ULTRASONIC NONDESTRUCTIVE EVALUATION

Engineering and Biological Material Characterization

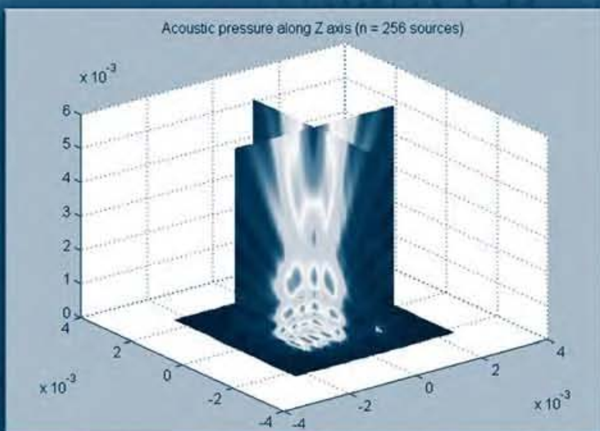

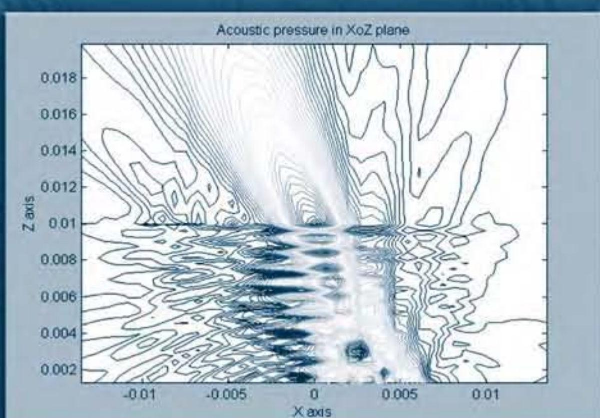

Edited by
Tribikram Kundu

CRC PRESS

ULTRASONIC NONDESTRUCTIVE EVALUATION

Engineering and Biological Material Characterization

ULTRASONIC NONDESTRUCTIVE EVALUATION

Engineering and Biological Material Characterization

Edited by

Tribikram Kundu

CRC PRESS

Boca Raton London New York Washington, D.C.

Library of Congress Cataloging-in-Publication Data

Kundu, T. (Tribikram)
Ultrasonic nondestructive evaluation : engineering and biological material characterization / Tribikram Kundu.
p. cm.
Includes bibliographical references and index.
ISBN 0-8493-1462-3 (alk. paper)
1. Ultrasonic testing. 2. Materials--Testing. 3. Biomolecules--Analysis. I. Title.

TA417.4K86 2003
620.1’1274—dc22 2003055770
Catalog record is available from the Library of Congress

International Standard Book Number 0-8493-1462-3
Library of Congress Card Number 2003055770
Printed in the United States of America 1 2 3 4 5 6 7 8 9 0
Printed on acid-free paper

Dedication

To my wife, Nupur

daughters, Ina and Auni

father, Makhan Lal Kundu

and mother, Sandhya Rani Kundu

Preface

Today, ultrasonic signal is being used for characterizing (detecting internal defects in) a variety of engineering structures, such as airplanes, buildings, nuclear power plants, pressure-vessels, and pipes, for inspecting human body parts, such as tumors, bones, and unborn fetuses. In spite of the ever increasing popularity and wide range of the use of this technology by researchers, medical technicians, factory workers, and engineers, we do not have any book that covers both the fundamentals and the advanced applications of this technology. Currently, books either concentrate on fundamental equation derivations, and thus are too theoretical, or consider only advanced applications, hoping that the readers have already gained the theoretical knowledge from another source. One reason that there have been no books written that cover both fundamental and advanced applications is there are many advanced applications of ultrasonic nondestructive evaluation (NDE); it is very difficult for any one author to cover all of those topics. The advanced topics are mostly covered in conference proceedings where different authors discuss different applications. Many advanced topics, such as guided wave technique, nonlinear ultrasonic technique, laser-ultrasonic technique, and acoustic microscopy, have matured enough to be included in a book.

The purpose of this book is to bridge the gap between the two types of books available in the market today — the one kind lacks the advanced analysis and the other kind lacks the fundamentals. This book starts with the fundamental principles of mechanics; derives the basic equations of the mechanics of elastic wave propagation; and then, step-by-step, expands its horizon to cover the state-of-the-art advanced topics of ultrasonic NDE that are in the forefront of today's research.

Chapter 1 derives the fundamental equations of mechanics related to ultrasonic NDE. It is written in such a way that any college graduate of science or engineering should be able to follow it. A good number of examples and exercise problems are provided for easier understanding and good comprehension of the subject. After studying this chapter the readers will be able to follow the remaining chapters on specialized topics.

Each chapter has been well written by authors who are experts in their fields and have many years of research experience related to the topics that they cover. These authors have nicely described many applications of ultrasonic techniques, from the traditional to the very advanced. All chapters are written in simple English that is understandable to practitioners, graduate students, and research scientists.

This book was created to assist people at each level. Some chapters have questions and problems appropriate for a graduate-level course on ultrasonic NDE. Coverage of the traditional ultrasonic NDE applications with the derivation of basic equations should be attractive to practicing engineers and technicians. The advanced applications will be more appealing to research scientists.

Since Chapter 1 starts with the basic knowledge of science, derives all equations used in it, and gives a large number of solved problems and exercise problems, it can be an ideal syllabus for a graduate-level course on the mechanics of deformable solids (or continuum mechanics) with an emphasis on the elastic wave propagation study. Materials covered in the first few chapters, as well as one or two additional chapters, are ideal for a sequence of two consecutive graduate-level courses in mechanics, elastic wave propagation, and ultrasonic NDE.

Another distinguishing feature is that this book combines engineering and biological material characterization techniques. Both engineers (physical science community) and medical doctors (life science community) use ultrasonic techniques for material characterization and diagnosis. This is the first earnest attempt to bring these two communities together.

I would like to thank the authors for their time and effort. Without their contributions this project would not have been completed successfully. I would also like to thank my students, Rais Ahmad, Sourav Banerjee, and Heather Watson, for their assistance throughout the writing process. Finally, I want to give my sincere thanks to my wife, Nupur, and daughters Ina and Auni, for their patience and continuous encouragement.

Tribikram Kundu
Editor

Editor

Tribikram Kundu received his bachelor's degree in mechanical engineering from the Indian Institute of Technology, Kharagpur, in 1979. He earned his M.S. and Ph.D. from the Department of Mechanics and Structures at the University of California, Los Angeles (UCLA), in 1980 and 1983, respectively. He joined the University of Arizona as an assistant professor in August 1983 and was promoted to full professor in 1994.

Dr. Kundu has made significant and original contributions in both basic and applied research in nondestructive testing (NDT) techniques for engineering and biological material characterization by ultrasonic techniques. His fundamental research interests are in the analysis of elastic wave propagation in multilayered solids, fracture mechanics, computational mechanics, and geo- and biomechanics. Application areas of his research findings include civil and structural materials, aerospace materials, geo-materials, electronic and biological materials. He has edited 11 books, authored one textbook, four book chapters, and more than 150 technical papers; 80 of his papers have been published in refereed scientific journals. He has guided 18 Ph.D. students and 14 M.S. students. He is a fellow of the American Society of Mechanical Engineers (ASME) and American Society of Civil Engineers (ASCE), and a life member of Alexander von Humboldt Association of America (AvHAA). He is the current chairman of the ASME NDE Engineering Division. He is also a member of the American Academy of Mechanics (AAM), American Society of Nondestructive Testing (ASNT), Acoustical Society of America (ASA), International Association for Computer Methods and Advances in Geomechanics (IACMAG), and the International Society for Optical Engineering (SPIE). He has extensive collaborations with international and American scientists. He has spent a few months to a few years in each of the following institutes as an invited professor:

- Department of Biology, J.W. Goethe University, Frankfurt, Germany
- Department of Mechanics, Chalmers University of Technology, Gothenberg, Sweden
- Acoustic Microscopy Center, Semienov Institute of Chemical Physics, Russian Academy of Science, Moscow, Russia
- Department of Civil Engineering, Swiss Federal Institute of Technology in Lausanne (EPFL), Switzerland
- Department of Mechanical Engineering, University of Technology of Compiegne, France
- Materials Laboratory, University of Bordeaux, France

- Electrical Engineering Department, Ecole Normale Superior (ENS), Cachan, France
- Aarhus University Medical School, Aarhus, Denmark
- Institute of Experimental Physics, University of Leipzig, Germany
- Wright-Patterson Material Laboratory, Dayton, Ohio

Dr. Kundu has also received a number of recognitions:

- Humboldt Research Prize from Germany, Senior Scientist Award, 2003
- ASCE Fellowship Award, 2000
- ASME Fellowship Award, 1999
- SPIE Best Paper Award, 2000
- ASME NDE Division Best Paper Award, 2001 (where a graduate student is the leading author)
- Alexander von Humboldt Stiftung Fellowship from Germany, 1996–1997 and 1989–1990
- University of California Regents' Fellowship, 1979–1981
- UCLA Alumni Award as the Outstanding Graduate Student of the Year, College of Engineering, 1981
- President of India Gold Medal for ranking first among all graduating engineers from the Indian Institute of Technology, Kharagpur, India, 1979

Contributors

Marco G. Beghi Nuclear Engineering Department, Politecnico di Milano, Milano, Italy

Christopher Blase Kinematic Cell Research Group, Johann Wolfgang Goethe Universität, Frankfurt, Germany

Don E. Bray Don E. Bray, Inc., College Station, Texas

John. H. Cantrell NASA Langley Research Center, Hampton, Virginia

Fu-Kuo Chang Department of Aeronautics and Astronautics, Stanford University, Stanford, California

Arthur G. Every School of Physics, University of the Witwatersrand, South Africa

Jürgen Bereiter-Hahn Kinematic Cell Research Group, Johann Wolfgang Goethe Universität, Frankfurt, Germany

Jeong-Beom Ihn Department of Aeronautics and Astronautics, Stanford University, Stanford, California

Laurence Jacobs Georgia Institute of Technology, Atlanta, Georgia

Sridhar Krishnaswamy Northwestern University, Evanston, Illinois

Bruce Maxfield Industrial Sensors & Actuators, San Leandro, California

Dominique Placko Ecole Normale Superieure, Cachan, France

Jianmin Qu Georgia Institute of Technology, Atlanta, Georgia

Kay Raum Martin Luther University of Halle-Wittenberg, Germany

Wieland Weise Applied Acoustics, Physikalisch-Technische Bundesanstalt, Braunschweig, Germany

Pavel V. Zinin School of Ocean and Earth Science and Technology, University of Hawaii, Honolulu

Contents

1

Mechanics of Elastic Waves and Ultrasonic Nondestructive Evaluation

Tribikram Kundu

CONTENTS

0-8493-1462-3/02/$0.00+$1.50

It is necessary to have a good understanding of the fundamentals of mechanics to appreciate the physics of elastic wave propagation in solid and fluid materials. With this in mind, this chapter is divided into two focus areas. The first part is devoted to the theory of elasticity and continuum mechanics, while the basic equations of elastic wave propagation in materials are derived in the second part. It is very important to fully comprehend the first chapter before progressing to the rest of the book.

1.1 Fundamentals of the Continuum Mechanics and the Theory of Elasticity

Relations between the displacement, strain, and stress in an elastic body are derived in this section.

1.1.1 Deformation and Strain Tensor

Figure 1.1 shows the reference state (R) and the current deformed state (D) of a body in the Cartesian $x_1x_2x_3$ coordinate system. Deformation of the body and displacement of individual particles in the body are defined with respect to this reference state. As different points of the body move because of applied force or change in temperature, the configuration of the body changes from the reference state to the current deformed state. After reaching equilibrium in one deformed state, if the applied force or temperature changes again, the deformed state also changes. The current deformed state of the body is the equilibrium position under current state of loads. Typically, the stress-free configuration of the body is considered as the reference state, but it is not necessary for the reference state to always be stress free. Any possible configuration of the body can be considered as the reference state. For simplicity, if it is not stated otherwise, the initial stress-free configuration of the body before applying any external disturbance (force, temperature, etc.) will be considered as its reference state.

Consider two points, P and Q, in the reference state of the body. They move to P^* and Q^* positions after deformation. Displacement of points P and Q are denoted by vectors $\mathbf{u}$ and $\mathbf{u} + \mathbf{du}$, respectively. (Note: Here and in

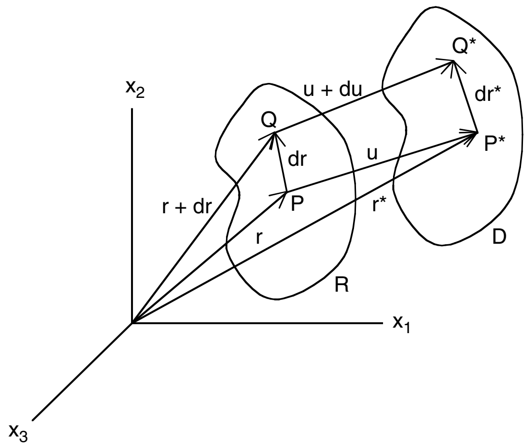

FIGURE 1.1
Deformation of a body. R is the reference state, and D is the deformed state.

subsequent derivations vector quantities will be denoted by bold letters.) Position vectors of P, Q, P^*, and Q^* are $\mathbf{r}$, $\mathbf{r} + \mathbf{dr}$, $\mathbf{r}^*$ and $\mathbf{r}^* + \mathbf{dr}^*$, respectively. Displacement and position vectors are related in the following manner:

$$\mathbf{r}^* = \mathbf{r} + \mathbf{u}$$
$$\mathbf{r}^* + \mathbf{dr}^* = \mathbf{r} + \mathbf{dr} + \mathbf{u} + \mathbf{du} \tag{1.1}$$
$$\therefore \mathbf{dr}^* = \mathbf{dr} + \mathbf{du}$$

In terms of the three Cartesian components the above equation can be written as

$$(dx_1^*\mathbf{e_1} + dx_2^*\mathbf{e_2} + dx_3^*\mathbf{e_3}) = (dx_1\mathbf{e_1} + dx_2\mathbf{e_2} + dx_3\mathbf{e_3}) + (du_1\mathbf{e_1} + du_2\mathbf{e_2} + du_3\mathbf{e_3}) \tag{1.2}$$

where $\mathbf{e_1}$, $\mathbf{e_2}$, and $\mathbf{e_3}$ are unit vectors in x_1-, x_2-, and x_3-directions, respectively.

In index or tensorial notation Equation 1.2 can be written as

$$dx_i^* = dx_i + du_i \tag{1.3}$$

where the free index (i) can take values of 1, 2, or 3.

Applying the chain rule, Equation 1.3 can be written as

$$dx_i^* = dx_i + \frac{\partial u_i}{\partial x_1}dx_1 + \frac{\partial u_i}{\partial x_2}dx_2 + \frac{\partial u_i}{\partial x_3}dx_3$$
$$\therefore dx_i^* = dx_i + \sum_{j=1}^{3}\frac{\partial u_i}{\partial x_j}dx_j = dx_i + u_{i,j}dx_j \tag{1.4}$$

In the above equation, the comma (,) means derivative, and the summation convention (repeated dummy index means summation over 1, 2, and 3) has been adopted.

Equation 1.4 can also be written in matrix notation in the following form:

$$\begin{Bmatrix} dx_1^* \\ dx_2^* \\ dx_3^* \end{Bmatrix} = \begin{Bmatrix} dx_1 \\ dx_2 \\ dx_3 \end{Bmatrix} + \begin{bmatrix} \frac{\partial u_1}{\partial x_1} & \frac{\partial u_1}{\partial x_2} & \frac{\partial u_1}{\partial x_3} \\ \frac{\partial u_2}{\partial x_1} & \frac{\partial u_2}{\partial x_2} & \frac{\partial u_2}{\partial x_3} \\ \frac{\partial u_3}{\partial x_1} & \frac{\partial u_3}{\partial x_2} & \frac{\partial u_3}{\partial x_3} \end{bmatrix} \begin{Bmatrix} dx_1 \\ dx_2 \\ dx_3 \end{Bmatrix} \quad \textbf{(1.5)}$$

In short form, Equation 1.5 can be written as

$$\{\mathbf{dr}^*\} = \{\mathbf{dr}\} + [\nabla \mathbf{u}]^{\mathrm{T}} \{\mathbf{dr}\} \quad \textbf{(1.6)}$$

If one defines

$$\varepsilon_{ij} = \frac{1}{2}(u_{i,j} + u_{j,i}) \quad \textbf{(1.7a)}$$

and

$$\omega_{ij} = \frac{1}{2}(u_{i,j} - u_{j,i}) \quad \textbf{(1.7b)}$$

then Equation 1.6 takes the following form:

$$\{\mathbf{dr}^*\} = \{\mathbf{dr}\} + [\boldsymbol{\varepsilon}]\{\mathbf{dr}\} + [\boldsymbol{\omega}]\{\mathbf{dr}\} \quad \textbf{(1.7c)}$$

1.1.1.1 Interpretation of ε_{ij} and ω_{ij} for Small Displacement Gradient

Consider the special case when **dr** = $dx_1\mathbf{e}_1$. After deformation the three components of $\mathbf{dr}^*$ can be computed from Equation 1.5.

$$\begin{aligned} dx_1^* &= dx_1 + \frac{\partial u_1}{\partial x_1} dx_1 = (1 + \varepsilon_{11}) dx_1 \\ dx_2^* &= \frac{\partial u_2}{\partial x_1} dx_1 = (\varepsilon_{21} + \omega_{21}) dx_1 \\ dx_3^* &= \frac{\partial u_3}{\partial x_1} dx_1 = (\varepsilon_{31} + \omega_{31}) dx_1 \end{aligned} \quad \textbf{(1.8)}$$

In this case, the initial length of the element PQ is $dS = dx_1$; the final length of the element P^*Q^* after deformation is

$$dS^* = [(dx_1^*)^2 + (dx_2^*)^2 + (dx_3^*)^2]^{\frac{1}{2}} = dx_1[(1+\varepsilon_{11})^2 + (\varepsilon_{21}+\omega_{21})^2 + (\varepsilon_{31}+\omega_{31})^2]^{\frac{1}{2}}$$
$$\approx dx_1[1+2\varepsilon_{11}]^{\frac{1}{2}} = dx_1(1+\varepsilon_{11}) \tag{1.9}$$

In Equation 1.9 we have assumed that the displacement gradients ($u_{i,j}$) are small. Therefore ε_{ij} and ω_{ij} are small, and the second-order terms involving ε_{ij} and ω_{ij} could be ignored.

Engineering normal strain (E_{11}) in x_1-direction, from its definition can be written as

$$E_{11} = \frac{dS^* - dS}{dS} = \frac{dx_1(1+\varepsilon_{11}) - dx_1}{dx_1} = \varepsilon_{11} \tag{1.10}$$

Similarly, one can show that ε_{22} and ε_{33} are engineering normal strains in x_2- and x_3-directions, respectively.

To interpret ε_{12} and ω_{12}, consider two mutually perpendicular elements, PQ and PR, in the reference state. In the deformed state these elements are moved to P^*Q^* and P^*R^* positions, respectively, as shown in Figure 1.2.

Let the vectors PQ and PR be $(\mathbf{dr})_{PQ} = dx_1\mathbf{e}_1$ and $(\mathbf{dr})_{PR} = dx_2\mathbf{e}_2$, respectively. After deformation, the three components of $(\mathbf{dr}^*)_{PQ}$ and $(\mathbf{dr}^*)_{PR}$ can be written

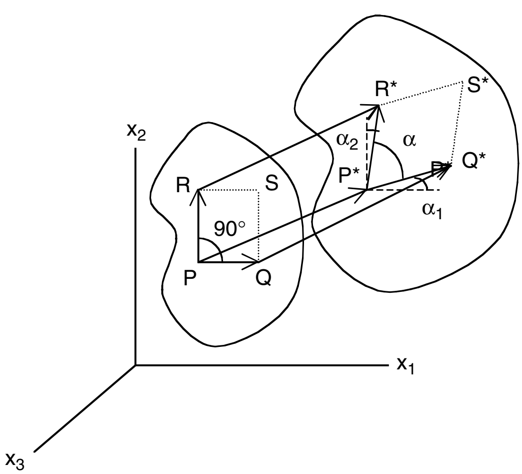

FIGURE 1.2
Two mutually perpendicular elements, PQ and PR, before deformation no longer remain perpendicular after deformation.

in the forms of Equation 1.11 and Equation 1.12, respectively, as given below:

$$
\begin{aligned}
(dx_1^*)_{PQ} &= dx_1 + \frac{\partial u_1}{\partial x_1} dx_1 = (1+\varepsilon_{11}) dx_1 \\
(dx_2^*)_{PQ} &= \frac{\partial u_2}{\partial x_1} dx_1 = (\varepsilon_{21} + \omega_{21}) dx_1 \\
(dx_3^*)_{PQ} &= \frac{\partial u_3}{\partial x_1} dx_1 = (\varepsilon_{31} + \omega_{31}) dx_1
\end{aligned}
\tag{1.11}
$$

$$
\begin{aligned}
(dx_1^*)_{PR} &= \frac{\partial u_1}{\partial x_2} dx_2 = (\varepsilon_{12} + \omega_{12}) dx_1 \\
(dx_2^*)_{PR} &= \frac{dx_2 \partial u_2}{\partial x_2} dx_2 = (1+\varepsilon_{22}) dx_2 \\
(dx_3^*)_{PR} &= \frac{\partial u_3}{\partial x_2} dx_2 = (\varepsilon_{32} + \omega_{32}) dx_1
\end{aligned}
\tag{1.12}
$$

Let α_1 be the angle between P^*Q^* and the horizontal axis, and let α_2 be the angle between P^*R^* and the vertical axis as shown in Figure 1.2. Note that $\alpha + \alpha_1 + \alpha_2 = 90°$. From Equation 1.11 and Equation 1.12 one can show the following:

$$
\begin{aligned}
\tan\alpha_1 &= \frac{(\varepsilon_{21} + \omega_{21}) dx_1}{(1+\varepsilon_{11}) dx_1} \approx \varepsilon_{21} + \omega_{21} = \varepsilon_{12} + \omega_{21} \\
\tan\alpha_2 &= \frac{(\varepsilon_{12} + \omega_{12}) dx_2}{(1+\varepsilon_{22}) dx_2} \approx \varepsilon_{12} - \omega_{21}
\end{aligned}
\tag{1.13}
$$

In the above equation we have assumed small displacement gradient and hence $1 + \varepsilon_{ij} \approx 1$. For small displacement gradient $\tan\alpha_i \approx \alpha_i$, one can write

$$
\begin{aligned}
\alpha_1 &= \varepsilon_{12} + \omega_{21} \\
\alpha_2 &= \varepsilon_{12} - \omega_{21} \\
\therefore\ \varepsilon_{12} &= \frac{1}{2}(\alpha_1 + \alpha_2) \quad \& \quad \omega_{21} = \frac{1}{2}(\alpha_1 - \alpha_2)
\end{aligned}
\tag{1.14}
$$

From Equation 1.14 it is concluded that $2\varepsilon_{12}$ is the change in the angle between the elements PQ and PR after deformation. In other words, it is the engineering shear strain, and ω_{21} is the rotation of the diagonal PS (see Figure 1.2) or the average rotation of the rectangular element PQSR about the x_3 axis after deformation.

In summary, ε_{ij} and ω_{ij} are the strain tensor and rotation tensor for small displacement gradients.

Example 1.1

Prove that the strain tensor satisfies the relation $\varepsilon_{ij,k\ell} + \varepsilon_{k\ell,ij} = \varepsilon_{ik,j\ell} + \varepsilon_{j\ell,ik}$.

This relation is known as the compatibility condition.

SOLUTION

$$\text{Left-hand side} = \varepsilon_{ij,k\ell} + \varepsilon_{k\ell,ij} = \frac{1}{2}(u_{i,jk\ell} + u_{j,ik\ell} + u_{k,\ell ij} + u_{\ell,kij})$$

$$\text{Right-hand side} = \varepsilon_{ik,j\ell} + \varepsilon_{j\ell,ik} = \frac{1}{2}(u_{i,kj\ell} + u_{k,ij\ell} + u_{j,\ell ik} + u_{\ell,jik})$$

Since the order or sequence of derivative should not make any difference, $u_{i,jk\ell} = u_{i,kj\ell}$; the other three terms in the two expressions can also be shown as equal. Thus the two sides of the equation are proved to be identical.

Example 1.2

Check if the following strain state is possible for an elasticity problem:

$$\varepsilon_{11} = k\left(x_1^2 + x_2^2\right), \quad \varepsilon_{22} = k\left(x_2^2 + x_3^2\right), \quad \varepsilon_{12} = kx_1x_2x_3, \quad \varepsilon_{13} = \varepsilon_{23} = \varepsilon_{33} = 0$$

SOLUTION

From the compatibility condition, $\varepsilon_{ij,k\ell} + \varepsilon_{k\ell,ij} = \varepsilon_{ik,j\ell} + \varepsilon_{j\ell,ik}$ given in Example 1.1, one can write

$\varepsilon_{11,22} + \varepsilon_{22,11} = 2\varepsilon_{12,12}$ by substituting $i = 1$, $j = 1$, $k = 2$, $\ell = 2$.

$$\varepsilon_{11,22} + \varepsilon_{22,11} = 2k + 0 = 2k$$

$$2\varepsilon_{12,12} = 2kx_3$$

Since the two sides of the compatibility equation are not equal, the given strain state is not a possible strain state.

1.1.2 Traction and Stress Tensor

Force per unit area on a surface is called traction. To define traction at a point P (see Figure 1.3), one needs to state on which surface, going through that point, the traction is defined. The traction value at point P will change if the orientation of the surface on which the traction is defined is changed.

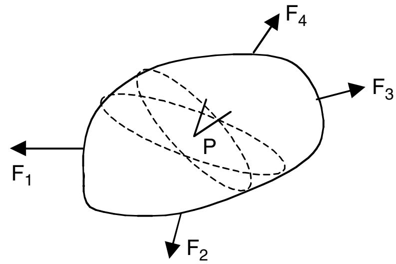

FIGURE 1.3
A body in equilibrium can be cut into two halves by an infinite number of planes going through a specific point P. Two such planes are shown in the figure.

Figure 1.3 shows a body in equilibrium under the action of some external forces, if it is cut into two halves by a plane going through point P. In general, to keep each half of the body in equilibrium some force will exist at the cut plane. Force per unit area in the neighborhood of point P is defined as the traction at point P. If the cut plane is changed, then the traction at the same point will change. To define traction at a point its three components must be given and the plane on which it is defined must be identified. The traction can be denoted as $\mathbf{T}^{(\mathbf{n})}$, where the superscript **n** denotes the unit vector normal to the plane on which the traction is defined, and where $\mathbf{T}^{(\mathbf{n})}$ has three components that correspond to the force per unit area in x_1-, x_2-, and x_3-directions, respectively.

Stress is similar to traction — both are defined as force per unit area. The only difference is that the stress components are always defined normal or parallel to a surface, while traction components are not necessarily normal or parallel to the surface. A traction $\mathbf{T}^{(\mathbf{n})}$ on an inclined plane is shown in Figure 1.4. Note that neither $\mathbf{T}^{(\mathbf{n})}$ nor its three components (T_{ni}) are necessarily normal or parallel to the inclined surface. Its two components (σ_{nn} and σ_{ns}) are perpendicular and parallel to the inclined surface, and are called normal and shear stress components.

Stress components are described by two subscripts. The first subscript indicates the plane (or normal to the plane) on which the stress component is defined, and the second subscript indicates the direction of the force per unit area or stress value. Following this convention, different stress components in $x_1x_2x_3$ coordinate system are defined in Figure 1.5.

Note that on each of the six planes, meaning the positive and negative x_1-, x_2-, and x_3-planes, three stress components (one normal and two shear stress components) are defined. If the outward normal to the plane is in the positive direction, then we call the plane a positive plane; otherwise it is a negative plane. If the force direction is positive on a positive plane or negative on a negative plane, then the stress is positive. All stress components shown on positive x_1-, x_2-, and x_3-planes and negative x_1-plane in Figure 1.5 are positive stress components. Stress components on the other two negative planes are not shown to keep the figure simple. Dashed arrows show three of the stress

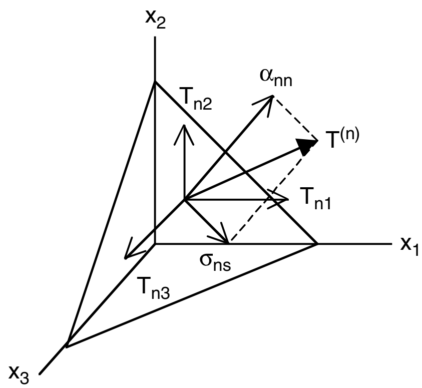

FIGURE 1.4
Traction $T^{(n)}$ on an inclined plane can be decomposed into its three components T_{ni}, or into two components — normal and shear stress components (σ_{nn} and σ_{ns}).

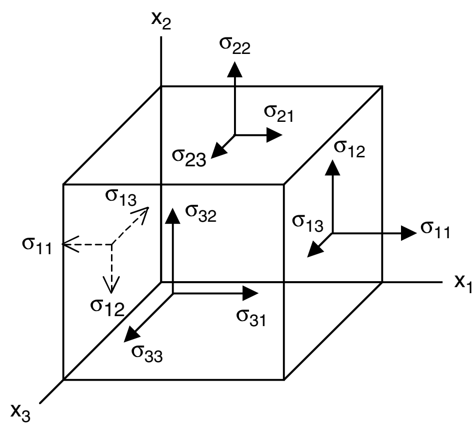

FIGURE 1.5
Different stress components in the $x_1x_2x_3$ coordinate system.

components on the negative x_1-plane, while solid arrows show the stress components on positive planes. If the force direction and the plane direction have different signs, one positive and one negative, then the corresponding stress component is negative. Referring to Figure 1.5, if we change the direction of the arrow of any stress component, then that stress component becomes negative.

1.1.3 Traction-Stress Relation

Let us take a tetrahedron OABC from a continuum body in equilibrium (see Figure 1.6). Forces (per unit area) acting in the x_1-direction on the four surfaces

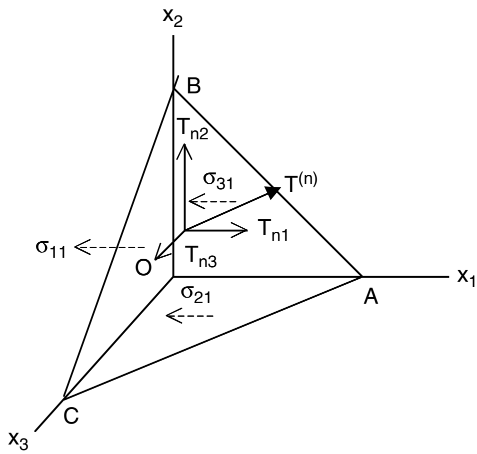

FIGURE 1.6
A tetrahedron showing traction components on plane ABC and x_1-direction stress components on planes AOC, BOC, and AOB.

of OABC are shown in Figure 1.6. From its equilibrium in the x_1-direction one can write

$$\sum F_1 = T_{n1}A - \sigma_{11}A_1 - \sigma_{21}A_2 - \sigma_{31}A_3 + f_1 V = 0 \tag{1.15}$$

where A is the area of the surface ABC; A_1, A_2, and A_3 are the areas of the other three surfaces OBC, OAC, and OAB, respectively; and f_1 is the body force per unit volume in the x_1-direction.

If n_j is the j-th component of the unit vector $\mathbf{n}$ that is normal to the plane ABC, then one can write $A_j = n_j A$ and $V = (Ah)/3$, where h is the height of the tetrahedron measured from the apex O. Equation 1.15 is simplified to

$$T_{n1} - \sigma_{11}n_1 - \sigma_{21}n_2 - \sigma_{31}n_3 + f_1\frac{h}{3} = 0 \tag{1.16}$$

In the limiting case when the plane ABC passes through point O, the tetrahedron height h vanishes and Equation 1.16 is simplified to

$$T_{n1} = \sigma_{11}n_1 + \sigma_{21}n_2 + \sigma_{31}n_3 = \sigma_{j1}n_j \tag{1.17}$$

In Equation 1.17 summation convention (repeated index means summation) has been used.

Similarly, from the force equilibrium in x_2- and x_3-directions one can write

$$\begin{aligned} T_{n2} &= \sigma_{j2}n_j \\ T_{n3} &= \sigma_{j3}n_j \end{aligned} \tag{1.18}$$

Combining Equation 1.17 and Equation 1.18, the traction-stress relation is obtained in index notation,

$$T_{ni} = \sigma_{ji} n_j \tag{1.19a}$$

where the free index (i) takes values of 1, 2, and 3 to generate three equations, and the dummy index (j) takes values of 1, 2, and 3 and is added inside each equation.

For simplicity the subscript n of T_{ni} is omitted and is written as T_i. It is implied that **n** is the unit normal vector to the surface, on which the traction is defined. Equation 1.19a can be rewritten as

$$T_i = \sigma_{ji} n_j \tag{1.19b}$$

1.1.4 Equilibrium Equations

If a body is in equilibrium, then the resultant force and moment on that body must be equal to zero.

1.1.4.1 Force Equilibrium

The resultant forces in the x_1-, x_2- and x_3-directions are equated to zero to obtain the governing equilibrium equations. First, x_1-direction equilibrium is studied. Figure 1.7 shows all forces acting in the x_1 direction on an elemental volume.

The zero resultant force in the x_1 direction gives

$$-\sigma_{11} dx_2 dx_3 + \left(\sigma_{11} + \frac{\partial \sigma_{11}}{\partial x_1} dx_1\right) dx_2 dx_3 - \sigma_{21} dx_1 dx_3 + \left(\sigma_{21} + \frac{\partial \sigma_{21}}{\partial x_2} dx_2\right) dx_1 dx_3$$
$$- \sigma_{31} dx_2 dx_1 + \left(\sigma_{31} + \frac{\partial \sigma_{31}}{\partial x_3} dx_3\right) dx_1 dx_2 + f_1\, dx_1 dx_2 dx_3 = 0$$

or

$$\left(\frac{\partial \sigma_{11}}{\partial x_1} dx_1\right) dx_2 dx_3 + \left(\frac{\partial \sigma_{21}}{\partial x_2} dx_2\right) dx_1 dx_3 + \left(\frac{\partial \sigma_{31}}{\partial x_3} dx_3\right) dx_1 dx_2 + f_1\, dx_1 dx_2 dx_3 = 0$$

or

$$\frac{\partial \sigma_{11}}{\partial x_1} + \frac{\partial \sigma_{21}}{\partial x_2} + \frac{\partial \sigma_{31}}{\partial x_3} + f_1 = 0$$

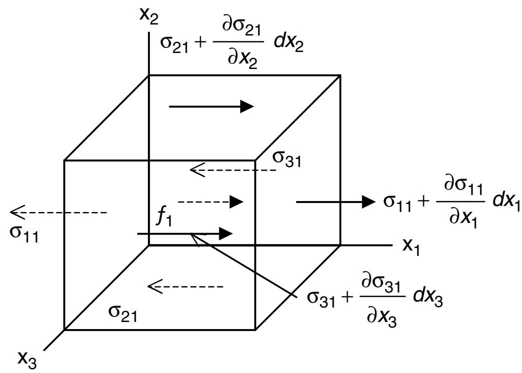

FIGURE 1.7
Forces acting in the x_1-direction on an elemental volume.

or

$$\frac{\partial \sigma_{j1}}{\partial x_j} + f_1 = 0 \tag{1.20}$$

In Equation 1.20 repeated index (j) indicates summation.

Similarly, equilibrium in x_2- and x_3-directions gives

$$\begin{aligned} \frac{\partial \sigma_{j2}}{\partial x_j} + f_2 = 0 \\ \frac{\partial \sigma_{j3}}{\partial x_j} + f_3 = 0 \end{aligned} \tag{1.21}$$

The three equations in Equation 1.20 and Equation 1.21 can be combined in the following form:

$$\frac{\partial \sigma_{ji}}{\partial x_j} + f_i = \sigma_{ji,j} + f_i = 0 \tag{1.22}$$

The force equilibrium equations given in Equation 1.22 are written in index notation, where the free index (i) takes three values of 1, 2, and 3 and corresponds to three equilibrium equations. The comma (,) indicates derivative.

1.1.4.2 Moment Equilibrium

Let us now compute the resultant moment in the x_3-direction (i.e., moment about the x_3-axis) for the elemental volume shown in Figure 1.8.

If we calculate the moment about an axis parallel to the x_3-axis and passing through the centroid of the elemental volume shown in Figure 1.8, then only

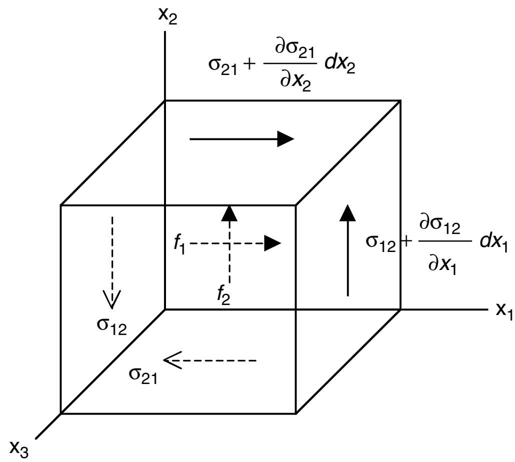

FIGURE 1.8
Forces on an element that may contribute to the moment in the x_3-direction.

four shear stresses shown on the four sides of the volume can produce moment. Body forces in x_1- and x_2-directions will not produce any moment because the resultant body force passes through the centroid of the volume. Since the resultant moment about this axis should be zero, one can write

$$\left(\sigma_{12} + \frac{\partial \sigma_{12}}{\partial x_1} dx_1\right) dx_2 dx_3 \frac{dx_1}{2} + (\sigma_{12}) dx_2 dx_3 \frac{dx_1}{2} - \left(\sigma_{21} + \frac{\partial \sigma_{21}}{\partial x_2} dx_2\right) dx_1 dx_3 \frac{dx_2}{2} - (\sigma_{21}) dx_1 dx_3 \frac{dx_2}{2} = 0$$

Ignoring the higher order terms one gets

$$2(\sigma_{12}) dx_2 dx_3 \frac{dx_1}{2} - 2(\sigma_{21}) dx_1 dx_3 \frac{dx_2}{2} = 0$$

or

$$\sigma_{12} = \sigma_{21}$$

Similarly, by applying moment equilibrium about the other two axes one can show that $\sigma_{13} = \sigma_{31}$ and $\sigma_{32} = \sigma_{23}$. In index notation, this is simplified as

$$\sigma_{ij} = \sigma_{ji} \tag{1.23}$$

Equation 1.23 shows that the stress tensor is symmetric. It should be noted here that if the body has internal body couple (or body moment per unit volume), then the stress tensor would not be symmetric.

Because of the symmetry of the stress tensor, Equation 1.19b and Equation 1.22 can also be written in the following form:

$$T_i = \sigma_{ij} n_j$$
$$\sigma_{ij,j} + f_i = 0 \tag{1.24}$$

1.1.5 Stress Transformation

Let us now investigate how the stress components in two Cartesian coordinate systems are related.

Figure 1.9 shows an inclined plane ABC where the normal is in the $x_{1'}$-direction, making the $x_{2'}x_{3'}$-plane parallel to the ABC plane. Traction $\mathbf{T}^{(1')}$ is acting on this plane. Three components of this traction in $x_{1'}$-, $x_{2'}$-, and $x_{3'}$-directions are the three stress components $\sigma_{1'1'}$, $\sigma_{1'2'}$ and $\sigma_{1'3'}$, respectively. Note that the first subscript indicates the plane on which the stress is acting and the second subscript gives the stress direction.

From Equation 1.19, one can write

$$T_{1'i} = \sigma_{ji} n_j^{(1')} = \sigma_{ji} \ell_{1'j} \tag{1.25}$$

where $n_j^{(1')} = \ell_{1'j}$ is the j-th component of the unit normal vector on plane ABC or, in other words, the direction cosines of the $x_{1'}$-axis.

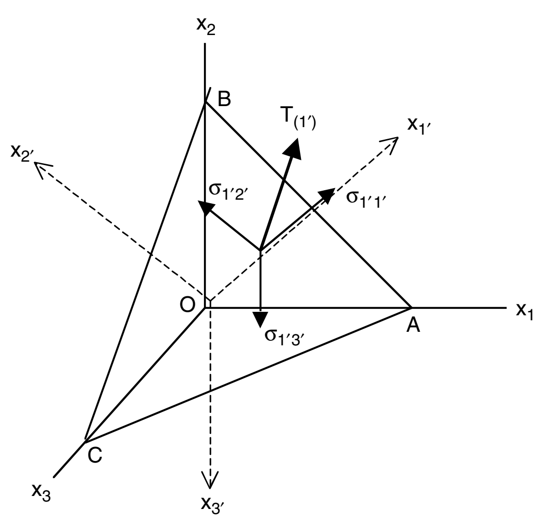

FIGURE 1.9
Stress components in the $x_{1'}x_{2'}\,x_{3'}$ coordinate system.

Note that the dot product between $\mathbf{T}^{(1')}$ and the unit vector $\mathbf{n}^{(1')}$ gives the stress component $\sigma_{1'1'}$; therefore,

$$\sigma_{1'1'} = T_{1'i}\ell_{1'i} = \sigma_{ji}\ell_{1'j}\ell_{1'i} \tag{1.26}$$

Similarly, the dot product between $\mathbf{T}^{(1')}$ and the unit vector $\mathbf{n}^{(2')}$ gives $\sigma_{1'2'}$, and the dot product between $\mathbf{T}^{(1')}$ and the unit vector $\mathbf{n}^{(3')}$ gives $\sigma_{1'3'}$.

$$\begin{aligned} \sigma_{1'2'} &= T_{1'i}\ell_{2'i} = \sigma_{ji}\ell_{1'j}\ell_{2'i} \\ \sigma_{1'3'} &= T_{1'i}\ell_{3'i} = \sigma_{ji}\ell_{1'j}\ell_{3'i} \end{aligned} \tag{1.27}$$

Equation 1.26 and Equation 1.27 can be written in index notation in the following form:

$$\sigma_{1'm'} = \ell_{1'j}\sigma_{ji}\ell_{m'i} \tag{1.28}$$

In Equation 1.28 the free index (m') can take values of 1′, 2′, or 3′.

Similarly, from the traction vector $\mathbf{T}^{(2')}$ on a plane whose normal is in the $x_{2'}$-direction one can show

$$\sigma_{2'm'} = \ell_{2'j}\sigma_{ji}\ell_{m'i} \tag{1.29}$$

and from the traction vector $\mathbf{T}^{(3')}$ on the $x_{3'}$-plane one can derive

$$\sigma_{3'm'} = \ell_{3'j}\sigma_{ji}\ell_{m'i} \tag{1.30}$$

Equation 1.28 through Equation 1.30 can be combined to obtain the following equation in index notation:

$$\sigma_{n'm'} = \ell_{n'j}\sigma_{ji}\ell_{m'i}$$

Note that in the above equation i, j, m' and n' can be interchanged to obtain

$$\sigma_{m'n'} = \ell_{m'i}\sigma_{ij}\ell_{n'j} = \ell_{m'i}\ell_{n'j}\sigma_{ij} \tag{1.31}$$

1.1.5.1 Kronecker Delta Symbol (δ_{ij}) and Permutation Symbol (ε_{ijk})

In index notation Kronecker delta symbol (δ_{ij}) and permutation symbol (ε_{ijk}). are often used. They are defined in the following manner:

$$\delta_{ij} = 1 \quad \text{for} \quad i = j$$

$$\delta_{ij} = 0 \quad \text{for} \quad i \neq j$$

and

$\varepsilon_{ijk} = 1$ for i, j, k having values 1, 2, 3; 2, 3, 1; or 3, 1, 2
$\varepsilon_{ijk} = -1$ for i, j, k having values 3, 2, 1; 1, 3, 2; or 2, 1, 3
$\varepsilon_{ijk} = 0$ for i, j, k not having three distinct values

ε_{ijk} is also known as the Levi-Civita symbol or alternating symbol.

1.1.5.1.1 Examples of Application of δ_{ij} and ε_{ijk}

Note that:

$$\frac{\partial x_i}{\partial x_j} = \delta_{ij}; \qquad \mathbf{e_i} \cdot \mathbf{e_j} = \delta_{ij}$$

$$\text{Det} \begin{vmatrix} a_{11} & a_{12} & a_{13} \\ a_{21} & a_{22} & a_{23} \\ a_{31} & a_{32} & a_{33} \end{vmatrix} = \varepsilon_{ijk} a_{1i} a_{2j} a_{3k}; \qquad \mathbf{b} \times \mathbf{c} = \varepsilon_{ijk} b_j c_k \mathbf{e_i}$$

where $\mathbf{e_i}$ and $\mathbf{e_j}$ are unit vectors in x_i-and x_j-directions, respectively, in the $x_1\ x_2 x_3$ coordinate system. Also note that **b** and **c** are two vectors, while $[a]$ is a matrix.

One can prove that the following relation exists between these two symbols:

$$\varepsilon_{ijk} \varepsilon_{imn} = \delta_{jm} \delta_{kn} - \delta_{jn} \delta_{km}$$

Example 1.3

Starting from the stress transformation law, prove that $\sigma_{m'n'}\ \sigma_{m'n'} = \sigma_{ij}\ \sigma_{ij}$, where $\sigma_{m'n'}$ and σ_{ij} are stress tensors in two different Cartesian coordinate systems.

SOLUTION

$$\sigma_{m'n'} \sigma_{m'n'} = (\ell_{m'i} \ell_{n'j} \sigma_{ij})(\ell_{m'p} \ell_{n'q} \sigma_{pq}) = (\ell_{m'i} \ell_{n'j})(\ell_{m'p} \ell_{n'q}) \sigma_{ij} \sigma_{pq}$$

$$= (\ell_{m'i} \ell_{m'p})(\ell_{n'j} \ell_{n'q}) \sigma_{ij} \sigma_{pq} = \delta_{ip} \delta_{jq} \sigma_{ij} \sigma_{pq} = \sigma_{ij} \sigma_{ij}$$

1.1.6 Definition of Tensor

A Cartesian tensor of order (or rank) 'r' in 'n' dimensional space is a set of n^r numbers (called the elements or components of tensor) that obey the following transformation law between two coordinate systems:

$$t_{m'n'p'q'\ldots} = (\ell_{m'i}\ell_{n'j}\ell_{p'k}\ell_{q'\ell}\ldots)(t_{ijk\ell\ldots}) \tag{1.32}$$

where $t_{m'n'p'q'\ldots}$ and $t_{ijk\ldots}$ each has 'r' number of subscripts. The 'r' number of direction cosines $(\ell_{m'i}\ell_{n'j}\ell_{p'k}\ell_{q'\ell}\ldots)$ are multiplied on the right-hand side.

Comparing Equation 1.31 with the definition of tensor Equation 1.32, one can conclude that the stress is a second-rank tensor.

1.1.7 Principal Stresses and Principal Planes

Planes on which the traction vectors are normal are called principal planes. Shear stress components on the principal planes are equal to zero. Normal stresses on the principal planes are called principal stresses.

In Figure 1.10 let **n** be the unit normal vector on the principal plane ABC, and let λ be the principal stress value on this plane. The traction vector on plane ABC can be written as

$$T_i = \lambda n_i$$

Again from Equation 1.24 we get the following:

$$T_i = \sigma_{ij} n_j$$

From the above two equations one can write

$$\sigma_{ij} n_j - \lambda n_i = 0 \tag{1.33}$$

The above equation is an eigen value problem that can be rewritten as

$$(\sigma_{ij} - \lambda\delta_{ij}) n_j = 0 \tag{1.34}$$

The system of homogeneous equations shown in Equations 1.33 and 1.34 gives nontrivial solution for n_j when the determinant of the coefficient matrix is zero. Thus, for nontrivial solution

$$Det\begin{bmatrix} (\sigma_{11}-\lambda) & \sigma_{12} & \sigma_{13} \\ \sigma_{12} & (\sigma_{22}-\lambda) & \sigma_{23} \\ \sigma_{13} & \sigma_{23} & (\sigma_{33}-\lambda) \end{bmatrix} = 0$$

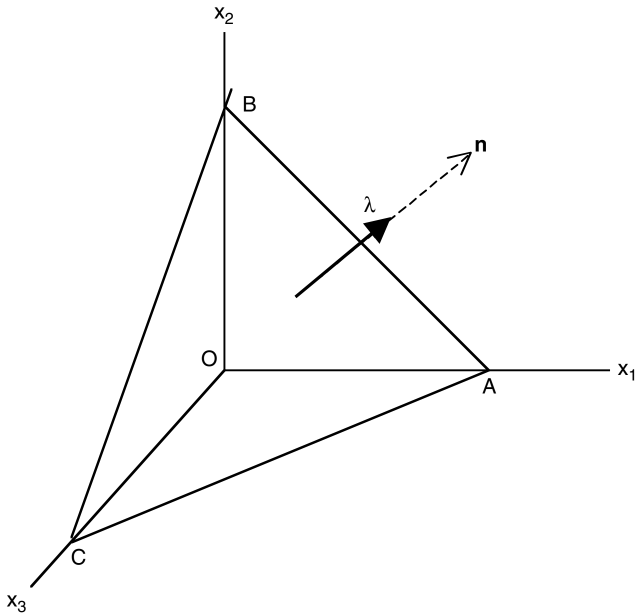

FIGURE 1.10
Principal stress λ on the principal plane ABC.

or

$$\lambda^3 - (\sigma_{11} + \sigma_{22} + \sigma_{33})\lambda^2 + \left(\sigma_{11}\sigma_{22} + \sigma_{22}\sigma_{33} + \sigma_{33}\sigma_{11} - \sigma_{12}^2 - \sigma_{23}^2 - \sigma_{31}^2\right)\lambda$$
$$- \left(\sigma_{11}\sigma_{22}\sigma_{33} + 2\sigma_{12}\sigma_{23}\sigma_{31} - \sigma_{11}\sigma_{23}^2 - \sigma_{22}\sigma_{31}^2 - \sigma_{33}\sigma_{12}^2\right) = 0 \quad \textbf{(1.35)}$$

In index notation, the above equation can be written as

$$\lambda^3 - \sigma_{ii}\lambda^2 + \frac{1}{2}(\sigma_{ii}\sigma_{jj} - \sigma_{ij}\sigma_{ji})\lambda - \varepsilon_{ijk}\sigma_{1i}\sigma_{2j}\sigma_{3k} = 0 \quad \textbf{(1.36)}$$

In Equation 1.36, ε_{ijk} is the permutation symbol that takes the values 1, –1, or 0. If the subscripts *i, j, k* have three distinct values of 1, 2, and 3 (or 2, 3, 1 or 3, 1, 2), respectively then its value is 1; if the values of the subscripts are in the opposite order of 3, 2, and 1 (or 2, 1, and 3 or, 1, 3 and 2) then ε_{ijk} is –1. If *i, j,* and *k* do not have three distinct values, then $\varepsilon_{ijk} = 0$.

Cubic Equation 1.36 should have three roots of λ. Three roots correspond to the three principal stress values. After getting λ, the unit vector components n_j can be obtained from Equation 1.34 and the constraint condition

$$n_1^2 + n_2^2 + n_3^2 = 1 \quad \textbf{(1.37)}$$

Note that for three distinct values of λ, there are three **n** values corresponding to the three principal directions.

Since the principal stress values should be independent of the starting coordinate system, the coefficients of the cubic equation should not change regardless whether we start from the $x_1x_2x_3$ coordinate system or $x_{1'}x_{2'}x_{3'}$ coordinate system. Thus,

$$\begin{aligned}
&\sigma_{ii} = \sigma_{i'i'} \\
&\sigma_{ii}\sigma_{jj} - \sigma_{ij}\sigma_{ji} = \sigma_{i'i'}\sigma_{j'j'} - \sigma_{i'j'}\sigma_{j'i'} \\
&\varepsilon_{ijk}\sigma_{1i}\sigma_{2j}\sigma_{3k} = \varepsilon_{i'j'k'}\sigma_{1'i'}\sigma_{2'j'}\sigma_{3'k'}
\end{aligned} \tag{1.38}$$

The three equations in Equation 1.38 are known as the three stress invariants. After some algebraic manipulations the second and third stress invariants can be further simplified and the three stress invariants can be written as

$$\begin{aligned}
&\sigma_{ii} = \sigma_{i'i'} \\
&\sigma_{ij}\sigma_{ji} = \sigma_{i'j'}\sigma_{j'i'} \quad or \quad \frac{1}{2}\sigma_{ij}\sigma_{ji} = \frac{1}{2}\sigma_{i'j'}\sigma_{j'i'} \\
&\sigma_{ij}\sigma_{jk}\sigma_{ki} = \sigma_{i'j'}\sigma_{j'k'}\sigma_{k'i'} \quad or \quad \frac{1}{3}\sigma_{ij}\sigma_{jk}\sigma_{ki} = \frac{1}{3}\sigma_{i'j'}\sigma_{j'k'}\sigma_{k'i'}
\end{aligned} \tag{1.39}$$

Example 1.4

a. Obtain the principal values and principal directions for the following stress tensor:

$$[\sigma] = \begin{bmatrix} 2 & -4 & -6 \\ -4 & 4 & 2 \\ -6 & 2 & -2 \end{bmatrix} \text{MPa}$$

given one value of the principal stress, is 9.739 MPa.

b. Compute the stress state in $x_{1'}x_{2'}x_{3'}$ coordinate system. Direction cosines of $x_{1'}x_{2'}x_{3'}$ axes are given below:

	$x_{1'}$	$x_{2'}$	$x_{3'}$
ℓ_1	0.7285	0.6601	0.1831
ℓ_2	0.4827	–0.6843	0.5466
ℓ_3	0.4861	–0.3098	–0.8171

SOLUTION

a. The characteristic equation is obtained from Equation 1.35.

$$\lambda^3 - (\sigma_{11}+\sigma_{22}+\sigma_{33})\lambda^2 + \left(\sigma_{11}\sigma_{22}+\sigma_{22}\sigma_{33}+\sigma_{33}\sigma_{11}-\sigma_{12}^2-\sigma_{23}^2-\sigma_{31}^2\right)\lambda$$
$$-\left(\sigma_{11}\sigma_{22}\sigma_{33}+2\sigma_{12}\sigma_{23}\sigma_{31}-\sigma_{11}\sigma_{23}^2-\sigma_{22}\sigma_{31}^2-\sigma_{33}\sigma_{12}^2\right)=0$$

For the given stress tensor it becomes:

$$\lambda^3 - 4\lambda^2 - 60\lambda + 40 = 0$$

The above equation can be written as

$$\lambda^3 - 9.739\lambda^2 + 5.739\lambda^2 - 55.892\lambda - 4.108\lambda + 40 = 0$$
$$\Rightarrow (\lambda - 9.739)(\lambda^2 + 5.739\lambda - 4.108) = 0$$
$$\Rightarrow (\lambda - 9.739)(\lambda + 6.3825)(\lambda - 0.6435) = 0$$

whose three roots are

$$\lambda_1 = -6.3825$$
$$\lambda_2 = 9.739$$
$$\lambda_3 = 0.6435$$

These are the three principal stress values.

Principal directions are obtained from Equation 1.34:

$$\begin{bmatrix} (\sigma_{11}-\lambda_1) & \sigma_{12} & \sigma_{13} \\ \sigma_{12} & (\sigma_{22}-\lambda_1) & \sigma_{23} \\ \sigma_{13} & \sigma_{23} & (\sigma_{33}-\lambda_1) \end{bmatrix} \begin{Bmatrix} \ell_{1'1} \\ \ell_{1'2} \\ \ell_{1'3} \end{Bmatrix} = 0$$

where $\ell_{1'1}$, $\ell_{1'2}$, $\ell_{1'3}$ are direction cosines for the principal direction associated with the principal stress (λ_1).

From the above equation one can write

$$\begin{bmatrix} (2+6.3825) & -4 & -6 \\ -4 & (4+6.3825) & 2 \\ -6 & 2 & (-2+6.3825) \end{bmatrix} \begin{Bmatrix} \ell_{1'1} \\ \ell_{1'2} \\ \ell_{1'3} \end{Bmatrix} = 0$$

The second and third equations of the above system of three homogeneous equations can be solved to obtain two direction cosines in terms of the third one, as given below:

$$\ell_{1'2} = 0.1333\ell_{1'1}$$
$$\ell_{1'3} = 1.3082\ell_{1'1}$$

Normalizing the direction cosines, as shown in Equation 1.37, we get the following:

$$1 = \ell_{1'1}^2 + \ell_{1'2}^2 + \ell_{1'3}^2 = \ell_{1'1}^2(1 + 0.1333^2 + 1.3082^2)$$
$$\Rightarrow \ell_{1'1} = \pm 0.605$$
$$\Rightarrow \ell_{1'2} = 0.1333\ell_{1'1} = \pm 0.081$$
$$\Rightarrow \ell_{1'3} = 1.3082\ell_{1'1} = \pm 0.791$$

Similarly, for the second principal stress ($\lambda_2 = 9.739$) the direction cosines are

$$\begin{Bmatrix} \ell_{2'1} = \pm 0.657 \\ \ell_{2'2} = \mp 0.612 \\ \ell_{2'3} = \mp 0.440 \end{Bmatrix}$$

and for the third principal stress ($\lambda_3 = 0.6435$) the direction cosines are

$$\begin{Bmatrix} \ell_{3'1} = \pm 0.449 \\ \ell_{3'2} = \pm 0.787 \\ \ell_{3'3} = \mp 0.423 \end{Bmatrix}$$

b. From Equation 1.31,

$$\sigma_{m'n'} = \ell_{m'i}\ell_{n'j}\sigma_{ij}$$

In matrix notation

$$[\sigma'] = [\ell][\sigma][\ell]^T$$

where

$$[\ell]^T = \begin{bmatrix} \ell_{1'1} & \ell_{2'1} & \ell_{3'1} \\ \ell_{1'2} & \ell_{2'2} & \ell_{3'2} \\ \ell_{1'3} & \ell_{2'3} & \ell_{3'3} \end{bmatrix} = \begin{bmatrix} 0.7285 & 0.6601 & 0.1831 \\ 0.4827 & -0.6843 & 0.5466 \\ 0.4861 & -0.3098 & -0.8171 \end{bmatrix}$$

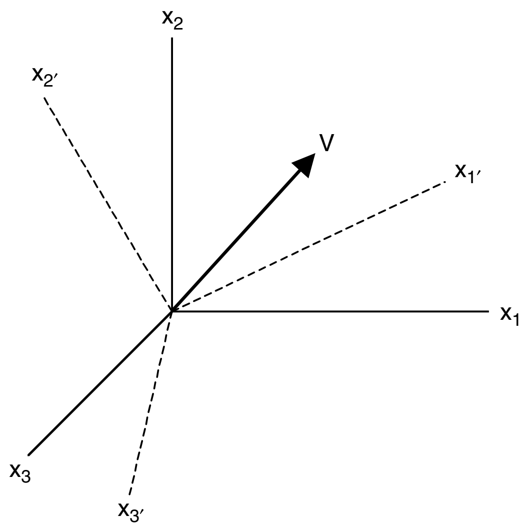

FIGURE 1.11
A vector **V** and two Cartesian coordinate systems.

Thus,

$$[\sigma'] = [\ell][\sigma][\ell]^T = \begin{bmatrix} -4.6033 & -0.8742 & 2.9503 \\ -0.8742 & 9.4682 & 1.6534 \\ 2.9503 & 1.6534 & -0.8650 \end{bmatrix} \text{MPa}$$

1.1.8 Transformation of Displacement and Other Vectors

The vector **V** can be expressed in two coordinate systems in the following manner (see Figure 1.11):

$$V_1e_1 + V_2e_2 + V_3e_3 = V_{1'}e_{1'} + V_{2'}e_{2'} + V_{3'}e_{3'} \quad \textbf{(1.40)}$$

If one adds the projections of V_1, V_2, and V_3 of Equation 1.40 along the $x_{j'}$-direction, then the sum should be equal to the component $V_{j'}$. Thus,

$$V_{j'} = \ell_{j'1}V_1 + \ell_{j'2}V_2 + \ell_{j'3}V_3 = \ell_{j'k}V_k \quad \textbf{(1.41)}$$

Comparing Equation 1.32 and Equation 1.41, one can conclude that vectors are first-order tensors, or tensors of rank 1.

1.1.9 Strain Transformation

Equation 1.7a gives the strain expression in the $x_1x_2x_3$ coordinate system. In the $x_{1'}x_{2'}x_{3'}$ coordinate system the strain expression is given by $\varepsilon_{i'j'} = \frac{1}{2}(u_{i',j'} + u_{j',i'})$. Now,

$$u_{i',j'} = \frac{\partial u_{i'}}{\partial x_{j'}} = \frac{\partial(\ell_{i'm}u_m)}{\partial x_{j'}} = \ell_{i'm}\frac{\partial(u_m)}{\partial x_{j'}} = \ell_{i'm}\frac{\partial u_m}{\partial x_n}\frac{\partial x_n}{\partial x_{j'}} = \ell_{i'm}\frac{\partial u_m}{\partial x_n}\ell_{nj'} = \ell_{i'm}\ell_{j'n}\frac{\partial u_m}{\partial x_n} \tag{1.42}$$

Similarly,

$$u_{j',i'} = \ell_{j'n}\ell_{i'm}\frac{\partial u_n}{\partial x_m} \tag{1.43}$$

Hence,

$$\begin{aligned} \varepsilon_{i'j'} &= \frac{1}{2}(u_{i',j'} + u_{j',i'}) = \frac{1}{2}(\ell_{i'm}\ell_{j'n}u_{m,n} + \ell_{j'n}\ell_{i'm}u_{n,m}) \\ &= \frac{1}{2}\ell_{i'm}\ell_{j'n}(u_{m,n} + u_{n,m}) = \ell_{i'm}\ell_{j'n}\varepsilon_{mn} \end{aligned} \tag{1.44}$$

It should be noted here that the strain transformation law (Equation 1.44) is identical to the stress transformation law (Equation 1.31). Therefore, strain is also a second-rank tensor.

1.1.10 Definition of Elastic Material and Stress-Strain Relation

Elastic or conservative material can be defined in many ways:

1. The material that has one-to-one correspondence between stress and strain is called elastic material.
2. The material that follows the same stress-strain path during loading and unloading is called elastic material.
3. For elastic materials, the strain energy density function (U_0) exists and it can be expressed in terms of the state of current strain only [$U_0 = U_0(\varepsilon_{ij})$], and independent of the strain history or strain path.

If the stress-strain relation is linear, then material is called linear elastic material; otherwise, it is nonlinear elastic material. Note that the elastic material does not necessarily mean that the stress-strain relation is linear, and the linear stress-strain relation does not automatically mean that the

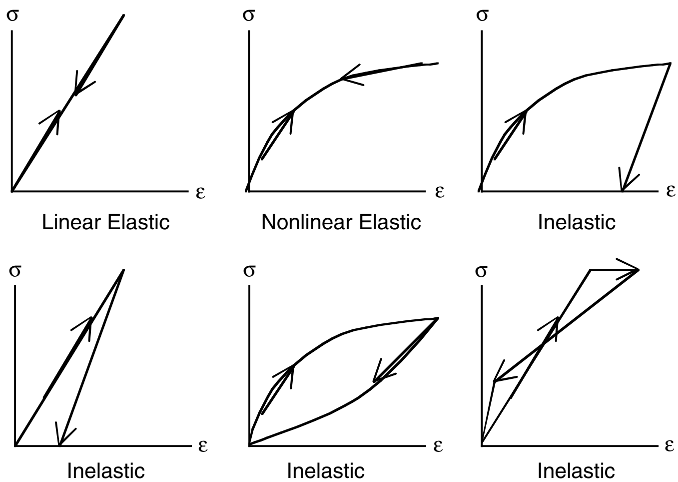

FIGURE 1.12
Stress-strain relations for elastic and inelastic materials.

material is elastic. If the stress-strain path is different during loading and unloading, then the material is no longer elastic even if the path is linear during loading and unloading. Figure 1.12 shows different stress-strain relations and indicates for each plot if the material is elastic or inelastic.

For conservative material the external work done on the material must be equal to the total increase in the strain energy of the material. If the variation of the external work done on the body is denoted by δW, and the variation of the internal strain energy, stored in the body, is δU, then $\delta U = \delta W$. Note that δU can be expressed in terms of the strain energy density variation (δU_0), and δW can be expressed in terms of the applied body force (f_i), the surface traction (T_i), and the variation of displacement (δu_i) thus:

$$\begin{aligned} \delta U &= \int_V \delta U_0 dV \\ \delta W &= \int_V f_i \delta u_i dV + \int_S T_i \delta u_i dS \end{aligned} \tag{1.45}$$

In Equation 1.45 integrals over V and S indicate volume and surface integrals, respectively. From Equation 1.45 one can write

$$\begin{aligned} \int_V \delta U_0 dV &= \int_V f_i \delta u_i dV + \int_S T_i \delta u_i dS = \int_V f_i \delta u_i dV + \int_S \sigma_{ij} n_j \delta u_i dS \\ &= \int_V f_i \delta u_i dV + \int_S (\sigma_{ij} \delta u_i) n_j dS \end{aligned}$$

Applying Gauss' divergence theorem on the second integral of the right-hand side, one gets

$$\int_V \delta U_0 dV = \int_V f_i \delta u_i dV + \int_V (\sigma_{ij}\delta u_i),_j dV = \int_V f_i \delta u_i dV + \int_V (\sigma_{ij,j}\delta u_i + \sigma_{ij}\delta u_{i,j})dV$$
$$= \int_V (f_i \delta u_i + \sigma_{ij,j}\delta u_i + \sigma_{ij}\delta u_{i,j})dV = \int_V ((f_i + \sigma_{ij,j})\delta u_i + \sigma_{ij}\delta u_{i,j})dV \quad \textbf{(1.46)}$$

After substituting the equilibrium equation (see Equation 1.24), the above equation is simplified to

$$\int_V \delta U_0 dV = \int_V (\sigma_{ij}\delta u_{i,j})dV = \int_V \frac{1}{2}(\sigma_{ij}\delta u_{i,j} + \sigma_{ij}\delta u_{i,j})dV = \int_V \frac{1}{2}(\sigma_{ij}\delta u_{i,j} + \sigma_{ji}\delta u_{j,i})dV$$
$$= \int_V \sigma_{ij}\frac{1}{2}(\delta u_{i,j} + \delta u_{j,i})dV = \int_V \sigma_{ij}\delta\varepsilon_{ij} dV \quad \textbf{(1.47)}$$

Since Equation 1.47 is valid for any arbitrary volume *V*, the integrand of the left- and right-hand sides must be equal to each other. Hence,

$$\delta U_0 = \sigma_{ij}\delta\varepsilon_{ij} \quad \textbf{(1.48)}$$

However, from the definition of elastic materials

$$U_0 = U_0(\varepsilon_{ij})$$
$$\therefore \delta U_0 = \frac{\partial U_0}{\partial \varepsilon_{ij}}\delta\varepsilon_{ij} \quad \textbf{(1.49)}$$

For arbitrary variation of $\delta\varepsilon_{ij}$ from Equation 1.48 and Equation 1.49 one can write

$$\sigma_{ij}\delta\varepsilon_{ij} = \frac{\partial U_0}{\partial \varepsilon_{ij}}\delta\varepsilon_{ij}$$
$$\therefore \sigma_{ij} = \frac{\partial U_0}{\partial \varepsilon_{ij}} \quad \textbf{(1.50)}$$

From Equation 1.50, the stress-strain relation can be obtained by assuming some expression of U_0 in terms of the strain components (Green's approach). For example, if one assumes that the strain energy density function is a quadratic function (complete second-degree polynomial) of the strain components as shown below:

$$U_0 = D_0 + D_{kl}\varepsilon_{kl} + D_{klmn}\varepsilon_{kl}\varepsilon_{mn} \tag{1.51}$$

then

$$\sigma_{ij} = \frac{\partial U_0}{\partial \varepsilon_{ij}} = D_{kl}\delta_{ik}\delta_{jl} + D_{klmn}(\delta_{ik}\delta_{jl}\varepsilon_{mn} + \varepsilon_{kl}\delta_{im}\delta_{jn}) = D_{ij} + D_{ijmn}\varepsilon_{mn} + D_{klij}\varepsilon_{kl}$$

$$= D_{ij} + (D_{ijkl} + D_{klij})\varepsilon_{kl}$$

Substituting $(D_{ijkl} + D_{klij}) = C_{ijkl}$ and $D_{ij} = 0$ (for zero stress; if strain is also zero then this assumption is valid), one gets the linear stress-strain relation (or *constitutive* relation) in the following form:

$$\sigma_{ij} = C_{ijkl}\varepsilon_{kl} \tag{1.52}$$

In Cauchy's approach, Equation 1.52 is obtained by relating the stress tensor with the strain tensor. Note that Equation 1.52 is a general linear relation between two second-order tensors.

In the same manner, for a nonlinear (quadratic) material the stress-strain relation will be

$$\sigma_{ij} = C_{ij} + C_{ijkl}\varepsilon_{kl} + C_{ijklmn}\varepsilon_{kl}\varepsilon_{mn} \tag{1.53}$$

In Equation 1.53 the first term on the right-hand side is the residual stress (stress for zero strain), the second term is the linear term, and the third term is the quadratic term. If one follows Green's approach, then this nonlinear stress-strain relation can be obtained from a cubic expression of the strain energy density function

$$U_0 = D_{kl}\varepsilon_{kl} + D_{klmn}\varepsilon_{kl}\varepsilon_{mn} + D_{klmnpq}\varepsilon_{kl}\varepsilon_{mn}\varepsilon_{pq} \tag{1.54}$$

In this chapter we limit our analysis to linear materials only. Our stress-strain relation is the one given in Equation 1.52.

Example 1.5

In the $x_1x_2x_3$ coordinate system, the stress-strain relation for a general anisotropic material is given by $\sigma_{ij} = C_{ijkm}\varepsilon_{km}$, and in the $x_{1'}x_{2'}x_{3'}$ coordinate system the stress-strain relation for the same material is given by $\sigma_{i'j'} = C_{i'j'k'm'}\varepsilon_{k'm'}$.

a. Starting from the stress and strain transformation laws, obtain a relation between C_{ijkm} and $C_{i'j'k'm'}$.

b. Is C_{ijkm} a tensor? If yes, what is its rank?

SOLUTION

a. Using Equation 1.52 and Equation 1.31 one can write

$$\begin{aligned}
&\sigma_{i'j'} = C_{i'j'k'm'}\varepsilon_{k'm'}\\
&\Rightarrow \ell_{i'r}\ell_{j's}\sigma_{rs} = C_{i'j'k'm'}\ell_{k'p}\ell_{m'q}\varepsilon_{pq}\\
&\Rightarrow (\ell_{i't}\ell_{j'u})\ell_{i'r}\ell_{j's}\sigma_{rs} = (\ell_{i't}\ell_{j'u})C_{i'j'k'm'}\ell_{k'p}\ell_{m'q}\varepsilon_{pq}\\
&\Rightarrow \delta_{tr}\delta_{us}\sigma_{rs} = (\ell_{i't}\ell_{j'u})C_{i'j'k'm'}\ell_{k'p}\ell_{m'q}\varepsilon_{pq} = \ell_{i't}\ell_{j'u}\ell_{k'p}\ell_{m'q}C_{i'j'k'm'}\varepsilon_{pq}\\
&\Rightarrow \sigma_{tu} = (\ell_{i't}\ell_{j'u}\ell_{k'p}\ell_{m'q}C_{i'j'k'm'})\varepsilon_{pq}
\end{aligned}$$

However,

$$\sigma_{tu} = C_{tupq}\varepsilon_{pq}$$

Therefore,

$$C_{tupq} = \ell_{i't}\ell_{j'u}\ell_{k'p}\ell_{m'q}C_{i'j'k'm'} = \ell_{ti'}\ell_{uj'}\ell_{pk'}\ell_{qm'}C_{i'j'k'm'}$$

Similarly, starting with the equation $\sigma_{pq} = C_{pqrs}\,\varepsilon_{rs}$ and applying stress and strain transformation laws, one can show that $C_{i'j'k'm'} = \ell_{i'p}\ell_{j'q}\ell_{k'r}\ell_{m's}$ C_{pqrs}.

b. Clearly C_{ijkm} satisfies the transformation law for a fourth-order tensor. Therefore, it is a tensor of order or rank = 4.

1.1.11 Number of Independent Material Constants

In Equation 1.52 the coefficient values C_{ijkl} depend on the material type and are called material constants or elastic constants. Note that *i*, *j*, *k*, and *l* can each take the three values of 1, 2, or 3. There are a total of 81 combinations possible, but not all 81 material constants are independent. Since stress and strain tensors are symmetric we can write

$$C_{ijkl} = C_{jikl} = C_{jilk} \tag{1.55}$$

The above relation in Equation 1.55 reduces the number of independent material constants from 81 to 36, and the stress-strain relation of Equation 1.52 can be written in the following form:

$$\begin{Bmatrix} \sigma_{11} \\ \sigma_{22} \\ \sigma_{33} \\ \sigma_{23} \\ \sigma_{31} \\ \sigma_{12} \end{Bmatrix} = \begin{bmatrix} C_{1111} & C_{1122} & C_{1133} & C_{1123} & C_{1131} & C_{1112} \\ C_{2211} & C_{2222} & C_{2233} & C_{2223} & C_{2231} & C_{2212} \\ C_{3311} & C_{3322} & C_{3333} & C_{3323} & C_{3331} & C_{3312} \\ C_{2311} & C_{2322} & C_{2333} & C_{2323} & C_{2331} & C_{2312} \\ C_{3111} & C_{3122} & C_{3133} & C_{3123} & C_{3131} & C_{3112} \\ C_{1211} & C_{1222} & C_{1233} & C_{1223} & C_{1231} & C_{1212} \end{bmatrix} \begin{Bmatrix} \varepsilon_{11} \\ \varepsilon_{22} \\ \varepsilon_{33} \\ 2\varepsilon_{23} \\ 2\varepsilon_{31} \\ 2\varepsilon_{12} \end{Bmatrix} \tag{1.56}$$

In the above expression only six stress and strain components are shown. The other three stress and strain components are not independent because of the symmetry of stress and strain tensors. The 6×6 C-matrix is known as the constitutive matrix. For elastic materials the strain energy density function can be expressed as a function of only strain; then its double derivative will have the form

$$\frac{\partial^2 U_0}{\partial \varepsilon_{ij} \partial \varepsilon_{kl}} = \frac{\partial}{\partial \varepsilon_{ij}} \left(\frac{\partial U_0}{\partial \varepsilon_{kl}} \right) = \frac{\partial}{\partial \varepsilon_{ij}} (\sigma_{kl}) = \frac{\partial}{\partial \varepsilon_{ij}} (C_{klmn} \varepsilon_{mn}) = C_{klmn} \delta_{im} \delta_{jn} = C_{klij} \tag{1.57}$$

Similarly,

$$\frac{\partial^2 U_0}{\partial \varepsilon_{kl} \partial \varepsilon_{ij}} = \frac{\partial}{\partial \varepsilon_{kl}} \left(\frac{\partial U_0}{\partial \varepsilon_{ij}} \right) = \frac{\partial}{\partial \varepsilon_{kl}} (\sigma_{ij}) = \frac{\partial}{\partial \varepsilon_{kl}} (C_{ijmn} \varepsilon_{mn}) = C_{ijmn} \delta_{km} \delta_{ln} = C_{ijkl} \tag{1.58}$$

In Equation 1.57 and Equation 1.58 the order or sequence of derivative has been changed. Since the order of derivative should not change the final results, one can conclude that $C_{ijkl} = C_{klij}$. In other words, the C-matrix of Equation 1.56 must be symmetric. Thus, the number of independent elastic constants is reduced from 36 to 21 and Equation 1.56 is simplified to

$$\begin{Bmatrix} \sigma_1 \\ \sigma_2 \\ \sigma_3 \\ \sigma_4 \\ \sigma_5 \\ \sigma_6 \end{Bmatrix} = \begin{bmatrix} C_{11} & C_{12} & C_{13} & C_{14} & C_{15} & C_{16} \\ & C_{22} & C_{23} & C_{24} & C_{25} & C_{26} \\ & & C_{33} & C_{34} & C_{35} & C_{36} \\ & & & C_{44} & C_{45} & C_{46} \\ & symm & & & C_{55} & C_{56} \\ & & & & & C_{66} \end{bmatrix} \begin{Bmatrix} \varepsilon_1 \\ \varepsilon_2 \\ \varepsilon_3 \\ 2\varepsilon_4 \\ 2\varepsilon_5 \\ 2\varepsilon_6 \end{Bmatrix} \tag{1.59}$$

In Equation 1.59 for simplicity we have denoted the six stress and strain components with only one subscript (σ_i and ε_i, where i varies from 1 to 6) instead of traditional notation of two subscripts. The material constants have been written with two subscripts instead of four.

1.1.12 Material Planes of Symmetry

Equation 1.59 has 21 independent elastic constants in absence of any plane of symmetry. Such material is called general anisotropic material or *triclinic* material. However, if the material response is symmetric about a plane or an axis, then the number of independent material constants is reduced.

1.1.12.1 One Plane of Symmetry

Let the material have only one plane of symmetry and this plane is the x_1-plane; in other words, the x_2x_3-plane whose normal is in the x_1-direction is the plane of symmetry. For this material, if the stress states $\sigma_{ij}^{(1)}$ and $\sigma_{ij}^{(2)}$ are mirror images of each other with respect to the x_1-plane, then the corresponding strain states $\varepsilon_{ij}^{(1)}$ and $\varepsilon_{ij}^{(2)}$ should be the mirror images of each other with respect to the same plane. Following the notations of Equation 1.59 we can say that the stress states $\sigma_{ij}^{(1)} = (\sigma_1, \sigma_2, \sigma_3, \sigma_4, \sigma_5, \sigma_6)$ and $\sigma_{ij}^{(2)} = (\sigma_1, \sigma_2, \sigma_3, \sigma_4, -\sigma_5, -\sigma_6)$ are of mirror symmetry with respect to the x_1-plane. Similarly, the strain states $\varepsilon_{ij}^{(1)} = (\varepsilon_1, \varepsilon_2, \varepsilon_3, \varepsilon_4, \varepsilon_5, \varepsilon_6)$ and $\varepsilon_{ij}^{(2)} = (\varepsilon_1, \varepsilon_2, \varepsilon_3, \varepsilon_4, -\varepsilon_5, -\varepsilon_6)$ are also of mirror symmetry with respect to the same plane. One can easily show by substitution that both states $(\sigma_{ij}^{(1)}, \varepsilon_{ij}^{(1)})$ and $(\sigma_{ij}^{(2)}, \varepsilon_{ij}^{(2)})$ can satisfy Equation 1.59 only when a number of elastic constants of the C-matrix become zero as shown below:

$$\begin{Bmatrix} \sigma_1 \\ \sigma_2 \\ \sigma_3 \\ \sigma_4 \\ \sigma_5 \\ \sigma_6 \end{Bmatrix} = \begin{bmatrix} C_{11} & C_{12} & C_{13} & C_{14} & 0 & 0 \\ & C_{22} & C_{23} & C_{24} & 0 & 0 \\ & & C_{33} & C_{34} & 0 & 0 \\ & & & C_{44} & 0 & 0 \\ & symm & & & C_{55} & C_{56} \\ & & & & & C_{66} \end{bmatrix} \begin{Bmatrix} \varepsilon_1 \\ \varepsilon_2 \\ \varepsilon_3 \\ 2\varepsilon_4 \\ 2\varepsilon_5 \\ 2\varepsilon_6 \end{Bmatrix} \tag{1.60}$$

Material with one plane of symmetry is called *monoclinic material*. From the stress-strain relation (Equation 1.60) of monoclinic materials one can see that the number of independent elastic constants is 13 for such materials.

1.1.12.2 Two and Three Planes of Symmetry

In addition to the x_1-plane, if the x_2-plane is also a plane of symmetry, then two stress and strain states that are symmetric with respect to the x_2-plane must also satisfy Equation 1.59. Note that the stress states $\sigma_{ij}^{(1)} = (\sigma_1, \sigma_2, \sigma_3, \sigma_4, \sigma_5, \sigma_6)$ and $\sigma_{ij}^{(2)} = (\sigma_1, \sigma_2, \sigma_3, -\sigma_4, \sigma_5, -\sigma_6)$ are states of mirror symmetry with respect to the x_2-plane and the strain states $\varepsilon_{ij}^{(1)} = (\varepsilon_1, \varepsilon_2, \varepsilon_3, \varepsilon_4, \varepsilon_5, \varepsilon_6)$ and $\varepsilon_{ij}^{(2)} = (\varepsilon_1, \varepsilon_2, \varepsilon_3, -\varepsilon_4, \varepsilon_5, -\varepsilon_6)$ are states of mirror symmetry with respect to the same plane. Like before, one can easily show by substitution that both states $(\sigma_{ij}^{(1)}, \varepsilon_{ij}^{(1)})$ and $(\sigma_{ij}^{(2)}, \varepsilon_{ij}^{(2)})$ can satisfy Equation 1.59 only when a number of elastic constants of the C-matrix become zero as shown below:

$$\begin{Bmatrix} \sigma_1 \\ \sigma_2 \\ \sigma_3 \\ \sigma_4 \\ \sigma_5 \\ \sigma_6 \end{Bmatrix} = \begin{bmatrix} C_{11} & C_{12} & C_{13} & 0 & C_{15} & 0 \\ & C_{22} & C_{23} & 0 & C_{25} & 0 \\ & & C_{33} & 0 & C_{35} & 0 \\ & & & C_{44} & C_{45} & 0 \\ & symm & & & C_{55} & 0 \\ & & & & & C_{66} \end{bmatrix} \begin{Bmatrix} \varepsilon_1 \\ \varepsilon_2 \\ \varepsilon_3 \\ 2\varepsilon_4 \\ 2\varepsilon_5 \\ 2\varepsilon_6 \end{Bmatrix} \quad \textbf{(1.61)}$$

Equation 1.60 is the constitutive relation when the x_1-plane is the plane of symmetry, and Equation 1.61) is the constitutive relation for the x_2-plane as the plane of symmetry. when both x_1- and x_2-planes are planes of symmetry, then the C-matrix has only 9 independent material constants as shown below:

$$\begin{Bmatrix} \sigma_1 \\ \sigma_2 \\ \sigma_3 \\ \sigma_4 \\ \sigma_5 \\ \sigma_6 \end{Bmatrix} = \begin{bmatrix} C_{11} & C_{12} & C_{13} & 0 & 0 & 0 \\ & C_{22} & C_{23} & 0 & 0 & 0 \\ & & C_{33} & 0 & 0 & 0 \\ & & & C_{44} & 0 & 0 \\ & symm & & & C_{55} & 0 \\ & & & & & C_{66} \end{bmatrix} \begin{Bmatrix} \varepsilon_1 \\ \varepsilon_2 \\ \varepsilon_3 \\ 2\varepsilon_4 \\ 2\varepsilon_5 \\ 2\varepsilon_6 \end{Bmatrix} \quad \textbf{(1.62)}$$

Note that Equation 1.62 includes the case when all three planes of x_1, x_2, and x_3 are planes of symmetry. Therefore, when two mutually perpendicular planes are planes of symmetry, then the third plane automatically becomes a plane of symmetry. Materials having three planes of symmetry are called *orthotropic* (or *orthogonally anisotropic* or *orthorhombic*) materials.

1.1.12.3 Three Planes of Symmetry and One Axis of Symmetry

If the material has one axis of symmetry in addition to the three planes of symmetry, then it is called *transversely isotropic* (*hexagonal*) material. If x_3-axis is the axis of symmetry, then the material response in x_1- and x_2-directions must be identical. In Equation 1.62, if we substitute $\varepsilon_1 = \varepsilon_0$ and all other strain components = 0, then we get the 3 nonzero stress components, $\varepsilon_1 = C_{11}\,\varepsilon_0$, $\sigma_2 = C_{12}\varepsilon_0$, $\sigma_3 = C_{13}\varepsilon_0$. Similarly, if the strain state has only 1 nonzero component $\varepsilon_2 = \varepsilon_0$, while all other strain components are 0, then the 3 normal stress components are $\sigma_1 = C_{12}\varepsilon_0$, $\sigma_2 = C_{22}\varepsilon_0$, $\sigma_3 = C_{23}\varepsilon_0$. Since x_3-axis is an axis of symmetry, σ_3 should be same for both cases; σ_1 for the first case should be equal to the σ_2 for the second case, and vice versa. Thus, $C_{13} = C_{23}$ and $C_{11} = C_{22}$. Then consider two more cases: (1) ε_{23} (or ε_4 in Equation 1.62) = ε_0, while all other strain components are 0; and (2) ε_{31} (or ε_5 in Equation 1.62) = ε_0, while all other strain components are 0. From Equation 1.62 one gets $\sigma_4 = C_{44}\varepsilon_0$ for case 1 and $\sigma_4 = C_{55}\varepsilon_0$. Since x_3-axis is the axis of symmetry, σ_4 and σ_5 should have equal values; therefore $C_{44} = C_{55}$. Substituting these constraint conditions in Equation 1.62, one gets

$$\begin{Bmatrix} \sigma_1 \\ \sigma_2 \\ \sigma_3 \\ \sigma_4 \\ \sigma_5 \\ \sigma_6 \end{Bmatrix} = \begin{bmatrix} C_{11} & C_{12} & C_{13} & 0 & 0 & 0 \\ & C_{11} & C_{13} & 0 & 0 & 0 \\ & & C_{33} & 0 & 0 & 0 \\ & & & C_{44} & 0 & 0 \\ & symm & & & C_{44} & 0 \\ & & & & & C_{66} \end{bmatrix} \begin{Bmatrix} \varepsilon_1 \\ \varepsilon_2 \\ \varepsilon_3 \\ 2\varepsilon_4 \\ 2\varepsilon_5 \\ 2\varepsilon_6 \end{Bmatrix} \tag{1.63}$$

In Equation 1.63 although there are 6 different material constants, only 5 are independent. Considering the isotropic deformation in the x_1x_2-plane, C_{66} can be expressed in terms of C_{11} and C_{12} in the following manner:

$$C_{66} = \frac{C_{11} - C_{12}}{2} \tag{1.64}$$

1.1.12.4 Three Planes of Symmetry and Two or Three Axes of Symmetry

If we now add x_1 as an axis of symmetry, then following the same arguments as before one can show that in Equation 1.63 the following three additional constraint conditions must be satisfied: $C_{12} = C_{13}$, $C_{11} = C_{33}$, and $C_{44} = C_{66}$.

The constitutive matrix is then simplified to:

$$\begin{Bmatrix} \sigma_1 \\ \sigma_2 \\ \sigma_3 \\ \sigma_4 \\ \sigma_5 \\ \sigma_6 \end{Bmatrix} = \begin{bmatrix} C_{11} & C_{12} & C_{12} & 0 & 0 & 0 \\ & C_{11} & C_{12} & 0 & 0 & 0 \\ & & C_{11} & 0 & 0 & 0 \\ & & & C_{66} & 0 & 0 \\ & symm & & & C_{66} & 0 \\ & & & & & C_{66} \end{bmatrix} \begin{Bmatrix} \varepsilon_1 \\ \varepsilon_2 \\ \varepsilon_3 \\ 2\varepsilon_4 \\ 2\varepsilon_5 \\ 2\varepsilon_6 \end{Bmatrix} \tag{1.65}$$

The addition of the third axis of symmetry does not modify the constitutive matrix any more. If two mutually perpendicular axes are the axes of symmetry, then the third axis must be an axis of symmetry. These materials have same material properties in all directions and are known as *isotropic* materials. From Equation 1.65 and Equation 1.64 one can see that isotropic materials have only two independent material constants. This chapter will concentrate on the analysis of the linear, elastic, isotropic materials.

Example 1.6

Consider an elastic orthotropic material for which the stress-strain relations are given by the following:

$$\varepsilon_{11} = \frac{\sigma_{11}}{E_1} - \nu_{21}\frac{\sigma_{22}}{E_2} - \nu_{31}\frac{\sigma_{33}}{E_3}$$

$$\varepsilon_{22} = \frac{\sigma_{22}}{E_2} - \nu_{12}\frac{\sigma_{11}}{E_1} - \nu_{32}\frac{\sigma_{33}}{E_3}$$

$$\varepsilon_{33} = \frac{\sigma_{33}}{E_3} - \nu_{13}\frac{\sigma_{11}}{E_1} - \nu_{23}\frac{\sigma_{22}}{E_2}$$

$$2\varepsilon_{12} = \frac{\sigma_{12}}{G_{12}} \qquad 2\varepsilon_{21} = \frac{\sigma_{21}}{G_{21}}$$

$$2\varepsilon_{13} = \frac{\sigma_{13}}{G_{13}} \qquad 2\varepsilon_{31} = \frac{\sigma_{31}}{G_{31}}$$

$$2\varepsilon_{23} = \frac{\sigma_{23}}{G_{23}} \qquad 2\varepsilon_{32} = \frac{\sigma_{32}}{G_{32}}$$

where E_i is the Young's Modulus in the x_i-direction, and ν_{ij} and G_{ij} represent Poission's ratio and shear modulus, respectively, in different directions for different values of i and j.

a. How many different elastic constants do you see in the above relations?

b. How many of those do you expect to be independent?

c. How many equations or constraint relations must exist among the above material constants?

d. Do you expect G_{ij} to be equal to G_{ji} for $i \neq j$? Justify your answer.

e. Do you expect ν_{ij} to be equal to ν_{ji} for $i \neq j$ Justify your answer.

f. Write down all equations (relating the material constants) that must be satisfied.

g. If the above relations are proposed for an isotropic material, then how many independent relations among the above material constants must exist? Do not write down those equations.

h. If the material is transversely isotropic, then how many independent relations among the above material constants must exist? Do not write down those equations.

SOLUTION

a. 15

b. 9

c. 6

d. Yes, because σ_{ij} and ε_{ij} are symmetric.

e. No, because symmetry of the constitutive matrix does not require that ν_{ij} be equal to ν_{ji}.

f. $$\begin{Bmatrix} \varepsilon_{11} \\ \varepsilon_{22} \\ \varepsilon_{33} \\ \varepsilon_{23} \\ \varepsilon_{31} \\ \varepsilon_{12} \end{Bmatrix} = \begin{bmatrix} \frac{1}{E_1} & -\frac{\nu_{21}}{E_2} & -\frac{\nu_{31}}{E_3} & 0 & 0 & 0 \\ -\frac{\nu_{12}}{E_1} & \frac{1}{E_2} & -\frac{\nu_{32}}{E_3} & 0 & 0 & 0 \\ -\frac{\nu_{13}}{E_1} & -\frac{\nu_{23}}{E_2} & \frac{1}{E_3} & 0 & 0 & 0 \\ 0 & 0 & 0 & \frac{1}{G_{23}} & 0 & 0 \\ 0 & 0 & 0 & 0 & \frac{1}{G_{31}} & 0 \\ 0 & 0 & 0 & 0 & 0 & \frac{1}{G_{12}} \end{bmatrix} \begin{Bmatrix} \sigma_{11} \\ \sigma_{22} \\ \sigma_{33} \\ \sigma_{23} \\ \sigma_{31} \\ \sigma_{12} \end{Bmatrix}$$

From symmetry of the above matrix (also known as compliance matrix),

$$\frac{\nu_{12}}{E_1} = \frac{\nu_{21}}{E_2}$$

$$\frac{\nu_{13}}{E_1} = \frac{\nu_{31}}{E_3}$$

$$\frac{\nu_{23}}{E_2} = \frac{\nu_{32}}{E_3}$$

the other three constraint conditions are $G_{12} = G_{21}$, $G_{13} = G_{31}$, $G_{32} = G_{23}$.

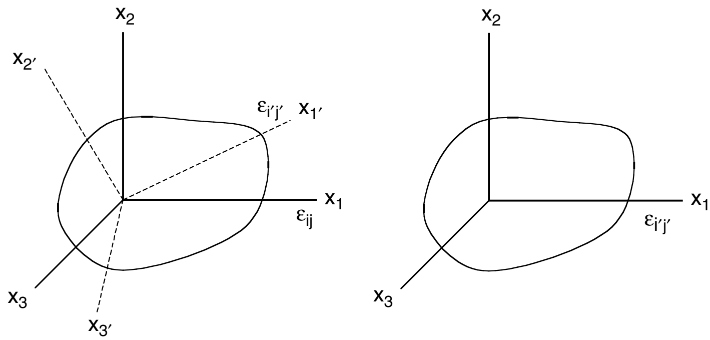

FIGURE 1.13
Isotropic material subjected to two states of strain.

g. Constraint relations must exist because isotropic material has only 2 independent material constants.

h. Relations should exist since the transversely isotropic solid has 5 independent material constants.

1.1.13 Stress-Strain Relation for Isotropic Materials — Green's Approach

Consider an isotropic material subjected to two states of strain as shown in Figure 1.13. The state of strain for the first case is ε_{ij} in the $x_1x_2x_3$ coordinate system as shown in the left figure and the strain state for the second case is $\varepsilon_{i'j'}$ in the $x_1x_2x_3$ coordinate system as shown in the right figure. Note that $\varepsilon_{i'j'}$ and ε_{ij} are numerically different. The numerical values for $\varepsilon_{i'j'}$ can be obtained from ε_{ij} by transforming the strain components ε_{ij} from the $x_1x_2x_3$ coordinate system to the $x_{1'}x_{2}x_{3'}$ coordinate system as shown on the left figure of 1.13. If the strain energy density function in the $x_1x_2x_3$ coordinate system is given by $U_0(\varepsilon_{ij})$, then the strain energy density for these two cases are $U_0(\varepsilon_{ij})$ and $U_0(\varepsilon_{i'j'})$. If the material is anisotropic, then these two values can be different since the strain states are different. If the material is isotropic, then these two values must be the same since, in the two figures of 1.13, identical numerical values of strain components ($\varepsilon_{i'j'}$) are applied in two different directions. For isotropic material equal strain values applied in two different directions should not make any difference in computing the strain energy density. For $U_0(\varepsilon_{ij})$ and $U_0(\varepsilon_{i'j'})$ to be identical U_0 must be a function of strain invariants because strain invariants are the only parameters that do not change when the numerical values of the strain components are changed from ε_{ij} to $\varepsilon_{i'j'}$.

Three stress invariants have been defined in Equation 1.39. In the same manner, three strain invariants can be defined as

$$I_1 = \varepsilon_{ii}$$
$$I_2 = \frac{1}{2}\varepsilon_{ij}\varepsilon_{ji} \tag{1.66}$$
$$I_3 = \frac{1}{3}\varepsilon_{ij}\varepsilon_{jk}\varepsilon_{ki}$$

Note that I_1, I_2, and I_3 are linear, quadratic, and cubic functions of strain components, respectively. To obtain linear stress-strain relation from Equation 1.50 it is clear that the strain energy density function must be a quadratic function of strain as shown below:

$$U_0 = C_1 I_1^2 + C_2 I_2$$
$$\therefore \sigma_{ij} = \frac{\partial U_0}{\partial \varepsilon_{ij}} = 2C_1 I_1 \frac{\partial I_1}{\partial \varepsilon_{ij}} + C_2 \frac{\partial I_2}{\partial \varepsilon_{ij}} = 2C_1 I_1 \delta_{ik}\delta_{km} + C_2 \frac{1}{2}(\delta_{im}\delta_{jn}\varepsilon_{nm} + \varepsilon_{mn}\delta_{in}\delta_{jm})$$
$$\therefore \sigma_{ij} = 2C_1 \varepsilon_{kk}\delta_{ij} + C_2 \varepsilon_{ij} \tag{1.67}$$

In Equation 1.67 if we substitute $2C_1 = \lambda$, and $C_2 = 2\mu$, then the stress-strain relation takes the following form:

$$\sigma_{ij} = \lambda\delta_{ij}\varepsilon_{kk} + 2\mu\varepsilon_{ij} \tag{1.68}$$

In Equation 1.68 coefficients λ and μ are known as Lame's first and second constants, respectively. This equation can be expressed in matrix form as in Equation 1.65 to obtain

$$\begin{Bmatrix} \sigma_1 = \sigma_{11} \\ \sigma_2 = \sigma_{22} \\ \sigma_3 = \sigma_{33} \\ \sigma_4 = \sigma_{23} \\ \sigma_5 = \sigma_{31} \\ \sigma_6 = \sigma_{12} \end{Bmatrix} = \begin{bmatrix} \lambda+2\mu & \lambda & \lambda & 0 & 0 & 0 \\ & \lambda+2\mu & \lambda & 0 & 0 & 0 \\ & & \lambda+2\mu & 0 & 0 & 0 \\ & & & \mu & 0 & 0 \\ & symm & & & \mu & 0 \\ & & & & & \mu \end{bmatrix} \begin{Bmatrix} \varepsilon_1 = \varepsilon_{11} \\ \varepsilon_2 = \varepsilon_{22} \\ \varepsilon_3 = \varepsilon_{33} \\ 2\varepsilon_4 = 2\varepsilon_{23} = \gamma_{23} \\ 2\varepsilon_5 = 2\varepsilon_{31} = \gamma_{31} \\ 2\varepsilon_6 = 2\varepsilon_{12} = \gamma_{12} \end{Bmatrix} \tag{1.69}$$

Note that the shear stress component (σ_{ij}) is simply equal to the engineering shear strain component (γ_{ij}) multiplied by Lame's second constant (μ). Therefore, Lame's second constant is the shear modulus.

Equation 1.68 and Equation 1.69 are also known as generalized Hooke's law in three-dimension. The law is named after Robert Hooke, who first proposed the linear stress-strain model. Equation 1.68 can be inverted to obtain strain components in terms of the stress components as given below.

By substituting the subscript j by i one can write

$$\sigma_{ii} = \lambda\delta_{ii}\varepsilon_{kk} + 2\mu\varepsilon_{ii} = (3\lambda + 2\mu)\varepsilon_{ii}$$
$$\therefore \varepsilon_{ii} = \frac{\sigma_{ii}}{(3\lambda + 2\mu)} \tag{1.70}$$

Substituting Equation 1.70 back into Equation 1.68 gives

$$\sigma_{ij} = \lambda\delta_{ij}\frac{\sigma_{kk}}{(3\lambda + 2\mu)} + 2\mu\varepsilon_{ij}$$

or

$$\varepsilon_{ij} = \frac{\sigma_{ij}}{2\mu} + \delta_{ij}\frac{\lambda\sigma_{kk}}{2\mu(3\lambda + 2\mu)} \tag{1.71}$$

1.1.13.1 Hooke's Law in Terms of Young's Modulus and Poission's Ratio

In undergraduate mechanics courses, strains are expressed in terms of stress components, Young's modulus (E), Poission's ratio (ν), and shear modulus (μ), in the following form:

$$\begin{aligned}
\varepsilon_{11} &= \frac{\sigma_{11}}{E} - \frac{\nu\sigma_{22}}{E} - \frac{\nu\sigma_{33}}{E} \\
\varepsilon_{22} &= \frac{\sigma_{22}}{E} - \frac{\nu\sigma_{11}}{E} - \frac{\nu\sigma_{33}}{E} \\
\varepsilon_{33} &= \frac{\sigma_{33}}{E} - \frac{\nu\sigma_{22}}{E} - \frac{\nu\sigma_{11}}{E} \\
2\varepsilon_{12} &= \gamma_{12} = \frac{\sigma_{12}}{\mu} = \frac{2(1+\nu)\sigma_{12}}{E} \\
2\varepsilon_{23} &= \gamma_{23} = \frac{\sigma_{23}}{\mu} = \frac{2(1+\nu)\sigma_{23}}{E} \\
2\varepsilon_{31} &= \gamma_{31} = \frac{\sigma_{31}}{\mu} = \frac{2(1+\nu)\sigma_{31}}{E}
\end{aligned} \tag{1.72}$$

In the above equation the relation between Young's modulus (E), Poission's ratio (ν), and shear modulus (μ) has been incorporated. Equation 1.72 can be expressed in index notation:

$$\varepsilon_{ij} = \frac{1+\nu}{E}\sigma_{ij} - \frac{\nu}{E}\delta_{ij}\sigma_{kk} \tag{1.73}$$

Equating the right-hand sides of Equation 1.71 and Equation 1.73, Lame's constants can be expressed in terms of Young's modulus and Poission's ratio. Similarly, the bulk modulus $K = \frac{\sigma_{ii}}{3\varepsilon_{ii}}$ can be expressed in terms of Lame's constants from Equation 1.70.

Example 1.7

For an isotropic material, obtain the bulk modulus K in terms of (a) E and ν, and (b) λ and μ.

SOLUTION

a. From Equation 1.70,

$$\sigma_{ii} = (3\lambda + 2\mu)\varepsilon_{ii}$$

Hence,

$$K = \frac{\sigma_{ii}}{3\varepsilon_{ii}} = \frac{3\lambda + 2\mu}{3}$$

b. From Equation 1.73,

$$\varepsilon_{ii} = \frac{1+\nu}{E}\sigma_{ii} - \frac{\nu}{E}\delta_{ii}\sigma_{kk} = \frac{1+\nu}{E}\sigma_{ii} - \frac{3\nu}{E}\sigma_{kk} = \frac{1-2\nu}{E}\sigma_{ii}$$

Hence,

$$K = \frac{\sigma_{ii}}{3\varepsilon_{ii}} = \frac{E}{3(1-2\nu)}$$

Since the isotropic material has only two independent elastic constants, any of the five commonly used elastic constants (λ, μ, E, ν, and K) can be expressed in terms of any other two elastic constants (see Table 1.1).

TABLE 1.1

Relations between Different Elastic Constants for Isotropic Materials

	λ	μ	E	ν	K
λ, μ	—	—	$\frac{\mu(3\lambda+2\mu)}{\lambda+\mu}$	$\frac{\lambda}{2(\lambda+\mu)}$	$\frac{3\lambda+2\mu}{3}$
λ, E	—	$\frac{(E-3\lambda)+\sqrt{(E-3\lambda)^2+8\lambda E}}{4}$	—	$\frac{-(E+3\lambda)+\sqrt{(E+3\lambda)^2+8\lambda^2}}{4}$	$\frac{(E+3\lambda)+\sqrt{(E+3\lambda)^2-4\lambda E}}{6}$
λ, ν	—	$\frac{\lambda(1-2\nu)}{2\nu}$	$\frac{\lambda(1+\nu)(1-2\nu)}{2\nu}$	—	$\frac{\lambda(1+\nu)}{3\nu}$
λ, K	—	$\frac{3(K-\lambda)}{2}$	$\frac{9K(K-\lambda)}{3K-\lambda}$	$\frac{\lambda}{3K-\lambda}$	—
μ, E	$\frac{(2\mu-E)\mu}{E-3\mu}$	—	—	$\frac{E-2\mu}{2\mu}$	$\frac{\mu E}{3(3\mu-E)}$
μ, ν	$\frac{2\mu\nu}{1-2\nu}$	—	$2\mu(1+\nu)$	—	$\frac{2\mu(1+\nu)}{3(1-2\nu)}$
μ, K	$\frac{3K-2\mu}{3}$	—	$\frac{9K\mu}{3K+\mu}$	$\frac{3K-2\mu}{2(3K+\mu)}$	—
E, ν	$\frac{\nu E}{(1+\nu)(1-2\nu)}$	$\frac{E}{2(1+\nu)}$	—	—	$\frac{E}{3(1-2\nu)}$
E, K	$\frac{3K(3K-E)}{9K-E}$	$\frac{3KE}{9K-E}$	—	$\frac{3K-E}{6K}$	—
ν, K	$\frac{3K\nu}{1+\nu}$	$\frac{3K(1-2\nu)}{2(1+\nu)}$	$3K(1-2\nu)$	—	—

1.1.14 Navier's Equation of Equilibrium

Substituting the stress-strain relation (Equation 1.68) into the equilibrium equation (Equation 1.24) one gets

$$
\begin{aligned}
&(\lambda\delta_{ij}\varepsilon_{kk}+2\mu\varepsilon_{ij})_{,j}+f_i=0\\
&\Rightarrow\left(\lambda\delta_{ij}u_{k,k}+2\mu\frac{1}{2}[u_{i,j}+u_{j,i}]\right)_{,j}+f_i=0\\
&\Rightarrow\lambda\delta_{ij}u_{k,kj}+\mu[u_{i,jj}+u_{j,ij}]+f_i=0\\
&\Rightarrow\lambda u_{k,ki}+\mu[u_{i,jj}+u_{j,ji}]+f_i=0\\
&\Rightarrow(\lambda+\mu)u_{j,ji}+\mu u_{i,jj}+f_i=0
\end{aligned}
\tag{1.74}
$$

In the vector form the above equation can be written as

$$
(\lambda+\mu)\underline{\nabla}(\underline{\nabla}\cdot\mathbf{u})+\mu\nabla^2\mathbf{u}+\mathbf{f}=0 \tag{1.75}
$$

Because of the vector identity $\nabla^2 \mathbf{u} = \underline{\nabla}(\underline{\nabla} \cdot \mathbf{u}) - \underline{\nabla} \times \underline{\nabla} \times \mathbf{u}$, Equation 1.75 can also be written as

$$(\lambda + 2\mu)\underline{\nabla}(\underline{\nabla} \cdot \mathbf{u}) - \mu\underline{\nabla} \times \underline{\nabla} \times \mathbf{u} + \mathbf{f} = 0 \tag{1.76}$$

In Equation 1.75 and Equation 1.76 the dot $(\cdot)$ is used to indicate the scalar or dot product, and the cross $(\times)$ is used to indicate the vector or cross product. In index notations, the above two equations can also be written as

$$(\lambda + \mu)u_{j,ji} + \mu u_{i,jj} + f_i = 0$$

or **(1.77)**

$$(\lambda + 2\mu)u_{j,ji} - \mu\varepsilon_{ijk}\varepsilon_{kmn}u_{n,mj} + f_i = 0$$

where ε_{ijk} and ε_{kmn} are permutation symbols, is defined in Equation 1.36. The equilibrium equations, expressed in terms of the displacement components (Equations 1.75 to 1.77) are known as Navier's equation.

Example 1.8

If a linear elastic isotropic body does not have any body force then prove that:

a. The volumetric strain is harmonic ($\varepsilon_{ii,jj} = 0$).

b. The displacement field is biharmonic ($u_{i,jjkk} = 0$).

SOLUTION

(a) From Equation 1.77 for zero body force one can write

$$(\lambda + \mu)u_{j,ji} + \mu u_{i,jj} = 0$$

$$\Rightarrow (\lambda + \mu)u_{j,jii} + \mu u_{i,jji} = 0$$

Note that

$$u_{i,jji} = u_{i,ijj} = \varepsilon_{ii,jj}$$

and

$$u_{j,jii} = \varepsilon_{jj,ii} = \varepsilon_{ii,jj}$$

The above equation is simplified to $(\lambda + 2\mu)\varepsilon_{ii,jj} = 0$.

Since $(\lambda + 2\mu) \neq 0$, the volumetric strain ε_{ii} must be harmonic.

(b) Again from Equation 1.77 for zero body force one can write

$$(\lambda + \mu)u_{j,ji} + \mu u_{i,jj} = 0$$

$$\Rightarrow ((\lambda + \mu)u_{j,ji} + \mu u_{i,jj})_{,kk} = (\lambda + \mu)u_{j,jikk} + \mu u_{i,jjkk} = 0$$

From part (a), $\varepsilon_{jj,kk} = u_{j,jkk} = 0$

Hence, $u_{j,jkki} = u_{j,jikk} = 0$. Substituting it into the above equation one gets

$$(\lambda + \mu)u_{j,jikk} + \mu u_{i,jjkk} = \mu u_{i,jjkk} = 0$$

$$\Rightarrow u_{i,jjkk} = 0$$

Example 1.9

Obtain the governing equation of equilibrium in terms of displacement for a material whose stress-strain relation is given by

$$\sigma_{ij} = \alpha_{ijkl}\varepsilon_{km}\varepsilon_{ml} + \delta_{ij}\gamma$$

where α_{ijkl} are material properties that are constants over the entire region, and γ is the residual state of stress that varies from point to point.

SOLUTION

Governing equation:

$$\sigma_{ij,j} + f_i = 0$$

$$\Rightarrow \alpha_{ijkl}(\varepsilon_{km}\varepsilon_{ml})_{,j} + \delta_{ij}\gamma_{,i} + f_i = 0$$

$$\Rightarrow \alpha_{ijkl}(\varepsilon_{km,j}\varepsilon_{ml} + \varepsilon_{km}\varepsilon_{ml,j}) + \gamma_{,i} + f_i = 0$$

$$\Rightarrow \frac{1}{4}\alpha_{ijkl}\{(u_{k,mj} + u_{m,kj})(u_{m,l} + u_{l,m}) + (u_{k,m} + u_{m,k})(u_{m,lj} + u_{l,mj})\} + \gamma_{,i} + f_i = 0$$

1.1.15 Fundamental Equations of Elasticity in Other Coordinate Systems

All equations derived so far have been expressed in the Cartesian coordinate system. Although the majority of elasticity problems can be solved in the Cartesian coordinate system for some problem geometries, such as axisymmetric problems, cylindrical and spherical coordinate systems are better suited for defining the problem and solving it. If the equation is given in vector form (Equations 1.75 and 1.76), then it can be used in any coordinate system with appropriate definitions of the vector operators in that coordinate system; when it is expressed in index notation in the Cartesian coordinate system (Equation 1.77), then that expression cannot be used in the cylindrical or spherical coordinatesystem. In Table 1.2 different vector operations, strain displacement relations, and equilibrium equations are given in the three coordinate systems that are shown in Figure 1.14.

1.2 Time Dependent Problems or Dynamic Problems

In all equations derived above it is assumed that the body is in static equilibrium. The resultant force acting on the body is equal to zero. If the body is subjected to a nonzero resultant force, then it will have an acceleration $\ddot{u}_i$ (time derivatives are denoted by dots over the variable), and the equilibrium equation (Equation 1.24) will be replaced by the following governing equation of motion:

$$\sigma_{ij,j} + f_i = \rho \ddot{u}_i \tag{1.78}$$

In the above equation ρ is the mass density.

Therefore, the Navier's equation for the dynamic case takes the following form:

$$(\lambda + 2\mu)\underline{\nabla}(\underline{\nabla} \cdot \mathbf{u}) - \mu \underline{\nabla} \times \underline{\nabla} \times \mathbf{u} + \mathbf{f} = \rho \ddot{\mathbf{u}} \tag{1.79}$$

1.2.1 Some Simple Dynamic Problems

Example 1.10

A time-dependent normal load on the surface of an elastic half-space is shown in Figure 1.15. Compute the displacement and stress field for this problem geometry.

TABLE 1.2

Important Equations in Different Coordinate Systems (Moon and Spencer, 1965) (ϕ and ψ are a Scalar and a Vector Function, Respectively)

Equations	Cartesian Coordinate System	Cylindrical Coordinate System	Spherical Coordinate System
Grad $\phi =$ $\underline{\nabla}\,\phi$	$\phi_{,i} = \phi_{,1}e_1 + \phi_{,2}e_2 + \phi_{,3}e_3$	$\frac{\partial\phi}{\partial r}e_r + \frac{\partial\phi}{\partial z}e_z + \frac{1}{r}\frac{\partial\phi}{\partial\theta}e_\theta$	$\frac{\partial\phi}{\partial r}e_r + \frac{1}{r}\frac{\partial\phi}{\partial\beta}e_\beta + \frac{1}{r\sin\beta}\frac{\partial\phi}{\partial\theta}e_\theta$
Div $\psi =$ $\underline{\nabla}\cdot\psi$	$\psi_{i,i} = \psi_{1,1} + \psi_{2,2} + \psi_{3,3}$	$\frac{\partial\psi_r}{\partial r} + \frac{\partial\psi_z}{\partial z} + \frac{1}{r}\frac{\partial\psi_\theta}{\partial\theta}$	$\frac{\partial\psi_r}{\partial r} + \frac{2}{r}\psi_r + \frac{1}{r}\frac{\partial\psi_\beta}{\partial\beta}$ $+\frac{\cot\beta}{r}\psi_\beta + \frac{1}{r\sin\beta}\frac{\partial\psi_\theta}{\partial\theta}$
Curl $\psi =$ $\underline{\nabla}\times\psi$	$\varepsilon_{ijk}\psi_{k,j} =$ $\begin{vmatrix} e_1 & e_2 & e_3 \\ \frac{\partial}{\partial x_1} & \frac{\partial}{\partial x_2} & \frac{\partial}{\partial x_3} \\ \psi_1 & \psi_2 & \psi_3 \end{vmatrix}$	$\frac{1}{r}\begin{vmatrix} e_r & re_\theta & e_z \\ \frac{\partial}{\partial r} & \frac{\partial}{\partial\theta} & \frac{\partial}{\partial z} \\ \psi_r & r\psi_\theta & \psi_z \end{vmatrix}$	$\frac{1}{r^2\sin\beta}\begin{vmatrix} e_r & re_\beta & r\sin\beta e_\theta \\ \frac{\partial}{\partial r} & \frac{\partial}{\partial\beta} & \frac{\partial}{\partial\theta} \\ \psi_r & r\psi_\beta & r\sin\beta\psi_\theta \end{vmatrix}$
Strain-Displacement Relation	Equation 1.7a $\varepsilon_{ij} = \frac{1}{2}(u_{i,j} + u_{j,i})$	$\varepsilon_{rr} = \frac{\partial u_r}{\partial r}$ $\varepsilon_{\theta\theta} = \frac{1}{r}\frac{\partial u_\theta}{\partial\theta} + \frac{u_r}{r}$ $\varepsilon_{zz} = \frac{\partial u_z}{\partial z}$ $\varepsilon_{rz} = \frac{1}{2}\left(\frac{\partial u_r}{\partial z} + \frac{\partial u_z}{\partial r}\right)$ $\varepsilon_{r\theta} = \frac{1}{2}\left(\frac{1}{r}\frac{\partial u_r}{\partial\theta} - \frac{u_\theta}{r} + \frac{\partial u_\theta}{\partial r}\right)$ $\varepsilon_{z\theta} = \frac{1}{2}\left(\frac{1}{r}\frac{\partial u_z}{\partial\theta} + \frac{\partial u_\theta}{\partial z}\right)$	$\varepsilon_{rr} = \frac{\partial u_r}{\partial r}$ $\varepsilon_{\beta\beta} = \frac{1}{r}\frac{\partial u_\beta}{\partial\beta} + \frac{u_r}{r}$ $\varepsilon_{\theta\theta} = \frac{1}{r\sin\beta}\frac{\partial u_\theta}{\partial\theta} + \frac{u_r}{r} + \frac{u_\beta}{r}\cot\beta$ $2\varepsilon_{r\beta} = \frac{1}{r}\frac{\partial u_r}{\partial\beta} + \frac{\partial u_\beta}{\partial r} - \frac{u_\beta}{r}$ $2\varepsilon_{r\theta} = \frac{1}{r\sin\beta}\frac{\partial u_r}{\partial\theta} - \frac{u_\theta}{r} + \frac{\partial u_\theta}{\partial r}$ $2\varepsilon_{\beta\theta} = \frac{1}{r\sin\beta}\frac{\partial u_\beta}{\partial\theta} + \frac{1}{r}\frac{\partial u_\theta}{\partial\beta} - \frac{u_\theta}{r}\cot\beta$
Equilibrium Equations	Equations 1.24 and 1.22 $\sigma_{ij,j} + f_i = 0$	$\frac{\partial\sigma_{rr}}{\partial r} + \frac{\partial\sigma_{rz}}{\partial z} + \frac{1}{r}\frac{\partial\sigma_{r\theta}}{\partial\theta}$ $+\frac{1}{r}(\sigma_{rr} - \sigma_{\theta\theta}) + f_r = 0$ $\frac{\partial\sigma_{rz}}{\partial r} + \frac{\partial\sigma_{zz}}{\partial z} + \frac{1}{r}\frac{\partial\sigma_{z\theta}}{\partial\theta}$ $+\frac{1}{r}\sigma_{rz} + f_z = 0$ $\frac{\partial\sigma_{r\theta}}{\partial r} + \frac{\partial\sigma_{z\theta}}{\partial z} + \frac{1}{r}\frac{\partial\sigma_{\theta\theta}}{\partial\theta}$ $+\frac{2}{r}\sigma_{r\theta} + f_\theta = 0$	$\frac{\partial\sigma_{rr}}{\partial r} + \frac{1}{r}\frac{\partial\sigma_{r\beta}}{\partial\beta} + \frac{1}{r\sin\beta}\frac{\partial\sigma_{r\theta}}{\partial\theta}$ $+\frac{1}{r}[2\sigma_{rr} + (\cot\beta)\sigma_{r\beta} - \sigma_{\beta\beta} - \sigma_{\theta\theta}] + f_r = 0$ $\frac{\partial\sigma_{r\beta}}{\partial r} + \frac{1}{r}\frac{\partial\sigma_{\beta\beta}}{\partial\beta} + \frac{1}{r\sin\beta}\frac{\partial\sigma_{\beta\theta}}{\partial\theta}$ $+\frac{1}{r}[3\sigma_{r\beta} + (\cot\theta)(\sigma_{\beta\beta} - \sigma_{\theta\theta})] + f_\beta = 0$ $\frac{\partial\sigma_{r\theta}}{\partial r} + \frac{1}{r}\frac{\partial\sigma_{\beta\theta}}{\partial\beta} + \frac{1}{r\sin\beta}\frac{\partial\sigma_{\theta\theta}}{\partial\theta}$ $+\frac{2\sigma_{\beta\theta}\cot\beta + 3\sigma_{r\theta}}{r} + f_\theta = 0$

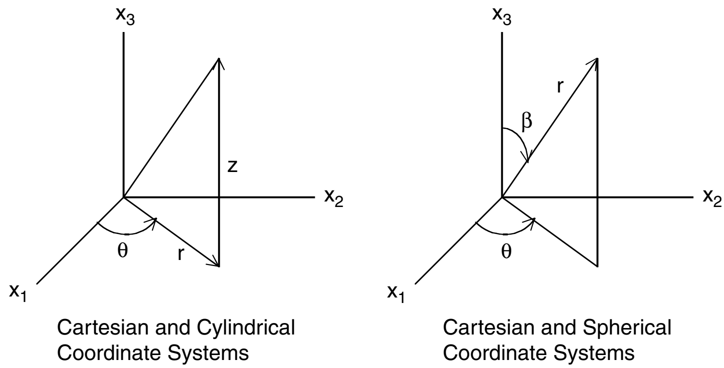

FIGURE 1.14
Cartesian ($x_1x_2x_3$), cylindrical ($r\theta z$), and spherical ($r\beta\theta$) coordinate systems.

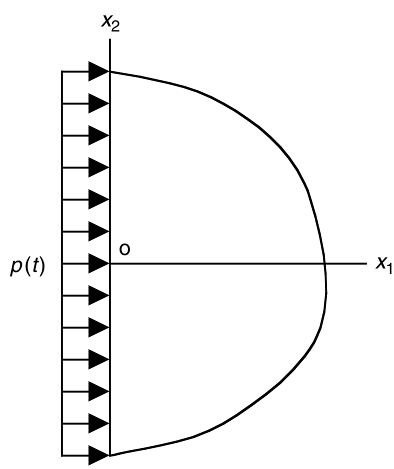

FIGURE 1.15
A time-dependent load $p(t)$ is applied on the surface ($x_1 = 0$) of an elastic half-space ($x_1 > 0$).

SOLUTION

Since the loading and the problem geometry are independent of x_2- and x_3-coordinates, the solution should be a function of x_1 only. The solution should also be symmetric about the x_1-axis, and this axis can be moved up or down or front or back without violating the symmetry conditions; u_2 and u_3 components of displacement must be equal to zero and the solution must have only one component of displacement, u_1, that will be a function of x_1 only.

Substituting $\mathbf{f} = 0$ (no body force), $u_2 = u_3 = 0$, and $u_1 = u_1(x_1)$ in Equation 1.79 one gets

$$(\lambda+2\mu)u_{1,11}=\rho\ddot{u}_1$$
$$\Rightarrow u_{1,11}=\frac{\rho}{\lambda+2\mu}\ddot{u}_1=\frac{1}{c_P^2}\ddot{u}_1 \tag{1.80}$$

Equation 1.80 is a one-dimensional wave equation that has a solution of the form

$$u_1=F\left(t-\frac{x_1}{c_P}\right)+G\left(t+\frac{x_1}{c_P}\right) \tag{1.81}$$

where

$$c_P=\sqrt{\frac{\lambda+2\mu}{\rho}} \tag{1.82}$$

Note that when Equation 1.81 is substituted into Equation 1.80, both left- and right-hand sides of Equation 1.80 become equal to

$$u_{1,11}=\frac{1}{c_P^2}\ddot{u}_1=\frac{1}{c_P^2}\left\{F''\left(t-\frac{x_1}{c_P}\right)+G''\left(t+\frac{x_1}{c_P}\right)\right\}$$

where F'' and G'' represent double derivatives of the functions with respect to their arguments.

From the initial condition of the problem, one can say that at $t = 0$, the displacement u_1 and the velocity $\dot{u}_1$ must be equal to zero for all $x_1 > 0$. Hence, for $x_1 > 0$:

$$u_1\Big|_{t=0}=F\left(-\frac{x_1}{c_P}\right)+G\left(\frac{x_1}{c_P}\right)=0 \tag{1.83}$$

$$\dot{u}_1\Big|_{t=0}=F'\left(-\frac{x_1}{c_P}\right)+G'\left(\frac{x_1}{c_P}\right)=0 \tag{1.84}$$

Taking the derivative of Equation 1.83 with respect to x_1 gives

$$-F'\left(-\frac{x_1}{c_P}\right)+G'\left(\frac{x_1}{c_P}\right)=0 \tag{1.85}$$

From Equation 1.84 and Equation 1.85 one gets

$$F'\left(-\frac{x_1}{c_P}\right)=G'\left(\frac{x_1}{c_P}\right)=0 \quad \textbf{(1.86a)}$$

Therefore,

$$F\left(-\frac{x_1}{c_P}\right)=A,\quad G\left(\frac{x_1}{c_P}\right)=B$$

where A and B are two constants.

Since Equation 1.83 must be satisfied for $x_1 > 0$, constant B must be equal to $-A$. In other words, if the arguments of F are negative and G is positive, then the function values are A and $-A$, respectively, where A can be any positive or negative constant. From Equation 1.81 one can see that for $t < \frac{x_1}{c_P}$, the argument $\left(t-\frac{x_1}{c_P}\right)$ of function F is negative, and the argument $\left(t+\frac{x_1}{c_P}\right)$ of function G is positive. Thus, $u_1 = F\left(t-\frac{x_1}{c_P}\right)+G\left(t+\frac{x_1}{c_P}\right)=0$, for $t<\frac{x_1}{c_P}$. For $t>\frac{x_1}{c_P}$, both arguments $\left(t-\frac{x_1}{c_P}\right)$ and $\left(t+\frac{x_1}{c_P}\right)$ are greater than zero. Then the function G should be a constant, but the function F is not necessarily a constant. From the initial condition we have proven that if the argument of F is less than zero, then only F should be a constant. Absorbing the constant value of $G\left(t+\frac{x_1}{c_P}\right)$ into F and defining a new function f as

$$f(t,x_1)=F\left(t-\frac{x_1}{c_P}\right)+G\left(t+\frac{x_1}{c_P}\right)=F\left(t-\frac{x_1}{c_P}\right)-A=f\left(t-\frac{x_1}{c_P}\right) \quad \textbf{(1.86b)}$$

one can write the displacement field in the following manner

$$\begin{aligned} u_1 &= 0 \quad \text{for } t\le\frac{x_1}{c_P} \\ u_1 &= f\left(t-\frac{x_1}{c_P}\right) \quad \text{for } t\ge\frac{x_1}{c_P} \end{aligned} \quad \textbf{(1.87)}$$

To obtain the function f we utilize the boundary condition at $x_1 = 0$, $\sigma_{11} = -p(t)$. Thus,

$$\sigma_{11} = (\lambda + 2\mu)\varepsilon_{11} + \lambda(\varepsilon_{22} + \varepsilon_{33}) = (\lambda + 2\mu)u_{1,1} = -\frac{(\lambda + 2\mu)}{c_p} f'(t) = -p(t)$$

$$\Rightarrow f'(t) = \frac{c_p}{(\lambda + 2\mu)} p(t) = \frac{1}{\rho c_p} p(t) \tag{1.88}$$

$$\Rightarrow f(t) = \frac{1}{\rho c_p} \int_0^t p(s)ds$$

The lower limit of the integral is zero since *f*(0) = 0, from Equation 1.87.

Combining Equations 1.87 and Equation 1.88 one gets

$$\begin{aligned} u_1 &= f\left(t - \frac{x_1}{c_P}\right) = \frac{1}{\rho c_P} \int_0^{t - \frac{x_1}{c_P}} p(s)ds \quad \text{for } t \geq \frac{x_1}{c_P} \\ u_1 &= 0 \qquad\qquad\qquad\qquad\qquad \text{for } t \leq \frac{x_1}{c_P} \end{aligned} \tag{1.89}$$

The stress field can be computed in the following manner:

$$\begin{aligned} \sigma_{11} &= (\lambda + 2\mu)u_{1,1} = -\frac{(\lambda + 2\mu)}{c_P} f'\left(t - \frac{x_1}{c_P}\right) \\ &= -\rho c_P f'\left(t - \frac{x_1}{c_P}\right) = -p\left(t - \frac{x_1}{c_p}\right) \qquad \text{for } t \geq \frac{x_1}{c_P} \\ \sigma_{11} &= 0 \qquad\qquad\qquad\qquad\qquad \text{for } t \leq \frac{x_1}{c_P} \end{aligned} \tag{1.90}$$

Equation 1.89 and Equation 1.90 show that the applied stress field $-p(t)$ at $x_1 = 0$ takes a time $t = \frac{x_1}{c_p}$ to propagate a distance of x_1. The propagation velocity of the disturbance is c_P. This wave only generates normal or longitudinal stress in the material, which is why this wave is known as the longitudinal or compressional wave. Velocity of the longitudinal wave is greater than that of the shear wave (discussed below); therefore, during an earthquake the longitudinal wave arrives first. That wave is also known as the primary wave or P-wave.

One can show that if the applied stress field in Figure 1.15 is parallel to the free surface, then the disturbance will propagate with a velocity $c_s = \sqrt{\frac{\mu}{\rho}}$, and only shear stress will be generated in the material. This wave is called a shear wave or secondary wave or S-wave. It is called secondary wave because during an earthquake it arrives second, after the P-wave.

In an infinite space if a spherical cavity is subjected to an uniform pressure $p(t)$, then one can show that P-waves are generated in the elastic medium that propagates with a velocity c_P away from the cavity.

Some simple problems like the ones described above can be solved directly from the Navier's equation. In these problems only one component of displacement is nonzero, and this nonzero displacement component is a function of only one variable. For the half-space problems, this variable is x_1 and for the spherical cavity problem it is the radial distance r. Those problems are simplified to one-dimensional problems.

If the applied load in Figure 1.15 does not extend to infinity in positive and negative x_2 directions, then the problem is no longer a one-dimensional problem. For example, suppose the applied load in Figure 1.15 extends to $\pm\, a$, in positive and negative x_2-directions, while it extends to infinity in the positive and negative x_3-directions. The displacement field in the half-space material will then have two components of displacement, u_1 and u_2, and both of them will be functions of x_1 and x_2 in general. In other words, now the problem becomes a two-dimensional problem. It is very difficult to solve two- and three-dimensional problems directly from the Navier's equation. Stokes-Helmholtz decomposition of the displacement field transforms the Navier's governing equation of motion into simple wave equations as in next section.

1.2.2 Stokes-Helmholtz Decomposition

If ϕ is a scalar function and **A** is a vector function, then any displacement field **u** can be expressed in the following manner:

$$\mathbf{u} = \underline{\nabla}\phi + \underline{\nabla} \times \mathbf{A} \tag{1.91}$$

The above decomposition is known as the Stokes-Helmholtz decomposition. Since the above vector equation has three parameters (u_1, u_2, u_3) on the left-hand side and four parameters (ϕ, A_1, A_2, A_3) on the right-hand side, one can define an additional relation (known as auxiliary condition or gauge condition)

$$\underline{\nabla} \cdot \mathbf{A} = 0 \tag{1.92}$$

to obtain unique relations between u_1, u_2, u_3 and ϕ, A_1, A_2, A_3.

Substituting Equation 1.91 in the Navier's equation, in absence of a body force, one gets

$$(\lambda+2\mu)\underline{\nabla}(\underline{\nabla}\cdot\mathbf{u})-\mu\underline{\nabla}\times\underline{\nabla}\times\mathbf{u}=\rho\ddot{\mathbf{u}}$$
$$\Rightarrow(\lambda+2\mu)\underline{\nabla}(\underline{\nabla}\cdot\{\underline{\nabla}\phi+\underline{\nabla}\times\mathbf{A}\})-\mu\underline{\nabla}\times\underline{\nabla}\times\{\underline{\nabla}\phi+\underline{\nabla}\times\mathbf{A}\}=\rho\{\underline{\nabla}\ddot{\phi}+\underline{\nabla}\times\ddot{\mathbf{A}}\} \quad \textbf{(1.93)}$$
$$\Rightarrow(\lambda+2\mu)\underline{\nabla}(\nabla^2\phi+\underline{\nabla}\cdot\{\underline{\nabla}\times\mathbf{A}\})-\mu\underline{\nabla}\times\underline{\nabla}\times\{\underline{\nabla}\phi+\underline{\nabla}\times\mathbf{A}\}=\rho\{\underline{\nabla}\ddot{\phi}+\underline{\nabla}\times\ddot{\mathbf{A}}\}$$

However, from the vector identity one can write

$$\underline{\nabla}\cdot(\underline{\nabla}\times\mathbf{A})=0$$
$$\underline{\nabla}\times(\underline{\nabla}\phi)=0 \quad \textbf{(1.94)}$$
$$\underline{\nabla}\times\underline{\nabla}\times\mathbf{A}=\underline{\nabla}(\underline{\nabla}\cdot\mathbf{A})-\nabla^2\mathbf{A}$$

Substituting Equation 1.94 and Equation 1.92 into Equation 1.93 one gets

$$(\lambda+2\mu)\underline{\nabla}(\nabla^2\phi)-\mu\underline{\nabla}\times(-\nabla^2\mathbf{A})=\rho\{\underline{\nabla}\ddot{\phi}+\underline{\nabla}\times\ddot{\mathbf{A}}\}$$
$$\Rightarrow\underline{\nabla}[(\lambda+2\mu)\nabla^2\phi-\rho\ddot{\phi}]+\underline{\nabla}\times[\mu\nabla^2\mathbf{A}-\rho\ddot{\mathbf{A}}]=0$$

Sufficient conditions for the above equation to be satisfied are

$$(\lambda+2\mu)\nabla^2\phi-\rho\ddot{\phi}=0$$
$$\mu\nabla^2\mathbf{A}-\rho\ddot{\mathbf{A}}=0$$

or

$$\nabla^2\phi-\frac{\rho}{(\lambda+2\mu)}\ddot{\phi}=\nabla^2\phi-\frac{1}{c_P^2}\ddot{\phi}=0$$
$$\nabla^2\mathbf{A}-\frac{\rho}{\mu}\ddot{\mathbf{A}}=\nabla^2\mathbf{A}-\frac{1}{c_S^2}\ddot{\mathbf{A}}=0 \quad \textbf{(1.95)}$$

The equations in Equation 1.95 are wave equations that have solutions in the following form:

$$\phi(\mathbf{x},t)=\phi(\mathbf{n}\cdot\mathbf{x}-c_Pt)$$
$$\mathbf{A}(\mathbf{x},t)=\mathbf{A}(\mathbf{n}\cdot\mathbf{x}-c_St) \quad \textbf{(1.96)}$$

The equations in Equation 1.96 represent two waves propagating in the **n** direction with the velocity of c_P and c_S, respectively. Note that **n** is the unit vector in any direction.

When **A** = 0 and ϕ = nonzero, then from the above solutions one gets

$$\mathbf{u} = \underline{\nabla}\phi = \mathbf{n}\phi'(\mathbf{n}\cdot\mathbf{x} - c_P t) \tag{1.97}$$

In Equation 1.97 the prime indicates derivative with respect to the argument. Here the direction of the displacement vector **u** and the wave propagation direction **n** are the same.

When **A** is not equal to 0 and ϕ is 0, then from the above solutions one gets

$$\mathbf{u} = \underline{\nabla}\times\mathbf{A} = \underline{\nabla}\times\mathbf{A}(\mathbf{n}\cdot\mathbf{x} - c_S t) \tag{1.98}$$

Three components of displacement in the Cartesian coordinate system can be written from Equation 1.98:

$$\begin{aligned} u_1 &= n_2 A_3'(\mathbf{n}\cdot\mathbf{x} - c_S t) - n_3 A_2'(\mathbf{n}\cdot\mathbf{x} - c_S t) \\ u_2 &= n_3 A_1'(\mathbf{n}\cdot\mathbf{x} - c_S t) - n_1 A_3'(\mathbf{n}\cdot\mathbf{x} - c_S t) \\ u_3 &= n_1 A_2'(\mathbf{n}\cdot\mathbf{x} - c_S t) - n_2 A_1'(\mathbf{n}\cdot\mathbf{x} - c_S t) \end{aligned} \tag{1.99}$$

Clearly the dot product between **n** and **u** (given in Equation 1.99) is zero; hence, the direction of the displacement vector **u** is perpendicular to the wave propagation direction **n**. Displacement fields given in Equation 1.97 and Equation 1.98 correspond to P- and S-waves, respectively.

1.2.3 Two-Dimensional In-Plane Problems

If the problem geometry is such that $u_1(x_1, x_2)$ and $u_2(x_1, x_2)$ are nonzero and u_3 is equal to zero, then the problem is called an in-plane problem. In Figure 1.15, if the load is applied over a finite length in the x_2- direction but the region of load application is extended to infinity in the x_3- direction, then it will be an in-plane problem. From Equation 1.99 one can see that if we substitute $A_1 = A_2 = 0$ and $A_3 = \psi$ then u_1 and u_2 components survive. To solve two-dimensional in-plane problems in the x_1x_2 plane we take two potential functions, $\phi\ (x_1, x_2, t)$ and $A_3 = \psi(x_1, x_2, t)$, to get the displacement components from Equation 1.97 and Equation 1.99 in the following form:

$$\begin{aligned} u_1 &= \frac{\partial\phi}{\partial x_1} + \frac{\partial\psi}{\partial x_2} \\ u_2 &= \frac{\partial\phi}{\partial x_2} - \frac{\partial\psi}{\partial x_1} \end{aligned} \tag{1.100a}$$

and the governing wave equations for this case are

$$\nabla^2\phi - \frac{1}{c_P^2}\ddot{\phi} = \phi_{,11} + \phi_{,22} - \frac{1}{c_P^2}\ddot{\phi} = 0$$
$$\nabla^2\psi - \frac{1}{c_S^2}\ddot{\psi} = \psi_{,11} + \psi_{,22} - \frac{1}{c_S^2}\ddot{\psi} = 0 \tag{1.100b}$$

If the in-plane problem is defined in the x_1x_3-plane, then to guarantee $u_2 = 0$ while u_1 and u_3 are nonzero, we need to substitute $A_1 = A_3 = 0$ and $A_2 = \psi$. In this case, the two potential functions $\phi(x_1, x_3, t)$ and $A_2 = \psi(x_1, x_3, t)$, give the following displacement components:

$$u_1 = \frac{\partial\phi}{\partial x_1} - \frac{\partial\psi}{\partial x_3}$$
$$u_3 = \frac{\partial\phi}{\partial x_3} + \frac{\partial\psi}{\partial x_1} \tag{1.101}$$

It should be noted here that Equation 1.100a and Equation 1.101 are similar except for their signs. Combining Equations 1.100a and 1.68 one can write

$$\begin{aligned}\sigma_{11} &= (\lambda+2\mu)u_{1,1} + \lambda(u_{2,2}+u_{3,3}) = (\lambda+2\mu)(\phi_{,11}+\psi_{,12}) + \lambda(\phi_{,22}-\psi_{,12})\\ &= (\lambda+2\mu)\{\phi_{,11}+\phi_{,22}\} + 2\mu(\psi_{,12}-\phi_{,22}) = \mu\{\kappa^2(\phi_{,11}+\phi_{,22}) + 2(\psi_{,12}-\phi_{,22})\}\\ &= \mu\{\kappa^2\nabla^2\phi + 2(\psi_{,12}-\phi_{,22})\}\end{aligned} \tag{1.102a}$$

where

$$k^2 = \frac{\lambda+2\mu}{\mu} = \left(\frac{c_P}{c_S}\right)^2 \tag{1.102b}$$

Similarly,

$$\begin{aligned}\sigma_{22} &= (\lambda+2\mu)u_{2,2} + \lambda(u_{1,1}+u_{3,3}) = (\lambda+2\mu)(\phi_{,22}-\psi_{,12}) + \lambda(\phi_{,11}+\psi_{,12})\\ &= (\lambda+2\mu)\{\phi_{,11}+\phi_{,22}\} - 2\mu(\psi_{,12}+\phi_{,11}) = \mu\{\kappa^2(\phi_{,11}+\phi_{,22}) - 2(\psi_{,12}+\phi_{,11})\\ &= \mu\{\kappa^2\nabla^2\phi - 2(\phi_{,11}+\psi_{,12})\}\\ \sigma_{12} &= 2\mu\times\frac{1}{2}(u_{1,2}+u_{2,1}) = \mu(\phi_{,12}+\psi_{,22}+\phi_{,12}-\psi_{,11}) = \mu(2\phi_{,12}+\psi_{,22}-\psi_{,11})\end{aligned} \tag{1.102c}$$

Following similar steps, from Equations 1.101 and 1.68 one gets

$$\begin{aligned}\sigma_{11} &= \lambda\nabla^2\phi + 2\mu(\phi,_{11} - \psi,_{13}) = \mu\{\kappa^2\nabla^2\phi - 2(\phi,_{33} + \psi,_{13})\}\\ \sigma_{33} &= \lambda\nabla^2\phi + 2\mu(\phi,_{33} - \psi,_{13}) = \mu\{\kappa^2\nabla^2\phi - 2(\phi,_{11} - \psi,_{13})\\ \sigma_{13} &= \mu\{2\phi,_{13} - \psi,_{33} + \psi,_{11}\}\end{aligned} \tag{1.103}$$

The above equations give stress and displacement components in terms of wave potentials for elastic waves propagating in x_1x_2- and x_1x_3-planes in an infinite isotropic solid medium in absence of any boundary. The effect of a plane boundary on the mechanics of elastic wave propagation is investigated later (Section 1.2.6).

1.2.4 P- and S-Waves

Important results presented above are summarized below.

Elastic waves in an infinite elastic solid can propagate in two different modes: P-wave mode and S-wave mode. When an elastic wave propagates as the P-wave, then only normal stresses (compressional or dilatational) are generated in the solid and the wave propagation speed is $c_P\left(=\sqrt{\frac{\lambda+2\mu}{\rho}}\right)$. When the elastic wave propagates as the S- wave, then only shear stresses are generated in the solid and the propagation speed is $c_S\left(=\sqrt{\frac{\mu}{\rho}}\right)$.

Wave potentials for these two types of waves, propagating in a three-dimensional space in direction **n,** are given by Equation 1.96. If the problem is simplified to an in-plane problem where the waves propagate in one plane (say x_1x_2-plane), then the wave potentials, ϕ and ψ, for these two types of waves can be written in the following form:

$$\begin{aligned}\phi(\mathbf{x},t) &= \phi(\mathbf{n}\cdot\mathbf{x} - c_Pt) = \phi(n_1x_1 + n_2x_2 - c_Pt) = \phi(x_1\cos\theta + x_2\sin\theta - c_Pt)\\ \psi(\mathbf{x},t) &= \psi(\mathbf{n}\cdot\mathbf{x} - c_St) = \psi(n_1x_1 + n_2x_2 - c_St) = \psi(x_1\cos\theta + x_2\sin\theta - c_St)\end{aligned} \tag{1.104}$$

Equation 1.104 represents waves propagating in direction **n** in the x_1x_2-plane as shown in Figure 1.16.

Displacement and stress components can be obtained from these wave potential expressions following Equation 1.100a and Equation 1.102. Note that in any plane normal to the wave propagation direction **n** the displacement and stress components are identical. In other words, every point on a plane normal to **n** has the same state of motion; these planes are called wavefronts, and the propagating P- and S-waves with plane wavefronts are called plane waves.

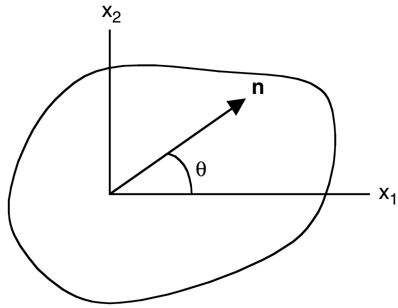

FIGURE 1.16
Elastic waves propagating in direction **n** in the x_1x_2-plane.

1.2.5 Harmonic Waves

If the time dependence of the wave motion is sin ωt, cos ωt, or $e^{\pm i\omega t}$ (i is the imaginary number $\sqrt{-1}$), then the wave is called a harmonic wave. Any function of time can be expressed as a superposition of harmonic functions by the Fourier series expansion or Fourier integral technique. If we have solutions for the harmonic time dependence, the solution for any other time dependence can be obtained by taking the inverse Fourier transform.

Unless otherwise specified, the time dependence in the subsequent analysis will be taken as $e^{-i\omega t}$. The advantage of this type of time dependence is that the problem becomes much simpler.

Equation 104 can have any expression for the functions ϕ and ψ. For harmonic time dependence $(e^{-i\omega t})$, ϕ and ψ must have the following forms:

$$\begin{aligned}\Phi(x_1,x_2,t) &= A\exp(ik_Px_1\cos\theta + ik_Px_2\sin\theta - i\omega t) = \phi(x_1,x_2)e^{-i\omega t}\\ \Psi(x_1,x_2,t) &= B\exp(ik_Sx_1\cos\theta + ik_Sx_2\sin\theta - i\omega t) = \psi(x_1,x_2)e^{-i\omega t}\end{aligned} \quad \textbf{(1.105)}$$

Comparing Equation 1.105 and Equation 1.104 one can see that

$$\begin{aligned}k_P &= \frac{\omega}{c_P}\\ k_S &= \frac{\omega}{c_S}\end{aligned} \quad \textbf{(1.106a)}$$

where k_P and k_S are P- and S-wave numbers, respectively. ω is known as the circular frequency (radian per second) and is related to the wave frequency (f in hertz or Hz) in the following manner:

$$\omega = 2\pi f \quad \textbf{(1.106b)}$$

A and B of Equation 105 are amplitudes of the wave potentials ϕ and ψ, respectively. For the time harmonic waves, the governing wave Equations 1.95 and 1.100b take the following form:

$$\nabla^2\phi + \frac{\omega^2}{c_p^2}\phi = \nabla^2\phi + k_p^2\phi = 0$$
$$\nabla^2\psi + \frac{\omega^2}{c_S^2}\psi = \nabla^2\psi + k_S^2\psi = 0 \tag{1.107a}$$

Since the time dependence $e^{-i\omega t}$ appears in every term for time harmonic motions, it is customary to ignore it while writing the expressions for potentials, displacements, and stresses.

From Equation 107a:

$$\nabla^2\phi = -k_P^2\phi$$

Therefore, from Equation 1.102b and the above relation

$$\kappa^2\nabla^2\phi = \left(\frac{c_P}{c_S}\right)^2\nabla^2\phi = \left(\frac{k_S}{k_P}\right)^2\nabla^2\phi = -k_S^2\phi \tag{1.107b}$$

Substituting Equation 1.107b into Equation 1.102 and Equation 1.103, we get the stress expressions for the harmonic waves in the x_1x_2-coordinate system:

$$\sigma_{11} = -\mu\left\{k_S^2\phi + 2(\phi,_{22} - \psi,_{12})\right\}$$
$$\sigma_{22} = -\mu\left\{k_S^2\phi + 2(\phi,_{11} + \psi,_{12})\right\} \tag{1.107c}$$
$$\sigma_{12} = \mu\{2\phi,_{12} + \psi,_{22} - \psi,_{11}\}$$

and in the x_1x_3-coordinate system:

$$\sigma_{11} = -\mu\left\{k_S^2\phi + 2(\phi,_{33} + \psi,_{13})\right\}$$
$$\sigma_{33} = -\mu\left\{k_S^2\phi + 2(\phi,_{11} - \psi,_{13})\right\} \tag{1.107d}$$
$$\sigma_{13} = \mu\{2\phi,_{13} + \psi,_{11} - \psi,_{33}\}$$

1.2.6 Interaction between Plane Waves and Stress-Free Plane Boundary

So far we have only talked about the elastic wave propagation in an unbounded elastic solid. Let us now try to understand how the presence of a stress-free surface affects the wave propagation characteristics.

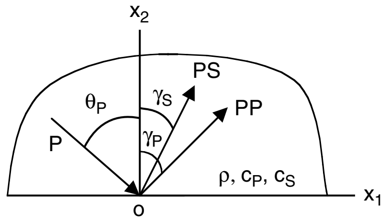

FIGURE 1.17
Reflection of the plane P-wave by a stress-free plane boundary.

1.2.6.1 P-Wave Incident on a Stress-Free Plane Boundary

First consider the effect of a stress-free boundary on the plane P-wave propagating in the direction as shown in Figure 1.17. It will be shown here that the reflected wave from the stress-free boundary will have two components: a P-wave component (denoted by PP) and an S-wave component (denoted by PS). In these notations the first letter indicates the type of wave that is incident on the stress-free surface, and the second subscript indicates the type of wave generated after the reflection at the surface.

In the absence of reflected waves PP and PS, let us first investigate if only the incident P-wave can satisfy the stress-free boundary conditions at $x_2 = 0$.

Wave potential for the incident P-wave shown in Figure 1.17 is given by

$$\phi = exp(ik_P x_1 sin\theta_P - ik_P x_2 cos\theta_P - i\omega t) = exp(ikx_1 - i\eta x_2 - i\omega t) \quad \textbf{(1.108)}$$

where $k = k_P \sin\theta_P$ and $\eta = k_P \cos\theta_P$. Amplitude of the incident wave is assumed to be 1. From Equation 1.102c one can compute the normal and shear stress components at the interface in the following form:

$$\sigma_{22} = \mu\{\kappa^2\nabla^2\phi - 2\phi,_{11}\} = \mu\{-\kappa^2(k^2 + \eta^2)\phi + 2k^2\phi\}$$
$$\sigma_{12} = \mu\{2\phi,_{12}\} = 2\mu k\eta\phi \quad \textbf{(1.109)}$$

Clearly, σ_{22} and σ_{12} are not equal to zero at $x_2 = 0$. To satisfy the stress-free boundary conditions at $x_2 = 0$ one needs to include two reflected waves, PP and PS. Readers can show that inclusion of only PP waves cannot satisfy the stress-free boundary conditions at $x_2 = 0$.

When both PP and PS waves are considered in the reflected field, then the total potential field (incident plus reflected) in the solid is given by

$$\begin{aligned}\phi &= \phi_I + \phi_R \\ &= \exp(ik_P x_1 \sin\theta_P - ik_P x_2 \cos\theta_P - i\omega t) \\ &\quad + R_{PP} \exp(ik_P x_1 \sin\gamma_P + ik_P x_2 \cos\gamma_P - i\omega t) \\ \psi &= \psi_R = R_{PS} \exp(ik_S x_1 \sin\gamma_S + ik_S x_2 \cos\gamma_S - i\omega t)\end{aligned} \quad \textbf{(1.110)}$$

Note that the ϕ expression of the above equation has two terms. The first term (ϕ_I) corresponds to the downward incident P-wave, and the second term (ϕ_R) corresponds to the upward reflected P-wave. Amplitude of the incident wave is 1, while that of the reflected P-wave is R_{PP}, and the amplitude of the reflected S-wave is R_{PS}. Inclination angles for these three waves are denoted by θ_P, γ_P and γ_S, respectively, in Figure 1.17.

From Equation 1.110 and Equation 1.102 one can compute the stress fields at $x_2 = 0$.

$$\begin{aligned}
\sigma_{22} &= \mu\{\kappa^2\nabla^2\phi - 2(\psi,_{12} + \phi,_{11})\} \\
&= \mu\{\kappa^2(-k_P^2[sin^2\theta_P + cos^2\theta_P]\phi_I - k_P^2[sin^2\gamma_P + cos^2\gamma_P]\phi_R) \\
&\quad + 2k_S^2 sin\gamma_S cos\gamma_S\psi + 2k_P^2 sin^2\theta_P\phi_I + 2k_p^2 sin^2\gamma_P\phi_R\} \\
&= \mu\{-\kappa^2k_P^2(\phi_I + \phi_R) + 2k_S^2 sin\gamma_S cos\gamma_S\psi + 2k_P^2 sin^2\theta_P\phi_I + 2k_S^2 sin^2\gamma_P\phi_R\} \\
\sigma_{12} &= \mu\{2\phi,_{12} + \psi,_{22} - \psi,_{11}\} \\
&= \mu\{2k_P^2(sin\theta_P cos\theta_P\phi_I - sin\gamma_P cos\gamma_P\phi_R) - k_S^2(cos^2\gamma_S - sin^2\gamma_S)\psi\}
\end{aligned} \tag{1.111}$$

For stress-free surface at $x_2 = 0$, both σ_{22} and σ_{12} must be zero at $x_2 = 0$. Substituting $x_2 = 0$ in Equation 1.111 and equating σ_{22} to zero one gets

$$\begin{aligned}
\sigma_{22} = \mu\Big\{&\left(2k_P^2\sin^2\theta_P - \kappa^2k_P^2\right)\exp(ik_Px_1\sin\theta_P - i\omega t) \\
&+ \left(2k_P^2\sin^2\gamma_P - \kappa^2k_P^2\right)R_{PP}\exp(ik_Px_1\sin\gamma_P - i\omega t) \\
&+ k_P^2\sin 2\gamma_S R_{PS}\exp(ik_Sx_1\sin\gamma_S - i\omega t)\Big\} = 0
\end{aligned} \tag{1.112}$$

If θ_P, γ_P and γ_S are independent of each other, then the only way one can satisfy the above equation is by equating the coefficient of each of the three terms to zero. This is not possible since the first coefficient cannot be zero for all θ_P. However, if we impose the condition

$$\exp(ik_Px_1\sin\theta_P - i\omega t) = \exp(ik_Px_1\sin\gamma_P - i\omega t) = \exp(ik_Sx_1\sin\gamma_S - i\omega t) \tag{1.113}$$

then Equation 1.112 will be satisfied if

$$\left(2k_P^2\sin^2\theta_P - \kappa^2k_P^2\right) + \left(2k_P^2\sin^2\gamma_P - \kappa^2k_P^2\right)R_{PP} + k_P^2\sin 2\gamma_S R_{PS} = 0 \tag{1.114}$$

Note that Equation 1.113 implies

$$\gamma_P = \theta_P$$
$$k_S \sin\gamma_S = k_P \sin\theta_P \Rightarrow \frac{\sin\gamma_S}{c_S} = \frac{\sin\theta_P}{c_P} \tag{1.115}$$

Equation 1.115 is known as Snell's law.

Then we introduce the following symbols:

$$k = k_P \sin\theta_P = k_S \sin\gamma_S$$
$$\eta = k_P \cos\theta_P = \sqrt{k_P^2 - k^2} \tag{1.116}$$
$$\beta = k_S \cos\gamma_S = \sqrt{k_S^2 - k^2}$$

in Equation 1.114 to obtain

$$\left(2k^2 - k_S^2\right) + \left(2k^2 - k_S^2\right)R_{PP} + 2k\beta R_{PS} = 0 \tag{1.117}$$

In Equation 1.117 we have also used the relation $\kappa^2 k_P^2 = k_S^2$, which is obvious from the definition of κ^2 (Equation 1.102b), k_P^2, and k_S^2 (Equation 1.106).

Similarly, satisfying $\sigma_{12} = 0$ at $x_2 = 0$ gives rise to the following equation:

$$2k\eta - 2k\eta R_{PP} - (\beta^2 - k^2)R_{PS} = 2k\eta - 2k\eta R_{PP} + \left(2k^2 - k_S^2\right)R_{PS} = 0 \tag{1.118}$$

Equation 1.117 and Equation 1.118 can be written in matrix form:

$$\begin{bmatrix} \left(2k^2 - k_S^2\right) & 2k\beta \\ -2k\eta & \left(2k^2 - k_S^2\right) \end{bmatrix} \begin{Bmatrix} R_{PP} \\ R_{PS} \end{Bmatrix} = \begin{Bmatrix} -\left(2k^2 - k_S^2\right) \\ -2k\eta \end{Bmatrix} \tag{1.119}$$

Equation 1.119 is then solved for R_{PP} and R_{PS}:

$$R_{PP} = \frac{4k^2\eta\beta - \left(2k^2 - k_S^2\right)^2}{4k^2\eta\beta + \left(2k^2 - k_S^2\right)^2}$$
$$R_{PS} = \frac{-4k\eta\left(2k^2 - k_S^2\right)}{4k^2\eta\beta + \left(2k^2 - k_S^2\right)^2} \tag{1.120}$$

1.2.6.2 Summary of Plane P-Wave Reflection by a Stress-Free Surface

When a plane P-wave strikes a stress-free surface at an inclination angle θ_P, as shown in Figure 1.17, a plane P-wave (PP) and a plane S-wave (PS) are generated as reflected waves to satisfy the stress-free boundary conditions at the plane surface. The angle of reflection for the P-wave is the same as the incident angle, and the angle of reflection for the S-wave is related to the incident angle by Snell's law (Equation 1.115). Potentials for the incident and reflected waves can be expressed as

$$\begin{aligned} \phi_P &= \phi_I = \exp(ikx_1 - i\eta x_2) \\ \phi_{PP} &= \phi_R = R_{PP}\exp(ikx_1 + i\eta x_2) \\ \psi_{PS} &= \psi_R = R_{PS}\exp(ikx_1 + i\beta x_2) \end{aligned} \tag{1.121}$$

with time dependence, $e^{-i\omega t}$ is implied to appear in every expression and is not shown explicitly. k, η and β are defined in Equation 1.116. Reflection coefficients R_{PP} and R_{PS} are given in Equation 1.120.

Example 1.11

Evaluate R_{PP} and R_{PS} for $\theta_P = 0$.

SOLUTION

From Equation (1.116) for $\theta_P = 0$, $k = 0$, $\eta = k_P$ and $\beta = k_S$.

Substituting these in Equation 1.120 one gets

$$R_{PP} = \frac{4k^2\eta\beta - \left(2k^2 - k_S^2\right)^2}{4k^2\eta\beta + \left(2k^2 - k_S^2\right)^2} = \frac{0 - k_S^4}{0 + k_S^4} = -1$$

$$R_{PS} = \frac{-4k\eta\left(2k^2 - k_S^2\right)}{4k^2\eta\beta + \left(2k^2 - k_S^2\right)^2} = \frac{0}{0 + k_S^4} = 0$$

For normal incidence, the reflected wave does not contain any shear wave. Incident and reflected wave potentials in this case are given by

$$\begin{aligned} \phi_P &= \phi_I = \exp(-i\eta x_2) = \exp(ik_P x_2) \\ \phi_{PP} &= \phi_R = -\exp(i\eta x_2) = -\exp(ik_P x_2) \end{aligned}$$

Example 1.12

Compute the displacement and stress fields for a plane P-wave striking a stress-free plane boundary at normal incidence ($\theta_P = 0$).

SOLUTION

As shown in the previous example for normal incidence of plane P-waves

$$\phi = \phi_P + \phi_{PP} = \exp(-ik_P x_2) - \exp(ik_P x_2)$$
$$\psi = 0$$

Hence, from Equation 1.100a

$$u_1 = \phi,_1 + \psi,_2 = 0$$
$$u_2 = \phi,_2 - \psi,_1 = -2ik_P \exp(-ik_P x_2)$$

and from Equation 1.102a

$$\sigma_{11} = \mu\{\kappa^2\nabla^2\phi + 2(\psi,_{12} - \phi,_{22})\}$$
$$\sigma_{22} = \mu\{\kappa^2\nabla^2\phi - 2(\psi,_{12} + \phi,_{11})\}$$
$$\sigma_{12} = \mu\{2\phi,_{12} + \psi,_{22} - \psi,_{11}\}$$

From Equation 1.107 and Equation 1.102b one can write

$$\kappa^2\nabla^2\phi = -\kappa^2 k_P^2\phi = -\frac{c_P^2}{c_S^2}\frac{\omega^2}{c_P^2}\phi = -k_S^2\phi$$

Substituting $\psi = 0$ and the above relation into the expressions for the stress field one gets

$$\sigma_{11} = \mu\left\{-k_S^2\phi - 2\phi,_{22}\right\} = -\mu\left\{\left(k_S^2 - 2k_P^2\right)[\exp(-ik_P x_2) - \exp(ik_P x_2)]\right\}$$
$$= 2i\mu\left(k_S^2 - 2k_P^2\right)\sin(k_P x_2)$$
$$\sigma_{22} = \mu\left\{-k_S^2\phi - 2\phi,_{11}\right\} = -\mu k_S^2[\exp(-ik_P x_2) - \exp(ik_P x_2)]$$
$$= 2i\mu k_S^2 \sin(k_P x_2)$$
$$\sigma_{12} = \mu\{2\phi,_{12}\} = 0$$

Note that all stress components vanish at the boundary at $x_2 = 0$.

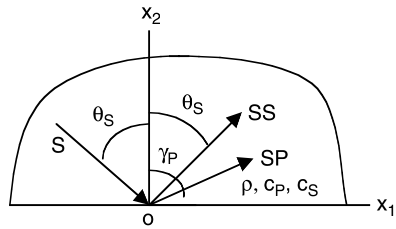

FIGURE 1.18
Reflection of the plane S-wave by a stress-free plane boundary.

1.2.6.3 Shear Wave Incident on a Stress-Free Plane Boundary

Figure 1.18 shows a shear wave incident on a stress-free plane boundary at an angle θ_S. Following a similar analysis as the P-wave incidence case, one can show that for S-wave incidence the reflected wave must also contain both S-wave and P-wave components to satisfy the stress-free boundary conditions. The two reflected waves are denoted by SS and SP, respectively. The wave potentials corresponding to the incident S and reflected SS and SP waves are

$$\begin{aligned} \psi_S &= \psi_I = \exp(ikx_1 - i\beta x_2) \\ \phi_{SP} &= \phi_R = R_{SP}\exp(ikx_1 + i\eta x_2) \\ \psi_{SS} &= \psi_R = R_{SS}\exp(ikx_1 + i\beta x_2) \end{aligned} \tag{1.122}$$

In Equation 1.122 time dependence $e^{-i\omega t}$ is implied and

$$\begin{aligned} k &= k_S \sin\theta_S = k_P \sin\gamma_P \\ \eta &= k_P \cos\gamma_P = \sqrt{k_P^2 - k^2} \\ \beta &= k_S \cos\theta_S = \sqrt{k_S^2 - k^2} \end{aligned} \tag{1.123}$$

θ_S and γ_P satisfy Snell's law,

$$\frac{\sin\theta_S}{c_S} = \frac{\sin\gamma_P}{c_P} \tag{1.124}$$

Note that for $\theta_S = \sin^{-1}\left(\frac{c_S}{c_P}\right)$ the angle γ_P becomes 90°. This angle is called the *critical angle*. Since $c_S < c_P$, the critical angle has a real value. If the angle of incidence exceeds the critical angle value, the reflected P-wave, as shown in Figure 1.18, is not generated since γ_P then becomes imaginary.

Reflection coefficients R_{SP} and R_{SS} can be obtained by satisfying the stress-free boundary conditions at $x_2 = 0$.

From Equation 1.102c,

$$\sigma_{22} = \mu\left\{\kappa^2\nabla^2\phi - 2(\psi,_{12} + \phi,_{11})\right\} = -\mu\left\{k_S^2\phi + 2(\psi,_{12} + \phi,_{11})\right\}$$
$$= -\mu\left\{\left(k_S^2 - 2k^2\right)^2 (R_{SP}e^{ikx_1 + i\eta x_2}) - 2k\beta(-e^{ikx_1 - i\beta x_2} + R_{SS}e^{ikx_1 + i\beta x_2})\right\}$$
$$\sigma_{12} = \mu\{2\phi,_{12} + \psi,_{22} - \psi,_{11}\} = \mu\{(-2k\eta)R_{SP}e^{ikx_1 + i\eta x_2} + (k^2 - \beta^2)(e^{ikx_1 - i\beta x_2} + R_{SS}e^{ikx_1 + i\beta x_2})$$

(1.125)

Since the two stress components of Equation 1.125 must be zero at $x_2 = 0$,

$$\sigma_{22}\big|_{x_2=0} = -\mu\left\{\left(k_S^2 - 2k^2\right)(R_{SP}e^{ikx_1}) - 2k\beta(-e^{ikx_1} + R_{SS}e^{ikx_1})\right\}$$
$$= \mu\left\{\left(2k^2 - k_S^2\right)R_{SP} + 2k\beta(-1 + R_{SS})\right\}e^{ikx_1} = 0$$
$$\sigma_{12}\big|_{x_2=0} = \mu\{(-2k\eta)R_{SP}e^{ikx_1} + (k^2 - \beta^2)(e^{ikx_1} + R_{SS}e^{ikx_1})\}$$
$$= \mu\left\{-2k\eta R_{SP} + \left(2k^2 - k_S^2\right)(1 + R_{SS})\right\}e^{ikx_1} = 0$$

The two equations above will be satisfied for all x_1 if

$$\begin{bmatrix} \left(2k^2 - k_S^2\right) & 2k\beta \\ -2k\eta & \left(2k^2 - k_S^2\right) \end{bmatrix} \begin{Bmatrix} R_{SP} \\ R_{SS} \end{Bmatrix} = \begin{Bmatrix} 2k\beta \\ -\left(2k^2 - k_S^2\right) \end{Bmatrix} \qquad \textbf{(1.126)}$$

Equation 1.126 can be solved for R_{SP} and R_{SS} to obtain

$$R_{SP} = \frac{4k\beta\left(2k^2 - k_S^2\right)}{4k^2\eta\beta + \left(2k^2 - k_S^2\right)^2}$$
$$R_{SS} = \frac{4k^2\eta\beta - \left(2k^2 - k_S^2\right)^2}{4k^2\eta\beta + \left(2k^2 - k_S^2\right)^2} \qquad \textbf{(1.127)}$$

Example 1.13

Evaluate R_{SP} and R_{SS} for $\theta_S = 0$

SOLUTION

From Equation 1.123 for $\theta_S = 0$, we get $k = 0$, $\eta = k_P$, and $\beta = k_S$.

Substituting these in Equation 1.127 one gets

$$R_{SP} = \frac{4k\beta\left(2k^2 - k_S^2\right)}{4k^2\eta\beta + \left(2k^2 - k_S^2\right)^2} = 0$$

$$R_{SS} = \frac{4k^2\eta\beta - \left(2k^2 - k_S^2\right)^2}{4k^2\eta\beta + \left(2k^2 - k_S^2\right)^2} = -1$$

For normal incidence the reflected wave does not contain any P-waves. The incident and reflected wave potentials for this case are given by

$$\psi_S = \psi_I = \exp(-ik_S x_2)$$

$$\psi_{SS} = \psi_R = -\exp(ik_S x_2)$$

Example 1.14

Compute displacement and stress fields for the in-plane S-wave striking a stress-free plane boundary at normal incidence ($\theta_S = 0$).

SOLUTION

As shown in the previous example, for normal incidence of the S-wave, the wave potentials are given by

$$\psi = \psi_I + \psi_R = \exp(-ik_S x_2) - \exp(ik_S x_2)$$

$$\phi = 0$$

Hence, from Equation 1.100a

$$u_1 = \phi,_1 + \psi,_2 = -ik_S\{e^{-ik_S x_2} + e^{ik_S x_2}\} = -2ik_S\cos(k_S x_2)$$

$$u_2 = \phi,_2 - \psi,_1 = 0$$

and from Equation 1.102

$$\sigma_{11} = \mu\{\kappa^2\nabla^2\phi + 2(\psi,_{12} - \phi,_{22})\}$$

$$\sigma_{22} = \mu\{\kappa^2\nabla^2\phi - 2(\psi,_{12} + \phi,_{11})\}$$

$$\sigma_{12} = \mu\{2\phi,_{12} + \psi,_{22} - \psi,_{11}\}$$

Substituting $\phi = 0$ in the above expressions one gets

$$\sigma_{11} = 2\mu\psi,_{12} = 0$$
$$\sigma_{22} = -2\mu\psi,_{12} = 0$$
$$\sigma_{12} = \mu\{\psi,_{22} - \psi,_{11}\} = -\mu k_S^2\{e^{-ik_S x_1} - e^{ik_S x_2}\} = 2i\mu k_S^2 \sin(k_S x_2)$$

Note that all stress components vanish at the boundary at $x_2 = 0$.

1.2.7 Out-of-Plane or Antiplane Motion — Shear Horizontal Wave

In earlier sections we have discussed the in-plane motion, where the displacements and wave propagation directions are confined in the x_1x_2-plane (see Section 1.2.3). Hence, x_3-components of displacement and wave velocity are zero. If the waves propagate in the x_1x_2-plane, but the particles have only x_3 component of nonzero displacement, then the wave motion is called antiplane or out-of-plane motion. For antiplane problems $u_1 = u_2 = 0$ and $u_3 = u_3(x_1, x_2, t)$.

Substituting the above displacement components into Navier's equation (Equation 1.79) and carrying out the dot and cross products (as given in Table 1.2), the following equations are obtained when the body force is absent:

$$(\lambda + 2\mu)\cdot 0 - \mu\cdot(-u_{3,11} - u_{3,22}) = \rho\ddot{u}_3$$
$$\Rightarrow u_{3,11} + u_{3,22} - \frac{\rho}{\mu}\ddot{u}_3 = 0 \qquad \textbf{(1.128)}$$
$$\Rightarrow \nabla^2 u_3 - \frac{1}{c_S^2}\ddot{u}_3 = 0$$

For harmonic waves, like before, we assume $e^{-i\omega t}$ time dependence and the above equation is simplified to

$$\nabla^2 u_3 + k_S^2 u_3 = 0 \qquad \textbf{(1.129)}$$

Note that the wave Equation 1.128 and Equation 1.129 are similar to Equation 1.100b and Equation 1.107, respectively. The only difference is in the definition of the unknown variable. For Equation 1.100b and Equation 1.107 the variables are the wave potentials, and for Equation 1.128 and Equation 1.129 it is the displacement. Following similar arguments as before one can show that Equation 1.128 gives a wave motion with velocity c_S like the shear wave. From the strain-displacement and stress-strain relations (for isotropic material) one can also show that the displacement field

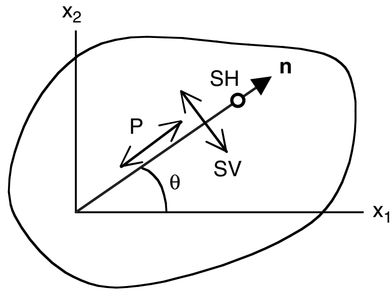

FIGURE 1.19
Particle displacement directions for a P, SV, or SH wave propagating in direction **n**. Particle motion for the SH-wave is in the x_3-direction, denoted by a circle.

$u_1 = u_2 = 0$ and $u_3 = u_3(x_1, x_2, t)$ can only produce shear strain (γ_{13} and γ_{23}) and shear stress (σ_{13} and σ_{23}). It should be noted here that the strain and stress fields corresponding to the in-plane shear wave, discussed earlier, produce nonzero shear strain (γ_{12}) and shear stress (σ_{12}). The antiplane shear wave and in-plane shear wave have a few things in common — they propagate with the same speed (c_S) and generate only shear stress in the medium. They also produce different components of nonzero shear stress because they have different particle displacement or polarization directions as shown in Figure 1.19. When a wave propagates in direction **n** in the x_1x_2-plane and the particle displacement is in the x_3-direction, then this antiplane shear wave is called the shear horizontal (SH) wave. If the particle displacement is normal to the wave propagation direction but lies in the same plane (in this case the x_1x_2-plane), then it is called a shear vertical (SV) wave, and when the particle displacement is parallel to the wave propagation direction, then the wave is a P-wave.

Note that Stokes-Helmholtz decomposition was not necessary for solving the antiplane problem. Direct substitution of $u_1 = u_2 = 0$ and $u_3 = u_3(x_1, x_2, t)$ into Navier's equation simplified it in the form of a wave equation, Equation 1.128 and Equation 1.129. Its solution for a harmonic wave is given by, as before,

$$u_3 = A\exp(ikx_1 + i\beta x_2 - i\omega t) \tag{1.130}$$

"A" of Equation 1.130 represents the amplitude of the wave; k and β must satisfy the relation $k^2 + \beta^2 = k_S^2$. In the subsequent analyses the time dependence $e^{-i\omega t}$ will be implied and will not be explicitly written.

1.2.7.1 Interaction of SH-Wave and Stress-Free Plane Boundary

Let us consider a plane SH-wave of unit amplitude striking a stress-free plane boundary at $x_2 = 0$ at an angle θ_S as shown in Figure 1.20. If the reflected

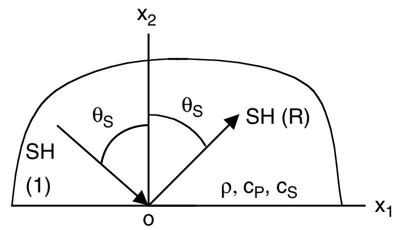

FIGURE 1.20
SH-wave reflected by a stress free boundary.

wave amplitude is R and angle of reflection is θ_S, then the total displacement field is given by

$$u_3 = \exp(ikx_1 - i\beta x_2) + R\exp(ikx_1 + i\beta x_2) \quad \textbf{(1.131)}$$

Time dependence $e^{-i\omega t}$ is implied. k and β have been defined in Equation 1.123.
The stress field can be obtained from this displacement field:

$$\sigma_{23} = 2\mu\varepsilon_{23} = 2\mu \times \frac{1}{2}(u_{2,3} + u_{3,2}) = \mu u_{3,2} = i\beta\mu\{-e^{-i\beta x_2} + Re^{i\beta x_2}\}e^{ikx_1} \quad \textbf{(1.132)}$$

at $x_2 = 0$, $\sigma_{23} = 0$; hence,

$$\sigma_{23}\big|_{x_2=0} = i\beta\mu\{-1 + R\}e^{ikx_1} = 0$$
$$\Rightarrow R = 1$$

The total displacement and stress fields are then given by

$$u_3 = \exp(ikx_1 - i\beta x_2) + \exp(ikx_1 + i\beta x_2) = \{e^{-i\beta x_2} + e^{i\beta x_2}\}e^{ikx_1} = 2\cos(\beta x_2)e^{ikx_1}$$
$$\sigma_{23} = i\beta\mu\{-e^{-i\beta x_2} + e^{i\beta x_2}\}e^{ikx_1} = -2\beta\mu\sin(\beta x_2)e^{ikx_1}$$
$$\sigma_{13} = \mu u_{3,1} = ik\mu\{e^{-i\beta x_2} + e^{i\beta x_2}\}e^{ikx_1} = 2ik\mu\cos(\beta x_2)e^{ikx_1}$$

Note, that at the boundary, σ_{23} is zero but σ_{13} is not.

From the above analysis it is clear that compared to in-plane waves (P and SV) the antiplane wave (SH) is much simpler to analyze, because no mode conversion occurs at the reflecting surface and the reflection coefficient ($R = 1$) has a much simpler expression than those given in Equation 1.120 or Equation 1.127. Also, the antiplane analysis does not require introduction of Stokes-Helmholtz potential functions, unlike the P-SV case. Because of these

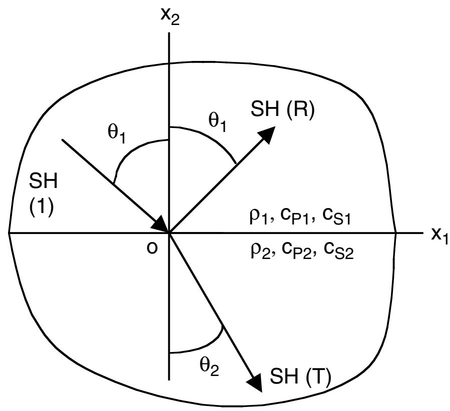

FIGURE 1.21
Reflection and transmission of the SH-wave at a plane interface.

simplicities, antiplane problems have been academically popular, but their practical applications are limited.

1.2.7.2 Interaction of SH-Wave and a Plane Interface

Let us consider the case where the SH-wave strikes a plane interface between two isotropic elastic solids as shown in Figure 1.21. Material properties (density, P-wave speed, and S-wave speed) for the two elastic solids are denoted by ρ_i, c_{Pi} and c_{Si}, where $i = 1$ and 2 for the two materials. The amplitudes of the incident, reflected, and transmitted waves are 1, R, and T, respectively. The angles of incidence and reflection are denoted by θ_1, while the transmission angle is θ_2, as shown in Figure 1.21.

To satisfy the displacement (u_3) and stress (σ_{23}) continuity conditions across the interface at $x_2 = 0$ for all x_1, the x_1-dependence term for all three waves must be the same. This condition gives rise to Snell's law:

$$\frac{\sin\theta_1}{c_{S1}} = \frac{\sin\theta_2}{c_{S2}} \quad \textbf{(1.133)}$$

The displacement fields corresponding to the incident, reflected, and transmitted waves then become

$$\begin{aligned} u_{3I} &= e^{ikx_1 - i\beta_1 x_2} \\ u_{3R} &= Re^{ikx_1 + i\beta_1 x_2} \\ u_{3T} &= Te^{ikx_1 - i\beta_2 x_2} \end{aligned} \quad \textbf{(1.134)}$$

In Equation 1.134 subscripts I, R, and T correspond to incident, reflected, and transmitted fields, respectively. Reflected and transmitted wave amplitudes are denoted by R and T, respectively, while the incident wave amplitude is 1.

Note that

$$\begin{aligned} k &= k_{S1}\sin\theta_1 = k_{S2}\sin\theta_2 \\ \beta_1 &= k_{S1}\cos\theta_1 \\ \beta_2 &= k_{S2}\cos\theta_2 \\ k_{S1} &= \frac{\omega}{c_{S1}}, \quad k_{S2} = \frac{\omega}{c_{S2}} \end{aligned} \tag{1.135}$$

From displacement and stress continuity at $x_2 = 0$ one can write

$$\begin{aligned} &(1+R)e^{ikx_1} = Te^{ikx_1} && \Rightarrow\ 1+R = T \\ &\mu_1\beta_1(-1+R)e^{ikx_1} = -\mu_2\beta_2 Te^{ikx_1} && \Rightarrow -1+R = -QT \end{aligned} \tag{1.136}$$

where

$$Q = \frac{\mu_2\beta_2}{\mu_1\beta_1} \tag{1.137}$$

Equation 1.136 can be solved for R and T,

$$\begin{aligned} R &= \frac{1-Q}{1+Q} \\ T &= \frac{2}{1+Q} \end{aligned} \tag{1.138a}$$

Note that when the two materials are identical $Q = 1$, $R = 0$, and $T = 1$. This is expected since in this special case there is no interface.

For normal incidence ($\theta_1 = \theta_2 = 0$) from Equation 1.135, $\beta_1 = k_{S1}$ and $\beta_2 = k_{S2}$. Therefore,

$$Q = \frac{\mu_2\beta_2}{\mu_1\beta_1} = \frac{\mu_2 k_{S2}}{\mu_1 k_{S1}} = \frac{\rho_2 c_{S2}^2 \dfrac{\omega}{c_{S2}}}{\rho_1 c_{S1}^2 \dfrac{\omega}{c_{S1}}} = \frac{\rho_2 c_{S2}}{\rho_1 c_{S1}} = \frac{Z_{2S}}{Z_{1S}}$$

then

$$\begin{aligned} R &= \frac{1-Q}{1+Q} = \frac{Z_{1S}-Z_{2S}}{Z_{1S}+Z_{2S}} \\ T &= \frac{2}{1+Q} = \frac{2Z_{1S}}{Z_{1S}+Z_{2S}} \end{aligned} \tag{1.138b}$$

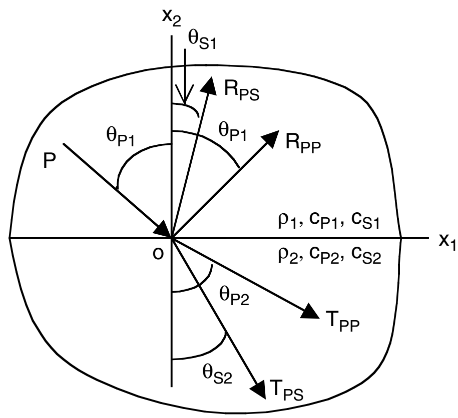

FIGURE 1.22
Reflected and transmitted waves near an interface for P-wave incidence.

1.2.8 Interaction of P- and SV-Waves with Plane Interface

These in-plane problems are more complex compared to the SH problem analyzed in the previous section, because of the mode conversion, as one can see below. First, the problem of P-wave incidence is solved.

1.2.8.1 P-Wave Striking an Interface

Figure 1.22 shows a plane P-wave of unit amplitude striking a plane interface between two linear elastic isotropic solids. Both reflected and transmitted waves have P- and SV-wave components and their amplitudes are denoted by R_{PP}, R_{PS}, T_{PP}, and T_{PS}.

Wave potentials for these five types of waves are given by

$$\begin{aligned}
\phi_{IP} &= e^{ikx_1 - i\eta_1 x_2} \\
\phi_{RPP} &= R_{PP} e^{ikx_1 + i\eta_1 x_2} \\
\phi_{TPP} &= T_{PP} e^{ikx_1 - i\eta_2 x_2} \\
\psi_{RPS} &= R_{PS} e^{ikx_1 + i\beta_1 x_2} \\
\psi_{TPS} &= T_{PS} e^{ikx_1 - i\beta_2 x_2}
\end{aligned} \tag{1.139}$$

where subscripts I, R, and T are used to indicate incident, reflected, and transmitted waves, respectively, and

$$
\begin{aligned}
&k = k_{P1}\sin\theta_{P1} = k_{S1}\sin\theta_{S1} = k_{P2}\sin\theta_{P2} = k_{S2}\sin\theta_{S2}\\
&\eta_1 = k_{P1}\cos\theta_{P1}\\
&\eta_2 = k_{P2}\cos\theta_{P2}\\
&\beta_1 = k_{S1}\cos\theta_{S1}\\
&\beta_2 = k_{S2}\cos\theta_{S2}\\
&k_{P1} = \frac{\omega}{c_{P1}}, \quad k_{P2} = \frac{\omega}{c_{P2}}, \quad k_{S1} = \frac{\omega}{c_{S1}}, \quad k_{S2} = \frac{\omega}{c_{S2}}
\end{aligned}
\tag{1.140}
$$

From the continuity of displacement components u_1 and u_2 and stress components σ_{12} and σ_{22} across the interface we get

$$
\begin{aligned}
&ik(1+R_{PP}) + i\beta_1 R_{PS} = ikT_{PP} - i\beta_2 T_{PS}\\
&i\eta_1(-1+R_{PP}) - ikR_{PS} = -i\eta_2 T_{PP} - ikT_{PS}\\
&\mu_1\left\{2k\eta_1(1-R_{PP}) - \beta_1^2 R_{PS} + k^2 R_{PS}\right\} = \mu_2\left\{2k\eta_2 T_{PP} - \beta_2^2 T_{PS} + k^2 T_{PS}\right\}\\
&-\mu_1\left\{\left(k_{S1}^2 - 2k^2\right)(1+R_{PP}) - 2k\beta_1 R_{PS}\right\} = -\mu_2\left\{\left(k_{S2}^2 - 2k^2\right)T_{PP} + 2k\beta_2 T_{PS}\right\}
\end{aligned}
$$

The above equations can be written in the following form:

$$
\begin{bmatrix}
k & \beta_1 & -k & \beta_2\\
\eta_1 & -k & \eta_2 & k\\
2k\eta_1 & -\left(2k^2 - k_{S1}^2\right) & 2k\eta_2\mu_{21} & \left(2k^2 - k_{S2}^2\right)\mu_{21}\\
\left(2k^2 - k_{S1}^2\right) & 2k\beta_1 & -\left(2k^2 - k_{S2}^2\right)\mu_{21} & 2k\beta_2\mu_{21}
\end{bmatrix}
\begin{Bmatrix} R_{PP}\\ R_{PS}\\ T_{PP}\\ T_{PS} \end{Bmatrix}
=
\begin{Bmatrix} -k\\ \eta_1\\ 2k\eta_1\\ -\left(2k^2 - k_{S1}^2\right) \end{Bmatrix}
\tag{1.141}
$$

In Equation 1.141 $\mu_{21} = \frac{\mu_2}{\mu_1}$; this equation set can be solved for R_{PP}, R_{PS}, T_{PP} and T_{PS}.

Example 1.15

For normal P-wave incidence ($\theta_{P1} = 0$ in Figure 1.22) calculate the reflected and transmitted wave amplitudes and potential fields in the two solids.

SOLUTION

From Equation 1.140 one can write for $\theta_{P1} = 0$

$$k = k_{P1}\sin\theta_{P1} = k_{S1}\sin\theta_{S1} = k_{P2}\sin\theta_{P2} = k_{S2}\sin\theta_{S2} = 0$$
$$\Rightarrow \theta_{S1} = \theta_{P2} = \theta_{S2} = 0$$
$$\eta_1 = k_{P1}\cos\theta_{P1} = k_{P1}$$
$$\eta_2 = k_{P2}\cos\theta_{P2} = k_{P2}$$
$$\beta_1 = k_{S1}\cos\theta_{S1} = k_{S1}$$
$$\beta_2 = k_{S2}\cos\theta_{S2} = k_{S2}$$

Equation 1.141 is simplified to

$$\begin{bmatrix} 0 & k_{S1} & 0 & k_{S2} \\ k_{P1} & 0 & k_{P2} & 0 \\ 0 & k_{S1}^2 & 0 & -k_{S2}^2\mu_{21} \\ -k_{S1}^2 & 0 & k_{S2}^2\mu_{21} & 0 \end{bmatrix} \begin{Bmatrix} R_{PP} \\ R_{PS} \\ T_{PP} \\ T_{PS} \end{Bmatrix} = \begin{Bmatrix} 0 \\ k_{P1} \\ 0 \\ k_{S1}^2 \end{Bmatrix}$$

From the first and third algebraic equations of the above matrix equation one gets $R_{PS} = T_{PS} = 0$; the remaining second and fourth equations form a two-by-two system of equations

$$\begin{bmatrix} k_{P1} & k_{P2} \\ -k_{S1}^2 & k_{S2}^2\mu_{21} \end{bmatrix} \begin{Bmatrix} R_{PP} \\ T_{PP} \end{Bmatrix} = \begin{Bmatrix} k_{P1} \\ k_{S1}^2 \end{Bmatrix}$$

that can be easily solved to obtain

$$R_{PP} = \frac{k_{P1}k_{S2}^2\mu_{21} - k_{P2}k_{S1}^2}{k_{P1}k_{S2}^2\mu_{21} + k_{P2}k_{S1}^2} = \frac{1 - \dfrac{k_{P2}k_{S1}^2}{k_{P1}k_{S2}^2\mu_{21}}}{1 + \dfrac{k_{P2}k_{S1}^2}{k_{P1}k_{S2}^2\mu_{21}}} = \frac{1 - \dfrac{\mu_1 c_{P1} c_{S2}^2}{\mu_2 c_{P2} c_{S1}^2}}{1 + \dfrac{\mu_1 c_{P1} c_{S2}^2}{\mu_2 c_{P2} c_{S1}^2}} = \frac{1 - \dfrac{\rho_1 c_{P1}}{\rho_2 c_{P2}}}{1 + \dfrac{\rho_1 c_{P1}}{\rho_2 c_{P2}}}$$

$$\Rightarrow R_{PP} = \frac{\rho_2 c_{P2} - \rho_1 c_{P1}}{\rho_2 c_{P2} + \rho_1 c_{P1}} = \frac{Z_2 - Z_1}{Z_2 + Z_1}$$

$$T_{PP} = \frac{2k_{P1}k_{S1}^2}{k_{P1}k_{S2}^2\mu_{21} + k_{P2}k_{S1}^2} = \frac{\dfrac{2k_{P1}k_{S1}^2}{k_{P1}k_{S2}^2\mu_{21}}}{1 + \dfrac{k_{P2}k_{S1}^2}{k_{P1}k_{S2}^2\mu_{21}}} = \frac{2\dfrac{\mu_1 c_{S2}^2}{\mu_2 c_{S1}^2}}{1 + \dfrac{\mu_1 c_{P1} c_{S2}^2}{\mu_2 c_{P2} c_{S1}^2}} = \frac{2\dfrac{\rho_1}{\rho_2}}{1 + \dfrac{\rho_1 c_{P1}}{\rho_2 c_{P2}}} \tag{1.142}$$

$$\Rightarrow T_{PP} = \frac{\rho_1}{\rho_2}\frac{2\rho_2 c_{P2}}{\rho_2 c_{P2} + \rho_1 c_{P1}} = \frac{\rho_1}{\rho_2}\frac{2Z_2}{Z_2 + Z_1}$$

In Equation 1.142 $Z_i = \rho_i c_{Pi}$ is known as the acoustic impedance. Note that when both materials are the same then $R_{PP} = 0$ and $T_{PP} = 1$.

For normal incidence of a plane P-wave at the interface of two materials

$$\phi_1 = \phi_{IP} + \phi_{RPP} = e^{-ik_{P1}x_2} + \frac{Z_2 - Z_1}{Z_2 + Z_1} e^{ik_{P1}x_2}$$

$$\phi_2 = \phi_{TPP} = \frac{\rho_1}{\rho_2} \frac{2Z_2}{Z_2 + Z_1} e^{-ik_{P2}x_2}$$

$$\psi_1 = \psi_2 = 0$$

Example 1.16

Compute stress and displacement fields in the two solids for normal P-wave incidence ($\theta_{P1} = 0$ in Figure 1.22).

SOLUTION

Potential fields for this case are shown in the above example. From these potential fields the displacement and stress components are obtained using the following relations (in this case $\psi = 0$):

$$u_1 = \phi_{,1} + \psi_{,2} = \phi_{,1}$$

$$u_2 = \phi_{,2} - \psi_{,1} = \phi_{,2}$$

$$\sigma_{11} = -\mu\left\{k_S^2\phi + 2\phi_{,22} - 2\psi_{,12}\right\} = -\mu\left\{k_S^2\phi + 2\phi_{,22}\right\}$$

$$\sigma_{22} = -\mu\left\{k_S^2\phi + 2\phi_{,11} + 2\psi_{,12}\right\} = -\mu\left\{k_S^2\phi + 2\phi_{,11}\right\}$$

$$\sigma_{12} = \mu\left\{2\phi_{,12} + \psi_{,22} - \psi_{,11}\right\} = 2\mu\phi_{,12}$$

Hence, for solid 1

$$u_1 = \phi_{,1} = 0$$

$$u_2 = \phi_{,2} = ik_{P1}\{-e^{-ik_{P1}x_2} + R_{PP}e^{ik_{P1}x_2}\}$$

$$\sigma_{11} = -\mu\left\{k_S^2\phi + 2\phi_{,22}\right\} = \mu_1\left(2k_{P1}^2 - k_{S1}^2\right)(e^{-ik_{P1}x_2} + R_{PP}e^{ik_{P1}x_2})$$

$$\sigma_{22} = -\mu\left\{k_S^2\phi + 2\phi_{,11}\right\} = -\mu_1 k_{S1}^2(e^{-ik_{P1}x_2} + R_{PP}e^{ik_{P1}x_2})$$

$$\sigma_{12} = 2\mu\phi_{,12} = 0$$

and for solid 2

$$u_1 = \phi_{,1} = 0$$

$$u_2 = \phi_{,2} = -ik_{P2}T_{PP}e^{-ik_{P2}x_2}$$

$$\sigma_{11} = -\mu\left\{k_S^2\phi + 2\phi_{,22}\right\} = \mu_2\left(2k_{P2}^2 - k_{S2}^2\right)T_{PP}e^{-ik_{P2}x_2}$$

$$\sigma_{22} = -\mu\left\{k_S^2\phi + 2\phi_{,11}\right\} = -\mu_2 k_{S2}^2 T_{PP}e^{-ik_{P2}x_2}$$

$$\sigma_{12} = 2\mu\phi_{,12} = 0$$

where R_{PP} and T_{PP} have been defined in Equation 1.142.

Note that at the interface (x_2 = 0) nonzero displacement and stress components can be computed from the expressions given for solids 1 and 2. Substituting x_2 = 0 in the expressions of the first solid one gets

$$u_2 = ik_{P1}\{-1 + R_{PP}\} = ik_{P1}\left\{-1 + \frac{Z_2 - Z_1}{Z_2 + Z_1}\right\} = \frac{-2ik_{P1}Z_1}{Z_2 + Z_1} = -\frac{2i\omega\rho_1}{Z_2 + Z_1}$$

$$\sigma_{11} = \mu_1\left(2k_{P1}^2 - k_{S1}^2\right)(1 + R_{PP}) = \left(\frac{2}{\kappa_1^2} - 1\right)\frac{2\rho_1\omega^2 Z_2}{Z_2 + Z_1}$$

$$\sigma_{22} = -\mu_1 k_{S1}^2(1 + R_{PP}) = -\frac{2\rho_1\omega^2 Z_2}{Z_2 + Z_1}$$

If $x_2 = 0$ is substituted in the expressions of the second solid, then we obtain

$$u_2 = -ik_{P2}T_{PP} = -i\frac{\omega}{c_{P2}}\frac{\rho_1}{\rho_2}\frac{2Z_2}{Z_2 + Z_1} = -\frac{2i\omega\rho_1}{Z_2 + Z_1}$$

$$\sigma_{11} = \mu_2\left(2k_{P2}^2 - k_{S2}^2\right)T_{PP} = \left(\frac{2}{\kappa_2^2} - 1\right)\frac{2\rho_1\omega^2 Z_2}{Z_2 + Z_1}$$

$$\sigma_{22} = -\mu_2 k_{S2}^2 T_{PP} = -\frac{2\rho_1\omega^2 Z_2}{Z_2 + Z_1}$$

Note that u_2 and σ_{22} are continuous across the interface, but σ_{11} is not since $\kappa_1\left(= \frac{c_{P1}}{c_{S1}}\right)$ and $\kappa_2\left(= \frac{c_{P2}}{c_{S2}}\right)$ are different.

1.2.8.2 SV-Wave Striking an Interface

Figure 1.23 shows a plane SV-wave of unit amplitude striking a plane interface between two linear elastic isotropic solids. Both reflected and transmitted

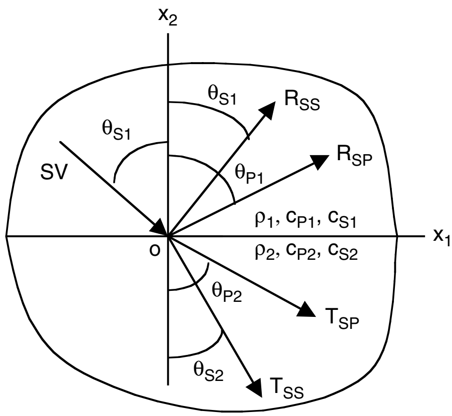

FIGURE 1.23
Reflected and transmitted waves at an interface for SV-wave incidence.

waves have P- and SV-wave components, and their amplitudes are denoted by R_{SP}, R_{SS}, T_{SP} and T_{SS}.

Wave potentials for these five types of waves are as follows:

$$\begin{aligned}
\psi_{IS} &= e^{ikx_1 - i\beta_1 x_2} \\
\phi_{RSP} &= R_{SP} e^{ikx_1 + i\eta_1 x_2} \\
\phi_{TSP} &= T_{SP} e^{ikx_1 - i\eta_2 x_2} \\
\psi_{RSS} &= R_{SS} e^{ikx_1 + i\beta_1 x_2} \\
\psi_{TSS} &= T_{SS} e^{ikx_1 - i\beta_2 x_2}
\end{aligned} \tag{1.143}$$

where subscripts I, R, and T are used to indicate incident, reflected, and transmitted waves, respectively. k, η_i and β_i are defined in Equation 1.140.

From continuity of displacement components (u_1 and u_2) and stress components (σ_{12} and σ_{22}) across the interface we get

$$\begin{aligned}
&ikR_{SP} + i\beta_1(-1 + R_{SS}) = ikT_{SP} - i\beta_2 T_{SS} \\
&i\eta_1 R_{SP} - ik(1 + R_{SS}) = -i\eta_2 T_{SP} - ikT_{SS} \\
&\mu_1\left\{-2k\eta_1 R_{SP} + \left(2k^2 - k_{S1}^2\right)(1 + R_{SS})\right\} = \mu_2\left\{2k\eta_2 T_{SP} + \left(2k^2 - k_{S2}^2\right)T_{SS}\right\} \\
&-\mu_1\left\{\left(k_{S1}^2 - 2k^2\right)R_{SP} + 2k\beta_1(1 - R_{SS})\right\} = -\mu_2\left\{\left(k_{S2}^2 - 2k^2\right)T_{SP} + 2k\beta_2 T_{SS}\right\}
\end{aligned}$$

The above equations can be also written in the following form:

$$\begin{bmatrix} k & \beta_1 & -k & \beta_2 \\ \eta_1 & -k & \eta_2 & k \\ 2k\eta_1 & -\left(2k^2 - k_{S1}^2\right) & 2k\eta_2\mu_{21} & \left(2k^2 - k_{S2}^2\right)\mu_{21} \\ \left(2k^2 - k_{S1}^2\right) & 2k\beta_1 & -\left(2k^2 - k_{S2}^2\right)\mu_{21} & 2k\beta_2\mu_{21} \end{bmatrix} \begin{Bmatrix} R_{SP} \\ R_{SS} \\ T_{SP} \\ T_{SS} \end{Bmatrix} = \begin{Bmatrix} \beta_1 \\ k \\ \left(2k^2 - k_{S1}^2\right) \\ 2k\beta_1 \end{Bmatrix} \tag{1.144}$$

In Equation 1.144 $\mu_{21} = \frac{\mu_2}{\mu_1}$; this equation can be solved for R_{SP}, R_{SS}, T_{SP}, and T_{SS}.

Example 1.17

For normal SV-wave incidence ($\theta_{S1} = 0$ in Figure 1.23) calculate the reflected and transmitted wave amplitudes and potential fields in the two solids.

SOLUTION

From Equation 1.140 one can write for $\theta_{S1} = 0$

$$k = k_{P1}\sin\theta_{P1} = k_{S1}\sin\theta_{S1} = k_{P2}\sin\theta_{P2} = k_{S2}\sin\theta_{S2} = 0$$

$$\Rightarrow \theta_{P1} = \theta_{P2} = \theta_{S2} = 0$$

$$\eta_1 = k_{P1}\cos\theta_{P1} = k_{P1} \qquad \eta_2 = k_{P2}\cos\theta_{P2} = k_{P2}$$

$$\beta_1 = k_{S1}\cos\theta_{S1} = k_{S1} \qquad \beta_2 = k_{S2}\cos\theta_{S2} = k_{S2}$$

Hence, Equation 1.144 is simplified to

$$\begin{bmatrix} 0 & k_{S1} & 0 & k_{S2} \\ k_{P1} & 0 & k_{P2} & 0 \\ 0 & k_{S1}^2 & 0 & -k_{S2}^2\mu_{21} \\ k_{S1}^2 & 0 & -k_{S2}^2\mu_{21} & 0 \end{bmatrix} \begin{Bmatrix} R_{SP} \\ R_{SS} \\ T_{SP} \\ T_{SS} \end{Bmatrix} = \begin{Bmatrix} k_{S1} \\ 0 \\ -k_{S1}^2 \\ 0 \end{Bmatrix}$$

From the second and fourth algebraic equations of the above matrix equation one gets $R_{SP} = T_{SP} = 0$; the remaining first and third equations form a two-by-two system of equations

$$\begin{bmatrix} k_{S1} & k_{S2} \\ k_{S1}^2 & -k_{S2}^2\mu_{21} \end{bmatrix} \begin{Bmatrix} R_{SS} \\ T_{SS} \end{Bmatrix} = \begin{Bmatrix} k_{S1} \\ -k_{S1}^2 \end{Bmatrix}$$

that can be easily solved to obtain

$$R_{SS}=\frac{k_{S1}k_{S2}^2\mu_{21}-k_{S2}k_{S1}^2}{k_{S1}k_{S2}^2\mu_{21}+k_{S2}k_{S1}^2}=\frac{1-\dfrac{k_{S2}k_{S1}^2}{k_{S1}k_{S2}^2\mu_{21}}}{1+\dfrac{k_{S2}k_{S1}^2}{k_{S1}k_{S2}^2\mu_{21}}}=\frac{1-\dfrac{\mu_1c_{S2}}{\mu_2c_{S1}}}{1+\dfrac{\mu_1c_{S2}}{\mu_2c_{S1}}}=\frac{1-\dfrac{\rho_1c_{S1}}{\rho_2c_{S2}}}{1+\dfrac{\rho_1c_{S1}}{\rho_2c_{S2}}}$$

$$\Rightarrow R_{SS}=\frac{\rho_2c_{S2}-\rho_1c_{S1}}{\rho_2c_{S2}+\rho_1c_{S1}}=\frac{Z_{2S}-Z_{1S}}{Z_{2S}+Z_{1S}}$$

$$T_{SS}=\frac{2k_{S1}^3}{k_{S1}k_{S2}^2\mu_{21}+k_{S2}k_{S1}^2}=\frac{\dfrac{2k_{S1}^3}{k_{S1}k_{S2}^2\mu_{21}}}{1+\dfrac{k_{S2}k_{S1}^2}{k_{S1}k_{S2}^2\mu_{21}}}=\frac{2\dfrac{\mu_1c_{S2}^2}{\mu_2c_{S1}^2}}{1+\dfrac{\mu_1c_{S2}}{\mu_2c_{S1}}}=\frac{2\dfrac{\rho_1}{\rho_2}}{1+\dfrac{\rho_1c_{S1}}{\rho_2c_{S2}}}$$

$$\Rightarrow T_{SS}=\frac{\rho_1}{\rho_2}\frac{2\rho_2c_{S2}}{\rho_2c_{S2}+\rho_1c_{S1}}=\frac{\rho_1}{\rho_2}\frac{2Z_{2S}}{Z_{2S}+Z_{1S}} \tag{1.145}$$

In Equation 1.145 $Z_{iS}=\rho_ic_{Si}$ is the acoustic impedance computed using shear wave speed, instead of the P-wave speed. Note that when both materials are the same $R_{SS}=0$ and $T_{SS}=1$.

Hence, for normal incidence of a plane SV-wave

$$\psi_1=\psi_{1S}+\psi_{RSS}=e^{-ik_{S1}x_2}+\frac{Z_{2S}-Z_{1S}}{Z_{2S}+Z_{1S}}e^{ik_{S1}x_2}$$

$$\psi_2=\psi_{TSS}=\frac{\rho_1}{\rho_2}\frac{2Z_{2S}}{Z_{2S}+Z_{1S}}e^{-ik_{S2}x_2}$$

$$\phi_1=\phi_2=0$$

Example 1.18

Compute the stress and displacement fields in the two solids for normal SV-wave incidence ($\theta_{S1}=0$ in Figure 1.23).

SOLUTION

Potential fields for this case are shown in the above example. From these potential fields, displacement and stress components are obtained using the following relations (in this case $\phi = 0$)

$$u_1 = \phi,_1 + \psi,_2 = \psi,_2$$

$$u_2 = \phi,_2 - \psi,_1 = -\psi,_1$$

$$\sigma_{11} = -\mu\left\{k_S^2\phi + 2\phi,_{22} - 2\psi,_{12}\right\} = -2\mu\psi,_{12}$$

$$\sigma_{22} = -\mu\left\{k_S^2\phi + 2\phi,_{11} + 2\psi,_{12}\right\} = -2\mu\psi,_{12}$$

$$\sigma_{12} = \mu\left\{2\phi,_{12} + \psi,_{22} - \psi,_{11}\right\} = \mu\{\psi,_{22} - \psi,_{11}\}$$

Hence, for solid 1

$$u_1 = \psi,_2 = ik_{S1}(-e^{-ik_{S1}x_2} + R_{SS}e^{ik_{S1}x_2})$$

$$u_2 = -\psi,_1 = 0$$

$$\sigma_{11} = -2\mu\psi,_{12} = 0$$

$$\sigma_{22} = -2\mu\psi,_{12} = 0$$

$$\sigma_{12} = \mu\{\psi,_{22} - \psi,_{11}\} = -\mu_1 k_{S1}^2(e^{-ik_{S1}x_2} + R_{SS}e^{ik_{S1}x_2})$$

and for solid 2

$$u_1 = \psi,_2 = -ik_{S2}T_{SS}e^{-ik_{S2}x_2}$$

$$u_2 = -\psi,_1 = 0$$

$$\sigma_{11} = -2\mu\psi,_{12} = 0$$

$$\sigma_{22} = -2\mu\psi,_{12} = 0$$

$$\sigma_{12} = \mu\{\psi,_{22} - \psi,_{11}\} = -\mu_2 k_{S2}^2 T_{SS}e^{ik_{S2}x_2}$$

where R_{SS} and T_{SS} have been defined in Equation 1.145.

Note that at the interface ($x_2 = 0$) nonzero displacement and stress components can be computed from the expressions given for solids 1 and 2. Substituting $x_2 = 0$ in the expressions for solid 1 one gets

$$u_1 = ik_{S1}(-1 + R_{SS}) = -\frac{i\omega}{c_{S1}}\frac{2Z_{1S}}{Z_{2S} + Z_{1S}} = \frac{-2i\omega\rho_1}{Z_{2S} + Z_{1S}}$$

$$\sigma_{12} = -\mu_1 k_{S1}^2(1 + R_{SS}) = -\rho_1\omega^2\frac{2Z_{2S}}{Z_{2S} + Z_{1S}} = \frac{-2\rho_1\omega^2 Z_{2S}}{Z_{2S} + Z_{1S}}$$

If $x_2 = 0$ is substituted in the expressions for solid 2, then we obtain

$$u_1 = -ik_{S2}T_{SS} = -i\frac{\omega}{c_{S2}}\frac{\rho_1}{\rho_2}\frac{2Z_{2S}}{Z_{2S}+Z_{1S}} = \frac{-2i\omega\rho_1}{Z_{2S}+Z_{1S}}$$

$$\sigma_{12} = -\mu_2 k_{S2}^2 T_{SS} = -\rho_2\omega^2\frac{\rho_1}{\rho_2}\frac{2Z_{2S}}{Z_{2S}+Z_{1S}} = \frac{-2\rho_1\omega^2 Z_{2S}}{Z_{2S}+Z_{1S}}$$

Note that u_1 and σ_{12} are continuous across the interface.

1.2.9 Rayleigh Wave in a Homogeneous Half Space

P, SV- and SH-type waves, propagate inside an elastic body and are known as body waves. When these waves meet a free surface or an interface they go through reflection and transmission. Some wave motions are confined near a free surface or an interface and are called surface waves or interface waves. The Rayleigh wave is a surface wave.

We have seen earlier that the stress-free boundary conditions at $x_2 = 0$. Figure 1.17 can be satisfied by the potential expressions given in Equation 1.121. Now let us try to satisfy the stress-free boundary conditions at $x_2 = 0$ with a different set of potential expressions, as given below. If it is possible to satisfy the appropriate boundary conditions with different potential expressions that give different type of particle motion, one can logically conclude that this new wave motion can exist in the half-space for that boundary condition. The potential expressions that are tried out now are

$$\begin{aligned} \phi &= A\exp(ikx_1 - \eta x_2) \\ \psi &= B\exp(ikx_1 - \beta x_2) \end{aligned} \tag{1.146}$$

Time dependence $\exp^{(-i\omega t)}$ is implied. Note that as x_2 increases, ϕ and ψ decay exponentially. Against the displacements and stresses associated with these potentials are confined near the free surface at $x_2 = 0$. Equation 1.146 represents a wave motion that propagate in the x_1-direction with a velocity c, where $c = \omega/k$.

Substituting Equation 1.146 into the governing wave equations (Equation 1.107) one gets

$$\begin{aligned} -k^2 + \eta^2 - k_P^2 = 0 \Rightarrow \eta = \sqrt{k^2 - k_P^2} \\ -k^2 + \beta^2 - k_S^2 = 0 \Rightarrow \beta = \sqrt{k^2 - k_S^2} \end{aligned} \tag{1.147}$$

From Equation 1.102

$$\sigma_{22} = -\mu\left\{k_S^2\phi + 2(\psi,_{12} + \phi,_{11})\right\}$$
$$= -\mu\left\{\left(k_S^2 - 2k^2\right)Ae^{ikx_1-\eta x_2} - 2ik\beta Be^{ikx_1-\beta x_2}\right\}$$
$$\sigma_{12} = \mu\{2\phi,_{12} + \psi,_{22} - \psi,_{11}\} = \mu\{(-2ik\eta)Ae^{ikx_1-\eta x_2} + (k^2+\beta^2)Be^{ikx_1-\beta x_2}\}$$

Satisfying the stress-free boundary conditions at $x_2 = 0$ one gets

$$\left\{\left(2k^2 - k_S^2\right)A + 2ik\beta B\right\}e^{ikx_1} = 0$$
$$\left\{-2ik\eta A + \left(2k^2 - k_S^2\right)B\right\}e^{ikx_1} = 0$$

The above equations are satisfied if

$$\begin{bmatrix} \left(2k^2 - k_S^2\right) & 2ik\beta \\ -2ik\eta & \left(2k^2 - k_S^2\right) \end{bmatrix} \begin{Bmatrix} A \\ B \end{Bmatrix} = \begin{Bmatrix} 0 \\ 0 \end{Bmatrix} \tag{1.148}$$

To have nontrivial solutions of A and B, the determinant of the coefficient matrix must be zero

$$\left(2k^2 - k_S^2\right)^2 - 4k^2\eta\beta = 0 \tag{1.149a}$$

Equation 1.149a can be also written as

$$\left(2\frac{\omega^2}{c^2} - \frac{\omega^2}{c_S^2}\right)^2 - 4\frac{\omega^2}{c^2}\left(\frac{\omega^2}{c^2} - \frac{\omega^2}{c_P^2}\right)^{\frac{1}{2}}\left(\frac{\omega^2}{c^2} - \frac{\omega^2}{c_S^2}\right)^{\frac{1}{2}} = 0$$
$$\Rightarrow \left(2 - \frac{c^2}{c_S^2}\right)^2 - 4\left(1 - \frac{c^2}{c_P^2}\right)^{\frac{1}{2}}\left(1 - \frac{c^2}{c_S^2}\right)^{\frac{1}{2}} = 0 \tag{1.149b}$$
$$\Rightarrow (2-\xi^2)^2 - 4\sqrt{(1-\xi^2)\left(1 - \frac{\xi^2}{\kappa^2}\right)} = 0$$

where $\xi = \frac{c}{c_S}$ and $\kappa = \frac{c_P}{c_S}$.

From Equation 1.147 $\eta = k\sqrt{1 - \frac{\xi^2}{\kappa^2}}, \beta = k\sqrt{1-\xi^2}$. Since $\kappa > 1$, if $\xi < 1$, then η and β will have real values. One can show that Equation 1.149a has only one root between 0 and 1 (Mal and Singh, 1991). To prove it let us remove the radicals from Equation 1.149b and, for simplicity, introduce the variable $p = 1/\kappa$ to obtain

$$\begin{aligned}
&(2-\xi^2)^4 = 16(1-\xi^2)(1-p^2\xi^2) \\
&\Rightarrow 16-32\xi^2+24\xi^4-8\xi^6+\xi^8 = 16-16(1+p^2)\xi^2+16p^2\xi^4 \\
&\Rightarrow -32+24\xi^2-8\xi^4+\xi^6 = -16(1+p^2)+16p^2\xi^2 \\
&\Rightarrow \xi^6-8\xi^4+(24-16p^2)\xi^2-16(1-p^2) = 0 = f(\xi^2)
\end{aligned} \tag{1.149c}$$

Note that $f(0) = -16(1-p^2) < 0$ and $f(1) = 1-8+24-16 = 1 > 0$. Equation 1.149c is a sixth-order polynomial equation of ξ or a third-order polynomial equation of ξ^2. Hence, ξ^2 can have a maximum of three roots. Since $f(\xi^2)$ changes sign between 0 and 1, it must have a minimum of 1 or a maximum of all three roots between 0 and 1. However, $f'(0) = 24 - 16p^2 > 0$ and $f''(\xi^2) = 6\xi^2 - 16 < 0$ for ξ between 0 and 1. Thus, a slope of $f(\xi^2)$ remains positive between 0 and 1. Equation 1.149c can have only 1 root of ξ^2 between 0 and 1. We will denote this root as ξ_R and corresponding c $(=\xi_R.c_S)$ as c_R. This wave that is confined near the free surface and has a velocity c_R is called Rayleigh wave.

Example 1.19

For an elastic solid with Poission's ratio $\nu = 0.25$, calculate c_R.

SOLUTION

From the definitions of p, c_S, c_P and the relations given in Table 1.1, one can write

$$p^2 = \left(\frac{c_S}{c_P}\right)^2 = \frac{\mu}{\lambda+2\mu} = \frac{\mu}{\dfrac{2\mu\nu}{1-2\nu}+2\mu} = \frac{\mu-2\mu\nu}{-2\mu\nu+2\mu} = \frac{1-2\nu}{2-2\nu} \tag{1.150}$$

For $\nu = 0.25$, $p^2 = 1/3$ and Equation 1.148b becomes

$$\xi^6-8\xi^4+\left(24-\frac{16}{3}\right)\xi^2-16\left(1-\frac{1}{3}\right) = 3\xi^6-24\xi^4+56\xi^2-32 = 0$$

Three real roots of the above equation are

$$\xi^2 = 4, \left(2+\frac{2}{\sqrt{3}}\right), \left(2-\frac{2}{\sqrt{3}}\right)$$

However, only one of these three roots is less than 1, which is necessary to have real values of η and β of Equation 1.145. Thus,

$$\xi_R^2 = \left(2 - \frac{2}{\sqrt{3}}\right) \Rightarrow \xi_R = 0.91948$$

and $c_R = 0.91948c_S$.

Similar to Example 1.19, Rayleigh wave speeds for other values of the Poission's ratio can be computed. Two approximate equations to compute the Rayleigh wave speed from the shear wave speed and Poission's ratio are given below:

$$c_R = \frac{0.862 + 1.14\nu}{1+\nu} c_S \tag{1.151a}$$

$$c_R = \frac{0.87 + 1.12\nu}{1+\nu} c_S \tag{1.151b}$$

Equations 1.151a and 1.151b are from Schmerr (1998) and Viktorov (1967), respectively. The ratio of the Rayleigh wave speed and the shear wave speed, computed from the exact and approximate equations for different Poission's ratios, are given in Table 1.3.

TABLE 1.3

Ratio of the Rayleigh Wave Speed and Shear Wave Speed for Different Poission's Ratios

ν	0	0.05	0.15	0.25	0.30	0.40	0.50
c_R/c_S (exact)	0.87	0.88	0.90	0.92	0.93	0.94	0.95
c_R/c_S Equation 151a	0.86	0.88	0.90	0.92	0.93	0.94	0.95
c_R/c_S Equation 151b	0.87	0.88	0.90	0.92	0.93	0.94	0.95

From Equation 1.148 one can write

$$\frac{B}{A} = \frac{2ik\eta}{(2k^2 - k_S^2)} = -\frac{(2k^2 - k_S^2)}{2ik\beta} \tag{1.152}$$

Hence, the displacement field is given by

$$\begin{aligned} u_1 &= \phi_{,1} + \psi_{,2} = (ikAe^{-\eta x_2} - \beta Be^{-\beta x_2})e^{ikx_1} = ikA\left(e^{-\eta x_2} + \left[2 - \frac{k_S^2}{2k^2}\right]e^{-\beta x_2}\right)e^{ikx_1} \\ u_2 &= \phi_{,2} - \psi_{,1} = (-\eta Ae^{-\eta x_2} + ikBe^{-\beta x_2})e^{ikx_1} = -\eta A\left(e^{-\eta x_2} + \frac{2k^2 - k_S^2}{2\eta\beta}e^{-\beta x_2}\right)e^{ikx_1} \end{aligned} \tag{1.153}$$

In Equation 1.153 there is only one undetermined constant '*A*' from which the amplitude of the Rayleigh wave can be computed.

At the surface ($x_2 = 0$)

$$u_1 = ikA\left(3 - \frac{k_S^2}{2k^2}\right)e^{ikx_1}$$
$$u_2 = -\eta A\left(1 + \frac{2k^2 - k_S^2}{2\eta\beta}\right)e^{ikx_1} \tag{1.154}$$

From Equation 1.154 it is clear that the two displacement components are 90° out-of-phase, because the coefficient of the exponential term of the u_1 expression is imaginary while that of the u_2 expression is real. After a detailed analysis of these displacement expressions one can show [Mal and Singh, 1991] that for a propagating Rayleigh wave the particles have an elliptic motion and the particles on the crest of the wave move opposite to the wave propagation direction. This type of motion is called *retrograde* elliptic motion.

1.2.10 Love Wave

In the previous section it has been shown that the Rayleigh wave propagates along a stress-free surface in a homogeneous solid. Let us now investigate if such propagation of antiplane motion is possible. To study this we consider an antiplane wave of the form

$$u_3 = Ae^{ikx_1 - \beta x_2}$$

propagating in the x_1-direction along the stress-free surface (at $x_2 = 0$) of an elastic half space. Note that the displacement field decays exponentially as one moves away from the surface.

Shear stress σ_{23} associated with this displacement field is given by

$$\sigma_{23} = \mu u_{3,2} = -\mu A\beta e^{ikx_1 - \beta x_2}$$

Note that at $x_2 = 0$ this stress component is nonzero unless A is zero. Therefore, the SH wave cannot propagate parallel to a stress-free surface.

Let us now consider antiplane motions in a layered half-space, as shown in Figure 1.24.

Inside the layer of thickness h down-going and up-going SH waves are propagating, and in the substrate an antiplane wave is propagating parallel to the interface. The strength of this horizontally propagating wave decays

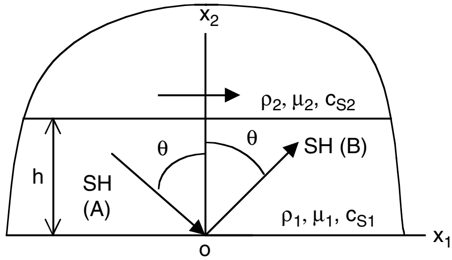

FIGURE 1.24
Possible antiplane motions in a layered half-space.

exponentially with x_2. Displacement fields associated with these antiplane waves can be written in the following form:

$$u_3^1 = Ae^{ikx_1 - i\beta_1 x_2} + Be^{ikx_1 + i\beta_1 x_2}$$
$$u_3^2 = Ce^{ikx_1 - \beta_2 x_2} \tag{1.155a}$$

In the above equation, A, B, and C are the amplitudes of the three waves, and the superscripts 1 and 2 indicate whether the displacement is computed in the layer or in the substrate. β_1 and β_2 are real numbers and are defined by

$$\beta_1 = \sqrt{k_{S1}^2 - k^2}$$
$$\beta_2 = \sqrt{k^2 - k_{S2}^2} \tag{1.155b}$$

From the stress-free boundary condition at $x_2 = 0$ we can write

$$\mu_1 u_{3,2}^1 \Big|_{x_2=0} = i\beta_1(-A+B)e^{ikx_1} = 0$$

Hence, $A = B$.

From displacement and stress continuity conditions at $x_2 = h$,

$$u_3^1\Big|_{x_3=h} = u_3^2\Big|_{x_3=h} \Rightarrow A(e^{-i\beta_1 h} + e^{i\beta_1 h})e^{ikx_i} = Ce^{ikx_1 - \beta_2 h} \Rightarrow 2A\cos(\beta_1 h) = Ce^{-\beta_2 h}$$

$$\mu_1 u_{3,2}^1\Big|_{x_3=h} = \mu_2 u_{3,2}^2\Big|_{x_3=h} \Rightarrow i\mu_1\beta_1 A(-e^{-i\beta_1 h} + e^{i\beta_1 h})e^{ikx_1} = -\mu_2\beta_2 Ce^{ikx_1 - \beta_2 h}$$

$$\Rightarrow 2A\sin(\beta_1 h) = \frac{\mu_2\beta_2}{\mu_1\beta_1} Ce^{-\beta_2 h}$$

From the above two equations one gets

$$tan(\beta_1 h) = \frac{\mu_2\beta_2}{\mu_1\beta_1} \Rightarrow tan\left(h\sqrt{k_{S1}^2 - k^2}\right) = \frac{\mu_2\sqrt{k^2 - k_{S2}^2}}{\mu_1\sqrt{k_{S1}^2 - k^2}} \quad \textbf{(1.156)}$$

Equation 1.156 can be solved for k, and from the relation $k = \omega/c_{Lo}$ the velocity c_{Lo} of the horizontally propagating wave of Figure 1.24 can be obtained. This wave is known as the *Love wave.* Note that k and c_{Lo} are functions of the wave frequency ω; in other words, this wave is *dispersive*. Equation 1.156 is known as the *dispersion equation* and it has multiple solutions for k and c_{Lo} for a given value of the frequency ω. For a given frequency ω, the displacement and stress fields inside the solid are different for different solutions of k and c_{Lo}. These displacement and stress profiles are called mode shapes. Different modes are associated with different wave speeds. Wave velocity of a specific mode at a certain frequency is constant, and this velocity is known as the *phase velocity*.

1.2.11 Rayleigh Wave in a Layered Half-Space

Rayleigh wave propagation in an isotropic half-space has been studied in Section 1.2.9. In Section 1.2.10, it was shown that unlike Rayleigh waves, SH-waves cannot propagate parallel to a stress-free surface in an isotropic solid half-space; however, a layered solid half-space can sustain SH motion (Love wave) propagating parallel to the stress-free surface as shown in Figure 1.24. Let us now investigate if the in-plane (P-SV) motion or the Rayleigh wave can propagate parallel to the stress free surface in a layered half space as shown in Figure 1.25.

In Figure 1.25 up-going and down-going P/SV-waves are shown in the layer, and horizontally propagating in-plane wave is shown in the substrate.

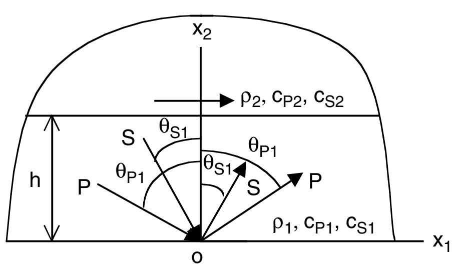

FIGURE 1.25
Possible in-plane motions in a layered half-space.

Potential fields for these different waves are given in Equation 1.157

$$\begin{aligned}
\phi_1 &= (a_1 e^{-i\eta_1 x_2} + b_1 e^{i\eta_1 x_2}) e^{ikx_1} \\
\psi_1 &= (c_1 e^{-i\beta_1 x_2} + d_1 e^{i\beta_1 x_2}) e^{ikx_1} \\
\phi_2 &= b_2 e^{-\eta_2 x_2} e^{ikx_1} \\
\psi_2 &= d_2 e^{-\beta_2 x_2} e^{ikx_1}
\end{aligned} \tag{1.157a}$$

where

$$\begin{aligned}
\eta_1 &= \sqrt{k_{P1}^2 - k^2} \\
\beta_1 &= \sqrt{k_{S1}^2 - k^2} \\
\eta_2 &= \sqrt{k^2 - k_{P2}^2} \\
\beta_2 &= \sqrt{k^2 - k_{S2}^2}
\end{aligned} \tag{1.157b}$$

Subscripts 1 and 2 are used for the layer and the substrate, respectively. Note that the potentials decay exponentially in the substrate. Relations between the unknown coefficients a_1, b_1, c_1, d_1, b_2, and d_2 can be obtained from the two boundary conditions at $x_2 = 0$ and four interface continuity conditions at $x_2 = h$. These six conditions are listed below:

$$1)\ \sigma_{22}^1\Big|_{x_2=0} = -\mu_1\left\{k_{S1}^2\phi_1 + 2(\psi_{1,12} + \phi_{1,11})\right\}_{x_2=0}$$

$$= -\mu_1\left\{\left(k_{S1}^2 - 2k^2\right)(a_1 + b_1) + 2k\beta_1(c_1 - d_1)\right\}e^{ikx_1} = 0$$

$$2)\ \sigma_{12}^1\Big|_{x_2=0} = \mu_1\{2\phi_{1,12} + \psi_{1,22} - \psi_{1,11}\} = \mu_1\left\{(2k\eta_1)(a_1 - b_1) + \left(k^2 - \beta_1^2\right)(c_1 + d_1)\right\}e^{ikx_1} = 0$$

$$3)\ \sigma_{22}^1\Big|_{x_2=h} = \sigma_{22}^2\Big|_{x_2=h} \Rightarrow -\mu_1\left\{k_{S1}^2\phi_1 + 2(\psi_{1,12} + \phi_{1,11})\right\}_{x_2=h} = -\mu_2\left\{k_{S2}^2\phi_2 + 2(\psi_{2,12} + \phi_{2,11})\right\}_{x_2=h}$$

$$\Rightarrow -\mu_1\left\{\left(k_{S1}^2 - 2k^2\right)\left(a_1E_1^{-1} + b_1E_1\right) + 2k\beta_1\left(c_1B_1^{-1} - d_1B_1\right)\right\}e^{ikx_1}$$

$$= -\mu_2\left\{\left(k_{S2}^2 - 2k^2\right)b_2E_2 - 2ik\beta_2 d_2B_2\right\}e^{ikx_1}$$

$$4.\ \sigma_{12}^1\Big|_{x_2=h} = \sigma_{12}^2\Big|_{x_2=h} \Rightarrow \mu_1\{2\phi_{1,12} + \psi_{1,22} - \psi_{1,11}\}_{x_2=h} = \mu_2\{2\phi_{2,12} + \psi_{2,22} - \psi_{2,11}\}_{x_2=h}$$

$$\Rightarrow \mu_1\left\{(2k\eta_1)\left(a_1E_1^{-1} - b_1E_1\right) + \left(k^2 - \beta_1^2\right)\left(c_1B_1^{-1} + d_1B_1\right)\right\}e^{ikx_1}$$

$$= \mu_2\left\{(-2ik\eta_2)b_2E_2 + \left(k^2 + \beta_2^2\right)d_2B_2\right\}e^{ikx_1}$$

$$5)\ u_1^1\Big|_{x_2=h} = u_1^2\Big|_{x_2=h} \Rightarrow \{\phi_{1,1} + \psi_{1,2}\}_{x_2=h} = \{\phi_{2,1} + \psi_{2,2}\}_{x_2=h}$$

$$\Rightarrow \{ik(a_1E_1^{-1} + b_1E_1) + i\beta_1(-c_1B_1^{-1} + d_1B_1)\}e^{ikx_1} = \{ikb_2E_2 - \beta_2 d_2 B_2\}e^{ikx_1}$$

$$6)\ u_2^1\Big|_{x_2=h} = u_2^2\Big|_{x_2=h} \Rightarrow \{\phi_{1,2} - \psi_{1,1}\}_{x_2=h} = \{\phi_{2,2} - \psi_{2,1}\}_{x_2=h}$$

$$\Rightarrow \{i\eta_1(-a_1E_1^{-1} + b_1E_1) - ik(c_1B_1^{-1} + d_1B_1)\}e^{ikx_1} = \{-\eta_2 b_2 E_2 - ikd_2B_2\}e^{ikx_1}$$

where

$$E_1 = e^{i\eta_1 h}$$

$$B_1 = e^{i\beta_1 h}$$

$$E_2 = e^{-\eta_2 h}$$

$$B_2 = e^{-\beta_2 h}$$

The above six conditions give the following matrix equation:

$$[A]\begin{Bmatrix} a_1 \\ b_1 \\ c_1 \\ d_1 \\ b_2 \\ d_2 \end{Bmatrix} = \begin{Bmatrix} 0 \\ 0 \\ 0 \\ 0 \\ 0 \\ 0 \end{Bmatrix} \qquad \textbf{(1.158)}$$

where the coefficient matrix (A) is given by

$$\begin{bmatrix} (2k^2 - k_{s1}^2) & (2k^2 - k_{s1}^2) & -2k\beta_1 & 2k\beta_1 & 0 & 0 \\ 2k\eta_1 & -2k\eta_1 & (2k^2 - k_{s1}^2) & (2k^2 - k_{s1}^2) & 0 & 0 \\ (2k^2 - k_{s1}^2)\mu_1 E_1^{-1} & (2k^2 - k_{s1}^2)\mu_1 E_1 & -2k\beta_1 B_1^{-1} & 2k\beta_1 B_1 & -(2k^2 - k_{s2}^2)\mu_2 B_2 & -2ik\beta_2\mu_2 B_2 \\ 2k\eta_1\mu_1 E_1^{-1} & -2k\eta_1\mu_1 E_1 & (2k^2 - k_{s1}^2)\mu_1 B_1^{-1} & (2k^2 - k_{s1}^2)\mu_1 B_1 & 2ik\eta_2\mu_2 E_2 & -(2k^2 - k_{s2}^2)\mu_2 B_2 \\ ikE_1^{-1} & ikE_1 & -i\beta_1 B_1^{-1} & i\beta_1 B_1 & -ikE_2 & \beta_2 B_2 \\ -i\eta_1 E_1^{-1} & i\eta_1 E_1 & -ikB_1^{-1} & -ikB_1 & \eta_2 E_2 & ikB_2 \end{bmatrix}$$

Since Equation 1.158 is a system of homogeneous equations, the determinant of the coefficient matrix $[A]$ must vanish for nontrivial solution of the coefficients, a_1, b_1, c_1, d_1, b_2, and d_2. The equation obtained by equating the determinant of $[A]$ to zero is called a dispersion equation, because this equation gives the values of k as a function of frequency. From the relation $k = \omega / c_R$, velocity (c_R) of the horizontally propagating wave can be obtained. Here, like Love waves, the wave velocity is dependent on the frequency and different modes propagate with different speeds. This wave is called a *generalized Rayleigh-Lamb wave* in a layered solid or simply the *Rayleigh wave*. Note that in the homogeneous solid the Rayleigh wave is not dispersive (wave speed is independent of the frequency) but in a layered half-space it is.

The procedure discussed above to solve the wave propagation problem in a layer over a half-space geometry can be generalized for the case when the solid has more than one layer. Note, that for the 2 layers over a half-space, the coefficient matrix (A) will have 10×10 dimension, and for the n-layers over a half-space case the dimension of this matrix will be $(4n + 2) \times (4n + 2)$.

1.2.12 Plate Waves

So far we have studied the mechanics of elastic wave propagation in a homogeneous or layered half-space and a homogeneous full space. Wave propagation in a plate with two stress-free surfaces is considered in this section. For simplicity, the antiplane (SH) problem will be studied first and then the in-plane (P/SV) problem will be considered.

1.2.12.1 Antiplane Waves in a Plate

Figure 1.26 shows possible SH motions in a plate with two stress-free boundaries.

The displacement field in the plate is taken as

$$\begin{aligned} u_3 &= (Ae^{-i\beta x_2} + Be^{i\beta x_2})e^{ikx_1} \\ \beta &= \sqrt{k_S^2 - k^2} \end{aligned} \tag{1.159}$$

From the two stress-free boundary conditions at $x_2 = \pm h$,

$$\begin{aligned} \mu u_{3,2}\big|_{x_2=h} &= 0 \Rightarrow i\beta\mu(-Ae^{-i\beta h} + Be^{i\beta h})e^{ikx_1} = 0 \\ \mu u_{3,2}\big|_{x_2=-h} &= 0 \Rightarrow i\beta\mu(-Ae^{i\beta h} + Be^{-i\beta h})e^{ikx_1} = 0 \end{aligned} \tag{1.160}$$

From Equation 1.160 one can write

$$\begin{bmatrix} -e^{-i\beta h} & e^{i\beta h} \\ -e^{i\beta h} & e^{-i\beta h} \end{bmatrix} \begin{Bmatrix} A \\ B \end{Bmatrix} = \begin{Bmatrix} 0 \\ 0 \end{Bmatrix} \tag{1.161}$$

For nontrivial solutions of A and B, the determinant of the coefficient matrix must vanish.

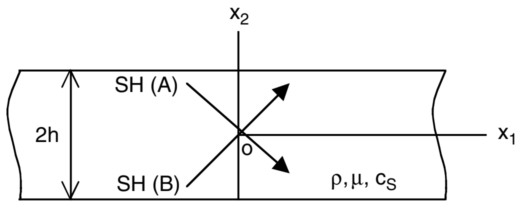

FIGURE 1.26
Possible SH motions in a plate.

Hence,

$$-e^{-2i\beta h} + e^{2i\beta h} = 2i\sin(2\beta h) = 0$$

$$\Rightarrow \sin(2\beta h) = 0 = \sin\{m\pi\}, \quad m = 0,1,2,.... \tag{1.162}$$

$$\Rightarrow \sqrt{k_S^2 - k^2} = \frac{m\pi}{2h}, \quad m = 0,1,2,....$$

k can be computed from the above equation. Clearly, k will be different for different values of m. Let us denote the solution by k_m.

$$k_S^2 - k_m^2 = \left(\frac{m\pi}{2h}\right)^2, \quad m = 0,\ 1,\ 2,....$$

$$\Rightarrow k_m = \sqrt{k_S^2 - \left(\frac{m\pi}{2h}\right)^2}, \quad m = 0,\ 1,\ 2,..... \tag{1.163}$$

$$\Rightarrow c_m = \frac{\omega}{k_m} = \frac{\omega}{\sqrt{k_S^2 - \left(\frac{m\pi}{2h}\right)^2}} = \frac{c_S}{\sqrt{1 - \left(\frac{m\pi}{2h}\right)^2\left(\frac{c_S}{\omega}\right)^2}}, \quad m = 0,\ 1,\ 2,....$$

Note that c_m is a function of ω, making these waves dispersive; however, for $m = 0$, $c_m = c_0 = c_S$. Thus, the 0-th order mode ($m = 0$) is not dispersive, but the higher-order modes ($m = 1, 2, 3, \ldots$) are (see Figure 1.27).

1.2.12.1.1 Mode Shapes

Let us now compute mode shapes for $m = 0, 1, 2, 3, \ldots$ etc.

For $m = 0$, $k_m = k_S$; hence, $\beta = 0$, and from Equation 1.161 $A = B$. Then from Equation 1.159 the displacement field becomes

$$u_3^0 = \left(Ae^{-i\beta x_2} + Be^{i\beta x_2}\right)e^{ikx_1} = 2Ae^{ikx_1}$$

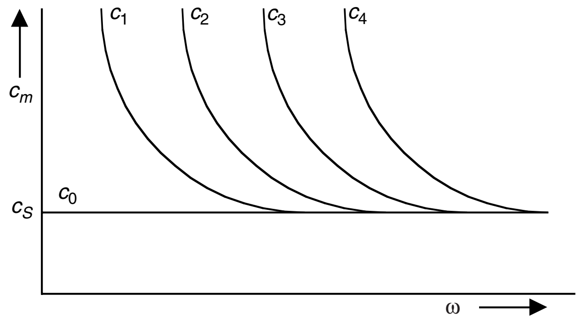

FIGURE 1.27
Dispersion curves for antiplane plate waves.

Clearly the displacement field is independent of x_2. Superscript "0" indicates 0-th order mode.

In the same manner for $m = 1$

$$k_m = \sqrt{k_S^2 - \left(\frac{\pi}{2h}\right)^2} \qquad \beta = \sqrt{k_S^2 - k_m^2} = \frac{\pi}{2h}$$

From Equation 1.161

$$\frac{B}{A} = e^{\pm i\pi}$$

Substituting it in Equation 1.159,

$$u_3^1 = (Ae^{-i\beta x_2} + Be^{i\beta x_2})e^{ikx_1} = A\left(e^{\frac{-i\pi x_2}{2h}} + e^{\pm i\pi}e^{\frac{i\pi x_2}{2h}}\right)e^{ikx_1}$$

$$= A\left(e^{\frac{-i\pi x_2}{2h}} - e^{\frac{i\pi x_2}{2h}}\right)e^{ikx_1} = -2iA\sin\left(\frac{\pi x_2}{2h}\right)e^{ikx_1}$$

For $m = 2$

$$k_m = \sqrt{k_S^2 - \left(\frac{2\pi}{2h}\right)^2} \qquad \beta = \sqrt{k_S^2 - k_m^2} = \frac{\pi}{h}$$

From Equation 1.161

$$\frac{B}{A} = e^{\pm 2i\pi}$$

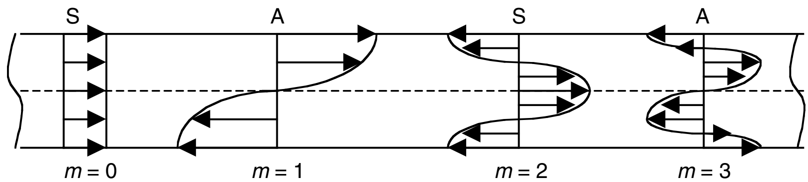

FIGURE 1.28
Mode shapes for different antiplane plate wave modes.

Substituting it in Equation 1.159

$$u_3^2 = (Ae^{-i\beta x_2} + Be^{i\beta x_2})e^{ikx_1} = A\left(e^{\frac{-i\pi x_2}{h}} + e^{\pm 2i\pi}e^{\frac{i\pi x_2}{h}}\right)e^{ikx_1}$$

$$= A\left(e^{\frac{-i\pi x_2}{2h}} + e^{\frac{i\pi x_2}{2h}}\right)e^{ikx_1} = 2A\cos\left(\frac{\pi x_2}{h}\right)e^{ikx_1}$$

In this manner x_2-dependence of the displacement field alternately becomes sine and cosine. Displacement field variation in the x_2-direction is known as the mode shape. Different mode shapes for this problem are plotted in Figure 1.28. Symmetric and antisymmetric modes, relative to the central plane of the plate, are denoted by *S* and *A*, respectively. Right and left arrows are used to indicate positive and negative directions of the displacement field, respectively.

1.2.12.2 In-plane Waves in a Plate (Lamb Waves)

Figure 1.29 shows possible in-plane (P/SV) motions in a plate with two stress- free boundaries.

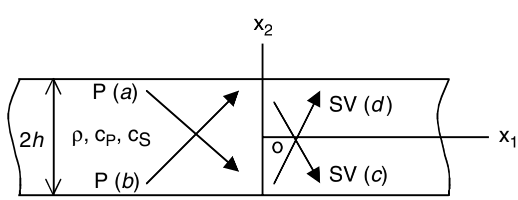

FIGURE 1.29
Possible in-plane motions in a plate.

P- and SV-wave potentials in the plate are given by

$$\begin{aligned} \phi &= (ae^{-i\eta x_2} + be^{i\eta x_2})e^{ikx_1} \\ \psi &= (ce^{-i\beta x_2} + de^{i\beta x_2})e^{ikx_1} \\ \eta &= \sqrt{k_P^2 - k^2} \\ \beta &= \sqrt{k_S^2 - k^2} \end{aligned} \tag{1.164}$$

From the stress free boundary conditions at $x_2 = \pm h$,

$$\begin{aligned}
&1.\ \sigma_{22}\big|_{x_2=h} = -\mu\left\{k_S^2\phi + 2(\psi,_{12} + \phi,_{11})\right\}_{x_2=h} \\
&\qquad = -\mu\left\{\left(k_S^2 - 2k^2\right)\left(aE^{-1} + bE\right) + 2/ik\beta\left(cB^{-1} - dB\right)\right\}e^{ikx_1} = 0 \\
&2.\ \sigma_{22}\big|_{x_2=-h} = -\mu\left\{k_S^2\phi + 2(\psi,_{12} + \phi,_{11})\right\}_{x_2=-h} \\
&\qquad = -\mu\left\{\left(k_S^2 - 2k^2\right)\left(aE + bE^{-1}\right) + 2/ik\beta\left(cB - dB^{-1}\right)\right\}e^{ikx_1} = 0 \\
&3.\ \sigma_{12}\big|_{x_2=h} = \mu\{2\phi,_{12} + \psi,_{22} - \psi,_{11}\}_{x_2=h} \\
&\qquad = \mu\left\{(2/ik\eta)\left(aE^{-1} - bE\right) + (k^2 - \beta^2)\left(cB^{-1} + dB\right)\right\}e^{ikx_1} = 0 \\
&4.\ \sigma_{12}\big|_{x_2=-h} = \mu\{2\phi,_{12} + \psi,_{22} - \psi,_{11}\}_{x_2=-h} \\
&\qquad = \mu\left\{(2/ik\eta)\left(aE - bE^{-1}\right) + (k^2 - \beta^2)\left(cB + dB^{-1}\right)\right\}e^{ikx_1} = 0
\end{aligned} \tag{1.165}$$

where

$$\begin{aligned} E &= e^{i\eta h} \\ B &= e^{i\beta h} \end{aligned}$$

From Equation 1.165 one can write

$$\begin{bmatrix} \left(2k^2 - k_S^2\right)E^{-1} & \left(2k^2 - k_S^2\right)E & -2k\beta B^{-1} & 2k\beta B \\ \left(2k^2 - k_S^2\right)E & \left(2k^2 - k_S^2\right)E^{-1} & -2k\beta B & 2k\beta B^{-1} \\ 2k\eta E^{-1} & -2k\eta E & \left(2k^2 - k_S^2\right)B^{-1} & \left(2k^2 - k_S^2\right)B \\ 2k\eta E & -2k\eta E^{-1} & \left(2k^2 - k_S^2\right)B & \left(2k^2 - k_S^2\right)B^{-1} \end{bmatrix} \begin{Bmatrix} a \\ b \\ c \\ d \end{Bmatrix} = \begin{Bmatrix} 0 \\ 0 \\ 0 \\ 0 \end{Bmatrix} \tag{1.166}$$

For nontrivial solutions of *a*, *b*, *c*, and *d*, determinant of the above 4 × 4 coefficient matrix must vanish. The equation obtained by equating the determinant of the above matrix to zero is called the dispersion equation because *k*, as a function of frequency, is obtained from this equation. Like the antiplane problem, multiple values of *k* are also obtained for a given frequency in this case. These multiple values (k_m) correspond to multiple modes of wave propagation. The wave speed c_L is obtained from k_m from the relation $c_L = \omega/k_m$. This wave is called the Lamb wave. Since k_m is dispersive, corresponding wave speed (c_L) is also dispersive (varies with frequency).

1.2.12.2.1 Symmetric and Antisymmetric Modes

The above analysis can be simplified significantly by decomposing the problem into symmetric and antisymmetric problems. To this aim, wave potentials in the plate are written in the following manner, instead of Equation 1.164:

$$\begin{aligned}
\phi &= (ae^{\eta x_2} + be^{-\eta x_2})e^{ikx_1} = \{A\sinh(\eta x_2) + B\cosh(\eta x_2)\}e^{ikx_1} \\
\psi &= (ce^{\beta x_2} + de^{-\beta x_2})e^{ikx_1} = \{C\sinh(\beta x_2) + D\cosh(\beta x_2)\}e^{ikx_1} \\
\eta &= \sqrt{k^2 - k_P^2} \\
\beta &= \sqrt{k^2 - k_S^2}
\end{aligned} \tag{1.167}$$

From the stress-free boundary conditions at $x_2 = \pm h$,

$$\begin{aligned}
&1)\ \sigma_{22}\big|_{x_2=h} = -\mu\left\{k_S^2\phi + 2(\psi,_{12} + \phi,_{11})\right\}_{x_2=h} \\
&\quad = -\mu\left\{\left(k_S^2 - 2k^2\right)[A\sinh(\eta h) + B\cosh(\eta h)] + 2ik\beta[C\cosh(\beta h) + D\sinh(\beta h)]\right\}e^{ikx_1} = 0 \\
&2)\ \sigma_{22}\big|_{x_2=-h} = -\mu\left\{k_S^2\phi + 2(\psi,_{12}\ \phi,_{11})\right\}_{x_2=-h} \\
&\quad = -\mu\left\{\left(k_S^2 - 2k^2\right)[-A\sinh(\eta h) + B\cosh(\eta h)] + 2ik\beta[C\cosh(\beta h) - D\sinh(\beta h)]\right\}e^{ikx_1} = 0 \\
&3)\ \sigma_{12}\big|_{x_2=h} = \mu\{2\phi,_{12} + \psi,_{22} - \psi,_{11}\}_{x_2=h} \\
&\quad = \mu\left\{(2ik\eta)[A\cosh(\eta h) + B\sinh(\eta h)] + (k^2 + \beta^2)[C\sinh(\beta h) + D\cosh(\beta h)]\right\}e^{ikx_1} = 0 \\
&4)\ \sigma_{12}\big|_{x_2=-h} = \mu\{2\phi,_{12} + \psi,_{22} - \psi,_{11}\}_{x_2=-h} \\
&\quad = \mu\left\{(2ik\eta)[A\cosh(\eta h) - B\sinh(\eta h)] + (k^2 + \beta^2)[-C\sinh(\beta h) + D\cosh(\beta h)]\right\}e^{ikx_1} = 0
\end{aligned} \tag{1.168}$$

Adding the first two equations of Equation 1.168 and subtracting the fourth equation from the third we get the following two equations:

$$\begin{aligned} &\left(2k^2 - k_s^2\right)B\cosh(\eta h) - 2ik\beta C\cosh(\beta h) = 0 \\ &2ik\eta B\sinh(\eta h) + \left(2k^2 - k_S^2\right)C\sinh(\beta h) = 0 \end{aligned} \tag{1.169a}$$

Adding the last two equations Equation 1.168 and subtracting the second equation from the first one gets the following:

$$\begin{aligned} &\left(2k^2 - k_s^2\right)A\sinh(\eta h) - 2ik\beta D\sinh(\beta h) = 0 \\ &2ik\eta A\cosh(\eta h) + \left(2k^2 - k_S^2\right)D\cosh(\beta h) = 0 \end{aligned} \tag{1.169b}$$

From Equation 1.168a one can write that for nontrivial solutions of *B* and *C*, the determinant of the coefficient matrix must vanish:

$$\begin{aligned} &\left(2k^2 - k_S^2\right)^2 \cosh(\eta h)\sinh(\beta h) - 4k^2\eta\beta\cosh(\beta h)\sinh(\eta h) = 0 \\ &\Rightarrow \frac{\tanh(\eta h)}{\tanh(\beta h)} = \frac{\left(2k^2 - k_S^2\right)^2}{4k^2\eta\beta} \end{aligned} \tag{1.170a}$$

Similarly, from Equation 1.169b, for nontrivial solutions of *A* and *D*, the determinant of the coefficient matrix must vanish

$$\begin{aligned} &\left(2k^2 - k_S^2\right)^2 \sinh(\eta h)\cosh(\beta h) - 4k^2\eta\beta\sinh(\beta h)\cosh(\eta h) = 0 \\ &\Rightarrow \frac{\tanh(\eta h)}{\tanh(\beta h)} = \frac{4k^2\eta\beta}{\left(2k^2 - k_S^2\right)^2} \end{aligned} \tag{1.170b}$$

If *A* and $D = 0$, but *B* and *C* do not, then Equation 1.170a must be satisfied and the potential field is given by

$$\begin{aligned} \phi &= (ae^{\eta x_1} + be^{-\eta x_2})e^{ikx_1} = B\cosh(\eta x_2)e^{ikx} \\ \psi &= (ce^{\beta x_2} + de^{-\beta x_2})e^{ikx_1} = C\sinh(\beta x_2)e^{ikx} \end{aligned}$$

Therefore, the displacement field is

$$u_1 = \phi,_1 + \psi,_2 = \{ikB\cosh(\eta x_2) + \beta C\cosh(\beta x_2)\}e^{ikx_1}$$

$$u_2 = \phi,_2 - \psi,_1 = \{\eta B\sinh(\eta x_2) - ikC\sinh(\beta x_2)\}e^{ikx_1}$$

Note that u_1 is an even function of x_2, while u_2 is an odd function of x_2. Therefore, in this case the displacement field will be symmetric about the central plane ($x_2 = 0$) of the plate. That is why these modes are called symmetric or extensional modes.

If B and C vanish, but A and D do not, then Equation 1.170b must be satisfied. In this case, u_1 will be an odd function of x_2, while u_2 will be an even function of x_2. The displacement field will be antisymmetric about the central plane ($x_2 = 0$) of the plate. These modes are known as antisymmetric or flexural modes.

Deformation of the plate for symmetric and antisymmetric modes of wave propagation is shown in Figure 1.30.

Equation 1.170a and Equation 1.170b are rather complex and have multiple solutions for k that can be obtained numerically. From the multiple k values the Lamb wave speed c_L (= ω/k) for different symmetric and antisymmetric modes of wave propagation can be obtained.

Let us investigate the dispersion Equation 1.170a and Equation 1.170b more closely for some special cases. For example, at low frequency, since η and β are small,

$$\frac{\tanh(\eta h)}{\tanh(\beta h)} \approx \frac{\eta h}{\beta h} - \frac{\eta}{\beta}$$

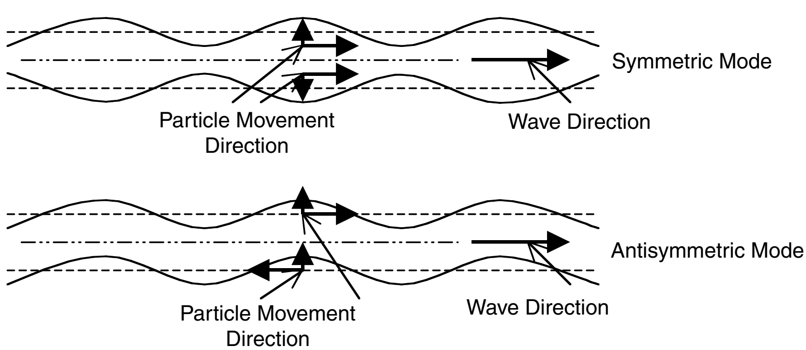

FIGURE 1.30
Deformation of the plate and particle movement directions for symmetric (top) and antisymmetric (bottom) modes of wave propagation.

Substituting it in Equation 1.170a, one gets for low frequency:

$$\frac{\eta}{\beta} = \frac{\left(2k^2 - k_S^2\right)^2}{4k^2\eta\beta} \Rightarrow 4k^2\eta^2 = \left(2k^2 - k_S^2\right)^2 \Rightarrow 4k^2\left(k^2 - k_P^2\right) = 4k^4 - 4k^2k_S^2 + k_S^4$$

$$\Rightarrow 4k^2\left(k_S^2 - k_P^2\right) = k_S^4 \Rightarrow k^2 = \frac{k_S^4}{4\left(k_S^2 - k_P^2\right)} \Rightarrow \frac{c_L^2}{\omega^2} = \frac{1}{k^2} = \frac{4\left(k_S^2 - k_P^2\right)}{k_S^4} = 4\frac{c_S^2}{\omega^2}\left(1 - \frac{c_S^2}{c_P^2}\right)$$

$$\Rightarrow c_L = 2c_S\sqrt{1 - \frac{c_S^2}{c_P^2}} = c_0 \tag{1.171}$$

Equation 1.170b can be solved by the perturbation technique (Bland, 1988; Mal and Singh, 1991) for small frequency to obtain

$$c_L = c_S\left\{\frac{4}{3}\left(1 - \frac{c_S^2}{c_P^2}\right)\right\}^{1/4}\left(\frac{\omega h}{c_S}\right)^{1/2} \tag{1.172}$$

Thus, at zero frequency, the phase velocity of the symmetric mode has a finite value (given in Equation 1.171), but that of the antisymmetric mode is zero. These modes are called fundamental symmetric and antisymmetric modes and are denoted by the symbols S_0 and A_0, respectively. At high frequencies, all modes have the Rayleigh wave speed, as shown below.

For high frequency, we have $\tanh(\eta h) \approx \tanh(\beta h) \approx 1$. Substituting it in Equation 1.170a and Equation 1.170b one gets

$$1 = \frac{\left(2k^2 - k_S^2\right)^2}{4k^2\eta\beta} \Rightarrow 4k^2\eta\beta = \left(2k^2 - k_S^2\right)^2 \Rightarrow \left(2k^2 - k_S^2\right)^2 - 4k^2\eta\beta = 0$$

The above equation is identical to the Rayleigh wave equation Equation 1.149a; its solution will give the Rayleigh wave speed. At high frequencies, Lamb modes attain Rayleigh wave speed.

Although Equation 1.170a and Equation 1.170b have only one solution each at low frequency, as the signal frequency increases the equations give multiple solutions. Typical plots of the variation of c_L as a function of frequency for an isotropic plate are shown in Figure 1.31.

1.2.13 Phase Velocity and Group Velocity

In Figure 1.27 and Figure 1.31 we see that the wave speeds are a function of frequency. If any mode of the wave propagates with a single frequency (monochromatic wave), then its velocity can be computed from the disper-

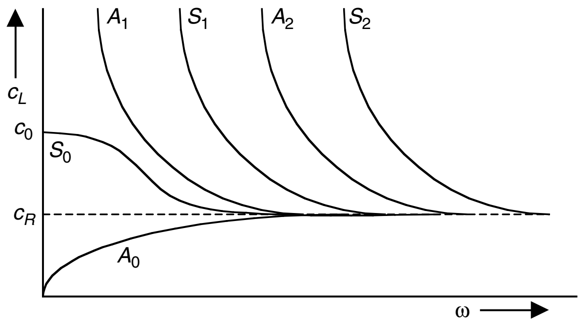

FIGURE 1.31
Dispersion curves for Lamb wave propagation in a plate.

sion curves like the ones in these figures. This velocity is called *phase velocity*. The schematic of the monochromatic wave velocity or phase velocity is shown in the top two plots of Figure 1.32.

In Figure 1.32, two waves, (1 and 2, top two plots) have slightly different frequencies and phase velocities. Wave 2 has a slightly higher frequency and phase velocity when compared with wave 1. A similar phase velocity–frequency relation (velocity increasing with frequency) is observed for the A_0 mode in Figure 1.31. If both waves exist simultaneously, then their total response will be as shown in the third and fourth plots of Figure 1.32. The third plot is obtained by simply adding the top two plots. The fourth plot is the same as the third plot; the only difference is that it is plotted in a different scale covering a wider range of x (0 to 15). The fourth plot clearly shows how two waves interfere constructively and destructively to form several groups or packets of waves separated by null regions. In this figure, the continuous lines show the displacement variations as functions of x at time $t = 0$, and dotted lines show the displacements at time t (slightly greater than 0). Propagation of these waves is evident in the figure. If the dotted lines are plotted at time $t = 1$, then the shift of the peak position represents the phase velocity and is denoted by c_{ph} in the figure. Similarly, the shift in the null position or the peak position of the modulation envelope of the summation of these two waves is the velocity of the envelope; this is called the *group velocity* and it is denoted by c_g in the bottom plot of Figure 1.32. The relation between the phase velocity and the group velocity is derived below.

Mathematical representations of two waves of different frequency and phase velocity are

$$u_i^1 = \sin(k_1 x - \omega_1 t)$$
$$u_i^2 = \sin(k_2 x - \omega_2 t) \tag{1.173a}$$

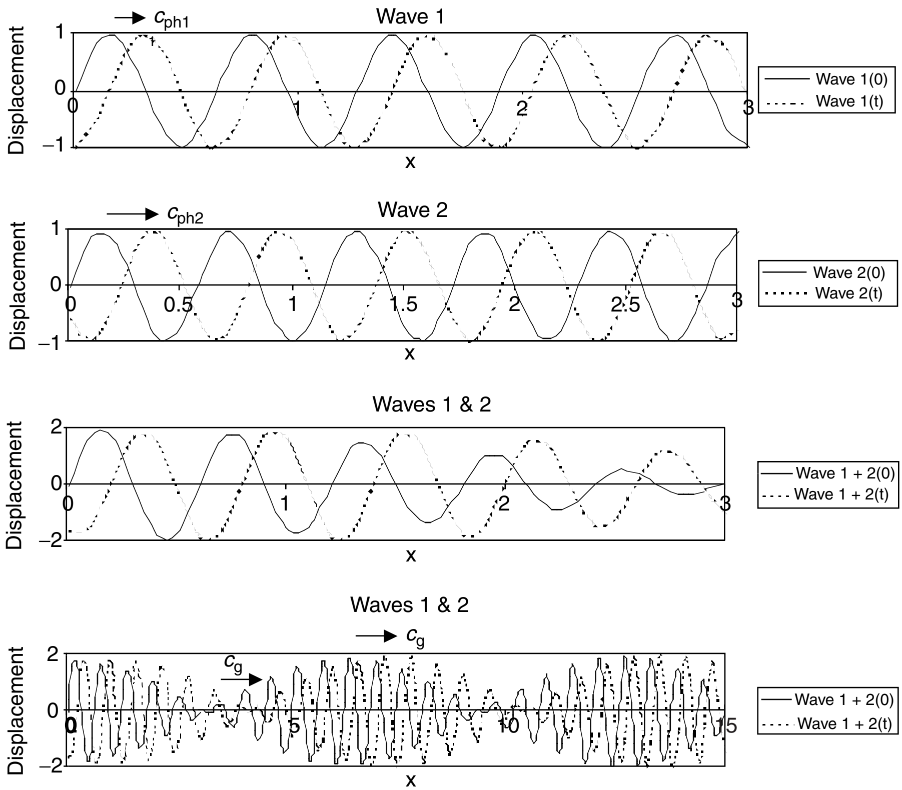

FIGURE 1.32
Propagation of elastic waves of single frequency (top two figures) and multiple frequencies (bottom two figures). Wave motions are shown at time 0 (continuous line) and t (dotted line).

where the subscript i can take any value of 1, 2, or 3 and the superscript 1 and 2 of u correspond to the first and second waves, respectively. Phase velocities for these two waves are

$$c_{ph1} = \frac{\omega_1}{k_1}$$
$$c_{ph2} = \frac{\omega_2}{k_2} \tag{1.173b}$$

Superposition of these two waves gives

$$u_i^1 + u_i^2 = \sin(k_1 x - \omega_1 t) + \sin(k_2 x - \omega_2 t) = \sin(a+b) + \sin(a-b) = 2\sin(a)\cos(b) \tag{1.174}$$

where

$$a = \frac{1}{2}(k_1 + k_2)x - \frac{1}{2}(\omega_1 + w_2)t = k_{av}x - \omega_{av}t$$
$$b = \frac{1}{2}(k_1 - k_2)x - \frac{1}{2}(\omega_1 - \omega_2)t = \left(\frac{\Delta k}{2}x - \frac{\Delta\omega}{2}t\right) \quad \textbf{(1.175)}$$

From Equation 1.174 and Equation 1.175,

$$u_i^1 + u_i^2 = 2\cos(b)\sin(a) = 2\cos\left(\frac{\Delta k}{2}x - \frac{\Delta\omega}{2}t\right)\sin(k_{av}x - \omega_{av}t) \quad \textbf{(1.176)}$$

Note that the cosine term shows how the modulation envelope is dependent on x and t. The above analysis shows that when two waves of slightly different wave number and frequency are superimposed, the resultant wave has the average wave number and frequency and is amplitude modulated. The velocity of the amplitude envelope is the *group velocity*, and is given by

$$c_g = \frac{d\omega}{dk} \quad \textbf{(1.177a)}$$

If the two waves that are superimposed have very close frequency and wave number,

$$\omega_1 \approx \omega_2 \approx \omega$$
$$k_1 \approx k_2 \approx k$$

then

$$\omega_{av} \approx \omega$$
$$k_{av} \approx k$$
$$d\omega = \Delta\omega$$
$$dk = \Delta k$$

and we can say that the wave formed by adding the two waves propagates with the same frequency (ω) and wave number (k) as its individual components. However, the envelope or group formed in between two successive nulls of the amplitude modulation curve travels with a velocity c_g where

$$c_g = \frac{d\omega}{dk} \quad \textbf{(1.177b)}$$

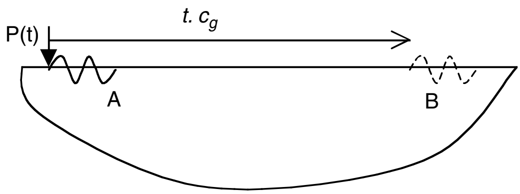

FIGURE 1.33
Finite pulse propagating with a speed equal to the group velocity.

The concept of group velocity is important because energy travels from one point to another in a solid with this velocity. This concept is illustrated in Figure 1.33.

Let a time dependent force $P(t)$ generate a finite pulse A as shown in Figure 1.33. This pulse can be assumed to be a superposition of a number of waves of different frequencies. Each of these waves can be assumed to exist in the region $-\infty < x < +\infty$. When all these waves are added, then a finite pulse like the one shown in Figure 1.33 is generated. This concept is similar to the Fourier series summation concept. Thus, the pulse A of Figure 1.33 is a group of waves and should travel with the group velocity (c_g). After a time t, the entire pulse will move to position B at a distance of $t.c_g$.

1.2.14 Point Source Excitation

So far we have discussed possible wave motions in solids of different geometry — infinite solid, half space, plate, etc. Except for some simple cases such as the one in Figure 1.15, we did not talk about how the waves are generated. In this section we will consider the source into our analysis and will calculate the wave motion in a solid due to a point source excitation. The derivation given in Mal and Singh (1991) for solid full space is followed here.

Let the concentrated time harmonic force $\mathbf{P}\delta(\mathbf{x})e^{-i\omega t}$ act at the origin of a solid full space. Where $\mathbf{P}$ is the force vector acting at the origin, $\delta(\mathbf{x})$ is the three-dimensional delta function that is zero everywhere except at the origin, where it is infinity. When the volume encloses the origin the volume integral of the delta function is 1. Without the loss of generality we can say that for this harmonic excitation the displacement field will also have the form $\mathbf{u} = \mathbf{u}(\mathbf{x})e^{-i\omega t}$. In the presence of a body force, which in this case is a concentrated force at the origin, Navier's equation Equation 1.79 takes the form

$$
\begin{aligned}
&(\lambda + 2\mu)\underline{\nabla}(\underline{\nabla}\cdot\mathbf{u}) - \mu\underline{\nabla}\times(\underline{\nabla}\times\mathbf{u}) + \mathbf{P}\delta(x) = -\rho\omega^2\mathbf{u} \\
&\Rightarrow c_P^2\underline{\nabla}(\underline{\nabla}\cdot \mathrm{u}) - c_S^2\underline{\nabla}\times(\underline{\nabla}\times\mathbf{u}) + \omega^2\mathbf{u} = -\frac{\mathrm{P}}{\rho}\delta(\mathrm{x})
\end{aligned}
\tag{1.178}
$$

To solve the above inhomogeneous equation $\delta(\mathbf{x})$ is represented in the following form:

$$\delta(\mathbf{x}) = -\nabla^2\left(\frac{1}{4\pi r}\right) \quad \textbf{(1.179)}$$

where $r = |\mathbf{x}|$ is the radial distance from the origin. To prove Equation 1.179, let us consider a function

$$\Phi = \frac{C}{r}$$

where C is a constant. Then one can easily show that

$$\nabla^2\Phi(\mathbf{x}) = 0, \quad \mathbf{x} \neq 0$$

Further, by the divergence theorem,

$$\int_V \nabla^2\Phi dV = \int_V \underline{\nabla}\cdot(\underline{\nabla}\Phi)dV = \int_S (\underline{\nabla}\Phi)\,\mathbf{n}dS = \int_S (\Phi_{,1}n_1 + \Phi_{,2}n_2 + \Phi_{,3}n_3)dS$$

$$= \int_S \frac{\partial\Phi}{\partial x_i}\frac{\partial x_i}{\partial n}dS$$

$$= \int_S \frac{\partial\Phi}{\partial n}dS = C\int_{\beta=0}^{\pi}\int_{\theta=0}^{2\pi}\left(-\frac{1}{r^2}\right)r^2\sin(\theta)d\theta d\beta = -4\pi C$$

If $C = -1/(4\pi)$, then the above volume integral becomes 1. Hence, $\nabla^2\left(-\frac{1}{4\pi r}\right)$ is zero for $\mathbf{x} \neq 0$ and its volume integral is 1. So it must be the three-dimensional delta function, as given in Equation 1.179.

Using the vector identity one can write

$$\mathbf{P}\delta(\mathbf{x}) = -\nabla^2\left(\frac{1}{4\pi r}\right) = -\frac{1}{4\pi}\left[\underline{\nabla}\left(\underline{\nabla}\cdot\frac{\mathbf{P}}{r}\right) - \underline{\nabla}\times\left(\underline{\nabla}\times\frac{\mathbf{P}}{r}\right)\right]$$

Therefore, the equation of motion (1.178) can be rewritten as

$$c_P^2\underline{\nabla}(\underline{\nabla}\cdot\mathbf{u}) - c_S^2\underline{\nabla}\times(\underline{\nabla}\times\mathbf{u}) + \omega^2\mathbf{u} = -\frac{1}{4\pi\rho}\left[\underline{\nabla}\left(\underline{\nabla}\cdot\frac{\mathbf{P}}{r}\right) - \underline{\nabla}\times\left(\underline{\nabla}\times\frac{\mathbf{P}}{r}\right)\right] \quad \textbf{(1.180)}$$

Let us now express $\mathbf{u}$ in terms of two scalar functions, ϕ and ψ, in the following manner:

$$\mathbf{u} = \underline{\nabla}(\underline{\nabla} \cdot \mathbf{P}\phi) - \underline{\nabla} \times (\underline{\nabla} \times \mathbf{P}\psi) \tag{1.181}$$

Then,

$$\underline{\nabla} \cdot \mathbf{u} = \nabla^2(\underline{\nabla} \cdot \mathbf{P}\phi) - \underline{\nabla} \cdot (\nabla^2 \mathbf{P}\phi)$$

$$\underline{\nabla} \times \mathbf{u} = -\underline{\nabla} \times [\underline{\nabla} \times (\underline{\nabla} \times \mathbf{P}\psi)] = \underline{\nabla} \times (\mathbf{P}\nabla^2\psi)$$

and Equation 1.180 becomes

$$\underline{\nabla}\underline{\nabla} \cdot \left[\mathbf{P}\left(c_P^2\nabla^2\phi + \omega^2\phi - \frac{1}{4\pi\rho r}\right)\right] - \underline{\nabla} \times \underline{\nabla} \times \left[\mathbf{P}\left(c_S^2\nabla^2\psi + \omega^2\psi - \frac{1}{4\pi\rho r}\right)\right] = 0 \tag{1.182}$$

The above equation is satisfied if ϕ and ψ are the solutions of the following inhomogeneous Helmholtz equations:

$$\begin{aligned} \nabla^2\phi + k_P^2\phi &= \frac{1}{4\pi\rho c_P^2 r} \\ \nabla^2\psi + k_S^2\psi &= \frac{1}{4\pi\rho c_S^2 r} \end{aligned} \tag{1.183}$$

One can easily show that the particular solutions of Equation 1.183 that are finite at $r = 0$ are

$$\begin{aligned} \phi &= \frac{1 - e^{ik_P r}}{4\pi\rho\omega^2 r} \\ \psi &= \frac{1 - e^{ik_S r}}{4\pi\rho\omega^2 r} \end{aligned} \tag{1.184}$$

From Equation 1.184 and Equation 1.181 the displacement field can be written as

$$\mathbf{u} = -\underline{\nabla}\underline{\nabla} \cdot \left[\mathbf{P}\frac{e^{ik_P r} - e^{ik_S r}}{4\pi\rho\omega^2 r}\right] + \frac{\mathbf{P}e^{ik_S r}}{4\pi\rho c_S^2 r} \tag{1.185}$$

or, in index notation,

$$
\begin{aligned}
u_i &= \frac{1}{4\pi\rho\omega^2}\left[k_S^2\frac{e^{ik_S r}}{r}P_i - \frac{\partial^2}{\partial x_i \partial x_j}\frac{e^{ik_P r}-e^{ik_S r}}{r}P_j\right] \\
&= \frac{1}{4\pi\rho\omega^2}\left[k_S^2\frac{e^{ik_S r}}{r}\delta_{ij} - \frac{\partial^2}{\partial x_i \partial x_j}\frac{e^{ik_P r}-e^{ik_S r}}{r}\right]P_j = G_{ij}(\mathbf{x};\mathbf{0})P_j
\end{aligned}
\tag{1.186}
$$

where $G_{ij}(\mathbf{x};\,\mathbf{0})\exp(-i\omega t)$ is the i-th component of the displacement produced at $\mathbf{x}$ by a concentrated force $\exp(-i\omega t)$ acting at the origin in the j-th direction. G_{ij} is known as the *steady-state Green's tensor* or, in simple words, *Green's function* for the infinite isotropic solid.

If the force acts in the j-th direction at $\mathbf{y}$, then the displacement component in the i-th direction is denoted by $G_{ij}(\mathbf{x};\mathbf{y})$ and is obtained by replacing r by $|\mathbf{x}-\mathbf{y}|$. Green's tensor in this case is given by Mal and Singh (1991):

$$
\begin{aligned}
G_{ij}(\mathbf{x};\mathbf{y}) = \frac{1}{4\pi\rho\omega^2}\Bigg\{&\frac{e^{ik_P r}}{r}\left[k_P^2 R_i R_j + (3R_iR_j-\delta_{ij})\left(\frac{ik_P}{r}-\frac{1}{r^2}\right)\right] \\
&+\frac{e^{ik_S r}}{r}\left[k_S^2(\delta_{ij}-R_iR_j) - (3R_iR_j-\delta_{ij})\left(\frac{ik_S}{r}-\frac{1}{r^2}\right)\right]\Bigg\}
\end{aligned}
\tag{1.187a}
$$

where

$$
R_i = \frac{x_i - y_i}{r} \tag{1.187b}
$$

If r is large compared to the wavelength, then $k_P r$ and $k_S r$ are large. An approximate expression for $G_{ij}(\mathbf{x};\mathbf{y})$ can be obtained by retaining only the terms containing $(k_P r)^{-1}$ and $(k_S r)^{-1}$ but ignoring all higher order terms. Thus, in the *far field*,

$$
G_{ij}(\mathbf{x};\mathbf{y}) = \frac{1}{4\pi\rho}\left[\frac{e^{ik_P r}}{c_P^2 r}R_iR_j + \frac{e^{ik_S r}}{c_S^2 r}(\delta_{ij}-R_iR_j)\right] \tag{1.188}
$$

and the displacement vector in the far field is given by

$$
\mathbf{u}(\mathbf{x};\mathbf{0}) = \frac{1}{4\pi\rho}\left[\frac{e^{ik_P r}}{c_P^2 r}(\mathbf{e_R}\cdot\mathbf{P})\mathbf{e_R} + \frac{e^{ik_S r}}{c_S^2 r}\left\{\mathbf{P}-(\mathbf{e_R}\cdot\mathbf{P})\mathbf{e_R}\right\}\right] \tag{1.189}
$$

1.2.15 Wave Propagation in Fluid

Since perfect fluid does not have any shear stress, the wave propagation analysis in a perfect fluid medium is much simpler and can be considered as a special case of that in the solid. In this book, unless otherwise specified, the fluid is assumed to be perfect fluid. The constitutive relation for a solid (Equation 1.68) can be specialized for the fluid case by substituting the shear modulus $\mu = 0$.

$$\sigma_{ij} = \lambda\delta_{ij}\varepsilon_{kk} \tag{1.190}$$

Since fluid can only sustain hydrostatic pressure p, the stress field in a fluid is given by

$$\sigma_{11} = \sigma_{22} = \sigma_{33} = -p \tag{1.191}$$

and all shear stress components are zero. The constitutive relation is then simplified to

$$\begin{aligned} &-p = \sigma_{11} = \sigma_{22} = \sigma_{33} = \lambda(\varepsilon_{11} + \varepsilon_{22} + \varepsilon_{33}) = \lambda(u_{1,1} + u_{2,2} + u_{3,3}) = \lambda\nabla\cdot\mathbf{u} \\ &\Rightarrow \nabla\cdot\mathbf{u} = -\frac{p}{\lambda} \end{aligned} \tag{1.192}$$

The governing equations of motion (Equation 1.78) can be specialized in the same manner:

$$\begin{aligned} &\sigma_{11,1} + f_1 = -p,_1 + f_1 = \rho\ddot{u}_1 \\ &\sigma_{22,2} + f_2 = -p,_2 + f_2 = \rho\ddot{u}_2 \\ &\sigma_{33,3} + f_3 = -p,_3 + f_3 = \rho\ddot{u}_3 \\ &\Rightarrow -\nabla p + \mathbf{f} = \rho\ddot{\mathbf{u}} = \rho\dot{\mathbf{v}} \end{aligned} \tag{1.193}$$

Hence,

$$\begin{aligned} &-\nabla\cdot\nabla p + \nabla\cdot\mathbf{f} = \nabla\cdot\rho\ddot{\mathbf{u}} = \rho\frac{\partial^2(\nabla\cdot\mathbf{u})}{\partial t^2} = -\frac{\rho}{\lambda}\frac{\partial^2 p}{\partial t^2} \\ &\Rightarrow -\nabla^2 p + \frac{1}{c_f^2}\frac{\partial^2 p}{\partial t^2} + \nabla\cdot\mathbf{f} = 0 \\ &\Rightarrow \nabla^2 p - \frac{1}{c_f^2}\frac{\partial^2 p}{\partial t^2} + f = 0 \end{aligned} \tag{1.194}$$

where

$$c_f = \sqrt{\frac{\lambda}{\rho}}$$
$$f = -\nabla \cdot \mathbf{f} \tag{1.195}$$

In absence of any body force, the above governing equation is simplified to the wave equation or Helmholtz equation

$$\nabla^2 p - \frac{1}{c_f^2}\frac{\partial^2 p}{\partial t^2} = 0 \tag{1.196}$$

Its solution is given by

$$p = f(\mathbf{n} \cdot \mathbf{x} - c_f t) \tag{1.197}$$

It represents a wave propagating in **n** direction with a velocity c_f. Note that this wave produces only normal stress like the P-wave in a solid, and its velocity c_f can be obtained from the P-wave speed expression (Equation 1.82) by substituting $\mu = 0$. This wave is the compressional wave or P-wave in the fluid. The S-wave cannot be generated in a perfect fluid.

For harmonic time dependence ($e^{-i\omega t}$) and two-dimensional problems like before, p can be expressed as $p(x_1, x_2, t) = p(x_1, x_2)e^{-i\omega t}$. The governing wave equation is simplified to

$$\nabla^2 p + k_f^2 p = 0 \tag{1.198}$$

where k_f ($=\omega/c_f$) is the wave number. The solution of Equation 1.198 is given by

$$p(x_1, x_2) = Ae^{ikx_1 + i\eta x_2} \tag{1.199}$$

where

$$\eta = \sqrt{k_f^2 - k^2} \tag{1.200}$$

Because of the plane wavefront, the wave defined by Equation 1.199 is called the plane wave.

1.2.15.1 Relation between Pressure and Velocity

In absence of any body force Equation 1.193 can be written as

$$-\nabla p = \rho\ddot{\mathbf{u}} = \rho\dot{\mathbf{v}} = \rho\frac{\partial \mathbf{v}}{\partial t}$$

Let us take the dot product on both sides of the equation with **n**, where **n** is some unit vector

$$-\nabla p \cdot \mathbf{n} = \rho\frac{\partial(\mathbf{v}\cdot\mathbf{n})}{\partial t} \tag{1.201}$$

Note that

$$-\nabla p \cdot \mathbf{n} = -\frac{\partial p}{\partial x_i}\frac{\partial x_i}{\partial n} = -\frac{\partial p}{\partial n}$$

$$\rho\frac{\partial(\mathbf{v}\cdot\mathbf{n})}{\partial t} = \rho\frac{\partial(\nu_n)}{\partial t}$$

Hence,

$$\rho\frac{\partial(\nu_n)}{\partial t} = -\frac{\partial p}{\partial n} \quad \Rightarrow \quad \nu_n = -\int\frac{1}{\rho}\frac{\partial p}{\partial n}dt \tag{1.202}$$

1.2.15.2 Reflection and Transmission of Plane Waves at the Fluid-Fluid Interface

Let us now investigate how plane waves in a fluid are reflected and transmitted at an interface between two fluids. Figure 1.34 shows a plane wave p_i of magnitude 1, incident at the interface between two fluids. Reflected and transmitted waves are denoted by p_R and p_T, respectively. Amplitudes of p_R and p_T are R and T, respectively (see Figure 1.34). Shear waves cannot be present in a fluid medium reflected and transmitted waves can only have a compressional wave or P-wave as shown in the figure.

Pressure fields corresponding to the incident, reflected, and transmitted waves are given by

$$\begin{aligned} p_i &= e^{ikx_1 - i\eta_1 x_2} \\ p_R &= R\cdot e^{ikx_1 + i\eta_1 x_2} \\ p_T &= T\cdot e^{ikx_1 - i\eta_2 x_2} \end{aligned} \tag{1.203}$$

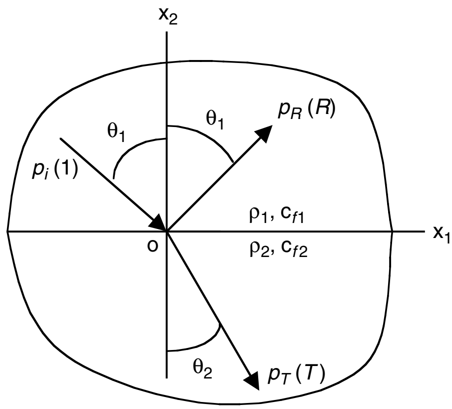

FIGURE 1.34
Incident, reflected and transmitted waves at a fluid-fluid interface

where

$$
\begin{aligned}
&k = k_{f1}\sin\theta_1 = k_{f2}\sin\theta_2 \\
&\eta_j = k_{fj}\cos\theta_j = \sqrt{k_{fj}^2 - k^2} \\
&k_{fj} = \frac{\omega}{c_{fj}}, \quad j = 1, 2
\end{aligned}
\tag{1.204}
$$

Since the pressure must be continuous across the interface.

$$
\begin{aligned}
&[(e^{-i\eta_1 x_2} + R\cdot e^{i\eta_1 x_2})e^{ikx_1}]_{x_2=0} = [T\cdot e^{-i\eta_2 x_2}e^{ikx_1}]_{x_2=0} \\
&\Rightarrow 1 + R = T
\end{aligned}
\tag{1.205}
$$

The second continuity condition that must be satisfied across the interface is the continuity of displacement or its derivative (velocity) normal to the interface. From Equation 1.202 one can therefore write

$$
\begin{aligned}
&v_2\Big|_{fluid1,x_2=0} = v_2\Big|_{fluid2,x_2=0} \\
&\Rightarrow \int \frac{1}{\rho_1}\frac{\partial(p_i + p_R)}{\partial x_2}dt\Bigg|_{x_2=0} = \int \frac{1}{\rho_2}\frac{\partial p_T}{\partial x_2}dt\Bigg|_{x_2=0} \\
&\Rightarrow \frac{1}{\rho_1}\frac{\partial(p_i + p_R)}{\partial x_2}\Bigg|_{x_2=0} = \frac{1}{\rho_2}\frac{\partial p_T}{\partial x_2}\Bigg|_{x_2=0} \\
&\Rightarrow \frac{i\eta_1}{\rho_1}(-1 + R) = -\frac{i\eta_2}{\rho_2}T
\end{aligned}
\tag{1.206}
$$

Equation 1.205 and Equation 1.206 can be written in matrix form:

$$\begin{bmatrix} -1 & 1 \\ \dfrac{\eta_1}{\rho_1} & \dfrac{\eta_2}{\rho_2} \end{bmatrix} \begin{Bmatrix} R \\ T \end{Bmatrix} = \begin{Bmatrix} 1 \\ \dfrac{\eta_1}{\rho_1} \end{Bmatrix} \tag{1.207}$$

Equation 1.206 gives

$$\begin{Bmatrix} R \\ T \end{Bmatrix} = \begin{bmatrix} -1 & 1 \\ \dfrac{\eta_1}{\rho_1} & \dfrac{\eta_2}{\rho_2} \end{bmatrix}^{-1} \begin{Bmatrix} 1 \\ \dfrac{\eta_1}{\rho_1} \end{Bmatrix} = \frac{1}{\left(\dfrac{\eta_1}{\rho_1} + \dfrac{\eta_2}{\rho_2}\right)} \begin{bmatrix} -\dfrac{\eta_2}{\rho_2} & 1 \\ \dfrac{\eta_1}{\rho_1} & 1 \end{bmatrix} \begin{Bmatrix} 1 \\ \dfrac{\eta_1}{\rho_1} \end{Bmatrix} = \frac{1}{\left(\dfrac{\eta_1}{\rho_1} + \dfrac{\eta_2}{\rho_2}\right)} \begin{Bmatrix} \dfrac{\eta_1}{\rho_1} - \dfrac{\eta_2}{\rho_2} \\ 2\dfrac{\eta_1}{\rho_1} \end{Bmatrix}$$

Hence,

$$\begin{aligned} R &= \frac{\dfrac{\eta_1}{\rho_1} - \dfrac{\eta_2}{\rho_2}}{\dfrac{\eta_1}{\rho_1} + \dfrac{\eta_2}{\rho_2}} = \frac{\dfrac{k_{f1}\cos\theta_1}{\rho_1} - \dfrac{k_{f2}\cos\theta_2}{\rho_2}}{\dfrac{k_{f1}\cos\theta_1}{\rho_1} + \dfrac{k_{f2}\cos\theta_2}{\rho_2}} = \frac{\rho_2 c_{f2}\cos\theta_1 - \rho_1 c_{f1}\cos\theta_2}{\rho_2 c_{f2}\cos\theta_1 + \rho_1 c_{f1}\cos\theta_2} \\ T &= \frac{2\dfrac{\eta_1}{\rho_1}}{\dfrac{\eta_1}{\rho_1} + \dfrac{\eta_2}{\rho_2}} = \frac{2\dfrac{k_{f1}\cos\theta_1}{\rho_1}}{\dfrac{k_{f1}\cos\theta_1}{\rho_1} + \dfrac{k_{f2}\cos\theta_2}{\rho_2}} = \frac{2\rho_2 c_{f2}\cos\theta_1}{\rho_2 c_{f2}\cos\theta_1 + \rho_1 c_{f1}\cos\theta_2} \end{aligned} \tag{1.208}$$

1.2.15.3 Plane Wave Potential in a Fluid

So far plane waves in a fluid have been expressed in terms of the fluid pressure p as given in Equations 1.197, 1.199, and 1.203. Plane waves in a solid were expressed in terms of P- and S-wave potentials. Since the elastic wave in a fluid is the P-wave, one can express the bulk wave in the fluid in terms of the P-wave potential ϕ also, as shown below:

$$\begin{aligned} \phi &= Ae^{i\mathbf{n}\cdot\mathbf{x} - i\omega t} \\ \mathbf{u} &= \underline{\nabla}\phi \end{aligned} \tag{1.209}$$

The above equation is identical for the P-wave propagation in a solid medium.

For two-dimensional time harmonic problems (time dependence $e^{-i\omega t}$ is implied) the wave potential, displacement, and stress fields in the x_1x_2 coordinate system are given by

$$\phi = Ae^{ikx_1 + i\eta x_2}$$

$$u_1 = \frac{\partial \phi}{\partial x_1} \tag{1.210}$$

$$u_2 = \frac{\partial \phi}{\partial x_2}$$

$$\sigma_{11} = \sigma_{22} = \lambda(u_{1,1} + \mathbf{u}_{2,2}) = \lambda\left(\frac{\partial^2\phi}{\partial x_1^2} + \frac{\partial^2\phi}{\partial x_2^2}\right)$$

$$= \lambda\nabla^2\phi = -\lambda k_f^2\phi = -\lambda\frac{\omega^2}{c_f^2}\phi = -\rho\omega^2\phi$$

$$\sigma_{12} = 0$$

$$p = -\sigma_{11} = -\sigma_{22} = \rho\omega^2\phi$$

In terms of the P-wave potential, the incident, reflected, and transmitted waves shown in Figure 1.34 can be expressed as

$$\phi_i = e^{ikx_1 - i\eta_1 x_2}$$

$$\phi_R = R \cdot e^{ikx_1 + i\eta_1 x_2} \tag{1.211}$$

$$\phi_T = T \cdot e^{ikx_1 - i\eta_2 x_2}$$

where k and η_j have been defined in Equation 1.204; it is assumed here that the incident wave amplitude is 1, while the reflected and transmitted wave amplitudes are R and T, respectively.

From continuity of normal displacement (u_2) and normal stress (σ_{22}) across the interface at $x_2 = 0$ one can write

$$\begin{aligned} i\eta_1(-1 + R) &= -i\eta_2 T \\ -\rho_1\omega^2(1 + R) &= -\rho_2\omega^2 T \end{aligned} \tag{1.212}$$

The above two equations can be written in matrix form

$$\begin{bmatrix} \eta_1 & \eta_2 \\ -\rho_1 & \rho_2 \end{bmatrix}\begin{Bmatrix} R \\ T \end{Bmatrix} = \begin{Bmatrix} \eta_1 \\ \rho_1 \end{Bmatrix} \tag{1.213}$$

From Equation 1.213 one gets

$$\begin{Bmatrix} R \\ T \end{Bmatrix} = \begin{bmatrix} \eta_1 & \eta_2 \\ -\rho_1 & \rho_2 \end{bmatrix}^{-1} \begin{Bmatrix} \eta_1 \\ \rho_1 \end{Bmatrix} = \frac{1}{(\eta_1\rho_2 + \eta_2\rho_1)} \begin{bmatrix} \rho_2 & -\eta_2 \\ \rho_1 & \eta_1 \end{bmatrix} \begin{Bmatrix} \eta_1 \\ \rho_1 \end{Bmatrix} = \begin{Bmatrix} \dfrac{\eta_1\rho_2 - \eta_2\rho_1}{\eta_1\rho_2 + \eta_2\rho_1} \\ \dfrac{2\eta_1\rho_1}{\eta_1\rho_2 + \eta_2\rho_1} \end{Bmatrix}$$

$$\Rightarrow \begin{Bmatrix} R \\ T \end{Bmatrix} = \begin{Bmatrix} \dfrac{\rho_2 c_{f2}\cos\theta_1 - \rho_1 c_{f1}\cos\theta_2}{\rho_2 c_{f2}\cos\theta_1 + \rho_1 c_{f1}\cos\theta_2} \\ \dfrac{2\rho_1 c_{f2}\cos\theta_1}{\rho_2 c_{f2}\cos\theta_1 + \rho_1 c_{f1}\cos\theta_2} \end{Bmatrix} \quad \textbf{(1.214a)}$$

R defined in Equations 1.208 and 1.214a are identical, but T has slightly different expressions. The reason is that in one case the wave expressions are given in terms of pressure and in another case it is in terms of potentials. The pressure-potential relation is given in Equation 1.210.

Example 1.20

Obtain Equation 1.208 from Equation 1.214a.

SOLUTION

From Equation 1.210 $p = \rho\omega^2\phi$

Hence,

$$p_i = \rho_1\omega^2\phi_i = \rho_1\omega^2 e^{ikx_1 - i\eta_1 x_2}$$

$$p_R = \rho_1\omega^2\phi_R = \rho_1\omega^2 R\cdot e^{ikx_1 + i\eta_1 x_2}$$

$$p_T = \rho_2\omega^2\phi_T = \rho_2\omega^2 T\cdot e^{ikx_1 - i\eta_2 x_2}$$

Thus,

$$\frac{|p_R|}{|p_i|} = R = \frac{\rho_2 c_{f2}\cos\theta_1 - \rho_1 c_{f1}\cos\theta_2}{\rho_2 c_{f2}\cos\theta_1 + \rho_1 c_{f1}\cos\theta_2}$$

$$\frac{|p_T|}{|p_i|} = \frac{\rho_2 T}{\rho_1} = \frac{2\rho_2 c_{f2}\cos\theta_2}{\rho_2 c_{f2}\cos\theta_1 + \rho_1 c_{f1}\cos\theta_2} = T_p \quad \textbf{(1.214b)}$$

These expressions are identical to the ones given in Equation 1.208.

Since the expressions of R are identical in the two cases, it is not necessary to specifically state if the reflection coefficient R is defined for fluid pressure or fluid potential. However, this is not the case for the transmission coefficient T, and one should use different symbols for the transmission coefficients for fluid pressure and fluid potential. Similar to the solid material, R and T without any subscript will be used to indicate reflection and transmission coefficients for fluid potentials, and the symbol T_p will be used to indicate transmission coefficient for fluid pressure. The relation between T_p and T is

$$T_p = \frac{\rho_2}{\rho_1} T \tag{1.215}$$

Note that for normal incidence

$$R = \frac{Z_2 - Z_1}{Z_2 + Z_1}$$

$$T_p = \frac{2Z_2}{Z_2 + Z_1}$$

1.2.15.4 Point Source in a Fluid

Let us analyze the wave propagation problem in a fluid when the waves are generated by a point source as shown in Figure 1.35. These concentrated pressure sources produce elastic waves with a spherical wavefront and are known as spherical waves.

If the time dependence of the point source is $f(t)$, then the governing equation of motion Equation 1.194 can be written as

$$\nabla^2 p - \frac{1}{c_f^2}\frac{\partial^2 p}{\partial t^2} = \delta(t)\delta(\mathbf{x} - \mathbf{0}) \tag{1.216}$$

where the three-dimensional delta function $\delta(\mathbf{x} - \mathbf{0})$ is zero at all points except at the origin. Because of the axisymmetric nature of the source it will generate an axisymmetric wave in the fluid. Since there is no body force in the fluid in the region that excludes the origin, the governing equation of motion in the fluid (excluding the origin) is

$$\nabla^2 p - \frac{1}{c_f^2}\frac{\partial^2 p}{\partial t^2} = 0$$

The problem is axisymmetric and its solution should be axisymmetric. In other words, p should be independent of angles θ and β of the spherical

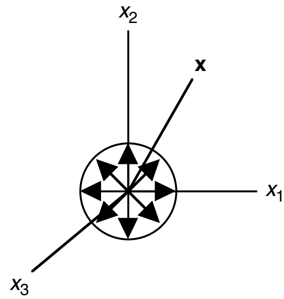

FIGURE 1.35
A point source at the origin generating spherical wave in a fluid.

coordinates and be a function of the radial distance *r* and time *t* only. For this special case the above governing equation is simplified to

$$\frac{1}{r^2}\left[\frac{\partial}{\partial r}\left(r^2\frac{\partial p}{\partial r}\right)\right]-\frac{1}{c_f^2}\frac{\partial^2 p}{\partial t^2}=0 \quad \textbf{(1.217)}$$

If we let $p = P(r, t)/r$, then the above equation is simplified to

$$\frac{\partial^2 P}{\partial r^2}-\frac{1}{c_f^2}\frac{\partial^2 P}{\partial t^2}=0 \quad \textbf{(1.218)}$$

That has a solution in the form

$$P = P_1\left(t-\frac{r}{c_f}\right)+P_2\left(t+\frac{r}{c_f}\right)$$

where P_1 and P_2 represent waves traveling in outward and inward directions, respectively. From physical considerations we cannot have an inward-propagating wave. The acceptable solution is

$$p(r,t)=\frac{P}{r}=\frac{1}{r}P_1\left(t-\frac{r}{c_f}\right)$$

It can be shown that the function P_1 has the following form (Schmerr, 1998):

$$P_1\left(t-\frac{r}{c_f}\right)=\frac{1}{4\pi}f\left(t-\frac{r}{c_f}\right)$$

The final solution of Equation 1.216 is

$$p(r,t) = \frac{1}{4\pi r} f\left(t - \frac{r}{c_f}\right) \tag{1.219}$$

If $f(t)$ is a delta function, then the governing equation and its solution are given by

$$\nabla^2 p - \frac{1}{c_f^2}\frac{\partial^2 p}{\partial t^2} = \delta(t)\delta(\mathbf{x} - \mathbf{0}) \tag{1.220}$$

$$p(r,t) = \frac{1}{4\pi r}\delta\left(t - \frac{r}{c_f}\right) \tag{1.221}$$

The Fourier transforms of Equation 1.220 and Equation 1.221 give

$$\begin{aligned} &\nabla^2 G + \frac{\omega^2}{c_f^2}\frac{\partial^2 G}{\partial t^2} = \delta(\mathbf{x} - \mathbf{0}) \\ &G(r,\omega) = \frac{e^{i\omega r/c_f}}{4\pi r} \end{aligned} \tag{1.222}$$

where G is the Fourier transform of p.

For harmonic excitation $f(t) = e^{-i\omega t}$ we can assume that the pressure field is also harmonic $p(r, t) = G(r)e^{-i\omega t}$. The equation of motion (Equation 1.215) becomes

$$\left[\nabla^2 G - \frac{\omega^2}{c_f^2}\frac{\partial^2 G}{\partial t^2}\right]e^{-i\omega t} = \delta(\mathbf{x} - \mathbf{0})e^{-i\omega t} \tag{1.223}$$

Comparing Equation 1.222 and Equation 1.223, one gets the solution for the harmonic case

$$G(r) = \frac{e^{ik_f r}}{4\pi r} \tag{1.224}$$

where $k_f = \omega/c_f$.

1.2.16 Reflection and Transmission of Plane Waves at a Fluid–Solid Interface

Figure 1.36 shows a plane P-wave of amplitude 1 striking an interface between a fluid half-space (density = ρ_f; P-wave speed = c_f) and a solid half-space (density = ρ_S; P-wave speed = c_P; S-wave speed = c_S). Reflected and

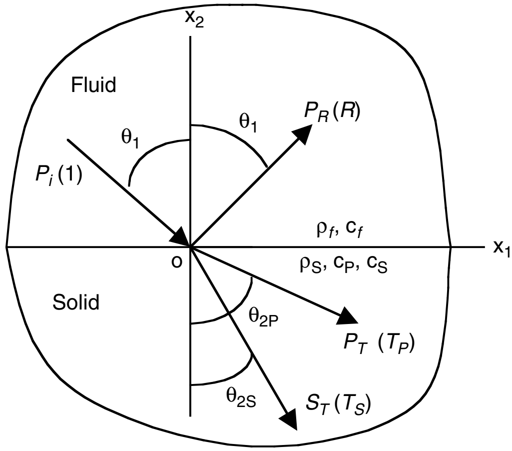

FIGURE 1.36
Incident, reflected, and transmitted waves near an interface between fluid ($x_2 \geq 0$) and solid ($x_2 \leq 0$) half-spaces.

transmitted wave directions in fluid and solid media are shown in the figure.The wave potentials in fluid and solid are

$$\begin{aligned}
\phi_i &= e^{ikx_1 - i\eta_f x_2} \\
\phi_R &= R \cdot e^{ikx_1 + i\eta_f x_2} \\
\phi_T &= T_p e^{ikx_1 - i\eta_S x_2} \\
\psi_T &= T_S e^{ikx_1 - i\beta_S x_2}
\end{aligned} \tag{1.225}$$

where

$$\begin{aligned}
k &= k_f \sin\theta_1 = k_P \sin\theta_{2P} = k_S \sin\theta_{2S} \\
\eta_f &= k_f \cos\theta_1 = \sqrt{k_f^2 - k^2} \\
\eta_S &= k_P \cos\theta_{2P} = \sqrt{k_P^2 - k^2} \\
\beta_S &= k_S \cos\theta_{2S} = \sqrt{k_S^2 - k^2} \\
k_f &= \frac{\omega}{c_f}, \quad k_P = \frac{\omega}{c_P}, \quad k_S = \frac{\omega}{c_S},
\end{aligned} \tag{1.226}$$

All waves have been expressed in terms of their potentials in Equation 1.225. From continuity of normal displacement (u_2) and stresses (σ_{22} and σ_{12}) across the interface (at $x_2 = 0$) one gets

$$
\begin{aligned}
&i\eta_f(-1+R) = i(-\eta_S T_P - kT_S)\\
&-\rho_f\omega^2(1+R) = -\mu\left\{-\left(2k^2-k_S^2\right)T_P + 2k\beta_S T_S\right\}\\
&\mu\left\{2k\eta_S T_P + \left(k^2-\beta_S^2\right)T_S\right\} = 0
\end{aligned}
\tag{1.227}
$$

The above equations can be written in matrix form:

$$
\begin{bmatrix} n_f & \eta_S & k \\ -\rho_f\omega^2 & -\mu\left(2k^2-k_S^2\right) & 2\mu k\beta_S \\ 0 & 2k\eta_S & \left(2k^2-k_S^2\right) \end{bmatrix}
\begin{Bmatrix} R \\ T_P \\ T_S \end{Bmatrix} = \begin{Bmatrix} \eta_f \\ \rho_f\omega^2 \\ 0 \end{Bmatrix}
\tag{1.228a}
$$

Equation 1.228a can be solved to obtain R, T_P, and T_S as shown below.

From the third equation in Equation 1.228a we get the following:

$$
T_S = -\frac{2k\eta_S}{\left(2k^2-k_S^2\right)}T_P
$$

Substituting this relation in the first two equations of Equation 1.228a, and after some simplification, one gets

$$
\begin{aligned}
&R - \frac{\eta_S}{\eta_f}\frac{1}{\left(\dfrac{2k^2}{k_S^2}-1\right)}T_P = 1\\
&R + \frac{\rho_S}{\rho_f}\left\{\frac{\left(\dfrac{2k^2}{k_S^2}-1\right)^2 + \dfrac{4k^2\eta_S\beta_S}{k_S^4}}{\left(\dfrac{2k^2}{k_S^2}-1\right)}\right\}T_P = -1
\end{aligned}
\tag{1.228b}
$$

Subtracting the first equation from the second equation of Equation 1.228b it is possible to obtain

$$\left\{ \frac{\rho_S}{\rho_f} \frac{\left(\frac{2k^2}{k_S^2}-1\right)^2 + \frac{4k^2\eta_S\beta_S}{k_S^4}}{\left(\frac{2k^2}{k_S^2}-1\right)} + \frac{\eta_S}{\eta_f} \frac{1}{\left(\frac{2k^2}{k_S^2}-1\right)} \right\} Tp$$

$$= \frac{\frac{\rho_S}{\rho_f}\left\{\left(\frac{2k^2}{k_S^2}-1\right)^2 + \frac{4k^2\eta_S\beta_S}{k_S^4}\right\} + \frac{\eta_S}{\eta_f}}{\left(\frac{2k^2}{k_S^2}-1\right)} T_P = -2$$

or

$$T_P = \frac{-2\left(\frac{2k^2}{k_S^2}-1\right)}{\frac{\rho_S}{\rho_f}\left\{\left(\frac{2k^2}{k_S^2}-1\right)^2 + \frac{4k^2\eta_S\beta_S}{k_S^4}\right\} + \frac{\eta_S}{\eta_f}} \qquad \textbf{(1.228c)}$$

Substituting the above expression of T_P into the first equation of Equation 1.228b one gets

$$R = 1 + \frac{\frac{\eta_S}{\eta_f}}{\left(\frac{2k^2}{k_S^2}-1\right)} \left\{ \frac{-2\left(\frac{2k^2}{k_S^2}-1\right)}{\frac{\rho_S}{\rho_f}\left\{\left(\frac{2k^2}{k_S^2}-1\right)^2 + \frac{4k^2\eta_S\beta_S}{k_S^4}\right\} + \frac{\eta_S}{\eta_f}} \right\}$$

$$= 1 + \frac{-2\frac{\eta_S}{\eta_f}}{\frac{\rho_S}{\rho_f}\left\{\left(\frac{2k^2}{k_S^2}-1\right)^2 + \frac{4k^2\eta_S\beta_S}{k_S^4}\right\} + \frac{\eta_S}{\eta_f}}$$

or

$$R = \frac{\dfrac{\rho_S}{\rho_f}\left\{\left(\dfrac{2k^2}{k_S^2}-1\right)^2+\dfrac{4k^2\eta_S\beta_S}{k_S^4}\right\}-\dfrac{\eta_S}{\eta_f}}{\dfrac{\rho_S}{\rho_f}\left\{\left(\dfrac{2k^2}{k_S^2}-1\right)^2+\dfrac{4k^2\eta_S\beta_S}{k_S^4}\right\}+\dfrac{\eta_S}{\eta_f}} \tag{1.228d}$$

Substituting Equation 1.228c into the third equation of Equation 1.228a we get

$$T_S = \frac{\dfrac{2k\eta_S}{k_S^2}}{\left(\dfrac{2k^2}{k_S^2}-1\right)}\frac{2\left(\dfrac{2k^2}{k_S^2}-1\right)}{\dfrac{\rho_S}{\rho_f}\left\{\left(\dfrac{2k^2}{k_S^2}-1\right)^2+\dfrac{4k^2\eta_S\beta_S}{k_S^4}\right\}+\dfrac{\eta_S}{\eta_f}}$$

$$= \frac{\dfrac{4k\eta_S}{k_S^2}}{\dfrac{\rho_S}{\rho_f}\left\{\left(\dfrac{2k^2}{k_S^2}-1\right)^2+\dfrac{4k^2\eta_S\beta_S}{k_S^4}\right\}+\dfrac{\eta_S}{\eta_f}} \tag{1.228e}$$

The above equations (1.228 c, d, and e) can be expressed in terms of the angles of incidence and transmission as shown below.

From Equation 1.226 one can write

$$\left(\frac{2k^2}{k_S^2}-1\right)^2 = \left(\frac{2k_S^2\sin^2\theta_{2S}}{k_S^2}-1\right)^2 = (-\cos 2\theta_{2S})^2 = \cos^2 2\theta_{2S}$$

$$\frac{\eta_S}{\eta_f} = \frac{k_P\cos\theta_{2S}}{k_f\cos\theta_1} = \frac{c_f\cos\theta_{2P}}{c_P\cos\theta_1} \tag{1.228f}$$

$$\frac{4k^2\eta_S\beta_S}{k_S^4} = \frac{4}{k_S^4}(k_S\sin\theta_{2S}\cdot k_P\sin\theta_{2P}\cdot k_S\cos\theta_{2S}\cdot k_P\cos\theta_{2P})$$

$$= \frac{k_P^2}{k_S^2}\sin 2\theta_{2P}\cdot\sin 2\theta_{2S} = \frac{c_S^2}{c_P^2}\sin 2\theta_{2P}\cdot\sin 2\theta_{2S}$$

Substituting the above relations into Equation 1.228d we get

$$R = \frac{\frac{\rho_S}{\rho_f}\left\{\left(\frac{2k^2}{k_S^2}-1\right)^2 + \frac{4k^2\eta_S\beta_S}{k_S^4}\right\} - \frac{\eta_S}{\eta_f}}{\frac{\rho_S}{\rho_f}\left\{\left(\frac{2k^2}{k_S^2}-1\right)^2 + \frac{4k^2\eta_S\beta_S}{k_S^4}\right\} + \frac{\eta_S}{\eta_f}}$$

$$= \frac{\frac{\rho_S}{\rho_f}\left\{\cos^2 2\theta_{2S} + \frac{c_S^2}{c_P^2}\sin 2\theta_{2P}\cdot\sin 2\theta_{2S}\right\} - \frac{c_f\cos\theta_{2P}}{c_P\cos\theta_1}}{\frac{\rho_S}{\rho_f}\left\{\cos^2 2\theta_{2S} + \frac{c_S^2}{c_P^2}\sin 2\theta_{2P}\cdot\sin 2\theta_{2S}\right\} + \frac{c_f\cos\theta_{2P}}{c_P\cos\theta_1}}$$

or

$$R = \frac{\frac{\rho_S c_P\cos\theta_1}{\rho_f c_f}\left\{\cos^2 2\theta_{2S} + \frac{c_S^2}{c_P^2}\sin 2\theta_{2P}\cdot\sin 2\theta_{2S}\right\} - \cos\theta_{2P}}{\frac{\rho_S c_P\cos\theta_1}{\rho_f c_f}\left\{\cos^2 2\theta_{2S} + \frac{c_S^2}{c_P^2}\sin 2\theta_{2P}\cdot\sin 2\theta_{2S}\right\} + \cos\theta_{2P}} = \frac{\Delta_2-\Delta_1}{\Delta_2+\Delta_1} \quad \textbf{(1.228g)}$$

where

$$\Delta_1 = \cos\theta_{2P}$$
$$\Delta_2 = \frac{\rho_S c_P\cos\theta_1}{\rho_f c_f}\left\{\cos^2 2\theta_{2S} + \frac{c_S^2}{c_P^2}\sin 2\theta_{2P}\cdot\sin 2\theta_{2S}\right\} \quad \textbf{(1.228h)}$$

Similarly, from Equation 1.228c we get

$$T_P = \frac{-2\left(\frac{2k^2}{k_S^2}-1\right)}{\frac{\rho_S}{\rho_f}\left\{\left(\frac{2k^2}{k_S^2}-1\right)^2 + \frac{4k^2\eta_S\beta_S}{k_S^4}\right\} + \frac{\eta_S}{\eta_f}}$$

$$= \frac{2\cos 2\theta_{2S}}{\frac{\rho_S}{\rho_f}\left\{\cos^2 2\theta_{2S} + \frac{c_S^2}{c_P^2}\sin 2\theta_{2P}\cdot\sin 2\theta_{2S}\right\} + \frac{c_f\cos\theta_{2P}}{c_P\cos\theta_1}}$$

or

$$T_P = \frac{\dfrac{2c_P\cos\theta_1\cos 2\theta_{2S}}{c_f}}{\dfrac{\rho_S c_P\cos\theta_1}{\rho_f c_f}\left\{\cos^2 2\theta_{2S} + \dfrac{c_S^2}{c_P^2}\sin 2\theta_{2P}\cdot\sin 2\theta_{2S}\right\} + \cos\theta_{2P}} = \frac{2c_P\cos\theta_1\cos 2\theta_{2S}}{c_f(\Delta_2+\Delta_1)} \tag{1.228i}$$

and from Equation 1.228e we get

$$T_S = \frac{\dfrac{4k\eta_S}{k_S^2}}{\dfrac{\rho_S}{\rho_f}\left\{\left(\dfrac{2k^2}{k_S^2}-1\right)^2 + \dfrac{4k^2\eta_S\beta_S}{k_S^4}\right\} + \dfrac{\eta_S}{\eta_f}}$$

$$= \frac{\dfrac{4k_S\sin\theta_1\cdot k_S\cos\theta_1}{k_S^2}}{\dfrac{\rho_S}{\rho_f}\left\{\cos^2 2\theta_{2S} + \dfrac{c_S^2}{c_P^2}\sin 2\theta_{2P}\cdot\sin 2\theta_{2S}\right\} + \dfrac{c_f\cos\theta_{2P}}{c_P\cos\theta_1}}$$

or

$$T_S = \frac{\dfrac{2c_S^2\sin 2\theta_{2P}}{c_P^2}\dfrac{c_P\cos\theta_1}{c_f}}{\dfrac{\rho_S c_P\cos\theta_1}{\rho_f c_f}\left\{\cos^2 2\theta_{2S} + \dfrac{c_S^2}{c_P^2}\sin 2\theta_{2P}\cdot\sin 2\theta_{2S}\right\} + \cos\theta_{2P}}$$

$$= \frac{2c_S^2\sin 2\theta_{2P}\cdot\cos\theta_1}{c_P c_f(\Delta_2+\Delta_1)} \tag{1.228j}$$

If the x_2-axis is defined as positive downward, then one can prove that the sign of T_S should change, but the signs of R and T_P remain unchanged.

Example 1.21

In Figure 1.36, suppose the incident and reflected fields in fluid are defined in terms of the fluid pressure instead of the P-wave potential, while the P- and S-waves in solid are defined in terms of the wave potentials. Obtain the reflection and transmission coefficients.

SOLUTION

The incident, reflected, and transmitted waves shown in Figure 1.36 are written in the following form:

$$\begin{aligned}
p_i &= e^{ikx_1 - i\eta_f x_2} \\
p_R &= R^* \cdot e^{ikx_1 + i\eta_f x_2} \\
\phi_T &= T_P^* e^{ikx_1 - i\eta_S x_2} \\
\psi_T &= T_S^* e^{ikx_1 - i\beta_S x_2}
\end{aligned} \tag{1.228k}$$

We would like to express R^*, T_P^*, and T_S^* in terms of R, T_P, and T_S.

Using Equation 1.210, it is possible to write from Equation 1.225

$$\begin{aligned}
p_i &= \rho_f \omega^2 \phi_i = \rho_f \omega^2 e^{ikx_1 - i\eta_f x_2} \\
p_R &= \rho_f \omega^2 \phi_R = \rho_f \omega^2 R \cdot e^{ikx_1 + i\eta_f x_2} \\
\phi_T &= T_P e^{ikx_1 - i\eta_S x_2} \\
\psi_T &= T_S e^{ikx_1 - i\beta_S x_2}
\end{aligned} \tag{1.228l}$$

Therefore, for unit amplitude of the incident pressure field the reflected and transmitted fields are modified in the following manner:

$$\begin{aligned}
p_i &= e^{ikx_1 - i\eta_f x_2} \\
p_R &= R \cdot e^{ikx_1 + i\eta_f x_2} \\
\phi_T &= \frac{T_P}{\rho_f \omega^2} e^{ikx_1 - i\eta_s x_2} \\
\psi_T &= \frac{T_S}{\rho_f \omega^2} e^{ikx_1 - i\beta_s x_2}
\end{aligned} \tag{1.228m}$$

Comparing Equation 1.228m and Equation 1.228k, one can write

$$R^* = R.$$

$$T_P^* = \frac{T_P}{\rho_f \omega^2} \tag{1.228n}$$

$$T_S^* = \frac{T_S}{\rho_f \omega^2}$$

R, T_P, and T_S expressions are given in Equations 1.228c to j.

1.2.17 Reflection and Transmission of Plane Waves by a Solid Plate Immersed in a Fluid

Figure 1.37 shows an acoustic pressure wave of amplitude 1 striking the top surface of a solid plate of thickness h immersed in a fluid. The solid plate divides the fluid space into two half-spaces. The top half-space contains the incident and reflected waves, while the bottom half-space contains the transmitted wave. The solid plate will have P- and S-waves generated in it. P- and S-wave potentials are denoted by ϕ and ψ, respectively. Subscripts U and D are used to denote upward and downward wave potentials, respectively.

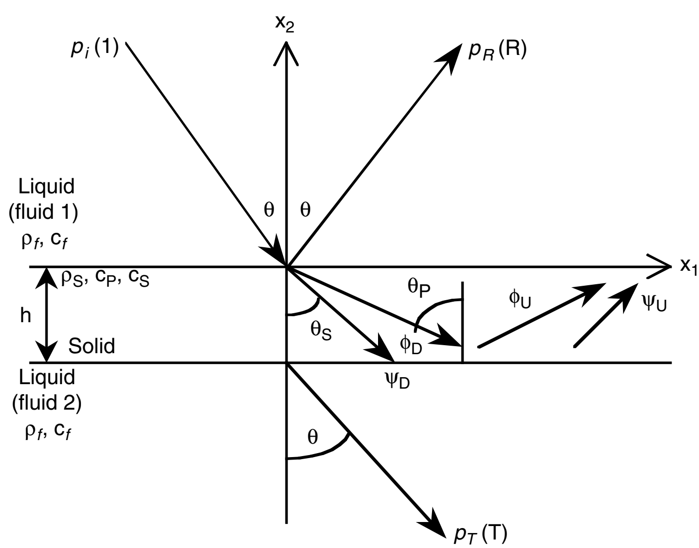

FIGURE 1.37
Incident, reflected, and transmitted pressure waves in fluid half-spaces separated by a solid plate containing upward and downward P- and S-waves.

Since the fluid properties are the same in the top and bottom-half spaces, the incident, reflected, and transmitted wave angles in the fluid are equal

(θ). The angles corresponding to the P- and S-waves in the solid plate are denoted by θ_P and θ_S, respectively.

As mentioned earlier, elastic waves in fluid can be mathematically expressed in terms of the pressure field or the potential field. In the previous section we have expressed it in terms of the potential field. Here we will express it in terms of the pressure field. Waves in the solid will be expressed in terms of the potential field. The seven waves shown by seven arrows in Figure 1.37 can be expressed in the following manner:

$$\begin{aligned}
p_i &= e^{ikx_1 - i\eta_f x_2} \\
p_R &= R \cdot e^{ikx_1 + i\eta_f x_2} \\
p_T &= T \cdot e^{ikx_1 - i\eta_f x_2} \\
\phi_D &= P_D \cdot e^{ikx_1 - i\eta_S x_2} \\
\phi_U &= P_U \cdot e^{ikx_1 + i\eta_S x_2} \\
\psi_D &= S_D \cdot e^{ikx_1 - i\beta_S x_2} \\
\psi_U &= S_U \cdot e^{ikx_1 + i\beta_S x_2}
\end{aligned} \tag{1.229}$$

where

$$\begin{aligned}
k &= k_f \sin\theta = k_P \sin\theta_P = k_S \sin\theta_S \\
\eta_f &= k_f \cos\theta = \sqrt{k_f^2 - k^2} \\
\eta_S &= k_P \cos\theta_P = \sqrt{k_P^2 - k^2} \\
\beta_S &= k_S \cos\theta_S = \sqrt{k_S^2 - k^2} \\
k_f &= \frac{\omega}{c_f}, \quad k_P = \frac{\omega}{c_P}, \quad k_S = \frac{\omega}{c_S},
\end{aligned} \tag{1.230}$$

From Equation 1.210 one can write

$$u_2 = \frac{\partial\phi}{\partial x_2} = \frac{1}{\rho\omega^2}\frac{\partial p}{\partial x_2}$$

and $\sigma_{22} = -p$.

From continuity of normal displacement (u_2) and stresses (σ_{22} and σ_{12}) across the interface (at $x_2 = 0$)

$$\frac{i\eta_f}{\rho_f\omega^2}(-1+R) = i(-\eta_S P_D + \eta_S P_U - kS_D - kS_U)$$

$$-(1+R) = -\mu\left\{-\left(2k^2 - k_S^2\right)(P_D + P_U) + 2k\beta_S(S_D - S_U)\right\} \quad \textbf{(1.2m31a)}$$

$$\mu\left\{2k\eta_S(P_D - P_U) + \left(k^2 - \beta_S^2\right)(S_D + S_U)\right\} = 0$$

and from continuity of normal displacement (u_2) and stresses (σ_{22} and σ_{12}) across the interface (at $x_2 = h$) one gets

$$-\frac{i\eta_f}{\rho_f\omega^2}TQ_f^{-1} = i\left(-\eta_S Q_P^{-1}P_D + \eta_S Q_P P_U - kQ_S^{-1}S_D - kQ_S S_U\right)$$

$$-TQ_f^{-1} = -\mu\left\{-\left(2k^2 - k_S^2\right)\left(Q_P^{-1}P_D + Q_P P_U\right) + 2k\beta_S\left(Q_S^{-1}S_D - Q_S S_U\right)\right\} \quad \textbf{(1.231b)}$$

$$\mu\left\{2k\eta_S\left(Q_P^{-1}P_D - Q_P P_U\right) + \left(k^2 - \beta_S^2\right)\left(Q_S^{-1}S_D + Q_S S_U\right)\right\} = 0$$

In Equation 1.231 μ is the shear modulus of the solid and

$$Q_f = e^{i\eta_f h}$$

$$Q_P = e^{i\eta_S h} \quad \textbf{(1.232)}$$

$$Q_S = e^{i\beta_S h}$$

The six equations given in Equation 1.231a and Equation 1.231b can be written in matrix form:

$$[A]\{X\} = \{b\} \quad \textbf{(1.233a)}$$

where

$$[A] = \begin{bmatrix} \frac{\eta_f}{\rho_f\omega^2} & 0 & \eta_S & -\eta_S & k & k \\ 1 & 0 & \mu\left(2k^2 - k_S^2\right) & \mu\left(2k^2 - k_S^2\right) & -2\mu k\beta_S & 2\mu k\beta_S \\ 0 & 0 & 2k\eta_S & -2k\eta_S & \left(2k^2 - k_S^2\right) & \left(2k^2 - k_S^2\right) \\ 0 & -\frac{\eta_f Q_f^{-1}}{\rho_f\omega^2} & \eta_S Q_P^{-1} & -\eta_S Q_P & kQ_S^{-1} & kQ_S \\ 0 & Q_f^{-1} & \mu\left(2k^2 - k_S^2\right)Q_P^{-1} & \mu\left(2k^2 - k_S^2\right)Q_P & -2\mu k\beta_S Q_S^{-1} & 2\mu k\beta_S Q_S \\ 0 & 0 & 2k\eta_S Q_P^{-1} & -2k\eta_S Q_P & \left(2k^2 - k_S^2\right)Q_S^{-1} & \left(2k^2 - k_S^2\right)Q_S \end{bmatrix}$$

(1.233b)

$$\{X\} = \begin{Bmatrix} R \\ T \\ P_D \\ P_U \\ S_D \\ S_U \end{Bmatrix}, \qquad \{b\} = \begin{Bmatrix} \dfrac{\eta_f}{\rho_f \omega^2} \\ -1 \\ 0 \\ 0 \\ 0 \\ 0 \end{Bmatrix}$$

Equation 1.233a can be solved for unknowns R, T, etc.

If the x_2-axis in Figure 1.37 is defined as positive downward, then $[A]$ matrix and $\{b\}$ vector of Equation 1.233a can be written in the following form after using the relations given in Equation 1.230:

$$[A] =$$

$$\begin{bmatrix} 0 & 0 & -\dfrac{\sin 2\theta_P}{c_P^2} & \dfrac{\sin 2\theta_P}{c_P^2} & -\dfrac{\cos 2\theta_S}{c_S^2} & -\dfrac{\cos 2\theta_S}{c_S^2} \\ 0 & 0 & -\dfrac{Q_P \sin 2\theta_P}{c_P^2} & -\dfrac{\sin 2\theta_P}{c_P^2 Q_P} & -\dfrac{Q_S \cos 2\theta_S}{c_S^2} & -\dfrac{\cos 2\theta_S}{Q_S c_S^2} \\ -1 & 0 & \rho_S \omega^2 \left(1 + 2\dfrac{c_S^2}{c_P^2} \sin^2 \theta_P\right) & \rho_S \omega^2 \left(1 + 2\dfrac{c_S^2}{c_P^2} \sin^2 \theta_P\right) & -\rho_S \omega^2 \sin 2\theta_S & \rho_S \omega^2 \sin 2\theta_S \\ 0 & -Q_f & \rho_S \omega^2 Q_P \left(1 + 2\dfrac{c_S^2}{c_P^2} \sin^2 \theta_P\right) & \dfrac{\rho_S \omega^2}{Q_P} \left(1 + 2\dfrac{c_S^2}{c_P^2} \sin^2 \theta_P\right) & -\rho_S \omega^2 Q_S \sin 2\theta_S & \dfrac{\rho_S \omega^2 \sin 2\theta_S}{Q_S} \\ \dfrac{\cos\theta}{\rho_f \omega^2 c_f} & 0 & \dfrac{\cos\theta_P}{c_P} & -\dfrac{\cos\theta_P}{c_P} & -\dfrac{\sin\theta_S}{c_S} & -\dfrac{\sin\theta_S}{c_S} \\ 0 & -\dfrac{\cos\theta}{\rho_f \omega^2 c_f} Q_f & \dfrac{Q_P \cos\theta_P}{c_P} & -\dfrac{\cos\theta_P}{c_P Q_P} & -\dfrac{Q_S \sin\theta_S}{c_S} & -\dfrac{\sin\theta_S}{c_S Q_S} \end{bmatrix}$$

(1.233c)

$$\{b\} = \begin{Bmatrix} 0 \\ 0 \\ 1 \\ 0 \\ \dfrac{\cos\theta}{\rho_f \omega^2 c_f} \\ 0 \end{Bmatrix}$$

1.2.18 Elastic Properties of Different Materials

The elastic wave speed and density of a number of materials are given in Table 1.4. These values have been collected from a number of references given in the reference list and from other sources. Three wave speeds — P-wave speed (c_P), shear wave speed (c_S), Rayleigh wave speed (c_R) and density (ρ) — are given for some materials. For other materials some information — shear wave speed, Rayleigh wave speed, or density — is missing.

1.3 Concluding Remarks

In this chapter a brief review of the fundamentals of the mechanics of elastic wave propagation in solid and fluid media are given, starting with the derivation of basic equations of the theory of elasticity and continuum mechanics. This is an important part of this book. The author's intention is not to devote the entire book to developing the theory of elastic wave propagation, but to include other advanced topics on the theory and application of ultrasonic nondestructive evaluation as done in the subsequent chapters. Only the basic and important topics on elastic waves related to ultrasonic NDE are covered in Chapter 1.

Elastic wave propagation in isotropic solids and fluids without material attenuation is discussed in detail in this chapter. Materials of this chapter can be covered in a graduate-level first course on elastic wave propagation. Some of the more advanced topics are covered in the following chapters of this book and in other books and papers listed in the references section. These include

1. Elastic wave propagation in multilayered anisotropic plates and pipes with and without material attenuation
2. Ultrasonic fields generated by sources of finite dimension
3. Nonlinear ultrasonics
4. Laser-ultrasonic techniques
5. Electro magnetic acoustics
6. Structural health monitoring by embedded ultrasonic sensors and actuators
7. Brillouin scattering
8. Acoustic microscopy
9. Ultrasonic characterization of biological materials and its clinical applications

TABLE 1.4

Elastic Wave Speeds (P-Wave Speed [c_P], S-Wave Speed [c_S], Rayleigh Wave Speed [c_R]), and Density (ρ) of Different Materials

Material	c_P (km/sec)	c_S [c_R] (km/sec)	ρ (g/cm)
Acetate, butyl (n)	1.27		0.871
Acetate, ethyl	1.18		0.900
Acetate, methyl ($C_3H_6O_2$)	1.15–1.21		0.928–0.934
Acetate, propyl	1.18		0.891
Acetone (C_3H_6O)	1.17		0.790
Acetonyl acetone ($C_6H_{10}O_2$)	1.40		0.729
Acrylic resin	2.67	1.12	1.18
Air (0°C)	0.33		0.0004
Air (20°C)	0.34		
Air (100°C)	0.39		
Air (500°C)	0.55		
Alcohol, butyl ($C_4H_{10}O$)	1.24		0.810
Alcohol, ethyl	1.18		0.789
Alcohol, methyl	1.12		0.792
Alcohol, propyl (i)	1.17		0.786
Alcohol, propyl (n)	1.22		0.804
Alcohol, t-Amyl ($C_5H_{12}O$)	1.20		0.810
Alcohol vapor (0°C)	0.231		
Alumina	10.82	6.16 [5.68]	3.97
Aluminum	6.25–6.5	3.04–3.13 [2.84–2.95]	2.70–2.80
Ammonia	0.42		
Analine ($C_6H_5NH_2$)	1.69		1.02
Argon	0.319		0.00178
Argon, liquid (−186°C to −189°C)	0.837–0.863		1.404–1.424
Bakelite	1.59		1.40
Barium titanate	4.00		6.02
Benzene (C_6H_6)	1.30		0.87
Benzol	1.33		0.878
Benzol, ethyl	1.34		0.868
Beryllium	12.7–12.9	8.71–8.88 [7.84–7.87]	1.82–1.85
Bismuth	2.18–2.20	1.10 [1.03]	9.80
Boron carbide	11.00		2.40
Bone	3.0–4.0	1.97–2.25 [1.84–2.05]	1.90
Brass (70% Cu, 30% Zn)	4.28–4.44	2.03–2.12 [1.96]	8.56
Brass, half hard	3.83	2.05	8.10
Brass naval	4.43	2.12 [1.95]	8.42
Bronze	3.53	2.23 [2.01]	8.86
Butyl rubber	1.70		1.11
Cadmium	2.78	1.50 [1.39]	8.64
Carbon bisulfide	1.16		
Carbon dioxide (CO_2)	0.258		
Curbon disulfide (CS_2)	1.15		1.26
Carbon disulfate	0.189		
Carbon monoxide (CO)	0.337		
Carbon tetrachloride (CCl_4)	0.93		1.60
Carbon, vitreous	4.26	2.68 [2.43]	1.47
Castor oil	1.48		0.969
Cesium (28.5°C)	0.967		1.88

(*Continued*)

TABLE 1.4 (Continued)

Elastic Wave Speeds (P-Wave Speed [c_P], S-Wave Speed [c_S], Rayleigh Wave Speed [c_R]), and Density (ρ) of Different Materials

Material	c_P (km/sec)	c_S [c_R] (km/sec)	ρ (g/cm)
Chlorine	0.205		
Chocolate (dark)	2.58	0.96	1.302
Choroform ($CHCl_3$)	0.987		1.49
Chromium	6.61	4.01 [3.66]	7.19
Columbium	4.92	2.10	8.57
Constantan	5.18–5.24	2.64 [2.45]	8.88–8.90
Copper	4.66–5.01	2.26–2.33 [1.93–2.17]	8.93
Duraluminium	6.40	3.12 [2.92]	2.80
Cork	0.051		0.24
Diesel oil	1.25		
Ether vapor (0°C)	0.179		
Ethyl ether ($C_4H_{10}O$)	0.986		0.713
Ethylene	0.314		
Flint	4.26	2.96	3.60
Fused quartz	5.96	3.76	2.20
Gasoline	1.25		0.803
Gallium (29.5°C)	2.74		5.95
Germanium	5.41		5.47
Glass, crown	5.26–5.66	3.26–3.52 [3.12]	2.24–3.60
Glass, heavy flint	5.26	2.96 [2.73]	3.60
Glass, quartz	5.57–5.97	3.43–3.77 [3.41]	2.2–2.60
Glass, window	6.79	3.43	
Glass, plate	5.71–5.79	3.43	2.75
Glass, pyrex	5.56–5.64	3.28–3.43 [3.01]	2.23
Glycerine ($C_3H_8O_3$)	1.92		1.26
Gold	3.24	1.20 [1.13]	19.3–19.7
Granite	3.90		
Hafnium	3.84		13.28
Helium	0.97		0.00018
Helium, liquid (–269°C)	0.18		0.125
Helium, liquid (–271.5°C)	0.231		0.146
Hydrogen	1.28		0.00009
Hydrogen, liquid (–252.7°C)	1.13		0.355
Ice	3.99	1.99	1.0
Inconel	5.70	3.0 [2.79]	8.25–8.39
Indium	2.22–2.56		7.30
Invar (63.8% Fe, 36% Ni, 0.2% Cu)	4.66	2.66 [2.45]	8.00
Iron, soft	5.90–5.96	3.22 [2.79–2.99]	7.7
Iron, cast	4.50–4.99	2.40–2.81 [2.3–2.59]	7.22–7.80
Kerosene	1.32		0.81
Kidney	1.54		1.05
Lead	2.16	0.70 [0.63–0.66]	11.34–11.40
Lead zirconate titanate (PZT)	3.79		7.65
Linseed oil	1.77		0.922
Liver	1.54		1.07
Lucite	2.68–2.70	1.05–1.10	1.15–1.18
Magnesium	5.47–6.31	3.01–3.16 [2.93]	1.69–1.83
Manganese	4.60–4.66	2.35	7.39–7.47

Marble	6.15		9.5

TABLE 1.4 (Continued)

Elastic Wave Speeds (P-Wave Speed [c_P], S-Wave Speed [c_S], Rayleigh Wave Speed [c_R]), and Density (ρ) of Different Materials

Material	c_P (km/sec)	c_S [c_R] (km/sec)	ρ (g/cm)
Mercury (20°C)	1.42–1.45		13.5–13.8
Methane	0.43		0.00074
Methylene iodide	0.98		
Molybdenum	6.30–6.48	3.35–3.51 [3.11–3.25]	10.2
Monel	5.35–6.04	2.72 [1.96–2.53]	8.82–8.83
Monochlorobenzene (C_6H_5Cl)	1.27		1.107
Morpholine (C_4H_9NO)	1.44		1.00
Motor oil (SAE 20)	1.74		0.87
Mylar	2.54		1.18
n-Hexanol ($C_6H_{14}O$)	1.30		0.819
Neon	0.43		
Neoprene	1.56		1.31
Nickel	5.61–5.81	2.93–3.08 [2.64–2.86]	8.30–8.91
Niobium	5.07	2.09 [1.97]	8.59
Nitric oxide	0.325		
Nitrobenzene ($C_6H_5NO_2$)	1.46		1.20
Nitrogen (0–20°C)	0.33–0.35		0.00116–0.00125
Nitrogen, liquid (–197°C)	0.869		0.815
Nitrogen, liquid (–203°C)	0.929		0.843
Nitromethane (CH_3NC_2)	1.33		1.13
Nitrous oxide	0.26		
Nylon	2.62	1.10 [1.04]	1.11–1.14
Oil	1.38–1.50		0.92–0.953
Olive oil	1.43		0.948
Oxygen (0–20°C)	0.32–0.33		0.00132–0.00142
Oxygen, liquid (–183.6°C)	0.971		1.143
Oxygen, liquid (–210°C)	1.13		1.272
Parrafin (15°C)	1.30		
Parracin oil	1.42		0.835
Peanut oil	1.46		0.936
Pentane	1.01		0.621
Perspex (PMMA)	2.70	1.33 [1.24]	1.19
Petroleum	1.29		0.825
Plastic, acrylic resin	2.67	1.12	1.18
Platinum	3.26–3.96	1.67–1.73 [1.60]	21.4
Plexiglas	2.67–2.77	1.12–1.43	1.18–1.27
Plutonium	1.79		15.75
Polycarbonate	2.22		1.19
Polyester casting resin	2.29		1.07
Polyethylene	2.0–2.67		0.92–1.10
Polythelyne (low density)	1.95	0.54 [0.51]	0.92
Polyethylene (TCI)	1.60		
Polypropylene	2.74		0.904
Polystyrene (Styron 666)	2.40	1.15 [1.08]	1.05
Polystyrene	2.67	1.10	2.80
Polyvinyl chloride	2.30		1.35
Polyvinyl chloride acetate	2.25		

(Continued)

TABLE 1.4 (Continued)

Elastic Wave Speeds (P-Wave Speed [c_P], S-Wave Speed [c_S], Rayleigh Wave Speed [c_R]), and Density (ρ) of Different Materials

Material	c_P (km/sec)	c_S [c_R] (km/sec)	ρ (g/cm)
Polyvinyl formal	2.68		
Polyvinylidene chorlide	2.40		1.70
Potassium (100°C)	1.86		0.818
Potassium (200°C)	1.81		0.796
Potassium (400°C)	1.71		0.751
Potassium (600°C)	1.60		0.707
Potassium (800°C)	1.49		0.662
Quartz	5.66–5.92	3.76	2.65
Refrasil	3.75		1.73
Rock salt (x direction)	4.78		
Rochelle salt	5.36	3.76	2.20
Rubber	1.26–1.85		
Salt solution (10%)	1.47		
Salt solution (15%)	1.53		
Salt solution (20%)	1.60		
Sandstone	2.92	1.84 [1.68]	
Sapphire	9.8–11.15		3.98
Silica (fused)	5.96	3.76 [3.41]	2.15
Silicon carbide	12.10	7.49 [6.81]	3.21
Silicone oil (25°C, Dow 710 fluid)	1.35		
Silicon nitride	10.61	6.20 [5.69]	3.19
Silver	3.60–3.70	1.70 [1.59]	10.5
Silver-18 Ni	4.62	2.31	
Silver epoxy, e-solder	1.90	0.98 [0.91]	2.71
Sodium (100°C)	2.53		0.926
Sodium (200°C)	2.48		0.904
Sodium (400°C)	2.37		0.857
Sodium (600°C)	2.26		0.809
Sodium (800°C)	2.15		0.759
Spleen	1.50		1.07
Stainless steel	5.98	3.3 [3.05]	7.80
Steel	5.66–5.98	3.05–3.3 [2.95–3.05]	7.80–7.93
Tantalum	4.16	2.04 [1.90]	16.67
Teflon	1.35–1.45		2.14–2.20
Thorium	2.40	1.56 [1.40]	11.73
Tin	3.32–3.38	1.59–1.67 [1.49]	7.3
Tissue (beef)	1.55		1.08
Tissue (brain)	1.49		1.04
Tissue (human)	1.47		1.07
Titanium	6.10–6.13	3.12–3.18 [2.96]	4.51–4.54
Titanium carbide	8.27	5.16 [4.68]	5.15
Titanium carbide with 6% Co	6.66	3.98 [3.64]	15.0
Tungsten	5.18–5.41	2.64–2.89 [2.46–2.67]	19.25
Transformer oil	1.39		0.92
Uranium	3.37	1.94 [1.78]	19.05
Uranium dioxide	5.18		10.96
Vanadium	6.02	2.77 [2.60]	6.09
Water (20°C)	1.48		1.00

TABLE 1.4 (Continued)

Elastic Wave Speeds (P-Wave Speed [c_P], S-Wave Speed [c_S], Rayleigh Wave Speed [c_R]), and Density (ρ) of Different Materials

Material	c_P (km/sec)	c_S [c_R] (km/sec)	ρ (g/cm)
Water (sea)	1.53		1.025
Water vapor (0°C)	0.401		
Water vapor (100°C)	0.405		
Water vapor (130°C)	0.424		
Wood (oak)	4.47–4.64	1.75	0.4615
Wood (pine, along the fiber)	3.32		
Wood (poplar, along the fiber)	4.28		
Zinc	4.17–4.19	2.42 [2.22]	7.10–7.14
Zinc oxide (c-axis)	6.40	2.95 [2.77]	5.61
Zircaloy	4.72	2.36 [2.20]	9.36
Zirconium	4.65	2.25 [2.10]	6.51

For some materials ranges (upper and lower bounds) for the material properties collected from different references are given.

EXERCISE PROBLEMS

Problem 1.1

Simplify the following expressions (note that δ_{ij} is the Kronecker delta, repeated index means summation and comma represents derivative):

(a) δ_{mm} (b) $\delta_{ij}\,\delta_{kj}$ (c) $\delta_{ij}\,u_{k,kj}$ (d) $\delta_{ij}\,\delta_{ij}$

(e) $\delta_{mm}\delta_{ij}\,x_j$ (f) $\delta_{km}u_{i,jk}\,u_{i,jm}$ (g) $\dfrac{\partial x_m}{\partial x_k}\dfrac{\partial x_m}{\partial x_k}$

Problem 1.2

Express the following mathematical operations in index notation

(a) $\underline{\nabla}\cdot\mathbf{u}$ (b) $\nabla^2\phi$ (c) $\nabla^2 \mathrm{u}$ (d) $\underline{\nabla}\phi$ (e) $\underline{\nabla}\times\mathbf{u}$ (f) $\underline{\nabla}\times(\underline{\nabla}\times\mathrm{u})$

(g) $[C]=[A][B]$ (h) $[A]^T[B]\neq[A][B]^T$ (i) $\{c\}=[A]^T\{b\}$ (j) $\underline{\nabla}\cdot(\underline{\nabla}\times\mathrm{u})$
(k) $\underline{\nabla}\times(\underline{\nabla}\phi)$ (l) $\underline{\nabla}(\underline{\nabla}\cdot\mathbf{u})$ (m) $\underline{\nabla}\cdot(\underline{\nabla}\phi)$

where **u** is a vector quantity and ϕ is a scalar quantity; A, B, and C are 3×3 matrix; c and b are 3×1 vectors.

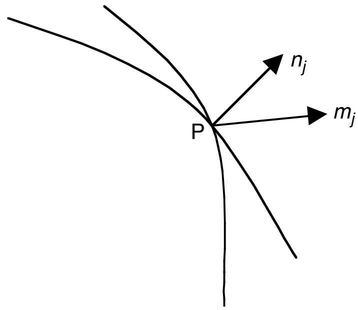

FIGURE 1.38

Problem 1.3

Consider two surfaces passing through the point P (see Figure 1.38). The unit normal vectors on these two surfaces at point P are m_j and n_j, respectively. The traction vectors on the two surfaces at point P are denoted by ($\overset{m}{T}_i$ and $\overset{n}{T}_i$), respectively. Check if the dot product between $\underline{\overset{m}{T}}$ and $\underline{n}$ is the same or is different from the dot product between $\underline{\overset{n}{T}}$ and $\underline{m}$.

Problem 1.4

(a) A thin triangular plate is fixed along the boundary OA and is subjected to a uniformly distributed horizontal load p_0 per unit area along the boundary AB as shown in Figure 1.39. Give all boundary conditions in terms of displacement or stress components in the x_1x_2-coordinate system.

(b) If p_0 acts normal to the boundary AB, what will be the stress boundary conditions along line AB?

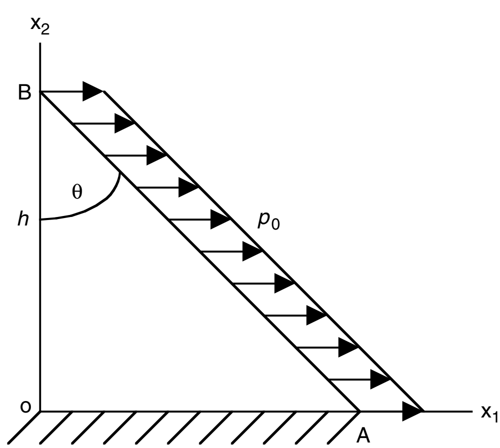

FIGURE 1.39

Problem 1.5

The quarter disk of radius a, shown in Figure 1.40, is subjected to a linearly varying shear stress that varies from 0 to T_0 along boundaries AO and CO and uniform pressure P_0 along the boundary ABC. Assume that all out-of-plane stress components are zero:

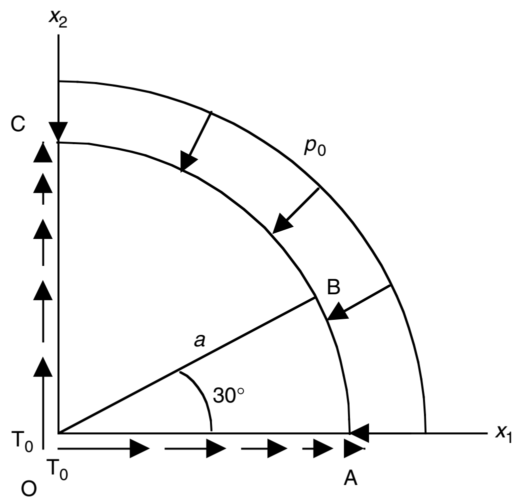

FIGURE 1.40

(a) Give all stress boundary conditions along the boundaries OA and OC in terms of stress components σ_{11}, σ_{22}, and σ_{12} in the Cartesian coordinate system.

(b) Give all stress boundary conditions along the boundaries OA and OC in terms of stress components σ_{rr}, $\sigma_{\theta\theta}$, and $\sigma_{r\theta}$ in the cylindrical coordinate system.

(c) Give all stress boundary conditions at point B in terms of stress components σ_{11}, σ_{22}, and σ_{12} in the Cartesian coordinate system.

(d) Give all stress boundary conditions along the boundary ABC in terms of stress components σ_{rr}, $\sigma_{\theta\theta}$, and $\sigma_{r\theta}$ in the cylindrical coordinate system.

Problem 1.6

(a) A dam made of isotropic material has two different water heads on two sides, as shown in Figure 1.41. Define all boundary conditions along the boundaries AB and CD in terms of stress components σ_{xx}, σ_{yy}, and τ_{xy}.

(b) If the dam is made of orthotropic material, what changes, if any, should be in your answer to part a?

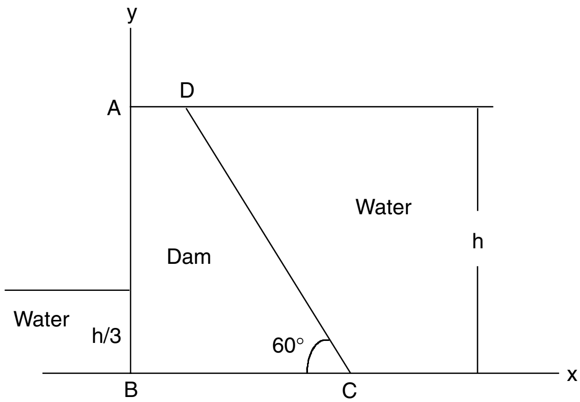

FIGURE 1.41

Problem 1.7

Express the surface integral $\oint_S x_i n_j \, dS$ in terms of the volume V bounded by the surface S (see Figure 1.42). n_j is the j-th component of the outward unit normal vector on the surface.

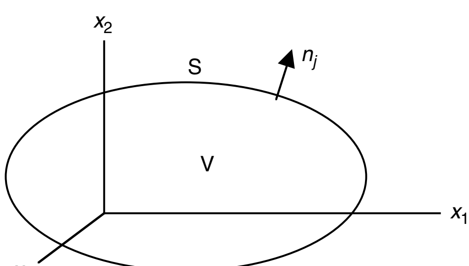

FIGURE 1.42

Problem 1.8

Obtain the principal stresses and their directions for the following stress state:

$$[\sigma] = \begin{bmatrix} 5 & -3 & 0 \\ -3 & 2 & 0 \\ 0 & 0 & 10 \end{bmatrix}$$

Problem 1.9

An anisotropic elastic solid is subjected to some load that gives a strain state ε_{ij} in the $x_1x_2x_3$ coordinate system. In a different (rotated) coordinate system $x_{1'}x_{2'}x_{3'}$, the strain state is transformed to $\varepsilon_{m'n'}$.

(a) Do you expect the strain energy density function U_0 to be a function of strain invariants only? Justify your answer.
(b) Do you expect the same or different expressions of U_0 when it is expressed in terms of ε_{ij} or $\varepsilon_{m'n'}$? Justify.
(c) Do you expect the same or different numerical values of U_0 when you compute it from its expression in terms of ε_{ij} and from its expression in terms of $\varepsilon_{m'n'}$? Justify.

Answer parts (a), (b), and (c) if the material is isotropic.

Problem 1.10

Stress-strain relation for a linear elastic material is given by $\sigma_{ij} = C_{ijkl}\varepsilon_{kl}$. Starting from the stress-strain relation for an isotropic material, prove that C_{ijkl} for the isotropic material is given by $\lambda\delta_{ij}\delta_{k\ell} + \mu(\delta_{ik}\delta_{j\ell} + \delta_{i\ell}\delta_{jk})$.

Problem 1.11

Obtain the governing equation of equilibrium in terms of displacement for a material whose stress-strain relation is given by

$$\sigma_{ij} = \alpha_{ijkl}\varepsilon_{km}\varepsilon_{ml} + \beta_{ijkl}\varepsilon_{kl} + \delta_{ij}\gamma$$

where α_{ijkl} and β_{ijkl} are material properties that are constants over the entire region, and γ is the residual hydrostatic state of stress that varies from point to point.

Problem 1.12

Starting from the three-dimensional stress transformation law, $\sigma_{i'j'} = l_{i'm}l_{j'n}\sigma_{mn}$, prove that for two-dimensional stress transformation the following equations hold good:

$$\sigma'_{11} = \sigma_{11}\cos^2\theta + \sigma_{22}\sin^2\theta + 2\sigma_{12}\sin\theta\cos\theta$$

$$\sigma'_{22} = \sigma_{11}\sin^2\theta + \sigma_{22}\cos^2\theta - 2\sigma_{12}\sin\theta\cos\theta$$

$$\sigma'_{12} = (-\sigma_{11} + \sigma_{22})\sin\theta\cos\theta + \sigma_{12}(\cos^2\theta - \sin^2\theta)$$

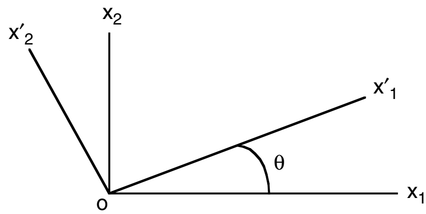

FIGURE 1.43

Problem 1.13

Consider a bar (one-dimensional structure with zero body force) for which the stress-strain relation is given by $\sigma_{11} = E\varepsilon_{11}$.

(a) Applying Newton's law (force = mass × acceleration) to an elemental segment of the bar, derive the governing equation of motion for the bar in the form of the wave equation.
(b) What should be the elastic wave speed in the bar?

Problem 1.14

An infinite plate of thickness $2h$ is subjected to a constant normal pressure p_0 at its two surfaces at time $t \geq 0$ (see Figure 1.44). Calculate the displacement field $\mathbf{u}$ at point P(δ,0,0), where $0 < \delta < h$, at time $t = h/c_P$, where c_P is the P-wave speed in the material.

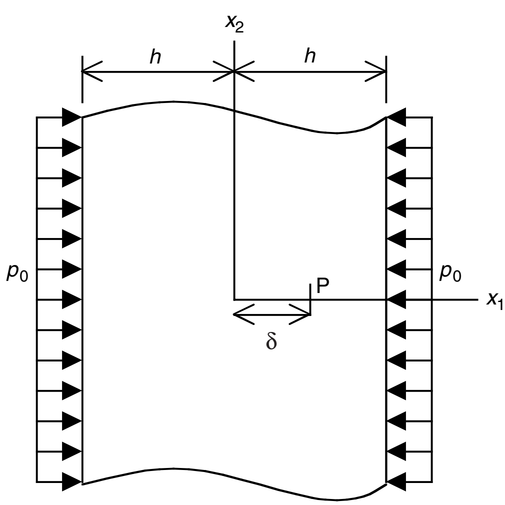

FIGURE 1.44

Problem 1.15

(a) A half-space is subjected to a time-dependent shear stress field p(t) at $x_1 = 0$ as shown in Figure 1.45. Find the stress and displacement fields at a point (x_1, x_2, x_3) at time $t > 0$.

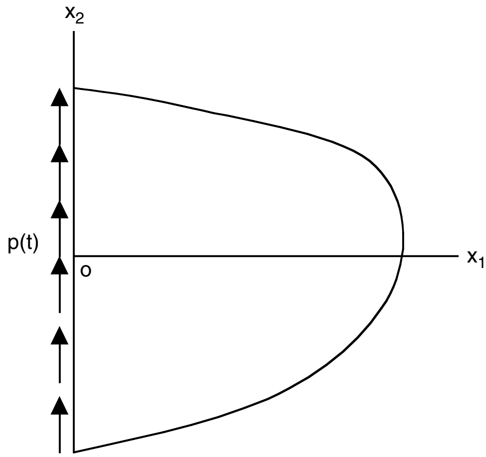

FIGURE 1.45

(b) Let $p(t)$ be 1 for $5 < t < 15$ and 0 for other values of t. Plot u_1, u_2, σ_{11}, and σ_{12} as a function of time at $x_1 = 5\sqrt{\frac{\mu}{\rho}}$, $x_2 = 0$, and $x_3 = 0$. Where μ and ρ are shear modulus and Poission's ratio, respectively.

Problem 1.16

A linear elastic half-space is subjected to a time-dependent inclined loading $p(t)$ on its surface as shown in Figure 1.46. Duration time of the load is T and its magnitude is P. The problem geometry and applied load are independent of the x_2- and x_3-coordinates. Plot the variation of two displacement components u_1 (by solid line) and u_2 (by dashed line) at point Q (x_1=X_0, x_2=Y_0) on the same plot as a function of time. Plot the variation of the two stress components σ_{11} (by solid line) and σ_{12} (by dashed line) as a function of time at the same point Q. Give important values in your plots. Lame's first and second constants and density of the solid are λ, μ, and ρ, respectively. You can directly plot the results without showing the intermediate steps. For both displacement and stress components plot positive quantities above the t-axis and negative quantities below the t-axis.

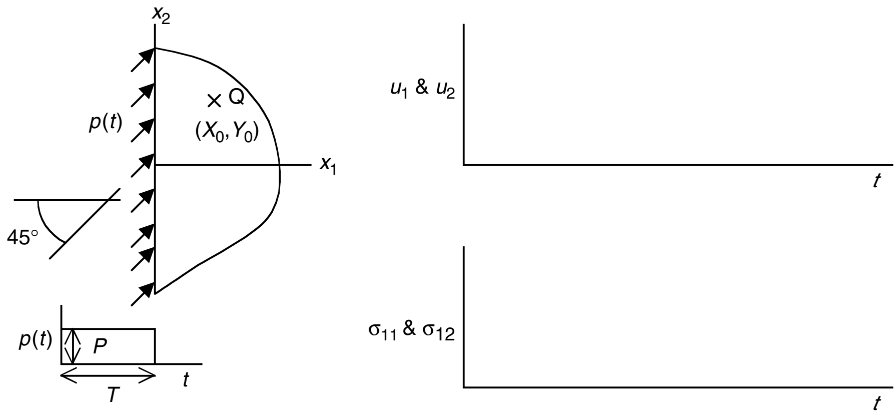

FIGURE 1.46

Problem 1.17

(a) For a vertically propagating SH-wave in a half-space (see Figure 1.47), calculate the total displacement and stress fields on a semicircle of radius 'a' in terms of α, a, and k_S (ω/c_S).

(b) Check if the stress-free boundary conditions are satisfied at the points, where the semicircle meets the surface at $x_3 = 0$.

(c) Find the amplitude of maximum displacement on the semicircle and locate the point where the displacement amplitude is maximum.

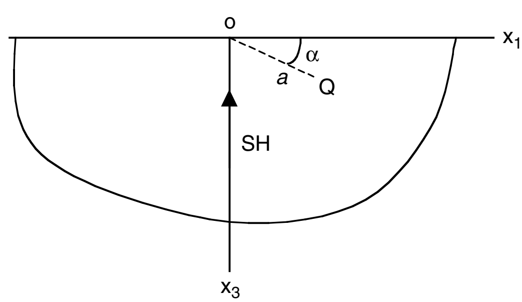

FIGURE 1.47

Problem 1.18

A uniform half-space is excited by a time harmonic incident plane P-wave as shown in Figure 1.48. If the incident field potential is given by
$\Phi_i(x_1, x_3, t) = \phi_i(x_1, x_3)e^{-i\omega t} = Ae^{i(kx_1 - \eta x_3)}e^{-i\omega t}$

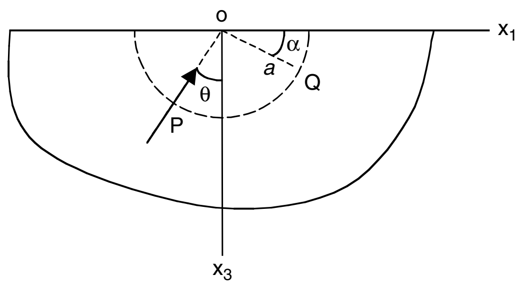

FIGURE 1.48

calculate the displacement field u_1 and u_3 at a point Q as a function of a, α and θ. α varies from 0 to π and θ varies from 0 to π/2. Assume that the reflection coefficients of the half-space are $R_{PP}(\theta)$ and $R_{PS}(\theta)$ for reflected P- and S-waves, respectively. Assume P- and S-wave speeds to be c_P and c_S, respectively. Express your final results in terms of $R_{PP}(\theta)$, $R_{PS}(\theta)$, a, α, ω, c_P, and c_S.

Problem 1.19

(a) Prove that the transfer coefficient (T) for an incident SH-wave in a layered half-space is given by

$$T = \frac{1}{\cos\left\{\dfrac{\omega h}{c_{S1}c_{S2}}\sqrt{c_{S2}^2 - c_{S1}^2 \sin^2\theta}\right\}}$$

where the transfer coefficient is defined as (see Figure 1.49).

$$T = \frac{u_2(x_1, 0)}{u_2(x_1, h)}$$

The equation of the incident wave is given by

$$u_{2i} = A\exp\left\{i\frac{\omega}{c_{S2}}(x_1\sin\theta - x_3\cos\theta - c_{S2}t)\right\}$$

(b) What is the value of the transfer function for: (1) $c_{S1} = c_{S2}$, (2) $h = 0$?

Problem 1.20

Obtain the expressions of the reflected wave amplitudes for a plane P-wave striking a plane rigid boundary at an inclination angle θ, after propagating through an elastic half-space. The inclination angle is measured from the axis normal to the rigid boundary.

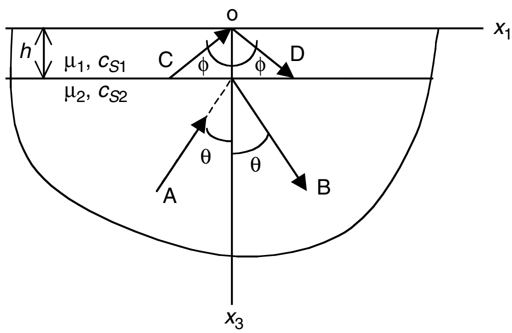

FIGURE 1.49

Problem 1.21

For two-dimensional wave propagation problems, P- and S-wave potentials are given by

$$\phi = \phi(n_1x_1 + n_2x_2 - c_Pt), \qquad \psi = \psi(n_1x_1 + n_2x_2 - c_St)$$

(a) Prove that the wave propagation direction and the wavefront are perpendicular to each other for both these waves.
(b) When the waves propagate in the x_1-direction, show that for

(1) $\phi \neq 0, \psi = 0, u_2 = \sigma_{12} = 0$, and for (2) $\phi = 0, \psi \neq 0, u_1 = \sigma_{11} = \sigma_{22} = 0$

Problem 1.22

A plane SH-wave propagating in a solid medium strikes the stress-free boundaries at $x_1 = 0$ and $x_2 = 0$ in the quarter space (see Figure 1.50). The displacement field associated with the incident SH-wave is given by $u_{3i} = e^{-ikx_1 - i\beta x_2}$; the time dependence $e^{-i\omega t}$ is implied. When the incident SH-wave encounters the two stress-free surfaces, reflected plane waves are generated to satisfy the boundary conditions.

Obtain the complete displacement field (considering incident as well as all reflected waves) in this quarter space, and show that the stress-free boundary conditions at the two surfaces are satisfied when the total field is considered.

Problem 1.23

From the Rayleigh wave dispersion equation

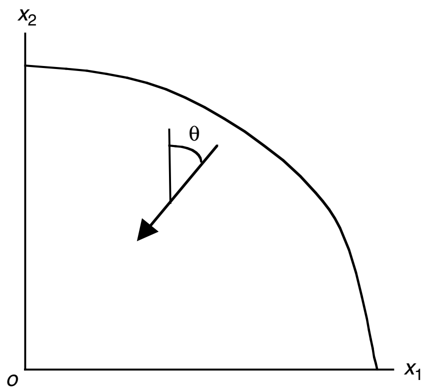

FIGURE 1.50

$$\left(2-\frac{c_R^2}{c_s^2}\right)^2-4\left(1-\frac{c_R^2}{c_p^2}\right)^{1/2}\left(1-\frac{c_R^2}{c_s^2}\right)^{1/2}=0$$

prove that when the Rayleigh wave speed is close to the shear wave speed (that is true for most materials) it is possible to approximately obtain the Rayleigh wave speed c_R from the relation

$$\frac{c_R}{c_s}=\frac{0.875+1.125\nu}{1+\nu}$$

where ν is Poission's ratio. (Hint: substitute $c/c_s = 1 + \Delta$, where Δ is a small number, and then ignore higher order terms in Δ).

Problem 1.24

Consider the horizontal shearing motions of a plate of thickness $2h$. Plate surfaces at $x_2 = +h$ and $-h$ are rigidly fixed.

(a) Determine the dispersion relation (guided wave speed as a function of frequency) for this problem geometry and plot the dispersion curves.
(b) Compute and plot the mode shapes for first few modes.
(c) Discuss the differences and similarities between the wave propagation characteristics (dispersion relation and mode shapes) of this problem and the stress-free plate problem discussed in Section 1.2.12.1.

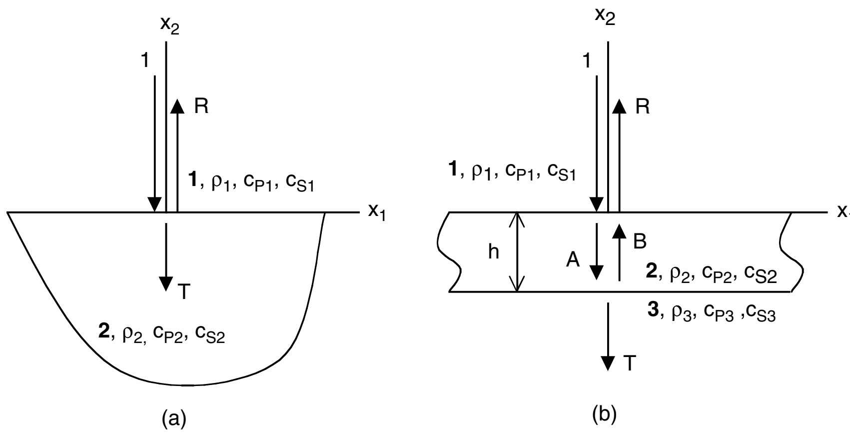

FIGURE 1.51

Problem 1.25

P-wave is normally incident at the interface of two solids, as shown in Figure 1.51a and Figure 1.51b. Incident P-wave amplitude is 1 and reflected wave amplitude is R. Material properties are shown in the figures.

(a) What is the value of R for the problem geometry shown in Figure 1.51a? You do not need to derive it; simply give its expression, using the material properties given.

(b) For the material properties shown in the two figures should the two R be the same? Note that there are a total of three materials in Figure 1.51b but only two in Figure 1.51a.

(c) Should the value of R in Figure 1.51b change when properties of material 3 are changed but those for materials 1 and 2 are unchanged?

(d) Stress and displacement continuity conditions at what interface of Figure 1.51b (top, bottom, or both) do you need to satisfy to solve for R?

(e) Stress and displacement continuity conditions at what interface of Figure 1.51b (top, bottom, or both) do you need to satisfy to solve for T?

(f) Write all necessary equations in terms of T and other unknown constants from which you can solve for T of Figure 1.51b. You do not need to give the final expression of T; only write the necessary equations.

Problem 1.26

Consider the phase velocity (c_{ph}) variation with frequency ω, as shown by the continuous line in the top plot of Figure 1.52. Obtain and plot the group velocity (c_g) variations, as a function of frequency ω, in 3 ranges (for ω between 0 and 1, between 1 and 2, and greater than 2). Give the group velocity values at $\omega = 0.5, 1.5$, and 2.5. If you use any relation other than the definitions of the phase velocity and group velocity, then you must derive it.

(Hint: From the definitions of phase velocity and group velocity, $c_{ph} = \frac{\omega}{k}$, $c_g = \frac{d\omega}{dk}$, first obtain the group velocity as a function of the phase velocity (c_{ph}) and its derivative $\left(\frac{dc_{ph}}{d\omega}\right)$. Then use that relation to solve the problem.)

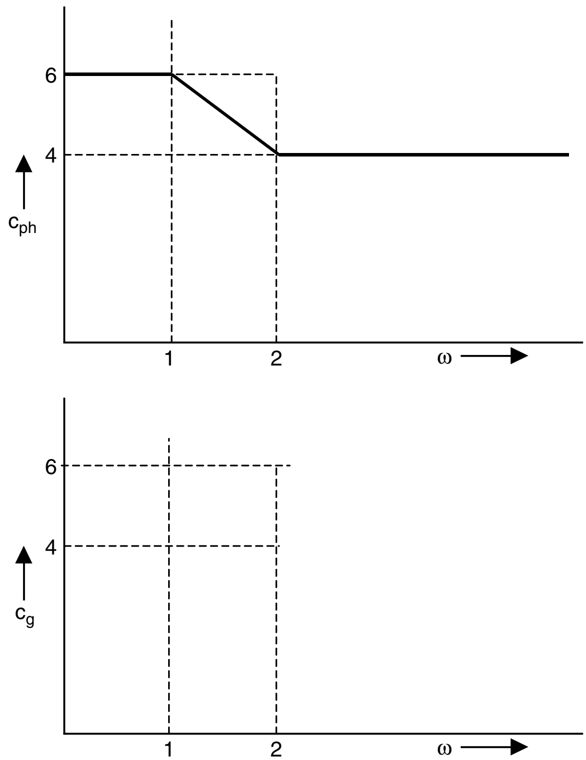

FIGURE 1.52

Problem 1.27

If a vector (such as force, velocity) has components A in both x_1- and x_2-directions, then the resultant vector has a magnitude $A\sqrt{2}$ and acts in x_1-direction (see Figure 1.53).

Two plane P-waves with harmonic time dependence, propagate in a material in x_1- and x_2-directions with a velocity c_P. Wave potentials for these two waves are given by

$$\phi_1 = Ae^{ik_P x_1 - i\omega t}$$

$$\phi_2 = Ae^{ik_P x_2 - i\omega t}$$

where $k_P = \dfrac{\omega}{c_P}$.

(a) In this material find the total particle displacement (magnitude and direction) at two points; (1) the origin, $x_1 = x_2 = 0$ and (2) at a second point for which $x_1 = x_2 = h$.

(b) It is suggested by a student that the combined effect of these two harmonic waves is a resultant wave propagating in the $x_{1'}$-direction with a wave amplitude $A\sqrt{2}$. Do you agree with this statement? Mathematically justify your answer.

(c) It is suggested by another student that the combined effect of these two harmonic waves is a resultant wave propagating in the $x_{1'}$-direction with a velocity $c_P\sqrt{2}$. Do you agree with this statement? Mathematically justify your answer.

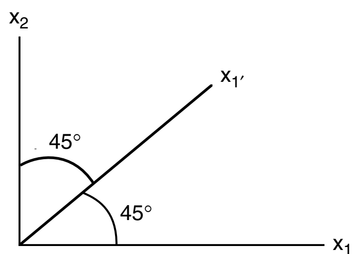

FIGURE 1.53

References

Achenbach, J. D., *Wave Propagation in Elastic Solids*, North-Holland, Amsterdam, 1973.

Auld, B. A., *Acoustic Fields and Waves in Solids*, 2nd ed., Vols. 1 and 2, Kreiger, Malabar, Florida, 1990.

Bland, D. R., *Wave Theory and Applications*, Oxford University Press, New York, 1988.

Brekhovskikh, L. M., *Waves in Layered Media*, Academic Press, New York, 1960.

Briggs, A., *Acoustic Microscopy*, Clarendon Press, Oxford, 1992.

Eringen, A. C., and Suhubi, E. S., *Linear Theory* (Elastodynamics, Vol. 2), Academic Press, New York, 1975.

Ewing, W. M., Jardetsky, W. S., and Press, F., *Elastic Waves in Layered Media*, McGraw-Hill, New York, 1957.

Graff, K. F., *Wave Motion in Elastic Solids*, Dover Publications, 1991.

Hung, B.-N. and Goldstein, A., Acoustic Parameters of Commercial Plastics, *IEEE Trans*., Vol. SU-30, pp. 249–254, 1983.

Jorgensen, C. S., and Kundu, T., Measurement of Material Elastic Constants of Trabecular Bone: A Micromechanical Analytic Study Using 1 GHz Acoustic Microscope, *Journal of Orthopaedic Research*, Vol. 20, pp. 151–158, 2002.

Kay, G. W. C., and Laby, T. H., *Tables of Physical and Chemical Constants,* Longman, London, 1986.

Kolsky, H., *Stress Waves in Solids*, Dover, New York, 1963.
Krautkramer, J., and Krautkramer, H., *Ultrasonic Testing of Materials*, 4th ed., Springer-Verlag, New York, 1990.
Liu, G. R., and Xi, Z. C., *Elastic Waves in Anisotropic Laminates*, CRC Press, 2002.
Mal, A. K., and Singh, S. J., *Deformation of Elastic Solids*, Prentice Hall, New Jersey, 1991.
Miklowitz, J., *The Theory of Elastic Waves and Wave Guides*, North-Holland, New York, 1978.
Moon, P., and Spencer, D. E., *Vectors*, Pub. D. Van Nostrand Company, Inc., Princeton, New Jersey, 1965.
Nayfeh, A. H., *Wave Propagation in Layered Anisotropic Media with Applications to Solids*, Elsevier, Amsterdam, 1995.
Rayleigh, J. W. S., *The Theory of Sound*, Dover, New York, 1945.
Rose, J. L., *Ultrasonic Waves in Solid Media*, Cambridge University Press, 1999.
Schmerr, L. W., *Fundamentals of Ultrasonic Nondestructive Evaluation — A Modeling Approach*, Plenum Press, New York, 1998.
Selfridge, A. R., Approximate Material Properties in Isotropic Materials, *IEEE Trans.*, Vol. SU-32, pp.381–394, 1985.
Viktorov, I. A., *Rayleigh and Lamb Waves — Physical Theory and Applications*, Plenum Press, New York, 1967.

2

Modeling of Ultrasonic Field by Distributed Point Source Method

Dominique Placko and Tribikram Kundu

CONTENTS

0-8493-1462-3/02/$0.00+$1.50

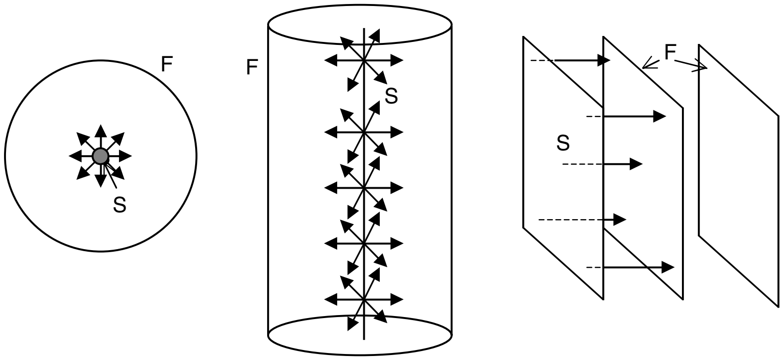

FIGURE 2.1
Point source (left), line source (middle), and infinite plane source (right) generating spherical, cylindrical, and plane wavefronts, respectively. Sources are denoted by S and the wavefronts by F.

In Chapter 1 we learned how plane waves and spherical waves propagate through a solid or fluid medium. Spherical waves are generated by a point source in an infinite medium, the cylindrical waves are generated by a line source, and plane waves are generated by an infinite plane (see Figure 2.1).

Harmonic waves are generated from harmonic (time dependence = $e^{-i\omega t}$) sources. The equation of the propagating spherical wave generated by a point source in a fluid space is given by Equation 2.1, and equations of a propagating plane waves in a fluid are given by Equation 2.2 and Equation 2.3:

$$G(r) = \frac{e^{ik_f r}}{4\pi r} \tag{2.1}$$

$$p(x_1) = e^{ik_f x_1} \tag{2.2}$$

$$\phi(x_1) = e^{ik_f x_1} \tag{2.3}$$

Note that these equations have been derived in Chapter 1 (see Equations 1.224 and 1.199.) Equation 2.2 and Equation 2.3 give pressure and potential fields of unit amplitude, respectively. G in Equation 2.1 can also be either pressure or potential. The potential-pressure relation is given in Chapter 1, Equation 1.210. k_f is the wave number of the fluid and has been defined in Chapter 1, after Equation 1.198. In Equation 2.1, r is the radial distance of the spherical wavefront from the point source at the origin. In Equation 2.2 and Equation 2.3 x_1 is the propagation direction of the plane wavefront.

If the wave sources of Figure 2.1 are located in a homogeneous solid instead of the fluid medium, then only compressional waves are generated in the solid and their expressions can be obtained by simply substituting k_P for k_f, where k_P is the P-wave number of the solid. In absence of any interface or

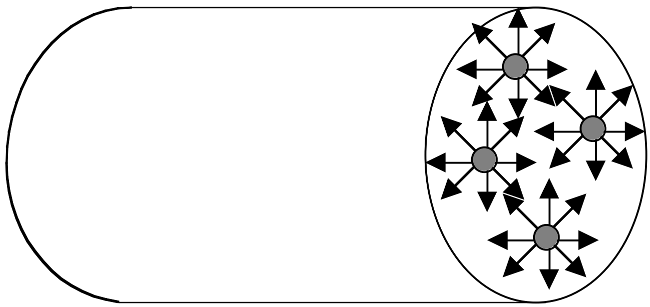

FIGURE 2.2
Four point sources distributed over a finite source.

boundary, the mode conversion does not occur and shear waves are not generated from the compressional waves.

In many nondestructive evaluation (NDE) applications elastic waves are generated by a source of finite dimension and the wavefronts are not spherical or cylindrical or plane. Typical dimensions of the commercially available ultrasonic transducers that are most commonly used for ultrasonic wave generation, vary from 1/4 to 1 in. in diameter. Of course, in special applications, the ultrasonic source can be much smaller (in the order of microns for high-frequency acoustic microscopy applications) or much larger (several inches for large structure inspection). To correctly predict the wavefront (displacement, stress, and pressure fields) generated by a finite source, it is necessary to follow some numerical or semianalytical techniques, as discussed in this chapter.

2.1 Modeling a Finite Plane Source by a Distribution of Point Sources

The pressure field due to a finite plane source can be assumed to be the summation of pressure fields generated by a number of point sources distributed over the finite source as shown in Figure 2.2. The finite source can be, for example, the front face of a transducer as shown in this figure.

This assumption can be justified in the following manner: A harmonic point source, which expands and contracts alternately, can be represented by a point and a sphere as shown in Figure 2.3(a). The point represents the contracted position and the sphere (circle in a two-dimensional figure) represents the expanded position. When a large number of these point sources are placed side-by-side on a plane surface, then the contracted and expanded positions of the point sources are shown in Figure 2.3(b). The combined effect of a large number of point sources, placed side by side, is shown in

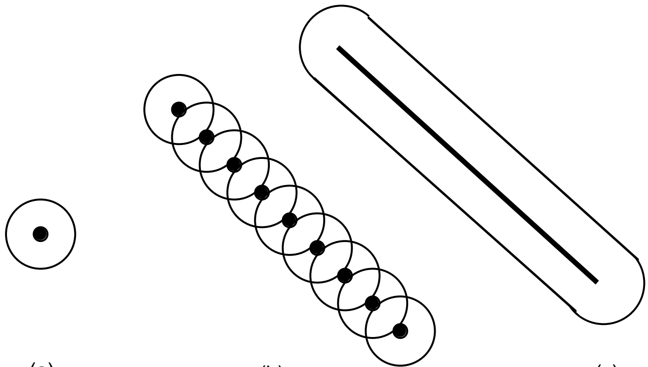

FIGURE 2.3
Contracted (dark) and expanded (thin line) positions of the particles for (a) a point source, (b) distributed finite number of point sources, and (c) a very large number of point sources.

Figure 2.3(c); in this figure the contracted (dark line) and expanded (thin line) positions of a line source or the cross section of a plane source are seen.

From Figure 2.3 it is clear that the combined effect of a large number of point sources distributed on a plane surface is the vibration of the particles in the direction normal to the plane surface. Non-normal components of motion at a point on the surface, generated by neighboring source points, cancel each other. However, non-normal components do not vanish along the edge of the surface. The particles not only vibrate normal to the surface but also expand to a hemisphere and contract to the point on the edge, as shown in Figure 2.3(c). If this edge effect does not have a strong contribution on the total motion, then the normal vibration of a finite plane surface can be approximately modeled by replacing the finite surface by a large number of point sources distributed over the surface.

2.2 Planar Piston Transducer in a Fluid

Let us compute the pressure field in a fluid for the planar piston transducer of finite diameter as shown in Figure 2.4. This problem can be solved in two ways as described below.

2.2.1 Conventional Surface Integral Technique

If one distributes the point sources over the transducer face, as discussed in Section 2.1, then the pressure field at position x in the fluid, which is due to

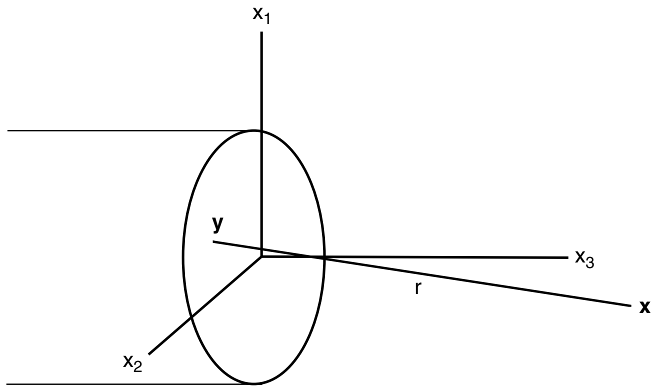

FIGURE 2.4
Point source *y* is on the transducer face; point *x* is where ultrasonic field is computed.

the point sources at position *y* distributed over the transducer surface, can be given by integrating Equation 2.1 over the transducer surface

$$p(\mathbf{x}) = \int_S B \frac{\exp(ik_f r)}{4\pi r}\, dS(\mathbf{y}) \tag{2.4a}$$

where *B* relates the source velocity and pressure. Thus, it is proportional to the source velocity amplitude. The above integral can be written in the following summation form:

$$p(\mathbf{x}) = \sum_{m=1}^{N} \left(\frac{B}{4\pi} \Delta S_m \right) \frac{\exp(ik_f r_m)}{r_m} = \sum_{m=1}^{N} A_m \frac{\exp(ik_f r_m)}{r_m} \tag{2.4b}$$

One can show from the Rayleigh-Sommerfield theory (Schmerr, 1998), that

$$p(\mathbf{x}) = -\frac{i\omega\rho}{2\pi} \int_S v_3(\mathbf{y}) \frac{\exp(ik_f r)}{r}\, dS(\mathbf{y}) \tag{2.5}$$

where, $v_3(y)$ is the particle velocity of the transducer surface; note that $v_1(y) = v_2(y) = 0$. For constant velocity of the transducer surface ($v_3 = v_0$) Equation 2.5 is simplified to

$$p(\mathbf{x}) = -\frac{i\omega\rho v_0}{2\pi} \int_S \frac{\exp(ik_f r)}{r}\, dS(\mathbf{y}) \tag{2.6a}$$

A comparison between Equation 2.4a and Equation 2.6a gives

$$B = -2i\omega\rho v_0 \tag{2.6b}$$

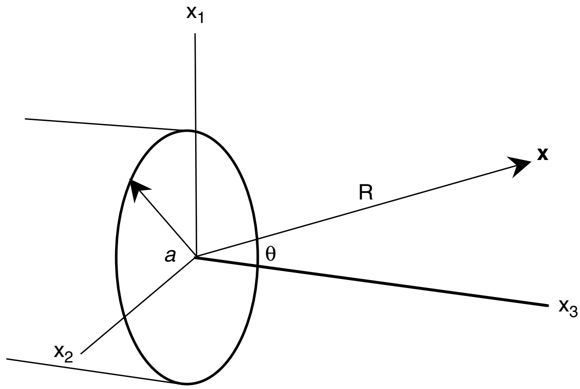

FIGURE 2.5
R and θ denote the far field point *x*.

Equation 2.6a can be evaluated in closed form for a circular transducer of radius *a* for the following two special cases (Schmerr, 1998):

1. When x is located on the x_3-axis

$$p(x_3) = \rho c_f v_0 \left[\exp(ik_f x_3) - \exp\left(ik_f \sqrt{x_3^2 + a^2} \right) \right] \tag{2.6c}$$

2. When x is in the far field. In other words, when r is much greater than the transducer radius

$$p(x_1, x_2, x_3) = -i\omega\rho v_0 a^2 \frac{\exp(ik_f R)}{R} \frac{J_1(k_f a \sin\theta)}{k_f a \sin\theta} \tag{2.6d}$$

R and θ of Equation 2.6c are shown in Figure 2.5. J_1 is the Bessel function of the first kind.

2.2.2 Alternative Distributed Point Source Method for Computing the Ultrasonic Field

An alternative technique to compute the strength of the distributed point sources is discussed in this section.

Let the strength of the m-th point source be A_m such that the pressure at a distance r_m from the point source is given by Equation 2.7 (also see Equation 2.4b):

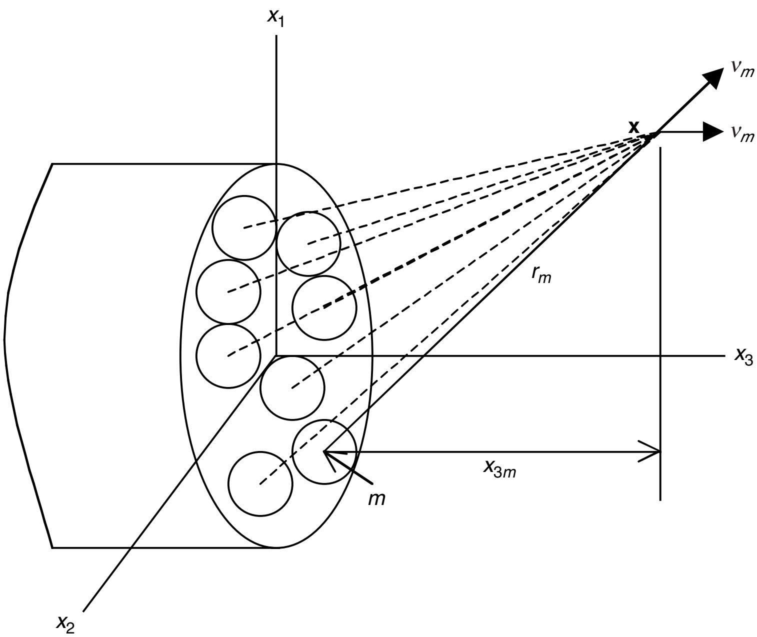

FIGURE 2.6
Velocity v_m at point **x** due to the m-th point source.

$$p_m(r) = A_m \frac{\exp(ik_f r_m)}{r_m} \tag{2.7}$$

If there are N point sources distributed over the transducer surface, as shown in Figure 2.6, then the total pressure at point x is given by

$$p(\mathbf{x}) = \sum_{m=1}^{N} p_m(r_m) = \sum_{m=1}^{N} A_m \frac{\exp(ik_f r_m)}{r_m} \tag{2.8}$$

where r_m is the distance of the m-th point source from point x. Note that Equations 2.8 and 2.4b are identical.

From the pressure-velocity relation (see Chapter 1, Equation 1.201 and Equation 1.202), it is possible to compute the velocity at x. From Equation 1.201 we get the following:

$$-\frac{\partial p}{\partial n} = \rho \frac{\partial v_n}{\partial t} = \pm i\omega\rho v_n \tag{2.9}$$

Note that for $e^{\pm i\omega t}$ time dependence of velocity, its derivative can be obtained by simply multiplying v_n by positive or negative $i\omega$. For $e^{-i\omega t}$ time dependence,

$$v_n = \frac{1}{i\omega\rho}\frac{\partial p}{\partial n} \tag{2.10}$$

Therefore, the velocity in the radial direction, at a distance r from the m-th point source, is given by

$$\begin{aligned} v_m(r) &= \frac{A_m}{i\omega\rho}\frac{\partial}{\partial r}\left(\frac{\exp(ik_f r)}{r}\right) = \frac{A_m}{i\omega\rho}\left(\frac{ik_f \exp(ik_f r)}{r} - \frac{\exp(ik_f r)}{r^2}\right) \\ &= \frac{A_m}{i\omega\rho}\frac{\exp(ik_f r)}{r}\left(ik_f - \frac{1}{r}\right) \end{aligned} \tag{2.11}$$

and the x_3-component of the velocity is

$$v_{3m}(r) = \frac{A_m}{i\omega\rho}\frac{\partial}{\partial x_3}\left(\frac{\exp(ik_f r)}{r}\right) = \frac{A_m}{i\omega\rho}\frac{x_3 \exp(ik_f r)}{r^2}\left(ik_f - \frac{1}{r}\right) \tag{2.12}$$

When contributions of all N sources are added (see Figure 2.6), then the total velocity in the x_3-direction at point x is obtained:

$$v_3(\mathbf{x}) = \sum_{m=1}^{N} v_{3m}(r_m) = \sum_{m=1}^{N} \frac{A_m}{i\omega\rho}\frac{x_{3m}\exp(ik_f r_m)}{r_m^2}\left(ik_f - \frac{1}{r_m}\right) \tag{2.13}$$

where x_{3m} is the x_3-value measured from the m-th source as shown in Figure 2.6.

If the transducer surface velocity in the x_3-direction is given by v_0 then for all x values on the transducer surface the velocity should be equal to v_0. Therefore,

$$v_3(\mathbf{x}) = \sum_{m=1}^{N} \frac{A_m}{i\omega\rho}\frac{x_{3m}\exp(ik_f r_m)}{r_m^2}\left(ik_f - \frac{1}{r_m}\right) = v_0 \tag{2.14}$$

By taking N points on the transducer surface it is possible to obtain a system of N linear equations to solve N unknowns (A_1, A_2, A_3, …. A_N). Difficulty arises when the point source location and the point of interest (x) coincide, because then r_m becomes zero and v_{3m}, from Equation 2.14 is unbounded. If point sources as well as points of interest x are both located on the transducer surface, then only r_m can be zero, sometimes. To avoid this possibility, the point sources are located slightly behind the transducer surface as shown in Figure 2.7. In this arrangement the smallest value that r_m can take is r_S.

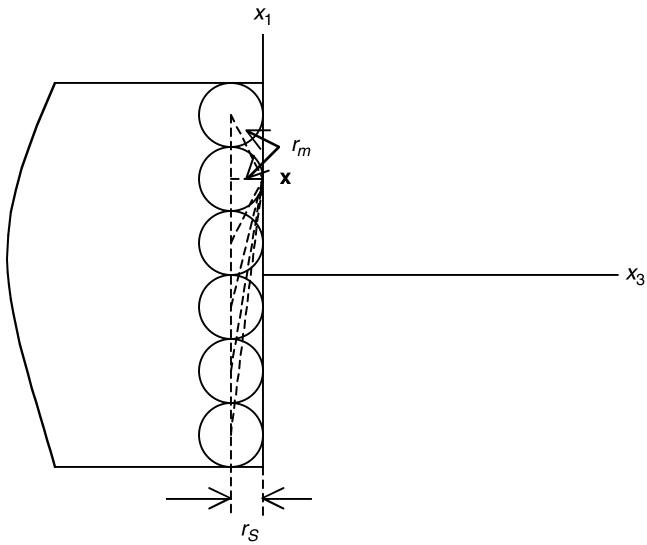

FIGURE 2.7
Point sources are located at $x_3 = -r_S$, while the transducer surface is at $x_3 = 0$.

Point x at which the x_3-component of velocity is matched with the transducer surface velocity v_0 is taken on the transducer surface at the apex of the small spheres that touch the transducer surface (see Figure 2.7). Point sources are placed at the centers of these small spheres. In addition to matching the v_3-component to v_0, if one also wants to equate the other two components, v_1 and v_2, to zero then for each point x on the transducer surface there are a total of three equations given in Equation 2.14 and Equation 2.15a.

$$v_1(\mathbf{x}) = \sum_{m=1}^{N} \frac{A_m}{i\omega\rho} \frac{x_{1m} \exp(ik_f r_m)}{r_m^2} \left(ik_f - \frac{1}{r_m} \right) = 0$$
$$v_2(\mathbf{x}) = \sum_{m=1}^{N} \frac{A_m}{i\omega\rho} \frac{x_{2m} \exp(ik_f r_m)}{r_m^2} \left(ik_f - \frac{1}{r_m} \right) = 0 \tag{2.15a}$$

Thus, from N points on the sphere surfaces $3N$ equations are obtained, and we get more equations than unknowns. To get the same number of unknowns as equations, the number of unknowns can be increased from N to $3N$ by replacing each point source by a triplet. A triplet is a combination of three point sources with different strengths put together as shown in Figure 2.8. All sources are placed in the same plane at $x_3 = -r_S$ parallel to the transducer surface. The three point sources of each triplet are located at three vertices of an equilateral triangle; these triangles are oriented randomly (see Figure 2.8) to

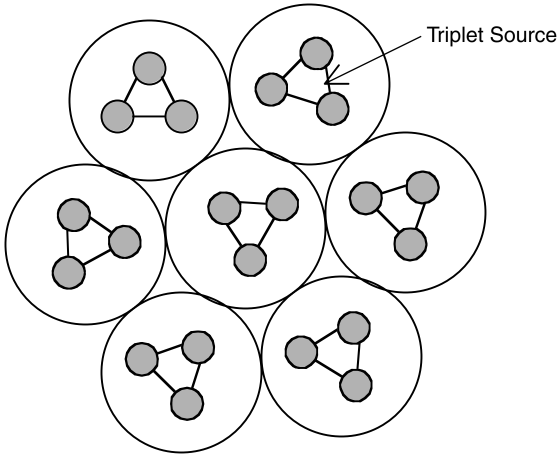

FIGURE 2.8
Randomly oriented triplet sources.

preserve the isotropic material properties and prevent any preferential orientation. By solving a system of 3N linear equations (for triplet sources) or a system of N linear equations (for simple point sources), the source strengths A_m associated with all point sources can be obtained. After getting A_m, the pressure $p(x)$ can be calculated at any point from Equation 2.8, on the transducer surface or away. The pressure field obtained in this manner should be same as that from Equation 2.6a.

2.2.2.1 Matrix Formulation

The matrix formulation for the steps described above to compute the source strengths is given below.

Equation 2.14 and Equation 2.15a can be combined into the following matrix equation:

$$\mathbf{V}_S = \mathbf{M}_{SS}\mathbf{A}_S \quad \textbf{(2.15b)}$$

where V_S is the $3N \times 1$ vector of the velocity components at N number of surface points x, and A_S is the $3N \times 1$ vector containing the strengths of 3N number of point sources. M_{SS} is the $3N \times 3N$ matrix relating the two vectors V_S and A_S. From Equation 2.14 and Equation 2.15a one can write

$$\{\mathbf{V}_S\}^T = \left[v_1^1 \quad v_2^1 \quad v_3^1 \quad v_1^2 \quad v_2^2 \quad v_3^2 \quad \ldots\ldots\ldots \quad v_1^N \quad v_2^N \quad v_3^N\right] \quad \textbf{(2.15c)}$$

Note that the transpose of the column vector V_S is a row vector of dimension $1 \times 3N$. Elements of this vector are denoted by v_j^n where the subscript

j can take values of 1, 2, or 3 and indicate the direction of the velocity component. Superscript n can take any value between 1 and N corresponding to the point on the transducer surface at which the velocity component is defined.

For most ultrasonic transducers $v_j^n = 0$ for $j = 1$ and 2 (the velocity component parallel to the transducer face) and $v_j^n = v_0$ for $j = 3$ (the velocity component normal to the transducer face). Equation 2.15c is then simplified to

$$\{\mathbf{V}_S\}^T = [0 \quad 0 \quad v_0 \quad 0 \quad 0 \quad v_0 \quad \ldots\ldots.. \quad 0 \quad 0 \quad v_0] \tag{2.15d}$$

Vector A_S of the source strengths is given by

$$\{\mathbf{A}_S\}^T = [A_1 \quad A_2 \quad A_3 \quad A_4 \quad A_5 \quad A_6 \quad \ldots\ldots.. \quad A_{3N-2} \quad A_{3N-1} \quad A_{3N}] \tag{2.15e}$$

Note that the upper limits of Equation 2.14 and Equation 2.15a are changed from N to $3N$ when triplet sources are considered, because then for each of the N small spheres three point sources exist (see Figure 2.8).

Finally, the square matrix M_{SS} is obtained from Equation 2.14 and Equation 2.15a

$$\mathbf{M}_{SS} =$$

$$\begin{bmatrix} f\left(x_{11}^1, r_1^1\right) & f\left(x_{12}^1, r_2^1\right) & f\left(x_{13}^1, r_3^1\right) & f\left(x_{14}^1, r_4^1\right) & \ldots & \ldots & f\left(x_{1(3N-1)}^1, r_{3N-1}^1\right) & f\left(x_{1(3N)}^1, r_{3N}^1\right) \\ f\left(x_{21}^1, r_1^1\right) & f\left(x_{22}^1, r_2^1\right) & f\left(x_{23}^1, r_3^1\right) & f\left(x_{24}^1, r_4^1\right) & \ldots & \ldots & f\left(x_{2(3N-1)}^1, r_{3N-1}^1\right) & f\left(x_{2(3N)}^1, r_{3N}^1\right) \\ f\left(x_{31}^1, r_1^1\right) & f\left(x_{32}^1, r_2^1\right) & f\left(x_{33}^1, r_3^1\right) & f\left(x_{34}^1, r_4^1\right) & \ldots & \ldots & f\left(x_{3(3N-1)}^1, r_{3N-1}^1\right) & f\left(x_{3(3N)}^1, r_{3N}^1\right) \\ f\left(x_{11}^2, r_1^2\right) & f\left(x_{12}^2, r_2^2\right) & f\left(x_{13}^2, r_3^2\right) & f\left(x_{14}^2, r_4^2\right) & \ldots & \ldots & f\left(x_{1(3N-1)}^2, r_{3N-1}^2\right) & f\left(x_{1(3N)}^2, r_{3N}^2\right) \\ f\left(x_{21}^2, r_1^2\right) & f\left(x_{22}^2, r_2^2\right) & f\left(x_{23}^2, r_3^2\right) & f\left(x_{24}^2, r_4^2\right) & \ldots & \ldots & f\left(x_{2(3N-1)}^2, r_{3N-1}^2\right) & f\left(x_{2(3N)}^2, r_{3N}^2\right) \\ f\left(x_{31}^2, r_1^2\right) & f\left(x_{32}^2, r_2^2\right) & f\left(x_{33}^2, r_3^2\right) & f\left(x_{34}^2, r_4^2\right) & \ldots & \ldots & f\left(x_{3(3N-1)}^2, r_{3N-1}^2\right) & f\left(x_{3(3N)}^2, r_{3N}^2\right) \\ \ldots & \ldots & \ldots & \ldots & \ldots & \ldots & \ldots & \ldots \\ f\left(x_{31}^N, r_1^N\right) & f\left(x_{32}^N, r_2^N\right) & f\left(x_{33}^N, r_3^N\right) & f\left(x_{34}^N, r_4^N\right) & \ldots & \ldots & f\left(x_{3(3N-1)}^N, r_{3N-1}^N\right) & f\left(x_{3(3N)}^N, r_{3N}^N\right) \end{bmatrix}_{3N \times 3N} \tag{2.15f}$$

where

$$f\left(x_{jm}^n, r_m^n\right) = \frac{x_{jm}^n \exp(ik_f r_m^n)}{i\omega\rho\left(r_m^n\right)^2}\left(ik_f - \frac{1}{r_m^n}\right) \tag{2.15g}$$

In Equation 2.15g, the first subscript j of x can take values of 1, 2, or 3 and indicate whether x is measured in the x_1-, x_2-, or x_3-direction. The subscript m of x and r can take values from 1 to $3N$ depending on which point source is considered, and the superscript n can take any value between 1 and N

corresponding to the point on the transducer surface where the velocity component is computed. As mentioned earlier in this formulation from $3N$ point sources, three boundary conditions on the velocity are satisfied at every point of the N boundary points.

If point x in Figure 2.7 is denoted by x_n, indicating that this point is located on the n-th boundary point, then the position vector connecting the m-th point source and the n-th boundary point is denoted by r_m^n and its three components in x_1, x_2, and x_3-directions are x_{jm}^n, $j = 1, 2, 3$, in Equation 2.15f and Equation 2.15g.

From Equation 2.15b one gets the point source strengths by inverting the matrix M_{SS}:

$$\mathbf{A}_S = [\mathbf{M}_{SS}]^{-1}\mathbf{V}_S = \mathbf{N}_{SS}\mathbf{V}_S \quad \textbf{(2.15h)}$$

If point sources are located very close to the transducer surface (r_S in Figure 2.7 is small), then the point source strengths (A_S) should be approximately equal to the source strengths on the transducer surface. From Equation 2.4a and Equation 2.6a we get

$$A_m = \frac{B}{4\pi}\Delta S_m = -\frac{2i\omega\rho v_0}{4\pi}\frac{S}{N} \quad \textbf{(2.15i)}$$

In Equation 2.15i S is the transducer surface area. Note that this equation gives the same source strength for all values of m. Therefore, the vector A_S, obtained from this equation, should have the following form:

$$\{\mathbf{A}_S\}^T = -\frac{i\omega\rho v_0 S}{2\pi N}[1 \quad 1 \quad 1 \quad \ldots \quad \ldots \quad 1] \quad \textbf{(2.15j)}$$

After getting the source strength vector A_S from Equation 2.15h or Equation 2.15j, the pressure $p(x)$ or velocity vector $V(x)$ at any point (on the transducer surface or away) can be obtained from Equation 2.8 (for pressure) or Equation 2.14 and Equation 2.15a (for velocity components). If the points in the fluid where the pressure and velocity vector are to be computed are called observation points or target points, then the pressure and velocity components, at these observation or target points, are obtained from the following matrix relation:

$$\begin{aligned} \mathbf{P}_T &= \mathbf{Q}_{TS}\mathbf{A}_S \\ \mathbf{V}_T &= \mathbf{M}_{TS}\mathbf{A}_S \end{aligned} \quad \textbf{(2.15k)}$$

where P_T is a $M \times 1$ vector containing pressure values at M number of target points and V_T is a $3M \times 1$ vector containing three velocity components at every target point. The V_T expression is similar to the V_S expression given in Equation 2.12b. The only difference is that its dimension is $3M \times 1$ instead of $3N \times 1$. Matrix M_{TS} will be the same as M_{SS} of Equation 2.15f if the target points are identical to the transducer surface points where the velocity components are matched to obtain the point source strength vector A_S in Equation 2.12g. However, for computing the velocity field at different points, the expression for M_{TS} will be slightly different from the M_{SS} expression given in Equation 2.15f. Then its dimension will be $3M \times 3N$ as shown below:

$$\mathbf{M}_{TS} =$$

$$\begin{bmatrix} f(x_{11}^1, r_1^1) & f(x_{12}^1, r_2^1) & f(x_{13}^1, r_3^1) & f(x_{14}^1, r_4^1) & \cdots & \cdots & f(x_{1(3N-1)}^1, r_{3N-1}^1) & f(x_{1(3N)}^1, r_{3N}^1) \\ f(x_{21}^1, r_1^1) & f(x_{22}^1, r_2^1) & f(x_{23}^1, r_3^1) & f(x_{24}^1, r_4^1) & \cdots & \cdots & f(x_{2(3N-1)}^1, r_{3N-1}^1) & f(x_{2(3N)}^1, r_{3N}^1) \\ f(x_{31}^1, r_1^1) & f(x_{32}^1, r_2^1) & f(x_{33}^1, r_3^1) & f(x_{34}^1, r_4^1) & \cdots & \cdots & f(x_{3(3N-1)}^1, r_{3N-1}^1) & f(x_{3(3N)}^1, r_{3N}^1) \\ f(x_{11}^2, r_1^2) & f(x_{12}^2, r_2^2) & f(x_{13}^2, r_3^2) & f(x_{14}^2, r_4^2) & \cdots & \cdots & f(x_{1(3N-1)}^2, r_{3N-1}^2) & f(x_{1(3N)}^2, r_{3N}^2) \\ f(x_{21}^2, r_1^2) & f(x_{22}^2, r_2^2) & f(x_{23}^2, r_3^2) & f(x_{24}^2, r_4^2) & \cdots & \cdots & f(x_{2(3N-1)}^2, r_{3N-1}^2) & f(x_{2(3N)}^2, r_{3N}^2) \\ f(x_{31}^2, r_1^2) & f(x_{32}^2, r_2^2) & f(x_{33}^2, r_3^2) & f(x_{34}^2, r_4^2) & \cdots & \cdots & f(x_{3(3N-1)}^2, r_{3N-1}^2) & f(x_{3(3N)}^2, r_{3N}^2) \\ \cdots & \cdots & \cdots & \cdots & \cdots & \cdots & \cdots & \cdots \\ f(x_{31}^{N_T}, r_1^{N_T}) & f(x_{32}^{N_T}, r_2^{N_T}) & f(x_{33}^{N_T}, r_3^{N_T}) & f(x_{34}^{N_T}, r_4^{N_T}) & \cdots & \cdots & f(x_{3(3N-1)}^{N_T}, r_{3N-1}^{N_T}) & f(x_{3(3N)}^{N_T}, r_{3N}^{N_T}) \end{bmatrix}_{3M \times 3N}$$

(2.15l)

where $f(x_{jm}^n, r_m^n)$ is identical to the expression given in Equation 2.15g. Definitions of the subscripts j and x do not change from those in Equation 2.15g. The superscript n of x and r can take any value between 1 and M depending on which target point is considered. Note that M_{TS} is not a square matrix when M and N are different.

From Equation 2.8 the matrix Q_{TS} can be obtained when there are $3N$ point sources and M target points:

$$\mathbf{Q}_{TS} = \begin{bmatrix} \frac{\exp(ik_f r_1^1)}{r_1^1} & \frac{\exp(ik_f r_2^1)}{r_2^1} & \frac{\exp(ik_f r_3^1)}{r_3^1} & \cdots & \cdots & \frac{\exp(ik_f r_{3N}^1)}{r_{3N}^1} \\ \frac{\exp(ik_f r_1^2)}{r_1^2} & \frac{\exp(ik_f r_2^2)}{r_2^2} & \frac{\exp(ik_f r_3^2)}{r_3^2} & \cdots & \cdots & \frac{\exp(ik_f r_{3N}^2)}{r_{3N}^2} \\ \frac{\exp(ik_f r_1^3)}{r_1^3} & \frac{\exp(ik_f r_2^3)}{r_2^3} & \frac{\exp(ik_f r_3^3)}{r_3^3} & \cdots & \cdots & \frac{\exp(ik_f r_{3N}^3)}{r_{3N}^3} \\ \cdots & \cdots & \cdots & \cdots & \cdots & \cdots \\ \cdots & \cdots & \cdots & \cdots & \cdots & \cdots \\ \frac{\exp(ik_f r_1^{N_T})}{r_1^{N_T}} & \frac{\exp(ik_f r_2^{N_T})}{r_2^{N_T}} & \frac{\exp(ik_f r_3^{N_T})}{r_3^{N_T}} & \cdots & \cdots & \frac{\exp(ik_f r_{3N}^{N_T})}{r_{3N}^{N_T}} \end{bmatrix}_{M \times 3N} \quad \textbf{(2.15m)}$$

The definition of r_m^n is identical for Equation 2.15k and Equation 2.15l; it is the distance between the *m*-th point source and *n*-th target point.

This alternative method and matrix formulation for computing the ultrasonic field in a homogeneous fluid was first proposed by Placko and Kundu (2001); it was then extended to solve different ultrasonic problems by Placko et al. (2001, 2002) and Lee et al. (2002). This technique has been named by the authors as the distributed point source method (DPSM). The advantage of the DPSM technique is not obvious for this simple case of homogeneous medium. It will be evident later in this chapter when the ultrasonic field, in the presence of a finite inclusion or scatterer, will be computed.

The DPSM technique, discussed in this section, is a general technique. It is not restricted to the case of small value of r_S (see Figure 2.7).

For small r_S Equation 2.15j can be used; otherwise Equation 2.15h will have to be used. When Equation 2.15h is used then Equation 2.15k is modified to

$$\begin{aligned} \mathbf{P}_T &= \mathbf{Q}_{TS}\mathbf{N}_{SS}\mathbf{V}_S \\ \mathbf{V}_T &= \mathbf{M}_{TS}\mathbf{N}_{SS}\mathbf{V}_S \end{aligned} \tag{2.15n}$$

Example 2.1

Give the modified expressions for $\mathbf{V}_S$ (Equation 2.15d) and $\mathbf{M}_{SS}$ (Equation 2.15f) for the case when the triplet sources are replaced by single point sources, located at the centers of the small spheres (see Figure 2.6 and Figure 2.7), and only the normal displacement components (normal to the transducer surface) at the apex (or collocation points) on the transducer surface are equated to the transducer surface velocity v_0.

SOLUTION

For N number of spheres distributed over the transducer surface there will be N point sources and N collocation points. The velocity vector V_S of Equation 2.15d will have N entries instead of $3N$ entries.

$$\{\mathbf{V}_S\}^T = [v_0 \quad v_0 \quad v_0 \quad \ldots\ldots.. \quad v_0]_{N\times 1} \tag{2.15o}$$

The matrix M_{SS} of Equation 2.15f will have a dimension of $N \times N$ instead of $3N \times 3N$, since the displacement components, in the x_3-direction only, are to be matched. The final form of M_{SS} is given below:

$$
\mathrm{M}_{SS} =
\begin{bmatrix}
f(x_{31}^1, r_1^1) & f(x_{32}^1, r_2^1) & f(x_{33}^1, r_3^1) & f(x_{34}^1, r_4^1) & \cdots & \cdots & f(x_{3(N-1)}^1, r_{N-1}^1) & f(x_{3N}^1, r_N^1) \\
f(x_{31}^2, r_1^2) & f(x_{32}^2, r_2^2) & f(x_{33}^2, r_3^2) & f(x_{34}^2, r_4^2) & \cdots & \cdots & f(x_{3(N-1)}^2, r_{N-1}^2) & f(x_{3N}^2, r_N^2) \\
f(x_{31}^3, r_1^3) & f(x_{32}^3, r_2^3) & f(x_{33}^3, r_3^3) & f(x_{34}^3, r_4^3) & \cdots & \cdots & f(x_{3(N-1)}^3, r_{N-1}^3) & f(x_{3N}^3, r_N^3) \\
f(x_{31}^4, r_1^4) & f(x_{32}^4, r_2^4) & f(x_{33}^4, r_3^4) & f(x_{34}^4, r_4^4) & \cdots & \cdots & f(x_{3(N-1)}^4, r_{N-1}^4) & f(x_{3N}^4, r_N^4) \\
\cdots & \cdots & \cdots & \cdots & \cdots & \cdots & \cdots & \cdots \\
\cdots & \cdots & \cdots & \cdots & \cdots & \cdots & \cdots & \cdots \\
\cdots & \cdots & \cdots & \cdots & \cdots & \cdots & \cdots & \cdots \\
f(x_{31}^N, r_1^N) & f(x_{32}^N, r_2^N) & f(x_{33}^N, r_3^N) & f(x_{34}^N, r_4^N) & \cdots & \cdots & f(x_{3(N-1)}^N, r_{N-1}^N) & f(x_{3N}^N, r_N^N)
\end{bmatrix}_{N\times N}
\tag{2.15p}
$$

where, from Equation 2.15g

$$
f(x_{3m}^n, r_m^n) = \frac{x_{3m}^n \exp(ik_f r_m^n)}{i\omega\rho (r_m^n)^2}\left(ik_f - \frac{1}{r_m^n}\right) \tag{2.15q}
$$

Example 2.2

For a large number of point sources distributed along the transducer surface, as shown in Figure 2.6 and Figure 2.7, evaluate the source strength vector A_S using Equation 2.15h for the M_{SS} and V_S expressions given in Equations 2.15o and 2.15p, respectively.

SOLUTION

For a large number of distributed point sources, the radius of the individual spheres becomes small (see Figure 2.7). As the number of point sources approaches infinity, the radius of individual spheres reduces to zero. Therefore, r_m^n, the distance between the m-th point source and n-th collocation point (or apex point), becomes zero for $m = n$. In other words, when the source is at the center of a sphere and the collocation point is at the apex of the same sphere, then the distance between the source and the collocation point is reduced to zero, as the number of point sources approaches infinity.

Note that in Equation 2.15qr_m^n appears in the denominator. Therefore, for small values of r_m^n Equation 2.15q can be simplified in the following manner:

$$
f(x_{3m}^n, r_m^n) = \frac{x_{3m}^n \exp(ik_f r_m^n)}{i\omega\rho (r_m^n)^2}\left(ik_f - \frac{1}{r_m^n}\right) \approx \frac{x_{3m}^n \exp(ik_f r_m^n)}{i\omega\rho (r_m^n)^2}\left(-\frac{1}{r_m^n}\right)
$$

$$
= -\frac{x_{3m}^n \exp(ik_f r_m^n)}{i\omega\rho (r_m^n)^3}
$$

Note that all spheres have the same radius $r_m = r_S = r$, and therefore $x_{3m}^n = r$. Substituting it into the above expression and expanding the exponential term in its series expansion we get

$$f\left(x_{3m}^n, r_m^n\right) \approx -\frac{x_{3m}^n \exp\left(ik_f r_m^n\right)}{i\omega\rho\left(r_m^n\right)^3} \approx -\frac{r}{i\omega\rho\left(r_m^n\right)^3}\left(1 + ik_f r_m^n + \ldots\right)$$
$$\approx -\frac{r}{i\omega\rho\left(r_m^n\right)^3} \tag{2.15r}$$

For $m = n$, $r_m^n = r_m^m = r$. Substituting it in Equation 2.15r, we get (no summation on m is implied)

$$f\left(x_{3m}^m, r_m^m\right) \approx -\frac{r}{i\omega\rho\left(r_m^m\right)^3} \approx -\frac{r}{i\omega\rho r^3} \approx -\frac{1}{i\omega\rho r^2} \tag{2.15s}$$

Substitution of Equation 2.15r and Equation 2.15s into Equation 2.15p yields

$$\mathbf{M}_{SS} = -\frac{1}{i\omega\rho r^2}\begin{bmatrix} 1 & \left(\frac{r}{r_2^1}\right)^3 & \left(\frac{r}{r_3^1}\right)^3 & \ldots & \left(\frac{r}{r_N^1}\right)^3 \\ \left(\frac{r}{r_1^2}\right)^3 & 1 & \left(\frac{r}{r_3^2}\right)^3 & \ldots & \left(\frac{r}{r_N^2}\right)^3 \\ \left(\frac{r}{r_1^3}\right)^3 & \left(\frac{r}{r_2^3}\right)^3 & 1 & \ldots & \left(\frac{r}{r_N^3}\right)^3 \\ \ldots & \ldots & \ldots & \ldots & \ldots \\ \left(\frac{r}{r_1^N}\right)^3 & \left(\frac{r}{r_2^N}\right)^3 & \left(\frac{r}{r_3^N}\right)^3 & \ldots & 1 \end{bmatrix}_{N\times N}$$

It should be noted here that, for $m \neq n$, $r_m^n > r$. Therefore, in the above matrix expression, the off-diagonal terms are smaller than the diagonal terms. With an increasing number of point sources as r approaches zero, all off-diagonal terms vanish and the above matrix simplifies to

$$\mathbf{M}_{SS} = -\frac{1}{i\omega\rho r^2}\begin{bmatrix} 1 & 0 & 0 & \ldots & 0 \\ 0 & 1 & 0 & \ldots & 0 \\ 0 & 0 & 1 & \ldots & 0 \\ \ldots & \ldots & \ldots & \ldots & \ldots \\ 0 & 0 & 0 & \ldots & 1 \end{bmatrix}_{N\times N}$$

Therefore, from Equation 2.15h

$$\mathbf{A}_S = [\mathbf{M}_{SS}]^{-1}\mathbf{V}_S$$

$$= -i\omega\rho r^2 \begin{bmatrix} 1 & 0 & 0 & \dots & 0 \\ 0 & 1 & 0 & \dots & 0 \\ 0 & 0 & 1 & \dots & 0 \\ \dots & \dots & \dots & \dots & \dots \\ 0 & 0 & 0 & \dots & 1 \end{bmatrix} \begin{Bmatrix} v_0 \\ v_0 \\ v_0 \\ \dots \\ v_0 \end{Bmatrix} = -i\omega\rho v_0 r^2 \begin{Bmatrix} 1 \\ 1 \\ 1 \\ \dots \\ 1 \end{Bmatrix} \quad \textbf{(2.15t)}$$

Example 2.3

Prove that the coefficients of Equation 2.15j and Equation 2.15t are identical.

SOLUTION

Total surface area from N hemispheres, associated with the N point sources, is equated to the transducer surface area S. Therefore,

$$S = 2\pi r^2 \times N = 2\pi N r^2$$

$$\Rightarrow r^2 = \frac{S}{2\pi N}$$

Substituting it in the coefficient of Equation 2.15t gives

$$-i\omega\rho v_0 r^2 = -\frac{i\omega\rho v_0 S}{2\pi N}$$

2.2.3 Restrictions on r_S for Point Source Distribution

It is evident from Figure 2.7 that as the number of point sources to model the transducer surface increases, r_S decrease. It is expected that with larger number of point sources the computation time and accuracy both should increase. What optimum number of point sources should produce reliable results? To answer this question the following analysis is conducted:

For a very small transducer of surface area dS vibrating with a velocity of amplitude v_0 in the x_3-direction the pressure at point x (at a distance r from the source at point y) can be computed from Equation 2.6a

$$p(\mathbf{x}) = -\frac{i\omega\rho v_0}{2\pi}\frac{\exp(ik_f r)}{r}\,dS \quad \textbf{(2.16)}$$

Using Equation 2.10, the particle velocity in the radial direction can be computed from the above pressure field,

$$\begin{aligned} v_r &= \frac{1}{i\omega\rho}\frac{\partial p}{\partial r} = \frac{1}{i\omega\rho}\left(\frac{-i\omega\rho v_0}{2\pi}\right)\left(\frac{ik_f \exp(ik_f r)}{r} - \frac{\exp(ik_f r)}{r^2}\right) dS \\ &= -\frac{v_0(ik_f r - 1)}{2\pi r^2}\exp(ik_f r)\, dS \end{aligned} \tag{2.17}$$

and the velocity in the x_3-direction

$$v_3 = \frac{1}{i\omega\rho}\frac{\partial p}{\partial x_3} = \frac{1}{i\omega\rho}\frac{\partial p}{\partial r}\frac{\partial r}{\partial x_3} = -\frac{v_0(ik_f r - 1)}{2\pi r^2}\exp(ik_f r) dS \frac{x_3 - y_3}{r} \tag{2.18}$$

where x_3 and y_3 are the x_3-coordinate values of points x and y, respectively.
If the point x is taken on the surface of sphere of radius r_S as shown in Figure 2.7, then $r = r_S = x_3 - y_3$, and v_3 of Equation 2.18 is simplified to

$$\begin{aligned} v_3 &= -\frac{v_0(ik_f r_S - 1)}{2\pi r_S^2}\exp(ik_f r_S) dS = v_0(1 - ik_f r_S)\left(1 + ik_f r_S + O\left(k_f^2 r_S^2\right)\right)\frac{dS}{2\pi r_S^2} \\ &\approx v_0\left(1 + k_f^2 r_S^2\right)\frac{dS}{2\pi r_S^2} \end{aligned} \tag{2.19}$$

The right-hand side of Equation 2.19 should be equal to v_0, since the pressure computed in Equation 2.16 is obtained from the transducer surface velocity v_0 in the x_3-direction. Hence, the velocity at x when x is taken on the transducer surface should be equal to v_0. The right hand side of Equation 2.19 is v_0 when $dS = 2\pi r_S^2$ and $k_f^2 r_S^2 << 1$. Therefore, dS should be the surface area of a hemisphere of radius r_S, and the second condition implies the following:

$$\begin{aligned} k_f^2 r_S^2 &= \left(\frac{2\pi f}{c_f} r_S\right)^2 << 1 \\ \Rightarrow r_S &<< \frac{c_f}{2\pi f} \\ \Rightarrow r_S &<< \frac{\lambda_f}{2\pi} \end{aligned} \tag{2.20}$$

where λ_f is the wavelength in the fluid. Equation 2.20 is used to compute the number of point sources in the following manner: Take a value of r_S

satisfying the condition in Equation 2.20 and compute the number of point sources (N) from the transducer surface area (S) from the relation

$$N = \frac{S}{2\pi r_S^2} \tag{2.21a}$$

Note that the spacing between two neighboring point sources is different from r_S. If the point sources are arranged uniformly at the vertex points of squares of side length a, then each point source should be associated with an area of a^2 of the flat transducer face. This area is then equated to the hemispherical surface area of each point source to obtain:

$$\begin{aligned} a^2 &= 2\pi r_S^2 \\ \Rightarrow a &= r_S\sqrt{2\pi} \end{aligned} \tag{2.21b}$$

Substituting Equation 2.20 in the above equation we get

$$\begin{aligned} a &= r_S\sqrt{2\pi} << \sqrt{2\pi}\,\frac{\lambda_f}{2\pi} \\ \Rightarrow a &<< \frac{\lambda_f}{\sqrt{2\pi}} \end{aligned} \tag{2.21c}$$

2.3 Focused Transducer in a Homogeneous Fluid

For a focused transducer (see Figure 2.9), the ultrasonic field in the fluid can be modeled by distributing the point sources along the curved transducer face. O'Neil (1949) argued that for transducers with small curvature Ray-

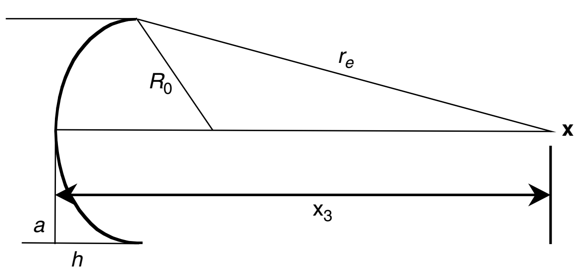

FIGURE 2.9
Focused transducer. R_0 is the radius of curvature of the transducer and a is its radius.

leigh-Sommerfield integral representation (Equation 2.6a) holds if the surface integral is carried out over the curved surface. Therefore, the DPSM technique, discussed in Section 2.2.2, holds good for the curved transducer face as well. The only difference is that, in this case the point sources are distributed over a curved surface, instead of a flat surface.

The integral representation of the pressure field in the fluid for a focused transducer should be same as Equation 2.6a. This integral can be evaluated in closed form, for computing the pressure variation on the central axis of the transducer (i.e., for the on-axis pressure computation). The on-axis pressure field is given by (Schmerr, 1998)

$$p(x_3) = \frac{\rho c v_0}{q_0}\left[\exp(ik_f x_3) - \exp\left(ik_f\sqrt{x_3^2 + a^2}\right)\right] = \frac{\rho c v_0}{q_0}[\exp(ik_f x_3) - \exp(ik_f r_e)] \tag{2.22}$$

where

$$q_0 = 1 - \frac{x_3}{R_0} \tag{2.23}$$

R_0 is the radius of curvature of the transducer face. r_e is the distance of the point of interest from the transducer edge.

At the geometric focus point, $x_3 = R_0$, the pressure is given by (Schmerr, 1998)

$$p(R_0) = -i\rho c v_0 k_f h \exp(ik_f R_0) \tag{2.24}$$

If, at $x_3 = z$, the on-axis pressure is maximum then z should satisfy the following equation (Schmerr, 1998):

$$\cos\left(\frac{k_f\delta}{2}\right) = \frac{2(\delta + z)\sin\left(\frac{k_f\delta}{2}\right)}{(\delta + h)q_0 k_f R_0} \tag{2.25a}$$

where

$$\delta = r_e - z = [(z-h)^2 + a^2]^{\frac{1}{2}} - z \tag{2.25b}$$

2.4 Ultrasonic Field in a Nonhomogeneous Fluid in Presence of an Interface

If the fluid in front of the transducer is not homogeneous but is made of two fluids with an interface between the two, the ultrasonic signal generated by the transducer will go through reflection and transmission at the interface

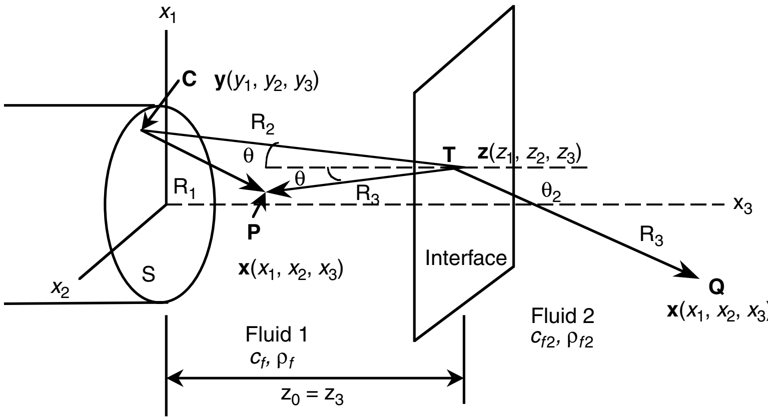

FIGURE 2.10
Transducer in front of the interface between two fluids of different properties.

(see Figure 2.10). In this case, the pressure field in fluid 1, at point P, can be computed by adding the contributions of the direct incident ray (R_1) and reflected ray. To compute the pressure at point Q in fluid 2, the contribution of only the transmitted ray needs to be considered. Acoustic wave speed and density of the two fluids are denoted by c_f and ρ_f for fluid 1, and c_{f2} and ρ_{f2} for fluid 2, as shown in Figure 2.10.

In Figure 2.10, point C is either on the transducer surface for Rayleigh-Sommerfield integral representation of the pressure field, or just behind the transducer surface (see Figure 2.7) for the DPSM modeling as discussed in Section 2.2.2. We are interested in computing the acoustic pressure at point P in fluid 1, and at point Q in fluid 2. As shown in the figure, point P receives a direct ray (R_1) from point C and a ray (R_3) reflected by the interface at point T. Point Q can only receive a ray from point C after it is transmitted at the interface at point T. Position vectors of points C, T, P, and Q are denoted by y, z, x, and x, respectively, as shown in the figure. Because both points P and Q are the points where the pressure field is to be computed, we use the same symbol x for denoting the positions of these two points although those are not at the same location.

When the coordinates x_1, x_2, and x_3 and y_1, y_2, and y_3 are known, then how can we obtain the coordinates z_1, z_2, and z_3 of T on the interface, where the ray is reflected or transmitted to reach point P or Q? This question can be answered from geometric considerations given below.

2.4.1 Pressure Field Computation in Fluid 1 at Point P

Let vectors $\underline{A}$ and $\underline{B}$ represent CT and TP, respectively, in Figure 2.10

$$\underline{A} = (z_1 - y_1)\underline{e_1} + (z_2 - y_2)\underline{e_2} + (z_3 - y_3)\underline{e_3}$$
$$\underline{B} = (x_1 - z_1)\underline{e_1} + (x_2 - z_2)\underline{e_2} + (x_3 - z_3)\underline{e_3} \quad \textbf{(2.26)}$$

Note that the magnitudes of vectors $\underline{A}$ and $\underline{B}$ are R_2 and R_3, respectively.

$$R_2 = \left\{(z_1 - y_1)^2 + (z_2 - y_2)^2 + (z_3 - y_3)^2\right\}^{\frac{1}{2}}$$
$$R_3 = \left\{(x_1 - z_1)^2 + (x_2 - z_2)^2 + (x_3 - z_3)^2\right\}^{\frac{1}{2}} \quad \textbf{(2.27)}$$

Unit vectors $\hat{A} = \frac{A}{R_2}, \hat{B} = \frac{B}{R_3}$
Unit vector $\hat{n}$ normal to the interface is given by

$$\hat{n} = \begin{Bmatrix} 0 \\ 0 \\ 1 \end{Bmatrix}$$

Note that for an inclined interface

$$\hat{n} = \begin{Bmatrix} n_1 \\ n_2 \\ n_3 \end{Bmatrix}$$

From the problem geometry one can easily see that

$$\hat{n} \times \hat{A} = \hat{n} \times \hat{B} \quad \textbf{(2.28)}$$

$$\hat{n} \cdot \hat{A} = -\hat{n} \cdot \hat{B} \quad \textbf{(2.29)}$$

Let

$$\hat{A} = \begin{Bmatrix} a_1 \\ a_2 \\ a_3 \end{Bmatrix}, \qquad \hat{B} = \begin{Bmatrix} b_1 \\ b_2 \\ b_3 \end{Bmatrix} \quad \textbf{(2.30)}$$

Substituting the above unit vector expressions in Equation 2.28 one gets

$$Det\begin{bmatrix} e_1 & e_2 & e_3 \\ n_1 & n_2 & n_3 \\ a_1 & a_2 & a_3 \end{bmatrix} = Det\begin{bmatrix} e_1 & e_2 & e_3 \\ n_1 & n_2 & n_3 \\ b_1 & b_2 & b_3 \end{bmatrix}$$

or, in an alternate representation,

$$\begin{bmatrix} 0 & -n_3 & n_2 \\ n_3 & 0 & -n_1 \\ -n_2 & n_1 & 0 \end{bmatrix}\begin{Bmatrix} a_1 \\ a_2 \\ a_3 \end{Bmatrix} = \begin{bmatrix} 0 & -n_3 & n_2 \\ n_3 & 0 & -n_1 \\ -n_2 & n_1 & 0 \end{bmatrix}\begin{Bmatrix} b_1 \\ b_2 \\ b_3 \end{Bmatrix}$$

or

$$\begin{bmatrix} 0 & -1 & 0 \\ -1 & 0 & 0 \\ 0 & 0 & 0 \end{bmatrix}\begin{Bmatrix} a_1 \\ a_2 \\ a_3 \end{Bmatrix} = \begin{bmatrix} 0 & -1 & 0 \\ -1 & 0 & 0 \\ 0 & 0 & 0 \end{bmatrix}\begin{Bmatrix} b_1 \\ b_2 \\ b_3 \end{Bmatrix}$$

or

$$\begin{Bmatrix} -a_2 \\ a_1 \\ 0 \end{Bmatrix} = \begin{Bmatrix} -b_2 \\ b_1 \\ 0 \end{Bmatrix}$$

or

$$\begin{Bmatrix} -\dfrac{z_2 - y_2}{R_2} \\ \dfrac{z_1 - y_1}{R_2} \end{Bmatrix} = \begin{Bmatrix} \dfrac{z_2 - x_2}{R_3} \\ -\dfrac{z_1 - x_1}{R_3} \end{Bmatrix} \tag{2.31}$$

Similarly, from Equation 2.29

$$[n_1 \quad n_2 \quad n_3]\begin{Bmatrix} a_1 \\ a_2 \\ a_3 \end{Bmatrix} = -[n_1 \quad n_2 \quad n_3]\begin{Bmatrix} b_1 \\ b_2 \\ b_3 \end{Bmatrix}$$

or

$$[0 \quad 0 \quad 1]\begin{Bmatrix} a_1 \\ a_2 \\ a_3 \end{Bmatrix} = -[0 \quad 0 \quad 1]\begin{Bmatrix} b_1 \\ b_2 \\ b_3 \end{Bmatrix}$$

or

$$a_3 = -b_3 \Rightarrow \frac{z_3 - y_3}{R_2} = \frac{z_3 - x_3}{R_3} \tag{2.32}$$

Solving the above equations we get the following:

$$\begin{aligned} z_1 &= \frac{y_1(x_3 - z_3) - x_1(z_3 - y_3)}{x_3 - 2z_3 + y_3} \\ z_2 &= \frac{y_2(x_3 - z_3) - x_2(z_3 - y_3)}{x_3 - 2z_3 + y_3} \end{aligned} \tag{2.33}$$

Note that if point C is on the x_1x_2-plane then $y_3 = 0$, and for fluid 1 x_3 is between 0 and z_3; the denominator of Equation 2.33 should never become zero. After obtaining z_1 and z_2, from Equation 2.33, the lengths R_2 and R_3 can be easily obtained from Equation 2.27. To evaluate R_1 one does not need z_1 and z_2. It is simply equal to

$$R_1 = \left\{(x_1 - y_1)^2 + (x_2 - y_2)^2 + (x_3 - y_3)^2\right\}^{\frac{1}{2}} \tag{2.34}$$

Then the pressure field at point P can be obtained from the following equation:

$$p_P(x) = -\frac{i\omega\rho_f v_o}{2\pi}\int_S \frac{\exp(ik_f R_1)}{R_1}dS - \frac{i\omega\rho_f v_o}{2\pi}\int_S \frac{R.\exp\{ik_f(R_2 + R_3)\}}{R_2 + R_3}dS \tag{2.35}$$

In Equation 2.35 the first integral corresponds to the wave path CP and the second integral corresponds to the wave path CTP. Both these integrals are similar to the expression given in Equation 2.6a; the only difference is that in the second integral expression the reflection coefficient R has been included because this wave reaches point P after being reflected at the interface. Expression of the reflection coefficient R is given in Equation 1.214b):

$$R = \frac{\rho_2 c_{f2}\cos\theta_1 - \rho_1 c_{f1}\cos\theta_2}{\rho_2 c_{f2}\cos\theta_1 + \rho_1 c_{f1}\cos\theta_2}$$

In this case, the incident angle is θ, the transmitted angle is θ_2, the fluid densities are ρ_f and ρ_{f2}, and the acoustic wave speeds in the two fluids are c_f and c_{f2}. The transmitted angle θ_2 can then be expressed in terms of the incident angle θ using Snell's law (see Chapter 1, Equation 1.204):

$$\cos\theta_2 = \sqrt{1-\sin^2\theta_2} = \sqrt{1-\left(\frac{c_{f2}\sin\theta}{c_f}\right)^2} = \left\{1-\left(\frac{c_{f2}}{c_f}\right)^2+\left(\frac{c_{f2}}{c_f}\cos\theta\right)^2\right\}^{\frac{1}{2}} \tag{2.36}$$

Therefore, R takes the following form:

$$R = \frac{\rho_2 c_{f2}\cos\theta - \rho c_f\left\{1-\frac{c_{f2}^2}{c_f^2}+\frac{c_{f2}^2}{c_f^2}\cos^2\theta\right\}^{\frac{1}{2}}}{\rho_2 c_{f2}\cos\theta + \rho c_f\left\{1-\frac{c_{f2}^2}{c_f^2}+\frac{c_{f2}^2}{c_f^2}\cos^2\theta\right\}^{\frac{1}{2}}} \tag{2.37}$$

In the above equation cos θ can be obtained from the relation given below. The dot product between the unit vectors $\hat{n}$ and $\hat{A}$ is given by

$$\hat{n}\cdot\hat{A} = |\hat{n}||\hat{A}|\cos\theta = n_1a_1 + n_2a_2 + n_3a_3$$
$$\Rightarrow \cos\theta = n_3a_3 = a_3 = \frac{z_3-y_3}{R_2} \tag{2.38}$$

2.4.2 Pressure Field Computation in Fluid 2 at Point Q

Let us define two vectors $\underline{A}$ and $\underline{C}$ where $\underline{A}$ = CT and $\underline{C}$ = TQ

$$\underline{A} = (z_1-y_1)\underline{e_1} + (z_2-y_2)\underline{e_2} + (z_3-y_3)\underline{e_3}$$
$$\underline{C} = (x_1-z_1)\underline{e_1} + (x_2-z_2)\underline{e_2} + (x_3-z_3)\underline{e_3} \tag{2.39}$$

The magnitudes of vectors $\underline{A}$ and $\underline{C}$ are R_2 and R_3, respectively

$$R_2 = \left\{(z_1-y_1)^2 + (z_2-y_2)^2 + (z_3-y_3)^2\right\}^{\frac{1}{2}}$$
$$R_3 = \left\{(x_1-z_1)^2 + (x_2-z_2)^2 + (x_3-z_3)^2\right\}^{\frac{1}{2}} \tag{2.40}$$

Unit vectors $\hat{A} = \frac{A}{R_2}$, $\hat{C} = \frac{C}{R_3}$
Unit vector $\hat{n}$ normal to the interface is given by

$$\hat{n} = \begin{Bmatrix} 0 \\ 0 \\ 1 \end{Bmatrix}$$

Note that for an inclined interface

$$\hat{n} = \begin{Bmatrix} n_1 \\ n_2 \\ n_3 \end{Bmatrix}$$

From the problem geometry shown in Figure 2.10, the following equations are obtained:

$$\begin{aligned} |\hat{n} \times \hat{A}| &= \sin\theta \\ \hat{n} \cdot \hat{A} &= \cos\theta \\ |\hat{n} \times \hat{C}| &= \sin\theta_2 \\ \hat{n} \cdot \hat{C} &= \cos\theta_2 \end{aligned} \tag{2.41}$$

Let

$$\hat{A} = \begin{Bmatrix} a_1 \\ a_2 \\ a_3 \end{Bmatrix}, \qquad \hat{C} = \begin{Bmatrix} c_1 \\ c_2 \\ c_3 \end{Bmatrix}$$

from Equation 2.41 and Equation 2.39

$$\begin{aligned} c_3 &= \cos\theta_2 = \frac{x_3 - z_3}{R_3} \\ a_3 &= \cos\theta = \frac{z_3 - y_3}{R_2} \end{aligned} \tag{2.42}$$

and

$$\hat{n}\times\hat{C} = Det\begin{bmatrix} e_1 & e_2 & e_3 \\ n_1 & n_2 & n_3 \\ c_1 & c_2 & c_3 \end{bmatrix} = \begin{bmatrix} 0 & -n_3 & n_2 \\ n_3 & 0 & -n_1 \\ -n_2 & n_1 & 0 \end{bmatrix}\begin{Bmatrix} c_1 \\ c_2 \\ c_3 \end{Bmatrix} = \begin{bmatrix} 0 & -1 & 0 \\ -1 & 0 & 0 \\ 0 & 0 & 0 \end{bmatrix}\begin{Bmatrix} c_1 \\ c_2 \\ c_3 \end{Bmatrix} = \begin{Bmatrix} -c_2 \\ c_1 \\ 0 \end{Bmatrix} \tag{2.43}$$

$$\Rightarrow \left|\hat{n}\times\hat{C}\right|^2 = c_1^2 + c_2^2 = \sin^2\theta_2$$

or

$$\sin^2\theta_2 = \frac{(x_1 - z_1)^2 + (x_2 - z_2)^2}{R_3^2} \tag{2.44}$$

Similarly,

$$|\hat{n}\times\hat{A}|^2 = a_1^2 + a_2^2 = \frac{(z_1 - y_1)^2 + (z_2 - y_2)^2}{R_2^2} = \sin^2\theta \tag{2.45}$$

Because $\hat{A},\hat{n},\hat{C}$ are located on the same plane

$$\begin{aligned} \hat{n}\times\hat{A} &= \hat{e}_S \sin\theta \\ \hat{n}\times\hat{C} &= \hat{e}_S \sin\theta_2 \end{aligned} \tag{2.46}$$

where $\hat{e}_S$ is the unit vector normal to the plane containing $\hat{A},\hat{n},\hat{C}$.

From Equation 2.46 and Snell's law (see Chapter 1, Equation 1.204) one can write

$$\begin{aligned} &\frac{\hat{n}\times\hat{A}}{\sin\theta} = \frac{\hat{n}\times\hat{C}}{\sin\theta_2} \\ &\Rightarrow \frac{\hat{n}\times\hat{A}}{c_f} = \frac{\hat{n}\times\hat{C}}{c_{f2}} \end{aligned} \tag{2.47}$$

or

$$\begin{aligned} &\frac{1}{c_f}\begin{Bmatrix} -a_2 \\ a_1 \\ 0 \end{Bmatrix} = \frac{1}{c_{f2}}\begin{Bmatrix} -c_2 \\ c_1 \\ 0 \end{Bmatrix} \\ &\Rightarrow \begin{Bmatrix} -\dfrac{z_1 - y_1}{c_f R_2} \\ \dfrac{z_2 - y_2}{c_f R_2} \\ 0 \end{Bmatrix} = \begin{Bmatrix} -\dfrac{x_1 - z_1}{c_{f2} R_3} \\ \dfrac{x_2 - z_2}{c_{f2} R_3} \\ 0 \end{Bmatrix} \end{aligned} \tag{2.48}$$

z_1 and z_2 can be obtained from Equation 2.45 by minimizing the following error function

$$E = \left(\frac{z_1 - y_1}{c_f R_2} + \frac{z_1 - x_1}{c_{f2} R_3} \right)^2 + \left(\frac{z_2 - y_2}{c_f R_2} + \frac{z_2 - x_2}{c_{f2} R_3} \right)^2 \quad \textbf{(2.49)}$$

E can be minimized by some optimization technique such as simplex algorithm. In MATLAB code the fminsearch function can be used for this purpose. After evaluating z_1 and z_2, the pressure at point Q can be obtained from the following equation:

$$p(x_1, x_2, x_3) = -\frac{i\omega\rho_f v_o}{2\pi} \int_S \frac{T_p \exp[ik_f R_2 + k_{f2} R_3)]}{\sqrt{R_2 + \frac{c_{f2}}{c_f} R_3} \sqrt{R_2 + R_3 \frac{c_{f2} \cos^2\theta}{c_f \cos^2\theta_2}}} dS \quad \textbf{(2.50)}$$

The numerator of the above integrand is similar to that in Equation 2.6a. The only difference is that in Equation 2.50 the numerator has been multiplied by T_p, the transmission coefficient at the interface, and the argument of the exponential term has two entries that correspond to the ray paths CT and TQ. The denominator of Equation 2.50 is much more complex compared to the one given in Equation 2.6a. The derivation of this denominator expression can be found in Schmerr (1998).

The transmission coefficient is given in Chapter 1, Equation 1.214b

$$T_p = \frac{2\rho_2 c_{f2} \cos\theta_2}{\rho_2 c_{f2} \cos\theta_1 + \rho_1 c_f \cos\theta_2}$$

As mentioned above, in this case, the incident angle is θ, the angle of transmission is θ_2, the fluid densities are ρ_f and ρ_{f2}, and the acoustic wave speeds in the two fluids are c_f and c_{f2}. Angle θ_2 can be expressed in terms of the incident angle θ (see Equation 2.36); T_p then takes the following form:

$$T_p = \frac{2\rho_{f2} c_{f2} \cos\theta}{\rho_{f2} c_{f2} \cos\theta + \rho_f c_f \left\{ 1 - \frac{c_{f2}^2}{c_f^2} + \frac{c_{f2}^2}{c_f^2} \cos^2\theta \right\}^{\frac{1}{2}}} \quad \textbf{(2.51)}$$

2.5 DPSM Technique for Ultrasonic Field Modeling in Nonhomogeneous Fluid

The steps discussed in Section 2.4 are based on the Rayleigh-Sommerfield integral representation for the pressure field computation in fluids 1 and 2. In this section, an alternative technique, called the DPSM technique, developed

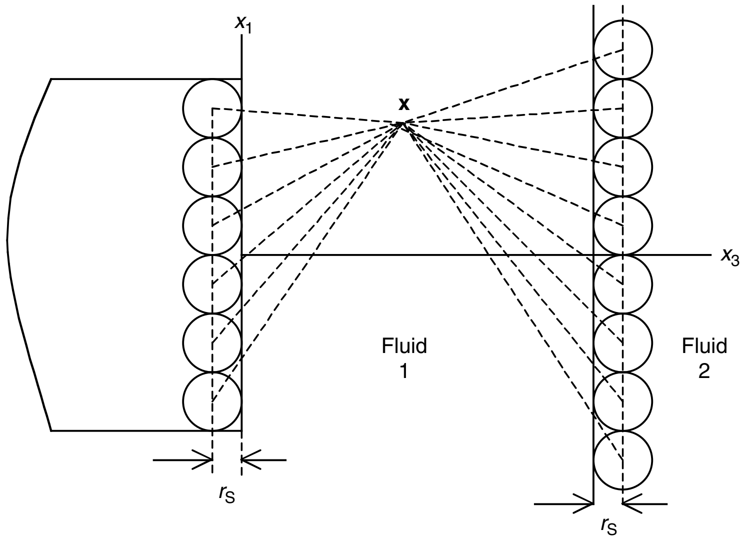

FIGURE 2.11
Point sources (at the center of small circles) for computing the ultrasonic field in fluid 1.

by Placko and Kundu (2001) for ultrasonic modeling, is generalized to include the inhomogeneous fluid case. In the DPSM technique, the interface is replaced by a layer of equivalent point sources instead of tracing the rays from the transducer face to the point of interest in fluid media 1 or 2.

2.5.1 Field Computation in Fluid 1

The field in fluid 1 is computed by superimposing the contributions of two layers of point sources distributed over the transducer face and the interface, respectively (see Figure 2.11). Two layers of sources are located at a small distance r_S away from the transducer face and interface, respectively, such that the apex of the spheres (of radius r_S) touch the transducer face or interface.

The strength of the point sources distributed along the transducer surface can be obtained from Equation 2.15h or Equation 2.15j. For finding the strength of the point sources attached to the interface, velocity components at the interface due to the reflected waves at the interface are to be matched as described below.

As shown in Figure 2.12, any point P in fluid 1 can receive only two rays, 1 and 2, from a single point source on the transducer surface. Ray 1 is the direct ray reaching P, and ray 2 arrives at P after being reflected at the interface. Total ultrasonic field at point P can be obtained by superimposing the contributions of a number of point sources (y_m) distributed over the transducer surface. The total field at P, generated only by the reflected rays

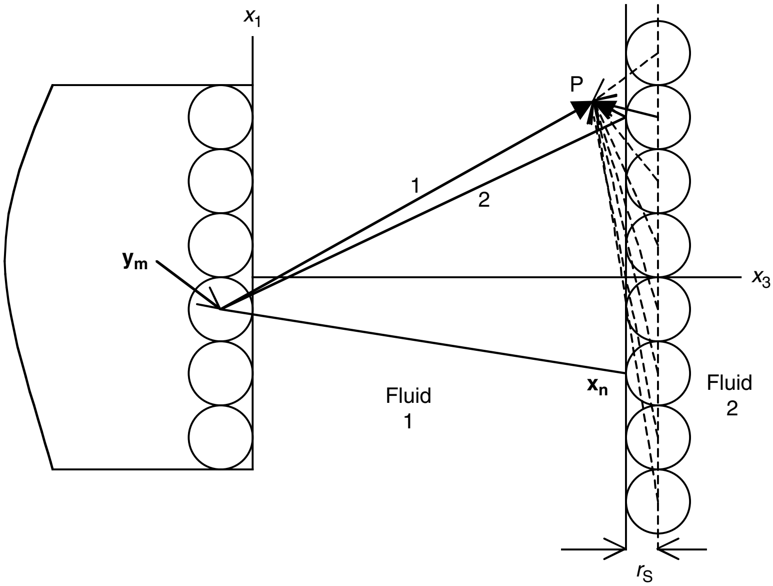

FIGURE 2.12
Point P can receive two rays, 1 and 2, from a single point source y_m.

(ray 2) from all point sources on the transducer surface, should be same as the total contributions of all point sources distributed over the interface.

Let us take a point P at x_n on the interface. In Figure 2.12, the point P is shown very close to the interface. Let us assume that this point is now moved to the interface. Let there be N point sources ($y_{m,}$ $m = 1, 2, \ldots N$) on the transducer surface and M points (x_n, $n = 1, 2, \ldots M$) on the interface where the boundary conditions should be satisfied. If the boundary conditions are to be satisfied for three components of velocity at all M points, then there are a total of $3M$ boundary conditions.

Velocity components at M interface points due to ray 1 only (ignoring reflection) can be easily obtained from the N triplet sources in the following manner (see Equation 2.15k):

$$\mathbf{V}_T^i = \mathbf{M}_{TS}^i \mathbf{A}_S \tag{2.52}$$

where $\mathbf{V}_T^i$ is the $3M \times 1$ vector of the velocity components at the target points (x_n) on the interface due to the incident beam only. $\mathbf{A}_S$ is the $3N \times 1$ vector of the point source strengths on the transducer surface. Because of the triplet type source, there are three point sources inside every small sphere. The normal velocity component (v_0) at the transducer surface is known. As a result, $\mathbf{A}_S$ can be obtained from Equation 2.15h or Equation 2.15j. $\mathbf{M}_{TS}^i$ is the

$3M \times 3N$ matrix that relates the two vectors $\mathbf{V}_T^i$ and $\mathbf{A}_S$ of Equation 2.52. The components of $\mathbf{M}_{TS}^i$ are identical to those for M_{TS} given in Equation 2.15l.

In Equation 2.52 and subsequent equations, the superscripts and subscripts are defined as follows:

Superscripts
- i — direct incident ray
- r — reflected ray
- t — transmitted ray

Subscripts
- S — ultrasonic source or transducer points
- I — interface points
- T — target points or observation points (These points can be placed anywhere - in fluid 1, fluid 2, on the transducer surface, or on the interface.)

For the reflected field computation at the interface, the velocity vector and the source strength vector are computed in a similar manner:

$$\mathbf{V}_T^r = \mathbf{M}_{TS}^r \mathbf{A}_S \tag{2.53}$$

where $\mathbf{V}_T^r$ is the $3M \times 1$ vector of the three velocity components at the target points (x_n) on the interface due to the reflected beam only (ray 2 of Figure 2.12) and $\mathbf{M}_{TS}^r$ is the $3M \times 3N$ matrix that relates the two vectors $\mathbf{V}_T^r$ and $\mathbf{A}_S$ of Equation 2.53. Components of $\mathbf{M}_{TS}^r$ can be obtained by multiplying $\mathbf{M}_{TS}^i$ by appropriate reflection coefficients, given in Equation 2.37.

Next we would like to obtain the same $\mathbf{V}_T^r$ vector from the $3M$ point sources distributed along the interface. Within each sphere shown in Figure 2.12 three point sources or triplet (see Figure 2.8) are placed; thus from M spheres one gets $3M$ sources. The interface point sources are located around the centers of the small spheres of Figure 2.12, and three sources of each triplet are placed parallel to the interface. Points x_n are located on the surface of the small spheres. $\mathbf{V}_T^r$ at M points, generated by the $3M$ sources at the interface, can be written as

$$\mathbf{V}_T^r = \mathbf{M}_{TI}^i \mathbf{A}_I \tag{2.54}$$

where $\mathbf{V}_T^r$ is the $3M \times 1$ vector, same as in Equation 2.53 and $\mathbf{A}_I$ is the $3M \times 1$ vector of the strength of interface sources; this vector is unknown. $\mathbf{M}_{TI}^i$ is the $3M \times 3M$ matrix that relates the 2 vectors $\mathbf{V}_T^r$ and $\mathbf{A}_I$ of Equation 2.54. The components of $\mathbf{M}_{TI}^i$ are similar to those for M_{SS} given in Equation 2.15f and M_{TS} of Equation 2.15l. Two variables, x_{jm}^n and r_m^n, for $\mathbf{M}_{TI}^i$ computation can be obtained after knowing the point source coordinates z_m ($m = 1, 2, \ldots 3M$)

distributed along the interface, and coordinates x_n (n = 1, 2, … M) of the interface points.

From Equation 2.53 and Equation 2.54

$$\mathbf{A}_I = \left[\mathbf{M}_{TI}^i\right]^{-1}\mathbf{V}_T^r = \left(\left[\mathbf{M}_{TI}^i\right]^{-1}\mathbf{M}_{TS}^r\right)\mathbf{A}_S \tag{2.55}$$

Equation 2.55 gives the strength of the interface sources. After obtaining the interface source strengths, the ultrasonic field at any set of target points x_n (n = 1, 2, … N_T) between the transducer face and interface can be obtained by adding the contributions of the incident waves from the two layers of point sources at the transducer face and interface as shown in Figure 2.11. In other words, a field at any point can be obtained by adding the expressions, given in Equation 2.52 and Equation 2.54.

$$\mathbf{V}_T = \mathbf{V}_T^i + \mathbf{V}_T^r = \mathbf{M}_{TS}^i\mathbf{A}_S + \mathbf{M}_{TI}^i\mathbf{A}_I \tag{2.56a}$$

The only difference between the two components of Equation 2.56a and those in Equation 2.52 and Equation 2.54 is in the definitions of x_{jm}^n and r_m^n for $\mathbf{M}_{TI}^i$ and $\mathbf{M}_{TS}^i$. In Equation 2.52 and Equation 2.54 the target points are located on the interface, while in Equation 2.56a the target points are in between the transducer face and the interface. Therefore, the values of x_{jm}^n and r_m^n will change accordingly. As mentioned earlier, r_m^n is the distance between the m-th point source and n-th target point, and x_{jm}^n are the three components of r_m^n.

2.5.1.1 Approximations in Computing the Field

The approximation of the above section in deriving Equation 2.56a is that the presence of the interface does not affect the source strength vector $\mathbf{A}_S$. Note that $\mathbf{A}_S$ of Equation 2.52 is computed from Equation 2.15h or Equation 2.15j. With this assumption, the velocity vector computed on the transducer surface, using Equation 2.56a, will give a different value than v_0. If the interface is close to the transducer surface then the transducer surface velocity will be significantly different from v_0 because of the interface effect.

To make sure that the velocity vector on the interface is equal to a constant (v_0) in the x_3-direction and zero in x_1- and x_2-directions, the following formulation is followed.

Similar to the previous section, it is again assumed that there are N triplet sources on the transducer surface and M sources along the interface. Velocity vector on the transducer surface, due to the point sources representing the transducer effect only, can be obtained from Equation 2.52:

$$\mathbf{V}_S^i = \mathbf{M}_{SS}^i\mathbf{A}_S \tag{2.56b}$$

$\mathbf{V}_S^i$ is the ($3N \times 1$) vector of the velocity components at the transducer surface, $\mathbf{A}_S$ is the $3N \times 1$ vector of the point source strengths distributed over the transducer face, and $\mathbf{M}_{SS}^i$ is the $3N \times 3N$ matrix that is identical to the one given in Equation 2.15f.

In the same manner, velocity components on the transducer surface due to the interface sources are given by

$$\mathbf{V}_S^r = \mathbf{M}_{SI}^i \mathbf{A}_I \tag{2.56c}$$

The above equation is obtained from Equation 2.54 when the target points are placed on the transducer surface. Here, $\mathbf{V}_S^r$ is a $3N \times 1$ vector of the velocity components at N points on the transducer surface, $\mathbf{A}_I$ is the ($3M \times 1$) vector of the interface source strengths, and $\mathbf{M}_{SI}^i$ is the $3N \times 3M$ matrix that is similar to the one given in Equation 2.15l.

Adding Equation 2.56b and Equation 2.56c, the total velocity at the transducer surface is obtained:

$$\mathbf{V}_S = \mathbf{V}_S^i + \mathbf{V}_S^r = \mathbf{M}_{SS}^i \mathbf{A}_S + \mathbf{M}_{SI}^i \mathbf{A}_I \tag{2.56d}$$

Substituting Equation 2.55 into Equation 2.56d we get

$$\begin{aligned} \mathbf{V}_S &= \mathbf{M}_{SS}^i \mathbf{A}_S + \mathbf{M}_{SI}^i \mathbf{A}_I = \mathbf{M}_{SS}^i \mathbf{A}_S + \mathbf{M}_{SI}^i \left[\mathbf{M}_{TI}^i\right]^{-1} \mathbf{M}_{TS}^r \mathbf{A}_S \\ \Rightarrow \mathbf{V}_S &= \left[\mathbf{M}_{SS}^i + \mathbf{M}_{SI}^i \left[\mathbf{M}_{TI}^i\right]^{-1} \mathbf{M}_{TS}^r\right] \mathbf{A}_S \end{aligned} \tag{2.56e}$$

or

$$\mathbf{A}_S = \left[\mathbf{M}_{SS}^i + \mathbf{M}_{SI}^i \left[\mathbf{M}_{TI}^i\right]^{-1} \mathbf{M}_{TS}^r\right]^{-1} \mathbf{V}_S \tag{2.56f}$$

where

$$\mathbf{V}_S = [0 \quad 0 \quad v_0 \quad 0 \quad 0 \quad v_0 \quad \ldots\ldots\ldots\ldots \quad 0 \quad 0 \quad v_0]^T \tag{2.56g}$$

If $\mathbf{A}_S$ is computed from Equation 2.56f instead of Equation 2.15h, then the constant velocity at the transducer surface is guaranteed even when the interface is located very close to the transducer surface.

2.5.2 Field in Fluid 2

For ultrasonic field computation in fluid 2, only one layer of point sources, adjacent to the interface, is considered (see Figure 2.13). The total field at x should be the superposition of fields generatedby all these point sources,

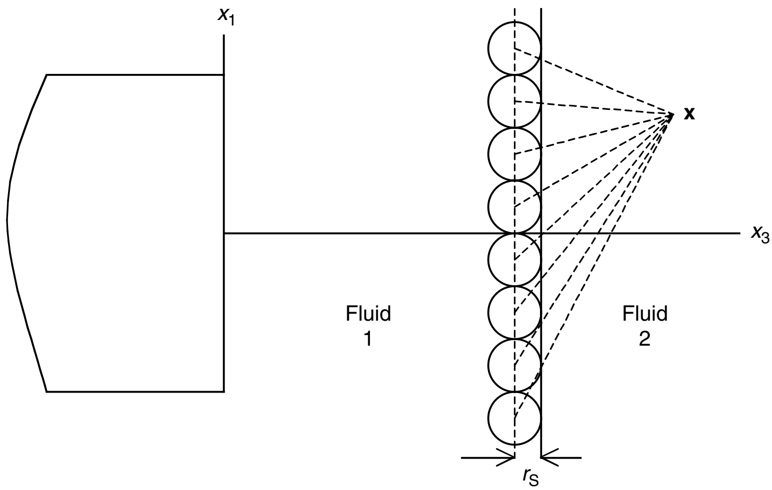

FIGURE 2.13
One layer of point sources (at the center of small circles) for computing the ultrasonic field in fluid 2.

located at various distances from x, as shown by the dotted lines in the figure. Strengths of these sources are obtained as before by equating the velocity components computed by the point sources, distributed along the interface, to those obtained from the transmitted wave contribution.

After following an analysis similar to that outlined in Section 2.5.1, strengths of the interface point sources in this case can be obtained from the relation (see Equation 2.55):

$$\mathbf{A}_I = \left[\mathbf{M}_{TI}^i\right]^{-1}\mathbf{V}_T^t = \left(\left[\mathbf{M}_{TI}^i\right]^{-1}\mathbf{M}_{TS}^t\right)\mathbf{A}_S \quad \textbf{(2.57)}$$

where $\mathbf{A}_I$ is the $3M \times 1$ vector of the interface source strengths, $\mathbf{M}_{TI}^i$ is the $3M \times 3M$ matrix that relates the two vectors $\mathbf{V}_T^t$ and $\mathbf{A}_I$, and $\mathbf{M}_{TS}^t$ is the $3M \times 3N$ matrix relating the velocity vector $\mathbf{V}_T^t$ at the interface points, and $\mathbf{A}_S$ is the source strength vector for point sources distributed along the transducer face.

In this case, the equations relating the interface velocity components to the transducer source strengths and interface source strengths are similar to Equation 2.53 and Equation 2.54 and can be written as follows:

$$\mathbf{V}_T^t = \mathbf{M}_{TS}^t\mathbf{A}_S \quad \textbf{(2.58)}$$

$$\mathbf{V}_T^t = \mathbf{M}_{TI}^i\mathbf{A}_I \quad \textbf{(2.59)}$$

After computing the interface source strengths using Equation 2.57, the ultrasonic field at any new target points x_n ($n = 1, 2, \ldots N_T$) on the right side of the interface (or in fluid 2) can be obtained from Equation 2.59. While computing the field at new points, appropriate changes in the values of x_{jm}^n and r_m^n appearing in matrix $\mathbf{M}_{TI}^i$ should be taken into account. As mentioned earlier, r_m^n is the distance between the m-th point source and n-th target point, and x_{jm}^n are the three components of r_m^n.

2.6 Ultrasonic Field in Presence of a Scatterer

The DPSM technique is then applied to the model ultrasonic field near a scatterer of finite dimensions for which no closed form analytical solution exists. Problem geometry showing the transducer and scatterer is given in Figure 2.14.

To compute the ultrasonic field in front of a scatterer (left of the scatterer), point sources are distributed along the transducer face and the solid-fluid interface as well as along the imaginary interface (extending the front face of the solid scatterer, shown by the dotted line in Figure 2.14). Triplet sources are located around the centers of the small spheres. The strength of the point sources on the transducer face is known from the normal velocity component (v_0) of the transducer surface (Equation 2.15j or Equation 2.56f). The strength of the point sources distributed along the real and imaginary interface is not known. This is carried out in a manner similar to the one described in Section 2.5.1. The only difference here is that in Equation 2.53 $\mathbf{M}_{TS}^r$ must be obtained by multiplying $\mathbf{M}_{TS}^i$ by appropriate reflection coefficients. The technique to compute the reflection coefficient for this case differs from the one given in Section 2.5.1. In the previous case, the same expression of the reflection coefficient (Equation 2.37) was used for all interface points x_n. However for this problem geometry when the interface points x_n are located on the scatterer surface, then the reflection coefficient for a solid plate immersed in a fluid (Chapter 1, Equation 1.233a) should be used. However, when the interface points x_n are located on the dotted line, along the imaginary interface between two identical fluids, then the reflection coefficient should be zero. Except for this difference in the reflection coefficient definition the steps to compute the interface source strengths for these two problem geometries are identical, and the source strength vector can be obtained from Equation 2.55

$$\mathbf{A}_I = \left[\mathbf{M}_{TI}^i\right]^{-1}\mathbf{V}_T^r = \left(\left[\mathbf{M}_{TI}^i\right]^{-1}\mathbf{M}_{TS}^r\right)\mathbf{A}_S$$

For computing the ultrasonic field behind the scatterer, or on the right side of the dotted line, the point sources should be taken as shown in Figure 2.15. Note that now some of the point sources are aligned with the right edge of

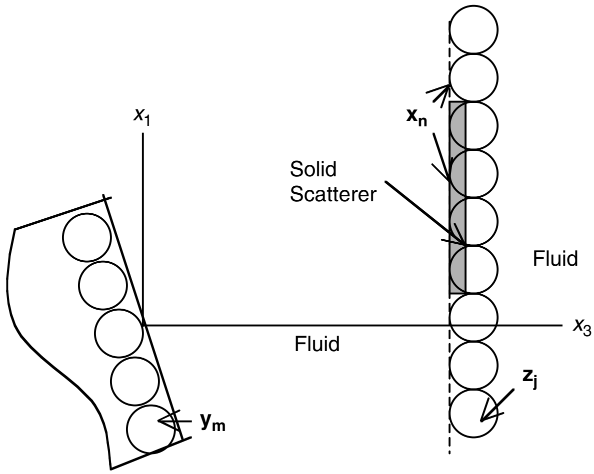

FIGURE 2.14
A finite solid scatter immersed in a fluid in front of a transducer face.

the scatterer, while the rest are aligned with the imaginary interface along the left edge, and marked by the dotted line. For thin scatterers these two planes coincide.

Following similar steps as in Section 2.5.2, the strengths of the interface point sources in this case can be obtained from Equation 2.57

$$\mathbf{A}_I = \left[\mathbf{M}_{TI}^i\right]^{-1}\mathbf{V}_T^t = \left(\left[\mathbf{M}_{TI}^i\right]^{-1}\mathbf{M}_{TS}^t\right)\mathbf{A}_S$$

where $\mathbf{A}_I$ is the $3M \times 1$ vector of the interface source strengths, $\mathbf{M}_{TI}^i$ is the $3M \times 3M$ matrix that relates the velocity vector $\mathbf{V}_T^t$ at the interface points x_n to the interface source strengths $\mathbf{A}_I$, and $\mathbf{M}_{TS}^t$ is the $(3M \times 3N)$ matrix that relates the velocity vector $\mathbf{V}_T^t$ at the interface points to the transducer source strength vector $\mathbf{A}_S$.

In this case equations relating the interface velocity components to the transducer source strengths and interface source strengths are similar to Equation 2.53 and Equation 2.54 and can be written as

$$\mathbf{V}_T^t = \mathbf{M}_{TS}^t\mathbf{A}_S$$

$$\mathbf{V}_T^t = \mathbf{M}_{TI}^i\mathbf{A}_I$$

After computing the interface source strengths using Equation 2.57, the ultrasonic field at any new target points x_n ($n = 1, 2, \ldots N_T$) on the right side

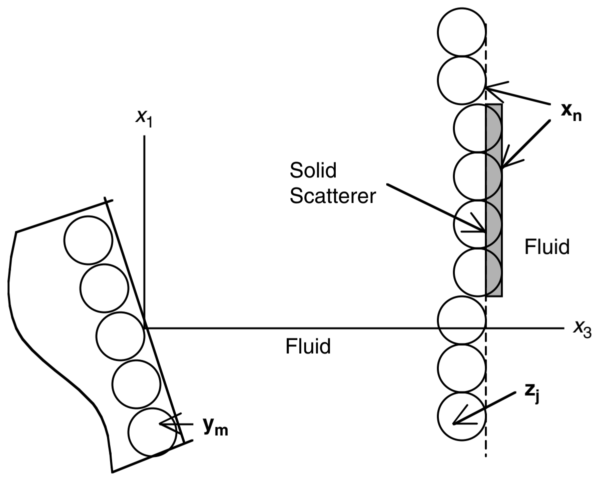

FIGURE 2.15
A finite solid scatter immersed in a fluid in front of a transducer face — distribution of interface sources for computing ultrasonic field in fluid 2.

of the interface can be obtained from Equation 2.59. For computing the field at new points, appropriate changes in the values of x_{jm}^n and r_m^n appearing in matrix $\mathbf{M}_{TI}^i$ should be taken into account. As mentioned earlier, r_m^n is the distance between the m-th point source and n-th target point, and x_{jm}^n are the three components of r_m^n.

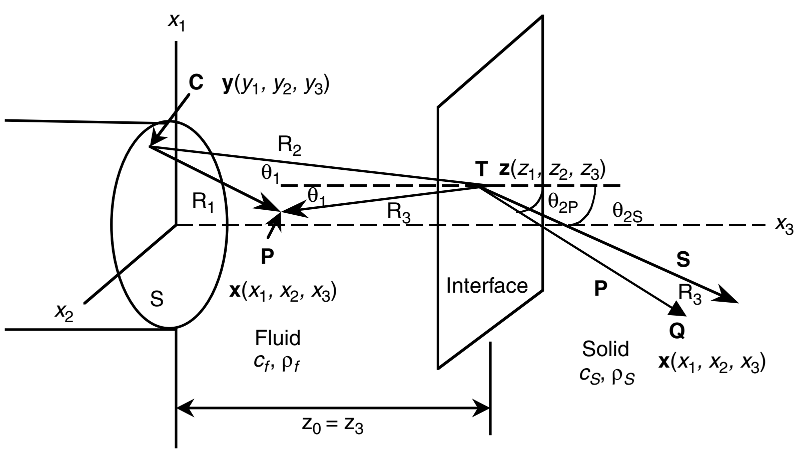

FIGURE 2.16
Ultrasonic transducer in front of a fluid-solid interface — incident and reflected P-waves in the fluid medium and transmitted P- and S-waves in the solid medium are shown.

2.7 Ultrasonic Field in Presence of a Fluid-Solid Interface

Up to this point we have computed the ultrasonic field in the fluid medium only. Three cases that have been considered so far are homogeneous fluid (Section 2.2 and Section 2.3), two fluids with an interface (Section 2.4 and Section 2.5), and a solid inclusion in a homogeneous fluid (Section 2.6). Even for the solid inclusion case (Section 2.6), only the ultrasonic field in the fluid medium has been computed. Now let us compute the field inside the solid. The problem geometry considered here is shown in Figure 2.16; it is similar to the ones shown in Figure 2.10 through Figure 2.13; the only difference is that fluid 2 in those figures is replaced here by a solid medium, while fluid 1 and transducer locations remain unchanged.

2.7.1 Ultrasonic Field in Fluid

The steps for computing the ultrasonic field inside the fluid for the problem geometry of Figure 2.16 are similar to the steps described in Section 2.4.1 (the surface integral technique) and Section 2.5.1 (the DPSM technique). The only difference is that in Section 2.4.1 and Section 2.5.1 the reflection coefficient was for the fluid-fluid interface, and now it should be for the fluid-solid interface. Therefore, Equation 2.37 should be replaced by the reflection coefficient for the fluid-solid interface with Equation 1.228d or Equation 1.228g in Chapter 1. When the transmission angles become imaginary, then it is easier to use Equation 1.228d.

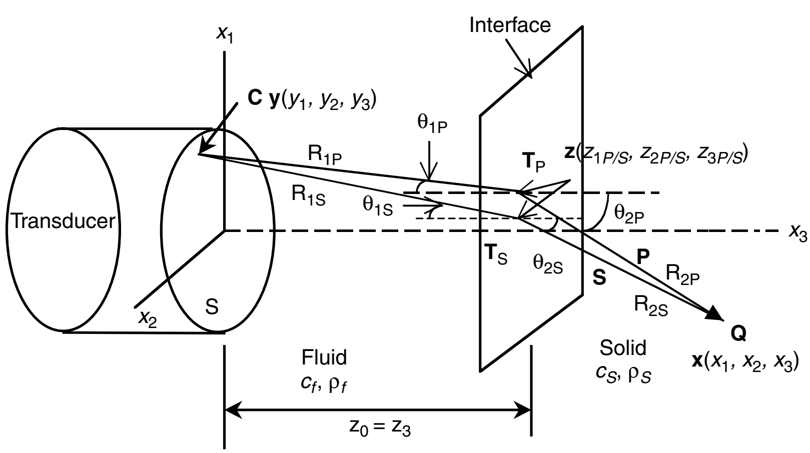

FIGURE 2.17
Transducer immersed in a fluid in front of a fluid-solid interface.

2.7.2 Ultrasonic Field in Solid

Computation of the ultrasonic field inside the solid medium is more cumbersome. When longitudinal waves strike a fluid-solid interface, both longitudinal (P) and shear (S) waves are generated in the solid (see Figure 2.16), unlike the fluid-fluid interface where only longitudinal waves are generated. Thus, if we are interested in computing the ultrasonic field at a point inside the solid medium for a specific point source on the transducer surface, we need to consider contributions of two rays: one generating the P-wave and the second one generating the S-wave, as shown in Figure 2.17.

In Figure 2.17 only the transmitted waves, traveling from point C on the transducer face to point Q in the solid medium, are shown. One ray travels along the path CT_PQ, and the second ray path is CT_SQ. The ray traveling a distance R_{1P} from C to T_P strikes the interface with an incident angle θ_{1P}. It should generate one reflected P-wave ray and two transmitted rays corresponding to P- and S-waves in the solid. To keep the figure simple, only the transmitted P-wave ray is shown traveling a distance of R_{2P} to point Q. Since the transmitted S-wave generated at point T_P has a different transmission angle, it cannot reach point Q for this incident angle and is not shown. However, for another incident angle θ_{1S}, the transmitted S-wave will reach point Q. For this incident angle, the transmitted P-wave cannot reach point Q and is not shown. If points C and Q are fixed, then only two rays can contribute to the ultrasonic field at point Q. It should be mentioned here that P- and S-wave path lengths in the solid are denoted by R_{2P} and R_{2S}, respectively; both R_{1P} and R_{1S} in the fluid medium represent P-wave path lengths. Subscripts P and S of R_1 indicate what type of transmitted waves (P or S) in the solid reach point Q for the P-wave path in the fluid.

Mathematical steps similar to the ones described in Section 2.4.2 are now followed to compute the ultrasonic field at point Q.

Let us define four vectors $\underline{A_P}$, $\underline{A_S}$, $\underline{C_P}$, and $\underline{C_S}$ where $\underline{A_P} = CT_P$, $\underline{A_S} = CT_S$, $\underline{C_P} = T_PQ$, and $\underline{C_S} = T_SQ$:

$$
\begin{aligned}
\underline{A_P} &= (z_{1P} - y_1)\underline{e_1} + (z_{2P} - y_2)\underline{e_2} + (z_{3P} - y_3)\underline{e_3} \\
\underline{A_S} &= (z_{1S} - y_1)\underline{e_1} + (z_{2S} - y_2)\underline{e_2} + (z_{3S} - y_3)\underline{e_3} \\
\underline{C_P} &= (x_1 - z_{1P})\underline{e_1} + (x_2 - z_{2P})\underline{e_2} + (x_3 - z_{3P})\underline{e_3} \\
\underline{C_S} &= (x_1 - z_{1S})\underline{e_1} + (x_2 - z_{2S})\underline{e_2} + (x_3 - z_{3S})\underline{e_3}
\end{aligned}
\quad (2.60)
$$

Note that the magnitudes of vectors $\underline{A_P}$, $\underline{A_S}$, $\underline{C_P}$, and $\underline{C_S}$ are R_{1P}, R_{1S}, R_{2P}, and R_{2S}, respectively.

$$R_{1P} = \left\{(z_{1P} - y_1)^2 + (z_{2P} - y_2)^2 + (z_{3P} - y_3)^2\right\}^{\frac{1}{2}}$$
$$R_{1S} = \left\{(z_{1S} - y_1)^2 + (z_{2S} - y_2)^2 + (z_{3S} - y_3)^2\right\}^{\frac{1}{2}}$$
$$R_{2P} = \left\{(x_1 - z_{1P})^2 + (x_2 - z_{2P})^2 + (x_3 - z_{3P})^2\right\}^{\frac{1}{2}} \tag{2.61}$$
$$R_{2S} = \left\{(x_1 - z_{1S})^2 + (x_2 - z_{2S})^2 + (x_3 - z_{3S})^2\right\}^{\frac{1}{2}}$$

Unit vectors $\hat{A}_P = \frac{A_P}{R_{1P}}, \hat{A}_S = \frac{A_S}{R_{1S}}, \hat{C}_P = \frac{C_P}{R_{2P}}, \hat{C}_S = \frac{C_S}{R_{2S}}$
Unit vector $\hat{n}$ normal to the interface is given by

$$\hat{n} = \begin{Bmatrix} 0 \\ 0 \\ 1 \end{Bmatrix}$$

Note that for an inclined interface

$$\hat{n} = \begin{Bmatrix} n_1 \\ n_2 \\ n_3 \end{Bmatrix}$$

From the problem geometry shown in Figure 2.17 one can write

$$\begin{aligned}
&|\hat{n} \times \hat{A}_P| = \sin\theta_{1P}, \qquad &|\hat{n} \times \hat{A}_S| = \sin\theta_{1S} \\
&\hat{n}.\hat{A}_P = \cos\theta_{1P}, \qquad &\hat{n}.\hat{A}_S = \cos\theta_{1S} \\
&|\hat{n} \times \hat{C}_P| = \sin\theta_{2P}, \qquad &|\hat{n} \times \hat{C}_S| = \sin\theta_{2S} \\
&\hat{n}.\hat{C}_P = \cos\theta_{2P}, \qquad &\hat{n}.\hat{C}_S = \cos\theta_{2S}
\end{aligned} \tag{2.62}$$

Let

$$\hat{A}_P = \begin{Bmatrix} a_{1P} \\ a_{2P} \\ a_{3P} \end{Bmatrix}, \quad \hat{A}_S = \begin{Bmatrix} a_{1S} \\ a_{2S} \\ a_{3S} \end{Bmatrix}, \quad \hat{C}_P = \begin{Bmatrix} c_{1P} \\ c_{2P} \\ c_{3P} \end{Bmatrix}, \quad \hat{C}_S = \begin{Bmatrix} c_{1S} \\ c_{2S} \\ c_{3S} \end{Bmatrix} \tag{2.63}$$

From Equation 2.60, Equation 2.62, and Equation 2.63 we get

$$c_{3P} = \cos\theta_{2P} = \frac{x_3 - z_{3P}}{R_{2P}}, \qquad c_{3S} = \cos\theta_{2S} = \frac{x_3 - z_{3S}}{R_{2S}}$$
$$a_{3P} = \cos\theta_{1P} = \frac{z_{3P} - y_3}{R_{1P}}, \qquad a_{3S} = \cos\theta_{1S} = \frac{z_{3S} - y_3}{R_{1S}} \tag{2.64}$$

and

$$\hat{n} \times \hat{C}_{P/S} = Det\begin{bmatrix} e_1 & e_2 & e_3 \\ n_1 & n_2 & n_3 \\ c_{1P/S} & c_{2P/S} & c_{3P/S} \end{bmatrix} = \begin{bmatrix} 0 & -n_3 & n_2 \\ n_3 & 0 & -n_1 \\ -n_2 & n_1 & 0 \end{bmatrix}\begin{Bmatrix} c_{1P/S} \\ c_{2P/S} \\ c_{3P/S} \end{Bmatrix}$$
$$= \begin{bmatrix} 0 & -1 & 0 \\ -1 & 0 & 0 \\ 0 & 0 & 0 \end{bmatrix}\begin{Bmatrix} c_{1P/S} \\ c_{2P/S} \\ c_{3P/S} \end{Bmatrix} = \begin{Bmatrix} -c_{2P/S} \\ c_{1P/S} \\ 0 \end{Bmatrix} \tag{2.65}$$
$$\Rightarrow \left|\hat{n} \times \hat{C}_{P/S}\right|^2 = c_{1P/S}^2 + c_{2P/S}^2 = \sin^2\theta_{2P/S}$$

or

$$\sin^2\theta_{2P/S} = \frac{(x_1 - z_{1P/S})^2 + (x_2 - z_{2P/S})^2}{R_{2P/S}^2} \tag{2.66}$$

Similarly,

$$\left|\hat{n} \times \hat{A}_{P/S}\right|^2 = a_{1P/S}^2 + a_{2P/S}^2 = \frac{(z_{1P/S} - y_1)^2 + (z_{2P/S} - y_2)^2}{R_{1P/S}^2} = \sin^2\theta_{1P/S} \tag{2.67}$$

In Equation 2.65 through Equation 2.67 and in subsequent equations subscript $_{P/S}$ indicates one set of equations with subscript P and another set of equations with subscript S. Since $\hat{A}_{P/S}$, $\hat{n}$, $\hat{C}_{P/S}$ are located on the same plane

$$\hat{n} \times \hat{A}_{P/S} = \hat{e}_{P/S} \sin\theta_{1P/S}$$
$$\hat{n} \times \hat{C}_{P/S} = \hat{e}_{P/S} \sin\theta_{2P/S} \tag{2.68}$$

where $\hat{e}_P$ and $\hat{e}_S$ are the unit vectors normal to the planes containing $\hat{A}_P$, $\hat{n}$, $\hat{C}_P$ and $\hat{A}_S$, $\hat{n}$, $\hat{C}_S$, respectively.

From Equation 2.68 and Snell's law (see Chapter 1, Equation 1.204) one can write

$$\frac{\hat{n}\times\hat{A}_{P/S}}{\sin\theta_{1P/S}} = \frac{\hat{n}\times\hat{C}_{P/S}}{\sin\theta_{2P/S}}$$
$$\Rightarrow \frac{\hat{n}\times\hat{A}_{P/S}}{c_f} = \frac{\hat{n}\times\hat{C}_{P/S}}{c_{P/S}} \tag{2.69}$$

or

$$\frac{1}{c_f}\begin{Bmatrix} -a_{2P/S} \\ a_{1P/S} \\ 0 \end{Bmatrix} = \frac{1}{c_{P/S}}\begin{Bmatrix} -c_{2P/S} \\ c_{1P/S} \\ 0 \end{Bmatrix}$$
$$\Rightarrow \begin{Bmatrix} -\dfrac{z_{1P/S}-y_1}{c_f R_{1P/S}} \\ \dfrac{z_{2P/S}-y_2}{c_f R_{1P/S}} \\ 0 \end{Bmatrix} = \begin{Bmatrix} -\dfrac{x_1-z_{1P/S}}{c_{P/S} R_{2P/S}} \\ \dfrac{x_2-z_{2P/S}}{c_{P/S} R_{2P/S}} \\ 0 \end{Bmatrix} \tag{2.70}$$

$z_{1P/S}$ and $z_{2P/S}$ are obtained from Equation 2.70 by minimizing the following error function:

$$E = \left(\frac{z_{1P/S}-y_1}{c_f R_{1P/S}} + \frac{z_{1P/S}-x_1}{c_{P/S} R_{2P/S}}\right)^2 + \left(\frac{z_{2P/S}-y_2}{c_f R_{1P/S}} + \frac{z_{2P/S}-x_2}{c_{P/S} R_{2P/S}}\right)^2 \tag{2.71}$$

E of Equation 2.71 are minimized by some optimization technique such as simplex algorithm. In MATLAB code the *fminsearch* function can be used for this purpose. After obtaining $z_{1P/S}$ and $z_{2P/S}$ all angles of incidence and transmission can be evaluated from Equation 2.61 and Equation 2.64. Then the P- and S-wave potentials at point Q are obtained in the following manner.

Let the ultrasonic field in the fluid medium be expressed in terms of the fluid pressure. From Equation 2.6a and Equation 2.16 the pressure fields generated by the source point C (see Figure 2.17) at the interface points T_P and T_S can be written as

$$p(z_{1P}, z_{2P}, z_{3P}) = \frac{-i\omega\rho_f v_0 dS}{2\pi} \frac{\exp(ik_f R_{1P})}{R_{1P}}$$
$$p(z_{1S}, z_{2S}, z_{3S}) = \frac{-i\omega\rho_f v_0 dS}{2\pi} \frac{\exp(ik_f R_{1S})}{R_{1S}} \quad \textbf{(2.72)}$$

where v_0 is the transducer surface velocity in the direction normal to the transducer face and dS is the elemental area of the point source at point C.

Two pressure waves of Equation 2.72 strike the fluid-solid interface at angles θ_{1P} and θ_{1S}, respectively. Transmission coefficients for P- and S-wave generation in the solid, for a P-wave striking the fluid-solid interface from the fluid side, are given in Chapter 1, Equations 1.228n, c, e, i, and j. Equation 1.228n gives the relation between two sets of transmission and reflection coefficients:

$$R^* = R.$$
$$T_P^* = \frac{T_P}{\rho_f \omega^2}$$
$$T_S^* = \frac{T_S}{\rho_f \omega^2}$$

Coefficients with the superscript (*) are for the incident field expressed in terms of the fluid pressure; and the coefficients without the superscript is for the incident field expressed in terms of wave potentials. In both cases, elastic waves in the solid are expressed in terms of the P- and S-wave potentials only. After multiplying the pressure fields of Equation 2.72 by appropriate transmission coefficients of Equation 1.228n, one gets the P- and S-wave potentials in the solid at points T_P and T_S (Figure 2.17), respectively. To obtain P and S wave potentials at point Q one must multiply the P- and S-wave potentials in the solid at points T_P and T_S by appropriate wave propagation terms, to mathematically represent the propagating P- and S-waves along the path lengths R_{2P} and R_{2S} (Figure 2.17), respectively. Finally, from the wave potential terms the displacement components are obtained by taking derivatives of the potentials (see Chapter 1, Equation 1.91, Equation 1.100, and Equation 1.101).

After going through these steps the final expression of the displacement field in the solid will have the following form (Schmerr, 1998):

$$\mathbf{u}(\mathbf{x}) = \frac{-\rho_f v_o}{2\pi\rho_S}\left\{\frac{\hat{\mathbf{e}}_P}{c_P}\int_S \frac{T_P^* \exp[ik_f R_{1P} + k_P R_{2P})]}{\sqrt{R_{1P} + \frac{c_P}{c_f}R_{2P}}\sqrt{R_{1P} + R_{2P}\frac{c_P\cos^2\theta_{1P}}{c_f\cos^2\theta_{2P}}}}\,dS\right.$$

$$\left. + \frac{\hat{\mathbf{e}}_S}{c_S}\int_S \frac{T_S^* \exp[ik_f R_{1S} + k_S R_{2S})]}{\sqrt{R_{1S} + \frac{c_S}{c_f}R_{2S}}\sqrt{R_{1S} + R_{2S}\frac{c_S\cos^2\theta_{1S}}{c_f\cos^2\theta_{2S}}}}\,dS\right\} \qquad \textbf{(2.73)}$$

where $\hat{\mathbf{e}}_P$ and $\hat{\mathbf{e}}_S$ are unit vectors in the direction T_PQ and normal to the direction T_SQ, respectively. In other words, $\hat{\mathbf{e}}_P$ and $\hat{\mathbf{e}}_S$ are polarization unit vectors in the direction of the particle displacements for propagating P- and S-waves, respectively. Transmission coefficients T_P^* and T_S^* are obtained from Chapter 1, Equations 1.228n, c, e, i, and j, as shown below. Note that the integrands of Equation 2.73 are similar to the integrand of Equation 2.50.

$$T_P^* = \frac{T_P}{\rho_f\omega^2} = \frac{2c_P\cos\theta_{1P}\cos 2\theta_{2P}}{c_f\rho_f\omega^2(\Delta_{2P}+\Delta_{1P})} = \frac{\frac{-2}{\rho_f\omega^2}\left(\frac{2[k^P]^2}{k_S^2}-1\right)}{\frac{\rho_S}{\rho_f}\left\{\left(\frac{2[k^P]^2}{k_S^2}-1\right)^2 + \frac{4[k^P]^2\eta_{SP}\beta_{SP}}{k_S^4}\right\} + \frac{\eta_{SP}}{\eta_{fP}}} \qquad \textbf{(2.74)}$$

$$T_S^* = \frac{T_S}{\rho_f\omega^2} = -\frac{2c_S^2\cos\theta_{1S}\cdot\sin 2\theta_{2S}}{c_P c_f\rho_f\omega^2(\Delta_{2S}+\Delta_{1S})} = \frac{\frac{-4k^S\eta_{SS}}{\rho_f\omega^2 k_S^2}}{\frac{\rho_S}{\rho_f}\left\{\left(\frac{2[k^S]^2}{k_S^2}-1\right)^2 + \frac{4[k^S]^2\eta_{SS}\beta_{SS}}{k_S^4}\right\} + \frac{\eta_{SS}}{\eta_{fS}}}$$

where

$$k^{P/S} = k_f\sin\theta_{1P/S}$$

$$\eta_{fP/S} = k_f\cos\theta_{1P/S} = \sqrt{k_f^2 - (k^{P/S})^2}$$

$$\eta_{SP/S} = \sqrt{k_P^2 - (k^{P/S})^2} \qquad \textbf{(2.75a)}$$

$$\beta_{SP/S} = \sqrt{k_S^2 - (k^{P/S})^2}$$

$$k_f = \frac{\omega}{c_f},\quad k_P = \frac{\omega}{c_P},\quad k_S = \frac{\omega}{c_S},$$

and

$$\Delta_{1P} = \cos\theta_{2P}$$

$$\Delta_{1S} = \sqrt{1-\left(\frac{c_P}{c_S}\sin\theta_{2S}\right)^2}$$

$$\Delta_{2P} = \frac{\rho_S c_P \cos\theta_{1P}}{\rho_f c_f}\left\{\left[1-2\left(\frac{c_S}{c_P}\sin\theta_{2P}\right)^2\right]^2 \right. \tag{2.75b}$$

$$\left. +2\frac{c_S^3}{c_P^3}\sin 2\theta_{2P}\cdot\sin\theta_{2P}\left[1-\left(\frac{c_S}{c_P}\sin\theta_{2P}\right)^2\right]^{\frac{1}{2}}\right\}$$

$$\Delta_{2S} = \frac{\rho_S c_P \cos\theta_{1S}}{\rho_f c_f}\left\{\cos^2 2\theta_{2S} + 2\frac{c_S}{c_P}\sin 2\theta_{2S}\cdot\sin\theta_{2S}\left[1-\left(\frac{c_P}{c_S}\sin\theta_{2S}\right)^2\right]^{\frac{1}{2}}\right\}$$

Expressions of T_P given in Equation 2.74 and Equation 1.228c and Equation 1.228i are identical. However, signs of T_S given in Equations 2.71 and 1.227d, i are different. This change of sign is the result of the change of the coordinate direction relative to the wave propagation direction. In Chapter 1, Figure 1.36, the incident and transmitted waves are propagating in the negative x_2-direction, while in Figure 2.17, these waves are propagating in the positive x_3-direction. In Chapter 1, after Equation 1.228j, it has been mentioned and can be easily verified that the signs of some transmission coefficients change if one changes the direction of the coordinate axis.

2.7.3 Transducer Surface Inclined to the Fluid–Solid Interface

If the transducer has some inclination relative to the interface as shown in Figure 2.18, such that the central axis of the transducer is not normal to the interface, then the basic steps of the analysis described in Section 2.7.1 and Section 2.7.2 do not change. The only difference in the analysis between the two problem geometries of Figure 2.17 and Figure 2.18 is that for the problem geometry of Figure 2.17, $y_3 = 0$ or constant for all point sources on the transducer surface, but that is not the case for Figure 2.18. Therefore, the inclined incidence case can be modeled in the same manner with minor modifications in the formulation.

2.8 Numerical Results

Sections 2.1 through Section 2.7 describe the theory of the ultrasonic field modeling by using the DPSM technique in homogeneous and nonhomoge-

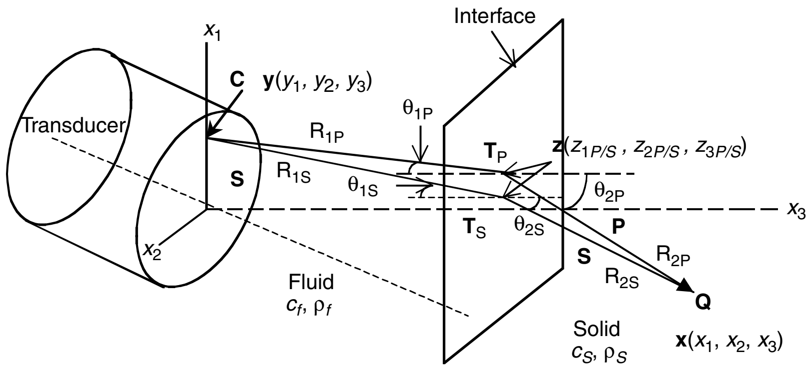

FIGURE 2.18
Transducer surface is not parallel to the fluid-solid interface.

neous fluids and in the fluid-solid media. Based on this theory the authors have developed a number of MATLAB computer codes to model the ultrasonic fields generated by the ultrasonic transducers of finite dimension that are immersed in a fluid. In the simplest case, the transducer is immersed in a homogeneous fluid. More complex problem geometries involve two fluids with a plane interface, fluid-solid medium with a plane interface, and a solid scatterer of finite size immersed in a homogeneous fluid. The numerical results clearly show how the ultrasonic field decays as the distance from the transducer increases, and the field becomes more collimated as the size of the transducer increases. It also shows that the field is reflected and transmitted at an interface, and how a finite size scatterer can give rise to the reflection, transmission, and diffraction of the incident field. A sample computer code is placed on the publisher's Web site (http://www.crcpress.com) as well as a brief description of the code, so that the readers can run the MATLAB code and reproduce some of the results presented here and also generate new results for other problem geometries.

2.8.1 Ultrasonic Field in a Homogeneous Fluid

In this example the ultrasonic field in front of a flat circular, flat rectangular, and concave circular transducer faces, are generated. The transducer front face geometries are shown in Figure 2.19. The area of the flat transducer face is 5 mm^2 for both circular and square transducers. Note that a 0.1-in. diameter circular transducer gives an area of 5 mm^2. A concave transducer face has different dimensions; its diameter is 12.7 mm (0.5 in.), and its radius of curvature is 8 mm. All of the dimensions in the figure are given in meter, but the scales are not necessarily the same in the horizontal and vertical directions. These three transducers are denoted as circular, square, and focused transducers. Note that the flat transducer face is located on the *xy*-plane. We would like to compute the ultrasonic field in front of the trans-

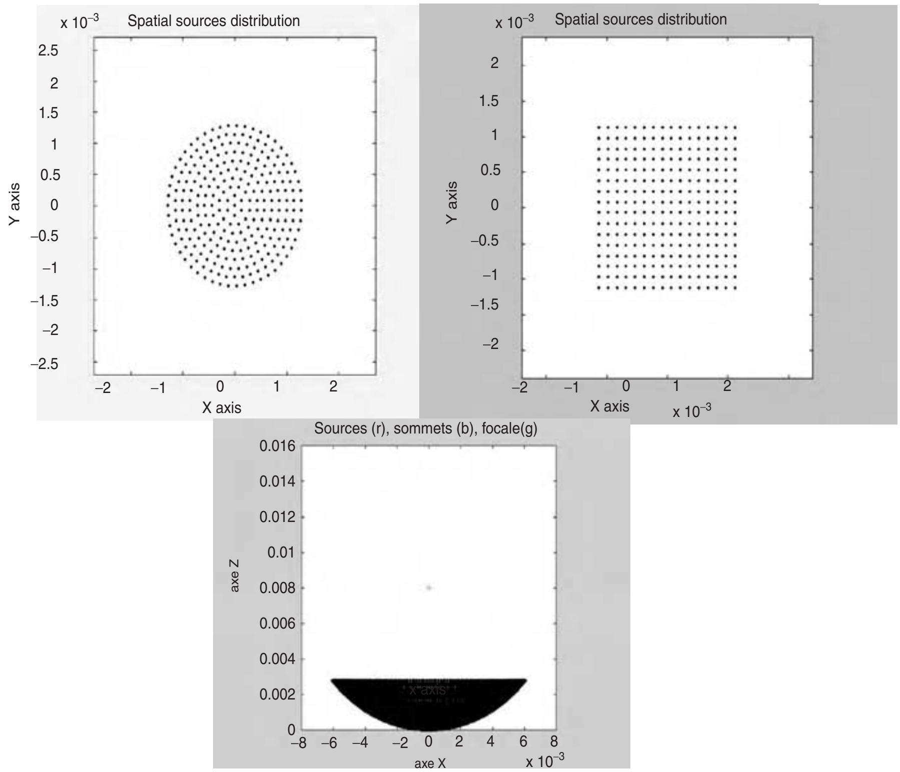

FIGURE 2.19
Distribution of the point sources at the front face of a flat circular (top left) and flat square (top right) transducer. Bottom figure: side view of the concavefront face of a transducer.

ducer face in the *xz*- or the *yz*-plane. Both *xz*- and *yz*-planes are planes of symmetry and are perpendicular to each other.

The ultrasonic pressure field variations along the *xz*- and *yz*-planes in front of the transducer face are shown in Figure 2.20 for 1-MHz frequency of the transducers. The top-left and top-right images of this figure are for the circular and square transducers, respectively. The field is less collimated for the square transducer. For both transducer geometries the ultrasonic field has a number of peaks (or maxima denoted by the red color) and dips (or minima denoted by the blue color) along the central axis (*z*-axis) of the transducer near the transducer face. The peaks and dips are a result of constructive and destructive interferences between the fields generated by different point sources on the transducer face.

For the concave transducer the field intensity increases as we approach the focal point. The focal point is at a distance of 8 mm from the transducer face, while the plot is shown for a distance varying from 3 to 6 mm.

It should be mentioned here that the focused transducer surface area is 25 times that of the flat transducers. To maintain the same spacing between

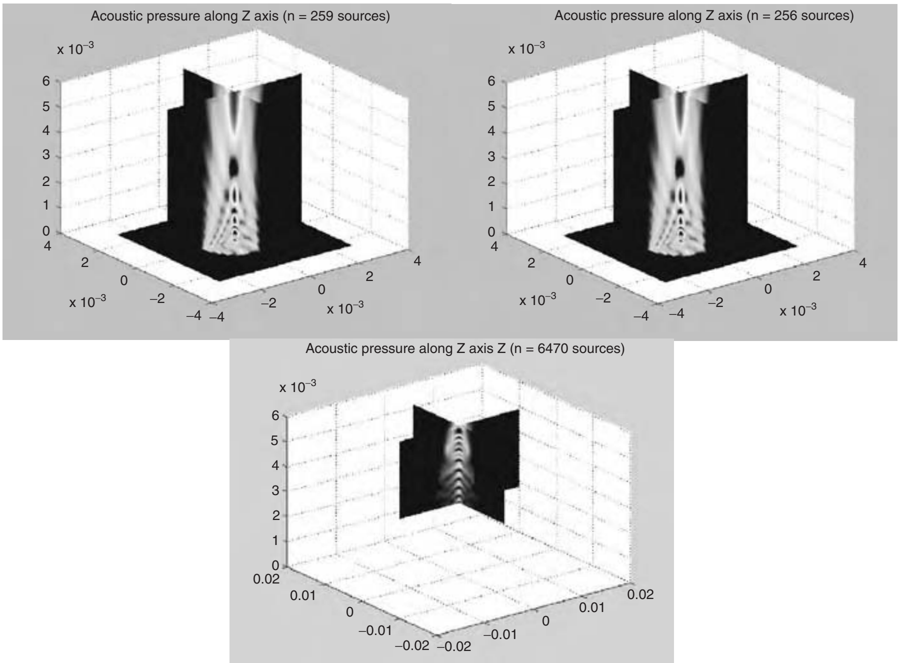

FIGURE 2.20
Ultrasonic pressure fields generated by a circular (top left), a square (top right), and a concave circular (bottom) transducer. Transducer face geometries are shown in Figure 2.19. Transducer frequency is 1 MHz. The surface area of the flat transducers is 5 mm^2. The concave transducer has a radius of curvature of 8 mm, and the diameter of its periphery is 12.7 mm. The number of point sources is 259 for the top-left figure, 256 for the top-right figure, and 6470 for the bottom figure. The ultrasonic field is plotted up to an axial distance of 6 mm. Note that the focal point for the concave transducer is at a distance of 8 mm, which is beyond the plotted region.

neighboring point sources (see Section 2.2.3), the number of point sources for the focused transducer is made about 25 times that of the flat transducers. Thus the number of point sources for the focused transducer is 6470, while for the flat transducers the two numbers are 256 and 259, respectively.

Variations of the pressure field along the z-axis, in front of the transducer face, are clearly shown in Figure 2.21. The top two figures are for the circular and square transducers and the bottom figure is for the focused transducer. The analytical solutions (Equation 2.6a for the flat circular transducer and Equation 2.22 for the focused transducer) give results that are very close to the one obtained by the DPSM technique (Equation 2.15k; see Figure 2.21). Three peaks between 0 and 4 mm along the z-axis, in Figure 2.21 correspond for both circular and square transducers to the three dots in Figure 2.20 along the central axis of the ultrasonic beam.

Example 2.4

Check whether Equation 2.20 is satisfied for the flat circular cylinder with 259 point sources.

SOLUTION

The area for each point source (A_S) is computed from the surface area of the transducer face in the following manner:

$$A_S = \frac{\pi r^2}{n} = \frac{\pi 1.27^2}{259} = 0.01956 \text{ mm}^2$$

Because $A_S = 2\pi r_S^2$ (see Figure 2.7 and also the discussion between Equation 2.19 and Equation 2.20) we can write

$$r_S = \sqrt{\frac{0.01956}{2\pi}} = 0.0558 \text{ mm}$$

From the wavelength (λ_f), wave speed (c_f) and frequency (f) relation, we get the wavelength in water for 1-MHz frequency

$$\lambda_f = \frac{c_f}{f} = \frac{1.5 \times 10^6}{10^6} = 1.5 \text{ mm}$$

From Equation 2.20 we get

$$r_S << \frac{1.5}{2\pi} \text{ mm}$$

$$\Rightarrow r_S << 0.24 \text{ mm}$$

Because $r_S = 0.0558$ mm, the above condition is satisfied.

Pressure field variations in front of the transducer face along the *xz*-plane for the three transducer geometries of Figure 2.19 are shown in Figure 2.22. In this figure one can clearly see how the pressure field oscillates near the transducer face and decays laterally (in the positive and negative *x*-directions) and axially (in the *z*-direction) for the flat transducers. For the focused transducer a clear peak can be observed near the focal point. Contour plots for the pressure field variations in the *xz*-plane for the same three transducer geometries are shown in Figure 2.23.

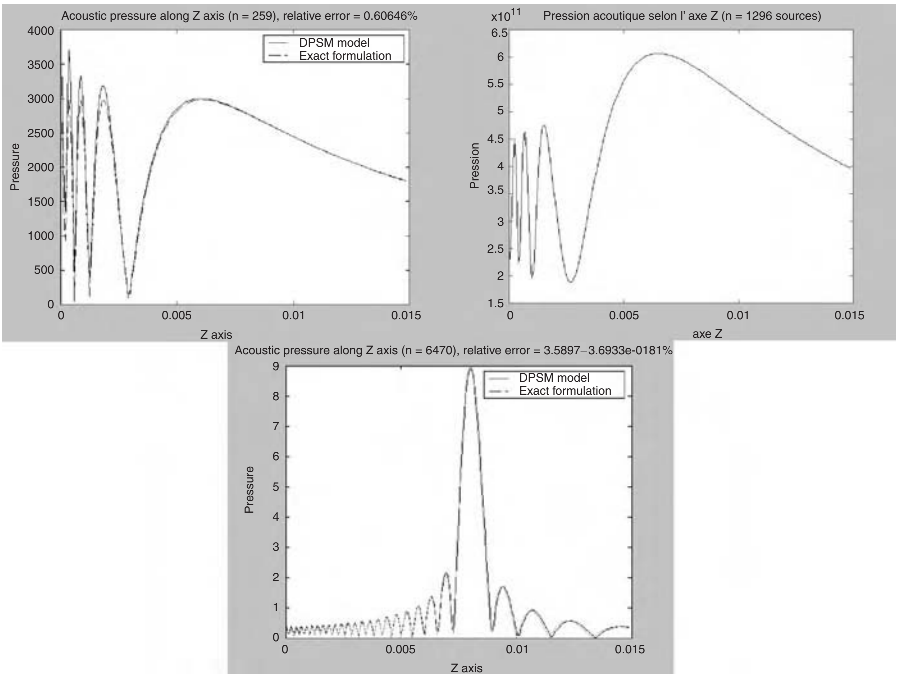

FIGURE 2.21
Ultrasonic pressure fields generated by circular (left top), square (right top), and focused (bottom) transducers. Thin dashed curves in left top and bottom figures have been generated by the closed form expressions (Equation 2.6c for the flat circular transducer and Equation 2.22 for the focused transducer). Continuous curves are obtained by the DPSM technique (Equation 2.15k).

Figure 2.24 shows the effect of increasing the number of point sources. As more sources are considered, the computed field becomes smoother. Since the oscillating velocity amplitudes at the transducer surface are different for the left and right columns of this figure, as well as the scales along the vertical axes, the numerical values in the two columns should not be compared. A comparison of the relative variations of the pressure fields between the two columns clearly demonstrates the effect of the increasing number of point sources on the computed pressure field.

The effect of the presence of a small circular hole at the center of a 2.54-mm (0.1-in.) diameter flat circular transducer is shown in Figure 2.25. The pressure field in the *xz*-plane (top right plot of Figure 2.25) is very similar to the one given in Figure 2.23 (top left). Therefore, a small hole at the center of a flat circular transducer does not significantly affect the generated pressure field in the fluid. The bottom two plots of Figure 2.25 show the pressure and normal velocity (V_z) variations in the *xy*-plane, very close to the transducer surface. It should be noted here that an oscillating pattern is present in the pressure plot but not in the velocity plot. Theoretically, the velocity compo-

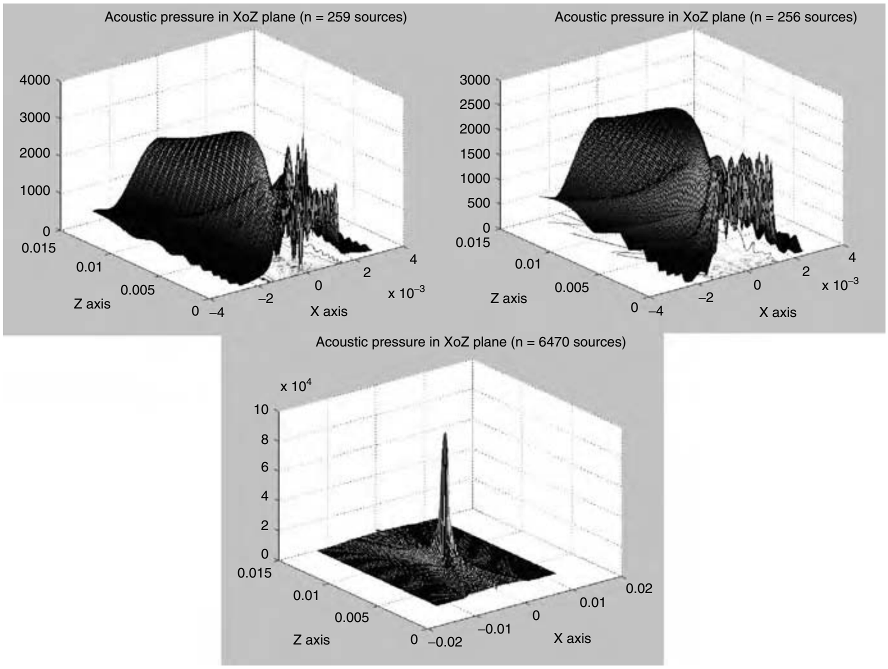

FIGURE 2.22
Ultrasonic pressure fields in the *xz*-plane are generated by circular (left top), square (right top), and focused (bottom) transducers. The central axis of the transducer coincides with the *z*-axis.

nent should be a constant and equal to v_0 on the transducer surface; see Equation 2.6a and Equation 2.15d. A small level of noise in the velocity plot exists due to the numerical error.

2.8.2 Ultrasonic Field in a Nonhomogeneous Fluid — DPSM Technique

The pressure field generated by a circular transducer placed parallel to the interface of two fluids is computed. As before, the transducer frequency is set at 1 MHz and its diameter is 2.54 mm. The distance between the transducer face and the interface between two fluids is 10 mm. The transducer is immersed in fluid 1 (P-wave speed = 1.49 km/sec; density = 1 gm/cm^3). The P-wave speed and density of fluid 2 are set at 2 km/sec and 1.5 gm/cm^3, respectively.

One hundred point sources are used to model the transducer surface and four hundred point sources (each point source is a triplet source) model the interface effect (see Figure 2.11 and Figure 2.12). Point sources distributed over the interface, which are also called target sources, are distributed over a square area of 20-mm side length. The interface source positions change when computing the acoustic fields in fluids 1 and 2.

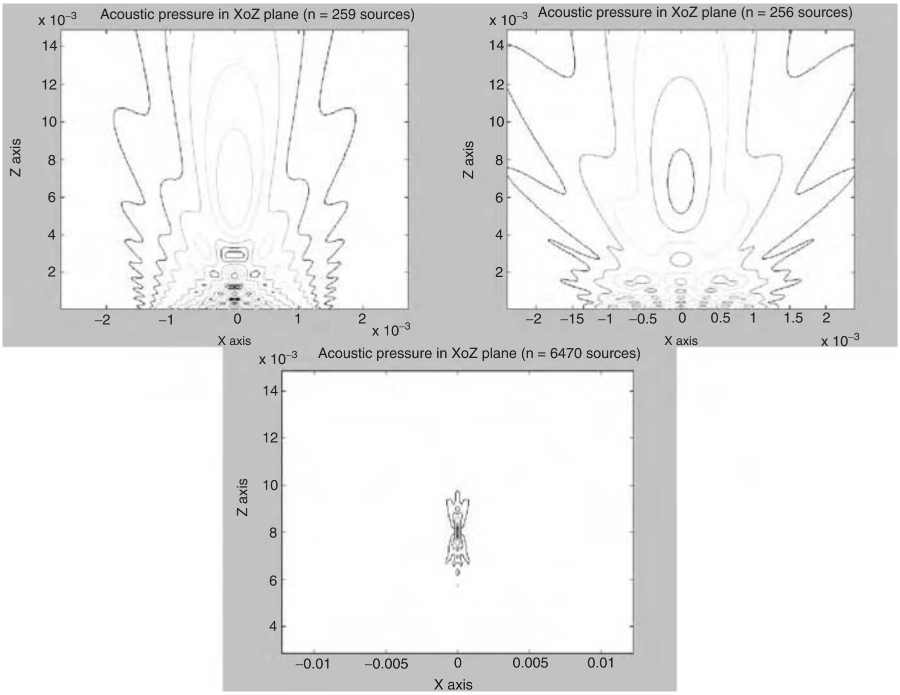

FIGURE 2.23
Contour plots for the ultrasonic pressure fields in the *xz*-plane are generated by circular (left top), square (right top), and focused (bottom) transducers. This figure is the same as Figure 2.22, but contour plots are given here instead of surface plots.

Pressure fields computed in the two fluids are plotted in Figure 2.26. Note how the pressure variation in the *xy* plane is changed, as the distance of the *xy*-plane from the transducer surface is increased from 0 (middle left figure) to 10 mm (bottom left figure). Pressure variations in the *xz*-plane in both fluids are shown as a contour plot (top right) and a surface plot (middle right). Pressure along the *z*-axis is plotted in the bottom right figure. Oscillations in the acoustic pressure in fluid 1 are the effects of constructive and destructive interferences between two rays that can reach a point in fluid 1. The first ray travels from the transducer face to the point of interest, and the second ray reaches the same point after being reflected at the interface (see Figure 2.10).

Pressure and velocity variations in the two fluids for an inclined transducer (inclination angle = 20°) are shown in Figure 2.27. The fluid properties and the transducer dimension are the same as those in this figure and Figure 2.26. The only difference between the problem geometries of Figure 2.26 and Figure 2.27 is that in Figure 2.26 the transducer face is parallel to the interface and in Figure 2.27 it is inclined.

From Snell's law the transmission angle in the second fluid can be computed:

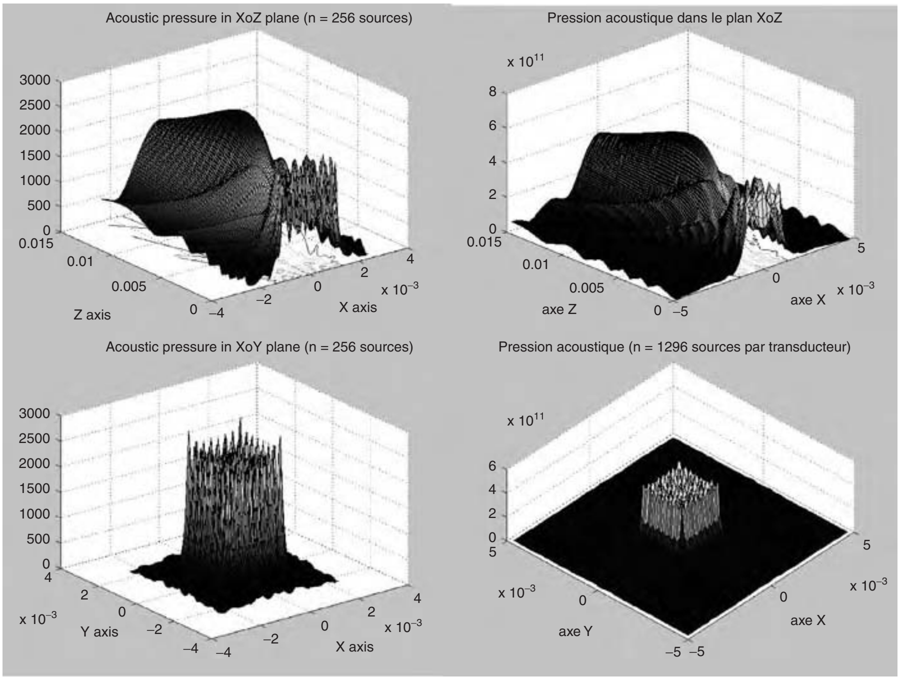

FIGURE 2.24
Pressure variations in the *xz*-plane (top row) and *xy*-plane, close to the transducer surface (bottom row) for a rectangular transducer. Left (256 point sources) and right (1296 point sources) columns correspond to two different discretizations of the transducer surface and two different transducer velocity amplitudes, v_0 of Equation 2.6a.

$$\theta_T = \sin^{-1}\left(\frac{2}{1.49}\sin(20)\right) = 27.33° \text{ o}$$

Incident and transmission angles, measured from the middle left plot of Figure 2.27, give values close to 20° and 27.33°, respectively. Note that the V_z variation (bottom right) and the pressure variation (middle right) in the two fluids are similar.

2.8.3 Ultrasonic Field in a Nonhomogeneous Fluid — Surface Integral Method

The ultrasonic field in the nonhomogeneous fluid can also be computed by the conventional surface integral technique instead of the DPSM technique. Unlike the DPSM technique, in the surface integral method the fluid–fluid interface is not modeled by the distributed point sources. Here only the transducer surface is discretized into the distributed point sources. In this method, the pressure fields in fluids 1 and 2 are computed by Equation 2.35

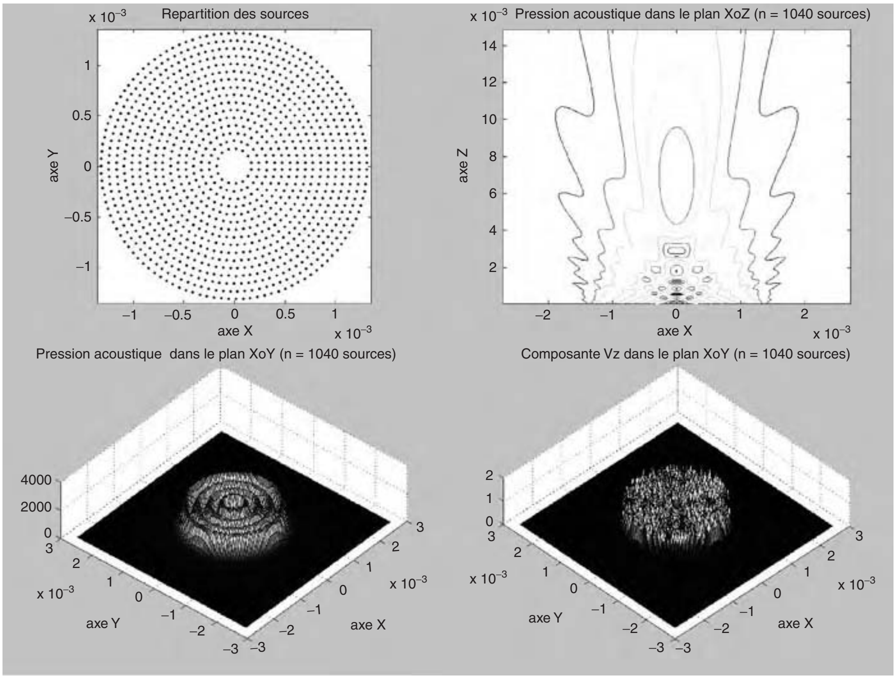

FIGURE 2.25
Top left: Circular transducer with a small hole at the center is modeled by 1040 point sources; top right: pressure field in the *xz* plane; bottom left: pressure field in the *xy* plane, close to the transducer surface; bottom right: normal velocity component (V_z) in the *xy*-plane, close to the transducer surface.

and Equation 2.50, respectively. The theory of this computation is given in Section 2.4 while the theory of the DPSM computation is given in Section 2.5. Figure 2.28 shows the pressure field along the *z*-axis in fluids 1 and 2, computed by the surface integral technique. A comparison of Figure 2.28 with the bottom-right plot of Figure 2.26 shows a perfect match between the results obtained by these two methods.

2.8.4 Ultrasonic Field in Presence of a Finite Size Scatterer

Following the theory described in Section 2.6, a computer code has been developed to compute the ultrasonic pressure field in the presence of a finite size scatterer. This computer code is used to solve the problem of ultrasonic field scattering by a finite size steel plate, immersed in water. The problem geometry is shown in Figure 2.29. A finite size thin steel plate (1 mm thick) is placed at the interface between two fluids: fluid 1 and fluid 2. The results are presented for the case in which both fluids are water. Scattered fields are computed for a large plate (20 × 20 mm, shown by the dashed line in Figure 2.29), and for a small plate (5 × 5 mm, shown by the solid line in Figure 2.29).

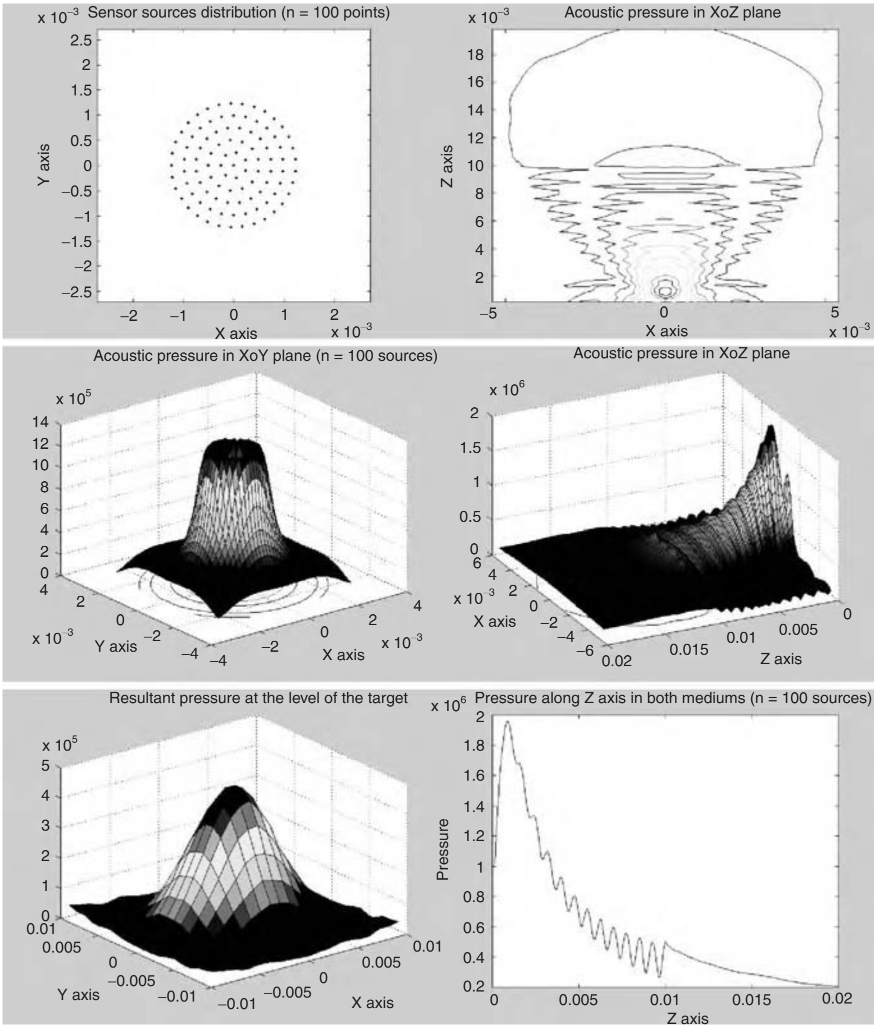

FIGURE 2.26
Circular transducer in a nonhomogeneous fluid. Top left: 2.54 mm diameter transducer modeled by 100 point sources; middle left: acoustic pressure in the *xy*-plane, close to the transducer surface ($z \sim 0$ mm); bottom left: acoustic pressure in the *xy* plane in fluid 1 at the interface position ($z = 10$ mm); top right: contour plot of the pressure variation in fluid 1 ($z = 0$ to 10 mm) and fluid 2 ($z = 10$ to 20 mm); middle right: surface plot of the pressure variation in fluid 1 ($z = 0$ to 10 mm) and fluid 2 ($z = 10$ to 20 mm); bottom right: pressure variation along the *z*-axis in fluid 1 ($z = 0$ to 10 mm) and fluid 2 ($z = 10$ to 20 mm).

The ultrasonic beam, generated by a 6.28-mm diameter cylindrical transducer, strikes the plate at an angle $\theta_i = 25°$ and 38.37°. Signal frequency is 1 MHz. The ultrasonic fields for these two striking angles are computed and

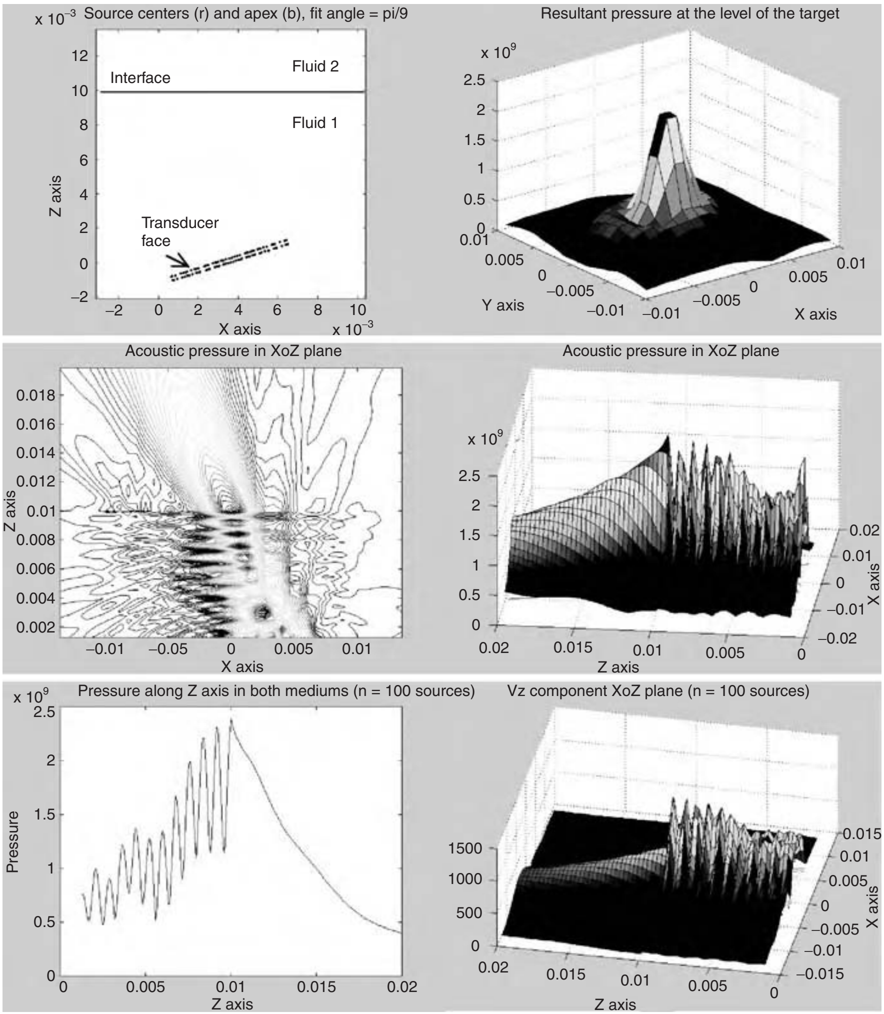

FIGURE 2.27
Top left: Inclined transducer face modeled with 100 point sources, angle between the interface and the transducer face is 20°; top right: acoustic pressure in the *xy*-plane in fluid 1 at the interface position (z = 10 mm); middle left: contour plot of the pressure field variation in fluid 1 (z = 1 to 10 mm) and fluid 2 (z = 10 to 20 mm); middle right: surface plot of the pressure field variation in fluid 1 (z = 1 to 10 mm) and fluid 2 (z = 10 to 20 mm); bottom left: pressure variation along the z-axis in fluid 1 (z = 1 to 10 mm) and fluid 2 (z = 10 to 20 mm); bottom right: surface plot of the velocity (V_z) variation in fluid 1 (z = 1 to 10 mm) and fluid 2 (z = 10 to 20 mm).

plotted in Figure 2.30 and Figure 2.31, respectively (Placko et al., 2003). Material properties for this computation are shown in Table 2.1.

The plate is placed at a distance of 10 mm from the transducer face. Thirty-two point sources distributed slightly behind the transducer face (see Figure 2.7) model the transducer.

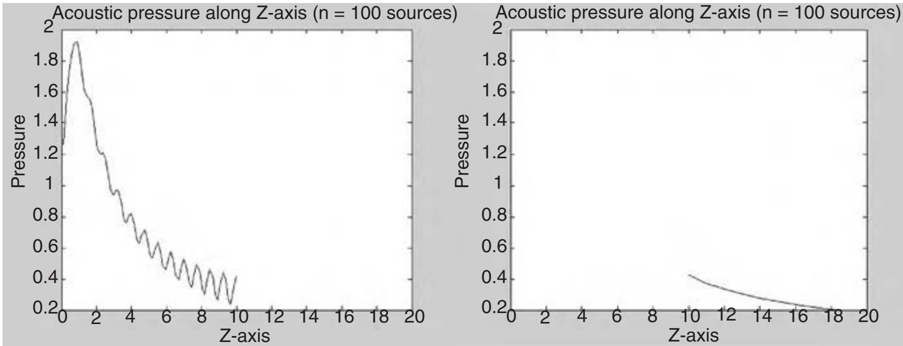

FIGURE 2.28
Pressure variation along the *z*-axis in fluid 1 (left) and fluid 2 (right).

Note that in both Figure 2.30 and Figure 2.31, scattered fields behind the steel plate are much stronger for the small plate than that for the large plate. For the large steel plate very little acoustic energy is transmitted into the fluid, behind the plate, because of the large impedance mismatch between the steel plate and the water. It should also be noted that in addition to the transmitted field, the reflected field for the large plate is also relatively weaker. The weak specular reflection for the large plate is more evident in Figure 2.31. A specular reflected beam is the reflected beam in the position predicted by the optics theory. The probable cause for a weak specular reflection by the large plate is that part of the ultrasonic energy generates leaky guided waves in the plate and propagates away from the striking zone. Therefore, less energy is specularly reflected by the larger plate. In Figure 2.32 we can see that for a 38.37° incident angle a guided wave mode is generated; less energy is specularly reflected for this incident angle when the plate is large.

As discussed above, the semianalytical/numerical techniques given in this chapter are useful for modeling the ultrasonic field generated by a finite size ultrasonic transducer for finite size specimens and in the presence of inclusions and cracks of finite dimensions.

TABLE 2.1

Water and Steel Properties for the Results Presented in Figure 2.30 through Figure 2.32

Material & Properties	P-wave Speed (km/sec)	S-wave Speed (km/sec)	Density (gm/cm^3)
Steel	5.96	3.26	7.93
Water	1.49	—	1

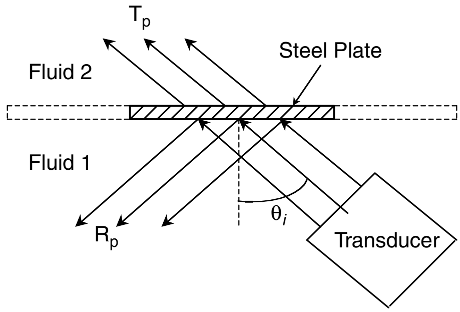

FIGURE 2.29
A bounded ultrasonic beam from an inclined transducer strikes a finite steel plate immersed in water at an angle θ_i (fluid 1 = fluid 2 = water).

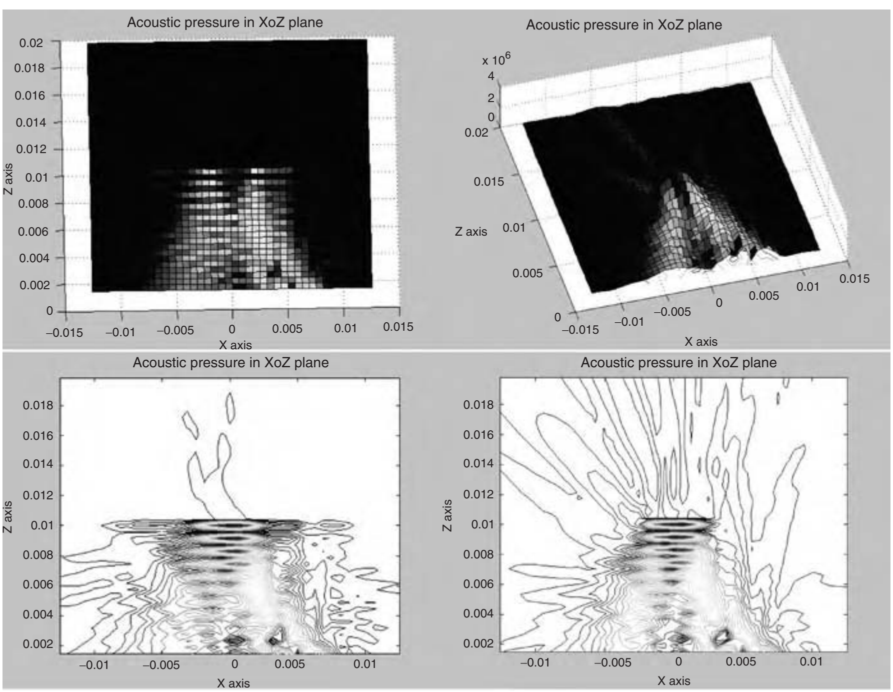

FIGURE 2.30
Total ultrasonic pressure distributions (incident plus scattered fields) near a steel plate scatterer, immersed in water. Left and right columns are for large (20 × 20 mm) and small (5 × 5 mm) plates, respectively. Incident angle is 25°. In top and bottom rows, the same pressure fields are plotted in two different ways.

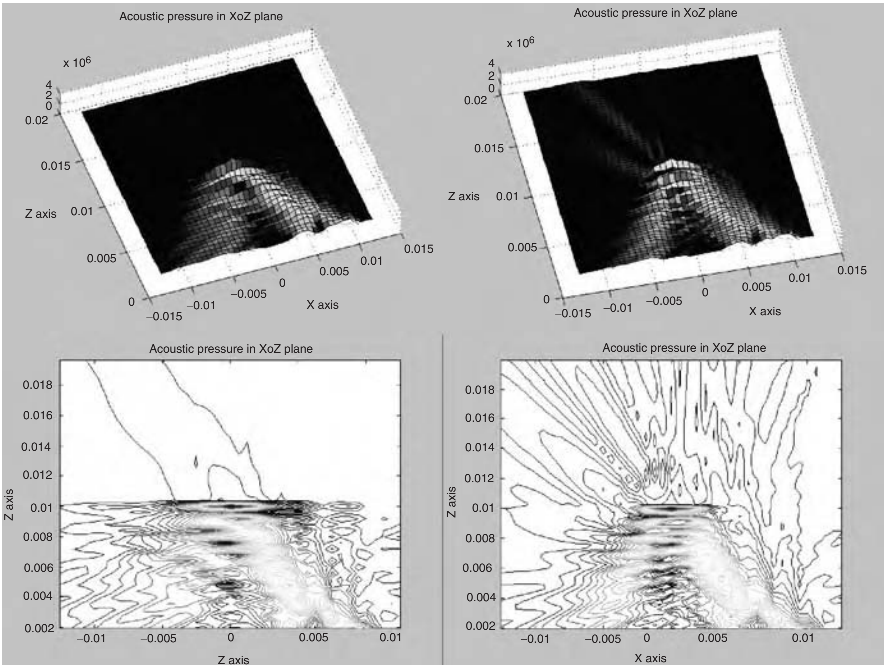

FIGURE 2.31
This figure is the same as Figure 2.30, but these plots are for a 38.37° angle of incidence.

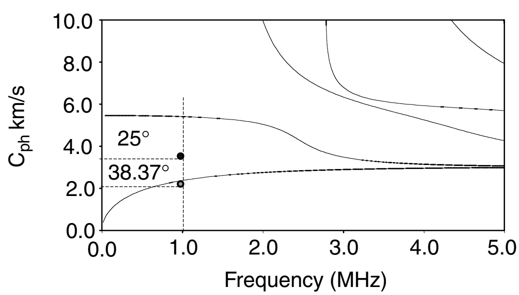

FIGURE 2.32
Dispersion curves for 1-mm thick steel plate (properties given in Table 2.1). Phase velocities corresponding to the two striking angles of Figure 2.30 (25°) and Figure 2.31 (38.37°) are shown. Note that the 38.37° incidence is capable of generating guided wave in the plate.

References

Lee, J.P., Placko, D., Alnuaimi, N., and Kundu, T., Distributed Point Source Method (DPSM) for Modeling Ultrasonic Fields in Homogeneous and Non-Homogeneous Fluid Media in Presence of an Interface, First European Workshop on Structural Health Monitoring, Balageas, D., Ed., Ecole Normale Superieure de Cachan, France, July 10–12, 2002.

O'Neil, H. T., Theory of Focusing Radiators, *Journal of the Acoustical Society of America*, Vol. 21, No. 5., 1949, pp. 516–526.

Placko, D. and Kundu, T., A Theoretical Study of Magnetic and Ultrasonic Sensors: Dependence of Magnetic Potential and Acoustic Pressure on the Sensor Geometry, *Advanced NDE for Structural and Biological Health Monitoring*, *Proceedings of SPIE,* Kundu, T., Ed., SPIE's 6th Annual International Symposium on NDE for Health Monitoring and Diagnostics, Mar. 4–8, Newport Beach, CA, Vol. 4335, 2001, pp. 52–62.

Placko, D., Kundu, T., and Ahmad, R., Distributed Point Source Method (DPSM) for Modeling Ultrasonic Fields in Homogeneous and Non-Homogeneous Fluid Media, Second International Conference on Theoretical, Applied, Computational and Experimental Mechanics, Paper No. 114, Kharagpur, India, Globenet Computers, India, Dec. 27–30, 2001.

Placko, D., Kundu, T., and Ahmad, R., Theoretical Computation of Acoustic Pressure Generated by Ultrasonic Sensors in Presence of an Interface, *Smart NDE and Health Monitoring of Structural and Biological Systems,* Kundu, T. Ed., SPIE's 7th Annual International Symposium on NDE for Health Monitoring and Diagnostics, Mar. 18–21 San Diego, CA, Vol. 4702, 2002, pp. 157–168.

Placko, D., Kundu, T., and R. Ahmad, Ultrasonic Field Computation in Presence of a Scatterer of Finite Dimension, *Smart Nondestructive Evaluation and Health Monitoring of Structural and Biological Systems*, Kundu, T., Ed., SPIE's 8th Annual International Symposium on NDE for Health Monitoring and Diagnostics, Mar. 3–5, San Diego, CA, Vol. 5047, 2003.

Placko, D., Liebeaux, N., and Kundu, T., Presentation d'une methode generique pour La Modelisation des Capteurs de type Ultrasons, Magnetiques et Electrostatiques, Instrumentation, Mesure, Metrologie: Evaluation nondestructive, (in French), Vol. 1, 2001 pp.101–125.

Schmerr, L. W., *Fundamentals of Ultrasonic Nondestructive Evaluation — A Modeling Approach*, Plenum Press, New York, 1998.

3

Ultrasonic Systems for Industrial Nondestructive Evaluation

Don E. Bray

CONTENTS

Globally competitive industries need efficient, reliable, and accurate inspection methods. While all nondestructive evaluation (NDE) methods offer particular capabilities suitable for special needs, ultrasonics has wide-ranging capabilities and is most adaptable to automation and flaw characterization. Ultrasound is able to interrogate both the surface and interior of a part. Moreover, a wide variety of waves with various particle motions and frequencies give almost unbounded capabilities for ultrasound. Limitations of ultrasound often are based on the physical properties of the material being

0-8493-1462-3/02/$0.00+$1.50

TABLE 3.1

Worldwide NDE Market in the 1990s

Industry	Distribution of NDE Users (%)
Aerospace	26
Automotive	15
Metals	15
Utilities	14
Petrochemical	10
Others	20

Source: Adapted from Wells, C.D., *Insight*, 36, 1994.

inspected, the need for a physical couplant, and the training of the inspectors and supervisors. Suitable applications of ultrasound are very dependent on knowledgeable engineers and inspectors.

Ultrasound in the 1990s accounted for 28% of the NDE marketplace, over twice the market share of the 1950s (Wells, 1994). Table 3.1 shows the distribution of NDE users in the 1990s, with the majority of the users in the aerospace industry, followed by the automotive, metals, utilities, and petrochemical industries. While none of these industrial groups has shown significant growth in recent years, the overall worldwide market is significant and was estimated to be $960 million in the 1990s. The market trends above did not include the electronics industry, which has become significant.

The opportunity for ultrasound to be used in automated inspection systems, and to offer improved flaw characterization as needed for more stringent fitness for service and code requirements indicates that there should be growth in the design and manufacture of ultrasonic systems.

Initially, ultrasound was mostly used for flaw detection and characterization. Since the ultrasonic wave speeds are elastic constants, ultrasonic applications have evolved into a variety of material characterization processes. In addition to attenuation data indicating stress corrosion cracking (SCC), for example, wave speed measurements are capable of indicating texture and elastic properties in crystalline materials as well as stress in a variety of solids. Hardness and grain size determination are among the capabilities of ultrasonic measurements.

Because of the opportunities in ultrasonic systems engineering, the material to follow is focused on automated and handheld devices and systems. Specific techniques will be discussed only briefly, with some specific industrial applications described dealing with automated inspection, time-of-flight (TOF), and phased arrays as applied to flaw characterization. Data analysis for bond integrity determination as well as pipe, pipelines, and aircraft inspection are included. In general, a discussion of individual, small component inspection has been omitted from this chapter. Examples of such components are automotive crankshafts and engine blocks, flow control valves used in chemical processes, and aircraft clevises and pins. While these items are important NDE subjects, they are not included here.

The reader should note that in-depth presentations of various ultrasonic techniques also have been avoided in this chapter since extensive coverage occurs elsewhere in the volume. For example, Chapter 4 and Chapter 5 discuss guided waves applied to plates and pipes, while Chapter 7 and Chapter 8 cover laser ultrasonics and electromagnetic-acoustic transducers (EMATs). These important topics deserve extensive coverage. Other chapters also may contain information relative to specific industries that are not covered here, and the reader is urged to seek this information from the rest of the book.

3.1 Flaw Sizing Principles and Applications

Flaw sizing historically has been based on amplitude change (i.e., the larger the reflection, the larger the flaw). The tendency of this technique to underestimate the actual flaw size and the lack of good information on material fracture properties led to conservative engineering designs that have a large safety factor. As a result, some American Society Mechanical Engineers (ASME) Boiler and Pressure Vessel Codes allow the manufacture of pressure vessels without inspection. These designs are inefficient, and the modern movement is to develop specifications with better inspection techniques and lower safety factors (Bray, 2003).

Tip diffraction techniques enable the inspector to determine with better accuracy the location of various aspects of cracks, namely the root and tip. This has increased the accuracy in the sizing of flaws and anomalies. Silk and Liddington (1975) reported early results that provided much of the basis for the tip diffraction or time-of-flight diffraction (TOFD) technique. Later descriptions and reviews of this technique are given in a number of sources, including Harumi et al. (1989), Avioli et al. (1991), and Bray and Stanley (1997).

The following description of TOFD is summarized from Bray and Stanley (1997):

> Tip-diffraction techniques utilize the principle that an edge of a crack struck by a wave will radiate (diffract) individual signals to other locations on the surface of the part. With this radiated energy, the tip depth below the surface may be determined for surface breaking flaws, and the depth below opposite surfaces for embedded flaws.

The methods for calculating flaw size (tip locations) for an angled, embedded flaw using TOFD is described as follows for a 45° inclined flaw AB in Figure 3.1. Here, the transverse wave (T) launched by an angle-beam probe approaches the flaw AB, which is also oriented at 45°. Striking the flaw, the transverse wave (T′) is reflected back to the probe, and the crack tips launch circular compressional waves, shown by wavefronts A and B in Figure 3.2.

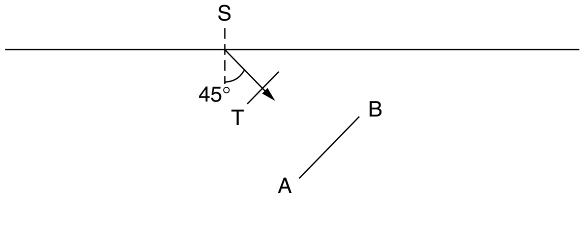

FIGURE 3.1
Incident 45° transverse wave (T) launched from position S toward 45° inclined flaw. (From Bray, D.E. and Stanley, R.K., *Nondestructive Evaluation*, CRC Press, Boca Raton, FL, 1997. With permission.)

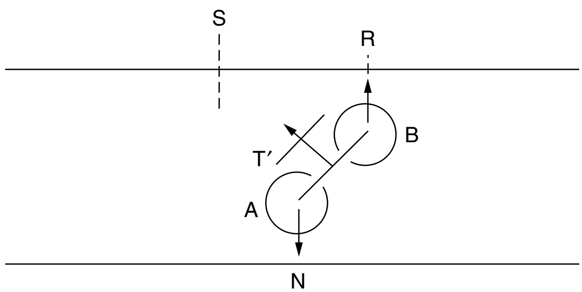

FIGURE 3.2
Compressional waves A and B launched from crack tip along with reflected wave T′. (From Bray, D.E. and Stanley, R.K., *Nondestructive Evaluation*, CRC Press, Boca Raton, FL, 1997. With permission.)

The reflected transverse wave T′ provides an approximate location for the flaw with the reflected pulse S in Figure 3.3. A compressional receiving probe located at R in Figure 3.2 will produce an indication R in Figure 3.3. When displayed on the same screen, the separation of R from S is indicative of the depth of the crack tip below the surface of the part. Modern instrumentation has greatly enhanced the capability of the TOFD systems to accurately predict the locations of crack tips. Error sources for this technique, such as irregular tip shapes and ultrasonic frequency effects are evident. Even with these limitations, the superiority of the technique for flaw sizing led to the implementation of the ASME of Code Case 2235 (1996), allowing its use for the first time in ASME code inspections.

Cowfer and Hedden (1991) have reviewed several of these studies related to inspections for the nuclear power industry. Using a variety of sources, they showed that there is a variation in the probability of detection [P(D)] for ultrasonics, depending on the type of flaw. For example, in the size range less than 25 mm, volumetric defects, slag, and inclusions tend to have a higher P(D) than smooth cracks with sharp edges. For sizing machined notches, the amplitude-based techniques, using 45 and 60° shear wave wedges, showed

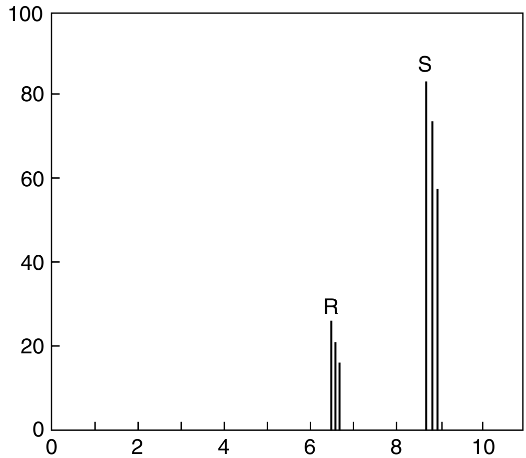

FIGURE 3.3
Composite view of received signals from directly reflected transverse wave at S and diffracted wave from B received at R. (From Bray, D.E. and Stanley, R.K., *Nondestructive Evaluation*, CRC Press, Boca Raton, FL, 1997. With permission.)

poor performance in comparison with the diffraction techniques in the ranging from 0 to 30 mm (0 to 1.2 in.). In the range of 0 to 6 mm in depth (0 to 0.25 in.) none of the techniques showed good performance. Above that threshold, the tip diffraction techniques show a very good correlation with the actual notch depth, while the amplitude-based methods appear to significantly undersize the flaw. While the performance in machined notch studies is not always transferable to actual flaws, comparisons within the test are significant. In the present case, the superior performance of the tip diffraction methods for the larger flaws is notable.

3.2 Phased Array Transducers

Efficient inspection and correct flaw sizing obviously are enhanced with signals obtained from multiple probe locations. The mechanical manipulation of the probe required for obtaining these multiple signals through either handheld or automated means is tedious and time consuming. Another important point is significant probe manipulation may lead to interpretation error since a large number of signals must be diagnosed. An improved means for obtaining multiple signals is through the use of phased array transducers. With this technique, instead of a single probe moved to all of the locations on the part to be inspected, the part may be covered by a single array of very small ultrasonic elements that blanket an area. The scan of the area is conducted with an electronic manipulation of the individual elements.

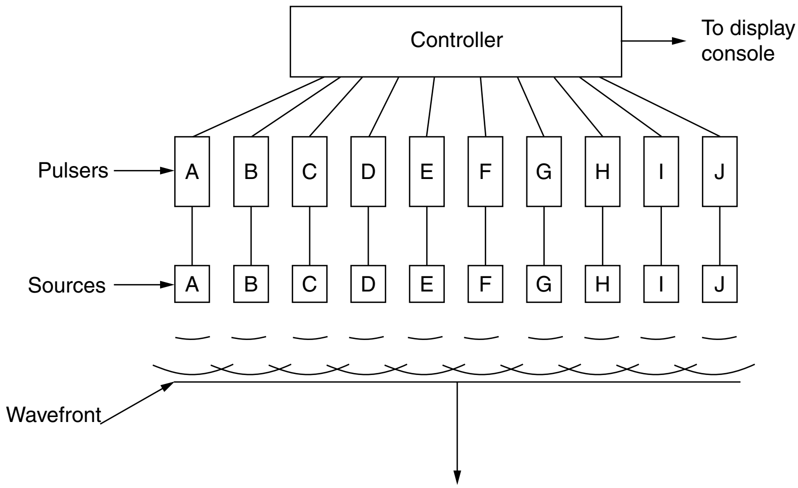

FIGURE 3.4
Phases array multiplexer system. Wavefront for normally incident longitudinal wave shown. (From Bray, D.E. and Stanley, R.K., *Nondestructive Evaluation*, CRC Press, Boca Raton, FL, 1997. With permission.)

Multiplexer circuits used for phased arrays are described in a number of sources, including Singh and Davies (1991) and Bray and Stanley (1997). Moles and Cancre (2001) have reported more recently on the subject of phased arrays, where they show a variety of characteristics such as beam focusing and other manipulations with some examples applied to electric resistance welds in piping and billets.

The following is summarized from Bray and Stanley (1997). Figure 3.4 shows circuits A through J consisting of a separate pulser and transducer. Each probe element is assumed to be a point or very small source, and the firing sequence of the pulsers is controlled through other circuitry. Where each pulser fires simultaneously, a normal wavefront as shown in Figure 3.4 will be generated. Pulsing the probes in phased sequences can create a variety of beam patterns, including angle-beam and focus configurations. For example, the angle-beam pattern shown in Figure 3.5 results when the firing sequence is evenly phased from A through J. The inclination angle (θ) is given by

$$\theta = \sin^{-1} \frac{C\Delta t}{w} \tag{3.1}$$

where

C = phase speed in the material
Δt = phase delay in pulsing each probe
w = probe center-line spacing

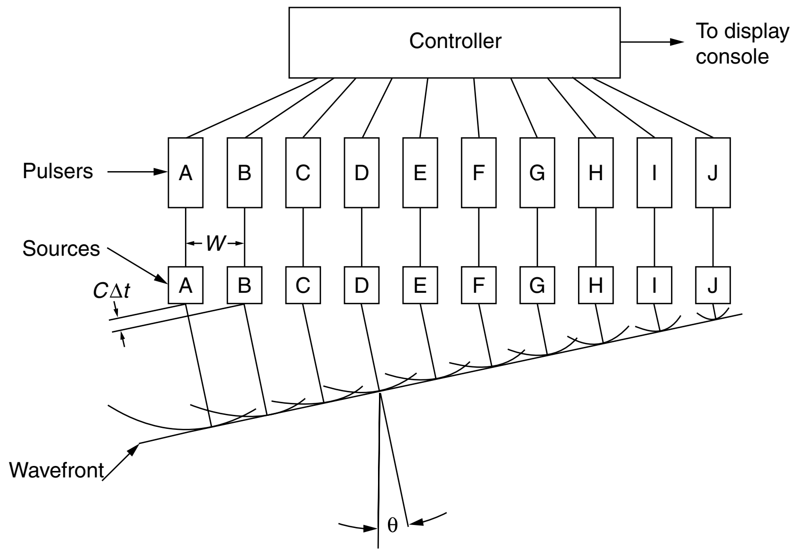

FIGURE 3.5
Inclined wavefront obtained by phased left to right firing sequence of probe elements. (From Bray, D.E. and Stanley, R.K., *Nondestructive Evaluation*, CRC Press, Boca Raton, FL, 1997. With permission.)

Varying the delay between pulses would change the angle. Firing the pulsers in the reverse order, J through A, would result in an angle beam with the opposite orientation. Further, firing from the outside to the inside (i.e., A and J simultaneously, then B and I, etc.) will create a focused beam. Large, phased arrays have great ability to electronically scan considerable areas with the manipulation of the pulsing sequence of the probes.

3.3 Automated Ultrasonic and Hybrid Systems

Industry is keenly interested in automation because of its advantages in inspecting large surfaces or large numbers of parts and its good repeatability of results. Generally, handheld manual inspection and a good operator are capable of finding defects smaller than those found by automated systems. Automated systems, on the other hand, will usually perform very reliably at an established sensitivity level. The overall benefit of automated systems is that more inspection may be performed with time, reducing the number of defective parts and systems placed into service. Requirements for automation are summarized in Table 3.2.

In addition to fully ultrasonic systems, many applications are using hybrid systems that combine two or more techniques. For example, magnetic flux

TABLE 3.2

Ultrasonic Characteristics Affecting Automation

Requirement	Comment
Probe size	Both small and large sizes possible; small size is more maneuverable, but requires more manipulation to cover an area; small size gives better resolution.
Probe manipulation	Ability to miniaturize probes gives small sizes, which are better for high speed manipulation.
Couplant	Typical grease, gel, or water couplants can be a problem where high speed is needed; noncontact methods such as EMAT and laser techniques offer benefits, but have seen only limited field or shop use.
Data capture and analysis	Digitization of data is well developed for ultrasonics; fully digitized ultrasonic systems have existed for some time; specific arrival information as well as complete signals can be transferred to a computer for analysis.

leakage may be used to find corrosion areas in pipe and plate, and automated ultrasonic may be used to characterize the corrosion. Additionally, automated full-system aircraft inspection may involve both low-frequency acoustic excitation and laser sensors. The examples discussed below will include hybrid as well as fully ultrasonic systems.

3.3.1 Automated, Phased Array Inspections of Aerospace Structures

Due to the overwhelming use of composites by the aerospace industry, there is considerable inspection activity for these materials. The capability of phased array systems to interrogate large areas is appealing to this application. Further, the software-controlled manipulation of the phased array elements enables improved characterization of the defects.

Smith, et al. (1999) report the development of 9 element and 17 element arrays applied to inspecting aircraft composite structures. Pulse frequencies from 12 to 20 MHz were used in a 128-mm-long multielement array of 5×2 mm elements.

Composite tanks are very amenable to automated inspection due to their regular shape. Whittle et al. (2000) present a fully automated system for composite rocket motor cases. The structure is a filament wound carbon fiber motor case. The initial step in the manufacture is for thermally insulating rubber to be laid onto the mandrel and vulcanized. The carbon fiber is overlayed on the rubber and cured. The result is a highly attenuating inner layer and a fiber structure on the outside. The case is a cylinder 2×4 m. Delaminations and voids as well as bonding integrity are the concerns in the inspection. The case is fitted into a sturdy manipulator and robot arms with pulse-echo (PE) sensors scanning both the inside and outside of the tank. Thickness also is measured. The domes are not inspected automatically because of the interweaving fibers and excess resin in that region.

The inspection scheme first established zones that were affected by the local geometry. Each had specific test requirements. The same manipulator was used for inside and outside the case, being withdrawn and replaced for the proper application.

Fifteen probes for the cylindrical section in array format and with a multichannel flaw detector reduce the inspection time. From the inside, 0° compressional wave delay line probes were developed. A 2-MHz source frequency was used with a 1-MHz filter to give superior thickness measurement for inside measurements. Outside, 5-MHz immersion probes were used. Thickness measurement accuracy of better than 0.5 mm was achieved. Thicknesses for the carbon fibers ranged from 4.2 to 18 mm and the thermal protection insulating rubber was from 2 to 45 mm. Thickness accuracies of 0.1 and 0.15 mm were achieved for the fiber and thermal layers, respectively. Typically, the target size for defect detection was 8×8 mm. Once the manipulators were in place and the automatic datuming sequence completed by the software, the inspections were executed under complete software control.

3.3.2 Automated, Hybrid Aircraft Inspection Systems

Full-body aircraft inspection is a highly desired objective of the airline industry. One such system using a low frequency acoustic source and a laser vibrometer is reported to be able to perform a full-body inspection of business and commercial aircrafts (Morris, 2002). Reports show that the system can detect cracks, corrosion, disbanding, and delaminations in a single, 10- to 12-h robotic inspection. The system can penetrate 300 mm into the aircraft structure.

3.4 Automated Ultrasonic Pipeline Inspection Systems

Pipeline inspection is uniquely challenging. Since pipe is a round, uniform shape, the initial idea is that it should be easy to inspect. They are usually buried, limiting access to the outside surface. Further, many defects occur inside the pipe, which is not easily accessible. Where in-line inspection tools, or pigs, are used for the inspection, there is limited input to the system once the pig is launched; there is also limited chance for data retrieval during the test. Finally, there are great differences in pipe diameter, joints, curves, and turns that create a complex collection of shapes and circumstances. To respond to these challenges, the pipeline industry has developed very effective inspection systems, using ultrasound and other techniques such as magnetics and radiography.

Ultrasound has been an effective NDE tool for pipelines. Conditions evaluated or detected with ultrasound include corrosion, usually at the bottom of the pipe; SCC; and weld defects. Other anomalies also exist, such as dents and gouges from the outside. These may go unnoticed and then be the source of cracking.

One description of an ultrasonic inspection tool is given by Katz et al. (2002). The tested pig was developed for pipelines 0.61 m (24 in.) or greater, but was modified for testing a 0.41-m (16-in.) pipe. Wall thickness for the inspected pipe was 6.35 mm (0.25 in.). The in-line inspection tool uses 45° shear waves. Oil or water as the transmission medium also serves as the couplant. The rate of batch flow controlled the inspection speed within ±1 m/sec. Data were collected over a 27-km (17-mi) length of pipe with an 80 m elevation change. The line tested had seen earlier failures due to longitudinal SCC. Redundancy in the system enables each defect to be seen by six different sensors on the inspection tool.

The data were reported in B and C scan in two groups. The first group showed features exceeding 80 mm in length and 2 mm in depth, and the second showed features over 50 mm in length and 1 mm in depth. The C-scan results showed good correlation with found SCC defects. One found crack field was 1.1 m in length with intermittent occurrence of cracking from 12.5 to 25% of the wall thickness. Another field was 220 mm in length at the same depth range. Excavation and photomicrography revealed the features of the cracks, which coincided with the ultrasonic results.

3.4.1 Comparison of Ultrasonic and Magnetic Pipeline Inspection Systems

Ultrasonics and magnetics have been used in hybrid pipeline inspection pigs. Where liquid couplant is not easily available, as in gas pipelines, ultrasonics requires that the pig contain a separate couplant supply that must be released on demand. Often these gas pipeline ultrasonic units have the probes in liquid-filled wheels, but a small amount of couplant is still required at the contact surface. Magnetics, on the other hand, can operate freely in a gas environment. In some cases, magnetics can be used to locate suspect areas, while ultrasonics can be used to define the problem.

Wilkie et al. (2002) report a comparison of the performance of ultrasonic and magnetic in-line inspection tools. The tests were on a 864-mm (34-in.) line from Canada's Enbridge Pipelines, Inc. Two ultrasonic pigs were tested, one with 96 sensors mounted in liquid-filled wheels and another with 480 sensors on an offset sensor skid exciting 45° shear waves and 32 sensors exciting longitudinal waves. In the offset sensor skid, signals are transmitted in both clockwise and counterclockwise directions. The specifications for the 96-sensor pig were that it could detect flaws 75 mm (3 in.) in length or longer and detect wall thickness (t) from 0.2 to 0.25 t or greater. Inspection speed was 3 m/sec (6.7 mi/h) in liquid and 8 m/sec (17.8 mi/h) in gas. Two 2-MHz sensors were used. For the 480 sensor pig, the minimum length of defect detectable was 30 mm (1.2 in.) at 1 m/sec speed and 60 mm (2.2 in.) at 2 m/sec.

The minimum depth detectable was given to be 1 mm. The magnetic tool excited a flux field in the circumferential direction. Specifications for the magnetic tool were a minimum detection depth of 0.25 t for flaws over 50 mm in length, and 0.5 t for flaws ranging from 25 to 50 mm. Because of the significant difference in the type and configuration of each pig, there would be some expected differences in the performance.

Defects expected were cracks in welds and in the wall as well as metal loss. Data were collected on board the pig and presented in C scan upon analysis. The relative position of each defect was reported.

The overall results for the pig with 480 sensors were more detailed than those for the 96-probe pig, and the ultrasonic results were more detailed than those obtained with the magnetics pig. The magnetics pig was more economical to run, and there were circumstances where the investigators felt that it was a better choice than the more expensive ultrasonic pig.

3.5 Pipe Inspection in Chemical and Petroleum Processing Plants

Pipe inspection in processing plants is in some ways easier than inspecting buried pipelines. The obvious reason is that the processing pipes are above ground and may be more accessible. They might also be inspected from the outside and not have the restriction of internal pig inspection. There are complications that render these inspections difficult in cases where the pipes are nested in piping groups or are covered with insulating material.

Inspection of single-pipe sections before welding into long lengths is the simplest inspection since each section can be inspected in an automated environment at a pipe inspection plant. Typically, pipe inspection involves angle beam shear wave probes and normal beam longitudinal probes in a configuration where the pipe and probe system rotate and move longitudinally relative to each other. Because of the added flexibility and efficiency, phased arrays are often used in inspecting pipe. More advanced schemes using guided waves for pipe inspection are included in this volume, and their descriptions will not be repeated here.

Clusters of pipe or tube in boiler heat exchangers are among the most difficult arrangements to inspect. The outer sections can be scanned by ultrasound and eddy current. The inner-nested sections are much more difficult to reach. Often these are inspected by automated systems that snake or crawl through the length of the pipe or tube.

Since both the angle beam and guided wave techniques depend on Snell's law of refraction, there is a need for characterizing the ultrasonic properties of advanced materials used for pipe. Ginzel and Ginzel (1995) report ultrasonic wave speed measurements in a variety of large-diameter pipes. They showed wave speeds in several directions in a collection of 11 pipes ranging

TABLE 3.3

Wave Speeds Measure in 11 Pipe Samples

Wave	Speed (m/sec)	Standard Deviation
Longitudinal in longitudinal pipe direction	5914	21.5
Longitudinal in circumferential direction	5931	63.5
Shear (SV) at 60° beam orientation to vertical	3273	46
Shear oriented radially	3293	57

Source: Adapted from Ginzel, E.A. and Ginzel, R.K., *Mater. Evaluation*, 53, 598–603, 1995.

in diameter from 42 to 48 in. (1067 to 1219 mm) and in thickness from 0.374 to 0.7 in. (9.5 to 17.8 mm) (Table 3.3). Four measurements were made on each pipe. The longitudinal wave speeds traveling in the longitudinal pipe direction averaged 5,914 m/sec, (232,834 in./sec) and the standard deviation was 21.5 m/sec (846 in/sec). Circumferential longitudinal wave speeds averaged 5931 m/sec (233,500 in./sec) with a standard deviation of 63.5 m/sec (2,500 in./sec). For shear (SV) waves at 60° (selected to simulate the refracted shear wave commonly used in angle beam inspection) the speeds averaged 3,273 m/sec (128,858 in./sec) with standard deviation of 46 m/sec (1,811 in./sec). For radially oriented SV waves, the speeds were 3,293 m/sec (129,645 in./sec) with a standard deviation of 57 m/sec (2,300 in./sec). In optimizing angle beams as well as guided waves, these variations will need to be considered.

3.6 Bond Inspection for Automobile and Aerospace Industries

Advanced production techniques in the automobile and aerospace industries are increasingly using some form of adhesive diffusion or solid-state bonding in place of rivets or welding. A proper bond can give a strong durable connection, but, like any joint it is susceptible to defects in the production. These defects affect the strength. A good solution to the problem of assessing bond integrity has been elusive, since a weak bond may have enough contact to transmit a moderately strong ultrasonic wave.

Ultrasonic signal analysis techniques have been presented as a method for assessing the bond quality of joints of dissimilar metals by Thomas and Chinn (1999). The reported work assembled a collection of diffusion bonded copper and aluminum for ultrasonic assessment. The quality of bond for the samples was affected in the experiment by temperature, surface preparation, and bonding time. PE ultrasonics was used from both the aluminum and copper sides, and the spectrum of the reflected signal was studied. Broadband transducers of 15 MHz were used. The findings showed that increased bond strength had a lower spectra value for reflected signals.

Acoustic resonance techniques have been applied by Allin et al. (2002) for evaluating bond strength for structural adhesives used in the automobile industry. Models for mode shapes were first produced for various bonded joints. Testing of the joint was performed over a mode 1 frequency range from 0 to 1.6 MHz for this model. For 2 mm aluminum adherends, predicted and measured bond strength showed very good correlation.

3.7 Ultrasonic Flaw Sizing, Fracture Mechanics, and Inspection Codes

Inspection codes have played an important role in assuring safe operation of engineering systems and components in industry. The ASME Boiler and Pressure Vessel Codes are used the world over for construction of pressure components. Much of the code is based on radiographic inspection techniques, not the newer ultrasonics tip diffraction or TOFD flaw sizing methods. Further, the time efficiencies of phase array technology are not being realized by these codes. The result often is inefficient designs, where more material is used in the construction without contributing to the safe operation of the system or component (Bray, 2003). Industries are pressing for improvement in the code that will enable adoption of these later ultrasonic techniques.

Both Moles et al. (2002a) and Cowfer and Hedden (1991) have reviewed the advantages of adopting TOFD in the ASME code and have shown comparison results indicating the superior ability of TOFD to size flaws. Recent sizing studies reviewed by these authors indicate that traditional amplitude techniques will typically undersize a defect. The codes compensate for this by specifying higher factors of safety, leading to overdesign. A more precise flaw estimation will enable more efficient engineering designs.

It is well known that repetition of inspection improves the probability of detection (POD). Phased arrays enable multiple approaches to a flaw, with fewer probe placements required. The software and electronic manipulation of the elements in the arrays enables welds and other areas to be scanned more effectively in order to increase this POD.

Moles et al. (2002b) have discussed the application of phased arrays to weld inspection, including pipeline girth welds. Figure 3.6 shows the single placement of sending and receiving probes for TOFD characterization of a weld defect. In this case, high-angle longitudinal wave probes are used. The earliest arrival at the receiver will be the lateral wave, which establishes an initial benchmark in the arrival pattern, since all other arrivals will be after this lateral wave arrives. Next will be the backwall reflection, which provides the longest travel path and the latest arrival in the pattern. Arrivals from the crack tips will then arrive between the lateral and backwall reflected signals. The arrival times of the diffracted waves are used in sizing the defects.

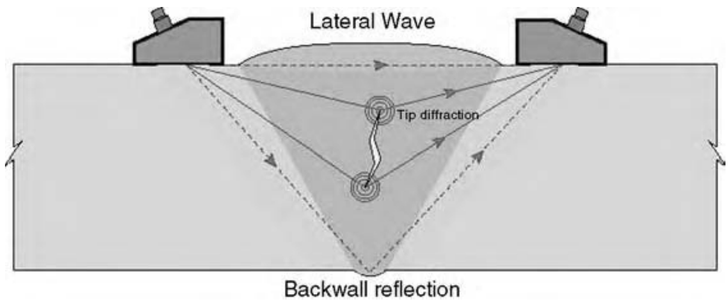

FIGURE 3.6
Send and receive transducers for tip diffraction flaw sizing. (From R/D Tech. With permission.)

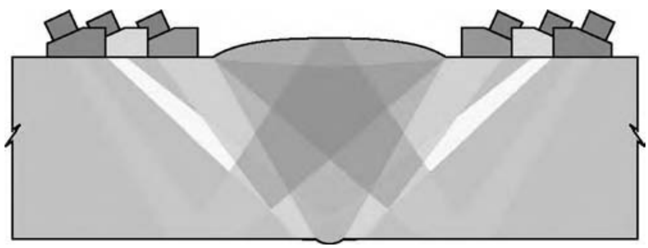

FIGURE 3.7
Probe arrangement for phased array scanning of weld. Outer probes are PE and the inner two are TOFD. (From R/D Tech. With permission.)

This is the scanning process that is done manually. The beam patterns for a combined PE and TOFD inspection of a weld are shown in Figure 3.7. Here the outer two probes are performing the PE inspection and the inner pair is for TOFD defect characterization. Clearly, with phased array technology, the various inspections may be performed with a single placement, by electronically manipulating the beam.

For weld inspection, devices as shown in Figure 3.8 that may be used to move the phased array assembly along the weld length are along the vertical axis. A typical interpretive display of the results is shown in Figure 3.9, where the weld length is vertical in the results illustration. The PE results are shown in the two outer displays, and the TOFD results are shown in the center. For the PE display, dark areas indicate echoes where the amplitude is above a preset threshold. For the TOFD display, the vertical dark line on the left is the similarly defined lateral wave, and the pair of vertical dark lines to the right is the same for the backwall echo. The dark images represent the pulse peak for each A-scan display, and the full image shown here is a summary of all of the A-scan displays of the inspection. The fan or shell shapes between the lateral wave and the backwall echo are associated with diffraction occurring between the lateral wave arrival and the backwall echo. One of the unique capabilities of phased array systems is the ability to scan for wave speeds and adjust the probes for optimum angle beam performance.

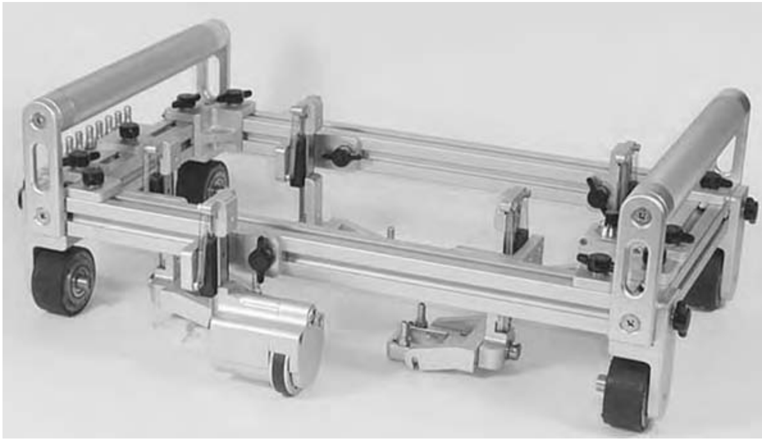

FIGURE 3.8
Carriage for scanning welds with phased array systems. (From R/D Tech. With permission.)

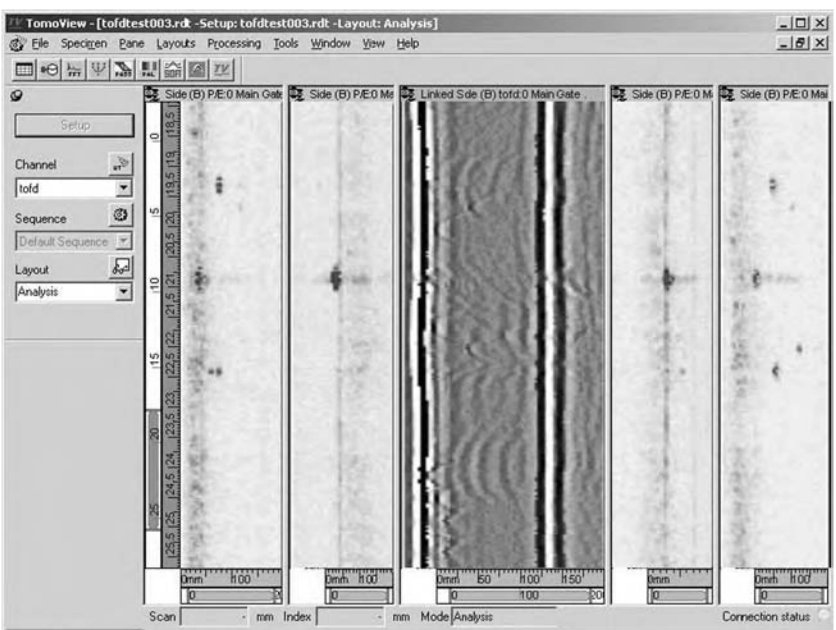

FIGURE 3.9
Scan results for weld. Outer areas are for PE tests and the inner are for TOFD. (From R/D Tech. With permission.)

3.8 Inspection with Airborne Ultrasonic Beams

Airborne ultrasonics has been applied in some cases to overcome the problem of liquid couplant. Generally, the problems of acoustic impedance mismatch between air (low impedance) and any solid (high impedance) severely restrict the energy transfer for this method. Further, the Snell's law of relationships for transfer between materials with severely different wave speeds requires high precision for the holding mechanism. Frequencies for airborne ultrasound may be around 50 kHz. The low frequencies used typically create long wavelengths and somewhat large sizes for minimum flaw discrimination. These problems have been resolved in some applications, allowing for useful inspection (Curlin Air Tech Note, 1998). Items typically inspected using airborne ultrasound include composites, urethane foam products, fiberglass, construction materials, honeycomb structures, and tires.

3.9 Liquid Content Determination in Tanks

Ultrasonics has been applied by Diaz of Pacific Northwest Laboratories (PNNL) to provide noninvasive container interrogation and material inspection capabilities (*Popular Mechanics*, 2002; Diaz, 2002). The convenient, portable handheld acoustic inspection device (AID) is shown in Figure 3.10. It was initially designed and fielded for noninvasive examination and identification of chemical warfare agents in munitions, and has been deployed worldwide in limited quantities over the past few years. The device is integrated with a palm-sized computer. The impedance differences of various known fluids and tank materials are stored in memory, and the echo characteristics at the interfaces are used to identify the contents.

Ultrasonic pulses easily penetrate dense materials, including liquids, which often defeat x-ray inspection methods. The return echoes from the injected ultrasonic pulses are analyzed in terms of TOF and amplitude decay to extract physical property measurements of the material in the container. These two parameters are used to sort and identify specific components in a sealed container. The device also measures ultrasonic velocity and attenuation to rapidly and reliably screen the contents of sealed containers and bulk-solid materials, augmenting on-site material interrogation efforts that use the expensive and time-consuming processes of direct sampling and laboratory analysis. The technique governing how the AID functions involves measurements of ultrasonic pulses in the range of 0.1 to 5 MHz that are launched into a container. The return echoes from these pulses are analyzed in terms of TOF and amplitude decay to extract physical property measurements of the material in the container. The handheld, battery-operated AID system performs an automated analysis of the return echoes to detect contraband and other

FIGURE 3.10
Acoustic inspection device for interrogating container contents. (From Pacific Northwest Laboratories. With permission.)

materials in submerged packages and concealed compartments in liquid-filled containers and solid-form materials. An inspector can quickly interrogate outwardly innocuous commodity items such as shipping barrels, tanker trucks, and metal ingots. Using two interchangeable ultrasonic sensor heads, containers interrogated can range in size from approximately 154 mm (6 in.) to over 2.4 m (96 in.) in diameter.

3.10 Residual Stress Measurement

Unfavorable residual stresses can lead to unexpected crack propagation due to a crack tip entering a tensile stress field and the warpage of parts in manufacture. Nondestructive measurement of these stresses has been a pressing need for industry for a number of years. In fact, an inability to measure these stresses is part of the justification for the conservative flaw sizing and design codes for the ASME Boiler and Pressure Vessel Code.

Reviews of ultrasonic stress measurement have been given by Thompson et al. (1996). Of the various physical principles used presently for stress measurement, ultrasonics has some unique characteristics. First, the ultrasonic wave can fully traverse a part, giving the capability to measure stresses throughout the cross section of the item. Second, ultrasonic waves are available in a variety of propagation paths and particle motions and frequencies.

The waves may propagate at the surface, near to the surface, and in the bulk, giving the possibility of gradient measurement. Bray and Tang (2001) have presented results using the L_{CR} technique for gradient measurement.

Several papers on ultrasonic residual stress measurement were presented at the 2001 ASME convention in Atlanta. Bray (2002) reported on data taken with the critically refracted longitudinal (LCR)-wave on pressure induced stress in a pressure vessel, as well as weld induced stresses in the same vessel. Miyasaka et al. (2002) reported on characterizing stress at a ceramic/metal interface using scanning acoustic microscopy. Chance and Bray (2001) described work on stress relaxation in welded steel plates. Walaszek et al. (2002) described the effect of microstructure on ultrasonic stress measurements, and dos Santos and Bray (2002) compared the acoustoelastic methods used to evaluate stresses. While each of these papers reports success in the various techniques, work still remains in building a database so that results obtained from a variety of materials can be correctly interpreted.

3.11 Summary

Global industry is focusing on more efficient designs with well-defined life expectancies. These requirements are demanding that NDE in general, and ultrasonics in particular, be able to deliver efficient inspection with repeatable and precise results. There is ample opportunity for growth in ultrasonics, even in an environment where industrial growth may not be significant.

For this next generation of ultrasonic NDE, much of the systems engineering may be transferable from system to system. For example, the technology developed for the overall inspection of full-sized aircrafts may be transferable to the inspection of polymer and composite tanks or vice versa. Further, the data handling and analysis used in phased array technology should be fitted to a number of inspections. Ultrasonic material analysis and stress measurement should further improve the confidence in engineering designs.

Ultrasonics is a high-tech field, and suitable education and training are required to take full advantages of the capabilities that it offers.

References

Allin, J.M., Cawley, P., and Lowe, M.J.S., A robust technique for disbond detection in the automotive industry, *Rev. Quant. Nondestructive Evaluation*, 21, 1172–1179, 2002.

American Society of Mechanical Engineers, Boiler and Pressure Vessels Code, Section VIII, Code Case 2235, New York, 1996.

Avioli, M. et al., Ultrasonic testing applications in utilities, Vol. 7, Sec. 17, Ultrasonic Testing, *Nondestructive Testing Handbook*, McIntire, P.E., Sec. Ed., American Society for Nondestructive Testing, Columbus, OH, 1991, pp. 570–591.

Bray, D.E., ASME in the Global Pressure Equipment Arena, 10° Congresso Nazionale dell'AIPnD, Conferenza Nazionale sulle, Prove non Distruttive Monitoraggio Diagnoistica, (10th Congress on Nondestructive Testing, Italian Society for NDT), Ravenna, Italy, Apr. 2–4, 2003, http://www.asme.org/groups/materialsandstructures/ravennaitalydbray1.pdf.

Bray, D.E., Ultrasonic stress measurement and material characterization in pressure vessels, piping and welds, *Trans. ASME, J. Pressure Vessel Tech.*, 124, 326–335, 2002.

Bray, D.E. and Stanley, R.K., *Nondestructive Evaluation*, CRC Press, Boca Raton, FL, 1997.

Bray, D.E. and Tang, W., Subsurface stress evaluation in steel plates and bars using the L_{CR} ultrasonic wave, *Nucl. Eng. Design*, 207, 231–240, 2001.

Chance, B.H. and Bray, D.E., Nondestructive monitoring of stress relaxation in welded steel plates, *Trans. ASME, J. Pressure Vessel Tech.*, 124, 343–348, 2002.

Cowfer, C.D. and Hedden, O.F., Overview of the ASME Section XI Code Relating to NDE and ultrasonic examination performance demonstration, *Trans. ASME, J. Pressure Vessel Tech.*, 113, 170–179, 1991.

Curlin Air Tech Note, Nondestructively inspect material integrity with an airborne ultrasonic beam, NDT.net, 3, 1998.

Diaz, A., personal communication, 2002.

Ginzel, E.A. and Ginzel, R.K., Study of acoustic velocity variations in line pipe steel, *Mater. Evaluation*, 53, 598–603, 1995.

Harumi, K., Ogura, Y., and Uchida, M., Eds. *Ultrasonic Defect Sizing*, Japanese Society for Non-Destructive Inspection, Tokyo, 1989.

Katz, D.C., Rú́hle, U., and Wolfe, T., 16 inch Williams Gas pipeline inspected for SCC using PII's new ultrasonic tool, Paper No. IPC2002-27005, *Proc. IPC'02, 4th Int. Pipeline Conf.*, Calgary, Alberta, Canada, Sep. 29–Oct. 3, 2002.

Miyasaka, C., Tittmann, B., and Tanaka, S-I., Characterization of stress at a ceramic/metal jointed interface by the V(z) technique of scanning acoustic microscopy, *Trans. ASME, J. Pressure Vessel Tech.*, 124, 336–342, 2002.

Moles, M.D.C., Ginzel, E., and Dubé, N., Quantitative NDT and fitness for purpose, PVP-Vol.450/NDE-Vol-22, *NDE Eng.: Applications, Proc. 2002 Pressure Vessels Piping Conf.*, Vancouver, B.C., Paper PVP2002-1628, 2002a, pp. 5–10.

Moles, M., Dubé, N., and Ginzel, E., Pipeline girth weld inspections using ultrasonic phased arrays, Paper No. IPC2002-27393, *Proc. IPC'02, 4th Int. Pipeline Conf.*, Calgary, Alberta, Canada, Sep. 29–Oct 3, 2002.

Moles, M. and Cancre, F., Element parameters for ultrasonic phased arrays, *Rev. Quantitative Nondestructive Evaluation*, Thompson, D.O. and Chementi, D., Eds., AIP Conf. Proc., 615, American Institute of Physics, Melville, NY, 2001, pp. 855–860.

Morris, J., Honeywell develops 'cat scan' inspection for business jets, *Aviation Week Space Technol.*, Nov. 18, 2002, p. 70.

dos Santos, A. and Bray, D.E., Comparison of acoustoelastic methods to evaluate stresses in steel plates and bars, *Trans. ASME, J. Pressure Vessel Tech.*, 124, 354–358, 2002.

Silk, M.G. and Lidington, B.H., The potential of diffracted ultrasound in the determination of crack depth, *Nondestructive Testing*, 8, pp. 146–151, 1975.

Singh, G.P., and Davies, J.W., Multiple transducer ultrasonic techniques, Vol. 7, Sec. 9, Ultrasonic Testing, *Nondestructive Testing Handbook*, McIntire, P.E., Sec. Ed., American Society for Nondestructive Testing, Columbus, OH, 1991, pp. 269–309.

Smith, R.A., Willsher, S., and Bending, J., Linear-array systems for aerospace NDE, *Nondestructive Characterization of Materials IX*, Green, R.E., Jr., Ed., American Institute of Physics, AIP Conf. Proc. 497, Melville, NY, 1999, pp. 502–509.

Sounding out hiding places, *Popular Mechanics*, Nov. 2002, p. 24.

Thomas, G. and Chinn, D., Signal analysis approach to ultrasonic evaluation of diffusion bond quality, *Nondestructive Characterization of Materials IX*, Green, R.E., Jr., Ed., AIP Proc., Sydney, Australia, American Institute of Physics, Melville, NY, 1999, pp. 536–542.

Thompson, R.B., Lu, W.-Y., and Clark, A.V., Jr., Ultrasonic methods, *Handbook of Measurement of Residual Stresses*, Lu, J., James, M., and Roy, G., Eds., Society for Experimental Stress Analysis, Bethel, CT, 1996, chap. 7, pp. 149–178.

Walaszek, H., Lieurade, H.P., Peyrac, C., Hoblos, J., and Rivenez, J., Potentialities of ultrasonics for evaluating residual stresses: influences of microstructure, *Trans. ASME, J. Pressure Vessel Tech.*, 124, 3349–3353, 2002.

Wells, C.D., The commercial role of NDT in the context of a changing world, *Insight*, 36, 1994.

Whittle, A.C. and Gatta, A., Automated high integrity ultrasonic examination of composite rocket motor cases, World Conf. NDT, Rome, Italy 2000, http://www.ndt.net/article/wcndt00/papers/ind082.htm.

Wilkie, G.H., Elm, T.J., and Engen, D.L., Enbridge comparison of crack detection in-line inspection tools, Paper No. IPC2002-27307, *Proc. IPC'02, 4th Int. Pipeline Conf.*, Calgary, Alberta, Canada, Sep. 29–Oct 3, 2002.

4

Guided Waves for Plate Inspection

Tribikram Kundu

CONTENTS

0-8493-1462-3/02/$0.00+$1.50

In recent years Lamb waves have been successfully used for detecting defects in plate type structures such as composite plates, metal plates, and concrete slabs. This chapter gives the theoretical background for such inspection, lists advantages of the guided wave inspection technique over conventional ultrasonic techniques, and presents experimental results for a number of plate specimens. Recent developments by the author and other investigators on the plate inspection technique, which uses guided waves, are also presented here.

4.1 Guided Waves and Waveguides

An elastic wave that propagates through a waveguide is called a *guided wave*. A waveguide is a structure with boundaries that help elastic waves to propagate from one point to another. An elastic full space cannot be considered as a waveguide because it does not have any boundary, but an elastic half space with a stress-free boundary can act as a waveguide if the elastic wave propagates along the boundary. The stress-free boundary can help elastic waves to propagate from one point of the boundary to another point (see Chapter 1, Section 1.2.9). The guided wave, propagating along the stress-free boundary of an elastic half-space, is called the Rayleigh wave. A single-layered half-space can be a waveguide for Love waves (antiplane motions, Chapter 1, Section 1.2.10) or Rayleigh waves, also known as generalized Rayleigh-Lamb waves (in-plane motions, Chapter 1, Section 1.2.11). Waveguides can be of any shape or size. Common types of waveguides are plates, pipes, cylindrical rods (solid or hollow), and bars (of rectangular cross sections or other geometric shapes). Even though the cross section of a waveguide often remains constant, independent of the axial distance from its end, it can also be a function of the position. Figure 4.1 shows different types of waveguides: (a) plate; (b–d) bars with rectangular, circular, and I cross-section; (e–f) rods with varying cross sections. In some of these waveguides the elastic wave can easily propagate, while in other cases the propagating guided waves decay fast.

The *Lamb wave* is the *guided wave* that propagates in a plate as shown in Figure 4.1(a). The two traction-free boundary surfaces of the plate help the Lamb wave modes to propagate. A Lamb wave, observed in a plate, is also known as the *plate wave*. Similarly, a guided wave propagating through a

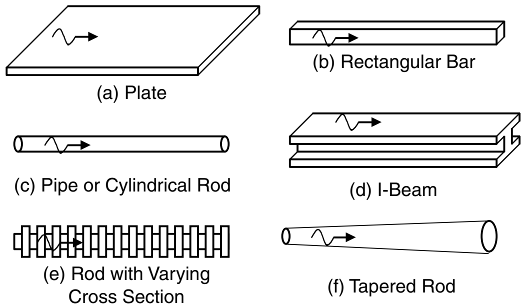

FIGURE 4.1
Different waveguides.

rectangular or cylindrical rod is known as a *rod wave*, and guided waves in a pipe or cylindrical rod are known as *cylindrical guided waves*. All these guided waves have one thing in common; they propagate through a waveguide satisfying the stress-free boundary conditions of the waveguide. Rayleigh (1885) and Lamb (1917) first solved the guided wave propagation problems in an elastic half-space and elastic plate, respectively. Guided waves in these two waveguides are named after them. One big difference between these two guided waves is that the Rayleigh wave speed in an elastic half-space is nondispersive, meaning it is independent of the frequency (see Chapter 1, Section 1.2.9). The Lamb wave speed is dispersive, or dependent on the frequency (see Chapter 1, Section 1.2.12). Another difference is that at a given frequency a Rayleigh wave in a half-space can propagate with only one speed while the Lamb wave can propagate with multiple speeds. Different plate wave modes, associated with various types of particle motion in the plate (see Chapter 1, Figure 1.28), propagate with different wave speeds at the same frequency (see Chapter 1, Figure 1.27 and Figure 1.31). Like Lamb waves, the guided waves through a rectangular bar or a cylindrical rod also show multiple mode characteristics, and the wave speeds for these modes are generally dispersive. Because of these similarities, sometimes the guided waves propagating through a pipe, a rectangular plate of finite width, or a rectangular bar are also called Lamb waves. Strictly speaking, those waves are not Lamb waves and should be identified as guided waves and not Lamb waves.

4.1.1 Lamb Waves and Leaky Lamb Waves

When the plate is immersed in a liquid, the surfaces at the liquid-solid interface are not traction free and the energy of the propagating wave leaks into the surrounding liquid; the propagating wave is called the *leaky Lamb wave (LLW)*. Strictly speaking, Lamb waves without any leaky energy are observed only in a plate in vacuum. When the plate is immersed in air, Lamb waves propagating in the plate leak energy into the air; a propagating wave in a plate immersed in air is therefore also a leaky Lamb wave. Since the intensity of the energy, leaking into the surrounding air, is very small, it is generally ignored and the wave is not called a leaky Lamb wave when the plate is in the air. For a plate immersed in a liquid the intensity of energy leaking into the surrounding liquid is not negligible and should not be ignored.

4.2 Basic Equations — Homogeneous Elastic Plate in Vacuum

Fundamental equations of the Lamb wave propagation in a solid plate have been derived in Chapter 1, Section 1.2.12.2. Those equations are briefly reviewed here. For a linear, elastic, isotropic plate of thickness 2*h* (see Chapter 1, Figure 1.29) the phase velocity dispersion curves are obtained by solving the following dispersion equations (see Chapter 1, Equation 1.170a and Equation 1.170b):

$$\frac{\tanh(\eta h)}{\tanh(\beta h)} = \frac{\left(2k^2 - k_S^2\right)^2}{4k^2\eta\beta} \tag{4.1a}$$

$$\frac{\tanh(\eta h)}{\tanh(\beta h)} = \frac{4k^2\eta\beta}{\left(2k^2 - k_S^2\right)^2} \tag{4.1b}$$

Equation 4.1a and Equation 4.1b give phase velocity dispersion curves for symmetric and antisymmetric modes, respectively. In the above equations,

$$\begin{aligned}
k &= \frac{\omega}{c_L} \\
\eta &= \sqrt{k^2 - k_P^2} \\
\beta &= \sqrt{k^2 - k_S^2} \\
k_P &= \frac{\omega}{c_P} \\
k_S &= \frac{\omega}{c_S}
\end{aligned} \tag{4.2}$$

where, c_L is the Lamb wave speed (phase velocity), c_P is the primary wave (P-wave) speed, and c_S is the secondary wave (S-wave) speed of the plate material. ω is the circular frequency (rad/sec, $\omega = 2\pi f$) of the propagating wave.

The potential field, displacement field, and stress field for the symmetric and antisymmetric Lamb modes can be obtained from Chapter 1, Equation 1.167 and Equation 1.168,
Symmetric modes:

$$\begin{aligned} \phi &= B\cosh(\eta x_2)e^{ikx_1} \\ \psi &= C\sinh(\beta x_2)e^{ikx_1} \end{aligned} \tag{4.3}$$

$$\begin{aligned} u_1 &= \phi_{,1} + \psi_{,2} = \{ikB\cosh(\eta x_2) + \beta C\cosh(\beta x_2)\}e^{ikx_1} \\ u_2 &= \phi_{,2} - \psi_{,1} = \{\eta B\sinh(\eta x_2) - ikC\sinh(\beta x_2)\}e^{ikx_1} \end{aligned} \tag{4.4}$$

$$\begin{aligned} \sigma_{22} &= -\mu\left\{k_S^2\phi + 2(\psi_{,12} + \phi_{,11})\right\} = -\mu\left\{\left(k_S^2 - 2k^2\right)B\cosh(\eta x_2) + 2ik\beta C\cosh(\beta x_2)\right\}e^{ikx_1} \\ \sigma_{12} &= \mu\{2\phi_{,12} + \psi_{,22} - \psi_{,11}\} = \mu\{(2ik\eta)B\sinh(\eta x_2) + (k^2 + \beta^2)C\sinh(\beta x_2)\}e^{ikx_1} \end{aligned} \tag{4.5}$$

Antisymmetric modes:

$$\begin{aligned} \phi &= A\sinh(\eta x_2)e^{ikx_1} \\ \psi &= D\cosh(\beta x_2)e^{ikx_1} \end{aligned} \tag{4.6}$$

$$\begin{aligned} u_1 &= \phi_{,1} + \psi_{,2} = \{ikA\sinh(\eta x_2) + \beta D\sinh(\beta x_2)\}e^{ikx_1} \\ u_2 &= \phi_{,2} - \psi_{,1} = \{\eta A\cosh(\eta x_2) - ikD\cosh(\beta x_2)\}e^{ikx_1} \end{aligned} \tag{4.7}$$

$$\begin{aligned} \sigma_{22} &= -\mu\left\{k_S^2\phi + 2(\psi_{,12} + \phi_{,11})\right\} = -\mu\left\{\left(k_S^2 - 2k^2\right)A\sinh(\eta x_2) + 2ik\beta D\sinh(\beta x_2)\right\}e^{ikx_1} \\ \sigma_{12} &= \mu\{2\phi_{,12} + \psi_{,22} - \psi_{,11}\} = \mu\{(2ik\eta)A\cosh(\eta x_2) + (k^2 + \beta^2)D\cosh(\beta x_2)\}e^{ikx_1} \end{aligned} \tag{4.8}$$

From Chapter 1, Equation 1.169a and Equation 1.169b we get

$$\frac{B}{C} = \frac{2ik\beta}{\left(2k^2 - k_S^2\right)}\frac{\cosh(\beta h)}{\cosh(\eta h)} = -\frac{\left(2k^2 - k_S^2\right)}{2ik\eta}\frac{\sinh(\beta h)}{\sinh(\eta h)} \tag{4.9a}$$

and

$$\frac{A}{D} = \frac{2ik\beta}{\left(2k^2 - k_S^2\right)}\frac{\sinh(\beta h)}{\sinh(\eta h)} = -\frac{\left(2k^2 - k_S^2\right)}{2ik\eta}\frac{\cosh(\beta h)}{\cosh(\eta h)} \tag{4.9b}$$

Substituting Equation 4.9a and Equation 4.9b in the displacement and stress expressions, we obtain the following for symmetric modes:

$$
\begin{aligned}
u_1 &= \{ikB\cosh(\eta x_2) + \beta C\cosh(\beta x_2)\}e^{ikx_1} \\
&= B\left\{ik\cosh(\eta x_2) + \frac{\left(2k^2 - k_S^2\right)}{2ik}\frac{\cosh(\eta h)}{\cosh(\beta h)}\cosh(\beta x_2)\right\}e^{ikx_1} \\
u_2 &= \{\eta B\sinh(\eta x_2) - ikC\sinh(\beta x_2)\}e^{ikx_1} \\
&= B\left\{\eta\sinh(\eta x_2) - \frac{\left(2k^2 - k_S^2\right)}{2\beta}\frac{\cosh(\eta h)}{\cosh(\beta h)}\sinh(\beta x_2)\right\}e^{ikx_1}
\end{aligned}
\tag{4.10}
$$

$$
\begin{aligned}
\sigma_{22} &= -\mu\left\{\left(k_S^2 - 2k^2\right)B\cosh(\eta x_2) + 2ik\beta C\cosh(\beta x_2)\right\}e^{ikx_1} \\
&= -\mu B\left\{\left(k_S^2 - 2k^2\right)\cosh(\eta x_2) + 2ik\beta\frac{\left(2k^2 - k_S^2\right)}{2ik\beta}\frac{\cosh(\eta h)}{\cosh(\beta h)}\cosh(\beta x_2)\right\}e^{ikx_1} \\
&= \mu B\left(2k^2 - k_S^2\right)\left\{\cosh(\eta x_2) - \frac{\cosh(\eta h)}{\cosh(\beta h)}\cosh(\beta x_2)\right\}e^{ikx_1} \\
\sigma_{12} &= \mu\{(2ik\eta)B\sinh(\eta x_2) + (k^2 + \beta^2)C\sinh(\beta x_2)\}e^{ikx_1} \\
&= \mu B\left\{(2ik\eta)\sinh(\eta x_2) + \left(2k^2 - k_S^2\right)\frac{C}{B}\sinh(\beta x_2)\right\}e^{ikx_1} \\
&= \mu B\left\{(2ik\eta)\sinh(\eta x_2) - \left(2k^2 - k_S^2\right)\frac{2ik\eta}{\left(2k^2 - k_S^2\right)}\frac{\sinh(\eta h)}{\sinh(\beta h)}\sinh(\beta x_2)\right\}e^{ikx_1} \\
&= 2ik\eta\mu B\left\{\sinh(\eta x_2) - \frac{\sinh(\eta h)}{\sinh(\beta h)}\sinh(\beta x_2)\right\}e^{ikx_1}
\end{aligned}
\tag{4.11}
$$

For antisymmetric modes we obtain

$$
\begin{aligned}
u_1 &= \{ikA\sinh(\eta x_2) + \beta D\sinh(\beta x_2)\}e^{ikx_1} \\
&= A\left\{ik\sinh(\eta x_2) + \frac{\left(2k^2 - k_S^2\right)}{2ik}\frac{\sinh(\eta h)}{\sinh(\beta h)}\sinh(\beta x_2)\right\}e^{ikx_1} \\
u_2 &= \{\eta A\cosh(\eta x_2) - ikD\cosh(\beta x_2)\}e^{ikx_1} \\
&= A\left\{\eta\cosh(\eta x_2) - \frac{\left(2k^2 - k_S^2\right)}{2\beta}\frac{\sinh(\eta h)}{\sinh(\beta h)}\cosh(\beta x_2)\right\}e^{ikx_1}
\end{aligned}
\tag{4.12}
$$

$$\begin{aligned}
\sigma_{22} &= -\mu\left\{\left(k_S^2 - 2k^2\right)A\sinh(\eta x_2) + 2ik\beta D\sinh(\beta x_2)\right\}e^{ikx_1} \\
&= -\mu A\left\{\left(k_S^2 - 2k^2\right)\sinh\left(\eta x_2\right) + 2ik\beta\frac{\left(2k^2 - k_S^2\right)}{2ik\beta}\frac{\sinh(\eta h)}{\sinh(\beta h)}\sinh(\beta x_2)\right\}e^{ikx_1} \\
&= \mu A\left(2k^2 - k_S^2\right)\left\{\sinh(\eta x_2) - \frac{\sinh(\eta h)}{\sinh(\beta h)}\sinh(\beta x_2)\right\}e^{ikx_1} \\
\sigma_{12} &= \mu\{(2ik\eta)A\cosh(\eta x_2) + (k^2 + \beta^2)D\cosh(\beta x_2)\}e^{ikx_1} \\
&= \mu A\left\{(2ik\eta)\cosh(\eta x_2) + \left(2k^2 - k_S^2\right)\frac{D}{A}\cosh(\beta x_2)\right\}e^{ikx_1} \\
&= \mu A\left\{(2ik\eta)\cosh(\eta x_2) - \left(2k^2 - k_S^2\right)\frac{2ik\eta}{2k^2 - k_S^2}\frac{\cosh(\eta h)}{\cosh(\beta h)}\cosh(\beta x_2)\right\}e^{ikx_1} \\
&= 2ik\eta\mu A\left\{\cosh(\eta x_2) - \frac{\cosh(\eta h)}{\cosh(\beta h)}\cosh(\beta x_2)\right\}e^{ikx_1}
\end{aligned} \tag{4.13}$$

The time dependence ($e^{-i\omega t}$) is implied in the above expressions.

4.2.1 Dispersion Curves and Mode Shapes

As explained in Chapter 1, variation of the wave velocity as a function of the frequency is known as the dispersion curve. Displacement and stress field variations across the plate thickness are called mode shapes. The steps involved in solving the dispersion equation and mode shapes are discussed in this section.

4.2.1.1 Dispersion Curves

It is necessary to solve Equation 4.1 (Equation 4.1a for symmetric modes and Equation 4.16 for antisymmetric modes) to obtain the dispersion curves. It can be solved in one of two ways: (1) fix the frequency (ω) and then try to get the Lamb wave speed (c_L) by satisfying the dispersion equation (Equation 4.1a or Equation 4.16), or (2) fix the Lamb wave speed (c_L) and then investigate for what values of frequency ($f = \omega/2$) the dispersion equation is satisfied. If the first method is followed, the frequency is fixed and then a value for the Lamb wave speed c_L is assumed. Using these f and c_L values k, η and β are easily computed from Equation 4.2 since P- and S-wave speeds (c_P and c_S) in the plate material are known. The values of k, η, β, k_S, and h (plate thickness) are substituted into Equation 4.1a or Equation 4.16, and the left- and right-hand sides of the equation are compared. If the computed values on the two sides of the equation are different, then a new estimate of c_L is made. In other words, the nonlinear equation (Equation 4.1a or Equation 4.16) is solved for c_L for a given frequency using the standard techniques for solution of nonlinear equations, such as bisection method, secant method, and Newton-Raphson method.

The complications arise in this case due to the fact that for a single frequency the transcendental dispersion equations (Equation 4.1a and Equation 4.1b) have multiple roots. It is possible to miss some roots during the root-searching step. However, in principle, by taking a very small step size it is possible to capture all roots at a given frequency. After capturing all roots of the dispersion equation at one frequency, the frequency value is changed and then, following the same root finding technique, all roots for the new frequency are captured. In this manner, a number of roots of Equation 4.1a can be found and plotted in the frequency-phase velocity space, as shown in Figure 4.2. Here roots are found along the vertical grid lines at a 0.5-MHz interval.

Alternately, instead of fixing frequency it is possible to fix the Lamb wave speed (c_L) and vary the frequency (f) to capture all roots for a given c_L. Then the c_L value is changed and with varying f all roots are found for the new c_L value. Figure 4.3 shows all roots of Equation 4.1a captured in this manner. Roots are found along the horizontal grid lines, for the c_L interval of 0.5 km/sec. Note that, for the first mode, the roots, which appear along the horizontal lines in Figure 4.2, slightly below the c_L value of 3 and 5.5 km/sec, are not captured in Figure 4.3.

Connecting the neighboring roots in Figure 4.2 (or Figure 4.3), dispersion curves for the symmetric modes are obtained as shown in Figure 4.4. These modes are denoted as S_0, S_1, S_2, S_3, etc. Here, the letter S refers to the symmetric mode and the subscripts 0, 1, 2, 3, … are numbered from left to right starting with the lowest frequency mode. These numbers are called the order of the mode. Note that the S_0 mode starts at zero frequency, but the higher order modes (S_1, S_2, S_3, etc.) start at nonzero frequencies. The frequency value

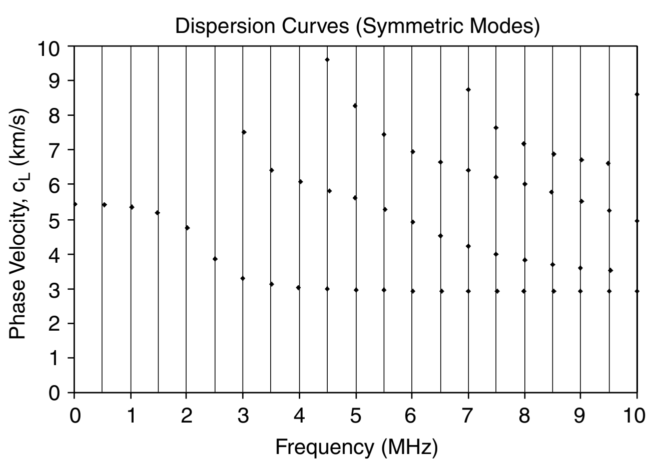

FIGURE 4.2
Roots of Equation 4.1a are plotted at 0.5 MHz frequency interval for a 1-mm thick aluminum plate (c_P = 6.32 km/sec, c_S = 3.13 km/sec, ρ = 2.7 g/cm³).

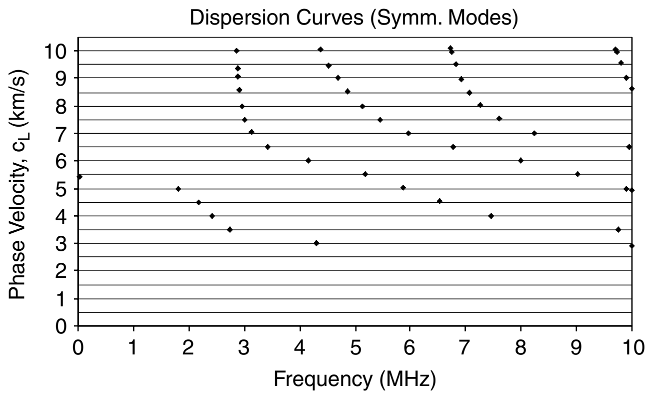

FIGURE 4.3
Roots of Equation 4.1a are plotted at a 0.5-km/sec interval of c_L for a 1-mm thick aluminum plate. Material properties are given in the caption of Figure 4.2.

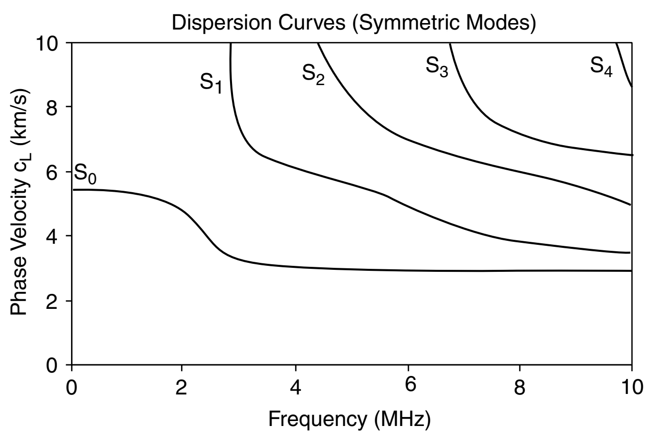

FIGURE 4.4
Symmetric modes for the Lamb wave propagation in a 1-mm thick aluminum plate (material properties are given in Figure 4.2). Dispersion curves are obtained after solving Equation 4.1a and then connecting the roots by continuous lines.

below which a specific mode is not observed is called the cutoff frequency for that mode. Note that there is no cutoff frequency for the S_0 mode; however, the higher order modes have nonzero cutoff frequency — if the order is higher, the cutoff frequency is higher.

In the same manner, the antisymmetric modes can be computed by solving Equation 4.1b. Antisymmetric modes for the same plate are shown in Figure 4.5. The antisymmetric modes are denoted by A_0, A_1, A_2, A_3, etc. The 0th-order antisymmetric mode A_0 does not have any cutoff frequency. The higher order modes (A_1, A_2, A_3, etc.) have nonzero cutoff frequency — the higher the order, the higher is the cutoff frequency like the symmetric modes.

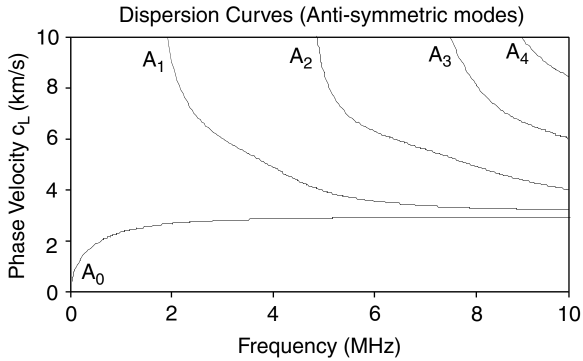

FIGURE 4.5
Antisymmetric modes for the Lamb wave propagation in a 1-mm thick aluminum plate (material properties are given in Figure 4.2). Dispersion curves are obtained after solving Equation 4.1b and then connecting the roots by continuous lines.

After superimposing these two sets of modes, the complete set of dispersion curves are obtained. The dispersion curves for aluminum, copper and steel plates are shown in Figure 4.6. This figure shows the effect of the change in material properties on the dispersion curves.

The effect of the variation of plate thickness on the dispersion curves is then investigated. This effect can be explicitly seen when Equation 4.1a and Equation 4.1b are rewritten in the following form:

$$\frac{\tanh\left(\omega h\sqrt{\frac{1}{c_L^2}-\frac{1}{c_P^2}}\right)}{\tanh\left(\omega h\sqrt{\frac{1}{c_L^2}-\frac{1}{c_S^2}}\right)} = \frac{\left(\frac{2}{c_L^2}-\frac{1}{c_S^2}\right)^2}{\frac{4}{c_L^2}\sqrt{\frac{1}{c_L^2}-\frac{1}{c_P^2}}\sqrt{\frac{1}{c_L^2}-\frac{1}{c_S^2}}} \tag{4.14a}$$

$$\frac{\tanh\left(\omega h\sqrt{\frac{1}{c_L^2}-\frac{1}{c_P^2}}\right)}{\tanh\left(\omega h\sqrt{\frac{1}{c_L^2}-\frac{1}{c_S^2}}\right)} = \frac{\frac{4}{c_L^2}\sqrt{\frac{1}{c_L^2}-\frac{1}{c_P^2}}\sqrt{\frac{1}{c_L^2}-\frac{1}{c_S^2}}}{\left(\frac{2}{c_L^2}-\frac{1}{c_S^2}\right)^2} \tag{4.14b}$$

In Equation 4.14a and Equation 4.14b, note that the half-thickness (h) of the plate and the wave frequency ($\omega = 2\pi f$) appear in the equation as a product term. From these equations it is possible to plot the variations of c_L as a function of fh, instead of a function of f only, since $\omega h = 2\pi fh$. The main advantage of this type of plot is that one plot covers multiple frequency and thickness combinations. From Equation 4.14a and Equation 4.14b it is easy to see that the c_L values for a 1-mm thick plate at 5 MHz should be identical

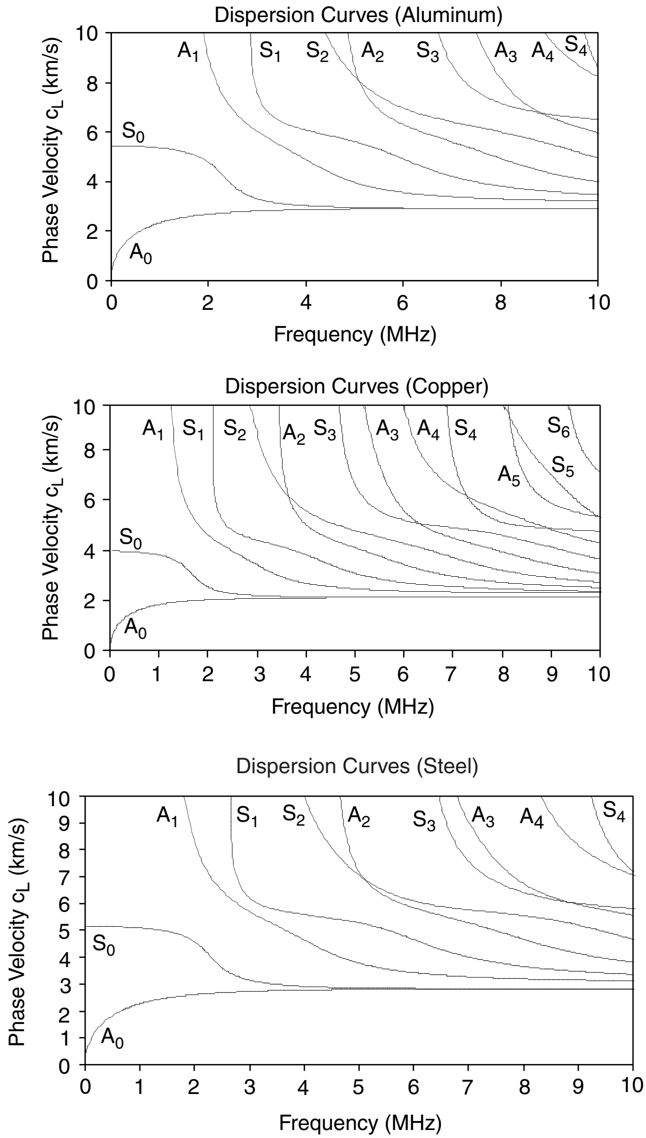

FIGURE 4.6
Dispersion curves for 1-mm thick aluminum, copper, and steel plates. Material properties: aluminum: $c_P = 6.32$ km/sec, $c_S = 3.13$ km/sec, $\rho = 2.7$ g/cm^3; copper: $c_P = 4.7$ km/sec, $c_S = 2.26$ km/sec, $\rho = 8.9$ g/cm^3; steel: $c_P = 5.96$ km/sec, $c_S = 3.26$ km/sec, $\rho = 7.9$ g/cm^3.

to those for a 5 mm thick plate at 1 MHz or 2.5 mm thick plate at 2 MHz since for all these combinations the plate thickness multiplied by the frequency value is equal to 5 MHz-mm. Three sets of dispersion curves of Figure 4.6 are given for the 1 mm thick plate for the frequency range varying from 0 to 10 MHz. The same curves will represent the dispersion curves for

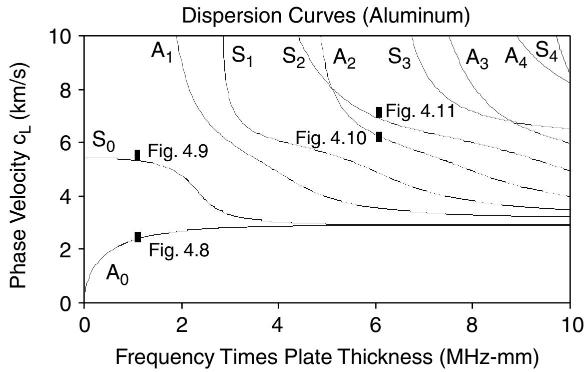

FIGURE 4.7
Dispersion curves for aluminum plates of different thickness. Displacement and stress variations inside the plate for four phase velocity-frequency combinations, marked by black squares, are shown in Figure 4.8 through Figure 4.11.

a 2 mm thick plate in the frequency range varying from 0 to 5 MHz, or for a 4-mm thick plate in the frequency range from 0 to 2.5 MHz. In other words, in Figure 4.6, if the frequency axis is changed to the frequency times the plate thickness (or $2fh$) value, as shown in Figure 4.7, then that plot represents dispersion curves for plates of different thickness. For a smaller plate thickness the frequency value should be greater and for a thicker plate the frequency should be smaller to obtain the same $2fh$ value along the horizontal axis of the dispersion curve plot shown in Figure 4.7.

4.2.1.2 Mode Shapes

Points on the dispersion curves of Figure 4.6 and Figure 4.7 give the frequency-phase velocity combinations for which Lamb wave can propagate. For the given frequency and phase velocity values, displacement and stress fields inside the plate can be obtained from Equations 4.10 and Equation 4.11 for symmetric modes, and from Equation 4.12 and Equation 4.13) for antisymmetric modes. Often we are interested in knowing the displacement and stress field variations inside the plate. In the wave propagation direction (x_1-direction), the field variation is sinusoidal for a given time and x_2 value, since the x_1-dependence is e^{ikx_1} (see Equation 4.10 through Equation 4.13). The x_2-dependence of the displacement and stress fields is called the mode shapes. Mode shapes for different displacement and stress components, for four different frequency-phase velocity combinations correspond to four modes (A_0, S_0, A_2 and S_2), which are shown in Figure 4.8 through Figure 4.11. For all four figures, the aluminum plate thickness is 1 mm and the field values are normalized with respect to their maximum values. The wave frequency is 1 MHz for Figure 4.8 and Figure 4.9, and 6 MHz for Figure 4.10 and Figure 4.11. Rectangular black markers in the dispersion curve plot (Figure 4.7) identify the region where the mode shapes are generated.

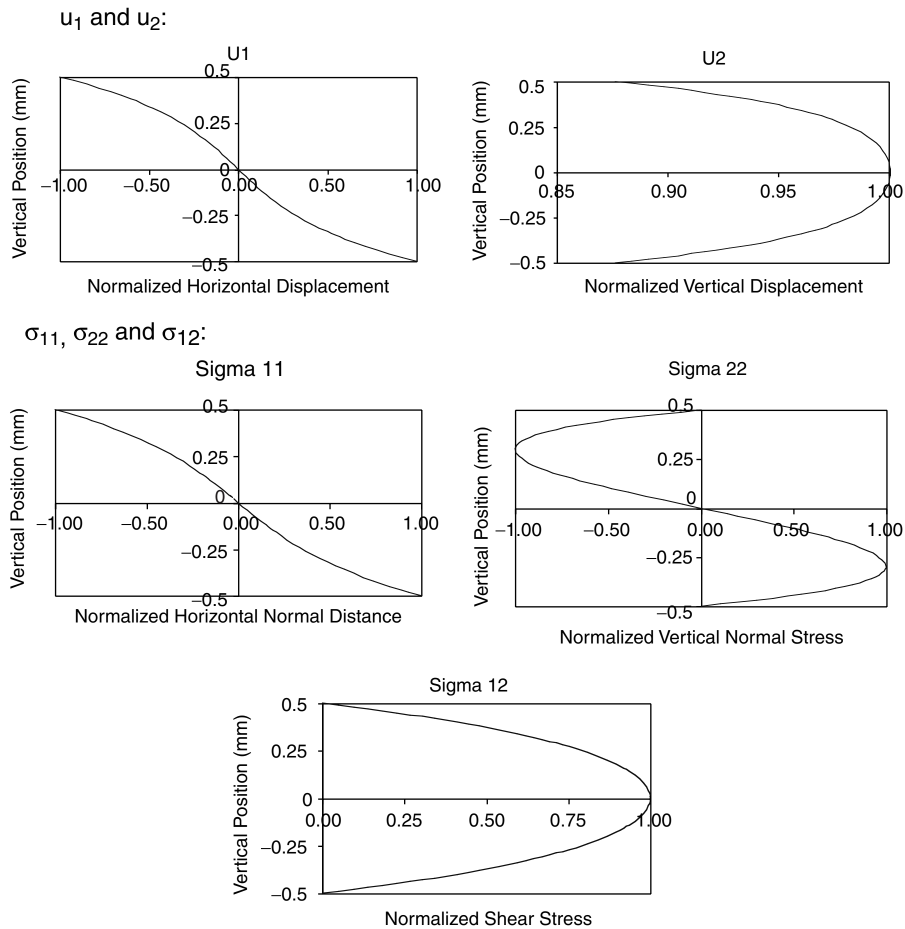

FIGURE 4.8
Displacement and stress variations along the plate thickness in a 1-mm thick aluminum plate for the A_0 mode of Lamb wave propagation at 1-MHz signal frequency. The corresponding point on the dispersion curve is shown in Figure 4.7.

As expected, the antisymmetric modes A_0 (Figure 4.8) and A_2 (Figure 4.10) show u_1, σ_{11}, σ_{22} as odd functions of x_2, while u_2 and σ_{12} are even functions. In Figure 4.9 and Figure 4.11, one can see that the symmetric modes (S_0 and S_2) generate u_1, σ_{11}, σ_{22} as even functions of x_2, while u_2 and σ_{12} are odd functions. It should also be noted here that the oscillations in the mode shapes increase as the frequency and the order of the mode increase.

What happens to a mode shape if the frequency is changed but the mode order is not? To investigate it, the displacement and stress amplitudes along the plate thickness are plotted for A_2 and S_2 modes in Figure 4.12 and Figure 4.13, respectively, for different phase velocities. Note that for both these modes, as the phase velocity increases, the frequency decreases. Details of

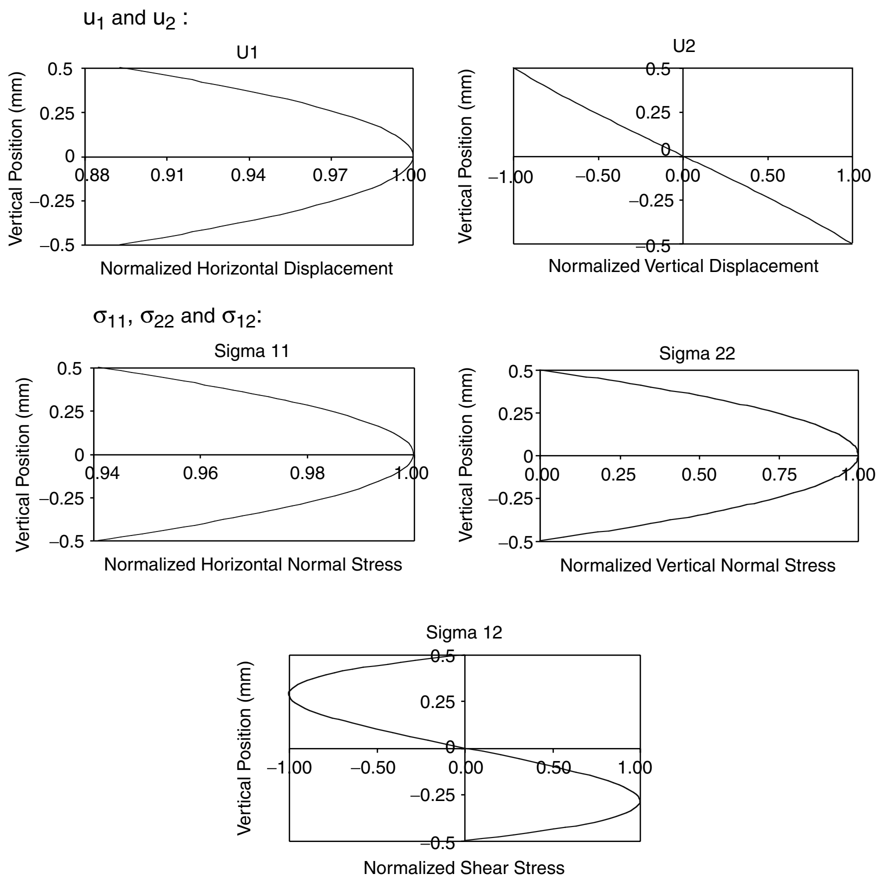

FIGURE 4.9
Displacement and stress variations along the plate thickness in a 1-mm thick aluminum plate for the S_0 mode of Lamb wave propagation at 1-MHz signal frequency. The corresponding point on the dispersion curve is shown in Figure 4.7.

the oscillation pattern vary with the phase velocity (and frequency), but the general nature of the variation remains approximately similar over a wide frequency and phase velocity range for most field variables. Note that the shear stress becomes almost equal to zero through the entire plate thickness near the phase velocity of 4.4 km/sec for both modes.

4.3 Homogeneous Elastic Plate Immersed in a Fluid

In the previous section we have learned how different modes of Lamb wave produce particle displacement in the plate, placed in a vacuum. Let us now study the effect of the presence of two fluid half-spaces, placed above

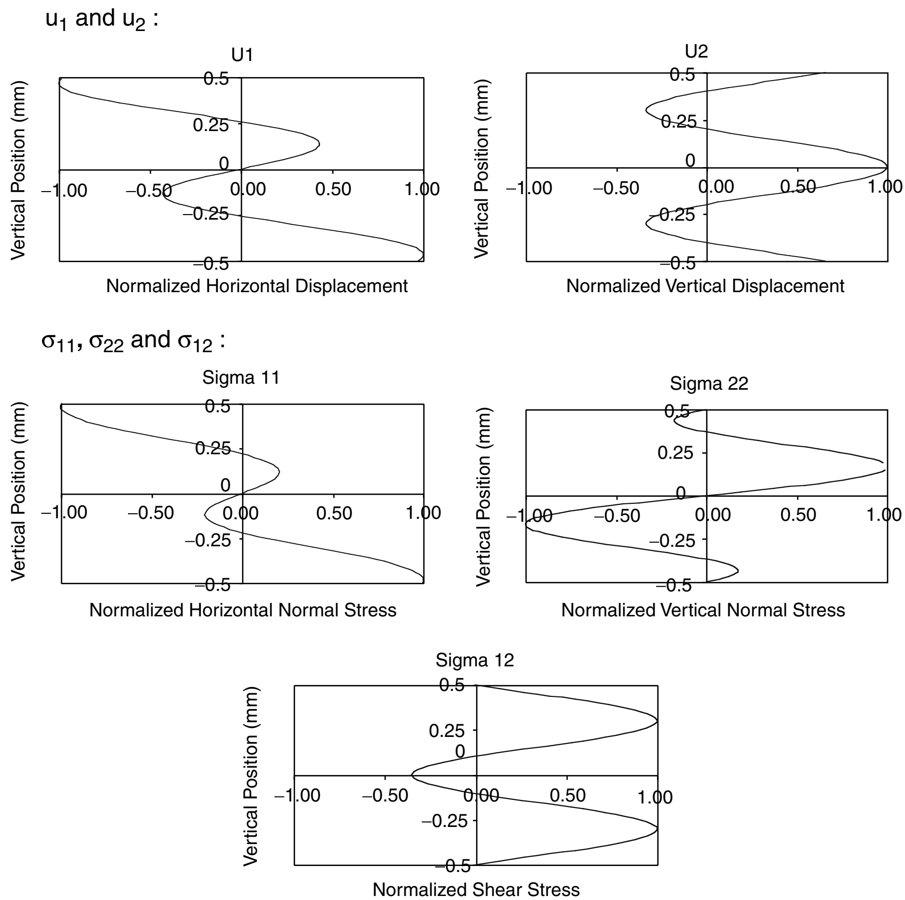

FIGURE 4.10
Displacement and stress variations along the plate thickness in a 1-mm thick aluminum plate for the A_2 mode of Lamb wave propagation at 6-MHz signal frequency. The corresponding point on the dispersion curve is shown in Figure 4.7.

and below an infinite plate. Unlike the previous case (plate in a vacuum), here the acoustic energy is no longer trapped inside the plate; it leaks into the surrounding fluid medium as shown in Figure 4.14.

From Chapter 1, Equation 1.167, the potential field in the solid plate is given by

$$\begin{aligned}
\phi &= (ae^{\eta x_2} + be^{-\eta x_2})e^{ikx_1} = \{A\sinh(\eta x_2) + B\cosh(\eta x_2)\}e^{ikx_1} \\
\psi &= (ce^{\beta x_2} + de^{-\beta x_2})e^{ikx_1} = \{C\sinh(\beta x_2) + D\cosh(\beta x_2)\}e^{ikx_1} \\
\eta &= \sqrt{k^2 - k_P^2} \\
\beta &= \sqrt{k^2 - k_S^2}
\end{aligned} \tag{4.15}$$

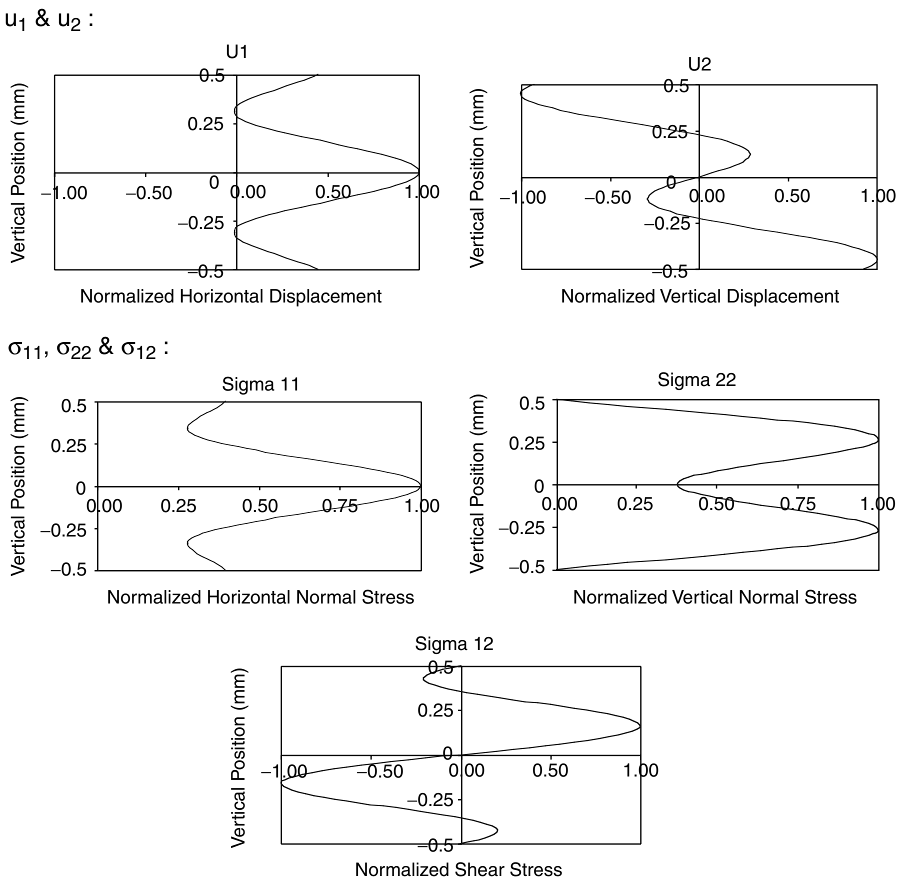

FIGURE 4.11
Displacement and stress variations along the plate thickness in a 1-mm thick aluminum plate for the S_2 mode of Lamb wave propagation at 6 MHz signal frequency. The corresponding point on the dispersion curve is shown in Figure 4.7.

The potential field in the fluid can be written as

$$\phi_{fL} = me^{\eta_f x_2}e^{ikx_1} = m\{\sinh(\eta_f x_2) + \cosh(\eta_f x_2)\}e^{ikx_1}$$

$$\phi_{fU} = ne^{-\eta_f x_2}e^{ikx_1} = n\{\cosh(\eta_f x_2) - \sinh(\eta_f x_2)\}e^{ikx_1} \quad \textbf{(4.16)}$$

$$\eta_f = \sqrt{k^2 - k_f^2}$$

where ϕ_{fL} and ϕ_{fU} correspond to the wave potentials in the lower and upper fluid half spaces, respectively.

Instead of considering the potentials in the above form, we can separate the symmetric and nonsymmetric components in the following manner:

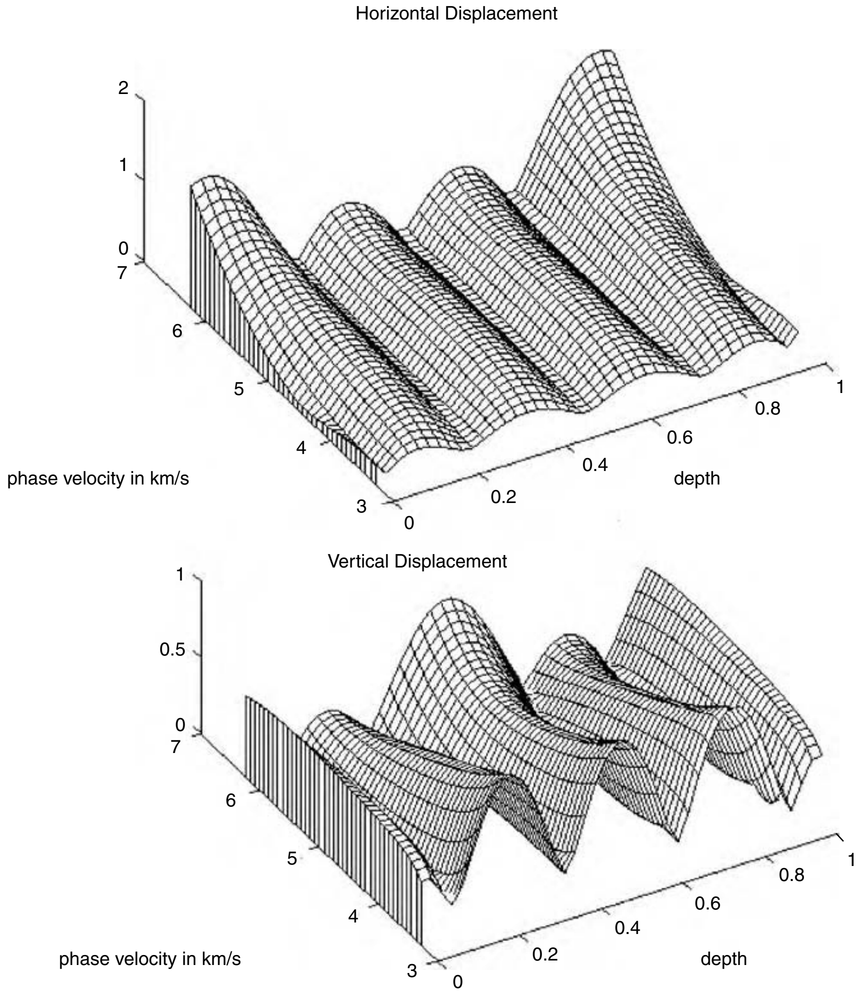

(a)

FIGURE 4.12
(a) Amplitude variations of horizontal (u_1 component, top figure) and vertical (u_2 component, bottom figure) displacements through the plate thickness for the A_2 mode, as the phase velocity varies from 3.4 to 6.3 km/sec; depth is 0 for the top of the plate and 1 for the bottom of the plate. Dispersion curves for the aluminum plate are shown in Figure 4.7. (b) Amplitude variations of horizontal normal stress (σ_{11} component, top figure), vertical normal stress (σ_{22} component, middle figure), and shear stress (σ_{12} component, bottom figure) through the plate thickness for the A_2 mode, as the phase velocity varies from 3.4 to 6.3 km/sec; depth is 0 for the top of the plate and 1 for the bottom of the plate. Dispersion curves for the aluminum plate are shown in Figure 4.7.

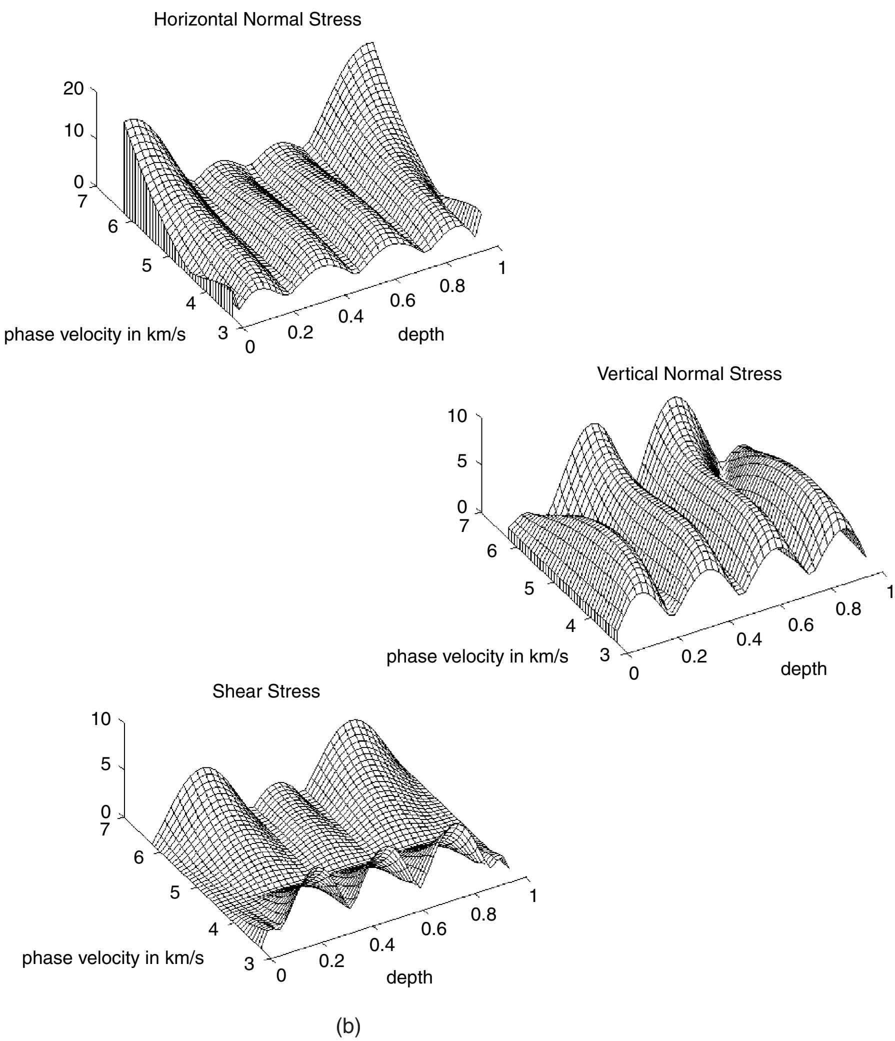

FIGURE 4.12
(continued)

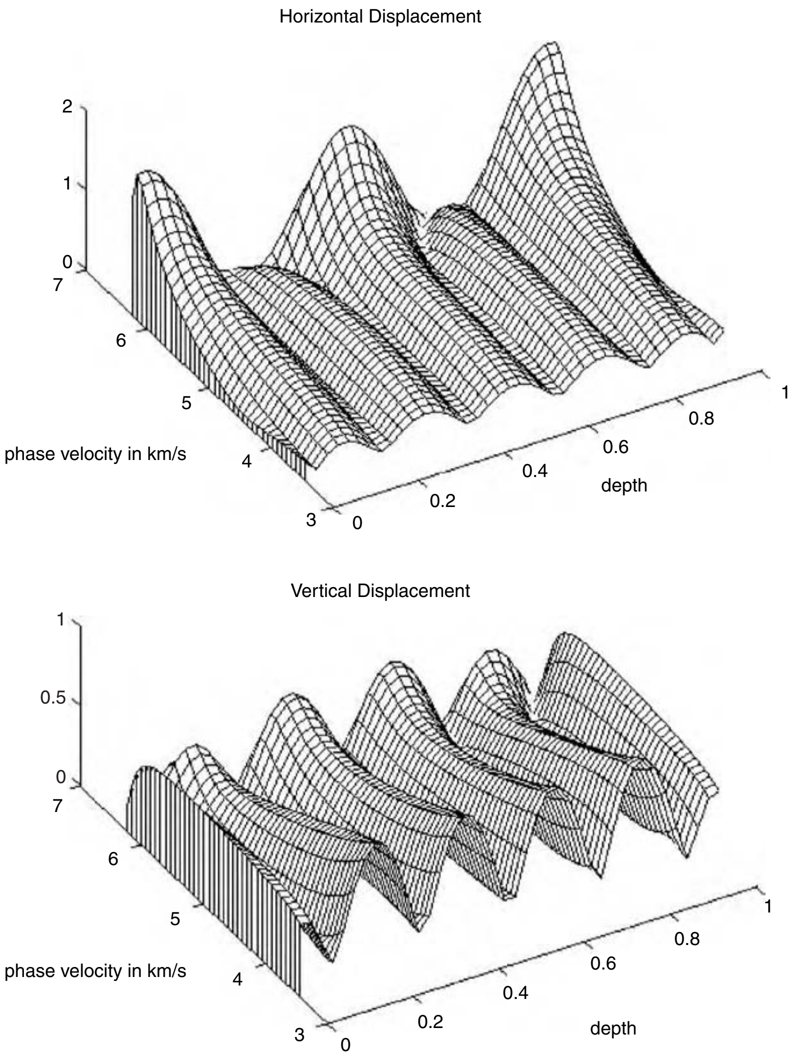

(a)

FIGURE 4.13

(a) Amplitude variations of horizontal (u_1 component, top figure) and vertical (u_2 component, bottom figure) displacements through the plate thickness for the S_2 mode, as the phase velocity varies from 3.5 to 6.3 km/sec; depth is 0 for the top of the plate and 1 for the bottom of the plate. Dispersion curves for the aluminum plate are shown in Figure 4.7. (b) Amplitude variations of horizontal normal stress (σ_{11} component, top figure), vertical normal stress (σ_{22} component, middle figure), and shear stress (σ_{12} component, bottom figure) through the plate thickness for the S_2 mode, as the phase velocity varies from 3.5 to 6.3 km/sec; depth is 0 for the top of the plate and 1 for the bottom of the plate. Dispersion curves for the aluminum plate are shown in Figure 4.7.

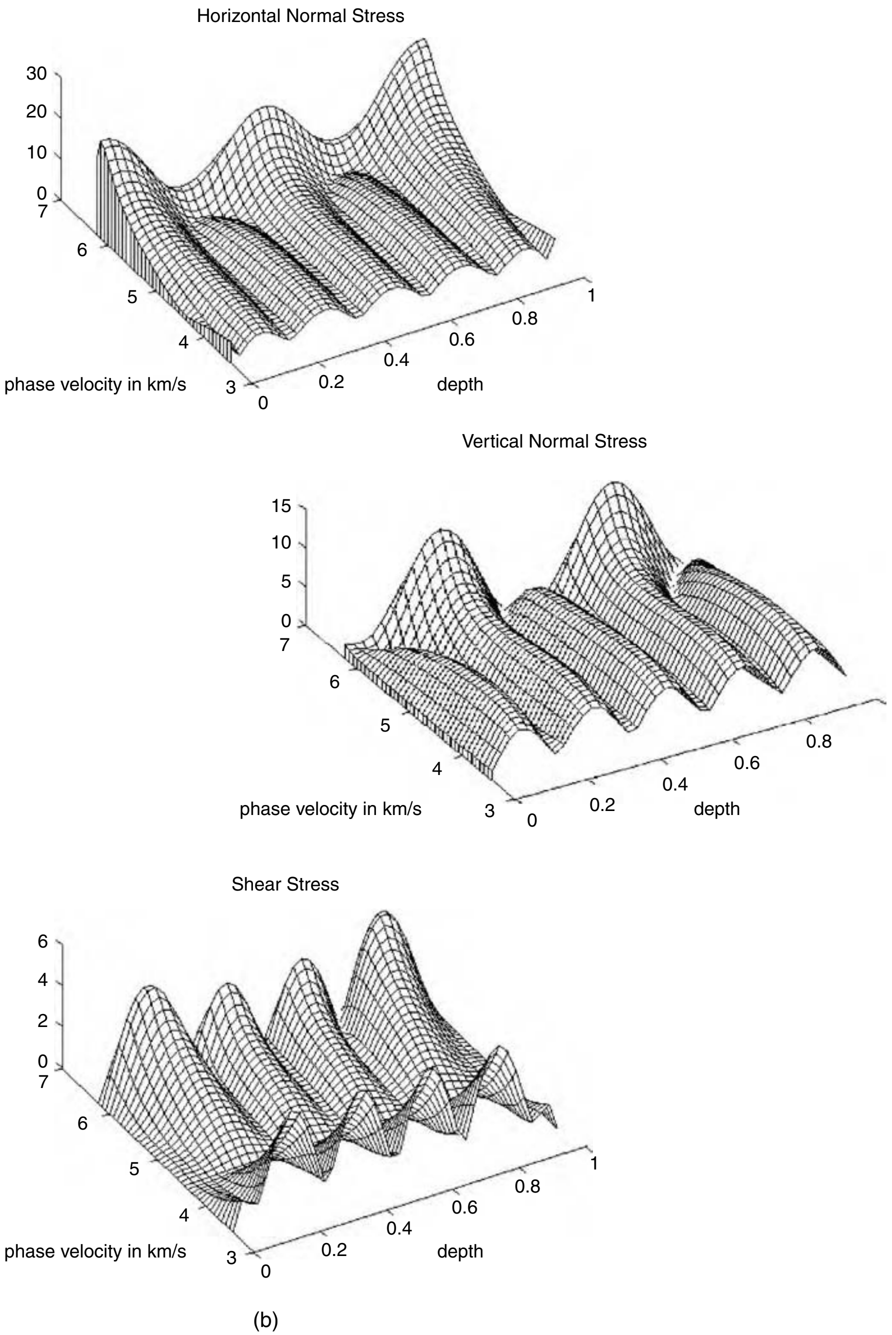

FIGURE 4.13
(continued)

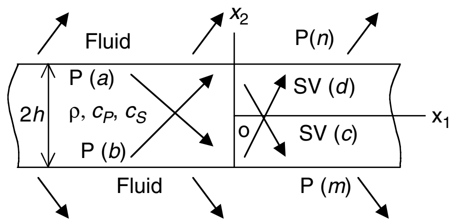

FIGURE 4.14
The Lamb wave is propagating in the positive x_1-direction, while the acoustic energy is leaking into the surrounding fluid medium, giving rise to the leaky Lamb wave propagation.

Symmetric motion:

$$\begin{aligned} \phi &= B\cosh(\eta x_2)e^{ikx_1} \\ \psi &= C\sinh(\beta x_2)e^{ikx_1} \\ \phi_{fL} &= Me^{\eta_f x_2}e^{ikx_1} \\ \phi_{fU} &= Me^{-\eta_f x_2}e^{ikx_1} \end{aligned} \tag{4.17}$$

Antisymmetric motion:

$$\begin{aligned} \phi &= A\sinh(\eta x_2)e^{ikx_1} \\ \psi &= D\cosh(\beta x_2)e^{ikx_1} \\ \phi_{fL} &= Ne^{\eta_f x_2}e^{ikx_1} \\ \phi_{fU} &= -Ne^{-\eta_f x_2}e^{ikx_1} \end{aligned} \tag{4.18}$$

Then the symmetric and antisymmetric motions are analyzed separately as given below. ϕ_{fL} and ϕ_{fU} in Equation 4.16 are defined differently from those given in Equation 4.17 and Equation 4.18. However, two definitions are equivalent (see Exercise Problem 4.7).

4.3.1 Symmetric Motion

At the fluid-solid interface the shear stress component should be zero, and normal stress and displacement components should be continuous across the interface. Therefore, we can write

$$\sigma_{12}\big|_{x_2=\pm h} = \mu\left\{(2ik\eta)[\pm B\sinh(\eta h)] + \left(2k^2 - k_s^2\right)[\pm C\sinh(\beta h)]\right\}e^{ikx_1} = 0$$

$$\Rightarrow 2ik\eta B\sinh(\eta h) + \left(2k^2 - k_s^2\right)C\sinh(\beta h) = 0$$

$$\sigma_{22}\big|_{x_2=\pm h} = +\mu\left\{\left(2k^2 - k_s^2\right)[B\cosh(\eta h)] - 2ik\beta[C\cosh(\beta h)]\right\}e^{ikx_1} = -\rho_f\omega^2 Me^{-\eta_f h}e^{ikx_1}$$

$$\Rightarrow \left(2k^2 - k_s^2\right)B\cosh(\eta h) - 2ik\beta C\cosh(\beta h) + \frac{\rho_f k_s^2}{\rho}Me^{-\eta_f h} = 0$$

$$u_2\big|_{x_2=\pm h} = \phi,_2 - \psi,_1 = \{\pm\eta B\sinh(\eta h) \mp ikC\sinh(\beta h)\}^{ikx_1} = \mp\eta_f Me^{-\eta_f h}e^{ik_1}$$

$$\Rightarrow \eta B\sinh(\eta h) - ikC\sinh(\beta h) + \eta_f Me^{-\eta_f h} = 0 \tag{4.19}$$

The 3 algebraic equations given in Equation 4.19 can be written as a matrix equation

$$\begin{bmatrix} 2ik\eta\sinh(\eta h) & \left(2k^2 - k_S^2\right)\sinh(\beta h) & 0 \\ \left(2k^2 - k_S^2\right)\cosh(\eta h) & -2ik\beta\cosh(\beta h) & \dfrac{\rho_f k_S^2}{\rho}e^{-\eta_f h} \\ \eta\sinh(\eta h) & -ik\sinh(\beta h) & \eta_f e^{-\eta_f h} \end{bmatrix}\begin{Bmatrix} B \\ C \\ M \end{Bmatrix} = \begin{Bmatrix} 0 \\ 0 \\ 0 \end{Bmatrix} \tag{4.20}$$

For nonzero solutions of B, C, and M, the determinant of the coefficient matrix must vanish. Therefore,

$$\eta_f e^{-\eta_f h}\left\{4k^2\eta\beta\sinh(\eta h)\cosh(\beta h) - \left(2k^2 - k_S^2\right)^2\cosh(\eta h)\sinh(\beta h)\right\}$$

$$-\frac{\rho_f k_S^2}{\rho}e^{-\eta_f h}\left\{2k^2\eta\sinh(\eta h)\sinh(\beta h) - \eta\left(2k^2 - k_S^2\right)\sinh(\eta h)\sinh(\beta h)\right\} = 0$$

$$\Rightarrow \eta_f\left\{4k^2\eta\beta\sinh(\eta h)\cosh(\beta h) - \left(2k^2 - k_S^2\right)^2\cosh(\eta h)\sinh(\beta h)\right\}$$

$$-\frac{\rho_f\eta k_S^4}{\rho}\sinh(\eta h)\sinh(\beta h) = 0 \tag{4.21}$$

$$\Rightarrow 4k^2\eta\beta\sinh(\eta h)\cosh(\beta h) - \left(2k^2 - k_S^2\right)^2\cosh(\eta h)\sinh(\beta h)$$

$$= \frac{\rho_f\eta k_S^4}{\rho\eta_f}\sinh(\eta h)\sinh(\beta h)$$

4.3.2 Antisymmetric Motion

For the potential field given in Equation 4.18, the plate motion should be antisymmetric with respect to the central plane of the plate. As in the previous section, if we apply the vanishing shear stress condition at the fluid-solid interfaces and continuity of the normal stress and displacement components across the two interfaces we get the following:

$$\sigma_{12}\big|_{x_2=\pm h} = \mu\left\{2ik\eta A\cosh(\eta h) + \left(2k^2 - k_S^2\right)D\cosh(\beta h)\right\}e^{ikx_1} = 0$$

$$\Rightarrow 2ik\eta A\cosh(\eta h) + \left(2k^2 - k_S^2\right)D\cosh(\beta h) = 0$$

$$\sigma_{22}\big|_{x_2=\pm h} = +\mu\left\{\pm\left(2k^2 - k_S^2\right)A\sinh(\eta h) - 2ik\beta[\pm D\sinh(\beta h)]\right\}e^{ikx_1} = \pm\rho_f\omega^2 Ne^{-\eta_f h}e^{ikx_1}$$

$$\Rightarrow \left(2k^2 - k_S^2\right)A\sinh(\eta h) - 2ik\beta D\sinh(\beta h) - \frac{\rho_f k_S^2}{\rho}Ne^{-\eta_f h} = 0$$

$$u_2\big|_{x_2=\pm h} = \phi_{,2} - \psi_{,1} = \{\eta A\cosh(\eta h) - ikD\cosh(\beta h)\}e^{ikx_1} = \eta_f Ne^{-\eta_f h}e^{ikx_1}$$

$$\Rightarrow \eta A\cosh(\eta h) - ikD\cosh(\beta h) - \eta_f Ne^{-\eta_f h} = 0$$

(4.22)

The three equations in Equation 4.22 can be written in the matrix form

$$\begin{bmatrix} 2ik\eta\cosh(\eta h) & \left(2k^2 - k_S^2\right)\cosh(\beta h) & 0 \\ \left(2k^2 - k_S^2\right)\sinh(\eta h) & -2ik\beta\sinh(\beta h) & \dfrac{\rho_f k_S^2}{\rho}e^{-\eta_f h} \\ \eta\cosh(\eta h) & -ik\cosh(\beta h) & -\eta_f e^{-\eta_f h} \end{bmatrix}\begin{Bmatrix} A \\ D \\ N \end{Bmatrix} = \begin{Bmatrix} 0 \\ 0 \\ 0 \end{Bmatrix} \qquad \textbf{(4.23)}$$

For nontrivial solutions of A, D, and N, the determinant of the coefficient matrix must vanish. Therefore,

$$-\eta_f e^{-\eta_f h}\left\{4k^2\eta\beta\cosh(\eta h)\sinh(\beta h) - \left(2k^2 - k_S^2\right)^2\sinh(\eta h)\cosh(\beta h)\right\}$$

$$+\frac{\rho_f k_S^2}{\rho}e^{-\eta_f h}\left\{2k^2\eta\cosh(\eta h)\cosh(\beta h) - \eta\left(2k^2 - k_S^2\right)\cosh(\eta h)\cosh(\beta h)\right\} = 0$$

$$\Rightarrow -\eta_f\left\{4k^2\eta\beta\cosh(\eta h)\sinh(\beta h) - \left(2k^2 - k_S^2\right)^2\sinh(\eta h)\cosh(\beta h)\right\}$$

$$+\frac{\rho_f\eta k_S^4}{\rho}\cosh(\eta h)\cosh(\beta h) = 0$$

$$\Rightarrow 4k^2\eta\beta\cosh(\eta h)\sinh(\beta h) - \left(2k^2 - k_S^2\right)^2\sinh(\eta h)\cosh(\beta h) = \frac{\rho_f\eta k_S^4}{\rho\eta_f}\cosh(\eta h)\cosh(\beta h)$$

(4.24)

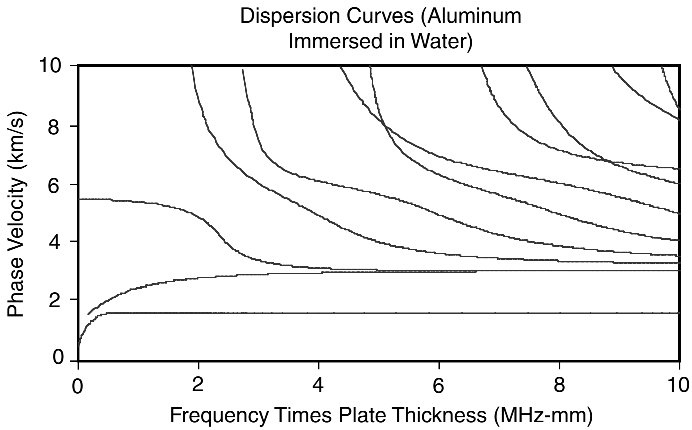

FIGURE 4.15
Dispersion curves for a 1-mm thick aluminum plate immersed in water. The mode, which is almost horizontal and has a phase velocity less than 2 km/sec, corresponds to the Scholte wave. Other curves correspond to the Lamb modes.

Equations 4.21 and Equation 4.24 give the dispersion equations for symmetric and antisymmetric modes, respectively, of leaky Lamb waves. Leaky Lamb wave dispersion curves for an aluminum plate immersed in the water are given in Figure 4.15. Similarities and differences between the Lamb wave dispersion curves (Figure 4.6) and leaky Lamb wave dispersion curves (Figure 4.15) should be noted here. Note that in Figure 4.15 one additional mode appears for c_L value below 2 km/sec. Viktorov (1967) has shown that for a solid plate immersed in a liquid one additional real root of the dispersion equation appears at every frequency for a phase velocity value that is less than the P-wave speed in the fluid or the shear wave speed in the solid. This wave mode at the fluid-solid interface was first identified by Scholte (1942) and is considered to be a special case of Stonely wave mode (Stonely, 1924) that is observed at the interface of two solids. Scholte wave mode is also known as the Stonely-Scholte wave mode. In absence of the fluid-solid or solid-solid interface such interface wave modes (Stonely and Scholte) are not observed in a free plate (Figure 4.6). Other than this additional mode the presence of water does not significantly affect the other Lamb modes of Figure 4.6. Note that when the plate is in a vacuum then the right-hand side of Equation 4.21 and Equation 4.24 vanish, the dispersion equations are simplified into those given in Equation 4.1a and Equation 4.1b, and the interface wave mode disappears.

Example 4.1

Without separating the symmetric and antisymmetric components of the plate motion obtain the dispersion equation for the leaky Lamb wave propagation in a homogeneous isotropic solid plate immersed in a liquid.

SOLUTION

For the problem geometry shown in Figure 4.14, the potential fields corresponding to the downward and upward P- and shear vertical (SV) waves are given by Equation 4.15 and Equation 4.16:

Wave potentials inside the solid plate:

$$\phi = (ae^{\eta x_2} + be^{-\eta x_2})e^{ikx_1}$$

$$\psi = (ce^{\beta x_2} + de^{-\beta x_2})e^{ikx_1}$$

$$\eta = \sqrt{k^2 - k_P^2}$$

$$\beta = \sqrt{k^2 - k_S^2}$$

Wave potentials in the lower and upper fluid half spaces:

$$\phi_{fL} = me^{\eta_f x_2}e^{ikx_1}$$

$$\phi_{fU} = ne^{-\eta_f x_2}e^{ikx_1}$$

$$\eta_f = \sqrt{k^2 - k_f^2}$$

If we apply the vanishing shear stress condition at the fluid-solid interfaces and continuity of the normal stress and displacement components across the two interfaces we get the following:

$$\sigma_{12}\big|_{x_2=h} = \mu\{2\phi_{,12} + \psi_{,22} - \psi_{,11}\}_{x_2=h}$$

$$= \mu\left\{(2ik\eta)(aE - bE^{-1}) + \left(2k^2 - k_S^2\right)(cB + dB^{-1})\right\}e^{ikx_1} = 0$$

$$\Rightarrow (2ik\eta)(aE - bE^{-1}) + \left(2k^2 - k_S^2\right)(cB + dB^{-1}) = 0$$

$$\sigma_{12}\big|_{x_2=-h} = \mu\{2\phi_{,12} + \psi_{,22} - \psi_{,11}\}_{x_2=-h}$$

$$= \mu\left\{(2ik\eta)(aE^{-1} - bE) + \left(2k^2 - k_S^2\right)(cB^{-1} + dB)\right\}e^{ikx_1} = 0$$

$$\Rightarrow (2ik\eta)(aE^{-1} - bE) + \left(2k^2 - k_S^2\right)(cB^{-1} + dB) = 0$$

$$\sigma_{22}\big|_{x_2=h} = -\mu\left\{k_S^2\phi + 2(\psi,_{12} + \phi,_{11})\right\}_{x_2=h}$$

$$= -\mu\left\{\left(k_S^2 - 2k^2\right)(aE + bE^{-1}) + 2ik\beta(cB - dB^{-1})\right\}e^{ikx_1}$$

$$= -\rho_f\omega^2 nE_f^{-1}e^{ikx_1}$$

$$\Rightarrow \left(2k^2 - k_S^2\right)(aE + bE^{-1}) - 2ik\beta(cB - dB^{-1}) + \frac{\rho_f k_S^2}{\rho}nE_f^{-1} = 0$$

$$\sigma_{22}\big|_{x_2=-h} = -\mu\left\{k_S^2\phi + 2(\psi,_{12} + \phi,_{11})\right\}_{x_2=-h}$$

$$= -\mu\left\{\left(k_S^2 - 2k^2\right)(aE^{-1} + bE) + 2ik\beta(cB^{-1} - dB)\right\}e^{ikx_1}$$

$$= -\rho_f\omega^2 mE_f^{-1}e^{ikx_1}$$

$$\Rightarrow \left(2k^2 - k_S^2\right)(aE^{-1} + bE) - 2ik\beta(cB^{-1} - dB) + \frac{\rho_f k_S^2}{\rho}mE_f^{-1} = 0$$

$$u_2\big|_{x_2=h} = \{\phi,_2 - \psi,_1\}_{x_2=h} = \{\eta(aE - bE^{-1}) - ik(cB + dB^{-1})\}e^{ikx_1} = -\eta_f nE_f^{-1}e^{ikx_1}$$

$$\Rightarrow \eta(aE - bE^{-1}) - ik(cB + dB^{-1}) + \eta_f nE_f^{-1} = 0$$

$$u_2\big|_{x_2=-h} = \{\phi,_2 - \psi,_1\}_{x_2=-h} = \{\eta(aE^{-1} - bE) - ik(cB^{-1} + dB)\}e^{ikx_1} = \eta_f mE_f^{-1}e^{ikx_1}$$

$$\Rightarrow \eta(aE^{-1} - bE) - ik(cB^{-1} + dB) - \eta_f mE_f^{-1} = 0 \qquad \textbf{(4.25)}$$

where

$$E = e^{i\eta h}$$
$$B = e^{i\beta h} \qquad \textbf{(4.26)}$$
$$E_f = e^{i\eta_f h}$$

The above six continuity conditions across the two fluid-solid interfaces can be written in matrix form

$$\begin{bmatrix} 2ik\eta E & -2ik\eta E^{-1} & \left(2k^2 - k_s^2\right)B & \left(2k^2 - k_s^2\right)B^{-1} & 0 & 0 \\ 2ik\eta E^{-1} & -2ik\eta E & \left(2k^2 - k_s^2\right)B^{-1} & \left(2k^2 - k_s^2\right)B & 0 & 0 \\ \left(2k^2 - k_s^2\right)E & \left(2k^2 - k_s^2\right)E^{-1} & -2ik\beta B & 2ik\beta B^{-1} & 0 & \frac{\rho_f k_s^2}{\rho}E_f^{-1} \\ \left(2k^2 - k_s^2\right)E^{-1} & \left(2k^2 - k_s^2\right)E & 2ik\beta B^{-1} & 2ik\beta B & \frac{\rho_f k_s^2}{\rho}E_f^{-1} & 0 \\ \eta E & -\eta E^{-1} & -ikB & -ikB^{-1} & 0 & \eta_f E_f^{-1} \\ \eta E^{-1} & -\eta E & -ikB^{-1} & -ikB & -\eta_f E_f^{-1} & 0 \end{bmatrix} \begin{Bmatrix} a \\ b \\ c \\ d \\ m \\ n \end{Bmatrix} = \begin{Bmatrix} 0 \\ 0 \\ 0 \\ 0 \\ 0 \\ 0 \end{Bmatrix}$$

(4.27)

For nonzero wave amplitudes (*a, b, c, d, m, n*), the determinant of the above 6×6 coefficient matrix must vanish. By equating the determinant of this matrix to zero the dispersion equation for the leaky Lamb wave propagation is obtained. Note that this dispersion equation gives both symmetric and antisymmetric modes. However, compared to Equation 4.21 and Equation 4.24 the determinant of the above 6×6 matrix is much more complicated. For this reason, symmetric and antisymmetric modes are computed separately from relatively simpler dispersion equations for symmetric and antisymmetric modes whenever possible.

4.4 Plane P-Wave Striking a Solid Plate Immersed in a Fluid

In Section 4.2 and Section 4.3, free Lamb wave propagation in a plate, which is in a vacuum or immersed in a fluid, has been studied by decomposing the particle motions into their symmetric and antisymmetric components. These Lamb waves are generated in the plate by some external excitations, such as a time dependent force or an elastic wave field striking the plate. In this section, the problem of a plane P-wave striking the plate at an angle θ, as shown in Chapter 1, Figure 1.37, is studied.

The pressure fields in the fluid and the potential fields in the solid are given in Chapter 1, Equation 1.229 for a plane P-wave striking a solid plate immersed in a fluid

$$
\begin{aligned}
p_i &= e^{ikx_1 - i\eta_f x_2} \\
p_R &= R \cdot e^{ikx_1 + i\eta_f x_2} \\
p_T &= T \cdot e^{ikx_1 - i\eta_f x_2} \\
\phi_D &= P_D \cdot e^{ikx_1 - i\eta_S x_2} \\
\phi_U &= P_U \cdot e^{ikx_1 + i\eta_S x_2} \\
\psi_D &= S_D \cdot e^{ikx_1 - i\beta_S x_2} \\
\psi_U &= S_U \cdot e^{ikx_1 + i\beta_S x_2}
\end{aligned}
$$

Equation 4.15 and Equation 4.16 are similar to Chapter 1, Equation 1.229; the only difference is that in Equation 1.229 one additional term (p_i) appears that corresponds to the incoming P-wave striking the plate. p_R and p_T of Equation 1.229 are similar to ϕ_{fU} and ϕ_{fL} of Equation 4.16; however, p_R and p_T are pressure fields while ϕ_{fU} and ϕ_{fL} are wave potentials in the fluid.

The relation between the pressure (p) and wave potential (ϕ) in a fluid is given in Chapter 1, Equation 1.210, $p = \rho\omega^2\phi$. It should also be mentioned that η_f, η_s, and β_s of Equation 1.229 and η_f, η, and β of Equation 4.15 and Equation 4.16 have slightly different definitions (see these equations for their definitions). The notations for wave amplitudes have also been changed in Equation 4.15 and Equation 4.16 from Equation 1.229.

Six equations that are obtained from the stress and displacement continuity conditions across the fluid-solid interfaces are given in Chapter 1, Equation 1.233a and Equation 1.233b. Note that Equation 1.233a is a system of non-homogeneous equations, while Equation 4.27 gives a system of homogeneous equations. Nonzero entries of the right-hand side vector of Equation 1.233a are due to the presence of the striking P-wave. The 6 × 6 coefficient matrix of Equation 1.233a and Equation 4.27 are similar, but these equations are not identical because the definitions of the wave potentials are slightly different in these two cases.

To obtain the identical coefficient matrix for the above two cases (in presence and in absence of the striking P-wave) the wave potentials in the solid plate and in the two fluid half-spaces are defined in the following manner. Wave potentials inside the solid plate:

$$\begin{aligned}
\phi &= (ae^{\eta x_2} + be^{-\eta x_2})e^{ikx_1} \\
\psi &= (ce^{\beta x_2} + de^{-\beta x_2})e^{ikx_1} \\
\eta &= \sqrt{k^2 - k_P^2} = -i\sqrt{k_P^2 - k^2} \\
\beta &= \sqrt{k^2 - k_S^2} = -i\sqrt{k_S^2 - k^2}
\end{aligned} \tag{4.28a}$$

Wave potentials in the lower and upper fluid half spaces:

$$\begin{aligned}
\phi_{fL} &= me^{\eta_f x_2}e^{ikx_1} \\
\phi_{fU} &= (e^{\eta_f x_2} + ne^{-\eta_f x_2})e^{ikx_1} \\
\eta_f &= \sqrt{k^2 - k_f^2} = -i\sqrt{k_f^2 - k^2} = -ik_f\cos\theta; \qquad k = k_f\sin\theta
\end{aligned} \tag{4.28b}$$

The extra term in the expression of ϕ_{fU} in Equation 4.28b in comparison to that in Equation 4.16 represents the incoming P-wave that strikes the plate. The reflected and transmitted P-wave amplitudes in the upper and lower fluid half spaces are denoted by n and m, respectively. Applying the continuity conditions across the two fluid-solid interfaces, the following equations are obtained:

$$\sigma_{12}\big|_{x_2=h}=0 \quad \Rightarrow (2ik\eta)(aE-bE^{-1})+\left(2k^2-k_S^2\right)(cB+dB^{-1})=0$$

$$\sigma_{12}\big|_{x_2=-h}=0 \quad \Rightarrow (2ik\eta)(aE^{-1}-bE)+\left(2k^2-k_S^2\right)(cB^{-1}+dB)=0$$

$$\sigma_{22}\big|_{x_2=h}=-\mu\left\{\left(k_S^2-2k^2\right)(aE+bE^{-1})+2ik\beta(cB-dB^{-1})\right\}e^{ikx_1}=-\rho_f\omega^2\left(E_f+nE_f^{-1}\right)e^{ikx_1}$$

$$\Rightarrow \left(2k^2-k_S^2\right)(aE+bE^{-1})-2ik\beta(cB-dB^{-1})+\frac{\rho_f k_S^2}{\rho}\left(E_f+nE_f^{-1}\right)=0$$

$$\sigma_{22}\big|_{x_2=-h}=-\mu\left\{\left(k_S^2-2k^2\right)(aE^{-1}+bE)+2ik\beta(cB^{-1}-dB)\right\}e^{ikx_1}=-\rho_f\omega^2 mE_f^{-1}e^{ikx_1}$$

$$\Rightarrow \left(2k^2-k_S^2\right)(aE^{-1}+bE)-2ik\beta(cB^{-1}-dB)+\frac{\rho_f k_S^2}{\rho}mE_f^{-1}=0$$

$$u_2\big|_{x_2=h}=\{\phi_{,2}-\psi_{,1}\}_{x_2=h}=\{\eta(aE-bE^{-1})-ik(cB+dB^{-1})\}e^{ikx_1}=\eta_f\left(E_f-nE_f^{-1}\right)e^{ikx_1}$$

$$\Rightarrow \eta(aE-bE^{-1})-ik(cB+dB^{-1})-\eta_f\left(E_f-nE_f^{-1}\right)=0$$

$$u_2\big|_{x_2=-h}=\{\phi_{,2}-\psi_{,1}\}_{x_2=-h}=\{\eta(aE^{-1}-bE)-ik(cB^{-1}+dB)\}e^{ikx_1}=\eta_f mE_f^{-1}e^{ikx_1}$$

$$\Rightarrow \eta(aE^{-1}-bE)-ik(cB^{-1}+dB)-\eta_f mE_f^{-1}=0$$

(4.29)

Definitions of E, B, and E_f are given in Equation 4.26. Putting these six equations in a matrix form we get

$$\begin{bmatrix} 2ik\eta E & -2ik\eta E^{-1} & \left(2k^2-k_S^2\right)B & \left(2k^2-k_S^2\right)B^{-1} & 0 & 0 \\ 2ik\eta E^{-1} & -2ik\eta E & \left(2k^2-k_S^2\right)B^{-1} & \left(2k^2-k_S^2\right)B & 0 & 0 \\ \left(2k^2-k_S^2\right)E & \left(2k^2-k_S^2\right)E^{-1} & -2ik\beta B & 2ik\beta B^{-1} & 0 & \frac{\rho_f k_S^2}{\rho}E_f^{-1} \\ \left(2k^2-k_S^2\right)E^{-1} & \left(2k^2-k_S^2\right)E & 2ik\beta B^{-1} & 2ik\beta B & \frac{\rho_f k_S^2}{\rho}E_f^{-1} & 0 \\ \eta E & -\eta E^{-1} & -ikB & -ikB^{-1} & 0 & \eta_f E_f^{-1} \\ \eta E^{-1} & -\eta E & -ikB^{-1} & -ikB & -\eta_f E_f^{-1} & 0 \end{bmatrix}$$

$$\times \begin{Bmatrix} a \\ b \\ c \\ d \\ m \\ n \end{Bmatrix} = \begin{Bmatrix} 0 \\ 0 \\ -\frac{\rho_f k_S^2}{\rho}E_f \\ 0 \\ \eta_f E_f \\ 0 \end{Bmatrix} \tag{4.30}$$

Note that the coefficient matrices in Equation 4.27 and Equation 4.30 are identical. The only difference between these two sets of equations is in the definition of their right-hand side vectors. Two problems, defined by Equation 4.27 and Equation 4.30, are analogous to the free vibration and forced vibration problems in structural dynamics, where the right-hand side vector represents the forcing function. Note that the wave number k in Equation 4.27 is obtained by satisfying the dispersion equation; in other words, it is obtained by equating the determinant of the coefficient matrix to zero. However, in Equation 4.30 k is no longer a variable; it is determined from the striking angle of the incident P-wave (see Equation 4.28b).

For generating a Lamb wave in the plate, the wave number k in Equation 4.30 must be the solution of the Lamb wave dispersion equation. In other words, if the striking angle of the incident P-wave is such that k becomes equal to ω/c_L (c_L is the Lamb wave speed in the plate) then the Lamb wave will be generated. For a given frequency, a number of wave speeds are observed in the Lamb wave dispersion curve plot (see Figure 4.6). Which Lamb mode is generated in the plate depends on what k value corresponds to the striking angle of the P-wave, $k = k_f \sin\theta$. To generate a Lamb mode with the phase velocity c_L it is necessary to satisfy the following condition:

$$
\begin{aligned}
& k_f \sin\theta = k = \frac{\omega}{c_L} \\
& \Rightarrow \sin\theta = \frac{\omega}{c_L k_f} = \frac{c_f}{c_L} \\
& \Rightarrow \theta = \sin^{-1}\left(\frac{c_f}{c_L}\right)
\end{aligned}
\tag{4.31}
$$

Equation 4.31 gives the incident angle (θ) necessary for generating a Lamb mode with a phase velocity (c_L) in a plate immersed in a fluid that has an acoustic wave speed (c_f). Equation 4.31 is known also as Snell's law.

Figure 4.16 shows a schematic diagram for the Lamb wave generation in a plate by striking the plate with a plane P-wave. If a plane P-wave strikes the left side of the plate with an incident angle (θ) that is appropriate for generating a Lamb mode, then the Lamb mode is generated in the plate. The generated Lamb wave then propagates to the right with a velocity c_L ($=\omega/k$). Note that Equation 4.30 and Equation 4.27 govern motions on the left side (forced vibration) and right side (free vibration) of the plate, respectively. From Equation 4.31 it is obvious that only the Lamb modes that have phase velocities higher than the acoustic wave speed in the surrounding fluid can be generated in this manner. The acoustic wave speed in water is 1.48 km/sec, while in alcohol it is between 1.12 and 1.24 km/sec (see Table 1.4). Therefore to generate a Lamb mode with a phase velocity between 1.2 and 1.48 km/sec the plate must be immersed in alcohol instead of water.

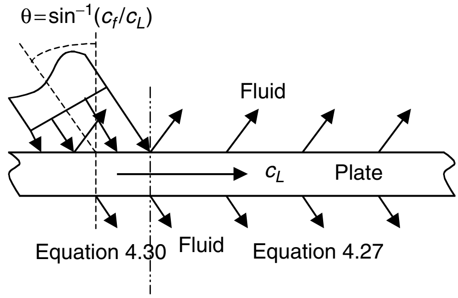

FIGURE 4.16
Lamb wave generation in a plate immersed in fluid. Equation 4.30 and Equation 4.27 govern the left side (forced vibration) and right side (free vibration) of the plate. The dashed-dotted line separates the left and right sides of the plate.

4.4.1 Plate Inspection by Lamb Waves

In the above sections we have learned how different modes of the Lamb wave can be generated in a plate by adjusting the striking angle and frequency of the incident P-wave. By placing an ultrasonic transducer at an angle relative to the plate, as shown in Figure 4.16, the required condition can be satisfied. Ultrasonic transducers generate P-waves of certain frequency. The signal frequency is determined by the natural frequency of the ceramic crystal in the transducer. The ultrasonic transducer frequency varies from 500 kHz to 10 MHz for conventional ultrasonic inspection applications. However, specially built ultrasonic transducers can generate ultrasonic signals with resonance frequency as low as 50 kHz or even lower, and as high as 100 MHz or more. In acoustic microscopy applications (discussed in Chapter 11), the signal frequency can be as high as 2 GHz, and in some applications even higher.

4.4.1.1 Generation of Multiple Lamb Modes by Narrowband and Broadband Transducers

Ultrasonic transducers that have well-defined natural frequency and always vibrate close to that frequency are called narrowband transducers. For example, a 5-MHz narrowband transducer can only generate ultrasonic waves with signal frequency equal to 5 MHz or very close to 5 MHz, say from 4.8 to 5.2 MHz. On the other hand, a broadband transducer can generate ultrasonic waves over a wide frequency range. For example, a 5-MHz broadband transducer can generate ultrasonic waves over a wide range of frequency around 5 MHz, say from 1 to 9 MHz. For generating different Lamb modes with a narrowband transducer, because it is not possible to change the signal frequency, it is necessary to change the angle of strike (θ of Figure 4.16). Note that changing θ implies changing the phase velocity (c_L) because θ and c_L are related by Equation 4.31.

Keeping the signal frequency constant and varying the incident angle implies moving along the vertical axis of the dispersion curve plots (see Figure 4.2). Lamb waves will be generated for the incident angle θ if $\theta = \sin^{-1}(\frac{c_f}{c_L})$, where c_f is the P-wave speed in the fluid and c_L is the Lamb wave speed. If we place two ultrasonic transducers, one acting as the transmitter (T) and the second one as the receiver (R) as shown in Figure 4.17a, and record the received signal strength as a function of the incident angle θ then we should get a curve as shown in Figure 4.17b. Peaks correspond to the incident angles for which a Lamb mode is generated. If the incident angle does not correspond to a Lamb mode-generating angle, then no ultrasonic energy reaches the receiver because no Lamb wave is generated and the directly reflected beam energy is mostly confined between the lines AB and CD (see Figure 4-17a). This directly reflected beam is also called a specularly reflected beam.

If the transducers are broadband type, then the signal frequency can be changed while maintaining a constant inclination angle of the transducers. Fixed inclination angle means constant phase velocity. Therefore, in this case,

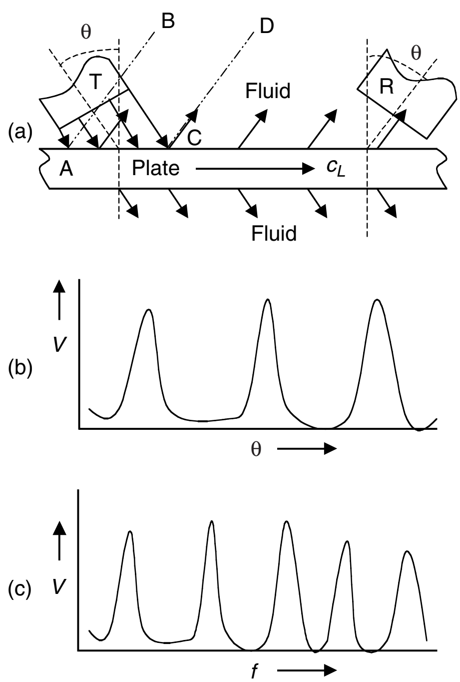

FIGURE 4.17
(a) Transmitter (T) and receiver (R) for generating and receiving Lamb waves in a plate; (b) received signal amplitude voltage as a function of the incident angle (peaks indicate generation of Lamb modes); (c) received signal amplitude voltage as a function of the signal frequency (peaks indicate generation of Lamb modes).

as we change frequency we move horizontally in the dispersion curve plot (see Figure 4.3). In this manner, received signal voltage versus frequency curve or $V(f)$ curve is generated (see Figure 4.17c). In this case, peaks will be observed at frequencies for which Lamb modes are generated. If the signal frequency does not correspond to a Lamb wave generation frequency, then the received signal strength should be close to zero; the reflected signal energy in this case remains mostly confined between lines AB and CD and does not reach the receiver.

4.4.1.2 Nondestructive Inspection of Large Plates

Following the technique presented above it is possible to generate multiple Lamb modes in a plate. In this section the interaction between Lamb modes and internal defects in a plate is investigated. Ghosh and Kundu (1998) have shown that strong and consistent Lamb modes can be generated in large plates by placing the transducers in small conical water containers attached to the plate as shown in Figure 4.18, instead of immersing the entire plate in a big water tank. The bottomless containers are attached to the plate in a watertight manner such that the water is in direct contact with the plate. Alleyne and Cawley (1992) also avoided immersing the entire plate in a water tank and generated Lamb waves in the plate by placing inclined transducers in cylindrical holes filled with water. In both of these cases water coupling is provided between the transducers and the plate — in one case the cylindrical water column, and in the other case the conical water volume provides this coupling. Between these two, conical water volumes are found to produce more consistent signals.

Using the transmitter-receiver arrangement shown in Figure 4.18, Lamb waves are generated in a 0.39-in. (9.9-mm) thick steel plate. Details of this experiment with steel and aluminum plates are given in Ghosh et al. (1998). Some experimental results generated for the steel plate are given in this chapter. Plate length and width are 60-in. (1524 mm) and 3.5-in. (88.9 mm), respectively. A 2-in. (50.8 mm) long hole of 0.125 in. (3.175 mm) diameter is drilled into the central plane of the plate parallel to its surface to artificially produce an internal defect (see Figure 4.19).

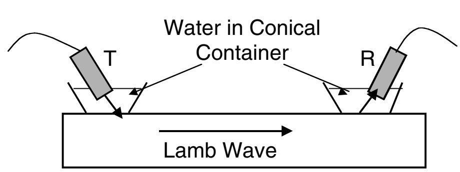

FIGURE 4.18
Transducers in conical water containers. (Source: From Ghosh, T. and Kundu, T., *J. Acoust. Soc. Am.*, 104, 1498–1502, 1998. With permission.)

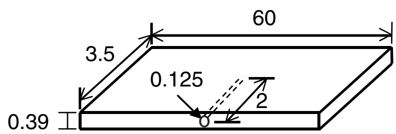

FIGURE 4.19
Steel plate with a hole. All dimensions are in inches. (Source: From Ghosh, T. et al., *Ultrasonics*, 36, 791–801, 1998. Reprinted with permission from Elsevier.)

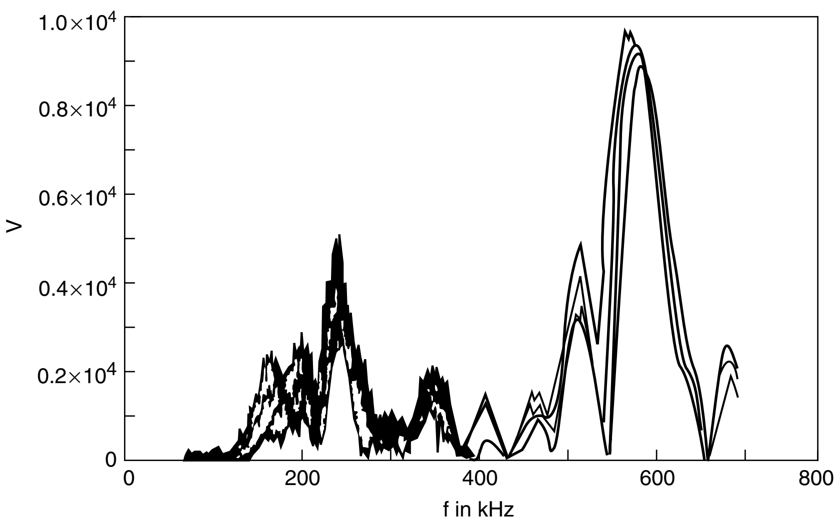

FIGURE 4.20
Four $V(f)$ curves generated by the setup of Figure 4.18 over the defect-free region of the plate of Figure 4.19 for 26° incident angle. (Source: From Ghosh, T. et al., *Ultrasonics*, 36, 791–801, 1998. Reprinted with permission from Elsevier.)

Figure 4.20 shows the $V(f)$ curves for the specimen of Figure 4.19 over the nondefective region (region that does not contain the hole) for 26° angle of incidence. The distance between the transmitter and the receiver for all experimental results is 12 in. (304.8 mm). This incident angle corresponds to a phase velocity of 3.4 km/sec, derived from Snell's law (Equation 4.31) with $c_f = 1.49$ km/sec.

The four curves of Figure 4.20 correspond to four different experiments carried out on four regions of the plate at four different times. They show some difference because at low frequency the signal is not well collimated. Directivity of the signal is controlled by the inclination of the transducer and relative positions of the inclined transducers with respect to the bottom section of the conical container. During different experiments the transducer position relative to the bottom section of the conical container slightly changes, giving rise to the variations in the $V(f)$ curves even when the plate dimension and its properties do not change. One can also see that the noise level is higher at lower frequencies because the signal is more scattered. In other words, its directivity is poorer at lower frequencies.

In spite of this noise and the variations of $V(f)$ curves from experiment to experiment, it is easy to observe two strong and distinguishable peaks — one near 230 kHz and the second one near 600 kHz in Figure 4.20. Another peak near 540 kHz is also observed in the $V(f)$ plot, but it is much weaker than the peak near 600 kHz.

Theoretical dispersion curves for this specimen are computed and plotted in Figure 4.21. The experimental points (frequencies at which peaks occur in Figure 4.20 are plotted along with the theoretical curves in Figure 4-21 to identify the Lamb modes that correspond to the two peaks of Figure 4.20. The strong peaks of the $V(f)$ curves have been denoted by the * symbol while the weak peaks are denoted by the + symbol in Figure 4.21. Since peak frequencies change from experiment to experiment, the experimental frequency scattering range (instead of a single value) is shown in Table 4.1 and on the dispersion curve plot (Figure 4.21) for every mode. After plotting the experimental points on the theoretical dispersion curves in Figure 4.21, it is clearly seen that the two peaks of Figure 4.20 correspond to the 0th-order symmetric (S_0) and first-order antisymmetric (A_1) modes.

$V(f)$ curves for the defective region are shown in Figure 4.22. For these plots the transmitter and the receiver are placed on opposite sides of the hole. The Lamb wave generated in the plate by the transmitter must propagate through the plate region containing the hole, before reaching the receiver. The four curves of Figure 4.22 are for four different experiments carried out at four different locations, but the defect (the hole) is located between the transmitter and the receiver in all four cases. Note that the S_0 mode has been

TABLE 4.1

Lamb Mode Peaks for 26° Incidence Angle (See Figure 4.20 and Figure 4.22)

Mode	**S_0**		**A_1**	
Frequency Range (kHz)	**224–241**		**588–617**	
Amplitude Information	**Non-def.**	**Def.**	**Non-def.**	**Def.**
Min.	3333	203	8782	8637
Max.	4782	1534	9797	9536
Average amp.	3713	785.5	9116	9034
Percentage change		–78.8		–0.89

Source: From Ghosh, T. et al., *Ultrasonics*, 36, 791–801, 1998. Reprinted with permission from Elsevier.

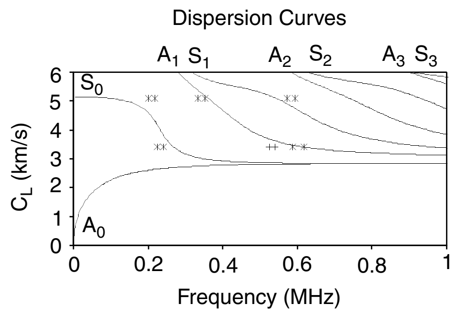

FIGURE 4.21
Theoretical dispersion curve for a 0.39-in. thick steel plate (c_P = 5.72 km/sec, c_S = 3.05 km/sec, ρ = 7.9 g/cm^3). Experimental points are shown by * and + symbols, for strong and weak peaks, respectively.

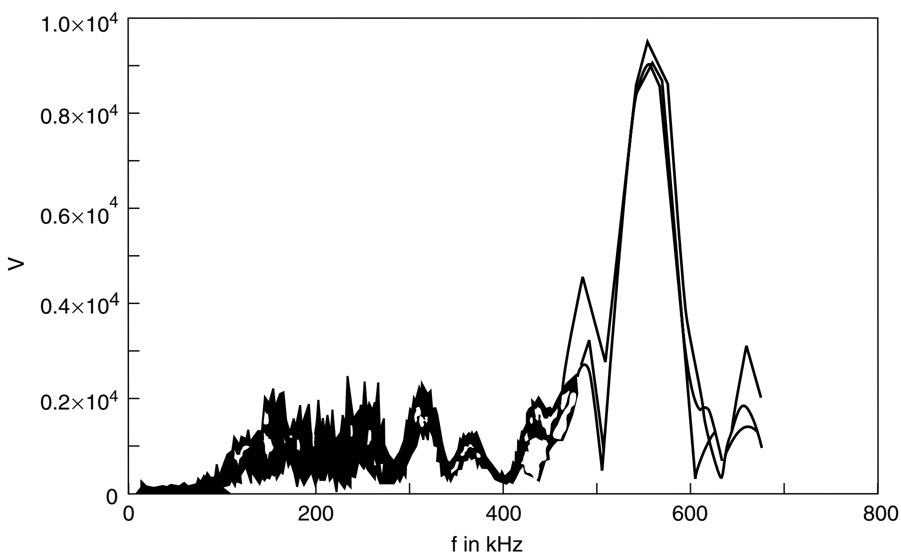

FIGURE 4.22
V(*f*) curves over the defective region of the steel plate for 26° angle of incidence. (Source: From Ghosh, T. et al., *Ultrasonics*, 36, 791–801, 1998. Reprinted with permission from Elsevier.)

strongly affected, almost disappeared, by the defect (hole), but the A_1 mode is quite insensitive to the defect.

Results from Figures 4.20 and 4.22 are summarized in Table 4.1. In this table the row identified as Frequency range describes the frequency range in which the Lamb wave peaks are observed for all four experiments. The rows identified as Min, Max, and Average amp. show the minimum, maximum, and average values of the four peaks corresponding to the four experimental curves over the nondefective (Non-def column) and defective regions (Def column). The percentage change of the average amplitude of the S_0 mode (see Table 4.1) due to the presence of the defect is –78.8%, where the minus sign implies a reduction in the peak amplitude. The change of the A_1 mode due to the defect is only –0.89%.

The computed stress patterns inside the plate for phase velocities varying from 3 to 5 km/sec for the S_0 and A_1 modes are shown in Figure 4.23 and Figure 4.24, respectively. The depth dimension is normalized with respect to the total plate thickness. In these figures, σ_{11}, σ_{22}, and σ_{13} stand for the horizontal normal stress, vertical normal stress, and the shear stress component, respectively. The x_1- and x_2-axes are located parallel and perpendicular to the plate surface, respectively. For the S_0 mode (Figure 4.23) at 3.4 km/sec phase velocity, the normal stress σ_{22} is large near the central plane of the plate (depth = 0.5), but σ_{12} is 0 there. In presence of the hole, these stress components are altered because the normal and shear stress components at the free surface of the hole must vanish; as a result, the propagating mode is affected. For the A_1 mode (Figure 4.24), normal stresses (σ_{11} and σ_{22}) are 0 at the central plane of the plate, and σ_{12} has a nonzero value at the central plane of the plate (σ_{12} is 0 in the entire plate near the phase velocity of 4 km/sec). However, since the two normal stress components are zero at the central plane, the defect has a smaller effect on the A_1 mode.

For 17° incident angle (phase velocity from Snell's law is 5.1 km/sec) strong peaks in the V(f) curves for the plate without any defect are observed near 210, 340, and 580 kHz (Figure 4.25). These correspond to S_0, A_1, and S_1 modes, respectively (see Figure 4.21). In Figure 4.21 one can notice that theoretical A_1 and S_1 modes are very close to the experimental values. The experimental points corresponding to the S_0 mode are not very close to the theoretical S_0 curve. This is due to the fact that the transducer response below 200 kHz is very weak (the transducers have a central frequency of 500 kHz). Second, although the transducer is inclined at 17° the 200-kHz signal that generated the Lamb wave in the plate probably did not strike the plate exactly at 17°, inclination but at a slightly larger angle. This makes the corresponding phase velocity smaller (from Snell's law, Equation 4.31) and thus bringing the experimental point closer to the theoretical curve.

The four $V(f)$ curves for the defective region are shown in Figure 4.26. One can clearly see that due to the presence of the defect S_0 and S_1 modes change significantly, but the A_1 mode is not very sensitive to the defect. This result is summarized in Table 4.2. The amplitude of the S_0 mode is reduced by more than 72% due to the defect; this reduction for the S_1 mode is more than 64%, while the reduction of the A_1 mode is only 3.5%. The justification for the symmetric modes being more sensitive to the defect is the same as before. Figure 4.23 shows that for the S_0 mode, for 5.1 km/sec phase velocity σ_{11} is very large and σ_{22} is moderately large at the central plane. As a result, this mode has been significantly affected (–72.79%) by the presence of the defect at the central plane of the plate. Figure 4.27 shows that, for the S_1 mode, for

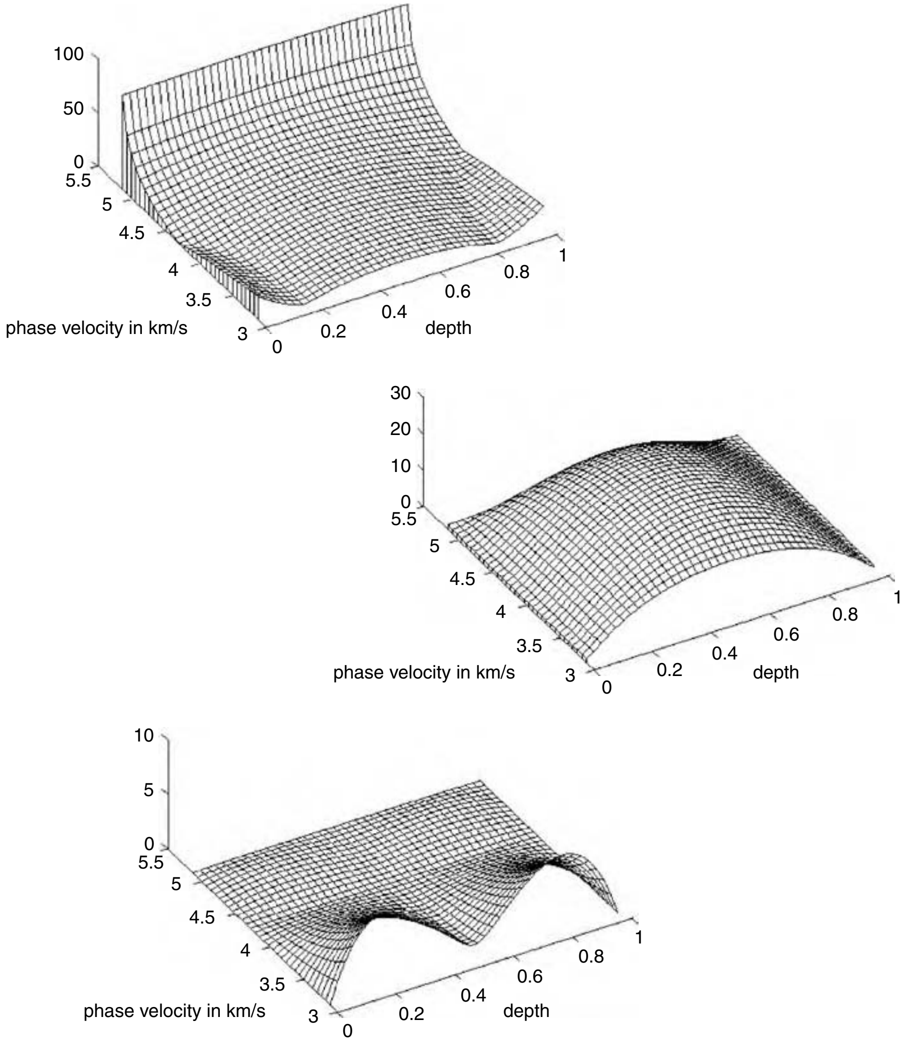

FIGURE 4.23
Amplitude variations of horizontal normal stress (σ_{11}, top figure), vertical normal stress (σ_{22}, middle figure), and shear stress (σ_{12}, bottom figure) inside the steel plate for S_0 mode, as the phase velocity varies from 3.1 to 5.1 km/sec; depth is 0 for the top of the plate and 1 for the bottom of the plate. Dispersion curves for this steel plate are shown in Figure 4.21.

5.1 km/sec phase velocity σ_{11} is small, but σ_{22} is large at the central plane of the plate. As a result, this mode has also been strongly affected (–64.48%) by the defect, although to a lesser degree than the S_0 mode (–72.8%). The A_1 mode on the other hand makes the shear stress component σ_{12} nonzero, but the normal

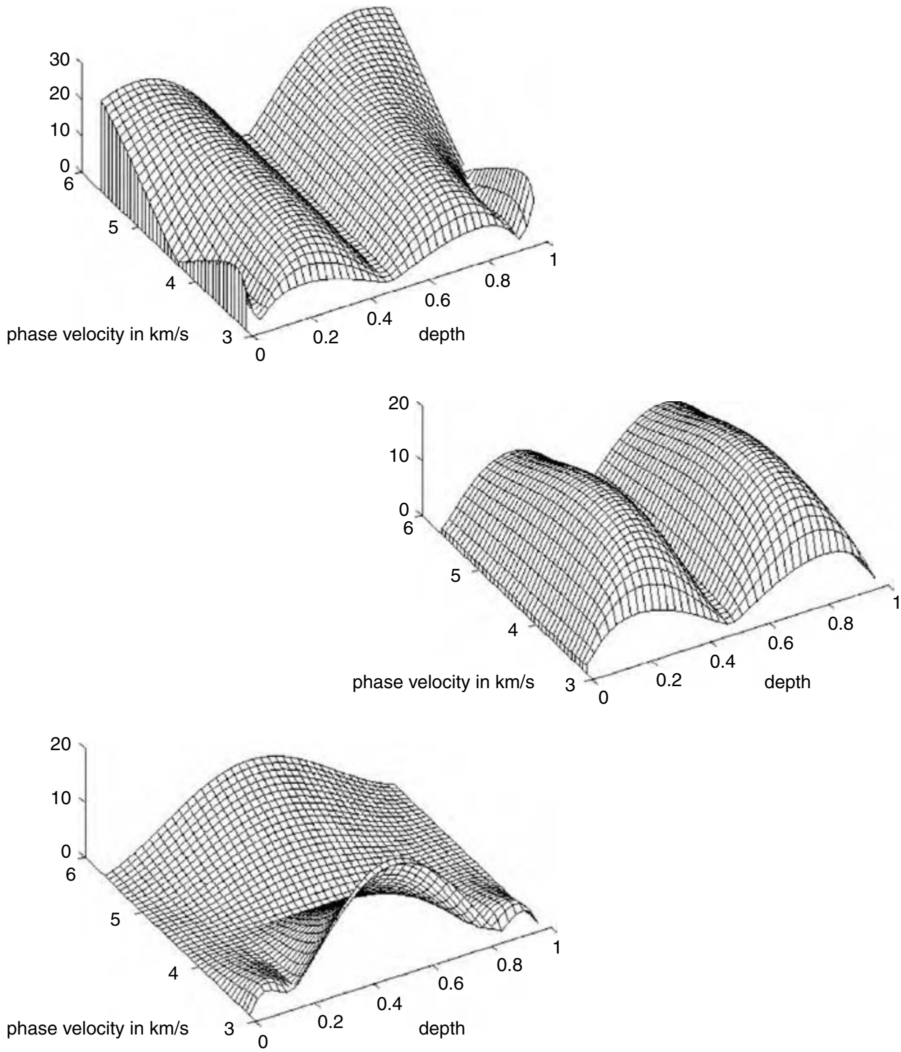

FIGURE 4.24
Amplitude variations of horizontal normal stress (σ_{11}, top figure), vertical normal stress (σ_{22}, middle figure), and shear stress (σ_{12}, bottom figure) inside the steel plate for A_1 mode as the phase velocity varies from 3.1 to 5.6 km/sec; depth is 0 for the top of the plate, and 1 for the bottom of the plate. Dispersion curves for this steel plate are shown in Figure 4.21.

stress components σ_{11} and σ_{22} are zero at the central plane (Figure 4.24); however, although σ_{12} is nonzero, it is small at the central plane for 5.1 km/sec phase velocity; this mode is not significantly affected by the presence of the hole (only –3.5% variation).

TABLE 4.2

Lamb Mode Peaks for 17° Incidence Angle (See Figure 4.25 and Figure 4.26)

Mode	S_0		A_1		S_1	
Frequency Range (kHz)	201–219		334–352		573–595	
Amplitude Information	Non- def.	Def.	Non-def.	Def.	Non-def.	Def.
Min.	2523	133	1294	1469	3504	950
Max.	4597	1544	2169	2335	4013	1830
Average amp.	3161	860	1625	1568	3714	1319
Percentage change		–72.79		–3.5		–64.48

Source: From Ghosh, T. et al., *Ultrasonics*, 36, 791–801, 1998. Reprinted with permission from Elsevier.

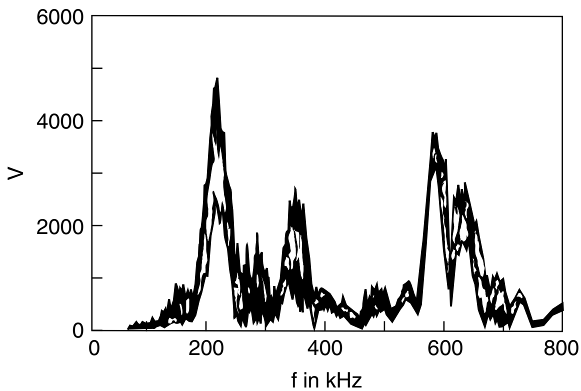

FIGURE 4.25
V(*f*) curves for the defect-free region of the plate, for 17° angle of incidence. (Source: From Ghosh, T. et al., *Ultrasonics*, 36, 791–801, 1998. Reprinted with permission from Elsevier.)

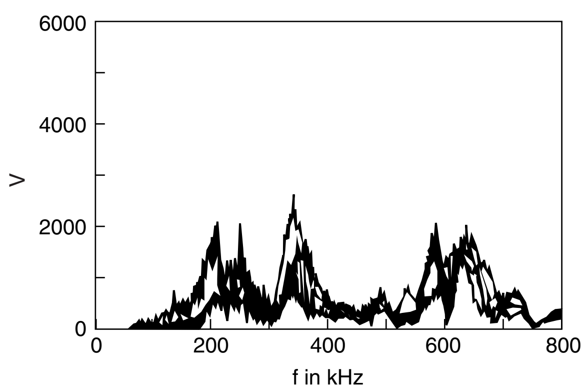

FIGURE 4.26
V(*f*) curves over the defective region of the plate for 17° angle of incidence. (Source: From Ghosh, T. et al., *Ultrasonics*, 36, 791–801, 1998. Reprinted with permission from Elsevier.)

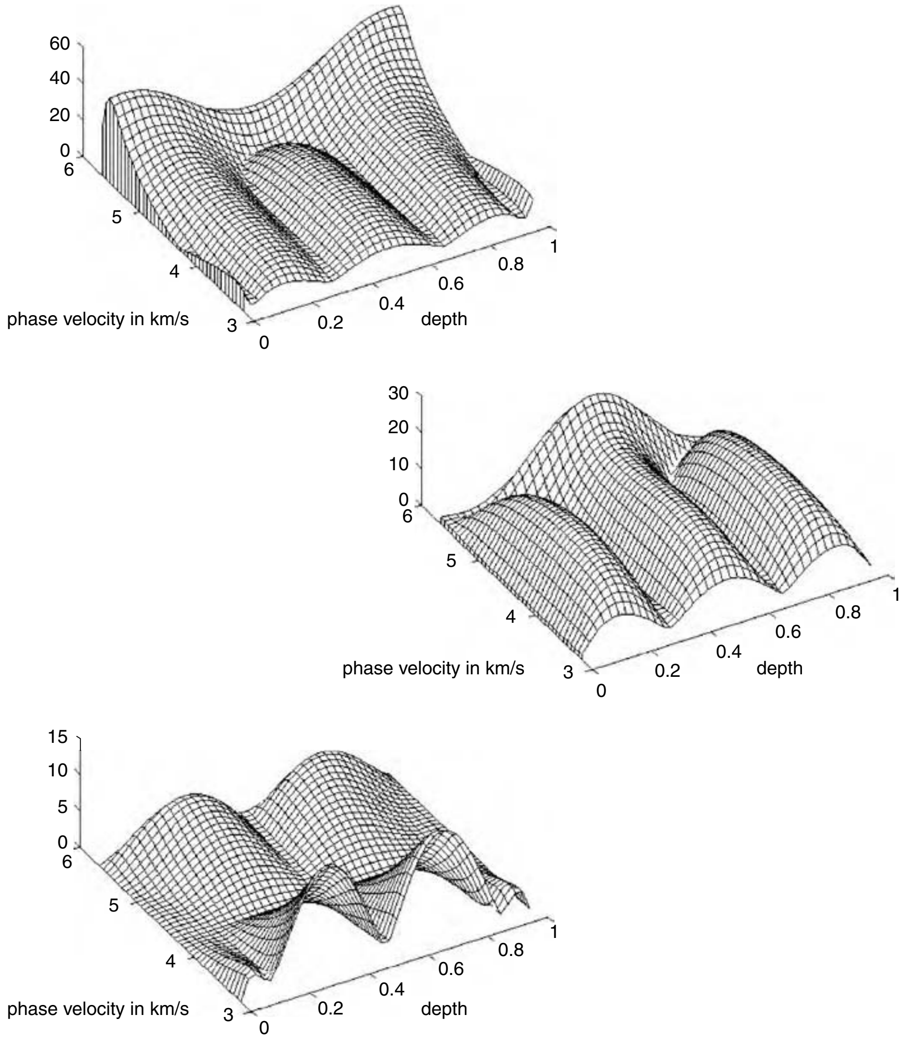

FIGURE 4.27
Amplitude variations of horizontal normal stress (σ_{11}, top figure), vertical normal stress (σ_{22}, middle figure), and shear stress (σ_{12}, bottom figure) inside the steel plate for S_1 mode, as the phase velocity varies from 3.1 to 5.6 km/sec; the depth is 0 for the top of the plate, and 1 for the bottom of the plate. Dispersion curves for this steel plate are shown in Figure 4.21.

4.5 Guided Waves in Multilayered Plates

So far we have analyzed Lamb wave propagation in a homogeneous isotropic plate in a vacuum or immersed in a fluid. In this section, the guided wave propagation in a multilayered solid plate is analyzed. Three problems that are considered here are:

1. Free vibration of a multilayered solid plate in a vacuum
2. Free vibration of a multilayered solid plate immersed in a fluid
3. Forced vibration of a multilayered solid plate immersed in a fluid — a plane P-wave propagating through the fluid half-space strikes the fluid-solid interface, creating the forcing excitation

Geometries of these three problems are shown in Figure 4.28.

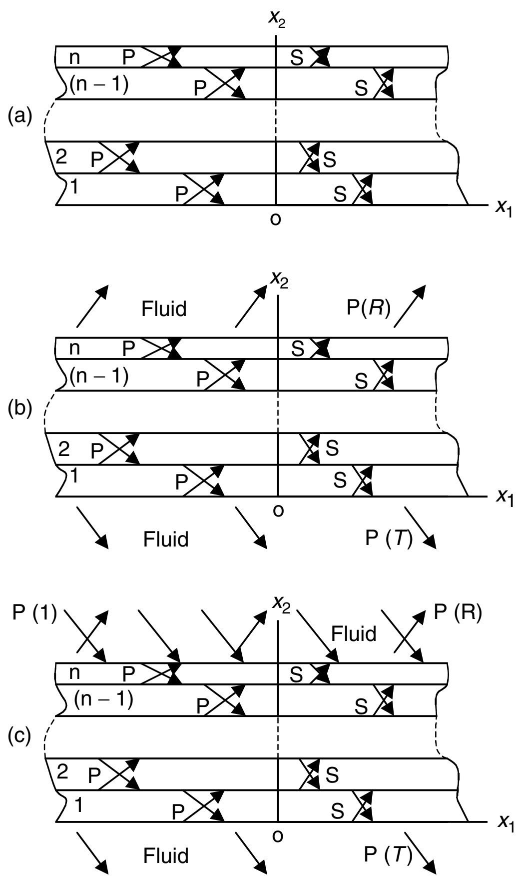

FIGURE 4.28
Guided wave propagation through the *n*-layered plate (a) in a vacuum, (b) in a fluid, and (c) the plate immersed in a fluid is struck by a downward P-wave of amplitude 1.

4.5.1 *n*-Layered Plate in a Vacuum

The problem geometry is shown in Figure 4.28a. The n number of layers of thickness $h_1, h_2, h_3, \ldots h_n$ are perfectly bonded (no slippage condition) along the $(n-1)$ interfaces at $x_2 = y_1, y_2, y_3 \ldots y_{n-1}$ where $y_1 = h_1$, $y_2 = h_1 + h_2$, $y_3 = h_1 + h_2 + h_3$, and, $y_{n-1} = h_1 + h_2 + h_3 + \ldots + h_{n-1}$. Therefore, the displacement components (u_1 and u_2), and the normal and shear stress components (σ_{22} and σ_{12}) across every interface must be continuous. In addition, normal and shear stress components at the two boundary surfaces at $x_2 = y_1 = h_1$, and $x_2 = y_n = h_1 + h_2 + h_3 + \ldots + h_n$ must vanish because the boundaries must be stress free when the plate is in vacuum. Thus, it is necessary to solve this boundary value problem, subjected to these boundary conditions and continuity conditions across the interface.

The governing equation inside of a general mth layer can be satisfied by considering upward and downward P- and S-waves in that layer. Note that the subscript m stands for the mth layer.

$$
\begin{aligned}
\phi_m &= \left\{a_m e^{-i\eta_m(x_2-y_{m-1})} + b_m e^{i\eta_m(x_2-y_{m-1})}\right\}e^{ikx_1} \\
\psi_m &= \left\{c_m e^{-i\beta_m(x_2-y_{m-1})} + d_m e^{i\beta_m(x_2-y_{m-1})}\right\}e^{ikx_1} \\
\eta_m &= \sqrt{k_{Pm}^2 - k^2} = i\sqrt{k^2 - k_{Pm}^2} \\
\beta_m &= \sqrt{k_{Sm}^2 - k^2} = i\sqrt{k^2 - k_{Sm}^2}
\end{aligned}
\quad (4.32)
$$

where a_m, b_m, c_m, and d_m represent wave amplitudes for the downward and upward P- and S-waves in the layer; k_{Pm} ($= \omega/c_{Pm}$) and k_{Sm} ($= \omega/c_{Sm}$) are P- and S-wave numbers, respectively. The exponential term is defined such that the phase term becomes zero at the lower interface of the layer. Note that the phase of the exponential terms can be equated to zero at any level y_p simply by replacing y_{m-1} by y_p. Real and imaginary components of a_m, b_m, c_m, and d_m are automatically adjusted during the satisfaction of continuity and boundary conditions.

Stress and displacement components at the top ($x_2 = y_m$) and bottom ($x_2 = y_{m-1}$) of the layer can be defined as:

$$
\begin{aligned}
\sigma_{12}\big|_{x_2=y_m} &= \mu_m\{2\phi_{m,12} + \psi_{m,22} - \psi_{m,11}\}_{x_2=y_m} \\
&= \mu_m\left\{2k\eta_m\left(a_m E_m^{-1} - b_m E_m\right) + \left(2k^2 - k_{Sm}^2\right)\left(c_m B_m^{-1} + d_m B_m\right)\right\}e^{ikx_1} \\
\sigma_{12}\big|_{x_2=y_{m-1}} &= \mu_m\{2\phi_{m,12} + \psi_{m,22} - \psi_{m,11}\}_{x_2=y_{m-1}} \\
&= \mu_m\left\{2k\eta_m(a_m - b_m) + \left(2k^2 - k_{Sm}^2\right)(c_m + d_m)\right\}e^{ikx_1}
\end{aligned}
$$

$$
\begin{aligned}
\sigma_{22}\big|_{x_2=y_m} &= -\mu_m\left\{k_{Sm}^2\phi_m + 2(\psi_{m,12} + \phi_{m,11})\right\}_{x_2=y_m} \\
&= -\mu_m\left\{\left(k_{Sm}^2 - 2k^2\right)\left(a_m E_m^{-1} + b_m E_m\right) + 2k\beta_m\left(c_m B_m^{-1} - d_m B_m\right)\right\}e^{ikx_1} \\
\sigma_{22}\big|_{x_2=y_{m-1}} &= -\mu_m\left\{k_{Sm}^2\phi_m + 2(\psi_{m,12} + \phi_{m,11})\right\}_{x_2=y_{m-1}} \\
&= -\mu_m\left\{\left(k_{Sm}^2 - 2k^2\right)(a_m + b_m) + 2k\beta_m(c_m - d_m)\right\}e^{ikx_1} \\
u_2\big|_{x_2=y_m} &= \{\phi_{m,2} - \psi_{m,1}\}_{x_2=y_m} = \left\{-i\eta_m\left(a_m E_m^{-1} - b_m E_m\right) - ik\left(c_m B_m^{-1} + d_m B_m\right)\right\}e^{ikx_1} \\
u_2\big|_{x_2=y_{m-1}} &= \{\phi_{m,2} - \psi_{m,1}\}_{x_2=y_{m-1}} = \{-i\eta_m(a_m - b_m) - ik(c_m + d_m)\}e^{ikx_1} \\
u_1\big|_{x_2=y_m} &= \{\phi_{m,1} + \psi_{m,2}\}_{x_2=y_m} = \left\{ik\left(a_m E_m^{-1} + b_m E_m\right) + i\eta_m\left(-c_m B_m^{-1} + d_m B_m\right)\right\}e^{ikx_1} \\
u_1\big|_{x_2=y_{m-1}} &= \{\phi_{m,1} + \psi_{m,2}\}_{x_2=y_{m-1}} = \left\{ik(a_m + b_m) + i\eta_m(-c_m + d_m)\right\}e^{ikx_1}
\end{aligned}
\tag{4.33}
$$

where

$$
\begin{aligned}
E_m &= e^{i\eta_m h_m} \\
B_m &= e^{i\beta_m h_m}
\end{aligned}
\tag{4.34}
$$

From Equation 4.33, displacement and stress components at the top and bottom of the mth layer can be written in terms of the wave amplitudes in the following matrix form:

$$
\begin{Bmatrix} u_1 \\ u_2 \\ \sigma_{22} \\ \sigma_{12} \end{Bmatrix}_{x_2=y_m} =
\begin{bmatrix}
ikE_m^{-1} & ikE_m & -i\eta_m B_m^{-1} & i\eta_m B_m \\
-i\eta_m E_m^{-1} & i\eta_m E_m & -ikB_m^{-1} & -ikB_m \\
\mu_m\left(2k^2 - k_{Sm}^2\right)E_m^{-1} & \mu_m\left(2k^2 - k_{Sm}^2\right)E_m & -2k\mu_m\beta_m B_m^{-1} & 2k\mu_m\beta_m B_m \\
2k\mu_m\eta_m E_m^{-1} & -2k\mu_m\eta_m E_m & \mu_m\left(2k^2 - k_{Sm}^2\right)B_m^{-1} & \mu_m\left(2k^2 - k_{Sm}^2\right)B_m
\end{bmatrix}
\begin{Bmatrix} a_m \\ b_m \\ c_m \\ d_m \end{Bmatrix}
\tag{4.35a}
$$

and

$$
\begin{Bmatrix} u_1 \\ u_2 \\ \sigma_{22} \\ \sigma_{12} \end{Bmatrix}_{x_2=y_{m-1}} =
\begin{bmatrix}
ik & ik & -i\eta_m & i\eta_m \\
-i\eta_m & i\eta_m & -ik & -ik \\
\mu_m\left(2k^2 - k_{Sm}^2\right) & \mu_m\left(2k^2 - k_{Sm}^2\right) & -2k\mu_m\beta_m & 2k\mu_m\beta_m \\
2k\mu_m\eta_m & -2k\mu_m\eta_m & \mu_m\left(2k^2 - k_{Sm}^2\right) & \mu_m\left(2k^2 - k_{Sm}^2\right)
\end{bmatrix}
\begin{Bmatrix} a_m \\ b_m \\ c_m \\ d_m \end{Bmatrix}
\tag{4.35b}
$$

Equation 4.35a and Equation 4.35b can be rewritten as

$$\{S_m\} = [G_m]\{C_m\} \tag{4.36a}$$

$$\{S_{m-1}\} = [H_m]\{C_m\} \tag{4.36b}$$

where $\{S_m\}$ and $\{S_{m-1}\}$ are 4×1 stress-displacement vectors at $x_2 = y_m$ and y_{m-1}, respectively, as given on the left-hand sides of Equation 4.35; $\{C_m\}$ is the 4×1 coefficient vector, $[a_m \;\; b_m \;\; c_m \;\; d_m]^T$, and $[G_m]$, $[H_m]$ are 4×4 square matrices given on the right-hand sides of Equation 4.35a and Equation 4.35b, respectively.

From Equation 4.36 we can write:

$$\{S_m\} = [G_m]\{C_m\} = [G_m][H_m]^{-1}\{S_{m-1}\} = [A_m]\{S_{m-1}\} \tag{4.37}$$

Equation 4.37 relates the stress-displacement components at the top and bottom of the mth layer. The matrix $[A_m](=[G_m][H_m]^{-1})$ is known as the Layer matrix or Propagator matrix (Thomson, 1950; Haskell, 1953; Kennett, 1983; Kundu and Mal, 1985).

Similarly, for the $m + 1$st layer it is possible to write

$$\{S_{m+1}\} = [G_{m+1}]\{C_{m+1}\} \tag{4.38a}$$

$$\{S_m\} = [H_{m+1}]\{C_{m+1}\} \tag{4.38b}$$

$$\{S_{m+1}\} = [A_{m+1}]\{S_m\} \tag{4.38c}$$

Note that from the displacement and stress continuity conditions across the interface at $x_2 = y_m$, $\{S_m\}$ of Equation 4.37 and Equation 4.38 must be identical. Therefore,

$$\{S_{m+1}\} = [A_{m+1}]\{S_m\} = [A_{m+1}][A_m]\{S_{m-1}\} \tag{4.39}$$

In this manner, the stress-displacement vector at the top boundary can be related to that at the bottom boundary:

$$\{S_n\} = [A_n][A_{n-1}][A_{n-2}]\ldots[A_2][A_1]\{S_0\} = [J]\{S_0\} \tag{4.40}$$

In Equation 4.40 $[J]$ is a 4×4 matrix obtained by multiplying n number of layer matrices. Equation 4.40 is written below in expanded matrix form and the stress-free boundary conditions are enforced. Unknown displacement components at the top and bottom boundaries are denoted as U_n, V_n, U_0, and V_0, as shown below.

$$\begin{Bmatrix} u_1 \\ u_2 \\ \sigma_{22} \\ \sigma_{12} \end{Bmatrix}_{x_2=y_n} = \begin{bmatrix} J_{11} & J_{12} & J_{13} & J_{14} \\ J_{21} & J_{22} & J_{23} & J_{24} \\ J_{31} & J_{32} & J_{33} & J_{34} \\ J_{41} & J_{42} & J_{43} & J_{44} \end{bmatrix} \begin{Bmatrix} u_1 \\ u_2 \\ \sigma_{22} \\ \sigma_{12} \end{Bmatrix}_{x_2=y_0}$$
$$\Rightarrow \begin{Bmatrix} U_n \\ V_n \\ 0 \\ 0 \end{Bmatrix} = \begin{bmatrix} J_{11} & J_{12} & J_{13} & J_{14} \\ J_{21} & J_{22} & J_{23} & J_{24} \\ J_{31} & J_{32} & J_{33} & J_{34} \\ J_{41} & J_{42} & J_{43} & J_{44} \end{bmatrix} \begin{Bmatrix} U_0 \\ V_0 \\ 0 \\ 0 \end{Bmatrix} \tag{4.41}$$

From Equation 4.41, four algebraic equations with four unknowns, U_n, V_n, U_0, and V_0, can be written in the following form:

$$\begin{bmatrix} -1 & 0 & J_{11} & J_{12} \\ 0 & -1 & J_{21} & J_{22} \\ 0 & 0 & J_{31} & J_{32} \\ 0 & 0 & J_{41} & J_{42} \end{bmatrix} \begin{Bmatrix} U_n \\ V_n \\ U_0 \\ V_0 \end{Bmatrix} = \begin{Bmatrix} 0 \\ 0 \\ 0 \\ 0 \end{Bmatrix} \tag{4.42}$$

If the Lamb wave propagates through the plate, then the displacement components at the top and bottom boundaries should not be equal to zero; in other words, there should be a nontrivial solution of the above system of equations. Therefore the determinant of the coefficient matrix must be zero, as shown below:

$$J_{31}J_{42} - J_{32}J_{41} = 0 \tag{4.43}$$

Equation 4.43 is the dispersion equation for the Lamb wave propagation through the n-layered plate in a vacuum (see Figure 4.28a).

By assigning a nonzero value to one of the four unknown quantities, U_n, V_n, U_0, and V_0, the remaining three can be obtained from Equation 4.43. Then the stress-displacement vector $\{S_m\}$ can be computed at any interface $x_2 = y_m$ using the relation $\{S_m\} = [A_m][A_{m-1}]\cdots[A_2][A_1]\{S_0\}$. To obtain the wave amplitudes inside the mth layer Equation 4.36 can be used. In this manner a_m, b_m, c_m, and d_m are obtained; then the stress and displacement variations (mode shapes) inside the plate are obtained from Equation 4.33.

4.5.1.1 Numerical Instability

The method described above is known as the transfer matrix method, the propagator matrix method, or the Thomson-Haskell matrix method, named after Thomson (1950) and Haskell (1953), who first proposed this technique. This technique works well as long as the product of the plate thickness and wave frequency is not very large. When this product becomes large, then numerical instabilities occur. The reason for this numerical instability is that in Equation 4.43 the difference between two very large but close numbers is computed. As the frequency times thickness increases, these two numbers become very large, but remain close to each other; a good number of significant figures are lost when the subtraction operation is carried out. Note that when the number of significant figures lost exceeds 32, then even the double precision computations are not accurate enough to solve the dispersion equation or mode shapes. The numerical precision problem can be removed by means of the delta matrix operation, a submatrix manipulation technique, developed by Dunkin (1965), Dunkin and Corbin (1970), Schwab and Knopoff (1970), and Kundu and Mal (1985).

4.5.1.2 Global Matrix Method

The multilayered plate problem can be solved by an alternate matrix formulation known as the global matrix method (Knopoff, 1964; Mal, 1988). The numerical precision problem can be avoided by following the formulation suggested by Mal (1988).

As mentioned earlier, the source of the numerical problem is the growing exponential terms in Equation 4.33 and in subsequent equations. From Equation 4.34 one can see that E_m^{-1} and B_m^{-1} grow exponentially when η_m and β_m become imaginary. It is possible to bypass this problem of growing exponential terms by defining the wave potentials in the mth layer in the following form:

$$\begin{aligned}
\phi_m &= \left\{a_m e^{-i\eta_m(x_2-y_m)} + b_m e^{i\eta_m(x_2-y_{m-1})}\right\}e^{ikx_1} \\
\psi_m &= \left\{c_m e^{-i\beta_m(x_2-y_m)} + d_m e^{i\beta_m(x_2-y_{m-1})}\right\}e^{ikx_1} \\
\eta_m &= \sqrt{k_{Pm}^2 - k^2} = i\sqrt{k^2 - k_{Pm}^2} \\
\beta_m &= \sqrt{k_{Sm}^2 - k^2} = i\sqrt{k^2 - k_{Sm}^2}
\end{aligned} \tag{4.44}$$

Note that the first terms of the potential expressions of Equation 4.44 are defined slightly differently from their counterparts in Equation 4.32. With this definition, for $y_{m-1} < x_2 < y_m$ all exponential terms decay instead of growing when η_m and β_m become imaginary.

With these potential expressions the stress and displacement components given in Equation 4.33 are changed to

$$
\begin{aligned}
\sigma_{12}\big|_{x_2=y_m} &= \mu_m\left\{2k\eta_m(a_m - b_m E_m) + \left(2k^2 - k_{Sm}^2\right)(c_m + d_m B_m)\right\}e^{ikx_1} \\
\sigma_{12}\big|_{x_2=y_{m-1}} &= \mu_m\left\{2k\eta_m(a_m E_m - b_m) + \left(2k^2 - k_{Sm}^2\right)(c_m B_m + d_m)\right\}e^{ikx_1} \\
\sigma_{22}\big|_{x_2=y_m} &= -\mu_m\left\{\left(k_{Sm}^2 - 2k^2\right)(a_m + b_m E_m) + 2k\beta_m(c_m - d_m B_m)\right\}e^{ikx_1} \\
\sigma_{22}\big|_{x_2=y_{m-1}} &= -\mu_m\left\{\left(k_{Sm}^2 - 2k^2\right)(a_m E_m + b_m) + 2k\beta_m(c_m B_m - d_m)\right\}e^{ikx_1} \\
u_2\big|_{x_2=y_m} &= \{-i\eta_m(a_m - b_m E_m) - ik(c_m + d_m B_m)\}e^{ikx_1} \\
u_2\big|_{x_2=y_{m-1}} &= \{-i\eta_m(a_m E_m - b_m) - ik(c_m B_m + d_m)\}e^{ikx_1} \\
u_1\big|_{x_2=y_m} &= \{ik(a_m + b_m E_m) + i\eta_m(-c_m + d_m B_m)\}e^{ikx_1} \\
u_1\big|_{x_2=y_{m-1}} &= \{ik(a_m E_m + b_m) + i\eta_m(-c_m B_m + d_m)\}e^{ikx_1}
\end{aligned}
\tag{4.45}
$$

E_m and B_m are defined in Equation 4.34.

From Equation 4.45, displacement and stress components at the top and bottom of the mth layer can be written in terms of the wave amplitudes in the following matrix form:

$$
\begin{Bmatrix} u_1 \\ u_2 \\ \sigma_{22} \\ \sigma_{12} \end{Bmatrix}_{x_2=y_m} = \begin{bmatrix} ik & ikE_m & -i\eta_m & i\eta_m B_m \\ -i\eta_m & i\eta_m E_m & -ik & -ikB_m \\ \mu_m\left(2k^2 - k_{Sm}^2\right) & \mu_m\left(2k^2 - k_{Sm}^2\right)E_m & -2k\mu_m\beta_m & 2k\mu_m\beta_m B_m \\ 2k\mu_m\eta_m & -2k\mu_m\eta_m E_m & \mu_m\left(2k^2 - k_{Sm}^2\right) & \mu_m\left(2k^2 - k_{Sm}^2\right)B_m \end{bmatrix} \begin{Bmatrix} a_m \\ b_m \\ c_m \\ d_m \end{Bmatrix}
\tag{4.46a}
$$

and

$$
\begin{Bmatrix} u_1 \\ u_2 \\ \sigma_{22} \\ \sigma_{12} \end{Bmatrix}_{x_2=y_{m-1}} = \begin{bmatrix} ikE_m & ik & -i\eta_m B_m & i\eta_m \\ -i\eta_m E_m & i\eta_m & -ikB_m & -ik \\ \mu_m\left(2k^2 - k_{Sm}^2\right)E_m & \mu_m\left(2k^2 - k_{Sm}^2\right) & -2k\mu_m\beta_m B_m & 2k\mu_m\beta_m \\ 2k\mu_m\eta_m E_m & -2k\mu_m\eta_m & \mu_m\left(2k^2 - k_{Sm}^2\right)B_m & \mu_m\left(2k^2 - k_{Sm}^2\right) \end{bmatrix} \begin{Bmatrix} a_m \\ b_m \\ c_m \\ d_m \end{Bmatrix}
\tag{4.46b}
$$

Equation 4.46a and Equation 4.46b can be written in the short form as given in Equations 4.36a and 4.36b. Similarly, for the m + 1st layer Equation 4.38a and Equation 4.38b are obtained. The only difference here is that no terms of [*G*] and [*H*] matrices contain E_m^{-1} or B_m^{-1}.

From the stress-displacement continuity conditions across the interface we get

$$\begin{aligned}&\{S_m\}=[G_m]\{C_m\}=[H_{m+1}]\{C_{m+1}\}\\&\Rightarrow [G_m]\{C_m\}-[H_{m+1}]\{C_{m+1}\}=\{0\}\quad \text{for } m=1,2,3,\ldots(n-1)\end{aligned} \tag{4.47}$$

From the stress-free boundary conditions at $x_2 = y_0$ and y_n we get

$$\begin{aligned}\{S_0\}=[H_1]\{C_1\}=\begin{Bmatrix}U_0\\V_0\\0\\0\end{Bmatrix}\\ \{S_n\}=[G_n]\{C_n\}=\begin{Bmatrix}U_n\\V_n\\0\\0\end{Bmatrix}\end{aligned} \tag{4.48}$$

In Equation 4.48 surface displacements U_0, V_0, U_n, and V_n are unknowns. Moving all unknowns to the left-hand side of Equation 4.48, it can be rewritten in the following form:

$$\begin{bmatrix}-1 & 0 & ikE_1 & ik & -i\eta_1B_1 & i\eta_1\\ 0 & -1 & -i\eta_1E_1 & i\eta_1 & -ikB_1 & -ik\\ 0 & 0 & \mu_1\left(2k^2-k_{S1}^2\right)E_1 & \mu_1\left(2k^2-k_{S1}^2\right) & -2k\mu_1\beta_1B_1 & 2k\mu_1\beta_1\\ 0 & 0 & 2k\mu_1\eta_1E_1 & -2k\mu_1\eta_1 & \mu_1\left(2k^2-k_{S1}^2\right)B_1 & \mu_1\left(2k^2-k_{S1}^2\right)\end{bmatrix}\begin{Bmatrix}U_0\\V_0\\a_1\\b_1\\c_1\\d_1\end{Bmatrix}=\begin{Bmatrix}0\\0\\0\\0\end{Bmatrix} \tag{4.49a}$$

$$\begin{bmatrix}ik & ikE_n & -i\eta_n & i\eta_nB_n & -1 & 0\\ -i\eta_n & i\eta_nE_n & -ik & -ikB_n & 0 & -1\\ \mu_n\left(2k^2-k_{Sn}^2\right) & \mu_n\left(2k^2-k_{Sn}^2\right)E_n & -2k\mu_n\beta_n & 2k\mu_n\beta_nB_n & 0 & 0\\ 2k\mu_n\beta_n & -2k\mu_n\beta_nE_n & \mu_m\left(2k^2-k_{Sm}^2\right) & \mu_n\left(2k^2-k_{Sn}^2\right)B_n & 0 & 0\end{bmatrix}\begin{Bmatrix}a_n\\b_n\\c_n\\d_n\\U_n\\V_n\end{Bmatrix}=\begin{Bmatrix}0\\0\\0\\0\end{Bmatrix} \tag{4.49b}$$

Note that there are a total of eight algebraic equations in two matrix equations of Equation 4.49, and a total of $4(n - 1)$ algebraic equations in $(n - 1)$ matrix equations of Equation 4.47. The total number of unknown parameters is defined by $(4n + 4)$, these are U_0, V_0, U_n, and V_n and a_m, b_m, c_m, and d_m ($m = 1, 2, 3, \ldots n$). This system of $4(n + 1)$ algebraic equations can be written in the following matrix form:

$$\begin{bmatrix} [H_1^*]_{4\times6} & [0]_{4\times4} & [0]_{4\times4} & [0]_{4\times4} & \cdots & [0]_{4\times4} & [0]_{4\times4} & [0]_{4\times6} \\ [[0]_{4\times2} \vdots [G_1]_{4\times4}] & -[H_2]_{4\times4} & [0]_{4\times4} & [0]_{4\times4} & \cdots & [0]_{4\times4} & [0]_{4\times4} & [0]_{4\times6} \\ [0]_{4\times6} & [G_2]_{4\times4} & -[H_3]_{4\times4} & [0]_{4\times4} & \cdots & [0]_{4\times4} & [0]_{4\times4} & [0]_{4\times6} \\ [0]_{4\times6} & [0]_{4\times4} & [G_3]_{4\times4} & -[H_4]_{4\times4} & \cdots & [0]_{4\times4} & [0]_{4\times4} & [0]_{4\times6} \\ \cdots & \cdots & \cdots & \cdots & \cdots & \cdots & \cdots & \cdots \\ [0]_{4\times6} & [0]_{4\times4} & [0]_{4\times4} & [0]_{4\times4} & \cdots & [G_{n-2}]_{4\times4} & -[H_{n-1}]_{4\times4} & [0]_{4\times6} \\ [0]_{4\times6} & [0]_{4\times4} & [0]_{4\times4} & [0]_{4\times4} & \cdots & [0]_{4\times4} & [G_{n-1}]_{4\times4} & -[[H_n]_{4\times4} \vdots [0]_{4\times2}] \\ [0]_{4\times6} & [0]_{4\times4} & [0]_{4\times4} & [0]_{4\times4} & \cdots & [0]_{4\times4} & [0]_{4\times4} & [G_n^*]_{4\times6} \end{bmatrix}_{4(n+1)\times4(n+1)}$$

$$\times \begin{Bmatrix} \begin{Bmatrix} U_0 \\ V_0 \end{Bmatrix}_{2\times1} \\ \{C_1\}_{4\times1} \\ \{C_2\}_{4\times1} \\ \{C_3\}_{4\times1} \\ \cdots \\ \{C_{n-1}\}_{4\times1} \\ \{C_n\}_{4\times1} \\ \begin{Bmatrix} U_n \\ V_n \end{Bmatrix}_{2\times1} \end{Bmatrix}_{4(n+1)\times1} = \begin{Bmatrix} 0 \\ 0 \\ 0 \\ 0 \\ \cdots \\ 0 \\ 0 \\ 0 \end{Bmatrix}_{4(n+1)\times1} \tag{4.50}$$

In Equation 4.50, $[H_1^*]$ and $[G_n^*]$ are 4×6 coefficient matrices given in Equation 4.49a and Equation 4.49b, respectively. Expressions of $[G_m]$, $[H_m]$, and $\{C_m\}$ are given on the right-hand side of Equation 4.46.

For nontrivial solution of the above system of homogeneous equations (also known as the global system of equations), the determinant of the banded square matrix of Equation 4.50 must be equal to 0. By equating the determinant to zero the dispersion equation is obtained. Then a unit value is assigned to one of the unknowns (for example, U_0 may be assumed to be 1), and the remaining $(4n + 3)$ unknowns can be solved. After solving the wave amplitudes a_m, b_m, c_m, and d_m ($m = 1, 2, 3, \ldots n$), the displacement and stress fields at any point can be computed from the displacement-potential and stress-potential relations.

4.5.2 *n*-Layered Plate in a Fluid

The problem geometry of the *n*-layered plate in a fluid is shown in Figure 4.28b. The plate dimensions and material properties are identical to those given in Section 4.5.1. The only difference here is that the plate is immersed in a fluid. Fluid properties are denoted by the subscript *f*.

The potential field in the fluid is given by

$$\phi_{fL} = Te^{-i\eta_f x_2} e^{ikx_1}$$
$$\phi_{fU} = R\, e^{i\eta_f (x_2 - y_n)} e^{ikx_1} \tag{4.51}$$
$$\eta_f = \sqrt{k_f^2 - k^2} = i\sqrt{k^2 - k_f^2}$$

Subscripts L and U correspond to the lower and upper fluid half-spaces, respectively. k_f is the wave number in the fluid. Normal stress and displacement components at the fluid-solid boundaries are obtained from the above potential fields.

$$\sigma_{22}\big|_{x_2=y_n} = -\rho_f \omega^2 \{\phi_{fU}\}_{x_2=y_n} = -\rho_f \omega^2 R\, e^{ikx_1}$$
$$\sigma_{22}\big|_{x_2=y_0} = -\rho_f \omega^2 \{\phi_{fL}\}_{x_2=y_0} = -\rho_f \omega^2 T e^{ikx_1} \tag{4.52}$$
$$u_2\big|_{x_2=y_n} = \{\phi_{fU,2}\}_{x_2=y_n} = i\eta_f R\, e^{ikx_1}$$
$$u_2\big|_{x_2=y_0} = \{\phi_{fL,2}\}_{x_2=y_0} = -i\eta_f T e^{ikx_1}$$

Wave potentials inside the *m*th layer are given in Equation 4.32. Subsequent derivation (up to Equation 4.40) remains the same for this problem as well. However, Equation 4.41 should be different in this case because the normal stress components at the fluid-solid interfaces are not equal to zero. Equating the vertical displacement and normal stress components at the fluid-solid interfaces, computed from the wave potentials in the fluid and solid, the following matrix equation is obtained:

$$\begin{Bmatrix} u_1 \\ u_2 \\ \sigma_{22} \\ \sigma_{12} \end{Bmatrix}_{x_2=y_n} = \begin{bmatrix} J_{11} & J_{12} & J_{13} & J_{14} \\ J_{21} & J_{22} & J_{23} & J_{24} \\ J_{31} & J_{32} & J_{33} & J_{34} \\ J_{41} & J_{42} & J_{43} & J_{44} \end{bmatrix} \begin{Bmatrix} u_1 \\ u_2 \\ \sigma_{22} \\ \sigma_{12} \end{Bmatrix}_{x_2=y_0}$$
$$\Rightarrow \begin{Bmatrix} U_n \\ i\eta_f R \\ -\rho_f \omega^2 R \\ 0 \end{Bmatrix} = \begin{bmatrix} J_{11} & J_{12} & J_{13} & J_{14} \\ J_{21} & J_{22} & J_{23} & J_{24} \\ J_{31} & J_{32} & J_{33} & J_{34} \\ J_{41} & J_{42} & J_{43} & J_{44} \end{bmatrix} \begin{Bmatrix} U_0 \\ -i\eta_f T \\ -\rho_f \omega^2 T \\ 0 \end{Bmatrix} \tag{4.53}$$

Note that the shear stress component is zero at the top and bottom boundaries of the plate because a perfect fluid cannot have any shear stress. Horizontal displacement components, U_0 and U_n, in the solid plate are unknowns; they are not necessarily equal to the horizontal displacement components in the fluid because of the possibility of slippage occurring between the fluid and solid particles at the fluid-solid interface. Equation 4.53 has four unknowns, R, T, U_0, and U_n, and can be rearranged in the following manner:

$$\begin{bmatrix} 0 & -\left(i\eta_f J_{12} + \rho_f\omega^2 J_{13}\right) & J_{11} & -1 \\ -i\eta_f & -\left(i\eta_f J_{22} + \rho_f\omega^2 J_{23}\right) & J_{21} & 0 \\ \rho_f\omega^2 & -\left(i\eta_f J_{32} + \rho_f\omega^2 J_{33}\right) & J_{31} & 0 \\ 0 & -\left(i\eta_f J_{42} + \rho_f\omega^2 J_{43}\right) & J_{41} & 0 \end{bmatrix} \begin{Bmatrix} R \\ T \\ U_0 \\ U_n \end{Bmatrix} = \begin{Bmatrix} 0 \\ 0 \\ 0 \\ 0 \end{Bmatrix} \tag{4.54}$$

For nontrivial solution of the above system of homogeneous equations, the determinant of the coefficient matrix must be equal to zero. Thus we get:

$$\begin{aligned} & i\eta_f\left[J_{31}\left(i\eta_f J_{42} + \rho_f\omega^2 J_{43}\right) - J_{41}\left(i\eta_f J_{32} + \rho_f\omega^2 J_{33}\right)\right] \\ & + \rho_f\omega^2\left[J_{21}\left(i\eta_f J_{42} + \rho_f\omega^2 J_{43}\right) - J_{41}\left(i\eta_f J_{22} + \rho_f\omega^2 J_{23}\right)\right] = 0 \end{aligned} \tag{4.55}$$

Equation 4.55 is the dispersion equation for the leaky Lamb wave propagation in an n-layered plate immersed in a fluid.

As in the previous section, after solving the dispersion equation and assuming $U_0 = 1$, the other three unknown quantities, R, T, and U_n, can be obtained from Equation 4.54. Then the stress-displacement vector $\{S_m\}$ can be computed at any interface $x_2 = y_m$ using the relation $\{S_m\} = [A_m][A_{m-1}] \ldots [A_2][A_1]\{S_0\}$. After evaluating $\{S_m\}$, Equation 4.36 is used to obtain the wave amplitudes inside the mth layer; a_m, b_m, c_m, and d_m are obtained as well. The stress and displacement variations (mode shapes) inside the plate can be obtained from the displacement-potential and stress-potential relations as given in Equation 4.33.

Example 4.2

Prove that the dispersion equation in Equation 4.42 is a special case of the dispersion equation in Equation 4.55. In other words, derive Equation 4.42 from Equation 4.55.

SOLUTION

Equation 4.42 is for a plate in a vacuum, while Equation 4.55 is for a plate in a fluid medium. Therefore, as the fluid property approaches the vacuum property, Equation 4.55 should approach Equation 4.42. Let us assume that the fluid density (ρ_f) and the acoustic wave speed in the fluid (c_f) are both very small, close to zero. In other words, the fluid is almost like the vacuum. Then the wave number ($k_f = \omega/c_f$) should be very large and we see that

$$\eta_f = \sqrt{k_f^2 - k^2} = k_f\sqrt{1 - \frac{k^2}{k_f^2}} \neq 0$$

Substituting $\rho_f = 0$ into Equation 4.55 we get

$$\begin{aligned}
&i\eta_f\left[J_{31}\left(i\eta_f J_{42} + \rho_f\omega^2 J_{43}\right) - J_{41}\left(i\eta_f J_{32} + \rho_f\omega^2 J_{33}\right)\right] \\
&\quad + \rho_f\omega^2\left[J_{21}\left(i\eta_f J_{42} + \rho_f\omega^2 J_{43}\right) - J_{41}\left(i\eta_f J_{22} + \rho_f\omega^2 J_{23}\right)\right] \\
&= i\eta_f[J_{31}(i\eta_f J_{42}) - J_{41}(i\eta_f J_{32})] \\
&= -\eta_f^2[J_{31}J_{42} - J_{32}J_{41}] = 0
\end{aligned}$$

Since η_f is not equal to zero,

$$J_{31}J_{42} - J_{32}J_{41} = 0$$

4.5.2.1 Global Matrix Method

As mentioned in Section 4.5.1, the numerical instability occurs for large values of the frequency multiplied by the plate thickness. This numerical precision problem can be avoided by following the delta-matrix manipulation (Dunkin and Corbin, 1970; Kundu and Mal, 1985) or global matrix method (Knopoff, 1964; Mal, 1988).

For this problem the first few steps of the global matrix formulation are identical to those from the previous problem. Thus Equation 4.44 through Equation 4.47 are valid in this case also. However, since the boundary conditions are different for this problem, Equation 4.48 should be changed to the following (see Equation 4.53):

$$\begin{aligned}
\{S_0\} = [H_1]\{C_1\} = \begin{Bmatrix} U_0 \\ -i\eta_f T \\ -\rho_f\omega^2 T \\ 0 \end{Bmatrix} \\
\{S_n\} = [G_n]\{C_n\} = \begin{Bmatrix} U_n \\ i\eta_f R \\ -\rho_f\omega^2 R \\ 0 \end{Bmatrix}
\end{aligned} \quad \textbf{(4.56)}$$

In Equation 4.56 U_0, U_n, R, and T are unknowns. The above equations can be rewritten in the following form:

$$\begin{bmatrix} -1 & 0 & ikE_1 & ik & -i\eta_1 B_1 & i\eta_1 \\ 0 & i\eta_f & -i\eta_1 E_1 & i\eta_1 & -ikB_1 & -ik \\ 0 & \rho_f\omega^2 & \mu_1(2k^2-k_{S1}^2)E_1 & \mu_1(2k^2-k_{S1}^2) & -2k\mu_1\beta_1 B_1 & 2k\mu_1\beta_1 \\ 0 & 0 & 2k\mu_1\eta_1 E_1 & -2k\mu_1\eta_1 & \mu_1(2k^2-k_{S1}^2)B_1 & \mu_1(2k^2-k_{S1}^2) \end{bmatrix} \begin{Bmatrix} U_0 \\ T \\ a_1 \\ b_1 \\ c_1 \\ d_1 \end{Bmatrix} = \begin{Bmatrix} 0 \\ 0 \\ 0 \\ 0 \end{Bmatrix} \tag{4.57a}$$

$$\begin{bmatrix} ik & ikE_n & -i\eta_n & i\eta_n B_n & -1 & 0 \\ -i\eta_n & i\eta_n E_n & -ik & -ikB_n & 0 & -i\eta_f \\ \mu_n(2k^2-k_{Sn}^2) & \mu_n(2k^2-k_{Sn}^2)E_n & -2k\mu_n\beta_n & 2k\mu_n\beta_n B_n & 0 & \rho_f\omega^2 \\ 2k\mu_n\beta_n & -2k\mu_n\beta_n E_n & \mu_m(2k^2-k_{Sm}^2) & \mu_n(2k^2-k_{Sn}^2)B_n & 0 & 0 \end{bmatrix} \begin{Bmatrix} a_n \\ b_n \\ c_n \\ d_n \\ U_n \\ R \end{Bmatrix} = \begin{Bmatrix} 0 \\ 0 \\ 0 \\ 0 \end{Bmatrix} \tag{4.57b}$$

Note that a total of eight algebraic equations are in the two matrix equations of Equation 4.57, and a total of $4(n - 1)$ algebraic equations in the $(n - 1)$ matrix equations of Equation 4.47. The total number of unknown parameters is $(4n + 4)$; these are U_0, U_n, R, and T and a_m, b_m, c_m, and d_m ($m = 1, 2, 3, \ldots n$). This system of $4(n + 1)$ algebraic equations can be written in the following matrix form:

$$\begin{bmatrix} [H_1^*]_{4\times6} & [0]_{4\times4} & \cdots & [0]_{4\times6} \\ [[0]_{4\times2} \vdots [G_1]_{4\times4}] & -[H_2]_{4\times4} & \cdots & [0]_{4\times6} \\ \cdots & \cdots & \cdots & \cdots \\ [0]_{4\times6} & [0]_{4\times4} & \cdots & [G_n^*]_{4\times6} \end{bmatrix}_{4(n+1)\times4(n+1)} \begin{Bmatrix} \begin{Bmatrix} U_0 \\ T \end{Bmatrix}_{2\times1} \\ \{C_1\}_{4\times1} \\ \{C_2\}_{4\times1} \\ \{C_3\}_{4\times1} \\ \cdots \\ \{C_{n-1}\}_{4\times1} \\ \{C_n\}_{4\times1} \\ \begin{Bmatrix} U_n \\ R \end{Bmatrix}_{2\times1} \end{Bmatrix}_{4(n+1)\times1} = \begin{Bmatrix} 0 \\ 0 \\ 0 \\ 0 \\ \cdots \\ 0 \\ 0 \\ 0 \end{Bmatrix}_{4(n+1)\times1} \tag{4.58}$$

The banded square matrix expression of Equation 4.58 is similar to the one given in Equation 4.50. However, in Equation 4.58, $[H_1^*]$ and $[G_n^*]$ are 4×6

coefficient matrices that are given in Equation 4.57a and Equation 4.57b, respectively. Note that these expressions differ from the ones given in Equation 4.49. Expressions for $[G_m]$, $[H_m]$, and $\{C_m\}$ are given on the right-hand side of Equation 4.46. The unknown vectors of Equation 4.58 and Equation 4.50 are also slightly different.

For a nontrivial solution of the above system of homogeneous equations, the determinant of the banded square matrix of Equation 4.58 must be equal to 0. The dispersion equation is obtained by equating this determinant to zero. Then a unit value is assigned to one of the unknowns (for example, U_0 may be assumed to be 1) and the remaining $(4n + 3)$ unknowns can be solved. After solving the wave amplitudes a_m, b_m, c_m, and d_m ($m = 1, 2, 3, \ldots n$), the displacement and stress fields at any point can be computed from the displacement-potential and stress-potential relations.

4.5.3 *n*-Layered Plate Immersed in a Fluid and Struck by a Plane P-Wave

In the previous two sections (Section 4.5.1 and Section 4.5.2), we have solved the free vibration problem — plate in a vacuum or in a fluid, in absence of any external excitation. In this section we consider the forced vibration problem — a multilayered plate is struck by a plane P-wave of amplitude 1 as shown in Figure 4.28c. This external excitation generates a reflected wave of amplitude R, a transmitted wave of amplitude T, and upward and downward waves inside the plate layers as shown in Figure 4.28c. Let the incident angle (measured from the vertical axis) of the incoming P-wave be θ. Then the horizontal wave number should be $k = k_f \sin\theta$.

The potential field in the fluid, in this case, should be similar to Equation 4.51, but with an additional term for the incoming P-wave in the upper fluid half-space

$$
\begin{aligned}
\phi_{fL} &= T e^{-i\eta_f x_2} e^{ikx_1} \\
\phi_{fU} &= \left\{ e^{-i\eta_f (x_2 - y_n)} + R e^{i\eta_f (x_2 - y_n)} \right\} e^{ikx_1} \\
\eta_f &= \sqrt{k_f^2 - k^2} = k_f \cos\theta; \quad k = k_f \sin\theta
\end{aligned}
\tag{4.59}
$$

Normal stress and displacement components at the fluid-solid boundaries are obtained from the above potential fields

$$
\begin{aligned}
\sigma_{22}\big|_{x_2 = y_n} &= -\rho_f \omega^2 \{\phi_{fU}\}_{x_2 = y_n} = -\rho_f \omega^2 (1 + R) e^{ikx_1} \\
\sigma_{22}\big|_{x_2 = y_0} &= -\rho_f \omega^2 \{\phi_{fL}\}_{x_2 = y_0} = -\rho_f \omega^2 T e^{ikx_1} \\
u_2\big|_{x_2 = y_n} &= \{\phi_{fU,2}\}_{x_2 = y_n} = i\eta_f (-1 + R) e^{ikx_1} \\
u_2\big|_{x_2 = y_0} &= \{\phi_{fL,2}\}_{x_2 = y_0} = -i\eta_f T e^{ikx_1}
\end{aligned}
\tag{4.60}
$$

Wave potentials inside the *m*th layer are given in Equation 4.32. Subsequent derivation (up to Equation 4.40) remains the same for this problem as well. However, Equation 4.41 should be different in this case because the normal stress components at the fluid-solid interfaces are not equal to zero. Equating the vertical displacement and normal stress components at the fluid-solid interfaces, computed from the wave potentials in the fluid and solid, the following matrix equation is obtained:

$$\begin{Bmatrix} u_1 \\ u_2 \\ \sigma_{22} \\ \sigma_{12} \end{Bmatrix}_{x_2=y_n} = \begin{bmatrix} J_{11} & J_{12} & J_{13} & J_{14} \\ J_{21} & J_{22} & J_{23} & J_{24} \\ J_{31} & J_{32} & J_{33} & J_{34} \\ J_{41} & J_{42} & J_{43} & J_{44} \end{bmatrix} \begin{Bmatrix} u_1 \\ u_2 \\ \sigma_{22} \\ \sigma_{12} \end{Bmatrix}_{x_2=y_0}$$

$$\Rightarrow \begin{Bmatrix} U_n \\ i\eta_f(-1+R) \\ -\rho_f\omega^2(1+R) \\ 0 \end{Bmatrix} = \begin{bmatrix} J_{11} & J_{12} & J_{13} & J_{14} \\ J_{21} & J_{22} & J_{23} & J_{24} \\ J_{31} & J_{32} & J_{33} & J_{34} \\ J_{41} & J_{42} & J_{43} & J_{44} \end{bmatrix} \begin{Bmatrix} U_0 \\ -i\eta_f T \\ -\rho_f\omega^2 T \\ 0 \end{Bmatrix} \tag{4.61}$$

Horizontal displacement components, U_0 and U_n, in the solid plate, are unknowns; they are not necessarily equal to the horizontal displacement components in the fluid because of the possibility of slippage occurring between the fluid and solid particles at the fluid-solid interface. Equation 4.61 has four unknowns, R, T, U_0, and U_n, and can be rearranged in the following manner:

$$\begin{bmatrix} 0 & -\left(i\eta_f J_{12} + \rho_f\omega^2 J_{13}\right) & J_{11} & -1 \\ -i\eta_f & -\left(i\eta_f J_{22} + \rho_f\omega^2 J_{23}\right) & J_{21} & 0 \\ \rho_f\omega^2 & -\left(i\eta_f J_{32} + \rho_f\omega^2 J_{33}\right) & J_{31} & 0 \\ 0 & -\left(i\eta_f J_{42} + \rho_f\omega^2 J_{43}\right) & J_{41} & 0 \end{bmatrix} \begin{Bmatrix} R \\ T \\ U_0 \\ U_n \end{Bmatrix} = \begin{Bmatrix} 0 \\ i\eta_f \\ \rho_f\omega^2 \\ 0 \end{Bmatrix} \tag{4.62}$$

The four unknowns, R, T, U_0, and U_n can be obtained from the above system of nonhomogeneous equations. Then the stress-displacement vector $\{S_m\}$ can be computed at any interface $x_2 = y_m$ using the relation $\{S_m\} = [A_m][A_{m-1}]\ldots[A_2]\,[A_1]\,\{S_0\}$. After evaluating $\{S_m\}$, Equation 4.36 is used to obtain the wave amplitudes inside the *m*th layer, obtaining a_m, b_m, c_m, and d_m as well; then the stress and displacement variations inside the plate can be obtained from the displacement-potential and stress-potential relations as given in Equation 4.33.

4.5.3.1 Global Matrix Method

As mentioned in Section 4.5.1 and Section 4.5.2, the numerical instability occurs for large values of the frequency multiplied by the plate thickness. This numerical precision problem can be avoided by following the delta-matrix manipulation or global matrix method.

For this problem, the first few steps of the global matrix formulation for this problem are identical to those from the previous problems. Equation 4.44 through Equation 4.47 apply to this problem as well. However, since the boundary conditions are different here, Equation 4.48 should be changed to the following (see Equation 4.61):

$$\{S_0\} = [H_1]\{C_1\} = \begin{Bmatrix} U_0 \\ -i\eta_f T \\ -\rho_f \omega^2 T \\ 0 \end{Bmatrix}$$

$$\{S_n\} = [G_n]\{C_n\} = \begin{Bmatrix} U_n \\ i\eta_f(-1+R) \\ -\rho_f \omega^2 (1+R) \\ 0 \end{Bmatrix} \tag{4.63}$$

In Equation 4.63 U_0, U_n, R, and T are unknown quantities. The above equations can be rewritten in the following form:

$$\begin{bmatrix} -1 & 0 & ikE_1 & ik & -i\eta_1 B_1 & i\eta_1 \\ 0 & i\eta_f & -i\eta_1 E_1 & i\eta_1 & -ikB_1 & -ik \\ 0 & \rho_f\omega^2 & \mu_1\left(2k^2 - k_{S1}^2\right)E_1 & \mu_1\left(2k^2 - k_{S1}^2\right) & -2k\mu_1\beta_1 B_1 & 2k\mu_1\beta_1 \\ 0 & 0 & 2k\mu_1\eta_1 E_1 & -2k\mu_1\eta_1 & \mu_1\left(2k^2 - k_{S1}^2\right)B_1 & \mu_1\left(2k^2 - k_{S1}^2\right) \end{bmatrix} \begin{Bmatrix} U_0 \\ T \\ a_1 \\ b_1 \\ c_1 \\ d_1 \end{Bmatrix} = \begin{Bmatrix} 0 \\ 0 \\ 0 \\ 0 \end{Bmatrix} \tag{4.64a}$$

$$\begin{bmatrix} ik & ikE_n & -i\eta_n & i\eta_n B_n & -1 & 0 \\ -i\eta_n & i\eta_n E_n & -ik & -ikB_n & 0 & -i\eta_f \\ \mu_n\left(2k^2 - k_{Sn}^2\right) & \mu_n\left(2k^2 - k_{Sn}^2\right)E_n & -2k\mu_n\beta_n & 2k\mu_n\beta_n B_n & 0 & \rho_f\omega^2 \\ 2k\mu_n\beta_n & -2k\mu_n\beta_n E_n & \mu_m\left(2k^2 - k_{Sm}^2\right) & \mu_n\left(2k^2 - k_{Sn}^2\right)B_n & 0 & 0 \end{bmatrix} \begin{Bmatrix} a_n \\ b_n \\ c_n \\ d_n \\ U_n \\ R \end{Bmatrix}$$

$$= \begin{Bmatrix} 0 \\ -i\eta_f \\ -\rho_f\omega^2 \\ 0 \end{Bmatrix} \tag{4.64b}$$

Note that Equation 4.64a is identical to Equation 4.57a, but Equation 4.64b differs from Equation 4.57b. There are eight algebraic equations in the two matrix equations of Equation 4.64, and a total of $4(n-1)$ algebraic equations in $(n-1)$ matrix equations of Equation 4.47. The total number of unknown parameters is $(4n+4)$; these are U_0, U_n, R, and T and a_m, b_m, c_m, and d_m (m = 1, 2, 3, … n). This system of $4(n+1)$ algebraic equations can be written in the following matrix form:

$$\begin{bmatrix} [H_1^*]_{4\times6} & [0]_{4\times4} & \cdots & [0]_{4\times6} \\ \left[[0]_{4\times2} \vdots [G_1]_{4\times4}\right] & -[H_2]_{4\times4} & \cdots & [0]_{4\times6} \\ \cdots & \cdots & \cdots & \cdots \\ [0]_{4\times6} & [0]_{4\times4} & \cdots & [G_n^*]_{4\times6} \end{bmatrix}_{4(n+1)\times4(n+1)} \begin{Bmatrix} \begin{Bmatrix} U_0 \\ T \end{Bmatrix}_{2\times1} \\ \{C_1\}_{4\times1} \\ \{C_2\}_{4\times1} \\ \{C_3\}_{4\times1} \\ \cdots \\ \{C_{n-1}\}_{4\times1} \\ \{C_n\}_{4\times1} \\ \begin{Bmatrix} U_n \\ R \end{Bmatrix}_{2\times1} \end{Bmatrix}_{4(n+1)\times1} = \begin{Bmatrix} 0 \\ 0 \\ 0 \\ 0 \\ 0 \\ \cdots \\ 0 \\ -i\eta_f \\ -\rho_f\omega^2 \\ 0 \end{Bmatrix}_{4(n+1)\times1} \quad \textbf{(4.65)}$$

The banded square matrix expression of Equation 4.65 is similar to the one given in Equation 4.50 and Equation 4.58. In Equation 4.65, $[H_1^*]$ and $[G_n^*]$ are 4×6 coefficient matrices that are given in Equation 4.64a and Equation 4.64b, respectively. Note that these matrices are identical to those given in Equation 4.57, but different from the ones given in Equation 4.49. Expressions of $[G_m]$, $[H_m]$, and $\{C_m\}$ are given on the right-hand side of Equation 4.46. Unknown vectors of Equation 4.65 and Equation 4.58 are the same, but the two vectors on the right-hand side of these two equations differ.

The system of nonhomogeneous equations in Equation 4.65 can be solved to obtain the $(4n+4)$ unknowns. After solving the wave amplitudes a_m, b_m, c_m, and d_m (m = 1, 2, 3, … n), the displacement and stress fields at any point can be computed from the displacement-potential and stress-potential relations.

4.6 Guided Waves in Single and Multilayered Composite Plates

Until now we have analyzed plates made of isotropic elastic layers only. All those analyses excluded the fiber-reinforced composite plates and any plate made of anisotropic layers. In this section, guided wave propagation through a unidirectional fiber-reinforced composite plate and multilayered composite plates, made of anisotropic layers, is studied. In the multilayered plate, fiber direction can vary from one layer to the next.

For this plate problem, it is possible to consider three separate problem geometries as shown in Figure 4.28: (1) plate in a vacuum, (2) plate in a fluid and (3) plane P-wave striking a plate in a fluid. We have already shown in the previous section (Example 4.2) that the plate in a vacuum is a special case of the plate in a fluid; therefore, it is not necessary to consider the plate in a vacuum problem separately. In the dispersion equation for the plate immersed in a fluid, if we set the fluid density equal to zero and the acoustic wave speed of the fluid to a small number, then we recover the dispersion equation for the plate in a vacuum. In Section 4.5 it is also shown that the dispersion equation for the free vibration problem (plate in a fluid) can be obtained from the forced vibration problem (plane P-wave striking a plate in a fluid), because the only difference between these two problems is that for the free vibration problem we get a system of homogeneous equations. The forced vibration problem results in a system of nonhomogeneous equations. The coefficient matrix from which the dispersion equation is derived is identical for the two problems (see Equation 4.65 and Equation 4.58 or Equation 4.62 and Equation 4.54). If we analyze the forced vibration problem and a plane P-wave striking a composite plate immersed in a fluid, then we solve the most general problem. The two free-vibration problems, plate in a vacuum and plate in a fluid, can be derived from this forced vibration problem. This problem is solved following the technique outlined by Mal et al. (1991).

Following Mal's notation, the coordinate axis for this problem geometry is slightly changed from our earlier assumptions. The vertical axis is changed from x_2 to x_3 (positive downward), and the wave propagation direction is inclined at an angle ϕ with respect to the x_1 axis as shown in Figure 4.29.

The stress-strain relation for a transversely isotropic solid is given in Chapter 1, Equation 1.63 and Equation 1.64. Those relations are given for the x_3-axis being the axis of symmetry. If the x_1-axis becomes the axis of symmetry,

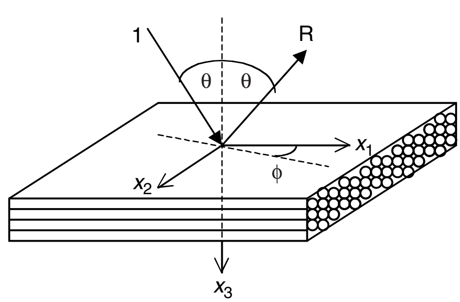

FIGURE 4.29
Reflection of a plane P-wave by a fiber-reinforced composite plate immersed in a fluid. Fiber direction is the x_1-direction. Plane containing the incident and reflected waves form an angle ϕ with the x_1-axis.

then, following the reasoning given in Chapter 1, it can be shown that Equation 1.63 is changed to

$$\begin{Bmatrix} \sigma_{11} \\ \sigma_{22} \\ \sigma_{33} \\ \sigma_{23} \\ \sigma_{31} \\ \sigma_{12} \end{Bmatrix} = \begin{bmatrix} C_{11} & C_{12} & C_{12} & 0 & 0 & 0 \\ & C_{22} & C_{23} & 0 & 0 & 0 \\ & & C_{22} & 0 & 0 & 0 \\ & & & C_{44} & 0 & 0 \\ & symm & & & C_{55} & 0 \\ & & & & & C_{55} \end{bmatrix} \begin{Bmatrix} \varepsilon_{11} \\ \varepsilon_{22} \\ \varepsilon_{33} \\ 2\varepsilon_{23} \\ 2\varepsilon_{31} \\ 2\varepsilon_{12} \end{Bmatrix} \quad \textbf{(4.66)}$$

where

$$C_{44} = \frac{C_{22} - C_{23}}{2} \quad \textbf{(4.67)}$$

This stress-strain relation can be found in any book on mechanics of anisotropic solids (Christensen, 1981). For comparison, the reader can also refer to Chapter 1, Equation 1.63 and Equation 1.64.

Buchwald (1961) proposed the following displacement-potential relation, which is useful for solving this problem:

$$\begin{Bmatrix} u_1 \\ u_2 \\ u_3 \end{Bmatrix} = \begin{bmatrix} \partial/\partial x_1 & 0 & 0 \\ 0 & \partial/\partial x_2 & \partial/\partial x_3 \\ 0 & \partial/\partial x_3 & -\partial/\partial x_2 \end{bmatrix} \begin{Bmatrix} \phi_1 \\ \phi_2 \\ \phi_3 \end{Bmatrix} \quad \textbf{(4.68)}$$

In absence of any body force, the equations of motion (Chapter 1, Equation 1.78) become

$$\begin{aligned} \sigma_{11,1} + \sigma_{12,2} + \sigma_{13,3} &= \rho\ddot{u}_1 \\ \sigma_{21,1} + \sigma_{22,2} + \sigma_{23,3} &= \rho\ddot{u}_2 \\ \sigma_{31,1} + \sigma_{32,2} + \sigma_{33,3} &= \rho\ddot{u}_2 \end{aligned} \quad \textbf{(4.69)}$$

Substituting Equation 4.66 into Equation 4.69 and specializing the equations for harmonic time dependence ($e^{-i\omega t}$), we obtain

$$\begin{aligned} &(C_{11}u_{1,11} + C_{12}u_{2,21} + C_{12}u_{3,31}) + C_{55}(u_{1,22} + u_{2,12}) + C_{55}(u_{1,33} + u_{3,13}) + \rho\omega^2 u_1 = 0 \\ &C_{55}(u_{1,21} + u_{2,11}) + (C_{12}u_{1,12} + C_{22}u_{2,22} + C_{23}u_{3,32}) + C_{44}(u_{2,33} + u_{3,23}) + \rho\omega^2 u_2 = 0 \\ &C_{55}(u_{1,31} + u_{3,11}) + C_{44}(u_{2,32} + u_{3,22}) + (C_{12}u_{1,13} + C_{23}u_{2,23} + C_{22}u_{3,33}) + \rho\omega^2 u_3 = 0 \end{aligned} \quad \textbf{(4.70)}$$

Then substitution of Equation 4.68 into Equation 4.70 gives

$$
\begin{aligned}
&(C_{11}\phi_{1,111} + C_{12}\phi_{2,221} + C_{12}\phi_{3,321} + C_{12}\phi_{2,331} - C_{12}\phi_{3,231}) \\
&\quad + C_{55}(\phi_{1,122} + \phi_{2,212} + \phi_{3,312}) + C_{55}(\phi_{1,133} + \phi_{2,313} - \phi_{3,213}) + \rho\omega^2\phi_{1,1} = 0 \\
&C_{55}(\phi_{1,121} + \phi_{2,211} + \phi_{3,311}) + (C_{12}\phi_{1,112} + C_{22}\phi_{2,222} + C_{22}\phi_{3,322} + C_{23}\phi_{2,332} - C_{23}\phi_{3,232}) \\
&\quad + C_{44}(\phi_{2,233} + \phi_{3,333} + \phi_{2,323} - \phi_{3,223}) + \rho\omega^2\phi_{2,2} + \rho\omega^2\phi_{3,3} = 0 \\
&C_{55}(\phi_{1,131} + \phi_{2,311} - \phi_{3,211}) + C_{44}(\phi_{2,232} + \phi_{3,332} + \phi_{2,322} - \phi_{3,222}) \\
&\quad + (C_{12}\phi_{1,113} + C_{23}\phi_{2,223} + C_{23}\phi_{3,323} + C_{22}\phi_{2,333} - C_{22}\phi_{3,233}) + \rho\omega^2\phi_{2,3} - \rho\omega^2\phi_{3,2} = 0
\end{aligned}
\tag{4.71}
$$

The first equation of Equation 4.71 can be written as

$$
\begin{aligned}
&\left[(C_{11}\phi_{1,11} + C_{12}\phi_{2,22} + C_{12}\phi_{3,32} + C_{12}\phi_{2,33} - C_{12}\phi_{3,23})\right. \\
&\quad \left. + C_{55}(\phi_{1,22} + \phi_{2,22} + \phi_{3,32}) + C_{55}(\phi_{1,33} + \phi_{2,33} - \phi_{3,23}) + \rho\omega^2\phi_1\right]_{,1} = 0 \\
&\Rightarrow \left[(C_{11}\phi_{1,11} + C_{12}\phi_{2,22} + C_{12}\phi_{2,33}) + C_{55}(\phi_{1,22} + \phi_{2,22} + \phi_{1,33} + \phi_{2,33}) + \rho\omega^2\phi_1\right]_{,1} = 0 \\
&\Rightarrow \left[\left(C_{11}\phi_{1,11} + C_{12}\nabla_1^2\phi_2\right) + C_{55}\nabla_1^2(\phi_1 + \phi_2) + \rho\omega^2\phi_1\right]_{,1} = 0 \\
&\Rightarrow \left[\left(C_{11}\phi_{1,11} + C_{55}\nabla_1^2\phi_1 + \rho\omega^2\phi_1\right) + (C_{12} + C_{55})\nabla_1^2\phi_2\right]_{,1} = 0
\end{aligned}
\tag{4.72}
$$

where

$$
\nabla_1^2 = \frac{\partial^2}{\partial x_2^2} + \frac{\partial^2}{\partial x_3^2}
$$

Similarly, the second equation of Equation 4.71 can be rewritten in the following form:

$$
\begin{aligned}
&\left[C_{55}(\phi_{1,11} + \phi_{2,11}) + (C_{12}\phi_{1,11} + C_{22}\phi_{2,22} + C_{23}\phi_{2,33}) + C_{44}(\phi_{2,33} + \phi_{2,33}) + \rho\omega^2\phi_2\right]_{,2} \\
&\quad + \left[C_{55}\phi_{3,11} + C_{22}\phi_{3,22} - C_{23}\phi_{3,22} + C_{44}(\phi_{3,33} - \phi_{3,22}) + \rho\omega^2\phi_3\right]_{,3} = 0 \\
&\Rightarrow \left[(C_{12} + C_{55})\phi_{1,11} + (C_{55}\phi_{2,11}) + (C_{22}\phi_{2,22} + C_{22}\phi_{2,33} - 2C_{44}\phi_{2,33}) + 2C_{44}\phi_{2,33} + \rho\omega^2\phi_2\right]_{,2} \\
&\quad + \left[C_{55}\phi_{3,11} + 2C_{44}\phi_{3,22} + C_{44}(\phi_{3,33} - \phi_{3,22}) + \rho\omega^2\phi_3\right]_{,3} = 0
\end{aligned}
$$

$$\Rightarrow \left[(C_{12}+C_{55})\phi_{1,11}+C_{55}\phi_{2,11}+C_{22}(\phi_{2,22}+C_{22}\phi_{2,33})+\rho\omega^2\phi_2\right]_{,2}$$

$$+\left[C_{55}\phi_{3,11}+C_{44}(\phi_{3,33}+\phi_{3,22})+\rho\omega^2\phi_3\right]_{,3}=0$$

$$\Rightarrow \left[(C_{12}+C_{55})\phi_{1,11}+C_{55}\phi_{2,11}+C_{22}\nabla_1^2\phi_2+\rho\omega^2\phi_2\right]_{,2}+\left[C_{55}\phi_{3,11}+C_{44}\nabla_1^2\phi_3+\rho\omega^2\phi_3\right]_{,3}=0 \tag{4.73}$$

and the third equation is rewritten as

$$C_{55}(\phi_{1,131}+\phi_{2,311}-\phi_{3,211})+C_{44}(\phi_{2,232}+\phi_{3,332}+\phi_{2,322}-\phi_{3,222})$$

$$+(C_{12}\phi_{1,113}+C_{23}\phi_{2,223}+C_{23}\phi_{3,323}+C_{22}\phi_{2,333}-C_{22}\phi_{3,233})+\rho\omega^2\phi_{2,3}-\rho\omega^2\phi_{3,2}=0$$

$$\left[C_{55}(\phi_{1,11}+\phi_{2,11})+C_{44}(\phi_{2,22}+\phi_{2,22})+(C_{12}\phi_{1,11}+C_{23}\phi_{2,22}+C_{22}\phi_{2,33})+\rho\omega^2\phi_2\right]_{,3}$$

$$+\left[-C_{55}\phi_{3,11}+C_{44}(\phi_{3,33}-\phi_{3,22})+(C_{23}\phi_{3,33}-C_{22}\phi_{3,33})-\rho\omega^2\phi_3\right]_{,2}=0$$

$$\left[(C_{55}+C_{12})\phi_{1,11}+C_{55}\phi_{2,11}+2C_{44}\phi_{2,22}+(C_{22}\phi_{2,22}-2C_{44}\phi_{2,22}+C_{22}\phi_{2,33})+\rho\omega^2\phi_2\right]_{,3}$$

$$+\left[-C_{55}\phi_{3,11}+C_{44}(\phi_{3,33}-\phi_{3,22})+(-2C_{44}\phi_{3,33})-\rho\omega^2\phi_3\right]_{,2}=0$$

$$\left[\left(C_{55}+C_{12}\right)\phi_{1,11}+C_{55}\phi_{2,11}+C_{22}\nabla_1^2\phi_2+\rho\omega^2\phi_2\right]_{,3}-\left[C_{55}\phi_{3,11}+C_{44}\nabla_1^2\phi_3+\rho\omega^2\phi_3\right]_{,2}=0 \tag{4.74}$$

Note that the sufficient conditions for satisfying Equation 4.72 through Equation 4.74 are

$$\begin{aligned}
&C_{11}\phi_{1,11}+C_{55}\nabla_1^2\phi_1+\rho\omega^2\phi_1+(C_{12}+C_{55})\nabla_1^2\phi_2=0\\
&(C_{12}+C_{55})\phi_{1,11}+C_{55}\phi_{2,11}+C_{22}\nabla_1^2\phi_2+\rho\omega^2\phi_2=0\\
&C_{55}\phi_{3,11}+C_{44}\nabla_1^2\phi_3+\rho\omega^2\phi_3=0
\end{aligned} \tag{4.75}$$

Equation 4.75 can be rewritten in the following form:

$$\begin{aligned}
&\left(\frac{C_{55}}{\rho}\nabla_1^2+\frac{C_{11}}{\rho}\frac{\partial^2}{\partial x_1^2}+\omega^2\right)\phi_1+\frac{(C_{12}+C_{55})}{\rho}\nabla_1^2\phi_2=0\\
&\frac{(C_{12}+C_{55})}{\rho}\frac{\partial^2}{\partial x_1^2}\phi_1+\left(\frac{C_{22}}{\rho}\nabla_1^2+\frac{C_{55}}{\rho}\frac{\partial^2}{\partial x_1^2}+\omega^2\right)\phi_2=0\\
&\left(\frac{C_{44}}{\rho}\nabla_1^2+\frac{C_{55}}{\rho}\frac{\partial^2}{\partial x_1^2}+\omega^2\right)\phi_3=0
\end{aligned} \tag{4.76}$$

Substituting

$$\frac{C_{22}}{\rho} = a_1$$
$$\frac{C_{11}}{\rho} = a_2$$
$$\frac{C_{12} + C_{55}}{\rho} = a_3 \qquad \textbf{(4.77)}$$
$$\frac{C_{44}}{\rho} = a_4$$
$$\frac{C_{55}}{\rho} = a_5$$

in Equation 4.76 we get

$$\left(a_5 \nabla_1^2 + a_2 \frac{\partial^2}{\partial x_1^2} + \omega^2 \right) \phi_1 + a_3 \nabla_1^2 \phi_2 = 0$$
$$a_3 \frac{\partial^2}{\partial x_1^2} \phi_1 + \left(a_1 \nabla_1^2 + a_5 \frac{\partial^2}{\partial x_1^2} + \omega^2 \right) \phi_2 = 0 \qquad \textbf{(4.78a)}$$
$$\left(a_4 \nabla_1^2 + a_5 \frac{\partial^2}{\partial x_1^2} + \omega^2 \right) \phi_3 = 0$$

Equation 4.78a can be written in matrix form

$$\begin{bmatrix} \left(a_5 \nabla_1^2 + a_2 \frac{\partial^2}{\partial x_1^2} + \omega^2 \right) & a_3 \nabla_1^2 & 0 \\ a_3 \frac{\partial^2}{\partial x_1^2} & \left(a_1 \nabla_1^2 + a_5 \frac{\partial^2}{\partial x_1^2} + \omega^2 \right) & 0 \\ 0 & 0 & \left(a_4 \nabla_1^2 + a_5 \frac{\partial^2}{\partial x_1^2} + \omega^2 \right) \end{bmatrix} \begin{Bmatrix} \phi_1 \\ \phi_2 \\ \phi_3 \end{Bmatrix} = \begin{Bmatrix} 0 \\ 0 \\ 0 \end{Bmatrix}$$

(4.78b)

The solution for the above system of differential equations is given by (Mal et al., 1991)

$$\begin{Bmatrix} \phi_1 \\ \phi_2 \\ \phi_3 \end{Bmatrix} = \begin{bmatrix} q_{11} & q_{12} & 0 \\ q_{21} & q_{22} & 0 \\ 0 & 0 & 1 \end{bmatrix} \left(\begin{bmatrix} e^{i\zeta_1 x_3} & 0 & 0 \\ 0 & e^{i\zeta_2 x_3} & 0 \\ 0 & 0 & e^{i\zeta_3 x_3} \end{bmatrix} \begin{Bmatrix} A_1^+ \\ A_2^+ \\ A_3^+ \end{Bmatrix} + \begin{bmatrix} e^{-i\zeta_1 x_3} & 0 & 0 \\ 0 & e^{-i\zeta_2 x_3} & 0 \\ 0 & 0 & e^{-i\zeta_3 x_3} \end{bmatrix} \begin{Bmatrix} A_1^- \\ A_2^- \\ A_3^- \end{Bmatrix} \right) e^{i(\xi_1 x_1 + \xi_2 x_2)}$$

or

$$\begin{Bmatrix} \phi_1 \\ \phi_2 \\ \phi_3 \end{Bmatrix} = \begin{bmatrix} q_{11} & q_{12} & 0 \\ q_{21} & q_{22} & 0 \\ 0 & 0 & 1 \end{bmatrix} \begin{Bmatrix} A_1^+ e^{i\zeta_1 x_3} + A_1^- e^{-i\zeta_1 x_3} \\ A_2^+ e^{i\zeta_2 x_3} + A_2^- e^{-i\zeta_2 x_3} \\ A_3^+ e^{i\zeta_3 x_3} + A_3^- e^{-i\zeta_3 x_3} \end{Bmatrix} e^{i(\xi_1 x_1 + \xi_2 x_2)} \tag{4.79}$$

where

$$\begin{aligned} q_{11} &= a_3 b_1 \\ q_{12} &= a_3 b_2 \\ q_{21} &= \omega^2 - a_2 \xi_1^2 - a_5 b_1 \\ q_{22} &= \omega^2 - a_2 \xi_1^2 - a_5 b_2 \end{aligned} \tag{4.80a}$$

$$\begin{aligned} b_{1,2} &= -\left(\frac{\beta}{2\alpha}\right) \mp \left[\left(\frac{\beta}{2\alpha}\right)^2 - \frac{\gamma}{\alpha}\right]^{1/2} \\ \alpha &= a_1 a_5 \\ \beta &= \left(a_1 a_2 + a_5^2 - a_3^2\right)\xi_1^2 - \omega^2 (a_1 + a_5) \\ \gamma &= \left(a_2 \xi_1^2 - \omega^2\right)\left(a_5 \xi_1^2 - \omega^2\right) \end{aligned} \tag{4.80b}$$

$$\begin{aligned} \zeta_1^2 &= -\xi_2^2 + b_1 \\ \zeta_2^2 &= -\xi_2^2 + b_2 \\ \xi_3^2 &= -\xi_2^2 + \left(\omega^2 - a_5 \xi_1^2\right) / a_4 \end{aligned} \tag{4.80c}$$

subject to $\text{Im}(\zeta_j) \geq 0, \quad j = 1, 2, 3$

From the potential expressions given in Equation 4.79, the three displacement components and the normal and shear stress components at a surface, x_3 = constant can be obtained using Equation 4.68 and Equation 4.66:

$$\begin{bmatrix} u_1 & u_2 & u_3 & \sigma_{13} & \sigma_{23} & \sigma_{33} \end{bmatrix}^T = \left\{S(x_3)\right\} e^{i(\xi_1 x_1 + \xi_2 x_2)} = \begin{bmatrix} Q_{11} & Q_{12} \\ Q_{21} & Q_{22} \end{bmatrix} [E] \begin{Bmatrix} A^+ \\ A^- \end{Bmatrix} e^{i(\xi_1 x_1 + \xi_2 x_2)} \tag{4.81}$$

where

$$[E] = \begin{bmatrix} e^{i\zeta_1 x_3} & 0 & 0 & 0 & 0 & 0 \\ 0 & e^{i\zeta_2 x_3} & 0 & 0 & 0 & 0 \\ 0 & 0 & e^{i\zeta_3 x_3} & 0 & 0 & 0 \\ 0 & 0 & 0 & e^{-i\zeta_1 x_3} & 0 & 0 \\ 0 & 0 & 0 & 0 & e^{-i\zeta_2 x_3} & 0 \\ 0 & 0 & 0 & 0 & 0 & e^{-i\zeta_3 x_3} \end{bmatrix} \quad \textbf{(4.82)}$$

$$\begin{bmatrix} A^+ & A^- \end{bmatrix}^T = \begin{bmatrix} A_1^+ & A_2^+ & A_3^+ & A_1^- & A_2^- & A_3^- \end{bmatrix}^T \quad \textbf{(4.83)}$$

$$[Q_{11}] = \begin{bmatrix} i\xi_1 q_{11} & i\xi_1 q_{12} & 0 \\ i\xi_2 q_{21} & i\xi_2 q_{22} & i\zeta_3 \\ i\zeta_1 q_{21} & i\zeta_2 q_{22} & -i\xi_2 \end{bmatrix}$$

$$[Q_{12}] = \begin{bmatrix} i\xi_1 q_{11} & i\xi_1 q_{12} & 0 \\ i\xi_2 q_{21} & i\xi_2 q_{22} & -i\zeta_3 \\ -i\zeta_1 q_{21} & -i\zeta_2 q_{22} & -i\xi_2 \end{bmatrix}$$

$$[Q_{21}] = \begin{bmatrix} -\rho a_5 \xi_1 \zeta_1 (q_{11} + q_{21}) & -\rho a_5 \xi_1 \zeta_2 (q_{12} + q_{22}) & \rho a_5 \xi_1 \xi_2 \\ -2\rho a_4 \xi_2 \zeta_1 q_{21} & -2\rho a_4 \xi_2 \zeta_2 q_{22} & \rho a_4 \left(\xi_2^2 - \zeta_3^2\right) \\ \delta_1 & \delta_2 & 2\rho a_4 \xi_2 \zeta_3 \end{bmatrix} \quad \textbf{(4.84a)}$$

$$[Q_{22}] = \begin{bmatrix} \rho a_5 \xi_1 \zeta_1 (q_{11} + q_{21}) & \rho a_5 \xi_1 \zeta_2 (q_{12} + q_{22}) & \rho a_5 \xi_1 \xi_2 \\ 2\rho a_4 \xi_2 \zeta_1 q_{21} & 2\rho a_4 \xi_2 \zeta_2 q_{22} & \rho a_4 \left(\xi_2^2 - \zeta_3^2\right) \\ \delta_1 & \delta_2 & -2\rho a_4 \xi_2 \zeta_3 \end{bmatrix}$$

$$\begin{aligned} \delta_1 &= \rho\left[(a_5 - a_3)\xi_1^2 q_{11} - (a_1 - 2a_4)\xi_2^2 q_{21} - a_1 \zeta_1^2 q_{21}\right] \\ \delta_2 &= \rho\left[(a_5 - a_3)\xi_1^2 q_{12} - (a_1 - 2a_4)\xi_2^2 q_{22} - a_1 \zeta_2^2 q_{22}\right] \end{aligned} \quad \textbf{(4.84b)}$$

The wave field due to the incident wave (see Figure 4.29) is given by:

$$e^{i(\xi_1 x_1 + \xi_2 x_2 + \zeta_0 x_3)} \quad \textbf{(4.85)}$$

where

$$\xi_1 = k_0 \sin\theta \cos\phi, \quad \xi_2 = k_0 \sin\theta \sin\phi, \quad \zeta_0 = k_0 \cos\theta, \text{ and } \quad k_0 = \omega/\alpha_0 \quad \textbf{(4.86)}$$

Acoustic wave potentials in the upper and lower fluids are denoted by ϕ_0 and ϕ_b, respectively. Then the displacement and stress components in the fluid are given by

$$u_i = \frac{\partial \phi_\alpha}{\partial x_i}, \quad i = 1, 2, 3$$
$$\sigma_{33} = -\rho_0 \omega^2 \phi_\alpha, \quad \sigma_{13} = \sigma_{23} = 0 \tag{4.87}$$

where the subscript α is either 0 (for the top fluid) or b (for the bottom fluid).

In terms of the reflection and transmission coefficients, R and T, the wave potentials in top and bottom fluid half-spaces are given by:

$$\phi_0 = (e^{i\zeta_0 x_3} + R e^{-i\zeta_0 x_3}) e^{i(\xi_1 x_1 + \xi_2 x_2)}$$
$$\phi_b = T e^{i[\zeta_0 (x_3 - H) + \xi_1 x_1 + \xi_2 x_2]} \tag{4.88}$$

Normal displacement and stress components should be continuous across the top and bottom interfaces, between the fluid half space and the plate. Shear stresses should vanish at the interfaces. Fluids and solids can have different horizontal displacement components across an interface. Therefore, the displacement and stress components at the top and bottom surfaces of the plate can be written as:

$$\{S(x_3)\}^T e^{i(\xi_1 x_1 + \xi_2 x_2)} = [u_1 \quad u_2 \quad \phi_{0,3} \quad 0 \quad 0 \quad -\rho_0 \omega^2 \phi_0], \quad x_3 = 0$$
$$= [u_1 \quad u_2 \quad \phi_{b,3} \quad 0 \quad 0 \quad -\rho_0 \omega^2 \phi_b], \quad x_3 = H \tag{4.89}$$

Substituting Equation 4.88 into Equation 4.89 yields:

$$\{S(x_3)\}^T e^{i(\xi_1 x_1 + \xi_2 x_2)} = [U_0 \quad V_0 \quad i\zeta_0(1-R) \quad 0 \quad 0 \quad -\rho_0 \omega^2 (1+R)] e^{i(\xi_1 x_1 + \xi_2 x_2)}, \quad x_3 = 0$$
$$= \left[U_1 \quad V_1 \quad i\zeta_0 T \quad 0 \quad 0 \quad -\rho_0 \omega^2 \phi_b T\right] e^{i(\xi_1 x_1 + \xi_2 x_2)}, \quad x_3 = H \tag{4.90}$$

where ζ_0, ζ_1, and ζ_2 are defined in Equation 4.86. Propagation term $e^{i(\xi_1 x_1 + \xi_2 x_2)}$ is implied in every term. Note, that u_1 and u_2 of Equation 4.89 are related to U_0, V_0, U_1, and V_1 of Equation 4.90 in the following manner:

$$u_1\big|_{x_3=0} = U_0 e^{i(\xi_1 x_1 + \xi_2 x_2)}, \quad u_2\big|_{x_3=0} = V_0 e^{i(\xi_1 x_1 + \xi_2 x_2)}, \quad u_1\big|_{x_3=H} = U_1 e^{i(\xi_1 x_1 + \xi_2 x_2)}, \quad u_2\big|_{x_3=H} = V_1 e^{i(\xi_1 x_1 + \xi_2 x_2)}$$

4.6.1 Single Layer Composite Plate Immersed in a Fluid

Equating $\{S(x_3)\}$ of Equation 4.90 and Equation 4.81 at $x_3 = 0$ and H, we get a total of 12 equations, with 12 unknowns: A_1^+, A_2^+, A_3^+, A_1^-, A_2^-, A_3^-, R, T, U_0, V_0, U_1, and V_1. Because it gives a system of nonhomogeneous equations, the 12 unknowns can be uniquely solved using the 12 equations. The dispersion equation is obtained by equating the determinant of the coefficient matrix to zero.

4.6.2 Multilayered Composite Plate Immersed in a Fluid

Like before, symbols and steps given in Mal et al. (1991) are followed in this section. A multilayered, multiorientation composite plate is analyzed here. The global coordinate system xyz is introduced, where the xy-plane is parallel to the surfaces of the plate. For each layer, or lamina, a local coordinate system $x_1x_2x_3$ is also introduced, with the x_1-axis along the fiber direction and the x_3-axis being identical to the z-axis. The fiber direction (x_1-axis) in each lamina makes an angle φ_m to the x-axis; φ_m, in general, varies from one lamina to the next.

The z-dependent parts of the three displacement components in the global coordinate system are denoted by $U(z)$, $V(z)$, and $W(z)$ and the three stress components σ_{13}, σ_{23}, and σ_{33} by $X(z)$, $Y(z)$, and $Z(z)$, respectively. The symbols u_i and σ_{i3} ($i = 1, 2, 3$) denote the z-dependent parts of the displacement and stress components in each local coordinate system.

The displacement and stress vectors in the global coordinate system are transformed from those in the local coordinate system by the following relations:

$$\begin{Bmatrix} U_m \\ V_m \\ W_m \end{Bmatrix} = [L(m)] \begin{Bmatrix} u_1^m \\ u_2^m \\ u_3^m \end{Bmatrix}$$
$$\begin{Bmatrix} X_m \\ Y_m \\ Z_m \end{Bmatrix} = [L(m)] \begin{Bmatrix} \sigma_{13}^m \\ \sigma_{23}^m \\ \sigma_{33}^m \end{Bmatrix} \quad \textbf{(4.91)}$$

where the subscript and superscript m represents the corresponding components in the mth layer, and the transformation matrix $[L(m)]$ is given by

$$[L(m)] = \begin{bmatrix} \cos(\phi_m) & -\sin(\phi_m) & 0 \\ \sin(\phi_m) & \cos(\phi_m) & 0 \\ 0 & 0 & 1 \end{bmatrix} \quad \textbf{(4.92)}$$

The stress-displacement vector $\{S(z)\}$ must be continuous across all interfaces parallel to the xy-plane. In the m-th lamina (for which $z_{m-1} \leq z \leq z_m$), the $\{S_m(z)\}$ vector is represented in the following partitioned matrix form, using Equation 4.81 and Equation 4.91:

$$\{S_m(z)\} = \begin{bmatrix} L(m) & 0 \\ 0 & L(m) \end{bmatrix} \begin{bmatrix} Q_{11}(m) & Q_{12}(m) \\ Q_{21}(m) & Q_{22}(m) \end{bmatrix} \begin{bmatrix} E^+(z,m) & 0 \\ 0 & E^-(z,m) \end{bmatrix} \begin{Bmatrix} A^+(m) \\ A^-(m) \end{Bmatrix} \quad \textbf{(4.93)}$$

where all partitioned submatrices and vectors are of order three. The vectors$\{A^{\pm}(m)\}$ and the matrices $[Q_{ij}(m)]$ have the same definitions as those for the uniform plate (see Equation 4.83 and Equation 4.84). For computing $[Q_{ij}(m)]$, material properties in Equation 4.84 should be substituted by those for the mth lamina. The matrices $[E^{\pm}(z,m)]$ are given by

$$[E^+(z,m)] = \begin{bmatrix} e^{i\zeta_1(z-z_{m-1})} & 0 & 0 \\ 0 & e^{i\zeta_2(z-z_{m-1})} & 0 \\ 0 & 0 & e^{i\zeta_3(z-z_{m-1})} \end{bmatrix}$$

$$[E^-(z,m)] = \begin{bmatrix} e^{i\zeta_1(z_m-z)} & 0 & 0 \\ 0 & e^{i\zeta_2(z_m-z)} & 0 \\ 0 & 0 & e^{i\zeta_3(z_m-z)} \end{bmatrix} \quad \textbf{(4.94)}$$

The continuity conditions across the interface z_m, $\{S_m\,(z_m)\} = \{S_{m+1}(z_m)\}$, can be written as:

$$[Q_m^-]\{A_m\} = [Q_{m+1}^+]\{A_{m+1}\} \quad \textbf{(4.95)}$$

where

$$\{A_m\} = \begin{Bmatrix} A_m^+ \\ A_m^- \end{Bmatrix}$$

$$[Q_m^+] = \begin{bmatrix} -L(m)Q_{11}(m) & -L(m)Q_{12}(m)E_m \\ -L(m)Q_{21}(m) & -L(m)Q_{22}(m)E_m \end{bmatrix}$$

$$[Q_m^-] = \begin{bmatrix} L(m)Q_{11}(m)E_m & L(m)Q_{12}(m) \\ L(m)Q_{21}(m)E_m & L(m)Q_{22}(m) \end{bmatrix} \quad \textbf{(4.96)}$$

$$[E_m] = \begin{bmatrix} e^{i\zeta_1 h_m} & 0 & 0 \\ 0 & e^{i\zeta_2 h_m} & 0 \\ 0 & 0 & e^{i\zeta_3 h_m} \end{bmatrix}$$

with $h_m = z_m - z_{m-1.}$ The superscripts – and + represent the upper and lower interface of the m-th lamina. Furthermore, the wave numbers ζ_j (j =1, 2, 3) are subject to the constraint $\mathrm{Im}(\zeta_j) > 0$ so that the diagonal elements of $[E_m]$ are always bounded.

Consider a multilayered, multiorientation composite plate, having N layers and subjected to a plane acoustic wave striking its top surface. The following equation can be obtained by satisfying boundary conditions at the fluid-solid interfaces and continuity conditions at the inner interfaces:

$$\begin{bmatrix} Q_0^- & Q_1^+ & 0 & 0 & \cdots & \cdots & \cdots & \cdots & 0 \\ 0 & Q_1^- & Q_2^+ & 0 & \cdots & \cdots & \cdots & \cdots & 0 \\ \cdots & \cdots & \cdots & \cdots & \cdots & \cdots & \cdots & \cdots & \cdots \\ 0 & \cdots & 0 & Q_{m-1}^- & Q_m^+ & 0 & \cdots & \cdots & 0 \\ 0 & \cdots & \cdots & 0 & Q_m^- & Q_{m+1}^+ & 0 & \cdots & 0 \\ \cdots & \cdots & \cdots & \cdots & \cdots & \cdots & \cdots & \cdots & \cdots \\ \cdots & \cdots & \cdots & \cdots & \cdots & \cdots & \cdots & \cdots & \cdots \\ \cdots & \cdots & \cdots & \cdots & \cdots & \cdots & \cdots & \cdots & \cdots \\ 0 & \cdots & \cdots & \cdots & \cdots & \cdots & 0 & Q_N^- & Q_b^+ \end{bmatrix} \begin{Bmatrix} A_0 \\ A_1 \\ \vdots \\ A_m \\ A_{m+1} \\ \vdots \\ \vdots \\ A_N \\ A_{N+1} \end{Bmatrix} = \begin{Bmatrix} P_1 \\ P_2 \\ 0 \\ 0 \\ 0 \\ \vdots \\ \vdots \\ 0 \\ 0 \end{Bmatrix} \quad \mathbf{(4.97)}$$

where the matrices $[Q_0^-]$ and $[Q_b^+]$ and vectors $\{P_1\}$ and $\{P_2\}$ are related to the fluid loading and are given by

$$[Q_0^-] = \begin{bmatrix} -1 & 0 & 0 \\ 0 & -1 & 0 \\ 0 & 0 & i\zeta_0 \\ 0 & 0 & 0 \\ 0 & 0 & 0 \\ 0 & 0 & \rho_0\omega^2 \end{bmatrix}^T, \quad [Q_b^+] = \begin{bmatrix} 1 & 0 & 0 \\ 0 & 1 & 0 \\ 0 & 0 & i\zeta_0 \\ 0 & 0 & 0 \\ 0 & 0 & 0 \\ 0 & 0 & -\rho_0\omega^2 \end{bmatrix}^T \quad \mathbf{(4.98)}$$

$$\{P_1\} = \{0 \quad 0 \quad i\zeta_0\}, \qquad \{P_2\} = \{0 \quad 0 \quad -\rho_0\omega^2\}$$

The unknown coefficients, R and T, and the tangential displacements on the fluid-solid interfaces are contained in $\{A_0\}$ and $\{A_b\}$ (or $\{A_{N+1}\}$) in the following form:

$$\{A_0\} = \{U_0 \quad V_0 \quad R\}, \quad \{A_{N+1}\} = \{U_{N+1} \quad V_{N+1} \quad T\} \qquad (4.99)$$

Equation 4.97 can be solved by standard numerical methods.

4.6.3 Multilayered Composite Plate in a Vacuum (Dispersion Equation)

To obtain the dispersion equation for a multiorientation composite laminate placed in a vacuum, the traction values at the two outer surfaces are set equal to zero. Then Equation 4.97 gives a system of homogeneous equations. A nontrivial solution for that system of equations exists if

$$\text{Det}\begin{bmatrix} \hat{Q}_1^+ & 0 & 0 & \cdots & \cdots & \cdots & \cdots & \cdots & 0 \\ Q_1^- & Q_2^+ & 0 & 0 & \cdots & \cdots & \cdots & \cdots & 0 \\ 0 & Q_2^- & Q_3^+ & 0 & \cdots & \cdots & \cdots & \cdots & 0 \\ \cdots & \cdots & \cdots & \cdots & \cdots & \cdots & \cdots & \cdots & \cdots \\ 0 & \cdots & 0 & Q_{m-1}^- & Q_m^+ & 0 & \cdots & \cdots & 0 \\ 0 & \cdots & \cdots & 0 & Q_m^- & Q_{m+1}^+ & 0 & \cdots & 0 \\ \cdots & \cdots & \cdots & \cdots & \cdots & \cdots & \cdots & \cdots & \cdots \\ 0 & \cdots & \cdots & \cdots & \cdots & 0 & Q_{N-1}^- & Q_N^+ & 0 \\ 0 & \cdots & \cdots & \cdots & \cdots & \cdots & \cdots & 0 & \hat{Q}_N^- \end{bmatrix} = 0 \quad \textbf{(4.100a)}$$

where

$$\begin{aligned} [\hat{Q}_1^+] &= [L(1)Q_{21}(1) \quad L(1)Q_{22}(1)E_1] \\ [\hat{Q}_N^-] &= [-L(N)Q_{21}(N)E_N \quad -L(N)Q_{22}(N)] \end{aligned} \quad \textbf{(4.100b)}$$

For waves propagating in a cross-ply laminate at 0 or 90° orientation to the fibers of the top lamina, the determinant becomes singular since it includes the antiplane (shear horizontal [SH]) motion. To remove this singularity, it is necessary to remove the elements associated with SH-wave motion and adjust the dimensions of the matrices appropriately (Mal et al., 1991).

4.6.4 Composite Plate Analysis with Attenuation

The solution technique discussed in Section 4.6.1 through Section 4.6.3 ignores the material attenuation. To incorporate the material attenuation in the formulation, the material constants of Equation 4.66 are to be made complex. The real parts give the stiffness properties and the imaginary parts are associated with the attenuation properties. Attenuation or dissipation of the waves in fiber reinforced composite materials is caused by the viscoelastic nature of the matrix and by scattering from fibers and other inhomogenities. Both of these effects can be modeled in the frequency domain by assuming that the material constants, C_{ij}, are complex and frequency dependent. For isotropic viscoelastic solid modeling, P- and S-wave speeds can be made complex and expressed in the following form (Mal et al., 1992):

$$\alpha = \sqrt{\frac{\lambda + 2\mu}{\rho}} = \frac{\hat{\alpha}}{1 + \dfrac{i}{2Q_\alpha}}$$
$$\beta = \sqrt{\frac{\mu}{\rho}} = \frac{\hat{\beta}}{1 + \dfrac{i}{2Q_\beta}} \tag{4.101a}$$

where Q_α and Q_β are called quality factors.

Laboratory measurements on a variety of materials have shown that (Mal et al., 1992): (1) $\hat{\alpha}$, $\hat{\beta}$, Q_α, and Q_β are independent of frequency in a broad frequency range; (2) Q_α and Q_β are proportional to the wave speeds $\hat{\alpha}$ and $\hat{\beta}$, respectively; and (3) numerical values of Q_α and Q_β for most materials are large. Therefore,

$$\frac{1}{Q_\beta} = \frac{1}{k \cdot \hat{\beta}} = p$$
$$\frac{1}{Q_\alpha} = \frac{1}{k \cdot \hat{\alpha}} = \frac{1}{k \cdot \hat{\beta}} \frac{\hat{\beta}}{\hat{\alpha}} = p \frac{\hat{\beta}}{\hat{\alpha}} \tag{4.101b}$$

From Equation 4.101a and Equation 4.101b we get

$$\alpha = \frac{\hat{\alpha}}{1 + \dfrac{i}{2Q_\alpha}} = \frac{\hat{\alpha}}{1 + \dfrac{1}{2} ip\left(\dfrac{\hat{\beta}}{\hat{\alpha}}\right)} = \frac{\hat{\alpha}}{\sqrt{1 + ip\left(\dfrac{\hat{\beta}}{\hat{\alpha}}\right)}}$$
$$\beta = \frac{\hat{\beta}}{1 + \dfrac{i}{2Q_\beta}} = \frac{\hat{\beta}}{1 + \dfrac{1}{2} ip} = \frac{\hat{\beta}}{\sqrt{1 + ip}} \tag{4.101c}$$

or

$$\alpha^2 = \frac{(\hat{\alpha})^2}{1 + ip\left(\frac{\hat{\beta}}{\hat{\alpha}}\right)}$$
$$\beta^2 = \frac{\left(\hat{\beta}\right)^2}{1 + ip} \tag{4.101d}$$

The material attenuation is expressed in terms of only one material parameter, p. This is possible due to the experimental fact that the quality factor, which is proportional to the inverse of the damping factor ($p/2$), is approximately proportional to the wave speed.

For a transversely isotropic solid, it can be shown that the five bulk wave speeds in the material are proportional to $\sqrt{a_i}$ for $i = 1$ to 5 (see Equation 4.77 for the definition of a_i). Thus, for such anisotropic solids with attenuation, a_i of Equation 4.77 can be made complex in the same manner as in Equation 4.101d, (Mal et al., 1992):

$$\begin{aligned}
\frac{C_{22}}{\rho} &= a_1 = \hat{a}_1\left(1 + ip\sqrt{\frac{\hat{a}_5}{\hat{a}_1}}\right)^{-1} \\
\frac{C_{11}}{\rho} &= a_2 = \hat{a}_2\left(1 + ip\sqrt{\frac{\hat{a}_5}{\hat{a}_2}}\right)^{-1} \\
\frac{C_{12} + C_{55}}{\rho} &= a_3 = \hat{a}_3\left(1 + ip\sqrt{\frac{\hat{a}_5}{\hat{a}_3}}\right)^{-1} \\
\frac{C_{44}}{\rho} &= a_4 = \hat{a}_4\left(1 + ip\sqrt{\frac{\hat{a}_5}{\hat{a}_4}}\right)^{-1} \\
\frac{C_{55}}{\rho} &= a_5 = \hat{a}_5(1 + ip)^{-1}
\end{aligned} \tag{4.102}$$

Note that in the above definition there is only one independent parameter p that is associated with the material attenuation, and $p/2$ is called the *damping factor* or *damping ratio*. The damping factor is frequency-independent at low-frequency range, when the wavelengths are long compared to the internal microstructure dimensions (grain size, fiber diameter, etc.). At higher frequencies the damping factor increases with the frequency because of the wave scattering by the internal microstructure. Mal et al. (1992) proposed the following frequency dependence of the damping factor:

$$p = p_0\left[1 + a_0\left(\frac{f}{f_0} - 1\right)^n H(f - f_0)\right] \quad \textbf{(4.103)}$$

where $H(f)$ is the Heaviside step function, p_0 and a_0 are material constants, $n = 2$ for 2-dimensional models, and $n = 3$ for 3-dimensional models. Equation 4.103 implies that wave attenuation is constant for frequency less than f_0, and it increases with frequency for frequency greater than f_0. The material parameter a_0 determines the rate of increase of attenuation with frequency.

The quality factor and damping factor are only two of many definitions associated with the material damping and attenuation. Other terminologies and symbols used for material damping are:

Ψ = Specific damping capacity
η = Loss factor
δ = Logarithmic decrement
ϕ = Phase angle by which stress leads strain
E'' = Loss modulus
ζ = $p/2$ = Damping ratio or damping factor
ΔW = Energy loss per cycle
α = Attenuation

Relations between these various definitions of material damping are given below for small values of material damping ($\tan\phi < 0.1$) (Kinra and Wolfenden, 1992):

$$\frac{1}{Q} = \frac{\Psi}{2\pi} = \eta = \frac{\delta}{\pi} = \tan\phi = \phi = \frac{E''}{E'} = 2\zeta = \frac{\Delta W}{2\pi W} = \frac{\lambda\alpha}{\pi} \quad \textbf{(4.104)}$$

where
Q = Quality factor
E' = Storage modulus
W = Maximum elastic stored energy
λ = Wavelength of elastic wave

4.7 Defect Detection in Multilayered Composite Plate

Following the theory described in Section 4.6, Mal et al. (1991) calculated the reflected spectra of defect-free and damaged (delaminated) composite plates. They have shown both theoretically and experimentally that delamination has a strong effect on the reflected signal spectra. Scanning a plate by Lamb waves to detect internal defects has been proposed by Nagy et al.

(1989), Chimenti and Martin (1991), Ditri, Rose and Chen (1992), Kundu et al. (1996), Maslov and Kundu (1997), and Kundu and Maslov (1997), among others. Yang and Kundu (1998) used the theory of guided wave propagation in multilayered anisotropic composite plates to conclude which Lamb mode should be used to detect defects in a specific layer of a 12-ply composite plate. Later, Kundu et al. (2001) analyzed the stress profiles in a multilayered composite plate generated by an ultrasonic beam striking the plate at an incident angle close to the Lamb critical angle and not exactly at the critical angle. Results showed that it is possible to detect different types of defect (delamination, broken fibers, missing fibers, etc.) in the composite plate and approximately predict in which ply the defect is located. A five-layer metal-matrix (Ti-6Al-4V) composite plate reinforced by SCS-6 fibers was studied by Kundu et al. (2001). The numerical and experimental results of this study are presented in Section 4.7.2.

4.7.1 Specimen Description

The specimen is a 5-layer metal matrix composite plate of dimension 80 × 33 × 1.97 mm^3. Five layers or plies of SCS-6 fibers in Ti-6Al-4V matrix are oriented in 90° and 0° directions in alternate layers. SCS is a copyrighted/registered name by the fiber manufacturer, Textron Inc. This fiber has a carbon core of about 25 μm diameter, two concentric layers of silicon carbide surround the carbon core, and two very thin (a few microns thick) layers of carbon coating are placed on the outside. The overall fiber diameter is about 152 μm. The fibers in the top, middle, and bottom layers are oriented in the x_2-direction or along the length of the plate; the other two plies are in the x_1-direction or along the width of the plate as shown in Figure 4.30. The composite was made by the foil-fiber-foil technique. The internal flaws in this figure were intentionally introduced in the plate during the fabrication process. The first (top) and the fifth (bottom) layers of fibers did not have any flaw. The left part of the second layer fibers was coated with boron nitride to impede the formation of good bonding between the fibers and the matrix. The fibers in the third layer were intentionally broken near the middle. The fourth layer had two areas of missing fibers; on the left side five fibers and on the right side ten fibers were removed. Photographs of the third and fourth layers are shown in Figure 4.31. These photographs were taken before fabricating the specimen. Broken and missing fiber zones can be clearly seen in these photographs.

Figure 4.30 shows how the specimen was scanned by propagating Lamb waves in the direction normal to the fiber direction of layers 1, 3, and 5 and parallel to the fibers of layers 2 and 4.

Before investigating the images generated by Lamb waves, the specimen was first scanned by the normal incidence C-scan technique. The C-scan images are shown in Figure 4.32. The three images of Figure 4.32 were generated by 10-MHz (top and middle) and 75-MHz (bottom) focused transducers used in the pulse-echo mode. The transducer axis is positioned nor-

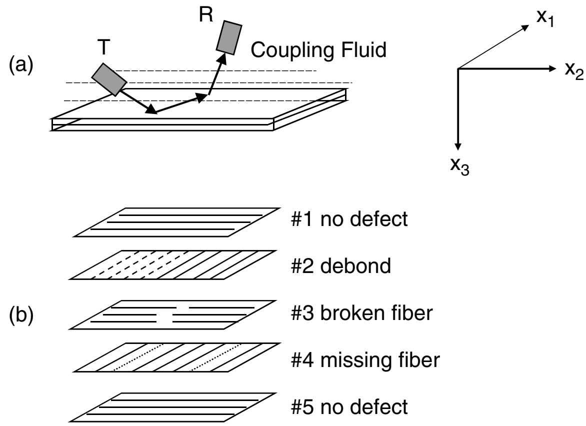

FIGURE 4.30
(a) Relative orientations of the transmitter, receiver, and the plate specimen and (b) schematic of the internal defects in the five layers of the composite plate specimen. (Source: From Kundu, T. et al., *Ultrasonics*, 39, 283–290, 2001. Reprinted with permission from Elsevier.)

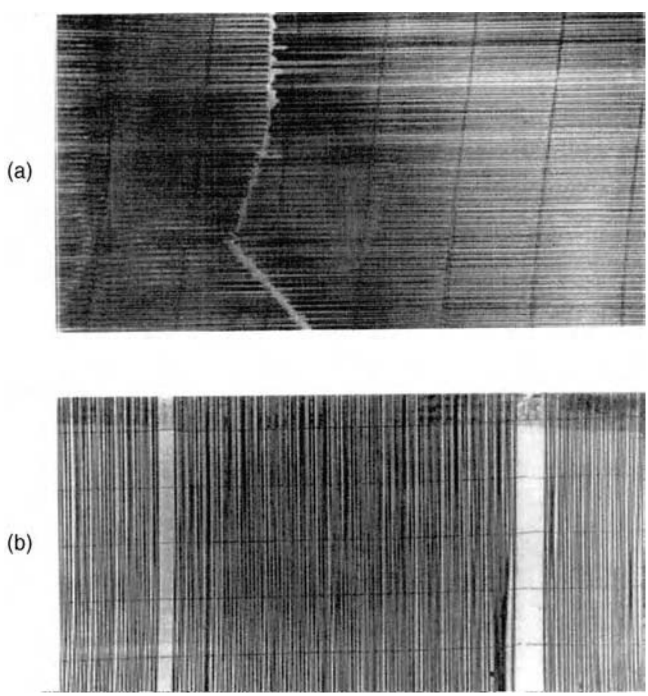

FIGURE 4.31
Photograph of (a) the broken fibers of the third layer and (b) missing fibers of the fourth layer, taken before fabricating the specimen. (Source: From Kundu, T. et al., *Ultrasonics*, 34, 49–49, 1996. Reprinted with permission from Elsevier.)

mal to the plate specimen. For the top and bottom images, the gate position is such that the reflected signals from the middle of the layer are received and the back surface echo is omitted; the internal defects should clearly be seen in these two images, for the middle image the back surface echo is also recorded. In all of these three images the debond can be clearly seen. The missing and broken fibers can be faintly seen in some images.

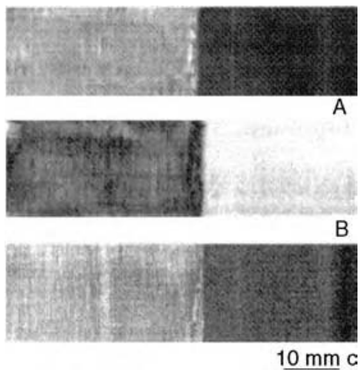

FIGURE 4.32
Conventional C-scan images generated by 10-MHz (top and middle) and 75-MHz (bottom) focused transducers, used in the pulse-echo mode. The back surface echo is omitted for constructing the top and bottom images, but it is considered for the middle image. (Source: From Kundu, T. et al., *Ultrasonics*, 34, 49–49, 1996. Reprinted with permission from Elsevier.)

For understanding and analyzing the Lamb wave generated images, it is necessary to compute the internal stress and displacement profiles when Lamb waves propagate in the direction normal to the fiber direction of layers 1, 3, and 5. In other words, the fiber orientation relative to the Lamb wave propagation direction is 90° for layers 1, 3, and 5, and 0° for layers 2 and 4. During the experiment the specimen was immersed in water.

4.7.2 Numerical and Experimental Results

For computing internal stresses and displacements in a multilayered plate all the elastic constants of individual layers must be indentified. However, the five independent elastic constants of the individual layers were not known and could not be measured easily. Only the density (4.1 g/cm^3) of the plate could be measured without any difficulty. The P-wave speed (1.49 km/sec) and the density (1 g/cm^3) of the coupling fluid (water) are also known quantities.

Huang et al. (1997), and Yang and Mal (1996) gave elastic properties of titanium (Ti) and silicon carbide (SiC) for SCS-6 fiber reinforced titanium matrix. These properties are listed in Table 4.3.

From Table 4.3, the stress-strain relation for Ti and SiC can be written in the following form. In the constitutive matrix (or [C] matrix) a range is given

TABLE 4.3

Elastic Properties of Titanium and Silicon Carbide

Material	Young's Modulus (E, GPa)	Poisson's ratio (ν)	Lame's First constant (λ, GPa)	Shear Modulus (G, GPa)	Density (ρ, g/cm³)
Titanium[1]	121.6	0.35	103.3	45.1	5.4
Titanium[2]	96.5		55.9	37.1	4.5
Silicon-Carbide[1]	415.0	0.17	91.4	177.4	3.2
Silicon-Carbide[2]	431.0		176	172.0	3.2

Note: Values given in these two references are marked by superscripts 1 and 2.

[1]Huang W., et al., *J. Acoust. Soc. Am.*, 101, 2031–3042, 1997.
[2]Yang, R.-B. and Mal A.K., *Int. J. Eng. Sci.*, 34, 67–79, 1996.

Source: From Kundu T. et al., *Ultrasonics*, 39, 283–290, 2001. With permission from Elsevier.

for each element. This range is obtained from the two sets of values of the elastic constants given in Table 4.3:

Stress-strain relation for Ti:

$$\begin{Bmatrix} \sigma_{11} \\ \sigma_{22} \\ \sigma_{33} \\ \sigma_{23} \\ \sigma_{31} \\ \sigma_{12} \end{Bmatrix} = \begin{bmatrix} 130.1-193.5 & 55.9-103.3 & 55.9-103.3 & 0 & 0 & 0 \\ & 130.1-193.3 & 55.9-103.3 & 0 & 0 & 0 \\ & & 130.1-193.3 & 0 & 0 & 0 \\ & & & 37.1-45.1 & 0 & 0 \\ & & & & 37.1-45.1 & 0 \\ & & & & & 37.1-45.1 \end{bmatrix} \begin{Bmatrix} \varepsilon_{11} \\ \varepsilon_{22} \\ \varepsilon_{33} \\ 2\varepsilon_{23} \\ 2\varepsilon_{31} \\ 2\varepsilon_{12} \end{Bmatrix} \quad \textbf{(4.105a)}$$

Stress-strain relation for SiC:

$$\begin{Bmatrix} \sigma_{11} \\ \sigma_{22} \\ \sigma_{33} \\ \sigma_{23} \\ \sigma_{31} \\ \sigma_{12} \end{Bmatrix} = \begin{bmatrix} 446-520 & 91.4-176 & 91.4-176 & 0 & 0 & 0 \\ & 446-520 & 91.4-176 & 0 & 0 & 0 \\ & & 446-520 & 0 & 0 & 0 \\ & & & 172-177.4 & 0 & 0 \\ & & & & 172-177.4 & 0 \\ & & & & & 172-177.4 \end{bmatrix} \begin{Bmatrix} \varepsilon_{11} \\ \varepsilon_{22} \\ \varepsilon_{33} \\ 2\varepsilon_{23} \\ 2\varepsilon_{31} \\ 2\varepsilon_{12} \end{Bmatrix} \quad \textbf{(4.105b)}$$

Constitutive matrices of both Ti and SiC, in Equation 4.105a and Equation 4.105b are isotropic and have two independent elastic constants. However, the SiC fiber reinforced Ti matrix composite has hexagonal symmetry. The [C] matrix for the composite should be anisotropic and have five independent elastic constants. Experimental values of phase velocity for different Lamb modes at various frequencies, as obtained by Kundu et al. (1996), are shown by 20 open triangles in Figure 4.33.

The [C] matrix for the individual layers of the five-layer composite plate was obtained by the trial and error method by matching the theoretical dispersion curves with the experimental points. After a number of trials, the following stress-strain relation gave the best fit between the theoretical curves and the experimental points:

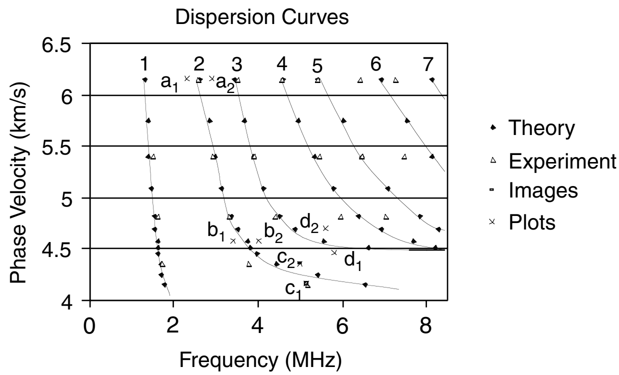

FIGURE 4.33
Numerically computed dispersion curves (diamond symbols connected by continuous lines). Twenty experimental points are shown by triangular symbols. Stress plots of Figure 4.34, Figure 4.35 and Figure 4.37 are generated for eight different frequency-phase velocity combinations (a_j, b_j, c_j and d_j, j = 1 and 2); those points are shown by cross markers. Square markers (points c_1 and c_2) show the frequency-phase velocity combinations used for generating the two images of Figure 4.36. The 7 modes, shown here, are numbered from 1 to 7. (Source: From Kundu, T. et al., *Ultrasonics*, 39, 283–290, 2001. With permission from Elsevier.)

$$\begin{Bmatrix} \sigma_{11} \\ \sigma_{22} \\ \sigma_{33} \\ \sigma_{23} \\ \sigma_{31} \\ \sigma_{12} \end{Bmatrix} = \begin{bmatrix} 325 & 103 & 103 & 0 & 0 & 0 \\ & 194 & 92 & 0 & 0 & 0 \\ & & 194 & 0 & 0 & 0 \\ & & & 51 & 0 & 0 \\ & & & & 100 & 0 \\ & & & & & 100 \end{bmatrix} \begin{Bmatrix} \varepsilon_{11} \\ \varepsilon_{22} \\ \varepsilon_{33} \\ 2\varepsilon_{23} \\ 2\varepsilon_{31} \\ 2\varepsilon_{12} \end{Bmatrix} \quad \textbf{(4.106)}$$

where x_1 is the fiber direction (elastic constants are given in GPa). Note that $C_{44} = (C_{22} - C_{23})/2$.

Theoretical leaky Lamb wave dispersion curves for the five-layer composite plate of 1.97 mm total thickness are shown in Figure 4.33 by black diamond symbols connected by continuous lines. These are computed with the individual layer properties given in Equation 4.106; for Lamb waves propagating normal to the fiber direction of the top layer, see Figure 4.30. Lamb modes are numbered from 1 to 7 from left (low frequency) to right (high frequency). It should be noted here that the matching between the experimental values and the theoretical dispersion curve is acceptable for the five modes. Fourteen out of the 17 experimental values for these five modes almost coincide with the theoretical curve, but the sixth and seventh modes did not match very well with the theoretical curves. This matching can be further improved by adjusting the elastic properties of the layers by more trial and error iterations or by implementing sophisticated optimization schemes such as the simplex algorithm (Nelder and Mead, 1965; Karim et al., 1990; Kundu, 1992; Kinra and Iyer, 1995).

After obtaining the elastic properties, stress profiles are computed for different frequency-phase velocity combinations on and around the second and third Lamb modes. These frequency-phase velocity combinations, for which stress profiles have been computed, are denoted by a_j, b_j, c_j, and d_j (j = 1 and 2) and shown by eight crosses in Figure 4.33. The plots are obtained for the plane longitudinal wave of a given frequency striking the composite plate at a specified angle. The corresponding phase velocity is obtained from the incident angle using Snell's law (Equation 4.31). If the phase velocity-frequency combination is such that it is near a leaky Lamb mode but does not coincide exactly with the dispersion curve, then the stress and displacement components would differ from those for the leaky Lamb wave propagation. It should be mentioned here that, for the stress field computations near Lamb modes, the contributions of incident, reflected, and transmitted waves in the upper and lower fluid half spaces are considered. The incident angle is set such that the phase velocity, computed from Snell's law, becomes close to a Lamb mode phase velocity. Because of the presence of the incident, reflected, and transmitted signals the normal stress components, at the top and bottom surfaces of the plate, do not have the same values.

Images of the composite plate have been generated for two different frequency-phase velocity combinations (c_1 and c_2). Both points are marked by two squares in Figure 4.33.

Figure 4.34 and Figure 4.35 show the computed stress profiles along the thickness or depth of the plate for 6 frequency-phase velocity combinations: two pairs (a_j and b_j) near the second mode and one pair (d_j) near the third mode. Figure 4.34 shows the shear stress (σ_{13}) variations along the depth of the plate. Figure 4.35 shows the normal stress variations (σ_{33} in the left column and σ_{11} in the right column). The phase velocity (c_L) and the incident angle (θ) are related by Snell's law.

The horizontal axes of Figure 4.34 and Figure 4.35 show the depth along the plate thickness (in the x_3-direction, see Figure 4.30a) varying from 0 (top of the plate) to 1.97 mm (bottom of the plate). Since the plate has five layers of identical thickness, the layer interfaces are located at 0.394, 0.788, 1.182, and 1.576 mm. In Figure 4.34 and Figure 4.35 the horizontal axis is marked at 0.4, 0.8, 1.2, and 1.6 mm, very close to the interface positions. In each plot of Figure 4.34 and Figure 4.35, two curves are shown. Dotted lines correspond to the frequency-phase velocity combinations that are located slightly below or left of the Lamb modes and the continuous lines correspond to the points slightly above or right of the Lamb modes. The curves in Figure 4.34 and Figure 4.35 are marked as SIJ-θ,f(αj) where θ is the angle of incidence in degree, f is the signal frequency in MHz, αj identifies the point (a_j, b_j, c_j, or d_j) of Figure 4.33, and SIJ stands for S13 for shear stress (σ_{13}) and S33 or

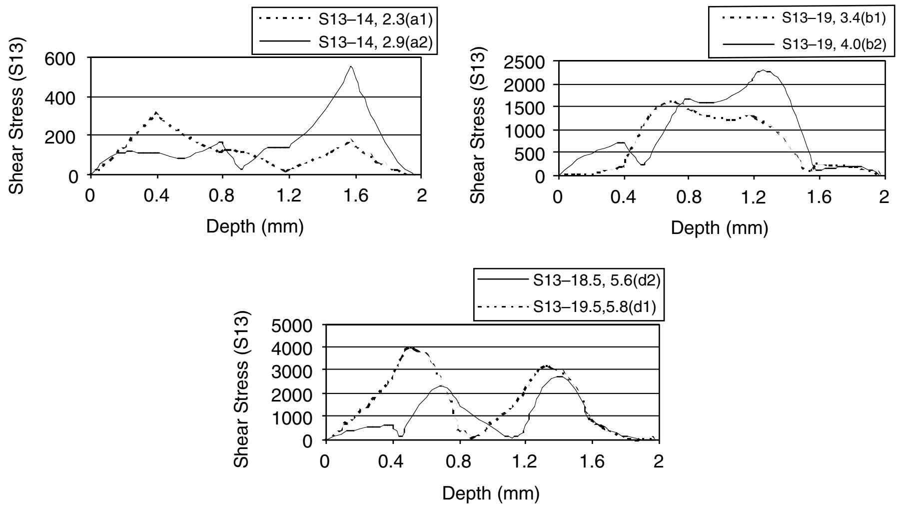

FIGURE 4.34
Shear stress variations inside the composite plate near second (top figures) and third (bottom figure) Lamb modes. Dotted lines have been generated for the frequency-phase velocity combinations denoted by points a_1, b_1, and d_1 in Figure 4.33. Points a_2, b_2, and d_2 of Figure 4.33 generate the continuous curves. (Source: From Kundu, T. et. al., *Ultrasonics*, 39, 283–290, 2001. Reprinted with permission from Elsevier.)

S11 for normal stresses (σ_{33} or σ_{11}). Note that the curves are not symmetric about the central plane of the plate. Therefore, these near Lamb modes, which are generated as the total effect of the incident, reflected, and transmitted waves near the Lamb critical angle of incidence, should be able to distinguish defects in a layer from similar defects in another layer of mirror symmetry.

It should be noted here that the continuous curves give relatively higher values in the lower half of the plate. For the frequency-phase velocity combinations a_2 and b_2 (of Figure 4.33), σ_{13} and σ_{11} in the fourth layer are much greater than those in the second layer. On the other hand, for a_1 and b_1 points, the first and second layer responses are greater than the fourth and fifth layer responses. This difference is less prominent for σ_{33}. This general trend is true for points d_1 and d_2 also. However, for the point d_2 the differences in the stress amplitude between the upper and lower halves of the plate are not as strong as those for points a_2 and b_2.

The results from Figure 4.34 and Figure 4.35 are summarized below:

1. Stress fields in the neighborhood of a Lamb mode are not symmetric with respect to the central plane of symmetry of the plate.
2. If moving in one direction relative to the Lamb mode causes the stresses to grow in the upper half of the plate, then an opposite direction movement will cause the stresses to grow in the lower half of the plate.

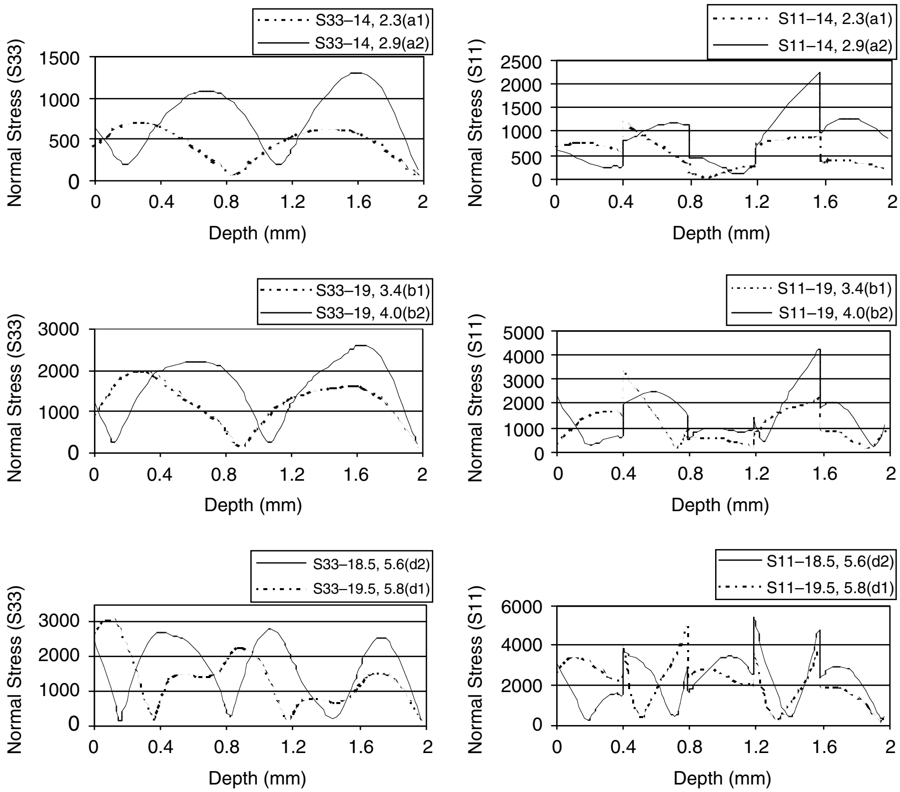

FIGURE 4.35
Normal stress variations inside the composite plate near second and third Lamb modes. Dotted lines have been generated for the frequency-phase velocity combinations denoted by points a_1, b_1, and d_1 in Figure 4.33. Points a_2, b_2, and d_2 of Figure 4.33 generate the continuous curves. σ_{33} and σ_{11} are shown in the left and right columns, respectively. (Source: From Kundu, T. et al., *Ultrasonics*, 39, 283–290, 2001. Reprinted with permission from Elsevier.)

3. The percentage difference in the stress values between two layers of mirror symmetry in the lower and upper halves of the plate is not same for all stress components.
4. The percentage difference in the stress values between two layers of mirror symmetry in the neighborhood of a Lamb mode varies from one Lamb mode to another.

Is this difference in stress amplitudes sufficient to distinguish between the defects in the upper and lower halves of the plate? To answer this question two images of the specimen were generated with the frequency-phase velocity combinations corresponding to points c_1 and c_2 of Figure 4.33. It should be mentioned here that point c_1 corresponds to a 21° incident angle and 5.15-MHz signal frequency, and point c_2 corresponds to a 20° incident angle and 5-MHz signal frequency. A laboratory-made ultrasonic scanner was used for generating the ultrasonic images. A broadband Panametrics transducer (0.5-in. diameter) was excited using the Matec 310 gated amplifier with tone-burst signals from the Wavetek function generator. The reflected signal was received by a Matec receiver and was digitized by a GAGE 40-MHz data acquisition board, and then the received signal was analyzed. The computer program computed either the peak-to-peak or the average amplitude of the signal in a given time window and then plotted it in a grayscale with respect to the horizontal (x_1, x_2) position of the transducers. The window was set near the first arrival time of the signal, avoiding reflections from the plate boundary.

FIGURE 4.36
Two images of the five-layer composite plate specimen generated by two different frequency-phase velocity combinations, shown by points c_1 and c_2 in Figure 4.33. The top image has been generated by 5-MHz signal incident at 20° (point c_2), and the bottom image has been produced by 5.15-MHz signal incident at 21° (point c_1). (Source: From Kundu, T. et al., *Ultrasonics*, 39, 283–290, 2001. Reprinted with permission from Elsevier.)

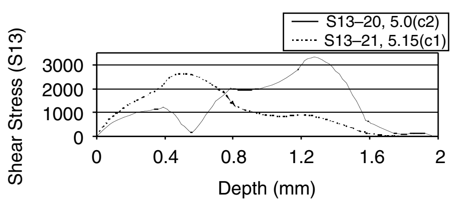

FIGURE 4.37
Shear stress variations inside the composite plate for frequency-phase velocity combinations, denoted by points c_1 (dotted curve) and c_2 (continuous curve) in Figure 4.33. Corresponding ultrasonic images are shown in Figure 4.36. (Source: From Kundu, T. et al., *Ultrasonics*, 39, 283–290, 2001. Reprinted with permission from Elsevier.)

The generated images are shown in Figure 4.36. The 5-MHz signal, with an incident angle of 20°, clearly shows themissing fiber defects of the fourth layer; the 5.15-MHz signal, with an incident angle at 21°, shows the delamination defect (darker region) of the 2nd layer. It also faintly shows the missing fibers of the fourth layer.

Delamination and missing fibers reduce the shear stress carrying capacity at the defect position. Note that the compressive normal stress (σ_{33}) can be present at the defect position from the nonvanishing contact pressure. Therefore, a study of the σ_{13} profile is critical for predicting the sensitivity of the propagating waves to delamination and missing fiber type defects. σ_{13} profiles for points c_1 and c_2 of Figure 4.33 are shown in Figure 4.37. For the 5-MHz signal, σ_{13} is very small in the second layer and it is maximum in the fourth layer. For this reason, in Figure 4.36 we see that the image generated by the 5-MHz signal clearly shows the missing fiber defects of the 4th layer and completely ignores the delamination defect of the second layer. On the other hand, with the 5.15-MHz signal (dotted line of Figure 4.37) the shear stress is maximum in the second layer and very small in the fourth layer. This explains why the image generated by the 5.15-MHz signal shows the delamination defect (darker region) of the 2nd layer, while the missing fiber defect of the fourth layer is not as clear.

The advantage of the near Lamb mode imaging is clearly demonstrated here. In the conventional C-scan image (Figure 4.32), the delamination defect guards the missing fiber defects. In the near Lamb wave image (Figure 4.36), the delamination defect does not have much effect on the detection of missing fiber defects when the appropriate combination of the striking angle and the signal frequency is selected.

Exercise Problems

Problem 4.1

Give the expression of σ_{11} for symmetric and antisymmetric modes for the Lamb wave propagating in the x_1-direction in a plate of thickness $2h$ as shown in Chapter 1, Figure 1.29.

Problem 4.2

For a solid plate in the vacuum the dispersion equations are given in Equation 4.1, and when it is immersed in a fluid the dispersion equations are given in Equation 4.21 and Equation 4.24.

a. If the P-wave speed in the fluid is a finite nonzero value α_f and the fluid density is close to 0, then should Equation 4.1 approximately give the dispersion equations for the plate immersed in that fluid? Justify your answer.
b. If the P-wave speed in the fluid is close to 0 and the fluid density is a finite nonzero value ρ_f, then should Equation 4.1 approximately give the dispersion equations for the plate immersed in that fluid? Justify your answer.

Problem 4.3

Stonely-Scholte waves propagate along a fluid-solid interface (at $x_2 = 0$) with wave amplitudes decaying exponentially in both fluid ($x_2 > 0$) and solid ($x_2 < 0$) media.

a. Obtain an equation from which the Stonely-Scholte wave speed can be computed.
b. Is this Stonely-Scholte wave dispersive?

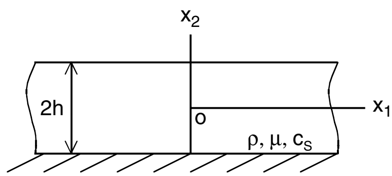

FIGURE 4.38
Problem geometry for Problem 4.5.

c. Specialize the dispersion equation in the limiting case as ρ_f approaches zero.

Problem 4.4

Stonely waves propagate along the interface (at $x_2 = 0$) of two solids with wave amplitudes decaying exponentially in both solids (at $x_2 > 0$ and $x_2 < 0$). Obtain the dispersion equation from which the Stonely wave speed can be computed. (Note: When one solid half-space is replaced by a fluid half-space, then the interface wave generated at the fluid-solid interface is a special case of Stonely wave and is known as Stonely-Scholte wave or Scholte wave.)

Problem 4.5

a. Phase velocity of the guided antiplane wave propagating through a plate of thickness $2h$ that is fixed at the bottom surface and free (stress-free) at the top surface (see Figure 4.38) is given by

$$c_m = \frac{c_S}{\sqrt{1 - f(c_S, m)}}$$

Derive the expression of the function $f(c_S, m)$.

b. Plot the variation of the phase velocity (c_0) as a function of frequency (ω) for the mode that has the lowest cutoff frequency. We will denote this mode as the fundamental mode. In your plot show the cutoff frequency (if any) and the asymptotic value of the curve. Is this mode dispersive?
c. Obtain and plot the mode shape for the fundamental mode.
d. Show how the mode shape that you have obtained in part c is satisfying the boundary conditions.

Problem 4.6

By expanding the Lamb wave dispersion equation for antisymmetric (or flexural) modes at low frequencies, prove that the wave speed (c_L) for the fundamental flexural mode at low frequency is approximately given by

$$c_L = \left(\frac{4\mu(\lambda+\mu)h^2}{3\rho(\lambda+2\mu)} \right)^{1/4} \omega^{1/2}$$

where $2h$ is the plate thickness, ρ is the density, ω is the wave frequency in radian/second, and λ and μ are Lame's 1st and 2nd constants, respectively.

Problem 4.7

ϕ_{fL} and ϕ_{fU} of Equation 4.17 and Equation 4.18 are defined differently, while keeping ϕ and ψ definitions unchanged as shown below:
Symmetric motion:

$$\phi = B\cosh(\eta x_2)e^{ikx_1}$$

$$\psi = C\sinh(\beta x_2)e^{ikx_1}$$

$$\phi_{fL} = \phi_{fU} = M\cosh(\eta_f x_2)e^{ikx_1}$$

Antisymmetric motion:

$$\phi = A\sinh(\eta x_2)e^{ikx_1}$$

$$\psi = D\cosh(\beta x_2)e^{ikx_1}$$

$$\phi_{fL} = \phi_{fU} = N\sinh(\eta_f x_2)e^{ikx_1}$$

Prove that for the above definitions the dispersion equations take the following form:
Symmetric motion:

$$\left(2k^2 - k_S^2\right)^2 \cosh(\eta h)\sinh(\beta h) - 4k^2\eta\beta\sinh(\eta h)\cosh(\beta h) = \frac{\rho_f \eta k_S^4}{\rho\eta_f}\frac{\sinh(\eta h)\sinh(\beta h)}{\tanh(\eta_f h)}$$

Antisymmetric motion:

$$\left(2k^2 - k_S^2\right)^2 \sinh(\eta h)\cosh(\beta h) - 4k^2\eta\beta\cosh(\eta h)\sinh(\beta h)$$
$$= \frac{\rho_f \eta k_S^4}{\rho\eta_f}\tanh(\eta_f h)\cosh(\eta h)\cosh(\beta h)$$

Note that the above dispersion equations are different from those given in Equation 4.21 and Equation 4.24.

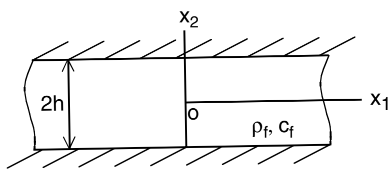

FIGURE 4.39
Fluid layer of thickness 2*h*, trapped between 2 rock half-spaces.

Explain why this difference appears. In other words, what are the shortcomings of the above definitions of ϕ_{fL} and ϕ_{fU}?

Problem 4.8

Calculate the inclination angles (measured from the axis normal to the plate surface) of two narrowband ultrasonic transducers of central frequency 1 and 5 MHz to generate A_0, S_0, A_1, and S_1 modes in a 1-mm thick aluminum plate when the plate is immersed in water (wave speed = 1.48 km/sec) and acetone (wave speed = 1.17 km/sec). You can assume that the dispersion curves for aluminum, shown in Figure 4.6, are not significantly affected when the plate is immersed in water or acetone.

Problem 4.9

a. A fluid layer of thickness 2*h* is trapped between two huge rocks (see Figure 4.39). The fluid density is ρ_f, and P-wave speed in the fluid is c_f. Obtain the dispersion equation for the guided wave propagation through the trapped fluid layer. In your derivation, model the rock as rigid blocks.

b. Solve the dispersion equation and plot the variation of the phase velocity as a function of frequency (ω) for the first three modes. In your plot, show the cutoff frequency (if any) and the asymptotic value of each curve.

c. Obtain and plot the mode shapes (displacement and stress variations) for all three modes.

References

Alleyne, D.N. and Cawley, P., The interaction of Lamb waves with defects, *IEEE Trans. Ultrasonic Ferroelectric Frequency Control*, 39, 381–396, 1992.

Buchwald, V.T., Rayleigh waves in transversely isotropic media, *Q. J. Mech. Appl*. 14, 293–317, 1961.

Chimenti, D.E., and Martin, R.W., Nondestructive evaluation of composite laminates by leaky Lamb waves, *Ultrasonics*, 29, 13–21, 1991.

Christesen, R.M., *Mechanics of Composite Materials*, John Wiley, New York, 1981, chap. 4.

Ditri, J.J., Rose, J.L., and Chen, G., Mode Selection criteria for defect detection optimization using Lamb waves, in *Review of Progress in Quantitative Nondestructive Evaluation*, Vol. 11, Thompson, D.O, and Chimenti, D.E., Eds., Plenum Press, New York, 1992, 2109–2115.

Dunkin, G.W., Computation of modal solutions in layered elastic media at high frequencies, *Bull. Seismological Soc. Am.*, 55, 335–358, 1965.

Dunkin, G.W. and Corbin, D.G., Deformation of a layered elastic half space by uniformly moving loads, *Bull. Seismological Soc. Am.*, 60, 167–191, 1970.

Ghosh, T. and Kundu, T., A new transducer holder mechanism for efficient generation and reception of Lamb modes in large plates, *J. Acoust. Soc. Am.*, 104, 1498–1502, 1998.

Ghosh, T., Kundu, T., and Karpur, P., Efficient use of lamb modes for detecting defects in large plates, *Ultrasonics*, 36, 791–801, 1998.

Haskell, N.A., The dispersion of surface waves on multilayered media, *Bull. Seismological Soc. Am.*, 43, 17–34, 1953.

Huang, W., Rokhlin, S.I., and Wang, Y.J., Analysis of different boundary condition models for study of wave scattering from fiber-matrix interphases, *J. Acoust. Soc. Am.*, 101, 2031–2042, 1997.

Karim, M.R., Mal, A.K., and Bar-Cohen, Y., Inversion of leaky Lamb wave data by simplex algorithm, *J. Acoust. Soc. Am.*, 88, 482–491, 1990.

Kennett, B.L.N., *Seismic Wave Propagation in Stratified Media*, Cambridge University Press, London, 1983.

Kinra, V.K., and Iyer, V.R., Ultrasonic measurement of the thickness, phase velocity, density or attenuation of a thin viscoelastic plate. II. The inverse problem, *Ultrasonics*, 33, 111–122, 1995.

Kinra, V.K. and Wolfenden, A., Eds., Relationship amongst various measures of damping, in *M3D: Mechanics and Mechanisms of Material Damping*, American Society for Testing and Materials, Philadelphia, 1992, p. 3.

Knopoff, L., A matrix method for elastic wave problems, *Bull. Seismological Soc. Am.*, 54, 431–438, 1964.

Kundu, T., Inversion of acoustic material signature of layered solids, *J. Acoust. Soc. Am.*, 91, 591–600, 1992.
Kundu, T. and Mal, A.K., Elastic waves in a multilayered solid due to a dislocation source, *Wave Motion*, 7, 459–471, 1985.
Kundu, T. and Maslov, K.I., Material interface inspection by Lamb waves, *Int. J. Solids Structures*, 34, 3885–3901, 1997.
Kundu, T., Maslov, K.I., Karpur, P., Matikas, T., and Nicolaou, P., A Lamb wave scanning approach for mapping defects in [0/90] titanium matrix composites, *Ultrasonics*, 34, 43–49, 1996.
Kundu, T., Potel, C., and de Belleval, J.F., Importance of the near Lamb mode imaging of multilayered composite plates, *Ultrasonics*, 39, 283–290, 2001.
Lamb, H., On waves in an elastic plate, *Proc. Roy. Soc. London, Ser. A*, 93, 114, 1917.
Mal, A.K., Wave propagation in layered composite laminates under periodic surface loads, *Wave Motion*, 10, 257–266, 1988.
Mal, A.K., Bar-Cohen, Y., and Lih, S.-S., Wave attenuation in fiber-reinforced composites, in *M3D: Mechanics and Mechanisms of Material Damping*, Kinra, V. K., and A. Wolfenden, A., Eds., American Society for Testing and Materials, Philadelphia, 1992, pp. 245–261.
Mal, A. K., Yin, C.-C., and Bar-Cohen, Y., Ultrasonic nondestructive evaluation of cracked composite laminates, *Composites Eng.*, 1, 85–101, 1991.
Maslov, K.I. and Kundu, T., Selection of Lamb modes for detecting internal defects in composite laminates, *Ultrasonics*, 35, 141–150, 1997.
Nagy, P.B., Adler, L., Mih, D., and Sheppard, W., Single mode Lamb wave inspection of composite laminates, in *Review of Progress in Quantitative Nondestructive Evaluation*, Vol. 8B, Thompson, D.O. and Chimenti, D.E., Eds., Plenum Press, New York, 1989, pp.1535–1542.
Nelder, J.A. and Mead, R., A simplex method for function minimization, *Computer J.*, 7, 308–315, 1965.
Rayleigh, L., On waves propagated along the plane surfaces of an elastic solid, *Proc. London Math. Soc.*, 17, 4–11, 1885.
Scholte, J.G., On the stonely wave equation, *Proc. Kon. Noderl. Akad. Wetensch*, 45, 159–164, 1942.
Schwab, F. and Knopoff, L., Surface wave dispersion computations, *Bull. Seismological Soc. Am.*, 60, 321–344, 1970.
Stonely, R., Elastic waves at the surface of separation of two solids, *Proc. R. Soc. London*, 106, 416–428.
Thomson, W.T., Transmission of elastic waves through a stratified solid medium, *J. Appl. Phys.*, 21, 89–93, 1950.
Viktorov, I.A., *Rayleigh and Lamb Waves: Physical Theories and Applications,* Plenum Press, New York, 1967.
Yang, R.-B. and Mal, A.K., Elastic waves in a composite containing inhomogeneous fibers, *Int. J. Eng. Sci.*, 34, 67–79, 1996.
Yang, W. and Kundu, T., Guided waves in multilayered anisotropic plates for internal defect detection, *ASCE J. Eng. Mech.*, 124, 311–318, 1998.

5

Cylindrical Waveguides and Their Applications in Ultrasonic Evaluation

Jianmin Qu and Laurence Jacobs

CONTENTS

5.1 Introduction

For over half a century, many investigators have studied wave propagation in cylindrical waveguides, such as rods, pipes, cylindrical shells, rings, and

0-8493-1462-3/02/$0.00+$1.50

annulus. Various theoretical approaches, approximate theories, and experimental investigations have been reported in the literature. Major results of these studies can be found in several classic books, including, Kolsky (1963), Achenbach (1973), Graff (1975) and Miklowitz (1978). The major objective of this chapter is to provide a comprehensive summary and systematic treatment of cylindrical waveguides. Basic approaches are presented for studying waves propagating in both the longitudinal and circumferential directions. Major results are discussed and the related references are cited for readers who are interested in more details. Furthermore, the emphasis of the discussions are toward nondestructive evaluation applications. It is hoped that this chapter will serve as a useful textbook or a reference tool for practitioners who need background information on cylindrical waveguides.

The chapter is divided into five sections. Fundamental governing equations of wave motion in cylindrical coordinates are listed in Section 5.2. Waves propagating in the longitudinal direction of the cylindrical waveguide are discussed in Section 5.3. Section 5.4 focuses on waves propagating in the circumferential direction. Some applications to nondestructive inspection of pipes and annular components are discussed in Section 5.5.

5.2 Governing Equations in Cylindrical Coordinates

As discussed in Chapter 1 (see also Achenbach, 1973, p. 236), the displacement equations of motion in a cylindrical coordinate system can be written as

$$\nabla^2 u_r - \frac{u}{r^2} - \frac{2}{r^2}\frac{\partial u_\theta}{\partial \theta} + \frac{1}{1-2\upsilon}\frac{\partial \Delta}{\partial r} = \frac{1}{c_T^2}\frac{\partial^2 u_r}{\partial t^2} \tag{5.1}$$

$$\nabla^2 u_\theta - \frac{u_\theta}{r^2} + \frac{2}{r^2}\frac{\partial u_r}{\partial \theta} + \frac{1}{1-2\upsilon}\frac{\partial \Delta}{\partial \theta} = \frac{1}{c_T^2}\frac{\partial^2 u_\theta}{\partial t^2} \tag{5.2}$$

$$\nabla^2 u_z + \frac{1}{1-2\upsilon}\frac{\partial \Delta}{\partial z} = \frac{1}{c_T^2}\frac{\partial^2 u_z}{\partial t^2} \tag{5.3}$$

where ∇^2 is the Laplacian operator

$$\nabla^2 = \frac{\partial^2}{\partial r^2} + \frac{1}{r}\frac{\partial}{\partial r} + \frac{1}{r^2}\frac{\partial^2}{\partial \theta^2} + \frac{\partial^2}{\partial z^2} \tag{5.4}$$

and the symbol Δ represents the dilatation

$$\Delta = \frac{\partial u_r}{\partial r} + \frac{1}{r}\left(\frac{\partial u_\theta}{\partial r} + u_r\right) + \frac{\partial u_z}{\partial z} \tag{5.5}$$

The corresponding stresses are given in terms of the displacements (Achenbach, 1973, pp. 75)

$$\sigma_{rr} = \lambda\left(\frac{\partial u_r}{\partial r} + \frac{u_r}{r} + \frac{1}{r}\frac{\partial u_\theta}{\partial \theta} + \frac{\partial u_z}{\partial z}\right) + 2\mu\frac{\partial u_r}{\partial r} \tag{5.6}$$

$$\sigma_{\theta\theta} = \lambda\left(\frac{\partial u_r}{\partial r} + \frac{u_r}{r} + \frac{1}{r}\frac{\partial u_\theta}{\partial \theta} + \frac{\partial u_z}{\partial z}\right) + 2\mu\left(\frac{u_r}{r} + \frac{1}{r}\frac{\partial u_\theta}{\partial \theta}\right) \tag{5.7}$$

$$\sigma_{zz} = \lambda\left(\frac{\partial u_r}{\partial r} + \frac{u_r}{r} + \frac{1}{r}\frac{\partial u_\theta}{\partial \theta} + \frac{\partial u_z}{\partial z}\right) + 2\mu\frac{\partial u_z}{\partial z} \tag{5.8}$$

$$\sigma_{r\theta} = \mu\left(\frac{\partial u_\theta}{\partial r} - \frac{u_\theta}{r} + \frac{1}{r}\frac{\partial u_r}{\partial \theta}\right) \tag{5.9}$$

$$\sigma_{\theta z} = \mu\left(\frac{1}{r}\frac{\partial u_z}{\partial \theta} + \frac{\partial u_\theta}{\partial z}\right) \tag{5.10}$$

$$\sigma_{zr} = \mu\left(\frac{\partial u_r}{\partial z} + \frac{\partial u_z}{\partial r}\right) \tag{5.11}$$

It follows from the Stokes-Helmholtz decomposition (see Chapter 1) that the displacement vector can be written in terms of a scalar and a vector potential function φ and $\psi = (\psi_r, \psi_\theta, \psi_z)^T$

$$u_r = \frac{\partial \varphi}{\partial r} + \frac{1}{r}\frac{\partial \psi_z}{\partial \theta} - \frac{\partial \psi_\theta}{\partial z} \tag{5.12}$$

$$u_\theta = \frac{1}{r}\frac{\partial \varphi}{\partial \theta} + \frac{\partial \psi_r}{\partial z} - \frac{\partial \psi_z}{\partial r} \tag{5.13}$$

$$u_z = \frac{\partial \varphi}{\partial z} + \frac{1}{r}\frac{\partial (r\psi_\theta)}{\partial r} - \frac{1}{r}\frac{\partial \psi_r}{\partial \theta} \tag{5.14}$$

It can be shown by direct substitution that the displacement equations of motion, Equation 5.1 through Equation 5.3, are identically satisfied if the potentials satisfy the following equations:

$$\nabla^2 \varphi = \frac{1}{c_L^2}\frac{\partial^2 \varphi}{\partial t^2} \tag{5.15}$$

$$\nabla^2 \psi_r - \frac{\psi_r}{r^2} - \frac{2}{r^2}\frac{\partial \psi_\theta}{\partial \theta} = \frac{1}{c_T^2}\frac{\partial^2 \psi_r}{\partial t^2} \tag{5.16}$$

$$\nabla^2\psi_\theta - \frac{\psi_\theta}{r^2} + \frac{2}{r^2}\frac{\partial\psi_r}{\partial\theta} = \frac{1}{c_T^2}\frac{\partial^2\psi_\theta}{\partial t^2} \tag{5.17}$$

$$\nabla^2\psi_z = \frac{1}{c_T^2}\frac{\partial^2\psi_z}{\partial t^2} \tag{5.18}$$

The stresses can be written in terms of the displacement potentials by substituting Equation 5.12 through Equation 5.14 into Equation 5.6 through Equation 5.11:

$$\sigma_{rr} = \lambda\nabla^2\varphi + 2\mu\left(\frac{\partial^2\varphi}{\partial r^2} - \frac{\partial^2\psi_\theta}{\partial r\partial z} - \frac{1}{r^2}\frac{\partial\psi_z}{\partial\theta} + \frac{1}{r}\frac{\partial^2\psi_z}{\partial r\partial\theta}\right) \tag{5.19}$$

$$\sigma_{\theta\theta} = \lambda\nabla^2\varphi + 2\mu\left(\frac{1}{r}\frac{\partial\varphi}{\partial r} + \frac{1}{r^2}\frac{\partial^2\varphi}{\partial\theta^2} + \frac{1}{r}\frac{\partial^2\psi_r}{\partial\theta\partial z} - \frac{1}{r}\frac{\partial\psi_\theta}{\partial z} + \frac{1}{r^2}\frac{\partial\psi_z}{\partial\theta} - \frac{1}{r}\frac{\partial^2\psi_z}{\partial r\partial\theta}\right) \tag{5.20}$$

$$\sigma_{zz} = \lambda\nabla^2\varphi + 2\mu\left(\frac{\partial^2\varphi}{\partial z^2} + \frac{1}{r}\frac{\partial^2\psi_r}{\partial\theta\partial z} + \frac{1}{r}\frac{\partial\psi_\theta}{\partial z} + \frac{\partial^2\psi_\theta}{\partial r\partial z}\right) \tag{5.21}$$

$$\sigma_{r\theta} = \mu\left(\frac{2}{r}\frac{\partial^2\varphi}{\partial r\partial\theta} - \frac{2}{r^2}\frac{\partial\varphi}{\partial\theta} - \frac{1}{r}\frac{\partial\psi_r}{\partial z} + \frac{\partial^2\psi_r}{\partial r\partial z} + \frac{1}{r}\frac{\partial^2\psi_\theta}{\partial\theta\partial z} + \frac{1}{r^2}\frac{\partial^2\psi_z}{\partial\theta^2} + \frac{1}{r}\frac{\partial\psi_z}{\partial r} - \frac{\partial^2\psi_z}{\partial r^2}\right) \tag{5.22}$$

$$\sigma_{z\theta} = \mu\left(\frac{\partial^2\psi_r}{\partial z^2} + \frac{1}{r^2}\frac{\partial\psi_\theta}{\partial\theta} + \frac{2}{r}\frac{\partial^2\varphi}{\partial z\partial\theta} - \frac{1}{r^2}\frac{\partial^2\psi_r}{\partial\theta^2} + \frac{\partial^2\psi_z}{\partial r\partial z} + \frac{1}{r}\frac{\partial^2\psi_\theta}{\partial r\partial\theta}\right) \tag{5.23}$$

$$\sigma_{zr} = \mu\left(-\frac{1}{r^2}\psi_\theta - \frac{\partial^2\psi_\theta}{\partial z^2} + \frac{1}{r^2}\frac{\partial\psi_r}{\partial\theta} + \frac{1}{r}\frac{\partial^2\psi_z}{\partial\theta\partial z} + \frac{1}{r}\frac{\partial\psi_\theta}{\partial r} + 2\frac{\partial^2\varphi}{\partial z\partial\theta} - \frac{1}{r}\frac{\partial^2\psi_r}{\partial r\partial\theta} + \frac{\partial^2\psi_\theta}{\partial r^2}\right) \tag{5.24}$$

5.3 Propagation in the Axial Direction

The propagation of free time-harmonic waves in an infinitely long cylindrical solid cylinder was first formulated on the basis of linear theory of elasticity by Pochhammer (1876) and Chree (1886). Similar waves in a hollow circular cylinder have been investigated, under the restriction of axial symmetry of motion, by McFadden (1954) and Hermann and Mirsky (1956). The corresponding non-axisymmetric case was studied by Gazis (1959). The disper-

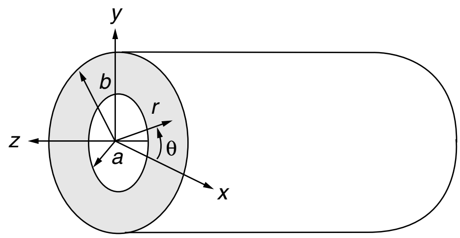

FIGURE 5.1
A cylindrical waveguide with the cylindrical coordinate system ($r\theta z$).

sion equations for these axially propagating waves are rather complex. They have been the subject of study by many researchers (e.g., Hudson, 1943; Holden, 1951; Pao and Mindlin, 1960; Mindlin, 1960; Mindlin and McNiven, 1960; Pao, 1962; Meeker, and Meitzler, 1964).

For time-harmonic waves propagating in the axial (the z-axis) direction of the cylindrical waveguide of circular cross section as shown in Figure 5.1, the displacement potentials can be written in the following form (Achenbach, 1973, p. 240):

$$\varphi = \Phi(r)\cos(m\theta + \theta_0)\exp[i(k_z z - \omega t)] \tag{5.25}$$

$$\psi_r = \Psi_r(r)\sin(m\theta + \theta_0)\exp[i(k_z z - \omega t)] \tag{5.26}$$

$$\psi_\theta = \Psi_\theta(r)\cos(m\theta + \theta_0)\exp[i(k_z z - \omega t)] \tag{5.27}$$

$$\psi_z = \Psi_z(r)\sin(m\theta + \theta_0)\exp[i(k_z z - \omega t)] \tag{5.28}$$

where θ_0 is an arbitrary constant, while m can only be either zero or integers, because the functions must be periodic in the circumferential direction for waves propagating in the axial direction. This will not be the case when considering waves propagating in the circumferential direction as will be discussed in Section 5.4. This particular form of solutions to the displacement potentials is motivated by the fact that the solutions are separable in the three coordinates. The exponential function in z is necessary to describe the propagation in the axial direction of the cylindrical waveguide. The trigonometric functions in θ are to ensure the periodicity in the circumferential directions. The variation in r will be determined by the satisfaction of the reduced wave equation (see Chapter 1).

Note that the form given above is somewhat different from that in the existing literature. The new constant θ_0 introduced here allows us to use the same general displacement potentials for both torsional motion and flexural motion.

As mentioned in Section 5.2, the three displacement components are related to four scalar potential functions: the scalar potential and the three components of the vector potential. An additional constraint condition must be imposed on the potential functions. For the problems considered in this chapter, it is more convenient to require that

$$\Psi_\theta(r) = -\Psi_r(r) \tag{5.29}$$

Upon substituting both Equation 5.25 through Equation 5.28 into Equation 5.15 through Equation 5.18 in conjunction with Equation 5.29, we obtain the following ordinary differential equations:

$$\frac{d^2\Phi}{dr^2} + \frac{1}{r}\frac{d\Phi}{dr} + p^2\Phi - \frac{m^2}{r^2}\Phi = 0 \tag{5.30}$$

$$\frac{d^2\Psi_z}{dr^2} + \frac{1}{r}\frac{d\Psi_z}{dr} + q^2\Psi_z - \frac{m^2}{r^2}\Psi_z = 0 \tag{5.31}$$

$$\frac{d^2\Psi_r}{dr^2} + \frac{1}{r}\frac{d\Psi_r}{dr} + q^2\Psi_r - \frac{(m+1)^2}{r^2}\Psi_r = 0 \tag{5.32}$$

where

$$p = \sqrt{\frac{\omega^2}{c_L^2} - k_z^2} = k_z\sqrt{\frac{c_z^2}{c_L^2} - 1}, \quad q = \sqrt{\frac{\omega^2}{c_T^2} - k_z^2} = k_z\sqrt{\frac{c_z^2}{c_T^2} - k_z^2} \tag{5.33}$$

and $c_z = \omega/k_z$ is the phase velocity of waves propagating in the axial direction.

Equation 5.30 through Equation 5.32 are Bessel equations. Their solutions are the Bessel functions of the first and second kinds of order m for $\Phi(r)$ and $\Psi_z(r)$, and order $m+1$ for $\Psi_r(r)$,

$$\Phi(r) = A_1 J_m(pr) + A_2 Y_m(pr) \tag{5.34}$$

$$\Psi_r = B_1 J_{m+1}(qr) + B_2 Y_{m+1}(qr) \tag{5.35}$$

$$\Psi_z = C_1 J_m(qr) + C_2 Y_m(qr) \tag{5.36}$$

The constants A_n, B_n, and C_n are to be determined by the boundary conditions of the given problem.

Substituting Equation 5.25 through Equation 5.28 into Equation 5.12 through Equation 5.14 yields the corresponding displacements

$$u_r = u_1(r)\cos(m\theta + \theta_0)\exp(ik_z z) \tag{5.37}$$

$$u_\theta = u_2(r)\sin(m\theta + \theta_0)\exp(ik_z z) \tag{5.38}$$

$$u_z = u_2(r)\cos(m\theta + \theta_0)\exp(ik_z z) \tag{5.39}$$

where

$$u_1(r) = \Phi' + \frac{m}{r}\Psi_z + ik_z\Psi_r \tag{5.40}$$

$$u_2 = -\frac{m}{r}\Phi + ik_z\Psi_r - \Psi_z' \tag{5.41}$$

$$u_z = ik_z\Phi - \frac{m+1}{r}\Psi_r - \Psi_r' \tag{5.42}$$

In the above and in what follows, the time factor $e^{-i\omega t}$ is omitted since it is common to all terms. The pertinent stress components are obtained by substituting Equation 5.25 through Equation 5.28 into Equation 5.19, Equation 5.22, and Equation 5.24, respectively,

$$\sigma_{rr} = \mu\sigma_{11}(r)\cos(m\theta + \theta_0)\exp(ik_z z) \tag{5.43}$$

$$\sigma_{r\theta} = \mu\sigma_{12}(r)\sin(m\theta + \theta_0)\exp(ik_z z) \tag{5.44}$$

$$\sigma_{rz} = \mu\sigma_{13}(r)\cos(m\theta + \theta_0)\exp(ik_z z) \tag{5.45}$$

where

$$\sigma_{11}(r) = \left[\frac{2m^2}{r^2} - \left(q^2 - k_z^2\right)\right]\Phi - \frac{2}{r}\Phi' + 2ik_z\Psi_r' - \frac{2m}{r^2}\Psi_z + \frac{2m}{r}\Psi_z' \tag{5.46}$$

$$\sigma_{12}(r) = \frac{2m}{r^2}(\Phi - r\Phi') - \frac{ik(1+m)}{r}\Psi_r + \left[q^2 - \frac{2m^2}{r^2}\right]\Psi_z + ik_z\Psi_r' + \frac{2}{r}\Psi_z' \tag{5.47}$$

$$\sigma_{13}(r) = \left(k_z^2 - q^2 - \frac{m(m+1)}{r^2}\right)\Psi_r - \frac{m}{r}\Psi_r' + 2ik_z\Phi' + ik_z\frac{m}{r}\Psi_z \tag{5.48}$$

Before concluding this section, we remark that the foregoing displacement potentials are general solutions in that they contain eight constants, A_n, B_n, C_n for $n = 1,2$, and m and θ_0. Regardless of the values of these constants, the displacements and stresses derived from these potentials satisfy the equations of motion. In what follows, we will assign particular values for these constants in order to investigate some specific motions of practical interest of the cylindrical waveguide.

5.3.1 Axial Waves in a Solid Cylinder

Consider a solid cylinder of circular cross section of radius b. Since the wave motion is finite at $r = 0$, the coefficients of the Bessel function of the second kind, $Y_n(\cdot)$, in the general solution must be zero. This yields

$$\varphi = A_1 J_m(pr)\cos(m\theta + \theta_0)\exp(ik_z z) \tag{5.49}$$

$$\psi_r = B_1 J_{m+1}(qr)\sin(m\theta + \theta_0)\exp(ik_z z) \tag{5.50}$$

$$\psi_\theta = -B_1 J_{m+1}(qr)\cos(m\theta + \theta_0)\exp(ik_z z) \tag{5.51}$$

$$\psi_z = C_1 J_m(qr)\sin(m\theta + \theta_0)\exp(ik_z z) \tag{5.52}$$

The above solution forms a complete set of modes for time-harmonic waves propagating in the axial direction of a solid cylinder of circular cross-section. For a given boundary value problem, the solution can be obtained as a linear superposition of these modes. In what follows, the dispersion equation will be derived; this dispersion equation relates the frequency, ω; the axial wavenumber, k_z; and the circumferential order, m.

To this end, assume the surface of the cylinder is free of traction. This means the boundary conditions at $r = b$ are

$$\sigma_{rr} = 0, \quad \sigma_{r\theta} = 0, \quad \sigma_{rz} = 0 \tag{5.53}$$

Substituting Equation 5.49 through Equation 5.52 into Equation 5.43 through Equation 5.45, respectively, and then making use of Equation 5.53 yields

$$\mathbf{D}(m, k_z, \omega)\mathbf{A} = \mathbf{0} \tag{5.54}$$

where $\mathbf{A} = (A_1, B_1, C_1)^T$ and

$$\mathbf{D}(m, k_z, \omega) = \begin{bmatrix} d_{11}^J(m,b) & d_{12}^J(m,b) & d_{13}^J(m,b) \\ d_{21}^J(m,b) & d_{22}^J(m,b) & d_{23}^J(m,b) \\ d_{31}^J(m,b) & d_{32}^J(m,b) & d_{33}^J(m,b) \end{bmatrix} \tag{5.55}$$

is a 3×3 matrix whose components $d_{\alpha\beta}^J$ are given in Appendix 5. Note that $d_{\alpha\beta}^J$ are functions of m and r, as well as the frequency, ω, and axial wavenumber, k_z. The dependence of $d_{\alpha\beta}^J$ on ω and k_z is explicitly indicated in the determinant of $d_{\alpha\beta}^J$, as shown in Equation 5.55. This is to emphasize that our intention is to derive a relationship between the frequency and wavenumber, the dispersion relationship.

For nontrivial solutions, the determinant of the coefficient matrix of this system of equations must vanish, i.e.,

$$\mathrm{Det}[\mathbf{D}(m, k_z, \omega)] = 0 \tag{5.56}$$

The above equation provides the desired dispersion relationship between the wavenumber and the frequency (i.e., the $\omega - k_z$ relationship). The curve of ω vs. k_z is called the frequency dispersion curve. For each given k_z value, Equation 5.56 may have many roots for ω. Solutions to this equation yield a family of dispersion curves. Each one is called a branch, which corresponds to a wave mode propagating in the axial direction of the cylinder.

Once a root corresponding to the given k_z is solved from Equation 5.56, it can be substituted back into Equation 5.54 to determine the corresponding eigenvector, **A**. Obviously, **A** can only be determined up to an arbitrary multiplier. Without loss of generality, one may require $\|\mathbf{A}\| = 1$.

For a given k_z value and a given value of m, let the nth root of Equation 5.56 be denoted by ω_n and the corresponding eigenvector be $\mathbf{A}_n$. It then follows from substituting Equation 5.49 through Equation 5.51 into Equation 5.40 through Equation 5.42 that the displacement components corresponding to this mode can be written as

$$\begin{bmatrix} u_r^{(n)} \\ u_\theta^{(n)} \\ u_z^{(n)} \end{bmatrix} = \begin{bmatrix} u_1^{(n)}(r)\cos(m\theta + \theta_0) \\ u_2^{(n)}(r)\sin(m\theta + \theta_0) \\ u_3^{(n)}(r)\cos(m\theta + \theta_0) \end{bmatrix} \exp(ik_z z) \tag{5.57}$$

where

$$\begin{bmatrix} u_1^{(n)} \\ u_2^{(n)} \\ u_3^{(n)} \end{bmatrix} = \begin{bmatrix} J_m'(pr) & ik_z J_{m+1}(qr) & \dfrac{mJ_m(qr)}{r} \\ -\dfrac{mJ_m(pr)}{r} & ik_z J_{m+1}(qr) & -J_m'(qr) \\ ik_z J_m(pr) & -qJ_m(qr) & 0 \end{bmatrix} \mathbf{A}_n \tag{5.58}$$

The waves described by the solutions in Equation 5.49 through Equation 5.52 are rather complicated. To gain some insight of the wave motion, let us consider some special cases of the general solutions.

5.3.1.1 Torsional Motion

In a pure torsional motion, u_θ should be the only nonzero displacement component. It should also be independent of θ. These conditions are met by setting $A_1 = B_1 = m = 0$, and $\theta_0 = \pi/2$ in the general solution given by Equation 5.49 through Equation 5.52. In this case, it follows from Equation 5.37 through Equation 5.39 that

$$u_r = u_z = 0\,, \quad u_\theta = C_1 q J_1(qr)\exp(ik_z z) \tag{5.59}$$

where we have used the property of Bessel functions $J_0'(x) = -J_1(x)$.

The corresponding stresses thus follow from Equations 5.43 through 5.45

$$\sigma_{rr} = \sigma_{rz} = 0 \tag{5.60}$$

$$\sigma_{r\theta} = C_1\mu\left[q^2 J_0(qr) - \frac{2q}{r} J_1(qr)\right]\exp(ik_z z) \tag{5.61}$$

The traction-free boundary condition at $r = b$ implies

$$qbJ_0(qb) - 2J_1(qb) = 0 \tag{5.62}$$

This is the dispersion equation for the torsional waves propagating in the axial direction of a solid cylinder of radius *b*. There are an infinite number of roots. Each represents a particular wave mode.
Since, for very small *x*

$$J_0(x) \approx 1, \quad J_1(x) \approx \frac{x}{2} \tag{5.63}$$

one can easily see that that $q = 0$ is a root of Equation 5.62. The other roots must be obtained numerically. The first five roots are

$$q_1 b = 0, \quad q_2 b \approx 5.136, \quad q_3 b \approx 8.417, \quad q_4 b \approx 11.62, \quad q_5 b \approx 14.79$$

Making use of Equation 5.63 in Equation 5.59 for the $q = 0$ mode, we have

$$u_\theta = Cr\exp(ik_z z) \tag{5.64}$$

This displacement represents the well-known lowest torsional mode. In this lowest mode, the displacement is proportional to the radius, and the motion is thus the rigid rotation of each cross section of the cylinder about its center. This mode is not dispersive, because $q = \sqrt{\omega^2/c_T^2 - k_z^2} = 0$ means $c_z = c_T$.

The higher torsional modes are dispersive with frequencies which follow from the definition of *q* as

$$\left(\frac{\omega b}{c_T}\right)^2 = (q_n b)^2 + (k_z b)^2 \tag{5.65}$$

where $q_n b$ are the roots of Equation 5.62. It is noted that given a real-valued frequency, the wavenumber may be real-valued or imaginary. This is similar to the case of shear waves in a layer, where the branches are hyperboles for real-valued k_z and circles for imaginary values of the wavenumber.

It follows the behavior of Bessel functions that Equation 5.62 has no roots for $q^2 < 0$. This means that the phase velocity of the torsional waves is always greater than or equal to the shear wave speed c_T.

5.3.1.2 Longitudinal Waves

Longitudinal waves refer to the axially symmetrical motion in the cylinder. They are characterized by the presence of displacement components in the radial and axial directions, but none in the θ-direction. Furthermore, these nonzero displacement components must be independent of θ because of the axisymmetric requirement. It is seen that these conditions are met by setting $C_1 = m = 0$, and $\theta_0 = 0$ in the general solution given by Equation 5.49

through Equation 5.52. In this case, it follows from Equation 5.37 through Equation 5.39 that

$$u_r = (\Phi' + ik_z\Psi_r)\exp(ik_z z) = [-A_1 pJ_1(pr) + iB_1 k_z J_1(qr)]\exp(ik_z z) \quad \textbf{(5.66)}$$

$$u_\theta = 0 \quad \textbf{(5.67)}$$

$$u_z = \left(ik_z\Phi - \Psi_r' - \frac{1}{r}\Psi_r \right)\exp(ik_z z) = [iA_1 k_z J_0(pr) - C_1 qJ_0(qr)]\exp[ik_z z] \quad \textbf{(5.68)}$$

where we used the relationship (Stakgold, 1979)

$$\frac{d}{dx}J_v(x) = J_{v-1}(x) - \frac{v}{x}J_v(x) \quad \textbf{(5.69)}$$

The corresponding pertinent stresses are found from Equation 5.43 and Equation 5.45 by setting $C_1 = m = 0$, and $\theta_0 = 0$ in Equation 5.49 through Equation 5.52:

$$\begin{bmatrix} \sigma_{rr} \\ \sigma_{rz} \end{bmatrix} = \mu \begin{bmatrix} d_{11}^J(0,r) & d_{12}^J(0,r) \\ d_{21}^J(0,r) & d_{22}^J(0,r) \end{bmatrix} \begin{bmatrix} A_1 \\ B_1 \end{bmatrix} \quad \textbf{(5.70)}$$

where the functions $d_{\alpha\beta}^J(m,r)$ are given in Appendix 5. As mentioned earlier, they are functions of the circumferential mode number, *m;* and the radial coordinate, *r*; the frequency, ω; and wavenumber, k_z.

The traction-free boundary conditions on the surface $r = b$ thus yields

$$\begin{bmatrix} d_{11}^J(0,b) & d_{12}^J(0,b) \\ d_{21}^J(0,b) & d_{22}^J(0,b) \end{bmatrix} \begin{bmatrix} A_1 \\ B_1 \end{bmatrix} = \begin{bmatrix} 0 \\ 0 \end{bmatrix} \quad \textbf{(5.71)}$$

The requirement that the determinant of the coefficients must vanish presents us with the dispersion equation as follows:

$$\left[\frac{2p}{b}\left(q^2 + k_z^2\right)J_1(pb) - \left(q^2 - k_z^2\right)^2 J_0(pb) \right] J_1(qb) - 4k_z^2 pqJ_1(pb)J_0(qb) = 0 \quad \textbf{(5.72)}$$

This is the well-known Pochhammer (1876) dispersion equation. Once the roots of the dispersion equation are found, the corresponding eigenvectors can be obtained from Equation 5.71. Thus the displacements are also known from Equation 5.66 through Equation 5.68.

By introducing the dimensionless variables

$$\hat{k} = k_z b, \quad \hat{c} = \frac{c_z}{c_T}, \quad \kappa = \frac{c_L}{c_T}, \quad \hat{p} = \frac{p}{k_z} = \sqrt{\frac{\hat{c}^2}{\kappa^2} - 1}, \quad \hat{q} = \frac{q}{k_z} = \sqrt{\hat{c}^2 - 1} \quad \textbf{(5.73)}$$

we can rewrite Equation 5.72 into a nondimensional form

$$\frac{J_0(\hat{k}\hat{p})J_1(\hat{k}\hat{q})}{J_1(\hat{k}\hat{p})J_0(\hat{k}\hat{q})}+\frac{4\hat{p}\hat{q}}{(\hat{q}^2-1)^2}=\frac{2\hat{p}(\hat{p}^2+1)}{\hat{k}(\hat{q}^2-1)^2}\frac{J_1(\hat{k}\hat{q})}{J_0(\hat{k}\hat{q})} \quad \textbf{(5.74)}$$

This equation contains three independent dimensionless variables, the phase velocity, $\hat{c}_z$; the wavenumber, $\hat{k}$; and variable, κ, which is a function of the Poisson's ratio of the cylinder material. In other words, once the Poisson's ratio is given, Equation 5.74 defines a relationship between $\hat{c}$ and $\hat{k}$ that is independent of the geometry of the cylinder. This is typical of waveguides. The advantage of the nondimensional form of the dispersion equation is that once it is solved for a given material, the $\hat{c}$- $\hat{k}$ curves are applicable to cylinders of any diameter.

The dispersion equation (Equation 5.74) has been discussed in great detail including real, imaginary, and complex braches by Onoe et al. (1962). The results for real-valued wavenumbers are included in the work of Armenàkas et al. (1969). Plots showing both the frequency and velocity dispersion curves can be found in these works for various values of the Poisson's ratio.

From a practical application point of view, the low modes are more important. To find the lower modes, one may assume $\hat{k} \ll 1$. In this case, the Bessel functions in Equation 5.74 can be approximated by their asymptotic representations for small argument (Stakgold, 1979)

$$J_0(x) \sim 1-\frac{x^2}{4}, \quad J_1(x) \sim \frac{x}{2}-\frac{x^3}{16} \quad \text{for } x \to 0 \quad \textbf{(5.75)}$$

Making use of the above approximations in Equation 5.74, we obtain an asymptotic representation of the dispersion equation valid for $\hat{k} \ll 1$:

$$c=\sqrt{\frac{E}{\rho}}\left(1-\frac{\nu^2}{4}\hat{k}^2\right)+O(\hat{k}_4) \quad \textbf{(5.76)}$$

where $E=\mu(3\lambda+2\mu)/(\lambda+\mu)$ is the Young's modulus of the material. In the limit when $\hat{k} \to 0$, the phase velocity thus becomes equal to $\sqrt{E/\rho}$. This is called the bar velocity and is the value found from the simplest theory of thin rods.

To investigate the behavior of Equation 5.74 for high frequency (or large diameter), consider the asymptotic expansions of the Bessel functions (Stakgold, 1979) for $|x| \to \infty$

$$J_n(x) \approx \begin{cases} \sqrt{\dfrac{2}{\pi x}}\cos\left(x-\dfrac{n\pi}{2}-\dfrac{\pi}{4}\right) & \text{when } \operatorname{Im}(x)=0 \\ \dfrac{i^n \exp(-ix)}{\sqrt{-2\pi i x}} & \text{when } \operatorname{Re}(x)=0 \end{cases} \quad \textbf{(5.77)}$$

For the case of $c_z < c_T$ (or equivalently $\hat{c} < 1$), both $\hat{p}$ and $\hat{q}$ are pure imaginary. In this case, when $\hat{k} \to \infty$, we have, from Equation 5.74 that

$$\left(2 - \frac{c_z^2}{c_T^2}\right) - 4\sqrt{1 - \frac{c_z^2}{c_L^2}}\sqrt{1 - \frac{c_z^2}{c_T^2}} = 0 \tag{5.78}$$

This is identical to the Rayleigh wave equation. This result is expected because large $\hat{k}$ means either a very thick cylinder or very high frequency. In both cases, the waves propagate as if they were in a semi-infinite space that supports only the Rayleigh surface wave. Because the Rayleigh equation has only one root, this result also indicates that as the frequency increases, all modes whose velocity is less than c_T will asymptotically approach the Rayleigh wave.

For modes with $c_L > c_z > c_T$, $\hat{p}$ is still imaginary, but $\hat{q}$ becomes real. It thus follows from Equation 5.77 that the dispersion equation (Equation 5.74) can be written asymptotically for large $\hat{k}$ as

$$\frac{\tan[\hat{k}(\hat{c}^2 - 1)^{1/2}]}{1 + \tan[\hat{k}(\hat{c}^2 - 1)^{1/2}]} - \frac{4(\hat{c}^2 - 1)^{1/2}(1 - \hat{c}^2/\kappa^2)^{1/2}}{(\hat{c}^2 - 2)^2} = 0 \tag{5.79}$$

Clearly, one of the roots to the above equation is $\hat{c} = 1$ or $c_z = c_T$. All the modes whose velocity is in between c_T and c_L gravitate to the shear wave speed c_T for large $\hat{k}$.

When $c_z > c_L$, both $\hat{p}$ and $\hat{q}$ are real. The dispersion equation can therefore be written asymptotically for large $\hat{k}$ as

$$\frac{\tan[\hat{k}(\hat{c}^2 - 1)^{1/2} - \pi/4]}{\tan[\hat{k}(\hat{c}^2/\kappa^2 - 1)^{1/2} - \pi/4]} + \frac{4(\hat{c}^2 - 1)^{1/2}(\hat{c}^2/\kappa^2 - 1)^{1/2}}{(\hat{c}^2 - 2)^2} = 0 \tag{5.80}$$

The close resemblance between this and the Rayleigh-Lamb dispersion equation exhibits the fact that the frequency spectra for a cylinder and a plate, for axially symmetric and symmetric waves, respectively, are very similar.

5.3.1.3 Flexural Waves

Now consider the solution in Equation 5.49 through Equation 5.52 for $m = 1$ and $\theta_0 = 0$. The corresponding displacement components follow from Equation 5.40 through Equation 5.42:

$$u_r = \left[A_1 J_1'(pr) + \frac{C_1}{r} J_1(qr) + ik_z B_1 J_2(qr)\right]\cos(\theta)\exp(ik_z z) \tag{5.81}$$

$$u_\theta = \left[-\frac{A_1}{r} J_1(pr) + ik_z B_1 J_2(qr) - C_1 J_1'(qr)\right]\sin(\theta)\exp(ik_z z) \tag{5.82}$$

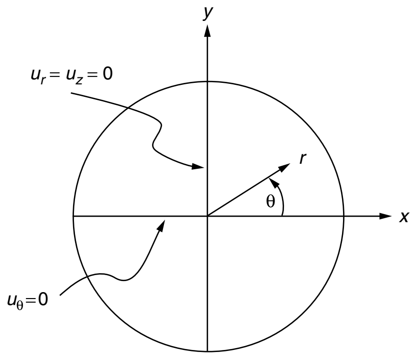

FIGURE 5.2
Flexural waves.

$$u_z = [ik_z A_1 J_1(pr) - B_1 q J_1(qr)]\cos(\theta)\exp(ik_z z) \quad \textbf{(5.83)}$$

To illustrate the motion represented by these displacement components, consider Figure 5.2. The cross section of the cylinder at $y = 0$ (which is the same as $\theta = 0, \pi$) remains in the $y = 0$ plane, because $u_\theta = 0$ on this plane. The material particles that lie in this plane can only move in the *x*- or the *z*-direction within the *xz*-plane. Furthermore, all the material particles that lie in the vertical plane $x = 0$ (which is the same as $\theta = \pm\pi/2$) can move only in the *x*-direction, because both $u_r = u_z = 0$. Looking from the top (down from the positive *y*-axis), the overall motion of the cylinder resembles the motion of a snake moving on the ground (the *xz*-plane). These observations suggest the terminology flexural waves for the motion described by Equation 5.81 through Equation 5.83.

The pertinent stresses of the flexural waves are

$$\begin{bmatrix} \sigma_{rr} \\ \sigma_{rz} \\ \sigma_{r\theta} \end{bmatrix} = \mu \begin{bmatrix} d_{11}^J(1,r) & d_{12}^J(1,r) & d_{13}^J(1,r) \\ d_{21}^J(1,r) & d_{22}^J(1,r) & d_{23}^J(1,r) \\ d_{31}^J(1,r) & d_{32}^J(1,r) & d_{33}^J(1,r) \end{bmatrix} \begin{bmatrix} A_1 \\ B_1 \\ C_1 \end{bmatrix} \quad \textbf{(5.84)}$$

where the functions $d_{\alpha\beta}^J(m,r)$ are given in Appendix 5. By using the traction-free boundary conditions, $\sigma_{rr} = 0$, $\sigma_{rz} = 0$, and $\sigma_{r\theta} = 0$ at $r = b$, we arrived at the eigenvalue problem

$$\mathbf{D}(1, k_z, \omega)\mathbf{A} = \mathbf{0} \quad \textbf{(5.85)}$$

where $\mathbf{A} = (A_1, B_1, C_1)^T$

$$\mathbf{D}(1, k_z, \omega) = \begin{bmatrix} d_{11}^J(1,b) & d_{12}^J(1,b) & d_{13}^J(1,b) \\ d_{21}^J(1,b) & d_{22}^J(1,b) & d_{23}^J(1,b) \\ d_{31}^J(1,b) & d_{32}^J(1,b) & d_{33}^J(1,b) \end{bmatrix} \quad \textbf{(5.86)}$$

is a 3 × 3 matrix whose components are functions of k_z and ω.

For nontrivial solutions, the determinant of the coefficient matrix of this system of equations must vanish, meaning

$$\mathrm{Det}[\mathbf{D}(1, k_z, \omega)] = 0 \tag{5.87}$$

This is the desired dispersion equation for flexural waves propagating in the axial direction of the cylinder of radius b.

Numerical computations on the frequency spectrum were carried out by Armenàkas et al. (1969). The asymptotic behavior of the frequency spectrum was examined in considerable detail by Pao and Mindlin (1960). Similar to the analysis of the axially symmetric waves, they have shown that, as $\hat{k} \to \infty$, the velocities of all propagating modes will asymptotically approach one of the three speeds, Rayleigh wave speed, the shear wave speed, or the dilatational wave speed. In the low frequency range, it can be shown (Achenbach, 1973, p. 248) that

$$c_z = \frac{1}{2}\sqrt{\frac{E}{\rho}}\hat{k} \quad \text{for } \hat{k} \to 0 \tag{5.88}$$

5.3.2 Axial Waves in a Hollow Cylinder

Consider a hollow cylinder of inner radius a and outer radius b as shown in Figure 5.1. It is assumed that both the inner and outer surfaces are traction free, i.e.,

$$\sigma_{rr} = 0, \quad \sigma_{r\theta} = 0, \quad \sigma_{rz} = 0 \quad \text{at } r = a, b$$

The general solution to the waves propagating in the axial direction of this hollow cylinder is given by Equation 5.25 through Equation 5.28 with the r-dependent functions given by Equation 5.34 through Equation 5.36. The Bessel functions of second kind should be retained in this case, because the presence of both incoming (toward the center) and outgoing (away from the center) waves is necessary to satisfy the traction-free boundary conditions on both the inner and outer surfaces. Thus, the displacement components are given by Equation 5.37 through Equation 5.39, and the corresponding stresses can be computed from Equation 5.43 through Equation 5.45:

$$\begin{bmatrix} \sigma_{rr} \\ \sigma_{rz} \\ \sigma_{r\theta} \end{bmatrix} = \mu \begin{bmatrix} d_{11}^J(m,r) & d_{12}^J(m,r) & d_{13}^J(m,r) & d_{11}^Y(m,r) & d_{12}^Y(m,r) & d_{13}^Y(m,r) \\ d_{21}^J(m,r) & d_{22}^J(m,r) & d_{23}^J(m,r) & d_{21}^Y(m,r) & d_{22}^Y(m,r) & d_{23}^Y(m,r) \\ d_{31}^J(m,r) & d_{32}^J(m,r) & d_{33}^J(m,r) & d_{31}^Y(m,r) & d_{32}^Y(m,r) & d_{33}^Y(m,r) \end{bmatrix} \mathbf{A} \tag{5.89}$$

where $\mathbf{A} = \left[A_1, B_1, C_1, A_2, B_2, C_2\right]^T$ and the elements $d_{\alpha\beta}^Z(m,r)$ are given in Appendix 5. The traction-free condition on both surfaces $r = a, b$ results in the following eigenvalue problem:

$$\begin{bmatrix} d^J_{11}(m,b) & d^J_{12}(m,b) & d^J_{13}(m,b) & d^Y_{11}(m,b) & d^Y_{12}(m,b) & d^Y_{13}(m,b) \\ d^J_{21}(m,b) & d^J_{22}(m,b) & d^J_{23}(m,b) & d^Y_{21}(m,b) & d^Y_{22}(m,b) & d^Y_{23}(m,b) \\ d^J_{31}(m,b) & d^J_{32}(m,b) & d^J_{33}(m,b) & d^Y_{31}(m,b) & d^Y_{32}(m,b) & d^Y_{33}(m,b) \\ d^J_{11}(m,a) & d^J_{12}(m,a) & d^J_{13}(m,a) & d^Y_{11}(m,a) & d^Y_{12}(m,a) & d^Y_{13}(m,a) \\ d^J_{21}(m,a) & d^J_{22}(m,a) & d^J_{23}(m,a) & d^Y_{21}(m,a) & d^Y_{22}(m,a) & d^Y_{23}(m,a) \\ d^J_{31}(m,a) & d^J_{32}(m,a) & d^J_{33}(m,a) & d^Y_{31}(m,a) & d^Y_{32}(m,a) & d^Y_{33}(m,a) \end{bmatrix} \begin{bmatrix} A_1 \\ B_1 \\ C_1 \\ A_2 \\ B_2 \\ C_2 \end{bmatrix} = \mathbf{0} \tag{5.90}$$

By setting the determinant to zero, we obtain the dispersion equation for waves propagating in the axial direction of a hollow cylinder of inner radius a and outer radius b.

Similar to the solid cylinder case, let us consider some specific wave motions of practical interest.

5.3.2.1 Torsional Motion

In a pure torsional motion, u_θ should be the only nonzero displacement component. Furthermore, it should be independent of θ. These conditions are met by setting $A_n = B_n = m = 0$ and $\theta_0 = \pi/2$ in the general solution. The corresponding dispersion equation is thus deduced from Equation 5.90:

$$\begin{bmatrix} d^J_{33}(0,b) & d^Y_{33}(0,b) \\ d^J_{33}(0,a) & d^Y_{33}(0,a) \end{bmatrix} \begin{bmatrix} C_1 \\ C_2 \end{bmatrix} = \begin{bmatrix} 0 \\ 0 \end{bmatrix} \tag{5.91}$$

The vanishing of the determinant yields $q = 0$, or

$$J_2(qb)Y_2(qa) - J_2(qa)Y_2(qb) = 0 \tag{5.92}$$

Clearly, the modes determined from Equation 5.92 are all dispersive. The lowest mode corresponding to $q = 0$, however, is nondispersive. Its displacement field is similar to Equation 5.64. In fact, one can easily show that in the limit $a \to 0$, Equation 5.92 reduces to Equation 5.62, as expected. For the case $b > a \to \infty$, one can use the asymptotic expressions of the Bessel functions in Equation 5.92, which results in

$$\sin(qh) = 0 \tag{5.93}$$

where $h = b - a$ is the wall thickness of the hollow cylinder. This is identical to the dispersion equation for the symmetric horizontally polarized shear waves in a plate of thickness $2h$ (Achenbach, 1973, p.206).

Similar to the solid cylinder case, it can be shown (Gazis, 1959) that Equation 5.92 does not have any real roots for $q^2 < 0$. Thus, it can be ascertained that the phase velocity of the torsional waves in a hollow cylinder is always greater than or equal to the shear velocity c_T.

5.3.2.2 Longitudinal Waves

Longitudinal waves refer to the axially symmetrical motion in the cylinder. They are characterized by the presence of displacement components in the radial and axial directions, but none in the θ-direction. Furthermore, these nonzero displacement components must be independent of θ because of the axisymmetric requirement. It is seen that these conditions are met by setting $C_n = m = 0$ and $\theta_0 = 0$ in the general solution. The corresponding eigenvalue problem is thus obtained from Equation 5.90:

$$\begin{bmatrix} d_{11}^J(0,b) & d_{12}^J(0,b) & d_{11}^Y(0,b) & d_{12}^Y(0,b) \\ d_{21}^J(0,b) & d_{22}^J(0,b) & d_{21}^Y(0,b) & d_{22}^Y(0,b) \\ d_{11}^J(0,a) & d_{12}^J(0,a) & d_{11}^Y(0,a) & d_{12}^Y(0,a) \\ d_{21}^J(0,a) & d_{22}^J(0,a) & d_{21}^Y(0,a) & d_{22}^Y(0,a) \end{bmatrix} \begin{bmatrix} A_1 \\ B_1 \\ A_2 \\ B_2 \end{bmatrix} = \mathbf{0} \tag{5.94}$$

Vanishing of the determinant yields the dispersion equation. Some numerical results of the dispersion curves are presented in Rose (1999, p. 161).

5.3.2.3 Flexural Waves

As in the solid cylinder case, flexural waves in a hollow cylinder are defined by setting $m = 1$, and $\theta_0 = 0$ in the general solution. The corresponding eigenvalue problem is thus obtained from Equation 5.90 by setting $m = 1$. Some numerical results of the dispersion curves are given in Rose (1999, p. 167).

5.4 Propagation in the Circumferential Direction

Unlike waves propagating in the longitudinal direction, waves propagating in the circumferential direction of a cylinder follow a curved path. The simplest case of wave propagation along a curve path is the Rayleigh type of surface waves on a curved surface. Cook and Valkenburg (1954) investigated the possibility of Rayleigh waves propagating along a cylindrical surface. The analytical work on Rayleigh-type waves on a cylindrical surface was presented by Viktorov (1958), Grace and Goodman (1966), Keller and Karal (1960, 1964), Grimshaw (1968), Rulf (1969), and Gregory (1971). More recent works in this area include Smith (1977) and Harris (2002).

It is known that unlike the Rayleigh wave on a planar surface, frequency dispersion takes place for surface waves propagating along a curved surface. In addition, in the case of a curvilinear (convex) boundary of a solid, it is also possible for other modes of surface waves to propagate, confined near

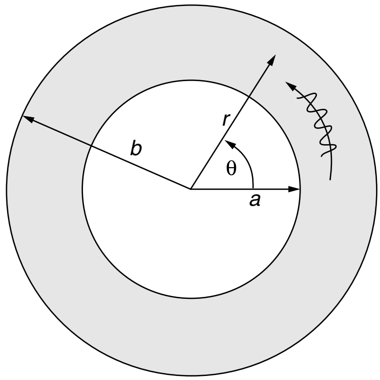

FIGURE 5.3
A circular annulus with inner radius a, outer radius b, in the polar coordinate system (r, θ).

the curved boundary (Brekhovskikh, 1968). These waves are sometimes called the *whispering gallery* waves. Famous examples of such whispering gallery waves include the Temple of Heaven in Beijing and the dome of St. Paul's Cathedral in London, which was described in Rayleigh's classic book, *The Theory of Sound* (1945).

The dispersion of elastic waves and Rayleigh-type waves in a thin disc was investigated by Červ (1988). The focus was to study the displacement amplitude of the various circumferential modes in a thin disc. In the case of a hollow cylinder, multiple reflection may take place between the walls. Consequently, guided waves (similar to the Rayleigh-Lamb waves) between the inner and outer surfaces can propagate in the circumferential direction. This problem was solved by Liu and Qu (1998a,b).

Consider, again, Figure 5.1. For time-harmonic waves propagating in the circumferential (the θ-axis) direction of a cylindrical body, the motion is independent of the z-axis. Therefore, it is sufficient to consider a two-dimensional motion with r and θ being the only independent spatial variables. The hollow cylinder can then be considered as either a ring or an annulus (see Figure 5.3). The displacement potentials can be written as (Liu and Qu, 1998a)

$$\varphi = \Phi(r)\exp[i(k_\theta\theta - \omega t)], \quad \psi_z = \Psi_z(r)\exp[i(k_\theta\theta - \omega t)] \tag{5.95}$$

Note that the interest here is to study the waves that propagate in the circumferential direction of the cylindrical body. Therefore, the periodic requirement on the variable θ should not be imposed (i.e., the wavenumber k_θ does not need to be an integer.) Furthermore, unlike the longitudinal wavenumber k_z, the circumferential wavenumber k_θ defined here is dimensionless. The unknown functions $\Phi(r)$ and $\Psi_z(r)$ can be determined by substituting Equation 5.95 into Equation 5.15 and Equation 5.18, respectively,

$$\Phi'' + \frac{1}{r}\Phi' + \left[\left(\frac{\omega}{c_L}\right)^2 - \left(\frac{k_\theta}{r}\right)^2\right]\Phi = 0 \tag{5.96}$$

$$\Psi_z'' + \frac{1}{r}\Psi_z' + \left[\left(\frac{\omega}{c_T}\right)^2 - \left(\frac{k_\theta}{r}\right)^2\right]\Psi_z = 0 \tag{5.97}$$

These are Bessel equations of order k_θ. Their general solutions can be written as

$$\Phi(r) = A_1 J_{k_\theta}\left(\frac{\omega}{c_L}r\right) + A_2 Y_{k_\theta}\left(\frac{\omega}{c_L}r\right) \tag{5.98}$$

$$\Psi_z(r) = B_1 J_{k_\theta}\left(\frac{\omega}{c_T}r\right) + B_2 Y_{k_\theta}\left(\frac{\omega}{c_T}r\right) \tag{5.99}$$

where $J_{k_\theta}(\cdot)$ and $Y_{k_\theta}(\cdot)$ are, respectively, the first and second kind of Bessel functions of order k_θ. Making use of Equation 5.98 through Equation 5.998 in Equation 5.95 yields the solutions for the displacement potentials

$$\varphi = \left[A_1 J_{k_\theta}\left(\frac{\omega}{c_L}r\right) + A_2 Y_{k_\theta}\left(\frac{\omega}{c_L}r\right)\right]\exp[i(k_\theta\theta - \omega t)] \tag{5.100}$$

$$\psi_z = \left[B_1 J_{k_\theta}\left(\frac{\omega}{c_T}r\right) + B_2 Y_{k_\theta}\left(\frac{\omega}{c_T}r\right)\right]\exp[i(k_\theta\theta - \omega t)] \tag{5.101}$$

The corresponding displacements are

$$u_r = W_r(r)\exp[i(k_\theta\theta - \omega t)], \quad u_\theta = W_\theta(r)\exp[i(k_\theta\theta - \omega t)] \tag{5.102}$$

where the displacement amplitudes are

$$W_r(r) = \frac{1}{r}\left[A_1\frac{\omega r}{c_L}J_{k_\theta}'\left(\frac{\omega r}{c_L}\right) + ik_\theta B_1 J_{k_\theta}\left(\frac{\omega r}{c_T}\right) + A_2\frac{\omega r}{c_L}Y_{k_\theta}'\left(\frac{\omega r}{c_L}\right) + ik_\theta B_2 Y_{k_\theta}\left(\frac{\omega r}{c_T}\right)\right] \tag{5.103}$$

$$W_\theta(r) = \frac{1}{r}\left[ik_\theta A_1 J_{k_\theta}\left(\frac{\omega r}{c_L}\right) + B_1\omega r J_{k_\theta}'\left(\frac{\omega r}{c_T}\right) + ik_\theta A_2 Y_{k_\theta}\left(\frac{\hat{\omega} r}{c_L}\right) + B_2\omega r Y_{k_\theta}'\left(\frac{\hat{\omega} r}{c_T}\right)\right] \tag{5.104}$$

Substituting Equation 5.95 into Equation 5.19 and Equation 5.22 yields the pertinent stresses

$$\sigma_{rr} = \frac{\mu\exp[i(k_\theta\theta - \omega t)]}{r^2}[\kappa^2 r^2\Phi'' + (\kappa^2 - 2)r\Phi' - (\kappa^2 - 2)k_\theta^2\Phi + 2ik_\theta r\Psi' - 2ik_\theta \tag{5.105}$$

$$\sigma_{r\theta} = \frac{\mu \exp[i(k_\theta \theta - \omega t)]}{r^2}[-r^2\Psi'' + r\Psi' - k_\theta^2\Psi + 2ik_\theta r\Phi' - 2ik_\theta\Phi] \quad \textbf{(5.106)}$$

The above solution represents a wave field that has constant phase along any radial line. In other words, material points having identical phase lie in the same radial line that rotates about the center $r = 0$ with the angular velocity $c(r)/r$, where $c(r)$ is the linear phase velocity for a material particle located at a distance r from the center. It is clear that $c(r)$ must be a linear function of r, because the angular velocity must be independent of r. The fact that the phase velocity $c(r)$ depends on r creates some apparent ambiguity on the definition of the circumferential wavenumber k_θ. It will be seen later that such apparent ambiguity is immaterial. For convenience, one may define the wavenumber k_θ by

$$k_\theta = \frac{\omega b}{c(b)} = \frac{\omega r}{c(r)} \quad \textbf{(5.107)}$$

5.4.1 Circumferential Waves in a Solid Disk

Consider a solid cylinder of circular cross-section of radius b. Since the circumferential motion is independent of the z-axis, the problem is essentially a two dimensional disk. Because the waves must be finite at $r = 0$, the coefficients of the Bessel function of the second kind, $Y_n(\cdot)$, must be zero. This yields from Equation 5.100 and Equation 5.101,

$$\varphi = A_1 J_{k_\theta}\left(\frac{\omega}{c_L} r\right)\exp[i(k_\theta\theta - \omega t)] \quad \textbf{(5.108)}$$

$$\psi_z = B_1 J_{k_\theta}\left(\frac{\omega}{c_T} r\right)\exp[i(k_\theta\theta - \omega t)] \quad \textbf{(5.109)}$$

The above equations form a complete set of modes for time-harmonic waves propagating in the circumferential direction of a solid cylinder with circular cross section. For a given boundary value problem, the solution can be obtained as a linear superposition of these modes. In what follows, the dispersion equation will be derived that relates the frequency, ω, and the circumferential wavenumber, k_θ.

To this end, assume the surface of the cylinder is free of traction, meaning the boundary conditions at $r = b$ are

$$\sigma_{rr} = 0, \ \sigma_{r\theta} = 0 \quad \textbf{(5.110)}$$

Substituting Equation 5.108 through Equation 5.109 into Equation 5.19 Equation 5.22, respectively, and then making use of Equation 5.110 yields

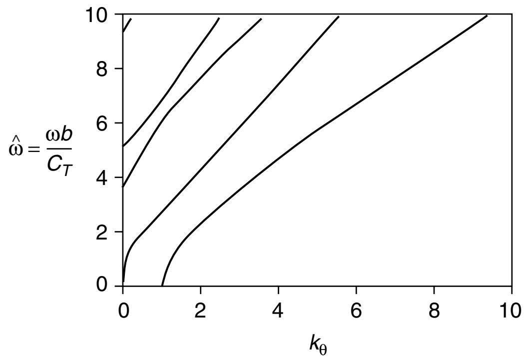

FIGURE 5.4
First five branches of the dispersion curves for circumferential waves in a solid disk.

$$\begin{bmatrix} d_{11}^J(b) & d_{12}^J(b) \\ d_{21}^J(b) & d_{22}^J(b) \end{bmatrix} \mathbf{A} = \begin{bmatrix} 0 \\ 0 \end{bmatrix} \quad \textbf{(5.111)}$$

where the coefficients $d_{mn}^Z(r)$ are given in Appendix 5 and the unknown vector $\mathbf{A} = (A_1, B_1)^T$ is to be determined from the eigenvalue problem (Equation 5.111). For a nontrivial solution, the determinant of the above equation must vanish, which yields the dispersion relationship

$$J_{k_\theta-2}\left(\frac{\hat{\omega}}{\kappa}\right) J_{k_\theta+2}(\hat{\omega}) - (\kappa^2 - 1) J_{k_\theta}\left(\frac{\hat{\omega}}{\kappa}\right) [J_{k_\theta-2}(\hat{\omega}) + J_{k_\theta+2}(\hat{\omega})] + J_{k_\theta+2}\left(\frac{\hat{\omega}}{\kappa}\right) J_{k_\theta-2}(\hat{\omega}) = 0 \quad \textbf{(5.112)}$$

where

$$\hat{\omega} = \frac{\omega b}{c_T} \quad \textbf{(5.113)}$$

is the dimensionless circular frequency. This equation* was derived by Viktorov (1957).

For each given value of the circumferential wavenumber, k_θ, the root of Equation 5.112 gives the corresponding frequencies of the various modes (branches). Figure 5.4 shows the first five branches of the dispersion curves. Once the dispersion equation is solved, the eigenvector $\mathbf{A}$ can be determined from Equation 5.111 up to an arbitrary multiplier. Without loss of generality, one may require $\|\mathbf{A}\| = 1$.

* There is an error in Viktorov's equation 8.

For a given k_θ value, let the nth root of Equation 5.112 be denoted by $\hat{\omega}_n$ and the corresponding eigenvector be $\mathbf{A}_n$. It then follows from Equation 5.102 that the displacement components corresponding to this mode can be written as

$$u_r^{(n)} = W_r^{(n)}(r)\exp(ik_\theta\theta), \quad u_\theta^{(n)} = W_\theta^{(n)}(r)\exp(ik_\theta\theta) \tag{5.114}$$

where the displacement amplitudes are

$$W_r^{(n)}(r) = \frac{1}{r}\left[A_1^{(n)}\frac{\hat{\omega}_n r}{\kappa}J'_{k_\theta}\left(\frac{\hat{\omega}_n r}{\kappa}\right) + ik_\theta B_1^{(n)}J_{k_\theta}(\hat{\omega}_n r)\right] \tag{5.115}$$

$$W_\theta^{(n)}(\bar{r}) = \frac{1}{r}\left[ik_\theta A_1^{(n)}J_{k_\theta}\left(\frac{\hat{\omega}_n r}{\kappa}\right) + B_1^{(n)}\hat{\omega}_n r J'_{k_\theta}(\hat{\omega}_n r)\right] \tag{5.116}$$

It is clear from Equation 5.108 through Equation 5.109 that for the time-harmonic waves propagating in the θ-direction, all material particles located on the same radial line should have the same phase factor given by

$$\exp[i(k_\theta\theta - \omega t)] = \exp\left[i\omega\left(\frac{k_\theta\theta}{\omega} - t\right)\right] = \exp\left[i\omega\left(\frac{\theta}{\alpha} - t\right)\right] \tag{5.117}$$

where

$$\alpha = \frac{\omega}{k_\theta} \tag{5.118}$$

is called the *angular phase velocity* of the circumferential wave (Liu and Qu, 1998a). In other words, each radial line of the cylinder can be viewed as a wave front of the circumferential wave. Propagation of the circumferential wave can be described by the rotation of the radial line with an angular velocity α as defined by Equation 5.118. Variation of the wave amplitude on each wavefront (radial line of the cylinder) is characterized by $W_r^{(n)}(r)$ and $W_\theta^{(n)}(r)$.

5.4.2 Circumferential Waves in a Hollow Cylinder

Consider steady-state, time-harmonic waves in a circular annulus of inner radius a and outer radius b as shown in Figure 5.3. It is assumed that the surface of the annulus is traction-free, meaning,

$$\sigma_r = \sigma_{r\theta} = 0 \quad \text{at } r = a, b \tag{5.119}$$

The displacement potentials for this problem are given by Equation 5.100 and Equation 5.101. Making use of these displacement potentials in Equation 5.105 and Equation 5.106 in conjunction with the traction-free boundary conditions Equation 5.119 yields a system of four homogeneous equations for the constants $\mathbf{A} = (A_1, B_1, A_2, B_2)^T$

$$\begin{bmatrix} d_{11}^J(b) & d_{12}^J(b) & d_{11}^Y(b) & d_{12}^Y(b) \\ d_{21}^J(b) & d_{22}^J(b) & d_{21}^Y(b) & d_{22}^Y(b) \\ d_{11}^J(a) & d_{12}^J(a) & d_{11}^Y(a) & d_{12}^Y(a) \\ d_{21}^J(a) & d_{22}^J(a) & d_{21}^Y(a) & d_{22}^Y(a) \end{bmatrix} \mathbf{A} = \mathbf{0} \tag{5.120}$$

where components $d_{mn}^Z(r)$ were derived by Liu and Qu (1998a) and reproduced here in Appendix 5. They are all functions of the nondimensional wavenumber, k_θ; nondimensional frequency, $\hat{\omega}$; and nondimensional wall thickness parameter, η.

$$\eta = \frac{a}{b} \tag{5.121}$$

For nontrivial solutions, the determinant of the coefficient matrix of this system of equations must vanish, meaning

$$\mathrm{Det}\left[d_{mn}^Z\right] = f(k_\theta, \hat{\omega}) = 0 \tag{5.122}$$

The above equation provides the dispersion relationship between the circumferential wavenumber and the frequency (i.e., the $\hat{\omega} - k_\theta$ relationship). For each given k_θ value, Equation 5.122 may have many roots for $\hat{\omega}$. Therefore, solutions to Equation 5.122 yield a family of dispersion curves. Each one is called a branch, which corresponds to a wave mode propagating in the circumferential direction. For future reference, three additional variables are introduced

$$h = b - a, \quad \bar{k} = k_\theta(1-\eta) = k_\theta h/b, \quad \bar{\omega} = \hat{\omega}(1-\eta) = \omega h/c_T \tag{5.123}$$

Here h is the wave thickness of the hollow cylinder, and $\bar{k}$ and $\bar{\omega}$ are dimensionless wavenumber and frequency, respectively. The relevance of these new variables will be discussed later in this section. For now, it is worth mentioning that once the $\hat{\omega} - k_\theta$ relationship is solved from Equation 5.122, the $\bar{k} - \bar{\omega}$ relationship is readily obtained from Equation 5.123.

Once a root corresponding to a given value of k_θ is solved from Equation 5.122, it can be substituted back into Equation 5.120 to determine the corresponding eigenvector, $\mathbf{A}$. Obviously, $\mathbf{A}$ can only be determined up to an arbitrary multiplier. Without loss of generality, one may require $\|\mathbf{A}\| = 1$.

For a given k_θ value, let the nth root of Equation 5.122 be denoted by $\hat{\omega}_n$ and the corresponding eigenvector be $\mathbf{A}_n$. It then follows from Equation 5.102 that the displacement components corresponding to this mode can be written as,

$$u_r^{(n)} = W_r^{(n)}(r)\exp[i(k_\theta\theta - \omega t)], \quad u_\theta^{(n)} = W_\theta^{(n)}(\bar{r})\exp[i(k_\theta\theta - \omega t)] \quad \textbf{(5.124)}$$

where the displacement amplitudes are

$$W_r^{(n)}(r) = \frac{1}{r}\left[A_1^{(n)}\frac{\hat{\omega}_n r}{\kappa}J'_{k_\theta}\left(\frac{\hat{\omega}_n r}{\kappa}\right) + B_1^{(n)}\frac{\hat{\omega}_n r}{\kappa}Y'_{k_\theta}\left(\frac{\hat{\omega}_n r}{\kappa}\right)\right.$$
$$\left. + ik_\theta A_2^{(n)}J_{k_\theta}(\hat{\omega}_n r) + ik_\theta B_2^{(n)}Y_{k_\theta}(\hat{\omega}_n r)\right] \quad \textbf{(5.125)}$$

$$W_\theta^{(n)}(r) = \frac{1}{r}\left[ik_\theta A_1^{(n)}J_{k_\theta}\left(\frac{\hat{\omega}_n r}{\kappa}\right) + ik_\theta B_1^{(n)}Y_{k_\theta}\left(\frac{\hat{\omega}_n r}{\kappa}\right)\right.$$
$$\left. - A_2^{(n)}\hat{\omega}_n r J'_{k_\theta}(\hat{\omega}_n r) - B_2^{(n)}\hat{\omega}_n r Y'_{k_\theta}(\hat{\omega}_n r)\right] \quad \textbf{(5.126)}$$

The amplitude of the total displacement of the n^{th} mode is thus given as a function of the radial distance from the center of the cylinder

$$W_n(r) = \frac{1}{H_n}\sqrt{\left|W_r^{(n)}(r)\right|^2 + \left|W_\theta^{(n)}(r)\right|^2} \quad \textbf{(5.127)}$$

where H_n is the maximum amplitude across the thickness for the nth mode, meaning

$$H_n = \max\left\{\sqrt{\left|W_r^{(n)}(r)\right|^2 + \left|W_\theta^{(n)}(r)\right|^2}, 0 \le r \le b\right\} \quad \textbf{(5.128)}$$

In this section, some numerical examples of the steady-state circumferential waves are carried out for $\nu = 0.2817$; $c_T = 3200$ m/sec.; $c_L = 5660$ m/sec.; and $\eta = 0.1$, 0.5, and 0.95. The numerical solutions of the dispersion curves are obtained by giving a value of $\bar{k}$, then finding the root of Equation 5.122 for the corresponding values of $\bar{\omega}$. An infinite number of real roots exist. Each represents a propagating mode. Note that care must be taken in the root-finding procedure because the determinant (Equation 5.122) changes its value very rapidly.

The first 10 modes, (i.e., the first 10 branches of the $\bar{\omega} - \bar{k}$ curves) are plotted in Figure 5.5(a) through Figure 5.5(c) for $\eta = 0.1$, 0.5 and 0.95, respectively. Notice that at high frequencies, the first mode for all cases is almost a straight line, indicating that it is almost nondispersive.

It is also seen, for example, from Figure 5.5b that there is a crossover point between the seventh and eighth modes around $\bar{k} = 4$ for the annulus with $\eta = 0.5$. For a thinner annulus, e.g., $\eta = 0.95$, there are more crossover points between different modes. This crossover phenomenon also occurs in the case of a flat plate, where the symmetric and antisymmetric modes may have crossover points. Physically, a cross-over point indicates that at that particular frequency, the mechanical energy may be exchangeable between the two neighboring modes (Meeker and Meitzler, 1964). However, unlike the plate case where the symmetric and antisymmetric modes are clearly defined, it is no longer possible to define the symmetric and antisymmetric modes in the annulus because of the curvature. For this reason, the modes are defined somewhat arbitrarily when two of them cross each other. Therefore, the concept of energy exchange between these two modes becomes somewhat of an artifact.

Once the frequency dispersion relationship is determined, one can compute the linear phase velocity in the circumferential direction for a material particle at distance r from the center

$$c(r) = r\alpha = \frac{\bar{\omega}}{\bar{k}} \frac{r}{b} c_T \tag{5.129}$$

For example, the circumferential wave travels along the outer surface, $r = b$, with the speed of

$$c(b) = \frac{\bar{\omega}}{\bar{k}} c_T = \frac{\omega b}{k_\theta} \tag{5.130}$$

This is consistent with Equation 5.107. Now the advantage of defining k_θ through this equation is clear. Once the dispersion equation is solved, the propagating (phase) velocity at the outer surface of the annulus, $c(b)$, is obtained from Equation 5.130. On the other hand, since $c(b)$ can be measured easily on the outer surface of the annulus, Equation 5.130 provides a tool to determine the dispersion curves experimentally.

The phase velocities of the first 10 modes are plotted in Figure 5.6a through Figure 5.6c for $\eta = 0.1$, 0.5, and 0.95, respectively. It is seen from these results that, at higher frequencies, the first modes are almost nondispersive for the three cases considered ($\eta = 0.1, 0.5, 0.95$). They all asymptotically approach the Rayleigh wave velocity, which is non-dispersive (here $c_R/c_T = 0.9214$ for $\nu = 0.2817$). Except for the first three modes, all higher modes have phase velocities greater than the shear wave speed in the wavenumber range considered. For the first mode at higher frequencies, the phase velocity $c(b)$ varies with the wall thickness: $c(b) > c_T$ for very thick annulus ($\eta = 0.1$) and $c(b) < c_T$ for very thin annulus ($\eta = 0.95$). It has been shown (Viktorov, 1958) that the phase velocity of the second mode should be greater than the

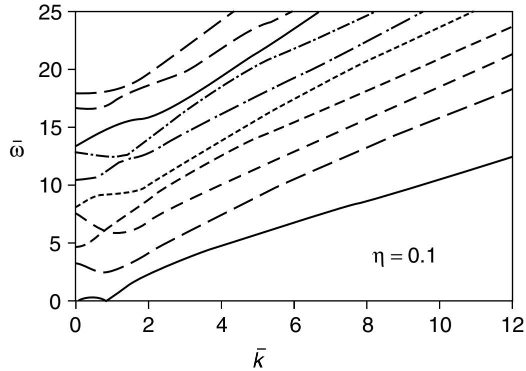

(a)

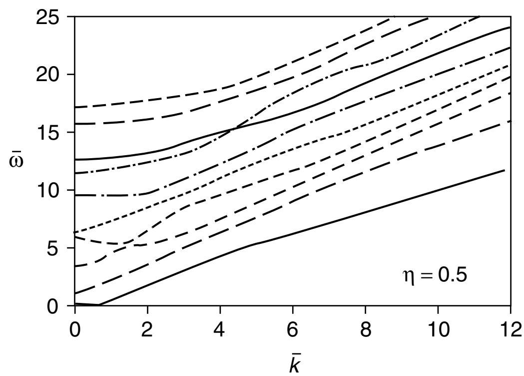

(b)

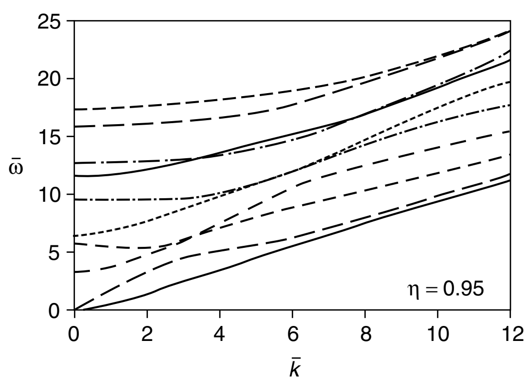

(c)

FIGURE 5.5
The first 10 branches of the $\bar{\omega}-\bar{k}$ relationship for (a) $\eta = 0.1$; (b) $\eta = 0.5$; (c) $\eta = 0.95$.

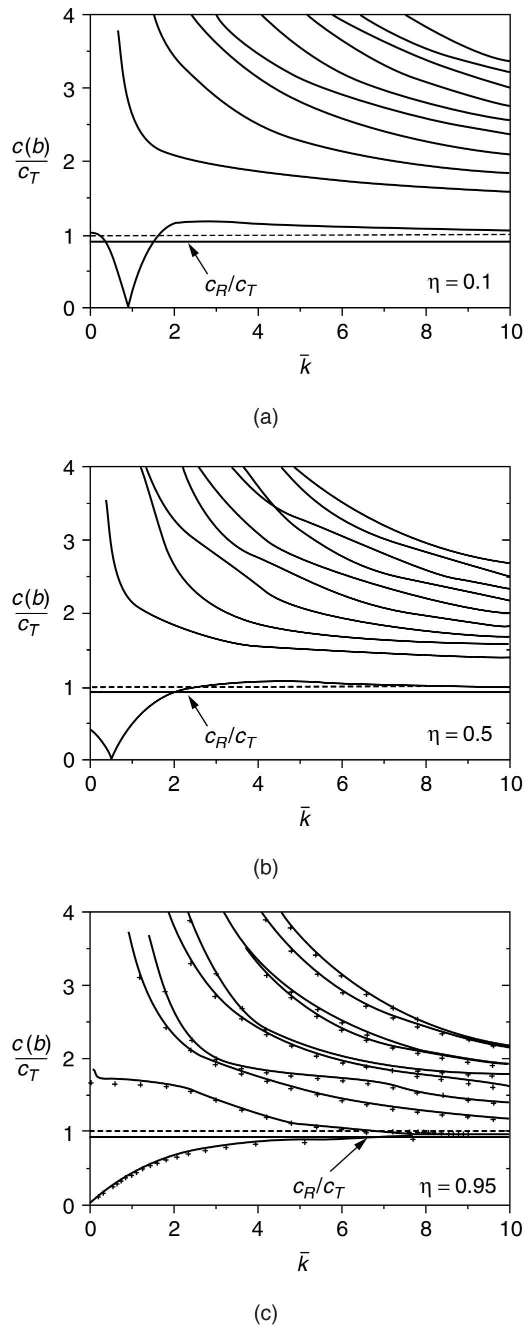

FIGURE 5.6
The first 10 branches of the $c(b)-\bar{k}$ relationship for (a) $\eta = 0.1$ (b) $\eta = 0.5$ (c) $\eta = 0.95$. Solid lines are for the annulus and cross-hair symbols are for a flat plate of thickness h.

Rayleigh wave velocity and approaches the Rayleigh wave velocity as $\bar{k} \to \infty$. However, the first two modes shown in Figure 5.6c were not mentioned in Viktorov (1958) and Červ (1988), which seem to be the most complex modes to analyze.

Knowing the $\bar{\omega} - \bar{k}$ relationship, one can also compute the group velocity of the circumferential waves (Achenbach, 1973)

$$c_g = \frac{\partial \omega}{\partial k} = \frac{\partial \bar{\omega}}{\partial \bar{k}} c_T \tag{5.131}$$

The group velocities of the first 10 modes are plotted in Figure 5.7a through Figure 5.7c for $\eta = 0.1$, 0.5, and 0.95, respectively. Unlike waves in a flat plate (Weaver and Pao, 1982), the group velocity may exceed the longitudinal wave speed ($c_L = 1.814c_T$ here) for a thicker annulus (Figure 5.7a and Figure 5.7b). Since it is the overall wave group that propagates at the group velocity, c_g, it can be interpreted that $c_g > c_L$ means that the waves will appear to originate at the front of the group, travel to the rear, and disappear (Graff, 1975).

Intuitively, one may expect that the size of the annulus (consequently, the curvature) would affect the dispersion relationship. However, the dispersion curves shown in Figure 5.5 through Figure 5.7 are somewhat curvature independent. This is because the $\bar{\omega} - \bar{k}$ curves obtained from Equation 5.122 depend on only the shape factor, η, which characterizes only the shape, not the radius of the annulus (e.g., the size). Consequently, the curves in Figure 5.5 through Figure 5.7 can be used for circular annuli of different radii, as long as they all have the same shape (e.g., the same η). The question is, "How does the curvature get involved?"

To this end, we return to the angular phase velocity defined in Equation 5.118. Making use of the nondimensional variables introduced in Equation 5.123, one can easily show that

$$\alpha = \frac{\omega}{kb} = \frac{\bar{\omega}}{\bar{k}} \frac{c_T}{b} \tag{5.132}$$

It is clear from Equation 5.132 that, although the $\bar{\omega} - \bar{k}$ curves obtained from Equation 5.122 depend on only the shape (not the radii of the annulus), the angular phase velocity of the circumferential waves does depend on the radius b. In other words, the curvature is involved through the angular phase velocity. Consequently, once the $\bar{\omega} - \bar{k}$ relationship is solved from Equation 5.122 for a given shape factor, η, the angular phase velocity for annuli of different radii can be easily obtained from Equation 5.132, as long as they all have the same shape factor, η. In this sense, the dispersion equation can be viewed as universal in that it provides the solutions for all annuli that have the same shape factor.

Another point worth mentioning is the limits of the geometrical parameters. Note that in addition to the wavelength, $2\pi b/k_\theta$, there are two other independent length parameters in this problem. Although the choice is some-

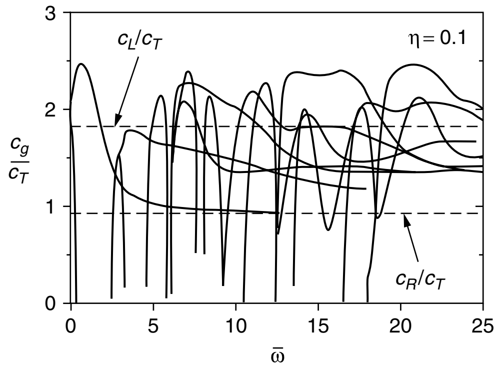

(a)

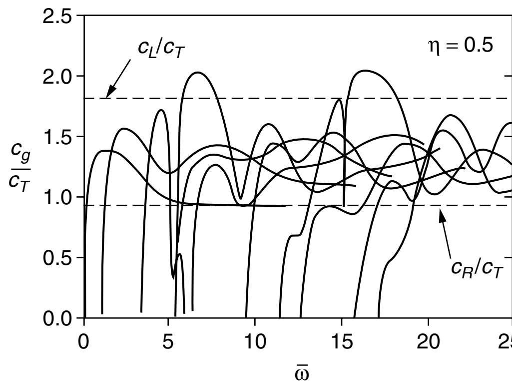

(b)

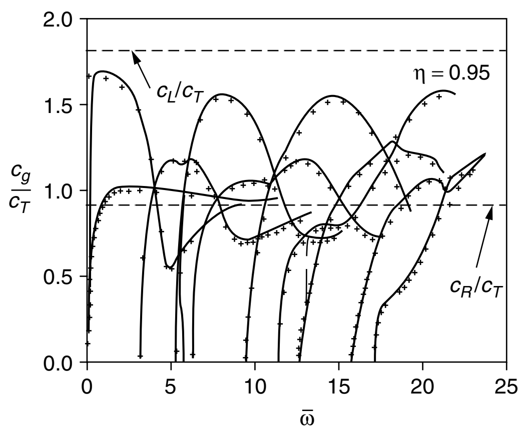

(c)

FIGURE 5.7
The first 10 branches of the $c_g - \bar{k}$ relationship for (a) $\eta = 0.1$ (b) $\eta = 0.5$ (c) $\eta = 0.95$. Solid lines are for the annulus and crosshair symbols are for a flat plate of thickness *h*.

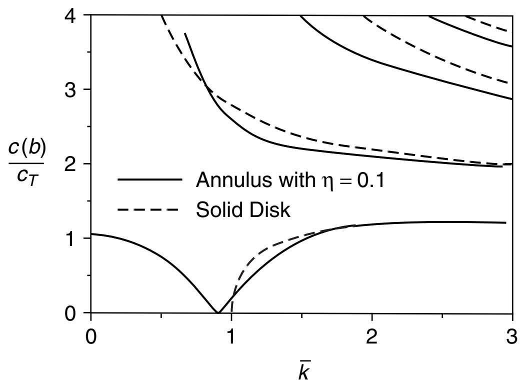

FIGURE 5.8
Comparison of phase velocity dispersion curves between a solid disk and an annulus with $\eta = 0.1$.

what arbitrary, the outer radius, *b*, and the wall thickness, *h*, are taken to be the two independent parameters in this section. For convenience, a nondimensional parameter, $\eta = a/b$, was introduced to characterize the shape or the aspect ratio of the annulus. The use of η makes the dispersion equation independent of the curvature as discussed in previous paragraphs. However, the limits of η must be carefully examined in order to correctly interpret the results.

It appears that $\eta = 0$ (i.e., $a = 0$ for finite b) corresponds to a solid disk. However, careful examination of the equations reveals that this is not the case. The limit of $a \to 0$ in Equation 5.122 does not yield the dispersion equation for a solid disk. This may be understood physically by considering two disks, one that is solid and another that has a hole of infinitesimal radius at the center. For the solid disk, displacement at the center must be kept finite on physical grounds. Therefore, the displacement fields only consist of the Bessel functions of the first kind. On the other hand, for the disk with a center hole, the free surface of the hole requires the Bessel function of the second kind in the displacement fields in order to satisfy the traction-free boundary condition. In fact, the multiple reflections between the outer surface and the surface of the hole form a caustic at the center. A strong stress concentration arises when the hole diameter becomes very small. The wave fields become unbounded in the limit of $a \to 0$. The unbounded displacement field is characterized by the singularity of the Bessel function of the second kind.

To illustrate the above argument, a comparison of the phase velocity dispersion curves between a solid disk and an annulus of $\eta = 0.1$ is shown in Figure 5.8. It is seen that the cutoff wavenumber of the first mode is $\bar{k} = 1$ for the solid disk and $\bar{k} = 1 - \eta$ for the annulus. In both cases, this corresponds to $k_\theta = 1$, which means that the wavelength on the outer surface is equal to $2\pi b$, the outer circumference. Since this mode is analogous to the first flexural mode (in the limit of $\eta \to 1$ it approaches the first flexural mode in the plate see Figure 5.6c), its wavelength must be smaller than the circumference for it to propagate along the circumferential direction. However, the dispersion curves of the annulus have an extra branch extended from $\bar{k}=0$ to $\bar{k}=1-\eta=0.9$, labeled as the 0th mode in this chapter. This propagating mode is unique to the annulus due to the multiple reflections between the inner and outer surfaces. The outer surface of the annulus is a convex surface and the inner surface is a concave surface. The Rayleigh-type surface waves are different for these two cases (Viktorov, 1958). A convex surface admits a Rayleigh-type surface wave with real-valued wavenumber whose wave speed is slightly higher than the Rayleigh wave speed on a flat surface. On the other hand, a concave surface only admits a Rayleigh-type surface wave with complex wavenumber. Consequently, the surface wave on a concave surface propagates with attenuation due to the radiation of energy into the medium. This radiated energy will be reflected back to the center by the outer surface if there is one.

Consequently, the attenuated surface wave on the inner surface is enhanced by this reflected energy to form a propagating wave. Thus, it is fair to say that the existence of the extra branch is to accommodate the inability of the concave surface to sustain propagating surface waves. As the wavenumber increases, the phase velocity of this extra mode decreases. The velocity (both phase and group), as well as the frequency, becomes zero when $\bar{k}=1-\eta$ (see also Figure 5.5a through Figure 5.5c). This corresponds to $k_\theta=1$, which means that the wavelength on the outer surface is equal to $2\pi b$, the outer circumference. In this case, no wave propagation takes place in the circumferential direction since the nodal points on the outer surface stay at the same position all the time due to the 2π periodicity. Since each radial line of the annulus is a wavefront propagating in the circumferential direction with the angular velocity defined by Equation 5.118, one may conclude that there will be no wave propagation at any radius $a \le r < b$ if there is no wave propagation on the outer surface $r=b$. Asymptotic analysis as $k_\theta \to 1$, $\omega \to 0$ shows that the displacement field is indeed zero everywhere. Numerical computations also confirm this.

Next, consider the limit of $\eta \to 1$. Notice that

$$h=b-a=b(1-\eta) \tag{5.133}$$

Therefore, two limiting cases may result:

Case 1 $\eta \to 1$ with h being a nonzero value

Case 2 $\eta \to 1$ with b being a finite value

It follows from Equation 5.133 that Case 1 yields $b \to \infty$. Consequently, this limiting case corresponds to a flat plate of thickness h. On the other hand, Case 2 yields $h \to 0$, which corresponds to a thin annulus (ring) of radius b.

Note from the preceding discussion that the two limiting cases are differentiated by only different values of b. Now recall that the dispersion equation is independent of b. Therefore, one may conclude that the dispersion curves for guided waves in a plate and for the circumferential waves in a thin annulus are the same in the limit of $\eta \to 1$. For example, the dispersion relationship of a plate with thickness h represents an approximation to the dispersion relationship of an annulus with $\eta = 0.95$. This is demonstrated by the comparisons shown in Figure 5.6c and Figure 5.7c, where the phase and group velocities for the 1st 10 modes in a plate of thickness h and that in an annulus with η =).95 are plotted, respectively. The solid lines are from the annulus and the crosshair symbols are from the plate. It is seen that the two cases are very close. Furthermore, based on the foregoing discussion, these are also approximate solutions to the velocity dispersion curves of a thin annulus of finite radius b. This discovery extends the utility of the Rayleigh-Lamb dispersion equation for plates to annuli and cylindrical thin shells when circumferential waves are of interest. In other words, instead of going through complicated calculations to obtain the dispersion curves in the circumferential direction for a thin cylindrical shell, one can simply use the Rayleigh-Lamb equation to obtain an approximate solution.

It seems that the above result is somewhat counterintuitive in that even if the wavelength is of the order of the circumference, there will still be a distinction between a thin cylindrical shell and a flat plate regardless of the value of η. This is indeed true. The above result simply states that in the limit of $\eta \to 1$, the dispersion curves for these two cases are the same when $\bar{k} = k_\theta h/b$ is used in the plot regardless of the value of b. Since the phase factor, $\exp[i(k_\theta \theta - \omega t)]$ does depend on b, the actual wave fields in the shell and in the plate are indeed different. The conclusion is, therefore, that although the wave fields may be quite different between a thin shell and a flat plate, their dispersion curves are identical if both are plotted as functions of $\bar{k}$. For example, the dispersion curves for a thin shell are conventionally plotted as functions of k_θ. From the above discussions, one can obtain these curves from the Rayleigh-Lamb equations of a plate by converting $\hat{k} = k_z h$ to $\bar{k} = k_\theta h/b$ through Equation 5.123.

Finally, consider the displacements. For the nth mode, the displacement variation as function of r is characterized by $W_r^{(n)}(r)$ and $W_\theta^{(n)}(r)$. Interestingly enough, our numerical solutions show that $W_r^{(n)}(r)$ is real and $W_\theta^{(n)}(r)$ is pure imaginary, which indicates that the two components are always 90° out of phase.

The normalized displacement amplitudes $W_n(r)$ are shown in Figure 5.9a through Figure 5.9c for $\eta = 0.1, 0.5$, and 0.95, respectively. Generally speaking, for a fixed value of $\bar{\omega}$, higher modes have smaller wavenumbers. The values of $\bar{k}$ corresponding to $\bar{\omega} = 10$ for each mode are indicated in these figures. In reading these figures, please note that the relative magnitude between different modes is meaningless because each mode is normalized by itself. The purpose of these figures is to show how each individual mode varies along the radial direction.

It is seen that in all three cases, the first mode is a Rayleigh-type surface wave either on the inner or outer surfaces, depending upon the shape factor

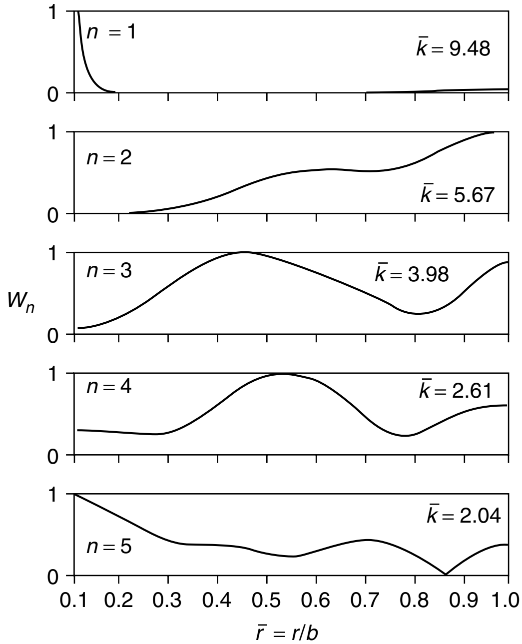

(a)

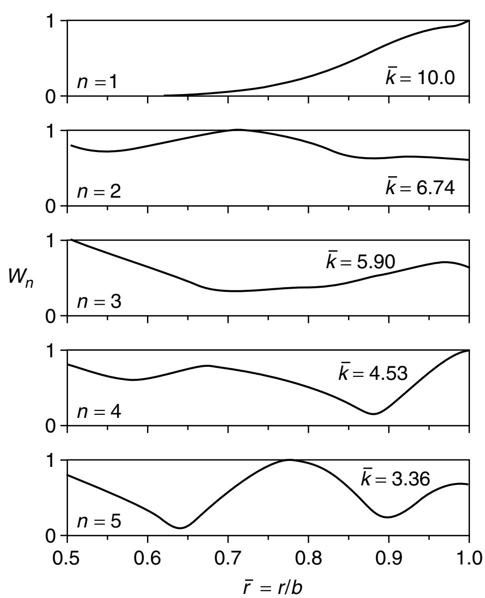

(b)

FIGURE 5.9
Displacement profiles across the wall thickness of the first five modes for (a) $\eta = 0.1$ (b) $\eta = 0.5$ (c) $\eta = 0.95$. They are normalized by their respective maximum amplitude through the thickness.

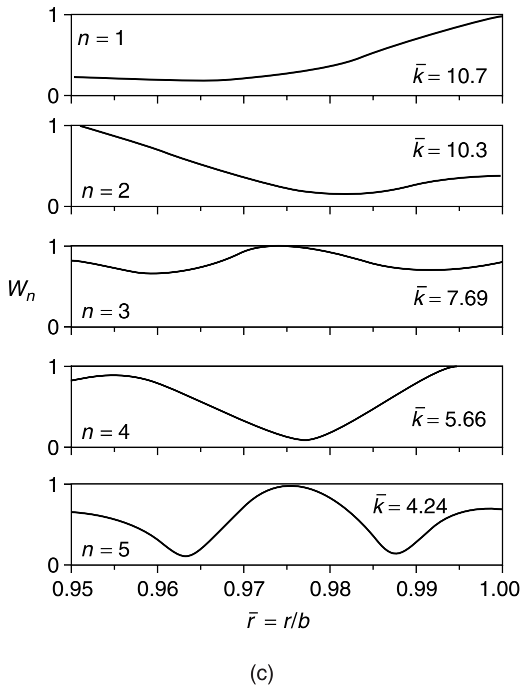

FIGURE 5.9
(Continued)

of the annulus, η. Notice the large amplitude of the first mode near the inner surface, as shown in Figure 5.9a. This mode is primarily due to the presence of the inner free surface. Because the inner surface has such a small radius, the caustic effect previously mentioned gives rise to a large displacement amplitude. For relatively thinner annulus (e.g., η = 0.5), the caustic effect becomes less important and the first mode becomes a Rayleigh-type surface wave on the outer surface. For the case η = 0.95, the annulus become even thinner and approaches to a plate. In this case, one may still call the first mode a Rayleigh-type surface on the outer surface, for its amplitude on the outer surface is still several times of that on the inner surface. However, the decay rate is much slower as shown in Figure 5.9c.

5.5 Flaw Detection in Pipes and Annular Components

Testing large structures using conventional bulk ultrasonic wave techniques is slow because the test region is limited to the area immediately surrounding the transducer. Therefore, scanning is required if the entire structure is to be tested. Ultrasonic guided waves provide an attractive alternative solution to this problem because they can be excited at one location on the structure and propagate over a long distance. By analyzing the characteristics of the guided waves such as the returning echoes, change of dispersion relationships, etc., the presence of flaws may be detected. However, because of the multimode nature of guided waves, ultrasonic tests using guided waves are more complicated.

A thorough understanding of the wave fields is critical to extract useful information from the vast amount of data collected from guided waves tests. Basic theories of guided waves and their applications to nondestructive evaluation can be found in the works by many pioneers in this field, including Achenbach and Keshava (1967); Achenbach (1973); Guyott and Cawley (1988); Lowe (1997); Lowe et al. (2000); Chimenti and Nayfeh (1985, 1989); Nayfeh (1995); Shah and Datta (1982); Datta et al. (1991); Mal (1988); Mal et al. (1991); Nagy and Kent (1995); Nagy et al. (1994); Rokhlin and Wang (1988); Rose (1999); Rose and Soley (2000). A recent review paper by Rose (2002) gives an excellent account of the historical development of guided wave methods in ultrasonic nondestructive evaluation. In this section, we will discuss several examples of how to use guided waves for the nondestructive detection of flaws in pipes and annular structural components.

5.5.1 Applications of Guided Waves in the Longitudinal Direction

Pipes are extensively used for transporting chemicals, water, and other necessities. A nation's civil and chemical infrastructure depends to a large extent on the integrity of thousands of miles of pipes. Nondestructive inspection and monitoring of pipes are critical to these industries. Ultrasonic techniques have been used extensively for this purpose. One of the examples of such applications is the so-called smart pig, a robotic device that crawls through a pipe, carrying sensors. As the device moves along the pipe, the sensors generate and receive guided ultrasonic waves in the longitudinal direction of the pipes. By analyzing the data, sites with damage, such as corrosion, can be located (Guo and Kundu, 2001). Other examples of recent papers include detecting broken rails with guided waves (Rose et al., 2001), determining Poisson's ratio in wires (Nagy and Kent, 1995), and measuring fluid viscosity by using guided waves in a rod immersed in the fluid being measured (Costley et al., 1998).

Generating desired wave modes in the cylindrical waveguide is the first task for nondestructive testing. There are many ways of generating guided waves in cylindrical waveguides. Typically, an angle beam transducer is used for generating waves in a pipe, whereby refraction into the test pipe produces multiple reflection and transmission of ultrasonic energy and numerous mode conversions. A very short distance away from the transducer, clearly formed wave packets of ultrasonic energy are produced that can propagate along the pipe. Another common technique is to make use of a comb type transducer whereby ultrasonic energy is pumped into the structure at some particular spacing of the comb transducer where guided waves are generated in both directions (Rose et al., 1998). Guided waves can also be produced in a pipe by electromagnetic acoustic and magnetostrictive transducers (Thompson et al., 1972; Na and Kundu, 2002).

5.5.2 Application of Guided Waves in the Circumferential Direction

Fatigue cracks have been found to initiate and grow in the radial direction in many of the annular shaped components in aging helicopters. These include some of the most critical components such as the rotor hub, connecting links and pitch shaft, etc. At the present time, detection of such radial fatigue cracks relies mostly on visual inspection. More systematic, automated, and efficient methods to detect these cracks are needed.

Conventional ultrasonic imaging techniques can be used to detect such radial cracks. However, these techniques are impractical for real-time, integrated diagnosis. Nagy et al. (1994) proposed that guided ultrasonic waves that propagate in the circumferential direction may be used for the detection of radial fatigue cracks in annular components. Because of its potentials in nondestructive evaluation of annular components, extensive studies have been conducted to understand the generation and propagation of guided circumferential waves. Recently, a number of papers have been devoted to the study of the various properties of guided circumferential waves and their applications in nondestructive evaluation (e.g., Liu and Qu, 1998a,b; Kley et al., 1999; Valle et al., 1999, 2001; Qu et al., 1996, 2000; Towfighi et al., 2002; and Rose, 1999, 2002).

The main focus of this section is to develop methodologies that can determine the location and size of radial cracks in an annular component. To locate the crack, a time-frequency representation technique (the energy density of the short time Fourier transform [STFT; see Section 5.5.2.1] or spectrogram) is used to discern the arrival time of a given mode at a given frequency for both the incident and backscattered waves. By calculating the time delay of a specific mode in the spectrogram, the distance between the receiver and the crack can be determined. The crack is therefore located. For sizing the crack, a time domain counterpart of Auld's formula is derived. By using the time domain Auld's formula, the backscattering energy coefficient can be obtained directly from experimental measurements, as well as calculated from the synthetic, numerical data. By comparing the experimentally obtained and numerically calculated backscattering energy coefficients, the size of the crack can be determined.

In conducting ultrasonic nondestructive testing, the transient solutions to wave propagation problems are often needed. Solutions to transient waves propagating in the circumferential direction of an annular components can be written as a superposition of all steady-state normal modes (Liu and Qu, 1998b):

$$\mathbf{u} = \sum_{m=1}^{\infty} \mathbf{u}_m \tag{5.134}$$

where

$$\mathbf{u}_m = \sum_{i=1}^{2} \sum_{n=0}^{\infty} \frac{Q_{mn}^{(i)}}{M_{mn}^{(i)}} \mathbf{U}_{mn}^{(i)} \tag{5.135}$$

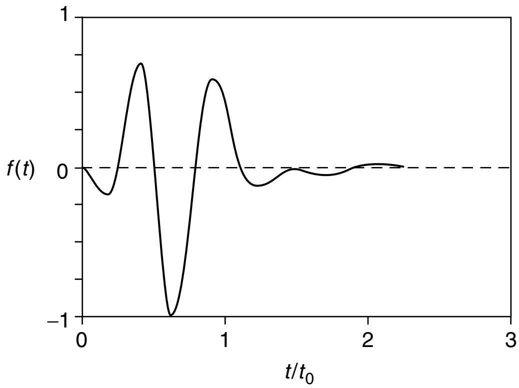

FIGURE 5.10
An excitation pulse.

TABLE 5.1

Geometry and Material Parameters

Inner Diameter	Outer Diameter	Ratio $\eta = a/b$	Poisson's Ratio	L-wave Speed	T-wave Speed
$a = 5.08$ cm	$b = 6.28$ cm	$\eta = 0.$	$\nu = 0.2817$	$c_L = 5660\ m/\text{sec}$	$c_T = 3120$ m/sec

In the above, $\mathbf{U}_{mn}^{(i)}$ is the solution of the steady-state problem discussed in Section 5.4 that satisfies the orthogonality condition

$$\int_V \rho \mathbf{U}_{mn}^{(i)} \mathbf{U}_{sk}^{(i)}\, dV = \begin{cases} 0, & m \neq s \quad \text{or} \quad n \neq k \\ \delta_{ij} M_{mn}^{(i)}, & m = s \quad \text{and} \quad n = k \end{cases} \tag{5.136}$$

and $Q_{mn}^{(i)}$ is related to the surface traction **F** through

$$Q_{mn}^{(i)} = \frac{1}{\omega_{mn}} \int_0^t P_{mn}^{(i)} \sin[\omega_{mn}(t-\tau)]\, d\tau \tag{5.137}$$

$$P_{mn}^{(i)} \int_S \mathrm{F} \cdot \mathbf{U}_{mn}^{(i)}\, dS \tag{5.138}$$

As a numerical example, consider a concentrated pulse applied normal to the outer surface at $\theta = 0$. The shape of the pulse is shown in Figure 5.10, which was measured directly from a 0.5-MHz lead zirconate titanate (PZT) transducer. The values of the geometry and material parameters used in the computation are given in Table 5.1. In these calculations, the infinite series was truncated at $n = 300$ and $m = 20$. Further increase of these values does not change the final results by more than 1%.

To present the data in a nondimensional form, two parameters are chosen

$$u_0 = \frac{f_0 t_0}{\rho c_T b} = 1.848 \times 10^{-5}\ \mu\boldsymbol{m}$$

$$t_0 = \frac{h}{c_T} = 3.846\ \mu\,\text{sec}$$

where $f_0 = \max\{|f(t)|\}$. These parameters are used to normalize the displacement and time. The solid line in Figure 5.4 shows the radial and tangential displacements on the outer surface at $\theta = 90°$ from this calculation.

The normal mode expansion method is a useful tool for effectively computing the wave propagation in a circular annulus. However, it is not applicable to annulus with cracks. Other numerical methods are needed in this case. The finite element method is one such numerical method for simulating wave propagation in an elastic medium. The advances in computer technology have made it possible to conduct the finite element simulation of wave propagation in rather complicated engineering components.

In using the finite element method for solving wave propagation problems, certain constraints must be imposed on the mesh size and time step of integration in order to ensure convergence and accuracy. In general, the velocity of the longitudinal wave (the fastest wave that can propagate in the medium) controls the integration time step, which must be chosen so that a disturbance cannot propagate through one element in less than one time step. The lowest phase velocity, and hence the shortest wavelength, sets the maximum permissible element size, which must be chosen so that spatial aliasing due to the finite element discretization does not occur (Alleyne and Cawly, 1991). Unfortunately, those theoretical estimates are not conservative. In practice, the actual element size has to be at least 15 to 20 times smaller than the theoretical estimate to obtain convergence (Moser et al., 1999).

In this work, the commercial general purpose finite element program ABAQUS/Explicit is used for the calculations. The simulation is first conducted for a perfect annulus subjected to a transient pulse on the outer surface at $\theta = 90°$. The dimensions and the material constants of the annulus are given in Table 5.1. Due to symmetry, only one half of the annulus needs to be modeled. The four-node plane strain elements are used. Several computations are conducted under the same loading and boundary conditions. Each time, the mesh is refined. It is found that for a load with 0.5-MHz center frequency, about 4000 elements are sufficient for the solution to become mesh-independent, corresponding to an element size about 15 times smaller than the theoretically estimated size based on the shear wave speed.

To check the accuracy, the finite element solutions are compared with the solution obtained using the normal mode expansion method for an uncracked annulus. The dashed line in Figure 5.11 shows the displacements from the finite element method. It is seen that the two solutions are very close.

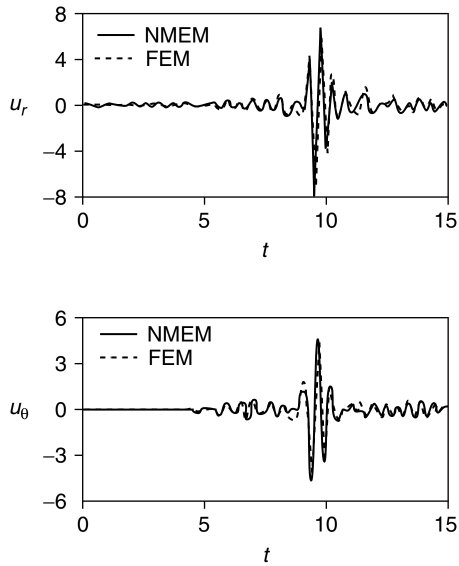

FIGURE 5.11
Comparison between waveforms from the finite element and the normal modal expansion methods.

To model the radial crack in an annulus, the nodes along the crack line are separated to form two traction-free crack surfaces. Such four-node elements near the crack tip cannot fully capture the singular crack-tip stress fields. Our interest is in the field far from the crack tip. The inaccuracy in the region near tip fields will not affect the accuracy of the far field.

Smaller cracks (less than 20% of the wall thickness) typically require a finer mesh to be accurately captured. Convergence is usually obtained after increasing the number of elements both in the thickness and in the waveguide axis directions. For very small cracks, the numerical computation becomes rather intensive. The smallest crack considered in this chapter is about 10% of the wall thickness.

5.5.2.1 Determining Crack Location

The main difficulty in determining the crack location comes from the dispersive nature of guided waves. Because of dispersion, the phase velocity of a guided wave depends on its frequency. In other words, a pulse changes its shape as it propagates along the waveguide. This makes it difficult (if not impossible) to track and identify the exact arrival time of the same feature of a propagating pulse. Consequently, methods based on the arrival time do not provide accurate information on the crack location. In order to alleviate this problem, the change in frequency content of the signal vs. time needs to be tracked so that dispersion can be taken into account.

For this purpose, the time-frequency representation (TFR) will be used in this work. The TFR of a time domain signal is a three-dimensional plot with frequency on the horizontal axis, time on the vertical axis, and the amplitude of the signal on the third axis (perpendicular to the plane of the horizontal and vertical axes). A TFR can also be represented as a two-dimensional contour plot. TFRs are obtained by first dividing the time domain into finite time intervals, or windows, then carrying out the spectrum analysis for the signals within each window. Within each time window, one can plot a frequency spectrum associated with that particular time window. By placing these spectra plots together according to their temporal sequence, a two dimensional TFR contour plot is obtained, displaying the frequency change with respect to time. Commonly used TFRs include wavelets, the STFT, and the Wigner-Ville distribution (WV). In this chapter, the STFT will be used. The STFT of a time domain signal, $s(t)$, is defined by

$$S(\omega,t)=\frac{1}{2\pi}\int_{-\infty}^{\infty}e^{-i\omega t}s(\tau)h(t-\tau)d\tau \tag{5.139}$$

where $h(t)$ is a window function defined by

$$h(t-\tau)=\begin{cases}1 & \text{for}\,|\tau-t|<\Delta t\\ 1 & \text{for}\,|\tau-t|\geq\Delta t\end{cases} \tag{5.140}$$

with Δt being the half window size. The STFT depends on the selection of window size; the larger the window, the more accuracy in frequency, but the less accuracy in time. The energy spectrum

$$E(\omega,t)=|S(\omega,t)|^2 \tag{5.141}$$

is called a spectrogram. The TFR plot is essentially a contour plot of the spectrogram as a function of time and frequency.

In addition to taking the spectrogram of the time domain signal based on Equation 5.139, a TFR plot can also be obtained from the dispersion curves. For example, consider a source-receiver system. Assume the frequency-wavenumber relationship (f–k) is known for the system. Therefore, the group velocity can be calculated through

$$c_g=2\pi\frac{\partial f}{\partial k} \tag{5.142}$$

for each of the different modes. Then, for a specific mode at frequency f, the arrival time from the source to the receiver is given by

$$t = \frac{s}{c_g(f)} \tag{5.143}$$

where s is the distance between the source and the receiver. This allows us to construct a TFR plot. Using this method, the TFR plot can be obtained by carrying out a time-harmonic analysis that yields the frequency-wavenumber relationship. The color (or gray scale) of such frequency-wavenumber plots show the amplitude of the signal strength.

In practice, the frequency-wavenumber dispersion curves are usually obtained numerically. In order to perform the numerical differentiation with reasonable accuracy, a very high precision is required for the frequency-wavenumber dispersion solution. A low-pass filter can reduce the numerical noise over the highly dispersive regions of the dispersion plot, and a moving average will further smooth the data for the nondispersive regions of the plot. Typically, the moving average procedure cannot be applied for frequencies below 2 MHz because the waves are highly dispersive below 2 MHz and the moving average could significantly distort the shape of the plot.

This alternative way of obtaining the TFR made it possible to compare the theoretically obtained TFR to a TFR obtained from experimental or purely numerical (e.g., finite element generated) signals. More interestingly, this experimental or numerical TFR is not limited to perfect geometries, even though the analytical dispersion curves usually can only be obtained for geometry without cracks. Thus, it is possible (and highly instructive) to compare analytically obtained dispersion curves (e.g., for a perfect annulus) to a TFR obtained from experimental signals measured on the same annulus with cracks. Such a comparison would allow the determination of the crack location.

Consider the setup shown in Figure 5.12. The goal is to determine the crack location, or find s. Let U be the incident wave at point B in the absence of the crack. For a given geometry and transducer, this field can be calculated using the finite element method discussed earlier. Let V be the total field at point B in the presence of the crack. This field is usually measured using a transducer. Then, $W = V - U$ gives the backscattered field at point B. Using the method discussed in previous paragraphs, the TFR of U can be obtained

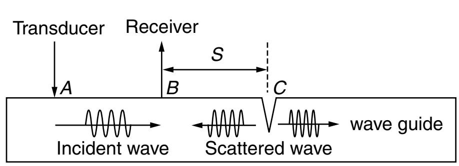

FIGURE 5.12
Experimental setup to determine crack location.

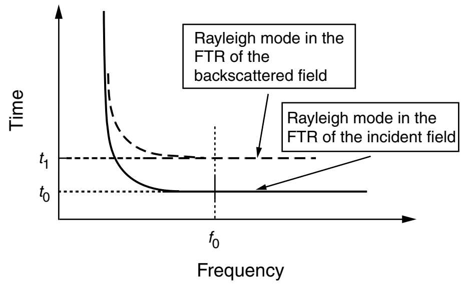

FIGURE 5.13
A measurement scheme to locate the crack.

from the finite element solution. Similarly, the TFR of W can also be obtained once U and V are measured. Now, focus on a particular mode in the TFRs, (e.g., the Rayleigh mode at a particular frequency, f_0). A schematic of the Rayleigh modes from both TFRs is shown in Figure 5.13. Clearly, t_0 is the time for the Rayleigh wave of frequency f_0 to travel from point A (source of the incident wave) to point B (position of the receiver).

Let us assume that it takes x seconds for the Rayleigh wave of frequency f_0 to travel from point B to point C where the crack is located. When this wave impinges on the crack, part of it will be scattered into the Rayleigh wave traveling back toward point B, and the portion with frequency f_0 arrives at point B after x seconds. As far as the backscattered field is concerned, the first time the Rayleigh wave with frequency f_0 arrives at point B is $2x$ seconds after the incident Rayleigh wave of the same frequency has passed point B. That is $t = t_1 - t_0 = 2x$. Therefore, it follows from Equation 5.143 that the distance between the receiver (point B) and the crack at point C (the source of the backscattered signals) is

$$s = xc_g(f_0) = \frac{1}{2}(t_1 - t_0)c_g(f_0) \quad \textbf{(5.144)}$$

The crack location is therefore known. It is seen that this method is independent of the source and source location. It requires neither selective generation nor detection of specific modes in order to alleviate the complexity due to dispersion. Therefore, it is very straightforward and easy to use once the TFRs of the incident and backscattered fields are obtained.

The accuracy of the above method depends on two factors. First, the dispersion curves of the incident wave must be calculated accurately so that a sharp and accurate TFR can be obtained. This, in principle, can be done by increasing the accuracy of the numerical solution of the dispersion curves in the uncracked annulus. Second, the experimentally measured backscattered field must be processed appropriately to obtain a sharp and accurate TFR. This is not very easy to achieve because of the noise in the measured signals.

Because of measurement uncertainties and noises in the signal, the TFR plot directly obtained from the experimental signal using Equation 5.139 usually has a very limited frequency-time resolution, which results in plots showing relatively large bands of energy, so that neither time nor frequency can be pinpointed accurately. To address this problem, the reassignment or the reallocation method is used to further process the TFRs. The idea is to move the energy value in a spectrogram from its point of computation to a center of gravity, adding it if necessary to other values coming from other calculation points. The reassignment method can greatly reduce "spreading" of the energy bands in a spectrogram along both the time and the frequency axis. This results in much sharper energy bands in the spectrogram and enables more accurate identification of the arrival time of a particular mode at a given frequency. Details of the reassignment method are described in Niethammer et al. (2001).

To test the method described above for locating the crack, experiments are conducted for an annulus with a radial crack. The crack extends from the inner wall of the annulus to 10% of the wall thickness. A 0.5-MHz transducer is used to generate the incident wave. The finite element simulation is conducted to obtain the incident field at an arbitrary location on the outer surface of the annulus. A PZT transducer is placed at the same location to measure the total wave field after the crack is introduced. The backscattered signal is then obtained by subtracting the incident signal (obtained from the uncracked annulus) from the total scattered signal. The reassigned STFT is then used to process the backscattered signals. For accuracy, the STFT of the inci-

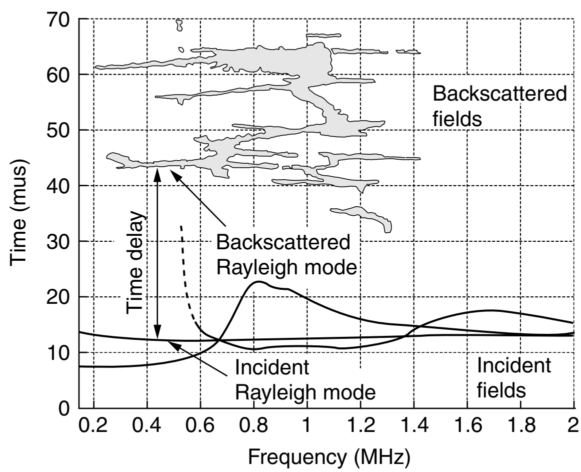

FIGURE 5.14
Methodology to locate the crack: comparison between the reassigned spectrogram for the backscattered energy and the analytical dispersion curves in the time-frequency domain.

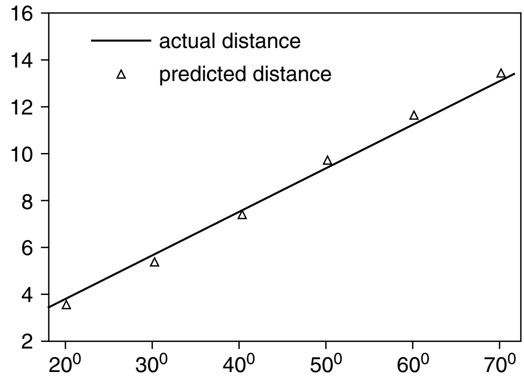

FIGURE 5.15
Distance between the crack and receiver; the solid line is the actual distance and the symbols represent the values estimated from the measurement.

dent wave is obtained numerically through the dispersion curves of the annulus. When these two STFTs are plotted on the same plot, each mode backscattered by the crack appears in the figure with a time delay between the incident and backscattered waves. As explained earlier, by measuring this delay for a given mode, one can determine the crack location (see Figure 5.14). In this example, the Rayleigh mode is used to compute the time delay. From there, the distance between the receiver and the crack is obtained. The measurements are carried out at several receiver locations. The comparison between the actual location and the location estimated from the experimental measurement is shown in Figure 5.15. The horizontal axis is the degree of separation between the receiver and the crack, and the vertical axis is the distance (in centimeters) between the crack and the receiver along the outer surface of the annulus. The solid line represents the actual distance, and the symbols are from the experimental estimates. One can see that the agreement is excellent.

This method works well even in the nearfield of the crack or the source. However, if the receiver is too close to the crack, the time delay between the backscattered and incident modes will be small and more difficult to discern. If the receiver is too close to the source transducer, modes in the incident field tend to cluster together, making it more difficult to identify the modes. Since the method is based on visual inspection of time delay, it is advantageous to have sufficient separation between the TFRs of the incident and backscattered fields.

5.5.2.2 Determining Crack Size

One challenge inherent to ultrasonic evaluation using guided waves is that even if a single mode can be generated inside the component, once that wave mode hits a crack, some of its energy may be converted into other modes. As a result, it is difficult to use the characteristics of a single mode to uniquely quantify a crack's attributes such as size and position. A method is needed that can take into account all possible modes.

To this end, the Auld's formula (Auld, 1979) can be used. For a two-transducer system, Auld derived a steady-state reciprocal relation that can be applied to flaw detection and characterization. Transducer I with power P produces the incident field. Transducer II is the receiver. The ratio of received electrical signal strength over incident signal strength is denoted by Γ. Auld's formula gives the change of Γ due to scattering by a scatter:

$$\delta\Gamma = ((E_{II})_{flaw} - (E_{II})_{noflaw})/(E_I)_{flaw} \quad \textbf{(5.145)}$$

Here E_I and E_{II} are the strength of the electrical signals in Transducers I and II.

For backscattering from a traction-free crack, the amplitude of the time-harmonic backscattered field is given by Qu and Achenbach (1987)

$$\delta\Gamma = -\frac{i\omega}{4P}\int_A \left(\sigma_{kj}^{(1)}\Delta u_k^{(2)}\right) n_1 \, dS \quad \textbf{(5.146)}$$

where P is the total power of the source transducer, ω is the frequency, $\sigma_{ij}^{(1)}$ is the incident stress field in the absence of the crack, and

$$\Delta u_k^{(2)} = u_k(x_2^-) - u_k(x_2^+) \quad \textbf{(5.147)}$$

is the crack opening displacement. The integration is over the crack surface A.

For transient problems, Equation 5.146 cannot be applied directly. Typically, the fast Fourier transform (FFT) must be applied to transform the signals into the frequency domain before using the Auld's formula (e.g., Lowe, 1997; Lowe et al., 2000). This procedure is rather involved and requires careful attention to the proper application of the FFT. In particular, zero-padding the time-domain data is absolutely necessary.

In this chapter, a different approach is taken. A counterpart of Equation 5.146 in the time domain will be derived so that it can be applied directly to time domain signals. This is done based on the fact that: (1) multiplication in the frequency domain is equivalent to convolution in the time domain; and (2) multiplying by $i\omega$ in the frequency domain is equivalent to differentiating with respect to time in the time domain. Thus, the counterpart of Equation 5.146 in the time domain can be written as

$$\delta\Gamma(t) = C\frac{d}{dt}\int_A \left(\sigma_{kj}^{(1)} * \Delta u_k^{(2)}\right) n_l \, dS \quad \textbf{(5.148)}$$

where C is a multiplicative constant and * stands for convolution. Conceivably, larger crack size leads to higher value of the backscattering amplitude.

To quantify the relationship between the backscattering amplitude and the crack size, the root-mean-square (RMS) of the frequency spectrum of the backscattering amplitude is calculated as

$$R = \sqrt{\frac{1}{4}\left|\int_{-\infty}^{\infty} e^{-i\omega t}\delta\Gamma(\tau)\,d\tau\right|^2 d\omega} \tag{5.149}$$

which can be regarded as the backscattered energy coefficient from the crack. It contains contributions from all relevant modes and frequencies.

The backscattered energy coefficient can be obtained in two ways. First, a numerical simulation (such as the finite element method) can be performed to obtain the displacements and stresses. These transient numerical solutions can be used in Equation 5.148 directly to obtain the backscattering amplitude. The backscattered energy coefficient is then obtained by applying the Fourier transform and computing the RMS as shown in Equation 5.149.

The second way of obtaining the backscattered energy coefficient is through Equation 5.145 by conducting experimental measurements. This can be done by using a single transducer that can generate and receive signals. The voltage received by this transducer will be proportional to the amplitude of the backscattered fields, as defined by Equation 5.145. The RMS of the amplitude of the backscattered field can then be computed to yield the experimentally obtained backscattered energy coefficient.

A method can now be devised to quantify the crack size in a given annulus. First, a series of numerical computations should be conducted for the same annulus with various crack sizes. Through this parametric study, a relationship (or a plot) between the crack size and the backscattered energy coefficient can be established. Such a plot is shown in Figure 5.16. Note that the

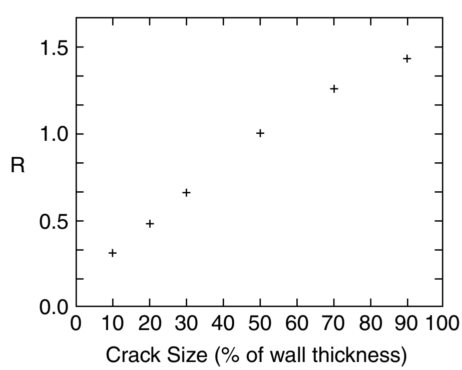

FIGURE 5.16
Backscattered energy coefficient vs. crack size.

TABLE 5.2

Comparison between Actual and Experimentally Estimated Crack Size (in % of Plate Thickness)

Actual (% of Plate Thickness)	Test 1	Test 2	Test 3	Test AVG
25	27.5	25.1	20.0	24.2
50	52.5	49.0	48.0	49.8

absolute value of R depends on the calibration of the measurement systems. What is important is the relative amplitude of R. So, in Figure 5.16, the amplitude of R is normalized by its value for the case where the crack is 50% of the wall thickness. Second, experimental measurements should be done on the same annulus with an unknown crack size. Based on these experimental data, the backscattered energy coefficient can be calculated as discussed in the previous paragraph. By comparing the experimentally obtained backscattered energy coefficient with the numerically obtained relationship between the crack size and backscattered energy coefficient, such as Figure 5.16, the crack size is determined. Note that the backscattered energy coefficient calculated numerically and the one that is obtained experimentally usually have different values. However, the difference is only up to a multiplicative constant. This constant can be calibrated by performing a measurement with a known crack size.

To illustrate the accuracy of this method, experiments were conducted on a flat plate with surface breaking cracks of various sizes. Table 5.2 shows the measured crack sizes against the actual crack size, and the agreement is very good.

In summary, methods to determine radial crack location and size are described. To locate the crack, a time-frequency representation technique (the STFT) is used to discern the arrival time of a given mode at a given frequency for both the incident and backscattered waves from the crack. By calculating the time delay of a specific mode in the spectrogram, the distance between the receiver and the crack can be determined and located. In using this method, the time-frequency representation of the incident wave is calculated from the finite element method. In addition, the reassignment method must be used to process the measured backscattered field in order to obtain a sharper time-frequency representation. It is found that this method is capable of characterizing cracks as small as 10% of the wall thickness. For smaller cracks, high frequency waves are needed and this requires more extensive numerical computations.

For sizing the crack, a time domain counterpart of the Auld's formula is developed. By using the time domain Auld's formula, the backscattering energy coefficient can be either obtained directly from experimental measurement, or calculated from the numerically synthetic data. By comparing the experimentally obtained and numerically calculated backscattering energy coefficients, the size of the crack can be determined.

It is important to note that the results presented here, both for crack sizing and crack locating, are dependent on the frequency of the input signal. The examples shown in this chapter are for signals in the frequency range 0.2 to 1.5 MHz (with most of the energy centered around 0.5 MHz). Even with this frequency range, the method is capable of detecting cracks as small as 0.3 mm. A Rayleigh wave of 0.3-mm wavelength would have a frequency of approximately 9.7 MHz in a steel annulus. The need for high-frequency waves to detect small flaws is significantly lessened by using techniques described here.

Finally, it should be mentioned that the methods described here can be applied not only to guided circumferential waves for detecting crack in an annular structure, but also to many other guided wave applications, such as detecting surface-breaking cracks using Rayleigh surface waves, and characterizing matrix cracks in laminated composites using Lamb waves.

Acknowledgment

Jianmin Qu acknowledges the financial support of NSFC under grant number 10228204.

Appendix 5

For waves in the longitudinal direction:

$$d_{11}^{Z}(m,r)=\left[\frac{2m(m-1)}{r^2}+k_z^2-q^2\right]Z_m(pr)+\frac{2p}{r}Z_{m+1}(pr)$$

$$d_{12}^{Z}(m,r)=2i\,k_z\left[qZ_m(qr)-\frac{m+1}{r}Z_{m+1}(qr)\right]$$

$$d_{13}^{Z}(m,r)=2m\left[\frac{(m-1)}{r^2}Z_m(qr)-\frac{q}{r}Z_{m+1}(qr)\right]$$

$$d_{21}^{Z}(m,r)=2ik_z\left[\frac{m}{r}Z_m(pr)-pZ_{m+1}(pr)\right]$$

$$d_{22}^{Z}(m,r)=-\frac{qm}{r}Z_m(qr)+\left(q^2-k_z^2\right)Z_{m+1}(qr)$$

$$d_{23}^{Z}(m,r)=\frac{ik_z m}{r}Z_m(qr)$$

$$d_{31}^{Z}(m,r) = -2m\left[\frac{m-1}{r^2}Z_m(pr) - \frac{p}{r}Z_{m+1}(pr)\right]$$

$$d_{32}^{Z}(m,r) = ik_z\left[qZ_m(qr) - \frac{2(m+1)}{r}Z_{m+1}(qr)\right]$$

$$d_{33}^{Z}(m,r) = \left[q^2 - \frac{2m(m-1)}{r^2}\right]Z_m(qr) - \frac{2q}{r}Z_{m+1}(qr)$$

where $Z_m(\bullet)$ can be either Bessel function of the first kind, $J_m(\bullet)$, or the second kind, $Y_m(\bullet)$. The superscript Z in $d_{\alpha\beta}^{Z}(m,r)$ is to indicate which Bessel function to use. For example,

$$d_{23}^{J}(m,r) = \frac{ik_z m}{r}J_m(qr)$$

while

$$d_{23}^{Y}(m,r) = \frac{ik_z m}{r}Y_m(qr)$$

For waves in the circumferential direction:

$$d_{11}^{Z}(r) = Z_{k_\theta-2}\left(\frac{\omega r}{\kappa c_T}\right) - 2(\kappa^2-1)Z_{k_\theta}\left(\frac{\omega r}{\kappa c_T}\right) + Z_{k_\theta+2}\left(\frac{\omega r}{\kappa c_T}\right)$$

$$d_{12}^{Z}(r) = i\kappa^2\left[Z_{k_\theta-2}\left(\frac{\omega r}{c_T}\right) - Z_{k_\theta+2}\left(\frac{\omega r}{c_T}\right)\right]$$

$$d_{21}^{Z}(r) = i\left[Z_{k_\theta-2}\left(\frac{\omega r}{\kappa c_T}\right) - Z_{k_\theta+2}\left(\frac{\omega r}{\kappa c_T}\right)\right]$$

$$d_{22}^{Z}(r) = -\kappa^2\left[Z_{k_\theta-2}\left(\frac{\omega r}{c_T}\right) + Z_{k_\theta+2}\left(\frac{\omega r}{c_T}\right)\right]$$

where $Z_m(\bullet)$ can be either Bessel function of the first kind, $J_m(\bullet)$, or the second kind Y_m. The superscript Z in $d_{\alpha\beta}^{Z}(r)$ is to indicate which Bessel function to use. For example,

$$d_{12}^{1}(b) = i\kappa^2\left[J_{k_\theta-2}\left(\frac{\omega b}{c_T}\right) - J_{k_\theta+2}\left(\frac{\omega b}{c_T}\right)\right]$$

References

Achenbach, J.D., *Wave Propagation in Elastic Solids*, North Holland, Amsterdam, 1973.

Achenbach, J.D. and Keshava, S.P., 1967, Free waves in a plate supported by a semi-infinite continuum, *J. Appl. Mech.*, 34, 397–404, 1967.

Alleyne, D. and Cawley, P., A two-dimensional fourier transform method for the measurement of propagating multimode signals, *J. Acoust. Soc. Am.*, 89, 1159–1168, 1991.

Armenàkas, A.E., Gazis, D.C., and Herrmann, G., *Free Vibration of Circular Cylindrical Shells*, Pergamon Press, New York, 1969.

Auld, B.A., General electromechanical reciprocity relations applied to the calculation of elastic wave scattering coefficients, *Wave Motion*, 1, 3–10, 1979.

Brekhovskikh, L.M., Surface waves confined to the curvature of the boundary in solid, *Soviet Physics — Acoust.*, 13, 462–472, 1968.

Červ, J., 1988, Dispersion of elastic waves and Rayleigh-type waves in a thin disc, *Acta Technica Csav*, 89, 89–99, 1988.

Chimenti, D.E. and Nayfeh, A.H., Leaky waves in fibrous composite laminates, *J. Appl. Phys*., 58, 4531, 1985.

Chimenti, D.E. and Nayfeh, A.H., Ultrasound reflection and guided wave propagation in biaxially laminated composite plates, *J. Acoust. Soc. Am.*, 87, 1409–1415, 1989.

Chree, C., Longitudinal vibrations of a circular bar, *Quart. J. Math.*, 21, 287–298, 1886.

Cook, E.G. and Valkenburg, H.E., Surface Waves at Ultrasonic Frequencies, *ASTM Bull.*, 3, 81–84, 1954.

Costley, R.D., Ingram, M., Simpson, J., Shah, V.V., and Balasubramaniam, K., Torsional waveguide sensor for molten materials, *Rev. Prog. Quant. Nondestructive Evaluation*, 17, 859–860, 1998.

Datta, S.K., Al-Nassar, Y., and Shah, A.K., 1991, Lamb wave scattering by a surface breaking crack in a plate, *Rev. Prog. Quant. Nondestructive Evaluation*, 10, 97–104, 1991.

Gazis, D., Three dimensional investigation of the propagation of waves in hollow circular cylinders, I. Analytical foundation. II. Numerical results, *J. Acoust. Soc. Am.*, 14, 1869–1876, 1959.

Grace, O.D. and Goodman, R.R., Circumferential waves on solid cylinders, *J. Acoust. Soc. Am.*, 39, 173–174, 1966.

Graff, K.F., *Wave Motion in Elastic Solids*, Ohio State University Press, Columbus, OH, 1975.

Gregory, R.D., The propagation of Rayleigh waves over curved surfaces at high frequency, *Proc. Cambridge Phil. Soc.*, 70, 103–121, 1971.

Grimshaw, R., Propagation of surface waves at high frequency, *J. Inst. Math. Appl.*, 4, 174–193, 1968.

Guo, D. and Kundu, T., A new transducer holder mechanism for pipe inspection, *J. Acoust. Soc. Am.*, 110, 303–309, 2001.

Guyott, C.C.H. and Cawley, P., 1988, The measurement of through thickness plate vibration using a pulsed ultrasonic transducer, *J. Acosut. Soc. Am.*, 83, 623–631, 1988.

Harris, J.G., Rayleigh wave propagation in curved waveguides, *Wave Motion*, 36, 425–441, 2002.

Herrmann, G. and Mirsky, I., Three-dimensional and shell-theory analysis of axially symmetric motions of cylinders, *Trans. ASME J. Appl. Mech.*, 78, 563–568, 1956.

Hudson, G.E., Dispersion of elastic waves in solid circular cylinders, *Phys. Rev.*, 63, 46–51, 1943.

Keller, J.B. and Karal, F.C., Surface wave excitation and propagation, *J. Appl. Phys.*, 31, 1039–1046, 1960.

Keller, J.B. and Karal, F.C., Geometrical theory of elastic surface-wave excitation and propagation, *J. Acoust. Soc. Am.*, 36, 32–40, 1964.

Kley, M., Valle, C., Jacobs, L.J., Qu, J., and Jarzynski, J., Development of dispersion curves for two-layered cylinders using laser ultrasonics, *J. Acost. Soc. Am.*, 106, 582–588, 1999.

Kolsky, H., *Stress Waves in Solids*, Dover, New York, 1963.

Liu, G. and Qu, J., Guided circumferential waves in a circular annulus, *J. Appl. Mech.*, 65, 424–430, 1998a.

Liu, G. and Qu, J., Transient wave propagation in a circular annulus subjected to impulse excitation on its outer surface, *J. Acost. Soc. Am.*, 104, 1210–1220, 1998b.

Lowe, M., Characteristics of the reflection of Lamb waves from defects in plates and pipes, *Rev. Prog. QNDE*, 17, 113–120, 1997.

Lowe, M.J.S., Cawley, P., Kao, J.K., and Diligent, O., Prediction and measurement of the reflection of the fundamental anti-symmetric Lamb wave from cracks and notches, *Rev. Prog. Quant. Nondestructive Evaluation*, 19A, 193–200, 2000.

Mal, A.K., Guided waves in layered solid with interface zones, *Int. J. Engng. Sci.*, 26, 873–881, 1988.

Mal, A.K., Yin, C.C., and Bar-Cohen, Y., Analysis of acoustic pulses reflection from the fiber-reinforced composite laminates, *J. Appl. Mech.*, 59, pp. 5136–5144, 1991.

McFadden, J.A., 1954, Radial vibrations of thick-walled hollow cylinders, *J. Acoust. Soc. Am.*, 26, 714–715.

Meeker, T.R. and Meitzler, A.H., Guided waves propagation in elongated cylinders and plates, in *Physical Acoustics*, Vol. 1, Part A, Mason, W.P., Ed., Academic Press, New York, 1964, pp. 111–167.

Miklowitz, J., *The Theory of Elastic Waves and Wave Guides*, North-Holland, Amsterdam, 1978.

Mindlin, R.D., Axially symmetric waves in elastic rods, *J. Appl. Mech.*, 82, 145–151, 1960.

Mindlin, R.D., and McNiven, H.D., Axially symmetric waves in elastic rods, *J. Appl. Mech.*, 82, 145–151, 1960.

Moser, F., Jacobs, L.J., and Qu, J., Modeling elastic wave propagation in wave guides with the finite element method, *NDT & E Int.*, 32, 225–234, 1999.

Na, W.B. and Kundu, T., EMAT-based inspection of concrete-filled steel pipes for inernal voids and inclusions, *J. Pressure Vessel Technol.*, 124, 265–272, 2002.

Nagy, P.B. and Kent, J., Ultrasonic assessment of poisson's ratio in thin rods, *J. Acoust. Soc. Am.*, 98, 2649, 1995.

Nagy, P.B., Blodgett, M., and Golis, M., Weep hole inspection by circumferential creeping waves, *NDT & E Int.*, 27, 131–142, 1994.

Nayfeh, A.H., *Wave Propagation in Layered Anistropic Media with Applications for Composites*, Elsevier, Amsterdam: North-Holland, 1995.

Niethammer, M., Jacobs, L.J., Qu, J., and Jarzynski, J., Time-frequency representation of Lamb waves using the reassigned spectrogram, *J. Acoust. Soc. Am.*, 109, 1841–1847, 2001.

Onoe, M., McNiven, H.D., and Mindlin, R.D., Dispersion of axially symmetric waves in elastic rods, *J. Appl. Mech.*, 28, 729–734, 1962.

Pao, Y.H., Dispersion of elastic waves in solid circular cylinders, Part II, *J. Appl. Mech.*, 28, 61–64, 1962.

Pao, Y.H. and Mindlin, R.D., Dispersion of flexural waves in an elastic, circular cylinder, *J. Appl. Mech.*, 27, 513–520, 1960.

Pochhammer, L., Ueber die Fortpflanzungsgeschwindigkeiten Kleiner Schwingungen in einem unbegrenzten isotropen Kreiscylinder, *Zeitschrift für Mathematik*, 81, 324–336, 1876.

Qu, J. and Achenbach, J.D., Backscattering from porosity in cross-ply composites, *Rev. Prog. Quant. Nondestructive Eval.*, 7, p.1029–1036, 1987.

Qu, J., Berthelot, Y., and Li, Z., Dispersion of guided circumferential waves in circular annulus, *Rev. Prog. Quant. Nondestructive Evaluation*, 15, 169–176, 1996.

Qu, J., Berthelot, Y., and Jacobs, L., Crack detection in thick annular components using ultrasonic guided waves, *Proc. Instn. Mech. Engrs. Part C*, 214, 1163–1171, 2000.

Rayleigh, J.W.S., *The Theory of Sound*, Dover, New York, 1945.

Rokhlin, S.I. and Wang W., Ultrasonic evaluation of in-plane and out-of-plane elastic properties of composite materials, *Rev. Prog. Quant. Nondestructive Evaluation*, 8B, 1489–1496, 1988.

Rose, J.L., *Ultrasonic Waves in Solid Media*, Cambridge Press, Cambridge, MA, 1999.

Rose, J.L., Standing on the shoulders of giants: an example of guided wave inspection, Mehl Honor Lecture, *Mater. Evaluation*, 60, 53–59, 2002.

Rose, J.L., Avioli, M.J., and Cho, Y., Elastic wave analysis for broken rail detection, *Rev. Progress QNDE*, Brunswick, Maine, 21B, 1806–1812, 2001.

Rose, J.L., Pelts, S., Quarry, M., A comb transducer model for guided wave NDE, *Ultrasonics*, 36, 163–168, 1998.

Rose, J.L. and Soley, L., Ultrasonic guided waves for the detection of anomalies in aircraft components, *Mater. Evaluation*, 50, 1080–1086, 2000.

Rulf, B., Rayleigh waves on curved surfaces, *J. Acoust. Soc. Am.*, 45, 493–499, 1969.

Shah, A.H. and Datta, S.K., Harmonic wave in a periodically laminated medium, *Int. J. Solids Structures*, 18, 397, 1982.

Smith, R., Propagation in slowly-varying wave-guides, *SIAM*, 33, 39–50, 1977.

Stakgold, I., *Green's Functions and Boundary Value Problems*, John Wiley, New York, 1979.

Thompson, R.B., Alers, G.A. and Tennison, M.A., Applications of Direct Eletromagnetic Lamb Wave Generation to Gas Pipeline Inspection, Proc. IEEE Ultrasonics Symp., 70–79, 91–94, 1972.

Towfighi, S., Kundu, T., and Ehsani, M., Elastic wave propagation in circumferential direction in anisotropic cylindrical curved plates, *J. Appl. Mech.*, 69, 283–291, 2002.

Valle, C., Qu, J., and Jacobs, L.J., Guided circumferential waves in layered cylinders, *Int. J. Eng. Sci.*, 37, 1369–1387, 1999.

Valle, C., Niethammer, M., Qu, J., and Jacobs, L.J., Crack characterization using guided circumferential waves, *J. Acoust. Soc. Am.*, 110, 1282–1290, 2001.

Viktorov, I.A., Rayleigh-type waves on a cylindrical surface, *Soviet Phys.–Acoust.*, 4, 131–136, 1958.

Weaver, R.L., and Pao, Y.H., Axisymmetric elastic waves excited by a point source in a plate, *J. Appl. Mech.*, 49, 821–836, 1982.

6

Fundamentals and Applications of Nonlinear Ultrasonic Nondestructive Evaluation

John H. Cantrell

CONTENTS

0-8493-1462-3/02/$0.00+$1.50

The increasing demand for new, more reliable materials, that are often used in hostile environments, has led to the necessity of establishing equally reliable, quantitative techniques for nondestructively evaluating and characterizing such materials. Although linear ultrasonic methods have long been among the most popular and useful of the nondestructive evaluation (NDE) methodologies, considerable effort has been expended in recent years on the development of NDE methodologies based on nonlinear ultrasonics. The focus of the present chapter is on the fundamental principles and applications of nonlinear ultrasonic NDE. Nonlinear ultrasonics generally entails the study of both finite amplitude ultrasonics and acoustoelasticity. Finite amplitude ultrasonics is concerned with the investigation of acoustic harmonics generated from the nonlinear interactions of an interrogative waveform (usually an initially pure sinusoidal wave) with basic lattice configurations of anharmonic materials; nano-/microstructures of solids including defects, and other organizational structures and boundaries in the material, including those of composite materials. Acoustoelasticity emphasizes the study of the variation of the sound velocity as a function of the state of stress of the material.

The chapter is divided into four parts. We begin in Section 6.1 with a consideration of the fundamental principles of finite amplitude ultrasonics with an emphasis on the connection of nonlinear ultrasonics generally to the basic atomic structures of the material and to thermodynamics. This connection is also emphasized in Section 6.2 where the fundamental aspects of acoustoelasticity is developed. The application of nonlinear ultrasonics to materials characterization is developed in Section 6.3; an emphasis on establishing the fundamental relationships between nonlinear ultrasonic parameters, both for finite amplitude ultrasonics and acoustoelasticity, and basic microstructural features, including defects, in materials is also addressed in this section. Section 6.4 concludes the chapter with a brief discussion of general measurement considerations.

6.1 Finite Amplitude Ultrasonics

In finite amplitude ultrasonics one generally measures the amplitude of harmonics generated by the nonlinear interactions of an initially pure sinusoidal sound wave with the material. The nonlinear interactions generally result from lattice anharmonicity (stemming from a nonquadratic intertomic potential) or from nonlinearities involving defects, microstructural features, or other disruptions in the lattice structure of the material. To emphasize the importance of the lattice structure to ultrasonic harmonic generation, the derivation of the basic equations for finite amplitude wave propagation begins with consideration of the coherent motion of discrete lattice points from which motion in the continuum limit (the nonlinear wave equation) is obtained. The acoustic nonlinearity parameter is defined and wave properties (attenuation and discontinuity distance) pertaining to harmonic generation are derived. The crystalline structure and symmetry dependences of the nonlinearity parameter are obtained, and the relationship to thermodynamics is established.

6.1.1 Coherent Motion of Discrete Lattice Points

Consider an infinite one-dimensional lattice of points connected by nonlinear springs as shown in Figure 6.1. For simplicity let each point represent an atom or particle and let the springs represent forces between each pair of particles. It is assumed that each point has a mass m and that in equilibrium, each point is separated from an adjacent point by the distance d. If the nth-point is displaced from its equilibrium position by the distance u_p, then the elastic potential energy V_{PE} of the collection of displaced masses is given by

$$V_{PE} = (V_{PE})_0 + \sum_p k_1(u_{p+1} - u_p) + \frac{1}{2}\sum_p k_2(u_{p+1} - u_p)^2 + \frac{1}{3!}\sum_p k_3(u_{p+1} - u_p)^3 + \cdots \quad \textbf{(6.1)}$$

where $(V_{PE})_0$ is a constant, k_1 is the first-order spring constant, k_2 is the second-order spring constant, and k_3 is the third-order spring constant. Note that the order of the spring constant is determined by the power of the displacement.

The initial positions (equilibrium configuration) of the set of mass points are referred to as the Lagrangian or material coordinates of the set. The theoretical development here will be performed with respect to the Lagrangian coordinates. It must be pointed out that the analytical development can also be performed with respect to the displaced positions (or

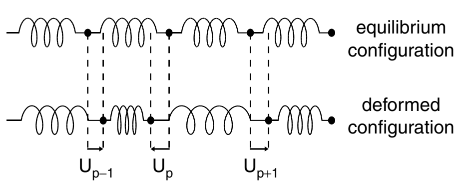

FIGURE 6.1
One-dimensional lattice of mass points connected by nonlinear springs.

present configuration) of the set of mass points. The set of present positions of the mass points is called the Eulerian or spatial coordinates. An analysis using Eulerian coordinates is often done for fluids but is rarely done for solids. It is important to recognize that both the Lagrangian and the Eulerian coordinates are defined with respect the same Cartesian reference frame. The designation Lagrangian or Eulerian refers to whether the analysis is carried out with respect to an initial position of particles or the present position of particles comprising the body.

We consider the action on the *n*th-lattice point by the forces from the remainder of the points in the lattice. Newton's law for the *n*th-lattice point is

$$m\frac{d^2u_n}{dt^2} = F_n = -\frac{dV_{PE}}{du_n} = -k_1\sum_p \frac{d}{du_n}(u_{p+1}-u_p)$$

$$-\frac{1}{2}k_2\sum_p \frac{d}{du_n}(u_{p+1}-u_p)^2 - \frac{1}{3!}k_3\sum_p \frac{d}{du_n}(u_{p+1}-u_p)^3 + \cdots = -k_1\sum_p\left(\frac{du_{p+1}}{du_n}-\frac{du_p}{du_n}\right)$$

$$-\frac{1}{2}k_2\sum_p\left[2(u_{p+1}-u_p)\frac{du_{p+1}}{du_n} - 2(u_{p+1}-u_p)\frac{du_p}{du_n}\right]$$

$$-\frac{1}{3!}k_3\sum_p\left[3(u_{p+1}-u_p)^2\frac{du_{p+1}}{du_n} - 3(u_{p+1}-u_p)^2\frac{du_p}{du_n}\right]+\cdots$$

$$= k_2[(u_{n+1}-u_n)-(u_n-u_{n-1})] + \frac{1}{2}k_3[(u_{n+1}-u_n)^2-(u_n-u_{n-1})^2]+\cdots. \quad \textbf{(6.2)}$$

where m is the mass of the lattice point and t is time. In obtaining the last equality in Equation 6.2 it is noted that $(du_{p+1}/du_n) = \delta_{p+1,n}$ and $(du_p/du_n) = \delta_{p,n}$ where $\delta_{p+1,n}$ and $\delta_{p,n}$ are Kronecker deltas. Hence, the first set of terms $\{-k_1\,\Sigma[(du_{p+1}/du_n) - (du_p/du_n)]\} = 0$ in Equation 6.2. F_n is the force exerted on the *n*th-lattice point by the remaining lattice points to restore the displaced point to its equilibrium position.

It is convenient to rewrite Equation 6.2 in the following form:

$$F_n = m\frac{d^2u_n}{dt^2} = \left[k_1 + k_2 d\left(\frac{u_{n+1}-u_n}{d}\right) + \frac{1}{2}k_3 d^2\left(\frac{u_{n+1}-u_n}{d}\right)^2\right]$$

$$-\left[k_1 + k_2 d\left(\frac{u_n-u_{n-1}}{d}\right) + \frac{1}{2}k_3 d^2\left(\frac{u_n-u_{n-1}}{d}\right)^2\right] + \cdot = [F_{n,n+1}] - [F_{n,n-1}] \quad \textbf{(6.3)}$$

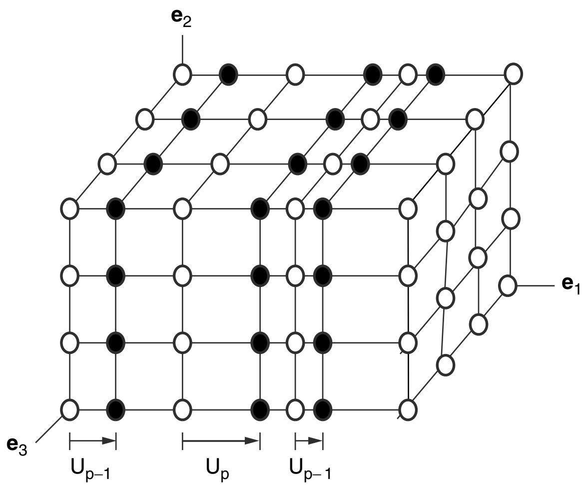

FIGURE 6.2
Three-dimensional lattice of points.

where $[F_{n,n+1}]$ is the force on lattice point n due to point $(n + 1)$ and is given by the terms in the first bracket in Equation 6.3. $[F_{n,n+1}]$ is the force on lattice point n due to point $(n - 1)$ and is given by the terms in the second bracket in Equation 6.3. We now assume an infinite three-dimensional lattice arrangement, a portion of which is shown in Figure 6.2. We consider the set of all points on the nth-plane normal to the direction e_1 and assume a uniform displacement of those points along e_1 (i.e., a longitudinal displacement along e_1). Equation 6.3 holds for each point on the nth plane. Since it is assumed that the particles are in equilibrium (i.e., no net forces) in the initial configuration, the force F_n on each particle in the nth plane must occur only when that plane is displaced from the initial configuration (i.e., when the plane is in the present configuration). We denote the force F_n on each particle in the nth-plane along the direction e_1 in the three-dimensional lattice by $F_{1,n}$. Let $S_1^{\,L}$ be a unit area of the nth-plane normal to e_1 in the initial lattice configuration. A stress is defined generally as a force per unit area. The longitudinal Lagrangian stress along direction e_1 on the nth plane $\sigma_{11,n}$ is defined as the normal force per unit area of the initial configuration, (i.e., $\sigma^{E}{}_{11,n} = F_{1,n}/S_1^{\,L}$).

The subscripted double one (i.e., 11) in $\sigma_{11,n}$ denotes a longitudinal stress. In general, a unit area S^L in the initial configuration is distorted during deformation such that the area S^L becomes S^E in the present configuration. The Eulerian stress $\sigma^E_{11,n}$ is defined by $\sigma^E_{11,n} = F_{1,n}/S^E_1$. It is important to note that, for simplicity, we are considering here a uniform displacement of the initial unit plane such that the initial unit plane is simply translated to the present position without distortion. Hence, in this case $S^L_1 = S^E_1$ and $\sigma_{11,n} = \sigma^E_{11,n}$.

From Equation 6.3 we obtain Newton's law for the longitudinal Lagrangian stress $\sigma_{11,n} = F_{1,n}/S_1^L$ (force normal to plane) to be

$$\frac{m}{S_1^L}\frac{d^2u_{1,n}}{dt^2} = \frac{F_{1,n}}{S_1^L} = \frac{[F_{1,n,n+1}]}{S_1^L} - \frac{[F_{1,n,n-1}]}{S_1^L}$$

$$= \frac{k_1}{S_1^L}(1-1) + \frac{k_2 d_1}{S_1^L}\left[\left(\frac{u_{1,n+1}-u_{1,n}}{d_1}\right) - \left(\frac{u_{1,n}-u_{1,n-1}}{d_1}\right)\right]$$

$$+\frac{1}{2}\frac{k_3 d_1^2}{S_1^L}\left[\left(\frac{u_{1,n+1}-u_{1,n}}{d_1}\right)^2 - \left(\frac{u_{1,n}-u_{1,n-1}}{d_1}\right)^2\right] + \cdots \tag{6.4}$$

where in Equation 6.4 the additional subscript 1 is added to the notation in Equation 6.3 to denote components along the e_1 direction. Thus, for example, $u_{1,n}$ denotes the particle displacement along $\mathbf{e}_1$ in the nth lattice plane normal to e_1.

6.1.2 Motion in the Continuum Limit — The Nonlinear Wave Equation

We pass to the continuum limit by letting the spacing d_1 between lattice points along the e_1-direction approach zero. The integer index n identifying a particular lattice point (or plane) now becomes the continuous index X_1 denoting a position coordinate. In the continuum limit, where $d_1 \to 0$, the discrete quantity $(u_{1,n+1} - u_{1,n})/d_1$ becomes

$$\lim_{d_1\to 0}\frac{u_{1,n+1}-u_{1,n}}{d_1} = \lim_{d_1\to 0}\frac{u_1(X_1+d_1)-u_1(X_1)}{d_1} = \frac{\partial u_1}{\partial X_1} \tag{6.5}$$

The partial derivative is used in Equation 6.5, since u_1 is in general a function of both X_1 and t. The last equality follows from the definition of the derivative where we identify $d_1 = dX_1$ in the continuum limit. The derivative $\partial u_1/\partial X_1$ in Equation 6.5 is a displacement gradient and is one component of the more general set of nine displacement gradients $\partial u_i/\partial X_j$, where $i, j = 1, 2,$ or 3, that may be defined in three dimensions (see Chapter 1). In the continuum limit Equation 6.4 becomes

$$\frac{m}{S_1^L}\frac{\partial^2 u_1}{\partial t^2} = \frac{F_1(X_1)}{S_1^L} - \frac{F_1(X_1-d_1)}{S_1^L} = \sigma_{11}(X_1) - \sigma_{11}(X_1-d_1)$$

$$= [A_1 - A_1] + A_{11}\left[\left(\frac{\partial u_1}{\partial X_1}\right)_{X_1} - \left(\frac{\partial u_1}{\partial X_1}\right)_{X_1-d_1}\right] + \frac{1}{2}A_{111}\left[\left(\frac{\partial u_1}{\partial X_1}\right)^2_{X_1} - \left(\frac{\partial u_1}{\partial X_1}\right)^2_{X_1-d_1}\right] + \cdots \tag{6.6}$$

where we define in the continuum limit $\sigma_{11}(X_1) = F_1(X_1)/S_1^L$ and

$$A_1 = \frac{k_1}{S_1^L},\ \ A_{11} = \frac{k_2 d_1}{S_1^L},\ \ A_{111} = \frac{k_3 d_1^2}{S_1^L} \tag{6.7}$$

Dividing Equation 6.6 by d_1 yields the expression

$$\frac{m}{S_1^L d_1}\frac{\partial^2 u_1}{\partial t^2} = \frac{\sigma_{11}(X_1) - \sigma_{11}(X_1 - d_1)}{d_1} = A_1\frac{1}{d_1}[1-1] + A_{11}\frac{1}{d_1}\left[\left(\frac{\partial u_1}{\partial X_1}\right)_{X_1} - \left(\frac{\partial u_1}{\partial X_1}\right)_{X_1-d_1}\right]$$

$$+\frac{1}{2}A_{111}\frac{1}{d_1}\left[\left(\frac{\partial u_1}{\partial X_1}\right)_{X_1}^2 - \left(\frac{\partial u_1}{\partial X_1}\right)_{X_1-d_1}^2\right] + \cdots \tag{6.8}$$

We note that $m/S_1^L d_1 = \rho_1$ is the mass density of the material in the initial configuration. In the continuum limit

$$\lim_{d_1\to 0}\frac{\sigma_{11}(X_1) - \sigma_{11}(X_1 - d_1)}{d_1} = \frac{\partial \sigma_{11}}{\partial X_1} \tag{6.9}$$

$$\lim_{d_1\to 0}\frac{1}{d_1}\left[\left(\frac{\partial u_1}{\partial X_1}\right)_{X_1} - \left(\frac{\partial u_1}{\partial X_1}\right)_{X_1-d_1}\right] = \left(\frac{\partial^2 u_1}{\partial X_1^2}\right)_{X_1} \tag{6.10}$$

and

$$\lim_{d_1\to 0}\frac{1}{d_1}\left[\left(\frac{\partial u_1}{\partial X_1}\right)_{X_1}^2 - \left(\frac{\partial u_1}{\partial X_1}\right)_{X_1-d_1}^2\right] = \lim_{d_1\to 0}\frac{1}{d_1}\left[\left(\frac{\partial u_1}{\partial X_1}\right)_{X_1} + \left(\frac{\partial u_1}{\partial X_1}\right)_{X_1-d_1}\right]$$

$$\times\left[\left(\frac{\partial u_1}{\partial X_1}\right)_{X_1} - \left(\frac{\partial u_1}{\partial X_1}\right)_{X_1-d_1}\right] = 2\left(\frac{\partial u_1}{\partial X_1}\right)\left(\frac{\partial^2 u_1}{\partial X_1^2}\right) \tag{6.11}$$

We thus find from Equation 6.9 through Equation 6.11 that in the continuum limit Equation 6.8 yields Newton's law for a continuum and the nonlinear wave equation for pure longitudinal nonlinear wave propagation

$$\rho_1\frac{\partial^2 u_1}{\partial t^2} = \frac{\partial \sigma_{11}}{\partial X_1} = A_{11}\frac{\partial^2 u_1}{\partial X_1^2} + A_{111}\left(\frac{\partial u_1}{\partial X_1}\right)\frac{\partial^2 u_1}{\partial X_1^2} + \cdots \tag{6.12}$$

It is important to note that Equation 6.12 is the continuum analog of Equation 6.4 for the system of discrete lattice points.

6.1.3 Acoustic Nonlinearity Parameter for Lattice Motion

The nonlinear wave equation, Equation 6.12, may be rewritten in the form

$$\frac{\partial^2 u_1}{\partial t^2} = c_1^2\left[1-\beta_1\left(\frac{\partial u_1}{\partial X_1}\right)\right]\frac{\partial^2 u_1}{\partial X_1^2} \tag{6.13}$$

where c_1 is the infinitesimal amplitude longitudinal wave speed given by

$$c_1 = \left(\frac{A_{11}}{\rho_1}\right)^{\frac{1}{2}} \tag{6.14}$$

and β_1 is the longitudinal wave acoustic nonlinearity parameter of the solid defined by

$$\beta_1 = -\frac{A_{111}}{A_{11}} \tag{6.15}$$

The acoustic nonlinearity parameter is a dimensionless parameter that quantifies the nonlinearity of the finite amplitude acoustic wave. When $\beta_1 = 0$, the nonlinear wave equation, Equation 6.13, reduces to the linear (i.e., infinitesimal amplitude) wave equation.

It may be inferred from Equation 6.6 that the relationship between the stress σ_{11} and the displacement gradient $\partial u_1/\partial X_1$ is

$$\sigma_{11} = A_1 + A_{11}\left(\frac{\partial u_1}{\partial X_1}\right) + \frac{1}{2}A_{111}\left(\frac{\partial u_1}{\partial X_1}\right)^2 + \cdots = A_1 + A_{11}\left[\left(\frac{\partial u_1}{\partial X_1}\right) - \frac{1}{2}\beta\left(\frac{\partial u_1}{\partial X_1}\right)^2 + \cdots\right] \tag{6.16}$$

We infer from the considerations of Chapter 1 and Equation 6.16 that, in general, the relationship between any stress σ_{ij} and the set of displacement gradients $\partial u_i/\partial X_j = u_{ij}$ may be obtained as[1]

$$\sigma_{ij} = A_{ij} + A_{ijkl}u_{kl} + \frac{1}{2}A_{ijklmn}u_{kl}u_{mn} + \cdots \tag{6.17}$$

where the coefficients A_{ij}, A_{ijkl}, and A_{ijklmn}, are the first-, second-, and third-order Huang coefficients written in full subscripted notation. The Einstein convention (summation of repeated indices) is used in Equation 6.17 and in all following equations except where noted.

A comparison of Equation 6.16 and Equation 6.17 reveals that the Huang coefficients A_1, A_{11}, and A_{111} are written in an abbreviated subscripted notation. The abbreviated notation is called the matrix or the Voigt contracted notation whereby the full tensor notation $A_{ijkl\ldots}$ is replaced by the contracted notation $A_{\alpha\beta\ldots}$ according to the following prescription:

ij = 11	22	33	23,32	13,31	12,21
α = 1	2	3	4	5	6

We infer from the considerations of Chapter 1 and Equation 6.12 that the generalized Newton's Law, referred to the initial configuration, may be written as[2,3]

$$\rho_1 \frac{\partial^2 u_i}{\partial t^2} = \frac{\partial \sigma_{ij}}{\partial X_j} \tag{6.18}$$

Substituting Equation 6.17 into Equation 6.18 yields the nonlinear acoustic wave equation in Lagrangian (material) coordinates

$$\rho_1 \frac{\partial^2 u_i}{\partial t^2} = \left(A_{ijkl} + A_{ijklmn} \frac{\partial u_m}{\partial X_n} \right) \frac{\partial^2 u_k}{\partial X_j \partial X_l} \tag{6.19}$$

6.1.4 Nonlinearity Parameter for Arbitrary Crystal Structure

Equation 6.19 may be simplified by introducing an orthogonal transformation R defined by

$$a_i = R_{ij} X_j \tag{6.20}$$

that rotates the X_1-axis into the transformed axis direction a_1 (the direction chosen to be the wave propagation direction). The components of the column vector R_{1i} (i = 1, 2, 3) of the transformation matrix are the direction cosines of the direction a_1 with respect to the set of axes X_i (i = 1, 2, 3). Thus $R_{1i} = N_i$ where N_i are the Cartesian components with respect to the X_i axes of the unit vector N along a_1. Application of this transformation to Equation 6.19 yields[4,5]

$$\rho_1 \frac{\partial^2 u_{pN}}{\partial t^2} = B_{pq,N} \frac{\partial^2 u_{qN}}{\partial a_1^2} + B_{pqr,N} \left(\frac{\partial u_{rN}}{\partial a_1} \right) \frac{\partial^2 u_{qN}}{\partial a_1^2} \tag{6.21}$$

where

$$B_{pq,\mathbf{N}} = R_{1j}R_{1l}R_{pi}R_{qk}A_{ijkl} = N_jN_lR_{pi}R_{qk}A_{ijkl} \quad \textbf{(6.22)}$$

and

$$B_{pqr,\mathbf{N}} = R_{1j}R_{1l}R_{1n}R_{pi}R_{qk}R_{rm}A_{ijklmn} = N_jN_lN_nR_{pi}R_{qk}R_{rm}A_{ijklmn} \quad \textbf{(6.23)}$$

It is possible to simplify Equation 6.21 further by introducing a second orthogonal transformation S^T defined by

$$u_i = S^T_{ik}P_k \quad \textbf{(6.24)}$$

that diagonalizes $B_{pq,\mathbf{N}}$. The column vector $S^T_{p\alpha}$ (p = 1, 2, 3 for a given α) represents the direction of particle displacement with respect to the transformed reference frame (a_1, a_2, a_3). Since $(R^{-1})_{ip} = R_{pi}$, $R_{pi}S_{p\alpha} = U^\alpha_i$ are the Cartesian coordinates (direction cosines) of the unit particle displacement vector **U** with respect to the initial reference frame (X_1, X_2, X_3) for a given α. Application of the transformation S^T to Equation 6.21 yields (no sum on **N**, α, β, or γ)

$$\rho_1 \frac{\partial^2 P_{\alpha\mathbf{N}}}{\partial t^2} = \mu_{\alpha\alpha,\mathbf{N}} \frac{\partial^2 P_{\alpha\mathbf{N}}}{\partial a_1^2} + \nu_{\alpha\beta\gamma,\mathbf{N}} \left(\frac{\partial P_{\gamma\mathbf{N}}}{\partial a_1}\right) \frac{\partial^2 P_{\beta\mathbf{N}}}{\partial a_1^2} \quad \textbf{(6.25)}$$

where $P_{\alpha N}$ is the transformed displacement

$$\mu_{\alpha\alpha,\mathbf{N}} = ((S^T)^{-1})_{\alpha p} B_{pq} (S^T)_{q\alpha} = R_{1j}R_{1l}(R_{pi}S_{p\alpha})(R_{qk}S_{q\alpha})A_{ijkl}$$
$$= N_jN_lU_iU_kA_{ijkl} \quad \textbf{(6.26)}$$

and

$$\nu_{\alpha\beta\gamma,\mathbf{N}} = ((S^T)^{-1})_{\alpha p} B_{pqr} (S^T)_{q\beta} (S^T)_{r\gamma} = R_{1j}R_{1l}R_{1n}(R_{pi}S_{p\alpha})(R_{qk}S_{q\beta})(R_{rm}S_{r\gamma})A_{ijklmn}$$
$$= N_jN_lN_nU^\alpha_iU^\beta_kU^\gamma_mA_{ijklmn} \quad \textbf{(6.27)}$$

In Equation 6.25 through Equation 6.27 and in all following equations there is no sum over repeated N, α, β, or γ subscripts. The subscripted **N** denotes the wave propagation direction. The subscripted α, β, and γ indicate the wave polarization and take the value 1 for quasi-longitudinal waves and the value 2 or 3 for quasi-transverse waves. The case α = β = γ corresponds to the situation where all polarizations in the last term in Equation 6.25 are in resonance with the first and second terms in Equation 6.25. The resonance terms are orders of magnitude larger than the nonresonance terms. To an excellent approximation the nonresonance terms may be neglected and Equation 6.25 reduces to

$$\rho_1 \frac{\partial^2 P_\psi}{\partial t^2} = \mu_\psi \frac{\partial^2 P_\psi}{\partial a_1^2} + \nu_\psi \left(\frac{\partial P_\psi}{\partial a_1} \right) \frac{\partial^2 P_\psi}{\partial a_1^2} \tag{6.28}$$

where the subscripted symbol $\psi = (\alpha, N)$ is an abbreviated mode index notation denoting a wave of polarization $\alpha = 1, 2,$ or 3 and propagation direction N. Thus, the choice $\alpha = 1$ corresponds to a quasi-longitudinal wave and $\alpha = 2, 3$ correspond to each of two independent quasi-shear waves for a chosen direction N in a material.

Noting that the infinitesimal amplitude (linear) sound velocity $c_\psi = (\mu_\psi/\rho_1)^{1/2}$, we may rewrite Equation 6.28 in the form[5]

$$\frac{\partial^2 P_\psi}{\partial t^2} = c_\psi^2 \left[1 - \beta_\psi \left(\frac{\partial P_\psi}{\partial a_1} \right) \right] \frac{\partial^2 P_\psi}{\partial a_1^2} \tag{6.29}$$

where the material elastic nonlinearity parameter β_ψ^e for nonlinear wave propagation is defined by

$$\beta_\psi^e = -\frac{\nu_{\alpha\alpha\alpha,N}}{\mu_{\alpha\alpha,N}} = -\frac{A_{ijklmn} N_j N_l N_n U_i U_k U_m}{A_{ijkl} N_j N_l U_i U_k} \tag{6.30}$$

Note in Equation 6.30 that the superscripts for the polarization components have been dropped (i.e., $U_i^\alpha = U_i$).

6.1.5 Ultrasonic Harmonic Generation

It is instructive to solve Equation 6.29 subject to the boundary condition that a pure sinusoidal wave given by $P_\psi = P_{\psi 0}\cos(\omega t) = P_{\psi 0}\cos(-\omega t)$ is launched into the material at $a_1 = 0$. It is expedient to employ a perturbation expansion of the displacement in the form

$$P_\psi = P_\psi^{(1)} + P_\psi^{(2)} + \cdots \tag{6.31}$$

The contribution $P_\psi^{(1)}$ is the solution to the linear wave equation

$$\frac{\partial^2 P_\psi^{(1)}}{\partial t^2} = c_\psi^2 \frac{\partial^2 P_\psi^{(1)}}{\partial a_1^2} \tag{6.32}$$

The plane wave solution of Equation 6.32, subject to the above boundary condition at $a_1 = 0$, is

$$P_\psi^{(1)} = P_{\psi 1} \cos(k_\psi a_1 - \omega t) \tag{6.33}$$

where k_ψ is the mode wave number and ω is the angular frequency.

A first-order perturbation equation for the contribution $P_\psi^{(2)}$ in Equation 6.31 is obtained by substituting the solution $P_\psi^{(1)}$ given by Equation 6.33 into the nonlinear term of Equation 6.29. The resulting expression is

$$\frac{\partial^2 P_\psi^{(2)}}{\partial t^2} = c_\psi^2 \frac{\partial^2 P_\psi^{(2)}}{\partial a_1^2} - \frac{1}{2} c_\psi^2 \beta_\psi k_\psi^3 (P_{\psi 1})^2 \sin 2(k_\psi a_1 - \omega t) \tag{6.34}$$

It is noted that the nonlinear term in Equation 6.34 is a second harmonic sinusoid. A solution to Equation 6.34, subject to the above boundary condition, is obtained by assuming a general solution of the form

$$P_\psi^{(2)} = f(a_1) \sin 2(k_\psi a_1 - \omega t) + g(a_1) \cos 2(k_\psi a_1 - \omega t) \tag{6.35}$$

It is assumed that f and g are functions of a_1 and that both functions vanish at $a_1 = 0$, since the boundary condition dictates that the second harmonic vanishes at $a_1 = 0$. Substitution of Equation 6.35 into Equation 6.34 yields the expression

$$\left(4k_\psi \frac{df}{da_1} + \frac{d^2 g}{da_1^2}\right) \cos 2(k_\psi a_1 - \omega t) - \left(4k_\psi \frac{dg}{da_1} - \frac{d^2 f}{da_1^2}\right) \sin 2(k_\psi a_1 - \omega t)$$
$$= \frac{1}{2} \beta_\psi k_\psi^3 (P_{\psi 1})^2 \sin 2(k_\psi a_1 - \omega t) \tag{6.36}$$

It is seen by equating coefficients of the sinusoidal terms in Equation 6.36 that

$$4k_\psi \frac{df}{da_1} + \frac{d^2 g}{da_1^2} = 0 \tag{6.37}$$

and

$$4k_\psi \frac{dg}{da_1} - \frac{d^2 f}{da_1^2} = -\frac{1}{2} \beta_\psi k_\psi^3 (P_{\psi 1})^2 \tag{6.38}$$

A consistent solution to Equation 6.37 and Equation 6.38 is found by assuming from Equation 6.37 that (df/da_1) and $(d^2 g/da_1^2)$ are zero. This implies that $f = f_0$ = constant, $(d^2 f/da_1^2) = 0$, and that $(dg/da_1) = g_1$ = constant. Hence, Equation 6.38 yields $(dg/da_1) = g_1 = -(1/8)\beta_\psi k_\psi^2(P_{\psi 1})^2$ or $g = [g_0 - (1/8)\beta_\psi k_\psi^2(P_{\psi 1})^2 a_1]$ where g_0 is an integration constant. Since the second harmonic must vanish at $a_1 = 0$, both f_0 (hence, f) and g_0 must be zero. A solution to the nonlinear wave equation, Equation 6.29, is then found from Equation 6.31, Equation 6.33, and Equation 6.35 to be

$$P_\psi = P_{\psi 1}\cos(k_\psi a_1 - \omega t) - \frac{1}{8}\beta_\psi k_\psi^2 (P_{\psi 1})^2 a_1 \sin 2(k_\psi a_1 - \omega t) + \cdots \quad \textbf{(6.39)}$$

Equation 6.39 shows that, in addition to the fundamental wave of amplitude $P_{\psi 1}$ and angular frequency ω, a second harmonic signal is generated of amplitude $P_{\psi 2} = (1/8)\beta_\psi k_\psi^2(P_{\psi 1})^2 a_1$. The second harmonic signal depends on the value of the nonlinearity parameter β_ψ and grows linearly with propagation distance a_1. Equation 6.39 thus suggests that β_ψ may be obtained experimentally by measuring the absolute amplitudes of the fundamental and second harmonic signals as

$$\beta_\psi = 8\frac{P_{\psi 2}}{k_\psi^2 P_{\psi 1}^2 a_1} \quad \textbf{(6.40)}$$

It is noted that when $\beta_\psi = 0$, the nonlinear wave Equation 6.29 reduces to the linear wave equation and the solution, Equation 6.39, reduces to the linear wave solution.

Example Problem 1

Show from Equation 6.30 that the nonlinearity parameter for longitudinal wave propagation in isotropic materials $\beta_{1,N}$ is given by Equation 6.15.

SOLUTION

For longitudinal waves in isotropic materials the wave polarization is parallel to the wave propagation direction for arbitrary propagation direction. Choosing the propagation direction to be along the X_1-axis, we can write $N_q = U_q = \delta_{1q}$ where δ_{1q} is the Kronecker delta. Substituting these values for N_q and U_q into Equation 6.30 yields $\beta_{1,N} = -(A_{ijklmn}\delta_{1i}\delta_{1j}\delta_{1k}\delta_{11}\delta_{1m}\delta_{1n}/A_{ijkl}\delta_{1i}\delta_{1j}\delta_{1k}\delta_{1l}) = -A_{111111}/A_{1111}$. In Voigt notation we obtain $\beta_{1,N} = -A_{111}/A_{11}$, in agreement with Equation 6.15.

6.1.6 Discontinuity Distance

Equation 6.39 predicts that the second harmonic signal $P_{\psi 2}$ increases linearly with propagation distance a_1, while the amplitude $P_{\psi 1}$ of the fundamental wave remains constant. Strictly, the amplitude of the fundamental wave does not remain constant, since the energy that generates the harmonic wave must come from the fundamental signal. Thus, the harmonic signal cannot grow indefinitely with propagation distance. Although Equation 6.39 is quite accurate for propagation distances typically encountered, it is of interest to access the distance at which the harmonics cease to grow. This distance is called the discontinuity distance and corresponds to the distance at which the waveform turns into a shock wave.

To obtain the discontinuity distance we rewrite the nonlinear wave equation (Equation 6.29) in the operator form[6]

$$\frac{\partial^2 P_\psi}{\partial t^2} - W^2 \frac{\partial^2 P_\psi}{\partial a_1^2} = \left(\frac{\partial}{\partial t} - W\frac{\partial}{\partial a_1}\right)\left(\frac{\partial}{\partial t} + W\frac{\partial}{\partial a_1}\right)P_\psi = 0 \quad \textbf{(6.41)}$$

where

$$W^2 = c_\psi^2\left[1 - \beta_\psi\left(\frac{\partial P_\psi}{\partial a_1}\right)\right] = c_\psi^2\left[1 - \frac{\beta_\psi}{c_\psi}\left(\frac{\partial P_\psi}{\partial t}\right)\right] \quad \textbf{(6.42)}$$

The particle velocity solution to Equation 6.41 takes the general form

$$\frac{\partial P_\psi}{\partial t} = F\left[\omega\left(t \pm \frac{a_1}{W}\right)\right] \quad \textbf{(6.43)}$$

where $(\partial P_\psi/\partial t)$ is the particle velocity. According to Equation 6.43, a wave with the boundary condition

$$\frac{\partial P_\psi}{\partial t} = \left(\frac{\partial P_\psi}{\partial t}\right)_0 \sin\omega t \quad \textbf{(6.44)}$$

at $a_1 = 0$, where $(\partial P_\psi/\partial t)_0 = \omega(P_{\psi 1})_0$, will have the general solution

$$\frac{\partial P_\psi}{\partial t} = \left(\frac{\partial P_\psi}{\partial t}\right)_0 \sin\left[\omega t - \frac{\omega a_1}{c_\psi}\left(1 - \frac{\beta_\psi}{2c_\psi}\frac{\partial P_\psi}{\partial t}\right)^{-1}\right] \quad \textbf{(6.45)}$$

The slope of the waveform described by Equation 6.45, evaluated at $(\partial P_\psi/\partial t) = 0$, is

$$\left[\frac{\partial}{\partial a_1}\left(\frac{\partial P_\psi}{\partial t}\right)\right]_{(\partial P_\psi/\partial t)=0} = -\left(\frac{\omega}{c_\psi}\right)\left[\frac{1}{\left(\frac{\partial P_\psi}{\partial t}\right)_0} - \frac{\omega a_1 \beta_\psi}{2c_\psi^2}\right]^{-1} \quad \textbf{(6.46)}$$

Discontinuity occurs at the distance $(a_1)_{disc}$ for which the slope becomes infinitely large, meaning $(\partial/\partial a_1)(\partial P_\psi/\partial t) = -\infty$ at $a_1 = (a_1)_{disc}$. From Equation 6.46 the discontinuity distance is obtained as

$$(a_1)_{disc} = \frac{2c_\psi^2}{\omega\beta_\psi\left(\dfrac{\partial P_\psi}{\partial t}\right)_0} = \frac{2c_\psi^2}{\omega^2\beta_\psi(P_{\psi 1})_0} \tag{6.47}$$

Example Problem 2

What is the discontinuity distance in polycrystalline aluminum alloy 2024-T4 for a 10 MHz ultrasonic wave having a typical displacement amplitude of 1.0 nm?

SOLUTION

The longitudinal sound velocity c_ψ for AA2024-T4 is 6.35×10^3 m/s^{-1} and the nonlinearity parameter β_ψ is 4.7. For an ultrasonic wave with angular frequency $\omega = 2\pi f = 2\pi \times 10^7$ Hz and displacement amplitude $(P_{\psi 1})_0 = 10^{-9}$ m the continuity distance is obtained from Equation 6.47 to be roughly 4.3 m.

These results indicate that the discontinuity distance is much larger than the wave propagation path in materials typically measured. The approximate solution given by Equation 6.39 is generally adequate for most applications of nonlinear ultrasonics.

6.1.7 Attenuation of Finite Amplitude Waves

Attenuation refers to the total loss of amplitude (or energy) of a sound wave along its propagation path resulting from all mechanisms responsible for such losses, including but not limited to, absorption, scattering, and diffraction. Absorption refers to the loss of amplitude (or energy) of an acoustic wave that results in an increase in temperature (however slight) in the propagation medium and is often associated with relaxation phenomena. Scattering and diffraction result in a redirection of wave energy from the original propagation direction. Before considering the attenuation of harmonically generated nonlinear ultrasonic waves, it is instructive to consider first the attenuation of the purely fundamental waveform.

One approach is to add a dissipative term to the linear wave Equation 6.32 for the fundamental wave $P_\psi^{(1)}$ to obtain[7]

$$\rho_1 \frac{\partial^2 P_\psi^{(1)}}{\partial t^2} = c_\psi^2 \frac{\partial^2 P_\psi^{(1)}}{\partial a_1^2} + \lambda_{dis} \frac{\partial^3 P_\psi^{(1)}}{\partial t \partial a_1^2} \tag{6.48}$$

where λ_{dis} is a damping constant. Assume a trial solution of the form

$$P_{\psi}^{(1)} = (P_{\psi 1})_0 e^{i(ka_1 - \omega t)} \tag{6.49}$$

Substituting Equation 6.49 into Equation 6.48 yields a solution providing that the dispersion relation

$$k^2 = \left(\frac{\omega}{c_{\psi}}\right)^2 \left[1 - i\left(\frac{\omega\lambda_{dis}}{\rho_1 c_{\psi}^2}\right)\right]^{-1} \tag{6.50}$$

is satisfied. If $\omega\lambda_{dis} << \rho_1 c_{\psi}{}^2$, Equation 6.50 can be expanded in a power series to give

$$k \approx \left(\frac{\omega}{c_{\psi}}\right) + i\left(\frac{\omega^2\lambda_{dis}}{2\rho_1 c_{\psi}^3}\right) + \cdots \tag{6.51}$$

Substitution of Equation 6.51 into Equation 6.49 yields

$$P_{\psi}^{(1)} = P_{\psi 1} e^{i(k_1 a_1 - \omega t)} \tag{6.52}$$

where

$$P_{\psi 1} = (P_{\psi 1})_0 e^{-\alpha_1 a_1} \tag{6.53}$$

$$k_1 = \omega / c_{\psi}$$

and

$$\alpha_1 = \frac{\omega^2 \lambda_{dis}}{2\rho_1 c_{\psi}^3} \tag{6.54}$$

is the attenuation coefficient; $(P_{\psi 1})_0$ is the amplitude of the fundamental wave at $a_1 = 0$. It is noted in this approximation that, according to Equation 6.54, the attenuation coefficient is proportional to ω^2. More generally, Equation 6.53 is used as a phenomenological expression to describe an attenuated fundamental wave, even in those cases where Equation 6.54 does not hold. It is usually assumed that the contributions from all sources to the attenuation are additive such that $\alpha_1 = \alpha_{abs} + \alpha_{sc} + \alpha_{diff} + \cdots$ where the subscripts refer to the absorption, scattering, and diffraction contributions, respectively. We note from Equation 6.53 that

$$\frac{dP_{\psi 1}}{da_1} = -\alpha_1 P_{\psi 1} \tag{6.55}$$

We now consider the attenuation of the generated second harmonic signal[8]. It is assumed that the attenuation of the second harmonic signal with attenuation coefficient α_2 is independent of the attenuation of the fundamental wave with attenuation coefficient α_1. The second harmonic signal amplitude $P_{\psi 2}$ thus decreases as the result of attenuation and we write the following in analogy to Equation 6.55:

$$\left(\frac{dP_{\psi 2}}{da_1}\right)_{attn} = -\alpha_2 P_{\psi 2} \tag{6.56}$$

where the subscript *attn* denotes the results of attenuation. According to Equation 6.39 the amplitude $P_{\psi 2}$ of second harmonic signal also increases with the propagation distance a_1 as $P_{\psi 2} = (1/8)\beta_\psi k_\psi^2 (P_{\psi 1})^2 a_1$. Hence,

$$\left(\frac{dP_{\psi 2}}{da_1}\right)_{HG} = \frac{1}{8}\beta_\psi k_\psi^2 P_{\psi 1}^2 \tag{6.57}$$

where the subscript *HG* denotes the results of harmonic generation.

The net spatial rate of change in $P_{\psi 2}$ is given by the sum of the attenuation and harmonic generation contributions from Equation 6.56 and Equation 6.57 as

$$\frac{dP_{\psi 2}}{da_1} = \left(\frac{dP_{\psi 2}}{da_1}\right)_{HG} + \left(\frac{dP_{\psi 2}}{da_1}\right)_{attn} = \frac{1}{8}\beta_\psi k_\psi^2 P_{\psi 1}^2 - \alpha_2 P_{\psi 2}$$

$$= \frac{1}{8}\beta_\psi k_\psi^2 (P_{\psi 1})_0^2 e^{-2\alpha_1 a_1} - \alpha_2 P_{\psi 2} \tag{6.58}$$

where the last equality follows from Equation 6.53. Equation 6.58 is a first-order differential equation. The solution to Equation 6.58 subject to the boundary condition that $P_{\psi 2} = 0$ at $a_1 = 0$ is

$$P_{\psi 2} = \frac{1}{8}\beta_\psi k_\psi^2 (P_{\psi 1})_0^2 \left[\frac{\exp(-2\alpha_1 a_1) - \exp(-\alpha_2 a_1)}{\alpha_2 - 2\alpha_1}\right] \tag{6.59}$$

Equation 6.53 and Equation 6.59 may be used to determine the true nonlinearity parameters from the nonlinearity parameters measured experimentally. The measured nonlinearity parameter $(\beta_\psi)_{meas}$ is determined from Equation 6.40 as

$$(\beta_\psi)_{meas} = 8\frac{P_{\psi 2}}{k_\psi^2 P_{\psi 1}^2 a_1} \tag{6.60}$$

where $P_{\psi 1}$ and $P_{\psi 2}$ are measured at a_1, the wave propagation distance. The true nonlinearity parameter β_ψ is determined by substituting Equation 6.53 and Equation 6.59 into Equation 6.60 and solving the resulting expression for β_ψ. The result is

$$\beta_\psi = (\beta_\psi)_{meas} \frac{a_1(\alpha_2 - 2\alpha_1)}{\{1 - \exp[-(\alpha_2 - 2\alpha_1)a_1]\}} \qquad \textbf{(6.61)}$$

For the case where $(\alpha_2 - 2\alpha_1)a_1 \ll 1$, Equation 6.61 reduces to $\beta_\psi = (\beta_\psi)_{meas}$.

6.1.8 Higher-Order Elastic Constants

Let us look more closely at the Huang coefficients A_1, A_{11}, and A_{111} (Voigt notation) that define the acoustic nonlinearity parameter for solids. In the continuum limit Equation 6.1 may be written in the form

$$\underset{d_1 \to 0}{Lim} V_{PE} = \int_{Vol} \left[\Phi_0 + A_1 \left(\frac{\partial u_1}{\partial X_1} \right) + \frac{1}{2} A_{11} \left(\frac{\partial u_1}{\partial X_1} \right)^2 + \frac{1}{3!} A_{111} \left(\frac{\partial u_1}{\partial X_1} \right)^3 + \cdots \right] dV \qquad \textbf{(6.62)}$$

where Φ_0 is a constant. A_1, A_{11}, and A_{111} are given by Equation 6.7 and the element of volume $dV = S_1 dX_1$, where S_1 is a unit of area normal to the X_1. The integrand of Equation 6.62 is the elastic potential energy (strain energy) per unit volume $\Phi(X_1, \partial u_1/\partial X_1)$ given by

$$\Phi\left(X_1, \frac{\partial u_1}{\partial X_1} \right) = \Phi_0 + A_1 \left(\frac{\partial u_1}{\partial X_1} \right) + \frac{1}{2} A_{11} \left(\frac{\partial u_1}{\partial X_1} \right)^2 + \frac{1}{3!} A_{111} \left(\frac{\partial u_1}{\partial X_1} \right)^3 + \cdots \qquad \textbf{(6.63)}$$

NOTE: We depart here from the notation for the elastic potential energy (strain energy) per unit volume used in other chapters of this book. In keeping with the notations often used in nonlinear thermoelasticity, the strain energy per unit volume is denoted by Φ and the internal energy per unit mass is denoted by U. We denote the internal energy per unit volume by U_V (see Section 6.1.10).

We see from Equation 6.63 that the order of the Huang coefficients A_1, A_{11}, and A_{111} are designated as first-, second-, and third-order according to the order of the displacement gradient $\partial u_1/\partial X_1$ of which it is a coefficient in the power series expansion of Equation 6.63. The displacement gradient is clearly used in Equation 6.63 as a measure of the strain.

Equation 6.62 and Equation 6.63 imply that the stress component σ_{11} is obtained as

$$\sigma_{11} = \frac{\partial \Phi}{\partial \left(\frac{\partial u_1}{\partial X_1} \right)}. \qquad \textbf{(6.64)}$$

Substituting Equation 6.63 into Equation 6.64 yields

$$\sigma_{11} = A_1 + A_{11}\left(\frac{\partial u_1}{\partial X_1}\right) + \frac{1}{2}A_{111}\left(\frac{\partial u_1}{\partial X_1}\right)^2 + \cdots \quad \textbf{(6.65)}$$

It is clear from Equation 6.65 that $A_1 = \sigma(X_1)$ is the static (initial) stress in the solid.

In general, the strain energy $\Phi(X, u_{ij})$ where $u_{ij} = \partial u_i/\partial X_j$ may be written (full notation)

$$\Phi(\boldsymbol{X}, u_{ij}) = \Phi_0 + A_{ij}u_{ij} + \frac{1}{2}A_{ijkl}u_{ij}u_{kl} + \frac{1}{3!}A_{ijklmn}u_{ij}u_{kl}u_{mn} + \cdots \quad \textbf{(6.66)}$$

The stress σ_{ij} is obtained as

$$\sigma_{ij} = \frac{\partial \Phi}{\partial u_{ij}} = A_{ij} + A_{ijkl}u_{kl} + \frac{1}{2}A_{ijklmn}u_{kl}u_{mn} + \cdots \quad \textbf{(6.67)}$$

in agreement with Equation 6.17.

It is important to recognize that the displacement gradients $\partial u_i/\partial X_j$ are in general not symmetric, (i.e., $u_{ij} \neq u_{ji}$). When dealing with finite deformations it is often convenient to use a strain measure that is not only symmetric but is also nonlinear. A commonly used strain measure for finite deformations is the Lagrangian strain obtained as follows:[9] A point in the initial configuration is represented by the vector $\boldsymbol{X}$. When the material is deformed the point moves to the present position x such that the point undergoes a displacement $\boldsymbol{u} = \boldsymbol{x} - \boldsymbol{X}$. Now consider two points in the initial configuration separated by the distance dl such that

$$dl^2 = |d\boldsymbol{X}|^2 = dX_i^2 \quad \textbf{(6.68)}$$

The distance between the same two points in the deformed configuration is separated by the distance dl' such that

$$dl'^2 = |d\boldsymbol{x}|^2 = dx_i^2 \quad \textbf{(6.69)}$$

From $\boldsymbol{u} = \boldsymbol{x} - \boldsymbol{X}$ we write

$$dl'^2 = (dX_i + du_i)^2 = (dX_i + u_{ij}dX_j)^2 \quad \textbf{(6.70)}$$

From Equation 6.68 and Equation 6.69 we obtain that the change in distance between the two particles resulting from the deformation is

$$dl'^2 - dl^2 = 2\eta_{ij}dX_idX_j \quad \textbf{(6.71)}$$

where the Lagrangian strains η_{ij} are defined by

$$\eta_{ij} = \frac{1}{2}(u_{ij} + u_{ji} + u_{ki}u_{kj}) \quad \textbf{(6.72)}$$

From Equation 6.72 it is seen that if we confine all displacements to that along a single direction X_1 (as would occur, for example, for longitudinal wave propagation in an isotropic material) the Lagrangian strain η_{11} is related to the displacement gradient $u_{11} = \partial u_1/\partial X_1$ as

$$\eta_{11} = u_{11} + \frac{1}{2}u_{11}^2 \quad \textbf{(6.73)}$$

The elastic potential energy per unit volume can also be expanded in a power series with respect to the Lagrangian strains as

$$\Phi(X_1, \eta_{11}) = \Phi_0 + C_1\eta_{11} + \frac{1}{2}C_{11}\eta_1^2 + \frac{1}{3!}C_{111}\eta_1^3 + \cdots \quad \textbf{(6.74)}$$

The coefficients C_1, C_{11}, and C_{111} (Voigt notation) are called the first-, second-, and third-order Brugger elastic constants, respectively.[10] Substituting Equation 6.73 into Equation 6.74 and equating coefficients of equivalent powers of the strain measure in the resulting equation to that of Equation 6.17, we obtain the relationship between the Huang coefficients and the Brugger elastic constants for longitudinal wave propagation in isotropic solids

$$A_1 = C_1 = \sigma_1(X_1) \quad \textbf{(6.75)}$$

$$A_{11} = \sigma_1(X_1) + C_{11} \quad \textbf{(6.76)}$$

and

$$A_{111} = 3C_{11} + C_{111} \quad \textbf{(6.77)}$$

Hence, the nonlinearity parameter may be written in terms of Brugger elastic constants as

$$\beta = -\frac{A_{111}}{A_{11}} = -\left(\frac{3C_{11} + C_{111}}{\sigma_1 + C_{11}}\right) \quad \textbf{(6.78)}$$

It is important to note from Equation 6.78 that the nonlinearity parameter is dependent on the initial stress in the solid σ_1 when the Brugger elastic constants are used.

In general, the elastic potential energy per unit volume $\mathbf{\Phi}(X, \boldsymbol{\eta}_{ij})$ may be written (full notation) as

$$\Phi(\boldsymbol{X}, \eta_{ij}) = \Phi_0 + C_{ij}\eta_{ij} + \frac{1}{2}C_{ijkl}\eta_{ij}\eta_{kl} + \frac{1}{3!}C_{ijklmn}\eta_{ij}\eta_{kl}\eta_{mn} + \cdots \quad \textbf{(6.79)}$$

where the Brugger elastic constants of order n are defined by[10]

$$C_{ijkl}\cdots = \left(\frac{\partial\Phi}{\partial\eta_{ij}\partial\eta_{kl}\cdots}\right)_{\mathbf{X}} \quad \textbf{(6.80)}$$

Substituting Equation 6.72 into Equation 6.79 and comparing the resulting expression term by term to Equation 6.66, we obtain the general relations

$$A_{ij} = C_{ij} = \sigma_{ij}(\boldsymbol{X}) \quad \textbf{(6.81)}$$

for the first-order Huang coefficients,

$$A_{ijkl} = \sigma_{jl}(\boldsymbol{X})\delta_{ik} + C_{ijkl} \quad \textbf{(6.82)}$$

for the second-order Huang coefficients, and

$$A_{ijklmn} = C_{jlmn}\delta_{ik} + C_{ijnl}\delta_{km} + C_{jnkl}\delta_{im} + C_{ijklmn} \quad \textbf{(6.83)}$$

for the third-order Huang coefficients.

It is important to recognize that the relationships given by Equation 6.81 to Equation 6.83 are referred to the initial state $\boldsymbol{X}$. In general, the initial state is assumed to have an initial stress $A_{ij} = C_{ij} = \sigma_{ij}(X)$. If the initial stress is zero, the particle configuration is defined by the set of position vectors $\{\overline{\mathbf{X}}\}$. The relationships given by Equation 6.81 to Equation 6.83 are then rewritten as

$$\overline{A}_{ij} = \overline{C}_{ij} = \sigma_{ij}(\overline{\boldsymbol{X}}) = 0 \quad \textbf{(6.84)}$$

for the first-order Huang coefficients,

$$\overline{A}_{ijkl} = \sigma_{jl}(\overline{\boldsymbol{X}})\delta_{ik} + \overline{C}_{ijkl} \quad \textbf{(6.85)}$$

for the second-order Huang coefficients, and

$$\overline{A}_{ijklmn} = \overline{C}_{jlmn}\delta_{ik} + \overline{C}_{ijnl}\delta_{km} + \overline{C}_{jnkl}\delta_{im} + \overline{C}_{ijklmn} \quad \textbf{(6.86)}$$

for the third-order Huang coefficients. The overbar above the quantities in Equation 6.84 Equation 6.86 and in all following quantities denote that the quantity is referred to the unstressed configuration. Hence, Equation 6.80, when referred to the unstressed configuration, becomes

$$\bar{C}_{ijkl}\cdots = \left(\frac{\partial \Phi}{\partial \bar{\eta}_{ij} \partial \bar{\eta}_{kl} \cdots} \right)_{\bar{X}} \quad \textbf{(6.87)}$$

and the modal nonlinearity parameter $\bar{\beta}^{e}_{\psi}$, referred to the zero stress state, is defined by

$$\bar{\beta}^{e}_{\psi} = -\frac{\bar{\nu}_{\alpha\alpha\alpha,N}}{\bar{\mu}_{\alpha\alpha,N}} = -\frac{\bar{A}_{ijklmn}\bar{N}_j\bar{N}_l\bar{N}_n\bar{U}_i\bar{U}_k\bar{U}_m}{\bar{A}_{ijkl}\bar{N}_j\bar{N}_l\bar{U}_i\bar{U}_k}. \quad \textbf{(6.88)}$$

The number of independent elastic constants depends on the symmetry of the material. Initial stresses can cause alterations in the material symmetry and so the number of independent elastic constants in initially stressed material may be different from the same materials with zero initial stress. There are in general $3^4 = 81$ second-order Brugger elastic constants and $3^6 = 729$ third-order Brugger elastic constants. However, the symmetries of the Lagrangian strains ($\eta_{ij} = \eta_{ji}$) and the invariance of the internal energy per unit volume with respect to an interchange of subscripted index pairs, reduce the number of independent elastic constants. These properties reduce the numbers of independent second-order and third-order constants to 21 and 56, respectively, corresponding to those of the triclinic crystal system. The crystal symmetry of the material may also reduce the number of independent constants, since the Brugger elastic constants are defined according to Equation 6.80 in terms of derivatives with respect to crystallographically equivalent strains η_{ij}.

The independent second-order constants are tabulated in Chapter 1. The independent third-order elastic constants for a given crystal symmetry are shown in Table 6.1. For cubic crystals of highest symmetry the independent third-order elastic constants reduce to three second-order and six third-order constants. For isotropic solids the numbers of independent Brugger elastic constants reduce to two second-order constants (C_{11} and C_{12} in Voigt notation) and three third-order constants (C_{111}, C_{112}, and C_{123} in Voigt notation).

For isotropic solids the second-order constants often used in the literature are the Lame′ constants λ and μ; and the third-order constants often used are the Murnaghan constants l, m, and n. The Lame′ constants are related to the second-order Brugger elastic constants as

$$\begin{aligned} \lambda + 2\mu &= C_{11} = C_{22} = C_{33} \\ \lambda &= C_{12} = C_{13} = C_{23} = C_{21} = C_{31} = C_{32} \\ \mu &= C_{44} = C_{55} = C_{66} \end{aligned} \quad \textbf{(6.89)}$$

TABLE 6.1

Indices of Independent Third-Order Brugger Elastic Constants (Voigt Notation) for a Given Crystal Symmetry

1 $\bar{1}$	2 2/*m* *m*	222 *mm*2 *mmm*	3 $\bar{3}$	3*m* $\bar{3}m$ 32	4 4/*m* $\bar{4}$	4*mm* $\bar{4}2m$ 422 4/*mmm*	23 *m*3	$\bar{4}3m$ 432 *m*3*m*	6 $\bar{6}$ 6/m	622 6/*mmm* $\bar{6}m2$ 6*mm*
111	111	111	111	111	111	111	111	111	111	111
112	112	112	112	112	112	112	112	112	112	112
113	113	123	113	112	113	113	113	112	113	113
114	0	0	114	114	0	0	0	0	0	0
115	115	0	115	115	0	0	0	0	0	0
116	0	0	116	115	116	0	0	0	116	0
122	122	122	113	112	112	112	113	112	a	a
123	123	123	123	123	123	123	123	123	123	123
124	0	0	124	124	0	0	0	0	0	0
125	125	0	125	124	0	0	0	0	0	0
126	0	0	126	126	0	0	0	0	–116	0
133	133	133	112	112	133	133	112	112	133	133
134	0	0	125	124	0	0	0	0	0	0
135	135	0	126	126	0	0	0	0	0	0
136	0	0	124	124	136	0	0	0	0	0
144	144	144	144	144	144	144	144	144	144	144
145	0	0	145	145	145	0	0	0	145	0
146	146	0	146	145	0	0	0	0	0	0
155	155	155	155	155	155	155	155	155	155	155
156	0	0	156	156	0	0	0	0	0	0
166	166	166	166	155	166	166	166	155	b	b
222	222	222	111	111	111	111	111	111	222	222
223	223	223	112	112	113	113	112	112	113	113
224	0	0	116	115	0	0	0	0	0	0
225	225	0	114	114	0	0	0	0	0	0
226	0	0	115	115	–116	0	0	0	116	0
233	233	233	113	112	133	133	113	112	133	133
234	0	0	126	126	0	0	0	0	0	0
235	235	0	124	124	0	0	0	0	0	0
236	0	0	125	124	–136	0	0	0	0	0
244	244	244	166	155	155	155	166	155	155	155
245	0	0	146	145	–145	0	0	0	–145	0
246	246	0	156	156	0	0	0	0	0	0
255	255	255	144	144	144	144	144	144	144	144
256	0	0	145	145	0	0	0	0	0	0
266	266	266	155	155	166	166	155	155	c	c
333	333	333	111	111	333	333	111	111	333	333
334	0	0	115	115	0	0	0	0	0	0
335	335	0	116	115	0	0	0	0	0	0
336	0	0	114	114	0	0	0	0	0	0
344	344	344	155	155	344	344	155	155	344	344
345	0	0	156	156	0	0	0	0	0	0
346	346	0	145	145	0	0	0	0	0	0
355	355	355	166	155	344	344	166	155	344	344

Continued

TABLE 6.1 CONTINUED

Indices of Independent Third-Order Brugger Elastic Constants (Voigt Notation) for a Given Crystal Symmetry

1 $\bar{1}$	2 2/*m* *m*	222 *mm*2 *mmm*	3 $\bar{3}$	3*m* $\bar{3}m$ 32	4 4/*m* $\bar{4}$	4*mm* $\bar{4}2m$ 422 4/*mmm*	23 *m*3	$\bar{4}3m$ 432 *m*3*m*	6 $\bar{6}$ 6/m	622 6/*mmm* $\bar{6}m2$ 6*mm*
356	0	0	146	145	0	0	0	0	0	0
366	366	366	144	144	366	366	144	144	d	d
444	0	0	444	444	0	0	0	0	0	0
445	445	0	445	445	0	0	0	0	0	0
446	0	0	446	445	446	0	0	0	145	0
455	0	0	446	445	0	0	0	0	0	0
456	456	456	456	456	456	456	456	456	e	e
466	0	0	445	445	0	0	0	0	0	0
555	555	0	444	444	0	0	0	0	0	0
556	0	0	445	445	–446	0	0	0	–145	0
566	566	0	446	445	0	0	0	0	0	0
666	0	0	444	444	0	0	0	0	–116	0

a = 111 − 222 + 112
b = (3/4) × 222 − (1/4) × 111 − (1/4) × 112
c = (1/2) × 111 − (1/4) × 222 − (1/4) × 112
d = (1/2) × (113 − 123)
e = (1/2) × (155 − 144)

Source: Reprinted from Huntington, H.B., The elastic constants of solids, in *Solid State Physics*, Vol. 7, 1958, pp. 38–39. With permission from Elsevier Science.

where all other second-order Brugger elastic constants are zero. Voigt notation is used in the above equations for the Brugger elastic constants. The relationships among the Murnaghan constants and the non-zero third-order Brugger elastic constants for isotropic solids are shown in Table 6.2 along with the relationships among various other isotropic third-order elastic constants that have been used in the literature.

Example Problem 3

Show from Equation 6.85, Equation 6.86, Equation 6.88, and Table 6.2 that the nonlinearity parameter for shear wave propagation in isotropic materials $\bar{\beta}_{2,N} = \bar{\beta}_{3,N} = 0$.

SOLUTION

For isotropic materials the results do not depend on the direction of propagation. Thus, it is convenient to align the Cartesian reference frame so that the wave propagation direction is along the [100] or $\bar{\mathbf{X}}_1$-axis such that $\bar{N}_q = \delta_{q1}$ and the wave polarization is along the [010] or $\bar{\mathbf{X}}_2$-axis such that $\bar{U}_q = \delta_{q2}$. From Equation 6.88 we write $\bar{\beta}_{2,N} = -\bar{A}_{212121}/\bar{A}_{2121}$ in full notation. From Equation 6.85 $\bar{A}_{212121} = 3\bar{C}_{1112} + \bar{C}_{212121}$ in full notation

TABLE 6.2

Relationships among Commonly Used Third-Order Elastic Constants for Isotropic Solids

Brugger	Truesdale Hyperelastic	Toupin and Bernstein	Landau and Lifshitz; Goldberg, Jones, and Kobett	Murnaghan; Hughes and Kelly
C_{111}	$2\lambda - 8\mu + 2\mu(\alpha_3 - \alpha_4 + \alpha_6)$	$\nu_1 + 6\nu_2 + 8\nu_3$	$2A + 6B + 2C$	$2l + 4m$
C_{112}	$2\lambda + 2\mu\alpha_3$	$\nu_1 + 2\nu_2$	$2B + 2C$	$2l$
C_{123}	$2\lambda + 2\mu\alpha_3 + \mu\alpha_4$	ν_1	$2C$	$2l - 2m + n$
C_{144}	$-\mu\alpha_4/2$	ν_2	B	$m - (n/2)$
C_{155}	$-2\mu - [\mu(\alpha_4 - \alpha_6)/2]$	$\nu_2 + 2\nu_3$	$B + (A/2)$	m
C_{456}	$-\mu + (\mu\alpha_6/3)$	ν_3	$A/4$	$n/4$
$[-\lambda + C_{144} + (1/2) C_{123}]/\mu$	α_3	$[-\lambda+\nu_2+(\nu_1/2)]/\mu$	$(-\lambda + B + C)/\mu$	$(-\lambda + l)/\mu$
$-2C_{144}/\mu$	α_4	$-2\nu_2/\mu$	$-2B/\mu$	$-[m - (n/2)]/\mu$
$2[\lambda - \mu + C_{144}]/\mu$	α_5	$2(\lambda - \mu + \nu_2)/\mu$	$(\lambda - \mu + B)/\mu$	$2[\lambda - \mu + m - (n/2)]/\mu$
$4[\mu + C_{456}]/\mu$	α_6	$4(\mu + \nu_3)/\mu$	$4\,[\mu + (A/4)]/\mu$	$4[\mu + (n/4)]/\mu$
C_{123}	$2\lambda + 2\mu\alpha_3 + \mu\alpha_4$	ν_1	$2C$	$2l - 2m + n$
C_{144}	$-\mu\alpha_4/2$	ν_2	B	$m - (n/2)$
C_{456}	$-\mu + (\mu\alpha_6/4)$	ν_3	$A/4$	$n/4$
$4C_{456}$	$-4\mu + \mu\alpha_6$	$4\nu_3$	A	n
C_{144}	$-\mu\alpha_4/2$	ν_2	B	$m - (n/2)$
$C_{123}/2$	$\lambda + \mu\alpha_3 + (\mu\alpha_4/2)$	$\nu_1/2$	C	$l - m + (n/2)$
$C_{112}/2$	$\lambda + \mu\alpha_3$	$(\nu_1/2) + \nu_2$	$B + C$	l
C_{155}	$-2\mu - [\mu(\alpha_4 - \alpha_6)/2]$	$\nu_2 + 2\nu_3$	$(A/2) + B$	m
$4C_{456}$	$-4\mu + \mu\alpha_6$	$4\nu_3$	A	n

Source: Reprinted from Green, R.E., Jr., Treatise on Materials Science and Technology, Vol. 3, Ultrasonic Investigation of Mechanical Properties, 1958, p.77. With permission from Elsevier Science.

or $\bar{A}_{666} = 3\bar{C}_{16} + \bar{C}_{666}$ in Voigt notation. In Voigt notation we find from Chapter 1 that the second-order constant $\bar{A}_{66} = \bar{C}_{66} = \bar{C}_{44}$ is not zero. From Table 6.1 we find $\bar{C}_{666} = 0$ (and only non-zero Brugger constants are listed in Table 6.2) and from Chapter 1 that the second-order constant $\bar{C}_{16} = 0$. Hence, $\bar{\beta}_{2,N} = 0$. A similar argument shows that $\bar{\beta}_{3,N} = 0$, since in this case $\bar{U}_q = \delta_{q3}$.

6.1.9 Structure and Symmetry Dependence of Nonlinearity Parameters

The acoustic nonlinearity parameters for harmonic generation have been determined[5] from literature values of the second- and third-order Brugger

TABLE 6.3

Comparison of Crystal Structure (Space Group), Bonding, and Range of Values of Longitudinal Mode Acoustic Nonlinearity Parameters along [100], [110], and [111] Directions of Cubic Crystals

Structure (Space Group)	Bonding	β[100] Range	β[110] Range	β[111] Range
NaCl (*Fm3m*)	Ionic	14.0–15.4	6.3–8.9	1.0–6.0
Perovskite (*Pm3m*)	Ionic	9.3–12.7	5.9–6.6	13.7–14.3
bcc (*Im3m*)	Metallic	7.4–8.8	6.2–6.3	8.1–11.4
fcc (*Fm3m*)	Metallic/ molecular	4.0–7.0	9.5–13.5	7.7–8.6
Fluorite (*Fm3m*)	Ionic	3.4–4.6	3.2–6.0	5.3–7.2
Zinc blende ($F\bar{4}3m$)/ diamond (*Fd3m*)	Covalent	1.8–3.0	4.3–6.0	2.7–5.4

Source: From Cantrell, J.H., *J. Appl. Phys.*, 76, 3372, 1994. With permission.

elastic constants for 29 initially stress-free crystals of cubic symmetry with point groups $m3m$ and $\bar{4}3m$. The nonlinearity parameters along the propagation directions [100], [110], and [111] are calculated from Equation 6.85, Equation 6.86, and Equation 6.88 and are shown in Table 6.3. We list in the table the structure of the cubic crystal, the type of interatomic bonding, and the range of values of the acoustic nonlinearity parameters for each of the propagation directions. It is seen that the nonlinearity parameters are strongly ordered for a given propagation direction according to the type of crystal structure. The relative lack of dependence on bonding compared to crystal structure is apparent upon surveying Table 6.3. For example, the magnitudes of the nonlinearity parameters along [100] and [110] of fluorite structured compounds with ionic tetrahedral linking of divalent and monovalent atoms are much closer to those of the zinc blende compounds with covalent tetrahedral linking of atoms than to the strongly ionic alkali halides with the NaCl structure.

The dependence of the acoustic nonlinearity parameters on the crystalline structure suggests that the geometry of the local atomic arrangement and shape, rather than the strength, of the interatomic potential are dominant factors in determining the magnitude of β. Some insight into the nature of the structure dependence can be gained by consideration of solids for which the elastic constants are dominated by a simple, short-range, two-body, central-force, repulsive contribution to the interatomic potential represented by the Born-Mayer potential.

We begin by reformulating Equation 6.1 in a three-dimensional form and restricting consideration only to nearest neighbor interactions of all atoms in a unit cell of the lattice. A unit cell is a volume containing the atoms that comprise the basis structure of the crystal. The entire crystal is generated by contiguous translations of the unit cell. The potential energy for all nearest neighbor (*nn*) particle pair interactions within the unit cell is

$$(V_{PE})_{cell} = \sum_{nn} V_{nn}^{PE}(\mathbf{u}_p - \mathbf{u}_q) \tag{6.90}$$

where

$$V_{nn}^{PE}(\mathbf{u}_p - \mathbf{u}_q) = \left(V_0^{PE}\right)_{nn} + [\mathbf{k}_1 \cdot (\mathbf{u}_p - \mathbf{u}_q)] + \frac{1}{2}[\mathbf{k}_2 \cdot (\mathbf{u}_p - \mathbf{u}_q)]^2 + \cdots \tag{6.91}$$

is the potential energy corresponding to a given nearest neighbor pair (p, q). The sum in Equation 6.90 is taken over all appropriate nn atomic pairs in the unit cell. For expediency we assume that the $V_{nn}{}^{PE}$ are central force potentials such that $(u_p - u_q) = (r - r_0)_{pq}e_{pq}$ where $(r - r_0)$ is the displacement along the direction given by the unit vector e_{pq} between the particle pair and r_0 is the equilibrium distance between the particle pair. Writing $V_{nn}^{PE}(u_p - u_q) = \phi_{nn}(r)$ and denoting the volume of the unit cell by V_{unit}, we define the elastic potential energy per unit volume $\Phi(r)$ by

$$\Phi(r) = \frac{1}{V_{unit}} \sum_{nn} \phi_{nn}(r) \tag{6.92}$$

The elastic potential energy per unit volume defined by Equation 6.92 is equivalent to that defined in the continuum approximation by Equation 6.66.

The relationship between the Lagrangian strain and the atomic pair separation is obtained directly from Equation 6.71. Writing $dl = r$, $dl_0 = r_0$, $dX_i = \xi_i$ where ξ_i is the difference in Cartesian coordinates of the two atoms in the initial state, we obtain from Equation 6.71

$$r^2 - r_0^2 = 2\xi_i \xi_j \eta_{ij} \tag{6.93}$$

From Equation 6.93 we may write

$$\frac{\partial}{\partial \eta_{ij}} = \xi_i \xi_j D \tag{6.94}$$

where

$$D = \frac{1}{r}\frac{d}{dr} \tag{6.95}$$

is a differential operator. We now assume that the initial stresses are zero. From Equation 6.87, Equation 6.92, Equation 6.94, and Equation 6.95, all referred to the unstressed configuration $\overline{\mathbf{X}}$, we get[11]

$$\bar{C}_{ijkl} = \frac{1}{2V_{unit}} \sum_{nn} \xi_i \xi_j \xi_k \xi_l [D^2 \phi(r)]_{r=r_0} \tag{6.96}$$

and

$$\bar{C}_{ijklmn} = \frac{1}{2V_{unit}} \sum_{nn} \xi_i \xi_j \xi_k \xi_l \xi_m \xi_n [D^3 \phi(r)]_{r=r_0} \tag{6.97}$$

where we have summed only over atomic nearest neighbors (nn) having the equilibrium distance $r = r_0$ in the unstressed configuration.

For definiteness, we consider acoustic waves propagating along the [100] direction in cubic crystals of all point groups. We find from Equation 6.85, Equation 6.86, Equation 6.88, Equation 6.96, and Equation 6.97 that the longitudinal acoustic nonlinearity parameter $\bar{\beta}[100]$ for harmonic generation, referred to the unstressed configuration, is given by

$$\bar{\beta}[100] = -\left\{ 3 + \frac{\sum_{nn} \xi_1^6 [D^3 \phi_{nn}(r)]_{r=r_0}}{\sum_{nn} \xi_1^4 [D^2 \phi_{nn}(r)]_{r=r_0}} \right\} \tag{6.98}$$

Equation 6.98 shows that the crystalline structure dependence of $\bar{\beta}[100]$ enters through ξ_1 and the geometry associated with the summation.

We now introduce the Born-Mayer potential energy in the form

$$\phi(r) = A \exp\left[-B\left(\frac{r}{r_0} - 1 \right) \right] \tag{6.99}$$

where B is the hardness parameter and A is the preexponential factor. The factor A contributes to the strength of the interatomic potential energy, while B and the equilibrium atomic pair separation r_0 govern the shape or curvature of the potential energy. From Equation 6.98 and Equation 6.99 and knowledge of the crystal structure we find for solids having the face-centered cubic (*fcc*) structure

$$\bar{\beta}[100]_{fcc} = \frac{B^2 - 3B - 3}{2(B+1)} \tag{6.100}$$

It is apparent from Equation 6.100 that the acoustic nonlinearity parameter in this model depends only on the Born-Mayer parameter B. The factor A does not enter the equation. This suggests that the shape more than the strength of the interatomic potential governs the magnitude of the nonlinearity parameter. We conjecture that the shape of the interatomic potential is roughly the same for all solids possessing a given crystal structure. This is consistent with the findings of Table 6.3 where similar values of the nonlinearity parameter were found for *fcc* crystals having bonds of greatly different strengths (metallic and molecular bonds).

A comparison of the experimentally determined nonlinearity parameters along [100] for the noble metal (*fcc*) crystals and the nonlinearity parameters calculated from Equation 6.100 may be obtained using independent, non-ultrasonic measurements of the Born-Mayer B parameter. For copper, silver, and gold, respectively, B is determined to be 13.0, 12.8, and 14.4, respectively. These values of B yield the calculated $\bar{\beta}[100]$ values 4.9, 4.8, and 5.6, respectively, for copper, silver, and gold. The calculated $\bar{\beta}[100]$ values are in very good agreement with the range of experimental values shown in Table 6.3 for *fcc* metals.

6.1.10 Connection with Thermodynamics

The analysis of acoustic nonlinearity so far has been based on the existence of an elastic potential energy function giving rise to stresses σ_{ij}. From the classical mechanics point of view the elastic potential energy is assumed to be that arising from the interaction of a collection of lattice particles initially at rest in some static lattice configuration. Although this is a good assumption for solids at low temperatures, it is less valid at higher temperatures and becomes even less valid at temperatures sufficiently high to produce a solid-liquid or a liquid-gas phase transformation. Indeed, for ideal gases the elastic potential energy is effectively zero. Yet, even an ideal gas gives rise to stresses (more appropriately pressures), and it is certainly true that gases can support the propagation of acoustic waves. So, how is this possible if the elastic potential energy is effectively zero? The answer lies in thermodynamics.

With increasing temperature the lattice particles acquire an increasing energy of vibration. This means that in addition to an elastic potential energy per unit volume Φ a collective kinetic energy per unit volume K is acquired from the kinetic energies of the individual lattice particles. The total energy per unit volume of the solid U_V is then

$$U_V = \mathbf{\Phi} + K \quad \textbf{(6.101)}$$

At temperatures corresponding to that of the solid-liquid phase transformation, the particle bonds of the solid begin break and reform in a random way, creating an ephemeral bonding of particle clusters that lead to the physical characteristics of the liquid state. In the liquid state the internal energy per unit volume can be dominated by the kinetic energy contribution. At higher temperatures corresponding to that of the liquid-gas phase transformation, the particles separate entirely. At sufficiently low mass density the particles of the gas are sufficiently separated that the particle bonding is effectively absent and the gas becomes an ideal gas. The contribution to U_V for the ideal gas is entirely due to the kinetic energy. The combined first and second laws of thermodynamics states that the change in the internal energy per unit volume dU_V is given by[12]

$$dU_V = dW_V + TdS \tag{6.102}$$

where T is the temperature of the system, S is the entropy per unit volume, and dW_V is the incremental work per unit volume done on the system. The work per unit volume done on the system is the sum of the stresses σ_{ij} times the corresponding incremental changes in strain (displacement gradient) given by

$$dW_V = \sigma_{ij} du_{ij} \tag{6.103}$$

Hence,

$$dU_V = \sigma_{ij} du_{ij} + TdS \tag{6.104}$$

Equation 6.104 implies that the internal energy per unit volume U_V is a function of the displacement gradient u_{ij} and the entropy per unit volume S

$$U_V = U_V(\boldsymbol{X}, u_{ij}, S) \tag{6.105}$$

and that the stress is

$$\sigma_{ij} = \frac{\partial U_V}{\partial u_{ij}} \tag{6.106}$$

Equation 6.106 states that the stress, in contrast to the limiting definition given by Equation 6.67, is defined more generally by the derivative of the internal energy per unit volume with respect to the displacement gradient.

All previous equations involving the power series expansions of the elastic potential energy per unit volume Φ may now be replaced by corresponding expansions of the internal energy per unit volume U_V. In particular, we may replace Equation 6.66 with

$$U_V(\mathbf{X}, u_{ij}, S) = (UV)_0 + A_{ij}u_{ij} + \frac{1}{2}A_{ijkl}u_{ij}u_{kl} + \frac{1}{3!}A_{ijklmn}u_{ij}u_{kl}u_{mn} + \tag{6.107}$$

and replace Equation 6.67 with

$$\sigma_{ij} = \frac{\partial U_V}{\partial u_{ij}} = A_{ij} + A_{ijkl}u_{kl} + \frac{1}{2}A_{ijklmn}u_{kl}u_{mn} + \cdot \tag{6.108}$$

The nonlinear equations of motion and the definition of the acoustic nonlinearity parameters are then obtained in the manner previously derived. However, the equations are now valid in materials other than solids at the absolute zero of temperature.

6.2 Acoustoelasticity

Traditionally, acoustoelasticity has been viewed as that aspect of material anharmonicity giving rise to the variation in sound velocity as a function of the state of stress of the material. Acoustoelastic measurements not only are a popular means of assessing stress fields, but are also a means of measuring higher-order elastic constants and for characterizing certain aspects of material microstructure.

6.2.1 Basic Concepts and Equations of Acoustoelasticity

We are interested in obtaining the elastic wave velocities as a function of applied or residual stress. It is convenient to exploit the difference between an initially stressed particle configuration and the unstressed configuration. The initial configuration, represented by the set of position vectors $\{X\}$, includes the effect of initial (residual or applied) stresses. We assume that the initial configuration is obtained by a finite deformation from an unstressed configuration of particles of the material represented by the set of position vectors $\{\bar{\mathbf{X}}\}$. With respect to the unstressed configuration $\{\bar{\mathbf{X}}\}$ the stress σ_{ij} may be expanded as

$$\sigma_{ij} = \bar{A}_{ijkl}\bar{u}_{kl} + \frac{1}{2}\bar{A}_{ijklmn}\bar{u}_{kl}\bar{u}_{mn} + \cdots \qquad \textbf{(6.109)}$$

where $\bar{\mathbf{u}} = \mathbf{x} - \bar{\mathbf{X}}$ and the displacement gradients with respect to $\bar{\mathbf{X}}$ are defined by

$$\bar{u}_{ij} = \partial\bar{u}_i/\partial\bar{X}_j \qquad \textbf{(6.110)}$$

where, as previously, an overbar above a quantity denotes that the quantity is defined with respect to the unstressed configuration. Note that the first-order Huang coefficients $\bar{A}_{ij} = 0$ in Equation 6.109, since the reference configuration $\bar{\mathbf{X}}$ is assumed to be stress free.

It is expedient to expand the stress σ_{ij} about the homogeneously deformed initial state $\mathbf{X}$. We write

$$\sigma_{ij} = (\sigma_{ij})_{\mathbf{X}} + \left(\frac{\partial \sigma_{ij}}{\partial \bar{u}_{kl}}\right)_{\mathbf{X}} [\bar{u}_{kl} - (\bar{u}_{kl})_{\mathbf{X}}] + \cdots = (\sigma_{ij})_{\mathbf{X}} + \left(\frac{\partial \sigma_{ij}}{\partial \bar{u}_{kl}}\right)_{\mathbf{X}} \tilde{u}_{kl} + \cdots \quad \textbf{(6.111)}$$

where in the last equality we define $\tilde{u}_i = \bar{u}_i - (\bar{u}_i)_{\mathbf{X}} = x_i - \bar{X}_i - (x_i - \bar{X}_i)_{\mathbf{X}}$ and $\tilde{u}_{ij} = \bar{u}_{ij} - (\bar{u}_{ij})_{\mathbf{X}}$; the subscripted **X** following a quantity denotes that the quantity is evaluated at the initial configuration. With respect to the unstressed configuration Newton's law may be written in analogy to Equation 6.18 as

$$\rho_0 \frac{\partial^2 x_i}{\partial t^2} = \rho_0 \frac{\partial^2 \tilde{u}_i}{\partial t^2} = \frac{\partial \sigma_{ij}}{\partial \bar{X}_j} \quad \textbf{(6.112)}$$

where ρ_0 is the mass density in the unstressed configuration. Substitution of Equation 6.111 into Equation 6.112 yields

$$\rho_0 \frac{\partial^2 \tilde{u}_i}{\partial t^2} = \frac{\partial \sigma_{ij}}{\partial \bar{X}_j} = \bar{L}_{ijkl} \frac{\partial^2 \tilde{u}_k}{\partial \bar{X}_l \partial \bar{X}_j} \quad \textbf{(6.113)}$$

where the propagation matrix $\bar{L}_{ijkl}$ is defined by

$$\bar{L}_{ijkl} = \left(\frac{\partial \sigma_{ij}}{\partial \bar{u}_{kl}}\right)_{\mathbf{X}} = \bar{A}_{ijkl} + \bar{A}_{ijklmn}(\bar{u}_{mn})_{\mathbf{X}} + \cdots \quad \textbf{(6.114)}$$

If only the linear term in Equation 6.114 is retained, then Equation 6.113) may be viewed as a linear wave equation for which the propagation matrix serves as a parametric coefficient, governing the sound velocity, that is dependent on the state of initial strain $(\bar{u}_{ij})_{\mathbf{X}}$ in the material.

We seek a linear wave solution to Equation 6.113. It is expedient to assume a solution of the form

$$\tilde{u}_k = \bar{U}_k \exp i(\omega t - \bar{\kappa} \cdot \bar{\mathbf{X}}) \quad \textbf{(6.115)}$$

where $\bar{\mathbf{N}} = \bar{\kappa} / |\bar{\kappa}|$ is the unit propagation direction referred to the unstressed configuration. It is convenient to define the natural velocity $\bar{W} = \omega / |\bar{\kappa}|$, since it is the velocity referred to the unstressed state.[13] Substituting Equation 6.115 into Equation 6.113, we obtain the set of linear equations for the unit polarization vectors $\bar{\mathbf{U}}$ given by

$$(\bar{L}_{ijkl}\bar{N}_j\bar{N}_l - \rho_0\bar{W}^2\delta_{ik})\bar{U}_k = 0 \quad \textbf{(6.116)}$$

Equation 6.116 is the basic equation of acoustoelasticity. It provides the variation in the sound velocity (here the natural velocity) as a function of applied or residual strains (via $\bar{L}_{ijkl}$), the wave propagation direction $\bar{\mathbf{N}}$, and the wave polarization $\bar{\mathbf{U}}$.

Let us consider the rate of change of the square of the natural velocity with respect to the applied stress p (uniaxial or hydrostatic) evaluated at the unstressed configuration (i.e., at $p = 0$). We write

$$\left[\frac{\partial(\rho_0\bar{W}^2)}{\partial p}\right]_{p=0} = \left[\left(\frac{\partial\sigma_{ab}}{\partial p}\right)\left(\frac{\partial\bar{u}_{rs}}{\partial\sigma_{ab}}\right)\left(\frac{\partial(\rho_0\bar{W}^2)}{\partial\bar{u}_{rs}}\right)\right]_{p=0}$$

$$= \bar{S}_{rsab}\left(\frac{\partial\sigma_{ab}}{\partial p}\right)_{p=0}\left(\frac{\partial(\rho_0\bar{W}^2)}{\partial\bar{u}_{rs}}\right)_{p=0} \quad \textbf{(6.117)}$$

where $\bar{S}_{rsab} = (\partial\bar{u}_{rs}/\partial\sigma_{ab})_{p=0}$ are the isothermal compliance coefficients referred to the unstressed configuration. For applied hydrostatic pressure of magnitude p or uniaxial compression of magnitude p in the unit direction $\bar{\mathbf{M}}$

$$\left(\frac{\partial\sigma_{ab}}{\partial p}\right)_{p=0} = -\delta_{ab} \ \text{ for hydrostatic pressure} \quad \textbf{(6.118)}$$

and

$$\left(\frac{\partial\sigma_{ab}}{\partial p}\right)_{p=0} = -\bar{M}_a\bar{M}_b \ \text{ for uniaxial compression} \quad \textbf{(6.119)}$$

where $\bar{M}_a$ are the Cartesian components of the direction vector $\bar{\mathbf{M}}$.

Substituting Equation 6.85 and Equation 6.86 into Equation 6.114, we obtain from Equation 6.116 and Equation 6.117 that

$$\left(\frac{\partial(\rho_0\bar{W}^2)}{\partial p}\right)_{p=0} = \left(\frac{\partial\sigma_{ab}}{\partial p}\right)_{p=0}[\bar{N}_a\bar{N}_b + \bar{U}_j\bar{U}_k(2\rho_0\bar{W}_0^2\bar{S}_{jkab} + \bar{N}_r\bar{N}_s\bar{S}_{iqab}\bar{C}_{jrksiq})] \quad \textbf{(6.120)}$$

where

$$(\rho_0\bar{W}^2)_{p=0} = \rho_0\bar{W}_0^2 = \bar{C}_{mrns}\bar{N}_r\bar{N}_s\bar{U}_m\bar{U}_n \quad \textbf{(6.121)}$$

TABLE 6.4

Stress Derivative of Natural Velocity for Various Wave Polarizations and Applied Stresses in Isotropic Solids

Applied Stress	Propagation Direction N	Polarization Direction U	$\rho_0 W_0^2$	$-\partial(\rho_0 W^2)/\partial p$
Hydrostatic	Arbitrary	$U \parallel N$	C_{11}	$1 + g[2C_{11} + C_{111} + 2C_{112}]$
Hydrostatic	Arbitrary	$U \perp N$	C_{44}	$1 + g[2C_{44} + (1/2)(C_{111} - C_{123})]$
Uniaxial	⊥ to stress	$U \parallel N$	C_{11}	$g\{C_{112} - (C_{12}/C_{44})[C_{11} + (1/4)(C_{111} - C_{112})]\}$
Uniaxial	⊥ to stress	$U \parallel$ stress	C_{44}	$g[C_{11} + C_{12} + (1/4)(C_{111} - C_{123}) + (C_{12}/8C_{44})(C_{111} - 3C_{112} + 2C_{123})]$
Uniaxial	⊥ to stress	$U \perp$ stress	C_{44}	$g[-C_{12} + (1/2)(C_{112} - C_{123}) + (C_{12}/4C_{44})(C_{111} - 3C_{112} + 2C_{123})]$

$g = (C_{11} + 2C_{12})^{-1}$

Source: Adapted from Thurston, R.N. and Brugger, K., *Phys. Rev.*, 133, A1604, 1964. With permission.

Equation 6.120 and Equation 6.121, derived for solids of arbitrary crystalline symmetry, specifically show the dependence of the natural velocity and the change of natural velocity with stress in terms of the second- and third-order elastic constants of the solid referred to the unstressed configuration. The equations suggest that one can determine the second- and third-order elastic constants of the material from experimental measurements of the natural velocity as a function of stress. Indeed, calculation of the elastic constants from such measurements has become quite well established.[14–18] Table 6.4 lists the stress derivatives of the natural velocity obtained for various combinations of wave polarizations and applied stresses in isotropic solids.

6.2.2 Measurement Considerations

In a typical ultrasonic experiment to measure the stress variation of the phase velocity, one generally measures as a function of applied stress the variation in time required for a generated plane wavefront to propagate between parallel sample surfaces. An inverse measure of that propagation time is the parameter F defined by

$$F = l^{-1} v \tag{6.122}$$

where v is the true velocity and l is the propagation distance in the sample in the homogeneouly deformed state. The true velocity is referred to the deformed state and is equal to the propagation length in the deformed state divided by the wave propagation time in the deformed state. The natural velocity $\overline{W}$ is referred to the unstressed state and is equal to the propagation length in the undeformed state divided by the propagation time in the stressed state. Hence, the relationship between the true sound velocity and the natural velocity is given by

$$v = l_0^{-1} l \overline{W} \tag{6.123}$$

where l_0 is the propagation distance in the undeformed sample.

There is an advantage in measuring changes in the natural velocity as a function of applied stress. The advantage is that such measurements are obtained from time measurements in the deformed state, but the length measurements are referred to the undeformed length of the solid. This is seen by substituting Equation 6.122 into Equation 6.123 to get

$$F = l_0^{-1} \overline{W} \tag{6.124}$$

From Equation 6.124 we may define the parameter H_p as[19]

$$H_p = -\left(\frac{1}{F}\frac{\partial F}{\partial p}\right)_{p=0} = -\frac{1}{F_0}\left(\frac{\partial F}{\partial p}\right)_{p=0} = -\frac{1}{\overline{W}_0}\left(\frac{\partial \overline{W}}{\partial p}\right)_{p=0} = -\frac{1}{2\rho_0 \overline{W}_0^2}\left[\frac{\partial(\rho_0 \overline{W}^2)}{\partial p}\right]_{p=0}. \tag{6.125}$$

H_p is a parameter of the material, often called the stress acoustic constant or the acoustoelastic constant that depends on the second- and third-order elastic constants of the material. It is cautioned that often in the literature one finds the measurements of H_p reported as an inverse measurement (i.e., H_p^{-1}).

The exact meaning of the experimental parameter F in Equation 6.122 and Equation 6.124 depends on the particular experimental technique used for the measurement. For example, if one uses a resonance or resonance-derived technique, then F is the acoustic standing-wave resonance frequency. If one uses a pulse coincidence technique, then F is the inverse pulse repetition rate. It is important to emphasize that all the above equations specifically refer to acoustic bulk wave propagation in materials. The elastic moduli or constants used to quantify this wave propagation are referred to bulk solids.

For any direction in isotropic solids a direct relationship exists between the uniaxial stress acoustic constant and the acoustic nonlinearity parameter. This relationship may be obtained from Equation 6.117 by noting that for a uniaxial stress we need to consider only the σ_{11} component of stress and the $\overline{u}_{11} = \partial \overline{u}_1 / \partial \overline{X}_1$ component of the displacement gradient. The appropriate stress-displacement gradient relationship, assuming an initially stress-free solid, is then given by

$$\sigma_{11} = \overline{A}_{11}\overline{u}_{11} + \frac{1}{2}\overline{A}_{111}\overline{u}_{11}^2 + \cdots. \tag{6.126}$$

Thus, $\sigma_{ab} = \sigma_{11}$, $\bar{u}_{rs} = \bar{u}_{11}$, and $\partial\sigma_{ab}/\partial p = 1$ in Equation 6.117. The compliance coefficient $\bar{S}_{rsab} = \bar{S}_{1111} = 1/\bar{A}_{1111}$ (full notation) or $\bar{S}_{\alpha\beta} = \bar{S}_{11} = 1/\bar{A}_{11}$ (Voigt notation). Hence, for isotropic solids Equation 6.117 is simplified to

$$\left(\frac{\partial(\rho_0\bar{W}^2)}{\partial p}\right)_{p=0} = \bar{S}_{11}\left(\frac{\partial(\rho_0\bar{W}^2)}{\partial\bar{u}_{11}}\right)_{p=0} = \frac{1}{\bar{A}_{11}}\left(\frac{\partial(\rho_0\bar{W}^2)}{\partial\bar{u}_{11}}\right)_{p=0} \quad \textbf{(6.127)}$$

From Equation 6.127 the natural velocity $\bar{\mathbf{W}}$ is obtained as

$$\rho_0\bar{W}^2 = \frac{\partial\sigma_{11}}{\partial\bar{u}_{11}} = \bar{A}_{11} + \bar{A}_{111}\bar{u}_{11} + \cdots. \quad \textbf{(6.128)}$$

From Equation 6.128, $[\partial(\rho_0\bar{W}^2)/\partial\bar{u}_{11}]_{p=0} = \bar{A}_{111}$. Finally, from Equation 6.125 and the relations $\rho_0\bar{W}_0^2 = \bar{A}_{11}$ and $\bar{\beta} = -(\bar{A}_{111}/\bar{A}_{11})$, we obtain the relationship between the uniaxial stress acoustic constant $\bar{\mathbf{H}}_{\mathbf{11}}$ and the acoustic nonlinearity parameter $\bar{\beta}$ as

$$\bar{H}_{11} = -\frac{1}{2\rho_0\bar{W}_0^2}\left(\frac{\partial(\rho_0\bar{W}^2)}{\partial p}\right)_{p=0} = -\frac{\bar{A}_{111}}{2\bar{A}_{11}^2} = \frac{\bar{\beta}}{2\bar{A}_{11}} \quad \textbf{(6.129)}$$

6.3 Characterization of Material Defects and Nano/Microstructures

Material defects and nano/microstructures can significantly alter the physical properties of the matrix material in which they occur. The structures are central to the development of new materials with specific design objectives, and the understanding of microstructure-physical property relationships is critical to material development. The nonlinear interaction of sound waves with material defects and nano/microstructures provides an important contribution to this understanding. Nonlinear ultrasonic measurements also serve as an effective and sometimes unique means for the quantitative NDE of such materials.

6.3.1 Acoustic Nonlinearity from Dislocation Monopoles

The strong crystalline structure and symmetry dependence of the acoustic nonlinearity parameters suggest that any changes in the crystal structure or symmetry could lead to changes in the values of the nonlinear ultrasonic parameters. The introduction of defects in the crystal structure can greatly disrupt the crystal lattice periodicity and may thus produce large changes in the nonlinearity parameters. A defect of some importance is the dislocation. An edge dislocation may be viewed as a disruption in the crystal lattice

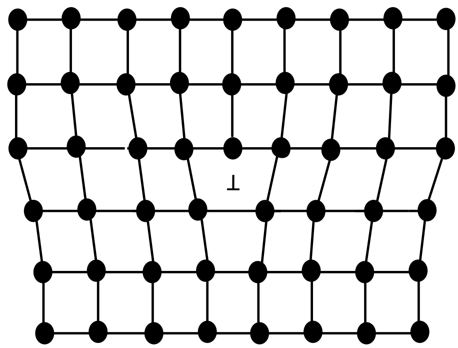

FIGURE 6.3
Edge dislocation in a simple cubic lattice.

caused by the introduction of an extra half-plane of atoms introduced into the lattice as illustrated for the simple cubic lattice structure shown in Figure 6.3. By convention, if the extra half-plane of atoms is inserted at the top, the dislocation is called a positive edge dislocation and is denoted by the symbol ⊥; if inserted at the bottom the dislocation is called a negative edge dislocation and is denoted by the symbol T. The insertion of the half-plane of atoms produces a compressive stress in the half-space volume containing the extra atoms and tensile stresses in the half-space volume below the terminus of the extra atoms. The dislocation line is defined by the linear array of atoms along the edge (terminus) of the extra half-plane of atoms. An isolated dislocation is called a dislocation monopole.

The application of a shear stress results in a plastic shear strain in the crystal as the result of dislocation motion. The plastic shear strain occurs in addition to the elastic strain in the solid. The plastic shear strain resulting from dislocation glide may be obtained from a consideration of Figure 6.4. Under an applied shear stress the positive dislocations of line length L glide to the right along the slip or glide planes in the crystal appropriate to the applied stress. The negative dislocations of line length L glide to the left along the appropriate glide planes. Since the motion of dislocations is actually the movement of half-planes of atoms, the top surface of the crystal will be displaced relative to the bottom surface. If a dislocation moves completely across the crystal through the distance d_{mp}, the crystal will be displaced by a distance corresponding to a lattice spacing b, called the Burgers vector. Such a dislocation will thus contribute b to the total displacement of D, shown in Figure 6.4. A dislocation that moves only a distance x_i contributes only a fraction (x_i/d_{mp}) of b. If the total number of mobile dislocations is N, then the total displacement D is given by

$$D = \frac{b}{d_{mp}} \sum_{i=1}^{N} x_i \tag{6.130}$$

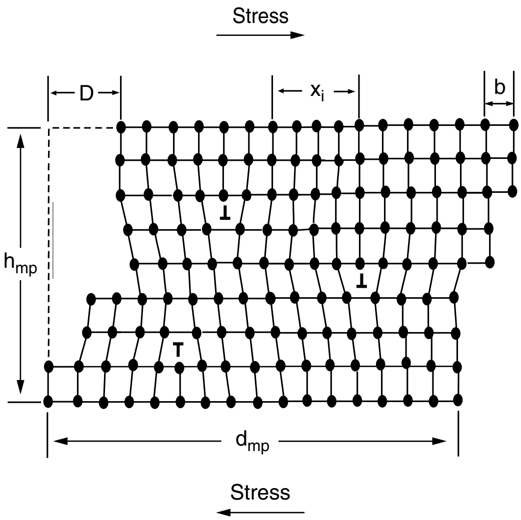

FIGURE 6.4
Plastic shear strain resulting from dislocation glide.

Let h_{mp} be the distance normal to the slip planes that include the slip planes of all mobile dislocations under consideration. The plastic shear strain is then given by

$$\bar{\gamma}_{mp} = \frac{D}{h_{mp}} = \frac{b}{h_{mp} d_{mp}} \sum_{i=1}^{N} x_i = b\Lambda_{mp}\bar{x} \tag{6.131}$$

where $\Lambda_{mp} = NL/h_{mp}Ld_{mp}$ is the density of mobile dislocation monopoles and

$$\bar{x} = \frac{1}{N} \sum_{i=1}^{N} x_i \tag{6.132}$$

is the average distance moved by a dislocation. The subscripted *mp* denotes dislocation monopole in the above expressions. Because the average area of slip plane $\bar{S}$ swept by a dislocation is $L\,\bar{x}$, then Equation 6.131 may be rewritten as

$$\bar{\gamma}_{mp} = b\left(\frac{\Lambda_{mp}}{L}\right)\bar{S} = bn\bar{S} \tag{6.133}$$

where $n = \Lambda_{mp}/L$ is the number of dislocation lines per unit volume.

The dislocation line is generally broken into segments, often called loops, as the result of pinning sites along the line caused by point defects in the

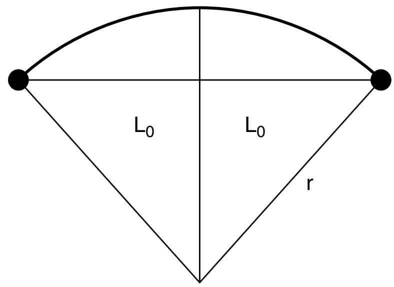

FIGURE 6.5
Bowing of pinned dislocation from application of shear stress. (From Hikata A. et al., *J. Appl. Phys.*, 36, 229, 1965. With permission.)

solid or by the intersection of the dislocation with other dislocations. The application of a shear stress τ on a pinned dislocation segment will cause the segment to bow out like a string and form an arc of radius r as shown in Figure 6.5. The dislocation loop length $L \approx 2L_0$ in Figure 6.5. The application of a longitudinal stress $\sigma = \sigma_{11}$ will result in a resolved shear stress along the slip direction on a glide plane given by $\tau = R\sigma$, where R is the resolving factor. In equilibrium the shear stress is balanced by the line tension (energy per unit length of the dislocation) $T_{mp} \approx \mu b^2$, where μ is the shear modulus of the solid, such that

$$\tau = \frac{T_{mp}}{rb} = \frac{\mu b}{2r}. \tag{6.134}$$

The corresponding shear strain $\bar{\gamma}_{mp}$, referred to the unstressed configuration, on the dislocation monopole resulting from the dislocation motion is obtained from Equation 6.133 as

$$\bar{\gamma}_{mp} = \frac{\Lambda b}{2L_0}\bar{S} \tag{6.135}$$

where $\bar{S}$, the area swept out by the dislocation, is given by

$$\bar{S} = r^2\left(\theta - \frac{1}{2}\sin 2\theta\right) \tag{6.136}$$

and θ is the half-angle subtended by the arc. We write $\theta = \sin^{-1}(L_0/r)$ and expand θ in a power series with respect to (L_0/r), where we assume (L_0/r) is small. Keeping terms to fifth power in (L_0/r) yields the expression[20]

$$\bar{\gamma}_{mp} = \frac{2}{3}\left(\frac{\Lambda_{mp}L_0^2}{\mu}\right)\tau + \frac{4}{5}\left(\frac{\Lambda_{mp}L_0^4}{\mu^2 b^2}\right)\tau^3 \tag{6.137}$$

The longitudinal lattice strain $\bar{\varepsilon}_{lat} = \bar{u}_{11} = \partial\bar{u}_1 / \partial\bar{X}_1 = \partial\bar{u} / \partial\bar{X}$ due to the longitudinal stress σ can be obtained from Equation 6.111 for zero initial stress by writing

$$\frac{\partial\bar{u}}{\partial\bar{X}} = \bar{u}_{11} = \bar{\varepsilon}_{lat} = \left(\frac{\partial\bar{u}_{11}}{\partial\sigma}\right)_{\bar{\mathbf{X}}}\sigma + \frac{1}{2}\left(\frac{\partial^2\bar{u}_{11}}{\partial\sigma^2}\right)_{\bar{\mathbf{X}}}\sigma^2 + \cdots$$

$$= \left(\frac{\partial\sigma}{\partial\bar{u}_{11}}\right)_{\bar{\mathbf{X}}}^{-1}\sigma - \frac{1}{2}\left[\left(\frac{\partial^2\sigma}{\partial\bar{u}_{11}^2}\right)_{\bar{\mathbf{X}}}\left(\frac{\partial\sigma}{\partial\bar{u}_{11}}\right)_{\bar{\mathbf{X}}}^{-3}\right]\sigma^2 + \cdots$$

$$= \frac{1}{\bar{A}_{11}}\sigma - \frac{1}{2}\frac{\bar{A}_{111}}{\bar{A}_{11}^3}\sigma^2 + \cdots \tag{6.138}$$

The subscripted $\bar{\mathbf{X}}$ in Equation 6.138 means that the derivative is evaluated at the zero stress state. The total longitudinal strain $\bar{\varepsilon}$ in the solid containing a network of dislocation monopoles is the sum of the longitudinal plastic strain due to the dislocation network $\bar{\varepsilon}_{mp} = \Omega\bar{\gamma}_{mp}$ and the longitudinal lattice strain $\varepsilon_{lat} = \bar{u}_{11}$ given as

$$\bar{\varepsilon} = \bar{\varepsilon}_{lat} + \bar{\varepsilon}_{mp} = \bar{u}_{11} + \Omega\bar{\gamma}_{mp} \tag{6.139}$$

where Ω is a conversion factor from shear strain to longitudinal strain. From Equation 6.137 through Equation 6.139, we get the total longitudinal strain-longitudinal stress relationship for the solid as

$$\bar{\varepsilon} = \left(\frac{1}{\bar{A}_{11}} + \frac{2}{3}\frac{\Omega\Lambda_{mp}L_0^2R^3}{\mu^3 b^2}\right)\sigma - \frac{1}{2}\frac{\bar{A}_{111}}{\bar{A}_{11}^2}\sigma^2 + \frac{4}{5}\frac{\Omega\Lambda_{mp}L_0^4R^3}{\mu^3 b^2}\sigma^3 + \cdots \tag{6.140}$$

Let us assume that the initial stress in the material is σ_1 that gives rise to an initial total strain $\bar{\varepsilon}_1$. If the stress in the material is then increased infinitesimally from σ_1 to σ, then the total strain is increased infinitesimally from $\bar{\varepsilon}_1$ to $\bar{\varepsilon}$. A power series of the stress with respect to the initial total strain is then

$$\sigma = \sigma_1 + \left(\frac{\partial\sigma}{\partial\bar{\varepsilon}}\right)_{\mathbf{X}}(\bar{\varepsilon} - \bar{\varepsilon}_1) + \frac{1}{2}\left(\frac{\partial^2\sigma}{\partial\bar{\varepsilon}^2}\right)_{\mathbf{X}}(\bar{\varepsilon} - \bar{\varepsilon}_1)^2 + \cdots$$

$$= \sigma_1 + \left(\frac{\partial\bar{\varepsilon}}{\partial\sigma}\right)_{\mathbf{X}}^{-1}(\bar{\varepsilon} - \bar{\varepsilon}_1) - \left(\frac{1}{2}\right)\left[\left(\frac{\partial^2\bar{\varepsilon}}{\partial\sigma^2}\right)_{\mathbf{X}}\left(\frac{\partial\bar{\varepsilon}}{\partial\sigma}\right)_{\mathbf{X}}^{-3}\right](\bar{\varepsilon} - \bar{\varepsilon}_1$$

$$= \sigma_1 + P(\bar{\varepsilon} - \bar{\varepsilon}_1) + \frac{1}{2}Q(\bar{\varepsilon} - \bar{\varepsilon}_1)^2 + \cdots \tag{6.141}$$

where from Equation 6.141 for values of the initial stress σ_1 is small compared to the Huang coefficients and the shear elastic constant μ

$$P = \left(\frac{\partial \bar{\varepsilon}}{\partial \sigma}\right)_X^{-1} \approx \left(\frac{1}{\bar{A}_{11}} + \frac{2}{3}\frac{\Omega\Lambda_{mp}L_0^2 R}{\mu}\right)^{-1} \quad \textbf{(6.142)}$$

and

$$Q = -\left(\frac{\partial^2 \bar{\varepsilon}}{\partial \sigma^2}\right)_X \left(\frac{\partial \bar{\varepsilon}}{\partial \sigma}\right)_X^{-3} \approx \left[\frac{\bar{A}_{111}}{\bar{A}_{11}^2} - \frac{24}{5}\frac{\Omega\Lambda_{mp}L_0^4 R^3}{\mu^3 b^2}\sigma_1\right]\left[\frac{1}{\bar{A}_{11}} + \frac{2}{3}\frac{\Omega\Lambda_{mp}L_0^2 R}{\mu}\right]^{-3}. \quad \textbf{(6.143)}$$

The subscripted **X** in Equation 6.141 through Equation 6.143 means that the derivative is evaluated at the initially stressed configuration **X** where the initial stress is σ_1.

The total acoustic nonlinearity $\bar{\beta}_{total}$ is obtained to good approximation for most materials as

$$\bar{\beta}_{total} = -\frac{Q}{P} \approx -\frac{\bar{A}_{111}}{\bar{A}_{11}} + \frac{24}{5}\frac{\Omega\Lambda_{mp}L_0^4 R^3 \bar{A}_{11}^2}{\mu^3 b^2}|\sigma_1| \quad \textbf{(6.144)}$$

It is interesting to note that the first term on the right-hand side of Equation 6.144 is the lattice contribution to the total nonlinearity parameter given by

$$\bar{\beta}_{lat} = -\frac{\bar{A}_{111}}{\bar{A}_{11}}. \quad \textbf{(6.145)}$$

The second term on the right-hand side of Equation 6.144 is the contribution to the total nonlinearity parameter from the network of dislocation monopoles in the solid given by

$$\bar{\beta}_{mp} = \frac{24}{5}\frac{\Omega\Lambda_{mp}L_0^4 R^3 \bar{A}_{11}^2}{\mu^3 b^2}|\sigma_1|. \quad \textbf{(6.146)}$$

It is important to note that the contribution from dislocation monopoles requires the presence of an initial stress σ_1. The magnitude of the initial stress $|\sigma_1|$ is used in Equation 6.144 and Equation 6.146, since $\bar{\beta}_{mp}$ is independent of the direction of dislocation bowing resulting from a positive or negative initial stress.

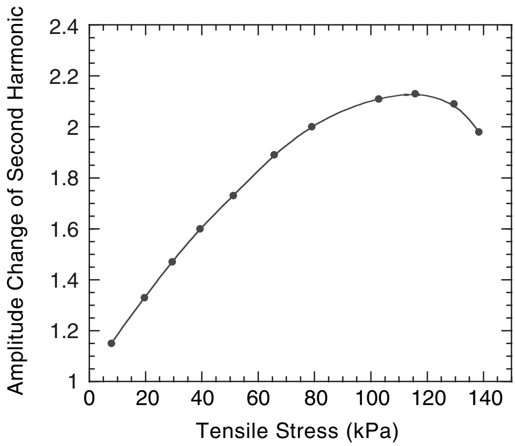

FIGURE 6.6
Acoustic second harmonic signal (amplitude change) plotted as a function of uniaxial stress applied to single crystal aluminum. (From Hikata, A. et al., *J. Appl. Phys.*, 36, 229, 1965. With permission.)

6.3.2 Dislocation Monopole Characterization of Metallic Materials

Figure 6.6 shows a graph of the amplitude of the generated second harmonic signal in pure single crystal aluminum plotted as a function of the applied stress in the material (from Hikata et al., *J. Appl. Phys.*, 36, 229, 1965, with permission). The linear dependence of the amplitude (or equivalently $\bar{\beta}_{mp}$) on the applied stress is in agreement with Equation 6.146 for low stresses. With increasing applied stress many dislocations become unpinned from their pinning sites and the average loop length of the dislocations increases. The increase in loop length leads to an increase in the attenuation. As indicated in Equation 6.61 the measured nonlinearity parameter increases exponentially with increasing attenuation. At a sufficiently large average loop length the reduction in measured signal due to attenuation dominates harmonic generation and leads to the nonlinear behavior in Figure 6.6 at higher applied stresses.

Equation 6.146 also predicts that the amplitude of the generated acoustic second harmonic depends on the fourth power of the dislocation loop length. Although direct verification of this prediction has not been reported, an indirect verification of the strong dependence of the nonlinearity parameter on the applied stress is shown in Figure 6.7 for aluminum alloy 2024-T4. The applied stress given in Figure 6.7 is the resolved shear stress amplitude of the fundamental longitudinal acoustic wave. The graph shows that the nonlinearity parameter $\bar{\beta}_{mp}$ for aluminum 2024-T4 is relatively constant from zero stress up to a stress of 2.7 to 2.9 MPa. The longitudinal stress of 2.7 to 2.9 MPa corresponds to a resolved acoustic shear stress amplitude of roughly 0.9 to 1.0 MPa. At higher acoustic stress amplitudes a substantial increase in

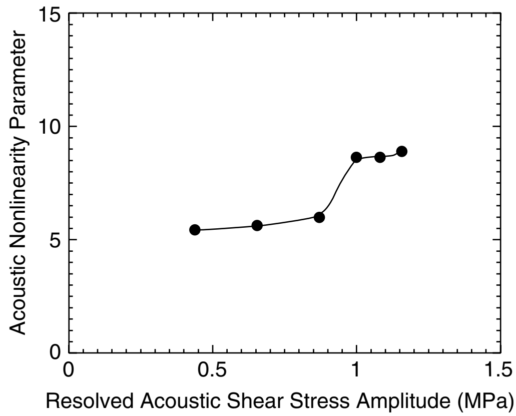

FIGURE 6.7
Acoustic nonlinearity parameter of aluminum alloy 2024-T4 plotted as a function of the driving (fundamental), wave-resolved shear stress amplitude.

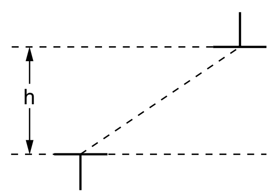

FIGURE 6.8
Illustration of dislocation dipole formed by the mutual trapping of two dislocations by the force fields of the interacting dislocation pair.

β, hence acoustic harmonic generation, is seen to occur. Resolved shear stress amplitudes in the range 0.9 MPa to 1.0 MPa correspond to that required for dislocation breakaway from weak pinning sites (e.g., Guinier-Preston zones) in the material. The resulting increase in dislocation loop length following breakaway is a likely explanation for the dramatic increase in $\bar{\beta}_{mp}$ with increased acoustic stress amplitude.

6.3.3 Acoustic Nonlinearity from Dislocation Dipoles

As shown in Section 6.3.2, a stress applied to a material will produce motion of the monopole dislocations in the material. If two dislocations move sufficiently close to each other, the dislocations can become mutually trapped in the force fields of the interacting dislocations. A trapped dislocation pair is known as a dislocation dipole and is illustrated in Figure 6.8. A stress applied to a dislocation dipole will cause the dislocations in the dipole pair to move relative to each other, but the center of mass of the dipole will remain fixed.

The equations of motion, neglecting body forces and referring to the unstressed configuration, are obtained from Equation 6.18 by setting $\rho_1 = \rho_0$,

$u_i = \bar{u}_i$, and $X_j = \bar{X}_j$. For simplicity we consider only longitudinal wave propagation in an isotropic medium and drop the subscripts to obtain

$$\rho_0 \frac{\partial^2 \bar{u}}{\partial t^2} = \frac{\partial \sigma}{\partial \bar{X}} \tag{6.147}$$

We assume that the total longitudinal displacement $\bar{u}$ consists of a lattice displacement contribution $\bar{u}_{lat}$ and a dipole displacement contribution $\bar{u}_{dp}$ as

$$\bar{u} = \bar{u}_{lat} + \bar{u}_{dp} \tag{6.148}$$

Substituting Equation 6.148 into Equation 6.147 and differentiating with respect to $\bar{X}$ of the resulting expression yields

$$\rho_0 \frac{\partial^2}{\partial t^2}\left(\frac{\partial \bar{u}_{lat}}{\partial \bar{X}} + \frac{\partial \bar{u}_{dp}}{\partial \bar{X}}\right) = \frac{\partial^2 \sigma}{\partial \bar{X}^2} \tag{6.149}$$

We consider launching a pure sinusoidal acoustic stress wave of amplitude B_1 into the solid. For generality we assume that the total stress perturbation σ in the solid is composed of a static stress component σ_1 (an applied or residual stress) and an oscillatory component (acoustic stress wave) consisting of the fundamental wave of amplitude B_1 and generated second harmonic waves of amplitudes B_2 and C_2 as

$$\sigma = \sigma_1 + B_1 \cos(\omega t - k\bar{X}) + B_2 \cos 2(\omega t - k\bar{X}) + C_2 \sin 2(\omega t - k\bar{X}) \tag{6.150}$$

where ω is the angular frequency and k is the wavenumber. To first approximation the coefficient B_1 is assumed to be constant, independent of wave propagation distance. However, the coefficients B_2 and C_2 are assumed to be functions of the distance of propagation $\bar{X}$ (where $\bar{X} = 0$ is the value of the coordinate at the launch site) and satisfy the boundary conditions

$$\begin{aligned} B_2 &= B_2(\bar{X}), \quad B_2(0) = 0 \\ C_2 &= C_2(\bar{X}), \quad C_2(0) = 0 \end{aligned} \tag{6.151}$$

In order to obtain the appropriate nonlinear wave equation we must find the constitutive equations between the lattice and dipole displacement gradients $\partial \bar{u}_{lat}/\partial \bar{X}$ and $\partial \bar{u}_{dp}/\partial \bar{X}$, respectively, and the stress σ in Equation 6.149.

6.3.3.1 Constitutive Equations

For edge dislocation pairs of opposite polarity the shear force per unit length F_x on a given dislocation due to the other dislocation in the pair is given as[21]

$$F_x = -\frac{\mu b^2}{2\pi(1-\nu)} \frac{x(x^2 - y^2)}{(x^2 + y^2)^2} \tag{6.152}$$

where μ is the shear modulus, b is Burgers vector, ν is Poission's ratio, and (x, y) are the Cartesian coordinates of one dislocation in the pair relative to the coordinates (0, 0) of the second. We assume motion of the dipole pairs only along parallel slip planes (i.e., along the x-direction) separated by a distance $y = h$, called the dipole height. At equilibrium, with no residual or applied stresses, Equation 6.152 asserts that $\pm x = \pm y = h$. The equation of motion of the equivalent one-body problem for the dislocation dipole pair under the influence of a driving stress σ is

$$m_{eff}\frac{\partial^2 x}{\partial t^2} = F_x + b\sigma R \tag{6.153}$$

where m_{eff} is the effective reduced mass of the dipole pair (of the order $\rho_0 b^2$) and R is the conversion factor from longitudinal displacement along the direction of the propagating acoustic wave to displacement of the dislocation along the slip plane. We expand Equation 6.152 in a power series in x with respect to h, keeping terms to second order, and approximate Equation 6.153 as

$$m_{eff}\frac{\partial^2 \zeta}{\partial t^2} + \frac{\mu b^2}{4\pi h^2(1-\nu)}\zeta - \frac{\mu b^2}{8\pi h^3(1-\nu)}\zeta^2 = b\sigma R \tag{6.154}$$

where $\zeta = (x - h)$ is the displacement of the dislocation with respect to the equilibrium position h.

Equation 6.154 may be solved, using a standard iterative procedure, by first obtaining the solution ζ_1 to Equation 6.154 in which the nonlinear term (squared term) is ignored and where the approximation of Equation 6.150 without the second harmonic terms is used for the driving stress. The differential equation for ζ_1 is then

$$m_{eff}\frac{\partial^2 \zeta_1}{\partial t^2} + \frac{\mu b^2}{4\pi h^2(1-\nu)}\zeta_1 = bR[\sigma_1 + B_1\cos(\omega t - k\bar{X})] \tag{6.155}$$

The solution to Equation 6.155 is

$$\zeta_1 = \frac{4\pi R\sigma_1 h^2(1-\nu)}{\mu b} + \frac{4\pi R\sigma_1 h^2(1-\nu)B_1}{\mu b - 4\pi^2\omega^2 b^{-1} m_{eff} h^2(1-\nu)}\cos(\omega t - k\bar{X}) \tag{6.156}$$

The inertial term, $4\pi^2\omega^2 b^{-1} m_{eff} h^2(1-\nu)$, in the denominator of the second term after the equal sign in Equation 6.156 is negligible compared to μb for the typical ultrasonic range of frequencies and may be ignored.

The solution ζ_1 is now substituted for ζ in the ζ^2 term of Equation 6.154 to obtain

$$m_{eff}\frac{\partial^2 \zeta}{\partial t^2} + \frac{\mu b^2}{4\pi h^2(1-\nu)}\zeta - \frac{\mu b^2}{8\pi h^3(1-\nu)}\zeta_1^2 = b\sigma R \tag{6.157}$$

Substituting Equation 6.156 and Equation 6.150 into Equation 6.157 and solving the resulting expression, we obtain the approximate solution to Equation 6.154 as

$$\zeta = \left(\frac{4\pi R h^2 (1-\nu)\sigma_1}{\mu b} + \frac{8\pi^2 R^2 h^3 (1-\nu)^2 \sigma_1^2}{\mu^2 b^2} + \frac{4\pi^2 R^2 h^3 (1-\nu)^2 B_1^2}{\mu^2 b^2} \right)$$
$$+ \left(\frac{4\pi R h^2 (1-\nu) B_1}{\mu b} + \frac{16\pi^2 R^2 h^3 (1-\nu)^2 \sigma_1 B_1}{\mu^2 b^2} \right) \cos(\omega t - k\bar{X})$$
$$+ \left(\frac{4\pi R h^2 (1-\nu) B_2}{\mu b} + \frac{4\pi^2 R^2 h^3 (1-\nu)^2 B_1^2}{\mu^2 b^2} \right) \cos 2(\omega t - k\bar{X})$$
$$+ \left(\frac{4\pi R h^2 (1-\nu) B_2}{\mu b} \right) \sin 2(\omega t - k\bar{X}) \quad \textbf{(6.158)}$$

where the negligible inertial terms have been dropped.

The acoustic wave displacement gradient $\partial \bar{u}_{dp}/\partial \bar{X}$ is related to the plastic shear strai $\bar{\gamma}_{dp}$ resulting from dipole motion as

$$\frac{\partial \bar{u}_{dp}}{\partial \bar{X}} = \Omega \bar{\gamma}_{dp} \quad \textbf{(6.159)}$$

where Ω, as before, is the conversion factor from dislocation displacement in the slip plane to longitudinal displacement $\bar{u}_{dp}$ along the propagation direction of the acoustic wave. The relationship between $\bar{\gamma}_{dp}$ and the dislocation displacement ζ may be written in analogy to Equation 6.131 as

$$\bar{\gamma}_{dp} = \Lambda_{dp} b \zeta \quad \textbf{(6.160)}$$

where Λ_{dp} is the dislocation dipole density. The constitutive equation for the dislocation dipole contribution to the wave equation is obtained by substituting Equation 6.158 into Equation 6.160 and then substituting the resulting expression into Equation 6.159.

The constitutive equation for the lattice contribution to the wave equation, referred to the unstressed configuration, may be found by expanding the stress σ in terms of the lattice displacement gradients $\partial \bar{u}_{lat}/\partial \bar{X}$ to second order as

$$\sigma = \bar{A}_{11} \left(\frac{\partial \bar{u}_{lat}}{\partial \bar{X}} \right) + \frac{1}{2} \bar{A}_{111} \left(\frac{\partial \bar{u}_{lat}}{\partial \bar{X}} \right)^2 + \cdots \quad \textbf{(6.161)}$$

Using, again, the iteration approach leading to Equation 6.158, we first write from Equation 6.161 and Equation 6.150 the linear approximation to $\partial\bar{u}_{lat}/\partial\bar{X}$ as

$$\left(\frac{\partial\bar{u}_{lat}}{\partial\bar{X}}\right)_1 = \frac{\sigma}{\bar{A}_{11}} = \frac{\sigma_1}{\bar{A}_{11}} + \frac{B_1}{\bar{A}_{11}}\cos(\omega t - k\bar{X}) \tag{6.162}$$

where the second harmonic terms of Equation 6.150 for the driving stress are suppressed in Equation 6.162. The next iteration is obtained by substituting Equation 6.150 and Equation 6.162 into the equation

$$\bar{A}_{11}\left(\frac{\partial\bar{u}_{lat}}{\partial\bar{X}}\right) + \frac{1}{2}\bar{A}_{111}\left(\frac{\partial\bar{u}_{lat}}{\partial\bar{X}}\right)_1^2 = \sigma \tag{6.163}$$

The solution to the resulting equation and the lattice contribution to the wave equation is

$$\left(\frac{\partial\bar{u}_{lat}}{\partial\bar{X}}\right) = \left(\frac{\sigma_1}{\bar{A}_{11}} - \frac{1}{4}\frac{\bar{A}_{111}B_1^2}{\bar{A}_{11}^3} - \frac{1}{2}\frac{\bar{A}_{111}\sigma_1^2}{\bar{A}_{11}^3}\right) + \left(\frac{B_1}{\bar{A}_{11}} - \frac{\bar{A}_{111}B_1\sigma_1}{\bar{A}_{11}^3}\right)\cos(\omega t - k\bar{X})$$
$$+\left(\frac{B_2}{\bar{A}_{11}} - \frac{1}{4}\frac{\bar{A}_{111}B_1^2}{\bar{A}_{11}^3}\right)\cos 2(\omega t - k\bar{X}) + \left(\frac{C_2}{\bar{A}_{11}}\right)\sin 2(\omega t - k\bar{X}) \tag{6.164}$$

6.3.3.2 Solution to Wave Equation

The differential equation governing the propagation of an acoustic wave in an isotropic solid containing dislocation dipoles is obtained to second order in the nonlinearity by substituting Equation 6.150 and Equation 6.158 through Equation 6.160 into Equation 6.149. Assuming that the fundamental amplitude B_1 is constant, we obtain the following set of coupled differential equations governing the in-phase and quadrature stress amplitudes B_2 and C_2, respectively, of the second harmonic of the acoustic wave

$$\frac{\partial^2 B_2}{\partial\bar{X}^2} + \frac{16\pi\rho_0\omega^2\Omega R\Lambda_{dp}h^2(1-\nu)}{\mu}B_2 - 4k\frac{\partial C_2}{\partial\bar{X}}$$
$$= \rho_0\omega^2\left(\frac{\bar{A}_{111}}{\bar{A}_{11}^3} - \frac{16\pi^2\Omega R^2\Lambda_{dp}h^3(1-\nu)^2}{\mu^2 b}\right)B_1^2 \tag{6.165}$$

and

$$\frac{\partial^2 C_2}{\partial \overline{X}^2} + \frac{16\pi\rho_0\omega^2\Omega R\Lambda_{dp}h^2(1-\nu)}{\mu}C_2 + 4k\frac{\partial B_2}{\partial \overline{X}} = 0 \tag{6.166}$$

The solutions to Equation 6.165 and Equation 6.166, subject to the boundary conditions given by Equation 6.151, are

$$B_2 = 0 \tag{6.167}$$

and

$$C_2 = -\frac{\rho_0\omega^2 B_1^2 \overline{X}}{4k}\left(\frac{\overline{A}_{111}}{\overline{A}_{11}^3} - \frac{16\pi^2\Omega R^2\Lambda_{dp}h^3(1-\nu)^2}{\mu^2 b}\right) \tag{6.168}$$

6.3.3.3 Displacement Amplitudes and Acoustic Nonlinearity Parameters

Experimental measurements of the nonlinearity parameters for harmonic generation are commonly performed by measuring the absolute amplitudes of the fundamental and harmonically generated displacements, rather than stress amplitudes. A quantitative measure of the nonlinearity is given by the acoustic nonlinearity parameter $\overline{\beta}$ defined in analogy to Equation 6.40 as

$$\overline{\beta} = 8\frac{C_2'}{k^2 B_1'^2 \overline{X}} \tag{6.169}$$

where B_1' and C_2' are the fundamental and second harmonic displacement amplitudes, respectively.

The displacement amplitudes may be obtained from the stress amplitudes B_1 and C_2 by noting that, to within the same approximation used in our iterative approximation procedure to derive Equation 6.167 and Equation 6.168, we can write

$$\frac{\partial \overline{u}}{\partial t} \approx -\frac{\omega}{kA_{11}}\sigma = -\frac{\omega}{kA_{11}}[\sigma_1 + B_1\cos(\omega t - k\overline{X}) + C_2\sin 2(\omega t - k\overline{X})] \tag{6.170}$$

Integrating Equation 6.170 with respect to time, we obtain the displacement amplitudes

$$B_1' = -\frac{1}{kA_{11}}B_1 = \text{constant} \tag{6.171}$$

and

$$C_2' = \frac{1}{2kA_{11}} C_2 = -\frac{1}{8} k^2 B_1'^2 \overline{X} \left(\frac{\overline{A}_{111}}{\overline{A}_{11}} - \frac{16\pi^2 \Omega R^2 \Lambda_{dp} h^3 (1-\nu)^2 \overline{A}_{11}^2}{\mu^2 b} \right) \quad \textbf{(6.172)}$$

where the last equality in Equation 6.172 follows from Equation 6.168.

The total acoustic nonlinearity parameter $\overline{\beta}$, referred to the unstressed configuration, is obtained by substituting Equation 6.172 into Equation 6.169 to get

$$\overline{\beta} = \overline{\beta}_{lat} + \overline{\beta}_{dp} = -\frac{\overline{A}_{111}}{\overline{A}_{11}} + \frac{16\pi^2 \Omega R^2 \Lambda_{dp} h^3 (1-\nu)^2 \overline{A}_{11}^2}{\mu^2 b} \quad \textbf{(6.173)}$$

The first term on the right-hand side of Equation 6.173 is the lattice contribution $\overline{\beta}_{lat}$ to the total nonlinearity parameter obtained previously, Equation 6.145, and the last term is the contribution $\overline{\beta}_{dp}$ from the dislocation dipoles given by

$$\overline{\beta}_{dp} = \frac{16\pi^2 \Omega R^2 \Lambda_{dp} h^3 (1-\nu)^2 \overline{A}_{11}^2}{\mu^2 b} \quad \textbf{(6.174)}$$

It is important to note that in contrast to dislocation monopoles, the nonlinearity parameter associated with dislocation dipoles does not depend on the applied or residual stresses in the material or on the dislocation loop lengths. $\overline{\beta}_{dp}$ does depend on the third power of the dipole height h.

6.3.4 Harmonic Generation and Metal Fatigue

Cyclic loading in metal fatigue promotes the formation of dislocation dipoles as the result of the mutual trapping of individual dislocations moving to and fro in response to the cyclic stresses. Dipole formation occurs when the encounters between dislocations of opposite polarity become sufficiently close. The dipoles are composed almost exclusively of edge dislocations because screw dislocations are annihilated by cross-slip. With increasing levels of fatigue the dominant dislocation structures formed consist not of arrays of isolated single dislocations monopoles or dipoles, but rather of complex, self-organized substructural arrangements formed from dislocation dipoles and multipoles. The first substructures formed in pure metals are vein structures followed by the formation of persistent slip bands (PSBs) at stress amplitudes corresponding to the saturation stress of the material in strain-controlled loading.

It is instructive to estimate the change in the acoustic nonlinearity parameter resulting from cyclic stressing for highly fatigued aluminum alloy 2024-T4.[22] Measurements in virgin material yield the values $\mu \approx 28.6$ GPa, $\overline{A}_{11} \approx 109$ GPa, and the lattice contribution $\overline{\beta}_{lat} = 4.7$ in Equation 6.173. For high cycle, highly fatigued polycrystalline Al2024-T4, reasonable estimates of the alloy parameters are $h \approx 4$ nm, $b \approx 0.4$ nm, $\Omega = R = 0.33$, and $\nu = 0.33$. If it is assumed that the distribution of dipoles throughout the material in dislocation substructures occupies a total volume fraction of roughly 0.5, then Equation 6.174 yields the value $\overline{\beta}_{dp} \approx 14.8$ for the dipole contribution to the total nonlinearity parameter. The model predicts that the contribution to $\overline{\beta}$ from dislocation dipoles is roughly 3.1 times that from the lattice contribution in highly fatigued material.

Figure 6.9 shows an experimental plot of the value of the total acoustic nonlinearity as a function of the number of fatigue cycles of American Society for Testing and Materials (ASTM) standard dogbone specimens of AA2024-T4 cyclically stressed at a rate of 10 Hz under uniaxial, stress-controlled load from zero stress to 276 MPa.[22] Each specimen was fatigued for a different number of cycles. The maximum measured values of $\overline{\beta}$ are plotted as a function of the number fatigue cycles. The $\overline{\beta}$ parameter is seen to increase monotonically with increasing fatigue cycles, although the increase in the range from 10 to 100 kc is relatively smaller. It is found with single crystal and polycrystalline copper that stress-controlled loading produces a slow but monotonic increase in the volume fraction of persistent slip bands throughout the fatigue life. It is presumed that the range 10 to 100 kc for AA20243-T4 in Figure 6.9 is dominated by the similar growth of persistent

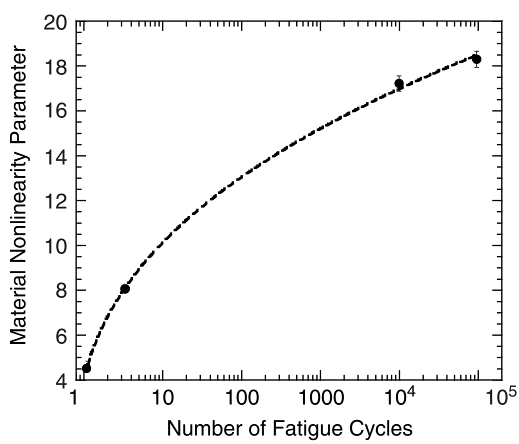

FIGURE 6.9
Total acoustic nonlinearity parameter plotted as a function of the number of fatigue cycles of aluminum alloy 2024-T4. (From Cantrell, J.H. and Yost, W.T., *Int. J. Fatigue*, 23, S487, 2001. With permission.)

slip bands. The value of $\bar{\beta}$ measured at 100 kc of fatigue is roughly three times larger than that obtained for the virgin material, in good agreement with the model prediction of 3.1. These data suggest that the nonlinearity parameter does, indeed, track substructural changes in the material associated with the fatigue process; they also suggest that the origin of the increase in $\bar{\beta}$ is associated with the growth and transformation of dislocation dipole substructures formed in the material during fatigue.

6.3.5 Effects of Precipitation on Ultrasonic Harmonic Generation

One of the principal strengthening and hardening mechanisms of alloys involves the precipitation of secondary phases from a solid solution of material. The presence of secondary phases alters the nonlinear properties of the material in a manner that depends on the volume fraction of secondary phases precipitated in the alloy material. We shall restrict our considerations to compressional waves in quasi-isotropic solids (i.e., solids consisting of randomly oriented grains). For generality the solid is assumed to consist of any number of distinct phases *N*. We assume that the grain orientations are perfectly random (no texture) and that the number such grains contained within a path length of sound is sufficiently large to provide a good statistical sampling for an arbitrary phase *i*. To the extent that such conditions are maintained the value of the effective nonlinearity parameter $\bar{\beta}$ is expected to be independent of grain size.

From Equation 6.138 and Equation 6.145 we write

$$\frac{\partial \bar{u}}{\partial \bar{X}} = \frac{1}{\bar{A}_{11}}\sigma - \frac{1}{2}\frac{\bar{A}_{111}}{\bar{A}_{11}^3}\sigma^2 + \cdots = \frac{1}{\bar{A}_{11}}\sigma + \frac{1}{2}\frac{\bar{\beta}}{\bar{A}_{11}^2}\sigma^2 + \cdots \tag{6.175}$$

We seek the appropriate mixing law for $\bar{\beta}$ that accounts for the effects of the various phases *i*. We define V_0 and ρ_0 to be the initial (unperturbed) volume and mass density, respectively, of the solid. The local transformation from the initial state to the deformed state *V* or ρ is defined through the Jacobian

$$J = \frac{V}{V_0} = \frac{\rho_0}{\rho} \tag{6.176}$$

It is assumed that the volume *V* at any time consists of a number *N* of constituent phases *i* such that

$$V = \sum_{i=1}^{N} V_i \tag{6.177}$$

From Equation 6.176 and Equation 6.177 we get

$$J = \frac{1}{V_0}\sum_i V_i = \frac{1}{V_0}\sum_i J_i (V_0)_i = \sum_i J_i f_i \tag{6.178}$$

where $J_i = V_i/(V_0)_i$ is the Jacobian for phase i and $f_i = (V_0)_i/V_0$ is the volume fraction of phase i. The Jacobian may be written in terms of the displacement gradients $\bar{u}_{ij} = \partial\bar{u}_i/\partial\bar{X}_j$ as

$$J = 1 + \bar{u}_{kk} + \cdots \tag{6.179}$$

Substituting Equation 6.179 into Equation 6.178 yields

$$\bar{u}_{kk} = \sum_i (\bar{u}_{mm})_i f_i \tag{6.180}$$

where in obtaining Equation 6.180 it is assumed that $\Sigma f_i = 1$.

We now assume that for a given phase i the grain orientations are sufficiently random and of sufficiently large number that each phase responds independently as an isotropic structure. Under such conditions we obtain from Equation 6.180 the relationship

$$\frac{\partial\bar{u}}{\partial\bar{\bar{X}}} = \sum_i \left(\frac{\partial\bar{u}}{\partial\bar{\bar{X}}}\right)_i f_i \tag{6.181}$$

in the notation of Equation 6.175 where for each phase i we assume

$$\left(\frac{\partial\bar{u}}{\partial\bar{\bar{X}}}\right)_i = \frac{1}{(\bar{A}_{11})_i}\sigma + \frac{1}{2}\frac{\bar{\beta}_i}{(\bar{A}_{11})_i^2}\sigma^2 + \cdots \tag{6.182}$$

From Equation 6.175, Equation 6.181, and Equation 6.182 and the assumption of local equality of stresses we write

$$\frac{1}{\bar{A}_{11}}\sigma + \frac{1}{2}\frac{\bar{\beta}}{\bar{A}_{11}^2}\sigma^2 = \left(\sum_i (\bar{A}_{11})_i^{-1} f_i\right)\sigma + \frac{1}{2}\left(\sum_i \bar{\beta}_i (\bar{A}_{11})_i^{-2} f_i\right)\sigma^2 \tag{6.183}$$

Equating like powers of σ, we obtain

$$\bar{A}_{11}^{-1} = \sum_i (\bar{A}_{11})_i^{-1} f_i \tag{6.184}$$

and

$$\bar{\beta} = A_{11}^2 \sum_i \bar{\beta}_i (A_{11})_i^{-2} f_i \tag{6.185}$$

Equation 6.184 and Equation 6.195 are general expressions that provide the dependence of the effective Huang coefficient $\bar{A}_{11}$ and the effective nonlinearity parameter $\bar{\beta}$ on the volume fractions of constituent phases making up the material.

We now consider the application of Equation 6.184 and Equation 6.195 to determinations of the effective Huang coefficient and nonlinearity parameter that account for the nominal kinetic aspects of the precipitation process. For simplicity we consider a precipitation process for which the total volume fraction of the second-phase precipitates f_p changes during the precipitation process, but the relative volume fractions of constituent second-phase precipitates for the alloy remain constant. The effective nonlinearity parameter $\bar{\beta}_p$ and the effective second-order Huang coefficient $\left(\bar{A}_{11}^p\right)$ of the second-phase precipitates taken collectively remain unchanged. We may thus rewrite Equation 6.84 and Equation 6.185 in terms of volume fractions of precipitate f_p and solid solution constituents f_i^{ss} as

$$\frac{1}{\bar{A}_{11}} = \frac{1}{\left(\bar{A}_{11}^p\right)} f_p + \sum_i \frac{1}{\left(\bar{A}_{11}^{ss}\right)_i} f_i^{ss} \tag{6.186}$$

and

$$\bar{\beta} = (\bar{A}_{11})^2 \left[\frac{\bar{\beta}_p}{\left(A_{11}^p\right)^2} f_p + \sum_i \frac{\bar{\beta}_i}{\left(A_{11}^{ss}\right)_i^2} f_i^{ss} \right] \tag{6.187}$$

where $(\bar{A}_{11}^{ss})_i$ is an effective second-order Huang coefficient for the *i*-th constituent.

The invariance of the relative volume fractions of second-phase precipitates must come at the expense of the solid solution constituents. It is assumed that the constituents of a solid solution are depleted linearly with increasing volume fraction of precipitates as

$$f_i^{ss} = (f_i^{ss})_0 - e_i f_p \tag{6.188}$$

where f_i^{ss} is the present volume fraction of solid solution constituent i, f_p is the total volume fraction of second-phase precipitates, $(f_i^{ss})_0$ is the volume fraction of constituent i in pure solid solution (i.e., when $f_p = 0$), and e_i is the depletion constant for the *i*-th constituent.

Substituting Equation 6.188 into Equation 6.186 yields

$$\frac{1}{\bar{A}_{11}} = \frac{1}{\left(\bar{A}_{11}^{ss}\right)_0}\left\{1 + f_p\left[\frac{\left(\bar{A}_{11}^{ss}\right)_0}{\left(\bar{A}_{11}^{p}\right)} - \sum_i \frac{\left(\bar{A}_{11}^{ss}\right)_0}{\left(\bar{A}_{11}^{ss}\right)_i} e_i\right]\right\} \tag{6.189}$$

where the effective second-order Huang coefficient for pure solid solution $\left(\bar{A}_{11}^{ss}\right)_0$ is given by

$$\left(\bar{A}_{11}^{ss}\right)_0 = \left(\sum_i \frac{f_i^{ss}}{\left(\bar{A}_{11}^{ss}\right)_i}\right)^{-1} \tag{6.190}$$

Similarly, from Equation 6.187 through Equation 6.189 we find that the effective nonlinearity parameter $\bar{\beta}$ of the solid in terms of total volume fraction of second-phase precipitates f_p is given by

$$\bar{\beta} = \left\{1 + f_p\left[\frac{\left(\bar{A}_{11}^{ss}\right)_0}{\left(\bar{A}_{11}^{p}\right)} - \sum_i \frac{\left(\bar{A}_{11}^{ss}\right)_0}{\left(\bar{A}_{11}^{ss}\right)_i} e_i\right]\right\}^{-2}\left\{\bar{\beta}_0 + f_p\left[\frac{\left(\bar{A}_{11}^{ss}\right)_0^2}{\left(\bar{A}_{11}^{p}\right)^2}\bar{\beta}_p - \sum_i \frac{\left(\bar{A}_{11}^{ss}\right)_0^2}{\left(\bar{A}_{11}^{ss}\right)_i^2}\bar{\beta}_i e_i\right]\right\} \tag{6.191}$$

where

$$\bar{\beta}_0 = \sum_i \frac{\left(\bar{A}_{11}^{ss}\right)_0^2 \bar{\beta}_i}{\left(\bar{A}_{11}^{ss}\right)_i^2}\left(f_i^{ss}\right)_0 \tag{6.192}$$

is the nonlinearity parameter for pure solid solution. For typical values of the various $\bar{A}_{11}$'s and $\bar{\beta}_i$'s the coefficients of the terms containing f_p in Equation 6.191 are estimated to be of order unity. Expanding Equation 6.191 in a power series for small values of f_p and keeping only the linear terms, we obtain

$$\bar{\beta} = \bar{\beta}_0(1 + R_c f_p) \tag{6.193}$$

where the constant

$$R_c = \sum_i \left[\frac{\left(\bar{A}_{11}^{ss}\right)_0}{\left(\bar{A}_{11}^{ss}\right)_i}\left(2 - \frac{\bar{\beta}_i\left(\bar{A}_{11}^{ss}\right)_0}{\bar{\beta}_0\left(\bar{A}_{11}^{ss}\right)_i}\right)e_i\right] - \frac{\left(\bar{A}_{11}^{ss}\right)_0}{\left(\bar{A}_{11}^{p}\right)}\left(2 - \frac{\bar{\beta}_p\left(\bar{A}_{11}^{ss}\right)_0}{\bar{\beta}_0\left(\bar{A}_{11}^{p}\right)}\right) \tag{6.194}$$

Equation 6.193 is a linear approximation to Equation 6.191. A survey of typical values of $(\bar{A}_{11})_i$ and $\bar{\beta}_i$ indicates that Equation 6.193 should be accurate

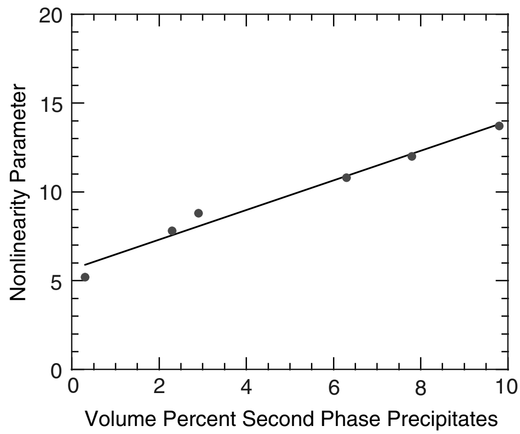

FIGURE 6.10
Measured acoustic nonlinearity parameter of aluminum alloy 7075 plotted as a function of the volume fraction of coarsened second-phase precipitates. (From Cantrell, J.H. et al., *Proc. IEEE Ultrasonics Symposium*, Cat No. 86CH2375-4, Institute of Electrical and Electronic Engineers, New York, 1986, p. 1075. Copyright 1986 IEEE. With permission.)

for most materials to within typical experimental uncertainty for volume fractions as high as approximately 10%. Figure 6.10 shows a graph of the measured acoustic nonlinearity parameter of aluminum alloy 7075 plotted as a function of the volume fraction of coarsened second-phase precipitates.[23] It is seen that the functional dependence is linear as predicted by Equation 6.193.

It must be pointed out that the above results do not account for the effect on the nonlinearity parameter of the interactions of the second-phase precipitates with dislocations that occur in the matrix (i.e., primary phase) of the alloy. Such interactions are minimized when the precipitates are sufficiently large (coarsened) that coherency (one-to-one lattice matching across interfaces) between the precipitates and the matrix material is lost. Coherency loss results in a dramatic decrease in the internal stresses at dislocation sites in the material. Such conditions are termed overaging and result in a loss in overall strength of the alloy. In the above derivation we have treated these materials as initially stress free. Such an assumption appears to be justified by the experimental data for coarsened precipitates.

The dependence of the nonlinearity parameter on the volume fraction of second-phase precipitates for metallic alloys suggests a possible relationship between the nonlinearity parameter and the engineering hardness number (e.g., Brinell hardness, Rockwell hardness, etc.). The reason for this relationship is that the flow resistance of such alloys is dependent on the presence of both coherent and incoherent second-phase material. Measurements of the nonlinearity parameters on 18 Ni Maraging steel as a function of Rockwell-C hardness is shown in Figure 6.11.[24] The strong correlation between

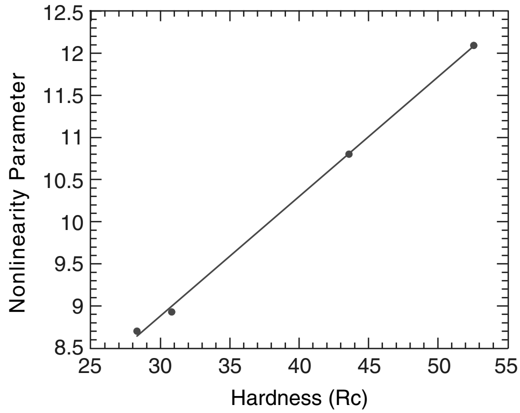

FIGURE 6.11
Measured acoustic nonlinearity parameter of 18 Ni maraging steel plotted as a function of Rockwell-C hardness. (From Yang, H. et al., *Proc. IEEE Ultrasonics Symposium*, Cat No. 87CH2492-7, Institute of Electrical and Electronic Engineers, New York, 1987, p. 1131. Copyright 1987 IEEE. With permission.)

the measured nonlinearity parameters and the engineering hardness number is evident. The physical basis of the engineering hardness parameters is rather different from the hardness parameter of the Born-Mayer potential. However, it is clear from Figure 6.11 that the microstructural properties of the alloys that govern material hardness also govern in large part the magnitude of the nonlinearity parameters.

6.3.6 Effect of Precipitation on Acoustoelastic Constants

The focus of Section 6.3.5 is on the effect on harmonic generation of coarsened second-phase precipitates in alloys. It is also of interest to explore the sensitivity of the acoustoelastic constants to the volume fraction of the second phase following a terminal heat treatment. In steel alloys, carbon in excess of the solubility limit (0.02 wt%) forms iron carbide (cementite) as a second phase that precipitates from (softer) solid-ferrite. A graph of the measured longitudinal mode acoustoelastic constant H_{11} plotted as a function of volume fraction of carbide precipitate (cementite) is shown in Figure 6.12.[25] The acoustoelastic constant increases linearly as the amount of carbide (cementite) phase is increased in the alloy up to a volume fraction of roughly 15%. In this study the amount of carbide phase is calculated using the level rule and the nominal carbon content in the alloy. The constant of proportionality between the relative change of the acoustoelastic constant and the volume fraction of second phase in the steel alloys is obtained from the figure to be approximately equal to 15.3(TPa vol%)$^{-1}$. This means that the acoustoelastic constants in these alloys can be calculated empirically using the values of this quantity in the 100% solid-solution material and the volume fraction of second phase in the alloy.

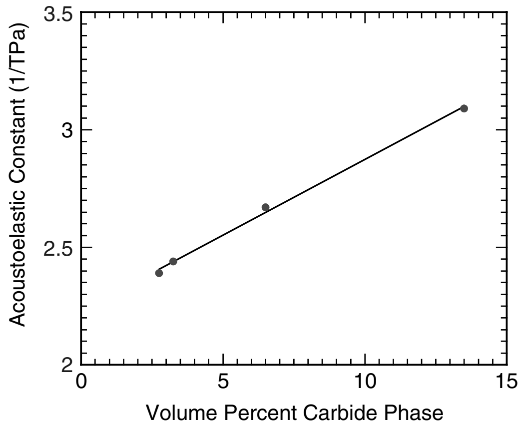

FIGURE 6.12
Measured acoustoelastic constant of steel alloys plotted as a function of volume fraction of carbide (cementite) phase. (From Allison, S. et al., *Proc. IEEE Ultrasonics Symposium*, Cat No. 84CH2112-1, Institute of Electrical and Electronic Engineers, New York, 1984, p. 997. Copyright 1984 IEEE. With permission.)

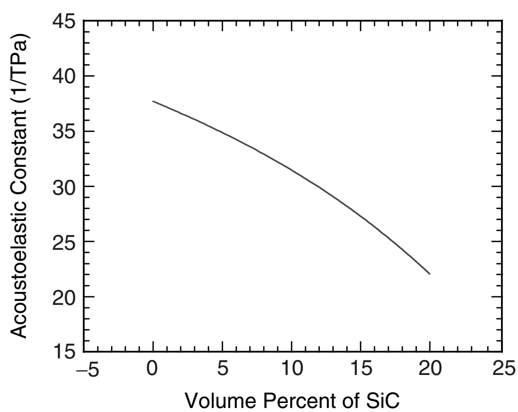

FIGURE 6.13
Longitudinal wave acoustoelastic constant of AA7064 metal matrix composite plotted as a function of embedded SiC particles.

Considerable research effort has been devoted in recent years to the development of metal-matrix composites and more recently of nanocomposites. Metal-matrix composites consist of small particles, typically micron-size or smaller intermetallics or ceramics that are embedded in a metal matrix. The nondestructive characterization of the elastic and nonelastic behavior of such materials is essential to their manufacturing processes. Of particular interest here are the measured values of the acoustoelastic constants as a function of the volume percent of particles embedded in the matrix. Figure 6.13 shows a plot of the measured longitudinal wave acoustoelastic constants for SiC particles embedded in a 7064 aluminum alloy matrix obtained from referenced data.[26] The relationship between the acoustoelastic constant and the percent SiC is seen to be approximately linear up to roughly 10% volume fraction. Thereafter, the curve rapidly becomes nonlinear. The results depicted in Figure 6.12 and Figure 6.13 are somewhat similar to the results predicted by Equation 6.193 for harmonic generation in alloy material as a function of volume fraction of second phase precipitates. This is not particularly surprising because according to Equation 6.129, the acoustoelastic constant for isotropic solids is proportional to the acoustic nonlinearity parameter for such solids.

In general, for a given combination of stress, propagation, and polarization directions, the relationship between the natural sound velocity and stress may be obtained by integrating Equation 6.125 to get

$$\overline{W}(p) = \overline{W}_0 + \overline{W}_0 H_p p \tag{6.195}$$

where $\overline{W}_0 = \overline{W}(0)$ is the natural velocity at zero stress. As suggested by Equation 6.185, unknown stresses can be determined when both the natural velocity in the absence of stress and the acoustoelastic constant are known independently. This approach may be used as a practical method for determining applied and residual stresses in engineering materials. In principle, one could even calculate the acoustoelastic constants from Equation 6.120, Equation 6.121, and Equation 6.125 if the second- and third-order elastic constants are known. Unfortunately, measurements of the third-order elastic constants have been performed mostly on pure materials and some simple alloys. Indeed, the technique mostly used for such measurements have been that of determining the stress dependence of the natural velocity (i.e., the acoustoelastic constant of the material).

It is important to point out here that the measured velocity and stress-dependent velocity changes in engineering materials depend strongly on microstructural features that make it necessary to perform a calibration between velocity and stress (i.e., determine the acoustoelastic constant) for each material in order for the method to be used in the determination of unknown stresses. Microhomogeneity, texture, and weak anisotropy of the material, which are usually neglected in engineering applications of the theory of elasticity, cannot be neglected in the applications of acoustoelasticity. The third-order elastic constants for polycrystalline materials can differ widely, even for alloys having only slightly different compositions. For structural aluminum of slightly different composition, differences as large as 50% are observed.[27]

6.3.7 Harmonic Generation from Precipitate-Dislocation Interactions

The results of Section 6.3.5 are derived for the case of coarsened precipitates and do not account for the effects of the interaction of precipitated second phases

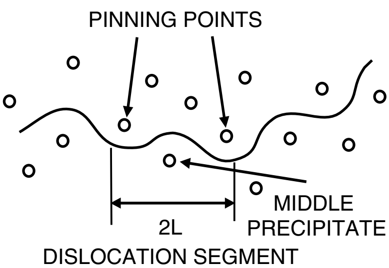

FIGURE 6.14
Bowing of matrix dislocations resulting from the nucleation and growth of coherent precipitates. (From Cantrell, J.H. and Yost, W.T., *Appl. Phys. Lett*., 77, 1952, 2000. With permission.)

with dislocations that occur naturally in the matrix of the alloy. Prior to coarsening, the nucleation and growth of second-phase precipitates in metallic alloys cause dislocations near the precipitates to bow under the action of local precipitate-matrix coherency stresses as illustrated in Figure 6.14.[28] The coherency stresses produce measurable changes in the magnitude of the acoustic nonlinearity parameters that allow a quantitative assessment of precipitation kinetics, as we shall now show.

For ease of calculation it is assumed that the precipitates are spherical, elastically isotropic, and randomly distributed in the matrix. We assume that the bowing of a given dislocation segment of length $2L_0$ involves three precipitates such that the middle precipitate serves to bend the dislocation segment relative to the two end pinning precipitates. For expediency the three precipitates are assumed to be crudely collinear such that a distance L_0 separates adjacent precipitates. The fractional change in the acoustic nonlinearity parameter $\Delta\bar{\beta}/\bar{\beta}_{lat}$ resulting from the application of a stress σ_1 on a pinned dislocation segment of length $2L_0$ is obtained from Equation 6.146 as

$$\frac{\Delta\bar{\beta}}{\bar{\beta}_{lat}} = \frac{24}{5}\frac{\Omega\Lambda_{mp}L_0^4R^3\bar{A}_{11}^2}{\bar{\beta}_{lat}\mu^3b^2}|\sigma_1| \tag{6.196}$$

where $\Delta\bar{\beta} = \bar{\beta}_{total} - \bar{\beta}_{lat} = \bar{\beta}_{mp}$ is the change in the nonlinearity parameter resulting from the nucleation and growth of precipitates. It is assumed in arriving at Equation 6.196 that prior to precipitation the material is stress free, hence $\sigma_1 = 0$, and that nonzero values of σ_1 occur only as the result of coherency stresses from precipitate-matrix misfit.

The radial stress σ_1 in the matrix at a radius r from a spherical precipitate of radius r_1 embedded in a finite body is given by[21,29]

$$\sigma_1 = -\frac{4\mu\delta r_1^3}{r^3} \tag{6.197}$$

where δ is the precipitate-matrix lattice misfit parameter. The misfit parameter is a measure of the amount of atomic spacing (lattice) mismatch at the interface between two adjacent materials. We assume that a given dislocation line roughly follows the contour of the minimum interaction energy between adjacent precipitates and evaluate the stress σ_1 on the dislocation segment at $r = L_0/2$. Substituting Equation 6.197 into Equation 6.196 and evaluating the resulting expression at $r = L_0/2$ yields

$$\frac{\Delta\bar{\beta}}{\bar{\beta}_{lat}} = 154\frac{\Omega\Lambda_{mp}L_0R^3\bar{A}_{11}^2\,|\,\delta\,|\,r_1^3}{\bar{\beta}_{lat}\mu^2b^2} \tag{6.198}$$

Nucleation of a precipitate occurs when a cluster of solute atoms statistically attains a critical radius r_{crit}. The precipitate spacing L_0 in a random particle distribution is determined from the volume fraction of critical nuclei f_n as

$$L_0 = \left(\frac{4\pi}{3}\right)^{1/3}\frac{r_{crit}}{f_n^{1/3}} \tag{6.199}$$

According to Equation 6.197, the stress on a dislocation segment increases as r_1^3, where r_1 is the radius of a growing precipitate. This radius can be related to the volume fraction of precipitate growth by assuming that the volume of growing precipitate $V_g = (4\pi/3)(r_1^3 - r_{crit}^3)$. The volume fraction of precipitate growth is given by $f_g = V_g/L_0^3$. Thus, from Equation 6.199, we obtain

$$r_1 = r_{crit}\left(1+\frac{f_g}{f_n}\right)^{1/3} \tag{6.200}$$

Substituting Equation 6.199 and Equation 6.200 into Equation 6.198 yields

$$\frac{\Delta\bar{\beta}}{\bar{\beta}_{lat}} \approx 248\frac{\Lambda_{mp}\Omega R^3r_{crit}^4\bar{A}_{11}^2\,|\,\delta\,|}{\bar{\beta}_{lat}\mu^2b^2}\left(f_n^{-1/3} + f_n^{-4/3}f_g\right) \tag{6.201}$$

Equation 6.201 shows that the acoustic nonlinearity parameter decreases as the volume fraction of critical nuclei increases, while the parameter increases with precipitate growth. The opposing effects allow independent determinations of precipitate nucleation and growth rates by curve fitting Equation 6.201 to measurements of the nonlinearity parameter taken as a function of alloy heat treatment time. It is convenient to recast Equation 6.201 in terms of heat treatment times. This is accomplished by noting that the time dependencies of the volume fractions of critical nuclei and growing precipitates may be written in the form

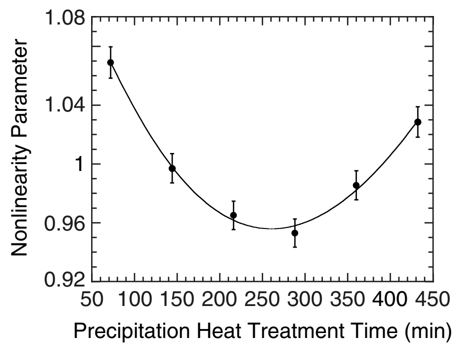

FIGURE 6.15
Normalized acoustic nonlinearity parameter of AA2024 plotted as a function of heat treatment time. (From Cantrell, J.H. and Yost, W.T., *Appl. Phys. Lett.*, 77, 1952, 2000. With permission.)

$$f_i = f_i^0 + k_i(t - t_0)^{m_i} \quad \textbf{(6.202)}$$

where the subscripted i denotes either n for critical nuclei or g for growing precipitates. The number of critical nuclei per unit volume N can be obtained by noting that $N = L_0^{-3}$ and writing from Equation 6.199 and Equation 6.202

$$N = N_0\left[1 + \frac{k_n}{f_n^0}(t - t_0)^{m_n}\right] \quad \textbf{(6.203)}$$

where

$$N_0 = \frac{3f_n^0}{4\pi r_{crit}^3} \quad \textbf{(6.204)}$$

We consider an application of the above model to the assessment of S′ precipitation in aluminum alloy 2024 during artificial aging at 463 K (190°C) from the T4 to the T6 temper. Figure 6.15 shows a graph of the normalized nonlinearity parameter, $(\bar{\beta}_{total}/\bar{\beta}_{lat}) = 1 + (\Delta\bar{\beta}/\bar{\beta}_{lat})$, plotted as a function of heat treatment time.[28] The experimental data, represented by the solid circles, are normalized with respect to the value $\bar{\beta}_{lat}$ of the T4 temper. The minimum in the data corresponds to the point at which the contribution to $\bar{\beta}_{total}$ from the growth of precipitates equals that from nucleation.

The solid curve in Figure 6.15 is a Levenberg-Marquardt curve fit of Equation 6.201 using the functional form in Equation 6.202 for the appropriate volume fractions. The curve fit yields the values $f_n^0 = 7.4 \times 10^{-7}$, $k_n = 7.1 \times 10^{-10}$, and $m_n = 1.0$ for precipitate nucleation. These values indicate a constant nucleation rate of $(dN/dt) = 5.4 \times 10^{15}$ m^{-3}s^{-1} according to Equation 6.203 with $N_0 = 3.4 \times 10^{20}$ m^{-3}. The curve fit also yields the values $f_g^0 = 3.2 \times 10^{-2}$, $k_g =$

3.2×10^{-8}, and $m_g = 2.2$ for the growth of precipitates. The growth rate is calculated from the fractional transformation parameter f defined as $f = f_g / f_g^{max}$ where f_g^{max} is the volume fraction of precipitates at maximum growth. Microscopical examination reveals that $f_g^{max} = 5\%$. Hence, a growth rate (s^{-1}) of $(df/dt) = 2.4 \times 10^{-8} (t - 72)^{1.2}$ is calculated from Equation 6.202. These results are consistent with that expected from rapid early growth of S′ precipitates. Generally, information on the kinetics of phase transformations in alloy systems is obtained from time-sequenced electron microscopical examination and differential scanning microcalorimetry — a labor intensive process. The present results show that acoustic harmonic generation is a useful, time-saving tool that is complementary to the existing methodologies for the characterization of precipitation processes in materials.

6.3.8 Acoustic Nonlinearity from Cracks

The nonlinear interaction of sound waves with cracks or other contacting interfaces has attracted much interest in recent years. Generally, the contacting surfaces are modeled as free,[30] partially clamped or clapping,[31,32] or ideally bonded.[33,34] A model of contact nonlinearity for rough surfaces based on a statistical distribution of asperity heights[35] has been applied to cracks with rough surfaces.[36] We consider the application of the rough surface model to a region of material containing a uniform distribution of cracks.

Consider a boundless isotropic solid containing a uniform distribution of thin penny-shaped cracks of radius R and surface area $\bar{S} = \pi R^2$ in the manner given by Nazarov and Sutin.[36] A typical single crack is depicted in Figure 6.16. The coordinates $\bar{X}_i$ are fixed in the solid. The coordinate system $\bar{X}_i'$ is attached to the crack such that $\bar{X}_3'$ is normal to the crack surface $\bar{S}$. The coordinate $\bar{X}_3'$ makes an angle ϕ with the $\bar{X}_3$-coordinate. The projection of $\bar{X}_3'$ onto the $\bar{X}_1$-$\bar{X}_2$ plane makes the angle θ with the $\bar{X}_2$ coordinate. Let a longitudinal stress $\sigma_{33} = \sigma$ act along the $\bar{X}_3$-coordinate axis. The stress σ produces a longitudinal stress $\sigma'_{33} = \sigma'$ normal to the crack surface given by

$$\sigma' = \sigma \cos^2 \phi \tag{6.205}$$

The stress σ' produces a change in the crack volume ΔV_{crk} that results in a crack-induced strain (displacement gradient) $(d\bar{u}'_{33})_{crk} = d\varepsilon'_{crk}$ in the solid given by

$$d\varepsilon'_{crk} = \Delta V_{crk}(\phi) N_{crk}(\phi, \theta) \sin\phi \, d\phi \, d\theta \tag{6.206}$$

where $N_{crk}(\phi,\theta)$ is the normalized crack distribution function (i.e., the number of cracks per unit volume per unit solid angle). It is assumed that the variation in crack volume ΔV_{crk} is dependent on the stress σ' normal to the

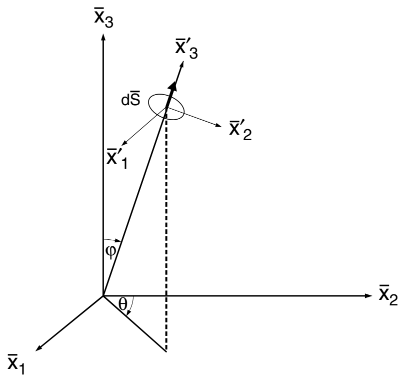

FIGURE 6.16
Coordinate system for a single penny-shaped crack.

crack surface as $\Delta V_{crk} = F(\sigma'/\bar{A}_{11})$ where F is some function. For small variations we may expand ΔV_{crk} in a Taylor series as

$$\Delta V_{crk} = \alpha'\left(\frac{\sigma'}{\bar{A}_{11}}\right) + \frac{\beta'}{2}\left(\frac{\sigma'}{\bar{A}_{11}}\right)^2 + \cdots \quad \textbf{(6.207)}$$

where α′ and β′ are the second- and third-order elastic crack coefficients.

The strain $d\bar{\varepsilon}'_{crk}$ in the $\bar{X}'_i$ coordinate frame may be express as $d\bar{\varepsilon}_{crk}$ in the $\bar{X}_i$ coordinate frame according to the transformation

$$d\bar{\varepsilon}_{crk} = d\bar{\varepsilon}'_{crk}\cos^2\phi \quad \textbf{(6.208)}$$

Integrating Equation 6.208 over all cracks in the solid and substituting Equation 6.205 into the resulting expression yields

$$\bar{\varepsilon}_{crk} = \int_{\theta=0}^{2\pi}\int_{\phi=0}^{\pi/2} N_{crk}(\phi,\theta)\sin\phi\cos^4\phi\left[\alpha'\left(\frac{\sigma}{\bar{A}_{11}}\right) + \frac{\beta'}{2}\left(\frac{\sigma}{\bar{A}_{11}}\right)^2 + \cdots\right]d\phi\, d\theta \quad \textbf{(6.209)}$$

for the strain due to all cracks. The total strain $\bar{\varepsilon} = \bar{\varepsilon}_{lat} + \bar{\varepsilon}_{crk}$. In order to emphasize the nonlinear contribution of the crack to the stress-strain relationship, we consider only the linear contribution from the lattice and write $\bar{\varepsilon}_{lat} = \sigma/\bar{A}_{11}$. Thus, from Equation 6.209 we obtain

$$\bar{\varepsilon} = \bar{\varepsilon}_{lat} + \bar{\varepsilon}_{crk} \approx \frac{1+g_1}{\bar{A}_{11}}\sigma + \frac{g_2}{\bar{A}_{11}^2}\sigma^2 + \cdots \quad \textbf{(6.210)}$$

where

$$g_1 = \alpha' \int_{\theta=0}^{2\pi} \int_{\phi=0}^{\pi/2} N_{crk}(\phi,\theta) \sin\phi \cos^4 \phi d\phi d\theta \quad \textbf{(6.211)}$$

and

$$g_2 = \frac{\beta'}{2} \int_{\theta=0}^{2\pi} \int_{\phi=0}^{\pi/2} N_{crk}(\phi,\theta) \sin\phi \cos^6 \phi d\phi d\theta \quad \textbf{(6.212)}$$

From Equation 6.210) we obtain

$$\sigma \approx \bar{A}_{11}(1+g_1)^{-1}[\bar{\varepsilon} - g_2(1+g_1)^{-2}\bar{\varepsilon}^2 + \cdots] = \bar{A}_{11}(1+g_1)^{-1}\left[\bar{\varepsilon} - \frac{1}{2}\beta_{crk}\bar{\varepsilon}^2 + \cdots\right] \quad \textbf{(6.213)}$$

where

$$\beta_{crk} = 2g_2(1+g_1)^{-2} \quad \textbf{(6.214)}$$

is the acoustic nonlinearity parameter for cracks. For a uniform, completely random distribution of cracks $N_{crk}(\phi,\theta) = N_0^{crk}/2\pi$ where N_0^{crk} = constant. For such a case $g_1 = \alpha' N_0^{crk}/5$ and $g_2 = \beta' N_0^{crk}/14$, and $\beta_{crk} = (\beta' N_0^{crk}/7)[1 + (\alpha' N_0^{crk}/5)]^{-2}$. For sufficiently small crack densities $\beta_{crk} \approx (\beta' N_0^{crk}/7)$. A comparison of experimental measurements of materials with and without cracks allows a determination of β_{crk}. Equation 6.214 may then be used to compare the experimental measurements with analytical crack models. We now consider one such model.

It is assumed that the penny-shaped crack is composed of two rough surfaces, each of area $\bar{S} = \pi R^2$, pressed together in contact from internal stresses from solid material surrounding the crack. The points of contact are dependent on the relative profiles of the contacting surfaces. For analytical expediency the points of contact of the two rough surfaces may be replaced by the points of contact resulting from a plane, rigid surface in contact with a surface having the relative profile of the two rough surfaces prior to contact, as illustrated in Figure 6.17. The plane, rigid surface is denoted by the dotted line. The relative profile is characterized by a distribution function $W(h_{asp})$ of asperities where the height of the asperity h_{asp} is measured from some middle or mean reference line, also shown in Figure 6.17. Hence, $W(h_{asp})dh_{asp}$ is the number of asperities having a height between h_{asp} and $h_{asp} + dh_{asp}$ per unit area of crack surface area measured from the mean reference line. The tops of the asperities are assumed to have one of three possible shapes: (a)

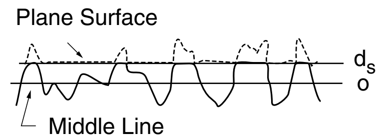

FIGURE 6.17
Illustration of a rough (relative profile) surface in contact with a plane, rigid surface.

a hemisphere of radius r_1; (b) an obtuse cone with apex angle 2ψ; or (c) a cylinder of radius r_1.

When the asperities in the relative profile surface make contact with the rigid, plane surface under an applied stress σ_{appl}, the tops of the asperities are compressed and become planar (i.e., flatten). If the distance between the middle line and the plane surface is d_s under the applied stress σ_{appl}, then all asperities for which $h_{asp} > d_s$ will be flattened. The force required to flatten a given asperity depends on the shape of the asperity and the asperity displacement $\delta_{asp} = h_{asp} - d_s$. The force f necessary to flatten a single asperity is: (a) $f = (2E/3)(1 - \nu^2)^{-1}(r_1\delta_{asp}/2)^{1/2}$ for the hemisphere, (b) $f = (\pi E/2)(1 - \nu^2)^{-1}\,\delta_{asp}^2 \tan\psi$ for the cone, and (c) $f = 2E(1 - \nu^2)^{-1} r_1\delta_{asp}$ for the cylinder. E is Young's modulus.

In equilibrium the applied stress σ_{appl} is balanced by the reactive stress of the asperities σ_{asp} such that

$$\sigma_{appl} + \sigma_{asp} = 0 \tag{6.215}$$

The reactive stress σ_{asp} resulting collectively from the asperities is then

$$\sigma_{asp} = -\int_{d}^{\infty} f(h_{asp} - d_s)W(h_{asp})dh_{asp} \tag{6.216}$$

A commonly used distribution function for cracks is

$$W(h_{asp}) = n(\pi R^2 h_s)\exp(-h_{asp}/h_s) \tag{6.217}$$

where n is the number of asperities in a single crack and $h_s = 2^{1/2}h_0$ where h_0 is the characteristic height of the asperities. Substituting Equation 6.217 into Equation 6.216 yields

$$\sigma_{asp} = -nH_1\exp(-d_s/h_s) \tag{6.218}$$

where (a) $H_1 = (8\pi)^{-1/2}h_s^{3/2}r_1^{1/2}R^{-2}E(1 - \nu^2)^{-1}$ for hemispherical asperities; (b) $H_1 = h_s^2R^{-2}E(1 - \nu^2)^{-1}$ for conical asperities; and (c) $H_1 = 2\pi^{-1}h_s r_1 R^{-2}E(1 - \nu^2)^{-1}$ for cylindrical asperities.

It is assumed that the applied stress is the sum of an internal stress in the material applied normally to the crack surface that tends to close the crack and a perturbative stress σ' resulting, for example, from an acoustic wave. Thus,

$$\sigma_{appl} = \sigma' + \sigma_{mat} \tag{6.219}$$

We now consider an estimate of σ_{mat}.

For a plane crack (i.e., no asperities) the normal displacement $u_{crk}(r)$ of surfaces in response to a stress σ_{open}, tending to open the crack, is

$$u_{crk}(r) = 4(1-\nu^2)(R^2 - r^2)^{1/2}\sigma_{open}/\pi E \tag{6.220}$$

where r is the radial coordinate in the plane of the crack. The volume of the crack V_{crk} is obtained from Equation 6.220 to be

$$V_{crk} = 16(1-\nu^2)R^3\sigma_{open}/3E \tag{6.221}$$

If it is assumed that Equation 6.221 also holds for rough cracks under the stress $\sigma_{mat} = -\sigma_{open}$ tending to close the crack, and that $V_{crk} = \pi R^2 d_s$, then from Equation 6.221 we obtain

$$\sigma_{mat} = -3\pi E d_s/16R(1-\nu^2) \tag{6.222}$$

Equation 6.215, Equation 6.218, Equation 6.219, and Equation 6.222 provide that in the absence of a perturbative stress (i.e., $\sigma' = 0$), the condition of equilibrium yields

$$3\pi E(d_s)_0/16R(1-\nu^2) = -nH_1\exp[-(d_s)_0/h_s] \tag{6.223}$$

where $(d_s)_0$ is the equilibrium distance between the middle line and the plane surface.

In the presence of a perturbative stress σ' the equilibrium conditions are

$$\sigma' = -(\sigma_{mat} + \sigma_{asp}) \tag{6.224}$$

Substituting Equation 6.218 and Equation 6.222 into Equation 6.224 and expansion of the resulting expression in a power series about $(d_s)_0$ yields

$$\frac{\sigma'}{(\sigma_{mat})_0} = \left(1 + \frac{h_s}{d_0}\right)\frac{d_s - (d_s)_0}{h_s} - \frac{1}{2}\left(\frac{d_s - (d_s)_0}{h_s}\right)^2 + \cdots \tag{6.225}$$

where

$$(\sigma_{mat})_0 = 3\pi E(d_s)_0/16R(1-\nu^2) \quad \textbf{(6.226)}$$

Solving Equation 6.225 for $[d_s - (d_s)_0]$ and substituting the resulting expression into the expression $\Delta V_{crk} = \pi R^2[d_s - (d_s)_0]$ for the change in crack volume yields

$$\Delta V_{crk} = \pi R^2[d_s - (d_s)_0]$$

$$= \pi R^2 h_s\left[\left(1+\frac{h_s}{(d_s)_0}\right)^{-1}\left(\frac{\sigma'}{(\sigma_{mat})_0}\right) + \frac{1}{2}\left(1+\frac{h_s}{(d_s)_0}\right)^{-3}\left(\frac{\sigma'}{(\sigma_{mat})_0}\right)^2 + \cdots\right] \quad \textbf{(6.227)}$$

Comparing Equation 6.227 with Equation 6.207 yields the relationship between the elastic crack coefficients (α' and β') and the crack model parameters as

$$\alpha' = \frac{16h_sR^3(1-\nu^2)}{3(d_s)_0}\left(1+\frac{h_s}{(d_s)_0}\right)^{-1} \quad \textbf{(6.228)}$$

and

$$\beta' = \frac{256h_sR^4(1-\nu^2)^2}{9\pi(d_s)_0^2}\left(1+\frac{h_s}{(d_s)_0}\right)^{-3} \quad \textbf{(6.229)}$$

Example Problem 4

What is the acoustic nonlinearity parameter from cracks for a material having a relatively small crack density of 3×10^7 m^{-3}, a crack radius of 10^{-3} m, a crack equilibrium separation of 3×10^{-8} m between the asperity middle line and the plane surface, a characteristic asperity height of 10^{-8} m, and a Poission's ratio of 0.25?

SOLUTION

For these parameters Equation 6.228 yields $\alpha' = 1.2 \times 10^{-9}$ m^3 and Equation 6.229) yields $\beta' = 3.7 \times 10^{-5}$ m^3. Substituting these values of α' and β' into Equation 6.214 gives $\beta_{crk} \approx 156$.

A comparison of these results to the typical lattice contribution to the acoustic nonlinearity parameter is given in Table 6.3 reveals that even in the presence of relatively small crack densities the contribution of cracks to the acoustic nonlinearity parameter can be orders of magnitude larger than the lattice contribution.

6.4 General Measurement Considerations and Conclusion

The emphasis of the present chapter has been on the development of the fundamental principles that link bulk wave nonlinear ultrasonic measurements to the physical origin of many of the most common material nonlinearities. The development generally has been performed assuming an infinite or semi-infinite material to emphasis on the physical basis of the nonlinearity without regard to a specific measurement methodology or technique. The choice of measurement method is to some extent a matter of preference or experience, but the physical dimensions, ultrasonic attenuation, and accessibility of the material to be measured often place limitations on the choice of technique to be used. The most common measurement techniques both for finite amplitude measurements and for acoustoelastic measurements use either toneburst or continuous wave approaches. Page limitations prevent a detailed discussion of the techniques reported in the literature. However, a brief discussion of the salient features of the general methodologies with appropriate references, some of which are reviews, is presented.

Toneburst techniques[37–39] employ the injection of narrowband pulses (usually from a gated continuous wave source) into the material by means of a piezoelectric element (transducer) bonded to the surface of the material to be measured. The determination of the nonlinearity parameter using finite amplitude measurements is made from absolute measurements of the amplitudes of the fundamental and harmonically generated signals. The most commonly used transducer materials for such measurements are lithium niobate and quartz because of their relatively low harmonic distortion, an essential feature for such measurements. Detection of finite amplitude signals are most often made using capacitive (electrostatic ultrasonic) transducers,[37,38,42,43] calibrated piezoelectric transducers,[40,41] and to a lesser extent laser interferometry.[43,44] Tonebrurst approaches are also used in acoustoelastic measurements where variations of the sound velocity are measured as a function of the stress applied to the material.[44,45]

Continuous wave approaches utilize resonance conditions within the bounded material established by the injection of a continuous wave from a transducer attached to the surface. For acoustoelastic measurements continuous wave techniques take maximum advantage of sensitivity enhancement resulting from the superposition of waveforms reflected from the bounding surfaces.[45] A variation of the amplitude of the superposed waveforms also leads to resonant frequency shifts that may be used to assess material nonlinearity parameters.[45,46] Several variations of the continuous wave approach have emerged that utilize dual frequency modulation techniques.[46] Finally, progress in understanding the propagation of nonlinear surface acoustic waves[47,48] has supported the development of corresponding measurement techniques[46] for the determination of surface and near-surface nonlinearities.

References

1. Huang, K., On the atomic theory of elasticity, *Proc. Roy. Soc. London*, A203, 178, 1950.
2. Thurston, R.N., Wave propagation in fluids and normal solids, in *Physical Acoustics*, Vol. 1, Part A, Mason, W.P., Ed., Academic Press, New York, 1964, chap. 1.
3. Wallace, D.C., Thermoelastic theory of stressed crystals and higher-order elastic constants, in *Solid State Physics*, Vol. 25, Ehrenreich, H., Seitz, F., and Turnbull, D., Eds., Academic Press, New York, 1970, p. 301.
4. Holt, A.C. and Ford, J., Theory of ultrasonic pulse measurements of third-order elastic constants for cubic crystals, *J. Appl. Phys.*, 38, 42, 1967.
5. Cantrell, J.H., Crystalline structure and symmetry dependence of acoustic nonlinearity parameters, *J. Appl. Phys.*, 76, 3372, 1994.
6. Thurston, R.N. and Shapiro, M.J., Interpretation of ultrasonic experiments on finite-amplitude waves, *J. Acoust. Soc. Am.*, 41, 1112, 1967.
7. Landau, L.D. and Lifshitz, E.M., *Theory of Elasticity*, Addison-Wesley, Reading, MA, 1959, p. 171.
8. Thuras, A.L. et al., Extraneous frequencies generated in air carrying intense sound waves, *J. Acoust. Soc. Am.*, 6, 17, 1935.
9. Murnaghan, F.D., *Finite Deformation of an Elastic Solid*, Wiley, New York, 1951, p. 27.
10. Brugger, K., Thermodynamic definition of higher order elastic coefficients, *Phys. Rev.*, 133, A1611, 1961.
11. Reif, F., *Fundamentals of Statistical and Thermal Physics*, McGraw-Hill International, Singapore, 1983, p. 153.
12. Thurston, R.N. and Brugger, K., Third-order elastic constants and the velocity of small amplitude elastic waves in homogeneously stressed media, *Phys. Rev.*, 133, A1604, 1964.
13. Hughes, D.S. and Kelly, Second-order elastic deformation of solids, *Phys. Rev.*, 92, 1145, 1953.
14. Bateman, T. et al. Third-order elastic moduli of germanium, *J. Appl. Phys.*, 32, 928, 1961.
15. Hiki, Y. and Granato, A.V., Anharmonicity in noble metals: higher order elastic constants, *Phys. Rev.*, 144, 411, 1966.
16. Salama, K. and Alers, G., Third-order elastic constants of copper a low temperature, *Phys. Rev.*, 161, 673, 1967.
17. Thomas, J.F., Jr., Third-order elastic constants of aluminum, *Phys. Rev.*, 175, 955, 1968.
18. Egle, D.M. and Bray, D.E., Measurement of acoustoelastic and third-order elastic constants for rail steel, *J. Acoust. Soc. Am.*, 60, 741, 1976.
19. Cantrell, J.H., Anharmonic properties of solids from measurements of the stress acoustic constant, *J. Testing Evaluation*, 10, 223, 1982.
20. Hikata, A. et al., Dislocation contribution to the second harmonic generation of ultrasonic waves, *J. Appl. Phys.*, 36, 229, 1965.
21. Hull, D. and Bacon, D.J., *Introduction to Dislocations*, 3rd ed., Pergamon, Oxford, 1984, p. 86.
22. Cantrell, J.H. and Yost, W.T., Nonlinear ultrasonic characterization of fatigue microstructures, *Int. J. Fatigue*, 23, S487, 2001.

23. Cantrell, J.H. et al., Effective nonlinearity parameters of aluminum alloys as a function of volume fraction of second phase precipitates, in *Proc. IEEE Ultrasonics Symposium*, Cat No. 86CH2375-4, Institute of Electrical and Electronic Engineers, New York, 1986, p. 1075.
24. Yang, H. et al., Effect of aging on the third-order elastic moduli of 18Ni maraging steel, in *Proc. IEEE Ultrasonics Symp.*, Cat. No. 87 CH 2492-7, Institute of Electrical and Electronic Engineers, New York, 1987, p. 1131.
25. Allison, S.G. et al., Effect of prestrain upon the acoustoelastic properties of carbon steel, in *Proc. IEEE Ultrasonics Symp.*, Cat. No. 84 CH2112-1, Institute of Electrical and Electronic Engineers, New York, 1984, p. 997.
26. Mohrbacher, H. and Salama, K., Elastic nonlinearity in metal-matrix composites, *Res. Nondestr. Eval.*, 3, 159, 1991.
27. Smith, A.T. et al., Third-order elastic moduli of polycrystalline metals from ultrasonic velocity measurements, *J. Acoust. Soc. Am.*, 40, 1966, p. 1002.
28. Cantrell, J.H. and Yost, W.T., Determination of precipitate nucleation and growth rates from ultrasonic harmonic generation, *Appl. Phys. Lett.*, 77, 1952, 2000.
29. Eringen, A.C., *Mechanics of Continua*, Krieger, Huntington, NY, 1980, p. 219.
30. Solodov, I. Yu., Acoustic nonlinearity of a piezoelectric crystal surface, *J. Appl. Phys.*, 64, 2901, 1988.
31. Richardson, J.M., Harmonic generation at an unbonded interface. I. Planar interface between semi-infinite media, *Intn'l J. Eng. Sci.*, 17, 73, 1979.
32. Len, K.S. et al., Experimental observation of the influence of contact nonlinearity on the reflection of bulk acoustic waves and propagation of surface acoustic waves, *Sov. Phys. Acoust.*, 37, 610, 1991.
33. Zhou, S. and Shui, Y., Nonlinear reflection of bulk acoustic waves at an interface, *J. Appl. Phys.*, 72, 5070, 1992.
34. Zhou, S. et al., Nonlinear bulk acoustic waves in anisotropic solids: Propagation, generation, and reflection, *J. Appl. Phys.*, 78, 39, 1995.
35. Rudenko, O.V. and Wu, C., Nonlinear properties of rough surface contact and acousto-diagnostic of a roughness height distribution, *Acoust. Phy.*, 40, 1994.
36. Nazarov,V. E. and Sutin, A M., Nonlinear elastic constants of solids with cracks, *J. Acoust. Soc. Am.*, 102, 3349, 1997.
37. Gauster, W.B. and Breazeale, M.A., Ultrasonic measurements of the nonlinearity parameters of copper single crystals, *Phys. Rev.*, 168, 655, 1968.
38. Cantrell, J.H. and Salama, K., Acoustoelastic characterization of materials, *Int. Mat. Rev.*, 36, 125,1991.
39. Yost, W.T. and Cantrell, J.H., Absolute ultrasonic displacement amplitude measurements with a submersible electrostatic acoustic transducer, *Rev. Sci. Instrum.*, 63, 4182, 1992.
40. Dace, G.E. et al., Nonlinear acoustics. A technique to determine microstructural changes in materials, in *Review of Progress in Quantitative Nondestructive Evaluation*, Vol. 10B, Thompson, D.O. and Chimenti, D.E., Eds., Plenum, New York, 1991, p. 1685.
41. Hurley, D. et al., A comparison of three techniques to determine the nonlinear ultrasonic parameter b, in *Review of Progress in Quantitative Nondestructive Evaluation*, Vol. 16, Thompson, D.O. and Chimenti, D.E., Eds., Plenum, New York, 1997, p. 1383.
42. Moreau, A., Detection of acoustic second harmonic in solids using heterodyne laser interferometer, *J. Acoust. Soc. Am.*, 98, 2745, 1995.

43. Cantrell, J. H., Ultrasonics, in *Encyclopedia of Applied Physics*, Vol. 22, Trigg, G.L., Ed., Wiley-VCH Verlag, 1998, p. 495.
44. Yost, W.T. et al., Fundamental aspects of pulse phase-locked loop technology-based methods for measurement of ultrasonic velocity, *J. Acoust. Soc. Am.*, 91, 1456, 1992.
45. Bolef, D.I. and Miller, J.G., High-frequency continuous wave ultrasonics, in *Physical Acoustics*, Vol. VIII, Mason, W.P. and Thurston, R.N., Eds., Academic, New York, 1964, chap. 3.
46. Zheng, Y. et al., Nonlinear acoustic applications for material characterization: a review, *Can. J. Phys.*, 77, 927, 1999.
47. Shui, Y. and Solodov, I.Yu., Nonlinear properties of Rayleigh and Stonely waves, *J. Appl. Phys.*, 64, 6155, 1988.
48. Skull, D.J. et al., Harmonic generation in plane and cylindrical nonlinear Rayleigh waves, *J. Acoust. Soc. Am.*, 94, 418, 1993.

7

Theory and Applications of Laser-Ultrasonic Techniques

Sridhar Krishnaswamy

CONTENTS

0-8493-1462-3/02/$0.00+$1.50

7.1 Introduction

Laser ultrasonics deals with the generation and detection of ultrasound in a solid, liquid, or gaseous medium using laser light. Typically, the technique uses modulated laser irradiation to induce ultrasound by either ablating the medium or using rapid thermal expansion. The resulting ultrasonic wave packets are also typically measured using optical probes. Laser ultrasonics therefore provides a noncontact way of carrying out ultrasonic interrogation of a medium to provide information about its properties.

Laser ultrasonic measurement systems are particularly attractive to nondestructive structural and materials characterization of solids because:

1. They are noncontact, leading to increased speed of inspection.
2. They can be nondestructive if the optical power is kept sufficiently small.
3. They can be used for *in situ* measurements in an industrial setting.
4. They are couplant independent (unlike contact acoustic microscopy techniques), providing absolute measurements of ultrasonic wave displacements.
5. They have a very small footprint and can be operated on curved complex surfaces.
6. They are broadband systems providing information from the kHz to the GHz range, enabling the probing of macrostructures to very thin films.

Laser ultrasonics does have its drawbacks. In particular, optical detection techniques generally offer lower sensitivity than contact piezoelectric transducers. Laser ultrasonic systems are also relatively more expensive than other conventional ultrasonic techniques. Laser ultrasonic techniques are of interest only for certain special applications.

In this chapter, the basics of laser ultrasonics primarily as they relate to nondestructive characterization of solid materials are discussed. In Section 7.2, the basic process of laser generation of ultrasound is briefly described. The major techniques of optical detection of ultrasound are then addressed in Section 7.3. Section 7.4 is devoted to recent applications of laser ultrasonics. It must be mentioned that this chapter is not intended to be a comprehensive review of laser ultrasonics. Rather, the focus here is to describe the basic principles involved and to provide illustrative applications that take specific advantage of some of the unique features of the technique. For a more comprehensive discussion of the principles of laser ultrasonics, the reader is referred to the books by Scruby and Drain (1990) and Gusev and Karabutov (1993), as well as several excellent review articles on laser generation of ultrasound (Hutchins, 1988) and optical detection of ultrasound (Monchalin, 1986; Wagner, 1990; and Dewhurst and Shan, 1999).

7.2 Laser Generation of Ultrasound

Laser generation of ultrasound was first demonstrated by White (1963). Since then, lasers have been used to generate ultrasound in solids, liquids, and gases for a number of applications. A comprehensive review of laser generation of ultrasound is given in Hutchins (1988) and Scruby and Drain (1990). Here we will restrict attention to the generation of ultrasound in solids using pulsed lasers.

7.2.1 Generation Mechanisms

The dominant mechanisms involved in laser generation of ultrasound in a solid are easy to outline. A pulsed laser beam impinges on a material and is partially absorbed by it. The optical power that is absorbed by the material is converted to heat, leading to rapid localized temperature increase. This results in rapid thermal expansion of a local region, which leads to generation of ultrasound into the medium. If the optical power is kept sufficiently low enough that the material does not melt and ablate, the generation regime is called thermoelastic (see Figure 7.1a). If the optical power is high enough to lead to melting of the material and plasma formation, once again ultrasound is generated, but in this case via momentum transfer due to material ejection (see Figure 7.1b). The ablative regime of generation is typically not acceptable

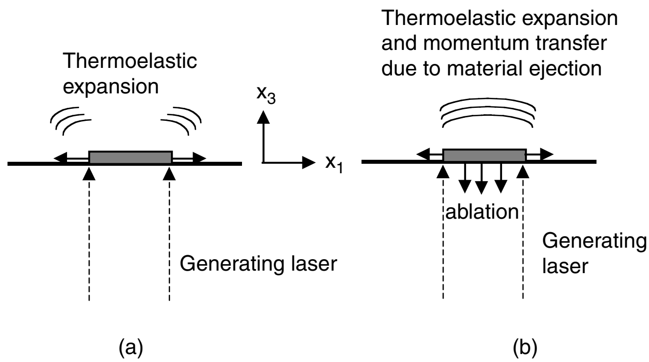

FIGURE 7.1
Laser generation of ultrasound in (a) thermoelastic regime and (b) ablative regime.

for nondestructive characterization of materials. However, it is useful in some process-monitoring applications, especially since it produces strong bulk wave generation normal to the surface. In some cases where a strong ultrasonic signal is needed but ablation is unacceptable, a sacrificial layer (typically a coating or a fluid) is used either unconstrained on the surface of the test medium or constrained between the medium and an optically transparent plate. The sacrificial layer is then ablated by the laser, again leading to strong ultrasound generation in the medium due to momentum transfer.

It is important to characterize the ultrasound generated by laser heating of a material in order to determine the amplitude, frequency content, and directivity of the ultrasound generated. If the material ablates, the ultrasound that results from momentum transfer can be modeled as arising from a normal impulsive force applied to the surface. Analytical solutions to this problem can be obtained by appropriate temporal and spatial convolution of the elastodynamic solution for a point impulsive force on a half-space (Achenbach, 1973). Recently, a complete model of ultrasound generation in the ablative regime was given by Murray et al. (1999). As ablative generation is typically not used in nondestructive evaluation, we will not explore this further here.

For thermoelastic generation on materials such as metals where the optical energy is absorbed in a very thin layer on the surface, Scruby et al. (1980) have argued that the relevant elastodynamic problem is that of shear dipoles acting on the surface of the body. Their argument was based on the consideration that a point expansion source in the interior of a solid can be modeled as three mutually orthogonal dipoles (Achenbach, 1973), and this degenerates into a pair of orthogonal dipoles as the expansion source moves to a free surface (see Figure 7.1a). This approach was given a rigorous basis in the form of a surface center of expansion (SCOE) model proposed by Rose (1984). A full thermoelastic model was subsequently developed by McDonald (1989) and further developed by Spicer (1991). This model predicts all the major features that have been observed in thermoelastic generation, and we will consider it in greater detail.

7.2.2 Thermoelastic Generation of Ultrasound

For simplicity a fully decoupled linear analysis for homogeneous, isotropic materials is considered. The basic problem of thermoelastic generation of ultrasound can be decomposed into three subproblems: (1) electromagnetic energy absorption by the medium, (2) the consequent thermal diffusion problem with heat sources (due to the electromagnetic energy absorbed), (3) the resulting elastodynamic problem with volumetric sources (due to thermal expansion). The analysis is *decoupled* and *linear* in that electromagnetic energy absorption is assumed not to change the thermal, elastic, or electromagnetic properties; the temperature increase is assumed not to change the elastic, electromagnetic, or thermal properties; and the mechanical deformation is assumed not to alter the thermal profile of the material.

The optical energy that is absorbed depends on the wavelength of the laser light and the properties of the absorbing material. The optical intensity variation with depth inside an absorbing medium that is illuminated by a light beam at normal incidence (see Figure 7.1) is given by an exponential decay relation

$$I(x_1, x_2, x_3, t) = I_o(x_1, x_2, t)\exp[-\gamma x_3] \quad \textbf{(7.1)}$$

where $I_o(x_1, x_2, t)$ is the incident intensity distribution at the surface (which is a function of the laser parameters) and γ is an absorption coefficient characteristic of the material for the given wavelength of light. For most metallic materials, the absorption coefficient is high enough that the optical energy does not penetrate very much into the material. The optical penetration depth defined as $1/\gamma$ is on the order of a few nanometers for most metals over the optical wavelengths typically used for laser generation of ultrasound. The wavelength of the ultrasound generated using typical nanosecond laser pulses is much larger than this, and therefore the surface shear dipole model of Scruby et al. (1980) is appropriate in this case. For polymeric materials such as epoxy or for semiconductor materials, the optical penetration depth can be much larger, and the problem has to be treated as one of volumetric expansion sources distributed into the bulk of the material.

The optical energy absorbed by the material leads to a distributed heat source in the material given by

$$q(x_1, x_2, x_3, t) = q_o(x_1, x_2, t)\gamma\exp[-\gamma x_3] \quad \textbf{(7.2)}$$

where q_o is proportional to I_o and has the same spatial and temporal characteristics as the incident laser source. The corresponding thermal problem is then solved for the given thermal source distribution using the equations of heat conduction. For numerical convenience, McDonald (1989) and Spicer (1991) use the hyperbolic heat conduction equation

$$\frac{\kappa}{c_{th}^2}\frac{\partial^2 T}{\partial t^2}+\rho C\frac{\partial T}{\partial t}=\kappa\nabla^2 T+q \tag{7.3}$$

where T is the temperature, ρ is the material density, C is heat capacity, κ is the thermal diffusivity, and c_{th} is the thermal wave speed usually taken as equal to the longitudinal wave speed. It has been argued that the hyperbolic heat conduction considerably simplifies the numerical calculations and, for the ultrasonic time scales of interest, it provides essentially indistinguishable results from those obtained using the more classical parabolic heat conduction equation. The necessary thermal boundary conditions arise from the fact that there is no heat flux across the surface, and initially the medium is at uniform temperature.

The temperature distribution can be calculated for a given laser source and material by solving the heat conduction equation (Equation 7.3). For insulators, heat conduction may be neglected and the resulting adiabatic temperature rise is readily obtained by setting $\kappa \to 0$ in this equation. For most metals, heat diffusion can be significant and needs to be taken into account by solving the full heat conduction equation.

The temperature rise from the laser energy absorbed leads to a volumetric expansion source given by

$$\phi_T=\frac{3\lambda+2\mu}{\lambda+2\mu}\alpha_T T \tag{7.4}$$

where α_T is the coefficient of linear thermal expansion, and λ and μ are the Lame elastic constants of the material. The elastodynamic equations in terms of the scalar and vector displacement potentials, including the volumetric expansion source, then becomes

$$\begin{aligned}\nabla^2\phi-\frac{1}{c_P^2}\ddot{\phi}&=\phi_T\\ \nabla^2\underline{\psi}-\frac{1}{c_S^2}\ddot{\underline{\psi}}&=0\end{aligned} \tag{7.5}$$

where ϕ and ψ are the scalar and vector potentials respectively; and c_P and c_S are the longitudinal and shear wave speeds of the material, respectively; and superposed dot indicates time differentiation. The above elastodynamic equations need to be solved along with the boundary conditions that the surface tractions vanish. The elastic displacement field **u** is then obtained from

$$\mathrm{u}=\underline{\nabla}\phi+\underline{\nabla}\times\underline{\psi} \tag{7.6}$$

Given the laser source parameters, the resulting temperature and elastodynamic fields are obtained from the above system of equations using transform techniques (McDonald, 1989; Spicer, 1991). The heat conduction and the elastodynamic equations are transformed using one-sided Laplace transform in time, and either a Fourier (for a line source) or Hankel (for a point source) transform in space. Closed-form solutions can be obtained analytically in the transformed domain and numerically inverted back into the physical domain (McDonald, 1989; Spicer, 1991; Arias, 2003).

If the optical penetration depth is very small (i.e., $\gamma \to \infty$), and the laser beam is assumed to be focused into an infinitely long line along the x_1-direction, with a delta function temporal dependence, the resulting heat source simplifies to

$$q(x_1, x_2, x_3, t) = Q_o \delta(x_1)\delta(x_3)\delta(t) \tag{7.7}$$

where Q_o is the strength of the heat source proportional to the laser energy input. If thermal diffusion is also neglected, the resulting simplified problem can be explicitly solved (McDonald, 1989; Arias, 2003). It is then possible to obtain the corresponding in-plane stresses (Arias, 2003)

$$\sigma_{31} = D\delta'(x_1)H(t) \tag{7.8}$$

where prime indicates differentiation with respect to the argument, and $H(t)$ is the Heaviside step function. The above indicates that the shear dipole model of Scruby et al. (1980) is indeed valid in this limit of no thermal diffusion and no optical penetration. The dipole magnitude D is given by (Arias, 2003)

$$D = \frac{2\mu}{\lambda + 2\mu}(3\lambda + 2\mu)\frac{\alpha_T Q_o}{\rho C} \tag{7.9}$$

Solutions to the more general case where the temporal and spatial characteristics are more typical of real laser pulses can be readily obtained from the above solution using a convolution over space and time. If optical penetration depth is significant or if thermal diffusion is important, solutions to the complete system of equations will have to be obtained numerically (Spicer, 1991; Arias, 2003).

7.2.2.1 Directivity of Bulk Wave Generation

Figure 7.2 shows the surface normal displacement at the epicentral location generated by a point-focused thermoelastic source and measured using a homodyne interferometer (described in Section 7.3). The arrival of a longi-

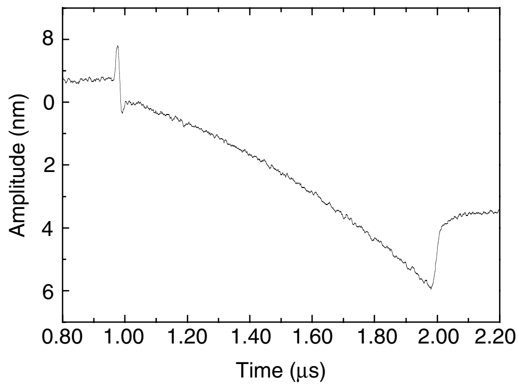

FIGURE 7.2
Experimentally measured epicentral surface normal displacement.

tudinal wave is distinctly seen, followed by a slowly increasing wash, until the shear wave arrives. The initial positive going precursor pulse has been attributed to thermal diffusion, and should disappear in the limit that diffusion is neglected (Doyle, 1986).

The directivity (i.e., the wave amplitude at different angles to the surface normal) of longitudinal and shear waves generated by a thermoelastic source has been calculated theoretically and measured experimentally by a number of researchers (Scruby and Drain, 1990). The longitudinal and shear wave directivity using a shear dipole model for the thermoelastic laser source has been obtained using a mass-spring lattice elastodynamic calculation (Sohn and Krishnaswamy, 2003). These are shown in Figure 7.3. It is seen that for thermoelastic generation, longitudinal waves are most efficiently generated in directions that are at an angle to the surface normal. Epicentral longitudinal waves are much weaker. These are consistent with the results of other models and experiments (Hutchins et al., 1981). The exception is that some of the theoretical models do not predict the surface-skimming longitudinal waves along the surface that are observed in the experiments.

7.2.2.2 Rayleigh Wave Generation

Rayleigh waves that propagate on the surface of a thick solid are widely used in ultrasonic nondestructive characterization of structures (Viktorov, 1967). Thermoelastic generation of Rayleigh waves has therefore been extensively studied (Scruby and Drain, 1990). Figure 7.4a shows the theoretically calculated surface displacements in the far field of a thermoelastic point source. A strong bipolar Rayleigh wave is seen to be generated by the thermoelastic source. Shown in Figure 7.4b are measurements of the far-field surface normal displacement made using a homodyne inteferometer (discussed in Section 7.3). If the laser source is a line source rather than a point-

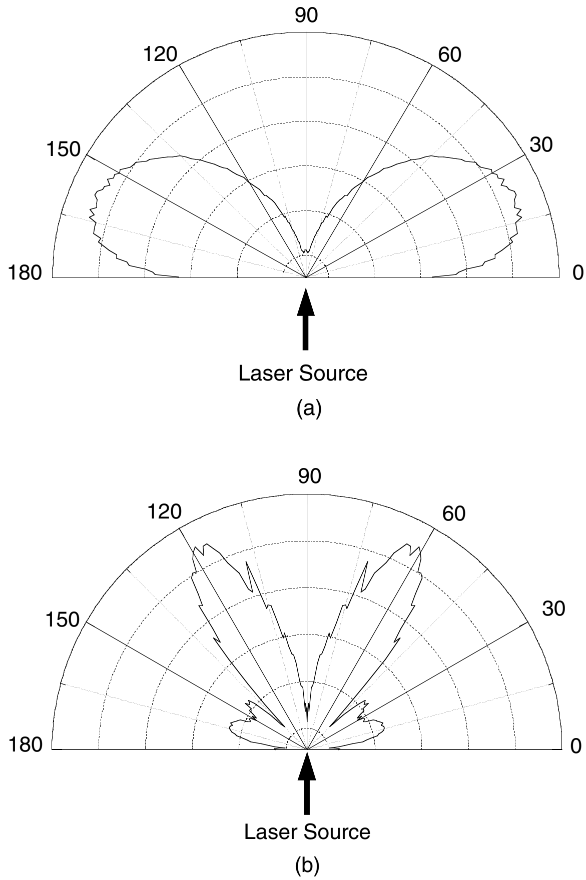

FIGURE 7.3
Calculated directivity pattern of thermoelastic laser generated ultrasound: (a) longitudinal waves, (b) shear waves. (From Sohn, Y. and Krishnaswamy, S., personal communication, 2003. With permission.)

focused source, the Rayleigh wave becomes a monopolar pulse as shown both theoretically and experimentally in Figure 7.5 (Sohn and Krishnaswamy, 2003).

7.2.2.3 Lamb Wave Generation

It is well known from Lamb wave theory that ultrasonic wave propagation in a plate consists of different propagating guided wave modes that are dispersive (Viktorov, 1967; Achenbach, 1973). Thermoelastic Lamb wave generation in thin plates has been experimentally studied by Dewhurst et al. (1987), and has been modeled by Spicer et al. (1990). Figure 7.6 shows the Lamb waves that are generated by a single thermoelastic line source on a thin aluminum plate. The detection system used was a broadband multiplexed

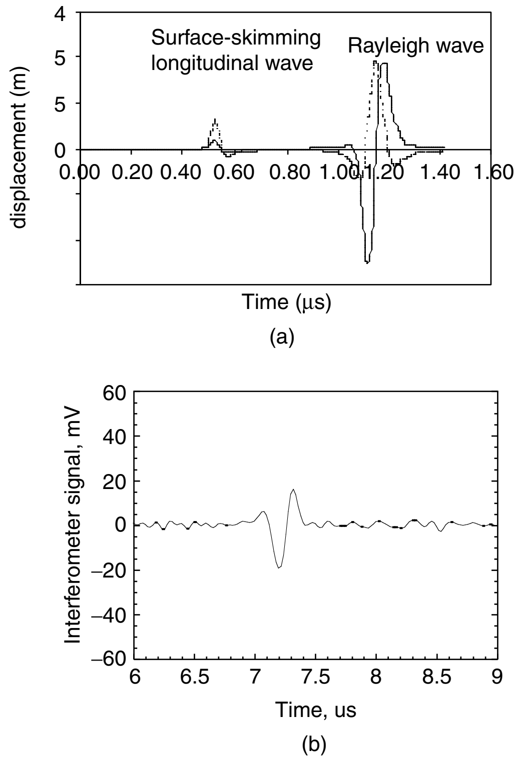

FIGURE 7.4
Rayleigh wave generation: (a) Theoretical calculations of the surface normal (solid) and horizontal (dotted) displacements, (b) experimental results for surface normal displacements. (From Sohn, Y. and Krishnaswamy, S., personal communication, 2003. With permission.)

two-wave mixing interferometer (Section 7.3). The figure shows the surface ultrasonic displacement at different source-to-receiver distances, demonstrating the dispersive nature of the wave propagation.

7.2.2.4 Guided-Wave Generation in Multilayered Structures

Thermoelastic generation of ultrasound on multilayered structures has also been demonstrated, motivated by potential applications to the characterization of coatings. In these cases, again the various guided modes are generally dispersive. Murray and Wagner (1999) have performed comparisons of theoretical and experimental signals in layered structures on a substrate. High frequency ultrasonic guided waves were generated with a miniature Nd:YAG laser with a 1-nsec pulse width and 3 μJ per pulse, focused down to a point source of about 40 μm diameter (Figure 7.7). Figure 7.7b shows the ultrasonic surface displacements measured using a broadband stabilized Michelson interferometer (described in Section 7.3) at a distance of 1.5 mm

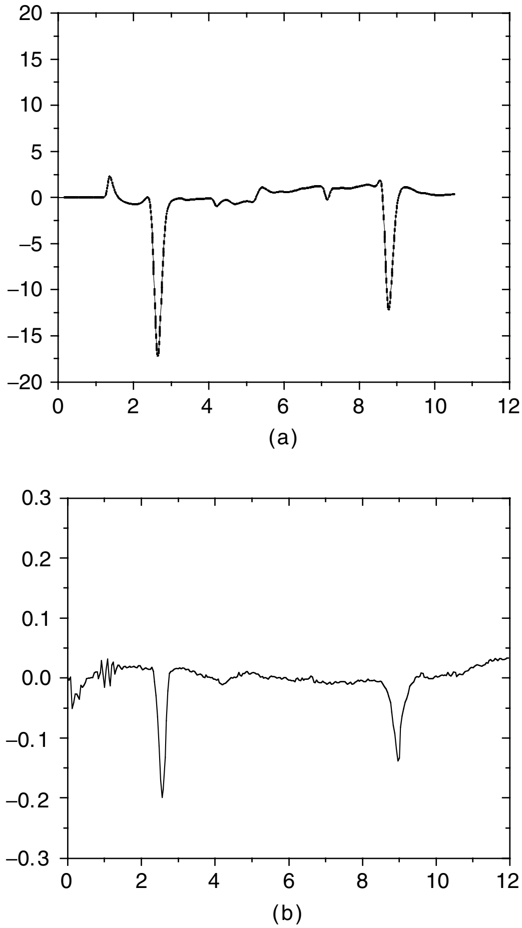

FIGURE 7.5
Surface normal displacement showing monopolar Rayleigh wave from a thermoelastic line source: (a) theoretical, (b) experimental (From Sohn et al., 2003).

from the laser source. The specimen was a 2.2-μm Ti coating on aluminum. Also, shown in Figure 7.7c are the theoretically expected signals using the thermoelastic model described above appropriately extended for the two-layer case. It is seen that the thermoelastic model adequately captures the experimental behavior.

7.2.2.5 Array of Sources

Several systems have been demonstrated for the generation of ultrasound at an array of points or lines on a test object. The development of these systems has been primarily motivated by the fact that the maximum ultra-

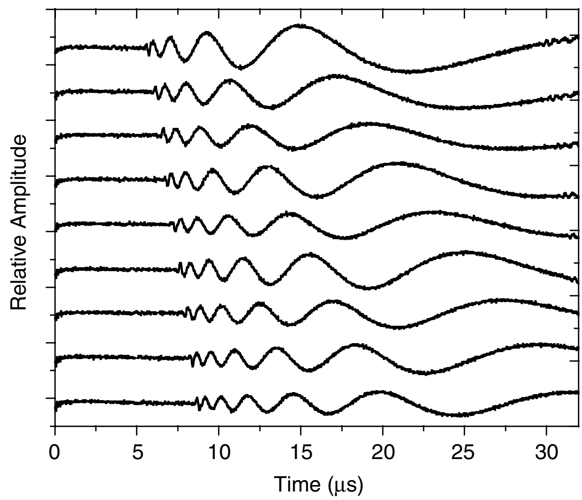

FIGURE 7.6
Thermoelastically generated Lamb waves in a thin aluminum plate. The surface normal displacements at several distances from the generating source are shown.

sonic signal amplitude that can be generated by a single laser source is limited by the damage threshold of the material under inspection. By distributing the laser energy in both time and space, the generated acoustic signals can be focused at the desired location, the acoustic signal bandwidth can be narrowed, and the signal-to-noise ratio (SNR) of laser ultrasonic systems can be improved. Techniques developed to create laser pulses that are spatially and temporally modulated for use in laser ultrasonic phased array generation systems include multiple laser heads (Noroy et al., 1993; Murray et al., 1996), optical fiber arrays (Yang et al., 1993), and free space optical delay lines based on a White cell configuration (Steckenrider et al., 1995). Systems such as these require the ability to pulse the different array elements at different times. As these systems are either very expensive or do not provide sufficient flexibility for timing the pulses, they have remained primarily laboratory devices.

Array generation of surface acoustic waves in blocks, plates, and layered media has met with greater success because they only require a spatial distribution of the laser generation source. A number of schemes have been proposed for generating narrowband surface acoustic waves. These include using illumination through periodic surface masks (Royer et al., 1984), repetitive illumination by a lenticular array (Wagner et al., 1990), optical-fiber-guided laser arrays (Jarzynski et al., 1989), and holographic diffraction gratings (Huang et al., 1992). In all these cases, the generating laser source is a periodic array of spacing ‘d’. The wave number of the waves that will constructively build up at any point on the surface is determined by the spacing ‘d’.

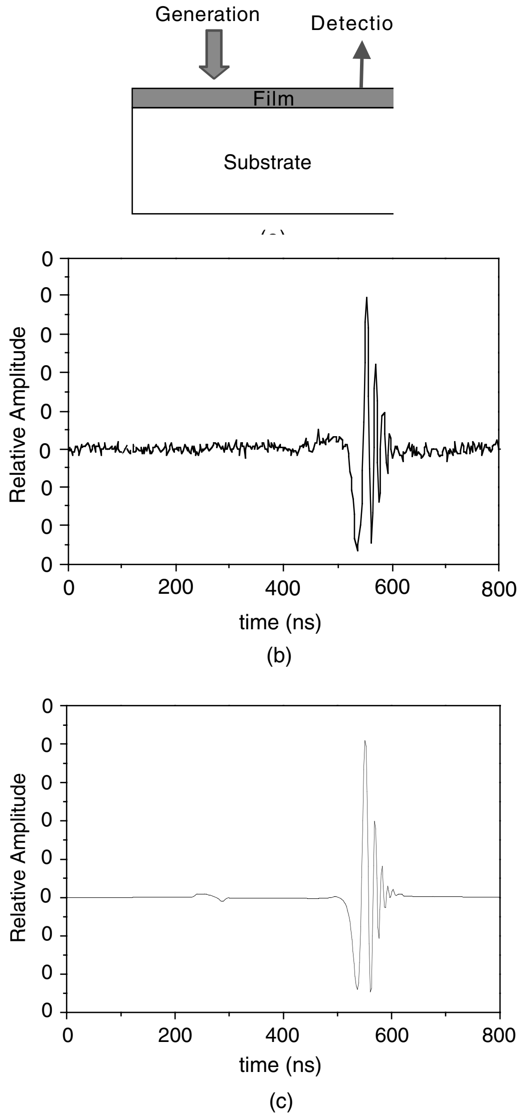

FIGURE 7.7
(a) Schematic of thermoelastic generation on a 2.2-µm Ti thin film coating on an aluminum substrate. Surface normal displacement at a distance of 1.5 mm.(b) measured experimental and (c) predicted by the theoretical model.

The scheme of Huang et al. (1992) is shown in Figure 7.8a. A line array of essentially identical laser pulses is formed by line-focusing an Nd:YAG laser beam using cylindrical lenses, and then diffracting the line beam into an array of lines using a holographic diffraction grating, prior to focusing on the specimen. By adjusting the spacing and line width of the array, a tone-burst-like acoustic wave of the desired frequency can be generated. The signal detected using a broadband heterodyne interferometer (see Section 7.3) and its spectrum are shown in Figure 7.8b and Figure 7.8c. Also shown in Figure 7.8c is the spectrum of the broadband signal generated by a single line of zeroth order from the line array. It can be seen that a significant bandwidth reduction has been achieved. This method allows for tuning the surface acoustic wave (SAW) frequency by varying the line spacing and line width by adjusting the distances between the lenses and the specimen.

To provide narrowband generation at very high frequencies (needed for testing thin films and coatings), the wave number and the array spacing has to be very small. In this case, a simpler approach is to create an optical intensity grating by interfering two crossed laser beams both obtained from the same generating laser source (Nelson et al., 1982). Figure 7.9a shows a schematic of the setup. In this case, the interference grating pitch determines the wave number and is given by the wavelength of the generating laser and the angle between the crossed beams. The latter can be adjusted to provide tunable narrowband generation. Figure 7.9b and Figure 7.9c show the surface ultrasonic displacement and its spectrum as measured by a balanced broadband homodyne interferometer (see Section 7.3).

7.2.3 Types of Lasers Used for Generation

Selecting the type of laser to use depends on the material in which the ultrasound is to be generated, and the desired frequency content of the ultrasound. The main parameters of the generating laser are its wavelength, energy, pulse duration, and repetition rate. The repeti tion rate is important for speed of testing. The pulse duration plays a significant role in the frequency content of the ultrasound generated (other parameters such as spatial extent also affect the frequency content). A modulated continuous wave laser is possibly adequate for low-frequency (order of tens of kHz) generation. Typically, laser pulses on the order of 10 nsec are used for generation of ultrasound in the order of 10-Mhz frequency range. For even higher frequencies, pulse widths on the order of 100 psec (resulting in ultrasound in the order of 100-MHz frequency range) or even femtosecond (for GHz range) laser systems may be necessary.

The optical power depends on the material to be tested and whether laser damage is acceptable or not. Lasers with optical power ranging from nanojoules to microjoules to several hundred millijoules have all been used to produce ultrasound in structures.

Finally, the choice of laser wavelength primarily depends on the material absorption. Laser wavelengths ranging from the ultraviolet to the infrared and higher have been used for laser generation of ultrasound.

7.3 Optical Detection of Ultrasound

Optical detection of ultrasound is attractive because it is noncontact, with high detection bandwidth (unlike resonant PZT transducers), and it can

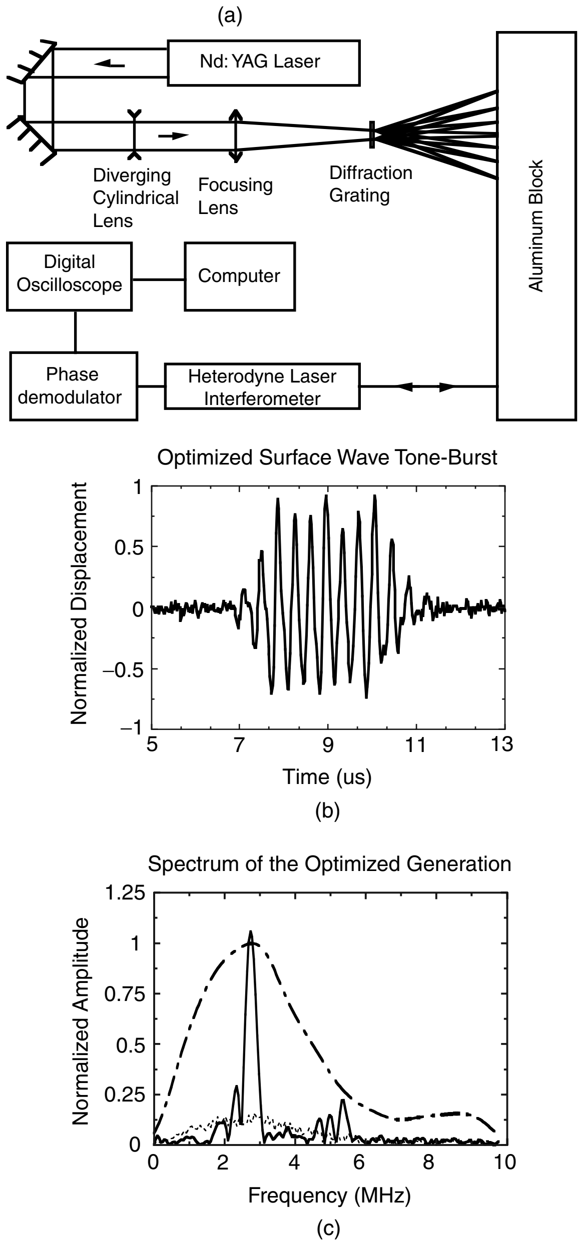

FIGURE 7.8
(a) Schematic of a laser ultrasonic system for narrowband generation of surface acoustic waves. (b) Narrowband signal and (c) its spectra (solid line). Also shown is the spectrum of the Rayleigh wave generated by a single line source (as measured: dots; smoothed and scaled: dashed line).

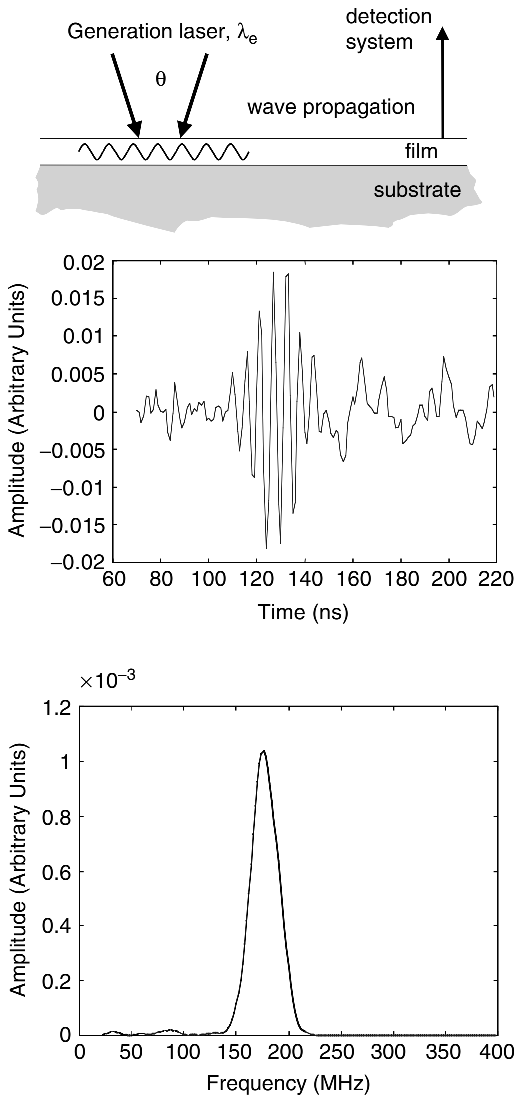

FIGURE 7.9
Crossed beam interference for narrowband generation of high frequency surface acoustic waves. Time-domain signal of a narrowband surface acoustic wave on a thin film. Spectrum of the narrowband surface acoustic wave showing high-frequency generation.

provide absolute measurement of the ultrasonic signal. Optical detection sensitivity is at least an order of magnitude poorer than contact transducers, especially on objects that scatter light diffusively. Much of the recent work in laser ultrasonics has therefore been devoted toward improving the sensitivity of optical detection (Monchalin, 1986; Wagner, 1990; and Dewhurst and Shan, 1999). In this section, the ways in which ultrasonic signal information can be encoded onto a light beam are first described, followed by a discussion of some of the more common methods of demodulating the encoded information using optical interferometry.

7.3.1 Encoding of Ultrasound Information onto an Optical Beam

To optically monitor ultrasound, a light beam should be made to interact with the object undergoing such motion. Interaction of acoustic waves and light waves in transparent media has a long history (see for instance Fleury, 1970) and will not be reviewed here. Attention will be confined here to opaque solids that either reflect or scatter light. In this case, the light beam can only be used to monitor the *surface* motion associated with the ultrasound.

Typically laser beams are used as the optical source, and these can provide monochromatic, linearly polarized, plane light beams. The electric field of such beams can be expressed as

$$E = a\exp[j(\omega_{opt}t - \phi)] \tag{7.10}$$

where E is the electric field of amplitude a, frequency ω_{opt}, and phase ϕ. It is important to note that extant photodetectors cannot directly track the optical phase (the optical frequency ω_{opt} is just too high), and as such only the optical intensity (proportional to $P = EE^* = a^2$, where $*$ represents the complex conjugate) can be directly measured.

There are a number of ways in which ultrasound can affect the light beam. These can be broadly classified into intensity-modulated techniques and phase- (or frequency-) modulated techniques.

7.3.1.1 Intensity Modulation Induced by Ultrasound

The intensity of the reflected light beam can change due to ultrasound-induced changes in the refractive index of the medium, and this can be monitored directly using a photodetector. Though these changes are typically very small for most materials, this method has been used successfully in picosecond ultrasonics (Grahn et al., 1989) to measure the properties of thin films (Thompsen et al., 1985) and nanostructures (Antonelli et al., 2002). Another intensity-based technique utilizes the surface tilt associated with ultrasonic motion (Adler et al., 1967). The probe light beam is tightly focused onto an optically reflective object surface. A partial aperture (usually called a knife-edge in this context) is placed behind a recollimating lens located in the path of the reflected beam prior to being focused onto a photodetector. The reflected light beam will undergo a slight tilt because of the ultrasonic displacement. This action will cause varying portions of light to be blocked by the knife-edge, resulting in an intensity change at the photodetector. A third class of intensity-based techniques is applicable to continuous or tone-burst SAW packets of known frequency and velocity. In this case, the ultrasonic surface displacement acts like a surface diffraction grating, and an incident plane light beam will undergo diffraction in the presence of the SAW wave packet. A photodetector placed in the direction of either of the two expected diffracted first-order beams can be used to monitor the SAW wave packet (Lean et al., 1970). Recently, diffraction detection has been used to measure the mechanical properties of thin films (Rogers, 2000). In general, intensity-modulated techniques are typically less sensitive than phase- (or frequency-) modulated techniques. As such, their use in nondestructive characterization has been limited. The reader is referred to the review papers of Monchalin (1986) and Wagner (1990) for further information on intensity-modulated techniques.

7.3.1.2 Phase or Frequency Modulation Induced by Ultrasound

Ultrasonic motion on the surface of a body also affects the phase or frequency of the reflected or scattered light. For simplicity, consider an object surface illuminated at normal incidence by a light beam as shown in Figure 7.10. Let the surface normal displacement at the point of measurement be $u(t)$ due to ultrasonic motion, where t is time. We shall assume that the surface tilt is not so large that the reflected optical beam is tilted significantly away. The object surface displacement just changes the phase of the light by causing a change in the path length (equal to twice the ultrasonic normal displacement) that the light has to travel. In the presence of ultrasonic displacement, the electric field can therefore be expressed as

$$E_s = a_s \exp[j\{\omega_{opt}t - 2k_{opt}u(t) - \varphi_s\}] \tag{7.11}$$

where $k_{opt} = 2\pi / \lambda_{opt}$ is the optical wave number, λ_{opt} is the optical wavelength, and φ_s is the optical phase (from some common reference point) in the absence of ultrasound.

For time-varying phase modulation such as caused by an ultrasonic wave packet, it is also possible to view the optical interaction with the surface motion as an instantaneous doppler shift in optical frequency. To see this, note that Equation 7.11 can be equivalently written in terms of the surface velocity $V(t) = \frac{du}{dt}$ as

$$E_s = a_s \exp[j\{\tilde{\omega}_{opt}t - \varphi_s\}] \tag{7.12}$$

where the instantaneous optical frequency is now given by

$$\tilde{\omega}_{opt}t = \int_0^t \omega_{opt}\left\{1 - \frac{2V}{c}\right\}dt \tag{7.13}$$

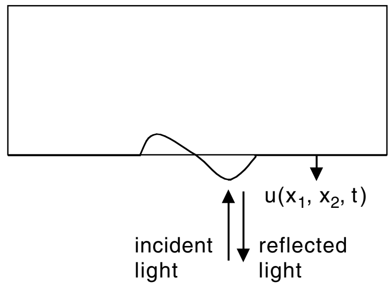

FIGURE 7.10
Phase modulation of light due to ultrasonic displacement.

where c is the speed of light. The surface velocity associated with the ultrasonic motion therefore leads to a frequency shift of the optical beam.

7.3.2 Optical Interferometry

The phase of a single optical beam cannot be measured directly since the optical frequency is too high to be monitored directly by any extant photodetector. Therefore, a demodulation scheme has to be used to retrieve phase-encoded information. There are a number of optical interferometers that perform this demodulation (see Malacara [1992] for a general discussion on optical interferometry). Here we will only consider some of the more common systems that have found application in laser ultrasonics.

7.3.2.1 Reference Beam Interferometers

In this class of interferometers, the optical signal beam from the object is mixed with a separate planar reference beam. As such, they perform best on an optically mirror-polished surface.

7.3.2.1.1 Two-Beam Homodyne Interferometers

The simplest optical interferometer is the two-beam Michelson setup shown in Figure 7.11. The output from a laser is split into two at a beam splitter; one of the beams is sent to the test object, and the other is sent to a reference mirror. Upon reflection, the two beams are recombined parallel to each other and made to interfere at the photodetector. The electric fields at the photodetector plane can be written as

$$E_R = a_R \exp[j\{\omega_{opt} t - k_{opt} L_R\}] \tag{7.14}$$

$$E_s = a_s \exp[j\{\omega_{opt} t - k_{opt}(L_s + 2u(t)\}] \tag{7.15}$$

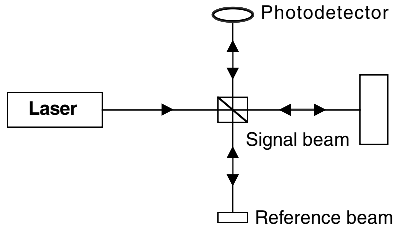

FIGURE 7.11
Two-beam homodyne interferometer (Michelson).

where (i = R, S) refer to the reference and signal beams, respectively. Here E_i are the electric fields of the two beams of amplitudes a_i and optical frequency ω_{opt}. The phases $\phi_i = k_{opt}L_i$ are due to the different path lengths L_i that the two beams travel *from a point of common phase* (say at the point just prior to the two beams splitting at the beam splitter). Here it is convenient to consider the phase term for the signal beam as being comprised of a static part $k_{opt}L_s$ due to the static path length, and a time-varying part due to the time-varying ultrasonic displacement $u(t)$. The total electric field at the photodetector plane is then the sum of the fields of the two beams, and the resulting intensity is obtained as

$$\begin{aligned} P_D &= (E_R + E_s)(E_R + E_s)^* \\ &= P_R + P_s + 2\sqrt{P_R P_s}\cos\{k_{opt}(L_R - L_s) - 2k_{opt}u(t)\} \\ &= P_{tot}[1 + M\cos\{k_{opt}(L_R - L_s) - 2k_{opt}u(t)\}] \end{aligned} \tag{7.16}$$

where $P_i = a_i^2$ are the optical intensities (directly proportional to the power in watts) of the two beams individually. In the last expression above, we have defined the total optical power $P_{tot} = P_R + P_s$. The factor $M = \frac{2\sqrt{P_R P_s}}{P_{tot}}$ is known as the modulation depth of the interference and ranges between 0 (when one of the beams is not present) to 1 (when the two beams are of equal intensity).

If the phase change due to the signal of interest is $2k_{opt}u(t) \ll 1$ — as is typically the case for typical ultrasonic displacements — the best sensitivity is obtained by ensuring that the static phase difference is maintained at quadrature, (i.e., at k_{opt} $(L_R - L_s)$ $\frac{\pi}{2}$) (see Figure 7.12). This can be achieved by choosing the reference and signal beam path lengths appropriately. The two-beam Michelson interferometer that is maintained at quadrature provides an output optical power at the photodetector given by

$$P_D = P_{tot}\{1 + M(2k_{opt}u(t))\}, \quad k_{opt}u \ll 1 \tag{7.17}$$

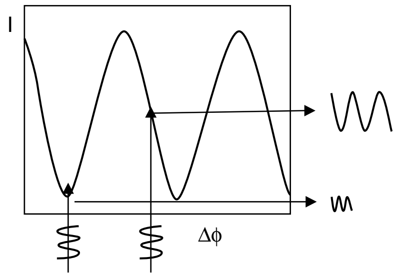

FIGURE 7.12
Two-beam interferometer output intensity as a function of phase change. The largest variation in output intensity for small phase changes occurs at quadrature.

This shows that the output of a Michelson interferometer that is operated at quadrature is proportional to the ultrasonic displacement. In reality, even the static optical path is not quite static because of low-frequency ambient vibration that can move the various optical components or the object around. If the signal of interest is high-frequency (say several kHz or higher) — and this is the case for ultrasonic signals — it is possible to use an active stabilization system using a moving mirror (typically mounted on a piezoelectric stack) on the reference leg such that the static (or more appropriately, low-frequency) phase difference is always actively kept constant by means of a feedback controller.

The piezoelectric mirror can also be used to calibrate the full fringe interferometric output by intentionally inducing an optical phase change in the reference leg that is larger than 2π. This will provide both the total power P_{tot} and the modulation depth M. An absolute measurement of the ultrasonic displacement can be obtained from Equation 7.17.

It is important to characterize the SNR, or equivalently the minimum detectable displacement of the optical interferometer. There are several possible noise sources in an optical-detection system. These include noise from the laser source, in the photodetector, in the electronics, and in the optical path due to ambient vibrations and thermal currents. Most of these noise sources can be stabilized against or minimized by careful design and isolation, leaving only quantum or shot noise arising from random fluctuations in the photocurrent. Shot noise increases with increasing optical power, and it basically sets the absolute limit of detection for optical-measurement systems.

The optical power incident on the photodetector generates a photocurrent given by

$$i_D = \frac{\eta e}{h\nu_{opt}} P_D \tag{7.18}$$

where η is the detector quantum efficiency, e is the charge of an electron, ν_{opt} is the optical (circular) frequency in hertz, and h is Planck's constant. The photocurrent associated with the signal of interest is only that part that is related to the ultrasonic displacement (see Equation 7.17):

$$i_{sig} = \frac{\eta e}{h\nu_{opt}} MP_{tot}(2k_{opt}u(t)) \quad \textbf{(7.19)}$$

The mean-squared shot noise current depends on the total photocurrent and is given by

$$\left\langle i_n^2 \right\rangle = 2eB\langle i_D \rangle \quad \textbf{(7.20)}$$

where < > represents time-average (over a relevant time scale of interest) of the quantity inside it, and B is the detection bandwidth. The SNR is then defined as

$$SNR = \left\{ \frac{\left\langle i_{sig}^2 \right\rangle}{\left\langle i_n^2 \right\rangle} \right\}^{1/2} \quad \textbf{(7.21)}$$

Without loss of generality, the object displacement can be assumed to be harmonic (more general transient signals can be handled by the Fourier transform), $u(t) = U \sin \omega_u t$, where U is the magnitude and ω_u represents the ultrasonic frequency. The shot-noise limited SNR of a stabilized Michelson interferometer operating at quadrature is then given by

$$SNR = k_{opt}MU \sqrt{\frac{\eta P_{tot}}{h\nu_{opt}B}} \quad \textbf{(7.22)}$$

The minimum detectable ultrasonic signal, based on the somewhat arbitrary criterion that a signal is detectable if it is equal to the noise magnitude (i.e., if $SNR = 1$), is then given by

$$U_{\min} = \frac{1}{k_{opt}M} \sqrt{\frac{h\nu_{opt}B}{\eta P_{tot}}} \quad \textbf{(7.23)}$$

For a detection bandwidth of 1 Hz, detector efficiency of 0.5, modulation depth of 0.8, total collected optical power of 1 W from a green laser (514 nm), the minimum detectable sensitivity is on the order of 10^{-17} m.

Of all possible configurations, the two-beam homodyne interferometer provides the best shot-noise detection sensitivity as long as the object beam is specularly reflective.

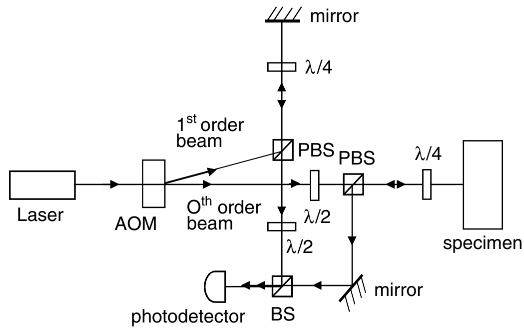

FIGURE 7.13
Two-beam heterodyne interferometer.

7.3.2.1.2 Two-Beam Heterodyne Interferometers

In this class of interferometers, one of the two beams to be mixed is of a slightly different optical frequency. Typically this frequency shift is obtained by passing a laser beam through an acousto-optic modulator (a Bragg cell), the first diffracted order of which provides a frequency shifted beam. Figure 7.13 shows a typical heterodyne interferometer. The reference and signal beams in this case can be expressed as

$$E_R = a_R \exp[j((\omega_{opt} + \omega_B)t - \phi_R)] \quad \textbf{(7.24)}$$

$$E_s = a_s \exp[j(\omega_{opt}\, t - \phi_s)] \quad \textbf{(7.25)}$$

where ω_B is the frequency shift introduced by the acousto-optic modulator. The resulting interference intensity at the photodetector is

$$P_D = P_{tot}\,[1 + M \cos\{\omega_B t + \varphi_n(t) - 2k_{opt}\, u(t)\}] \quad \textbf{(7.26)}$$

As before, we have decomposed the phase difference in terms of a term $\varphi_n(t)$, which includes the static path difference, the effect of possible low-frequency noise, and a signal term due to object displacement. Once again, considering a sinusoidal object displacement the amplitude of which is a fraction of the optical wavelength $u(t) = U \sin \omega_u t,\ 2k_{opt}U \ll 1$, we have

$$P_D = P_{tot}[1 + M\{\cos(\omega_B t + \varphi_n(t) - 2k_{opt}U \sin\omega_u t)\}]$$

$$= P_{tot}\left[1 + M\left\{\cos(\omega_B t + \varphi_n(t)) - 2k_{opt}U\left[\underbrace{\cos((\omega_B + \omega_u)t + \varphi_n(t))}_{\text{signal at upper side-band}} - \underbrace{\cos((\omega_B - \omega_u)t + \varphi_n(t))}_{\text{signal at lower side-band}}\right]\right\}\right] \quad \textbf{(7.27)}$$

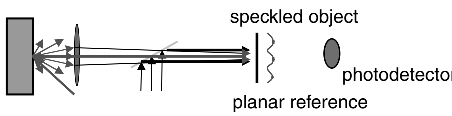

FIGURE 7.14
Ultrasound detection on rough surfaces; interference of speckled signal and planar reference beams is nonoptimal.

Note that the object displacement information can be directly monitored on a spectrum analyzer and is proportional to the amplitude of the signals at the upper and lower sidebands around the optical heterodyne frequency ω_B. Alternatively, the signal can be extracted using either phase locked loops or frequency discriminators. The former provides a signal proportional to the surface displacement, and the latter to the surface velocity (Monchalin, 1986). The SNR of the heterodyne interferometer can be shown to be slightly less (typically a factor of half, depending on the signal demodulation scheme used) than the homodyne setup (Monchalin, 1986).

The heterodyne interferometer also provides an absolute measure of the ultrasonic signal. For instance, in a spectrum analyzer, the ratio of the sideband amplitude to the carrier amplitude at the heterodyne frequency is directly proportional to the ultrasonic displacement. Furthermore, the heterodyne setup does not require active mechanical stabilization such as the one used for homodyne interferometers. As such, the heterodyne interferometer is more suited for application in industrial settings (Monchalin, 1993). The performance of the heterodyne interferometer also degrades significantly if the object is a diffuse scatterer.

In the discussion above we have implicitly assumed that the object surface is optically specularly reflective, so that the reflected object beam can be recollimated into a plane wave. If the object surface is rough, the scattered object beam will in general be a speckled beam. In this case, the performance of the interferometer will be several orders of magnitude poorer due to two factors. First, the total optical power P_{tot} collected will be lower than from a mirror surface. Second, the mixing of a non-planar object beam (one where the optical phase varies randomly across the beam) with a planar reference beam is not efficient (see Figure 7.14). This could be counterproductive with the worst case situation, leading to complete signal cancellation. Therefore, interferometers such as the Michelson, which use a planar reference beam, are best used in the laboratory on optically mirror-like surfaces.

7.3.2.2 Self-Referential Interferometers

On rough surfaces, self-referential interferometers offer significantly improved performance. The speckled object beam containing information about the object displacement is mixed with a *wavefront-matched reference*

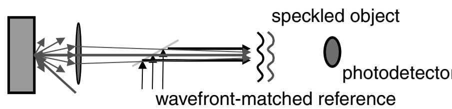

FIGURE 7.15
Ultrasound detection on rough surfaces; wavefront-matched interference.

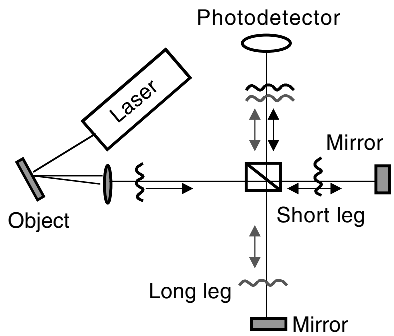

FIGURE 7.16
Long-path time-delay interferometer.

beam that may or may not contain signal information. Since the two beams are now wavefront-matched, it is possible to efficiently spatially mix the two beams to pull out the signal of interest (see Figure 7.15). Some of the common self-referential interferometers are: (1) time-delay interferometers, (2) Fabry-Perot (FP) interferometers, (3) adaptive holographic interferometers.

7.3.2.2.1 *Time-Delay Interferometers*

Consider the long-path time-delay interferometer shown in Figure 7.16. The scattered beam from the object is collected and split into two copies. Both these copies are reflected back by mirrors, but one of them travels via a short leg and the other travels via a long leg. Since both the beams that interfere arise from the scattered beam from the object surface, and as such are essentially wavefront-matched (assuming that the path difference is not so large that beam spreading becomes an issue), the spatial mixing will be optimal. However, one of the beams travels a longer distance than the other. The ultrasonic information contained in each leg arises from different times. The two beams that interfere can therefore be expressed as

$$E_s = a_s \exp[j\{\omega_{opt} t - k_{opt}(L_s + 2u(t)\}] \quad \textbf{(7.28)}$$

$$E_L = a_L \exp[j\{\omega_{opt} t - k_{opt}(L_L + 2u(t-\tau)\}]$$

(7.29)where $\tau = (L_L - L_S)/c$ denotes the fact that the ultrasonic signal is sampled at different times by the long and short beams. The interference intensity at the photodetector is therefore

$$P_D = P_{tot}[1 + M\cos[k_{opt}(L_L - L_S) - 2\{u(t-\tau) - u(t)\}]] \quad \textbf{(7.30)}$$

In this case, the path length difference needs to be stabilized at quadrature to provide detection at maximum sensitivity. If the ultrasonic signal of interest is of sufficiently short duration compared to the time delay τ, the interferometer measures the ultrasonic displacement directly. In practice this implies very long optical path length difference, necessitating the use of long coherence laser sources. For shorter path length difference, this interferometer provides time-differential information about the ultrasonic motion. Some alternative configurations of the time-delay interferometer such as the Sagnac interferometer (Bowers, 1982; Fomitchov et al., 2000) do not require a long coherence laser source, and furthermore they are common path, providing an added measure of stability against ambient noise.

Unfortunately, the frequency response of time-delay interferometers is very non-uniform. This is readily understood by referring to Equation 7.30. Clearly, the output signal is insensitive to low frequencies (where the ultrasonic displacement is slowly varying over time τ). Also, no output signal will be seen if the ultrasonic signal is periodic with period τ/n where n is any integer. Time-delay interferometers are useful only for detecting fairly narrowband ultrasonic signals of known frequency range.

7.3.2.2.2 Fabry-Perot Interferometers

In this configuration, the light from the test object is collected into a device that consists of two planar or confocal mirrors (curved mirrors facing each other with coincident focal point) that form an FP cavity. The mirror reflectivites are usually kept very high such that the light is multiply reflected between the two mirrors and a part of it leaks out from each end at every reflection. For illustrative purposes, let us consider the planar FP cavity shown in Figure 7.17, even though it is the confocal one that is preferred in practice in view of its better light gathering capacity (Monchalin, 1986). Note that the FP is a self-referential interferometer in that interference occurs between *multiple copies* of the object beam. Consider the total light transmitted by a planar free-space FP cavity of cavity length L

$$E_{tr} = \sum_{n=1}^{\infty} E_{tr}^{(n)} = \frac{a_O t^2 e^{-j\phi_O} e^{-jk_{opt}L}}{1 - r^2 e^{-jk(2L)}} \quad \textbf{(7.31)}$$

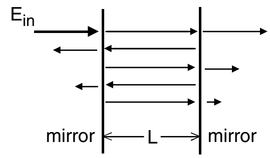

FIGURE 7.17
Fabry-Perot interferometer.

where $E_{in} = a_O e^{-j\phi_O}$ is the beam from the object that is incident into the cavity and t and r are the *amplitude* transmission and reflection coefficients, respectively. The net transmitted optical power is therefore

$$\frac{P_{tr}(\omega_{opt})}{P_O} \equiv \hat{P}_{tr}(\omega_{opt}) = \frac{(1-R)^2}{1+R^2-2R\cos(2\pi\omega_{opt}/\omega_{fsr})} \tag{7.32}$$

where $P_O = a_O^2$ is the object beam power and $R = rr^*$, $T = tt^*$, $R + T = 1$ are the *intensity* reflection and transmission coefficients, respectively, that sum to unity in the absence of energy absorption. Also,

$$\omega_{fsr} = \frac{c}{2L} \tag{7.33}$$

is called the free-spectral-range of the FP. The normalized transmitted optical power is plotted in Figure 7.18. We note the following:

1. The transmitted optical power exhibits periodic maxima at integral multiples of the free-spectral range. These are called the passbands of the instrument. Outside of the passbands, the light transmitted is rather small, especially as the mirror reflectivity R approaches unity.
2. The transmitted optical power does not depend on the object beam static phase but does depend on the optical frequency. It is therefore important to think of the Fabry-Perot as an optical frequency discriminator (an optical filter) that allows selective transmission of certain optical frequencies (passbands). For sufficiently high mirror reflectivities, the full-width at half-maximum at each of the passbands of the FP is

$$\frac{\Delta\omega_{whm}}{\omega_{fsr}} = \frac{(1-R)}{\pi\sqrt{R}} \equiv \frac{1}{\Im} \tag{7.34}$$

where $\Im$ is called the finesse of the Fabry-Perot cavity. Note that the closer to unity the mirror reflectivities, the higher the finesse and the narrower the passbands of the instrument, the higher the sensitivity of the instrument to small frequency shifts.

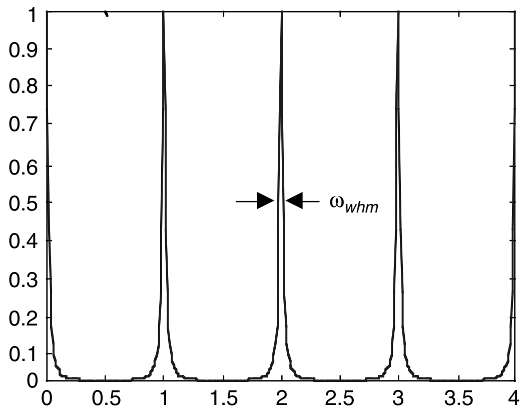

FIGURE 7.18
Fabry-Perot interferometer response in transmission (plot of $\hat{P}_{tr}$ vs. $\omega_{opt}/\omega_{fsr}$ for R = 0.9)

In practice, the FP is set to operate at one of its half-maximum points. This is achieved by tuning the cavity length L (which is usually actively stabilized against drift). The response curve at the half-maximum point is almost linear with a slope

$$\left.\frac{d\hat{P}_{tr}}{d\omega_{opt}}\right|_{half-\max point} = \frac{\Im}{\omega_{fsr}} \tag{7.35}$$

The normalized transmitted intensity variation due to a small optical frequency shift of $\Delta\omega_{opt}$ about the operating point is then given by $\Delta p_{tr} = \frac{\Im}{\omega_{fsr}}\Delta\omega_{opt}$.

Again considering a harmonic ultrasonic displacement, $u(t) = U \sin\omega_u t$, $2k_{opt}U \ll 1$, the corresponding surface velocity is $V(t) = \omega_u U \cos\omega_u t$. The corresponding optical frequency shift is $\Delta\omega_{opt} = \frac{2\omega_{opt}}{c}\,\omega_u U \sin\omega_u t$ (see Equation 7.13).

Therefore, the FP output can be written as:

$$P_{tr} = P_O\left[\frac{1}{2} + \frac{\Im}{\omega_{fsr}}.\frac{2\omega_{opt}}{c}\omega_u U \sin\omega_u t\right] \tag{7.36}$$

where it is assumed that in the absence of ultrasonic signals the FP will be tuned to the half-maximum point. The associated SNR becomes

$$SNR = \frac{\left\langle i_{sig}^2 \right\rangle}{\left\langle i_n^2 \right\rangle} = \left\{\frac{2\eta P_o}{h\nu_{opt}B}\right\}^{1/2}\left\{\frac{\Im}{\omega_{fsr}}\frac{\omega_{opt}}{c}\omega_u U\right\} \tag{7.37}$$

The minimum detectable displacement therefore becomes

$$U_{\min} = \left[\frac{h\nu_{opt} B}{2\eta P_O} \right]^{1/2} \frac{\omega_{fsr} c}{\Im \omega_{opt} \omega_u} \tag{7.38}$$

Note that the FP response varies inversely as the ultrasonic frequency. This means that its response at low frequencies is poor. This is good in that ambient vibrations of the test object will not really affect the instrument (ambient vibrations that change the FP cavity length are another matter, and need to be stabilized against). FP interferometers have therefore been of considerable interest in industrial applications (Monchalin, 1993). At moderate frequencies, the FP is actually a very good instrument. At even higher ultrasonic frequencies, the response will move out of the linear region in Figure 7.18, and Equation 7.38 is no longer applicable. The response will in fact get poorer as the frequency shifts beyond the operating pass band of the instrument. In reality, the response is even more complicated by the fact that the multiple beams that interfere actually must have been incident on the object at different times, and therefore would likely have sampled the ultrasonic wave packet at different times. The precise nature of the response curve depends on the particular instrument.

7.3.2.2.3 Dynamic Holographic Interferometers

This class of interferometers is based on dynamic holographic recording typically in photorefractive media. One approach is to planarize the speckled object beam by using optical phase conjugation (Paul et al., 1987; Delaye et al., 1995a). The planarized object beam can then be effectively interfered with a planar reference beam in a two-beam homodyne or heterodyne interferometer. Alternatively, a reference beam with the same speckle structure as the static object beam can be holographically reconstructed for interference with the object beam containing the ultrasonic information (Ing and Monchalin, 1991; Delaye et al., 1995b; Pouet et al., 1996). This is most readily achieved by using the process of two-wave mixing in photorefractive media (Yeh, 1993).

Two-wave mixing is essentially a dynamic holographic process where two coherent optical beams (pump/reference and probe/signal beams) interact within a photorefractive crystal (PRC). The process of two-wave mixing can be briefly summarized as: (1) creation of optical intensity gratings due to coherent interference of the interacting beams leading to (2) nonuniform photoexcitation of electric charges in the PRC, which then diffuse/drift to create (3) a space-charge field within the PRC, which in turn creates (4) a refractive index grating via the electro-optical effect, and which causes (5) diffraction of the interacting beams. A net consequence of this is that at the output of the PRC we have not only a portion of the transmitted probe beam, but also a part of the pump beam that is diffracted into the direction of the probe beam.

The pump beam diffracted into the signal beam direction has the same wavefront structure as the transmitted signal beam.

Since the PRC process has a certain response time (depending on the material, the applied electric field, and total incident optical intensity), it turns out that it is unable to adapt to sufficiently high-frequency modulations in the signal beam. The PRC can only adapt to changes in the incident beams that are slower than the response time. This makes two-wave mixing interferometers especially useful for ultrasound detection. High-frequency ultrasound-induced phase modulations are essentially not seen by the PRC, and therefore the diffracted pump beam will have the same wavefront structure as the *unmodulated* signal beam. The transmitted signal beam will contain the ultrasound-induced phase modulation. By interfering the diffracted (but unmodulated) pump beam with the transmitted (modulated) signal beam (both otherwise with the same wavefront structure), one obtains a highly efficient interferometer. Furthermore, any low frequency modulation in the interfering beams (such as those caused by noise from ambient vibration or slow motion of the object) will be compensated for by the PRC as it adapts and creates a new hologram. Two-wave mixing interferometers therefore do not need any additional active stabilization against ambient noise.

Several different types of photorefractive two-wave mixing interferometers have been described in the literature (Ing and Monchalin, 1991; Delaye et al., 1995b; Pouet et al., 1996). Here we will describe the isotropic diffraction configuration (Delaye et al., 1997). shown in Figure 7.19. The Bismuth silicon oxide (BSO) crystal used in this setup was oriented with grating vector along the (001) crystal axis. For simplicity, optical activity and birefringence effects in the PRC will be neglected.

Let the signal beam obtained from the scatter from the test object be s-polarized. As shown in Figure 7.19, a half-wave plate (HWP) is used to rotate the incident signal beam polarization by 45° leading to both *s*- and *p*-polarized phase-modulated components of equal intensity given by

$$E_{s0} = \frac{a}{\sqrt{2}} \exp[j(\omega_{opt} t - \phi(t))] \tag{7.39}$$

A photorefractive grating is created by the interference of the *s*-polarized component of the signal beam with the *s*-polarized pump beam. The diffracted pump beam (also *s*-polarized for this configuration of the PRC) upon exiting the crystal is then given by (Delaye et al., 1997)

$$E_R = \frac{a}{\sqrt{2}} \exp[j\omega_{opt} t][\exp[-\alpha L/2]\{[\exp(\gamma L) - 1] + \exp[-j\phi(t)]\} \tag{7.40}$$

where $\gamma = \gamma_r + j\gamma_i$ is the complex photorefractive gain, α is the intensity absorption coefficient of the crystal, and L is the length of the crystal. The *p*-polarized component of the signal beam is transmitted by the PRC undisturbed (except for absorption) and can be written as

$$E_S = \frac{a}{\sqrt{2}}\exp[-\alpha L/2]\exp[j(\omega_{opt}t - \phi(t))] \quad \textbf{(7.41)}$$

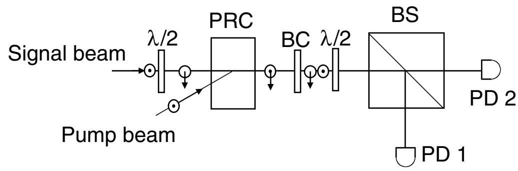

FIGURE 7.19
Configuration of isotropic diffraction setup. λ/2: Half-wave plate; PRC: Photorefractive crystal; BC: Berek compensator; BS: beam splitter; PD: photodetector.

Upon exiting the PRC, the diffracted pump and the transmitted signal beams are now orthogonally polarized. A Berek's wave plate is interposed so as to introduce an additional phase shift of ϕ_L in the transmitted signal beam to put the interference at quadrature. The two beams are then passed through a polarizing beam splitter oriented at 45° to *s*- and *p*-directions, giving rise to two sets of optical beams that interfere at the two photodetectors. The intensities recorded at the two photodetectors are then given by (for $\phi(t) \ll \pi/2$)

$$P_{D1} = \frac{P_{tot}}{4}e^{-\alpha L}\{e^{2\gamma_r L} + 2e^{2\gamma_r L}[\cos(\gamma_i L - \phi_L) + \phi(t)(\sin(\gamma_i L - \phi_L) + \sin(\gamma_i L)] + 2\phi(t)\sin\phi_L + 1\}$$

$$P_{D2} = \frac{P_{tot}}{4}e^{-\alpha L}\{e^{2\gamma_r L} - 2e^{2\gamma_r L}[\cos(\gamma_i L - \phi_L) + \phi(t)(\sin(\gamma_i L - \phi_L) - \sin(\gamma_i L)] - 2\phi(t)\sin\phi_L + 1\}$$

(7.42)

where $P_{tot} = a^2$ is proportional to the optical power collected in the scattered object beam. In the case of a pure real photorefractive gain (i.e., the diffracted beam phase is unaffected by the two-wave mixing process), quadrature is obtained by setting $\phi_L = \pi/2$. In this case, upon electronically subtracting the two photodetector signals using a differential amplifier, the output signal is

$$S = P_{tot}e^{-\alpha L}\{e^{\gamma L} - 1\}\varphi(t) \quad \textbf{(7.43)}$$

In the case of a pure real photorefractive gain, we therefore have linear phase demodulation. Since the phase modulation is $\phi(t) = 2k_{opt}u(t)$, the output signal is directly proportional to the ultrasonic displacement. The SNR of the two-wave mixing interferometer in the isotropic configuration for real photorefractive gain follows directly from Equation 7.42:

$$SNR = 2k_{opt}U\sqrt{\frac{\eta P_{tot}}{h\upsilon_{opt}}e^{-\frac{\alpha L}{2}}}\frac{e^{\gamma L} - 1}{(e^{2\gamma L} + 1)^{1/2}} \quad \textbf{(7.44)}$$

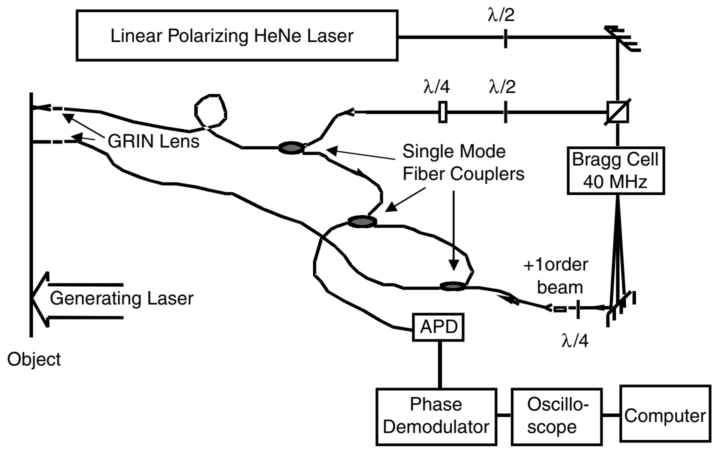

FIGURE 7.20
A dual-probe heterodyne interferometer.

It is clear that the lower the absorption and the higher the photorefractive gain, the better the SNR.

7.3.2.2.4 Multibeam Interferometers

There are many instances where ultrasonic detection from more than a single point on the object surface is desired. For instance, ultrasonic attenuation measurements require that the same ultrasonic wave packet be measured at two distinct locations on the object. Similarly, dispersion of ultrasonic guided waves can be effectively obtained by measuring a broadband ultrasonic signal at two locations a known distance apart. Ultrasonic detection at multiple points can also be used as phased-array receivers (Murray and Krishnaswamy, 2001) and for anisotropy characterization (Zhou et al., 2002).

Huang et al. (1994) have configured a dual-probe system that can monitor ultrasonic displacement at two different locations on a test object. This system is based on heterodyne interferometry as shown in Figure 7.20. The output of a laser is passed through a 40-MHz Bragg cell providing the beam splitting and frequency shifts needed for heterodyne interferometry. The zeroth-order and the first-order beams are used for heterodyne interference. The two beams are coupled into two single-mode 1×2 fiber-optic couplers. The output beams are terminated with microfocusing lenses and focused to the detecting points on the sample surface. The reflected light from the surface is collected by the same lens and coupled back into the fiber. A third coupler recombines the two returning beams and delivers them to the photodetector. As in any heterodyne interferometer, the surface displacement information is carried in the phase shift of the heterodyne signal output from the photodetector. In this dual-probe interferometer, the phase shift is proportional to the difference of the displacements in the two probing points (Huang et al., 1994). A noteworthy

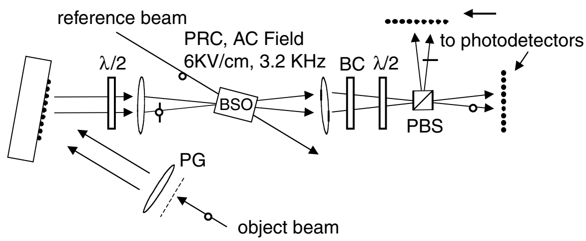

FIGURE 7.21
Multiplexed two-wave mixing interferometer for simultaneous detection of ultrasound at a number of locations.

feature of this dual-probe interferometer is that the detection sensitivity at the two probe points is exactly the same and is independent of surface reflectivity at the two probing locations.

Murray and Krishnaswamy (2001) have recently developed a multibeam interferometer that allows for the simultaneous detection of acoustic waves from a number of points on the surface of a specimen. This interferometer is based on multiplexed two-wave mixing in photorefractive crystals. The optical setup is illustrated in Figure 7.21 and is similar to the isotropic diffraction setup discussed earlier. The primary difference is that multiple two-wave mixing processes occur simultaneously in a single PRC. Murray and Krishnaswamy (2001) show that by keeping the pump beam sufficiently strong compared to the signal beams, cross-talk can be minimized. The multibeam mixing in the PRC therefore acts as multiple two-wave mixing. This essentially provides multiple independent interferometers all demodulated in parallel by a single PRC. Multiplexed two-wave mixing interferometers can be used as phased-array receivers (Murray and Krishnaswamy, 2001) and matched-filters for narrowband and chirped surface-acoustic wave detection (Murray et al., 2000). They can also be used for anisotropy characterization of materials (Zhou et al., 2002).

7.3.2.2.5 Intrinsic Fiber-Optic Ultrasound Sensors

Most of the interferometers described above can be used in conjunction with optical fibers to pipe the light to and from the test object (such as the dual-probe system shown in Figure 7.20). In such systems, the transduction of ultrasound to light occurs outside the fiber, and as such, the fiber does not play any role in the transduction process. If the transduction of ultrasound to light occurs inside an optical fiber, the sensor is referred to as an intrinsic fiber-optic ultrasound sensor. Such sensors can be embedded in a medium to monitor ultrasound inside the medium and not just at the surface. A number of intrinsic fiber optic ultrasonic sensors have been described in the literature. The majority of these sensors such as fiberized Mach-Zehnder (DePaula et al., 1983a), Michelson (Dandridge, 1991), Sagnac (Fomitchov et al., 2000) or Fabry-Perot (Dorighi et al., 1995) detectors are based on fiber

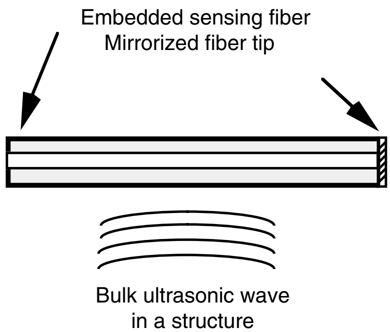

FIGURE 7.22
Intrinsic transduction of ultrasound to optical phase shift inside an optical fiber.

optic interferometry. Alternative approaches such as polarization-based (DePaula et al., 1983b) and fiber Bragg gratings based sensors (Fisher et al., 1997) have also been proposed.

The simplest fiber-optic ultrasound sensor is a piece of optical fiber that is embedded in the medium (Figure 7.22). Light from a laser is coupled into one end of the fiber and can be either reflected back (if the tip of the fiber is mirrorized) or be transmitted to a demodulating interferometer. When ultrasound impinges on the fiber, the phase of the light is affected by changes in dimension of the fiber and the strain-induced changes in the refractive index of the optical fiber. For the case of a single mode fiber immersed in a fluid upon which a plane ultrasonic wave (of wavelength much greater than the fiber diameter) impinges at normal incidence (Figure 7.22), the changes in the physical length L and refractive index n of the fiber can be written as a function of the acoustic pressure ΔP as

$$\frac{\Delta L}{\mathrm{L}} = -\frac{(1-2\nu)\Delta P}{E} \tag{7.45}$$

$$\frac{\Delta n}{n} = \frac{n^2 \Delta P}{2E}(1-2\nu)(2p_{12}+p_{11}) \tag{7.46}$$

where E and ν are the Young's modulus and Poission's ratio of the fiber, respectively; ΔP is the pressure variation caused by ultrasound; and p_{12} and p_{11} are components of the strain-optic tensor for the fiber material (Hocker et al., 1979). If the fiber sensor is embedded in a solid, or if the wavelength is comparable to the fiber dimensions, if the ultrasound impinges at an angle

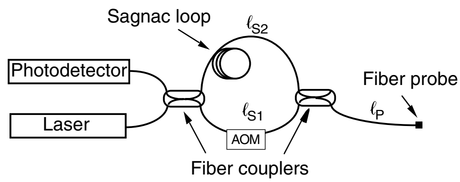

FIGURE 7.23
An intrinsic Sagnac ultrasound sensor.

to the fiber, the fiber response to ultrasound is considerably more complicated (Dorighi et al., 1997).

The ultrasound-induced phase modulation in the light beam propagating in the fiber can be demodulated in any of the standard interferometers described earlier. Figure 7.23 shows an implementation of a fiber-optic ultrasound sensor based on a Sagnac demodulation scheme (Fomitchov et al., 2000).

7.4 Applications

Laser ultrasonics has found wide-ranging applications both in industry and academic research. Here we will consider some illustrative applications of laser ultrasonics in nondestructive flaw identification, materials characterization, and process monitoring.

7.4.1 Laser Ultrasonics for Flaw Detection

Laser ultrasonic techniques have been used for nondestructive flaw detection in metallic and composite structures. Here we describe a few representative example applications in flaw imaging using bulk waves, surface acoustic waves, and Lamb waves.

7.4.1.1 Laser Ultrasonic Flaw Imaging Using Bulk Waves

As discussed in Section 7.2, thermoelastic generation of bulk waves in the epicentral direction is generally weak in materials for which the optical penetration depth and thermal diffusion effects are small. Laser ultrasonic techniques using bulk waves have been used primarily for imaging of defects in composite structures (where the penetration depth is large), or on structures that are coated with a sacrificial film that enhances epicentral generation.

Lockheed Martin has recently installed a large-scale laser ultrasonic facility for inspecting polymer-matrix composite structures in aircraft such as the joint strike fighter (Yawn et al., 1999). In this system, a pulsed CO_2-laser was

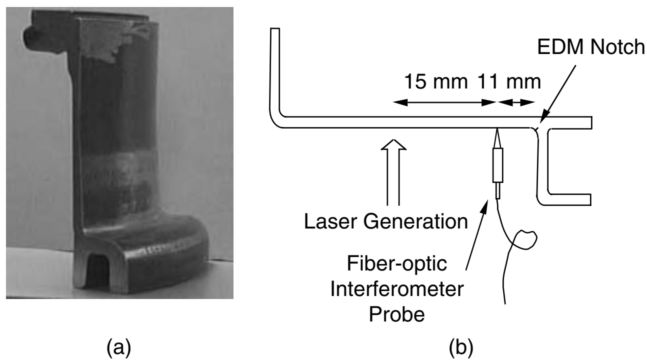

FIGURE 7.24
(a) Aircraft wheel part containing cracks. (b) Schematic of the scanning setup.

used to thermoelastically generate bulk waves into the composite part. A coaxial long-pulse Nd:YAG detection laser demodulated by a confocal FP was used to monitor the back reflections of the bulk waves. The system has been demonstrated on prototype F-22 inlet ducts. Yawn et al. (1999) estimate that the inspection time using the non-contact laser system is about 70 minutes as opposed to about 24 hours for a conventional ultrasonic squirter system.

Choquet et al. (2001) have demonstrated that laser ultrasonics can be used to detect hidden corrosion in painted metallic aircraft lap-joint structures. They use spectral analysis to assess the residual thickness of the metal layer, and state that their technique can identify a 1% loss in thickness due to corrosion.

7.4.1.2 Laser Ultrasonic Flaw Imaging Using Surface Acoustic Waves

Laser ultrasonic systems can also be used to generate and detect surface acoustic waves on specimens such as the aircraft wheel shown in Figure 7.24. Here the high degree of double curvature of the wheel makes the use of contact transducers difficult. Huang et al. (1994) used laser generation along with dual-probe heterodyne interferometer detection. The presence of cracks along the doubly curved location is indicated by the presence of reflected ultrasound signals in some locations but not in others (Figure 7.25 and Figure 7.26). A reflection coefficient, calculated as the ratio of the reflected signal to the original signal power, is plotted in Figure 7.27 and provides a measure of the length of the crack. Such pitch-catch approaches to detecting cracks using laser ultrasonics is feasible on cracks that are large enough to provide a sufficiently strong reflected signal.

7.4.1.3 Laser Ultrasonic Tomographic Imaging Using Lamb Waves

Tomographic imaging of plate structures using Lamb waves is often desired when the test area is not directly accessible and so must be probed from

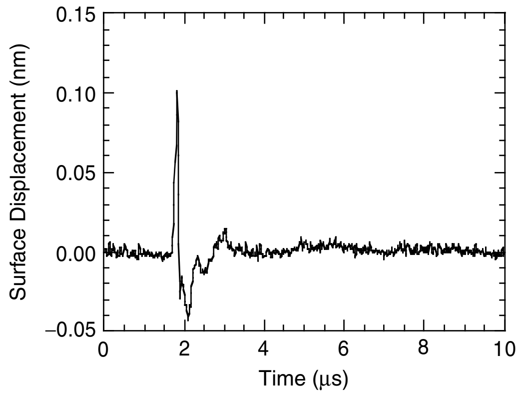

FIGURE 7.25
Inspection for cracks in aircraft wheels. Signal from locations without a crack.

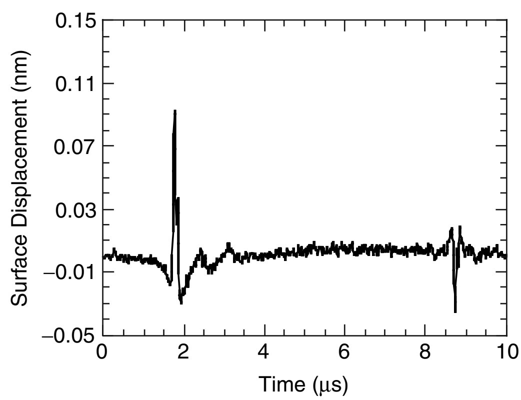

FIGURE 7.26
Inspection for cracks in aircraft wheels. Signal from locations with a crack, indicated by presence of reflections.

outside the area. Computer algorithms are used to reconstruct variations of a physical quantity (such as ultrasound attenuation) within a cross-sectional area from its integrated projection in all directions across that area. Laser ultrasonic tomographic systems using attenuation of ultrasound for tomographic reconstruction need to take into account the high degree of variability in the generated ultrasound arising from variation in the thermal absorption at different locations on the plate.

To avoid erroneously interpreting this variation as differences in the projected attenuation along different directions, Huang et al. (1994) have used a dual-probe Michelson interferometer with the first probe serving as a reference to normalize the signal from the second probe. The normalized signal is therefore dependent only on the true attenuation along the wave

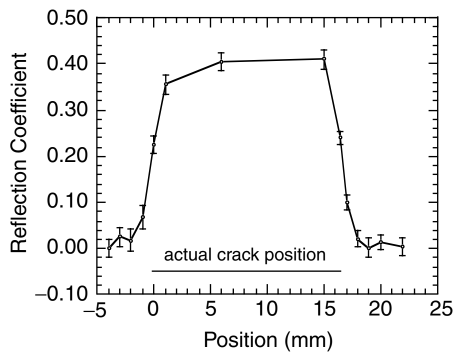

FIGURE 7.27
Reflection coefficient measured at different scanning locations of the wheel.

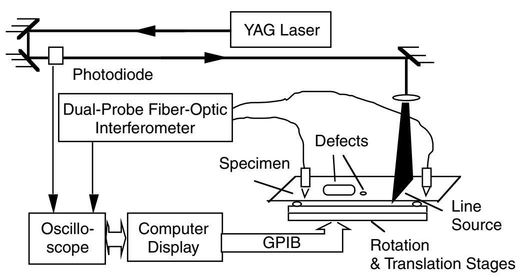

FIGURE 7.28
Laser ultrasonic Lamb-wave tomographic setup.

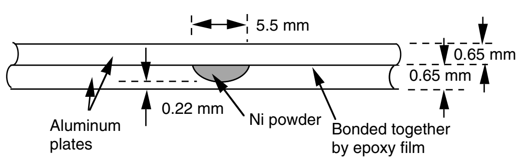

FIGURE 7.29
Cross section of bonded thin plates containing an inclusion.

propagation path. Narrowband Lamb waves were generated using an array of thermoelastic sources. A schematic of the setup is shown in Figure 7.28. Figure 7.29 shows a cross section of the simulated corrosion defect produced in epoxy-bonded aluminum plates. The specimen is composed of 2 0.65-mm thick aluminum plates of thickness 0.65 mm and an approximately 13-µm thick epoxy film. Corrosion was simulated by partially removing the surface of the bottom plate and inserting a fine nickel powder in the cavity prior to bonding. Figure 7.30 shows typical narrowband Lamb waves detected using

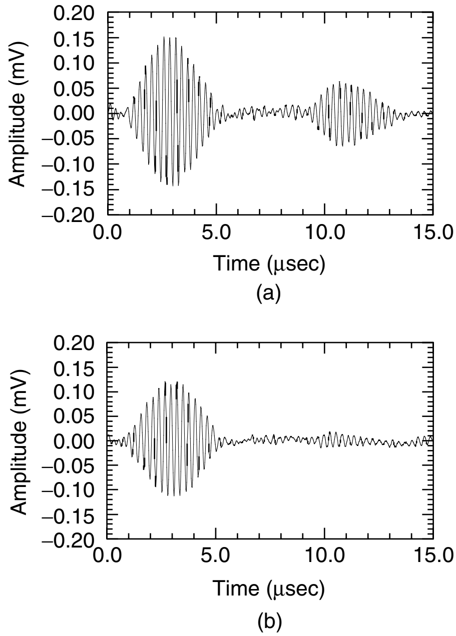

FIGURE 7.30
Typical Lamb wave signals after bandpass filtering: (a) without defect, (b) with the defect between the two detecting points.

the dual-probe interferometer in the presence and absence of the inclusion. By tomographically scanning the plate, Huang et al. (1994) were able to create a tomographic image of the specimen as shown in Figure 7.31. Also shown superposed in Figure 7.31 is a C-scan image of the same sample obtained using a commercial scanning acoustic microscope. The size and the shape of the tomographically reconstructed image is consistent with that of the C-scan.

7.4.1.4 Scanning Laser Source Imaging of Surface-Breaking Flaws

In the applications described thus far, laser ultrasonics has been used in a conventional pitch-catch ultrasonic inspection mode, except that lasers were used to generate and detect the ultrasound. For detecting very small cracks, the pitch-catch technique requires that the crack reflect a significant fraction of the incident wave, and that the generating and receiving locations be in line and normal to the crack. Recently, Kromine et al. (1998, 2000) have developed a scanning laser source (SLS) technique for detecting very small surface-breaking cracks that are arbitrarily oriented with respect to the generating and detecting directions. The SLS technique has no counterpart in conventional ultrasonic inspection methodologies, as it relies on near-field scattering and

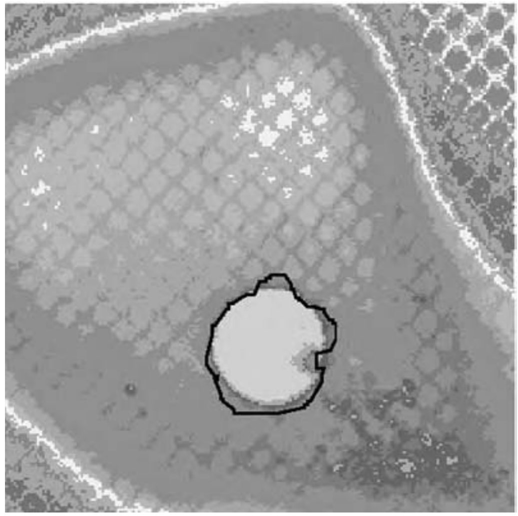

FIGURE 7.31
Superposed image of the tomographic image (solid line) and a conventional ultrasonic C-scan image.

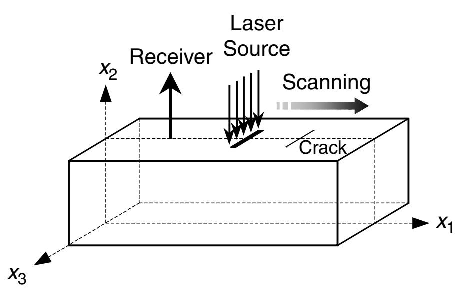

FIGURE 7.32
Schematic of the SLS technique.

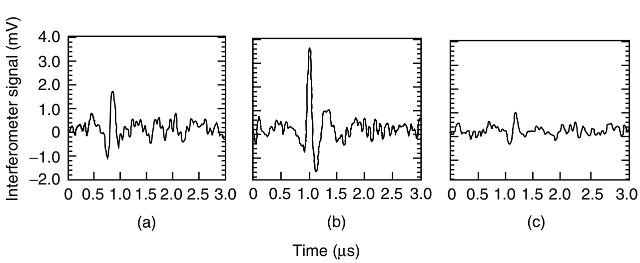

FIGURE 7.33
Ultrasonic surface normal displacement at three locations of the scanning laser source: (a) far from the defect; (b) close to the defect, and (c) behind the defect.

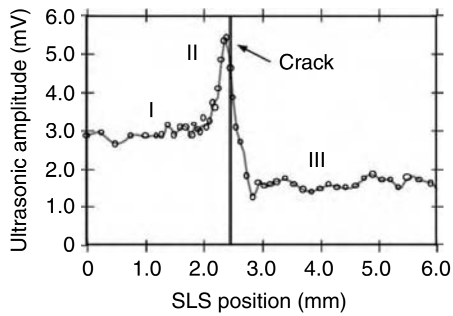

FIGURE 7.34
Typical characteristic signature of ultrasonic peak-to-peak amplitude vs. SLS location as the source is scanned over a surface-breaking defect.

variations in thermoelastic generation of ultrasound in the presence and absence of defects.

In the SLS technique, the ultrasound generation source, which is a point or a line-focused high-power laser beam, is swept across the test specimen surface and passes over surface-breaking flaws (see Figure 7.32). The generated ultrasonic wave packet is detected using an optical interferometer or a conventional contact PZT transducer either at a fixed location on the specimen or at a fixed distance between the source and receiver. The ultrasonic signal that arrives at the Rayleigh wave speed is monitored as the SLS is scanned. Kromine et al. (2000) and Sohn and Krishnaswamy (2002) have shown that the amplitude and frequency of the measured ultrasonic signal have specific variations when the laser source approaches, passes over, and moves behind the defect.

Kromine et al. (2000) have experimentally verified the SLS technique on an aluminum specimen with a surface-breaking fatigue crack of 4-mm length and 50-μm width. A broadband heterodyne interferometer with 1- to 15-MHz bandwidth was used as the ultrasonic detector. The SLS was formed by focusing a pulsed Nd:YAG laser beam (pulse duration = 10 nsec; energy = 3 mJ). The detected ultrasonic signal at three locations of the SLS position is presented in Figure 7.33. The Rayleigh wave amplitude as a function of the SLS position is shown in Figure 7.34. Several revealing aspects of the Rayleigh wave amplitude signature should be noted:

1. In the absence of a defect or when the source is far ahead of the defect, the amplitude of the generated ultrasonic direct signal is constant (see zone I in Figure 7.34). The Rayleigh wave signal is of sufficient amplitude above the noise floor to be easily measured by the laser detector (see Figure 7.33a), but the reflection is within the noise floor.
2. As the source approaches the defect, the amplitude of the detected signal significantly increases (zone II in Figure 7.34). This increase

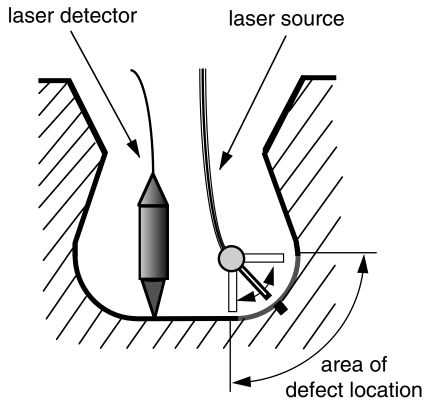

FIGURE 7.35
SLS inspection of turbine disk attachment slots.

is readily detectable even with a low sensitivity laser interferometer as compared to weak echoes from the flaw (see Figure 7.33b).

3. As the source moves behind the defect, the amplitude drops lower than in zone I due to scattering of the generated signal by the defect (see zone III in Figure 7.34).

The variation in signal amplitude is due to two mechanisms: (1) near-field scattering by the defect, and (2) changes in the conditions of generation of ultrasound when the SLS is in the vicinity of the defect. As such, the SLS technique is not very sensitive to flaw orientation (Kromine et al., 2000). In addition to the amplitude signature shown above, spectral variations in the detected ultrasonic signal also show characteristic features (Kromine et al., 2000). Both amplitude and spectral variations can form the basis for an inspection procedure using the SLS technique.

The SLS technique has been applied to detect small electrical discharge machining (EDM) notches in titanium engine disk blade attachment slots (Kromine et al., 1998) (see Figure 7.35). Cracking usually occurs on the slot-to-face transition region in these specimens. In view of the complicated and small geometry of these slots, a multimode optical fiber was used to pipe the generating laser source to the specimen. A special rotary fixture was used to house the generating fiber and scan the laser ultrasonic source within the turbine slot. The detection of the ultrasonic signal can be done using either an adaptive two-wave mixing interferometer focused within the slot, or a PZT transducer located on the easily accessible outside surface of the engine disk. The inspected slot was an EDM calibration notch of 0.05-nm width, 0.75-nm length, and 0.375-nm depth. The amplitude signature of the defect obtained using the SLS technique is shown in Figure 7.36.

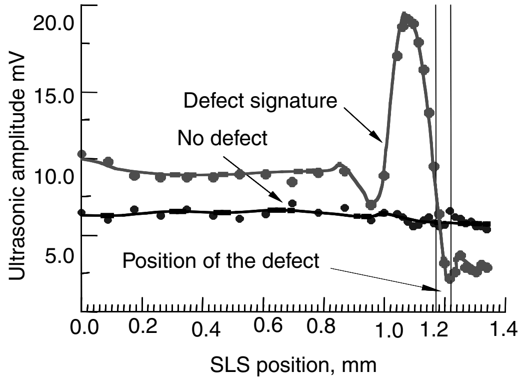

FIGURE 7.36
Amplitude signature of SLS inspection of turbine disk slots.

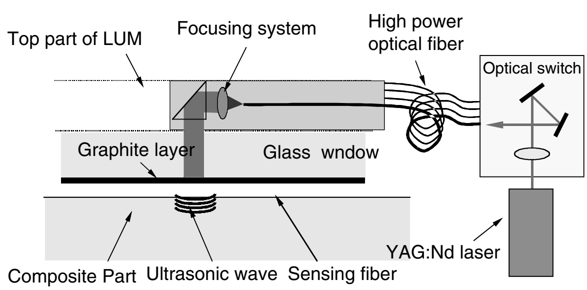

FIGURE 7.37
Schematic of a laser ultrasonic instrumented mold for graphite-epoxy composite laminate fabrication.

7.4.2 Laser Ultrasonics for Process Monitoring

Real-time laser ultrasonic systems that are rugged enough to perform in an industrial setting have been demonstrated. These systems typically use optical fibers to pipe in the generation laser beam and to gather the detection laser beam to a remote demodulation unit. Monchalin (1993) reports one of the earliest uses of laser ultrasonics in a steel mill for the measurement of wall thickness in seamless tubing. The measurements were made online at a temperature of 1000°C. An excimer KrF laser was used in the ablative mode to generate ultrasound. The back wall echoes were picked up using a confocal FP, and the wall thickness profile of the tube along its length was directly measured. The results were found to agree with handheld thickness gauge measurements.

More recent applications of laser ultrasonics in process monitoring have been to measure the properties of paper (Blouin et al., 2001), the thickness of glass (Shih et al., 2001), the evolution of microstructure (Kruger et al.,

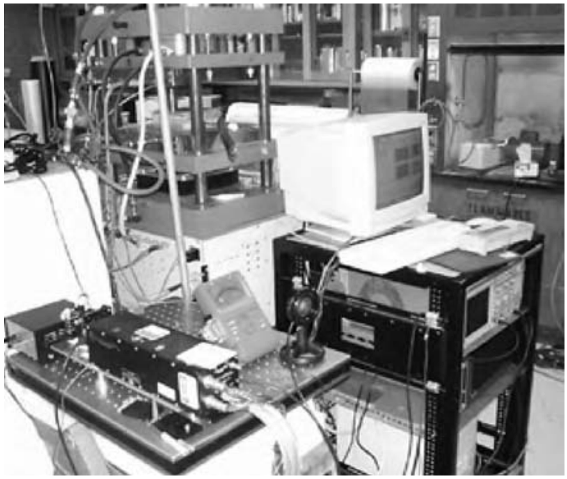

FIGURE 7.38
Photograph of the laser ultrasonic instrumented mold integrated into a resin transfer molding machine.

2002), and the curing of polymer matrix composites (Fomitchov et al., 2002). Again, in all these works, Lamb waves and bulk waves are generated and ultrasonic time-of-flight, modal dispersion, or attenuation are used to obtain the material properties. As a representative example, we will describe a laser ultrasonic method to monitor the cure of polymer matrix composites (Fomitchov et al., 2002).

A schematic of the laser ultrasonic cure monitoring system is shown in Figure 7.37. The device consists of a laser ultrasound generation system and embedded intrinsic fiber-optic Sagnac ultrasound sensors. The ultrasonic generation source is a Nd:YAG laser switch-coupled into one of four multimode optical fibers (see Figure 7.37) to provide generation capability at four locations. The output beams from the fiber are deflected 90° by a mini-prism. The deflected laser beams transmit through a glass window in an aluminum mold and are absorbed by a graphite layer deposited on the inner face of the window. Ultrasonic pulses are generated due to rapid thermal expansion of the graphite layer, and these are transmitted into the composite part. Fomitchov et al. (2002) report that the glass-graphite sandwich configuration provides higher efficiency of generation in comparison with metal or ceramic targets, and it can withstand the high temperatures inside the mold.

Fomitchov et al. (2002) have use the instrumented mold to fabricate graphite-epoxy composite laminates processed in a resin-transfer mold (see Figure 7.38). The resin material used was a mixture of three components: Araldite GY 6010 epoxy, HY 917 hardener and DY 070 accelerator (Ciba Specialty Chemicals Corporation). Typical time-domain ultrasonic signals obtained at four locations at a specific instant in time are shown in Figure 7.39. To obtain a qualitative overview of the entire cure process, the time-domain ultrasonic data obtained at four different locations at various times during the entire

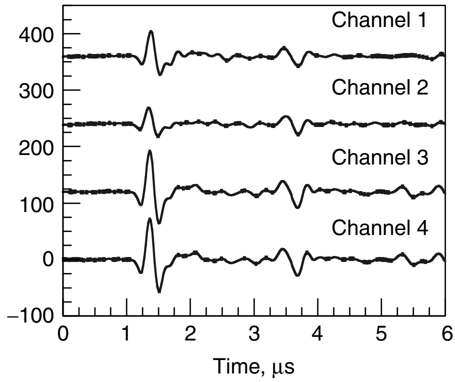

FIGURE 7.39
Time trace of typical ultrasonic signals from the four channels obtained at a specific instant during cure.

cure cycle are shown plotted as B-scans in Figure 7.40. The horizontal axis represents the cure time (in seconds) at which data were acquired, and the vertical axis represents ultrasonic *flight* time (in microseconds). The ultrasonic amplitudes are plotted as gray-level values. The B-scans contain a wealth of information about the cure state. Specifically, note that:

1. The arrival times for the generated ultrasonic wave and its reflection from the bottom of the mold have significant variations during the curing cycle.
2. Ultrasonic attenuation (as seen from the gray-level variation) changes during the cure cycle. At certain times during the cure, the attenuation is high enough that the signals are barely detected.
3. When the epoxy is a liquid (0 to 35 min), only longitudinal waves are detected.
4. Once the epoxy solidifies (after about 50 min), shear wave arrivals are observed.
5. Scatter from the various plies of the composite laminate can be clearly seen.

The ultrasonic velocities calculated from the data at various times during the cure cycle are plotted in Figure 7.41. Data from different locations and specimens are shown in the figure. Clearly there is some variation between the data obtained at different locations (possibly indicative of local variations in the cure state). Initially there is a decrease in velocity followed by a rapid increase to a final value. Fomitchov et al. (2002) have correlated the initial decrease and subsequent rise to changes in the state of the polymer as the liquid epoxy polymerizes into a solid state. Measurements such as these can

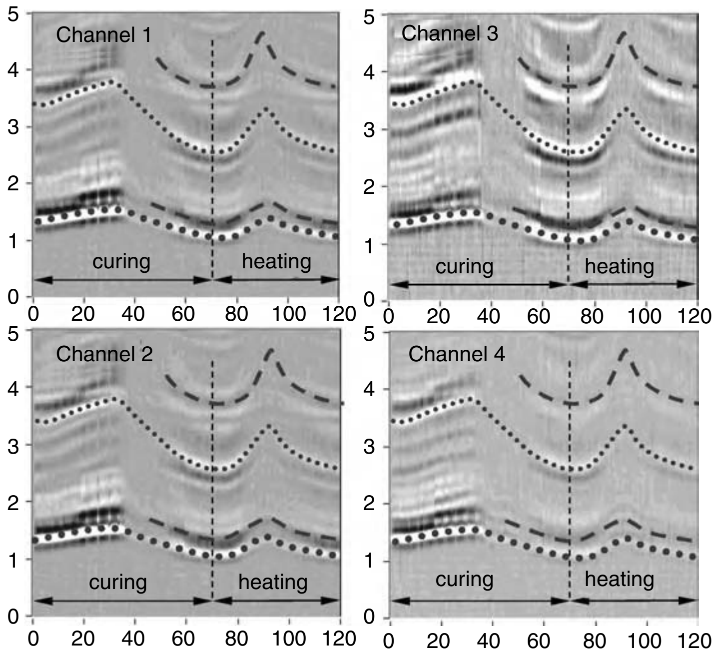

FIGURE 7.40
Laser ultrasonic data shown as B-scans for the four channels. Horizontal axis: curing time in minutes; vertical axis: ultrasonic time of flight in μs; dotted line: longitudinal wave; dashed line: shear wave.

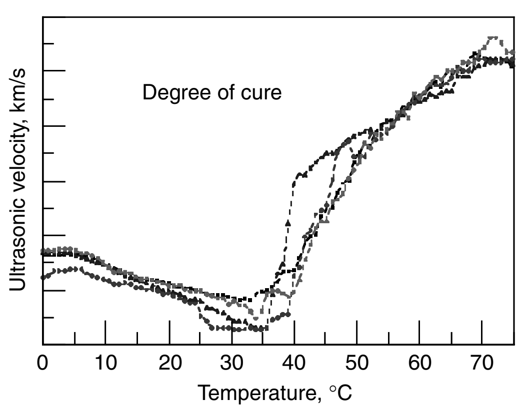

FIGURE 7.41
Ultrasonic velocity vs. curing time in minutes measured at the four locations. Vertical axis ranges from 1600 to 2800 m/sec.

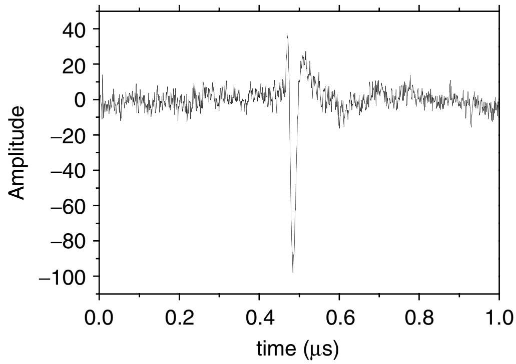

FIGURE 7.42
Broadband surface acoustic guided waves in a 1-μm TiN coating on a steel substrate: time-domain trace.

be used in real time to control process parameters to ensure that the specimen cure is uniform and complete.

7.4.3 Laser Ultrasonics for Materials Characterization

Laser ultrasonic techniques have been used to characterize the properties of materials ranging from the macro- to the microscale. Here we describe applications to thin film and coating characterization and to the determination of material anisotropy.

7.4.3.1 Characterization of the Mechanical Properties of Thin Films

The small footprint and noncontact nature of laser ultrasonic methods make them especially useful for characterizing thin films. Several optical techniques have been devised and implemented. A pump-probe technique has been used in which very high frequency (in gigahertz) acoustic waves are generated that propagate perpendicular to the film and reflect off the film–substrate interface (Thompsen et al., 1985, 1986). This bulk wave technique requires an ultrafast laser source, and material attenuation of high-frequency ultrasound limits the useful measurement range to reasonably thin films. For thicker films, guided-wave ultrasonic techniques are more practical. The impulsive stimulated thermal scattering (Duggal et al., 1992) technique and the phase velocity scanning (Harata et al., 1990) technique both use a spatially periodic irradiance pattern to generate single frequency SAW tone bursts that are detected through probe-beam diffraction, interferometry, or contact transducers. Broadband techniques (Schneider et al., 1997; Murray et al., 1999) can also be used where SAWs are generated with a simple pulsed laser point or line source that are then detected with an interferometer after some propagation distance along the film.

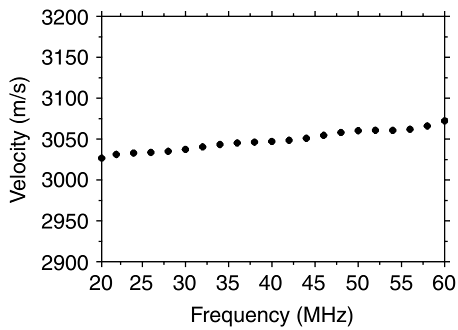

FIGURE 7.43
Surface acoustic guided waves in a 1-μm TiN coating on a steel substrate: dispersion curve.

Murray et al. (1999) have reported laser ultrasonic characterization of hard coatings. They used a broadband laser generation source by focusing a Nd:YAG laser with a 1-nsec pulse width and 3 μJ per pulse to a spot of about 40 μm diameter. The ultrasonic displacements were monitored using a stabilized Michelson interferometer with a 100-mW frequency doubled Nd:YAG laser for detection. The detection spot size was focused down to approximately 5 μm. The bandwidth of the detection system was 100 MHz. Typical ultrasonic signals in a 1-μm TiN coating on a stell substrate is shown in Figure 7.42. Since these are broadband signals, the corresponding dispersion curve can be readily obtained by measuring the ultrasonic signal at two distinct distances from the laser source (Figure 7.43). It is then possible to

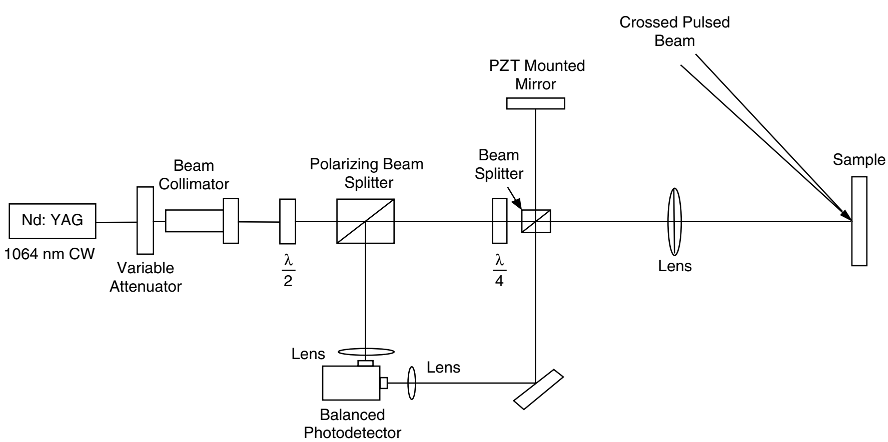

FIGURE 7.44
Schematic of the laser ultrasonic microscope for thin film characterization.

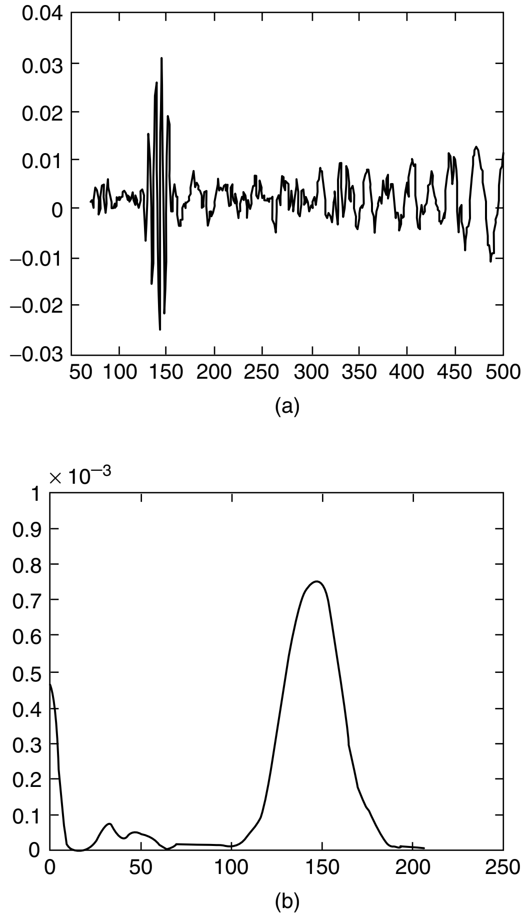

FIGURE 7.45
S_0 mode propagating on 420-nm Al/236-nm silicon nitride: (a) displacement vs. time (nsec) and (b)spectrum (MHz).

extract the material properties by minimizing the error in the dispersion curves obtained theoretically and experimentally.

Laser ultrasonic techniques can also be used to characterize the properties of *free-standing* nanometer-sized thin films (Rogers, 2000; Hernandez et al., 2002). Such thin films are widely used in microelectrical mechanical systems (MEMS) devices such as radio frequency switches, pressure sensors, and micromirrors. Figure 7.44 shows the experimental setup of Hernandez et al. (2002). In this case, narrowband laser generation is achieved by the coherent interference of two crossed pulsed laser beams that are obtained from a microchip laser that deposits pulsed laser energy (10 μJ in 300 psec) in the form of a spatially periodic source on the structure. The resulting

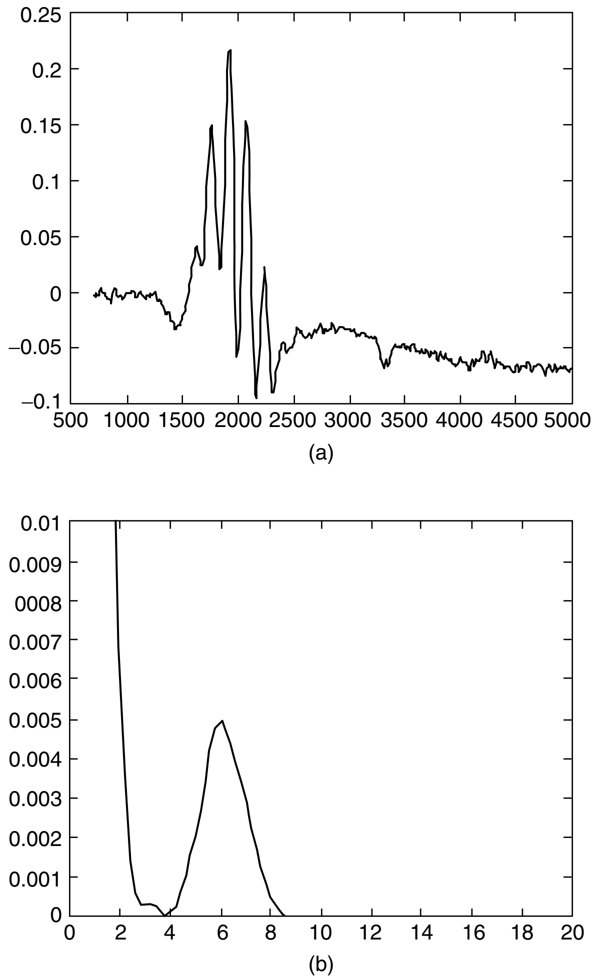

FIGURE 7.46
A_0 mode propagating on 420-nm Al/236-nm silicon nitride: (a) displacement vs. time (nsec) and (b) spectrum (MHz).

narrowband ultrasonic modes of fixed wavelength are monitored using a broadband Michelson interferometer. Since the wave numbers are fixed by the laser source, and the ultrasonic frequencies can be measured from the signals, the phase velocities of these modes are directly obtained. By varying the geometry of the spatially periodic source, a wide range of wave numbers can be probed, and the guided-wave dispersion curves can be obtained.

Figure 7.45 and Figure 7.46 show the ultrasonic signals corresponding to one wave number for the two lowest-order modes in a two-layer Al/Si3N4 membrane (aluminum thickness: 300 to 500 nm; silicon nitride thickness: 240

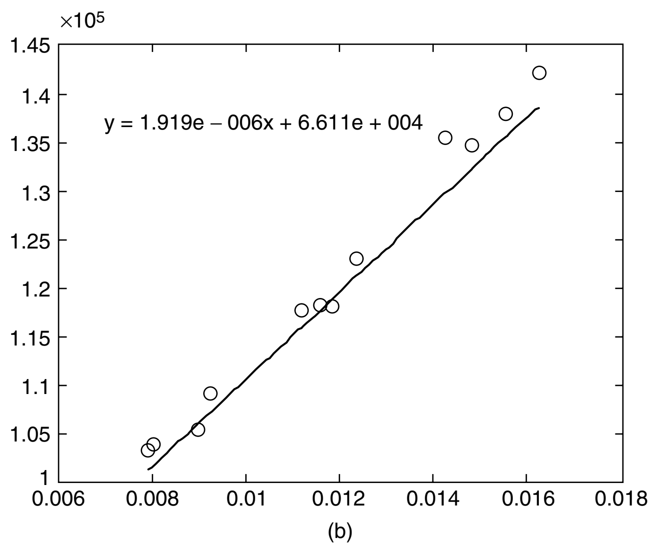

FIGURE 7.47
(a) S_0 mode dispersion curve for 420-nm Al/236-nm silicon nitride: velocity (v_{so}) in (m/sec) vs. $(kh)^2$. (b) A_0 mode dispersion curve for 420-nm-Al/236-nm silicon nitride: velocity $(v_{so})^2$ in $(m/sec)^2$ vs. $(kh)^2$.

to 400 nm). The corresponding dispersion curves for these two modes are also shown. By varying the crossing-beam angle, Hernandez et al. (2002) have obtained the dispersion curves for these two lowest order modes (Figure 7.47). From these dispersion curves, elastic properties and residual stress in the thin films have been extracted (Hernandez et al., 2002).

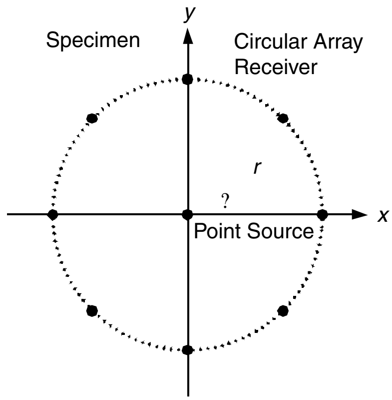

FIGURE 7.48
Point source generation and multiplexed array detection of SAWs in anisotropic materials.

7.4.3.2 Characterization of Material Anisotropy

Laser ultrasonics has been used by a number of researchers to investigate the anisotropy of materials (Maznev et al., 1999; Hurley et al., 2001; Audoin et al., 1996; Neubrand and Hess, 1992; Every and Sachse 1990). Both point- and line-focused laser sources have been used to generate the ultrasound. The ultrsaound generated by a point laser source is typically detected by a point receiver and group velocity information is obtained at different angles. Doyle and Scala (1991) have used a line-focused laser to determine the elastic constants of composite materials using the measured phase velocities of SAWs. Huang and Achenbach (1994) used a line source and a dual-probe Michelson interferometer to provide accurate measurements of time of flight of SAWs on silicon.

Zhou et al. (2002) have recently used a multiplexed two-wave mixing interferometer with eight detection channels to provide group velocity slowness images. Figure 7.48 shows the configuration of the optical beams for anisotropic material characterization using SAWs. In this setup, a pulsed Nd:YAG laser (pulse energy of approximately 1 mJ) is focused by a lens system on to the sample surface to generate the SAWs. The eight optical probe beams are obtained using a circular diffraction grating and focused on to the sample surface by a lens system to fall on a circle of radius *r* centered about the generation spot. The whole array of 8 points was rotated every 2° to obtain the material anisotropy over the entire 360° range. Since a point source and point receiver configuration is used, the surface wave group velocity is obtained in this case.

Figure 7.49a shows the time-domain SAW signals on (001) silicon from 0 to 90°. The group velocity slowness in each direction is obtained from the time-domain data through a cross-correlation technique and is shown in Figure 7.49b where the filled circles are the experimental values. Also shown in this figure is the theoretical group velocity slowness calculated

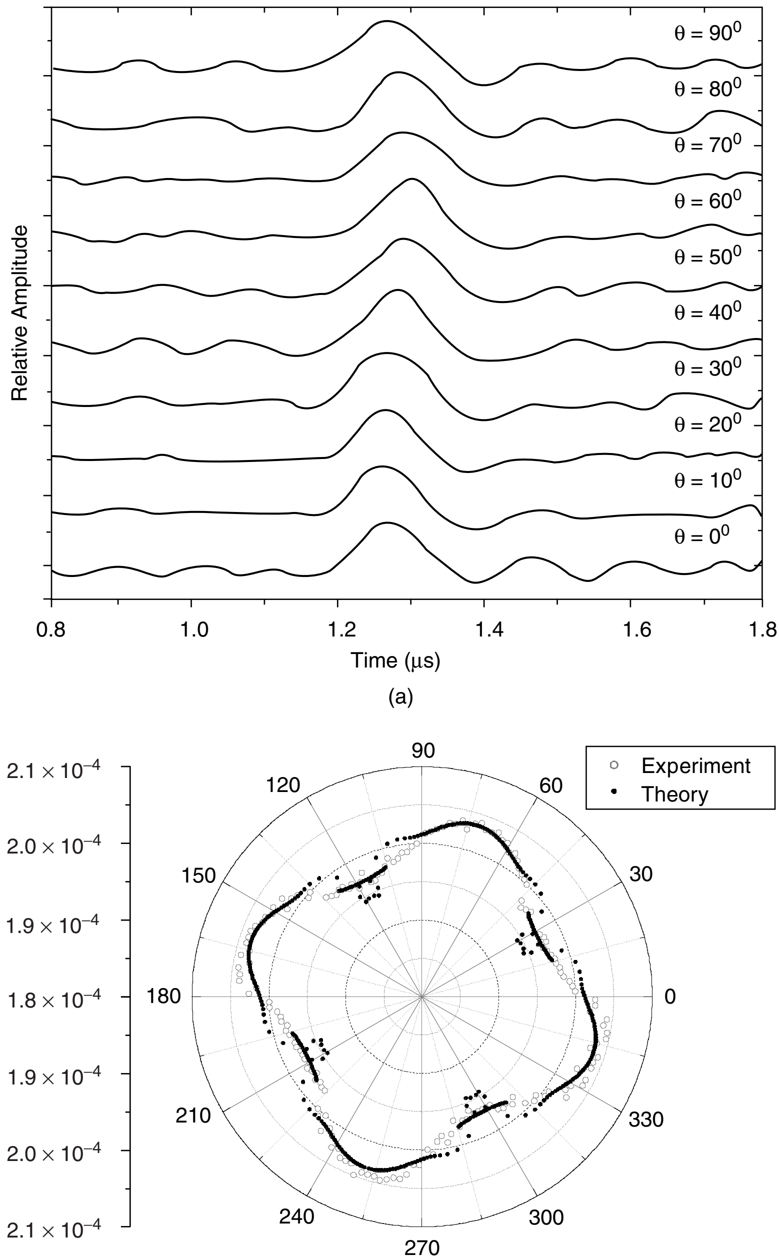

FIGURE 7.49
(a) Signals detected in different directions on *z*-cut silicon. (b) Slowness curve for *z*-cut silicon.

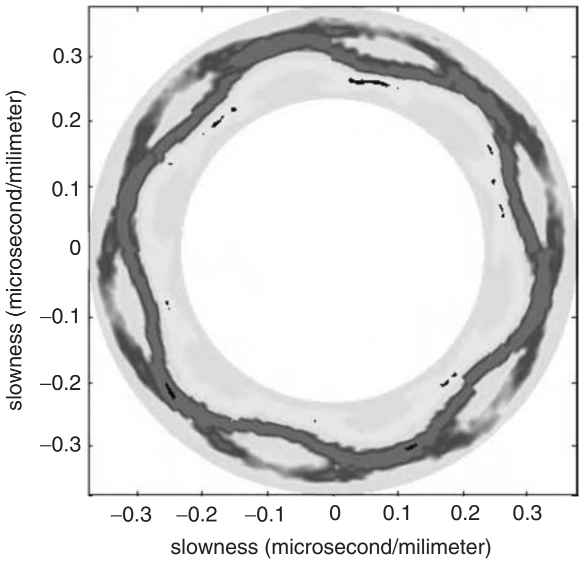

FIGURE 7.50
Group velocity slowness of *z*-cut quartz.

using nominal material values. The discontinuities that appear in both the experimental and the theoretical curves are due to the presence of pseudo-surface waves. Zhou et al. (2002) have also obtained group velocity slowness curves on the (0001) surface of a block of quartz. The time-domain traces and the corresponding group velocity slowness curves are shown in Figure 7.50. The multiple pulses observed are due to a combination of the presence of SAWs and pseudo-SAWs, as well as the energy folding that occurs in anisotropic materials such as (0001) quartz. The group velocity slowness curves obtained experimentally can be further processed to obtain the anisotropic material constants as described by Castagnede et al. (1991).

7.5 Conclusion

In this chapter, various laser ultrasonic techniques and their applications are outlined. The material discussed here represents only a small cross section of the topic. It is not meant to be exhaustive, but rather to be illustrative.

Acknowledgments

The author would like to thank Jan Achenbach, John Dorighi, Pavel Fomitchov, Carmen Hernandez, Jin Huang, Alex Kromine, Todd W. Murray, Yasuaki Nagata, Bruno Pouet, Younghoon Sohn, Hemmo Tuovinen, and Yi Zhou for many of the results that are presented in this chapter. The author is also grateful to the National Science Foundation, the Federal Aviation Administration, and the Air Force Office of Scientific Research for support of the author's research efforts.

References

Achenbach, J.D., *Wave Propagation in Elastic Solids*, North-Holland/Elsevier, Amsterdam, 1973.

Adler, R., Korpel, A., and Desmares, P., An instrument for making surface waves visible, *IEEE Trans. Sonics and Ulrasonics*, SU-15, 157, 1967.

Antonelli, G.A., Maris, H.J., Malhotra, S.G. et al., Picosecond ultrasonics study of the vibrational modes of a nanostructure, *J. Appl. Phys.*, 91, 3261–3267, 2002.

Arias, I., Modeling of the Detection of Surface Breaking Cracks by Laser Ultrasonics, Ph.D. dissertation, Northwestern University, Evanston, IL, 2003.

Audoin, B., Bescond, C., and Deschamps, M., Measurement of stiffness coefficients of anistropic materials from pointlike generation and detection of acoustic waves, *J. Appl. Phys.*, 80, 3760–3771, 1996.

Blouin, A., Reid, B., and Monchalin, J.P., Laser ultrasonic measurements of the elastic properties of a static and a moving paper web and of web tension, in *Review of Progress in Quantitative Nondestructive Evaluation*, Vol. 20, Thompson, D.O. and Chimenti, D.E., Eds., American Institute of Physics, New York, 2001, pp. 271–279.

Bowers, J.E., Fiber optical sensor for surface acoustic waves, *Appl. Phys. Lett.*, 41, 3, 1982.

Castagnede, B., Kim, K.Y., Sachse, W., Thompson, M.O., Determination of the elastic constants of anistropic materials using laser-generated ultrasonic signals, *J. Appl. Phys.*, 70, 150–157, 1991.

Choquet, M., Levesqu, D., Massabki, M., Neron, C., Bellinger, N.C., Forsyth, D., Chapman, C.E., Gould, R., Komorowski, J.P., and Monchalin, J.P., Laser-ultrasonic detection of hidden corrosion in aircraft lap joints :Results from corroded samples in *Review of Progress in Quantitative Nondestructive Evaluation*, Vol. 20, Thompson, D.O. and Chimenti, D.E., Eds., American Institute of Physics, New York, 2001, pp. 300–307.

Dandridge, A., Fiber optic sensors based on the Mach-Zehnder and Michelson interferometers, in *Fiber Optic Sensors: An Introduction for Engineers and Scientists*, Ed. E. Udd, John Wiley & Sons, New York, 1991.

Delaye, P., Blouin, A., Drolet, D., and Monchalin, J.P., Heterodyne-detection of ultrasound from rough surfaces using a double-phase conjugate mirror, *Appl. Phys. Lett.*, 67, 3251–3253, 1995a.

Delaye, P., de Montmorillon, L.A., and Roosen, G., Transmission of time modulated optical signals through an absorbing photorefractive crystal, *Opt. Commun.*, 118, 154–164, 1995b.

Delaye, P., Blouin, A., Drolet, D., Montmorillon, L.A., Roosen, G., and Monchalin, J.P., Detection of ultrasonic motion of a scattering surface by photorefractive in P:Fe under an applied DC field, *J. Opt. Soc. Am.*, B 14, 1723–1734, 1997.
De Paula, R.P., Cole, J.H., and Bucaro, J.A., Broad-band ultrasonic sensor based on induced optical phase shifts in single-mode fibers, *J. of Lightwave Technol.*, LT-1, 390–393, 1983a.
De Paula, R.P., Flax, L., Cole, J.H., and Bucaro, J.A., Single-mode fiber ultrasonic sensor, *IEEE J Quantum Electron.*, QE-18, 680–683, 1983b.
Dewhurst, R.J., Edwards, C., McKie, A.D.W., and Palmer, S.B., Estimation of the thickness of thin metal sheet using laser generated ultrasound, *Appl. Phys. Lett.*, 51, 1066–1068, 1987.
Dewhurst, R.J., and Shan, Q., Optical remote measurement of ultrasound, *Meas. Sci. Technol.*, 10, R139–R168, 1999.
Dorighi, J.F., Krishnaswamy, S., and Achenbach, J.D., Stabilization of an embedded fiber optic Fabry-Perot sensor for ultrasound detection, *IEEE Trans. Ultrason. Ferroelecteric Frequency Control*, 42, 820–824, 1995.
Dorighi J.F., Krishnaswamy, S., and Achenbach, J.D., Response of an embedded fiber-optic ultrasound sensor, *J. Acoust. Soc. Am.*, 101, 257–263, 1997.
Doyle, P.A., Laser generated ultrasonic waveforms in metals, *J. of Phys. D: Appl. Phys.*, 19, 1613, 1986.
Doyle, P.A. and Scala, C.M., Ultrasonic measurement of elastic constants for composite overlays, *Rev. Prog. Quant. Nondestructive Evaluation*, 10B, 1453–1459, 1991.
Duggal, A.R., Rogers, J.A., and Nelson, K.A., Real-time optical characterization of surface acoustic modes of polyimide thin-film coatings, *J. Appl. Phys.*, 72, 2823, 1992.
Every, A.G. and Sachse, W., Determination of the elastic constants of anisotropic solids from acoustic-wave group-velocity measurements, *Phys. Rev. B*, 42, 8196–8205, 1990.
Fisher, N.E., Surowiec, J., Webb, D.J., Jackson, D.A., Gavrilov, L.R., Hand, J.W., Zhang, L., Bennion, I., In-fibre Bragg gratings for ultrasonic medical applications, *Meas. Sci. Technol.*, 8, 1050–1054, 1997.
Fleury, P.A., Light scattering as a probe of phonons and other excitations, in *Physical Acoustics*, Vol. VI, Academic Press, New York, 1970.
Fomitchov P., Krishnaswamy, S., and Achenbach, J.D., Extrinsic and intrinsic fiber optic Sagnac ultrasound sensors, *Opt. Eng.*, 39, 1972–1984, 2000.
Fomitchov, P.F., Kim, Y., Kromine, A., and Krishnaswamy, S., Laser ultrasonic array for cure monitoring of polymer-matrix composites, *J. Composite Mater.*, 36, 1889–1901, 2002.
Grahn, H.T., Maris, H.J., and Tauc, J., Picosecond ultrasonics, *IEEE J. Quantum Electron.*, 25, 2562–2569, 1989.
Gusev, V.E., and Karabutov, A.A., *Laser Optoacoustics*, American Institute of Physics, New York, 1993.
Harata, A., Nishimura, H., Sawada, T., Laser-induced surface acoustic waves and photothermal surface gratings generated by crossing two pulsed laser beams, *Appl. Phys. Lett.*, 57, 132–134, 1990.
Hocker, G.B., Fiberoptic Sensing of Pressure and Temperature, *Appl. Opt.*, 18, 1445–1448, 1979.
Huang, J., Nagata, Y., Krishnaswamy, S., Achenbach, J.D., Laser based ultrasonics for flaw detection, IEEE Ultrasonic Symp., Levy, M. and Schneider, S.C., Eds., IEEE, New York, 1994, pp. 1205–1209.

Huang, J., and Achenbach, J.D., Measurement of material anisotropy by dual-probe laser interferometer, *Res. Nondestructive Evaluation*, 5, 225–235, 1994.

Hurley, D.C., Tewary, V.K., Richards, A.J., Surface acoustic wave methods to determine the anisotropic elastic properties of thin films, *Meas. Sci. Technol.*, 12, 1486–1494, 2001.

Hutchins, D.A., Dewhurst, R.J., and Palmer, S.B., *J. Acoust. Soc. Am.*, 70, 1932, 1981.

Hutchins, D.A., Ultrasonic generation by pulsed lasers, in *Physical Acoustics*, Vol. XVIII, Mason, W.P., and Thurston, R.N., Academic Press, New York, 1988, pp. 21–123.

Ing, R.K. and Monchalin, J.P., Broadband optical detection of ultrasound by two-wave mixing in a photorefractive crystal, *Appl. Phys. Lett.*, 59, 3233, 1991.

Jarzynski, J. and Berthelot, Y.H., The use of optical fibers to enhance the laser generation of ultrasonic waves, *J. Acoust. Soc. Am.*, 85, 158–162, 1989.

Kromine, A.K., Fomitchov, P.A., Krishnaswamy, S., and Achenbach, J.D., (1998), Scanning Laser Source Technique and its Applications to Turbine Disk Inspection, in *Review of Progress in Quantitative Nondestructive Evaluation*, Vol. 18A, Thompson, D.O. and Chimenti, D.E., Eds., Plenum Press, New York, 2001, pp. 381–386.

Kromine, A.K., Fomitchov, P.A., Krishnaswamy, S., and Achenbach, J.D., Laser ultrasonic detection of surface breaking discontinuities: scanning laser source technique, *Mater. Evaluation*, 58, 173, 2000.

Kruger, S.E., Bolognini, S., Lamouche G., and Moreau, A., Monitoring microstructure evolution of nickel at high temperature, in *Review of Progress in Quantitative Nondestructive Evaluation*, Vol. 21, Thompson, D.O. and Chimenti, D.E., Eds., American Institute of Physics, New York, 2002, pp. 1518–1526.

Lean, E.G.H., Tseng, C.C., and Powell, C.G., Optical probing of acoustic surface waves, *Appl. Phys. Lett.*, 16, 32–35, 1970.

Malacara, D., *Optical Shop Testing*, John Wiley, New York, 1992.

Maznev, A.A., Akthakul, A., Nelson, K.A., Surface acoustic modes in thin films on anisotropic substrates, *J. Appl. Phys.,* 86, 2818–2824, 1999.

McDonald, F.A., Practical quantitative theory of photoacoustic pulse generation, *Appl. Phys. Lett.*, 54, 1504–1506, 1989.

Monchalin, J.P, Optical detection of ultrasound, *IEEE Trans. Ultrasonics, Ferroelectrics, Frequency Control*, UFCC-33, 485–499, 1986.

Monchalin, J.P., Progress towards the application of laser-ultrasonics in industry, in *Review of Progress in Quantitative Nondestructive Evaluation*, Vol. 12, Thompson, D.O. and Chimenti, D.E., Eds., Plenum Publishers, New York, 1993.

Murray, T.W., Deaton, J.B., Jr., and Wagner, J.W., Experimental evaluation of enhanced generation of ultrasonic waves using an array of laser sources, *Ultrasonics* 34, 69–77, 1996.

Murray, T.W. and Wagner, J.W., Laser generation of acoustic waves in the ablative regime, *J. Appl. Phys.*, 85, 2031–2040, 1999.

Murray, T.W., Krishnaswamy, S., and Achenbach, J.D., Laser generation of ultrasound in films and coatings, *Appl. Phys. Lett.*, 74, 3561–3563, 1999.

Murray, T.W., Tuovinen, H., and Krishnaswamy, S., Adaptive optical array receivers for detection of surface acoustic waves, *Appl. Opt.*, 39, 3276–3284, 2000.

Murray, T.W. and Krishnaswamy, S., Multiplexed interferometer for ultrasonic imaging applications, *Opt. Eng.*, 40, 1321–1328, 2001.

Nagata, Y., Huang, J., Achenbach, J.D., and Krishnaswamy, S., Computed tomography using laser-based ultrasonics, in *Review of Progress in Quantitative Nondestructive Evaluation*, Vol. 14, Thompson, D.O. and Chimenti, D.E., Eds., Plenum Publishers, New York, 1995.

Nelson, K.A., Dwayne Miller, R.J., Lutz, D.R. and Fayer, M.D., (Optical generation of tunable ultrasonic waves, *J. Appl. Phys.*, 53, 1144–1149, 1982.

Neubrand, A., and Hess, P., Laser generation and detection of surface acoustic waves: elastic properties of surface layers, *J. Appl. Phys.,* 71, 227–238, 1992.

Noroy, M.H., Royer, D., and Fink, M., The laser-generated phased array: analysis and experiments, *J. Acoust. Soc. Am.,* 94, 1934–1943, 1993.

Paul, M., Betz, B., and Arnold, W., Interferometric detection of ultrasound from rough surfaces using optical phase conjugation, *Appl. Phys. Lett.*, 50, 1569–1571, 1987.

Pouet, B.F., Ing, R.K., Krishnaswamy, S., and Royer, D., Heterodyne interferometer with two-wave mixing in photorefractive crystals for ultrasound detection on rough surfaces, *Appl. Phys. Lett.*, 69, 3782–3784, 1996.

Rogers, J.A., Optical generation and characterization of acoustic waves in thin films: Fundamentals and applications, *Ann. Rev. Mat. Sci.*, 30, 117, 2000.

Rose, L., Point-source representation for laser generated ultrasound, *J. Acoust. Soc. Am.*, 75, 723–732, 1984.

Royer, D. and Dieulesant, E., *J. Appl. Phys.*, 56, 2507–2511, 1984.

Schneider, D., Schwartz, T., Bradfordm, A.S., Shan, Q., and Dewhurst, R.J., *Ultrasonics*, 35, 345, 1997.

Scruby, C.B., Dewhurst, R.J., Hutchins, D., and Palmer, S., Quantitative studies of thermally-generated elastic wave in laser irradiated solids, *J. Appl. Phys.*, 51, 6210–6216, 1980.

Scruby, C.B. and Drain, L.E., *Laser Ultrasonics: Techniques and Application*, Adam Hilder, New York, 1990.

Shih, F.J., Pouet, B.F., Klein, M.B., McKie, A.D.W., Determination of glass thickness using laser-based ultrasound, in *Review of Progress in Quantitative Nondestructive Evaluation*, Vol. 20, Thompson, D.O. and Chimenti, D.E., Eds., American Institute of Physics, New York, 2001, pp. 287–293.

Sohn, Y. and Krishnaswamy, S., personal communication, 2003.

Sohn, Y., and Krishnaswamy, S., Mass-spring lattice model of the scanning laser source technique, *Ultrasonics*, 39, 543–551, 2002.

Spicer, J., McKie, A.D.W., and Wagner, J.W., Quantitative theory for laser ultrasonic waves in a thin plate, *Appl. Phys. Lett.*, 57, 1882–1884, 1990.

Spicer, J., Laser Ultrasonics in Finite Structures: Comprehensive Modeling with Supporting Experiments, Ph.D. dissertation, Johns Hopkins University, Baltimore, Maryland, 1991.

Steckenrider, J.S., Murray, T.W., Wagner, J.W., and Deaton, J.B., Jr., Sensitivity enhancement in laser ultrasonics using a versatile laser array system, *J. Acoust. Soc. Am.*, 97, 273–279, 1995.

Thompsen, C., Grahn, H.T., Maris, H.J., and Tauc, J., Ultrasonic experiments with picosecond time resolution, *J. Physiq*, colloque C10, 46, 765, 1985.

Thompsen, C., Grahn, H.T., Maris, H.J., and Tauc, J., Surface generation and detection of phonons by picosecond light pulses, *Phys. Rev. B*, 34, 4129, 1986.

Viktorov, I.A., *Rayleigh and Lamb Waves*, Plenum Publishers, New York, 1967.

Wagner, J.W., Optical detection of ultrasound, in *Physical Acoustics*, Vol. XIX, Academic Press, New York, 1990.

Wagner, J.W., McKie, A.D.W., Spicer, J.B. and Deaton, J.B., Modulated laser array sources for generation of narrowband and directed ultrasound, *J. Nondestructive Eval*. 9, 263-270 (1990).

White, R.M., Generation of elastic waves by transient surface heating, *J. Appl. Phys.*, 24, 3559–3567, 1963.

Yang, Y., DeRidder, N., Ume, C., and Jarzynski, J., Noncontact optical fiber phased array generation of ultrasound for non-destructive evaluation of materials and processes, *Ultrasonics,* 31, 387–394, 1993.

Yawn, K.R., Drake, T.E., Osterkamp, M.A., Chuang, S.Y., Kaiser, D., Marquardt, C., Filkins, B., Lorraine, P., Martin, K., and Miller, J., Large-scale laser ultrasonic facility for aerospace applications, in *Review of Progress in Quantitative Nondestructive Evaluation*, Vol. 18, Thompson, D.O. and Chimenti, D.E., Kluwer Academic/Plenum Publishers, New York, 1999, pp. 387–393.

Yeh, P., *Introduction to Photorefractive Nonlinear Optics*, John Wiley, New York, 1993.

Zhou, Y., Murray, T.W., and Krishnaswamy, S., Photoacoustic imaging of surface wave slowness using multiplexed two-wave mixing interferometry, *IEEE UFFC*, 49, 1118–1123, 2002.

8

Electromagnetic Acoustic Transducers

Bruce Maxfield

CONTENTS

8.1 Introduction

In many ways, electromagnetic acoustic transducers (EMATs) are very simple devices; a pulse of current through one or several wires (a coil) placed in a magnetic field generates a pulse of ultrasonic energy in a metal. The underlying physics of this coupling (going from energy in an electromagnetic field to energy in an elastic wave) is very well understood. In addition to first principles derivations of practical quantities such as insertion loss or

0-8493-1462-3/02/$0.00+$1.50

transfer impedance (these are defined later), there are simpler models that yield the same results. The first principles derivations are useful as they show exactly where the various models break down.

Although this is a text with an academic orientation, our discussion of EMATs will not begin with a first principles derivation of the coupling between an external electromagnetic field and the atomic lattice in a metal. A first principles discussion is very lengthy and it adds little to one's understanding about how EMATs work and where they can be applied. Later in this chapter, we give some references to first principles derivations. With the assistance of much published literature, we will develop an accurate, quantitative description of the response of a wide variety of EMATs by applying the widely used Lorentz force model. This treatment is valid for nonmagnetic metals and magnetic metals when in a large applied field (near magnetic saturation, magnetostriction does not contribute much to the electromechanical coupling). Near the end of this chapter, we discuss some of the uses that have been made of EMATs in magnetic metals and give references to quantitative descriptions of how EMATs work in magnetic metals. In many cases, no special consideration of the magnetic properties of the metal is needed.

It is not very useful to discuss practical applications of EMATs (after all, this is an engineering text) without making direct and detailed references to how EMATs (the coil) are excited when operating in the transmit mode and how the EMAT (the coil) is used with the receiver electronics in the receive mode. Additional considerations are needed when the same EMAT is used for both transmission and reception of elastic waves, the so-called pulse-echo (PE) mode. To this end, a portion of this chapter is devoted to the circuit and other practical aspects of using EMATs.

This chapter is not intended to be a review of the EMAT literature. EMAT theory and practice has been discussed in several review articles. The reader can refer to Alers and Burns (1987), Dobbs (1976), Frost (1979), Maxfield et al. (1987), and Thompson (1990) for a general review of EMAT theory and applications and to Alers et al. (1990) for a review of how EMATs are used in nondestructive testing (NDT). These reviews and other chapters in this text are all one really needs for a complete understanding of EMAT theory and practice. Where additional details are desired, the reader is referred to the other literature cited at the end of this chapter as well as references in the above-mentioned review articles.

8.2 A Basic Yet Practical EMAT

Before getting involved in a description of the coupling between an external electromagnetic field and the atoms within a metal, I first want to describe how one particular real EMAT works. Figure 8.1 is a drawing of an EMAT that uses a cylindrical permanent magnet (PM) and a spiral-wound coil like

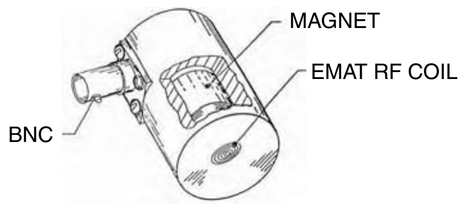

FIGURE 8.1
A small permanent magnet shear wave EMAT about 25 mm in diameter and 40 mm high.

FIGURE 8.2
Efficient planar coils that can be used for EMAT construction: (a) spiral coil, (b) double-elongated spiral coil, and (c) single-elongated spiral coil. Frequently, all but the darkened area is shielded so that eddy currents are generated in the metal surface only beneath the darkened area. The return current in the surface covers a much larger area. One advantage of placing the entire coil near the surface is that the return current path is tighter.

the one shown in more detail in Figure 8.2a. Although this EMAT does not generate a pure mode (one gets a combination of radially polarized shear waves and longitudinal waves, both propagating perpendicular to the surface), it is an efficient and practical EMAT for nondemanding tasks like thickness gauging. This EMAT is placed on or very near a metal surface. A one- or two-cycle pulse of radio frequency (RF) current (at the frequency of the ultrasonic wave one wishes to generate) is passed through the coil. Maxwell's equations (Jackson, 1962) tell us that this coil current generates a mirror image current in the metal surface (in electromagnetics, this is called the eddy current). The magnetic field produced by the PM covers the entire area over which eddy currents are generated. The magnetic Lorentz force on these eddy currents is transferred to the atomic lattice in the metal.

As described in Section 3.1, it is this Lorentz force on the eddy currents that generates the elastic wave. Electromechanical coupling takes place within the skin depth. Since the skin depth is an intimate part of the metal, no mechanical bond or impedance mismatch accompanies this coupling process. In terms of previous discussions in this book, the Lorentz force on the induced current is a body force that appears, for instance, in Chapter 1, Equation 1.79. This chapter uses mostly the same general notation for parameters like displacement, force, frequency, etc. as in Chapter 1. In order to maintain consistency with the published literature, some deviations from the notation in Chapter 1 have been introduced. These are pointed out at appropriate points within this chapter.

Although the operation of this EMAT sounds rather simple, there are many important details that enter into designing and building a useful EMAT (of course, the same is true for designing and building piezoelectric transducers that are also widely used for nondestructive testing). In Sections 8.4, 8.5, and 8.6 of this chapter, we look at many aspects that must be considered in the design, construction, and use of EMATs. I hope that this brief introduction to a real EMAT is sufficient to motivate the reader to work through the details of EMAT responses that follow.

8.3 The Lorentz Force Model

8.3.1 Generating an Elastic Wave

When an EMAT is used as a transmitting device, electromagnetic energy is converted or transformed into elastic energy. When an EMAT is used as a receiver, the reverse occurs; namely, elastic energy is converted into electromagnetic energy. These basic processes are illustrated by the elementary EMAT structures shown in Figure 8.3. Figure 8.3a shows a time varying current, I, in a thin strip near the metal surface and its image current density, J. A static magnetic field, B_O, is applied at some angle to the metal surface in the x-z plane. As shown in Figure 8.3a, the magnetic Lorentz force, f, on the eddy current lies in the surface and perpendicular to J. This body force is given by

$$\mathbf{f} = \mathbf{J} \times \mathbf{B_O} \tag{8.1}$$

NOTE: In this chapter, vector quantities are indicated by bold script.

It is shown below that this body force generates a shear displacement polarized (with displacement motion) in the direction of the Lorentz force and propagating away from the surface.

Figure 8.3b illustrates the inverse or reception process where a shear wave of peak displacement, u, is reflected from the metal surface beneath the strip. We will return to this after our description of elastic wave generation.

An EMAT being used as a transmitter is fundamentally a current operated device. This means that the elastic amplitude is proportional to the current through the wire. Many wires can be placed in close proximity to give a reasonable approximation to a current sheet (more about this later). If the current is the same in all wires, then one obtains a reasonable approximation to a plane wavefront propagating away from this part of the surface.

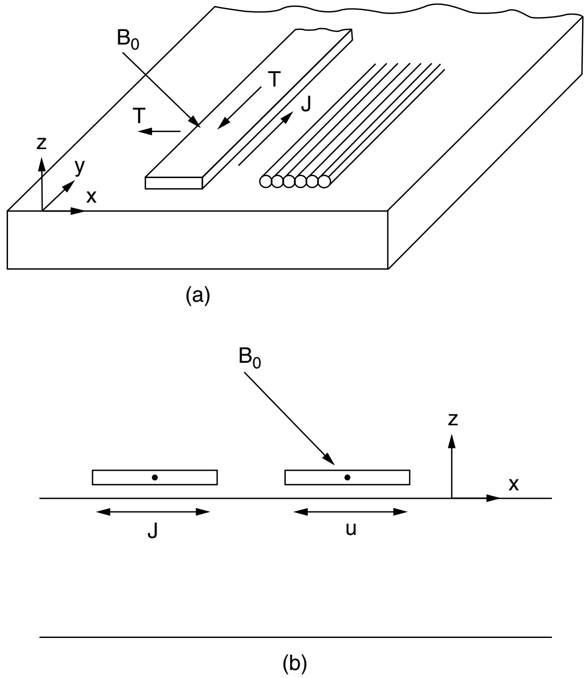

FIGURE 8.3
Representations of elemental EMATs consisting of a wire/strip or wires/strips of metal in magnetic field placed on or near a metal surface: (a) a strip carrying a current, I, placed above the surface induces a surface current density, J, in the region beneath the strip or a set of wires (a coil) of n turns per meter produces a surface magnetic field given by Equation 8.3 and (b) a metal strip bonded to the surface moves horizontally in the magnetic field when a shear wave is reflected from the surface. This generates an electric field along the strip given by Equation 8.24.

These arguments describe generally how there can be direct conversion of energy in an external electromagnetic field to energy in an elastic wave and how a plane wave might be generated. As mentioned in the introduction, a completely general, quantitative description, though reasonably straightforward, is a great deal more complex. Such a treatment is of little direct value from the point of view of understanding how practical EMATs work and how to use them. For further discussions of these electron-lattice interactions and how external electromagnetic fields can generate elastic waves in metals, in some cases without an applied magnetic field, the reader is referred to Gaerttner et al. (1969) and Dobbs (1976) and the many references contained in this chapter.

Any EMAT is a collection of wires placed in a static magnetic field. The body force (the driving force per unit volume), **f**, is given by Equation 8.1. This equation describes the driving force at each point in the metal surface. The magnetic field may be in any direction and the induced current density, **J**, may be arbitrarily complex. The propagating elastic displacement that results from any particular collection of wires and magnets is the sum of these body forces over the induced current distribution, **J(x,y)**. Pardee and Thompson (1980) have developed a formal structure to calculate the far-field radiation pattern of any EMAT (any collection of wires and magnets), and they have calculated the far-field radiation patterns for some of the practical coil-magnet structures that have been used to date to build EMATs. Other useful methods for calculating the elastic wave transmitter and receiver characteristics of EMATs (what I will refer to generally as the EMAT response) have been given by Maxfield and Hulbert (1975), Frost (1979), and Kawishima (1984).

As shown in the works cited above, calculating the actual response of even a simple EMAT can be a major task. These calculations sometimes obscure the basic physics and essential features needed to understand EMATs from a user's point of view. In order to develop an accurate understanding of the operation of EMATs in a simple and useful form, we turn to the Lorentz force model. This was first presented by Gaerttner et al. (1969) and since then it has been presented in various forms. The discussion below is a combination of what I believe to be the best features of several previous presentations. In particular, I have chosen to use almost the same notation as in the review paper of Thompson (1990). Following this work, I have chosen to express the Lorentz driving force in terms of the surface traction because this relates more directly to other work in ultrasonics. One obtains the surface traction by integrating the driving force, f, in the depth direction; namely,

$$\mathbf{T} = \int \mathbf{J(z)} \times \mathbf{B_O} dz \tag{8.2}$$

to obtain the surface driving stress or traction. Using the coordinate system defined in Figure 8.3, Maxwell's equations, and following methods given in Jackson (1962) and employed by Thompson (1990), the RF magnetic field in the vicinity of the center of the current sheet induced in the metal surface by a current of I amperes in a coil is given by

$$\mathbf{H}(z) = -n I \mathbf{j} \exp[(1 + j)z/\delta] \tag{8.3}$$

where $j = \sqrt{-1}$, n is the coil winding density in turns/meter and (**i, j, k**) are the unit vectors in the (x, y, z) coordinate system defined in Figure 8.3 (notice that the half-space occupied by the metal is z < 0). The electromagnetic skin depth, δ, is given by

$$d^2 = (2/\mu\sigma\omega) \tag{8.4}$$

where σ is the electrical conductivity in $(\Omega - m)^{-1}$; μ is the magnetic permeability in H/m; ω = 2πf; and f is the frequency in Hertz of the current, I, through the coil. If the metal is nonmagnetic, then $\mu = \mu_0$, the permeability of free space ($\mu_0 = 4\pi \times 10^{-7}$ Henries/m).

The induced current density can now be obtained from the Maxwell equation, **J** = **curl H,** where displacement currents are neglected because NDT ultrasonic measurements are always done at sufficiently low frequencies to make this an excellent approximation. Solving this Maxwell equation gives

$$\mathbf{J}(z) = -nI[(1+j)/\delta]\,\mathbf{j}\exp[(1+j)z/\delta] \qquad \textbf{(8.5)}$$

Like the magnetic field, the current density decays exponentially into the metal. Using this in Equation 8.2 gives

$$\mathbf{T} = \mathbf{K} \times \mathbf{B_O}$$

where

$$\mathbf{K} = \int \mathbf{J(z)}\,dz \qquad \textbf{(8.6)}$$

The elemental EMATs shown in Figure 8.3 use wires/strips in a static magnetic field. This field may be at any angle to the surface; Figure 8.3 shows this field at some arbitrary angle in the x-z plane so the applied or bias field in the EMAT is given by

$$B_0 = B_{0X}\ i - B_{0Z}\mathbf{k}$$

Consequently, substituting this field and Equation 8.5 into Equation 8.1 gives

$$\mathbf{f} = n\ I\ [(1+j)/\delta]\ [B_{0Z}\mathbf{i} - B_{0X}\mathbf{k}]\ \exp[(1+j)z/\delta] \qquad \textbf{(8.7)}$$

This force has components in the plane of the metal surface (proportional to B_{0Z}) and perpendicular to the surface (proportional to B_{0X}). Navier's equation for the dynamic case written in vector notation for an elastically isotropic medium is given by Chapter 1, Equation 1.79 (see Chapter 1, Section 1.1.14) as

$$(\lambda+\mu)\underline{\nabla}(\underline{\nabla}\bullet\mathbf{u})+\mu\nabla^2\mathbf{u}+\mathbf{f}=0 \qquad \textbf{(8.8)}$$

where λ and μ are the Lame′ constants (which have units of Pascals) described in Chapter 1.

This is now sufficient information to allow the lattice equation of motion to be solved. Equation 8.8 is a vector equation that must be solved with appropriate boundary conditions. There are two useful boundary conditions for elastic wave problems: a stress free surface where $(\partial u_Z/\partial z)_{z=0} = 0$, and a fixed or rigid surface where $u(z = 0) = 0$. Two special cases of the magnetic field direction illustrate all of the important aspects of elastic wave generation with EMATs. The special cases are for the applied magnetic field (often referred to as the bias magnetic field) parallel and perpendicular to the metal surface. When the magnetic field is perpendicular to the surface, the **J** × **B** Lorentz force is in the plane of the surface; this configuration generates shear displacements in the metal. When the magnetic field is parallel to the surface, the **J** × **B** Lorentz force is perpendicular to the surface; this configuration generates longitudinal displacements in the metal. For these reasons, solutions of Equation 8.8 in the literature for the magnetic field perpendicular to the surface are sometimes designated with a subscript "S," and solutions for the magnetic field parallel to the surface are sometimes designated with a subscript "L."

The solution to Equation 8.8 with the body force given by Equation 8.7 has two components of displacements. The one generated by B_{0X} is a longitudinal wave given by

$$u_{ZF} = \{[jT_{ZZ}/(\lambda + 2\mu)\, k][1 + j(\delta^2 k^2/2)]^{-1}\}\{-\exp(jkz) + 0.5[(1+j)k\delta]\exp[(1+j)z/\delta]\} \tag{8.9}$$

for the stress-free boundary condition, $(\partial u_Z/\partial z)_{z=0} = 0$, and by

$$u_{ZR} = \{[jT_{ZZ}/(\lambda + 2\mu)k][1 + j(\delta^2 k^2/2)]^{-1}\}\{\delta k/2\}\{-\exp(jkz) + 0.5[(1 + j)k\delta]\exp[(1 + j)z/\delta]\} \tag{8.10}$$

for the rigid boundary condition, $u(z = 0) = 0$. The displacement generated by B_{0Z} is a shear wave given by

$$u_{XF} = \{[-jT_{XX}/\mu k]\, [1 + j(\delta^2 k^2/2)]^{-1}\}\, \{-\exp(jkz) + 0.5[(1 + j)k\delta]\exp[(1 + j)z/\delta]\} \tag{8.11}$$

for the stress-free boundary condition, $(\partial u_Z/\partial z)_{z=0} = 0$, and by

$$u_{XR} = \{[jT_{XX}/\mu k]\, [1 + j(\delta^2 k^2/2)]^{-1}\}\{\delta k/2\}\{-\exp(jkz) + 0.5[(1 + j)k\delta]\exp[(1 + j)z/\delta]\} \tag{8.12}$$

for the rigid boundary condition, $u(z = 0) = 0$.

In all these equations, $k = 2\pi/\Lambda$, Λ is the wavelength of the elastic wave that is generated and the surface tractions are given by

$$T_{XX} = nIB_{0Z} \tag{8.13}$$

$$T_{ZZ} = nIB_{0X} \tag{8.14}$$

The shear and longitudinal wave velocities are given in m/sec by c_S and c_L, respectively. The shear and longitudinal wavelengths are given in meters by Λ_S and Λ_L, respectively, where

$$c_S = [\mu/\rho]^{1/2} \tag{8.15}$$

$$c_L = [(\lambda + 2\mu)/\rho]^{1/2} \tag{8.16}$$

$$\Lambda_S f = c_S \tag{8.17}$$

$$\Lambda_L f = c_L \tag{8.18}$$

$$k_S = 2\pi/\Lambda_S \tag{8.19}$$

$$k_L = 2\pi/\Lambda_L \tag{8.20}$$

and ρ is the material density in kg/m^3.

It is also useful to define the shear and longitudinal wave acoustic impedances, ζ; namely,

$$\zeta_S = \rho c_S \tag{8.21}$$

$$\zeta_L = \rho c_L \tag{8.22}$$

Also, in earlier work, we have defined a parameter,

$$\beta = \delta^2 k^2/2 \tag{8.23}$$

since β, rather than the conductivity, is the important parameter when analyzing the EMAT response.

There are several features of the above solutions to Equation 8.8 that are worth noting. First, let us look at the role of β. This parameter is determined by the ratio of the electromagnetic skin depth to the wavelength of the elastic wave that is generated. This is the only parameter that couples the electromagnetic and elastic properties of the metal. Combining Equation 8.4 and Equation 8.23, it is clear that β is small at low frequencies. Looking at Equation 8.10 and Equation 8.12, we see that the leading term in the elastic displacement for rigid surface boundary conditions is proportional to β. The rigid surface displacement actually peaks around $\beta = 1$. The behavior of a free surface is quite different. Here, the displacement is independent of β for small β and decreases with increasing β.

The driving force is expressed in terms of tractions or surface stresses (see Chapter 1, Figure 1.4). As pointed out in Thompson (1990), to be completely accurate, the surface stresses, T_{XX} and T_{ZZ}, as defined by Equation 8.13 and Equation 8.14 should be called the effective stresses as they are only the tractions in the high conductivity limit, $\beta \ll 1$.

As noted, β is the only quantity in the displacement equations that couples the elastic and electromagnetic properties of the metal. Table 8.1

TABLE 8.1

Parameters for Various Metals

Units	Mass Density (kg/m^3)	Electrical Conductivity [1/(μΩ - m)]	Electrical Resistivity (nΩ - m)	Shear Velocity (m/sec)	Longitudinal Velocity (m/sec)	Shear Impedance (MRayl)	Longitudinal Impedance (MRayl)
Aluminum alloy, 2024	2700	35.7	28	3100	6400	8.4	17.3
Copper wire	8930	58.8	17	2270	5010	20.3	44.7
Steel, 1020 carbon	7860	10.0	100	3200	5900	25.2	46.4
Steel, 304 stainless	8020	1.4	720	3000	5700	24.1	45.7
Malleable iron, A47	7320	3.3	300	2900	5200	21.2	38.1

Note: Relevant parameters for a few metals. Values are approximate. Values are obtained from *The Handbook of Chemistry and Physics*, 73 ed., CRC Press, Boca Raton, FL, 1993; and Kino, G.S., *Acoustic Waves: Devices, Imaging and Analog Signal Processing*, Prentice-Hall, Inc., Upper Saddle River, NJ, 1987.

gives values of ρ, σ, c_S, c_L, ζ_S, and ζ_L for a few representative metals; Table 8.2 gives the values of δ, Λ_S, Λ_L, β_S, and β_L for frequencies of 0.3, 1.0, 3.0, 10, and 30 MHz for some of these materials. Having a quick reference to these values is useful when seeking approximate ranges in which to operate when using EMATs to generate any elastic wave, not just the bulk waves discussed above.

The role of β in reducing the efficiency of an EMAT is shown very clearly in Figure 8.4 where β is increased smoothly and continuously by increasing the temperature. Agreement with the theory discussed above is quite acceptable. Referring to Table 8.2, one sees that the high conductivity limit is valid for all of these materials except stainless steel at frequencies below 3 MHz. The free- and fixed-surface transmit and receive EMAT response for three representative metals — pure aluminum with σ = 37, tungsten with σ = 18, and lead with σ = 4.5, all in units of $(\mu\text{Ohm-m})^{-1}$ as a function of frequency is given in Figure 8.5 where the frequency dependence only enters through β.

8.3.2 Receiving an Elastic Wave

So far we have discussed how elastic waves are generated by an electromagnetic field external to the metal. All the processes involved are linear and all the conditions for reciprocity are satisfied. Consequently, the same mechanisms will work to allow the energy in an elastic wave to be converted into electromagnetic energy.

Before we get to an exact treatment of using EMATs as elastic wave receivers, we want to present a simple model that illustrates very directly how EMATs receive elastic waves. Figure 8.3b illustrates the inverse or reception process where a shear wave is reflected from the metal surface beneath a massless conducting strip that is bonded to the surface. The shear elastic wave polarized in the x-direction (perpendicular to the strip direction) will move the strip back and forth in the magnetic field. The charges of electric charge, e, in this moving conductor experience a magnetic Lorentz force given by $e\mathbf{v} \times \mathbf{B_O}$, where $\mathbf{v}$ is the elastic wave displacement velocity given by $\mathbf{v} = \omega A\mathbf{i}$ and A is the displacement amplitude. Using the standard constitutive equation for a conductor (the generalization of Ohm's law when a magnetic field is present [Landau, 1960, p. 205]), this force gives rise to an electric field given by (Jackson, 1962)

$$E = v \times B_O \tag{8.24}$$

This electric field integrated along that part of the strip, L′, illuminated by the shear wave gives an open circuit voltage of

$$V_{OC} = L' \omega A B_{OZ} \tag{8.25}$$

TABLE 8.2

Wavelength, *Skin Depth*, and β at Several Frequencies

Aluminum

Frequency (MHz)	Shear Wavelength (mm)	Longitudinal Wavelength (mm)	Skin Depth (mm)	β Shear	β Longitudinal
0.3	10.33	21.33	0.154	0.004	0.001
1	3.10	6.40	0.084	0.015	0.003
3	1.03	2.13	0.049	0.044	0.010
10	0.31	0.64	0.027	0.146	0.034
30	0.10	0.21	0.015	0.437	0.103

Steel

Frequency (MHz)	Shear Wavelength (mm)	Longitudinal Wavelength (mm)	Skin Depth (mm)	β Shear	β Longitudinal
0.3	10.67	19.67	0.291	0.015	0.004
1	3.20	5.90	0.159	0.049	0.014
3	1.07	1.97	0.092	0.146	0.043
10	0.32	0.59	0.050	0.488	0.144
30	0.11	0.20	0.029	1.465	0.431

Stainless Steel

Frequency (MHz)	Shear Wavelength (mm)	Longitudinal Wavelength (mm)	Skin Depth (mm)	β Shear	β Longitudinal
0.3	10.00	19.00	0.780	0.120	0.033
1	3.00	5.70	0.427	0.400	0.111
3	1.00	1.90	0.247	1.200	0.332
10	0.30	0.57	0.135	4.000	1.108
30	0.10	0.19	0.078	12.000	3.324

This is exactly the result we obtain below using the Lorentz force model and reciprocity theory.

8.3.3 The Transfer Impedance

In the remainder of this section, we present two different (but equivalent) approaches to describing the total EMAT response (generating the elastic wave and then receiving it at a later time such as is done in standard ultrasonic PE and pitch-catch [PC] measurements). Both of these treatments have been published elsewhere. We have found the first (Maxfield and Hulbert, 1975; Gaerttner et al., 1969) to be very useful when analyzing how best to incorporate an EMAT into an actual measurement circuit. The second treatment was developed by Thompson (1990); it has the important advan-

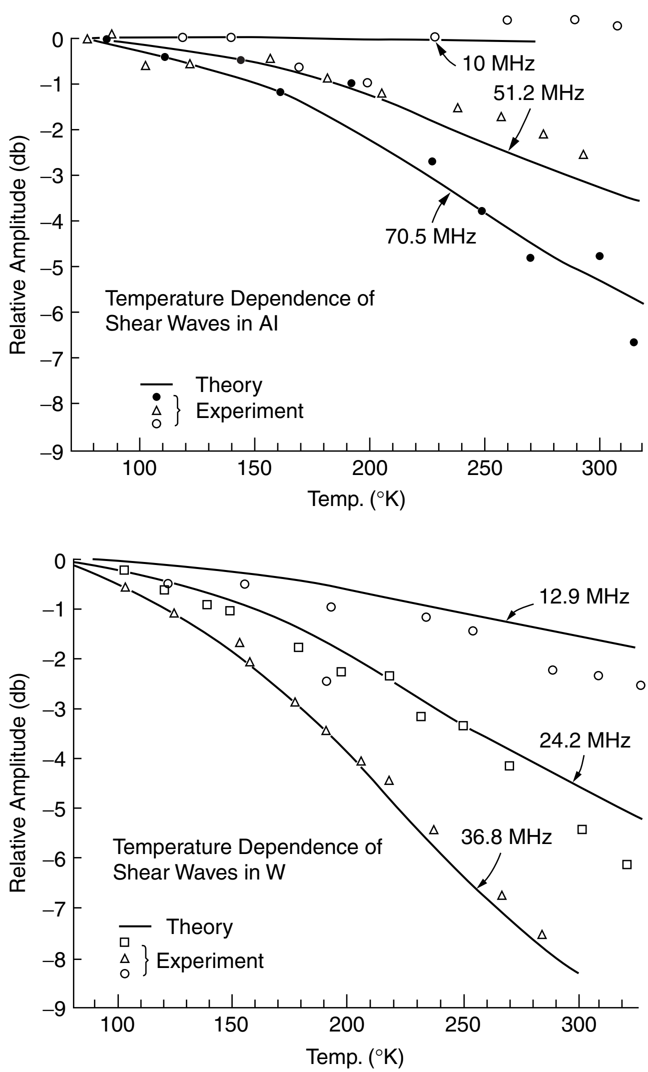

FIGURE 8.4
Dependence of the EMAT efficiency (insertion loss) upon the electromagnetic skin depth (the skin depth is changed by changing the temperature via the temperature dependent conductivity). (From Gaerttner et al., *Phys. Rev.*, 184, 702, 1969. With permission.)

tage that it can be directly related to the EMAT signal due to the presence of a flaw provided certain features of the flaw are known.

The equivalent circuit of an EMAT PC measurement is shown in Figure 8.6. The transmitter coil represented by Z_T is coupled to the receive coil represented by Z_R by an elastic wave that propagates through the metal. The acoustic power, P_{AI}, generated by a current I through Z_T is given by

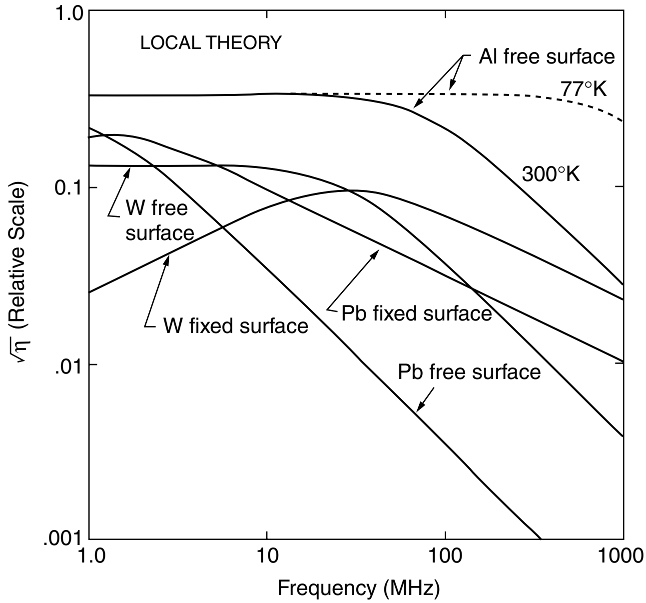

FIGURE 8.5
The calculated EMAT relative efficiency for three metals that cover the range of metal conductivities for both free- and fixed-surface boundary conditions. The frequency dependence comes from the electromagnetic skin depth (see Equation 8.4). Note the peak in response for fixed surface boundary conditions.

$$P_{AI} = 0.5\ \zeta_S\ \omega^2 \int |\, u_X(x,y)\, |^2 dxdy \tag{8.26}$$

where u is the peak displacement amplitude; for example, for a shear wave, this could be given by Equation 8.11. Equation 8.26 is a general expression valid for the power radiated from any elastic source. Integrating, we have

$$P_{AI} = 0.5\ \zeta_S\ \omega^2 |\, u_X(x,y)\, |^2 LW \tag{8.27}$$

where LW is the effective area over which elastic wave generation takes place and it is assumed that the displacement is uniform over the region beneath the coil. In order to generate this elastic power, the generator/driver must produce an electromagnetic power given by

$$P_{EI} = 0.5\ I^2\ \mathrm{Re}(Z_{TO} + Z_O) \tag{8.28}$$

where Re[Z] stands for the real part of the impedance. The input power coupling efficiency, η_I, is defined by

$$\eta_I = P_{AI}/P_{EI} \tag{8.29}$$

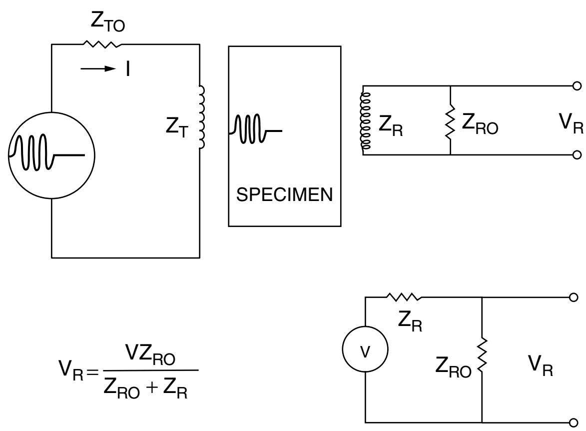

FIGURE 8.6
A schematic diagram of the transmitter and receiver coil circuits in an EMAT system; the coupling or transfer impedance is via the acoustic wave propagating in the metal. The receiver coil is a voltage source of internal impedance, Z_R.

The received acoustic power, P_{AR}, is just the input acoustic power reduced by the attenuation of the elastic wave as it propagates from the transmitter to the receiver so

$$P_{AR} = P_{AI}\exp(-2\alpha z) \tag{8.30}$$

where z is the absolute distance traveled by the wave before being received and α is the amplitude attenuation coefficient. Using the receiver equivalent circuit in Figure 8.6, the receiver output electromagnetic power, P_{ER}, is given by

$$P_{ER} = 0.5\ V^2/\mathrm{Re}[Z_R + Z_{RO}] \tag{8.31}$$

The receiver coupling efficiency, η_R, is given by

$$\eta_R = P_{ER}/P_{AR} \tag{8.32}$$

The main quantity of interest when working with EMATs is the transfer impedance, Z_T, defined as the open circuit output voltage divided by the current through the EMAT; namely,

$$Z_T = V/I \tag{8.33}$$

From Equation 8.11, Equation 8.13, and Equation 8.30, in the limit $\beta \ll 1$, for $\alpha = 0$ and for the coil area given by LW, we obtain (where n_T and n_R are the T and R coil winding densities)

$$\eta_1 = \left(n_T^2 B_O^2 LW\rho c_s\right)/[Re(Z_{TO} + Z_T)] \tag{8.34}$$

Reciprocity requires that the input and output coupling efficiencies only differ by geometrical and circuit factors. If coils of identical area are used on both sides, then

$$\eta_R = \left(n_R^2 B_O^2 LW/\rho c_s\right)/[\mathrm{Re}(Z_{RO} + Z_R)] \quad \textbf{(8.35)}$$

From Equation 8.11, Equation 8.13, Equation 8.21 and Equation 8.27 through Equation 8.35, we obtain

$$\mathrm{Z_T = n_T n_R B_O^2 LW/\rho c_s} \quad \textbf{(8.36)}$$

Similar expressions have been derived for a variety of elastic modes. This expression has been verified experimentally over the magnetic field range of 0.1 to 10 Tesla (Gaerttner et al., 1969) in aluminum.

I have found it useful to break the transfer impedance into four separate terms:

1. The intrinsic transfer impedance, Z_{TI}, calculated in the high conductivity limit and not incorporating any liftoff (coil or magnet) effects (this is the transfer impedance given above by Equation 8.36)
2. A magnet liftoff coefficient, $F_L(M)$
3. A coil liftoff coefficient, $F_L(C)$
4. A factor that includes the finite conductivity, $F(\beta)$, where $F(\beta) = 1$ for $\beta = 0$ for free surface boundary conditions

The total EMAT response is given by

$$Z_T = Z_{TI}\, F_L(M)\, F_L(C)\, F(\beta) \quad \textbf{(8.37)}$$

For example, for a liftoff distance, G, the coil liftoff coefficient for a circular coil of radius, R_C, is

$$F_L(C) = \exp(-4\pi G/R_C) \quad \textbf{(8.38)}$$

with a similar expression holding for a rectangular coil. For a meander coil (MC), we have

$$F_L(C) = \exp(-4\pi/GD) \quad \textbf{(8.39)}$$

where D is the period of the MC. This same expression holds for $F_L(M)$ for the periodic permanent magnet (PPM) EMAT described later with G being the magnet liftoff distance. When $F_L(C)$ cannot be calculated easily, it can be determined by measuring the coil impedance as a function of liftoff distance. The same is true for $F_L(M)$. $F(\beta) = (1 + \beta^2)^{-1}$ appears to be a reasonable

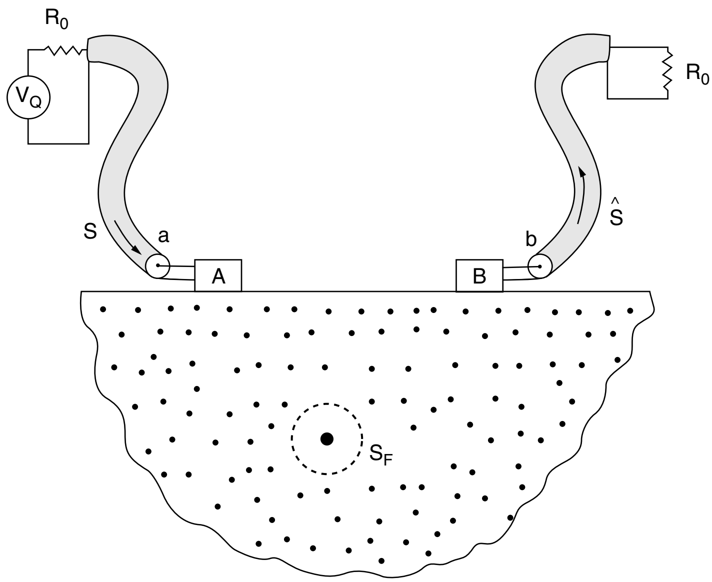

FIGURE 8.7
Conceptual view of an EMAT measurement as needed to apply the reciprocity theorem. (From Thompson, R.B., in *Physical Acoustics*, Academic Press, New York, 1991, pp. 157–200. With permission.)

approximation for all free surface boundary condition problems (it is an exact solution for normal beam shear and longitudinal waves), but this expression has not been tested very extensively. For plate and surface waves, one most likely should use separate shear and longitudinal values of β to describe the different overlap integrals for the forces driving the shear and longitudinal elastic displacements.

I have found the above treatment of transfer impedance to be useful for estimating the EMAT signals for cases such as a back wall reflection and for analyzing EMAT equivalent circuits such as the simple one shown in Figure 8.6 or the more complete one discussed in Section 8.6.

From the point of view of the physics of elastic wave scattering and estimating flaw signals, the best approach to understanding EMATs as either a transmitter or receiver is the one developed and described by Thompson (1990). Figure 8.7 shows a transmitter probe, A, connected to an exciter or driver having an output voltage, V_O, and internal impedance, R_O, by a transmission line of length, s. The receiver probe, B, is connected to the receiver preamplifier having an input resistance, R_O, by a transmission line of length s′. To avoid the need to consider reflections in the transmission lines, the generator output impedance and the receiver input impedance are both taken to be equal to the transmission line characteristic impedance, Z_O. Impedance matching can and should be used to satisfy these conditions.

As given by Thompson (1990), the voltage and current at any point in the transmission line connected to probe A is given by

$$V = V_I\,[\exp(-jks) + \Gamma_{aa}\exp(jks)] \tag{8.40}$$

$$I = [V_I/Z_O][\exp(-jks) - \Gamma_{aa}\exp(jks)] \tag{8.41}$$

where s is measured from the probe, Γ_{aa} is the voltage reflection coefficient at probe A, and V_I is the peak voltage. When the transmission line is matched to the probe, $\Gamma_{aa} = 0$. A similar set of equations can be written for probe B; namely,

$$V = V_I\,\Gamma_{ba}\exp(-jks')] \tag{8.42}$$

$$I = [V_I/Z_O][\Gamma_{ba}\exp(-jks')] \tag{8.43}$$

where s′ is measured from probe B and Γ_{ba} is the voltage transmission coefficient of the probe assembly (the combination of probes A and B).

As pointed out by Thompson (1990), one significant benefit of this approach is that Γ_{aa} and Γ_{ba} fully describe the output electrical signal. Moreover, Thompson (1990) and Auld (1990) show that

$$\delta\Gamma_{ba} = \Gamma_{ba}' - \Gamma_{ba} = (-1/4P)\int(\mathbf{v_1}\times\mathbf{T_2} - \mathbf{v_2}\times\mathbf{T_1})\times\mathbf{n}\,dS \tag{8.44}$$

where the integral is over the closed flaw surface, S_F, show n in Figure 8.7, Γ_{ba} is the transmission coefficient in the absence of the flaw, Γ^1_{ba} is the transmission coefficient in the presence of the flaw and **n** is the inward-directed unit vector normal to the flaw surface. Here, **v** is the material displacement velocity (this was used in Equation 8.24 and gave the term proportional to ωA in Equation 8.25) and **T** is the stress field radiated by the probes. The subscript "1" describes those fields that are excited when probe A is driven by an electrical power, $P = V_I^2/2Z_O$, in the absence of a flaw. The subscript "2" describes those fields that would have been excited had the receiving probe B been driven with the same power, P, and radiated into the medium with the flaw present. Reciprocity requires that $\Gamma_{ba} = \Gamma_{ab.}$ Following Thompson (1990), we will use the superscript "I" to denote flaw-free fields.

Equation 8.44 is really an amazing result because it gives the electrical signal produced by a flaw in terms of the flaw's response to the radiation patterns of the transmitter and receiver EMATs. These radiation patterns have been calculated for a few special cases and one can expect more cases to be calculated in the future.

Following Thompson (1990), we note that Γ_{ba} and not $\delta\Gamma_{ba}$ is actually measured. In the absence of elastic wave generation, the transmission coefficient would be Γ^e_{ab} and in the absence of a flaw, the response would be Γ^o_{ab}.

Consequently, the total transmission coefficient for a metal containing a flaw can be represented by

$$\Gamma_{ab} = \Gamma^{e}_{ab} + \Gamma^{o}_{ab} + \delta\Gamma_{ba} \tag{8.45}$$

The term, Γ^{e}_{ab}, is electrical cross talk between the probes. This can be made negligible for pulsed ultrasonic measurements by time gating, but it must be considered in continuous wave (cw) measurements such as some resonance EMAT work. Also, in a pulse-echo (PE) measurement, time gating can make $\Gamma^{o}_{ab} = 0$ for the time span being measured. Thus, for several practical EMAT measurement configurations where $\Gamma_{aa} = 0$, Equation 8.45 directly describes the EMAT signal.

The situation is quite different in a PC measurement where $\Gamma^{o}_{ab} \neq 0$. By placing an unbounded crack between probes A and B, Thompson (1990) developed an approximate expression for Γ^{o}_{ab} in the PC configuration; namely,

$$\Gamma^{opc}_{ab} \approx (-1/2P)\int \left(\mathbf{v}^{\mathbf{I}}_{\mathbf{2}} \cdot \mathbf{T}^{\mathbf{I}}_{\mathbf{1}}\right) \cdot n\, dS \tag{8.46}$$

The reader is referred to Thompson (1990), pp. 162 and 163 for additional discussions on the utility of this approach. It is particularily illustrative to note that Equation 8.46 is essentially the overlap integral of the radiation patterns (both in the absence of a flaw) of the two probes. Once one develops an understanding of the radiation patterns of EMATs, either from calculations such as presented by Pardee and Thompson (1980) or through actual measurements, it is possible to use this information to optimize any particular EMAT measurement configuration.

The PC method is used quite frequently with EMATs to measure the change in arrival time of an elastic wave (typically, a guided mode) due to some material anomaly in the path between the transmitter and receiver. Here, the total transmission coefficient is given approximately by

$$\Gamma_{ab} \approx \Gamma^{opc}_{ab} + \delta\Gamma_{ba} \tag{8.47}$$

where $\delta\Gamma_{ba}$ remains to be calculated or modeled for the particular anomaly of interest. For example, for a flaw small compared to the beam size, Gray and Thompson (1983) show that

$$\delta\Gamma_{ba} = j\left[\rho c^{2}_{w} A/2f\right]\left[V^{I}_{1} V^{I}_{2} / P\right] \tag{8.48}$$

where c_w is the propagation speed for the scattered wave and A is the scattered wave amplitude from the flaw. Although the tensor notation has been dropped, the material displacement velocities (v^I) should be taken in the direction of the wave polarizations linked by the scattering amplitude, A. In the PC mode, it is $\delta\Gamma_{ba}$ that produces the phase and amplitude changes in the received signal. (In real measurements, it is also possible for energy in a side lobe of the main beam to reflect from a large flaw or a material discontinuity, such as a weld, and arrive at the receiver location at the same time as the PC signal given by Γ_{ab}^{opc}, because this energy can easily be as large as that represented by a typical value of $\delta\Gamma_{ba,}$ one obtains a false flaw signal.)

In EMAT measurements, one normally measures the transfer impedance and not the transmission and reflection coefficients, Γ_{ab} and $\Gamma_{aa.}$ Referring to Figure 8.7 and Equation 8.40 through Equation 8.43, one can show that the transfer impedance, Z_{ba}, defined as the open circuit voltage from probe B divided by the current through probe A, is given by

$$Z_{ba} = (Z_{bb} + Z_o)\,(Z_{aa} + Z_o)\,\Gamma_{ba}/2Z_o \tag{8.49}$$

Following Thompson (1990), we note that in the general case, the transfer impedance is given by

$$Z_{ba} = -\int \left(\boldsymbol{V}_1'^{I} \bullet \boldsymbol{T}_2' - v_2' \bullet \boldsymbol{T}_2'^{I}\right) \bullet \boldsymbol{n}\, dS \tag{8.50}$$

where primes are used to denote radiated velocity and stress fields per unit drive current. For example, the transfer impedance for a small flaw is given by

$$Z_{ba} = j\left[2\rho c_W^2 A / f\right]\left[v_1'^{I} v_2'^{I}\right] \tag{8.51}$$

where the parameters have all been defined previously.

As originally presented by Thompson (1990) and refined by Wildebrand (1991), expressions for the transfer impedance show a commonality when expressed in terms of the radiation resistance. Following Thompson (1990), we define a normalized radiation resistance as

$$R_{L,S} = \left|(\rho c_{L,S}\omega A_{L,S}) / T^e\right| 2 \cos\theta \tag{8.52}$$

which is the stress of the radiated wave, $\rho c_{L,S}\omega\, A_{L,S}$, divided by the effective driving stress, T^e and the other quantities are as defined previously. The cosine factor accounts for the angular dependence of the power radiated per unit length of the transducer. After Thompson (1990), Figure 8.8 gives the normalized radiation resistance for aluminum for (a) longitudinal and (b) shear vertical (SV) and shear horizontal (SH) waves. Assuming free-surface boundary conditions, the transfer impedance for the MC EMAT (see Figure 8.9) is

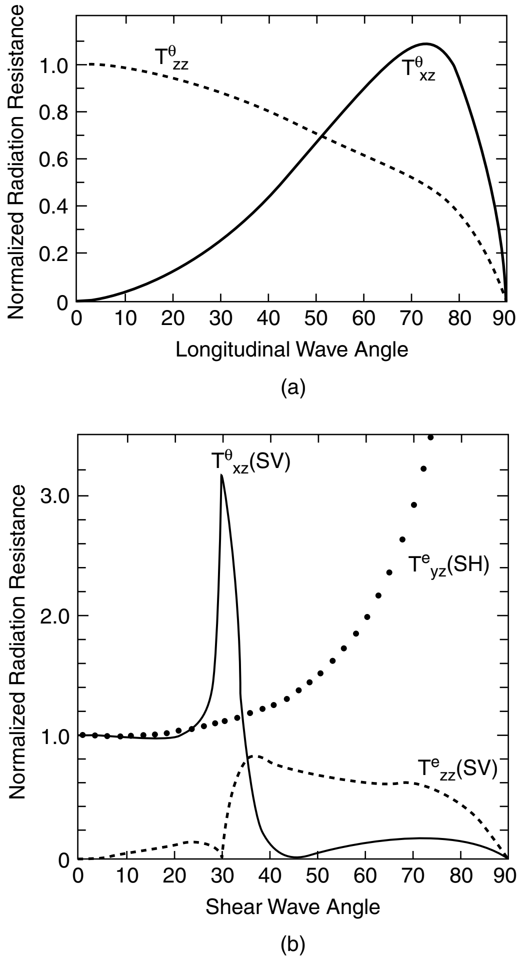

FIGURE 8.8
Normalized radiation resistance, $R_{L,S,}$ for plane wave generation by MC and PPM EMATs in aluminum. In each case, the curves are labeled by the component of driving traction considered. (a) longitudinal wave; (b) shear vertical and shear horizontal waves. (From Thompson, R.B., in *Physical Acoustics*, Academic Press, New York, 1991, pp. 157–200. With permission.)

$$|Z_{ba}| = [2/\rho c][2B_O/D]^2\{[\sin \pi a/D]/\pi a/D\}^2 \, R \, LW \qquad \textbf{(8.53)}$$

where R is the normalized radiation resistance given by Equation 8.52. The transfer impedance for a PPM EMAT in Figure 8.9 is

$$|Z_{ba}| = [8/\pi^2\rho c][nB_O]^2 \, R_S \, LW \qquad \textbf{(8.54)}$$

where R_S is the shear wave radiation resistance. Equation 8.53 and Equation 8.54 are the intrinsic transfer impedances as defined by Equation 8.37. This

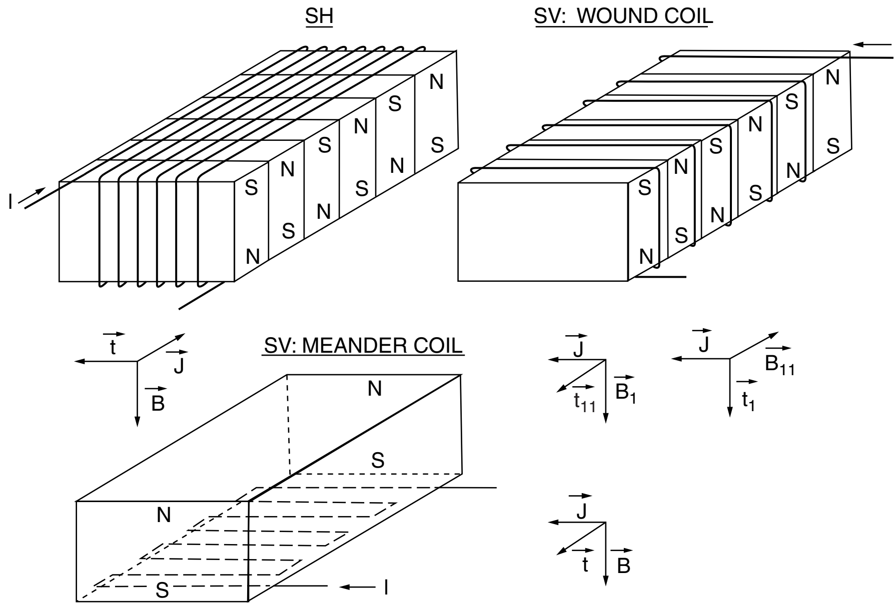

FIGURE 8.9
The three EMAT configurations with the currents, magnetic fields, and resulting forces schematically illustrated. (From Thompson, R.B., in *Physical Acoustics*, Academic Press, New York, 1991, pp. 157–200. With permission.)

treatment has the advantage of dividing the EMAT response into factors that describe the physical properties of the material and probe and the one factor, R, the radiation resistance, that describes the physics of the generation and reception processes.

8.3.4 EMAT Displacement Profiles and Radiation Patterns

The Lorentz force model, Maxwell's equations, and Equation 8.8 are used to calculate the displacement field of EMATs. The easiest real EMAT configuration to calculate is the spiral coil EMAT shown in Figure 8.1. Maxfield and Hulbert (1975) and Kawashima (1984) have given solutions to Equation 8.8, in both cases using the vector potential in the metal given by Dodd and Deeds (1968) or Onoe (1968). Although this calculation is relatively straightforward, it is lengthy. The interested reader can refer to the above references for more information.

The important conclusion that can be drawn from all of these works is that excellent quantitative agreement can be obtained between the calculated and measured response. Figure 8.10 compares the measured and calculated values for the voltage generated in a small receiver coil by the radial shear displacement generated by using a four-cycle pulse of current through a

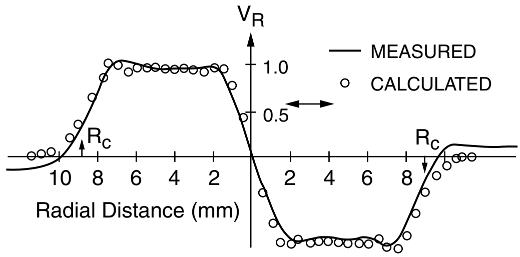

FIGURE 8.10
Comparison of the calculated (circles) response of a 19 mm diameter (R_C = 8.5 mm) spiral coil with the measured response (solid line). This signal was received on the opposite side of an aluminum plate with a 2 × 2 mm rectangular solenoid coil. The large coil was about 0.13 mm above the metal surface. There is a sign change in the voltage at the center because the receiver coil is scanned across the center of the spiral coil (the current is in opposite directions on opposite sides of the coil).

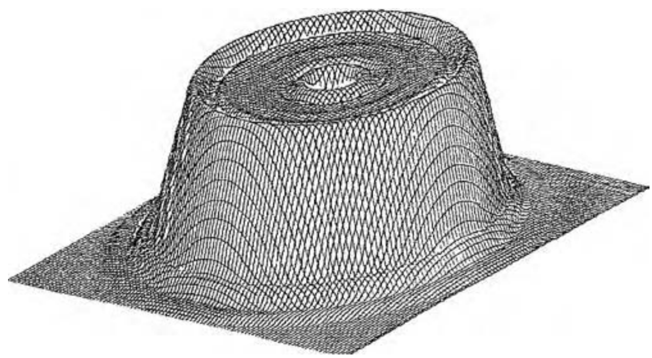

FIGURE 8.11
A reconstructed calculated acoustic mode pattern for the conditions specified in Figure 8.10. (From Maxfield et. al., *Mater. Evaluation*, 45, 1166, 1987. With permission.)

spiral coil like that shown in Figure 8.2a. The small rectangular receiver coil was scanned along a projection of the coil diameter on the metal face opposite the spiral coil (a PC configuration). The complete calculated response for this same transmitter coil is shown in Figure 8.11. Further details related to these measurements and calculations are available in Maxfield and Hulbert (1975) and Maxfield et al. (1987). A much more impressive set of calculations are presented by Kawashima (1984). Figure 8.12 shows the excellent quantitative agreement between the measured and calculated *pulse* response of a spiral coil like that in Figure 8.2a. Kawashima (1984) provides all the information needed to reproduce both the calculations and experiments that were conducted.

These calculations and measurements as well as calculations and measurements of EMAT radiation patterns given below provide ample evidence that

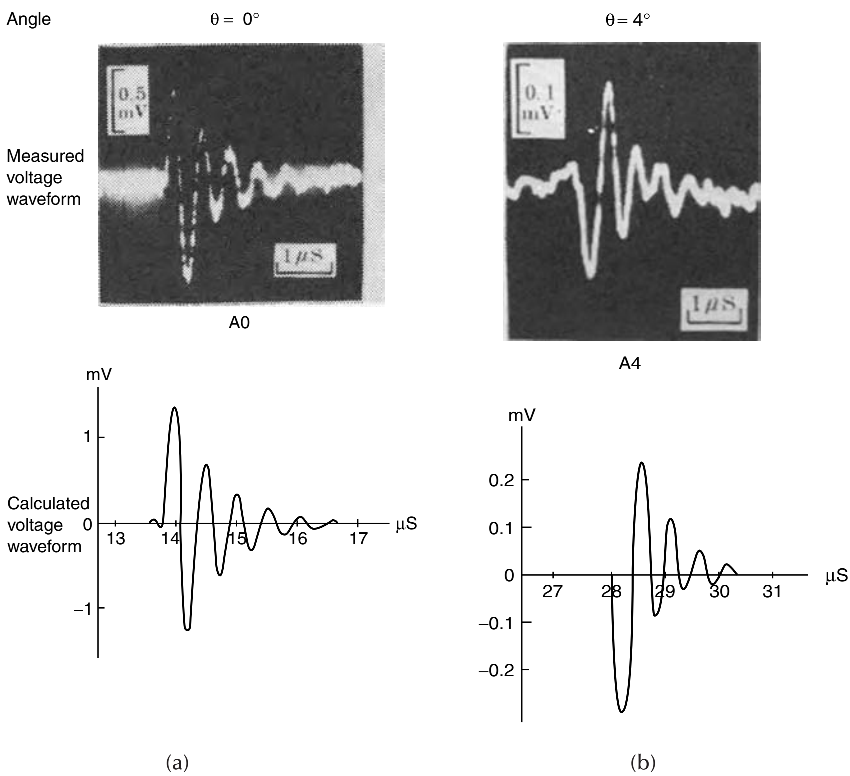

FIGURE 8.12
A comparison of the calculated output voltage (lower curve) and the measured (oscilloscope photo) ultrasonic wave pulse generated by an electromagnetic surface force: (a) longitudinal wave pulse. (b) shear wave pulse, both for propagation along the surface normal. Similar agreement is obtained for off-axis propagation (From Kawashima, H., *IEEE Trans. Sonics Ultrasonics*, SU-31, 83–94, 1984. With permission.)

we have (or could develop) an excellent quantitative understanding of all magnet-coil configurations that are used to construct EMATs. One interesting aspect of the ability to calculate the EMAT response very accurately is that it should be possible to develop an EMAT that could serve as a transfer standard for elastic energy in a metal.

So far, we have developed examples based on the generation and detection of bulk shear and longitudinal waves. As mentioned in Section 3.1, the Lorentz force model has been used by Pardee and Thompson (1980) to calculate the surface traction for different current and field distributions. Their work develops the basic equations needed to calculate the surface traction for the three types of EMATs shown in Figure 8.9. The results of calculations for a specific PPM and a specific MC EMAT are also given. Figures 6 to 14 in Pardee and Thompson (1980) are of great value when trying to understand the details of waves generated by these EMAT configurations. I recommend reading Pardee and Thompson (1980) before designing or building a practical EMAT even if one does not contemplate

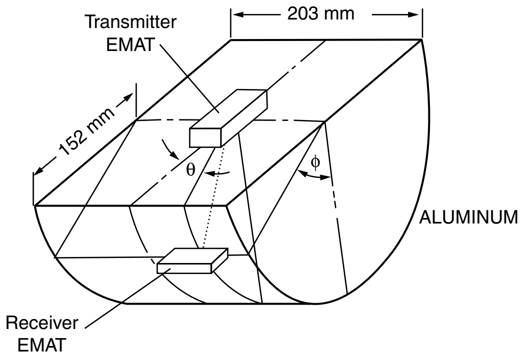

FIGURE 8.13
An experimental configuration that can be used for mapping EMAT directivity patterns. (From Maxfield and Fortunko, *Mater. Evaluation*, 41, 1399, 1983. With permission.)

actually doing the calculations described therein. Also of great value are calculations (or measurements) of the far-field radiation patterns of EMATs. There is a tremendous amount of information in the far-field EMAT radiation patterns; for example, see Figures 22 to 35 of Pardee and Thompson (1980). The reader should note that the far field can be several EMAT lengths (probably in the range up to 50 wavelengths for most EMATs currently being used) from the end of the EMAT.

EMAT radiation patterns are often not that difficult to measure. Methods are described, for example, in Maxfield and Hulbert (1975), Maxfield and Fortunko (1983), and Kawashima (1984). The experimental configuration in Figure 8.13 was used to obtain the radiation patterns measured in the sagittal plane of the PPM SH EMAT shown in Figure 8.14. The three plots in Figure 8.15 are taken at different excitation frequencies that correspond to different main lobe angles. The solid lines in Figure 8.15 are not calculated results. These radiation patterns are qualitatively similar to the calculated response for a 6-wavelength-long PPM SH EMAT shown in Figure 24 of Pardee and Thompson (1980). The main lobe in Figure 24 is much narrower than the measured response in Figure 8.15 because the EMAT in the calculations is three times longer. Using the configuration in Figure 8.13, it is relatively easy to measure the beam characteristics of an EMAT. This can be a very important step in understanding the signals obtained in EMAT measurements.

8.3.5 Guided Modes

EMATs have found very widespread use for generating surface and guided waves in metals. The physics of surface and guided mode propagation has been described in many places. This text describes surface and plate wave generation and propagation in Chapter 1, Section 1.2.9 and Section 1.2.11, respectively. Another description of surface and plate waves, including many

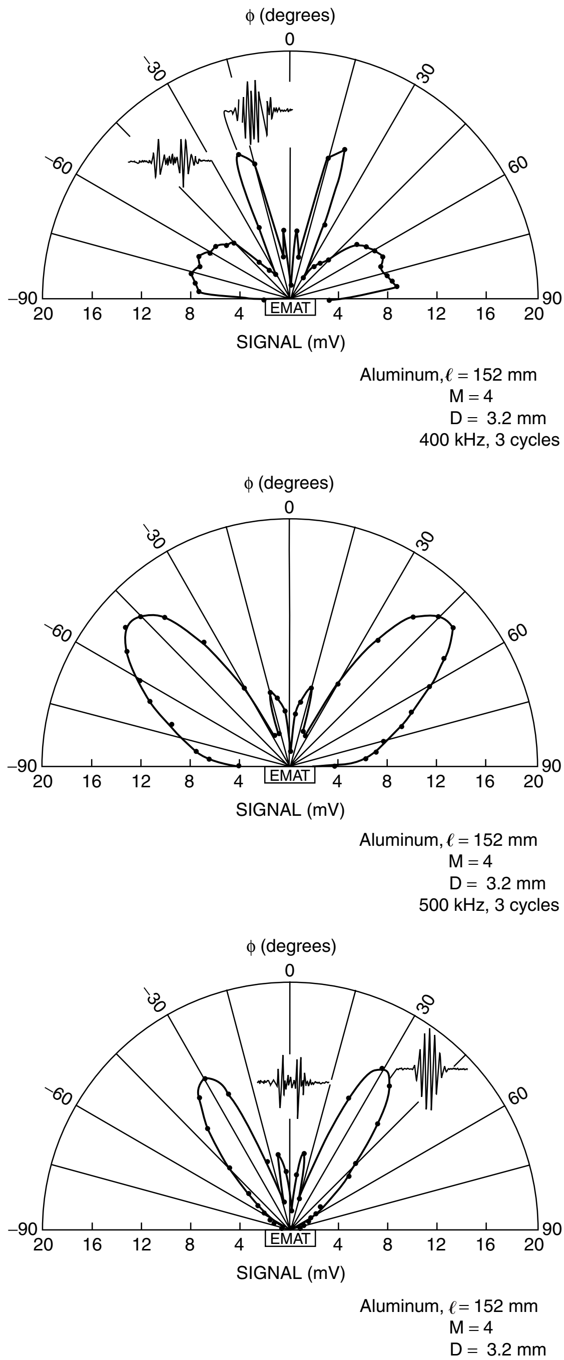

FIGURE 8.14
The SH-wave directivity pattern of a PPM SH EMAT for (a) 400 kHz, (b) 500 kHz, and (c) 700 kHz. (From Maxfield and Fortunko, *Mater. Evaluation*, 41, 1399, 1983. With permission.)

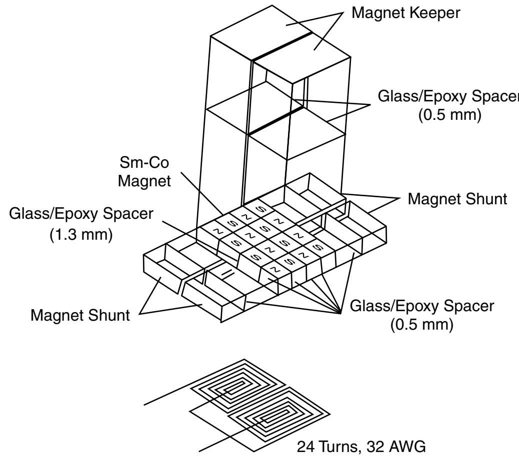

FIGURE 8.15
Cut-away view of a PPM EMAT that has good rejection of common mode electrical pickup. (From Maxfield and Fortunko, *Mater. Evaluation*, 41, 1399, 1983. With permission. Also, see Maxfield et. al., *Mater. Evaluation*, 45, 1166, 1987, for additional information on SH EMAT construction.)

calculations and practical examples, is given by Auld (1990). Rose (1999) gives a very detailed and easy-to-follow description of guided elastic waves in solids. Summarizing what was discussed in Chapter 1, no single plane wave will satisfy the free-surface boundary condition for waves propagating parallel to the surface of either a half space or plate. For these cases, one uses a superposition of partial waves. A surface wave requires the superposition of two partial waves, one longitudinal and the other shear. For a plate, two longitudinal waves and four shear waves are needed to satisfy the stress free boundary conditions at both surfaces. For a half-space, the solution is a Rayleigh wave consisting of two partial waves both decaying with depth and propagating parallel to the surface. For a plate, the partial wave solution separates into two parts; the first consists of two shear waves representing displacements both parallel to the surface and perpendicular to the propagation direction (these give rise to the SH plate modes), and the second consists of two shear waves and two longitudinal waves polarized in the sagittal x-z plane and propagating in the x-direction (these give rise to the symmetric and antisymmetric Lamb modes).

Exciting these waves requires periodic forces in order match the phase conditions for wave propagation. Guided and surface waves can be excited with exactly the same EMAT structures as used to generate bulk SH- (the PPM EMAT) bulk-SV waves and longitudinal waves (the MC EMAT). The transfer impedances, however, are quite different from the bulk wave cases. Using a normal mode formalism developed by Auld (1969) and Auld and Kino (1971), Thompson (1973) has shown that the surface displacement of a Lamb wave generated by a meander coil is given by

$$|u_x| = \left[\omega L/2Y_{Mx}^{1/2}\right]\left|\left[Txz/2Y_{Mx}^{1/2}\right] + \exp(-j\varphi)\left[Txz/2Y_{Mx}^{1/2}\right]\right| \tag{8.55}$$

$$|u_z| = \left[\omega L/2Y_{Mz}^{1/2}\right]\left|\left[Txz/2Y_{Mx}^{1/2}\right] + \exp(-j\varphi)\left[Txz/2Y_{Mx}^{1/2}\right]\right| \tag{8.56}$$

where the tractions (the high conductivity limit, $\beta \ll 1$, is assumed) are given by Equation 8.13 and Equation 8.14 and L is the EMAT length. The properties of the Lamb wave enter through the angle, φ, which is the relative phase angle between the normal and tangential surface displacements of the propagating mode and the mode admittance, Y_M, which depends upon the directions of the exciting current and applied magnetic field. For a description of the admittance parameter, see Thompson (1973). The normalized admittance curves for some symmetric and antisymmetric Lamb waves are given in Figure 8.16 through Figure 8.18. As shown in Figure 8.19, the Rayleigh wave admittance is a function of Poission's ratio. The relationship between the Rayleigh velocity and Poission's ratio is described in Chapter 1, Section 1.2.9. These admittance parameters (such as in Figures 8.16 to 8.18) and the Lamb wave dispersion curves (these can be calculated as described in Chapter 1, Section 1.2.12.2 with an example given in Chapter 1, Figure 1.31) are needed for designing plate wave EMATs. It is very important to pick modes that have a small admittance. Generally, the normalized admittance must be less than 10 in order for that mode to be excited with enough power to be useful for measurements.

Thompson (1990) shows that the surface tractions produced by an MC on a plate are given by

$$[T_{ZZ}/I] = B_{OX}[4/D][\{\sin(\pi a/D)\}/\{\pi a/D\}][\cos(2\pi x/D)]\exp(-2\pi G/D) \tag{8.57}$$

$$[T_{XZ}/I] = -B_{OZ}[4/D][\{\sin(\pi a/D)\}/\{\pi a/D\}][\cos(2\pi x/D)]\exp(-2\pi G/D) \tag{8.58}$$

from which it is shown that the transfer impedance is

$$|Z_{ba}| = [\omega^2/2]\left|\left[T_{XZ}/IY_{Mx}^{1/2}\right] - \exp(-j\varphi)\left[T_{ZZ}/IY_{Mx}^{1/2}\right]\right|^2 L^2 W \tag{8.59}$$

where the tractions include the coil liftoff coefficient. SH plate modes are excited by the surface forces produced by the PPM EMAT structure shown in Figure 8.9. Thompson (1990) shows that the surface traction and wave admittance for the PPM EMAT structure on a plate are given approximately by

$$[T_{YZ}/I] = [-4nB_O/\pi]\ [\cos(2\pi x/D)]\exp(-2\pi G/D) \tag{8.60}$$

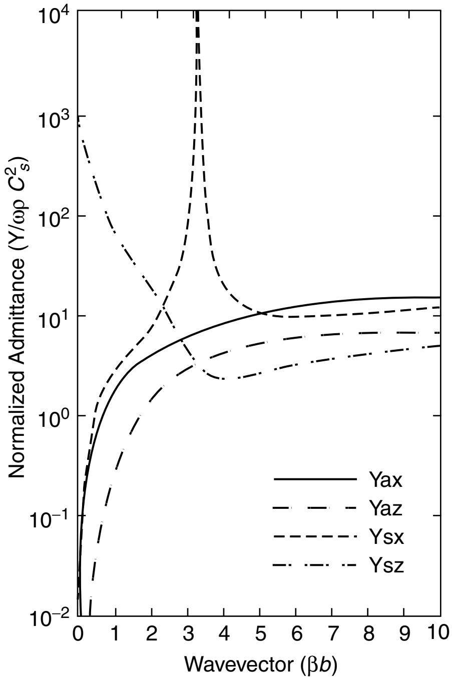

FIGURE 8.16
Normalized admittances for the n = 0 symmetric and antisymmetric Lamb modes. (From Thompson, R.B., in *Physical Acoustics*, Academic Press, New York, 1991, pp. 157–200. With permission.)

$$Y_{My} = \rho\omega c_s^2 b[(\omega/c_s)^2 - (n\pi/b)^2]^{1/2}/\varepsilon_n \tag{8.61}$$

where $\varepsilon_n = 1$ for $n = 0$ and $\varepsilon_n = 2$ for $n > 0$. From this, it can be shown that

$$|Z_{ba}| = [\omega^2/2]\left|\left[T_{YZ}/IY_{My}^{1/2}\right]\right|^2 \exp(-2\pi G/D)L^2W \tag{8.62}$$

where the traction includes the magnet liftoff coefficient. Chapter 1, Section 1.2.11 describes how one calculates the dispersion relation for SH-plate waves. Thompson (1990) also gives expressions for the dispersion relation and group and phase velocities for SH plate waves using the same notation as above.

8.4 Practical EMATs

This section gives EMAT designs for two of the EMAT structures that have been discussed above. In addition, we describe how these designs can be

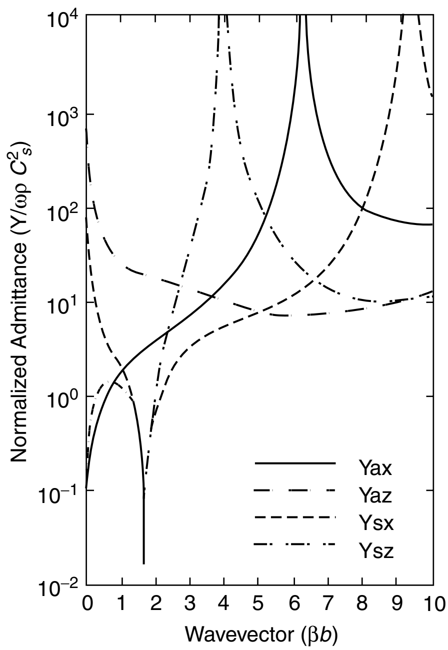

FIGURE 8.17
Normalized admittances for the n = 1 symmetric and antisymmetric Lamb modes. (From Thompson, R.B., in *Physical Acoustics*, Academic Press, New York, 1991, pp. 157–200. With permission.)

adapted to generate all of the other waves and modes that have been discussed in this chapter.

8.4.1 An EMAT for Generating Normal Beam Shear Waves

Figure 8.20 shows a practical EMAT design for normal beam shear waves (with SH polarization) for nonmagnetic metals, and Figure 8.21 shows a similar EMAT more suitable for use with a magnetic metal. These and several other useful EMATs are described in Papadakis et al. (1999). These EMATs both use the coil shown in Figure 8.2b. The EMATs are shown positioned relative to a test block. In one, a steel pole cap is used to increase the flux density in the vicinity of the coil near the magnetic surface. The dominant mode produced by these EMATs is a shear wave polarized perpendicular to the induced current. As described in the next paragraph, there is also a longitudinal wave generated, especially near the outer regions of the coil.

PMs do not produce spatially uniform magnetic fields. The magnetic field at various positions near the front face of a PM not having a pole cap is given in Figure 8.22 through Figure 8.24. The features to note are that the magnetic field at the metal surface (a distance h_2 from the magnet face, see

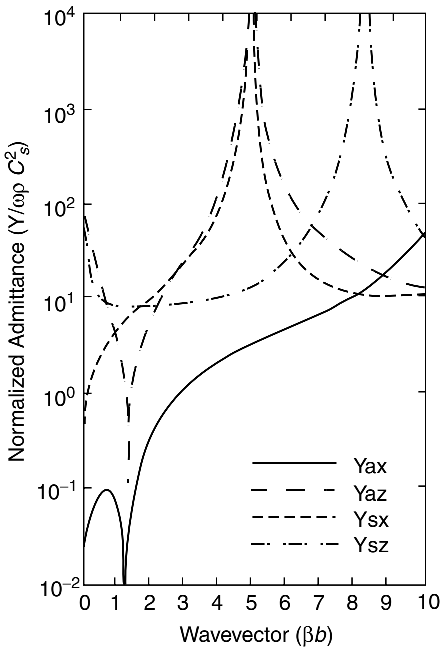

FIGURE 8.18
Normalized admittances for the n = 2 symmetric and antisymmetric Lamb modes. (From Thompson, R.B., in *Physical Acoustics*, Academic Press, New York, 1991, pp. 157–200. With permission.)

Figure 8.20 decreases with this liftoff distance as shown in Figure 8.22. Figure 8.23 shows that the perpendicular component of the field, H_Z, at and near the metal surface is reasonably constant over the central region of the PM. The magnetic field profile around an electromagnet of the same dimensions is very different so these curves are only valid for PMs. Within the different types of PMs, these curves will be a reasonable approximation to the actual field profiles if all fields are scaled by $H_Z(0,0)$, the z-component of the magnetic field at the center of the end of the PM. The radial component of the magnetic field of the cylindrical magnet is shown in Figure 8.24. Note that this field increases approximately linearly with distance from the cylindrical axis of the magnet, and that it can easily reach 0.1 to 0.2 T (1 to 2 kOe) near the magnet radius. Similar curves for a PM of rectangular cross section are not dramatically different for the central half of the magnet pole area. Magnetic field profiles around PMs can be calculated using one of several magnetic analysis software packages that are available commercially. Sometimes, suppliers of PMs will provide these profiles.

With this quantitative information about the fields produced by a cylindrical PM, it is instructive to look at how the EMAT shown in Figure 8.1 actually performs. Suppose that a spiral coil such as the one shown in Figure 8.2a with a radius of $0.8R_M$, where R_M is the magnet radius, is placed

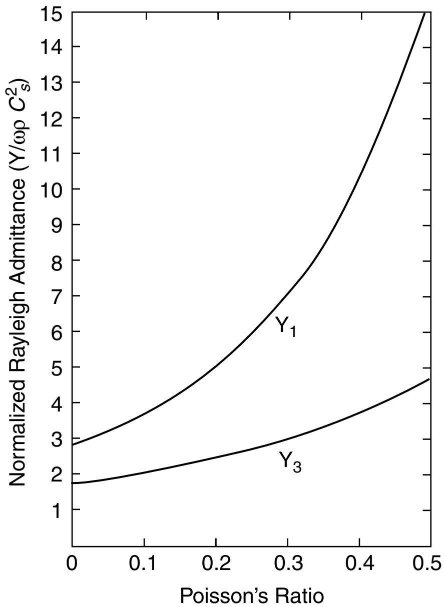

FIGURE 8.19
Normalized Rayleigh wave admittance as a function of Poission's ratio. (From Thompson, R.B., in *Physical Acoustics*, Academic Press, New York, 1991, pp. 157–200. With permission.)

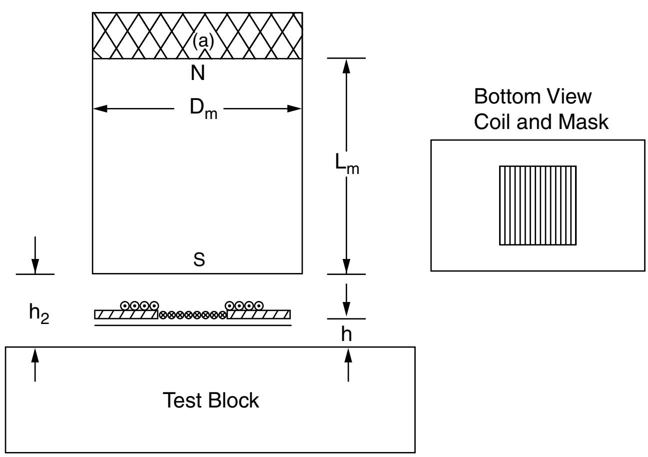

FIGURE 8.20
Sketch of a permanent magnet EMAT for the generation of linearly polarized shear waves.

near the PM so that the distance $(h_2 - h) = 1.4$ mm and $h = 0.5$ mm. The profile of the perpendicular component of magnetic field at the metal surface directly beneath this coil is given by curve (d) in Figure 8.23. The profile of the radial (horizontal) component of magnetic field at the metal surface

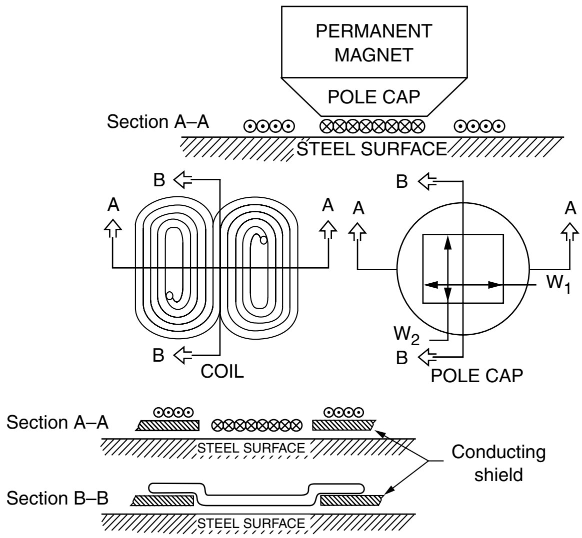

FIGURE 8.21
(a) Two elongated-spiral coils connected in series as shown in section A-A and biased by a magnetic field. The magnet pole cap shown in section B-B confines the magnetic field to the desired region for magnetic materials. (b) The central region of these coils is closer in elevation to the metal surface than the remainder of the coil. This generates a somewhat rectangular region of approximately linear current density surrounded by a much larger region of returning current. The pole cap confines the magnetic field primarily to the region where the induced current density is linear. The shield must be grounded and at least 50% larger than the total coil size.

beneath this coil is given approximately by curve (b) in Figure 8.24. The perpendicular field component generates a shear wave propagating away from the surface with a displacement given by Equation 8.11. The radial component of the magnetic field generates a longitudinal wave propagating away from the surface with a displacement given by Equation 8.9. The magnitude of the displacement profile for a spiral coil placed very near the surface is shown in Figure 8.11.

Several other features of this simple EMAT are worth noting. The actual displacement profile of a spiral coil is not a simple plane wave propagating away from the surface. Because the current on one side of the coil is exactly opposite in direction to the current on the other side of the coil, one displacement is 180° out of phase with the other. Looking at Figure 8.20 or Figure 8.21, it is also clear that the coil is also close to a PM. This means that eddy currents will be generated in the magnet. The magnetic field at the surface of the PM is given by curve (a) in Figure 8.23. Consequently, a shear elastic wave is also generated within the PM. If the other end of the PM is reasonably flat and parallel to the front surface, this elastic wave will return to the front surface at a later time where it may be detected by the EMAT coil acting as a receiver. This PM signal can be reduced substantially by

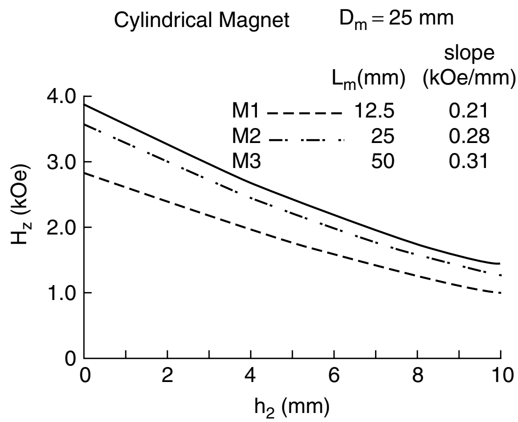

FIGURE 8.22
Magnetic field profiles: dependence of the axial component of magnetic field along the magnet symmetry axis as a function of the distance from the magnet face for three length-to-diameter ratios. These curves will scale approximately for other Sm-Co magnets if normalized to the magnetic field at the center of the magnet face. Nd-Fe-B permanent magnet curves can be derived approximately from these curves by dividing the Nd-Fe-B length-to-diameter ratio by 2, normalizing as described above and comparing with the Sm-Co curves.

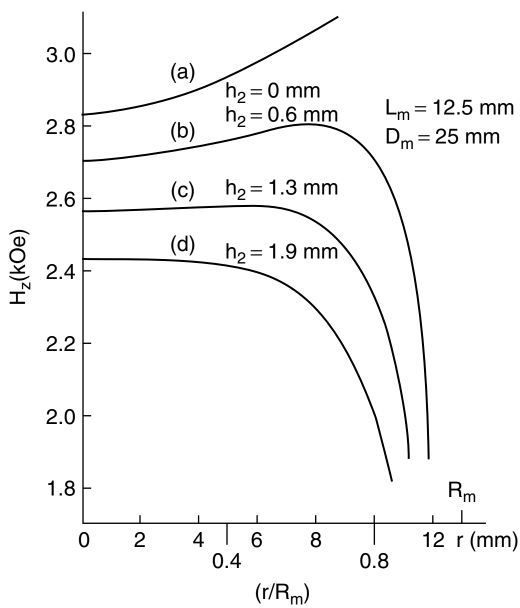

FIGURE 8.23
Radial dependence of the axial field component of a Sm-Co permanent magnet for different liftoff distances. The same scaling procedures as given in Figure 8.22 can be used to estimate the behavior of Sm-Co magnets of different length-to-diameter ratio and for Nd-Fe-B magnets.

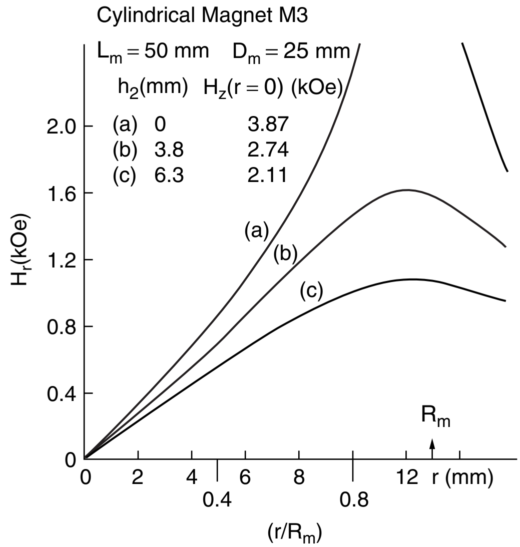

FIGURE 8.24
Radial dependence of the radial field component of a Sm-Co permanent magnet. Scaling procedures similar to those described for Figure 8.22 and Figure 8.23 apply.

placing a thin metal sheet between the coil and the PM and not bonding this thin strip to that part of the PM immediately behind the coil. It is often useful to place a piece of soft iron or cold-rolled steel on the backside of the PM. This material causes more of the magnetic flux in the PM to exit via the back face than would be the case if this iron were not used. This has the effect of making the PM a little longer than its true length. The curves shown in Figure 8.22 through Figure 8.24 depend upon the length-to-diameter ratio of the PM. For example, the perpendicular component of the magnetic field at the end of the magnet, $H_Z(0,0)$, increases with the length-to-diameter ratio. Placing a block of iron on the backside of the PM increases the front field by 10% or so at very little cost. Also, the PM sticks extremely well to cold-rolled steel. Since it is easy to drill holes in the steel and not in the PM, this backing material can be very useful for anchoring the PM to the EMAT housing (permanent magnet materials tend to be rather hard and brittle).

Figure 8.21 shows in cross section the planar (flat) coil in Figure 8.2b placed near a metal surface (Figure 8.21 shows the outer portions of the coil shielded by a conducting sheet [see the caption] and a little further from the metal surface). This approach is useful for defining the beam aperture.

8.5 EMATs and Magnetic Metals

In magnetic metals, the Lorentz force is only one of the electromechanical coupling mechanisms. The first description of electromechanical coupling

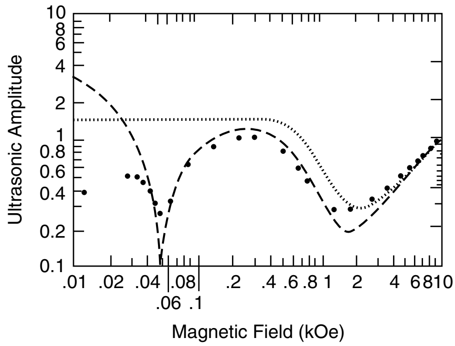

FIGURE 8.25
Magnetic field dependence of the amplitude of the first antisymmetric Lamb mode generated by a tangential field MC EMAT in steel (hot-rolled iron plate). The solid-broken line is a theoretical prediction based on measurement of magnetostrictive properties and the dotted line is a theoretical prediction based on a first principles model for grain rotation contributions to magnetostriction. (From Thompson, R.B., *IEEE Trans. Sonics Ultrasonics*, SU-20, 340–346, 1978. With permission.)

that generates elastic waves in magnetic metals was given by Thompson (1978). A good review of this coupling is contained in Thompson (1990). In addition to the Lorentz force, magnetic metals have electromechanical coupling because of magnetization and magnetostrictive forces. An exact treatment of electromechanical coupling in magnetic metals is beyond the scope of this chapter. Since magnetic steels are widely used engineering materials, it is important at least to summarize this subject here.

When the MC EMAT configuration shown in Figure 8.9 is used with magnetic metals, the transfer impedance depends much more strongly on the orientation of the magnetic field than is the case for nonmagnetic metals. Qualitative and quantitative differences in behavior are observed for both the field parallel and perpendicular to the surface. Some of the advantages of exploiting magnetic coupling mechanisms when they are available is evident in Figure 8.25. Note that the ultrasonic amplitude around 0.02 T where the contribution of magnetostriction is large is as great as in the Lorentz force regime at a field 50 times larger (1 T). This can be an enormous practical advantage.

Another important practical EMAT in magnetic materials uses the MC configuration with the magnetic field parallel to both the current and the surface (Thompson, 1991). In this case, the Lorentz force vanishes. The driving forces are such that SH-waves propagate parallel to the surface.

A practical implementation of this coupling mechanism has been developed by Davidson (1999); one configuration of this given in Figure 8.26. This EMAT has several features. First, both the transmit and receive EMATs use a pulsed magnetic field to provide the bias field. This EMAT requires a bias field parallel to the surface. It would require a magnet of large surface area (PM or electromagnet) to magnetize a thick plate even though the field requirement is not

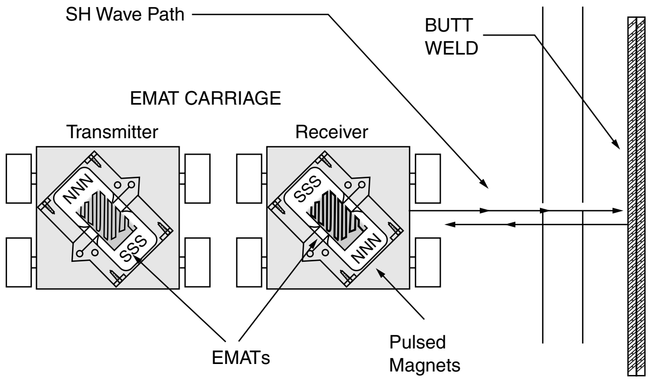

FIGURE 8.26
A magnet and coil structure that is useful for generating SH-waves by magnetostriction. Small, pulsed magnets are used to generate a biasing magnetic field parallel to the surface and at an angle to the propagation direction so as to maximize the transduction efficiency. (Figure provided by P.K. Davidson.)

great in magnitude. A pulsed magnetic field is naturally confined to the surface region. Also, notice that the surface magnetic field is neither perpendicular to the induced current nor the SH-wave propagation direction; this design feature optimizes performance of this EMAT.

Electromagnets can be very useful when working with magnetic metals because the applied field can be changed very easily. Similar performance can be realized with PMs by moving them an appropriate distance from the surface.

Magnetic properties of common magnetic steels depend upon material chemistry and mechanical processing (cold rolling, hot rolling, forging, etc.). A hammer impact on a steel pipe can create a local magnetic anomaly that will sometimes appear as a flaw or a region of small signal in an EMAT measurement. Also, some steels, such as Cr-Mo steel used in fossil fuel boilers, develop a magnetic coating and surface region that greatly enhance the generation of elastic waves. Although the electromechanical coupling efficiency of an EMAT can be greatly enhanced in magnetic metals, a successful application may require a more complete knowledge of the material than is the case for nonmagnetic metals.

Notwithstanding the above statements, many of the descriptions given in Section 8.3 and Section 8.4 of this chapter apply in a general sense to magnetic metals, especially in applied fields above 0.3 T in steel. Although the magnet liftoff coefficient is very different from that of nonmagnetic metals, the coil liftoff coefficient is exactly the same.

8.6 Using EMATs

To evaluate the displacements that are generated when using EMATs, we look at the displacement generated by the EMAT in Figure 8.21. For steel at

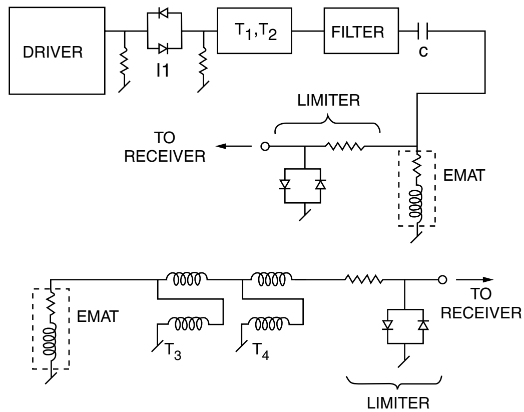

FIGURE 8.27
Schematic representation of methods for connecting an EMAT in an EMAT system.

1 MHz in an applied field of 1 T perpendicular to the surface and a current of 100 Amperes flowing through a coil having a winding density of 1000 turns/m (1 turn/mm), Equation 8.11 gives a peak displacement of 0.64 nm. This is between one and two orders of magnitude smaller than the displacement produced by a typical piezoelectric transducer (the damping or backing of an NDT piezoelectric transducer has a large influence on the output displacement). Some plate wave EMATs can generate displacements that are easily 10 times larger so EMATs used for plate wave generation will sometimes generate displacements that are as large as could be generated by a piezoelectric transducer producing the same mode. Some wave modes are easier to generate using EMATs, while others can only be generated with EMATs. However, under most conditions where EMATs are being used, they generate elastic displacements that are at least an order of magnitude smaller than those that could be generated using a piezoelectric transducer.

From the above discussion, it is clear that one should only consider using EMATs when one or more of their advantages are needed. The main advantage of EMATs is that they do not require a mechanical couplant between the transducer and test object. Another advantage related to this is the ability to operate at elevated temperatures. Although there has been much work in this area, a discussion of the many design factors related to high temperature EMATs is beyond the scope of this chapter. Some elevated temperature work is cited in Maxfield et al. (1987).

Because EMATs generate small voltage signals, it is necessary to give special attention to how EMATs are incorporated into the drive and receive electronics of the measurement system. Figure 8.27 shows a general schematic of how an EMAT may be connected to a measurement system. The upper portion is for a PE configuration. The lower portion shows how a separate coil would be connected as a receiver in the PC configuration. Below, we give the basic requirements for the various system components.

The EMAT driver is quite different from the exciter for a piezoelectric transducer. The objective of an EMAT driver is to pump current through the coil. In general, the driver output resistance will not be equal to the coil resistance so some form of impedance matching, represented by transformers, T_1 and T_2, should be used to make the best possible use of the power available in the driver. Because the current used to excite an EMAT can reach several hundred amperes, a matching transformer can require ferrite cores having a large cross-sectional area, sometimes as much as 100 mm^2. Another approach is to design the EMAT coil so that it matches the EMAT driver that is being used.

In the PE configuration, the receiver has a direct electrical connection to the driver even when the driver is not supplying current to the EMAT coil. Some form of isolator, represented here by I1, is needed between the receiver and driver. Figure 8.27 shows this isolator placed at the driver output (the resistors, which are much larger than the EMAT resistance, aid in pulse recovery of the drive circuit). If a long cable is used between the driver and EMAT (not a recommended approach), then there may be an advantage to placing the isolator and transformers near the EMAT. One type of EMAT driver uses semiconductors to alternately switch the EMAT between a positive voltage and ground or between a positive and negative voltage. In this way, one generates a square voltage pulse at the frequency one requires for EMAT operation. It is quite obvious that this is not the time dependence assumed in writing Equation 8.3 or in solving Equation 8.8. Most of the time, square wave voltage excitation works just fine, partly because the EMAT acts like a filter. This is especially true for the EMAT structures shown in Figure 8.9 because they are inherently fairly narrowband devices. If the user is concerned about this type of driver generating unwanted harmonic content in the elastic wave, then an appropriate filter can be placed as shown in the drive circuit.

The tuning capacitor, C, can be useful. This capacitor should be chosen so that it forms a slightly under damped or critically damped circuit with the EMAT resistance, inductance and shunt capacitance. It is usually best to place C close to the EMAT. There are many useful tips on working with RF circuits in *ARRL Handbook for Radio Amateurs* (2001). In particular, there is a description of narrowband matching between a transmitter and a load EMAT.

In the PE configuration, the receiver is connected directly to the driver while the excitation current is applied to the EMAT. Since the voltage across the EMAT can easily reach many hundreds of volts (the transient voltage can be several times the output voltage of the driver), it is easy to damage the sensitive electronics in the receiver circuit. The limiter is there to protect the receiver. The resistor in the limiter needs to be several times larger than the impedance of the EMAT to avoid shunting some of the driver current around the EMAT. In addition, the input resistance of the receiver preamplifier should be at least a few times larger than the series resistor in the limiter in order to avoid significant signal loss in this voltage divider. As described below, the receiver resistance is a source of noise. It can be a challenging task to balance all the competing factors, especially if receiver impedance matching transformers are used.

The above considerations sometimes dictate altering the EMAT system diagram shown in Figure 8.27. There are two common alternatives. The first is to use an active (electronic) switch to connect the EMAT to the receiver. Such a switch is opened just before the current pulse is applied to the EMAT so there is a high impedance between the driver and receiver (here, it can be important to give careful attention to capacitive coupling). After the drive current has returned to zero and most of the stored energy in the EMAT inductance has dissipated, the switch is closed so the receiver is connected to the EMAT coil. This allows for optimum matching of the EMAT to the receiver and enables one to obtain the lowest possible electronic noise in the receiver circuit. A second approach is to use a separate receiver coil. If one uses a printed circuit coil or a coil made of fine wire, the receiver coil may be placed beneath the transmitter coil without adding much additional liftoff or screening of fields generated by the transmitter coil. Using a second coil near the transmitter coil still leaves one with a large induced voltage to manage. This can be handled by the methods described above, but an active switch is probably the best method to use.

Additional discussions related to specific parts of the EMAT system are presented below.

8.6.1 Circuit and Electronic Considerations for EMATs

Using an EMAT as a receiver is a very different circuit function than using it as a transmitter. Here, we discuss optimizing receiver performance when separate transmitter and receiver coils are used.

A good first step in understanding EMATs as receivers in real circuits is to look at Equation 8.25. The displacement amplitude at the receiver is determined by the transmitting EMAT and the propagating medium so it is not a variable in receiver EMAT design. The magnetic field should be as large as possible but, beyond a few basic considerations, one is normally forced to work with B_O between 0.2 and 2 T. The length of wire that is placed adjacent to the metal surface (the wire that is effective in receiving an EMAT signal) can, in some cases, be made quite large but it is normally restricted by other design factors. The bottom line is that many factors often limit the design optimization process for the receiver EMAT coil even when it is different from the T coil. This means that one needs to look critically at how the receiver is connected into the EMAT system.

The most important factor to consider when using EMATs as receivers is to obtain good impedance matching between the EMAT receiver coil and the preamplifier. This requires matching the EMAT coil resistance, R_S, to the amplifier input resistance, R_A. The receiver EMAT coil resistance is sometimes as small as a fraction of 1 Ω, while the input resistance of a preamplifier is usually in the range of 30 to 300 Ω. Without proper impedance matching, this mismatch can result in an enormous loss of signal-to-noise ratio (SNR) (but not necessarily a loss in signal). One does not normally think of a 30-Ω input resistance amplifier as providing any significant problem when one has a 1-Ω source. However, without using impedance matching, the noise from the receiver input resistance can dominate the system noise behavior. The best SNR is achieved when the source resistance is as small as possible and yet dominates the system noise. This can be achieved, or at least approximated, through impedance matching.

Broadband impedance matching transformers, usually of the transmission line type, are available commercially. Since currents in the EMAT receiver circuit are usually very small, a receiver impedance matching transformer does not require ferrite cores of large cross-sectional areas (areas in the range of 1 to 5 mm^2 are normally used). The possible exception to this is when a receiver coil is connected to transformers without using an active switch.

Although it is common to use small diameter wire or printed circuits for EMAT receiver coils, the resistance of the rest of the receiver circuit before the impedance matching transformers should be made as small as possible in order to minimize the source noise resistance. A larger receiver bandwidth can be achieved if the distance between the receiver coil and the matching transformer is minimized because this minimizes the effective source capacitance. It is also important to shield the EMAT coil and any connecting wires from stray electromagnetic pickup because this noise will also appear directly as source noise. One very effective shield is a thin metal foil placed in front of the EMAT receiver coil (between the coil and the metal surface); this shield should be grounded to the object being measured using a very tight mechanical or, preferably, a soldered connection that is as short as possible. In a very noisy electrical environment, it is often beneficial to use a differential amplifier and treat the shield as a guard.

8.6.2 EMAT Noise Considerations

A combination of random electronic and coherent acoustic noise ultimately limits the performance of any EMAT system. Random electronic noise will always be present. The mean squared noise voltage of a resistance of R Ω, V_n^2, is given by

$$V_n^2 = 4kT_KR\Delta f \tag{8.63}$$

where $k = 1.38 \times 10^{-23}$ J/K, T_K is the temperature in Kelvin, and Δf is the system electronic noise bandwidth in hertz. As a practical example, let us take a bandwidth of 1 MHz and use a receiver coil having a resistance of 5 Ω (a reasonable value for either a wire wound or printed circuit EMAT coil that is near a permanent magnet and a metal surface). At T_K = 300 K, this gives a noise voltage of

$$V_n = 0.3\ \mu V_{rms} \tag{8.64}$$

Let us assume that we are working with a low-noise preamplifier having equivalent input noise resistance of 40 Ω; this will contribute a noise voltage of $V_{na} = 0.8\ \mu V_{rms}$. A 1:9 impedance matching transformer (a voltage transformation of 1:3) will give a total noise at the amplifier input of about $1.2\ \mu V_{rms}$ (the resultant noise is the square root of the sum of the squared noise voltages or $(V_n^2 + V_{na}^2)^{0.5}$. A 1-μV_{rms} signal from the EMAT coil gives a $3 = \mu\ V_{rms}$ signal at the amplifier input for an input SNR of 2.5. Without the transformer, the SNR is (1.0/0.85) = 1.2. Just using a matching transformer doubled the SNR. Some EMATs have a source resistance as small as 0.1 Ω; here, matching could achieve an increase of as much as 14 in the SNR. This is the difference between a signal that cannot even be seen on an oscilloscope and one that can be used directly for thickness gauging.

To put these numbers in perspective, the transfer impedance from Equation 8.36 is about 4 μΩ for steel at a field of 1 Tesla and using a coil that is 1 × 1 cm. A current of 100 A through this coil gives an EMAT output voltage of 400 μV, well above the noise of a well-matched EMAT system.

One factor that can nullify any effort at impedance matching is electromagnetic pickup. RF fields in the EMAT frequency operating range are everywhere (e.g., AM broadcasts). If reasonable attention has been paid to shielding and grounding, it is usually possible to reduce the general pickup noise in a receiver circuit to the range of 0.1 to 1.0 μV_{rms}. From the noise calculations given above, it is clear that good shielding and grounding methods are essential for reliable EMAT measurements. A good measure of system noise is obtained when the EMAT system is ready to operate, but there is no current in the drive coil.

Coherent acoustic noise is much more difficult to estimate. It has two main sources: grain scattering and multiple reflections in the material being studied and elastic waves generated in the EMAT magnet and case by the transmitter current that, at a later time, induces a voltage in the receiver coil. Spatial averaging, a signal processing method that is mentioned in Section 8.6.3, can be used to reduce coherent noise due to grain scattering and multiple reflections. Temporal averaging of electronic signals is much more common, but this does not reduce coherent acoustic noise.

The system electronic noise can also be reduced by decreasing the bandwidth. Although this is usually not of much use when a half-cycle or single-cycle excitation pulse is used, it can be of considerable benefit when multicycle tone bursts are used to drive the EMAT. The longer the tone bursts, the smaller the system bandwidth that is required to produce an undistorted signal of the system response. There are both analog and digital methods for reducing the signal bandwidth. Digital methods offer the greatest flexibility but analog methods can be an advantage if the system lacks sufficient dynamic range.

8.6.3 Signal Analysis Techniques

An extensive discussion of the many very useful signal analysis methods that are available when working with EMAT signals is beyond the scope of this chapter. In this section, we mention some methods that have proven useful.

Temporal averaging is the coherent summing of consecutive waveforms. Since the signal will add coherently and the noise will add randomly, temporal averaging improves the SNR of the overall waveform. The SNR improvement is proportional to the square root of the number of times the signal is summed. Many digitizing oscilloscopes have an averaging feature, and signal averaging software is available in many standard signal-processing software packages.

Spatial averaging requires that the receiving transducer be moved a small distance between each waveform acquisition. In this way, elastic scattering from grains and other internal structure is made more random in a small region where it is assumed the signal would otherwise be reasonably constant. Spatial averaging is accomplished by acquiring signals for a number of closely spaced EMAT positions. These signals must be added by shifting each in time by an appropriate amount (an amount related to the distance moved).

When working with tone bursts signals, the time between two signals can be calculated very accurately by calculating the cross-correlation function (CCF) of the two signals. For example, suppose that two receivers are used to measure a Lamb wave in a plate. The Lamb wave travel time between the two receivers can be obtained by calculating the CCF of the two signals. Many, perhaps up to 100, points in each signal are involved in this calculation. Using interpolation methods, the resolution available in this travel time calculation can be much better than the digitization interval of the waveform.

8.6.4 Magnet Considerations

Many different types of magnets can and have been used for EMATs. The most widely used and most convenient magnets are PMs. The curves in Figure 8.22 through Figure 8.24 give a good general summary of the behavior of PMs in EMATs on nonmagnetic metals. For a more detailed description of permanent magnets, the reader can refer to Parker (1990).

The magnetic field at the end of a PM depends upon the length-to-diameter ratio of the PM (L_M/D_M), the PM material, and the magnetic circuit. In an open magnetic circuit such as used in the EMAT in Figure 8.1 with a nonmagnetic metal, the magnetic field at the end of the PM will be about one-half the residual induction (for definitions of the magnetic terms used here as well as for a good description of designing magnetic circuits using PMs see Parker, 1990) for $(L_M/D_M) > 1$ for most rare earth PMs like SmCo and $(L_M/D_M) > 2$ for NdFe PMs.

Although electromagnets are not commonly used in commercial applications of EMATs, there are cases where they should at least be considered in EMAT design. For example, if an application requires a magnet of large area and the EMAT will be used on or around steel, the magnetic forces can be large and even hazardous to the operator. An electromagnet has the advantage that the field may be shut off. Some uses of electromagnets with EMATs are covered in Alers and Burns (1987) and Maxfield et al. (1987).

Another form of bias magnetic field was mentioned with respect to the EMAT configuration shown in Figure 8.26. Pulsed field EMATs were first reported by

Fortunko and MacLauchlan (1980) and there have been several successful applications of pulsed magnet EMATs since then (e.g., Alers and Burns, 1987).

Pulsed electromagnets are basically a coil with a core of laminated iron or air. Core lamination is needed so that eddy current generation does not seriously limit the rate at which fields can increase or decrease. Pulsed magnets in EMATs are useful primarily when relatively low fields (less than 0.1 T) or low repetition rates (less than a few Hz) are acceptable.

8.7 Summary

The objective of this chapter was to give the reader a quantitative description of EMATs, an appreciation of where they might be used, and an understanding of how to use them. The references cited herein are in no way a complete set of references to the large body of EMAT work that has been published as that is a job for review papers. Many of the references cited are to work that I have done or colleagues have done with whom I have worked or have otherwise been associated. This is no accident. It has been these workers and their contributions that, in many cases, have helped to shape my approach to understanding, designing, and using EMATs.

Some useful references, including some to work of myself and co-workers, have been omitted because they did not relate directly to the objectives of this chapter. I believe that the reader will find the cited literature adequate to fill in the background material needed to thoroughly understand what has been presented. I have tried to minimize the literature cited so the reader can focus attention on those few works that relate most directly to understanding and using EMATs. About half of the references are included because one or more figures were used. In most cases, the reader should only need to refer to the literatue cited and pertinent background given in Section 8.1. Finally, I would like dedicate this chapter to the memory of Dr. Christopher M. Fortunko who contributed so much to my understanding of EMATs and their use.

References

American Radio Relay League (ARRL), *ARRL Handbook for Radio Amateurs*, Newington, CT, 2001.

Alers, G.A., and Burns, L.R., EMAT designs for special applications, *Mater. Evaluation*, 45, 1184, 1987.

Alers, G.A., Huebschen, G., Maxfield, B.W., Repplinger, W., Salzberger, J., Thompson, R.B., and Willbrand, A., Section 10, Other Ultrasonic Techniques, in Nondestructive Testing Handbook, American Society of Nondestructive Testing, Columbus, OH, 1990.

Auld, B.A., Special microwave acoustics, *IEEE Trans. Microwave Theory Tech.*, MTT-17, 800–811, 1969.

Auld, B.A. and Kino, G.S., Normal mode theory for acoustic waves and its application to the interdigital transducer, *IEEE Trans. Electron Dev.*, ED-18, 898–908, 1971.

Auld, B.A., *Acoustic Fields in Solids*, 2nd ed., Vols. 1 and 2, Kreiger, Malabar, FL, 1990.

Davidson, P.K., and Alers, G.A., *Proc. ASNT Spring Conf.*, Houston, TX, March 1997; U.S. Patent No. 5,537,876, 1999.

Dobbs, E.R., Electromagnetic generation of ultrasonic waves, in *Physical Acoustics*, Vol. 10, Mason, W.P. and Thurston, R.N., Eds., Academic Press, New York, 1976, pp. 127–193.

Dodd, C.V., and Deeds, W.E., Analytical solutions to eddy current probe-coil problems, *J. Appl. Phys.*, 39, 2829, 1968.

Fortunko, C.M., and MacLauchlan, D., Pulsed Electromagnet EMATs, *Proc. DARPA/AFWAL Rev. Prog. QNDE*, La Jolla, CA, 1980, pp. 528–534.

Frost, H.M., Electromagnetic ultrasonic transducer: principles, practice and applications, in *Physical Acoustics*, Vol. 14, Mason, W.P. and Thurston, R.N., Eds., Academic Press, New York, 1979, pp. 179–276.

Gaerttner, M.R., Wallace, W.D., and Maxfield, B.W., Experiments relating to the theory of magnetic direct generation of ultrasound in metals, *Phys. Rev.*, 184, 702, 1969.

Gray, T.A., and Thompson, R.B., unpublished work (1983) referenced in Thompson, R.B., in *Physical Acoustics*, Vol. 19, Mason, W.P. and Thurston, R.N, Eds., Academic Press, New York, 1990, pp. 157–200.

Jackson, J.D., *Classical Electrodynamics*, John Wiley and Sons, Inc., New York, 1962, chap. 8.

Kawishima, H., Quantitative calculation and measurement of longitudinal and transverse ultrasonic wave pulses in solids, *IEEE Trans. Sonics Ultrasonics*, Vol. SU-31, 83–94, 1984.

Landau, L.D., and E.M. Lifshitz, *Electrodynamics of Continuous Media*, Pergamon Press, New York, 1960.

Maxfield, B.W., and Hulbert, J.K., Electromagnetic acoustic wave transducers (EMATs): their operation and mode patterns, *Proc. 10th Symp. NDE*, San Antonio, TX, 1975, pp. 44–62.

Maxfield, B.W., and Fortunko, C.M., The design and use of electromagnetic acoustic wave transducers (EMATs), *Mater. Evaluation*, 41, 1399, 1983.

Maxfield, B.W., Kuramoto, A., and Hulbert, J.K., Evaluating EMAT designs for selected applications, *Mater. Evaluation*, 45, 1166, 1987.

Onoe, 1968, as described in Kawashima (1984).

Papadakis, E.P., Fabrication and characterization of transducers, in *Physical Acoustics*, Vol. 11, Mason, W.P. and Thurston, R.N, Eds., Academic Press, New York, 1975, pp. 152–212.

Pardee, W.J., and Thompson, R.B., Half-space radiation by EMATs, *J. Nondestructive Evaluation*, 1, 157, 1980.

Parker, R.J., Advances in Permanent magnetism, John Wiley & Sons, New York, 1990.

Rose, J.L., *Ultrasonic Waves in Solid Media*, Cambridge University Press, London, 1999.

Thompson, R.B., A model for the electromagnetic generation and detection of rayleigh and lamb waves, *IEEE Trans. Sonics Ultrasonics*, SU-20, 340–346, 1973.

Thompson, R.B., Electromagnetic generation of rayleigh and Lamb waves in ferromagnetic metals, *IEEE Ultrasonics Symp. Proc.*, New York, 1975, p. 653.

Thompson, Meander line excitation of Lamb waves in magnetostrictive materials, R.B., *IEEE Trans. Sonics Ultrasonics*, SU-20, 340–346, 1978.

Thompson, R.B., The relationship between radiating body forces and equivalent surface stresses: Analysis and application to EMAT design, *J. Nondestructive Evaluation*, 1, 79, 1980.

Thompson, R.B., Physical principles of measurements with EMAT transducers, in *Physical Acoustics* Vol. 19, Pierce, A. and Thurston, R.N., Eds., Academic Press, New York, 1991, pp. 157–200.

Wildebrand, A., as quoted in Thompson, R.B., in *Physical Acoustics*, Vol. 19, Pierce, A. and Thurston, R.N, Eds., Academic Press, New York, 1990, pp. 157–200.

9

Ultrasonic Nondestructive Evaluation for Structural Health Monitoring: Built-In Diagnostics for Hot-Spot Monitoring in Metallic and Composite Structures

Jeong-Beom Ihn and Fu-Kuo Chang

CONTENTS

0-8493-1462-3/02/$0.00+$1.50

9.1 Introduction

There have been a number of recent advances in sensing technologies and material/structural damage characterization combined with current developments in computation and communication. These developments have resulted in a significant interest in creating new diagnostic technologies for monitoring the integrity of both existing and new structures in real time with minimal human intervention. Using distributed sensors to monitor the health state of in-service structures is possible if sensor signals can be accurately interpreted to reflect *in situ* structural condition through real-time data processing. The complete system can be integrated and automated to perform real-time inspection or damage detection.

The essence of structural health monitoring (SHM) technology is to develop autonomous systems for the continuous monitoring, inspection, and damage detection of structures with minimum human labor. The development of such systems would involve many disciplines such as structures, materials, sensors/actuators, signal processing, and intelligent software.

Although conventional nondestructive testing (NDT) techniques can be considered within the framework of structural health monitoring, there can be a difference in data interpretation between the traditional NDT and SHM. The traditional NDT techniques tend to use direct measurements to determine the physical condition of the structures. No historical data are needed. The accuracy of the diagnosis depends strongly on the resolution of the measurements, which rely heavily on the equipment. However, the SHM techniques would use the change in the measurements at the same location at two different times to identify the condition of the structures. Historical data are crucial for the technique. The accuracy of the identification depends strongly upon the sensitivity of sensors and the interpretation algorithm.

The potential direct benefits from such systems are enormous. These include:

1. Real-time monitoring and reporting — maintenance cost savings
2. Minimum human involvement — labor, downtime, and human error reduction
3. Automation — safety and reliability improvement

9.2 Existing Diagnostic Methods in SHM

Novel diagnostic methods or interpretation algorithms are needed to relate the sensor measurements to the physical conditions of structures in terms of damage. The current diagnostics methods in SHM can be classified as a vibration or wave propagation method.

9.2.1 Vibration-Based Method

9.2.1.1 Global Vibration Method

The global vibration-based method looks for changes in structural dynamic characteristics due to structural damage. The basic principle is that structural damage will change the physical properties of a given structure, such as mass, damping, and stiffness, which are also functions of modal parameters such as natural frequencies, mode shapes, and modal damping.

A large number of papers have been published on this method, and Doebling et al. have provided a detailed literature review on vibration-based damage detection.[1] The majority of the work presented in this review was limited to laboratory tests on representative structures (beams and simple plates), assuming linear damage detection where the initially linear-elastic structure remains linear-elastic after damage. The linear vibration approach results in inherently low sensitivity to defects such as cracks.[2] A body with a fatigue crack exhibits nonlinear vibrations because of the stiffness change at the instant of crack opening and closing.[5] Some researchers have focused only on crack detection using vibration characteristic with a crack modeled as a slit.[2–5]

The accuracy of relating small changes in modal parameters to small flaws such as cracks is very controversial since it is known to vary depending on test variables such as excitation type, measurement location, number of measurements, and boundary conditions. The method may not be sensitive to local damage such as a small crack that does not change the dynamic characteristic of the structure.

9.2.1.2 Local Vibration (Electromechanical Impedance) Method

The electromechanical (E/M) impedance method has been accepted as a structural health monitoring method because of its relative simplicity and applicability to complex structures.[6–9] The basic concept of this method is to use high-frequency vibrations to monitor a local area based on the changes in structural impedance that would indicate structural flaws. The method uses small-sized piezoelectric sensors bonded to an existing structure with a self-sensing mechanism. These piezoelectric active sensors placed at critical locations measure changes in local vibration characteristics and relate them to the extent of the structural damage.

9.2.2 Wave Propagation Method

The wave propagation method uses a transmitter and receiver, as in a pitch and catch configuration, to send a diagnostic stress wave along the structure and measure the changes in the received signal due to structural flaws. Piezoelectric sensors can be used as a both actuator (transmitter) and sensor (receiver) because of its piezoelectric effect. In plate-like structures, Lamb waves can propagate relatively long distance and are found to be sensitive to various types of structural damage (e.g., delamination, cracks, and cutouts, for example).[10–14] This method is effective for detecting local damage in a large area (or hot spot) of the structure. The chapter will focus on this method.

9.3 Built-In Structural Health Monitoring System

Based on sensor functionality, all the structural health monitoring systems can be classified into two types: passive sensing and active sensing.

For a passive sensing system, only sensors are installed in the structures. Sensor measurements are constantly taken in real time, while the structures are in service, and are compared with a set of reference (healthy data). The sensor-based system estimates the condition of the structure based on the data comparison. Because the input energy to the structure is typically random and unknown, the corresponding sensor measurements reflect the response of the structures to the unknown inputs. This type of diagnostics has been primarily applied to determining unknown inputs that cause changes in sensor measurements such as external loads, incipient cracks, temperature, and pressure.

For an active sensing system, known external mechanical or nonmechanical loads are input to the structures through built-in devices such as transducers or actuators. Since the inputs are known, the difference in the local sensor measurements based on the same input is strongly related to a physical change in the structural condition such as the introduction of damage.

The chapter will focus on an active sensing system based on piezoelectric materials. Typically, the system would consist of three parts: an integrated sensor network, a controller, and diagnostic software. This chapter will primarily address the diagnostic software for the piezoelectric-based active sensing system. Both the integrated sensor network and the controller will be briefly mentioned. More related information can be found in the references section.[15–17]

9.4 Integrated Sensor Network and Controller

9.4.1 SMART Layer

Chang and Lin[15] recently invented a manufacturing technique to integrate a network of piezoelectric sensors into a dielectric film (so-called SMART Layer™ [Acellent Technologies]) using electronic circuit printing techniques. A SMART layer can be surface mounted on metallic structures or embedded inside composite structures. Figure 9.1 shows the typical rectangular shape of the SMART layer with embedded 12 lead zirconate titanate (PZT) sensor networks. The SMART layers can be customized in different shapes depending on the applications or geometry of the structures (Figure 9.2).[16–17]

In this chapter, the SMART layer is selected for deployment of the piezoelectric sensor network. Various sizes of the SMART layer will be customized for each selected applications to be discussed later.

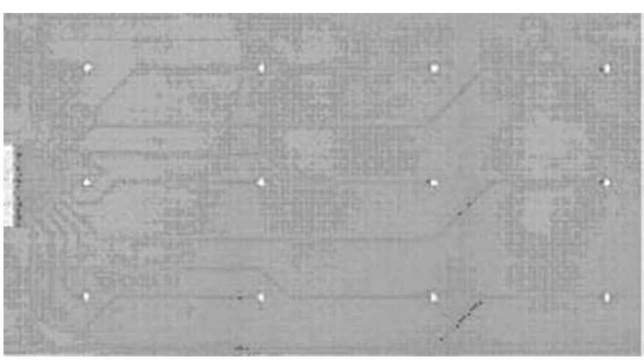

FIGURE 9.1
Rectangular SMART layer with embedded sensor networks.

FIGURE 9.2
SMART layers in different shapes.

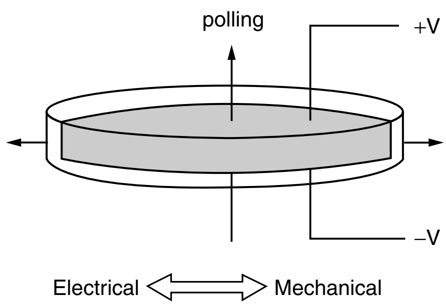

FIGURE 9.3
Deformation of piezoelectric disk by applied voltage.

9.4.2 Piezoelectric Effect

Typically, the SMART layers use the thin disk types of piezoelectric materials of PZT ceramic as actuators and sensors. As illustrated in Figure 9.3, when an electric field is applied, the material produces dimensional changes. Conversely, when mechanical pressure is applied, the crystalline structure produces a voltage proportional to the pressure. The mechanical and electrical axes of operation are set during "polling," the process that induces piezoelectric properties in the ceramic. Because of the anisotropic nature of piezoelectric materials after polling process, its effects depend on direction.

The following electromechanical equations describe the effects of a piezoelectric material:

$$S_{ij} = s^{E}_{ijkl} T_{kl} + d_{kij} E_k \tag{9.1}$$

$$D_i = d_{ikl} T_{kl} + \varepsilon^{T}_{ik} E_k \tag{9.2}$$

where

S_{ij} = strain tensor
s^{E}_{ijkl} = compliance tensor (constant electric filed)
E_k = applied electric filed

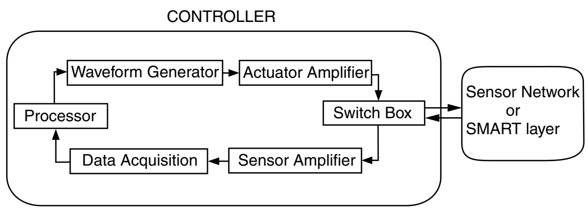

FIGURE 9.4
Components in controller.

E_{ik}^{T} = dielectric constant (at constant stress)
T_{kl} = stress tensor
d_{kij} = piezoelectric constant
D_i = dielectric displacement

9.4.3 Controller

The controller interfaces with the sensor network or SMART layer for the waveform generation and the multichannel data acquisition. The components of the controller include the waveform generator, actuator/sensor amplifier, switch box, and data acquisition (Figure 9.4). The controller is operated by the diagonostic software embedded in the processor.

9.5 Diagnostic Software

The damage detection technique uses sensor signals generated from nearby piezoelectric actuators built into the structures to detect any structural flaws. It consists of three major components: diagnostic signal generation, signal processing, and damage diagnostics.

9.5.1 Signal Generation

9.5.1.1 Diagnostic Waveform

A piezoelectric actuator can generate diagnostic waves that propagate along the structure for damage interrogation. The changes in the received signals can then be analyzed to reveal structural flaws. An appropriate diagnostic waveform has to be chosen for the easy signal interpretation process. The five-cycle windowed sine-burst signal shown in Figure 9.5a is widely used in the field of nondestructive evaluation (NDE) for its good dispersion characteristic and its sensitivity to structural flaws. A Hanning window is used to concentrate the maximum amount of energy at the desired driving frequency.

As Figure 9.5b shows, the waveform has a narrowband frequency spectrum with its spectral density concentrated at the driving frequency. The narrower

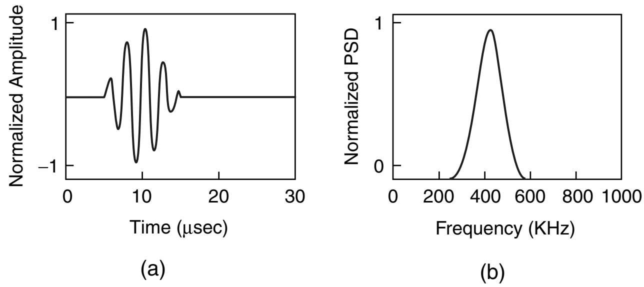

FIGURE 9.5
Diagnostic input waveform at driving frequency of 420 kHz. (a) Windowed burst signal with five cycles; (b) frequency spectrum (power spectral density).

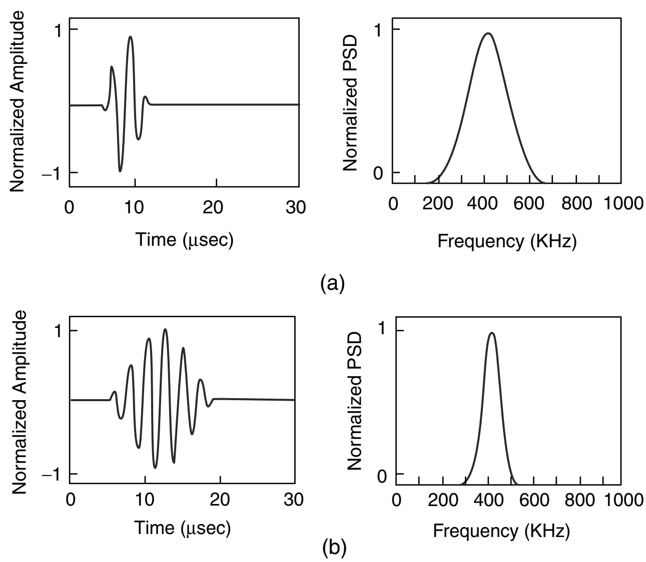

FIGURE 9.6
Effects of varying number of cycles on burst waveforms. (a) Burst signal with three cycles; (b) burst signal with seven cycles.

the band width is, the less dispersion where the input waveform remains about the same as it travels along the medium. If the number of cycles of the input function is increased, the bandwidth will narrow but the time duration of the wave will lengthen (Figure 9.6). When the time duration of a wave is longer, the time resolution gets lower. There is always a trade-off between a good dispersion characteristic and time resolution.

9.5.1.2 Lamb Waves for Damage Detection

Lamb waves are a type of guided ultrasonic wave propagation between two parallel surfaces of a plate-like structure. Lamb waves can be excited by the surface mounted or imbedded piezoelectric actuators.

Lamb waves have been adopted extensively as an effective tool for evaluating defects by detecting changes in the received waveforms. Roh and Chang[10] proposed a built-in diagnostic technique to identify an anomaly such as a hole in plates using scattering waves. The interaction of Lamb waves with defects on plates was best investigated by Alleyne and Cawley,[11] whose results showed that the sensitivity of individual Lamb waves to defects was strongly dependent on the frequency. Chang and Mal[12] have studied the scattering Lamb waves from a single rivet hole with artificial edge cracks both theoretically and numerically.

9.5.1.2.1 Theory of Lamb Wave Propagation

Lamb waves represent two-dimensional propagating vibrations in plates, which are described by known mathematical equations originally formulated by H. Lamb in 1917.[18] There are two groups of waves, the symmetric waves and the antisymmetric waves, that satisfy the wave equation and the boundary conditions. The velocities of these waves depend on the frequency and the thickness of the plate (the dispersion relation), and there are a finite number of symmetric and antisymmetric modes that travel independently. The dispersion relation is found by numerical solution of the Rayleigh-Lamb equation:

$$\frac{\tan(\bar{d}\sqrt{1-\alpha^2})}{\tan(\bar{d}\sqrt{\beta^2-\alpha^2})} + \left[\frac{4\alpha^2\sqrt{1-\alpha^2}\sqrt{\beta^2-\alpha^2}}{(2\alpha^2-1)^2}\right]^{\pm 1} = 0 \tag{9.3}$$

(+1 for symmetric roots; −1 for antisymmetric roots)

$$\alpha^2 = \frac{c_t^2}{c_{ph}^2}, \quad \beta^2 = \frac{c_t^2}{c_l^2}, \quad \bar{d} = \frac{k_t h}{2} \tag{9.4}$$

$$c_t^2 = \frac{\mu}{\rho}, \quad c_l^2 = \frac{(\lambda+2\mu)}{\rho}, \quad k_t = \frac{\omega}{c_t} \tag{9.5}$$

where

$$\mu = \frac{E}{2(1+\nu)}, \quad \lambda = \frac{E\nu}{(1-2\nu)(1+\nu)}$$

With a given material, Young's modulus E, Poission's ratio ν and the density ρ, the phase velocity C_{ph}, and the frequency-thickness product ωh

have to be iteratively solved. Once the phase velocity dispersion curve is obtained, the group velocity dispersion curve can be obtained from

$$f = 2\pi\omega, \quad k = \frac{2\pi}{wavelength}, \quad c_{ph} = \frac{\omega}{k} \tag{9.6}$$

$$v_g = \frac{\partial\omega}{\partial k} \tag{9.7}$$

where
v_g = the group velocity
ω = the angular frequency
k = the real wave number

9.5.1.2.2 Dispersion Curve

Figure 9.7 shows the group velocity dispersion curve for aluminum. Depending on the frequency-thickness values, a different number of modes may propagate. In a practical application of Lamb waves, for the simplicity of analysis, the values of frequency-thickness values are kept below the cut-off frequency of the a1 mode, where there is only a fundamental symmetric mode (s0) and a fundamental antisymmetric mode (a0) (the shaded area in Figure 9.7).

When the wavelengths are large in relation to the thickness of the plate, the fundamental symmetric mode and the fundamental antisymmetric mode are equivalent to the extensional and flexural waves, respectively. The antisymmetric mode is widely used in damage detection in composite structures due to its sensitivity to delamination damages.[13–14] The fundamental symmetric mode has been used to detect surface crack growth in metallic structures[11] and is utilized in this chapter for fatigue crack detection.

9.5.2 Signal Processing

Before sensor measurements can be interpreted and related to structural flaws (e.g., crack, delamination), the raw sensor measurements should be represented for an easier and more effective interpretation. The raw sensor measurements from sensors can be represented as the following forms with different characteristics (Table 9.1).[19]

As Table 9.1 shows, the time and frequency representation will give us the most information about the sensor measurements. The plots of spectral amplitude information in time and frequency axes are called spectrograms. A Matlab™ function from a signal processing tool box, *specgram.m*, was used to generate spectrograms. The *specgram.m* computes the windowed discrete-time Fourier transform of a signal using a sliding window (short-time Fourier Transform [STFT]). The spectrogram is the magnitude of this function.

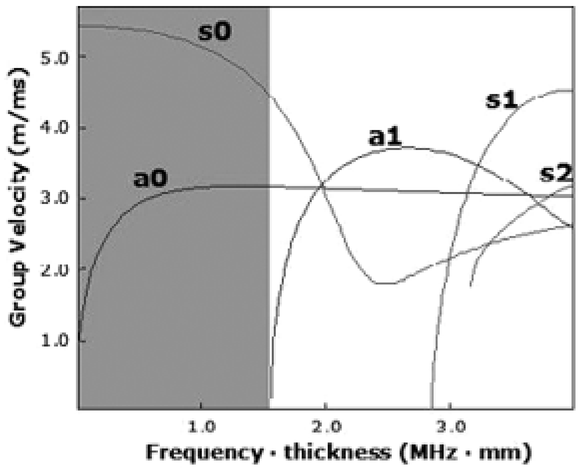

FIGURE 9.7
Group velocity dispersion curve for aluminum.

TABLE 9.1
Signal Representations

	Pros	Cons
Time domain	Amplitude, wave speed	Inaccurate or impossible for complicated signal
Frequency domain	Natural frequencies	No time information
Time and frequency	All of the above	Trade-off between frequency and time resolution

The STFT of a signal, *s(t)*, is defined as

$$S(\omega,t)=\frac{1}{2\Pi}\int_{-\infty}^{\infty}e^{-iwt}s(\tau)h(\tau-t)d\tau \tag{9.8}$$

where *h(t)* is a window function. Since the window function *h(t)* has a short time duration, by moving *h(t)* with Fourier integrals, the signal's local frequency properties evolving over time can be revealed. The Hanning window is typically used as a window function.

A joint time-frequency analysis method based on the STFT can be used for generating the envelope of the time varying signal and extracting time of flight (TOF) information from sensor measurements.[10] The group velocity measurements can be then obtained from the following:

$$Group\ velocity=\frac{Sensor\ spacing}{TOF} \tag{9.9}$$

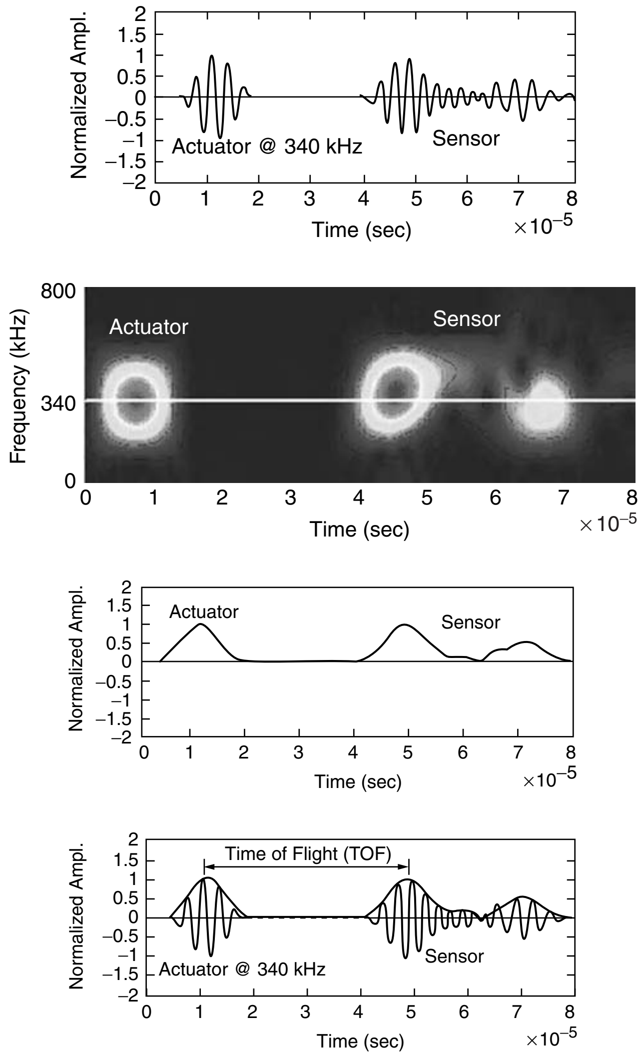

FIGURE 9.8
Extracting TOF information.

The group velocity measurement is used as key information for the signal interpretation as it reveals the types of modes traveling along the structure. Figure 9.8 illustrates the procedure of obtaining the TOF information and the group velocity of the sensor measurement. Roh[10] previously used this approach to obtain the TOF information of the scattered wave from an anomaly on an aluminum plate. Plot A in Figure 9.8 shows the input wave and corresponding sensor measurement in time axis. Plot B is the spectrogram with time represented by the horizontal axis, frequency is represented by the vertical axis, and spectral amplitude is represented by the axis coming

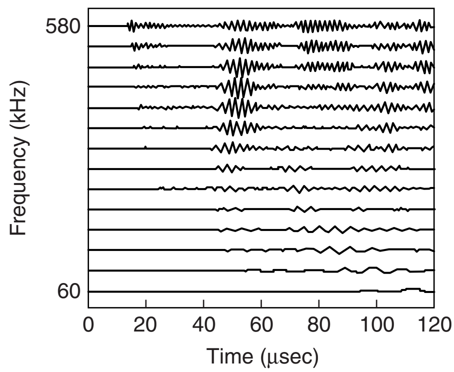

FIGURE 9.9
Collected sensor signal.

out of the page. It shows the maximum spectral amplitude at a driving input center frequency of 340 kHz. Plot C shows the distribution of the spectral amplitude in the time axis along the line of the center frequency. This spectral amplitude plot in time represents the envelope of the time signal after normalization (plot D). Since the time signal contains lots of peaks and valleys, the unique peak of the envelope on the first arrival wave packet well defines the reference point for the TOF information. The TOF on the first arrival wave packet can be obtained by taking the time difference between the peak of the actuator and the peak of the first arrival envelope.

The wide-band spectrogram can be constructed from the STFT processes of the collected data at different center frequencies. Figure 9.9 and Figure 9.10 show the collected sensor signals from 60 to 580 kHz input center frequencies and corresponding sensor spectrogram, respectively. The wide-band sensor spectrogram shows how the amplitude of the sensor signals distributes in a wide range of frequencies and the time domain. It also helps to decide the driving center frequency where it gives the best wave propagating resolution or the highest signal-to-noise ratio. It also shows the dispersion relation of Lamb waves in time and frequency axis as we connect the peaks of the first and the second arrival wave packet (Figure 9.10).

When a structural flaw such as a fatigue crack is introduced near the actuator and sensor diagnostic path, changes in the sensor signals will occur, allowing us to obtain the scatter signal representing these changes. As we collect the scattered signal at a wide range of center frequencies, we can obtain the wide-scatter spectrogram through the same procedure as the wide-band sensor spectrogram.

9.5.3 Damage Diagnostics

When an elastic wave travels through a region where there is a change in material properties, scattering occurs in all directions. The directly transmitted signals are modified to the forward scattering waves, and the scattered energy

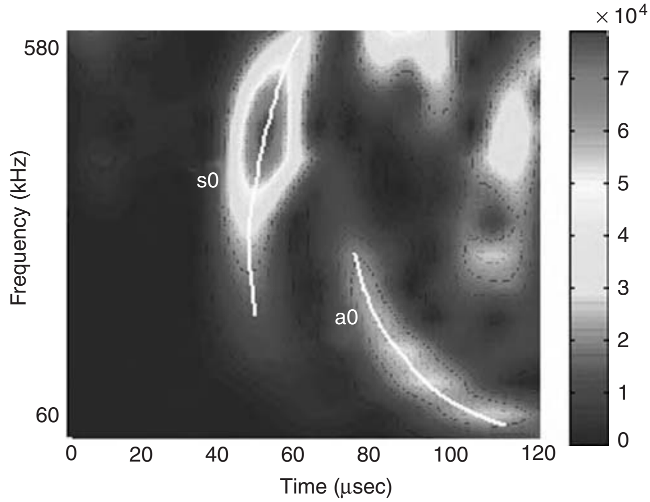

FIGURE 9.10
Wide-band sensor spectrogram.

provides good information about a presence of damage across the actuator and sensor path. The scatter wave in the time domain can be obtained by subtracting the baseline data recorded for the structure with the initial damage size from the sensor data for the structure with the extended damagesize.

The damage diagnostics in this chapter utilize an interactive Microsoft® Windows program called Disperse, first developed by Pavlakovic and Lowe[20–21] to generate dispersion curves for a wide range of composite structures. Using Disperse, a group velocity dispersion curve for an aluminum plate can be generated. Using the STFT-envelope method previously described, the group velocity dispersion curve of an aluminum plate can be plotted for fundamental modes and compared with the numerical results. Figure 9.11 shows the good match between the numerical and experimental results. The experiments results were obtained from a 3.175-mm thick aluminum plate.

9.5.3.1 Damage Index

Since it is possible to compare the experimental group velocity with the group velocity estimate by Disperse numerical results, it is easy to identify the s0 mode wave packet. The damage index (DI) is defined as the relative ratio of the scatter energy contained in the s0 mode wave packet to the baseline energy contained in the s0 mode wave packet. This ratio can be obtained by the time integration of the power scatter spectral density within the s0 time-window at a specified frequency, which then can be nondimensionalized by baseline information such that

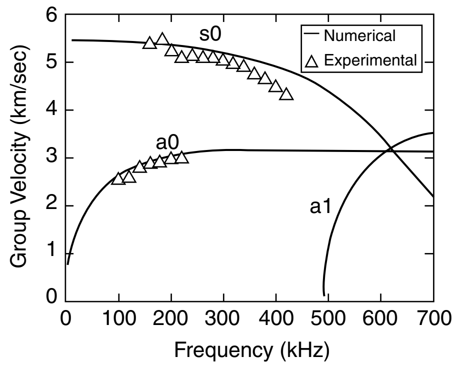

FIGURE 9.11
Group velocity dispersion curve (3.175-mm thick aluminum plate).

$$\mathrm{DI} \equiv \left(\frac{\int_{t_i}^{t_f} \left| S_{sc}(\omega_0, t) \right|^2 dt}{\int_{t_i}^{t_f} \left| S_b(\omega_0, t) \right|^2 dt} \right)^{\alpha} \tag{9.10}$$

where

S_{sc} = the time varying spectral amplitude of scatter signal
S_b = the time varying spectral amplitude of baseline signal
ω_0 = the selected driving frequency (usually taken at the driving frequency that gives the highest signal-to-noise ratio)
t_f and t_i = the upper bound and lower bound of the fundamental symmetric mode in time domain, respectively
α = the gain factor $0 < \alpha \sum 1$ ($\alpha = 0.5$ was taken for this chapter since DI with $\alpha = 0.5$ gave the good linear response to real fatigue crack growth by experiments)

Figure 9.12 graphically shows how the baseline and scatter energy can be extracted from the spectrograms. The energy is directly related to the area under the time varying power spectral amplitude.

9.5.3.2 Crack Detection Scheme

Figure 9.13 describes the damage detection scheme. Sensor measurements are taken from the sensor network or the SMART layer installed on the structure. The initial measurement is considered as a baseline that represents the initial condition of the structure. After a signal-processing routine, we can measure the group velocity from the baseline and using only a group

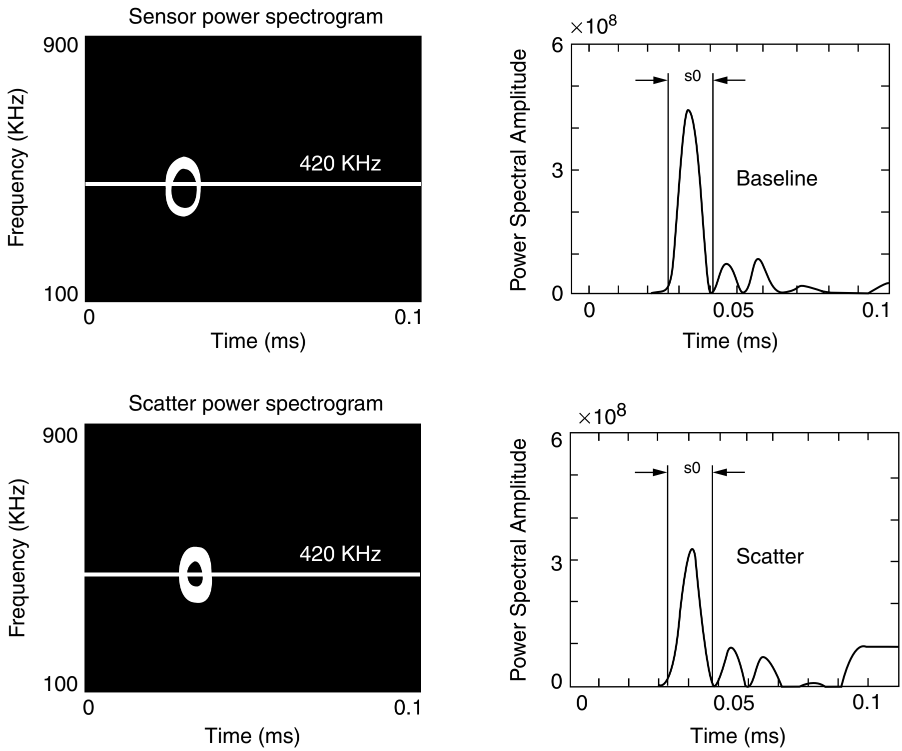

FIGURE 9.12
Energy contents in s0 mode.

velocity estimate from a wave model by Disperse,[20–21] we can then select the s0 mode in time domain. This information is fed to the DI routine. The sensor measurements at later times are subtracted from the baseline and represent the signal changes or scatter signals. The damage index is then evaluated based on the s0 mode wave packet selected initially. The procedure indicated by the solid line in Figure 9.13 will be repeated for continuous structural health monitoring. In this scheme only a minimal analytical work is required and complex waveform simulations are not needed.

9.6 Validating the Scheme

The crack detection scheme developed in earlier sections can be applied to aircraft structures for crack detection. Examples include riveted aluminum lap joints and a cracked aluminum plate repaired by a composite repair patch.

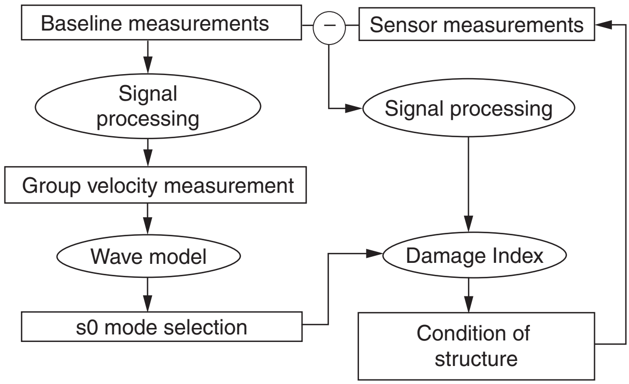

FIGURE 9.13
Crack detection scheme.

The SMART layers can be customized in different shapes depending on the applications or geometry of the structures.[16–17] As illustrated in Figure 9.14, for monitoring multisite cracks on fuselage lap joints, the SMART layers will have the shape of a strip known as a SMART strip. An actuator SMART strip will be installed between rivet rows, and a sensor SMART strip will be installed at a distance. This is a pitch and catch configuration where multiline inspection is possible for covering a large area.

As Figure 9.15 shows, to monitor cracks underneath the bonded repair patch, a SMART layer with the same shape as the repair layers will be inserted into the conventional composite repair layers with minimum intervention. Since a crack can grow in any direction, sensors and actuators will be distributed around the initial crack location to monitor the entire repaired region.

9.6.1 Riveted Lap Joints

9.6.1.1 Experiment Setup

Two identical aluminum single lap joints (936 × 462 mm), called Airbus lap joint 1 and Airbus lap joint 2, with two artificial 1.27-mm edge cracks at the center rivet were used for a constant amplitude fatigue test under tensile loading. Three SMART Layers by Acellent Technologies were surface mounted as shown in Figure 6.3. The center strip located between the two rivet rows was used as an actuator strip and the top and bottom strips were used as sensor strips. Between specified cyclic loading intervals, ultrasonic scans and eddy current tests were performed in order to detect crack initiation and growth around 21 rivet holes. No visual inspection was possible on the lap joints.

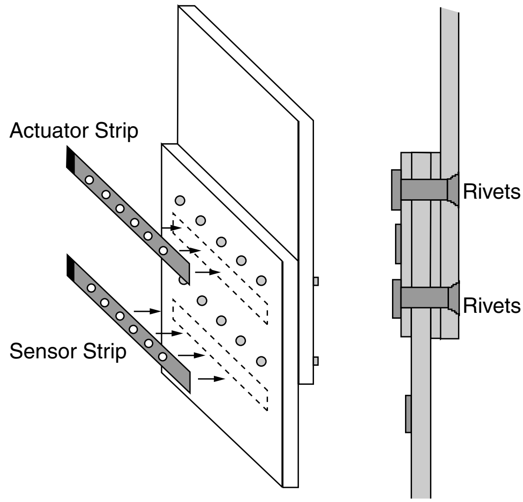

FIGURE 9.14
The sensor network design for riveted lap joints.

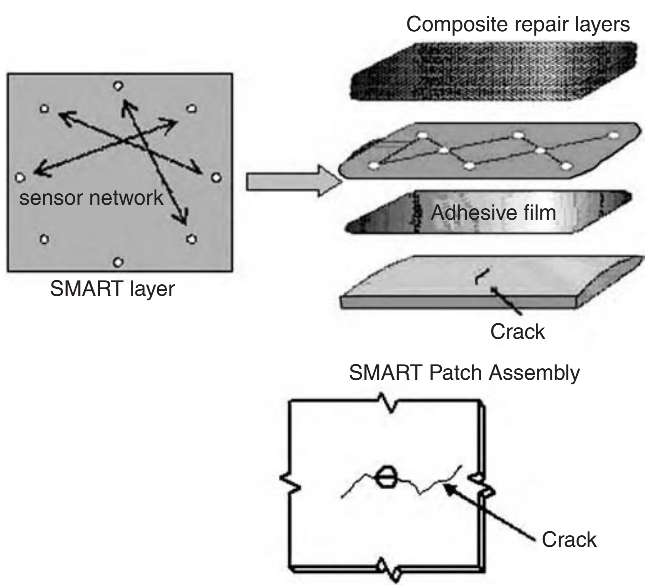

FIGURE 9.15
The sensor network design for composite repair patches.

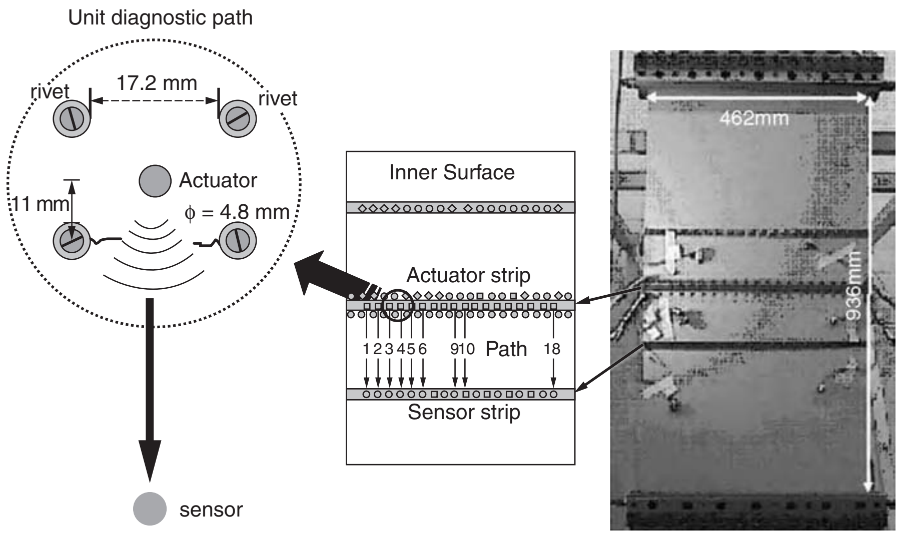

FIGURE 9.16
Lap joint specimen with SMART strips and diagnostic paths.

In parallel with NDT evaluations, a SMART suitcase[16–17] (a portable active diagnostic instrument designed to interface with piezoelectric transducers) was implemented to generate diagnostic signals from the actuator strip and record measurements from the sensor strips. Using a built-in waveform generator, a windowed sine-burst wave was generated as an input signal over a wide frequency range of 100 to 900 kHz and corresponding sensor measurements were collected at a sampling rate of 25 Msample/sec. The processing time for signal generations and sensor data storage took 22 sec to cover 19 rivets, which is significantly faster than conventional NDT methods. This processing time is based on the current specification of the SMART suitcase by Acellent Technologies and test setups such as sampling points, number of averaging points, and frequency bandwidth. Considering only one frequency excitation likely gives enough information for damage diagnostics, the entire processing time, including interpretation processing time, can be reduced even further.

9.6.1.2 Conventional NDT Results

Between the specified cycle loading intervals, the ultrasonic scan and eddy current test were performed in order to detect crack initiation and growth around 21 rivet holes. The NDT technician looked for two possible cracks at each rivet hole and marked the estimated crack lengths at different loading cycles. Since the crack estimates by NDT had to be compared with SMART strip results, the estimated crack lengths by NDT for the comparison purpose were obtained from the summation of two crack lengths based on the diagnostic path location. For example, the estimated crack length by NDT at path

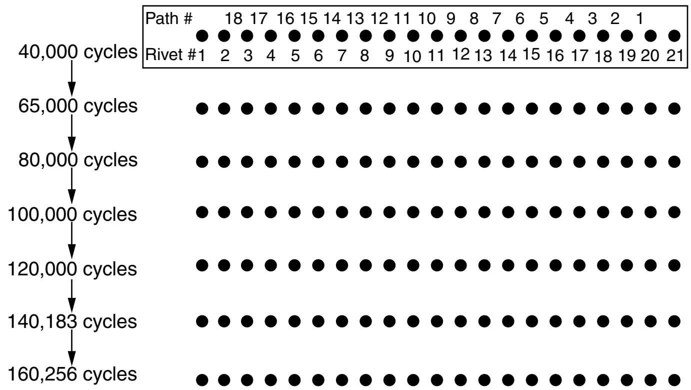

FIGURE 9.17
Ultrasonic estimates of crack lengths (Airbus lap joint 1).

10 location is the summation of the estimated crack length at the left-hand side of rivet #10 and the estimated crack length at the right-hand side of rivet #11 (Figure 9.17).

The crack growth estimates on both specimens by NDT methods at different loading cycles are shown in Figure 9.18 and Figure 9.19. There were 18 path locations for each specimen but, for the simplicity of the plot, only some of them were selected in the results. Figure 9.20 compares the two methods of crack detection. The ultrasonic technique in these experiments usually tends to find cracks longer than the eddy current estimates with a maximum estimate difference of 7.7 mm. No visual inspection was possible because of the doublers installed at the joints.

9.6.1.3 SMART Strip Results

9.6.1.3.1 s0 Mode Selection

In order to evaluate the DI for crack detection at the lap joint specimens, the s0 mode wave packet must be identified. The analytical results and experimental results of TOF are shown in Figure 9.21. The results strongly suggest that the first arrival wave packet is the s0 mode wave for the DI evaluation for crack detection at the lap joint specimens.

9.6.1.3.2 DI Results and Comparison

The DI was evaluated with the sensor measurements from 420-kHz input signals where it gave the highest signal to noise ratio. As seen in Figure 9.16 and Figure 9.17, since each actuator-sensor diagnostic path is located between a pair of rivet holes, the crack length detected by the path will be the sum of the two crack lengths that can be initiated from each rivet hole.

Among the crack estimate results at 18 actuator-sensor paths for each lap joint specimen, Figure 9.22 shows the DI vs. the number of cycles along with the NDT estimates on the secondary axis at the selected paths. Since different NDT techniques have different crack detection resolution (Figure 9.20), the

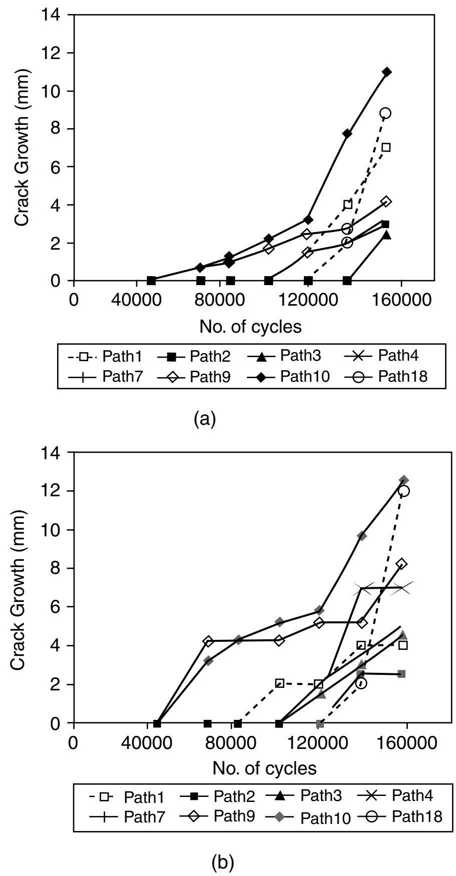

FIGURE 9.18
Conventional NDT results (Airbus lap joint 1). (a) Eddy current crack growth estimate; (b) Ultrasonic crack growth estimate.

DI shows a different correlation with the ultrasonic and eddy current crack estimates in Figure 9.23.

The probability of detection (POD) is a characteristic that allows us to quantify the quality of any NDT technique.[22] To obtain the POD, the different crack events monitored by NDT were ranked from the largest down to the smallest crack length and then compared with the results obtained with the DI:

$$POD = \frac{SC}{M+1-N} \tag{9.11}$$

where

SC = sum of crack events recorded by the DI
M = total number of crack events recorded by NDT
N = serial event

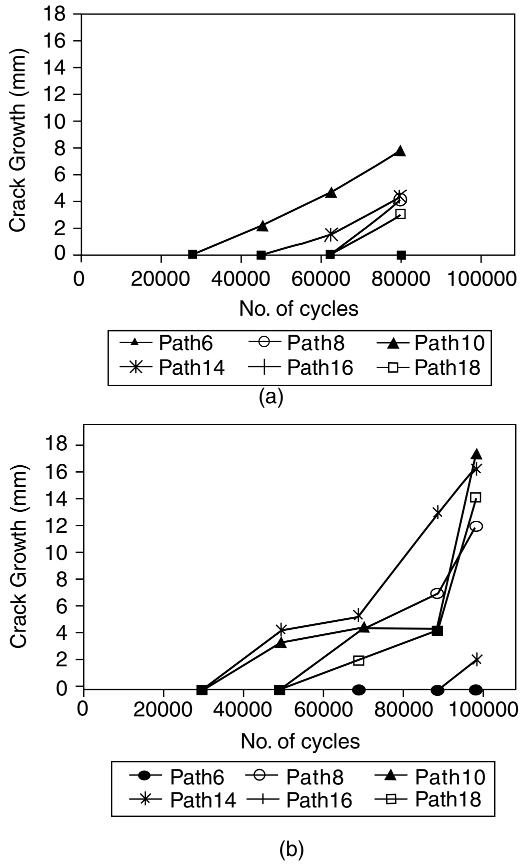

FIGURE 9.19
Conventional NDT results from Airbus lap joint 2. (a) Eddy current crack growth estimate; (b) ultrasonic crack growth estimate.

Using the formula above, POD was evaluated in Figure 9.24, Figure 9.25, and Figure 9.26. In Figure 9.24 and Figure 9.25, the two threshold levels of the DI were used for the POD. A DI of 0.1 is a good threshold level where crack lengths down to 5 mm can be detected, while avoiding false calls when compared with conventional NDT estimates (Figure 9.23). The DI also shows a higher probability of damage detection with the eddy current than the ultrasonic technique (Figure 9.26).

9.6.2 Bonded Repair Patch

The same damage detection scheme was applied to the cracked aluminum plate repaired by the boron/epoxy repair patch for detecting the crack growth on the plate. Two specimens (SMART patch 1 and SMART patch 2) were manufactured and tested. One of the specimens (SMART patch 2)

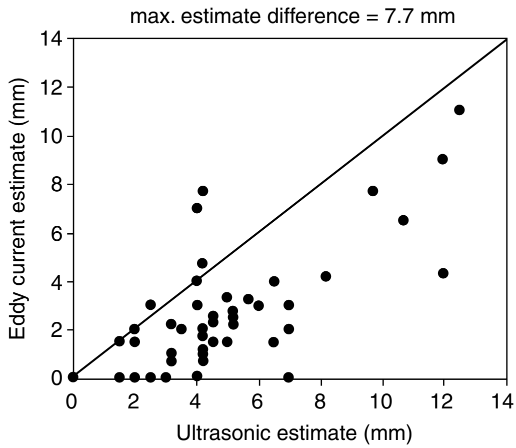

FIGURE 9.20
Eddy current vs. ultrasonic (Airbus lap joints 1 and 2).

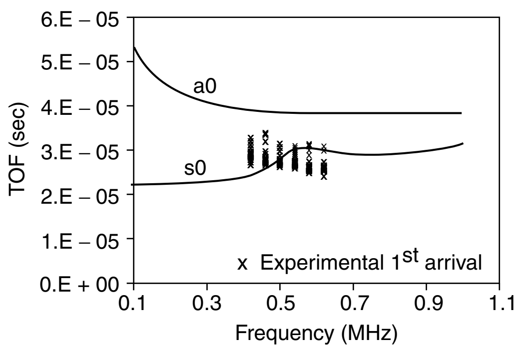

FIGURE 9.21
Analytical and experimental results of s0 mode TOF.

had a patch debond test prior to the fatigue crack test. The results of the fatigue crack tests from both specimens are presented next, and the results from the debond tests on SMART patch 2 specimen will be presented in Section 9.6.2.5.

9.6.2.1 Specimen Construction

As Figure 9.14 shows, two rectangular aluminum plates with 2-mm-long Electric Discharge Machining (EDM) notches at a center hole (8 mm diameter) were repaired with a unidirectional boron/epoxy patch. The thickness of the boron and aluminum patch was chosen based on the stiffness match design criteria such as

$$E_p h_p \approx E_a h_a \tag{9.12}$$

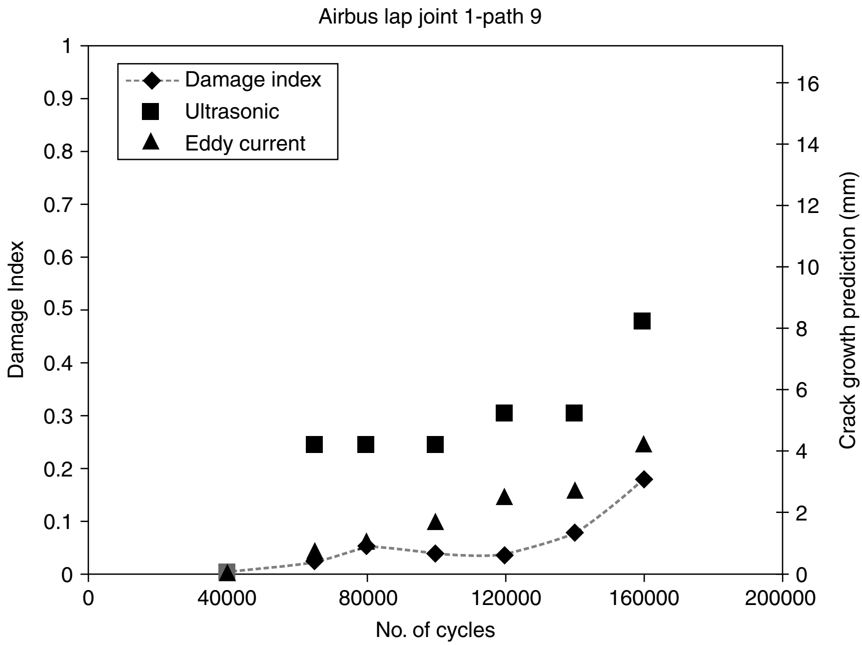

(a)

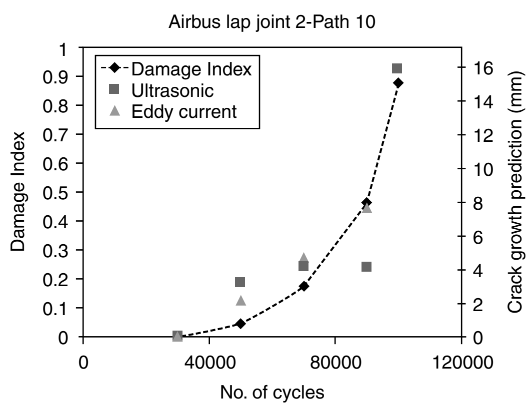

(b)

FIGURE 9.22
DI vs. number of cycles with NDT estimate in secondary axis. (a) Airbus lap joint 1 — path 9; (b) Airbus lap joint 2 — path 10.

where
E_p = boron patch stiffness
E_a = aluminum stiffness
h_p = boron patch thickness
h_a = aluminum thickness

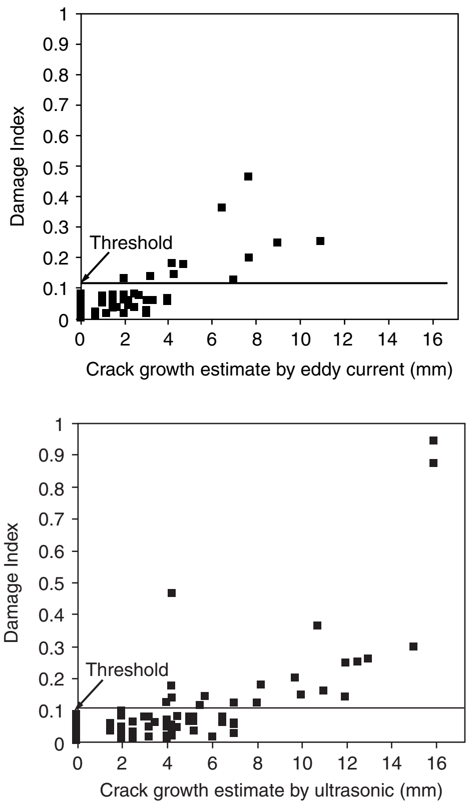

FIGURE 9.23
DI vs. NDT crack growth estimate.

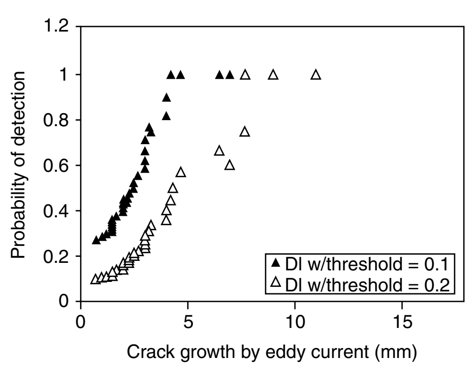

FIGURE 9.24
Probability of damage detection by the DI when compared with the eddy current NDT.

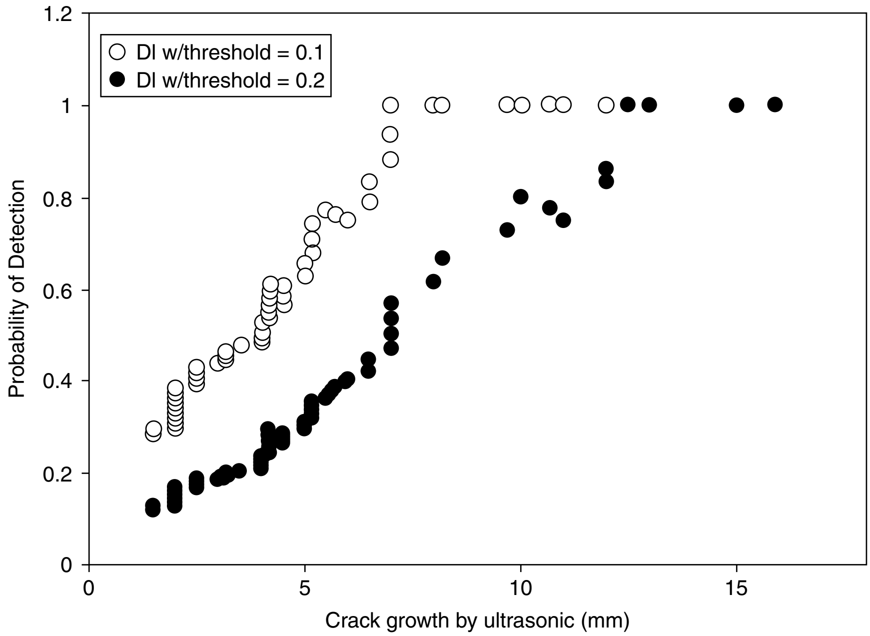

FIGURE 9.25
Probability of damage detection by the Damage Index when compared with the ultrasonic NDT.

The repair materials used in these tests are listed in Table 9.2. Two SMART layers were fabricated with an embedded network of piezoelectric actuators/sensors and inserted into the patch at different ply locations (Figure 9.14). The lower SMART layer (layer 10) was inserted right on the interface as close to the neutral axis as possible to excite a more symmetric mode. Conversely, the upper SMART layer (layer 3) was inserted near the top layer to excite a more antisymmetrical mode.

The lower SMART layer targets for the crack growth on the aluminum plate, and the upper SMART layer targets for the possible patch disbond from the aluminum plate. The locations of the piezoelectric actuator and sensors with diagnostic paths on the SMART layers are shown in Figure 9.28. The repair layers and SMART layers were stacked as seen in Figure 9.27 and co-cured with aluminum plate with a vacuum bag under a constant temperature of 250°F for 90 min.

Two specimens were manufactured with different geometries. One specimen (SMART patch 1) had a 140 × 350-mm aluminum base with a tapered patch design and the other (SMART patch 2) has a 420 × 478-mm aluminum base with the same patch design but without the tapered edge (Figure 9.29).

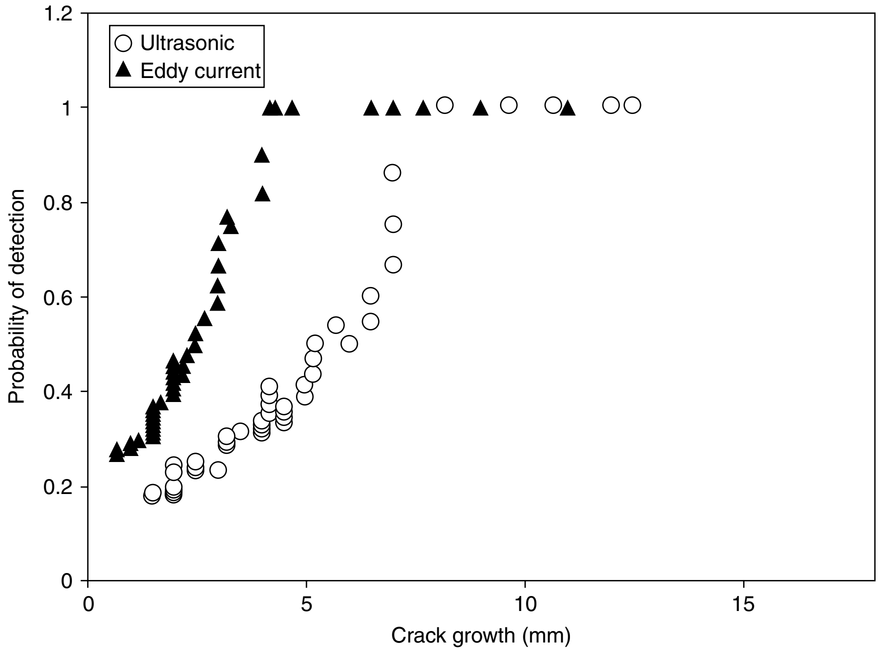

FIGURE 9.26
Probability of damage detection by the damage index when compared with the ultrasonic and eddy current NDT.

TABLE 9.2
Bonded Patch Specimen Repair Materials

Material	Supplier	Thickness (mm)
5521 Boron/epoxy prepreg	Textron	0.127
FM 73 adhesive	Cytec	0.254
SMART layer	Acellent	0.1016

9.6.2.2 Experimental Setup for the Fatigue Test

The repaired specimens were fatigued by tensile cyclic loading and crack propagation was visually identified from the back side of the repaired panel. The lower SMART layer (layer 10, Figure 9.27) was used for monitoring crack growth. Using a SMART suitcase, we generated an input signal over a frequency range of 100 to 600 kHz and collected sensor measurements after different loading cycles while the specimen was unloaded. The corresponding crack lengths were visually measured.

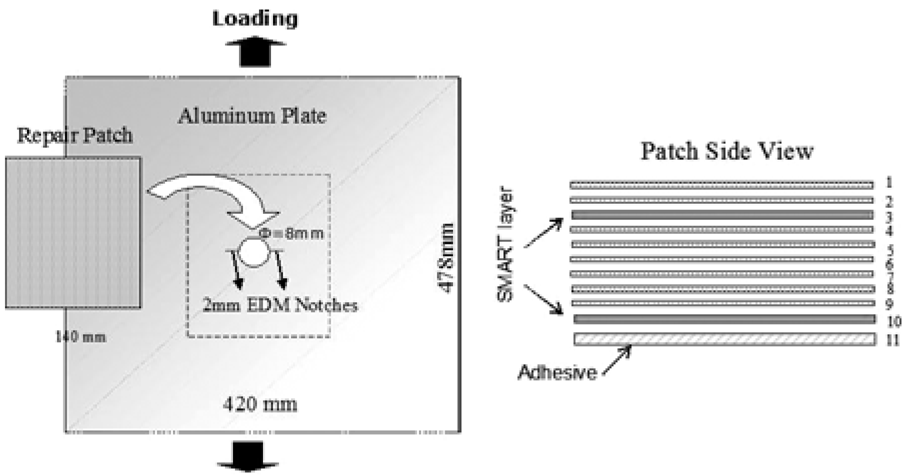

FIGURE 9.27
Bonded patch specimen assembly (SMART patch 2).

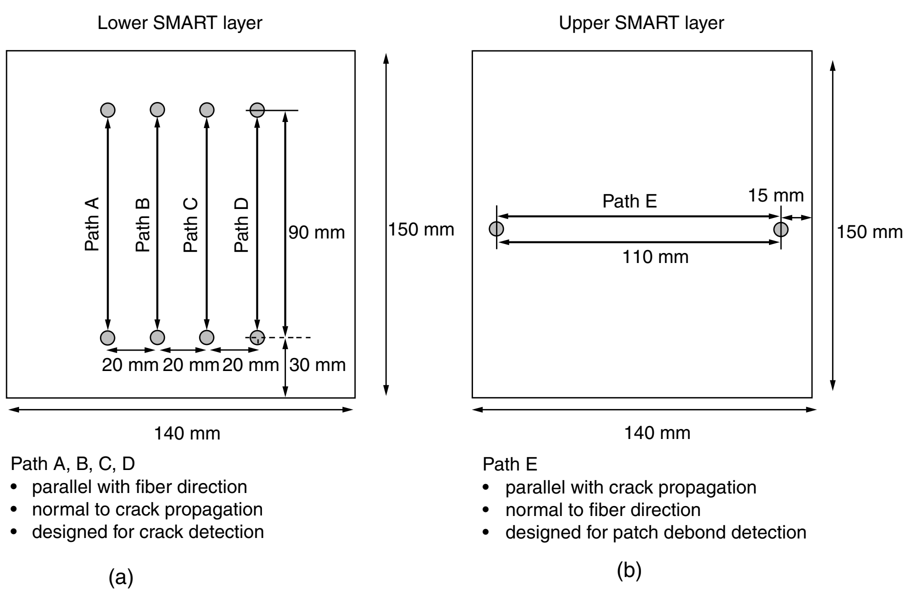

FIGURE 9.28
SMART layers with diagnostic paths. (a) SMART patch 1; (b) SMART patch 2.

9.6.2.3 Crack Detection Results

9.6.2.3.1 s0 Mode Selection

The boron/epoxy patch-adhesive layer-aluminum plate specimen described earlier was modeled using the Disperse code[20–21] and used to generate the

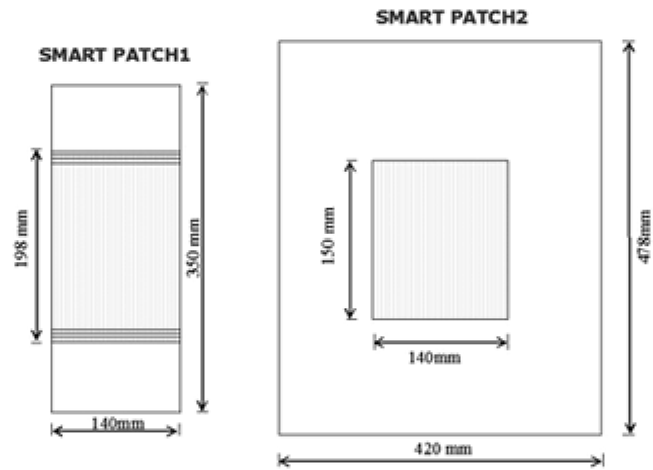

FIGURE 9.29
Bonded patch specimens.

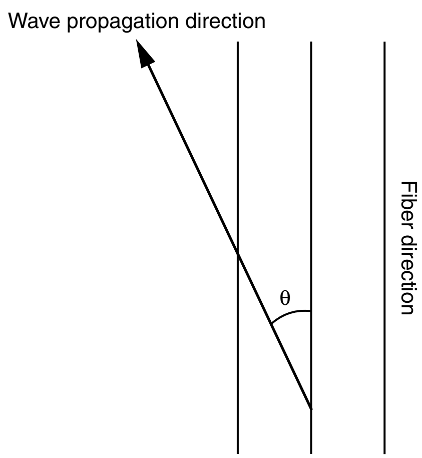

FIGURE 9.30
Angle between the wave propagation and boron fiber direction.

group velocity dispersion curve in various modes (Figure 9.31). The stiffness of the boron/epoxy patch was taken as C_{11} = 210.1 GPa, $C_{12} = C_{13}$ = 5.64 GPa, $C_{22} = C_{33}$ = 26.3 GPa, C_{23} = 4.5 GPa, with shear stiffness C_{44} = 10.3 GPa, $C_{55} = C_{66}$ = 7.2 GPa. A Young's modulus of 2.07 GPa and a Poission's ratio of 0.34 were used for the adhesive layer.

Because of the directional properties of the patch, the group velocity dispersion curves at various wave propagation angles (Figure 9.30) can also be obtained from the Disperse code.

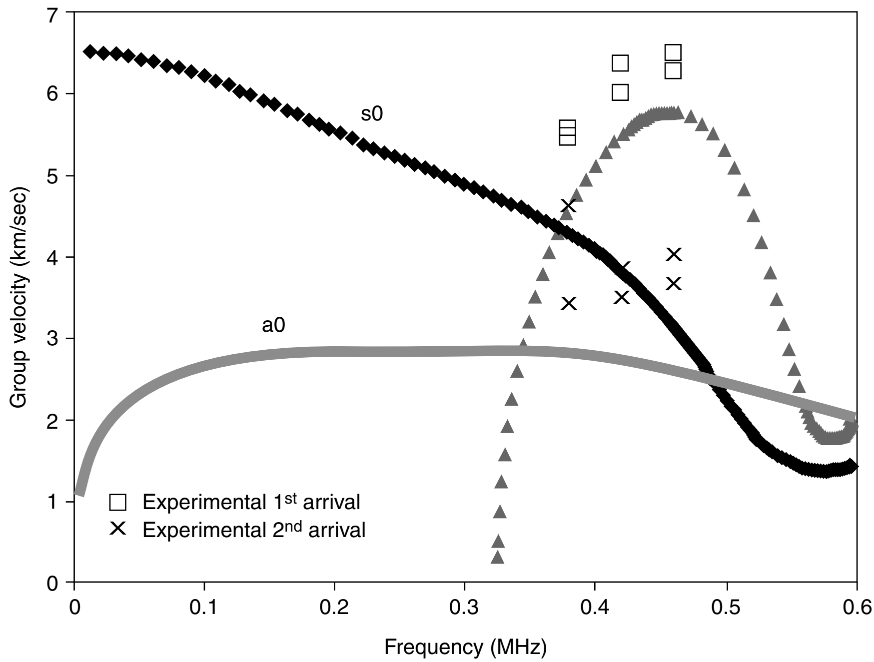

FIGURE 9.31
Group velocity dispersion curve of boron/epoxy-adhesive-aluminum (fiber direction, θ = 0).

Since the lower SMART layer is used for crack detection and the diagnostic paths are parallel with the boron fibers, the group velocity dispersion curve of Lamb wave modes with θ = 0 was obtained by the numerical results. Figure 9.31 shows a good agreement between the numerical results and the experimental measurements at a frequency range of 380 to 460 kHz where the experimental second arrival packet was identified as the fundamental symmetric Lamb wave mode (s0).

9.6.2.3.2 DI Results

The sensor data from the 420-kHz input signal were used for the analysis since these data have the highest signal-to-noise ratio. The DI was evaluated based on the time arrival of the second arrival wave packet. The baseline was taken after the specimens were cycled until an initial crack growth of 2 mm had occurred.

The crack growth was defined as

$$\text{Crack growth} = \text{the final crack length} - \text{initial crack length}$$

$$= 2a_f - 2a_i \quad \textbf{(9.13)}$$

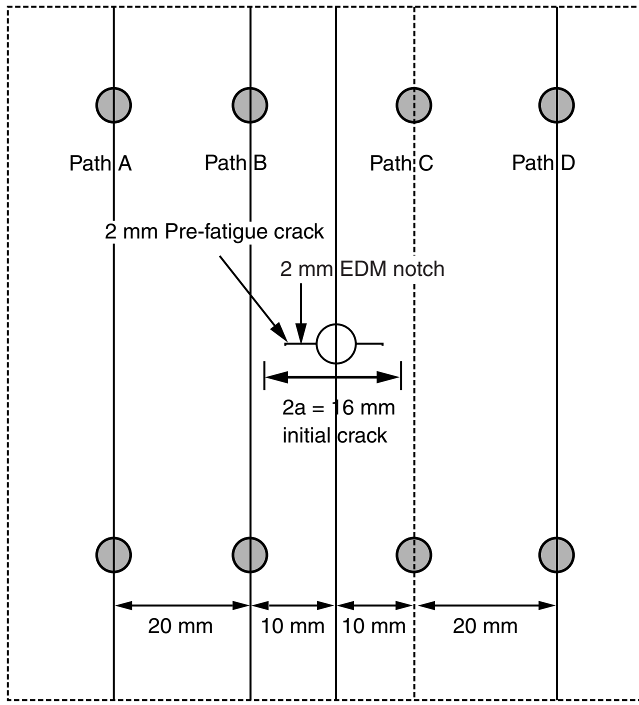

FIGURE 9.32
Diagnostic paths in lower SMART layer.

where $a_i = 16$ mm including an 8-mm hole diameter.

Further crack growth was visually identified and at the same time monitored by the DI, which was evaluated at different diagnostic paths (Figure 9.32). The results are plotted in Figure 9.33, which indicates the clear crack growth detection capability of the DI. It also shows in a consistent manner the higher sensitivity of the damage index as the diagnostic paths (paths B and C) are closer to the initial crack tip location.

In order to evaluate the cyclic loading effect on the DI, the sensor measurements were continuously taken at the specified loading intervals even before any visual identification of crack initiation was possible. Figure 9.34 shows the changes of the DI at different loading cycles, but the variation remains at a value less than 0.1.

9.6.2.4 Patch Debonding Effect

What if the repair patch debonds from the host structure? In real applications, the patch disbond can arise from fatigue loading, impact, or long-term environmental exposures.

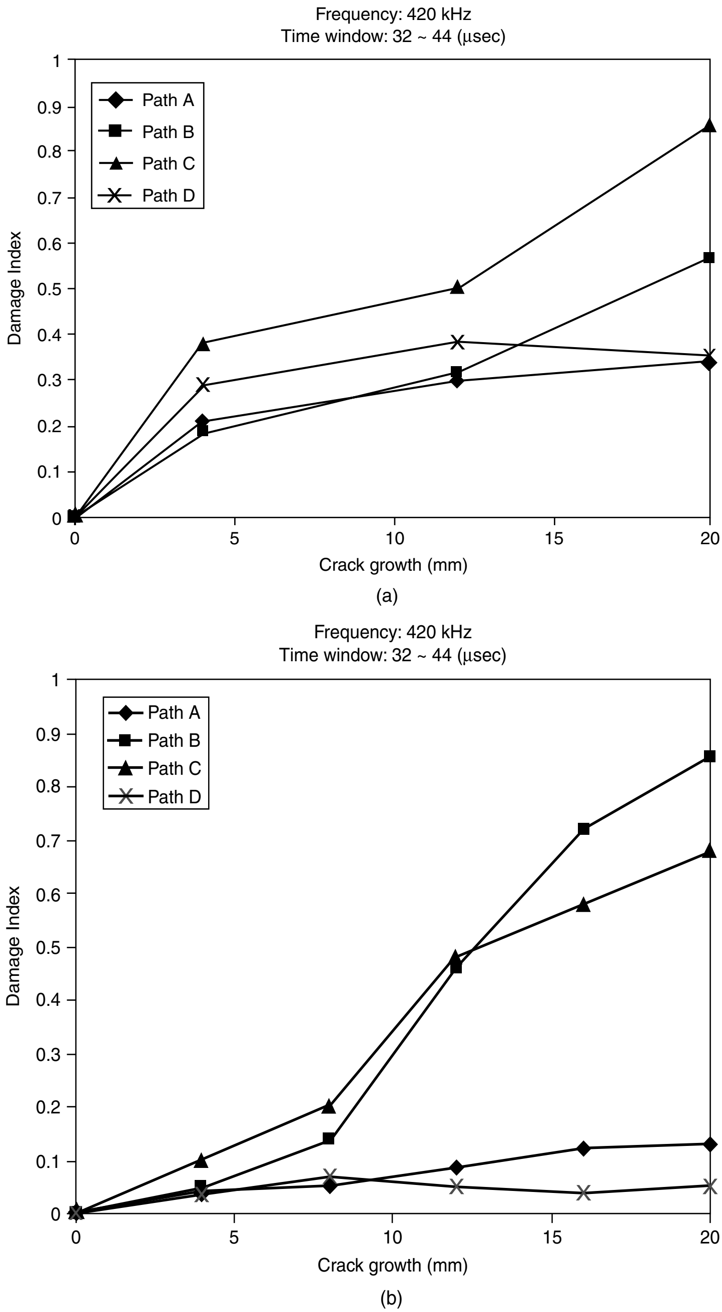

FIGURE 9.33
DI vs. crack growth. (a)SMART patch 1; (b) SMART patch 2.

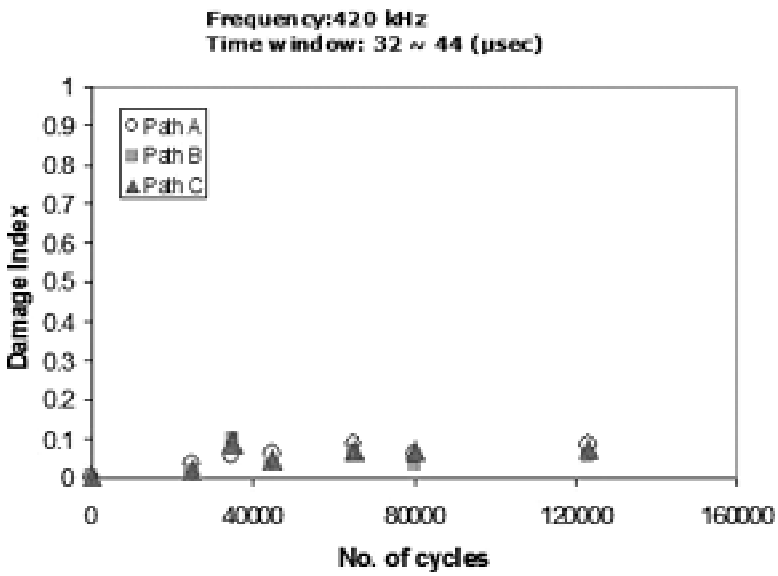

FIGURE 9.34
Cyclic loading effect on the DI.

9.6.2.4.1 Push-Down Test Setup

In order to assess the effects of the patch disbond on the DI, one of the specimens (SMART patch 2) was taken for the patch disbond test. As seen in Figure 9.35, the compression force was applied through the hole on the back side of the specimen to locally debond the patch around the center hole. A ring with a 1.5-in. inner diameter was placed at the bottom to limit the size of the debond.

Two incremental compression loads were applied to the specimen. After each load, the sensor measurements from the SMART layers were taken and the specimen was taken to the Boeing Company for patch disbond inspection. The Through Thickness Ultrasonic (TTU) test was then performed. Figure 9.36 shows the progressive debond damages as darker areas at the center of the patch with corresponding approximate debond areas.

9.6.2.4.2 Lamb Wave Mode Verification

The upper SMART layer was designed for the patch disbond detection. Since the diagnostic path on the upper SMART layer is orthogonal to the boron fiber direction, and has the same material properties as the boron/epoxy patch-adhesive layer-aluminum plate specimen described earlier, it was possible to obtain the numerical dispersion curves for the wave propagation direction of $\theta = 90°$. As Figure 9.37 shows, the experimental first arrival signal is most probably the fundamental symmetric mode and the experimental second arrival signal is most probably the fundamental antisymmetric mode in the frequency range from 220 to 500 kHz.

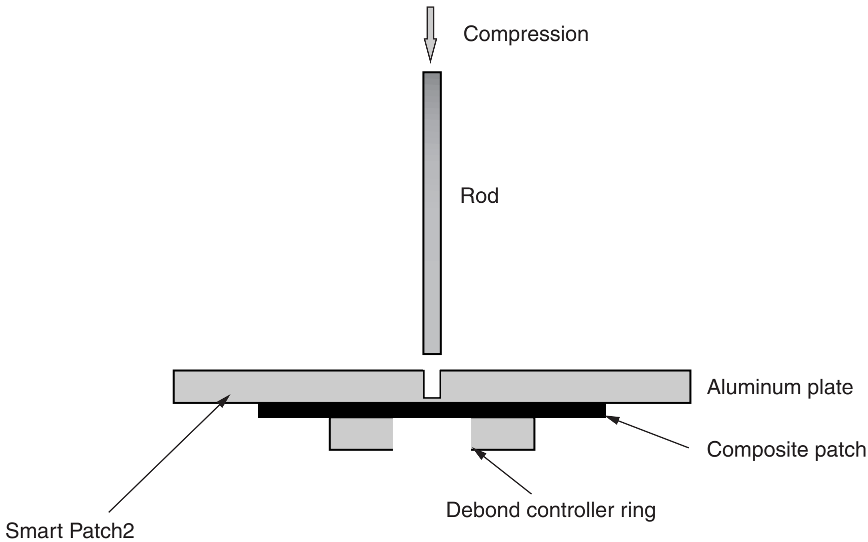

FIGURE 9.35
Push-down test setup.

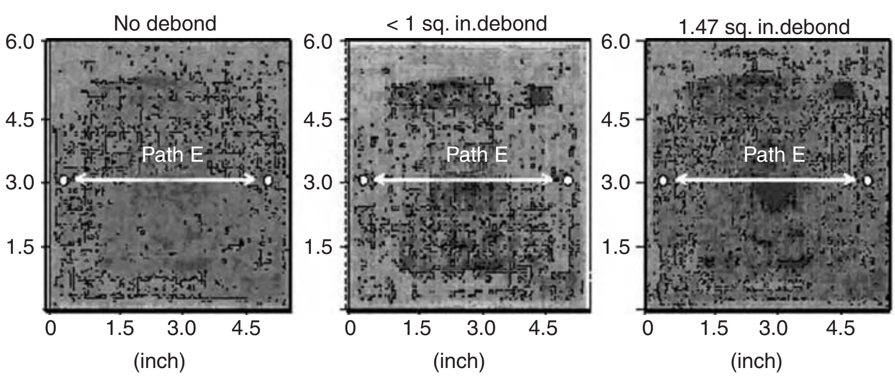

FIGURE 9.36
TTU results from Boeing Company with diagnostic path location (top view of repair patch area only).

Sensor measurements were taken from path E in the upper SMART layer. Figure 9.38 shows the amplitude spectrums of both the a0 and s0 modes before and after the debond damage where the amplitude was normalized by the maximum value of the a0 amplitude spectrum. As expected, the fundamental antisymmetric mode (the experimental second arrival) shows higher sensitivity to the disbond damage.

We can also use the same DI for crack detection described previously to detect disbond damage when the a0 mode is considered instead of the s0

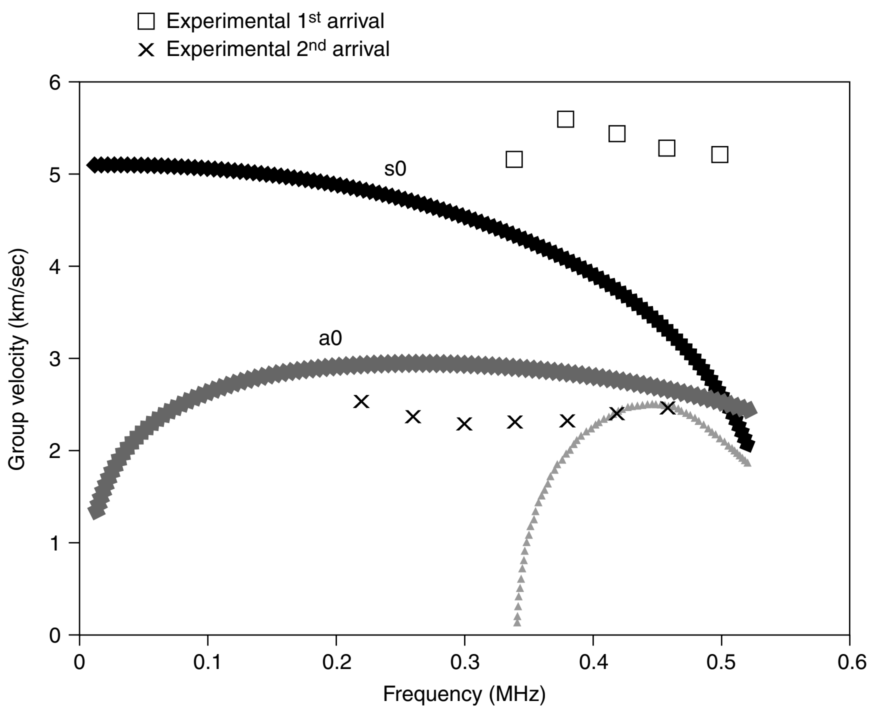

FIGURE 9.37
Group velocity dispersion curve of boron/epoxy-adhesive-aluminum (θ = 90°).

mode. The DI for detecting the two different damage types will have the following forms:

$$DI \text{ for crack detection} = \left[\frac{\textit{Scatter} \text{ energy of s0 wave}}{\text{Baseline energy of s0 wave}}\right]^{1/2}$$

$$DI \text{ for debond detection} = \left[\frac{\textit{Scatter} \text{ energy of a0 wave}}{\text{Baseline energy of a0 wave}}\right]^{1/2}$$

9.6.2.5 Variations of the DI

As Figure 9.39 shows, the various tests were conducted at different times, which are denoted as "serial events" on the specimen (SMART patch 2). The specimen was first tested only for the patch debond (Section 9.6.2.4) and then fatigued under cyclic loading for the fatigue crack growth (Section 9.6.2.2).

The DI by the upper SMART layer shows good sensitivity to the debond damage and remains with small variation afterward. On the other hand, the

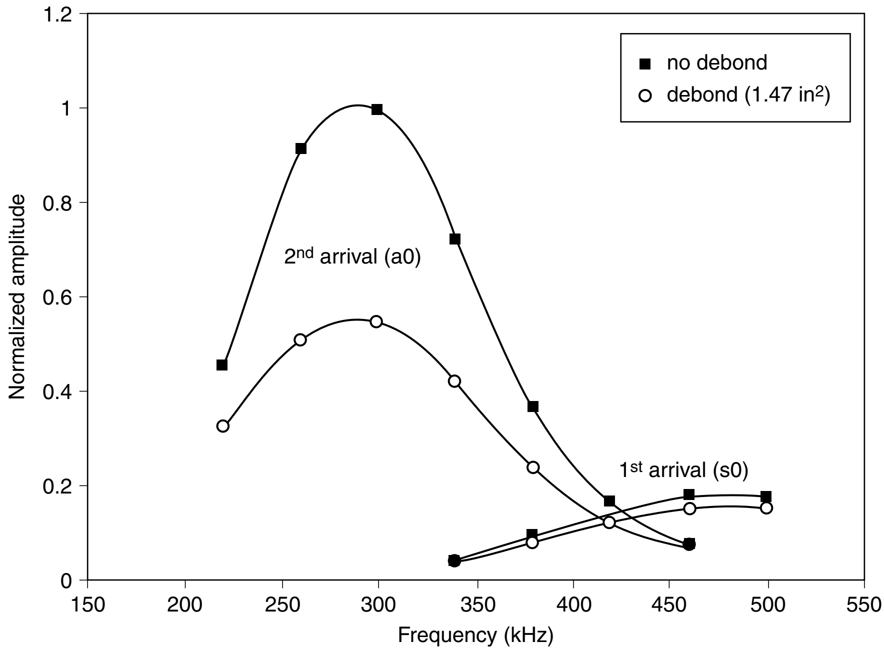

FIGURE 9.38
Normalized amplitude responses of the upper SMART layer (path E) to debond damage.

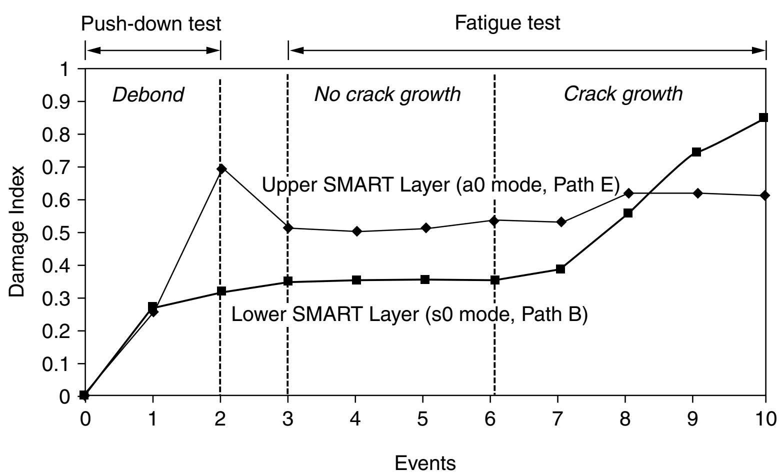

Serial Events	0	1	2	3	4	5	6	7	8	9	10
Debond (in^2)	0	<1	1.47	N/A	N/A	N/A	N/A	N/A	N/A	N/A	1.54
Cycle (×1000)				65	80	123	429	616	852	902	948
Crack growth 2a (mm)	0	0	0	0	0	0	8	12	16	20	24

FIGURE 9.39
Variation of the DI in the series of tests.

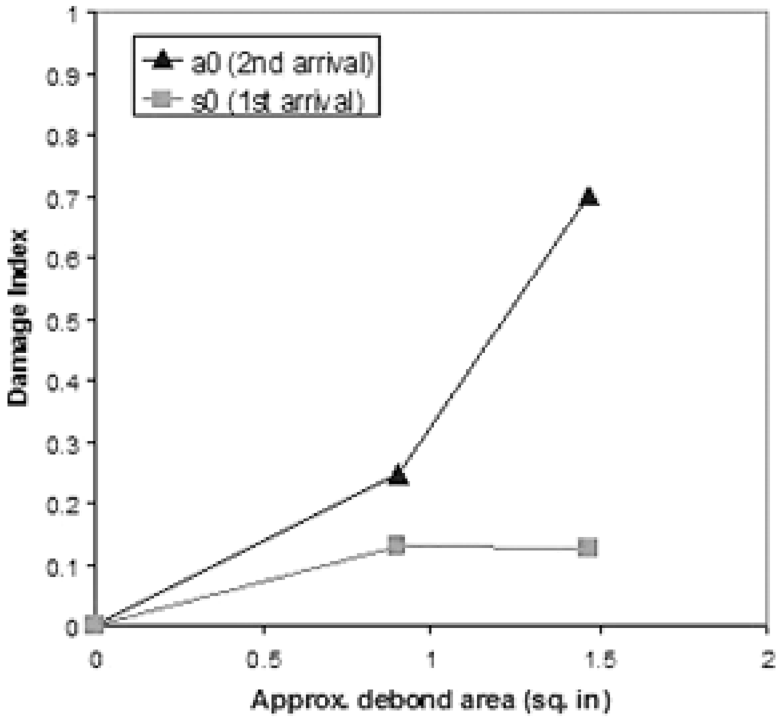

FIGURE 9.40
The response of s0 and a0 modes to debond damage (upper SMART layer).

Damage Index by the lower SMART layer shows good sensitivity only to the crack growth. Figure 9.40 and Figure 9.41 show the sensitivity of the s0 and the a0 modes generated by the upper SMART layer to the debond damage and the crack growth respectively. As previously observed in the amplitude spectrum plot (Figure 9.38), the a0 mode is more sensitive to debond damage than the s0 mode. Both the a0 and the s0 modes generated by the upper SMART layer were also not sensitive to the crack growth compared with the s0 mode of the lower SMART layer. The insensitivity of the s0 mode of the upper SMART layer (path E) may be the result of its wave propagation direction, which was parallel to the crack propagation direction.

9.7 Conclusions

An active sensing diagnostic technique for metallic and composite structures using built-in piezoelectric sensor/actuator networks was investigated and discussed. It consists of three major components: diagnostic signal generation, signal processing, and damage diagnostics. In diagnostic signal generation,

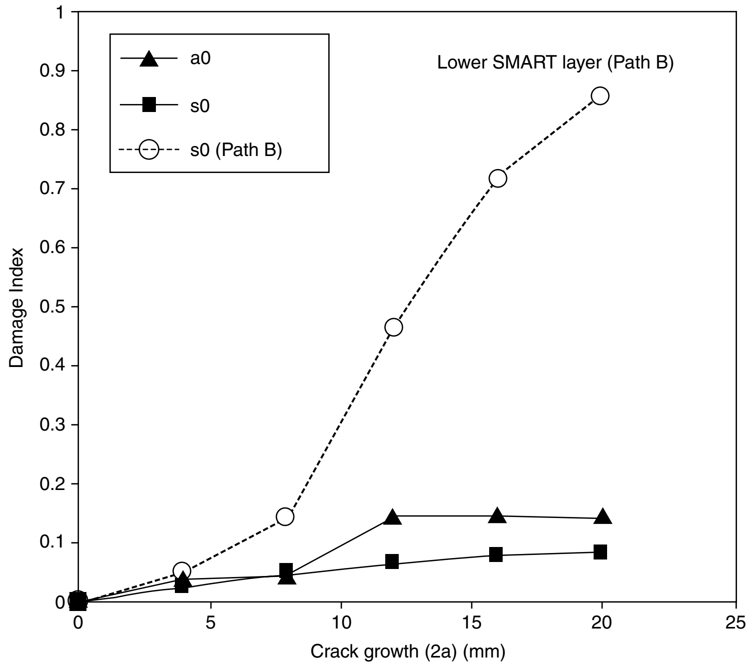

FIGURE 9.41
The response of s0 and a0 modes to crack growth (upper SMART layer).

appropriate diagnostic signals were selected for actuators to maximize receiving sensor measurements. In signal processing, methods were discussed to maximize signal-to-noise ratio in recorded sensor signals and derive experimental dispersion curves. A physics-based DI was developed from extracting features in sensor signals related to crack growth.

As demonstrated, the technique was used to detect crack lengths as small as 5 mm on riveted fuselage joints with certainty equal to conventional NDT such as the eddy current testing and the ultrasonic scan methods.

The results from the repair patch specimens also correlate quite well with visual inspections and clearly indicate that the technique can detect crack propagation underneath the patch. In case of the repair patch disbond, the technique using the additional SMART layers inserted at different ply locations can detect both crack growth and debond damage.

The damage detection ability using the proposed system can be further improved by selecting the optimal actuator-sensor location, which is a function of structural geometry and initial structure conditions.[23]

Acknowledgments

The financial support of the Air Force Office of Scientific Research and European Aeronautic Defence and Space Company (EADS) on this investigation is gratefully appreciated. The author would like to thank Dr. Christian Boller of EADS, Holger Speckmann of EADS Airbus for the support of the single-lap tests, and Dr. Roy Ikegami of Boeing Company for his support on the repair patch tests.

References

1. Doebling, S.W., Farrar, C.R., Prime, M.B., Shevitz, D.W., *Damage Identification and Health Monitoring of Structural and Mechanical Systems from Changes in Their Vibration Characteristics: A Literature Review,* Tech. Rep. No.: LA-13070-MS, Los Alamos National Laboratory, Los Alamos, NM, 1996.
2. Imam, I., Azarro, S., Bankert, R., and Scheibel, J., Development of an on-line rotor crack detection and monitoring system, *J. Vibration, Acoustics, Stress, Reliability Design*, 3, 241–250, 1989.
3. Doyle, J.F., Determining the size and location of transverse cracks in beams, *Exp. Mech.*, Sept. 1995, 272–280.
4. Tsyfansky, S.L. and Beresnevich, V.I., Non-linear vibration method for detection of fatigue cracks in aircraft wings, *J. Sound Vibration*, 236, 49–60, 2000.
5. Matveev, V.V. and Bovsunovsky, A.P., Vibration-based diagnostics of fatigue damage of beam-like structures, *J. Sound Vibration,* 249, 23–40, 2002.
6. Giurgiutiu, V., Damage metric algorithms for active-sensor structural health monitoring, *Proc. First Eur. Workshop Structural Health Monitoring*, Cachan (Paris), France, July 10–12, 2002, pp. 433–441.
7. Zagrai, A.N. and Giurgiutiu, V., Electro-mechanical impedance method for crack detection in thin wall structures, *Proc. 3rd Int. Workshop Structural Health Monitoring*, Stanford, CA, 2001, pp. 177–186.
8. Peairs, D.M., Park, G., and Inman, D.J., Investigation of self-monitoring and self-healing bolted joints, *Proc. 3rd Int. Workshop Structural Health Monitoring*, Stanford, CA, 2001 pp. 430–439.
9. Castanien K.E. and Liang, C., Application of active structural health monitoring technique to aircraft fuselage structures, *Proc. Smart Structures Materials: Industrial Commercial Applications of Smart Structures Technol.*, SPIE, San Diego, CA, 2721, 38–49, 1996.
10. Roh, Y.S. and Chang, F.-K., Built-In Diagnostics for Identifying an Anomaly in Plates Using Wave Scattering, Ph.D. dissertation, Department of Aeronautics and Astronautics, Stanford University, Stanford, CA,1999.
11. Alleyne, D. N. and Cawley, P., The interaction of Lamb waves with defects, *IEEE Trans. Ultrasonics, Ferroelectrics, Frequency Control*, 39, 381–397, 1992.
12. Chang, Z. and A. Mal, Scattering of Lamb waves from a rivet hole with edge cracks, *Mech. Mater.*, 21, 197–204, 1999.
13. Wang, C.S. and Chang, F.-K., "Built-In Diagnostics for Impact Damage Identification of Composite Structures, *Proc. 3rd Int. Workshop Structural Health Monitoring*, Stanford, CA, 2001, pp. 612–621.
14. Kessler, S.S., Spearing, S.M., and Soutis, C., Structural health monitoring in composite materials using Lamb wave methods, *Smart Mater. Structures*, 11, 269–278, 2002.

15. Lin, M. and Chang, F.-K., Manufacturing of Composite Structures with a Built-In Network of Piezoceramics, Ph.D. dissertation, Department of Mechanical Engineering, Stanford University, Stanford, CA, 1998.
16. Lin, M., Qing, X., Kumar, A., and Beard, S., SMART layer and SMART suitcase for structural health monitoring applications, *Proc. SPIE Smart Structures Mater. Systems*, Long Beach, CA, March 2001.
17. Acellent Technologies, http://www.acellent.com.
18. Viktrov, I.A., *Rayleigh and Lamb Waves, Physical Theory and Applications*, Plenum Press, New York, 1967.
19. Qian S. and Chen, D., *Joint Time-Frequency Analysis: Methods and Applications*, Prentice Hall, Upper Saddle River, NJ, 1996.
20. Pavlakovic, B., Lowe, M., A System for Generating Dispersion Curves: User's Manual for Disperse v. 2.0, June 2000.
21. Lowe, M.J.S., Pavlakovic, B.N., and Cawley, P., Guided wave NDT of structures: a general purpose computer model for calculating waveguide properties, *Proc. 3rd Int. Workshop Structural Health Monitoring*, Stanford, CA, 2001, pp. 880–888.
22. Boller, C., Ihn, J.-B., Staszewski, W.J., and Speckmann, H., Design principles and inspection techniques for long life endurance of aircraft structures, *Proc. 3rd Int. Workshop Structural Health Monitoring*, Stanford, CA, 2001, pp. 275–283.
23. Ihn, J.-B., Built-in Diagnostics for Monitoring Fatigue Crack Growth in Aircraft Structures, Ph.D. dissertation, Department of Aeronautics and Astronautics, Stanford University, Stanford, CA, 2003.

10

Brillouin Scattering Measurement of SAW Velocities for Determining Near-Surface Elastic Properties

Marco G. Beghi, Arthur G. Every, and Pavel V. Zinin

CONTENTS

0-8493-1462-3/02/$0.00+$1.50

10.1 Introduction

Surface Brillouin scattering (SBS) is a noncontact measurement technique that exploits light scattering to probe the properties of surface acoustic waves (SAWs), either at the surface of homogeneous solids or in thin supported layers. The objective is to obtain information on the elastic properties of the near-surface region, extending down to a depth of the order of a micron. The near-surface elastic properties of solids often differ markedly from those of the underlying bulk material. They are a sensitive indicator of residual stress, annealing, and other near-surface physical conditions. SBS is widely used in the characterization of thin (submicron) supported layers, whose elastic properties can differ from those of the corresponding bulk material. It can alternatively be exploited to measure other properties, such as the layer thicknesses or mass density or the presence of interfacial layers. The systems that have been studied to date are many and diverse. They include inorganic materials such as silicon and silicides; a variety of carbonaceous materials such as diamond, chemical vapor deposited (CVD) diamond, and diamond-like films; various types of hard coatings like carbides and nitrides; Langmuir-Blodgett (LB) films; and various types of multilayers.

The SBS technique does not involve the excitation of SAWs, but relies on spontaneous thermal fluctuations in these modes. It does not observe SAW propagation over macroscopic distances, but is based on local inelastic scattering of light, and is therefore applicable to small samples. Most other SAW techniques are based on the excitation of surface waves, at frequencies determined by the particular technique and experimental conditions; quantitative acoustic microscopy, for example, measures SAW at frequencies ranging from 30 MHz to 2 GHz,[1] while typical frequencies of the broadband SAW pulses obtained by laser excitation lie within the range 5 to 500 MHz.[2] In

SBS the wave vector is determined by the experimental conditions, and with visible light the explored SAW wavelengths are of the order of half a micron or less; typical SAW speeds of such wavelengths correspond to frequencies ranging from a few GHz up to 30 GHz. Surface Brillouin scattering is the only technique able to detect SAWs in this frequency range.[3,4] In order to cover broader frequency ranges, and thus obtain fuller information on the near surface properties, SBS has also been used in conjunction with other techniques such as acoustic microscopy,[5] laser-ultrasonic techniques, or microindentation.[6,7] Wavelengths of a fraction of a micron are still orders of magnitude larger than interatomic distances, and their analysis by a continuum model is therefore fully appropriate.

Thermal fluctuations are governed by the equipartition principle of thermodynamics, which says that at a temperature T each vibrational degree of freedom of a mechanical system is endowed with on average an amount of energy $k_B T$, where $k_B = 1.38 \times 10^{-23}$ J/K is Boltzmann's constant. In an elastic continuum the vibrational degrees of freedom correspond to acoustic modes of any wave vector. The thermal noise can thus be seen as a superposition of all the acoustic modes. In SBS the scattering geometry selects a specific wave vector and probes the thermal noise at that wave vector, performing a sampling of the surface wave dispersion. This is done by illuminating the surface with a laser beam and examining the spectrum of the scattered light. The laser is of fairly modest power (usually less than a watt) and supposedly causes minimal heating of the surface; it is not the driving force producing the fluctuations, but it is the tool used to detect them. For a highly polished surface, most of the incident light is specularly reflected, refracted, or absorbed. However, because of the thermal fluctuations, a small amount is diffusely scattered, undergoing a change in frequency in the process. This is akin to Raman scattering, but entailing long wavelength acoustic modes rather than molecular vibrations (in microscopic terms, acoustic phonons rather than optical phonons). From the spectrum of the inelastically scattered light and the scattering geometry, one can derive the SAW dispersion relation for the surface and infer the elastic properties of the near-surface region. How this is done is the subject matter of this chapter.

SBS is commonly but not invariably observed in opaque or semiopaque materials, in which the scattering volume is the surface and the small region near the surface that the light is able to penetrate. Some materials studied in SBS are transparent or semitransparent, and in these cases one observes a substantial amount of light scattering from within the bulk. While the main focus of this chapter is on SBS, for completeness we will address some remarks at the issue of bulk Brillouin scattering. Bulk Brillouin scattering is, among other things, used to study the elastic properties of transparent materials as a function of temperature and pressure, particularly with regard to their behavior near phase transitions. When bulk scattering can also be observed, it can be advantageously exploited, since it provides additional information on which to base elastic properties determination. Brillouin spectrometry is particularly suited to measurements under controlled temperature and/or pressure, because the measurements are contactless, and require only one (for the backscattering configuration) or two (for other configurations) optical windows to access the specimen. This has allowed measurements in furnaces equipped with optical windows,[8–10] and in diamond anvil cells, exploiting the transparency of diamond.[11]

The outline of this chapter is as follows. In Section 10.2 we discuss the underlying physics of SBS, the mechanisms for the scattering of light by thermally excited acoustic vibrations, and the nature of the various bulk and guided waves that play a role in the scattering. An analysis of the various acoustic modes was already presented in Chapter 1 for the case of isotropic media and layers. However, much of the recent experimental work in the area of SBS has been concerned with crystals, epitaxial layers, superlattices, and other types of solids that are elastically anisotropic. The analysis of Chapter 1 is therefore extended to anisotropic media and follows a somewhat different approach, giving results in a form that is more directly linked to the scattering cross section.

In Section 10.3, the SBS technique is described in more detail, and some classical applications are discussed. The observation of SBS has greatly benefited in recent years from developments in multipass tandem Fabry-Perot interferometry and low noise high sensitivity detectors.[12] These developments have brought about improvements in resolution and have significantly reduced the data collection time required to achieve adequate signal-to-noise ratio. Finally, Section 10.4 contains a review of recent SBS applications to the study of single- and multilayers, particularly hard and superhard materials.

This chapter presupposes familiarity with the elementary principles of elasticity, as expounded in Chapter 1 of this book and in the reviews.[13–15] It is a fairly self-contained overview of the SBS technique and its application in the nondestructive characterization of materials. We draw attention to a number of other recent reviews on the subject of SBS.[3,4,12,16] Theoretical treatments of SBS have been published by a number of authors.[17–26] Bulk Brillouin scattering has been reviewed by Dil.[27]

10.2 Theory

10.2.1 Brillouin Scattering: The Principle

The principle of Brillouin scattering is shown in Figure 10.1. A laser beam of angular frequency Ω_i and wave vector $\mathbf{q}_i$ is incident on the highly polished surface of a sample at angle θ to the normal. Most of this light is specularly reflected, refracted at angle θ', or absorbed. However, as a result of thermally excited dynamic fluctuations in the strain field within the solid and dynamic rippling of the surface, a small amount of light is diffusely scattered, undergoing in the process a fractional change in frequency of the order of $c_{acoust}/c_{light} \sim 10^{-5}$, where c_{acoust} is the acoustic wave speed and c_{light} is

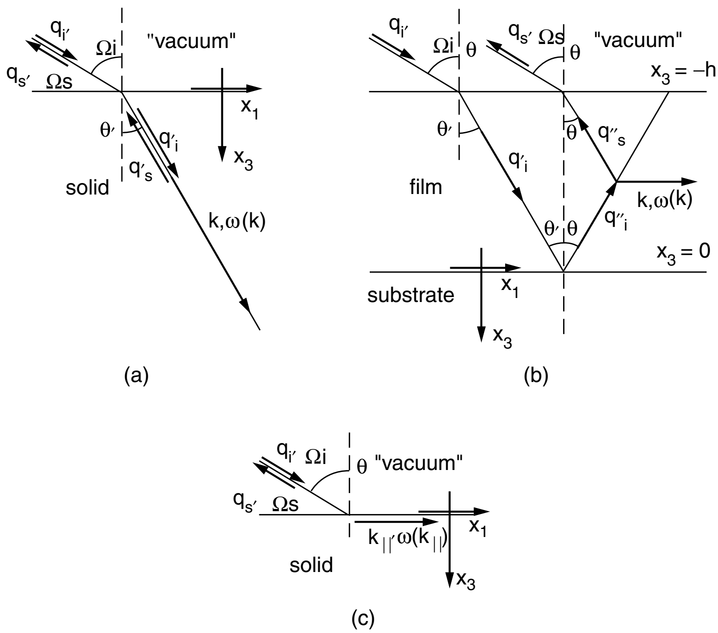

FIGURE 10.1
Brillouin scattering geometry. Ω_i, Ω_s incident and scattered optical circular frequencies; ω: acoustical circular frequency; $\mathbf{q}_i$, $\mathbf{q}_s$: incident and scattered optical wave vectors, in vacuum; $\mathbf{q}_1'$, $\mathbf{q}_i''$, $\mathbf{q}_s'$, $\mathbf{q}_s''$: incident and scattered optical wave vectors, in the solid; **k**: acoustical wave vector. (a) transparent solid, of refractive index n: $q_i \sin\theta \cong q_i' \sin\theta'$, by Snell's law, $\mathbf{k} = \mathbf{q}_i' - \mathbf{q}_s'$, $q_s' \cong q_i' = nq_i$, $k = 2nq_i$; (b) supported transparent film, of refractive index n : $q_i \sin\theta \cong q_i' \sin\theta'$, by Snell's law, $\mathbf{k} = \mathbf{q}_i'' - \mathbf{q}_s''$, $q_s'' \cong q_i'' = q_i' = nq_i$, $k = 2q_i''\sin\theta' = k = 2q_i \sin\theta$. (c) opaque solid: $k_{||} = (q_i - q_s)_{||}$, $q_s \cong q_i$, $k_{||} = 2q_i \sin\theta$.

the speed of light (see Section 10.3.1.1). Present in the spectrum of scattered radiation is a relatively intense central peak, unshifted in frequency, which is due to static inhomogeneities and surface roughness in the sample. Because of the fluctuations, in the spectrum there are two more or less mirror image sidebands straddling the central peak. The frequency-downshifted one is called the Stokes band, and the frequency-upshifted one the anti-Stokes band. The inelastic (frequency-shifted) spectrum, which is our concern here, depends on the optical and elastic properties of the sample, the scattering geometry, and the vibrational modes of the solid that the light is able to couple to. Since, as already mentioned, the average amount of energy per vibrational degree of freedom is $k_B T$, the intensity of the inelastic spectrum turns out to be proportional to the absolute temperature.

From a quantum mechanical point of view, the scattering is interpreted as a phonon creation (Stokes) or annihilation (anti-Stokes) process in which the photon loses or gains the energy of the phonon. It must also be noted that the quantum of energy $\hbar\omega$ ($\hbar$ is Planck's constant) associated with an oscillator of 30 GHz frequency corresponds to an equivalent temperature $\hbar\omega/k_B$

of about 1.5 K. This means that even at rather low temperatures the classical approach adopted in this chapter is adequate for calculating the spectrum. It is only at extremely low temperatures where $k_B T$ becomes comparable to $\hbar\omega$, and quantum mechanical effects become pronounced so that a more sophisticated approach is required.

In the usual implementation of SBS, the backscattered light of frequency Ω_s, and wave vector $\boldsymbol{q}_s$ in a small cone around $-\boldsymbol{q}_i$, is collected and analyzed. Three common scattering processes are depicted in Figure 10.1 pertaining to a (a) transparent solid, (b) transparent supported layer, and (c) an opaque or semiopaque solid or supported layer. Because of the small frequency shift $|\omega| = |\Omega_s - \Omega_i| \ll \Omega_i$, it follows that the incident and scattered light wavelengths differ only very slightly, so that to a good approximation $q_s \approx q_i$. Taking into account the change in the wavelength due to the refractive index n for the light when it is in the solid, it follows that $q_s' \approx q_s'' \approx q_s' \approx q_s'' \approx nq_i$ (see Section 10.2.1.1). Further, Snell's law of refraction requires that $q_i' \approx q_s'' \approx q_s' \approx q_s'' \approx nq_i$ and $q_i \sin\theta \approx q_i' \sin\theta'$.

10.2.1.1 Acoustic Modes in Anisotropic Media

Interpretation of SBS spectra can become a complex task when the spectra contain several peaks and when an estimate of the specimen's elastic properties is not available *a priori*. A proper assignment for each peak requires an understanding the basics of SAW propagation in layered solids, especially when the layers are anisotropic. Extensive discussions of bulk and surface waves can be found in a number of books.[15,28–35] We discuss only some salient features here.

The theoretical approach we present here is formulated for anisotropic media and includes as a special case isotropic solids. It was shown in Chapter 1 that in isotropic solids two types of bulk acoustic modes exist: primary waves, longitudinally polarized, and secondary waves, transversely polarized. Two independent (orthogonal) transverse polarization directions exist. In isotropic solids the secondary waves are perfectly equivalent, while in anisotropic solids they are not. These modes, called fast transverse (FT) and slow transverse (ST) from their generally different velocities, have phase velocities and polarization vectors that depend on the propagation direction. Also the phase velocity and polarization vector of the longitudinal (P) mode depend on the propagation direction. Although in the anisotropic case the polarization vectors are generally neither exactly parallel nor exactly perpendicular to the wave vector (and therefore, in strict terms, the modes are quasi longitudinal and quasi-transverse) the above names and the corresponding labels P, ST, and FT are customarily used in this context, and are also adopted in this chapter.

At surfaces other acoustic modes are encountered. The Rayleigh wave (RW) at the free surface of a semi-infinite isotropic elastic half-space and at the surface of an isotropic substrate covered by an isotropic layer were discussed in detail in Chapter 1. The RW propagating along the stress-free boundary of a homogeneous solid is a nondispersive acoustic wave which has its energy and displacement field confined near the surface.[36,37] Similar waves existing on anisotropic surfaces are called generalized RW (GRW).[38] The solutions of the wave equation for such waves differ from the true RW on isotropic media only in the form of the variation of the displacement with depth.[36] Antiplane and in-plane modes in free-standing plates (Lamb waves) were also discussed in Chapter 1, as well as transverse modes in a layered half-space (Love waves). Unattenuated waves traveling along interfaces between two solids (Stoneley waves)[39] exist in certain cases; the conditions for their existence have been established.[40] The existence of attenuated interfacial waves was also shown.[41]

Along a stress-free boundary, surface skimming longitudinal (LA) and transverse (T) acoustic waves can exist. The former, from being encountered in different contexts, has acquired various names, including the high frequency pseudo-surface wave (HFPSW),[42] leaky longitudinal surface wave (LLSW), and longitudinal guided wave (LGW) or mode (LGM). Furthermore, waves exist that are surface-like but slowly radiate energy away from the surface and for which the displacement field does not vanish at infinite depth. They are not surface waves in the strict sense, but since their energy is mainly confined near the surface they are called pseudo-surface acoustic waves (PSAWs).[36] PSAWs have a phase velocity higher than that of the lowest of the bulk waves in the substrate. The presence of a layer over a substrate leads to the appearance of a number of waves confined within the layer.[43] For a single layer on solid substrate, these waves are called generalized Lamb[32] or Sezawa waves,[26] because of their similarity to Lamb waves in free-standing isotropic plates. Degenerate Lamb modes have been identified by Sezawa. The behavior of generalized Lamb waves depends on the thickness of the layer in relation to the wavelength, on whether the layer is stiffer or less stiff than the substrate, and the relative densities of the layer and substrate.

In addition to Chapter 1, reviews of the SAW propagation on plates and layered materials can be found in references at the end of this chapter.[33,36,37,43,44]

10.2.1.2 Transparent Solids: The Elasto-Optic Scattering Mechanism

In the case of a transparent solid (Figure 10.1a), most of the scattered light emanates from the refracted beam in a region well away from the surface, and the kinematic conditions relating wave vector and frequency shift of the light pertain to bulk acoustic wave scattering. The scattering in this case is mediated by the *elasto-optic scattering mechanism*, in which dynamic fluctuations in the strain field ε_{ij} bring about fluctuations in the dielectric constant, and these in turn translate into fluctuations in the refractive index. These fluctuating optical inhomogeneities result in inelastic scattering of the light as it passes through the solid. In the general anisotropic case the dielectric constant is a tensor χ_{ij} of rank 2, and its fluctuations are given by $\delta\chi_{ij} = p_{ijkl}\,\varepsilon_{kl}$, where p_{ijkl} is the tensor of the elasto-optic constants.

The strain field in the bulk, well away from the surface, can be expressed as the superposition of the displacement fields of all the bulk P, FT, and ST acoustic waves of the solid. For a particular scattering geometry (i.e., specific incident light wave vector $\mathbf{q}_i'$ and scattered light wave vector $\mathbf{q}_s'$ [both within the solid), the scattering wave vector is $\mathbf{k} = \mathbf{q}_i' - \mathbf{q}_s'$, and only acoustic waves having precisely this wave vector **k** contribute to the detected signal. Bearing in mind that $\mathbf{q}_i'$ and $\mathbf{q}_s'$ differ only very slightly in magnitude, it follows that for backscattering $k = 2q_i'$. The spectrum of the scattered radiation thus contains in principle three pairs of peaks, at frequency shifts

$$\omega = \pm 2q_i' c_{acoust} = \pm 2nq_i c_{acoust} \tag{10.1}$$

where c_{acoust} stands for phase velocity of the P, FT, or ST wave in the direction of **k**. The intensities of these peaks vary considerably, depending on the elasto-optic constants p_{ijkl} of the solid, wave polarization, and direction and other factors; it is quite common for one or more of the peaks to be too faint to be detected or even to be zero. These peaks yield up to three bulk wave velocities as a function of direction θ′, from which individual elastic constants or combinations of constants can be inferred.[45] In bulk wave scattering the frequency shifts of Equation 10.1 are much larger (up to 150 GHz or so) than for surface wave scattering (typically below 30 GHz). The presence of bulk wave peaks, well separated from surface wave scattering, is of advantage in determining elastic constants using SBS.

10.2.1.3 Brillouin Scattering in Thin Supported Transparent Layers

In the case of a transparent layer on a substrate (Figure 10.1b), in addition to Brillouin scattering from the refracted beam, there have been several reported observations of scattering from the beam of wave vector $\mathbf{q}_i''$ that is reflected from the interface. From the geometry of Figure 10.1b, one readily infers that the scattering wave vector $\mathbf{k} = \mathbf{q}_i' - \mathbf{q}_s'$ of the acoustic modes that are coupled to, is parallel to the surface, and of magnitude $k = 2q_i'' \sin\theta'$. Invoking Snell's law, it follows that $k = 2q_i \sin\theta$, which is, somewhat surprisingly at first sight, independent of the refractive index. Bulk waves are thus detected, having direction parallel to the surface, and frequency

$$\omega = \pm 2q_i c_{acoust} \sin\theta \tag{10.2}$$

yielding one or more bulk wave velocities parallel to the surface.

10.2.1.4 Opaque Solids: Surface Ripple Scattering Mechanism

In the case of an opaque or semiopaque solid or layer, the Brillouin scattering occurs at or near the surface. In this case the wave vector constraint on the acoustic modes that are coupled to is limited to the component $k_{||}$ parallel to the surface, which is of magnitude

$$k_{||} = 2q_i \sin\theta \tag{10.3}$$

This allows coupling to a continuous spectrum of bulk modes, incident on the surface and having this value of $\mathbf{k}_{||} = (k_1, k_2)$ and any value of k_3, the component of $\boldsymbol{k}$ normal to the surface. This part of the spectrum is called the Lamb shoulder. Also coupled are surface waves of various kinds that have this value of $\boldsymbol{k}_{||}$. The modes detected in backscattering have frequencies

$$\omega = \pm 2q_i c_{acoust} \sin\theta \tag{10.4}$$

yielding a continuum of values of c_{acoust} for the bulk modes and discrete values of wave velocity for the surface modes.

In the case of an opaque solid, SBS is mediated by the *surface ripple scattering mechanism* (i.e., scattering by dynamic corrugations in the surface profile)[17,46] due to the wave displacements. The dynamic rippling of the surface can be resolved into a superposition of harmonic waves, which act as moving diffraction gratings at the surface, traveling in the reverse (+) or forward (-) directions at velocity c_{acoust}. These cause diffraction of the light together with a Doppler frequency shift. It can be shown that in the classical regime, the cross section for scattering of light with frequency change ω and surface scattering wave vector $k_{||}$, is proportional to the power spectrum $<|u_3(k_{||}, \omega)|^2>$ of the normal fluctuations in the surface profile.[16,20] According to the fluctuation dissipation theorem for the normal displacement u_3 of the surface

$$<|u_3(\mathbf{k}_{||}, \omega)|^2> \propto \frac{T}{\omega} \operatorname{Im} G_{33}(\mathbf{k}_{||}, \omega) \tag{10.5}$$

where $\operatorname{Im} G_{33}(\mathbf{k}_{||}, \omega)$ is the imaginary (dissipative) part of the Fourier $(\mathbf{k}_{||}, \omega)$ domain surface dynamic response function (Green's function) for force and displacement normal to the surface. Hence, the scattering cross section for dynamic ripple mediated scattering is given by

$$\frac{d^2\sigma}{d\Omega d\omega} = \frac{AT}{\omega} \operatorname{Im} G_{33}(\mathbf{k}_{||}, \omega) \tag{10.6}$$

where A is a constant that depends on the scattering geometry, the frequency and polarization of the incident light, and the optical properties of the medium. How $\mathrm{Im}\, G_{33}(\mathbf{k}_{||},\omega)$ is calculated will be explained shortly.

In the case of a semiopaque solid, there can also be a contribution to the scattering from the elasto-optic effect in the region close to the surface that the light is able to penetrate. This scattering can be expressed in terms of the Green's function tensor G_{ij}, in this case not limited to the normal component G_{33} or to the response exactly at the surface. Accurate calculations of the elasto-optic scattering in semi-opaque solids require a knowledge of the complex dielectric constant as well as the p_{ijkl}, which are not always readily available. We will not treat this aspect further here, but refer the reader to the investigations by various authors.[47–51]

Note that the angular dependences given by Equation 10.2 and Equation 10.4 are exactly the same, but the physical interpretation is quite different. Regarding bulk modes, Equation 10.2 refers to isolated peaks in the Brillouin spectrum associated with modes with $\boldsymbol{k}$ parallel to the surface, while Equation 10.4 pertains to a continuum of bulk modes. In SBS, it is tempting to take a $\sin\theta$ dependence of the frequency shift of a peak as the tell-tale sign of a surface mode. As we have seen here, this can also be an indication of a surface skimming bulk wave.

10.2.2 Computation of Brillouin Spectra

10.2.2.1 Green's Function for Anisotropic Layered Media

Here we briefly describe the derivation of the Fourier $(\mathbf{k}_{||},\omega)$ domain surface dynamic response function (Green's function) $G_{33}(\mathbf{k}_{||},\omega)$ for an anisotropic layer of thickness h perfectly bonded to an anisotropic half space, following Every.[52] In the following sections we also discuss the nature of the various surface and guided waves, and how some of their properties can be obtained from $G_{33}(\mathbf{k}_{||},\omega)$. We adopt the coordinate system shown in Figure 10.1, with the x_1- and x_2-axes in the interface between the layer and substrate and the x_3-axis normal to the surface and directed into the substrate. By letting h tend to zero, the properties of the substrate alone are obtained. We consider a general anisotropic elastic continuum of mass density ρ^+ and elastic modulus tensor C^+_{ijkl} in the half-space $x_3 > 0$ and a layer of density ρ^- and elastic modulus tensor C^-_{ijkl} in the region $-h < x_3 < 0$ (Figure 10.1). The superscripts + and − will also be used for other quantities such as stress or displacement to distinguish them when they pertain specifically to the substrate or respectively to the layer.

We first provide a brief introduction to the subject of bulk waves in anisotropic solids, extending the detailed analysis presented in Chapter 1 for the isotropic case. We then show how bulk waves are used as partial waves in the calculation of the surface dynamic response of a layered solid. The wave equation for an infinite anisotropic elastic solid is

$$\rho \frac{\partial^2 u_i}{\partial t^2} = C_{ijkl} \frac{\partial^2 u_k}{\partial^2 x_j x_l} \quad \textbf{(10.7)}$$

summation over repeated indices being implied. Equation 10.7 admits plane wave solutions of the form

$$u_i = U_i \exp[i(\mathbf{k} \cdot \mathbf{x} - \omega t)] \quad \textbf{(10.8)}$$

where the wave vector ***k***, angular frequency ω and polarization vector ***U*** are related by the set of three linear equations

$$(C_{ijkl} k_j k_l - \rho \omega^2 \delta_{ik}) U_k = 0 \quad \textbf{(10.9)}$$

δ_{ik} being the Kronecker symbol, and the corresponding secular equation being

$$D(\mathbf{k}, \omega) = | C_{ijkl} k_j k_l - \rho \omega^2 \delta_{ik} | = 0 \quad \textbf{(10.10)}$$

The Christoffel equations (10.9) and their secular equation (10.10), represent the bulk wave dispersion relation for the anisotropic medium. It is more convenient to analyze wave propagation in anisotropic media using the slowness vector $\mathbf{s} = \mathbf{k}/\omega$ instead of the wave vector. In terms of the slowness vector, Equations 10.9 and 10.10 take the forms

$$(C_{ijkl} s_j s_k - \rho \omega^2 \delta_{il}) U_l = 0 \quad \textbf{(10.11)}$$

$\Omega(\mathbf{s}) = | C_{ijkl} s_j s_k - \rho \delta_{il} | = 0$ **(10.12)**

A section of the slowness surface of GaAs in the (001) plane, defined by Equation 10.12, is shown by the solid lines in Figure 10.2. It is a centrosymmetric surface of three sheets corresponding to the P, FT, and ST modes. The slowness surface depicts the directional dependence of the slowness or inverse phase velocity $s = 1/c_{acoust}$. In the case of isotropic solids all three sheets of the slowness surface are spherical, the outer two sheets coincide and correspond to pure transverse (secondary) waves, and the inner sheet corresponds to pure longitudinal (primary) waves. For anisotropic solids, the

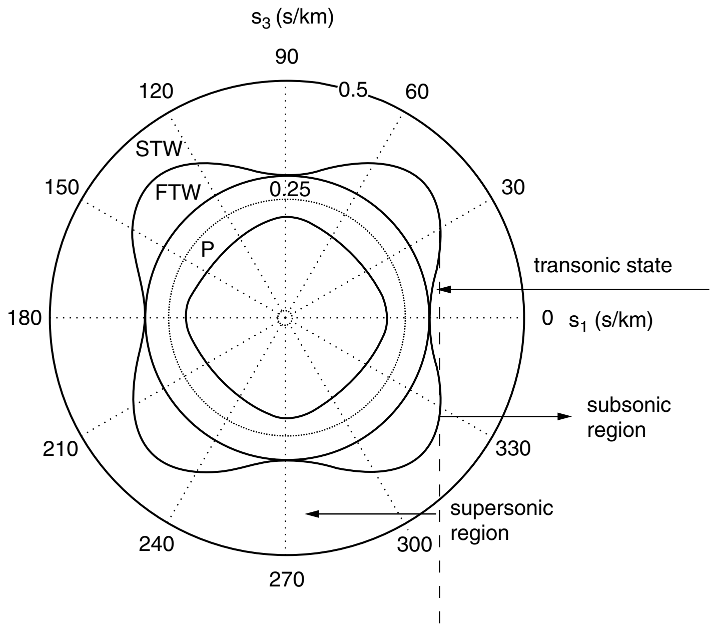

FIGURE 10.2
The slowness curve of GaAs for the (001) plane. The dashed line corresponds to the transonic state. The solid curves correspond to the slowness curves for longitudinal (P), fast transverse (FT), and slow transverse (ST) waves.

outer two sheets (corresponding to FT and ST quasi-transverse waves) are separated. They are in contact only in isolated directions, known as acoustic axes, which can be found in both symmetry and nonsymmetry directions.The energy flow velocity for a plane homogeneous wave is the ray or group velocity vector $\mathbf{c}_g = \nabla_\mathbf{k}\omega(\mathbf{k}) = \nabla_\mathbf{s}\Omega(\mathbf{s})$, which has the property of being normal to the constant frequency surface at any point. The direction of the ray vector is an important consideration when selecting partial waves in the boundary problem we discuss in the next section.

The dashed line in Figure 10.2 is the slow transverse threshold.[26] It corresponds to the limiting point on the ST slowness curve where $s_{||} = k_{||}/\omega$ is a maximum, and where the ray vector, which is perpendicular to the slowness surface, is parallel to the physical surface of the sample. At larger values of $s_{||}$, corresponding to smaller velocities, all solutions for the slowness component $s_3 = k_3/\omega$ are complex and correspond to inhomogeneous waves; the maximum value of $s_{||}$ is thus known as the limiting transonic state. For an isotropic solid, the slowness curves are circles, and the transonic state coincides with the transverse slowness along the surface, $s_S = (\rho/C_{44})^{1/2}$, but this is not generally true for anisotropic solids as Figure 10.2 demonstrates.

We now determine the Green's function, following the procedure of Cottam and Loudon.[53] It is assumed that the medium is subjected to a time- and position-dependent distribution of body force **F**(**x**, t), defined per unit mass and having a harmonic time dependence

$$\mathbf{F}(\mathbf{x},\mathbf{t}) = \mathbf{F}(\mathbf{x})\exp(-i\omega t) \tag{10.13}$$

The equation of motion for the components of the elastic displacement field $\boldsymbol{u}(x,\omega)\exp(-i\omega t)$ in the medium is then given by

$$C_{ijkl}\frac{\partial^2 u_l}{\partial^2 x_j x_k} + \rho\omega^2 u_i = -F_i(\mathbf{x}), \quad x_3 > 0 \tag{10.14}$$

summation over repeated indexes being again implied. The particular integral of Equation 10.14 can be written formally

$$u_i(\mathbf{x},\omega) = -\int_{-\infty}^{\infty} d^3\mathbf{x}' g_{ij}(\mathbf{x},\mathbf{x}',\omega)F_j(\mathbf{x}') \tag{10.15}$$

where $g_{ij}(x,\omega)$ is the elastodynamic Green's tensor. When the point force is located at the surface of the film $[\mathbf{F}_j(\mathbf{x}') = \mathbf{F_j}\delta(x_1')\delta(x_2')\delta(x_3'+h)]$ where $\delta(x)$ is the delta function], g_{ij} is called the surface Green's function; if the point force is applied at the film/substrate interface ($x_3 = 0$) we call $g_{33}(x_{||}, x_3 = 0, \omega)$ the interface Green's function. For a concentrated point force acting at the top surface we have

$$u_i(\mathbf{x},\omega) = g_{ij}(\mathbf{x},\omega)F_j \tag{10.16}$$

The Fourier $(k_{||}, \omega)$ domain surface dynamic response function (Green's function) G_{ij} is defined as a double Fourier integral of the elastodynamic Green's tensor $g_{ij}(\mathbf{x}, \omega)$ in the variables x_1 and x_2.

$$G_{ij}(\mathbf{k}_{||},x_3,\omega) = \int_{-\infty}^{\infty} d^2\mathbf{x}_{||} g_{ij}(\mathbf{x}_{||},x_3,\omega)\exp\{-i\mathbf{k}_{||}\mathbf{x}_{||}\}, \tag{10.17}$$

where $x_{||} = (x_1,x_2)$ and $k_{||} = (k_1, k_2)$; the inverse transform is

$$g_{ij}(\mathbf{x}_{||},x_3,\omega) = \frac{1}{(2\pi)^2}\int_{-\infty}^{\infty} d^2\mathbf{k}_{||} G_{ij}(\mathbf{k}_{||},x_3,\omega)\exp\{i\mathbf{k}_{||}\mathbf{x}_{||}\} \tag{10.18}$$

The purpose of the following simulations is to find a response of the system to an external harmonic force (Equation 10.13) applied at the layer's upper surface

$$\sigma^{-}_{l3}(\mathbf{x}_{||}, x_3 = -h, \omega) = -F_l\delta(\mathbf{x}_{||}l = 1, 2, 3 \quad \textbf{(10.19)}$$

where $\delta(x_{||}) = \delta(x_1)\delta(x_2)$ is the two-dimensional δ-function. In Equation 10.19, superscript in the stress componentσ^{-}_{l3} indicates that it has been calculated in the layer. The negative sign in Equation 10.19 has to do with the fact that the surface tractions $\sigma_{j3}(x_{||}, x_3 = -h, \omega)$ are in reaction to the applied force.

Equation 10.19 is written in the spatial or Cartesian coordinate system, but we can also write it in the Fourier domain (*k*-space) using properties of the delta function[54]

$$\delta(x) = \frac{1}{(2\pi)}\int_{-\infty}^{\infty} dk \exp\{ikx\} \quad \textbf{(10.20)}$$

and it can then be rewritten as an inverse Fourier transform:

$$\sigma^{-}_{l3}(\mathbf{x}_{||}, x_3 = -h, \omega) = -\frac{1}{(2\pi)^2}\int_{-\infty}^{\infty} d^2\mathbf{k}_{||}F_l \exp\{i\mathbf{k}_{||}\mathbf{x}_{||}\}, \quad l = 1, 2, 3 \quad \textbf{(10.21)}$$

In order to calculate the Brillouin spectrum (Equation 10.6) we need only the component of the external force **F** normal to the surface [**F** = (0,0,*F*)]. Therefore, the conditions (Equation 10.21) can be rewritten as

$$\sigma^{-}_{33}(\mathbf{x}_{||}, x_3 = -h, \omega) = -\frac{F}{(2\pi)^2}\int_{-\infty}^{\infty} d^2\mathbf{k}_{||} \exp\{i\mathbf{k}_{||}\mathbf{x}_{|} \quad \textbf{(10.22)}$$

$$\sigma^{-}_{l3}(\mathbf{x}_{||}, x_3 = -h, \omega) = 0, \quad l = 1, 2 \quad \textbf{(10.23)}$$

To find the response of the system to the force *F* we seek the solution of the equations of motion (Equation 10.14) in the form of a superposition of outgoing plane waves whose amplitudes are proportional to *F*. In the film the displacement field is given by

$$u^{-}_{i}(\mathbf{x}, \omega) = \frac{F}{(2\pi)^2}\int_{-\infty}^{\infty} d^2\mathbf{k}_{||}\sum_{n=1}^{6} A^{(n)}U^{(n)}_{i} \exp\left\{i\left(\mathbf{k}_{||}\mathbf{x}_{||} + k^{(n)}_{3}x_3\right.\right. \quad \textbf{(10.24)}$$

and in the substrate it is given by

$$u_i^+(\mathbf{x},\omega) = \frac{F}{(2\pi)^2}\int_{-\infty}^{\infty} d^2\mathbf{k}_{||}\sum_{n=7}^{9} A^{(n)}U_i^{(n)} \exp\left\{i\left(\mathbf{k}_{||}\mathbf{x}_{||} + k_3^{(n)}x_3\right)\right\} \quad \textbf{(10.25)}$$

For each value of $\boldsymbol{k}_{||}$ and ω, the coefficients $A^{(n)}$ in Equations 10.24 and 10.25 are the nine unknown constants for the decomposition into plane waves. The third component k_3 of k and the polarization vector **U** are related by the Christoffel equations (10.9) where $k_3^{(n)}$ are roots of the characteristic sextic equation (Equation 10.10). Generally Equation 10.10 yields six solutions; in the substrate the 3 ($n = 7,8,9$) are chosen which correspond to outgoing waves, on the basis that they are either homogeneous (bulk) waves ($k_3^{(n)}$ real) with ray or group velocity vectors, $\boldsymbol{c}_g$, directed into the interior ($c_{g3} > 0$), or they are inhomogeneous (evanescent) waves ($k_3^{(n)}$ complex or pure imaginary) which decay into the interior ($Im\ k_3^{(n)} > 0$). In the film all six partial waves (n = 1, 2, 3, 4, 5, 6) must be taken into account.

In computer codes[52] the slowness equation is written in the form of a polynomial equation

$$\sum_{i,j,k=1}^{6} D_{ijk}s_1^i s_2^j s_3^k = 0 \quad \textbf{(10.26)}$$

where the coefficients D_{ijk} depend on the C_{ijkl} and ρ. For a given $s_{||} = (s_1, s_2)$ this becomes a sextic equation

$$E_{3k}s_3^k = 0,\quad E_{3k} = \sum_{i,j=1}^{6} D_{ijk}s_1^i s_2^j$$

in s_3. For s_3 perpendicular to a mirror plane, all odd powers of s_3 are zero, and it reduces to a cubic in $(s_3)^2$. To obtain the component along x_3 of the group velocity when s_3 is real, we simply differentiate the above equation and do similarly for the other two components. The calculation of the roots of Equation 10.26 can be simplified by first rotating the crystal to the coordinate frame, where the surface of the sample defines the x_1x_2 plane, and the propagation direction is always along x_1. For monoclinic symmetry, the implicit form of the coefficients in Equation 10.26 is given by Nayfeh.[55] For triclinic symmetry, the implicit form of the polynomial Equation 10.26 can be found elsewhere.[56]

From the stress-strain relationship, $\sigma_{lm} = C_{lmpq}\partial u_p/\partial x_q$, and Equation 10.24 and Equation 10.25, it follows that the surface tractions are given by

$$\sigma_{l3}^-(\mathbf{x}_{||}, x_3 = -h, \omega) = \frac{i\omega F}{(2\pi)^2}\int_{-\infty}^{\infty} d^2\mathbf{k}_{||}\sum_{n=1}^{6} A^{(n)}B_l^{(n)} \exp\{i(\mathbf{k}_{||}\mathbf{x}_| \quad \textbf{(10.27)}$$

where the matrix $B_l^{(n)}$ has been introduced

$$B_l^{(n)} = C_{3lpq}^{-} U_p^{(n)} k_q^{(n)} \exp\left\{-ik_3^{(n)} h\right\}/\omega \quad n = 1,2,3,4,5,6; \quad l = 1, 2, 3 \quad \textbf{(10.28)}$$

Summation is implied over repeating indexes (p,q) in Equation 10.28. Comparing Equation 10.27, Equation 10.28 and Equation 10.23, we arrive at a set of three linear equations for the partial wave amplitudes $A_j^{(n)}$

$$\sum_{n=1}^{6} B_l^{(n)} A^{(n)} = \frac{i\delta_{3l}}{\omega}, \quad l = 1,2,3 \quad \textbf{(10.29)}$$

Another three equations for the amplitudes arise from the continuity of stress at the interface

$$\sigma_{j3}^{+}(\mathbf{x}_{||}, x_3 = 0_+, \omega) - \sigma_{j3}^{-}(\mathbf{x}_{||}, x_3 = 0_-, \omega) = 0 \quad \textbf{(10.30)}$$

which yield

$$\sum_{n=1}^{9} B_l^{(n)} A^{(n)} = 0, \quad l = 4, 5, 6 \quad \textbf{(10.31)}$$

where

$$B_l^{(n)} = C_{3(l-3)pq}^{+} U_p^{(n)} k_q^{(n)}/\omega, \quad n = 7, 8, 9; \quad l = 4, 5, 6 \quad \textbf{(10.32)}$$

and

$$B_l^{(n)} = -C_{3(l-3)pq}^{-} U_p^{(n)} k_q^{(n)}/\omega, \quad n = 1, 2, 3, 4, 5, 6; \quad l = 4, 5, 6 \quad \textbf{(10.33)}$$

Finally there are three equations for the partial wave amplitudes arising from continuity of the displacement field at the boundary

$$u_i^{+}(\mathbf{x}_{||}, x_3 = 0_+, \omega) - u_i^{-}(\mathbf{x}_{||}, x_3 = 0_-, \omega) = 0 \quad \textbf{(10.34)}$$

which yield

$$\sum_{n=1}^{9} B_l^{(n)} A^{(n)} = 0, \quad l = 7, 8, 9 \quad \textbf{(10.35)}$$

where

$$B_l^{(n)} = U_{l-6}^{(n)}, \quad l = 7, 8, 9; \quad n = 7, 8, 9 \tag{10.36}$$

and

$$B_l^{(n)} = -U_{l-6}^{(n)}, \quad l = 7, 8, 9; \quad n = 1, 2, 3, 4, 5, 6 \tag{10.37}$$

Note the – sign in the defining Equation 10.37 for $B_l^{(n)}$.

Combining Equation 10.29, Equation 10.31, and Equation 10.35 we arrive at a system of nine linear equations in nine unknown $A^{(n)}$ and a right-hand-side vector Y.

$$\mathrm{B}^* A = \frac{i}{\omega} Y \tag{10.38}$$

where $Y_l = 0$ for $l \neq 3$ and $Y_l = 1$ for $l = 3$. The solution of Equation 10.38 takes the form

$$A^{(n)} = \frac{i}{\omega}(\mathbf{B}^{-1})^{(n)} = \frac{i}{\omega}\frac{adj(\mathbf{B})^{(n)}}{\det|\mathbf{B}|} \tag{10.39}$$

adj denoting matrix adjoint. From Equation 10.19, Equation 10.24, and Equation 10.39 it follows

$$g_{33}(\mathbf{x}_{||}, x_3 = -h, \omega) = \frac{1}{(2\pi)^2}\int_{\infty}^{-\infty} d^2\mathbf{k}_{||}\left\{\sum_{n=1}^{6}\frac{i}{\omega}(\mathbf{B}^{-1})^{(n)}U_3^{(n)}\exp\left(-ik_3^{(n)}h\right)\right\}\exp(i\mathbf{k}_{||}\mathbf{x}_{||}) \tag{10.40}$$

Comparing Equation 10.40 with Equation 10.18 we finally obtain the surface Green's function

$$G_{33}(\mathbf{k}_{||}, x_3 = -h, \omega) = \frac{i}{\omega}\sum_{n=1}^{6}(\mathbf{B}^{-1})^{(n)}U_3^{(n)}\exp\left(-ik_3^{(n)}h\right) \tag{10.41}$$

Green's function for interface is obtained in a similar way. Instead of Equation 10.19 we have

$$\sigma_{33}(\mathbf{x}_{||}, x_3 = 0, \omega) = -F\,\delta(\mathbf{x}_{|} \tag{10.42}$$

the stresses at the outer surface of the layer are null

$$\sigma_{l3}^{-}(\mathbf{x}_{||}, x_3 = -h, \omega) = 0, \quad l = 1, 2, 3 \tag{10.43}$$

while the stress at the interface is continuous only in the interface plane

$$\sigma_{l3}^{+}(\mathbf{x}_{||}, x_3 = 0_+, \omega) - \sigma_{l3}^{-}(\mathbf{x}_{||}, x_3 = 0_-, \omega) = 0, \quad l = 1, 2 \tag{10.44}$$

and is discontinuous in x_3-direction

$$\sigma_{33}^{-}(\mathbf{x}_{||}, x_3 = 0, \omega) - \sigma_{33}^{-}(\mathbf{x}_{||}, x_3 = 0, \omega) = -\frac{F}{(2\pi)^2}\int_{-\infty}^{\infty} d^2\mathbf{k}_{||} \exp\{i\mathbf{k}_{||}\mathbf{x} \tag{10.45}$$

A set of linear equations is accordingly obtained, which differs from Equation 10.38 only in the right-hand side: $Y_l = 0$ for $l \neq 6$ and $Y_l = 1$ for $l = 6$. For the interfacial Green's function we obtain

$$G_{33}(\mathbf{k}_{||}, x_3 = 0, \omega) = \frac{i}{\omega}\sum_{n=1}^{6}(\mathbf{B}^{-1})^{(n)}U_3^{(n)} \tag{10.46}$$

Equation 10.6 was said earlier to describe Brillouin scattering from the free surface of a semi-infinite solid. It has been shown[52] that it can also be applied to more complicated situations such as (1) scattering from the interface between two perfectly bonded solids, one transparent and the other opaque; (2) scattering from the surface of an opaque film supported on a substrate; and (3) scattering from the interface between a thin supported film and substrate when either the film or substrate are transparent. In cases where the light passes through a transparent medium before or after meeting a scattering surface, there will also be elasto-optic scattering and interference between this and the ripple scattering. The emphasis in the present treatment is on the surface dynamics, and no account is taken of elasto-optic scattering.

By way of example, Figure 10.3 shows the anti-Stokes (frequency upshifted) component of the SBS spectrum of the (110) surface of the cubic crystal $VC_{0.75}$ for $k_{||}$ in the $[1\bar{1}0]$ direction obtained by Zhang et al.[57] Only that part of the spectrum well away from the central peak is shown. The dominant features in the spectrum are a sharp peak due to the RW, and the Lamb shoulder continuum, due to the continuum of bulk modes that participate in surface scattering. As can be seen, the measured spectrum is well accounted for by the theoretical spectrum calculated from $ImG_{33}(\boldsymbol{k}_{||}, \omega)$.

10.2.2.2 Computation of Dispersion Relations

The maxima of the surface Green's function (Equation 10.41) or the interfacial one (Equation 10.46) identify the dispersion relations for surface and interface acoustic modes, respectively. These Green's functions are inversely pro-

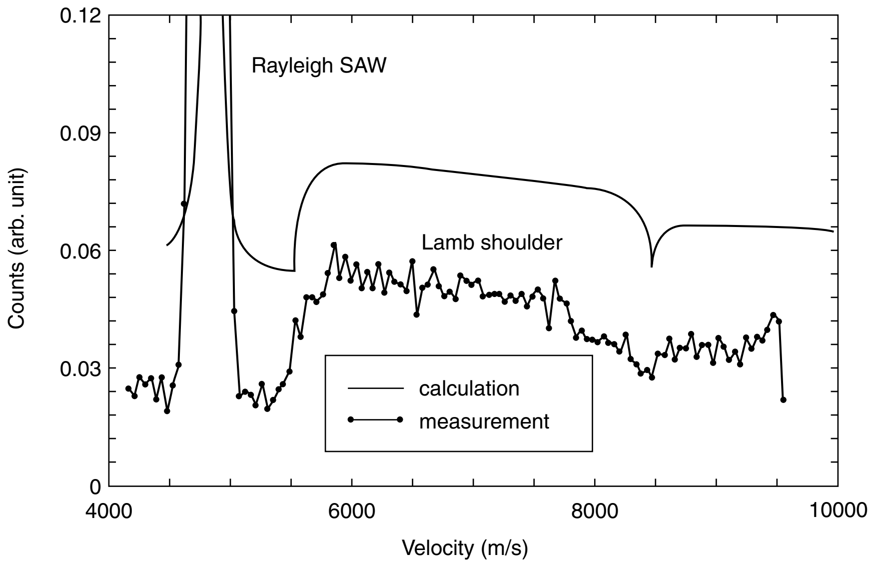

FIGURE 10.3
Theoretical and measured spectra of $VC_{0.75}$ for the $[1\bar{1}0]$ direction in the (110) surface. (From Zhang, X. et al., *Int. J. Refrac. Metals Hard Mater.*, 16, 303, 1998. With permission.)

portional to the determinant $\det|\mathbf{B}|$ (see also Equation 10.39); divergencies are therefore expected when

$$\det|\mathbf{B}| = 0 \tag{10.47}$$

and maxima are possibly (but not exclusively) found when $\det|\mathbf{B}|$ is minimum.

Equation 10.47 is essentially the equation obtained by the approach presented in Chapter 1, which considers the free motion of the medium in the absence of the external forces and identifies the resonant frequencies. The meaning of the corresponding divergences of the Green's function is straightforward. Since the model considered here (Equation 10.14) is perfectly elastic and does not include dissipation mechanisms, the response to a resonant harmonic external force (Equation 10.13) is divergent. Equation 10.47 identifies the true surface waves. Their displacement field vanishes at infinite depth, and typically falls off to a negligible amplitude within a few wavelengths from the surface; their power flow is exclusively parallel to the surface. Nondivergent maxima of the Green's function instead identify damped resonances. Damping is not provided by dissipative mechanisms, but by a component of the power flow that is perpendicular to the surface and irradiates part of the wave energy toward the interior of the medium. Such resonances are the PSAWs, also called leaky surface waves (see Section 10.2.1.1), whose displacement field does not vanish at infinite depth, but still behaves similarly to SAWs because the displacement field is still mainly confined close to the surface. In numerical computations divergencies can be avoided by a simulation of a dissipative mechanism, obtained by attributing a non null imaginary part to the frequency ω. Delta function resonances are thus transformed into finite and broadened peaks.[58]

The dispersion equation (Equation 10.47) can be solved for $k_{||}$ for fixed ω. The roots of Equation 10.47 located on the real axis $k_{||}$ correspond to the true RWs and generalized Lamb surface waves, while PSAWs are attenuated by energy leakage, and correspond to complex values of $k_{||}$ (pole).[36] The velocity of the PSAW is determined by the real part of the reciprocal of $k_{||}$ ($c_{PSAW} = Re[\omega/k_{||}]$) and the attenuation is given by the imaginary part.

In Green's function calculations for SBS the wave vector component $k_{||}$ is kept fixed and the imaginary part of the Green's function is calculated as a function of frequency $Im[G_{33}(\omega)]$. True surface waves, such as the RW, show up as δ-function singularities. The RW corresponds to a singularity at ω_R, its velocity being $\omega_R/k_{||}$. For the true surface waves the velocities obtained by solving Equation 10.47 or by locating the divergencies of the Green's function are identical. In Green's function calculations PSAWs show up as resonances of finite height and width centered at frequency ω_{MAX}, and the velocity of the PSAW is $c_{PSAW} = \omega_{MAX}/k_{||}$. The higher the attenuation or the farther the pole from the real axis, the broader is the PSAW peak in the Green's function, and the higher is the discrepancy between the modal (Equation 10.47) and Green's function solutions for PSAW velocity.

For the surface of an isotropic half-space, Equation (10.47) can be written in analytical form. It is the famous Rayleigh equation, already analyzed in Chapter 1:

$$\chi^6 - 8\chi^4 + 8(3 - 2\varsigma^2)\chi^2 - 16(1 - \varsigma^2) = 0 \qquad \textbf{(10.48)}$$

where $\chi = c/c_S$ and $\zeta = c_S/c_P$. It can be simplified by introducing another variable $y = \chi^2 - 8/3$

$$y^3 + 3py + 2q = 0 \qquad \textbf{(10.49)}$$

where $p = 8/9(1 - 6\zeta_2)$ and $q = 8/3(17/9 - 5\zeta^2)$. Rayleigh's equation was derived more than a century ago, but still attracts the attention of researchers.[59–61] Nkemzi[62] applied the theory of Cauchy integrals to derive an explicit form for the RW velocity in an elastic solid. The solution of Equation 10.49 derived by Lord Rayleigh and discussed in Chapter 1 is the Rayleigh surface wave RW of velocity c_R. The RW at the stress-free surface of a solid is a superposition of three phase-matched evanescent waves that satisfies the free surface boundary conditions. The absence of any power flow normal to the surface comes from the absence of any incoming or outgoing bulk waves.

For isotropic solids $c_R < c_S$, and c_R lies in the range[44] $0.87\ c_S < c_R < 0.96\ c_S$. Measurements of the Rayleigh wave velocity give a lower bound for c_S, and hence a lower bound for C_R. The value of C_R can be obtained from the approximate relation[44]

$$c_R = c_S \frac{0.718 - (c_S/c_R)^2}{0.75 - (c_S/c_R)^2} \quad \textbf{(10.50)}$$

or using Poission's ratio ν

$$c_R = c_S \frac{0.87 + 1.12\nu}{1 + \nu} \quad \textbf{(10.51)}$$

Turning back to Green's function calculations, for an isotropic half-space, the power spectrum $<|u_3(\mathbf{k}_{||},\omega)|^2>$ can be written in closed form[18,63]

$$<|u_3(\mathbf{k}_{||},\omega)|^2> = \frac{k_B T}{S\pi\rho k_{||} c_S^3} I_3(\mathbf{k}_{||},\omega) \quad \textbf{(10.52)}$$

$$I_3(\mathbf{k}_{||},\omega) = \mathrm{Re}\left\{ \frac{k_{p3} k_s k_{||}^2}{4k_{p3}k_{s3}k_{||}^2 + \left(k_{s3}^2 - 2k_{||}^2\right)^2} \right\} \quad \textbf{(10.53)}$$

where $k_p = \omega/c_P$ and $k_s = \omega/c_S$ are wave numbers for the longitudinal and shear modes respectively, and $k_{p3} = \sqrt{k_p^2 - k_{||}}$ and $k_{s3} = \sqrt{k_s^2 - k_{||}}$ are the wave vector components normal to the surface.

A PSW can be found in the form of a surface skimming longitudinal wave. The computation is performed considering in Equation 10.21 a harmonic force (Equation 10.13) directed along x_1 instead of x_3, and computing the longitudinal power spectrum[19,46] $<|u_1(\mathbf{k}_{||},\omega)|^2>$. The latter can be written in closed form for isotropic half-space[63]

$$<|u_1(\mathbf{k}_{||},\omega)|^2> = \frac{k_B T}{S\pi\rho k_{||} c_S^3} I_1(\mathbf{k}_{||},\omega) \quad \textbf{(10.54)}$$

$$I_1(\mathbf{k}_{||},\omega) = \mathrm{Re}\left\{ \frac{k_{s3} k_s k_{||}^2}{4k_{p3}k_{s3}k_{||}^2 + \left(k_{s3}^2 - 2k_{||}^2\right)^2} \right\} \quad \textbf{(10.55)}$$

its form being very similar to that of $<|u_3(\mathbf{k}_{||},\omega)|^2>$. This mode, called LLSW or longitudinal mode (LM) (see Figure 10.4), does not cause surface corrugations, but it does interact with light by the elasto-optic mechanism.[46] Sandercock[64] first observed the LLSW in the Brillouin spectrum of the (110)

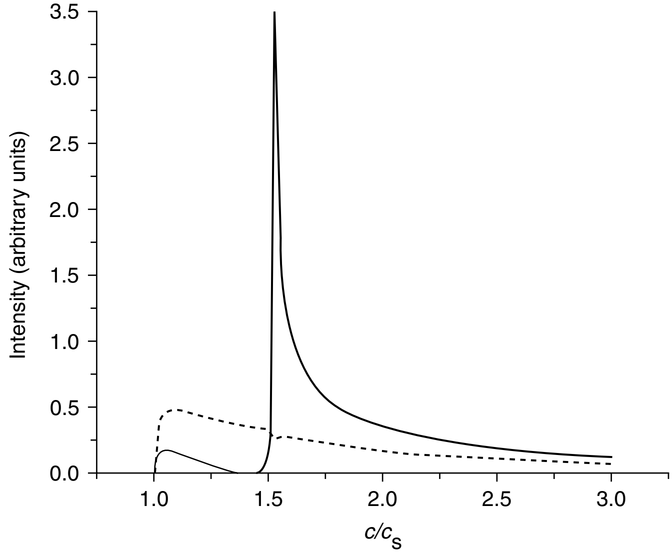

FIGURE 10.4
The factors I_P (broken line) and I_S (solid line) as function of c/c_S at fixed $k_{||}$ simulated for hard amorphous carbon synthesized from C_{60}, (sample B) with elastic parameters given in Table10. 2. Region of c/c_S with RW is omitted.

surface in GaAs. Detailed studies of the detection of LLSW by SBS solid were performed.[22,63,65] It was shown[65] that the peak in the longitudinal spectrum corresponds to a leaky surface wave; it was found[63] that when the Poission's ratio ν is smaller than 1/3, the longitudinal power spectrum $<|u_1(\mathbf{k}_{||},\omega)|^2>$ exhibits a sharp and well-defined peak, very close to c_P (see Figure 10.4). For ν > 1/3 the peak becomes broader and lies between $2c_S$ and c_P. Note, however, that in the power spectrum for $<|u_3(\mathbf{k}_{||},\omega)|^2>$, there is a sharp dip at the LLSW, and so this mode can also be measured even if there is only ripple scattering.

It must be mentioned that for ν < 0.263 the Rayleigh equation has three distinct real roots. One is the RW velocity, lying in the (0, c_S) interval, and another one, out of this interval, coincides with the longitudinal velocity c_P.[66] Mozhaev et al.[66] described this high-velocity solution as the Brewster angle reflections of homogeneous (along the plane front) bulk acoustic waves. Analytical expressions for the roots of the Rayleigh equation were derived in several articles.[60,62,67]

10.3 Experimental Method

10.3.1 Experimental Setup

The most common configuration for Brillouin scattering experiments is presented in Figure 10.1 (see Section 10.2.1). The specimen is illuminated by a

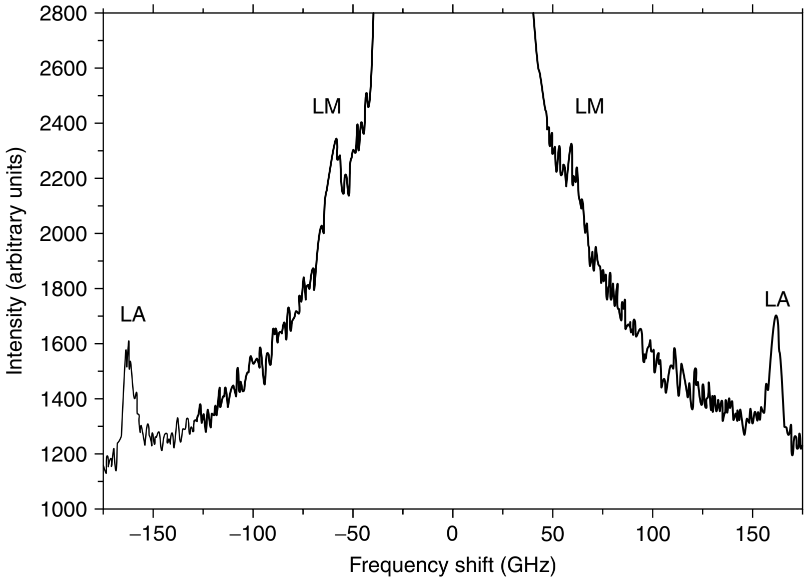

FIGURE 10.5
Experimental Brillouin spectrum, at θ = 70°, of amorphous carbon synthesized from C_{60} sample B. (From Manghnani, M.H. et al., *Phys. Rev. B*, 6412, 121403, 2001. With permission.)

laser beam, the light scattered in a given direction is collected and its spectrum is analyzed. Figure 10.1 presents the usual configuration of backscattering which, as discussed below, is often advantageous; in volume Brillouin scattering other geometries are also adopted, in which the collection direction forms an angle other than 180° (typically 90°[45,68,69]) with the incidence direction. Other types of configuration have sometimes been used and will be mentioned below.

The common configuration will be discussed here in some detail, although not limited exclusively to the backscattering case. The incident laser light is monochromatic: it has wavelength (in vacuum) λ_0, wave vector q_i, and circular frequency Ω_i ($|q_i| = q_i = 2\pi/\lambda_0$ and $\Omega_i = c_{light}\, q_i$, c_{light} being the velocity of light). The spectrum of scattered light was already introduced in Section 10.2.1. The most intense feature is the sharp peak at Ω_i, due to light elastically reflected by static inhomogeneities; a weaker and much broader feature, still centered at Ω_i, can be present. It is due to scattering by dynamic, but non-traveling, excitations, and is called quasi-elastic scattering (see Figure 10.5). Scattering by dynamic and traveling excitations (i.e., acoustic waves) produces symmetric doublets. The scattered light collected along the direction of a wave vector q_s interacted with an acoustic wave, of any kind, of wave vector

$$\boldsymbol{k} = \pm\,(\boldsymbol{q}_s - \boldsymbol{q}_i) \qquad \textbf{(10.56)}$$

the ± sign referring to anti-Stokes and Stokes events, respectively (see Section 10.2.1), and contains a doublet at frequencies

$$\Omega_s = \Omega_i \pm \omega \tag{10.57}$$

where the ± sign refers again to anti-Stokes and Stokes events, and $\omega = c_{acoust} |k|$ is the frequency of the acoustic wave, of velocity c_{acoust}. In the analysis of Equation 10.57 and Equation 10.56 the wide difference between the velocity of light and any acoustic velocity allows some simplification.

10.3.1.1 Scattering Geometry

Volume Brillouin scattering is the scattering by bulk acoustic waves of velocity c_{acoust}, where c_{acoust} stands for the velocity of any of the three bulk waves P, FT, and ST (see Section 10.2.1.1). In this case the optical wave vectors appearing in Equation 10.56 are those ($\boldsymbol{q}_i'$ and $\boldsymbol{q}_s'$) present in the bulk; their directions are determined by the incidence and collection directions out of the sample, and by the refractive index n, with $q_i' = n\, q_i$ and $q_s' = n\, q_s$ (see Section 10.2.1). The angular frequencies are $\omega = c_{acoust}\, k$, $\Omega_i = (c_{light}/n)q_i'$ and $\Omega_s = c_{light}/n)q_s'$, (c_{light}/n) being the light velocity in the medium. Equation 10.56 implies that $|\mathbf{k}|$ can possibly be much smaller than $|\boldsymbol{q}_s'|$ and $|\boldsymbol{q}_i'|$, but not larger than their sum. Since $|\mathbf{k}|$ is at most of the same order as $|\boldsymbol{q}_s'|$ and $|\boldsymbol{q}_i'|$, the ratio ω / Ω_i is at most of the order of the ratio $c_{acoust}/(c_{light}/n)$ (i.e., at most 10^{-4} to 10^{-5}) for any physical values of c_{acoust} and n). The relative difference $|\Omega_s - \Omega_i| / \Omega_i$ is therefore at most of the same order as $c_{acoust}/(c_{light}\ /n)$ (see Equation 10.57), as well as the relative difference $|\boldsymbol{q}_s' - \boldsymbol{q}_i'| / q_i'$. The scattering event can therefore be analyzed neglecting the difference between the magnitudes of the two moduli: $q_i' \cong q_s'$ (see Section 10.2.1). This means that the directions of $\mathbf{q}_i'$ and $\mathbf{q}_s'$ (i.e., the directions of the incident and scattered beams, identify uniquely the scattering configuration and the acoustic wave vector $\boldsymbol{k}$**)**. In particular, the backscattering geometry ($\mathbf{q}_s' = -\mathbf{q}_i'$, and therefore $\mathbf{q}_s = -\mathbf{q}_i$) maximizes the modulus of k: in this geometry

$$k = 2\frac{2\pi}{\lambda_0} n \tag{10.58}$$

Equation 10.1 accordingly holds, and $|\boldsymbol{q}_s - \boldsymbol{q}_i| / q_i$ reaches its maximum achievable value of $2(c_{acoust}/c_{light})n$, which is typically of the order of 10^{-5}.

In SBS (i.e., scattering by SAWs), Equation 10.56 holds only for the wave vector components parallel to the surface, due to the breaking of translational invariance in the direction normal to the surface:

$$k_{||} = \pm (\boldsymbol{q}_s - \boldsymbol{q}_i)_{||} \tag{10.59}$$

Since Snell's law means that upon refraction both $\boldsymbol{q}_{i||}$ and $\mathbf{q}_{s||}$ remain unchanged, Equation 10.59 is conveniently analyzed in terms of the optical wave vectors $\boldsymbol{q}_i$ and $\boldsymbol{q}_s$ outside of the sample. Also in this case their directions determine the acoustic wave vector $\boldsymbol{k}_{||}$. The scattered direction $\boldsymbol{q}_s$ is conveniently taken in the incidence plane, defined by $\boldsymbol{q}_i$ and the normal to the surface. In this case $\boldsymbol{k}_{||}$ also belongs to the incidence plane and

$$k_{||} = q_i(\sin \theta_i - \sin \theta_s) \tag{10.60}$$

θ_i and θ_s being the incidence and scattering angles, referred to the surface normal. In Equation 10.60 the sign of θ_s indicates forward (positive θ_s) or backward (negative θ_s) scattering. As already noted in Sections 10.2.1.3 and 10.2.1.4 the wave vectors probed by surface scattering do not depend on the refractive index. The very small upper limit for the relative difference $|\boldsymbol{q}_s - \boldsymbol{q}_i|/q_i$ discussed above is even smaller in SBS; in backscattering ($\theta_s = -\theta_i$), again a typical choice since it maximizes $k_{||}$,

$$k_{||} = 2q_i \sin\theta_i = 2\frac{2\pi}{\lambda_0}\sin\theta_i \tag{10.61}$$

Equation 10.4 accordingly holds, and $|\boldsymbol{q}_s - \boldsymbol{q}_i|/q_i = 2(c_{\text{SAW}}/c_{light}) \sin\theta_i$, which is always (also for diamond) well below 10^{-4}, down to below 10^{-6}.

Equation 10.58 and Equation 10.61 imply that in transparent or semitransparent samples, in which surface and volume scattering can be simultaneously observed, in backscattering the bulk acoustic waves are probed at wavelength $\lambda_0/(2n)$, while the surface waves are probed at wavelength $\lambda_0/(2\sin\theta_i)$. Since the RW is slower than bulk waves, the spectral contributions from surface waves and from bulk waves are well separated. In any scattering geometry, and for both types of waves, the wave vector k or $k_{||}$ is determined by the scattering geometry; the frequency ω is obtained by the spectrum of the scattered light (see Section 10.2.2), and the velocity of acoustic waves is immediately derived as ω/k for bulk waves and $\omega/k_{||}$ for SAWs. It can be mentioned that silicon, with a penetration depth for green light of ≈ 1 µm, is transparent enough to give a good scattering signal from bulk waves; from truly transparent materials, such as glass, the scattering volume for bulk waves is large and gives a signal from bulk waves much more intense than that from surface waves.

10.3.1.2 The Backscattering Configuration

A typical experimental setup for an SBS measurement in backscattering is shown in Figure 10.6. The laser beam is directed onto the specimen by a small mirror, called here the incidence mirror, and focused onto the specimen surface by a lens, called here the front lens. The same lens also collects the scattered light, transforming the light coming from the focusing spot into a parallel beam that is sent to the spectrometer. Typically, spatial filtering is

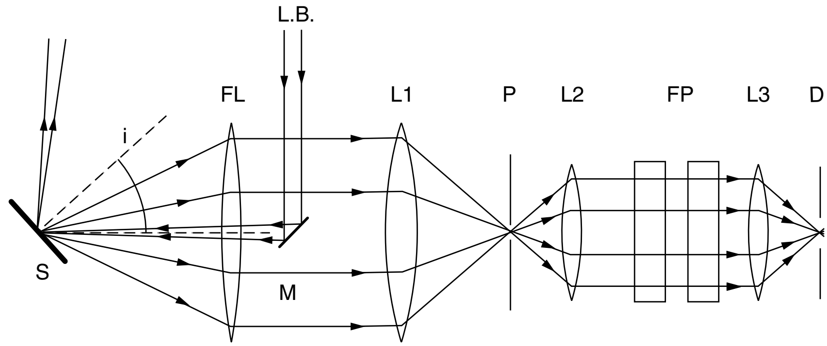

FIGURE 10.6
Experimental setup in backscattering. LB: laser beam; M: mirror; FL: front lens; S: sample, L1, P, and L2: spatial filtering by two lenses and a pinhole; FP: Fabry-Perot interferometer (for simplicity, a single interferometer is shown, instead of the tandem multipass one); D: light detector.

needed and is provided by a pinhole: the scattered beam is focused onto the pinhole by a lens and can then be reconverted to a parallel beam. On the optical path to the spectrometer a couple of steering mirrors can be inserted to give additional degrees of freedom, which is useful for alignment purposes. A similar configuration is obtained using, instead of the incidence mirror, a larger mirror that deflects all the scattered light with a hole drilled in it, the incident beam passing through the hole.

Beside the maximization of the exchanged wave vector, another advantage of backscattering emerges clearly: a single lens focuses the incident beam and collects the scattered light. In any other scattering geometry two separate lenses must be adopted, and their focal points must coincide to high precision. For this reason other geometries have been adopted in volume scattering,[68] but very rarely in SBS. In volume scattering, due to the finite extension of the waist of the focused incident beam, the requirement of coincident foci is less stringent than in SBS, where the additional requirement of precise coincidence at the surface must be satisfied. Another advantage of backscattering is that, at least for incidence not too close to the normal, the collection direction is far from the specular reflection one, and in the collected beam the amount of light that is elastically scattered is therefore minimized.

Example 1

Determine the range of SAW wavelengths probed in backscattering, with incidence angle varying from 20 to 70°, and with: (a) the λ_0 = 532-nm light of a frequency-doubled Nd:YAG laser, and (b) the λ_0 = 488-nm light of the blue line of an Ar ion laser.

SOLUTION

Equation 10.61 states that

$$k_{||} = 2q_i \sin\theta_i = 2\frac{2\pi}{\lambda_0}\sin\theta_i$$

therefore $\lambda_{||} = \lambda_0/(2\sin\theta_i)$. With $20° \leq \theta_j \leq 70°$, we have $0.342 \leq \sin\theta_j \leq 0.940$. For the two cases, 778 nm $\geq \lambda_{||} \geq$ 283 nm and 713 nm $\geq \lambda_{||} \geq$ 260 nm.

Example 2

Estimate the frequencies of bulk acoustic waves (if any) and of SAWs probed in backscattering, with incidence angles of 30° and of 70°, by the λ_0 = 514.5 nm light of the green line of an Ar ion laser, for a) silicon, b) diamond, c) aluminum.

SOLUTION

From Example 1, the parallel wavelengths probed in backscattering with λ_0 = 514.5 and θ_i = 20° and 70°, (i.e., sin θ_i = 0.5 and 0.94) are $\lambda_{||}$ = 514.5 and 273.8 nm. From Equation 10.58 the bulk wavelength probed in backscattering with λ_0 = 514.5 is $\lambda = \lambda_0/(2n) = 257.2/n$, where n is the refractive index. An estimate of the frequency requires an estimate of the velocity.

In aluminum, only the Rayleigh surface wave can be observed. Polycrystalline aluminum is isotropic. From the SBS point of view, if the focusing spot of the incident laser beam is smaller than a single grain, the properties of that grain, which is anisotropic, are mainly probed. However, beside the possibility of focusing close to the grain border, single grain properties can realistically be probed only with grains of several tens of microns. The isotropic properties of polycrystalline aluminum (i.e., $c_S \cong 3$ km/secec [see Chapter 1] and $\nu \cong 0.35$) are then considered here. It was discussed in Section 10.2.2.2 that in the isotropic case, $0.87c_S < c_R < 0.96c_S$, with the approximate expression (see Equation 10.50) $c_R = c_S(0.87 + 1.12\,\nu)/(1 + \nu)$. This gives respectively $2.61 < c_R < 2.88$ km/sec, and c_R = 2.80 km/sec (the uncertainty in c_S, see Chapter 1, limits the precision of this number), meaning f_{SAW} = 5.44 and 10.2 GHz.

Crystalline diamond and silicon have cubic anisotropy. Cubic symmetry guarantees the isotropy of quantities like the refractive index, represented by tensors of rank 2, but the elastic behavior is anisotropic. Available values or mass density, elastic constants and refractive index are, for silicon, $\rho = 2.33 \times 10^3$ kg/m^3, C_{11} = 166 GPa, C_{44} = 79.6 GPa, C_{12} = 64 GPa, and $n \sim 4$ (real part), and for diamond [70] $\rho = 3.51 \times 10^3$ kg/m^3, C_{11} = 1080 GPa, C_{44} = 578 GPa and C_{12} = 125 GPa, and n = 2.43. In crystalline media the velocities depend on the direction, and the usual formulas for bulk waves, $c_P = (C_{11}/\rho)^{1/2}$ and $c_S = (C_{44}/\rho)^{1/2}$, give the appropriate values only for propagation along the [100] crystalline direction. Similarly, the RW velocity is direction dependent, and the above expressions are no longer valid. A detailed solution of this example would require the analysis of the anisotropic wave velocity. An estimate of bulk velocities can be obtained by the isotropic expressions. It can be noted that, due to the high values of the refractive indexes, for incidence not too far from normal on a (100) face the propagation direction of the probed bulk waves is close to the [100]. It can also be noted that for propagation exactly along the [100] direction the scattering cross section for the shear waves is null. An even rougher estimate for the Rayleigh velocity can be taken as the velocity c_S of the shear wave given by the isotropic formula.

With the above values, c_S = 5.84 km/secec and c_P = 8.44 km/secec for silicon, and c_S = 12.83 km/sec and c_P =17.54 km/sec for diamond. These values of velocity give the following estimates: for silicon, f_{SAW} = 11.3 and 21.3 GHz for the two incidence angles, f_S = 91 GHz and f_P = 131 GHz; for diamond, f_{SAW} = 24.9 and 46.9 GHz for the two incidence angles, f_S = 121 GHz and f_P = 166 GHz.

In reality, observed values of the RW velocity c_{SAW} vary with the propagation direction, and are closer to 5 km/sec for silicon [71] and to 11 km/sec for diamond,[72] with frequencies that are accordingly lower.

10.3.1.3 Other Scattering Configurations

Before proceeding in the present analysis, other types of experimental configurations are briefly mentioned. They have been used in Brillouin scattering measurements, but their applicability is less general than that of the scheme considered here.

Surface enhancement of Brillouin scattering by the excitation of surface plasmon polaritons was theoretically predicted[73,74] and observed.[75,76] This kind of experiment is interesting for the physics because it involves different types of excitations and it gives intense signals. However, it seems to be restricted to the special case of metal films of 40 to 80 nm thickness deposited on transparent substrates.

Brillouin scattering was observed in an optical waveguide, formed by a transparent film surrounded by two media of lower refractive index (including vacuum or air). The light propagates in the film by multiple total internal reflection, and repeatedly interacts with the acoustic wave. In various experiments,[24,77] prisms were exploited to insert the laser beam into the film and then to extract it. It can be mentioned that in the widely used signal transmission in optical fibers (specifically a transparent fiber surrounded by a medium of lower refractive index) Brillouin scattering occurs as an unwanted disturbance to be minimized, since it diverts power from the signal and thus introduces a transmission loss.

For transparent films a simple and effective geometry was developed, which allows simultaneous collection of the backscattered light and light scattered by bulk waves having wave vector parallel to the film surface.[78,79] The technique is applicable to transparent films with a reflecting substrate, or on which a metallic film has been evaporated.

10.3.2 Spectral Analysis

The analysis of Brillouin spectra, and especially of SBS spectra, is not a trivial task. The collected light contains (see Section 10.2.1) an intense elastic peak at the incident frequency Ω_i and one (or more) weak doublet at frequencies $\Omega_i \pm \omega$. The difficulty arises from the low intensity of the doublet and from its small relative frequency shift. The intensity is several orders of magnitude lower than that of the elastic peak, and the relative spectral shift ω/Ω_i is, for SBS, well below 10^{-4}, down to 10^{-6} (see Section 10.3.1.1). With green light the incident frequency is ~6×10^{14} Hz and the spectral shift is below 30 GHz. It can be noted that 30 GHz means exactly 1 cm^{-1}, and that typical frequency shifts observed in Raman scattering range from hundreds to thousands of cm^{-1}. The smallness of the frequency shift prevents the analysis by dispersive means such as diffraction gratings; also, even the triple grating configurations do not achieve a sufficient resolution.

Two methods have been exploited to overcome this difficulty: narrow bandwidth tunable band-pass filters and beating or heterodyne methods. Due to the optical frequency range, both types of instruments have to be implemented by optical means. Scanning multipass Fabry-Perot interferometers achieve the required filtering performances, and have become the standard choice. Most of the experimental SBS work published in the last decade was performed by this type of spectrometer, which is described here in some detail. In heterodyne methods, beating is observed, resulting from mixing the collected light with a reference beam. These methods have advantages and limitations. However since the limitations are severe for SBS applications, these applications are seldom used and are briefly outlined at the end of this section.

10.3.2.1 Multipass Fabry-Perot Interferometers

The Fabry-Perot interferometer[80] is an optical resonator that transmits only the light of its resonant wavelength, and thus acts as a band-pass filter. Since its resonant frequency is adjustable, it can exploited to scan the spectrum to be measured. Conventional Fabry-Perot interferometers do not achieve the contrast (the ratio of the maximum to the minimum transmissivity) needed to resolve the weak Brillouin doublets, and especially the SBS doublets. Sandercock first showed that the contrast could be significantly improved by multipassing (see below) the interferometer; after demonstrating, by a double pass,81 the potential of multipassing, he developed multipass interferometers.82 He then showed the advantage of tandem Fabry-Perot interferometers operated in series64 that avoid the overlapping of adjacent orders of interference, and introduced the configuration that exploits a single scanning stage common to the two interferometers, and thus automatically guarantees a synchronized scan.83 While other configurations were also exploited (single interferometers with three up to seven passes, tandem 3+3 passes with synchronous piezoelectric scanning,84 the tandem configuration with a common scanning stage85 evolved into the 3+3 passes tandem interferometer,3,12,64 which has become the type of interferometer most commonly adopted in Brillouin spectrometry. A fully computer-controlled version was described recently.[86] For specialized applications requiring extreme resolution, the combination of a plane multipassed Fabry-Perot and a spherical confocal one was also adopted.[87]

The basic principles of the operations of Fabry-Perot interferometers and multipass interferometers are summarized here, from the user's point of view, for readers not familiar with optical instrumentation. Reference is made to the mentioned configuration, commonly exploited for Brillouin spectroscopy. More detailed discussions can be found in existing excellent reviews, both general[80] and more specific.[3,12]

A single plane Fabry-Perot interferometer is an optical resonator (an optical cavity) formed by two plane parallel partially reflecting mirrors, at distance d from each other. Light enters the cavity through one of the incompletely reflecting mirrors, and is reflected back and forth, part of it being leaked at each reflection; the light leaking from the second mirror is the transmitted light. In the multiple reflection process the intensity of the wavelengths that satisfy the constructive interference condition is enhanced, while all the other wavelengths eventually interfere destructively and decay. The transmitted light contains only the wavelengths whose intensity in the cavity is high. For light of wavelength λ and frequency $f = c_{light}/\lambda$, entering the resonator with incidence normal to the mirrors, the constructive interference condition for a "round trip" between the mirrors is $2d = m\lambda$, where m is any positive integer. The equally spaced frequencies $f_m = m(c_{light}/2d)$ are thus selected, the frequency spacing being called the free spectral range: $\text{FSR} = c_{light}/2d$. For light entering the resonator with non-normal incidence, the resonance condition depends on the incidence angle, and the interferometer acts as a dispersive device, selecting a different frequency for any angle; this configuration is not useful in this context and will not be considered further.

More precisely, for normal incidence on mirrors of equal reflectivity R the phase delay φ between two consecutive round trips is $\varphi = 2d(2\pi/\lambda) = 2d(2\pi f/c_{light})$, and the superposition of the infinite reflections (having decreasing intensity due to incomplete reflection) gives a transmitted intensity

$$I = \frac{I_{\max}}{1 + R' \sin^2(\varphi/2)}$$

where $R' = 4R/(1 - R)^2$. The shape function $[1 + R' \sin_2(\varphi/2)]^{-1}$ is called the Airy function; it is a set of equally spaced maxima that become sharper for increasing R. Its maxima ($I = I_{\max}$) occur for $\varphi/2 = m\pi$, which identify the frequencies f_m mentioned above, and the minima ($I = I_{\max}/(1 + R')$) are at halfway between maxima. The ratio of maximum to minimum transmission is called contrast or extinction ratio; it is $(1 + R') = (1 + R^2)/(1 - R^2)$ and diverges when R approaches unity, exceeding 100 for $R > 0.82$ and 1000 for $R > 0.94$. The sharpness of the maxima is also an increasing function of R. The common characterization of sharpness by the full width at half maximum (FWHM) is usually presented in terms of the finesse F, defined as the ratio of the distance $\Delta\varphi = 2\pi$ between consecutive maxima to the FWHM. The Airy function gives a finesse $F = \pi\sqrt{R}/(1 - R)$, which exceeds 30 for $R > 0.9$ and 60 for $R > 0.95$; these values of F can be lowered by imperfections of the mirrors and by geometrical effects like the collection geometry discussed below.

Summarizing, the Fabry-Perot interferometer acts as a band-pass filter, transmitting all the frequencies f_m that are at equal spacing FSR from each other, with bandwidth FSR/F around each of them. High-performance filtering requires high values of the finesse F, in order to have a narrow transmitted bandwidth, and of the contrast, in order to have a strong attenuation of the nontransmitted wavelengths. Both parameters are increasing functions of the reflectivity R, and, beside the imperfections, are limited because for values of R too close to unity the maximum transmission declines.

The FSR, and therefore the transmitted frequencies f_m, can be modulated by modulating the distance d between the mirrors. Accordingly, the interferometer can be operated as a spectrometer using one of the transmitted frequencies as a narrow bandwidth band-pass filter, whose frequency is scanned across the spectral interval to be measured.

Operation of the interferometer as a Brillouin spectrometer is accomplished by first adjusting d to a central value $\bar{d}$ such that the incident laser frequency $\Omega_i/2\pi$ is transmitted, and then varying d around $\bar{d}$: $d = \bar{d} + \delta d$. This means that the $\bar{m}$th transmission peak coincides with the laser frequency: $f_{\bar{m}} = \bar{m}(c_{\text{light}}/2\bar{d}) = \Omega_i/2\pi$ (i.e., $\bar{d} = \bar{m}\,\lambda_0/2$); the selected FSR is $(c_{light}/2\bar{d})$. Then d is varied, typically by one order of interference (i.e., with $|\delta d| \le \lambda_0/2 = \bar{d}/\bar{m}$); the extrema of this interval are easily identified by the laser frequency being transmitted again by the $f_{\bar{m}-1}$ and $f_{\bar{m}+1}$ transmission peaks, respectively. By this distance scan the $f_{\bar{m}}$ transmission frequency scans the frequency range $\delta\Omega/2\pi = \pm(\Omega_i/2\pi)/\bar{m} = \pm(c_{light}/2\bar{d})$ = FSR around $\Omega_i/2\pi$. With frequency shifts to be measured ranging from a few GHz to some tens of giaghertz, FSR of tens of GHz are the typical choice, meaning distances $\bar{d}$ of a few millimeters. With $|\delta d| \le \lambda_0/2 = \bar{d}/\bar{m}$ such distances mean that $\bar{d}/|\delta d| = \bar{m} \sim 10^4$. Although the frequency is inversely proportional to the distance, with such small scanning amplitudes the relationship can be linearized: the relative accuracy of the linearized relationship is $|\delta d|/\bar{d} = 1/\bar{m}$ and is acceptable in most cases.

The Fabry-Perot interferometer is thus operated as a narrow band-pass filter that scans the frequency interval of interest. Light is then detected by a photomultiplier; due to the low intensity of SBS doublets, the photomultiplier is typically operated in the single photon counting mode. The distance (i.e., frequency) scan is usually performed by discrete steps. The distance is kept fixed for a given time, with photons being counted and attributed to that channel. The distance is then changed to a new value, and photons are counted and attributed to the new channel. The overall scanning amplitude is typically twice the FSR; the number of channels into which the scan is subdivided should be correlated to the finesse. Since the filtered bandwidth is FSR/F, and since the filter transfer function is an Airy function (which is similar to a Gaussian), if the number of channels is significantly smaller than 2F, the adjacent channels do not overlap and part of the spectral information is lost. On the other hand, if the number of channels is much higher than 2F the adjacent channels strongly overlap, and measurement time is consumed to collect redundant data. The optimal number of channels is therefore larger, but not much larger, than twice the finesse.

Since the finesse is a parameter of each specific interferometer and is independent of mirror distance, once the number of channels is fixed the only parameter to be chosen for each measurement is the FSR, (i.e., the mirror distance). Since the spectrum is measured in the ± FSR interval, the optimal choice of the FSR requires an estimate of the frequency of the peaks to be measured. The FSR must obviously be larger than the frequency to be measured, but not too much larger. As in any measurement, if the adopted full scale range is too large, the resolution becomes poor. As a rule of thumb, the FSR should not exceed twice the expected value of the frequency that should be measured. When performing sets of measurements, typically when measuring the spectrum at a set of different incidence angles, the practical requirement of not too often changing the mirror distance can lead to a partial relaxation of the above criterion.

As mentioned above, the filtering efficiency is measured by the finesse and the contrast. Measurement of Brillouin doublets has to face the proximity of the elastic peak, with orders of magnitude more intense; the contrast typically achievable by a single Fabry-Perot is not sufficient to effectively filter it off. Multipassing is therefore adopted. Passing the scattered light more times by the same interferometer increases both the contrast and the finesse, although the practically achieved values do not fully reach the theoretical limits (the product of the single-pass contrasts and the sum of the single-pass finesses). Similarly, tandem interferometers are adopted because in a single interferometer transmission simultaneously occurs by the $f_{\overline{m}}$, $f_{\overline{m}-1}$, and $f_{\overline{m}+1}$ transmission peaks, resulting in overlapping shifted replicas of the same spectrum and making the interpretation of the spectra more difficult. Two interferometers having slightly different FSR can be synchronously scanned, keeping their $f_{\overline{m}}$ transmission peaks coincident, with a high overall transmissivity; due to the different values of the FSR, if the $f_{\overline{m}}$ transmission peaks coincide and the $f_{\overline{m}-1}$ and $f_{\overline{m}+1}$ peaks of the two interferometers do not coincide, each of the interferometers cancels these transmission peaks of the other, avoiding replication of spectra.

In practice, full consideration of the detailed operation of a tandem multipass interferometer is not required. Such an interferometer, when properly synchronized, behaves as a peculiar single interferometer in which transmission from adjacent orders is almost completely suppressed, and which achieves high values of contrast and finesse, not realistically achievable by a single pass. The not perfect suppression shows up by the partial transmission of the intense laser light. This occurs at the extremes of the FSR, when only one of the interferometers does not transmit the laser frequency, giving rise to the instrumental ghosts typical of Fabry-Perot spectrometers. These ghosts, at ± FSR, can be usefully exploited for calibration purposes once the distance among the mirrors is known. Operationally, for each measurement two parameters have to be set: the number of channels and the FSR. The number of channels being optimally set at or above twice the finesse, and the finesse achievable by a multipass Fabry-Perot being of the order of 100, numbers of channels of 256 or 512 are typical choices. The FSR should instead be set, exactly as for a single-pass interferometer, above the expected frequency of the spectral feature to be measured, but not above twice or three times it.

It should finally be mentioned that operational modes slightly different from that outlined here can be useful for specific applications. For instance, frequency scanning by more than one FSR can be useful for high accuracy measurement of a peak frequency, when this frequency is already approximately known.[70]

Example 3

Evaluate the mirror distances to be adopted for the measurement of SAWs and respectively bulk acoustic waves (if any), for measurements performed in backscattering, with incidence angles of 30 and of 70°, by the $\lambda_0 = 514.5$-nm light of the green line of an Ar ion laser, for (a) silicon, (b) diamond, (c) aluminum.

SOLUTION

The evaluation is a straightforward consequence of the estimates of Example 2. Since $\text{FSR} = c_{light}/2d$ and, in the most common case, the FSR coincides with the full scale range of the measurements, d is immediately obtained keeping in mind that the numbers obtained in example 2 were only estimates. In order to observe the bulk waves in silicon and diamond, appropriate choices of the FSR could be at least 150 and 200 GHz, meaning a d of at most 1 mm and 0.75 mm, respectively. With these values of the FSR the RW can still be observed, but with a relatively poor resolution. In order to better measure the RW of the three materials, more appropriate choices of the FSR could be around 60, 30, and 15 GHz respectively, meaning a d of 2.5, 5, and 10 mm.

10.3.2.2 Optical Beating Methods

Optical beating methods are based on the heterodyne detection technique.[88] The scattered light is mixed, by beam splitters, with a reference beam derived from the incident beam, and the beating resulting from the interference of the two beams is observed. The measured signal is accordingly shifted to a frequency accessible by high-speed optical sensors, and frequency resolution becomes possible, which is much better than that achieved by optical filtering. After the method was first proposed, the first observation of a spectrum containing a Brillouin doublet from bulk waves was limited to frequencies below 100 MHz. A variant of the method achieved very high resolution, but remained limited to a few hundred megahertz. Scattering by surface waves was later observed in this frequency range. The upper frequency limit was extended to 800 MHz and to 1.7 GHz; more recently, by a more complex superheterodyne technique[89] a frequency range extending from 10 MHz to 3 GHz, with very high frequency resolution, was achieved. The optical beating methods intrinsically have a very small collection solid angle; since the collected light must interfere with a reference beam, its wave vector q_s must have a well-defined direction. This gives a good q_s resolution and allows the good frequency resolution, but with the usually weak surface scattering signals the larger collection angle allowed by filtering methods is typically necessary to gather a sufficient signal. The optical beating methods remain essentially devoted to transparent media, either solid or liquid.[88]

10.3.3 Nonideality of the Scattering Configuration

A further step in the analysis of the experimental setup involves the consideration of its geometrical nonidealities, which are at the origin of experimental uncertainties and of the broadening of spectral peaks. The analysis is presented mainly with reference to the case of backscattering from SAWs. Indications concerning scattering by SAWs in other geometries and scattering by bulk waves are also given.

10.3.3.1 Geometrical Imperfections

First, for the scattering geometry, the values of the incidence and scattering angles (see Equation 10.60) are known with finite accuracy. For both volume and surface scattering the backscattering configuration exploiting a single lens is better suited to minimize this error.[45,69] Once the alignment of the incidence mirror and the front lens is carefully performed (see the next section) the coincidence of the incident and scattered direction is automatically obtained, and the measurement uncertainties concern only the incidence angle θ_i. A given θ_i is obtained by specimen rotation from a reference position. Rotators are available by which rotations can be performed and measured with accuracy better than 0.1 mrad; the error in θ_i is essentially the error in the identification of the reference position. A practical reference position is normal incidence, identified by the perfect superposition of incident and reflected beams. By common procedures the exact superposition is typically found with an uncertainty in θ_i of at most $\delta\theta_i \cong 0.2° \cong 3.5$ mrad.[90] This means a relative uncertainty in $k_{||}$ of (see Equation 10.61) $\delta k_{||}/k_{||} = (\partial k_{||}/\partial\theta_i)\, \delta\theta_i/k_{||} = \delta\theta_i/\tan\theta_i$, which is nearly 1% at $\theta_i = 20°$, decreases to 0.6% at $\theta_i = 30°$, and falls to 0.13% at $\theta_i = 70°$. This uncertainty contributes to the uncertainty of the measured velocity. Its reduction requires some specific setup (e.g., a sufficiently long optical path with pinholes). The uncertainty $\delta\theta_i$ can thus be lowered to around 0.5 mrad, meaning that the relative uncertainty $\delta q_{||}/q_{||0}$ is reduced to 0.14% at $\theta_i = 20°$ and 0.1% at $\theta_i = 30°$, down to 0.02% at $\theta_i = 70°$.

10.3.3.2 Finite Collection Angle

In the outline presented above the wave vectors q_i and q_s were implicitly treated as perfectly determined vectors, implying a perfectly defined wave vector $k_{||}$. In reality, as it is discussed below and as it can be seen from Figure 10.6, both q_i and q_s lie within cones around their nominal values and correspond to a whole range of wave vectors $k_{||}$.

The incident beam is focused onto the sample, because otherwise the optical power density is not sufficient to give a detectable scattered signal. Due to the finite width of the laser beam, after focusing the incident beam contains all the wave vectors of given $|q_i|$ lying in a cone around the nominal incidence direction. More importantly, the front lens collects scattered light with all the directions of q_s falling within the solid angle Ω delimited by the lens aperture (i.e., with all the wave vectors within a cone around the nominal collection direction; see Figure 10.6). Due to the small width of the laser beam the spread of q_i is a minor effect, while the spread of q_s can be significant, since a wider collection angle means a higher signal intensity. A sufficiently accurate analysis can be performed considering only the spread of q_s.

A first consideration concerns the axis of the collection cone (i.e., the nominal scattering direction). The normal incidence can be identified as mentioned above by the perfect superposition of incident and reflected beams, but can also be found with superposed beams not passing through the center of the front lens. In that case the axis of the collection cone, which passes through the center of the lens, does not coincide with the incidence direction: backscattering is not perfectly achieved, an error $\delta\theta_s$ being present in the scattered direction alone. This error gives a relative uncertainty in $k_{||}$, evaluated for a fixed θ_i, of (see Equation 10.60) $\delta k_{||}/k_{||} = (\partial k_{||}/\partial\theta_s)\ \delta\theta_s/k_{||} = \delta\theta_s/(2\tan\theta_i)$. The same type of error occurs when the alignment of the collected light beam with the optical axis of the interferometer is not perfect. If this is the case, the finite apertures on the optical path of the interferometer can clip the light beam asymmetrically with respect to the beam axis. The light that is eventually analyzed is collected not symmetrically around the incidence direction.

This type of error is not easily detected, although it can be significant. An iris diaphragm mounted on the front lens can be of great help in the procedure of centering the beams.

A second consideration concerns the aperture of the collection cone. The lens, of numerical aperture N.A., collects all the wave vectors $\boldsymbol{q}_s$ whose direction differs from the nominal one by an angle smaller than $\gamma_{\text{lens}} = \arctan[1/(2\ \text{N.A.})]$; with a lens of aperture f/2 the collection cone has a semiangle $\gamma_{\text{lens}} \sim (1/4)$ radian ~ 14°, which is reduced to $\gamma_{\text{lens}} \sim (1/11)$ radian ~ 5° for a lens of aperture f/5.6. When a wide lens aperture is adopted the whole optical path, also within the interferometer, should be considered. Other finite apertures can be present, which can limit the collected light beam to a diameter smaller than that accepted by the front lens.

The wave vectors $\boldsymbol{q}_s$ belonging to the collection solid angle Ω are the outcome of interactions with SAWs whose wave vectors $\boldsymbol{k}_{||}$, determined by Equation 10.59, belong to a whole region in the $\mathbf{k}_{||}$ plane [4,90]. This region is symmetrically located around the incidence plane; the average $<\boldsymbol{k}_{||}>_\sigma$ of the wave vectors belonging to it can be computed integrating over the solid angle Ω and weighting each value of $\boldsymbol{k}_{||}$ by the corresponding cross section $d\sigma/d\Omega$, which is a function of both $\boldsymbol{q}_i$ and $\boldsymbol{q}_s$.[90]

$$\left\langle \mathbf{k}_{\|} \right\rangle_\sigma = \frac{\int_\Omega (\mathbf{q_i} - \mathbf{q_s})_{||} \frac{d\sigma(\mathbf{q_i}, \mathbf{q_s})}{d\Omega}}{\int_\Omega \frac{d\sigma(\mathbf{q_i}, \mathbf{q_s})}{d\Omega}} \quad \textbf{(10.62)}$$

The cross section for scattering by the ripple effect alone from an isotropic solid can be expressed in closed form.[20,90,91] If the elasto-optic mechanism is not negligible, the cross section is instead a function of the strain field within the material, and its evaluation is computationally much more expensive and requires the elasto-optic coefficients of the material, which are seldom known. An average value $<\boldsymbol{k}_{||}>_g$, which only takes into account geometric effects,[90] can be computed in a simpler way by ignoring the dependence of $d\sigma/d\Omega$ on $\boldsymbol{k}_s$: $<\boldsymbol{k}_{||}>_g = \frac{1}{\Omega}\int_\Omega(\boldsymbol{q}_i - \boldsymbol{q}_s)_{||}\, d\Omega$. In this integration, as well as in that of Equation 10.62, the small solid angle intercepted by the incidence mirror (or by any other means exploited to direct the incident beam onto the sample) should be eliminated from the integration solid angle; the scattered light impinging on it is reflected back toward the laser and is not collected.[4]

It should be noted that the relationship between $\boldsymbol{q}_s$ and $\boldsymbol{k}_{||}$ is nonlinear, since it involves a projection, (i.e., a trigonometric function). As a consequence, although the collection cone has perfect rotation symmetry around the nominal collection direction, meaning that the average collection direction coincides with the nominal one, the averages $<\boldsymbol{k}_{||}>_\sigma$ and $<\boldsymbol{k}_{||}>_g$ do not coincide with the nominal value of $k_{||}$, given by Equation 10.61. Due to the reflection symmetry with respect to the incidence plane the averages $<\boldsymbol{k}_{||}>_\sigma$ and $<\boldsymbol{k}_{||}>_g$ still belong to the incidence plane itself, but their modulus is not exactly given by Equation 10.61. The difference can be appreciated in a simplified way evaluating $<\boldsymbol{k}_{||}>_g$ by considering, instead of the whole solid angle Ω (Equation 10.62), only the collected wave vectors belonging to the incidence plane. This subset of collected wave vectors is significant, because it includes the minimum and the maximum of all the collected k_s, and is easily analyzed, because it is the set of wave vectors for which Equation 10.60 holds. It is the set of wave vectors for which θ_s lies in the interval $(-\theta_i - \gamma_{\text{lens}}, -\theta_i + \gamma_{\text{lens}})$; accordingly, the values of $k_{||}$ are spread over the interval

$$\frac{2\pi}{\lambda_0}(\sin\theta_i - \sin(-\theta_i \pm \gamma_{lens})) \cong 2\frac{2\pi}{\lambda_0}\sin\theta_i\left(1 \pm \frac{\gamma_{lens}}{\tan\theta_i}\right) \quad \textbf{(10.63)}$$

$$\langle k_{||}\rangle_g = \frac{2\pi}{\lambda_0}\frac{1}{2\gamma_{lens}}\int_{-\gamma_{lens}}^{\gamma_{lens}}(\sin\theta_i - \sin(-\theta_i \pm \gamma))d\gamma = 2\frac{2\pi}{\lambda_0}\sin\theta_i\left[1 \pm \frac{1}{2}\left(\frac{\sin\gamma_{lens}}{\gamma_{lens}} - 1\right)\right] \quad \textbf{(10.64)}$$

and the relative difference between this value and the nominal one given by Equation 10.61 is

$$\frac{1}{2}\left(\frac{\sin\gamma_{lens}}{\gamma_{lens}} - 1\right) = -\frac{1}{12}\gamma_{lens}^2 + \frac{1}{240}\gamma_{lens}^4 + \cdots \ (\gamma_{lens} \text{ in radians})$$

which does not depend on θ_i and can be not negligible when the best accuracy is needed with wide lens apertures. Similar conclusions are reached by the full integration of Equation 10.62.[90]

10.3.3.3 Instrumental Peak Width

The finite collection aperture also gives the main contribution to the instrumental width of the spectral peaks. An estimate is straightforwardly obtained in the simple case of a SAW propagating with velocity c_{SAW} independent of wavelength (a nondispersive SAW). In this case each collected wave vector corresponds to a circular frequency $\omega = c_{\mathrm{SAW}}|\boldsymbol{k}_{||}|$, and the spread of the frequencies is simply proportional to the spread of wave vectors given by Equation 10.63. In a more detailed analysis, still in the case of a SAW propagating with velocity c_{SAW} independent of wavelength and of the propagation direction, the actual spectrum of the collected light can be predicted by a procedure analogous to the integration of Equation 10.62.[4,90] The collection angle Ω is subdivided in infinitesimal angles $d\Omega$, each one corresponding to a specific direction of $\boldsymbol{q}_s$ (i.e., to a specific value of $\boldsymbol{k}_{||}$). Each infinitesimal angle contributes to the spectrum of the collected light an elemental peak centered at $\omega = c_{\mathrm{SAW}}|\boldsymbol{k}_{||}|$. The superposition of all the elemental peaks, possibly weighted by the corresponding scattering cross sections, supplies the spectrum of the collected light.

If the SAW velocity depends on wavelength or on the propagation direction, the spread in the value of the velocity further contributes to the spread of the frequencies of the elemental peaks. Other minor contributions to spectral broadening come from the finite width of the laser beam and from its finite spectral purity. In the above prediction procedure, if the intrinsic width of the spectral line corresponding to the acoustic mode is small, the width of each elemental peak is negligible, and the width of the measured peak is essentially the instrumental width. If instead the spectral line is broadened, by, for example, scattering or damping processes, each elemental peak has a finite width, and the width of the measured peak is the outcome of both the intrinsic and the instrumental width. This should be taken into account when the line width has to be measured (e.g., to assess damping coefficients).

A slit is sometimes inserted in the collected light beam.[4] The collection solid angle is thus reduced, achieving a significant reduction of both the difference between the average and the nominal $k_{||}$ and the spread of $k_{||}$. The instrumental peak width is thus significantly reduced, at the cost of a significant reduction of collected intensity, meaning an increase in measurement times.

For scattering by bulk waves the situation is slightly different. Projection of the wave vectors onto the surface is not involved; this implies that because of the perfect rotational symmetry of the collection cone around the nominal collection direction, the exchanged wave vectors are distributed with cylindrical symmetry around the nominal one. The average exchanged wave vector $<\boldsymbol{k}>$ has therefore the same direction as the nominal one. However all the wave vectors in the collection cone, except the nominal one, are not perfectly opposite to the incident wave vector, meaning that the exchanged wave vectors have a modulus slightly smaller than the nominal one (see Equation 10.56). Therefore, the finite collection angle causes a broadening of the spectral peak, with a shift in its center of mass.[80]

10.3.3.4 Measurement Accuracy

The overall precision and accuracy can be assessed by summarizing the above observations. First, the scattered intensity is measured by photon counting after narrow band-pass filtering by the Fabry-Perot interferometer (see above). Due to the weakness of Brillouin doublets the count rates can be very small (count rates of tens of counts per seconds are not rare) such that the total count numbers can be rather low. With low count numbers the intrinsically statistical nature of photon counting has evident consequences. For each channel of the spectrum analyzer the photon count n is a statistical variable; since the intensity is stationary it is the outcome of a Poissionian process which has an intrinsic variance of $\sqrt{n}$. The relative variance $\sqrt{n}\,/n$ is therefore a slowly decreasing function of the count number. This gives the spectra a granular or noisy appearance; the relative amplitude of the noise band in the spectra can only be decreased by increasing the measurement time. Since the decrease is slow, the advantage of a better definition of the spectrum has to be assessed against the increased measurement time. The central frequency ω of a spectral peak is typically found by fitting a predetermined line shape; the uncertainty $\delta\omega$ associated with the fitting procedure can typically be obtained by the procedure itself. It was mentioned in Section 10.3.2.1 that the most efficient number of spectral channels is of the order of twice the finesse. The uncertainty in the identification of the central frequency of a peak is typically below one channel, meaning that with a finesse of the order of 100 the uncertainty in the frequency measurement due to the photon counting process is of the order of a fraction of a percent. This uncertainty, although immediately evident, may not be the main cause of uncertainty. A comparable uncertainty comes from the calibration of the frequency scale. The most common calibration procedures are the measurement of a reference peak of known frequency and the attribution of the FSR frequency to the position of the ghosts. Both procedures involve the determination of the position of a spectral feature, which is affected by the same type of uncertainty discussed above.

Geometrical imperfections, whose effect is intrinsically deterministic, must also be analyzed in statistical terms because imperfections are, by definition, not known. If θ_i is measured with an uncertainty for which an upper bound $\delta\theta_i$ can be assigned, the value of $k_{||}$ is known to a relative uncertainty, which in backscattering is $\delta k_{||}/k_{||} = \delta\theta_i/\tan\theta_i$, as shown above. The backscattering geometry is generally the configuration that optimizes the accuracy of $k_{||}$. Remembering that $k_{||} = q_i(\sin\theta_i - \sin\theta_s)$ (Equation 10.60), where θ_i is positive and θ_s is taken positive in forward scattering and negative in backward scattering, in the latter case $k_{||}$ is the sum of two terms of the same sign (in particular in backscattering $\theta_i = -\theta_s$ and the two contributions have identical weight); in forward scattering $k_{||}$ is significantly smaller, being the sum of two terms of the opposite sign. Since the uncertainties $\delta k_{||}$ are the same, the relative uncertainty $\delta k_{||}/k_{||}$ is much worse in forward scattering. Furthermore, all the configurations other than backscattering require separate incidence and collection optics, introducing additional error causes.

The finite collection angle has the deterministic effect discussed in Section 10.3.3.2. It leads to a spread of the $k_{||}$ values (Equation 10.63), which affects the precision, since it increases the uncertainty in the identification of the central frequency of the spectral peak. More importantly, it affects the accuracy, because the average exchanged wave vector $\langle k_{||}\rangle_g$ or $\langle k_{||}\rangle_\sigma$ is shifted from the nominal one $k_{||0}$ (Equation 10.64)). The relative difference can reach 0.5% for an f/2 lens aperture, and is reduced well below 0.1% for an f/5.6 lens aperture. As discussed in Section 10.3.3.2, this shift can be computed and corrected for; it can also be strongly reduced by the adoption of a slit. However, in the case of the slit the simple estimates of Equation 10.63 and Equation 10.64 are no longer fully significant, because the subset of wave vectors considered by these equations is no longer fully representative, and the full computation of $\langle k_{||}\rangle$ must be considered.

Since $c_{SAW} = \omega/k_{||}$, uncertainties $\delta\omega$ and $\delta k_{||}$ induce velocity uncertainties δc_{SAW} of the measured velocity such that $|\delta c_{SAW}/c_{SAW}| = |\delta\omega/\omega|$ and $|\delta c_{SAW}/c_{SAW}| = |\delta k_{||}/k_{||}|$. The geometrical causes of bias and uncertainty are summarized and quantitatively evaluated in Table 10.1. Geometrical imperfections give relative uncertainties $|\delta v/v|$ proportional to $1/\tan\theta_i$, and are therefore more severe at small θ_i. In Table 10.1 estimates are given at the extremes of the commonly adopted interval $\theta_i = 30° \div 70°$. It can be noted that at large incidence angles and for the lower bounds of the primary uncertainties (meaning accurate alignment and positioning procedures) the

TABLE 10.1

Summary of the Geometrical Sources of Error in SBS Measurements

Cause	Effect	Primary Uncertainty	Velocity Uncertainty $\delta c/c$ (%)
Error in θ_i: $\delta\theta_i$	$\delta k_{\|\|}/k_{\|\|0} = \delta\theta_i/\tan\theta_i$	$\delta\theta_I = 0.5 \div 3.5$ mrad	$0.09 \div 0.61$ ($\theta_i = 30°$) $0.02 \div 0.13$ ($\theta_i = 70°$)
Error in θ_s: $\delta\theta_s$	$\delta k_{\|\|}/k_{\|\|0} = \delta\theta_s/(2\tan\theta_i)$	$\delta\theta_s = 5 \div 10$ mrad	$0.43 \div 0.86$ ($\theta_i = 30°$) $0.09 \div 0.18$ ($\theta_i = 70°$)
Collection angle	$\langle k_{\|\|}\rangle \neq k_{\|\|0}$	Lens aperture = f/2 ÷ f/5.6	$0.1 \div 0.5$

uncertainties in the velocity indicated in Table 10.1 are smaller than the intrinsically statistical ones, which have therefore a dominant role. Instead, for small incidence angles and for the upper bounds of the primary uncertainties (meaning not very accurate alignment and positioning procedures) the uncertainties of Table 10.1 are larger than the statistical ones, and are therefore the limiting factor for measurement accuracy.

10.3.4 Derivation of the Elastic Constants

A single Brillouin spectrum gives the circular frequencies ω of the observable spectral peaks. As discussed in Section 10.3.1.1 the scattering geometry and the laser wavelength fully determine the wave vector $\mathbf{k}_{||}$ exchanged with SAWs (see Equation 10.61 for the backscattering case), while the wave vector $\boldsymbol{k}$ exchanged with bulk waves also depends on the refractive index n (see Equation 10.58) for the backscattering case). The velocities of SAWs and of bulk waves are immediately obtained as $\omega/k_{||}$ and ω/k, respectively. Different values of k can be obtained by different scattering geometries, but this is seldom necessary since the bulk wave velocities do not depend on the modulus of $\boldsymbol{k}$, although they can depend on its direction. Different values of $\mathbf{k}_{||}$ are obtained with the same backscattering geometry by simply changing the incidence angle. The dispersion relation $c_{SAW}(\mathbf{k}_{||})$ is thus measured, and this is often useful since SAW velocities can depend on $k_{||}$. However, since measurements with an incidence angle close to zero are not practical (elastically reflected light becomes very intense because the scattered direction is too close to the specular reflection, and the effect of geometrical inaccuracies becomes more relevant, see Section 10.3.3.), with the standard configuration the range of $k_{||}$ that can be explored does not exceed a factor of 3. An experimental procedure to overcome this limitation was recently developed.[92]

Scattering by bulk waves has been extensively used to measure the elastic properties and the elasto-optic constants of bulk samples of nonmetallic materials.[45,69,70,93] In the simplest case of isotropic materials the velocities of longitudinal and transverse (primary and secondary) waves are simply given by $\sqrt{C_{11}/\rho}$ and $\sqrt{C_{44}/\rho}$, respectively, and the two moduli are immediately obtained when both the P and shear wave (S) peaks are measured, and when the mass density is known. For crystalline materials the number of independent elastic constants is higher, and measurements with different directions of k, possibly requiring crystals with different cuts, can be needed.

The analysis of scattering by SAWs depends on the nature of the sample. The cases of the semi-infinite homogeneous medium and of a supported film are the most relevant, and are considered here. It must be remembered (see Section 10.3.1.1) that in backscattering the bulk waves are probed at wavelength $\lambda_0/(2n)$ (see Equation 10.58), which is a fraction of a micrometer, and that SAWs are probed at parallel wavelength $\lambda_0/(2\sin\theta_i)$ (see Equation 10.61), which is larger but still smaller than a micrometer (with the usually adopted green light and with incidence not too close to normal). In supported films having thickness larger than a couple of micrometers, or even less, these wavelengths imply that bulk waves are already fully present and can be detected if the film is transparent enough. They also imply that since the decay depth of the RW is the same as the wavelength, the displacement field of the RW hardly reaches the substrate, meaning that such a wave is almost unaffected by the substrate. In other words, when the film thickness exceeds 1 μm, or little more than that, the presence of the substrate becomes irrelevant, and the data analysis can be performed as for a semi-infinite medium (i.e., a bare substrate).[7,72,94] Accordingly, a precise value of thickness is not needed, while the limitation of the scattering volume, due to the finite film thickness or to the limited transparency of the material, causes a peak broadening, but not a spectral shift. An exception occurs when high order resonances can be measured.[92]

It must also be remembered that the RWs that are detected propagate in the outermost layer, of depth of the order of 1 μm, and their behavior is determined by the properties of the material in this outermost layer. If, in a nominally homogeneous material, a gradient of material properties is present in the outermost layer, the sample is better schematized by one or more films, of different properties, on a substrate.

In the semi-infinite medium case the propagation velocity does not depend on the modulus of $\boldsymbol{k}_{||}$, but can depend on its direction if the material is anisotropic. In the case of a film of thickness h the propagation velocity also depends on the modulus of $\boldsymbol{k}_{||}$, namely through the nondimensional product $k_{||}h$. In both cases the dependence can be computed, as indicated in Section 10.2.2. Sets of velocities $c_i^{comp}(C_j)$ can be computed as a function of one or more free parameters C_j (typically, but not necessarily, elastic moduli), the index i typically standing for a set of values of $k_{||}h$ or a set of propagation directions (see below). If, for the same set of values of $k_{||}h$ or of propagation directions, the velocities c_i^{meas} are measured, and free parameters are determined by a standard least squares minimization procedure. The sum of squares is computed

$$\chi^2(C_j) = \sum_i \left(\frac{c_i^{comp}(C_j) - c_i^{meas}}{\sigma_i} \right)^2$$

where it has been assumed that the variances σ_i of each c_i^{meas} can be individually estimated; according to standard estimation theory the minimum of $\chi^2(C_j)$ identifies the most probable values ($\bar{C}_j$) of the parameters in the (C_j) space, and the isolevel curves of the ratio $\chi^2(C_j)/\chi^2(\bar{C}_j)$ identify the confidence region at any predetermined confidence level.[95,96] As discussed below for some cases, in some instances a well-defined minimum of $\chi^2(C_j)$ is found, allowing a good identification of the parameters,[96–98] while in other cases a broad minimum is found, in the shape for instance of a valley. In such cases a good identification of the parameters is not possible,[57,99,100] although sometimes some combination of the parameters can be identified with better precision than the individual parameters.[57,97,98] It was also shown that in some cases two significantly different sets of elastic constants fit the measured dispersion relation in a comparable way.[101]

The poor or good identification of the minimum of $\chi^2(C_j)$ depends on the amount of available information. When a single acoustic mode is detected, the values of $\chi^2(C_j)$ can remain low in a relatively wide region in the (C_j) space, meaning that the precision in the measurement of $\chi^2(\bar{C}_j)$ is poor. If additional information is obtained by the measurement of one or more other (surface or bulk) acoustic modes the precision in the measurement of the parameters can be significantly improved.[72,97–99,102–106] In these cases the minimization procedure can be split; if one of the modes allows a good determination of a first parameter, the others can be determined assuming a fixed value of the already identified one.[107] In other cases the relatively wide region in which $\chi^2(C_j)$ is not far from its minimum value has been delimited by imposing some physical acceptability criterion, like imposing an upper limit for the value of the bulk elastic modulus at the value of diamond.[108,109] In some cases a fixed value of Poission modulus was imposed *a priori*. [6] It can be noted that several published works only give the values of the parameters obtained by the minimization procedure, without presenting an analysis of the precision and reliability of the results.

It must also be noted that this least squares identification procedure is essentially independent of the technique by which the c_i^{meas} are measured, and the analysis of data obtained by, for example, acoustic microscopy (see Chapter 11) proceeds in the same way.[110] Differences are at most quantitative: acoustic microscopy operates at wavelengths that are two orders of magnitude larger than those probed by Brillouin spectroscopy, making its sensitivity to thin films much smaller.

The two cases of the semi-infinite homogeneous medium and of the supported film are discussed in more detail in the two following sections. It can be mentioned that Brillouin scattering has been exploited also in other cases such as LB films[111] and buried layers in silicon-on-insulator structures.[112] In addition, besides the determination of elastic constants in mesoscopically compact films, other applications have included the analysis of the transition between nonpropagating and propagating excitations in cluster assembled films. [113]

10.3.4.1 Semi-Infinite Medium

In a semi-infinite homogeneous medium (as noted above, a supported film having thickness of little more than 1 μm already behaves as a semi-infinite medium), the translational invariance is broken only by the free surface, and the sample has no intrinsic length scale; consequently, for any acoustic mode, the velocity is independent of the wavelength. Measurements at different values of $k_{||}$, which in backscattering means measurements at different incidence angles, are useful only because they allow detection of the modes whose frequency scales as $\sin\theta_i$, allowing the identification of the modes. Apart from this, measurements at various values of $k_{||}$ only give the same improvement in precision, coming from repeated measurements, that would be obtained by repeated measurements at the same $k_{||}$. Beside bulk waves, a semi-infinite homogeneous medium supports the RW and, as noted in Section 10.3.1.1., in sufficiently transparent materials in which the elasto-optic scattering mechanism is dominant, the so-called LGM, a mode traveling parallel to the surface, can also give a spectral peak.[72] In isotropic materials this mode has the same velocity as the longitudinal bulk wave, and directly supplies the value of the C_{11} elastic constant, or, if the longitudinal bulk wave is also measured, the values of C_{11} and of the refractive index n. In isotropic materials the Rayleigh velocity only identifies a combination of the elastic constants, and approximate expressions are often used (see Section 10.3.4); exact expressions for specific crystalline symmetries have also been used.[114] In anisotropic materials the dependence of the Rayleigh velocity on the propagation direction gives access to individual values of the constants.[8,10,94] If bulk waves can also be measured, the additional information improves the precision and the number of constants that can be determined, up to the determination of the whole set of elastic constants,[7,72,94] also in a low-symmetry case.[115] The dependence of the effective elastic constants on the propagation direction and on the position in the film has also been exploited to explore internal stresses.[79]

10.3.4.2 Supported Film

In a sample formed by a substrate and a supported film the film thickness h identifies a specific length scale, and the propagation velocity depends on the ratio of the acoustic length to h. This is typically expressed as a dependence of the acoustic velocity on the nondimensional product $k_{||}h$, and the behavior of the semi-infinite medium of the film material is asymptotically approached for high values of $k_{||}h$. Measurements at different values of $k_{||}$ allow measurement of the dispersion relation $c_{SAW}(k_{||}h)$. As noted at the beginning of Section 10.3.4, in backscattering the accessible range for $k_{||}$ does not exceed a factor of 3. In order to explore a wider range of $k_{||}h$, in some cases sets of films of different thicknesses have been used.[95,102,107,116] The independence of film properties on thickness is assessed checking that the parts of the dispersion relation measured on different samples fall on the same curve. This procedure was adopted also for unsupported films.[117] In other cases, in which the dependence of film properties on thickness was precisely the objective of the investigation,[109] this procedure could not be adopted.

As discussed in Section 10.1, in the case of a supported film, various types of modes can be present, according to the properties of the film and the substrate and to film thickness. As already discussed in Section 10.3.4, the quality of the information that can be obtained on the film material depends on the amount of information obtained from the observed acoustic branches. In addition to the RW modified by the presence of the film (modified Rayleigh wave), which is generally present, further information has been gained by the detection of the LGM[107,108] or of Sezawa or other modes.[10,95,103,105,116] The information that can be obtained from the modified Rayleigh wave was assessed in a model case (isotropic film on silicon substrate) by a sensitivity analysis.[118] It was found that the modified RW velocity is most sensitive to the values of the Young modulus and the shear modulus, meaning that both moduli can be determined with good precision, but least sensitive to the Poission's ratio ν, the bulk modulus B, and the C_{11} elastic constants, meaning that these parameters remain poorly determined. It was also found that the sensitivity to the film thickness and mass density is not high, meaning that for the identification of the elastic moduli an extreme accuracy in the measurement of thickness and density is not crucial. It was finally found, considering the possible detection of a second branch, that the LGM significantly contributes to the determination of ν and B, while the first Sezawa mode does not. These results justify the adoption of physical plausibility limits for ν and B, by which the Young modulus and shear modulus could be determined for films of thickness down to a couple of nanometers.[100,109]

In a case of a semitransparent layer on a solid, treated by a number of authors,[20–22,24,25] the full calculation requires a knowledge of the complex refractive indices and elasto-optic constants of the layer and substrate (which are not always readily available) and the near-surface dynamics, and takes account of the interference between ripple and elasto-optic scattering.[119] Where elasto-optic scattering plays a minor or subsidiary role, SBS spectra can often be semiquantitatively understood with just a knowledge of the surface dynamic response. In particular, the positions (but not the intensities) of the RW and Sezawa peaks are independent of the scattering mechanism. Interestingly, when elasto-optic scattering predominates, the dip in the Lamb shoulder at the P threshold reverses and becomes a peak very close to the P threshold, called the LGM.[46]

10.4 Case Studies in Surface Brillouin Scattering

Representative results obtained by SBS are reviewed in this section. As was mentioned in the introduction, SBS measures SAW velocities in the frequency range from a few GHz to 30 GHz with a lateral resolution of the order of several microns; the area subjected to the measurement is the focusing spot of the incident laser, which can be as small as ~ 5 μm on the focal plane. Within this area, light interacts with acoustic waves of submicrometric wavelength. The frequency range and spatial resolution determine the potential for SBS applications in nondestructive evaluation.

The ability to measure SAWs at high frequency has allowed the characterization of the elastic properties of the submicrometric films widely used in modern high-tech industry.[109] The high spatial resolution allows the study of the elastic properties of very small samples. A good example is offered by the new superhard phases synthesized at high pressure and high temperature (high P-T). The samples obtained by this technique are often not homogeneous and consist of several phases having different elastic properties and dimensions ranging from tens to hundreds of microns. The SBS technique is ideally suited for characterizing such specimens.[106]

10.4.1 Selected Results for Isotropic Bulk Solids

As already discussed in Section 10.3.4, in the supported films whose thickness exceeds about 1 μm, the behavior of SAWs is completely analogous to the behavior in semi-infinite media. The ability of Brillouin scattering to perform local measurement allows the characterization of very small samples. This is particularly relevant for materials, such as the new superhard materials obtained from fullerenes at high temperatures and pressures, which can be obtained only as extremely small specimens.

The discovery of the fullerene molecule C_{60} has led to extensive experimental studies of amorphous and nanocrystalline carbon phases in both bulk[19] and thin film[120] forms. Heating C_{60} at pressures above 8 GPa results in formation of 3-dimensional polymerized amorphous phases of C_{60}, and has fueled the debate on the existence of ultrahard fullerene-based phases with hardness higher than diamond.[121] Superhard phases can be obtained only in very small sizes, and they are opaque; Brillouin spectroscopy has allowed their elastic characterization. Manghnani et al. [106] reported the successful SBS measurements of the elastic properties of the superhard amorphous carbon synthesized from C_{60} under high pressure (13 to 13.5 GPa) and high temperature (800 to 900°C). The SBS spectra obtained from 2 bulk amorphous carbon (a-C) samples synthesized from C_{60} fullerite powder are shown in Figure 10.7. Surface scattering from the RW, at an incidence angle of 60°, gives the velocity of 6.49 km/sec for sample A (synthesized at 800°C) and 10.06 km/sec for sample B (synthesized at 900°C); these velocities are lower than that of diamond. For sample B scattering from the surface skimming longitudinal wave or longitudinal mode (see Sections 10.2.1.1 and 10.2.2.2) was also observed (see Figure 10.5).

The spectra were interpreted following the approach by Camley and Nizzoli,[63] computing the longitudinal power spectra $<|u_1(\boldsymbol{k}_{||},\omega)|^2>$ and the shear surface spectra $<|u_3(\boldsymbol{k}_{||},\omega)|^2>$ for the elastic properties of the sample given in Table 10.1 (see Figure 10.4). As can be seen from Figure 10.4, from which the RW was omitted for clarity, the power spectrum $<|u_3(\mathbf{k}_{||},\omega)|^2>$ associated with the ripple scattering mechanism vanishes for $\omega/k_{||}= c_P$ (the minimum is too deep and too thin to be visible in Figure 10.4), whereas the longitudinal power spectrum $<|u_1(k_{||},\omega)|^2>$ associated with elasto-optical interaction has a well defined maximum at $\omega/\boldsymbol{k}_{||}= c_P$. The significance of this maximum was discussed in Section 10.2.2.2.

The determination of the whole set of elastic constants by SBS[106] was made possible by the detection of the longitudinal mode. When only the RW velocity can be measured, the value of the elastic constants cannot be determined precisely, but it is possible to identify ranges for the Young modulus E and the shear modulus μ. Pastorelli et al.[122] used SBS to measure elastic properties of thick (600 nm) cubic boron nitride (cBN) using some *a priori* information. Elastic properties of the cBN films are of interest for industrial applications because cBN is the second-hardest material after diamond, and only recently a method to deposit cBN films was developed.[123] The measurement by SBS[122] was one of the first measurements of the elastic properties of the cBN films. It was done on thick cBN films that could be considered as semi-infinite media. Only the RW was detected in these films. To estimate the Young modulus and shear modulus Pastorelli et al. exploited two additional conditions: (1) Poission's ratio must lie between 0.0 and 0.5, and (2) the bulk modulus should not be greater than the bulk modulus of diamond (444 GPa). Applying these restrictions to the results of the RW measurements, a fairly narrow interval for elastic constants was obtained: 593 GPa $< E <$ 703 GPa, and 266 GPa $< \mu <$ 322 GPa.

In transparent media the interaction of the light with SAWs is expected to be weak, possibly too weak for experimental observation. Sussner et al.[124] showed that SAWs can be observed if the transparent material is coated by a thin aluminum layer. It was demonstrated that coating by a 40nm thick aluminum layer made it possible to detect SAWs in quartz, sapphire and polymethylmetacrylate (PMMA).

10.4.2 Selected Results for Anisotropic Bulk Solids

SBS has been successfully used for the detection of SAWs in anisotropic media, and SBS of cubic crystals is a good example showing the potential of the technique. Investigations of the SAW angular dispersion on cubic crystal surfaces revealed that, in addition to the GRW, a PSAW can exist.[36,38] Some properties of the PSAW for the three main planes of cubic crystals [i.e., (001), (110), and (111)] have been summarized by Farnell,[36] and an analysis of the use of SBS for detecting different types of waves propagating on the principal cubic crystal cuts has been reported by Velasco and Garcia-Moliner.[23]

The elastic properties of cubic crystals are determined by the three elastic constants C_{11}, C_{12}, and C_{44}, and the shape of the angular dispersion curve;

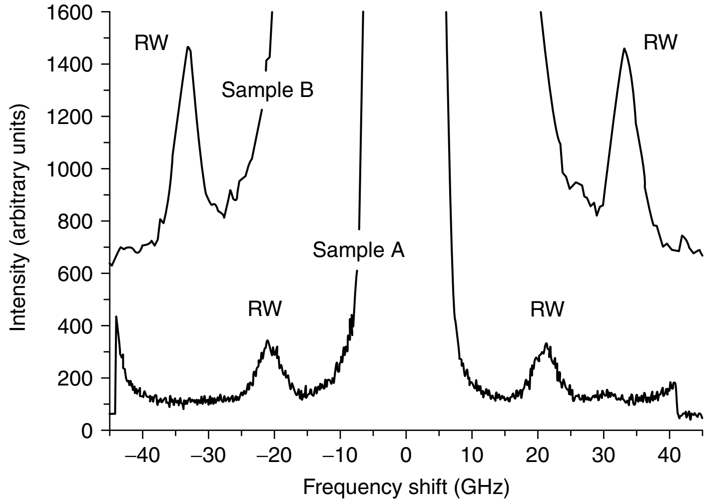

FIGURE 10.7
Experimental SBS spectra at θ = 60°, of superhard amorphous carbon synthesized from C_{60} under high pressure and high temperature. Sample A synthesized at 13 GPa and 800°C, and sample B synthesized at 13 GPa and 900°C. (From Manghnani, M.H. et al., *Phys. Rev. B,* 6412, 121403, 2001. With permission.)

hence the strategy in SBS measurements is determined largely by the anisotropy coefficient $\eta = 2C_{44}/(C_{11} - C_{12})$. Considering the (001) surface,[36,125] if $\eta < 1$, the variation of the GRW velocity with the propagation direction is small and the GRW is always distinct from the bulk slow transverse wave (STW) mode. In this case, the (001) plane is not very useful for the SBS characterization of the anisotropic elastic properties. For $\eta > 1$, as it is for silicon (Si) and gallium arsenide (GaAs), the angular variation of the velocity of the GRW and of the PSAW that exists in a certain angular range provides an opportunity for determining the elastic constants of a crystal from the angular dependence of the surface wave velocities alone, without the use of lateral wave data.[8,126,127]

Figure 10.8 is a grayscale image representing the calculated Brillouin intensity as a function of velocity $c = \omega/k_{||}$ and of direction φ measured from the [100] direction, for scattering from the (001) plane of gallium arsenide (GaAs). The grey scale intensity in this image is proportional to $\omega^{-1} Im\ [G_{33}(k_{||}, x_3 = 0, \omega + i0)]$ (see Equation 10.6). The elastic moduli of the GaAs were taken from reference[128] (see Table 10.2). The two bulk wave solutions for symmetry directions, the pure transverse vertical or fast transverse wave (FTW) and the pure transverse horizontal or STW, are displayed in Figure 10.8 as solid and dotted lines, respectively. Both the velocity and the intensity of the GRW velocity show considerable variation with direction. Toward the [110] direction the polarization of the GTW tilts over toward the horizontal it and

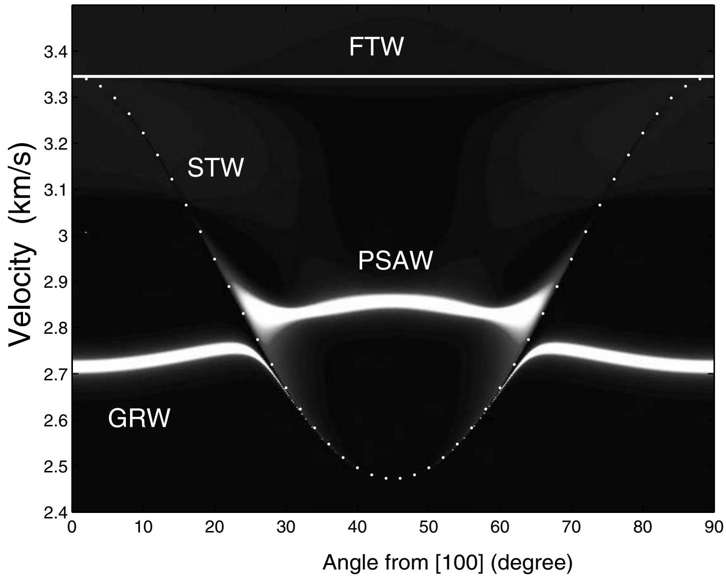

FIGURE 10.8
Green's function $G_{33}(\boldsymbol{k}_{||}, \omega)$ as a function of the GaAs(001) surface.

becomes more weakly coupled in G_{33}. As a result, the trace of the GRW shows decreasing intensity, ultimately vanishing as the GRW degenerates with the limiting STW bulk wave in the [110] direction. Also, as the GRW approaches this degenerate condition, its displacement field penetrates ever more deeply into the solid, which further diminishes its contribution to the surface response.

Extending out to about 20° on either side of the [110] direction is a sharp resonance within the bulk wave continuum, which is associated with a PSAW. This mode consists predominantly of two evanescent partial waves, but with the addition of a bulk wave component of small amplitude, which causes radiation of the energy of this wave into the substrate, resulting in attenuation of the wave as it travels along the surface. At the PSAW det$|\mathbf{B}|$ (see Section 10.2.2.2) is small but nonzero, except in isolated directions where the PSAW becomes a true supersonic SAW and det$|\mathbf{B}|$ vanishes.[129]

The angular dispersion curves in the (001) plane of cubic crystals have been investigated for nickel (Ni), [127] Si,[8,64] or GaP, [130] and for InSb,[131] and their behavior has been found to be properly predicted by the Green's function approach. Figure 10.9 illustrates the good agreement between theoretical simulation and experimental behavior of the SAW dispersion curve in the (001) plane of the GaAs.[132] SBS studies of GaAs[132] demonstrated the coexistence of GSW and PSAW around 20° as predicted by Green's function simulations (see Figure 10.8).

SAW propagation on the (111) plane in various cubic crystals has been extensively investigated by Kuok et al. (Si,[133] InSb,[131] GaAs,[132]). Figure 10.10

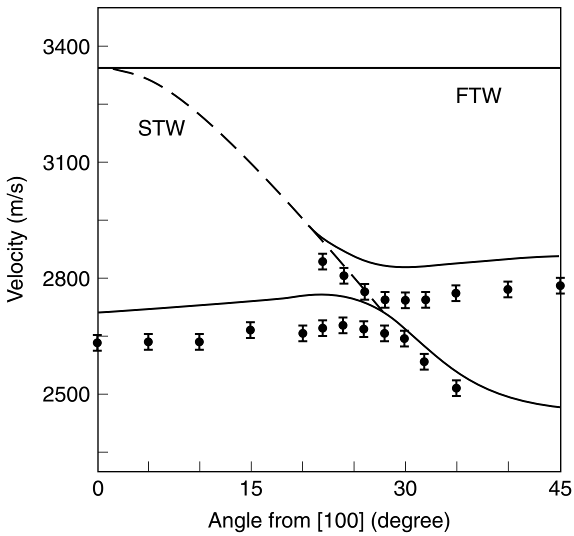

FIGURE 10.9
Angular dependence of the measured GSW and PSW velocities on (001) GaAs. Experimental data for GSW and PSW are denoted by circles. Solid curves represent the theoretical surface wave velocities, except the FTW and STW bulk wave velocity, which is shown as a dashed curve. (From Kuok, M.H. et al., *J. Appl. Phys.* 89, 7899, 2001. With permission.)

shows the measured angular dispersion curves of the three surface waves on (111) GaAs. It reveals that the PSW can propagate only in limited direction ranges on this surface. The velocities of GRW and LLSW on the (111) plane turn out to be less sensitive to the propagation direction than in the other two basal planes. Scattering from the PSW is strongest at azimuthal angle $\varphi = 0°$ ([110] direction), and its intensity decreases with increasing azimuthal angle until it is no longer measurable at $\varphi = 30°$. These observations are consistent with the theoretical findings of Lim and Farnell: they predicted that as φ approaches 30° the penetration depth of PSW into the bulk increases until it degenerates into a transverse bulk wave at $\varphi = 30°$.[134]

The SBS measurements of SAW dispersion on a (111) face of an fcc film of C_{60} (fullerite) grown on Ni(110) and BS data on longitudinal bulk wave allowed the determination of the three independent elastic constants of fcc C_{60} [94]. Similar work was done on chemical vapor deposited on polycrystalline diamond.[135]

SAWs on (110) faces of cubic GaAS, InSb, Ge and InAs ($\eta > 1$) have been investigated by Aleksandrov et al.[125] and more recently by Kuok et al. (GaAs,[132] InSb[131]). The angular dispersion curve of SAWs on the (110) plane in the cubic crystals represents a fascinating picture. Figure 10.11 represents Green's function simulations for the (110) plane of GaAs. In the (110) plane the FTW and STW curves meet each other at $\varphi = 55°$; beyond this point the PSAW does not exist, and it gradually disappears as the propagation direc-

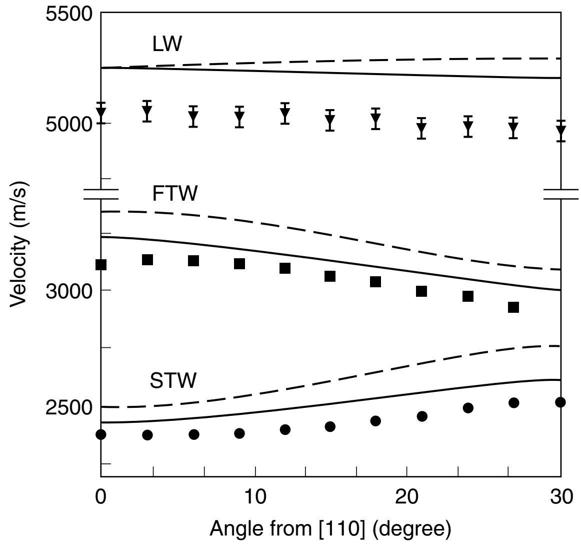

FIGURE 10.10
Angular dependence of the surface acoustic wave velocities on (111) GaAs. The experimental data for GSW, PSW, and HFPSW are represented by circles, squares and inverted triangles, respectively. LW means the longitudinal wave. (From Kuok, M.H. et al., *J. Appl. Phys.* 89, 7899, 2001. With permission.)

tion tends to [100]. Indeed, experimental SBS measurements (Figure 10.12) show that PSAW propagation on the (110) plane is restricted to the azimuthal angular region $10° < \varphi < 55°$.[132] The GRW was found to propagate in all directions on the surface with an intensity that is quite independent of direction. The LLSW has been detected on the (110) plane of GaAs as well. It is interesting to note that it was found that experimental data values for velocity were about 2%[64,132] lower than the calculated ones. Discussion on this subject can be found elsewhere.[8,64]

The most prominent features in a SBS spectrum are usually the RW and the PSAW peak, but with sufficient data collection times and adequate filtering the Lamb shoulder can be distinguished, and from it the bulk mode threshold velocities can be measured. SAW propagation in a vanadium carbide (VC) cubic crystal, for which $\eta \sim 0.8 < 1$, have been studied by Zhang et al.[57] In this study, two key features of the spectrum were exploited to determine the elastic constants of $VC_{0.75}$, namely the directional dependence in the (110) surface of the RW velocity, and the sharp dip in the Lamb shoulder lying at about 8500 m/sec, which corresponds to the P-wave threshold. The theoretical spectrum of $VC_{0.75}$ in Figure 10.3 has been calculated using Equation 10.5, and is in good agreement with the measured one.[57] The lateral wave LLSW is most sensitive to the longitudinal elastic constants[136] C_{11} and $C_{12} + 2C_{44}$, while the RW is more sensitive to C_{44} and $(C_{11} - C_{12})/2$.

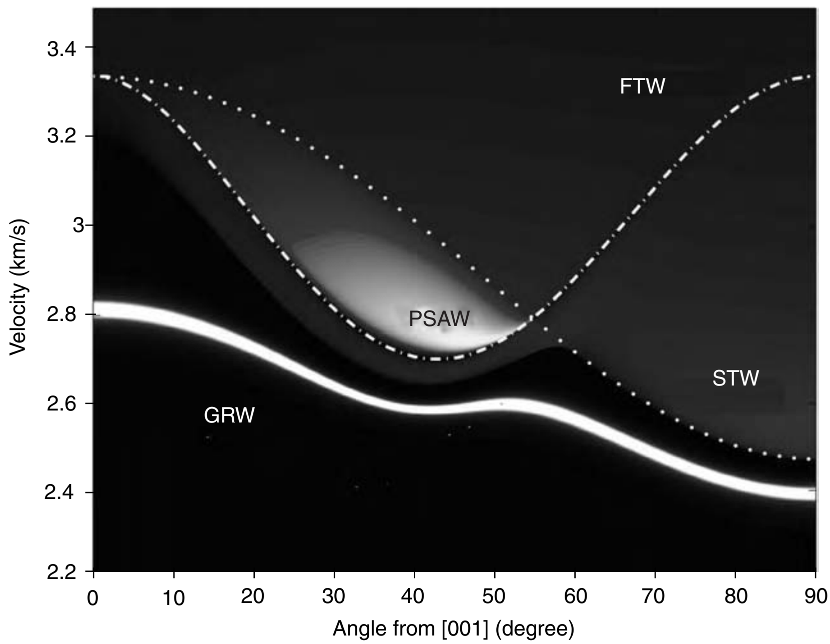

FIGURE 10.11
Green's function $G_{33}(\boldsymbol{k}_{||}, \omega)$ for the [100] direction in the GaAs (110) surface.

From the observed spectra, the elastic constants of $VC_{0.75}$ were determined to be C_{11} = 440 GPa, C_{12} = 92 GPa and C_{44} = 136 GPa.[57]

Most of the SBS studies of SAW propagation in anisotropic crystals have been performed on cubic crystals. For crystals of lower than cubic symmetry the detection of the GRW alone does not provide sufficient information for studying elastic properties of the crystals.[137] Carlotti et al.[138] were successful in determining five effective elastic constants of a thick (1.3 μm) transparent film (ZnO) of hexagonal symmetry. The constants C_{13}, C_{33}, and C_{44} were obtained from detection of the RW and of the longitudinal bulk mode propagation at different angles from the surface normal. The constant C_{11} was determined from the observation of the LLSW mode, and C_{66} was determined from detection of the shear horizontal mode traveling parallel to the film surface. As a rule, bulk Brillouin scattering is preferable[45] for low-symmetry crystals.[132]

10.4.3 Selected Results for Layered Media

One of the major applications for SBS is the study of the elastic properties of thin films. Thin films have a huge number of applications in modern industry. Ohring, in the preface of his monograph on science of thin films, wrote, "Thin-film science and technology plays a crucial role in the high-

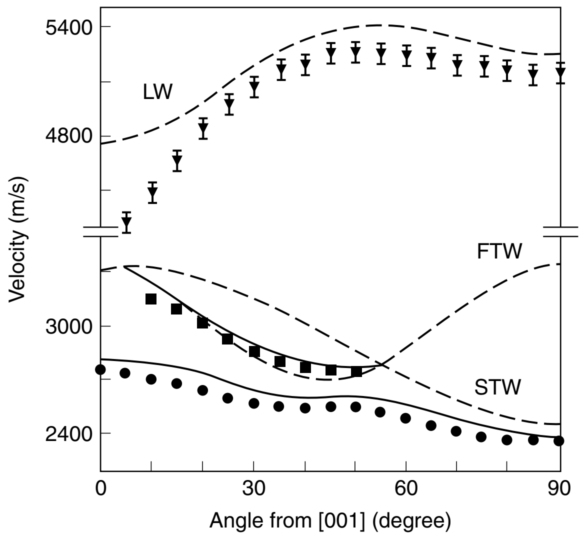

FIGURE 10.12
Angular dependence of the surface acoustic wave velocities on (110) GaAs. The experimental data for GRW, PSW, and LLPSW are represented by circles, squares, and inverted triangles, respectively. Solid curves represent theoretical surface wave velocities, while theoretical bulk wave velocities are shown as dashed curves. (From Kuok, M.H. et al., *J. Appl. Phys.* 89, 7899, 2001. With permission.)

tech industries that will bear the main burden of future American competitiveness."[139] In addition, elastic properties of the newly developed films, particularly superhard films, need to be determined experimentally because they strongly depend on the synthesis conditions, and cannot be derived from theoretical considerations alone. The thickness of such films ranges commonly from a few tens of nanometers up to the order of a micrometer. The nanoindentation technique widely used for mechanical characterization of thin micron films does not allow measurements of the hardness and elastic moduli of the submicron coating and substrate separately. Conventional methods usually employ SAWs. The surface wave displacements are concentrated within a wavelength from the surface and can probe the samples within a depth inversely proportional to the frequency used. For submicron films, frequencies in the range 5 to 30 GHz are needed, and therefore the SBS technique offers a unique opportunity to cover this range of frequencies.

SBS was used to study SAW in unsupported films (Lamb waves).[117,140] Measurements conducted on 23 nm unsupported Al films[140] illustrated that both the line and positions and relative intensities of the Lamb modes observed in the experimental spectra are well accounted for by theory. SBS of unsupported thin films are rather exceptional researches. The main direction of SBS in thin film characterization is the elastic characterization of thin supported films. For isotropic layered materials, the SAW velocity is dependent on the frequency (i.e., there is frequency dispersion). For anisotropic solids, the SAW velocity also exhibits a variation with the direction of propagation, called angular dispersion. The elastic properties of anisotropic solids can be extracted from measured dispersion curves. SBS usually operates within the frequency range of 10 to 30 GHz. At such frequencies the elastic properties of thin layers from several nanometers up to a micron or so can be determined. Thicker films generally behave as bulk media. Recent measurements of the SAW dispersion in ultrathin diamond-like carbon films[109] show that mechanical properties of 2-nm thick film can be extracted from SBS data.

The measurement of the SAW dispersion curve by SBS is highly dependent on the type of layer under investigation. Single layers on substrates are commonly divided into two classes: loading or slow-on-fast layers and stiffening or fast-on-slow layers. The origin of these designations seems to be the paper of Tiersten[141] in which he studies the slope of the dispersion curve for $kh > 0$. A layer is said to stiffen the substrate when its presence, at whatever thickness, increases the velocity of the surface wave above that of the RW velocity of the substrate[43] and vice versa. Farnell and Adler[43] have established sufficient conditions for the layer to be loading or stiffening: $c_S^- < \sqrt{2}c_S^+$ and $c_S^- > \sqrt{2}c_S^+$ (c_S^- is the shear velocity in the layer, c_S^+ is the shear velocity in the substrate).

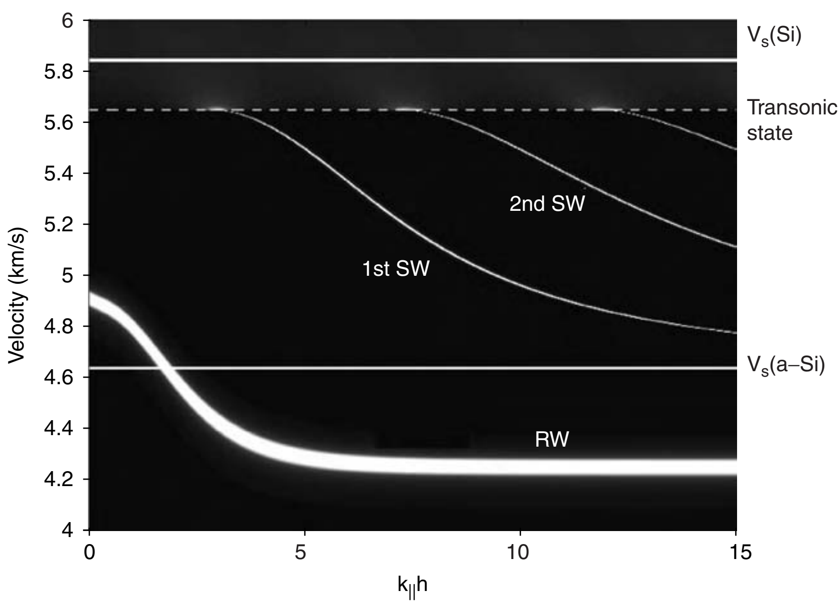

FIGURE 10.13
$ImG_{33}(k_{||}, \omega)/\omega$ for an amorphous silicon film on Si(001) for the [100] direction, a slow-on-fast system. It shows the dispersion of the Rayleigh and Sezawa waves.

10.4.3.1 Slow Film on Fast Substrate

Surface wave propagation in loading layers has been widely studied by SBS for various combinations of film and substrate: Al/Si,[142] gold/glass,[143] Al/NaCl,[101] CaF_2/Si,[144] ZnO/Si and ZnO/Al_2O_3,[14] polystyrene/Si,[146] and ZrB_3/Si.[71] An Al layer on Si was the first layered system where guided acoustic modes, detected by SBS, were satisfactorily explained in terms of ripple scattering at the film surface.[46] As an example, SAW propagation of an amorphous Si (*a*-Si) layer produced by ion bombardment will be considered here. Figure 10.13 depicts $ImG_{33}(k_{||}, \omega)/\omega$ by a grayscale as a function of $c = \omega/k_{||}$ and $k_{||}h$ for an amorphous silicon film on Si(001). In Figure 10.13, we plot only the modes with displacements in the sagittal plane. For the loading case, an infinite number of surface waves propagate:[43] RWs, PSAWs, Sezawa and Lamb modes, and various resonances within the continuum of bulk wave scattering. In Figure 10.13 the RW curve is much more intense than the Sezawa wave (SW) curves, because the RW is concentrated near the film surface to which $G_{33}(k_{||}, \omega)$ pertains. In the RW the displacement field is mainly concentrated near the free surface of the layer and it has a velocity that, with increasing layer thickness, approaches that of the RW of Si. It starts at the value of the RW on the substrate, 4.91 km/sec; for large $k_{||}h$, the Rayleigh SAW velocity tends asymptotically to a constant value of 4.25 km/sec, which is the phase velocity of the Rayleigh wave on the surface of bulk amorphous silicon.

The two horizontal lines labeled c_S(a-Si), 4.62 km/sec, and c(Si), 5.84 km/sec, are transverse bulk-wave-phase velocities in the layer and in the substrate, respectively. A lower transverse bulk-wave-phase velocity in the layer as compared with that of the substrate is necessary in order for SWs to exist. The horizontal-dashed line, $c = 5.65$ km/sec, corresponds to the transonic state in the substrate. The curves below the transonic state are the various orders of SWs, while curves for the pseudo-SWs lie above the transonic state. The essential difference between the SW and pseudo-SWs is understood in term of k_3 values of the partial waves. For the SW, which lies in the subsonic range in Figure 10.13, the partial waves in the substrate all have a complex value of k_3, and the corresponding displacement amplitudes decrease in an exponential fashion into the interior of the substrate. These properties allow the SW to propagate without attenuation along the surface, making it a true surface wave. In the case of a pseudo-SW, which lies in the supersonic range in Figure 10.13, one or more of the partial waves in the substrate has a real value of k_3. This bulk-wave component carries energy away from the surface into the interior of the substrate and causes the wave to decay with distance. We use the term pseudo-SW here because this particular pseudo-SAW is so closely related to the true Sezawa wave. The transition from one mode to the other is also clearly seen by the change in attenuation (Figure 10.13), which decreases suddenly when the wave no longer leaks energy into the substrate.

Figure 10.14 shows the measured and calculated dispersion curves for the Rayleigh SAW and Sezawa-type modes. For the dispersion curves of the

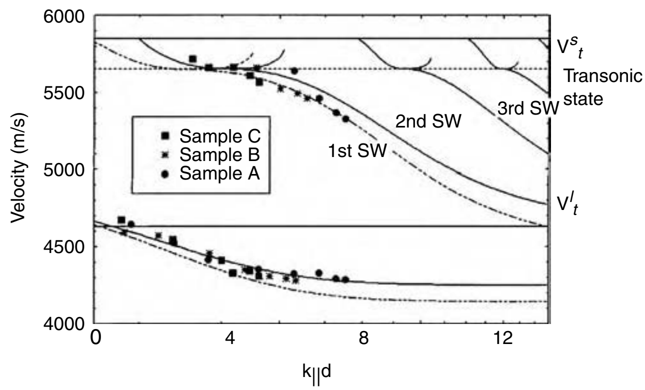

FIGURE 10.14
Dispersion relations for the [100] direction for an amorphous silicon film on Si(001). The two solid lines marked V_t^S and V_l^S represent the transverse bulk-wave velocity for the crystalline-silicon substrate and the amorphous silicon layer, respectively. The dotted-horizontal line indicates the transonic state. The solid curves represent calculated dispersion curves based on the model of a uniform amorphous layer on the (001) silicon surface and the elastic constants of the layer obtained from the present measurements. Dashed curves represent calculated dispersion curves from the elastic constants given in Table 10.2. RW: Rayleigh wave. 1st SW, etc. (From Zhang, X. et al., *Phys. Rev. B*, 58, 13677, 1998. With permission.)

Rayleigh and Sezawa-like modes, the solid lines are calculated using best fit elastic constants determined by comparison with SBS measurements in the paper.[26] There are also calculated curves for the higher-order Sezawa modes (Figure 10.14), but these modes were not observed for a-Si layer on Si.[26] For purposes of comparison, the dispersion curves of the Rayleigh-SAW and the first Sezawa-like excitation are also calculated using the literature values of the elastic constants of amorphous silicon. The agreement is within 2%.

The Sezawa and pseudo-Sezawa modes are commonly used in SBS for extracting elastic properties of slow-on-fast layers.[26,103] In the case of Brillouin spectroscopy measurements, very high velocity modes can be detected, so that for slow-on-fast layers numerous generalized Lamb modes can be measured on a single sample.[146]

The SAW dispersion for a-Si on Si mentioned above is representative of the slow-on-fast dispersion, although a small difference exists among these layers. Sklar[56] showed that depending on the layer/substrate combination, the pseudo-Sezawa mode for very thin layers tends to a different value. Values when $c_P < 2c_S$: for $k_{||}h \to 0$ the pseudo-Sezawa tends to the lateral wave, whose velocity is the longitudinal velocity of the substrate; values when $c_P > 2c_S$: the pseudo-Sezawa mode tends to a wave below the lateral longitudinal wave.

SAW wave propagation in the one-layer system, when layer and substrate have very close properties, has been discussed in detail by Lefeuvre.[147] The combination is situated near the border between stiffening and the loading layers. Such systems concern only a very few cases in practice, since the purpose of coatings is to change the surface properties of the material, generally affecting the elastic properties of the surface. For some combination of materials, a Stoneley wave can propagate.[43] A Stoneley wave is a localized mode that propagates along interface between two solids. It is nonattenuative because its velocity is lower than the bulk velocities of the two materials. When one of the materials is transparent, laser detection of interfacial waves is rendered possible.[48] Stoneley waves have thereby been measured by Brillouin spectroscopy by Bortolani et al.[148] for Ni on fused silica, by Bell et al.[149] at the interface molybdenum/fused silica, and by Jorna et al.[150] for Ni on ZnO.

10.4.3.2 Fast Film on Slow Substrate

Recent theoretical predictions[151] of the new superhard materials and production of the new superhard films such as cubic boron nitride (cBN), carbon nitride β-C_3N_4, B_4C, and CVD diamond films have excited considerable interest in the mechanical properties of thin hard and superhard films. Their hardness and abrasion resistant qualities, highly valued in technology and industry, are controlled by their large elastic moduli. Elastic properties of the superhard films need to be determined experimentally because they strongly depend on the synthesis conditions, and they cannot be derived from theoretical considerations alone. The thickness of such films commonly ranges from a few tens of nanometers up to the order of a micrometer. Recent studies have shown that SBS is an ideal technique for characterizing the new hard and superhard films.[95,105,107,152,153]

Despite the extensive literature on SAW propagation in layered solids, detailed study of SAW in stiffening layers (i.e., fast-on-slow systems) has only started recently.[152,154–156] Earlier computations of SAW propagation were usually restricted to true surface modes (surface waves that do not leak energy into bulk), but for stiffening layers the SAW propagation is mostly characterized by PSAWs. Also, the calculation of PSAWs is complicated by the attenuated nature of these modes; two parameters, the velocity and the attenuation of the SAW, should be computed. There have been only a few experimental studies performed on hard coatings because attenuation causes scattering in the results and lowers the quality of the signal.

Recent calculations of the dispersion of SAW above cutoff in stiffening systems[154] have revealed two types of SAW dispersion for fast-on-slow systems. It was shown that the SAW velocity initially grows with increasing $k_{||}h$. At a critical value $k_{||}h_{\text{cut}}$ the SAW meets and degenerates with the bulk wave continuum. Beyond this cutoff, while a true SAW no longer exists, there is a PSAW, which radiates energy into the substrate and attenuates with distance as it travels along the surface. The first type of behavior comes about when the elastic properties of the layer and the substrate are not very different, and has the velocity of the pseudo-SAW beyond cutoff increasing up to the RW velocity of the layer. This type of behavior is called the *nonsplitting* type and was first observed experimentally by Pang et al.[152,157] The second type of behavior arises when the elastic properties of the two

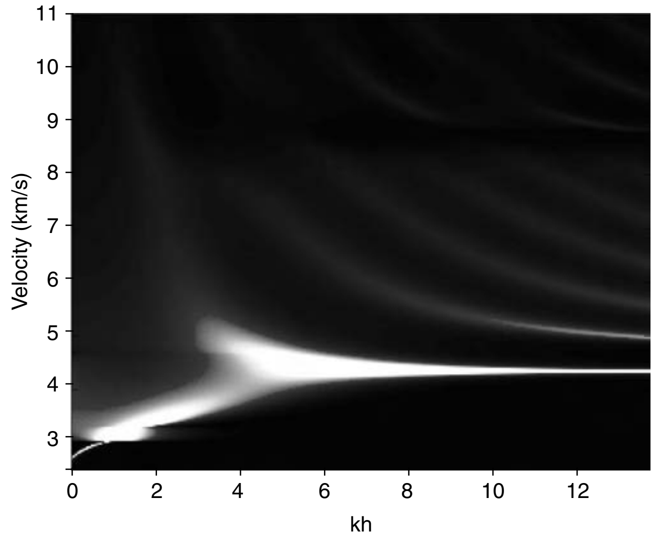

FIGURE 10.15
Two-dimensional grayscale image of the calculated Brillouin spectra of Si_3N_4/GaAs at the free Si_3N_4 surface. (From Zinin, P.V. et al., *Phys. Rev. B,* 60, 2844, 1999. With permission.)

materials are quite dissimilar and has the PSAW evolving into a strongly attenuated interfacial mode, while a second mode appears at a higher velocity and evolves into the RW at the free surface of the layer. This second type of behavior of the dispersion relation was called the *splitting type*.[154] A more detailed description of the behavior of the SAW dispersion curves for fast-on-slow systems for different combinations of films and substrates can be found elsewhere.[147]

The dispersion of SAWs in Si_3N_4 film on a GaAs substrate is an example of the splitting type of dispersion curve measured by SBS. Si_3N_4 film on GaAs is a stiffening system since c_S of the Si_3N_4 and GaAs are 4.7 km/sec and 3.3 km/sec, respectively.[105] In experiments, only one branch of the dispersion curve was measured. It corresponded to SAWs propagating in the [100] direction on the (001) GaAs surface. The Si_3N_4 film was assumed to be isotropic.[158] Grayscale images representing the calculated Brillouin intensity as a function of velocity $c = \omega/k_{||}$ and $k_{||}h$, for scattering from the free surface of the film and from the interface between the film and substrate for the [100] direction in the (001) surface of GaAs are presented in Figure 10.15 and Figure 10.16, respectively. The grayscale intensity in these images is proportional to $\omega^{-1}Im[G_{33}(k_{||}, x_3, \omega + i0)]$, with $x_3 = 0$ for the interface and $x_3 = -h$ for the surface of the film. Elastic constants used for the calculation are given in Table 10.2. For $k_{||}h = 0$, the velocity corresponds to the SAW velocity on the GaAs substrate. With increasing $k_{||}h$ the SAW velocity approaches the bulk wave threshold or limiting shear slowness $k_{||}/\omega$, which is reached at $k_{||}h_{cut} \approx 1.5$. Below $k_{||}h_{cut}$ the Brillouin spectrum displays a sharp peak that is

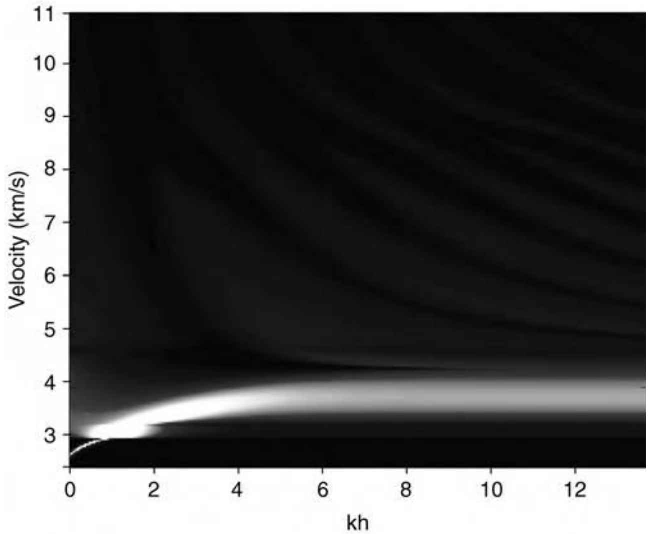

FIGURE 10.16
Two-dimensional gray image of the calculated Brillouin spectrum at the Si_3N_4/GaAs interface (From Zinin, P.V. et al., *Phys. Rev. B*, 60, 2844, 1999. With permission.)

TABLE 10.2
The Elastic Properties Used in the Calculations of the Power Spectra Shown in Figures 10.4, 10.8, 10.11, 10.13, 10.15, and 10.16

Materials	Density (kg/m^3)	C_{11} (GPa)	C_{22} (GPa)	C_{44} (GPa)	Ref.
a-carbon (sample B)	3150	868		376	106
Si	2332	165.7	63.9	79.6	26
a-Si	2230	138		48	26
GaAs	5318	118.1	53.2	59.4	128
Si_3N_4 (polycrystalline)	2500	189		56	158
bcc Co		212	165	53	159

associated with the true surface wave and a continuum extending from the bulk wave threshold to higher frequencies, which is known as the Lamb shoulder.

In our calculation of the Green's function (Equation 10.41), a small amount of artificial damping [58] is introduced to avoid a true singularity. In the region below cutoff, the position of the SAW peak is the same for surface and interface scattering. At $k_{||}h_{cut}$, the SAW degenerates with the bulk continuum, and beyond cutoff there is no true SAW. In its place there are broadened resonances that are associated with attenuated PSAWs at the interface or surface of the film and that leak energy into the substrate. Somewhat above the cutoff velocity, the Brillouin spectrum for the interface displays a broad peak that becomes independent of the film thickness beyond $k_{||}h \sim 4$. This peak is associated with a highly damped interfacial wave. Its broadening is

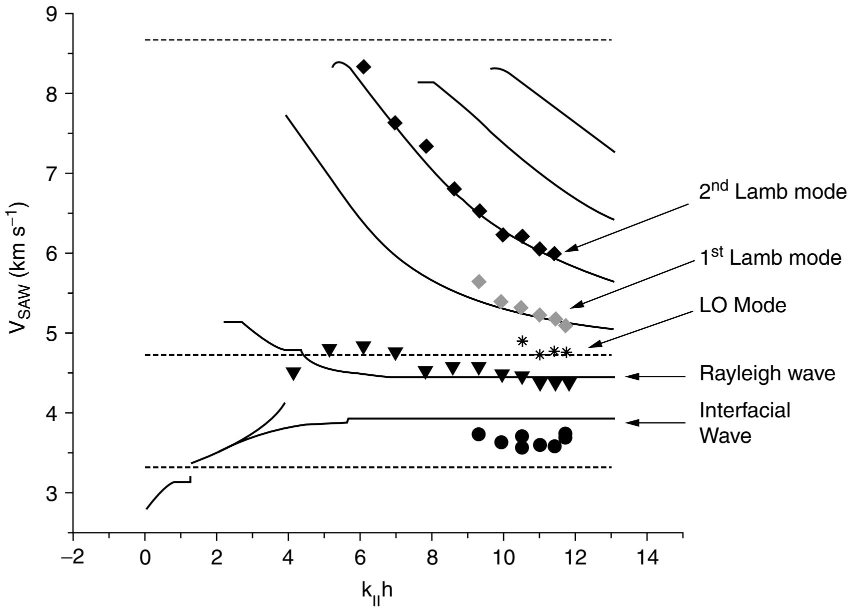

FIGURE 10.17
Dispersion curves calculated using the Green's function and experimental results of Si_3N_4/GaAs. Dashed lines are shear cutoff (lower line), longitudinal cutoff (middle line) for GaAs and longitudinal cutoff for Si_3N_4 (upper line). (From Zinin, P.V. et al., *Phys. Rev. B*, 60, 2844, 1999. With permission.)

due to leakage of energy into the substrate as discussed in Lefeuvre et al.[154] In the same spectral region, the calculated Brillouin spectrum for the surface of the film displays a broad peak that fades away by $k_{||}h \sim 4$. At this point another broad peak appears that becomes narrow with increasing $k_{||}h$ as the associated mode tends toward the Rayleigh mode of Si_3N_4. For very large $k_{||}h$ this becomes the true nondispersive Rayleigh SAW.

The dispersion curves in Figure 10.17 represent the traces of the maxima of the calculated Brillouin intensity (Figure 10.16) for the interface (the lowest solid line) and surface (Figure 10.15; the upper solid lines) and of the measured Brillouin intensity. The experimental data are found to be in excellent agreement with the theoretical predictions, except for the interfacial mode and the fact of the disappearance of the first Lamb mode in the measured spectrum at small $k_{||}h$. The former discrepancy suggests that the interface is more complicated than assumed in our model.

Among all hard or stiff films, diamond-like coatings (DLCs) appear to have the widest range of applications. It was found recently that SBS measurements of thin DLC films allow detection of the LGM.[107,108] Detection of the LGM allows both C_{11} and C_{44} of such films to be obtained from SBS measurements.

10.4.3.3 Anisotropic Supported Films

The elastic properties of anisotropic layered solids can be investigated either by measuring the frequency or angular dispersion curves by SBS. Experimental data[159] for a body-centered-cubic cobalt (Co) film on the (110) plane

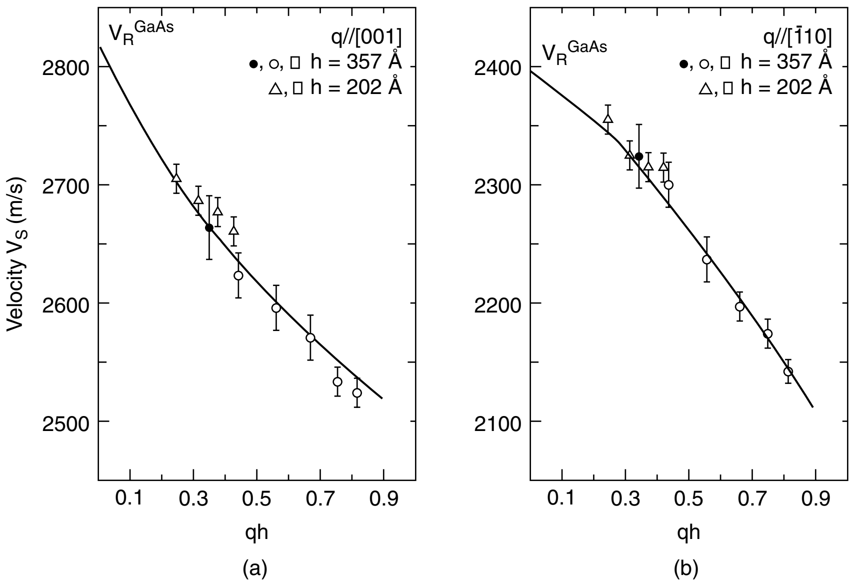

FIGURE 10.18
The measured (solid and triangles) and calculated (solid line) dispersion curves for the Rayleigh mode for 35.7- and 20.0-nm-thick bcc cobalt films of (110) GaAs. The two panels refers to propagation direction along [001] and $[\bar{1}10]$. Data represented by open circles and triangles were taken with 515-nm radiation, while solid circle was taken at 647 nm. (From Subramanian, S. et al., *Phys. Rev. B*, 49, 17319, 1994. With permission.)

of GaAs are presented in Figure 10.18. A strong RW peak is observed in the SBS spectrum along the [001] and $[\bar{1}10]$ directions in the (110) oriented film. To determine the elastic moduli of the cubic Co films (C_{11}, C_{12} and C_{44}), Subramanian et al.[159] proposed simultaneously fitting the frequency RW dispersions in these directions. Figure 10,18 shows the frequency dispersion curves for Co films along the [001] and $[\bar{1}10]$ directions in (110) oriented Co film on (110) GaAs. The study again demonstrated that values of the elastic moduli of thin films generally are different from the corresponding values in the bulk. Measurements of the frequency dispersion curve of the RW yield up to a 65% reduction in the values of C_{11} and C_{44} for the Co film.

Nizzoli at al.[111] reported SBS experiments on LB films, for which the anisotropy of the elastic properties could be regarded as having hexagonal symmetry, with the *c* axis, in the plane of the films. LB layers were grown on molybdenum and represent slow-on-fast systems. The stiffness matrix of anisotropic solids of hexagonal symmetry contains five independent elastic moduli (C_{11}, C_{12}, C_{13},C_{33} and C_{44}), and it is a nontrivial matter to determine all five constants[160] from conventional SBS measurements. In the article[111] the x_3-axis was chosen to be parallel to the molecular *c*-axis of the films and was in the plane of the film. The x_1-axis was chosen to be normal to the molecular *c*-axis of the films and was in the plane of the film. In such a coordinate system, C_{33} (C_{11}) is the longitudinal elastic modulus for phonons propagating parallel to the film and parallel (perpendicular) to the molecular axis. Observation of the LGM along the x_1-axis gave the value of the C_{11} modulus. SBS measurements along x_1 for different films thicknesses provided the dispersion curves for the RWs and SWs. A best fit to the data points of the RW and SW gave values of the C_{12} elastic modulus. The elastic modulus C_{33} was determined from the position of the LGM peak observed in the x_3-direction. To obtain the last two moduli, C_{44} and C_{13}, Nizzoli et al.[111] fitted the RW and bulk peaks in the SBS spectrum measured in the x_3-direction.

SAW propagation in hexagonal hBN films on a silicon substrate was studied by Wittkowski et al.[116] It was claimed that four independent elastic constants had been determined from the frequency dispersion of the Rayleigh and Sezawa modes. The elastic moduli obtained by Wittkowski et al. were used to describe SAW propagation in a two layer system: a stiff layer of cBN on a soft layer of hBN deposited on Si(111).[156] The GRW below shear cutoff and the PSAW above cutoff were detected by SBS. It was found that incorporating the hBN interlayer into a model of the SBS response and precise thickness measurement of the cBN layer and hBN interlayer fully describes the behavior of the SAW dispersion in deposited cBN layered systems. The most prominent example of application of SBS in studying elastic properties of multilayered systems is elastic characterization of superlattices, structures that consist of altering layers of different media with different thicknesses.[3] The ability to design a layered structure from films of different symmetry has resulted in a wide variety of superlattices with different elastic properties.[161–163] SBS has proved to be a powerful nondestructive tool for the elastic characterization of superlattices, but this is a subject beyond the scope of this chapter. For detailed discussion of the subject see Nizzoli et al.[3] and Comins.[16]

10.5 Concluding Remarks

Brillouin scattering, the scattering of an optical wave by an acoustical wave, provides a method to measure acoustical velocities at submicrometric wavelengths, corresponding to frequencies ranging from a few gigahertz to above 30 GHz for SAWs and up to above 100 GHz for bulk waves. Measurements are contactless, requiring only optical access to the sample, and local, allowing measurements on millimetric and submillimetric specimens. These characteristics qualify Brillouin scattering as a nondestructive ultrasonic testing technique. SBS has been extensively exploited to probe the acoustical properties and derive the elastic properties of bulk materials and thin films. SBS has a particular potential for the characterization of both submicrometric and nanometric films. The principles of the method have been reviewed, and the technical implementation has been discussed. An overview has finally been given of various recent applications of SBS to the characterization of various types of materials and of films.

The range of application of SBS has been growing in recent years as the dimensions of structures used in industry has moved down to the nanoscale region, for which SBS measurements of SAWs can be done most effectively. It must be noted that this is an active field of research; the performances of SBS for the elastic characterization of films are being pushed further, and nontraditional applications are being explored. Indeed, SBS has been used to study the melting transition of tin nanocrystals embedded in a silica film,[9] as well as probe residual stress through the acoustoelastic effect.[164] Thin films deposited on a substrate are usually in a state of stress that can reach several gigapascal, as in the case of epitaxial films such as Ge on Si, and surface wave velocity measurements constitute a valuable method for characterizing such a stress state. Other growing applications exploit the contactless nature of the technique to extend SBS measurements to high temperature[152] and high-pressure[104] regions. Measurements of the velocities of the RWs and SWs in thick gold film at 4.8 GPa demonstrated the potential of the SBS techniques in high-pressure physics of the elastic properties of opaque materials.

Acknowledgments

The authors would like to thank Diane Henderson for working with the manuscript. This research was supported for Pavel Zinin through a National Institutes of Standards and Technology Advanced Technology Program (ATP), cooperative agreement number 70NANBOH3048, U.S. Army Contract No. DAAD19-00-1-0569, and the National Science Foundation Grants No. DMR-0102215. Arthur Every's research was supported by the South African National Research Foundation under grant number 2053311.

References

1. Zinin, P.V., Quantitative acoustic microscopy of solids, in *Handbook of Elastic Properties of Solids, Liquids, and Gases. Volume I: Dynamic Methods for Measuring the Elastic Properties of Solids*, Levy, M., Bass, H., Stern, R., and Keppens, V., Eds., Academic Press, New York, 2001, pp. 187–226.

2. Lomonosov, A., Mayer, A.P., and Hess, P., Laser controlled surface acoustic waves, in *Handbook of Elastic Properties of Solids, Liquids, and Gases. Volume I: Dynamic Methods for Measuring the Elastic Properties of Solids*, Levy, M., Bass, H., Stern, R., and Keppens, V., Eds., Academic Press, New York, 2001, pp. 137–186.
3. Nizzoli, F. and Sandercok, J.R., Surface Brillouin scattering from phonons, in *Dynamical Properties of Solids*, Horton, G.K. and Maradudin, A.A., Eds., Elsevier, New York, 1990, pp. 285–335.
4. Mutti, P., Bottani, C.E., Ghislotti, G., Beghi, M., Briggs, G.A.D., and Sandercock, J.R., Surface Brillouin scattering: extending surface wave measurements to 20 GHz, in *Advanced in Acoustic Microscopy*, Briggs, A., Ed., Plenum Press, New York, 1995, pp. 249–300.
5. Sathish, S., Mendik, M., Kulik, A., Gremaud, G., and Wachter, P., Polish induced surface damage in nickel — scanning acoustic microscopy and Brillouin scatterings study, *Appl. Phys. Lett.*, 59, 167–168, 1991.
6. Jiang, X., Wang, M., Schmidt, K., Dunlop, E., Haupt, J., and Gissler, W., Elastic constants and hardness of ion beam sputtered TiNx films measured by Brillouin scattering and depth-sensing indentation, *J. Appl. Phys.*, 69, 3053–3057, 1991.
7. Jiang, X., Harzer, J.V., Hillebrands, B., Wild, C., and Koidl, P., Brillouin light scattering on chemical vapor deposited polycrystalline diamond: evaluation of the elastic moduli, *Appl. Phys. Lett*., 59, 1055–1057, 1991.
8. Stoddart, P.R., Comins, J.D., and Every, A.G., Brillouin-scattering measurements of surface-acoustic-wave velocities in silicon at high-temperatures, *Phys. Rev. B*, 51, 17574–17578, 1995.
9. Bottani, C.E., Li Bassi, A., and Kofman, R., Melting in metallic Sn nanoparticles studied by surface Brillouin scattering and synchrotron-x-ray diffraction, *Phys. Rev. B*, 59, R15601, 1999.
10. Zhang, X., Comins, J.D., Every, A.G., and Derry, T.E., Use of surface Brillouin scattering to examine a structural phase transition in carbon-ion-bombarded silicon during high-temperature annealing, *Phys. Rev. B*, 65, 012106, 2002.
11. Bassett, W.A., Dynamic measurements of elastic moduli of samples at high pressure and temperature, in *Handbook of Elastic Properties of Solids, Liquids, and Gases. Volume I: Dynamic Methods for Measuring the Elastic Properties of Solids*, Levy, M., Bass, H., Stern, R., and Keppens, V., Eds., Academic Press, New York, 2001, pp. 469–487.
12. Sandercock, J.R., Trends in Brillouin-scattering: studies of opaque materials, supported films, and central modes, in *Light Scattering in Solids. III. Recent Results*, Cardona, M. and Guntherodt, G., Eds., Springer-Verlag, Berlin, 1982, pp. 173–206.
13. Landau, L.D. and Lifshitz, E.M., *Mechanics*, 2nd ed., Pergamon Press, Oxford, New York, 1969.
14. Nye, J.F., *Physical Properties of Crystals,* Clarendon Press, Oxford, 1985.
15. Every, A.G., The elastic properties of solids: static and dynamic principles, in *Handbook of Elastic Properties of Solids, Liquids, and Gases. Volume I: Dynamic Methods for Measuring the Elastic Properties of Solids*, Levy, M., Bass, H., Stern, R., and Keppens, V., Eds., Academic Press, New York, 2001, pp. 3–36.
16. Comins, J.D., Surface Brillouin scattering, in *Handbook of Elastic Properties of Solids, Liquids, and Gases. Volume I: Dynamical Methods for Measuring the Elastic Properties of Solids*, Levy, M., Bass, H., Stern, R., and Keppens, V., Eds., Academic Press, New York, 2001, pp. 349–378.

17. Loudon, R., Theory of surface-ripple Brillouin scattering by solids, *Phys. Rev. Lett.*, 40, 581–583, 1978.
18. Loudon, R., Theory of lineshapes for normal-incidence Brillouin scattering by acoustic phonons, *J. Phys. C: Solid State Phys.*, 11, 403–417, 1978.
19. Subbaswamy, K.R. and Maradudin, A.A., Photoelastic and surface-corrugation contribution to Brillouin scattering from an opaque crystal, *Phys. Rev. B*, 18, 4181–4199, 1978.
20. Loudon, R. and Sandercock, J.R., Analysis of the light-scattering cross section for surface ripples on solids, *J. Phys. C: Solid State Phys.,*13, 2609–2622, 1980.
21. Marvin, A.M., Bortolani, V., and Nizzoli, F., Surface Brillouin scattering from acoustic phonons. I. General theory, *J. Phys. C: Solid State Phys.*, 13, 299–317, 1980.
22. Marvin, A.M., Bortolani, V., Nizzoli, F., and Santoro, G., Surface Brillouin scattering from acoustic phonons. II. Application to semiconductors, *J. Phys. C: Solid State Phys.*, 13, 1607–1616, 1980.
23. Velasco, V.R. and Garcia-Moliner, F., Theory of surface waves in anisotropic cubic crystals, *J. Phys. C: Solid St. Phys.*, 13, 2237–2256, 1980.
24. Rowell, N.L. and Stegeman, G.I., Theory of Brillouin scattering from opaque media, *Phys. Rev. B*, 18, 2598–2615, 1978.
25. Mills, D.L. and Subbaswamy, K.R., Surface and size effects on the light scattering spectra of solids, in *Progress in Optics*, Wolf, E., Ed., North Holland, Amsterdam, 1981, p. 45.
26. Zhang, X., Comins, J.D., Every, A.G., Stoddart, P.R., Pang, W., and Derry, T.E., Surface Brillouin scattering study of the surface excitations in amorphous silicon layers produced by ion bombardment, *Phys. Rev. B*, 58, 13677–13685, 1998.
27. Dil, J.G., Brillouin scattering in condensed matter, *Rep. Prog. Phys.*, 45, 285–334, 1982.
28. Fedorov, F.I., *Theory of Elastic Waves in Crystals*, Plenum Press, New York, 1968.
29. Musgrave, M.J.P., *Crystal Acoustics: Introduction to the Study of Elastic Waves and Vibrations in Crystals*, Holden-Day, San Francisco, 1970.
30. Achenbach, J.D., *Wave Propagation in Elastic Solids*, North-Holland, Amsterdam, 1973.
31. Dieulesaint, E. and Royer, D., *Elastic Waves in Solids: Applications to Signal Processing*, John Wiley, Chichester, 1980.
32. Auld, B.A., *Acoustic Fields and Waves in Solids*, Robert E. Krieger Publishing Company, Malabar, FL, 1990.
33. Nayfeh, A.H., *Wave Propagation in Layered Anisotropic Media: With Applications to Composites*, Elsevier, Amsterdam, New York, 1995.
34. Rose, J.L., *Ultrasonic Waves in Solid Media*, Cambridge University Press, London, 1999.
35. Wolfe, J.P., *Imaging Phonons: Acoustic Wave Propagation in Solids*, Cambridge University Press, London, 1998.
36. Farnell, G.W., Properties of elastic surface waves, in *Physical Acoustics*, Mason, W.P. and Thurston, R.N., Eds., Academic Press, New York, 1970, pp. 109–166.
37. Hickernell, F.S., Surface acoustic wave technology: macrosuccess through microseisms, in *Physical Acoustics*, Thurston, R.N., Pierce, A.D., and Papadakis, E., Eds., Academic Press, New York, 1999, pp. 136–208.
38. Every, A.G., Pseudosurface wave structures in phonon imaging, *Phys. Rev. B*, 33, 2719–2732, 1986.
39. Stoneley, R., Elastic waves at the surface of separation of two solids, *Proc. Roy. Soc.*, 106, 416–428, 1924.

40. Scholte, J.G., The range and existence of Rayleigh and Stoneley waves, *Mon. Not. Roy. Astron. Soc.*, (Geophys. Suppl.) 5, 120–126, 1947.
41. Pilant, W.L., Complex roots of the Stoneley-wave equation, *Bull. Seismol. Soc. Am.*, 62, 285–299, 1972.
42. Hillebrands, B., Lee, S., Stegeman, G.I., Cheng, H., Potts, J.E., and Nizzoli, F., A new class of guided longitudinal acoustic phonons in ZnSe films on GaAs found by surface Brillouin-scattering, *Surf. Sci*., 211, 387–393, 1989.
43. Farnell, G.W. and Adler, E.L., Elastic wave propagation in thin layers, in *Physical Acoustics*, Mason, W.P. and Thurston, R.N., Eds., Academic Press, New York, 1972, pp. 35–127.
44. Viktorov, I.A., *Rayleigh and Lamb Waves: Physical Theory and Applications*, Plenum Press, New York, 1967.
45. Grimsditch, M., Brillouin scattering, in *Handbook of Elastic Properties of Solids, Liquids, and Gases. Volume I: Dynamical Methods for Measuring the Elastic Properties of Solids*, Levy, M., Bass, H., Stern, R., and Keppens, V., Eds., Academic Press, New York, 2001.
46. Bortolani, V., Nizzoli, F., and Santoro, G., Surface density of acoustic phonons in GaAs, *Phys. Rev. Lett*., 41, 39–42, 1978.
47. Albuquerque, E.L., Loudon, R., and Tilley, D.R., Theory of normal incidence Brillouin scattering by acoustic phonons in a supported thin film, *J. Phys. C: Solid State Phys*., 12, 5297–5310, 1979.
48. Albuquerque, E.L., Theory of Brillouin scattering by Stoneley waves, *J. Physics C: Solid St. Phys*., 13, 2623–2639, 1980.
49. Albuquerque, E.L., Oliveros, M.C., and Tilley, D.R., Theory of Brillouin-scattering from an isotropic elastic film, *J. Phys. C. Solid State Phys.*, 17, 1451–1463, 1984.
50. Bortolani, V., Marvin, A.M., Nizzoli, F., and Santoro, G., Theory of Brillouin scattering from surface acoustic phonons in supported films, *J. Phys. C. Solid State Phys.*, 16, 1757–1776, 1983.
51. Byloos, C., Giovannini, L., and Nizzoli, F., Theory of the elasto optic coupling for surface Brillouin scattering in a supported bilayer, *Phys. Rev. B*, 51, 9867–9874, 1995.
52. Every, A.G., Surface Brillouin scattering mediated by the ripple mechanism, Unpublished, 1996.
53. Cottam, M.G. and Maradudin, A.A., Surface linear response functions, in *Surface Excitations*, Agranovich, V.M. and Loudon, R., Eds., Elsevier Science, London, 1984, pp. 5–193.
54. Byron, F.W. and Fuller, R.W., *Mathematics of Classical and Quantum Physics*, Dover Publications, New York, 1992, p. 248.
55. Nayfeh, A.H., The general problem of elastic wave propagation in multilayered anisotropic media, *J. Acoust. Soc. Am*., 89, 1521–1531, 1991.
56. Sklar, Z., *Quantitative Acoustic Microscopy of Coated Materials*, University of Oxford, 1993.
57. Zhang, X., Comins, J.D., Every, A.G., and Stoddart, P.R., Surface Brillouin scattering studies on vanadium carbide, *Int. J. Refrac. Metals Hard Mater.*, 16, 303–308, 1998.
58. Every, A.G., Kim, K.Y., and Maznev, A.A., The elastodynamic response of semi-infinite anisotropic solid to sudden elastic surface loading, *J. Acoust. Soc. Amer.*, 102, 1–10, 1997.
59. Malischewsky, P., *Surface Waves and Discontinuities*, Elsevier, Amsterdam, 1987.

60. Malischewsky, P.G., Comment to "A new formula for the velocity of Rayleigh waves" by D. Nkemzi, [*Wave Motion*, 26, 199–205, 1997], *Wave Motion*, 31, 93–96, 2000.
61. Royer, D., A study of the secular equation for Rayleigh waves using the root locus method, *Ultrasonics*, 39, 223–225, 2001.
62. Nkemzi, D., A new formula for the velocity of Rayleigh waves, *Wave Motion*, 26, 199–205, 1997.
63. Camley, R.E. and Nizzoli, F., Longitudinal resonance in surface acoustic phonons, *J. Phys. C. Solid Stat. Phys.*, 18, 4795–4804, 1985.
64. Sandercock, J.R., Light scattering from surface acoustic phonons in metals and semiconductors, *Solid State Commun.*, 26, 547–551, 1978.
65. Glass, N.E. and Maradudin, A.A., Leaky surface-elastic waves of both flat and strongly corrugated surfaces for isotropic, nondissipative media, *J. Appl. Phys.*, 54, 796–805, 1983.
66. Mozhaev, V.G., Bosia, F., and Weihnacht, M., Types of leaky SAW degeneracy in crystals, in Proc. *of 1998 IEEE Ultrasonics Symp.*, Levy, M., Schneider, S.C., and McAvoy, B.R., Eds., Institute of Electrical and Electronics Engineers, New York, 1998, pp. 143–148.
67. Rahman, N. and Barber, J.R., Exact expressions for the roots of the secular equation for Rayleigh waves, *ASME J. Appl. Mech.*, 62, 250–252, 1995.
68. Krüger, J.K., Brillouin spectroscopy and its application to polymers, in *Optical Techniques to Characterize Polymer Systems*, Bassler Elsevier, Amsterdam, 1989.
69. Zouboulis, E.S., Grimsditch, M., Ramdas, A.K., and Rodriguez, S., Temperature dependence of the elastic moduli of diamond: a Brillouin-scattering study, *Phys. Rev. B*, 57, 2889–2896, 1998.
70. Vogelgesang, R., Ramdas, A.K., Rodriguez, S., Grimsditch, M., and Anthony, T.R., Brillouin and Raman scattering in natural and isotopically controlled diamond, *Phys. Rev. B*, 54, 3989–3999, 1996.
71. Chirita, M., Xia, H., Sooryakumar, R., Tolle, J.B., Torres, V.M., Wilkens, B.J., Smith, D.J., Kouvetakis, J., and Tsong, I.S.T., Elastic properties of nanocrystalline zirconium–silicon–boron thin films, *J. Appl. Phys.*, 89, 4349–4353, 2001.
72. Djemia, P., Dugautier, C., Chauveau, T., Dogheche, E., De Barros, M.I., and Vandenbulcke, L., Mechanical properties of diamond films: A comparative study of polycrystalline and smooth fine-grained diamonds by Brillouin light scattering, *J. Appl. Phys.*, 90, 3771–3779, 2001.
73. Fukui, M., Toda, O., So, V.C.Y., and Stegemann, G.I., Surface plasmon enhanced Brillouin scattering from metal films, *Solid State Commun.*, 36, 995–1000, 1980.
74. Fukui, M., Toda, O., So, V.C.Y., and Stegemann, G.I., Enhanced Brillouin scattering involving surface plasmon polaritons, *J. Phys. C*, 14, 5591–5607, 1981.
75. Moretti, A.L., Robertson, W.M., Fisher, B., and Bray, R., Surface enhanced Brillouin scattering on silver films, *Phys. Rev. B*, 31, 3361–3368, 1985.
76. Robertson, W.M., Moretti, A.L., and Bray, R., Surface plasmon enhanced Brillouin scattering on silver films — double-resonance effect, *Phys. Rev. B*, 35, 8919–8928, 1987.
77. Rowell, N.L. and Stegeman, G.I., Brillouin scattering in thin film optical waveguides. II. Scattering theory, *Can. J. Phys.*, 60, 1804–1820, 1982.
78. Krüger, J.K., Embs, J., Brierley, J., and Jimenez, R., A new Brillouin scattering technique for the investigation of acoustic and opto-acoustic properties: application to polymers, *J. Phys. D: Appl. Phys.*, 31, 1913–1917, 1998.

79. Krüger, J.K., Embs, J., Lukas, S., Hartmann, U., Brierley, J., Beck, C.M., Jimenez, R., Alnot, P., and Durand, O., Spatial and angle distribution of internal stresses in nano- and microstructured chemical vapor deposited diamond as revealed by Brillouin spectroscopy, *J. Appl. Phys.*, 87, 74–77, 2000.
80. Vaughan, J.M., *The Fabry-Perot Interferometer*, Adam Hilger, Bristol, U.K., 1989.
81. Sandercock, J.R., Brillouin scattering study of SbSI using a double-passed, stabilized scanning interferometer, *Opt. Commun.*, 2, 73–76, 1970.
82. Sandercock, J.R., in *Proc. 2nd Int. Conf. on Light Scattering in Solids*, M. Balkanski, Ed., Flammarion, New York, 1971, pp. 9–12 and 219–223.
83. Sandercock, J.R., in *Proc. VII Int. Conf. on Raman Spectroscopy*, Ottawa 1980, W.F. Murphy, Ed., North Holland, Amsterdam, p. 364–367.
84a. Dil, J.G. and Brody, E.M., Brillouin scattering from isotropic metals, *Phys. Rev. B*, 14, 5218–5227, 1976.
84b. Lindsay, S. M., and Shepherd I. W., A high contrast multipass Fabry–Perot spectrometer, *J. Phys. E: Sci. Instrum*. 10, 150–154, 1977.
84c. Dil, J.G. and van Hijningen, N.C.J., Brillouin scattering near a rigid interface, *Phys. Rev. B*, 22, 5924–5935, 1980.
84d. Dil, J.G., van Hijningen, N.C.J., van Dorst, F., and Aarts, R.M., Tandem multipass Fabry-Perot interferometer for Brillouin scattering, *Appl. Opt.*, 20, 1374–1381, 1981.
85. Lindsay, S.M., Anderson, M.W., and Sandercock, J.R., Construction and alignment of a high performance multipass vernier tandem Fabry–Perot interferometer, *Rev. Sci. Instrum.*, 52, 1478–1486, 1981.
86. Hillebrands, B., Progress in multipass tandem Fabry–Perot interferometry: I. A fully automated, easy to use, self-aligning spectrometer with increased stability and flexibility, *Rev. Sci. Instrum.*, 70, 1589–1598, 1999.
87. Vacher, R. and Pelous, J., Behavior of thermal phonons in amorphous media from 4 to 300 K, *Phys. Rev. B*, 14, 823–828, 1976.
88. Tanaka, H. and Sonehara, T., Superheterodyne light beating spectroscopy for Rayleigh–Brillouin scattering using frequency-tunable lasers, *Rev. Sci. Instr.*, 73, 1998–2010, 2002.
89. Tanaka, H. and Sonehara, T., New method of superheterodyne light beating spectroscopy for Brillouin scattering using frequency-tunable lasers, *Phys. Rev. Lett.*, 74, 1609–1612, 1995.
90. Stoddart, P.R., Crowhurst, J.C., Every, A.G., and Comins, J.D., Measurement precision in surface Brillouin scattering, *J. Opt. Soc. Am. B*, 15, 2481–2489, 1998.
91. Agarwal, G.S., Interaction of electromagnetic waves at rough dielectric surfaces, *Phys. Rev. B*, 15, 2371–2383, 1977.
92. Zhang, X., Sooryakumar, R., Every, A.G., and Manghnani, M.H., Observation of organ-pipe acoustic excitations in supported thin films, *Phys. Rev. B*, 64, 081402(R), 2001.
93. Vacher, R. and Boyer, L., Brillouin scattering: A tool for the measurement of elastic and photoelastic constants, *Phys. Rev. B*, 6, 639–673, 1972.
94. Fioretto, D., Carlotti, G., Socino, G., Modesti, S., Cepek, C., Giovannini, L., Donzelli, O., and Nizzoli, F., Brillouin-scattering determination of the elastic constants of epitaxial fcc C_{60} film, *Phys. Rev. B*, 52, R8707–R8710, 1995.
95. Lefeuvre, O., Pang, W., Zinin, P., Comins, J.D., Every, A.G., Briggs, G.A.D., Zeller, B.D., and E.T.G., Determination of the elastic properties of a barrier film on aluminium by Brillouin spectroscopy, *Thin Solid Films*, 350, 53–58, 1999.

96. Beghi, M.G., Bottani, C.E., and Pastorelli, R., High accuracy measurement of elastic constants of thin films by surface Brillouin scattering, in *Mechanical Properties of Structural Films*, Muhlstein, C. and Brown, S.B., American Society for Testing and Materials, Conshohoken, PA, 2001, pp. 109–126.
97. Comins, J.D., Every, A.G., Stoddart, P.R., Zhang, X., Crowhurst, J.C., and Hearne, G.R., Surface Brillouin scattering of opaque solids and thin supported films, *Ultrasonics*, 38, 450–458, 2000.
98. Zhang, X., Stoddart, P.R., Comins, J.D., and Every, A.G., High-temperature elastic properties of a nickel-based superalloy studied by surface Brillouin scattering, *J. Phys. Condens. Matter.*, 13, 2281–2294, 2001.
99. Makarov, S., Chilla, E., and Frolich, H.J., Determination of elastic constants of thin films from phase velocity dispersion of different surface acoustic wave modes, *J. Appl. Phys.*, 78, 5028–5034, 1995.
100. Beghi, M.G., Ferrari, A.C., Bottani, C.E., Libassi, A., Tanner, B.K., Teo, K.B.K., and Robertson, J., Elastic constants and structural properties of nanometre-thick diamond-like carbon films, *Diamond Relat. Mater.*, 11, 1062–1067, 2002.
101. Nizzoli, F., Bhadra, R., Delima, O.F., Brodsky, M.B., and Grimsditch, M., Problems with the determination of elastic constants from higher order surface waves: results for Al on NaCl, *Phys. Rev. B*, 37, 1007–1010, 1988.
102. Lee, S., Hillebrands, B., Stegeman, G.I., Cheng, H., Potts, J.E., and Nizzoli, F., Elastic properties of epitaxial ZnSe(001) films on GaAs measured by Brillouin spectroscopy, *J. Appl. Phys.*, 63, 1914–1916, 1988.
103. Beghi, M.G., Bottani, C.E., Ossi, P.M., Lafford, T.A., and Tanner, K., Combined surface Brillouin scattering and x-ray reflectivity characterization of thin metallic films, *J. Appl. Phys.*, 81, 672–678, 1997.
104. Crowhurst, J.C., Hearne, G.R., Comins, J.D., Every, A.G., and Stoddart, P.R., Surface Brillouin scattering at high pressure: Application to a thin supported gold film, *Phys. Rev. B*, 60, R14990–R14993, 1999.
105. Zinin, P., Manghnani, M.H., Tkachev, S., Askarpour, V., Lefeuvre, O., and Every, A., Brillouin spectroscopy of surface in thin film Si3N4 on GaAs, *Phys. Rev. B*, 60, 2844–2850, 1999.
106. Manghnani, M.H., Tkachev, S., Zinin, P.V., Zhang, X., Brazhkin, V.V., Lyapin, A.G., and Trojan, I.A., Elastic properties of superhard amorphous carbon pressure synthesized from C_{60} by surface Brillouin scattering, *Phys. Rev. B*, 6412 (12), 121403, 2001.
107. Chirita, M., Sooryakumar, R., Xia, H., Monteiro, O.R., and Brown, I.G., Observation of guided longitudinal acoustic modes in hard supported layers, *Phys. Rev. B*, 60 (8), 5153–5156, 1999.
108. Ferrari, A.C., Robertson, J., Beghi, M.G., Bottani, C.E., Ferulano, R., and Pastorelli, R., Elastic constants of tetrahedral amorphous carbon films by surface Brillouin scattering, *Appl. Phys. Lett.*, 75, 1893–1895, 1999.
109. Beghi, M.G., Ferrari, A.C., Teo, K.B.K., Robertson, J., Bottani, C.E., Libassi, A., and Tanner, B.K., Bonding and mechanical properties of ultrathin diamond-like carbon films, *Appl. Phys. Lett.*, 81, 3804–3806, 2002.
110. Kim, J.O., Achenbach, J.D., Mirkarimi, P.B., Shinn, M., and Barnett, S.A., Elastic constants of single-crystal transition-metal nitride films measured by line-focus acoustic microscopy, *J. Appl. Phys.*, 72, 1805–1811, 1992.
111. Nizzoli, F., Hillebrands, B., Lee, S., Stegeman, G.I., Duda, G., Wegner, G., and Knoll, W., Determination of the whole set of elastic-constants of a polymeric Langmuir-Blodgett film by Brillouin spectroscopy, *Phys. Rev. B*, 40, 3323–3328, 1989.

112. Ghislotti, G. and Bottani, C.E., Brillouin scattering from shear horizontal surface phonons in silicon-on-insulator structures: theory and experiment, *Phys. Rev. B*, 50, 12131–12137, 1994.
113. Casari, C.S., LiBassi, A., Bottani, C.E., Barborini, E., Piseri, P., Podesta, A., and Milani, P., Acoustic phonon propagation and elastic properties of cluster-assembled carbon films investigated by Brillouin light scattering, *Phys. Rev.*, 64, 085417, 2001.
114. Lee, S.A. and Lindsay, S.M., Surface Brillouin scattering from graphite, *Phys. State Solid*, *B*, 157, K 83–K 86, 1990.
115. Boekholt, M., Harzer, J.V., Hillebrands, B., and Guntherodt, G., Determination of the sound velocities and the complete set of elastic-constants for $Bi_2Sr_2CaCu_2O_8$+delta single-crystals using Brillouin light scattering, *Physica C*, 179, 101–106, 1991.
116. Wittkowski, T., Jorzick, J., Jung, K., and Hillebrands, B., Elastic properties of thin h-BN films investigated by Brillouin light scattering, *Thin Solid Films*, 353, 137–143, 1999.
117. Grimsditch, M., Bhadra, R., and Schuller, I.K., Lamb waves in unsupported thin films: a Brillouin scattering study, *Phys. Rev. Lett.*, 58, 1216–1219, 1987.
118. Pastorelli, R., Tarantola, S., Beghi, M.G., Bottani, C.E., and Saltelli, A., Design of surface Brillouin scattering experiments by sensitivity analysis, Surf. Sci., 468, 37–50, 2000.
119. Bortolani, V., Nizzoli, F., Santoro, G., and Sandercock, J.R., Strong interference effects in surface Brillouin scattering from a supported transparent film, *Phys. Rev. B*, 25, 3442–3445, 1982.
120. Murugavel, P., Narayana, C., Govindaraj, A., Sood, A.K., and Rao, C.N.R., Brillouin scattering from C70 and C60 films: a comparative study of elastic properties, *Chem. Phys. Lett.*, 331, 149–153, 2000.
121. Blank, V.D., Buga, S.G., Serebryanaya, N.R., Dubitsky, G.A., Mavrin, B.N., Popov, M.Y., Bagramov, R.H., Prokhorov, V.M., Sulyanov, S.N., Kulniskiy, B.A., and Tatyanin, Y.V., Structures and physical properties of superhard and ultrahard 3D polymerized fullerites created from solid C_{60} by high pressure high temperature treatment, *Carbon*, 36, 665–670, 1998.
122. Pastorelli, R., Ossi, P.M., Bottani, C.E., Checchetto, R., and Miotello, A., Elastic constants of cubic boron nitride films, *Appl. Phys. Lett.*, 77, 2168–2170, 2000.
123. Mirkarimi, P.B., McCarty, K.F., and Medlin, D.L., Review of advances in cubic boron nitride film synthesis, *Mater. Sci. Eng.*, R21, 47–100, 1997.
124. Sussner, H., Pelous, J., Schmidt, M., and Vacher, R., Brillouin scattering from surface waves on Al-coated transparent media, *Solid State Commun.*, 36, 123–125, 1980.
125. Aleksandrov, V.V., Gladkevitch, A., Mozhaev, V.G., Giovannini, L., and Nizzoli, F., Brillouin scattering study of the pseudosurface acoustic mode on the (110) face of cubic-crystals having elastic anisotropy ratio above unity, *J. Appl. Phys.*, 76, 2176–2180, 1994.
126. Mendik, M., Sathish, S., Kulik, A., Gremaud, G., and Wachter, P., Surface acoustic wave studies on single crystal nickel using Brillouin scattering and scanning acoustic microscope, *J. Appl. Phys.*, 71, 2830–2834, 1992.
127. Mendik, M. and Sathish, S., Response to comment on Surface acoustic wave studies on single crystal nickel using Brillouin scattering and scanning acoustic microscope [*J. Appl. Phys.*, 75, 5459, 1994], *J. Appl. Phys.*, 75 (10 Pt1), 5461–5462, 1994.
128. Briggs, A., *Acoustic Microscopy*, Clarendon Press, Oxford, 1992.

129. Maznev, A.A. and Every, A.G., Secluded supersonic surface waves in germanium, *Phys. Lett. A*, 197, 423–427, 1995.
130. Zuk, J., Kiefte, H., and Clouter, M.J., Brillouin scattering study of surface acoustic waves in crystalline GaP, *J. Appl. Phys*., 72, 3504–3508, 1992.
131. Kuok, M.H., Ng, S.C., and Zhang, V.L., A Brillouin study of the angular dispersion of generalized surface and pseudosurface acoustic waves on the (001) surface of InSb, *Appl. Phys. Lett*., 77, 1296, 2000.
132. Kuok, M.H., Ng, S.C., and Zhang, V.L., Angular dispersion of surface acoustic waves on (001), (110), and (111) GaAs, *J. Appl. Phys*., 89, 7899–7902, 2001.
133. Kuok, M.H., Ng, S.C., and Liu, T., Brillouin scattering from pseudo surface acoustic waves in (111) silicon, *Solid State Commun*., 110, 185, 1999.
134. Lim, T.C. and Farnell, G.W., Character of pseudo surface waves on anisotropic crystals, *J. Acoust. Soc. Am*., 45, 845–851, 1969.
135. Jiang, X., Zhou, J.W., Reichelt, K., and Gruenberg, P., The study of mechanical properties of a-C:H films by Brillouin scattering and ultralow load indentation, *J. Appl. Phys*., 66, 4729–4735, 1990.
136. Every, A.G. and Sachse, W., Sensitivity of inversion algorithms for recovering elastic constants of anisotropic solids from longitudinal wavespeed data, *Ultrasonics*, 30, 43–48, 1992.
137. Yoshihara, A., Fujimura, T., Oka, Y., Fujisaki, H., and Shirotani, I., Surface Brillouin scattering in black phosphorus, *Phys. Rev. B,* 34, 7467–7470, 1986.
138. Carlotti, G., Fioretto, D., Socino, G., and Verona, E., Brillouin-scattering determination of the whole set of elastic constants of a single transparent film of hexagonal symmetry, *J. Phys.: Condens. Mater*., 7, 9147–9153, 1995.
139. Ohring, M., *The Materials Science of Thin Films*, Academic Press, Boston, 1992.
140. Bhadra, R., Grimsditch, M., Schuller, I. K., and Nizzoli, F., Brillouin scattering from unsupported Al films, *Phys. Rev. B*, 39, 12456–12459, 1989.
141. Tiersten, H.F., Elastic surface waves guided by thin films, *J. Appl. Phys*., 40, 770–789, 1969.
142. Bortolani, V., Nizzoli, F., Santoro, G., Marvin, A.M., and Sandercock, J. R., Brillouin scattering from surface phonons in Al-coated semiconductors, *Phys. Rev. Lett*., 43, 224–227, 1978.
143. Hillebrands, B., Baumgart, P., Mock, R., Guntherodt, G., and Bechthold, P.S., Dispersion of localized elastic modes in thin supported gold layers measured by Brillouin-scattering, *J. Appl. Phys*., 58, 3166–3168, 1985.
144. Karanikas, J.M., Sooryakumar, R., and Phillips, J.M., Dispersion of elastic waves in supported CaF_2 Films, *J. Appl. Phys*., 65, 3407–3410, 1989.
145. Carlotti, G., Socino, G., and Verona, E., Investigation of elastic properties of ZnO films by Brillouin scattering, *J. Appl. Phys*., 65, 1370–1372, 1989.
146. Sun, L., Dutcher, J.R., Giovannini, L., Nizzoli, F., Stevens, J.R., and Ord, J.L., Elastic and elasto-optic properties of thin-films of poly(styrene) spin-coated onto Si(001), *J. Appl. Phys*., 75, 7482–7488, 1994.
147. Lefeuvre, O., Characterisation of stiffening layers by acoustic microscopy and Brillouin spectroscopy, D. Phil. thesis, University of Oxford, 1998.
148. Bortolani, V., Nizzoli, F., and Santoro, G., Brillouin scattering at interfaces and long wave-length acoustic phonons, *J. De Physique*, 45, 45–53, 1984.
149. Bell, J.A., Zanoni, R., Seaton, C.T., Stegeman, G.I., Makous, J., and Falco, C.M., Elastic constants of, and Stonely waves in, molybdenum films measured by Brillouin scattering, *Appl. Phys. Lett*., 52, 610–612, 1988.

150. Jorna, R., Visser, D., Bortolani, V., and Nizzoli, F., Elastic and vibrational properties of nickel films measured by surface Brillouin scattering, *J. Appl. Phys.*, 65, 718–725, 1989.
151. Liu, A.Y. and Cohen, M.L., Prediction of new low compressibility solids, *Science*, 245, 841–842, 1989.
152. Pang, W., Stoddart, P.R., Comins, J.D., Every, A.G., Pietersen, D., and Marais, P.J., Elastic properties of TiN hard films at room and high temperatures using Brillouin scattering, *Int. J. Refrac. Metals Hard Mater.*, 15, 179–185, 1997.
153. Lefeuvre, O., Zinin, P., and Briggs, G.A.D., Leaky surface waves propagating on a fast on slow system and the implications for material characterization, *Ultrasonics*, 36, 229–232, 1998.
154. Lefeuvre, O., Zinin, P., Briggs, G.A.D., and Every, A., Surface wave dispersion beyond cutoff for a fast layer on a slow substrate, *Appl. Phys. Lett.*, 72, 856–857, 1998.
155. Wittkowski, T., Cortina, P., Jorzick, J., Jung, K., and Hillebrands, B., Brillouin light scattering from surface phonons in hexagonal and cubic boron nitride films, *Diamond Relat. Mater.*, 9, 1957–1964, 2000.
156. Zinin, P., Manghnani, M.H., Zhang, X., Feldermann, H., Ronning, C., and Hofsass, H., Surface Brillouin scattering of cBN films, *J. Appl. Phys.*, 91, 4196–4204, 2002.
157. Pang, W., Every, A.G., Comins, J.D., Stoddart, P.R., and Zhang, X., Brillouin scattering from acoustic excitations in TiN films on high speed steel — A stiffening system, *J. Appl. Phys.*, 86, 311–317, 1999.
158. Hickernell, T.S., Fliegel, F.M., and Hickernell, F.S., The elastic properties of thin-film siliconnitride, in *Proc. IEEE 1990 Ultrasonics Symp.*, McAvoy, B.R., Ed., Institute of Electrical and Electronics Engineers, New York, 1990, pp. 445–449.
159. Subramanian, S., Sooryakumar, R., Prinz, G.A., Jonker, B.T., and Idzerda, Y.U., Elastic constants of body-centered cubic cobalt films, *Phys. Rev. B*, 49, 17319–17324, 1994.
160. Lefeuvre, O., Kolosov, O.V., Every, A.G., Briggs, G.A.D., and Tsukahara, Y., Elastic measurements of layered nanocomposite materials by Brillouin spectroscopy, *Ultrasonics*, 38, 459–465, 2000.
161. Grimsditch, M., Effective elastic constants of superlattices, *Phys. Rev. B*, 31, 6818–6819, 1985.
162. Grimsditch, M. and Nizzoli, F., Effective elastic constants of superlattices of any symmetry, *Phys. Rev. B*, 33, 5891–5892, 1986.
163. Bell, J.A., Bennett, W.R., Zanoni, R., Stegeman, G.I., Falco, C.M., and Nizzoli, F., Elastic constants of Mo/Ta superlattices measured by Brillouin scattering, *Phys. Rev. B*, 35, 4127–4130, 1987.
164. Osetrov, A.V., Frohlich, H.J., Koch, R., and Chilla, E., Acoustoelastic effect in anisotropic layered structures, *Phys. Rev. B*, 62, 13963, 2000.

11

Theory and Applications of Acoustic Microscopy

Pavel V. Zinin and Wieland Weise

All things should be done as simple as possible, but not simpler.

Albert Einstein

CONTENTS

0-8493-1462-3/02/$0.00+$1.50

11.1 Introduction

Modern technologies require materials that withstand extreme conditions with high reliability. One of the key parameters that have a strong impact on the life expectancy of a material is its microstructure. The acoustic microscope was developed as a tool for studying the internal microstructure of nontransparent solids. In acoustic microscopy, a sample is imaged by ultrasound waves, and the contrast in reflection furnishes a map of the spatial distribution of the mechanical properties. Several books and handbook articles[1–4] give detailed historical outlines. Briefly, the development of the first high-frequency scanning acoustic microscope was motivated by the idea of using an acoustic field to study the spatial variations of the elastic material properties with nearly optical resolution. The first experiments date back to the 1940s when high-frequency acoustic images were obtained by the Leningrad scientist Sokolov.[5] He observed an acoustical image using the tube named after him, in which the acoustic picture was converted into a television display. The first scanning acoustic microscope was created by Lemons and Quate at Stanford University in 1973.[6] It was mechanically driven and operated in the transmission mode. Since then, gradual mechanical and electronic circuit improvements have been made and image recording has been automated. In general, acoustic microscopes now work in the reflection mode,[7] which will be described in the next section.

Many applications are described in the 1992 book *Acoustic Microscopy*.[2] Considerable progress in the acoustic microscopy of solid structures has been made since then. Developments in the theory of the image formation of subsurface defects[8] and three-dimensional objects[9,10] allow size and location of objects inside solids to be determined. Combining the time-of-flight technique with acoustic microscopy provides a powerful tool for investigating adhesion problems[11] as well as the microstructure of small superhard samples.[12] Acoustic microscopy can be used to visualize stress inside solid materials.[13] With the development of the ultrasonic force microscope[14] and the atomic force acoustic microscope,[15] the capability of the conventional acoustic microscope has been expanded to nanometer resolution. Recent developments in quantitative acoustic microscopy are described in the series *Advances in Acoustic Microscopy*.[16,17]

The main objective of this chapter is twofold. First, we will describe the main principles and the theory of image formation and interpretation in acoustic microscopy. Second, we will demonstrate the capabilities of acoustic microscopy as a nondestructive tool for studying the microstructure of modern materials.

11.2 Basic Principles of the SAM

The scanning acoustic microscope (SAM) can be characterized by a combination of operating principles distinguishing it from other microscope types.

These principles are image generation by scanning, far-field wave imaging, and the use of acoustic waves.

Image generation by scanning is basically different from the functionality of a conventional optical microscope, which is the oldest microscope type. The conventional microscope can be considered a parallel processing system[18] in which we can see all points of the object at the same time. In contrast to this, the SAM is a sequential imaging system in which a piezoelectric transducer emits a focused ultrasound beam that propagates through a coupling liquid, usually water, to the sample. The beam is scattered by the sample, and the scattered ultrasound wave is detected piezoelectrically. The output signal is just one single voltage. As the sample is scanned, the voltage is recorded in each scanning position of the focus and a grayscale image is generated. While medical ultrasound devices scan by electronic beam-steering, acoustic microscopes mechanically move either the microscope head or the sample.

The use of a focused beam leads to the second operating principle. As the focus is formed by converging propagating waves, the size of the focal spot (or focal area) is limited by diffraction. Also, as the detector is positioned remote from the sample, no near-field effects of the waves can be deployed. This distinguishes the SAM from near-field microscopes, including scanning atomic force acoustic microscopes. Two different techniques are commonly used to achieve convergence of the ultrasound wave in the SAM. The simplest way to generate a focused beam is to employ a piezoelectric transducer, which is already shaped like a spherical cap. Another technique is used in high-resolution microscopes, where the ultrasound wave is focused by means of an acoustic lens made from a buffer rod (Figure 11.1). A flat transducer is connected to one end face of the buffer rod. A spherical cavity

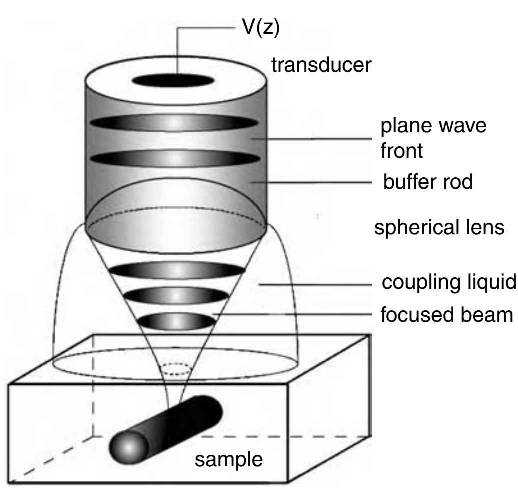

FIGURE 11.1
Schematic diagram of the reflection acoustic microscope.

is ground into the other face, which is coated with a quarter-wavelength matching layer to increase transmission. The ultrasound radiated from the lens is coupled by a fluid (usually water) to the surface of a solid sample. The spherical lens (i.e., the lens with a spherical cavity) focuses sound onto a spot whose size is comparable with the sound wavelength in the fluid (Figure 11.1). For nondestructive testing purposes, cylindrical lenses, which have a line focus, are often applied. Their performance is better than that of spherical lenses for the examination of surface waves propagating in anisotropic media.[19]

The acoustical microscopes for nondestructive testing usually operate in reflection mode. In the reflection microscope, the same lens and transducer as for emission are used to gather the waves reflected back from the sample (Figure 11.1). The reflection microscope therefore is always a confocal device. The term confocal indicates that both the detection and the emission are focused and that the two focal points coincide.[18] The confocal setup suppresses contrast from sample areas outside the focal point and thus yields higher resolution. In the transmission microscope, the forward scattered waves are detected by a second unit, and confocal operation is possible by adjustment of the detector.

The reflection acoustic microscope operates in the pulse-echo mode;[20] the same transducer emits the acoustic wave and receives the signal scattered from the sample. In most SAMs, the transducer is excited with a narrowband tone-burst. Time-limited excitation is used so that the first reflection from the sample can be gated out.[21] However, the theoretical framework for interpreting images is simpler when a single frequency is considered. More details regarding the electrical circuit and the type of signal used in the acoustic microscope can be found elsewhere.[2,20]

Imaging with ultrasound is the third operating principle. The operating frequencies of SAMs are between 100 MHz and 2 GHz; the high frequency provides the opportunity to obtain accurate measurement results for crack and void distributions with a resolution of up to 1 μm at a depth of 10 μm. The use of higher frequencies is restricted by the presence of wave attenuation in the coupling liquid, which is proportional to the frequency squared. The maximum possible working distance between the microscope and a sample therefore is about 60 μm at 2 GHz. The electroacoustic transducer always emits and detects the sound coherently. This is the reason why acoustical images can exhibit granular artifact structures, the so-called speckle. Speckle in ultrasound imaging (and all coherent imaging systems) is caused by the interference of waves from randomly distributed scatterers, which are too small to be resolved by the imaging system. The speckle degrades both the spatial and the contrast resolution in acoustical images, but in the SAM it fortunately does not often occur.

In optics a similar type of microscope exists — the scanning optical microscope (SOM). Though in this microscope light waves are used for imaging while acoustic waves are used in the SAM, the theory of image formation is very similar for the two types of microscopes.[22] Because of that similarity,

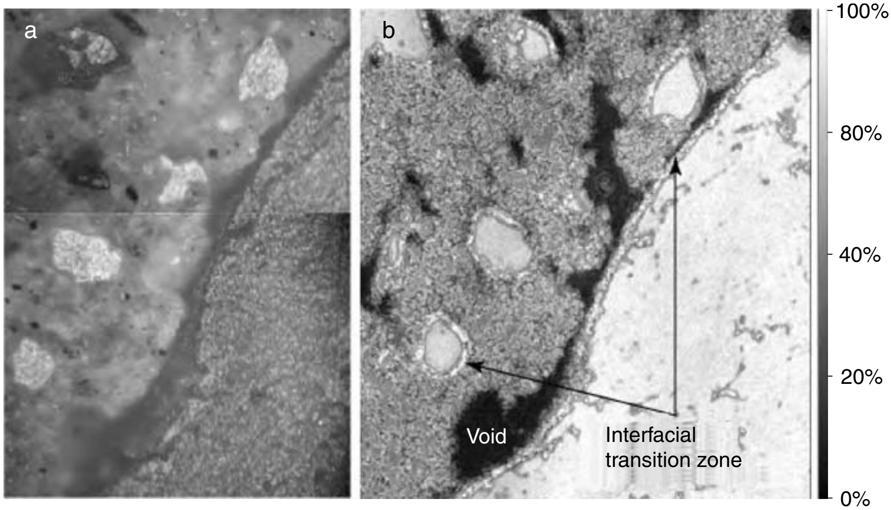

FIGURE 11.2
(a) Optical image of a concrete sample made with limestone aggregate grains. Magnification 50*1.25; (b) Acoustical image of the same sample. The acoustic image was made at ultrasound frequency 400 MHz, defocus value $Z = 0$. The image size is 1000*1000 μm.

most characteristic parameters developed for optical confocal microscopy, such as point spread function, optical transfer function,[23] and pupil function,[24] can also be used in scanning acoustic microscopy. We will describe all these functions in the next section. The type of microscope that is applied for a particular task depends on the difference in underlying contrast mechanisms that reveal different physical properties. Optical images reflect the variation of optical properties such as the refractive index of the sample surface; the contrast in acoustic images is determined by the variation of the acoustical impedance.[25] Figure 11.2 shows optical and acoustical images of a concrete sample loaded with ettringite. Two features can be distinguished in the acoustical image. First, there is a rim around the aggregates that is not visible in the optical micrograph; second, large voids can be seen in the acoustical image. The rim was identified as the interfacial transition zone filled with ettringite.[26] Identification of the interfacial transition zone is of importance for the concrete industry, as it is considered an important factor of concrete deterioration.

For some materals the SAM provides information invisible even in the scanning electron microscope. Figure 11.3 shows acoustic and scanning electron microscope images of a granitic aggregate in a cement matrix. The various mineral compositions were identified by energy dispersive (X-ray) spectroscopy analysis.[27] The acoustic image in Figure 11.3 demonstrates various types of aggregate grain boundaries within the matrix.[28] The quartz grains, and to some extent also the plagioclase grains, have sharp and well defined boundaries. The acoustical images are much sharper than the scanning electron

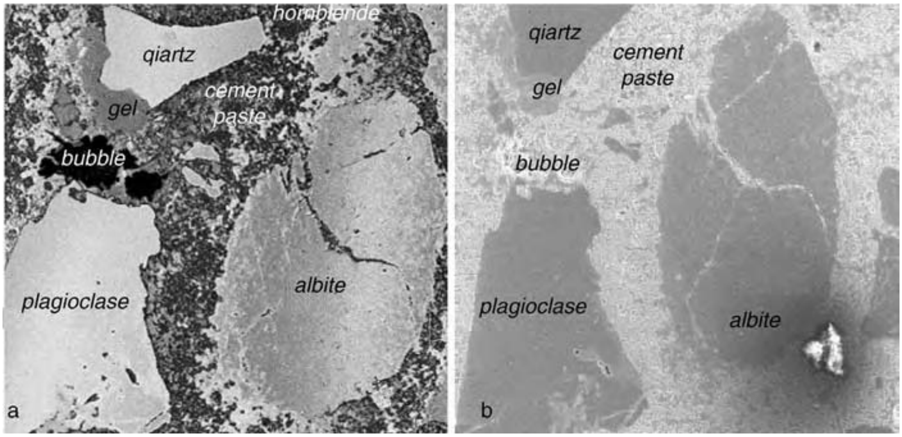

FIGURE 11.3
(a) Acoustic and (b) the scanning electron microscope images of a concrete sample made with granitic aggregate grains and Portland cement paste. The acoustic image was made at 400 MHz, $Z = 0$. The image size is 1000*1000 μm. (From Prasad, M. et al., *J. Mater. Sci.*, 35, 3607, 2000. With permission.)

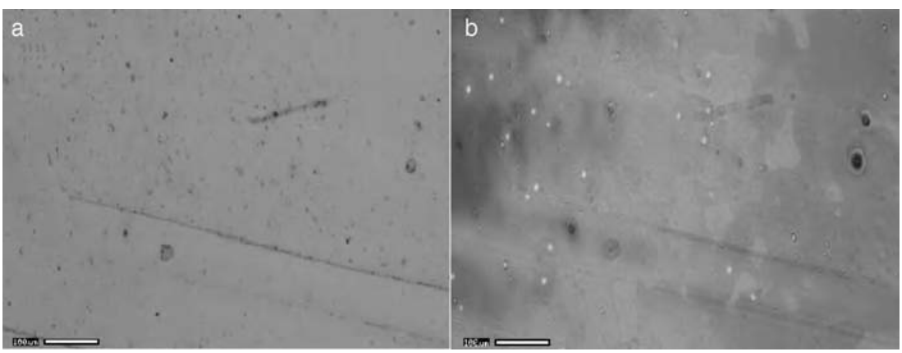

FIGURE 11.4
SAM image made by OXSAM of a standard epoxy layer on aluminum at 300 MHz: (a) $Z = 0$; (b) $Z = -20$ μm.

microscope image. This is important for analysis, as the smooth boundaries of quartz and plagioclase grains imply chemical inertness of the aggregates.

Images made by the SAM are called C-scans. They are obtained when the acoustic microscope mechanically scans a sample in a plane parallel to the sample surface. Figure 11.4 represents C-scan images of an epoxy layer on aluminum at different defocus positions (Z). Images obtained at different defocus positions allow the depth of voids to be located and their size to be estimated. Voids can be considered as strong scatterers and the brightness of the small void image is maximal when the focal point of the microscope is in coincidence with the void. The image of the side of an epoxy layer reveals many small surface defects as can be seen from Figure 11.4a. The image in Figure 11.4b is focused on the epoxy/aluminum interface; bright spots can therefore be attributed to voids or small bubbles close to the interface.

The first transmission SAM, created by Lemons and Quate, was a confocal microscope, as the focal point of the transmitting lens was in coincidence with that of the receiving lens. It is interesting to note that the transmission microscope is mostly used in nonconfocal mode, in a two-lens acoustic microscope.[4] Two-lens microscopy permits a variety of different techniques. In the ultrasonic flux imaging technique,[29,30] two point focus lenses are focused on the opposite faces of a crystal. Such a lens configuration makes visible a fascinating picture of bulk sound waves propagating in an anisotropic solid — a very effective method of determining elastic constants of crystals.[31] Tsukahara et al.[32] used a spherical lens as the transmitter and a planar transducer as the detector to measure the reflection coefficients of anisotropic solids.

Time-resolved acoustic microscopy adds an additional degree of freedom to visualize the internal microstructure of solids, namely time-of-flight. For layered materials, the reflected signal represents a train of pulses. The signal detected is displayed vs. the time of occurrence (A-scan). The first pulse is attributed to the reflection from the liquid/sample interface. The second pulse appears as a result of reflection from the first internal interface. The time delay of the pulses and their amplitudes provides information about the elastic properties and attenuation of sound in the layer. The combination of the time-of-flight method with mechanical scanning along a line is called B-scan. The B-scan produces a sectional view through the sample. Time-resolved acoustic microscopy helps to investigate adhesion problems,[11] and is a very powerful tool for characterizing subsurface cracks.[33] Figure 11.5 shows C- and B-scans of blister located at the interface between epoxy coating and aluminum at

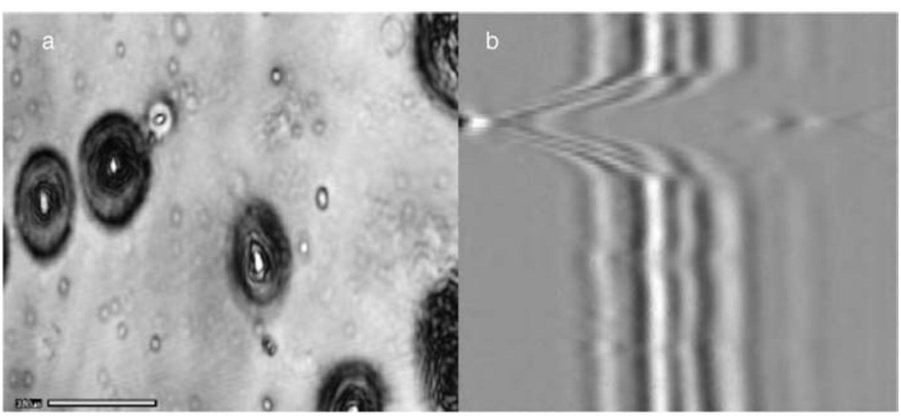

FIGURE 11.5
SAM image made by OXSAM of a 1-μm epoxy layer on 10-μm oxide anodized alumina on aluminum at 300 MHz: (a) $Z = -15$ μm; (b) time-resolved image made at $Z = -15$ μm, field of view is 50 nsec*300 μm.

300 MHz of a 1-μm epoxy layer on a 10-μm oxalic acid anodized oxide layer on aluminum. The blisters were developed in the sample during 11 days in hot water (60°C). Images were made by OXSAM, the microscope built in Oxford.[34] The time-resolved image (Figure 11.5b) makes the shape of the blister visible and also provides information about delaminations.

11.3 Theory of Image Formation in the SAM

One of the main features of acoustic microscopy is the possibility to visualize structures below the object surface, as no material is totally acoustically opaque. In acoustic microscopy we therefore have to do with three-dimensional image formation; reflected acoustic waves come not only from a single plane, but also from the layers located above and below the focal plane. As a result, SAM images are often difficult to interpret directly, and a theoretical formulation is required to understand their basic features. A theory is also necessary to obtain quantitative information about subsurface features such as location and size of voids and elastic properties of subsurface micro-objects.

To obtain the analytical solution of the output signal of the microscope we assume that the duration of the radio frequency signal of the microscope is long enough to justify continuous-wave analysis for the scattering problem. For example,[35] the field of the radiator may be described as a continuous wave solution if the pulse train contains several oscillations of the carrier frequency and the pulse length is large in comparison to the sample area relevant to contrast formation.

The direct way to derive the output signal of the acoustic microscope consists of five steps:

1. Simulation of the propagation inside a sapphire rod of the acoustical wave generated by a piezoelectric transducer situated at one end
2. Diffraction of the sound wave by a spherical cavity serving as the focusing lens at the other end and propagation of the focused wave through an immersion liquid to the sample
3. Analysis of the sound backscattered by the object
4. Diffraction of the backscattered waves by the spherical cavity
5. Propagation of the acoustic wave through the rod and generation of the electrical signal by the transducer

Each of these steps requires tedious simulations. Fortunately, application of the electromechanical reciprocity principle as formulated by Auld[36] and of the Fourier transform approach (spectrum approach) provides an elegant way to formulate the theory of image formation in scanning acoustic microscopy in an analytical form.[9,10,37,38] With the aid of the reciprocity principle,

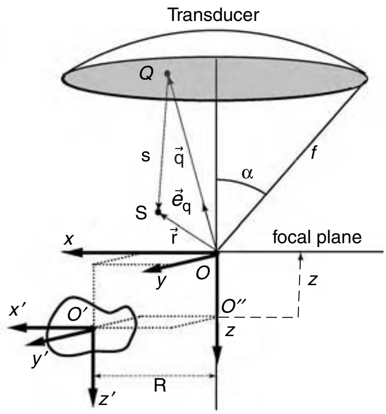

FIGURE 11.6
Model of the reflection acoustic microscope used for calculation: spherical transducer with focal length *f*, three-dimensional object defocused by *Z*, and shifted aside by *R*.

the detection properties of the microscope can be attributed to the emission properties.[37] With the spectrum approach the propagation of waves from one plane to another parallel one can be described simply by including a propagation factor. In the following paragraphs we will formulate the theory of the image formation in reflection and transmission microscopes using the Fourier spectrum approach.[9,10]

The model of the reflection acoustic microscope as it is used for calculation is presented in Figure 11.6. A time harmonic acoustic field at an arbitrary position in the immersion liquid can be represented by its scalar potential $\Phi(x,y,z)$ (see Chapter 1). The time factor exp(-*it*) is suppressed as follows, ω being angular frequency. As Φ must satisfy the Helmholtz equation, every solution can be decomposed into plane waves $\exp(ik_x x + ik_y y + ik_z z)$ with wave vector $\boldsymbol{k} = (k_x, k_y, k_z)$, $|\boldsymbol{k}| = \omega / c$, and *c* being the velocity of sound in the coupling liquid. If $k_x^2 + k_y^2 \leq k^2$, then $k_z = \pm\sqrt{k^2 - k_x^2 - k_y^2}$. Such waves are denoted as homogeneous waves. The positive or negative sign is for waves propagating in the positive or negative z-direction, respectively. If $k_x^2 + k_y^2 > k_z$, then $k_z = \pm i\sqrt{k_x^2 + k_y^2 - k^2}$ will be imaginary.[39] This means that the wave exponentially decays in the positive or negative *z*-direction, respectively. Such waves are denoted as evanescent waves. They are important to describe a field in the vicinity of irregular structures (near-field imaging). We assume that the whole acoustic wave with a potential Φ is propagating and evanescing either in the positive or in the negative *z*-direction, and the sign of k_z is therefore unambiguous. The two-dimensional angular spectrum $U(k_x, k_y, z)$ of $\Phi(x, y, z)$ at fixed coordinate $z = Z$ is then defined by the double Fourier integral[39]

$$U(k_x, k_y, Z) = \int_{-\infty}^{\infty}\int_{-\infty}^{\infty} \Phi(x, y, Z)\exp[-i(k_x x + k_y y)]dxdy \qquad \textbf{(11.1)}$$

Conversely, the potential can then be written as the inverse Fourier transform of the angular spectrum:

$$\Phi(x,y,Z) = \frac{1}{(2\pi)^2}\int_{-\infty}^{\infty}\int_{-\infty}^{\infty} U(k_x,\, k_y,\, Z)\exp[i(k_x x + k_y y)]dk_x dk_y \qquad \textbf{(11.2)}$$

The inverse Fourier transform (Equation 11.2) represents the acoustic field in the plane Z as a superposition of plane waves $\exp(ik_x x + ik_y y)$. A detailed description of the Fourier transform and its properties can be found elsewhere.[40] Atalar[37] applied Auld's reciprocity principle to derive the output voltage V of the detector of the reflection SAM in terms of angular spectra on an arbitrary plane z

$$V = \int_{-\infty}^{\infty}\int_{-\infty}^{\infty} U_i(-k_x,-k_x)U_s(k_x,k_x)k_z dk_x dk_y \qquad \textbf{(11.3)}$$

where $U_\mathrm{i}(k_x, k_y)$ is the angular spectrum of the field the microscope detector emits into the coupling liquid, $U_s(k_x, k_y)$ is the angular spectrum of the field resulting from scattering of the field incident on the object. It is the spectrum of the field the microscope detects. In Equation 11.3 a proportionality constant is omitted. The position of the plane z at which the spectra are evaluated is the same for both but z can be chosen arbitrarily. In the following, we will take the spectra in the focal plane where they might occur only virtually if the focus lies inside the object. We can interpret the signal generation as follows: A scattered field plane wave component with a particular wave vector (k_x, k_y, k_z) is weighted with the emission strength of the emitted plane wave with wave vector $(-k_x, -k_y, -k_z)$. So the weighting factor belongs to the emitted plane wave traveling exactly in the direction opposite to the detected plane wave. The weighting factor represents the detection properties of the transducer that are equal to the emission properties. This is a consequence of the electromechanical reciprocity principle for transducers. Finally, the detection is integrated coherently.

The expression in Equation 11.3 is also valid for the transmission microscope.[37] Then U_i is the spectrum the detecting transducer would emit if it were driven as the source. Note that for both microscope types U_i describes properties of the detector. A comprehensive derivation of Equation 11.3 can be found elsewhere.[41] Representation of the output signal in the form of Equation 11.3 provides a relatively simple way to omit steps (4) and (5) in the description. The problem of image formation therefore reduces to the simulation of the incident beam and to its scattering by an object.

The microscope is most easily modeled as a focusing transducer with the shape of a spherical cap radiating directly into the coupling liquid (Figure 11.6). We describe the strength of the emitted wave field along the transducer surface by the pupil function $P(\theta, \varphi)$, with θ and φ denoting the meridianal and azimuthal angles of the vector from a point on the transducer surface to the focal point (see Figure 11.6). The origin of the coordinate system is placed in the focus of the transducer. The positive z-direction is chosen away from the emitter. Due to reciprocity, the pupil function also describes the sensitivity of this transducer and might contain a phase factor to account for aberration.[1,22,24] The pupil function here does not have a unit. It may be regarded as proportional to the oscillation velocity.

Spherical transducers can be produced, for example, from piezoelectric plastic foils.[42] However, the spherical transducer can also serve as a model for the usual system consisting of a planar transducer, a buffer rod guiding the acoustic wave, and a spherical concave lens forming a converging wave. The two simply must emit the same angular spectrum. For numerical simulations several pupil functions are often used. The most elementary pupil function, which is discontinuous at the edge of the aperture with opening semiangle α, has the form

$$P(\theta) = \begin{cases} 1, \theta \le \alpha \\ 0, \theta > \alpha \end{cases} \tag{11.4}$$

Here every part of the transducer moves equally toward the coupling liquid. More realistic modelling for a plane transducer insonifying only a circular fraction of the lens is provided by a pupil function that is continuously differentiable at the edge:[43]

$$P(\theta) = \begin{cases} \frac{1}{2}\left[1 + \cos\left(\pi \frac{\cos\theta - 1}{\cos\alpha - 1}\right)\right], & \theta \le \alpha \\ 0, & \theta > \alpha \end{cases} \tag{11.5}$$

It has been shown that the pupil function of the microscope can be derived from images of a rigid spherical particle when the focal point is scanned along the sphere's half radius.[24] The two-dimensional pupil function (absolute value) of an acoustic microscope is presented in Figure 11.7. It is nonzero only inside the circle $\sqrt{(k'_x)^2 + (k'_y)^2} \le k \sin\alpha$. The broad fringes exhibit the sound field generated by the piston transducer, while the small rings are artifacts from imperfect scanning.

Our first task is to find the angular spectrum of the field emitted by a focusing transducer with given pupil function. We will calculate the (displacement) potential distribution in the focal plane, from which the angular spectrum is easily derived. By application of the Huygens-Fresnel principle,[44,p. 436] the field Φ at a point $\boldsymbol{r}$ whose distance from the focal point is small compared to the focal length f of the transducer is given by

$$\Phi_i(\bar{r}) = -\frac{1}{2\pi} \int_0^{2\pi} \int_0^{\pi/2} u_0 P(\theta, \varphi) \frac{\exp(iks)}{s} f^2 \sin\theta d\theta d\varphi \tag{11.6}$$

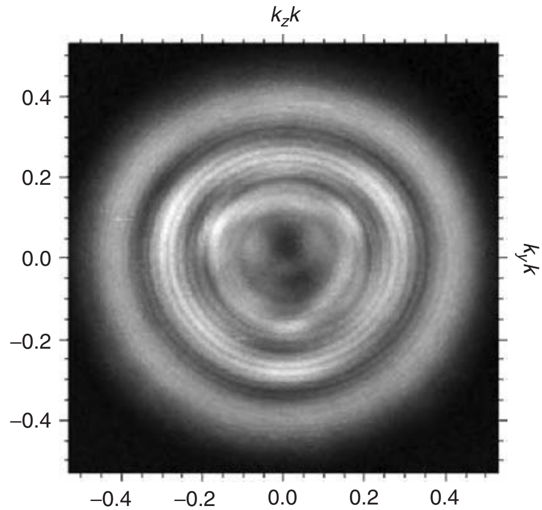

FIGURE 11.7
Experimental image of the pupil function of the ELSAM 400 MHz lens. Image was obtained by imaging a steel sphere (*ka* = 334), focusing at half radius of the sphere. (From Weise, W. et al., *J. Acoust. Soc. Am.*, 104, 181, 1998. With permission.)

where s denotes the distance between point Q on the transducer surface and point S, $\boldsymbol{s} = |\boldsymbol{r} - \boldsymbol{q}|$ (see Figure 11.6). The product $u_0\, P(\theta, \varphi)$ is the displacement of the transducer surface. The integration can be performed over the whole upper hemisphere, as the aperture is restricted by $P(\theta, \varphi)$. In the vicinity of the focal point, $r \ll f, s$, and we have in good approximation

$$(s - f) \approx \boldsymbol{e}_q \boldsymbol{r} \tag{11.7}$$

where $\boldsymbol{e}_q$ is the unit vector directed along vector $\boldsymbol{q}$. Introducing Equation 11.7 into the exponential function in Equation 11.6 and replacing s by f in the denominator of the integrand of Equation 11.6 we obtain the following:

$$\Phi_i(\bar{r}) = -\frac{u_0 \exp(ikf)}{2\pi} \int_0^{2\pi} \int_0^{\pi/2} \exp(ik\boldsymbol{e}_q(\theta,\varphi)\boldsymbol{r}) P(\theta,\varphi) f \sin\theta d\theta d\varphi \tag{11.8}$$

In the limit $f \to \infty$ (Debye approximation[45, p. 24]), this equation is valid throughout the whole space.[44, p. 436] It expresses the field in the focal region as a superposition of plane waves whose propagation vectors fall inside a geometrical cone formed by drawing straight lines from the edge of the aperture through the focal point, which, in contrast to the usual Debye integral,[45] are weighted with $P(\theta, \varphi)$. The vector $k\boldsymbol{e}_q\,(\theta, \varphi)$ has now assumed the meaning of the wave vector $\boldsymbol{k}$, and we may say that each point on $P(\theta, \varphi)$ is responsible for the emission (and, by reciprocity, for the detection) of the plane wave component emitted along the line from the point on $P(\theta,\varphi)$ through the focal point.

To find the angular spectrum of the emitted field in the focal plane, we set the third coordinate of $\boldsymbol{r}$ equal to zero and substitute Cartesian coordinates for the angular integration variables. For the vector components of $\boldsymbol{k}$ hold:

$$k_x = k \sin\theta \cos\varphi$$

$$k_y = k \sin\theta \sin\varphi \qquad \textbf{(11.9)}$$

$$k_z = \cos\varphi = \sqrt{k^2 - k_x^2 - k_y^2}$$

The Jacobi determinant corresponding to Equation 11.9 yields

$$\sin\theta d\theta d\varphi = \frac{1}{k^2 \cos\theta} dk_x dk_y = \frac{1}{kk_z} dk_x dk_y \qquad \textbf{(11.10)}$$

Denoting the Cartesian coordinates of $\boldsymbol{r}$ by x, y, z, Equation 11.8 can be rewritten

$$\Phi_i(x, y, z = 0) = \frac{1}{(2\pi)^2} \int_{-\infty}^{\infty} \int_{-\infty}^{\infty} P(k_x, k_y) \exp[i(k_x x + k_y y)] \frac{dk_x dk_y}{kk_z} \qquad \textbf{(11.11)}$$

Up to a constant $P(k_x,k_y)$ is defined as

$$P(k_x, k_y) = \begin{cases} P(\theta, \varphi), & k_x^2 + k_y^2 \leq k^2 \\ 0, & elsewhere \end{cases} \qquad \textbf{(11.12)}$$

with the relation between θ, φ, and k_x, k_y as given by Equation 11.9. From the definition of $P(k_x, k_y)$ we could set the integration limits in Equation 11.11 to infinity. In Equation 11.11 Φ_i obviously is the two-dimensional inverse Fourier transform of the function $P(k_x, k_y)/(k\ k_z)$. Comparison with Equation 11.2 shows that this is the angular spectrum of the transducer field in the focal plane provided that $\Phi_i(x, y, 0)$ has the same Fourier transform as the transducer field in the focal plane. However, Equation 11.11 might not describe the field in the focal plane far away from the focal point. But if both fields are focused, the squared field amplitude $|\Phi_i|^2$, integrated over the focal plane but excluding the region around the focal point, will for both give approximately zero (almost all the radiated energy passes through the focal region). Hence, from Parseval's theorem, the contribution of the field in these outer regions to the Fourier transformation may be neglected, and

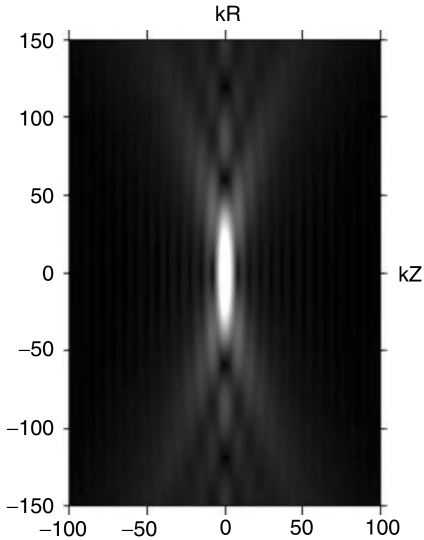

FIGURE 11.8
Calculated acoustic field near the focus of an elementary acoustic microscope lens with semiaperture angle α = 20°. (From Weise, W., PhD thesis, University of Bremen, 1997. With permission.)

the two fields can be described by the same angular spectrum throughout the focal plane. We can therefore write

$$U_i(k_x, k_y) = \frac{P(k_x, k_y)}{kk_z} \tag{11.13}$$

It should be noted that function $P(k_x,k_y)$ is defined in a spatial coordinate system rather than in the frequency (k) space, and it cannot be interpreted as an angular spectrum. Equation 11.13 is a result of the application of the Debye approximation. "In the Debye approximation, there is not an abrupt cut-off of the incident field, as in Kirchhoff approximation, but of the angular spectrum of the incident field."[45, p. 24] Figure 11.8 shows the amplitude of the acoustical field distribution near the focus of the spherical lens with the pupil function (Equation 11.4).[41] It is called point spread function (PSF) because it illustrates "what should be a point focus by geometrical optics is spread out by diffraction."[2] For the simple pupil function (Equation 11.4) the lateral distribution (field in the focal plane) is given by a *jinc* function

$$\Phi(r_t) = \frac{J_1(kr_t \sin\alpha)}{kr_t \sin\alpha} \tag{11.14}$$

where $r_t = \sqrt{x^2 + y^2}$ and J_1 is the cylindrical Bessel function. The axial field distribution (acoustical field along the z-axes: $x = 0$, $y = 0$) is described by a *sinc* function:

$$\Phi(z) = \frac{\sin[kz(1-\cos\alpha)]}{kz(1-\cos\alpha)} \quad \textbf{(11.15)}$$

Equation 11.14 and Equation 11.15 provide the lateral and the axial resolutions of the SAM. The jinc function has a maximum at $r_t = 0$, the first zero of $\Phi(r_t)$ is given by the Airy radius[39, p. 78]

$$r_{Airy} = \frac{0.61\lambda}{\sin\alpha} \quad \textbf{(11.16)}$$

where λ is the wavelength of the sound wave in the immersion liquid. The Rayleigh criterion states "that the images of two points may be considered resolved if the principal diffraction maximum of one falls exactly on the first diffraction minimum of the other."[46] Equation 11.16 gives the distance between the maximum and the first minimum of the acoustic field in the focal plane; it is called Rayleigh distance[47] and determines the axial resolution of the SAM. A detailed discussion of the different resolution criteria can be found in the book by Kino.[47]

The axial resolution (resolution along the z-axes) can be defined in the same way. The distance between the maximum and the first minimum along the z-axes is

$$z_{axial} = \frac{0.5\lambda}{(1-\cos\alpha)} \quad \textbf{(11.17)}$$

Equation 11.17 determines the axial resolution of the SAM. Figure 11.9 illustrates the behavior of the resolution of SAM operating at 1 GHz (Equation 11.16 and Equation 11.17) as a function of the aperture angle. The lateral resolution depends weakly on the aperture angle (Figure 11.9). It is 1.1-µm for a lens with a semiaperture angle of 60° at 1 GHz. In contrast to this, the axial resolution can be improved by a factor of 6 by increasing the semiaperture angle from 20 to 60°. For a microscope with a small angle lens, the focal length (the length of the main maximum of the field in the axial direction) is much longer (see Figure 11.8) than the focal width (the width of the main peak in the radial direction). Due to the high attenuation of sound in water, the highest frequency used in commercial microscopes is 2 GHz. In order to minimize the attenuation, Hamidioglu and Quate[48] used boiling water as the immersion liquid. They achieved a resolution of 0.2 µm at 4.4 GHz. Foster and Rugar[49] were able to obtain a resolution of 20 nm in low-velocity superfluid liquid helium at a temperature of 0.2 K.

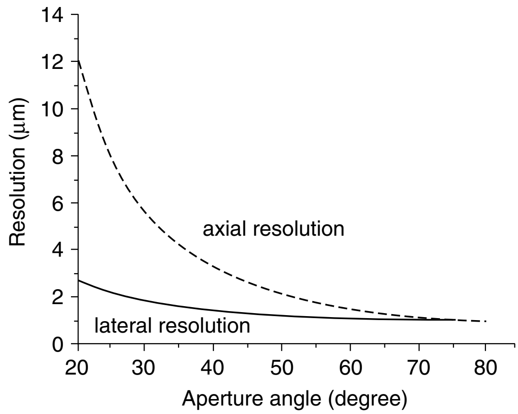

FIGURE 11.9
Calculated lateral (Equation 11.16) and axial (Equation 11.17) resolutions of a SAM operating at 1 GHz as a function of the aperture angle α. Water was chosen as the immersion liquid for simulations.

Now we know the spectrum incident on the object and we want to calculate the scattered spectrum. Consider imaging of a three-dimensional object as depicted in Figure 11.6. In the case of a reflection microscope, the same transducer serves as emitter and as detector, while for the transmission microscope the detector is situated confocally across from the emitter. We will use three coordinate systems, (x, y, z) with origin in the focal point and (x', y', z') in point O' linked to the particle. The z- and z'-axis are directed away from the emitter (Figure 11.7). The coordinates of the system O' are (X, Y, Z) from the focal point. We introduce also an intermediate coordinate system with its origin in point O'' with vector (x, y, z').

Following Somekh et al.[38] we determine the density of the backscattered spectrum or the scattering function $g_s(k_x, k_y, k_x', k_y')$ in the system O' linked to the particle as the spectrum of the reflected field in response to the incident spectral component with wave number coordinates (k_x', k_y'). The spectrum U_i' of the incident field as well as the spectrum U_s' of the reflected field are also given in the spatial coordinate system that originates at O'. Since the magnitude of $\boldsymbol{k}$ is fixed, the wave vector is completely specified by the vector $\boldsymbol{k}_t = (k_x, k_y)$; k_x, k_y denote the wave vector components of the scattered field, and k_x', k_y' denote the wave vector components of the incident field. To calculate the spectrum of the scattered field we must integrate over all incident spectral components

$$U_s'(k_x, k_y) = \frac{1}{(2\pi)^2} \int_{-\infty}^{\infty}\int U_i'(k_x', k_y') g_s(k_x, k_y, k_x', k_y') dk_x' \, dk_y' \qquad \textbf{(11.18)}$$

Now we have to determine the reflected spectrum with the help of the incident spectrum in system O, and then express the reflected spectrum in system O'. Let us first express the spectrum U_i incident in the focal plane system O in system O'' (see Figure 11.6). The spectrum U_i'' incident on the object plane at position Z is calculated by including a propagation factor $\exp(ik_z Z)$

$$U_i'(k_x', k_y') = U_i(k_x', k_y')\exp(ik_z' Z) \tag{11.19}$$

For the incident spectrum $k_z' = \sqrt{k^2 - (k_x')^2 - (k_y')^2}$. Here we introduce the notation for the incident and scattered spectra in system O'' as $U_i''(k_x', k_y')$ and $U_s''(k_x, k_y)$, respectively. It should be noted that as the incident wave propagates in the positive direction, the phase shift is positive if Z is positive. The spectrum in system O'' and O' can be linked with the help of the shift theorem.[39, p. 277] Since $x = x' + X, y = y' + Y$, the spectrum of the shifted object is

$$U_i'(k_x', k_y') = U_i''(k_x', k_y')\exp[i(k_x' X + k_y' Y)] \tag{11.20}$$

Introducing first Equation 11.20 and then Equation 11.19 into Equation 11.18, we obtain for $U_s'(k_x, k_y)$

$$U_s'(k_x, k_y) = \frac{1}{(2\pi)^2}\int_{-\infty}^{\infty}\int_{-\infty}^{\infty} U_i(k_x', k_y') g_s(k_x, k_y, k_x', k_y')\exp[i(k_x' X + k_y' Y + k_z' Z)]dk_x' dk_y' \tag{11.21}$$

To return to system O, the spectrum $U_s'(k_x, k_y)$ is first shifted to the O'' system by multiplying by $\exp[-i(k_x X + k_y Y)]$:

$$U_s''(k_x, k_y) = U_s'(k_x, k_y)\exp[-i(k_x X + k_y Y)] \tag{11.22}$$

Since the integration in Equation 11.3 is made on the focal plane we must return to the focal plane by multiplying Equation 11.22 by $\exp(-ik_z Z)$:

$$U_s(k_x, k_y) = U_s''(k_x, k_y)\exp[-i(k_z Z)] \tag{11.23}$$

For the reflection SAM, we have $k_z = -\sqrt{k^2 - (k_x)^2 - (k_y)^2}$, since the backscattered wave propagates opposite to the z-direction. Combining Equation 11.3, Equation 11.13, and Equation 11.21 to Equation 11.23, we obtain the output signal of the reflection SAM as

$$V(X, Y, Z) = \int_{-\infty}^{\infty}\int\int_{-\infty}^{\infty}\int P(-k_x, -k_y)P(k_x', k_y')g_s(k_x, k_y, k_x', k_y')$$

$$\exp[i(k_x' - k_x)X + (k_y' - k_y)Y + (k_z' - k_z)Z]\frac{dk_x' dk_y' dk_x dk_y}{kk_z'} \tag{11.24}$$

On an additional assumption, Equation 11.24 is valid for the transmission acoustic microscope as well. The main difference from the reflection microscope is that $k_z = +\sqrt{k^2 - (k_x)^2 - (k_y)^2}$. Additionally, in the transmission microscope, transmitting and receiving lenses may have different pupil functions. Then the first pupil function in Equation 11.24 belongs to the detector and the second to the emitter.

An analytical expression for the integral in Equation 11.24 can be derived only in a few cases of simply shaped objects: solid half-space,[50] spherical particle,[51] subsurface spherical cavity,[8] disk,[10] cylindrical inclusion,[52] and surface-breaking crack.[38,53] We will consider most of these cases in this chapter. When an analytical solution cannot be derived, several mathematical methods can be used to understand the basic features of image formation for complex objects. One of these is the method of stationary point.[45] Despite its complex rigorous formulation,[45] it is very often implicitly used in image interpretation. One prominent example is the derivation of the formula for the period of the $V(Z)$ oscillations related to the generation of the Rayleigh surface wave.[54] Parmon and Bertoni[54] postulated that the periodical character of the so-called $V(Z)$ curve is determined by interference of two rays: the central ray and the ray that excites the Rayleigh wave on the surface of the solid half-space (see Figure 11.10a). In this model only rays hitting the surface of the hemispherical transducer perpendicularly should be taken into account. These rays appear to come from the focus when they intersect the transducer[55] and have a stationary point in the integral in Equation 11.24. The use of the method of a stationary point for interpreting acoustical images is closely related to the fact that we used the Debye approximation for deriving Equation 11.24. According to Stamnes,[45] the Debye approximation "is a geometrical-optics approximation in the sense that only the contribution of the interior stationary points is accounted for the asymptotic evaluation of the angular spectrum; the end point contribution is neglected."

11.3.1 Two-Dimensional Objects

11.3.1.1 Signal from a Half-Space

Knowing the general expression for the output signal of the SAM, we can derive the expression of the images of simply shaped objects. We start with the simplest case, the SAM signal from a homogeneous half-space. In this case, we can present the spectrum of the reflected field as a simple multiplication of the incident field and the reflection coefficient:[56]

$$U_s(k_x, k_y) = \Re(k_x, k_y) U_i(k_x, k_y) \tag{11.25}$$

From Equation 11.3 and Equation 11.18 we obtain

$$g_s(k_x, k_y, k'_x, k'_y) = (2\pi)^2 \delta(k_x - k'_x)\delta(k_y - k'_y)\Re(k'_x, k'_y), \tag{11.26}$$

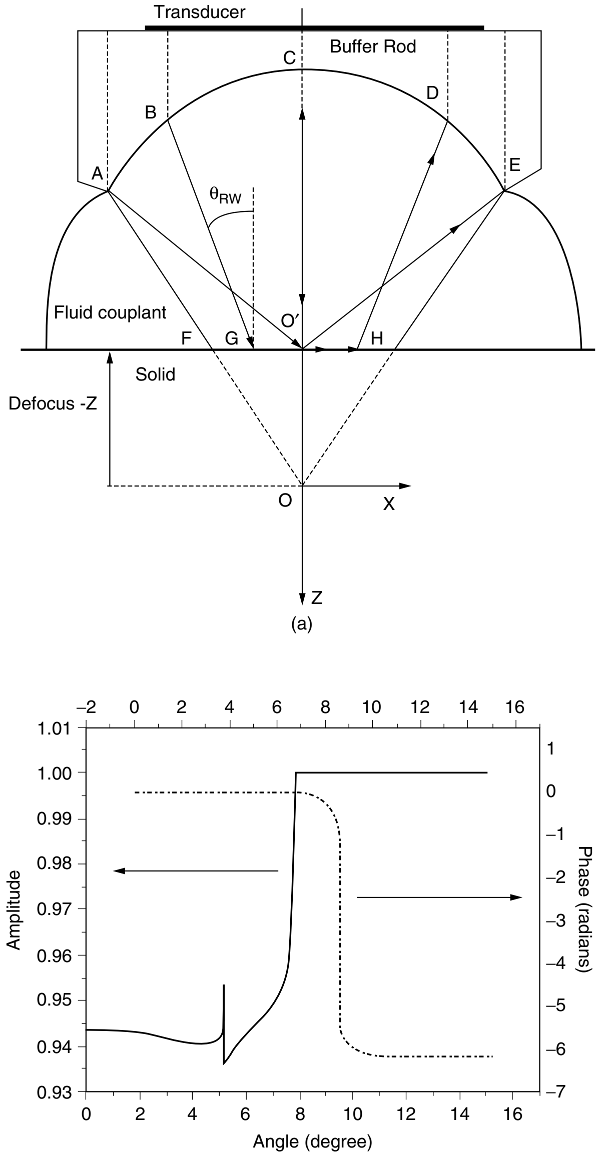

FIGURE 11.10
(a) Ray model interpretation for the paths of different wave components in the case of negative defocus ($Z < 0$). CO′ is the trajectory of a specular or geometrical wave. BGHD is the trajectory of a leaky (pseudo) Rayleigh wave. In the ray model the leaky Rayleigh wave is excited by ray BG, striking the surface at the angle $\theta_{SAW} = v_W / v_{SAW}$. AO′E is the trajectory of the edge wave. Rays AF, BG, HD, and EK are assumed to be normal to the hemispherical surface and appear to come from the focus when they intersect the transducer and liquid/solid interface. (b) Magnitude (solid line) and phase (dotted line) of the reflection coefficient from a water/superhard amorphous carbon interface.

where δ is the Dirac delta function. Substituting Equation 11.26 into Equation 11.24, we finally have as the output signal for the reflection microscope

$$V(Z) = \int_{-\infty}^{\infty}\int P(-k_x,-k_y)P(k_x,k_y)\Re(k_x,k_y)\exp(i2k_zZ)\frac{dk_x dk_y}{kk_z} \quad \textbf{(11.27)}$$

The fact that the signs in the arguments for the two pupil functions are different is important to investigating the inclined surfaces.[57] Taking into account that in the Debye approach the maximum angle of integration is restricted by the semiaperture angle α of the pupil to $\sqrt{(k_x')^2+(k_y')^2} \le k\sin\alpha$,[58] and introducing spherical coordinates in k space, we can replace Equation 11.27 by

$$V(Z) = \int_0^{2\pi} d\varphi_k \int_0^{\alpha} P(\theta_k,\varphi_k)P(\theta_k,\varphi_k+\pi)\Re(\theta_k,\varphi_k)\exp(i2k\cos\theta_k Z)\sin\theta_k d\theta_k \quad \textbf{(11.28)}$$

Assuming isotropy of the pupil function and integrating over φ_k we obtain an expression for the signal variation with the distance from the sample

$$V(Z) = \frac{V_o}{(1-\cos\alpha)}\int_0^{\alpha} P^2(\theta)\Re(\theta)\exp(i2kZ\cos\theta)\sin\theta d\theta \quad \textbf{(11.29)}$$

where V_0 is the signal of the acoustic microscope from a perfectly reflecting surface located in the focal plane.[59] The normalizing coefficient $V_0/(1-\cos\alpha)$ is important for simulating the signal from a subsurface defect described below. For a perfectly reflecting object ($\Re(\theta) = 1$) and a lens with elementary pupil function, the $V(Z)$ curve is a *sinc* function:

$$V(Z) = \frac{\sin[kZ(1-\cos\alpha)]}{kZ(1-\cos\alpha)} \quad \textbf{(11.30)}$$

The physical interpretation of the $V(Z)$ curve can be obtained by introducing the substitution[60,61] $t_\theta = 2/\lambda \cos\theta$ into the integral in Equation 11.29:

$$V(Z) = \int_{2/\lambda\cos\alpha}^{2/\lambda} P^2(t_\theta)\Re(t_\theta)\exp(i2\pi t_\theta k_z Z)dt_\theta \quad \textbf{(11.31)}$$

The normalizing constant in Equation 11.31 is omitted. Since the pupil function is unequal to zero only within $0 < \theta \le \alpha$, or when $(2/\lambda)\cos\alpha \le t\theta \le 2/\lambda$, the limits of the integral in Equation 11.31 can be extended from $-\infty$ to ∞

$$V(Z) = \int_{-\infty}^{\infty} P^2(t_\theta)\Re(t_\theta)\exp(i2\pi t_\theta k_z Z)dt_\theta \qquad \textbf{(11.32)}$$

Therefore, the $V(Z)$ curve is the Fourier transform of the product of the pupil function squared and the reflection coefficient. Equation 11.31 was used to reconstruct the complete reflection function of the solid sample and to study the surface acoustic wave propagation in multilayered solids.[43,60,62,63] An analytical expression of the reflection coefficient for a solid half-space is given in Appendix A. Figure 11.10b illustrates the behavior of amplitude and phase of the reflection coefficient for superhard amorphous diamond obtained at high-pressure (13.5 GPa) and high temperature (900 ± 100°C) (see parameters in Table 11.1). The amplitude shows a small dip associated with the longitudinal critical angle, sin $\theta_P^c = c/c_p$. The phase of the reflection coefficient has a small kink for the same angle. Obviously, above this angle, only shear waves penetrate into the substrate. Above the shear critical angle ($\sin\theta_S^c = c/c_s$), the magnitude of the reflection coefficient equals 1. At the Rayleigh angle, which is bigger than the shear angle, a phase change of 2π occurs, which is characteristic of Rayleigh surface wave propagation.[2]

The theory of the $V(Z)$ curve is important for understanding contrast formation in the SAM.[2] However, it is beyond the scope of this chapter, and we discuss this theory only briefly. To analyze the image formation in the reflection acoustic microscope, Atalar et al.[64] monitored the amplitude of the transducer voltage V as a function of lens-to-sample spacing Z, or the $V(Z)$ curve. A famous feature of the $V(Z)$ curve is the oscillation behavior[65](see Figure 11.11). The periodicity of dips appearing in the $V(Z)$ curves reported by Weglein and Wilson[65] soon was linked to surface wave propagation.[54,65,66] Invention of the line focus acoustic microscope with a cylindrical lens by Kushibiki et al.[67] made it possible to measure the anisotropy of surface acoustic waves on a crystal surface.[19] Considerable progress in contrast formation or $V(Z)$ curve theory has been made since then. Now the theory of the $V(Z)$ curve has been developed for multilayered solids,[68,69] plates,[70] for anisotropic materials,[71,72] and for different types of surface acoustic waves[73,74] and curved surfaces.[75,76] Detailed description of the $V(Z)$ curve formation and recent developments in application of the $V(Z)$ curve measurement for material characterization in quantitative acoustic microscopy can be found in references.[2,4,19]

11.3.1.2 Image Formation of Two-Dimensional Objects

Images of many solid samples in the SAM exhibit a strong Rayleigh wave contrast.[2] We will return to this point in the next paragraph and consider now image formation of two-dimensional objects when Rayleigh waves are not excited. Such an approach can be used for a SAM having a lens with a small semiaperture angle (α must be smaller than the Rayleigh angle), which

TABLE 11.1

Velocities, Critical Angles, Wavelength for the Rayleigh wave (Equal to the Penetration Depth of the Rayleigh Wave at 1 GHz) and Depth of the Longitudinal and Shear Waves Penetration for Different Isotropic Materials

Material	Density (kg/m^3)	c_p (km/sec)	θ_P^c (°)	c_S (km/sec)	θ_S^c (°)	c_{RW} (km/sec) λ_{RW} at 1 GHz (μm)	$Z_{P\text{-}30}$ (μm)	$Z_{S\text{-}30}$ (μm)	Ref.
Plexiglass	1100	2.70	33.7	1.10		1.04	16.7	40.9	
Gold	19281	3.24	27.6	1.2		1.13	13.8	37.5	2
Amorphous carbon film	2800	4.4	19.9	3.7	40.0	2.7	10.2	12.2	
Quartz (fused)	2200	5.97	14.6	3.2	27.9	3.0	7.5	14.1	2
Aluminum	2700	6.2	13.5	3.0	29.6	2.8	7.0	15	2
TiN	5300	9.4	9.2	5.7	15.2	5.2	4.8	7.9	154
Si_3N_4	3185	10.6	8.1	6.2	14.0	5.7	4.2	7.3	2
SiC	3210	12.1	7.1	7.5	11.5	6.8	3.7	6	2
cBN	3500	15.8	5.4	10.4	8.3	9.3	2.8	4.3	155
Amorphous carbon obtained from C^{60}	3150	16.6	5.2	10.2	8.5	9.8	2.7	4.4	87
Diamond	3515	18.1	4.7	12.3	6.9	10.9	2.5	3.7	156

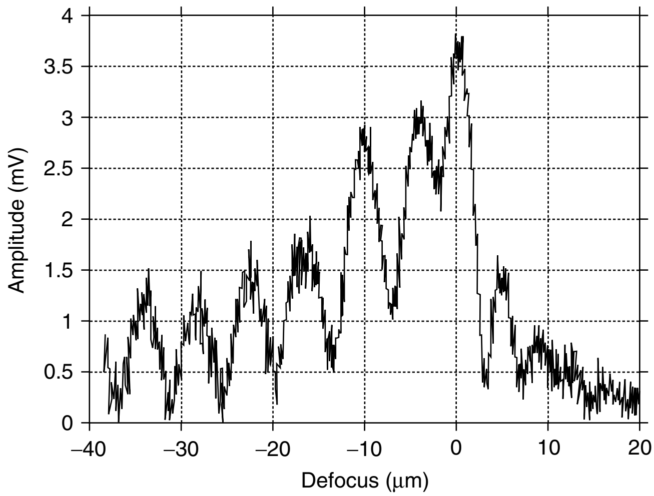

FIGURE 11.11
$V(Z)$ curve of 0.2-μm oxide film on aluminum measured at 980 MHz. Measurements were made at Oxford line focus microscope and modified for high frequency. (Briggs, A., *Advances in Acoustic Microscopy*, Plenum Press, New York, 1995, pp. 153–208.)

is widely used in nondestructive evaluation (NDE) for imaging subsurface structures.[77] In this approximation it is also assumed that at each point in the sample, the surface reflection is independent of the angle of the incident spectral component: $\Re(\theta) = \text{const}$.

Without excitation of surface acoustic waves, the problem can be simplified. The reflection properties can be defined by the reflectance function $R_o(x, y)$ of the object.[39, p52] The acoustic field Φ_s reflected from the sample is proportional to the product of the incident field and the reflectance function in the spatial domain

$$\Phi_s(x,y) = \Phi_i(x,y)R_o(x,y) \tag{11.33}$$

If we introduce the Fourier transform of the reflection function $R_o(x, y)$,

$$\Re_o(k_x,k_y) = \int_{-\infty}^{\infty}\int R_o(x',y')\exp[-i(k_x x' + k_x y')]\,dx'dy' \tag{11.34}$$

With the help of the convolution theorem of Fourier analysis, the Equation 11.33 can be rewritten as

$$U_s'(k_x,k_y) = \frac{1}{(2\pi)^2}\int_{-\infty}^{\infty}\int U_i'(k_x',k_y')\Re_o(k_x - k_x',k_y - k_y')\,dk_x'dk_y' \tag{11.35}$$

Comparing Equation 11.18 and Equation 11.35 we see that the density of the scattered spectrum is

$$g_s(k_x, k_y, k'_x, k'_y) = \Re_o(k_x - k'_x, k_y - k'_y) \quad \textbf{(11.36)}$$

The dependence of the scattering function g_s only of the variable differences enables us to present the output signal as an inverse Fourier integral of the object spectrum and the optical transfer function (OTF). We introduce Equation 11.36 into Equation 11.24 and substitute k'_x for $k_x - k'_x$ and k'_y for $k_{y^-} - k'_y$ and keep $k_{x,}\ k_y$. After changing the order of integration, we obtain

$$V(X,Y,Z) = \int\limits_{-\infty}^{\infty}\int \Re_o(k'_x, k'_y) H_R(k'_x, k'_y, Z) \exp[-i(k'_x X + k'_y Y)] dk'_x dk'_y \quad \textbf{(11.37)}$$

with the OTF for reflection SAM

$$H_R(k'_x, k'_y, Z) = \int\limits_{-\infty}^{\infty}\int dk_x dk_y P(k_x - k'_x, k_y - k'_y) P(-k_x, -k_y)$$

$$\frac{\exp\left[i\sqrt{k^2 - (k_x - k'_x)^2 - (k_y -)^2}\,Z\right]\left[i\sqrt{k^2 - k_x{}^2 - k_y{}^2}\,Z\right]}{\sqrt{k^2 - (k_x - k'_x)^2 - (k_y - k'_y)^2}} \quad \textbf{(11.38)}$$

In Equation 11.38 we have taken into account that $k_z = -\sqrt{k^2 - k_x^2 - k_y^2}$. The OTF describes the spectral properties of the imaging system. It determines how the different angular spectrum components of the object contribute to the image contrast.

The calculation of the OTF can be performed analytically only for the elementary pupil function in Equation 11.4.[10,78] The determination of the OTF for a real microscope system is a complex problem.[79] For a SAM it has been investigated elsewhere.[77,80] A direct method for measuring the OTF of a focused system ($Z = 0$) was presented by Atalar,[81] who has shown that the image scanned along the surface of a spherical particle exhibits the transfer function of the microscope. This method has been extended to measure the defocused OTF using three-dimensional images of steel spheres.[82] Figure 11.12a is an *X*-*Z*-scan of the top of a steel sphere. The value of the image amplitude is stored and the spherical scan extracted from the data. The method is valid for determination of the complex transfer function if phase measurement results are available. The moduli of the transfer function at different focal positions derived from Figure 11.12a are depicted in Figure 11.12b.

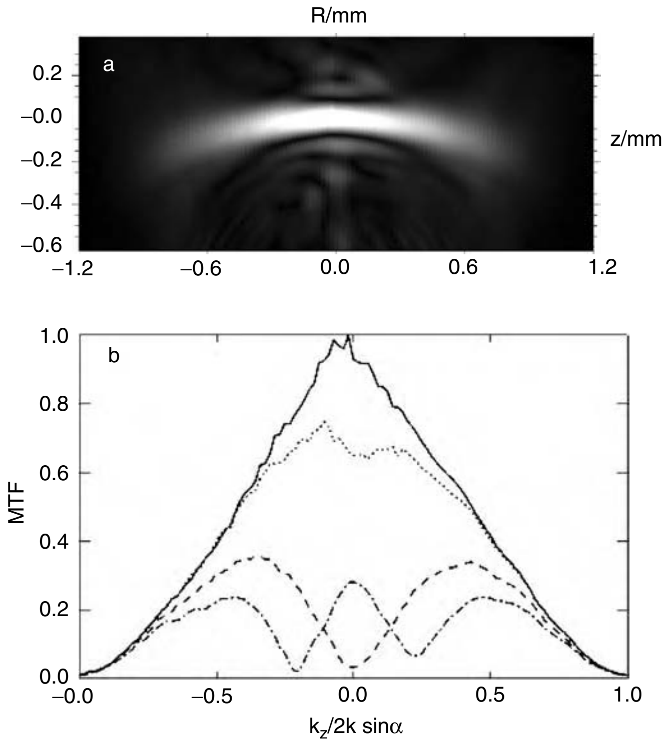

FIGURE 11.12
(a) *X-Z* scans of a steel ball of 2.5-mm radius taken at a frequency of 91 MHz. Semiaperture angle of the lens is equal to 27°. (b) Defocused OTF obtained in the LFM by scanning along an arc at different normalized defocusing positions $w = kZ\sin_2\alpha$. Solid line for $w = 0$, dotted for $w = 3$, dashed for $w = 6$, dash-dotted for $w = 8$. (From Zinin, P. et al., *Optik,* 107, 45, 1997. With permission.)

The basic features of two-dimensional objects imaging can be illustrated by using a perfectly reflecting disk. The circular disk is widely used as a model of penny shaped subsurface cracks. To calculate the images of a disk at different focal plane positions we will use the OTF in the paraxial approximation (k_x, $k_y \ll k$) for the SOM.[10,83] In the simplified Kirchhoff approximation, a perfecty reflecting disk is defined by the reflectance function of the object.[39, p. 52] $r_d(x,y)=1$ for (x, y) inside the disk, and $r_d(x,y)=0$, otherwise. The perfectly reflecting disk of radius a, has the angular spectrum[39,p. 64]

$$\Re_d(k_x,k_y) = 2\pi a \frac{J_o(k_t a)}{k_t} \tag{11.39}$$

Here we have defined the cylindrical transverse radial spatial frequency as $k_t = \sqrt{k_x^2 + k_y^2}$. The images of a rigid reflecting disk-shaped plane calculated

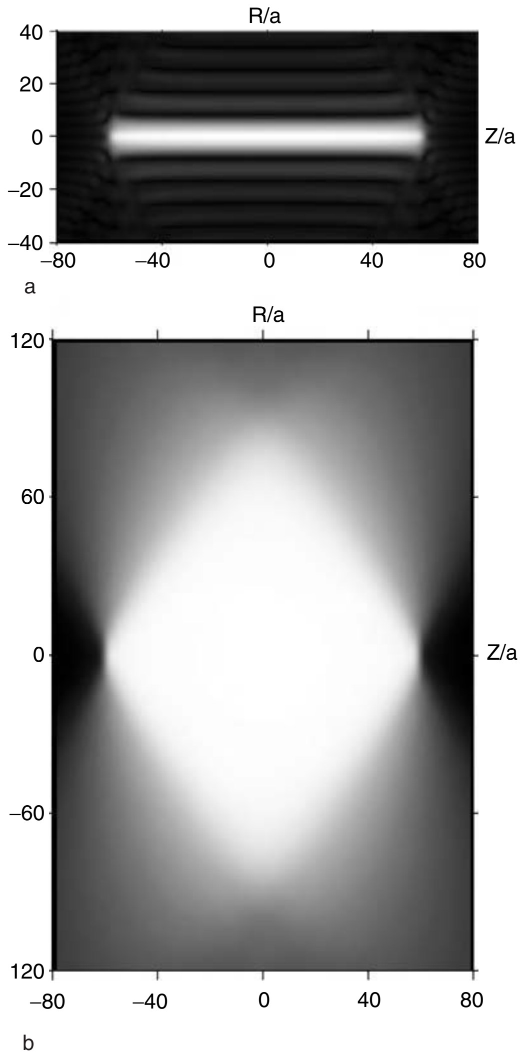

FIGURE 11.13
X-Z medial section of a rigid disk (*ka* = 60) calculated for a reflection SAM (top) and of a circular hole in a rigid screen (*ka* = 60) for a transmission SAM (bottom). Semiaperture angle of the transducer is equal to 60°. Axes scaled in units of the disk's radius. (From Zinin, P. et al., *Wave Motion*, 25, 213, 1997. With permission.)

with the help of Equation 11.39 in reflection and transmission SAMs are presented in Figure 11.13. In the reflection SAM, the three-dimensional area in which the image contrast mainly occurs can be regarded as a thin bright layer (Figure 11.13a). In the lateral direction, the dimension of the image is approximately equal to the dimension of the object. The thickness of this layer is proportional to the width of the main maximum of the $V(Z)$ curve/

(1 − cos α) (Equation 11.27). For the transmission microscope, we consider a circular hole in a perfectly reflecting screen. In contrast to the image in the reflection SAM, the image in Figure 11.13b is elongated, the elongation depending on the semiaperture angle. In the focus, the lateral size of the image coincides with that of the sample.

11.3.1.3 Image Formation of Surface Breaking Cracks

In this section we will take a closer look at the reflection coefficient in case Rayleigh surface waves are excited by the wave incident from the coupling liquid. The results will then be applied to investigate the effect of surface breaking cracks.

Along the surface of a solid sample, Rayleigh surface waves can propagate. If the surface is loaded with a liquid, these waves are denoted as leaky Rayleigh waves, as they can radiate into the liquid. Reciprocally, they can also be excited by waves arriving on the surface from the liquid. As Rayleigh waves exhibit a strong motion component orthogonal to the surface, they strongly interact with fluid waves.

The effect of Rayleigh waves on the SAM output signal may be included in the reflection coefficient $\Re$ in Equation 11.25 of an infinite half-space. In the simplest form, $\Re$ may be approximated by the sum of the reflection coefficient $\Re_o$ without the Rayleigh wave and a second term with singularities in the complex plane that contains the effect of the Rayleigh wave[38]

$$\Re(k_x, k_y) \approx \Re_o(k_x, k_y) + \frac{4i\alpha_R k_R}{k_x^2 + k_y^2 - k_p^2} \tag{11.40}$$

Here $k_p = k_R + i\alpha_R$ is the complex wave number of the Rayleigh wave. The imaginary part $i\alpha_R$ describes the exponential decay of the wave due to energy loss by irradiation into the coupling liquid. Real and imaginary parts must be equal in sign to describe a decaying wave; for convenience, we choose both to be positive. For Equation 11.40 to be valid it is assumed that the damping α_R is much smaller than k_R. The second term in Equation 11.40 describes the excitation and re-radiation into the coupling liquid of the leaky Rayleigh wave. It has a considerable influence on the reflection coefficient only if $\sqrt{k_x^2 + k_y^2} = k_R$. This is the condition for excitation and radiation of the surface wave. The angle θ_R the fluid wave then forms with the surface normal is given by $k \sin\theta_R = k_R$ in accordance with Snell's law.

If a lens with a semiaperture angle wider than the Rayleigh angle is used in the SAM, the *V*(*Z*) curve is strongly influenced by Rayleigh waves. On the detector the radiated Rayleigh wave signal and the specularly reflected wave signal will interfere. This interference changes when the distance between microscope and surface changes. But this will only hold if the defocus *Z* is negative. For positive defocus, the excited Rayleigh wave is not detected by the microscope, and the second term in Equation 11.40 does not give a signal. As the speed of the Rayleigh wave depends on the material properties, the signal recorded at changing distance, the $V(Z)$ curve, will exhibit a characteristic signature of the material for negative defocus, as can be observed from Figure 11.11. In general this $V(Z)$ curve is evaluated to investigate the properties of the sample. Instead of point focus lenses line focus lenses are often used for material investigation because the relative contribution of the Rayleigh wave and the specularly reflected wave to the microscope signal are more similar in this case. Material parameters may then be derived more precisely. The spectrum of line focus lenses can be assumed as independent of k_y.

In the following we will formulate the effect of Rayleigh waves on reflection in terms of a Green function. For simplicity, we will restrict to the case of the line focus lens. The one-dimensional relation between the reflected field distribution along the surface of a solid half-space and its angular spectrum is similar to that given by Equation 11.2:

$$\Phi_s(x) = \frac{1}{2\pi}\int_{-\infty}^{\infty} U_s(k_x)\exp(ik_x x)dk_x \quad \textbf{(11.41)}$$

The part of the reflected wave field $\Phi_s(x)$ that is due to the Rayleigh wave is obtained by inroducing Equation 11.25 into Equation 11.41, introducing the second term from Equation 11.40 and writing $U_i(k_x)$ as the Fourier transform of $\Phi_i(x)$

$$\Phi_s(x) = \frac{1}{2\pi}\int_{-\infty}^{\infty}\int_{-\infty}^{\infty} \frac{4i\alpha_R k_R}{k_x^2 - k_p^2}\Phi_i(x')\exp[ik_x(x-x')]dx'dk_x \quad \textbf{(11.42)}$$

After changing the order of integration, the integral over k_x is evaluated with the aid of the calculus of residues. For $x - x' > 0$ the path of integration is complemented through the upper half of the complex k_x plane enclosing the pole at k_p (remember we chose the real part of k_p greater than 0). For $x - x' < 0$ the path is complemented through the lower half and the pole at $-k_p$ is enclosed. Equation 11.42 yields

$$\Phi_s(x) = 2\alpha_R\left\{\int_{-\infty}^{x}\Phi_i(x')\exp[ik_p(x-x')]dx' + \int_{x}^{\infty}\Phi_i(x')\exp[ik_p(x'-x)]dx'\right\} \quad \textbf{(11.43)}$$

This may be rewritten with the aid of the Green function G(x, x'):

$$\Phi_s(x) = \int_{-\infty}^{\infty} G(x,x')\Phi_i(x')dx' \quad \textbf{(11.44)}$$

where $G(x, x')$ is defined by

$$G(x,x') = -2\alpha_R \exp(ik_p |x - x'|) \quad \textbf{(11.45)}$$

The Green function can be easily interpreted: It describes the field reflected from the sample surface at position x due to excitation at position x'. Equation 11.45 shows that the connection from x' to x is arranged by the decaying Rayleigh wave with wave vector k_p.

Interesting effects on the image obtained with the SAM will occur when there are surface discontinuities such as cracks or an abrupt change in the material properties and if a lens with a high semiaperture angle is used. Even if the width of a crack is much smaller than the resolution limit, it will immediately be recognized by fringes surrounding.[84,85] The reason for this is that Rayleigh waves generated on the surface will be reflected at the discontinuity. The reflected Rayleigh wave is then detected by the microscope.[86] Its phase will change when scanning parallel to the surface toward the discontinuity or away from it, leading to a change of the interference with the rest of the signal. This interference leads to fringes parallel to the crack, as can be observed in Figure 11.14. The Figure shows a SAM image of superhard amorphous carbon obtained at high pressure (13 GPa) and high temperature (800 ± 100°C) (for details see Manghnani et al.[87]). The defocus is $z = -20$ μm at 400 MHz. Strong fringes can be seen around the cracks and close to the sample edges. In the following paragraphs, we will quantitatively investigate the effect of a crack according to a derivation by Somekh et al.[38]

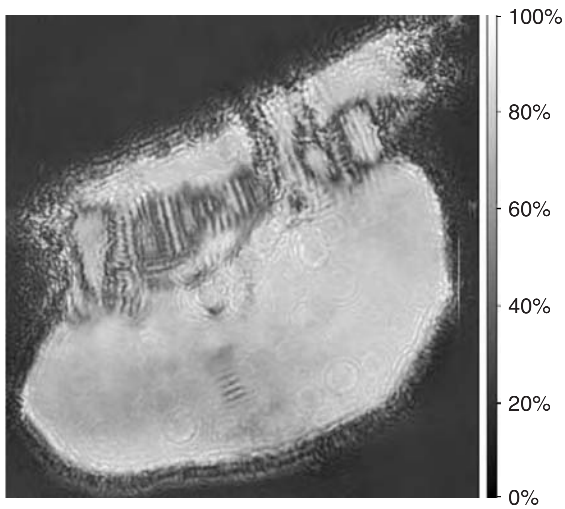

FIGURE 11.14
Acoustic image of amorphous carbon (the elastic properties are given in Table 11.1) at 400 MHz and at a defocus $z = -20$ μm.

The reflection in the vicinity of the crack will show a structural difference as compared to Equation 11.40. Let us assume that the crack runs in the y-direction. Then an incident plane wave with a wave vector component k_x will not simply be reflected with $k'_x = k_x$, but will include an additional part from the Rayleigh wave reflected at the discontinuity with the wave vector component $k'_x = -k_x$. We therefore will have to describe the reflected wave in terms of the scattering function $g_s(k_x, k_y, k'_x, k'_y)$ from Equation 11.18 instead of a reflection coefficient from Equation 11.40. It is now assumed that the reflection coefficient without the Rayleigh wave $\Re_o$ will not be influenced by the crack. This requires that the width of the crack be small in comparison to the wavelength in the coupling liquid and that its presence not change the surface elasticity or compliance so that no edge diffraction occurs. Moreover, we assume that no other surface waves are of importance. We will consider only the case that the field is constant in the y-direction, as for a SAM with a line focus lens oriented parallel to the crack. A treatment of the case of a point focus lens can be found in Rebinsky and Harris.[53] We will intuitively make use of the Green function (Equation 11.45) to construct the reflected field. We will assume that on the two sides of the crack the same material is found (for different materials see Somekh et al.[38]).

If a Rayleigh wave reaches the crack, it will in part be reflected with an in-plane reflection coefficient R and in part be transmitted with an in-plane transmission coefficient T. The values of R and T depend on the depth of the crack in comparison to the penetration depth of the Rayleigh wave. As some energy may be transformed into waves other than a Rayleigh surface wave, $R^2 + T^2$ may be less than 1. Without restriction of generality, we assume that the surface is located at $z = 0$ and the crack at position $x = 0$.

Let us first consider the field scattered into the coupling liquid from the surface left of the crack, hence $x < 0$. The Rayleigh waves arriving at position x will have different histories. Part of the Rayleigh wave is not affected by the crack. These waves have been excited either at positions x' with $x' < x$ traveling to the right, or at positions x' with $x < x' < 0$ traveling to the left. The contributions of these two parts are

$$-2\alpha_R\left[\int_{-\infty}^{x}\Phi_i(x')\exp[ik_p(x-x')]dx' + \int_{x}^{0}\Phi_i(x')\exp[-ik_p(x-x')]dx'\right] \qquad \textbf{(11.46)}$$

Another part has been excited at $x' < 0$; traveled to the right toward the crack; and after reflection at the crack, traveled to the left. Finally, one part has been excited at $x' > 0$, traveled to the left, and has been transmitted through the crack. The contributions of the latter two parts are

$$-2\alpha_R\exp[-ik_p(x-0)]\left[R\int_{-\infty}^{0}\Phi_i(x')\exp[ik_p(0-x')]dx' + T\int_{0}^{\infty}\Phi_i(x')\exp[-ik_p(0-x')]dx'\right] \qquad \textbf{(11.47)}$$

Note that in Equation 11.47 the Rayleigh wave is excited only before interaction with the crack. This restricts the integration over x'. The construction of the contributions arriving at a point x situated to the right of the crack is derived accordingly.

We now will assume that the whole expression for $\Phi_s(x)$, as given by the sum of the Equation 11.46 and Equation 11.47, is written with aid of a Green function in the form of Equation 11.45. We therefore may assume that the finite limits of the integrals are accounted for by multiplying the integrands with step functions. The different form of G for $x < 0$ and $x > 0$ may also be accounted for by step functions. To calculate the scattering function $g_s(k_x, k_x')$ we Fourier transform the whole expression and express $\Phi_i(x')$ as an inverse Fourier transform of $U_i(k_x')$ according to Equation 11.2 and Equation 11.1:

$$U_s(k_x) = \int_{-\infty}^{\infty}\int_{-\infty}^{\infty} G(x, x')\left\{\frac{1}{2\pi}\int_{-\infty}^{\infty} U_i(k_x')\exp(ik_x'x')dk_x'\right\}\exp(-ik_x x)dx'dx \qquad \textbf{(11.48)}$$

Changing the order of integration we find by comparison to Equation 11.18 that

$$g_s(k_x, k_x') = \int_{-\infty}^{\infty}\int_{-\infty}^{\infty} G(x, x')\exp(ik_x'x')\exp(-ik_x x)dx'dx \qquad \textbf{(11.49)}$$

For the evaluation of the integration over x' with an infinite boundary on one side, it may be utilized that the damping α_R leads to a decay of the integrand toward this boundary. The remaining integration over x can be carried out using a property of the delta function

$$\int_{-\infty}^{\infty} \exp\left[i(k_x' - k_x)x\right]dx = 2\pi\delta(k_x' - k_x) \qquad \textbf{(11.50)}$$

Including the term $\Re_o\delta(k_x' - k_x)$ that describes the specularly reflected field, we finally obtain

$$\begin{aligned} g(k_x, k_x') = \delta(k_x' - k_x)&\left[\Re_0 + \frac{4i\alpha_R k_R}{k_x^2 - k_p^2}\right] \\ &- \frac{\alpha_R(1-T)}{\pi}\left[\frac{1}{(k_x' - k_p)(k_x - k_p)} + \frac{1}{(k_x' - k_p)(k_x - k_p)}\right] \\ &- \frac{\alpha_R R}{\pi}\left[\frac{1}{(k_x' - k_p)(k_x - k_p)} + \frac{1}{(k_x' - k_p)(k_x - k_p)}\right] \end{aligned} \qquad \textbf{(11.51)}$$

The term in the first square brackets describes the reflection at the half-space without crack. It is the only part that remains for $T = 1$ and $R = 0$. The Rayleigh term there is a Lorentz function that is the Fourier transform of an exponential wave decaying to both sides of $x = 0$. The delta function makes the effect of this term translation invariant in the position space. The other terms are due to transmission or reflection of the surface wave. Their forms are due to the wave cutoff at the position of the crack. In both variables the terms are Fourier transforms of exponential waves that are set to 0 on either side of $x = 0$ and decay to the other side. The terms containing $(1 - T)$ reduce beyond the crack the amplitude of the waves that are due to the Lorentz function. For positive defocus besides the specular reflection, only the terms containing R have considerable influence on the microscope signal.

The fringe spacing around a surface breaking crack or a material boundary can be used to determine the Rayleigh velocity. It simply is half the wavelength of the Rayleigh wave. For the sample shown in Figure 11.14, this yields a Rayleigh wave velocity of (8.0 ± 2.1) km/sec, whereas Brillouin scattering measurements[87] of the Rayleigh wave velocity of the same sample yields (6.7 ± 0.3) km/sec. We note that though the error of the measured Rayleigh wave velocity by the SAM is greater than that determined by Brillouin scattering, the SAM measurements provide a reasonable estimate of the surface acoustic wave velocity of the superhard sample.

11.3.2 Image Formation of Three-Dimensional Objects

In confocal optical microscopy the theories of three-dimensional image formation are usually based on the Born approximation and so are valid only for weakly scattering objects.[88] In the case of biological materials, the Born approximation to the scattering problem can be used both in acoustics and in optics. Because acoustic microscopy is widely applied to hard materials involving strong scattering, it is necessary to extend the theories available today to include these objects. In this section, we will present a theory of image formation for strongly scattering spheres in the reflection SAM following a method proposed by Weise et al.[9] The imaging of spheres forms the basis for understanding the contrast of many objects, extending from bubbles or spherical inclusions in solids to curved surfaces in general. Moreover, beads are used as well-defined phantom objects for testing imaging systems.[89] From the theoretical point of view, spheres are the only three-dimensional particles for which an analytical solution of the scattering problem is available. Due to its sectioning ability, the confocal microscope is frequently used for surface profiling. It can be done by searching the axial contrast maximum.[90] However, spherical particles are an example that contrast maxima may also occur when the surface is considerably defocused (when the focus is in the center of the curvature).

In general the part of the scattering function describing the behavior of homogeneous (non-evanescent) waves, which is important for confocal imaging, can also be obtained directly from the far-field distribution of the scattered wave. The asymptotic behavior of the field distribution Φ_s scattered from a bounded obstacle for an incident plane wave with wave vector k' can be written as[91]

$$\Phi_s\left(\frac{\boldsymbol{k}}{k}r\right) = f\left(\frac{\boldsymbol{k}}{k'}\frac{\boldsymbol{k}'}{k'}\right)\frac{\exp(ikr)}{r}, \quad \text{as} \quad kr \to \infty \tag{11.52}$$

where r is the distance from the origin and $f\left(\frac{\boldsymbol{k}}{k'}\frac{\boldsymbol{k}'}{k'}\right)$ is the far-field scattering amplitude. The relation of the homogeneous wave part of the scattering function g to the far-field scattering amplitude $f\left(\frac{\boldsymbol{k}}{k'}\frac{\boldsymbol{k}'}{k'}\right)$ can be obtained using the angular spectrum representation of the far-field distribution[92, p.114]

$$g_s(k_x, k_y, k'_x, k'_y) = \frac{i}{2\pi k_z} f\left(\frac{\boldsymbol{k}}{k'}\frac{\boldsymbol{k}'}{k'}\right) \quad \text{for} \quad k_x{}^2 + k_y{}^2 < k^2. \tag{11.53}$$

Combining Equation 11.24 and Equation 11.53 and omitting the normalizing constant, we obtain

$$V(X,Y,Z) = \int_{-\infty}^{\infty}\int\int_{-\infty}^{\infty}\int P(-k_x, -k_x)P_s(k'_x, k'_x) f\left(\frac{\boldsymbol{k}}{k'}\frac{\boldsymbol{k}'}{k'}\right)$$

$$\exp[i(k'_x - k_x)X + (k'_y - k_y)Y + (k'_z - k_z)Z]\frac{dk'_x\, dk'_y\, dk_x\, dk_y}{kk'_z kk_z} \tag{11.54}$$

The same expression has been obtained in Zinin et al.,[10] but tedious calculation is required. The far-field angular distribution for scattering by a spherical particle can be found analytically[91]

$$f\left(\frac{k}{k'}\frac{\boldsymbol{k}'}{k'}\right) = \frac{1}{k}\sum_{n=0}^{\infty}(2n+1)A_n P_n(\cos\gamma_k) \tag{11.55}$$

where the A_n describe the scattering amplitudes that depend on particle size and material properties, and P_n are ordinary Legendre polynomials. γ_k is the angle between k and k'. In the scalar theory the A_{nm} are independent of m. [93]

In order to separate incident wave and reflected wave coordinates in Equation 11.55, we use the addition theorem for spherical harmonics[94] $Y_{n,m}$

$$P_n(\cos\gamma_k) = \frac{4\pi}{(2n+1)}\sum_{n=-m}^{m} Y^*_{n,m}\left(\frac{\boldsymbol{k}'}{k'}\right)Y_{n,m}\left(\frac{\boldsymbol{k}}{k}\right) \tag{11.56}$$

To evaluate the integral in Equation 11.54 we introduce spherical coordinates (Equation 11.9) and assume that P is independent of φ_k. After combining Equation 11.54 to Equation 11.56; writing $Y_{n,m}$ with the aid of the associated Legendre polynomials[94] $P_n^m(\cos\theta), Y_{n,m}(\theta_k,\varphi_k) = \sqrt{\frac{(2n+1)(n-m)!}{4\pi(n+m)!}}\, P_n^m(\cos\theta_k)\exp(im\varphi_k)$; and using the integral definition of the cylindrical Bessel functions J_m,

$$J_m(kR\sin\theta_k) = \frac{(\pm i)^m}{2\pi}\int_0^{2\pi}\exp\left[\pm i\left(kR\sin\theta_k\cos\theta_k + m\varphi_k\right)\right]d\varphi_k \qquad \textbf{(11.57)}$$

we finally obtain the output signal of the reflection SAM

$$V(R,Z) = \frac{V_o}{(1-\cos\alpha)}\sum_{n=0}^{\infty}\sum_{m=0}^{n}(-1)^n(2-\delta_{om})A_n I_{nm}^2(R,Z) \qquad \textbf{(11.58)}$$

$$I_{nm}(R,Z) = (-1)^m\int_0^{\alpha}P(\theta)\exp\left(ikZ\cos\theta\right)J_m(kR\sin\theta)\bar{P}_n^m(\cos\theta)\sin\theta\, d\theta \qquad \textbf{(11.59)}$$

where $\bar{P}_n^m(\cos\theta) = P_n^m(\cos\theta)N_{nm}$ and $N_{nm} = \sqrt{(2n+1)(n-m)!/\left[2(n+m)!\right]}$ are the normalizing coefficients and δ_{om} is the Kroneker delta symbol. To derive Equation 11.59, we also used properties of the Legendre polynomials: $P_n^m(-\cos\theta) = (-1)^{n+m}P_n^m(\cos\theta)$. For the transmission SAM the expression for the output signal has the form

$$V(R,Z) = \frac{V_o}{(1-\cos\alpha)}\sum_{n=0}^{\infty}\sum_{m=0}^{n}(-1)^n(2-\delta_{om})A_n I_{nm}(R,Z)I_{nm}^*(R,Z) \qquad \textbf{(11.60)}$$

where the superscript * denotes the complex conjugate. The model given by Equation 11.59 to Equation 11.60 describes contrast formation in the reflection SAM for spherical particles. C-scan images of spherical particles are formed by scanning in the *xy*-plane at a fixed Z position. If $Z = 0$, the focal plane passes through the center of the sphere. If $Z = a$, the focal plane touches the front surface of the sphere. Because of axial symmetry, the image of a sphere can be characterized by a curve that depends only on the distance R between the center of sphere and the axis of the lens ($V(R)$ curve). In such a case only the *X*-*Z* medial section (*X*-*Z*-scan) of the three-dimensional images may be considered.

Experimental and simulated *X*-*Z*-scans of a steel sphere are presented in Figure 11.15a and Figure 11.15b. To calculate the *X*-*Z*-scan of a spherical particle in the reflection and the transmission SAM, we use the elementary pupil function and expand the integral I_{nm} in a series.[93] The images of a steel particle are strongly dependent on the semiaperture angle, so the same

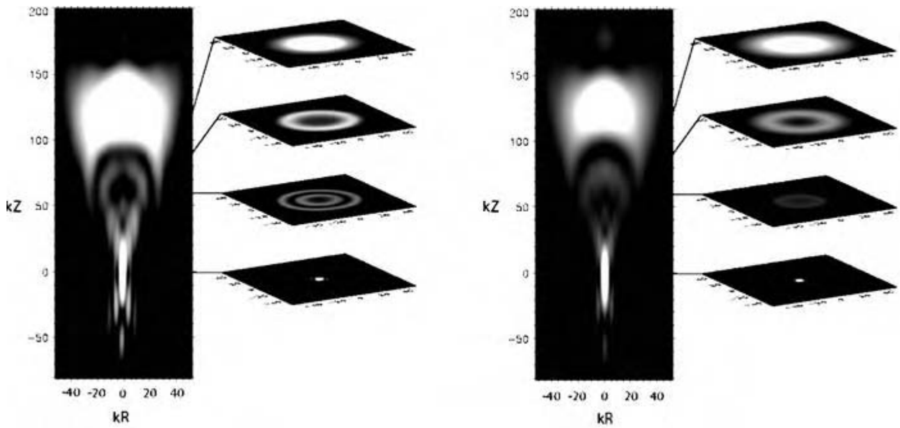

FIGURE 11.15
(a) *X-Z* scan through a steel sphere for a reflection microscope (OXSAM) at 105 MHz. The radius of the sphere was 560 μm. The semiaperture angle of the microscope lens was 26.5°. $Z = 0$ corresponds to focusing to the center of the sphere. (b) *X-Z* scan through a steel sphere for reflection microscope calculated with the same parameter as in (a). (From Zinin, P. et al., *Optik,* 107, 45, 1997. With permission.)

spherical particle has quite different *X-Z*-scans. Two regions of high image contrast occur. The maximum amplitude of the output signal is encountered when the focal point scans the top surface (top image) or the region close to the particle center. It has been shown that the image contrast obtained when scanning laterally or axially in the vicinity of the center of sphere reproduces the field emitted by the transducer contracted twice and is independent of the properties of the sphere.[93,95] A contraction by a factor of two of the center images in the lateral direction had been predicted by Atalar[37] and has been experimentally proven.[96] The image appears when the shape of the wavefront emitted by the transducer and the shape of the particle coincide. For an object whose shape is far from spherical, there is no such image.[95]

In an *X-Z*-scan, the contrast of the top images looks like a crescent. With increasing surface inclination, the thickness of this crescent increases while its contrast decreases. The bigger the semiaperture angle of the lens, the thinner the crescent. With increasing α, the images are even more similar to the object. The main features of contrast formation close to the surface can be well described quantitatively by the approximation proposed by Weise et al.[57] In that paper the signal obtained with a SAM from an uneven surface is approximated by the signal from a plane. This plane is tangential to the object surface at the point closest to the focal point of the transducer. It was shown that the image taken with the focus scanned at a fixed offset from the sphere's surface in the *z*-direction has the same form as the defocused OTF (see Figure 11.12). The normalized amplitude of the signal in a SAM for scanning along the surface of a rigid sphere is presented in Figure 11.12b. The contrast is inversely dependent on the inclination of the surface

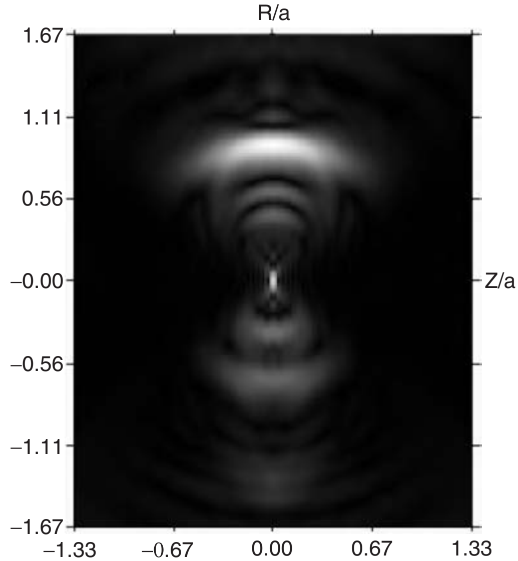

(a)

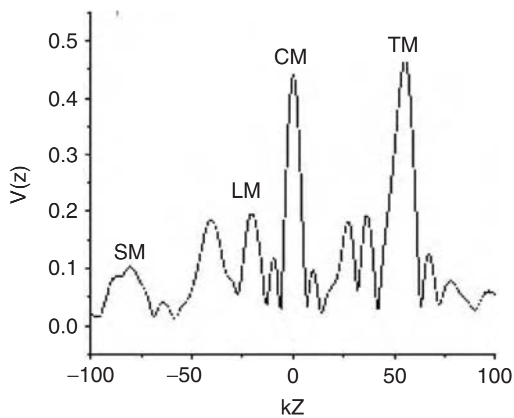

(b)

FIGURE 11.16
(a) *X-Z* medial section of a plexiglass sphere, $ka = 60$ calculated for reflection SAM. Axes scaled in units of the sphere's radius. (b) $V(Z)$ curve for a plexiglass sphere ($kR = 0$). TM = top maximum, CM = center maximum, LM = longitudinal maximum, SM = shear maximum. The semiaperture angle is equal to 60°. (From Zinin, P. et al., *Wave Motion,* 25, 213, 1997. With permission.)

under focus. The maximum follows the surface profile. An elegant analytical form of the top image of a sphere in the SOM was obtained recently.[97]

Let us now consider the effects of acoustical parameters of particles on the image contrast. In the case of particles that can be penetrated by sound, we can see the bottom of the particle — the dark side of the moon (see Figure

11.16, calculated for a Plexiglas sphere with parameters from Table 11.1). With increasing differences in the acoustical properties between particles and immersion liquids ($c > c_p$, c_p is the longitudinal velocity inside the particle) the dark side image moves toward the particle center. In the case of a solid particle, we can distinguish two bottom images as two kinds of waves that are focused inside the solid particles: the longitudinal and the transverse wave.[76] The radius of these images can be estimated from the position of the corresponding peaks on the $V(Z)$ curves (see Figure 11.16b). In Figure 11.16 there are four maxima on the $V(Z)$ curves for a liquid particle. The first maximum appears when the focal point is on the front surface of a sphere ($Z = a$, top maximum [TM]), and the second one appears when the center ($Z = 0$, center maximum [CM]) coincides with the focal point. The distance between these two maxima is equal to the sphere radius. The third maximum of the $V(Z)$ curves is due to focusing of the longitudinal waves onto the back of the sphere.[76] The top and bottom images have the form of an arc. The radius of the top arc is equal to that of the sphere, while the radius of the bottom arc is equal to the distance between CM and LM. For materials in which the shear waves can propagate we expect an image due to focusing of transverse waves by the bottom of the particle. The position of the maxima can be estimated by the following formula:[76]

$$Z_{P,S} = \frac{a}{2c_{P,S}/c - 1} \tag{11.61}$$

where $Z_{P,S}$ and $c_{P,S}$ are the positions of the maxima on the $V(Z)$ curve and sound velocities for longitudinal and shear wave, respectively. For a highly reflecting sphere such as steel or aluminum, the dark side images merge with the central image[76] (see Figure 11.15). The appearance of the region between CM and TM is influenced by the generation of Rayleigh waves.

For large spherical particles ($ka \gg 1$), the maximum radius of the top image appears to be reduced to about $ka \sin \alpha$. Hence the maximum area of contrast depends on the aperture of the microscope. This phenomenon was investigated theoretically[59] and experimentally[96] and was called the spherical particle size reduction effect. It arises because the reflection SAM cannot image surfaces inclined by an angle bigger than the semiaperture angle.[57] Therefore, from SAM images it is often not possible to attribute the vanishing of contrast to the edge of the object.

Now it is not difficult to predict the appearance of a three-dimensional image of an arbitrary uneven surface. The image must have the form of a thin layer whose shape follows the surface of the object. The thickness and brightness of this layer will be dependent on the surface inclination.

The images of spheres in transmission microscopes are quite different from those we have observed in the reflection SAM. In the transmission case, the width of the central dark spot or dark ring for $Z = 0$ is close to the real radius value of the sphere (see Figure 11.17). The dimension of the image in the

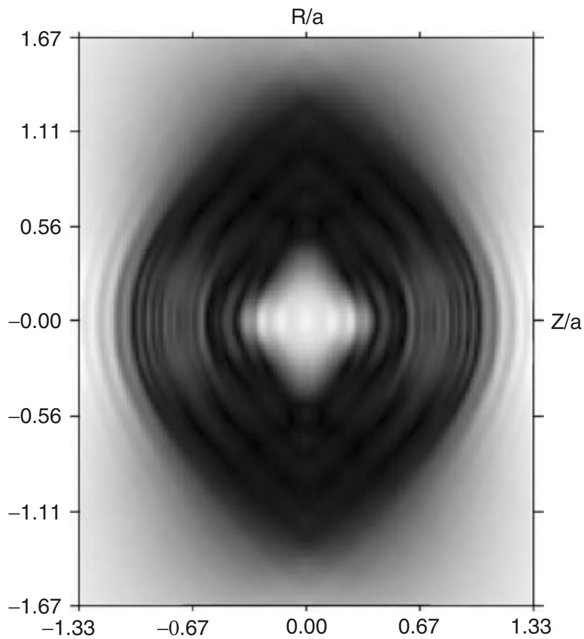

FIGURE 11.17
X-Z medial section of a plexiglass sphere calculated for transmission SAM. The parameters of the sphere are the same as in Figure 11.16. The semiaperture angle of the transducer is equal to 60°. Axes scaled in units of the sphere's radius. (From Zinin, P. et al., *Wave Motion*, 25, 213, 1997. With permission.)

axial direction equals $a/\sin\alpha$, and elongation can be simply described by

$$a_{elong} = \frac{a(1-\sin\alpha)}{\sin\alpha} \tag{11.62}$$

Interesting pictures are obtained when solid particles are investigated (see Figure 11.17). They exhibit a fringe pattern structure that is characteristic for the individual particle. It can be attributed to multiple reflection inside the particle, rainbow formation, and surface wave excitation.

11.3.3 Subsurface Imaging

Consider now imaging of a subsurface defect. The schematic diagram is given in Figure 11.18. The center of the spherical cavity is placed at point O′ with coordinates (X, Y, $Z + D$). Here ($Z + D$) is the distance from the center of curvature of the transducer to the cavity's center along the transducer axis. The distance between the liquid/solid interface and the center of the cavity O′ is D, and the distance from the center of curvature of the transducer

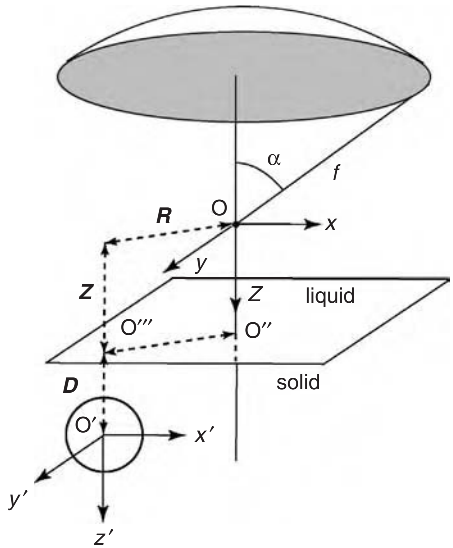

FIGURE 11.18
Problem geometry for subsurface imaging. 1 = spherical focusing transducer, 2 = liquid/solid interface, 3 = spherical cavity.

and the solid liquid interface is Z. The horizontal distance from the transducer axis is $\sqrt{X^2 + Y^2} = R$ and the radius of the cavity a.

To obtain an analytical solution for the output signal of the microscope for this system, it is necessary to make several assumptions. We will consider the waves scattered by the cavity only once and disregard the multiplied scattered waves. It is also assumed that the wave reflected at the liquid/solid interface is not disturbed by the cavity, so the signal due to reflection from the liquid/solid interface can be represented in the standard form of the $V(Z)$ curve for a half-space. This assumption is valid when the cavity is located below the Rayleigh wave penetration depth; it is also valid when the waves scattered from the cavity are weak compared to those reflected at the liquid/solid interface, so that their contribution to Rayleigh wave generation can be neglected. The latter holds for a cavity smaller than the wavelength of the Rayleigh wave. On these assumptions we will proceed with the theory.

It is convenient to write the output signal as a superposition of contributions of different wave types. First, the transducer receives a signal that is due to the wave reflected at the liquid/solid interface. This signal has the form of the $V(Z)$ curve of the solid in the absence of the cavity,[66] and we will denote it as V_R (R for reflection). The first signal from the cavity received by the transducer is the wave transmitted as a longitudinal wave into the solid and scattered by the cavity as a longitudinal wave. We will denote this wave as the PP wave and the output signal from this wave will be denoted as V_{PP}. Thereafter two waves reach the transducer simultaneously. A wave is transmitted into the solid as transverse wave and scattered by the cavity as longitudinal wave (PS wave) and its reverse (SP wave). The output signal corresponding to these two waves is ($V_{SP} + V_{PS}$). The slowest wave received by the transducer is the SS wave. It is transmitted into the solid as a transverse wave and scattered by the cavity as a transverse wave. The voltage corresponding to this signal is V_{SS}. The total output signal V generated by the scattered waves is equal to

$$V(R,Z) = V_R(Z) + V_{PP}(R,Z) + (V_{SP}(R,Z) + V_{PS}(R,Z)) + V_{SS}(R,Z) \quad \textbf{(11.63)}$$

A detailed derivation of each term of Equation 11.63 requires solving of the spherical particle diffraction problem of shear and longitudinal wave propagation in solids and would exceed the scope of this chapter. For a spherical cavity, the subject was discussed in detail by Lobkis et al.[8] Here we present only the final expression as developed there.[8] Omitting a constant, the terms in Equation 11.63 may be written as

$$V_{PP}(R,Z) = \frac{\rho_s c_P}{\rho\ c} \sum_{n=0}^{\infty} \sum_{m=0}^{n} (-1)^n (2-\delta_{0m}) A_n^{PP}\ L_{nm}^2(R,Z) \quad \textbf{(11.64)}$$

$$V_{SP}(R,Z) + V_{PS}(R,Z) = \frac{\rho_s}{\rho\ c} \sum_{n=0}^{\infty} \sum_{m=0}^{n} (-1)^n (2-\delta_{0m}) \left(c_P A_n^{PS} + c_S A_n^{SP}\right) L_{nm}(R,Z) T_{nm}^{SV}(R,Z) \quad \textbf{(11.65)}$$

$$V_{SS}(R,Z) = \frac{\rho_s c_S}{\rho\ c} \sum_{n=0}^{\infty} \sum_{m=0}^{n} (-1)^n (2-\delta_{0m}) \left[A_n^{SS} \left(T_{nm}^{SV}(R,Z)\right)^2 - A_n^{SH} \left(T_{nm}^{SH}(R,Z)\right)^2 \right] \quad \textbf{(11.66)}$$

with the definitions

$$L_{nm}(R,Z) = (-1)^m \int_0^{\alpha} P(\theta) T_P(\theta) \exp[i(kZ\cos\theta + k_P D\cos\theta_P)] J_m(kR\sin\theta) \bar{P}_n^m(\cos\theta_P) \sin\theta\, d\theta \quad \textbf{(11.67)}$$

$$T_{nm}^{SV}(R,Z) = (-1)^m \int_0^{\alpha} P(\theta) T_S(\theta) \exp[i(kZ\cos\theta + k_S D\cos\theta_S)] J_m(kR\sin\theta) \frac{\partial \bar{P}_n^m(\cos\theta_S)}{\partial\theta_S} \sin\theta\, d\theta \quad \textbf{(11.68)}$$

$$T_{nm}^{SH}(R,Z) = (-1)^m \int_0^{\alpha} P(\theta) T_S(\theta) \exp[i(kZ\cos\theta + k_S D\cos\theta_S)] J_m(kR\sin\theta) \frac{m\bar{P}_n^m(\cos\theta_S)}{\sin\theta_S} \sin\theta\, d\theta$$

(11.69)

where $A_n^{PP}, A_n^{SP}, A_n^{PS}, A_n^{SS}$, *and* A_n^{SH} are the scattering coefficients[8,98–100] for a spherical cavity inside a solid medium (see Appendix B); ρ_s is the density of the solid; c_P and c_S are the velocities of longitudinal and shear waves, respectively, in the solid; and $k_P = \omega / c_P$ and $k_S = \omega / c_S$ are the corresponding wave numbers. The angles θ, θ_P, θ_S follow Snell's law, $k \sin\theta = k_P \sin\theta_P = k_S \sin\theta_S$ (see Appendix A). T_P and T_S are the transmission coefficients for longitudinal and shear waves at the liquid/solid interface. Analytical expressions for the coefficients can be found in Appendix A.

Although Equation 11.64 through Equation 11.69 look cumbersome, they can, however, easily be interpreted using the Fourier spectrum approach. To understand the structure of Equation 11.64 through Equation 11.69, consider the spectrum of a wave incident on the cavity. Using Equation 11.19 and Equation 11.20, we can write it in the coordinate system originating in the center of the cavity

$$U_i(k_x, k_y) = \frac{P(k_x, k_y)}{k_z} T_{P,S}(k_x, k_y) \exp[i(k_x X + k_y Y + k_z Z + k_{P,Sz} D)] \quad \textbf{(11.70)}$$

The first term in Equation 11.70 is the spectrum of the wave incident on the focal plane, and the phase shift $\exp[i(k_x X + k_y Y + k_z Z)]$ moves the origin of the coordinate system to point *O‴*, which is located above the center of object *O′* on the liquid/solid interface. To calculate the spectrum inside the solid, we multiply the incident spectrum in the liquid by the coefficient $T_{P,S}(k_x, k_y)$, which is the transmission coefficient from a plane wave in the liquid to a longitudinal or transversal wave in the solid.[56,section 7] Finally, to get a spectrum originating in *O′* we multiply the spectrum at the liquid/solid interface by the propagation factor $\exp[ik_{P,Sz} D]$, with $k_{p,s} = \frac{\omega}{c_{P,S}}$ being the wave vector of the longitudinal wave in the solid. The wave is subject to refraction at the liquid/solid interface and Snell's law yields $k_{P,Sx} = k_x$, $k_{P,Sy} = k_y$, $k_{P,Sz} = \sqrt{k_{P,S}^2 - k_{P,Sx}^2 - k_{P,Sy}^2}$, with k_x, k_y as the components of the wave vector of the incident plane wave in the immersion liquid. Introducing spherical coordinates, we find that the angle θ is used for all operations in the immersion liquid: irradiation, represented by *P*(θ), and shifting the coordinate system from *O* to the system *O‴* in Figure 11.18, which is included in $\exp[ikZ \cos\theta] J_m(kR \sin\theta)$. The angles $\theta_{P,S}$ are used for operations within the solid such as shifting of the coordinate system from *O‴* to the system *O′* as included in $\exp[ik_{P,S} D \cos\theta_{P,S}]$ and scattering, represented by $P_{nm}(\cos\theta_{P,S})$.

Solving the inverse problem of determining size and location of a subsurface cavity from Equation 11.63 is a complex task. Lobkis et al.[101] used the method of stationary phase to derive an analytical expression for the *V*(*Z*) curve of a spherical cavity in a solid. Figure 11.19 shows theoretical and experimental *V*(*R* = 0, *Z*) curves for different solids. The $V_{PP}(R = 0, Z)$ curve (measuring only of longitudinal waves was achieved by separation of the reflected tone burst in time) exhibits three distinct peaks. The first is the

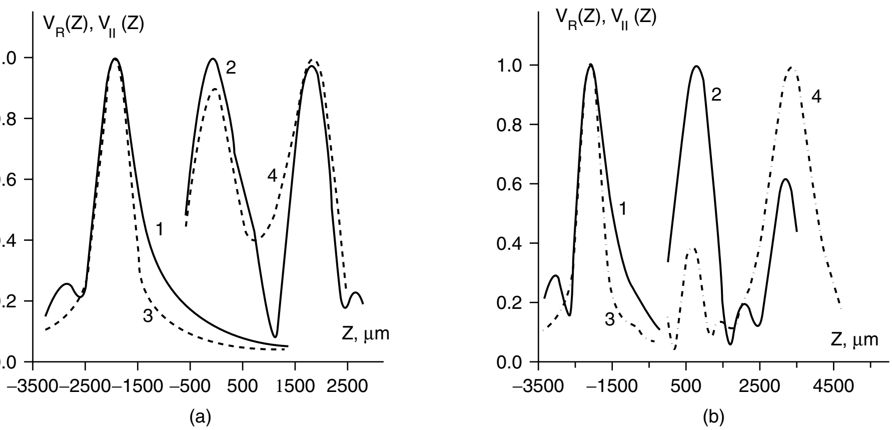

FIGURE 11.19
(a) The $V(0, Z)$ curve for a steel ball in epoxy (a = 0.99 mm, d = 1.95 mm, frequency = 25 MHz, $\alpha = 22°$); 1 = experimental $V(Z)$ curve, 2 = experimental $V_{PP}(Z)$ curve, 3 = theoretical $V(Z)$ curve with pupil function (Equation 11.5), 4 = theoretical $V_{PP}(Z)$ curve. (b) The $V(0, Z)$ curve for hemispherical cavity in glass (a = 1.22 mm, d = 1.95 mm, frequency = 25 MHz, $\alpha = 22°$). 1 = experimental $V(Z)$ curve, 2 = experimental $V_{SS}(Z)$ curve, 3 = theoretical $V(Z)$ curve with pupil function (Equation 11.5), 4. = theoretical $V_{SS}(Z)$ curve. (From Lobkis, O.I. et al., *J. Acoust. Soc. Am.*, 99, 33, 1996. With permission.)

ordinary $V(Z)$ curve from the liquid solid interface, where no Rayleigh waves occur because of the small lens aperture. The second and the third peaks are top maximum and center maximum of the cavity. The origin of the peaks is very similar to that of the peaks of a spherical particle as described in Section 11.3.2. The $V(Z)$ curve measured and simulated for shear waves $V_{TT}(R = 0, Z)$ contains three peaks as well. The positions of the TM and CM are different from those for $V_{PP}(R = 0, Z)$.

11.3.4 Theory of Time-Resolved Acoustic Microscopy

The time-of-flight acoustic microscopy technique provides an alternative method to visualize the internal microstructure of solid materials. It has been applied by Yamanaka[102] to measure the surface acoustic wave velocity. An essential contribution to the application of a time-resolving method for layered materials was made by a group from Oxford University.[33,34,103–105] The typical time-resolved signal from a solid sample is presented in Figure 11.20. Separation in time reflection for the different types of waves (P, PS, SS) from the structures located below the sample surface provides additional information about these structures and also allows their location to be determined (e.g., Figure 11.5).

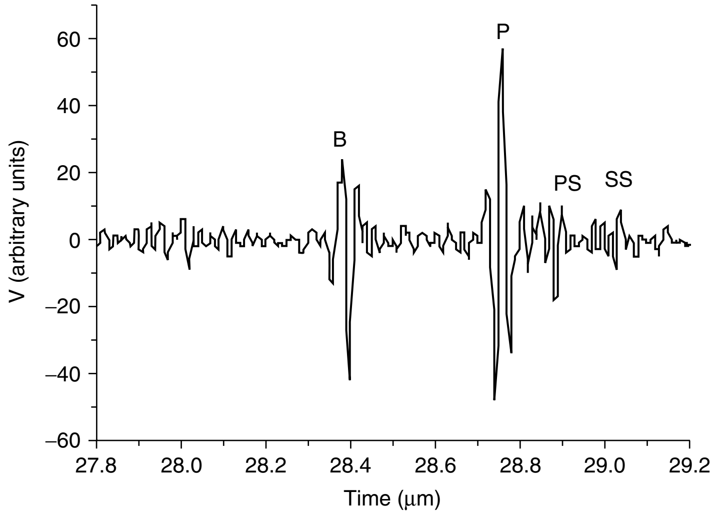

FIGURE 11.20
Time-resolved signal recorded from a hard amorphous carbon sample by a time-resolved SAM (developed at Institute of Biochemical Physics [From Levin V.M. et al., *J. Phys. Chem. Sol.*, 2001 (in press)]). The signals B and L are the result of reflection of the longitudinal wave from the front and back faces of the sample. Signals of the transverse wave arise due to conversion of longitudinal wave on the back face (mixed PS-signal) and due to conversion at the front sample face (SS-signal). (Figure courtesy of S. Berezina.)

The theory of time-resolved measurement can be found elsewhere.[104,106–108] Here we will obtain a simple solution using a Fourier spectrum approach. Let the defocus Z be fixed and a short acoustic pulse $s_o(t)$ be emitted by the lens toward the sample, and $s(t, Z)$ be the output signal. We suppose that the lens is aberration-free and that the pupil function is independent of frequency. The relationship between $s_o(t)$ and $s(t, Z)$ and their Fourier spectra $S_o(\omega)$, $S(\omega, Z)$ are

$$S_o(\omega) = \int_{-\infty}^{\infty} s_o(t)\exp(-i\omega t)dt \tag{11.71}$$

$$S(\omega, Z) = \int_{-\infty}^{\infty} s(t, Z)\exp(-i\omega t)dt \tag{11.72}$$

Because of the linearity of the system, the spectrum of the output signal of the SAM $S(\omega, Z)$ is a product of the spectrum of the input pulse $S_o(\omega)$ and the frequency response of the system $V(Z, \omega)$

$$S(\omega, Z) = S_o(\omega)V(\omega, Z) \tag{11.73}$$

The shape of a typical pulse $s_o(t)$ and its Fourier spectrum can be found elsewhere.[4] To get the time dependence of the output signal of the microscope $s(t, Z)$ in response to the excitation pulse, we apply the inverse Fourier transform to the spectrum $S(\omega, Z)$

$$s(t, Z) = \int_{-\infty}^{\infty} S_o(\omega)V(\omega, Z)\exp(i\omega t)d\omega \tag{11.74}$$

where the factor of $1/(2\pi)$ has been omitted. Taking into account the properties of the Fourier transform, the output signal $s(t, Z)$ can be presented in an alternative form:

$$s(t, Z) = \int_{-\infty}^{\infty} s_o(\xi - t)v(\xi, Z)d\xi \tag{11.75}$$

where $v(\xi, Z)$ is the inverse Fourier transform of the frequency response function $V(\omega, Z)$. The expression Equation 11.74 has been used in numerous papers.[103–105] The integral in Equation 11.75 has, however, some advantages for numerical simulations.

To calculate the integral in Equation 11.74 numerically, the spectra $S_o(\omega)$ and $V(\omega, Z)$ must be determined for both, positive and negative frequencies. Since the signals $s(t, Z)$ and $s_o(t)$ are real functions of time, functions $S_o(\omega)$ and $S(\omega, Z)$ must be Hermitian.[40,p. 16] Their real parts are even functions of frequency, and their imaginary parts are odd functions of frequency. This property can be succinctly written as $S_o(\omega) = S_o^*(-\omega)$ and $S(\omega, Z) = S^*(-\omega, Z)$, where the superscript * denotes the complex conjugate. To extend $V(\omega, Z)$ to the negative frequency range, we first have to extend the reflection coefficient into the negative frequency range. We recall that the reflection coefficient has been derived for an incident plane wave of monochromatic time dependence $\exp(-i\omega t)$. The phase of the reflection coefficient is just a phase shift for the plane wave due to reflection. Therefore,

$$\Re(-\omega, \theta) = |\Re(\omega, \theta)|\exp\left[-i\arg|\Re(-\omega, \theta)|\right] \tag{11.76}$$

where $\Re(\omega, \theta)$, and $V(\omega, Z)$ necessarily are Hermitian functions as well. Equation 11.76 denotes the argument of a complex function. Using the properties of Hermitian functions[109] and Equation 11.76, we can rewrite Equation 11.74 for the SAM

$$s(t,Z)=\int_0^{\alpha}P^2(\theta)\sin\theta d\theta\,\mathrm{Re}\left\{\int_0^{\infty}S_o(\omega)\Re(\theta,\omega)\exp\left[i\omega\left(t-\frac{2Z}{c}\cos\theta\right)\right]d\omega\right\}$$

(11.77)

where *Re* denotes the real part and $\Re$ (ω, θ) denotes the reflection coefficient. A normalizing coefficient has been omitted. The internal integral in Equation 11.77 is the Laplace transform of the function $S_o(\omega)$ $\Re$ (θ, ω) where time is replaced by the expression

$$t-\frac{2Z}{c}\cos\theta \quad \textbf{(11.78)}$$

where *c* is the velocity of sound in the liquid. The integral presentation in Equation 11.77 is of interest for analytical manipulations. We will consider some boundary cases. It can be seen from Equation 11.77 that if the reflection coefficient is real, the signal from the solid half-space *s*(*t*) has the form

$$s(t,Z)=\int_0^{\alpha}P^2(\theta)\Re(\theta,\omega)\sin\theta\, d\theta\,\mathrm{Re}\left\{\int_0^{\infty}S_o(\omega)\exp\left[i\omega\left(t-\frac{2Z}{c}\cos\theta\right)\right]d\omega\right\}$$

(11.79)

Equation 11.79 can be rewritten as

$$s(t,Z)=\int_0^{\alpha}P^2(\theta)\Re(\theta,\omega)s_o\left(t-\frac{2Z}{c}\cos\theta\right)\sin\theta\, d\theta \quad \textbf{(11.80)}$$

and repeats the shape of the initial signal $s_o(t)$ when the lens is focused on the surface of the solid (*Z* = 0).

$$s(t,Z=0)=s_o(t)\int_0^{\alpha}P^2(\theta)\Re(\theta,\omega)\sin\theta\, d\theta \quad \textbf{(11.81)}$$

To show the influence of the lens properties on the signal shape, consider a rectangular impulse ($S_o(\omega) = 1$, when ($-\Omega \le \omega \le \Omega$), and 0, when $|\omega| > \Omega$. Then s_o (T) = (sin ΩT)/(ΩT) and

$$s(t,Z) = \int_0^{\alpha} P^2(\theta)\Re(\theta,\omega) \frac{\sin\left[\Omega\left((t - \frac{2Z}{c}\cos\theta\right)\right]}{\Omega\left(t - \frac{2Z}{c}\cos\theta\right)} \sin\theta\, d\theta \qquad \textbf{(11.82)}$$

Let the pupil function be constant over the aperture angle (Equation 11.4) and let the half-space be rigid ($\Re(\theta) = 1$). Then Equation 11.82 has a simple form

$$s(t,Z) = \int_0^{\alpha} \frac{\sin\left[\Omega\left(t - \frac{2Z}{c}\cos\theta\right)\right]}{\Omega\left(t - \frac{2Z}{c}\cos\theta\right)} \sin\theta\, d\theta \qquad \textbf{(11.83)}$$

The integral in Equation 11.83 can be presented with the aid of the integral sine *Si*:

$$s(t,Z) = Si\left[\Omega\left(\frac{z}{c} - t\right)\right] - Si\left[\Omega\left(\frac{z}{c}\cos\alpha - t\right)\right] \qquad \textbf{(11.84)}$$

The solution in Equation 11.84 consists of two parts: one due to reflection of the central ray from the rigid surface and the second due to the rays radiated from the edge of the transducer (edge wave), marked in Figure 11.10 as AO′E. The contribution of the edge wave to the signal is smaller than that of the specularly reflected ray and the Rayleigh wave.[110] Detection of the edge wave has been demonstrated by Zhang et al.[110]

11.4 Applications of SAM in Nondestructive Evaluation

The use of acoustic microscopy is widespread and it is difficult to describe all areas in one chapter. We will only discuss the area of NDE where information often can be provided only by the SAM. In acoustic microscopy, the variation of the mechanical properties with depth can be studied by scanning the sample in various focal depth. The lens position in which the acoustic wave is focused onto the sample surface is termed as being in focus. When the focal point of the acoustic waves is at the position below the sample surface, the condition is termed defocused. Consider first the contrast of the acoustic microscope when the surface of the object is in focus (Z = 0). As can be seen from Equation 11.29, the signal from the surface for a microscope with the elementary pupil function in Equation 11.4 has the form

$$V(Z=0) = \frac{V_o}{(1-\cos\alpha)}\int_0^{\alpha} \Re(\theta)\sin\theta d\theta \quad \textbf{(11.85)}$$

The expression for the $V(Z)$ curve gives a clue to understanding the nature of the contrast in SAM images. It is obviously defined by the reflection coefficient $\Re(\theta)$, which has a simple form for a liquid/solid interface.[56] Its analytical expression is given in Appendix A. The reflection coefficient contains all relevant information about wave propagation in the sample.

The analysis of Equation 11.85 by Hirsekorn et al.[25] demonstrated that the magnitude of the gray levels in an image obtained with an acoustic microscope can be used as a measure of the acoustic impedance of a sample with the spatial resolution of the instrument[25] (see Figure 11.21).

Numerical calculations show that the reflection coefficient is nearly constant and equal to its value for the zero incidence angle within more than 90% of the region from θ = 0 to the longitudinal wave critical angle (see Figure 11.10b). Hirsekorn et al.[25] suggested the following procedure for the calibration curve: A set of polished samples of different materials covering a wide range of acoustic impedances is imaged with the SAM. The maximal amplitude of the specular reflection for each sample is recorded, stored, and plotted against the reflection coefficient for perpendicular incidence. This plot yields a straight line (Figure 11.21). The impedance of an unknown material can then be evaluated by interpolation from the maximal amplitude of the specular reflection.

11.4.1 Imaging of Subsurface Defects

The most common application of the acoustic microscope is likely the detection of subsurface defects.[111,112,113] Atalar distinguished between two methods of subsurface imaging.[114] The contrast of subsurface defects in heavy or stiff materials is determined by a Rayleigh surface acoustic wave. In stiff materials, the longitudinal and the shear waves cannot be focused deep enough because of the high-impedance mismatch between immersion liquid and sample, but the Rayleigh waves can be excited efficiently.[20] For stiff and heavy materials the penetration depth is therefore limited by the wavelength of the Rayleigh wave on the sample surface. On the other hand, "for low-impedance (light and soft) materials both longitudinal and shear waves can penetrate into the object with a reasonable focusing performance."[114] We illustrate these statements by considering the sound focusing below the solid surface at high frequency (1 GHz). Figure 11.22a shows the ray model of waves propagating in a solid.

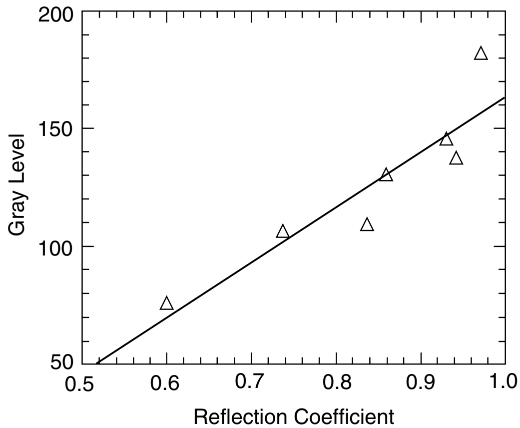

FIGURE 11.21
Grayscale values of maximal specular reflection amplitude of *V(Z)* curves as a function of the reflection coefficient for perpendicular sound incidence. The values are calculated from material densities and sound velocities of epoxy, Mg, Al, Si, Cu, Ni, and W (in order of increasing reflection coefficient). The zero grayscale value does not correspond to zero reflection. (From Hirsekorn, S. *et al., Appl. Phys. Lett.* 67, 745, 1995. With permission.)

As discussed in Section 11.3, in the geometrical optics approach we should only take into account rays that appear to come from the focus when intersecting the transducer. A set of curves of the power distribution of the longitudinal and the shear waves traveling in the solid for amorphous carbon is shown in Figure 11.22b. Here, the y-axis shows the normalized intensities for longitudinal and shear waves represented as E_P/E and E_S/E, and the x-axis represents the angle θ of the incident wave from liquid to solid. Expressions E_P/E and E_S/E are given in Appendix A. Simulations of the refraction of a focused beam into a stiff solid (see Figure 11.22) show that only a small part of the energy emitted from the lens penetrates into the solid. Only waves coming from the coupling liquid inside the cone with a vertical semiangle $\theta < \theta_P^c$ can be transmitted into the solid as longitudinal waves. The longitudinal critical angle θ_P^c can be derived from Snell's law. For solids with high longitudinal velocities, the critical angles can be very small (see Table 11.1). This is similar for the shear waves (Figure 11.22b). For the numerical simulations presented in Figure 11.22b, we used data for superhard amorphous carbon obtained from C_{60} at high pressure and high temperature[87] (see Table 11.1). For this sample the critical angles for longitudinal and shear waves are 5° and 8°, respectively.

Using a geometrical optics approach, it is easy to derive an expression for the locations of the focal points for longitudinal (Z_P) and shear waves (Z_S) inside a solid (see Figure 11.22a) if the (virtual) defocusing distance of the microscope is Z

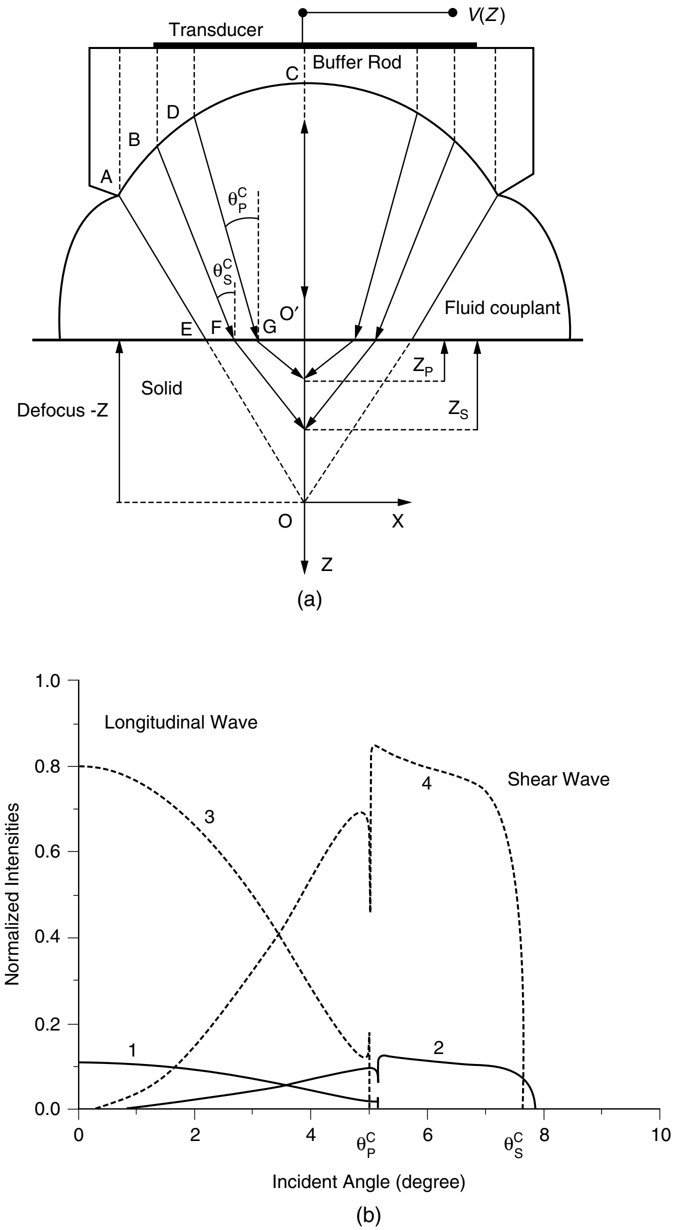

FIGURE 11.22
(a) Ray picture of shear and longitudinal waves focusing inside a solid sample in the case of negative defocus ($Z < 0$). Rays AF, BG, HD, and EK are normal to the transducer surface. (b) The calculated relative intensity distribution of the longitudinal and shear waves for wave propagation from water (mercury) into superhard amorphous carbon (see Figure 11.10b and Table 11.1 for elastic constants) as a function of incident angle: (1) longitudinal wave, and (2) shear wave crossing water-carbon interface; (3) longitudinal wave, and (4) shear wave crossing mercury-carbon interface.

$$Z_{P,S} = Z\frac{c}{c_{P,S}} \quad (11.86)$$

A realistic picture of elastic wave focusing inside the isotropic[115] and the anisotropic[116,117] solids can be simulated numerically using a Fourier spectrum approach. Table 11.1 presents calculations of the Rayleigh wave penetration depth and the depth of the focal positions of the longitudinal (Z_p) and shear (Z_S) wave at 1 GHz derived from Equation 11.86 for several hard materials. The defocusing distance (Z) was chosen as 30 µm for numerical simulations, as this is the maximal displacement of the lens operating at 1 GHz. Defocusing greater than 30 µm can damage the lens, as its focal length f usually does not exceed 80 µm. Analyzing the data in Table 11.1, we can conclude that for materials stiffer than silicon nitride in Table 11.1 the contrast of the subsurface images at 1 GHz is mainly determined by the Rayleigh wave. For these materials, the Rayleigh wave penetrates deeper than the location of the focal points of longitudinal and shear waves. A rigorous analysis of the image formation of micron-size defects in hard or superhard materials by high-frequency SAM has not yet been made.

Several techniques have recently been developed to improve the imaging of the subsurface defects, and we will mention several of them that seem to be the most promising. Miyasaka et al.[118] designed two kinds of lenses using the shear wave for subsurface imaging. One is a high-aperture acoustic lens operating at low-frequency (30 MHz), and the other is a center-sealed high-frequency (400 MHz or 1 GHz) acoustic lens. The latter has the central area of its aperture sealed to prevent longitudinal waves from traveling into the sample so that the acoustic image is essentially composed of shear wave components. The high-aperture acoustic lens has an aperture with a large aperture angle for exciting shear waves in the object. Miyasaka et al.[118] claim that the use of shear wave acoustic microscopy allows an increase in resolution for subsurface imaging of approximately 50%. Interesting results can be achieved with modern signal processing algorithms. Bechou et al.[119] applied advanced digital signal processing based on continuous wavelet transform time-resolved SAM images. Application of the technique to a nondestructive analysis of a dye-attached assembly showed the good abilities of the algorithm to detect and localize weak defects such as cracks in the dye.[120] Maslov et al.[121] monitored the phase of the signal reflected by the subsurface inclusion. It was shown that detection of the phase of the acoustical signal can be used to determine the nature of defects and to distinguish voids from solid inclusions in light casting alloys.

In the following we will consider the SAM application for imaging subsurface defects inside solids for three different types of materials as are used in modern industry: soft materials (epoxy, concrete), superhard materials (amorphous carbon synthesized from C_{60} at high pressure and temperature[122]), and intermediate case amorphous carbon films on steel (see Table 11.1).

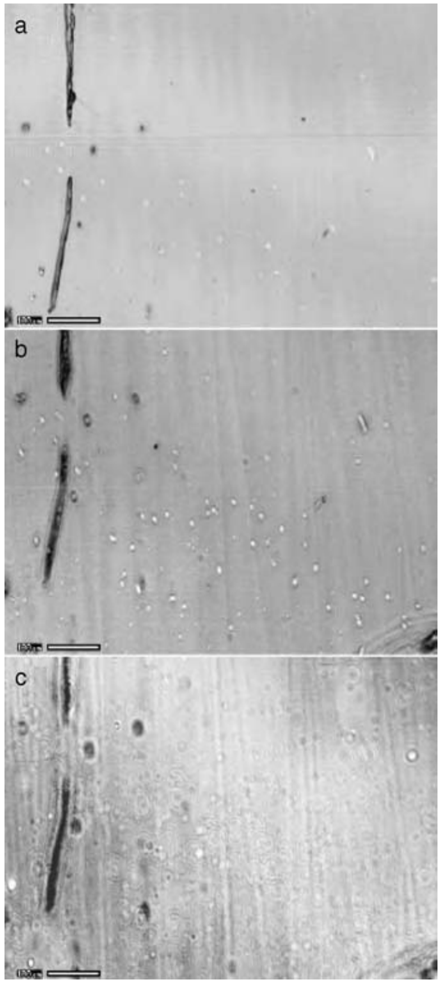

FIGURE 11.23
Acoustical images of the defects in epoxy layer on aluminum at 300 MHz made by OXSAM: (a) $Z = 0$, (b) $Z = -26$ μm, (c) $Z = -43$ μm.

11.4.1.1 Subsurface Imaging in Moderately Soft Solids

As has been noted above, the imaging of subsurface defects inside soft solids is an easy task. Figure 11.23 illustrates the imaging of defects located at the interface between aluminum and a 15-μm epoxy layer. Epoxy and polymer coatings are widely used by modern industry for protection purposes and as an adhesive. The surface image of the epoxy layer (Figure 11.23a) shows several defects as dark and bright spots. The velocity of the longitudinal wave in the epoxy imaged by SAM was 2.6 km/sec (Table 11.1). According to Equation 11.86, focusing of the acoustic beam onto the epoxy-aluminum

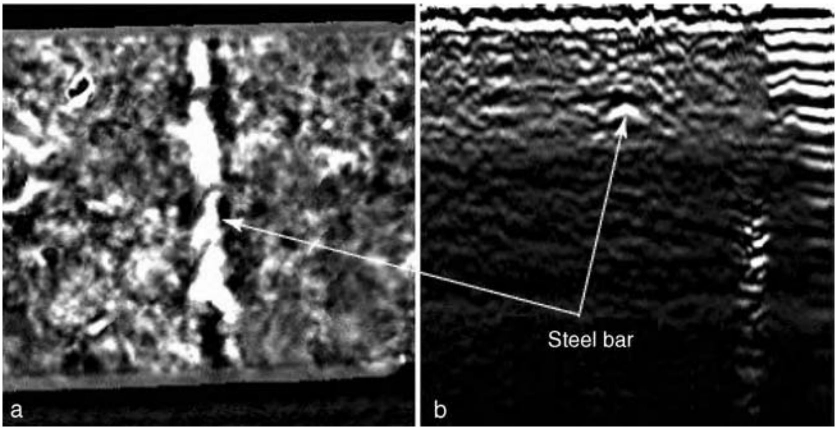

FIGURE 11.24
Acoustical image of the surface of a concrete sample at 50 MHz. (a) Subsurface image of a steel bar in concrete. The field of view is 36*36 mm. (b) Time-resolved image of the same sample, B-scan normal to the steel bar.

interface occurs when the defocus is 26 μm. A comparison of images of the epoxy surface (Figure 11.23a) and of the epoxy-aluminum interface (Figure 11.23b) shows that most of the defects (voids) are located near the interface. The contrast of the defects gets brighter as the SAM focus moves closer to the interface and more defects become visible. Further defocusing (Figure 11.23c) degrades the contrast of the defects at the epoxy-aluminum interface, showing several defects in the aluminum.

Steel bars in concrete provide another example of imaging subsurface structures in soft materials. This example attracts our attention because Portland cement concrete is one of the manmade materials most commonly used. Corrosion of reinforcing steel in concrete is one of the leading causes of infrastructure deterioration. Recently, it has been found that the time-resolved SAM is able to determine the mechanical properties of a thin layer of concrete of several millimeters around a steel bar and to perform subsurface imaging of the steel/concrete interface.

Figure 11.24a shows acoustical images of the reinforced concrete sample taken from the top surface at 50 MHz by the low-frequency acoustic microscope KSI 50 (Krämer Scientific Instruments). The image of the rebar located below the surface at a depth of 2 mm shows a good contrast[123] (see Figure 11.1). Attempts to get images of the rebar located deeper than 2 mm were not successful with the given frequency of the microscope. The image contains dark areas near the rebar, which can be attributed to high-porosity areas in which sound attenuation is very high.[123] The bright areas in the images (Figure 11.24a and b) represent voids (filled with air) and aggregates. The images of the rebar are fairly sharp and demonstrate that the acoustic microscope operating at 50 MHz is capable of evaluating the properties of the rebar/concrete interface. B-scans of the sample are presented in Figure

11.24b. In these images, the horizontal axis corresponds to the direction of the line scan. The vertical axis corresponds to the time measured for individual reflections to return to the transducer. The first reflection pulse is seen as a series of white-black-white lines due to reflection at the water/concrete interface. The pulse reflected at the concrete/rebar interface is represented as a signal with the same polarity (white-black-white lines), though the first positive peak (white) is not as pronounced as the second one. The sickle shape in the middle of the images is a signal reflected at the concrete/steel interface. The shape of the image in Figure 11.24 is in quantitative agreement with the theoretical prediction made for spherical objects in Section 11.3. It has been shown that the radius of the image of a spherical object is always smaller than the actual radius of the sphere and can be estimated as $ka \sin\alpha$.

As can be seen from the examples, SAM is a powerful tool for subsurface imaging of the defects inside soft opaque materials. As a result, acoustic microscopy is widely applied in the nondestructive inspection of electronic and optoelectronic structures,[124–128] integrated circuit packages,[129] electronic packaging,[130] and defect localization in the computer memory DRAM.[131]

11.4.1.2 Subsurface Imaging in Moderately Hard Solids

One of the expanding applications of the SAM is the inspection of the thin hard film as is widely used in current industrial developments. It is now recognized that new diamond-like carbon (DLC) coatings have an extraordinary potential to extend the life of machine components. The thicknesses of the DLC films used in industry are usually about several microns. The SAM operating at high frequency likely is an ideal device for studying film microstructures. Figure 11.25a through Figure 11.25d shows the 1.3-GHz acoustical images of a flat steel sample coated with a Cr-DLC film obtained with the Leitz ELSAM (Ernst Leitz SAM) acoustic microscope. The thickness of the film was 2.9 μm. The elastic properties measured by Brillouin scattering are given in Table 11.1. In the figures the acoustic microscope is focused onto the top surface and defocused to $Z = -6$ and -8 μm, respectively. All images reveal surface and subsurface defects in the coatings. A comparison of the brightness of the defects in the two images shows that the defects in the circles in Figure 11.25b are subsurface defects while those in the rectangles are surface defects.

A close look at the two images also shows that subsurface defects that were not visible in the in-focus image (Figure 11.25a) appeared in the defocused images (Figure 11.2c through Figure 11.25d), such as that marked in Figure 11.25c. The interpretation of the images is more complicated than for softer materials. The brightness of the contrast in Figure 11.25 also suggests that defects are in focus when $Z = -6$ μm. Equation 11.86 gives 2.04 μm for Z_p. The penetration depth of the Rayleigh wave is 2.1 μm at 1.3 GHz. Therefore, the Rayleigh wave does not interact with defects, and the images in Figure 11.25 are formed by longitudinal or shear waves. The wavelength of the longitudinal wave (3.8 μm) is greater than the film thickness (2.9 μm).

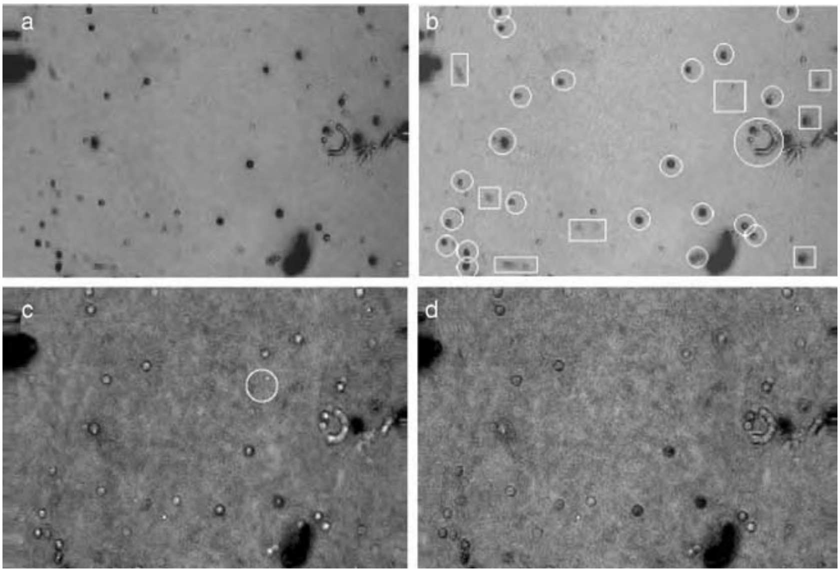

FIGURE 11.25
Acoustical image of the surface of the coated sample (Cr DCL) at 1.3 GHz. The field of view is 200*130 μm: (a–b) image was taken at focus. Defects inside the circles are subsurface defects, inside the squares are (c) surface defects image that were taken at defocus $Z = -6$ μm; (d) image was taken at defocus $Z = -8$ μm.

In such a case, images can be called near-field images. For near-field images, the ray theory does not provide the location of the defects, and the rigorous solution in Equation 11.63 through Equation 11.69 should be used. The characterization of the subsurface defects located in the near-field of the liquid/solid interface has not been extensively investigated in acoustic microscopy and will be a challenging future problem.

11.4.1.3 Subsurface Imaging in Stiff/Hard Solids

Imaging defects and the subsurface microstructure in stiff/hard materials are a complicated task. The behavior of the transmission coefficients (Figure 11.22b) provides a clear picture of the problems arising when the SAM is used to imagine the subsurface microstructure of stiff/hard materials (see also Jipson[132]). The transmission coefficient in Figure 11.22b was simulated for a superhard amorphous carbon synthesized at high pressure and high temperature. The elastic parameters of the sample are given in Table 11.1. Superhard materials synthesized from C_{60} at high pressure and high temperature can be obtained only in small amounts (several millimeters in length). The strong mismatch between the coupling liquid and the sample (as regards both velocities and impedances) significantly reduces the energy of the transmitted beam (see Figure 11.22b). To reduce the mismatch, mercury

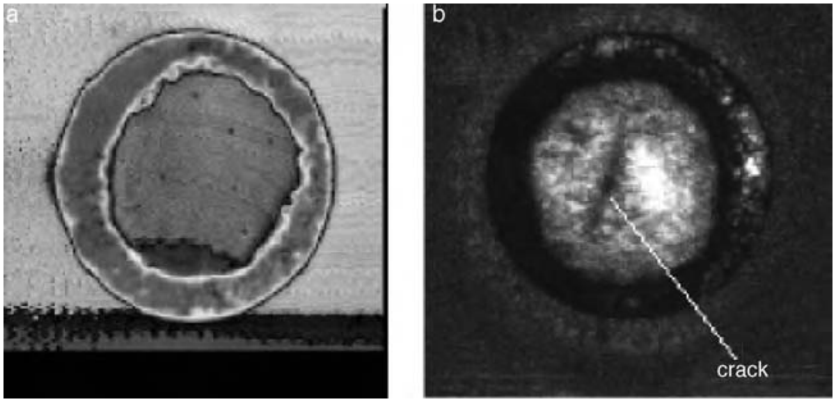

FIGURE 11.26
C-scan images of a hard amorphous carbon sample: (a) surface image, (b) interior image obtained by the impulse reflected from the back side of the sample. The field of view is 7*7 mm^2 (From Berezina, S. et al., *Ultrasonics*, 38, 327, 2000. With permission.)

can be used as a coupling liquid.[133] Figure 11.26 is a C-scan of hard amorphous carbon (c_p ~ 11 km/sec) synthesized at the pressure of 11 GPa and the temperature of 1450 K. The image was taken by SAM operating at 30 MHz, and the thickness of the sample was 2 mm. Use of mercury as an immersion liquid makes it possible to obtain an image of the back side of the sample. The impedance of mercury matches better with the impedance of the sample, and the energy transmitted into the sample increases (see Figure 11.22b). The back side image (Figure 11.26) revealed the crack and the gradient of the velocity (variation of the grayscale) in the hard amorphous carbon. It should be noted that very fast or superhard materials can be investigated only by low-frequency acoustic microscopes,[122] in which the defocusing distance is not limited by the attenuation of sound in the immersion liquid as in the case of a microscope operating at 1 GHz.

To conduct quantitative SAM measurements of the elastic properties of fast/hard materials, Wickramasinghe[134] suggested using a solid hemisphere (transformer) as an additional refraction surface to decrease the beam aberration inside the solid objects (Figure 11.27). A steel transformer was successfully used by Berezina[122] to detect a signal from the back side of fullerene ceramics. The steel hemisphere provided good acoustic impedance matching between mercury and the hard sample. Because of the transformer, the energy of the whole aperture (aperture angle $\theta = 23°$) beam is transmitted into the sample. Using a transformer, it is also possible to focus the beam onto the significant depth and to create the quasi-collinear beam by moving the transformer surface toward the lens. Figure 11.27a and 11.27b represents the pulse trains obtained at the frequency 13.5MHz when the beam is focused onto the front or back surface of the 5.68-mm glass plate. Figure 11.27c and 11.27d represents the acoustic responses of the plate to the collinear beams of longitudinal and shear waves. The transformer was then effectively

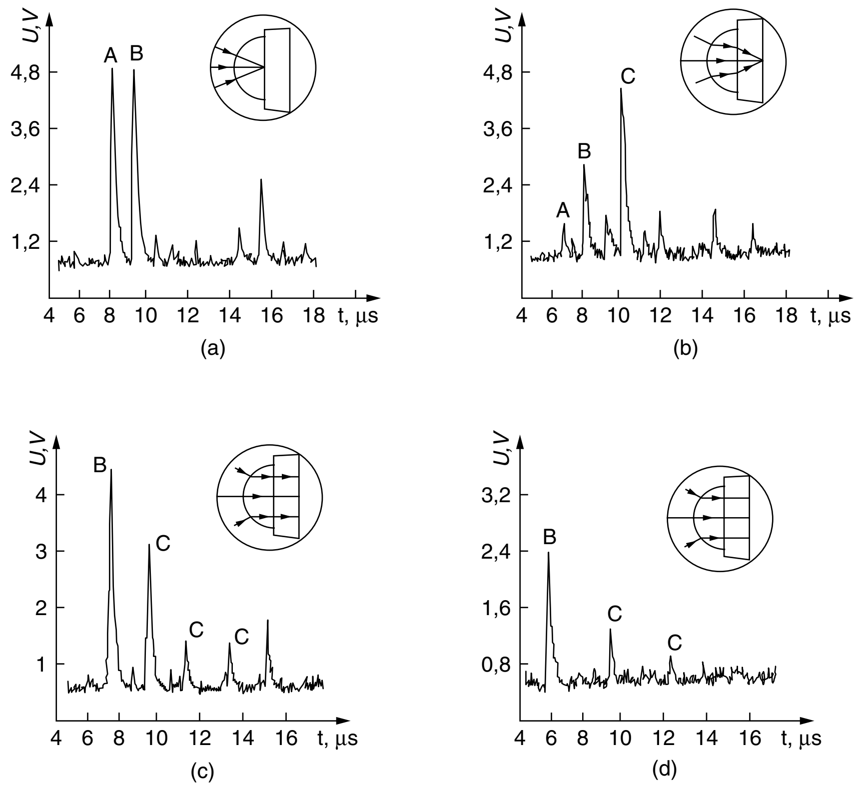

FIGURE 11.27
Pulse trains for a thick (5.68 mm) glass plate with spherical steel transformer (r = 3.36 mm) obtained at the frequency 13.5 MHz for focusing the beam on the (a) front and (b) back faces of the plate. In (c) and (d) the transformer body forms a narrow quasi-collinear beam of the longitudinal and shear wave, correspondingly.

applied for measuring the longitudinal sound velocity in the new hard phases of carbon.[122]

11.4.3 Evaluation of Adhesion by SAM

The detection of bond defects in layered structures is another area of nondestructive testing where acoustic microscopy has been successfully used for many years.[135,136] Recently, Parthasarathi et al.,[137] Wang,[138] and Gao et al.[139] discussed the theoretical aspects of the application of scanning acoustic microscopy for evaluating the adhesion between a film and a substrate and for inspection of layered solids with bond defects. Wang used a Fourier spectrum approach to model a confined bond defect between layer and substrate. The bond defect was characterized by shear ($s(x)$) and normal ($n(x)$) bond compliances. The total disbonding corresponds to $s = n = \infty$, and perfect bonding corresponds to $s = n = 0$. An analytical expression for the Green function of the bond defect can be obtained only when *n* and *s* are small (the Born approximation). It has a complicated form, and we will not present it in this chapter. To simulate responses of the acoustic microscope in the case of strong disbonding, numerical calculation is required. Results of the numerical simulations showed that the acoustic microscopy response was sensitive to the normal bond compliance in all defocus ranges. However, the shear bond compliance has an influence on the response only at large defocus.[138] Parthasarathi et al.[137] and Guo et al.[139] modeled the bond defect as an infinitely thin layer with normal and tangential stiffness parameters. They concluded that the SAM cannot directly measure the interface strength; however, interface stiffness parameters measured by the SAM may indicate the bond quality between film and substrate.

Characterization of the bonding by measuring bond compliances is one of the real future challenges to acoustic microscopy. Modern microscopes can distinguish two states of bonding: a perfect bond and full delaminations or disbonding. It has recently been proven that the acoustic microscope distinguishes regions of interfacial degradation at the earliest stages while optical microscopy remains insensitive.[136,140] An illustrative example of the use of SAM for studying disbonding is the research conducted at the University of Oxford.[11] Crossen et al. applied acoustic microscopy to monitor the propagation of the cathodic disbonding of an epoxy-polyamide coating on steel exposed to an NaCl solution. A linear scribe was made to initiate degradation. The disbonding (light area on both sides of the scratch in Figure 11.28a through Figure 11.28d) stops after about 50 min, with subsequent development of microblistering. Figure 11.28 shows the propagation of blisters beyond the disbonded region. Individual blisters grow with time and new blisters form at ever-increasing distances from the cut as time progresses. The separation between the substrate and the coating on blisters eventually leads to concentric fringes that reveal the heights and profiles of individual blisters.

Acoustic microscopy provides an opportunity not only to detect delaminations, but also to investigate the structure and shape of the disbonding. We demonstrate this capability by describing SAM studies on adhesive bonding as is widely used in the aircraft industry. In order to increase adhesion between aluminum and epoxy, a special surface pretreatment used on aluminum adherents in aerospace applications produces a honeycomb-like oxide structure on the adherent surface. The adhesive penetrates some distance into the honeycomb cells to form a microcomposite. The overall thickness of this interlayer between the bulk adhesive and the bulk adherent in a typical aluminum-epoxy joint is of the order of 1 μm only. Degradation of the boundary between the interlayer and epoxy can be observed only under severe degradation conditions.

Figure 11.29 shows the degradation of a sample comprising an anodized layer 1-μm thick and covered by 15 μm with epoxy after immersion in a 90°C water bath for 22 days. Blisters about 100 μm in diameter were found at the interface (see Figure 11.29a and Figure 11.29b). The SAM images

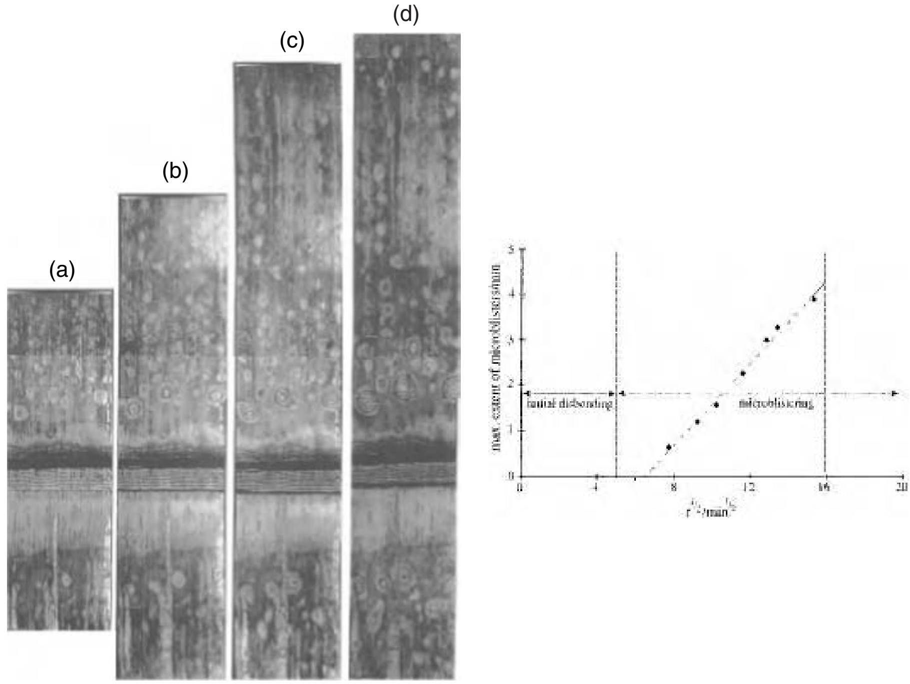

FIGURE 11.28
(a–d) SAM images (at 300 MHz) showing the developing of blisters beside a scribe in an epoxy-polyamide coating on mild steel. The exposure time to a 0.05-m NaCl solution increases to 4 hours. (d) The width of the bars is 100 μm. (e) The extent of the blister zone vs $(\text{time})^{1/2}$ during exposure; the points correspond to the time when images (a–d) were taken. (From Crossen, J.D. et al., *Faraday Discuss.*, 107, 417, 1997. With permission of the Royal Society of Chemistry.)

illustrate that degradation occur at discrete sites, rather than being uniformly distributed over the surface. After 49 days in 90°C water, a small blister, seen at a defocus z = 65 μm (Figure 11.29a), becomes visible at a defocus $z = -23$ μm (Figure 11.30b). In the time scan (Figure 11.30b) the vertical axis corresponds to the direction of the line scan 600 μm in length. The horizontal axis corresponds to the time individual reflections take to return to the transducer, with the frame width corresponding to 100 ns.

A pulse reflected at the epoxy water interface shows a light-dark-light contrast, whereas the signal reflected at the epoxy/blister interface has the reverse dark-light-dark contrast due to a phase shift. The phase shift occurs when the pulse is reflected at the interface between a fast medium and a soft substrate. Since the reflection at the substrate is not visible, the blister is likely due to corrosion of the aluminum rather than to disbonding at the interface.

11.4.4 Imaging Cracks

Cracking is a common cause for the degradation of materials used in industry; therefore, early nondestructive detection of cracks is of importance.

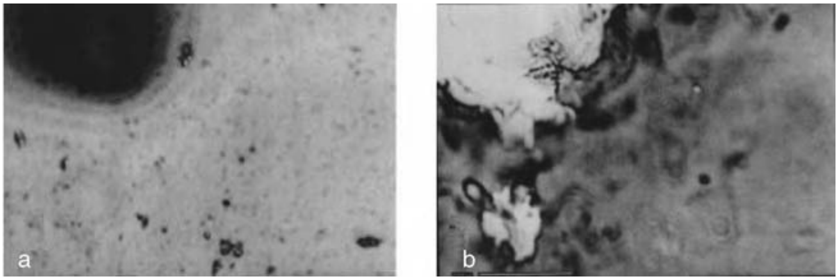

FIGURE 11.29
Acoustical images of a degraded joint between 15-μm epoxy layer and 1-μm oxide layer on pure aluminum. Sample was in 90°C water for 22 days. (a) Defocus distance z = –65 μm; superficial blister can be seen in the top-left corner. (b) Defocus distance = 65 μm; the start of degradation can be seen (bright spot in the left bottom corner).

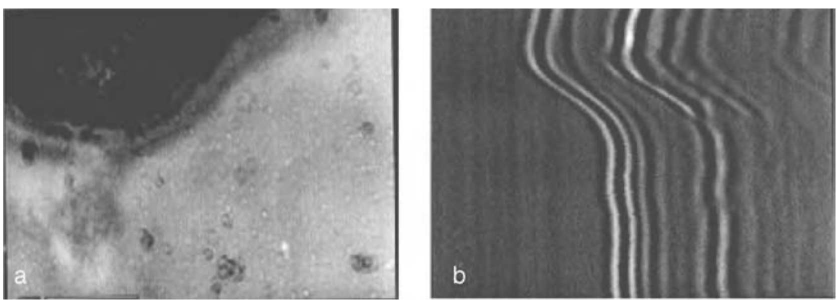

FIGURE 11.30
Acoustical images of the degraded joint of the same area as in Figure 11.29. Sample was in 90°C water for 49 days: (a) defocus distance = 23 μm; (b) time of flight SAM image shows cross section of the blister.

Scanning acoustic microscopy has proved to be of great value for the detection of cracks in a variety of materials such as ceramics,[2,141–143] metals,[144] and fiber composites.[145] Different types of cracks can be visualized by SAM, including surface-breaking cracks[33,86] and tensile cracks in hard coatings.[146]

For some materials SAM is the only method to detect cracks. For example, the ability to locate cracks at the aggregate/paste interface and subsurface cracks in aggregates in concrete is unique to SAM, since the cracks do not appear in optical images. In contrast, the scanning electron microscope can visualize only surface-breaking cracks. In addition, it may introduce cracks in the concrete as a result of sample preparation. Cracks that often appear during electron microscopy studies are due to the vacuum used for electron microscopy.

Acoustic microscopy shows its definite advantage over other techniques in identifying cracks within rocks and solids by the presence of the Rayleigh fringe contrast.[84] The theory of the fringe formation close to cracks is described in Section 11.3.1.3. Figure 11.31 shows a defocused acoustical image of granitic grains in Portland cement paste. The two acoustic images (Figure 11.31b and

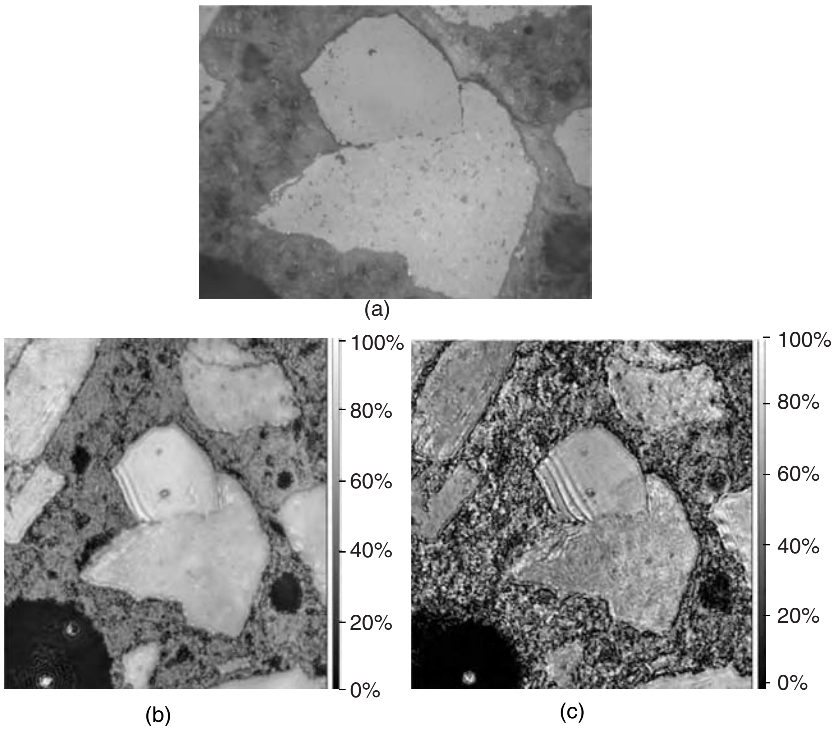

FIGURE 11.31
Concrete sample made with granitic aggregate grains and with plainement paste. (a) Reflected light microscopy; acoustic microscopy at 400 MHz. (b) $Z = -10$ μm, (c) $Z = -100$ μm (From Zinin, P., *Nondestructive Testing Evaluation Int.*, 33, 283, 2000. With permission.)

Figure 11.31c) were taken at 400 MHz. The Rayleigh wave fringes appear in the slightly defocused acoustical image ($Z = -10$ μm), indicating the existence of some cracks. At higher defocus ($Z = -100$ μm), two cracks are visible in the SAM image with excellent contrast. The reflected light optical micrograph (Figure 11.31a) does not show any cracks. It is difficult to estimate the depth of the cracks from the acoustical image in Figure 11.31 since the cracks are not visible in optical or in acoustical images focused on to the surface. They must be either very thin surface-breaking or subsurface cracks originating not deeper than the length of the Rayleigh wave.

SAM can be used not only for detection but also for crack characterization. Knauss *et al*. measured the depth of the short surface-breaking cracks by time-resolved microscopy.[33] Hidden from optical microscope, scratch-induced cracks have been observed in Al-Cu-Fe alloy coatings.[146] SAM can detect hidden fatigue cracks in riveted lap-joint samples (two aluminum alloys panels).[147] Arnold et al.[148] investigated the formation of microcracks in a frontal processing area around a crack. Lawrence et al. [142] demonstrated detection of cracks at the boundary between matrix and fiber in fiber composites.

11.4.5 Other SAM applications

A very interesting application for acoustic microscopy was found by Dresher-Krasiska. She demonstrated that time-resolved acoustic microscopy allows stress distribution to be visualized inside compressed aluminum.[149] Recently, Landa et al.[150] developed an approach that provides a quantitative description of the phenomena.

Conventionally, SAM images show variations of the amplitude of the acoustical signal. Reinholdtsen and Khuri-Yakub[21,77] measured amplitude and phase of the SAM signal at low frequency (3 to 10 MHz) to improve subsurface images. By modifying the two-dimensional point spread function, the transverse resolution was improved by about 20%, and the obscuring effect of surface roughness from images of subsurface features was eliminated.[77] Grill et al.[151] extended this technique to high frequency (1.2 GHz). This technique permits reconstruction of the surface relief of the sample with submicron resolution.[152]

The highest resolution in acoustic microscopy was achieved at low temperature.[49] However, high-temperature applications of the SAM appeared to be more attractive from the industrial point of view. Recently, an important step has been made in the direction of imaging subsurface structures in melts. Ihara et al.[153] developed a sound imaging technique to see a small steel object immerged in molten zinc at 600°C.

Exercise

Construct the contributions to the scattered field of the Rayleigh waves excited by the wavefield $\Phi_i(x')$ at a point x situated to the right of a crack at $x = 0$.

Acknowledgments

The authors would like to thank Dr. Sigrun Hirsekorn and Professor Arthur Every for making corrections; Prof. Tribikram Kundu for his animated scientific discussions; Professor Murli H. Manghnani and Dr. Sonya Berezina for their useful comments; and Hannelore Mewes, Diane Henderson, and Natalia Krokhina for working with the manuscript. This research was supported through a National Institutes of Standards and Technology (NIST) Advanced Technology Program (ATP), cooperative agreement number 70NANBOH3048, and U.S. Army Contract No. DAAD19-00-1-0569.

Appendix A

For solid liquid interface, the reflection coefficient can be expressed using acoustical impedances[2,115]

$$\Re(\theta) = \frac{\tilde{Z}_{tot} - \tilde{Z}}{\tilde{Z}_{tot} + \tilde{Z}} \quad \textbf{(11.A.1)}$$

here $\tilde{Z}$ are the acoustic impedances defined by

$$\tilde{Z}_P = \frac{\rho_S c_p}{\cos\theta_P},\ \tilde{Z}_S = \frac{\rho_S c_s}{\cos\theta_S},\ \tilde{Z} = \frac{\rho\ c}{\cos\theta},\ \tilde{Z}_{tot} = \tilde{Z}_P \cos^2(2\theta_S) + \tilde{Z}_S \cos^2(2\theta_S) \quad \textbf{(11.A.2)}$$

and ρ_s, $c_{p,}$ and c_s are density, longitudinal wave velocity, and shear wave velocity of the sample; ρ and c are density and longitudinal wave velocity of water. The angles θ_P and θ_S are determined from Snell's law

$$\sin\theta_P = \frac{c_p}{c}\sin\theta, \quad \sin\theta_S = \frac{c_s}{c}\sin\theta \quad \textbf{(11.A.3)}$$

The transmission coefficients for longitudinal (T_P) and shear waves (T_S) are given by[2]

$$T_P(\theta) = \frac{2\tilde{Z}_P\cos(2\theta_S)}{\tilde{Z}_{tot} + \tilde{Z}},\ T_S(\theta) = \frac{-2\tilde{Z}_S\cos(2\theta_S)}{\tilde{Z}_{tot} + \tilde{Z}} \quad \textbf{(11.A.4)}$$

For an incident energy flux E, the energy flux propagating away from the surface is[2]

$$E_T = |\Re(\theta)|^2 E \quad \textbf{(11.A.5)}$$

while the transmitted longitudinal is

$$E_P = \frac{\rho \tan\theta}{\rho_s \tan\theta_p} \left|T_P(\theta)\right|^2 E \tag{11.A.6}$$

and the transmitted shear is

$$E_S = \frac{\rho \tan\theta}{\rho_s \tan\theta_S} \left|T_S(\theta)\right|^2 E \tag{11.A.7}$$

Appendix B

For spherical elastic particles, the coefficients A_n are given by[157]

$$A_n = \frac{A_1^*(d_{22}d_{33} - d_{32}d_{23}) - A_2^*(d_{12}d_{33} - d_{32}d_{13})}{d_{11}(d_{22}d_{33} - d_{32}d_{23}) - d_{21}(d_{12}d_{33} - d_{32}d_{13})},$$

$$d_{11} = \frac{\rho}{\rho_i}(k_s a)^2 h_n(ka),$$

$$d_{12} = \left[2n(n+1) - (k_s a)\right]^2 j_n(k_p a) - 4(k_p a)^2 j_n'(k_p a),$$

$$d_{13} = 2n(n+1)\left[(k_s a) j_n'(k_s a) - j_n(k_s a)\right],$$

$$d_{21} = -(ka)h_n'(ka),$$

$$d_{22} = \left(k_p a\right) j_n'(k_p a), \tag{11.B.1}$$

$$d_{23} = n(n+1) j_n(k_s a),$$

$$d_{31} = 0,$$

$$d_{32} = 2[j_n(k_s a) - (k_p a) j_n'(k_p a)],$$

$$d_{33} = 2(k_s a)j_n'(k_s a) + [(k_s a)^2 - 2n(n+1) + 2]j_n(k_s a),$$

$$A_1^* = \frac{\rho}{\rho_s}(k_s a)^2 j_n(ka),$$

$$A_2^* = (ka)j_n'(ka)$$

here j_n are the spherical Bessel functions and $h^{(1)}$ the spherical Hankel functions of the first kind, $k_p = \frac{\omega}{c_p}$, $k_s = \frac{\omega}{c_s}$; c_p and c_s are longitudinal and shear velocities of the spherical particle. The stroke denotes the derivation.

Appendix C

The explicit form of the coefficients A_n^{ij} is

$$A_n^{SH} = -\frac{j_n(x_S) - x_S j_n'(x_S)}{h_n(x_S) - x_S h_n'(x_S)},$$
$$A_n^{PP} = -\frac{\Delta_n^{PP}}{\Delta_n}, \quad A_n^{PS} = -\frac{\Delta_n^{PS}}{\Delta_n}, \quad A_n^{SP} = -\frac{\Delta_n^{SP}}{\Delta_n}, \quad A_n^{SS} = -\frac{\Delta_n^{SS}}{\Delta_n} \quad \textbf{(11.C.1)}$$

where

$$\Delta_n = n(n+1)[h_n(x_P) - x_P h_n'(x_P)][h_n(x_S) - x_S h_n'(x_S)]$$
$$-[(\beta_n - 1)h_n(x_P) + 2x_P h_n'(x_P)][\beta_n h_n(x_S) + x_S h_n'(x_S)],$$

$$\Delta_n^{PP} = n(n+1)[j_n(x_P) - x_P j_n'(x_P)][h_n(x_S) - x_S h_n'(x_S)]$$
$$-[(\beta_n - 1)j_n(x_P) + 2x_P j_n'(x_P)][\beta_n h_n(x_S) + x_S h_n'(x_S)],$$

$$\Delta_n^{SS} = n(n+1)[h_n(x_P) - x_P h_n'(x_P)][j_n(x_S) - x_S j_n'(x_S)]$$
$$-[(\beta_n - 1)h_n(x_P) + 2x_P h_n'(x_P)][\beta_n j_n(x_S) + x_S j_n'(x_S)],$$

$$\Delta_n^{PS} = -\frac{i}{x_S}(1 + \beta_n), \quad \Delta_n^{SP} = -\frac{i}{x_P}(1 + \beta_n),$$

and

$$x_P = k_P a, \; x_S = k_S a, \; \beta_n = 1 + \frac{x_S^2}{2} - n(n+1).$$

References

1. Lemons, R.A. and Quate, C.F., Acoustic microscopy, in *Physical Acoustics*, Mason, W.P. and Thurston, R.N., Eds., Academic Press, London, 1979, pp. 1–92.
2. Briggs, A., *Acoustic Microscopy,* Clarendon Press, Oxford, 1992.
3. Gilmore, R.S., Industrial ultrasonic imaging/microscopy, in *Physical Acoustics*, Thurston, R.N., Pierce, A.D., and Papadakis, E., Eds., Academic Press, New York, 1999, pp. 275–346.
4. Zinin, P.V., Quantitative acoustic microscopy of solids, in *Handbook of Elastic Properties of Solids, Liquids, and Gases. Volume I: Dynamic Methods for Measuring the Elastic Properties of Solids*, Levy, M., Bass, H., Stern, R., and Keppens, V., Eds., Academic Press, New York, 2001, pp. 187–226.
5. Sokolov, S., The ultrasonic microscope, *Doklady Akademia Nauk SSSR* (in Russian), 64, 333–336, 1949.
6. Lemons, R.A. and Quate, C.F., Acoustic microscope-scanning version, *Appl. Phys. Lett.,* 24, 163–165, 1974.
7. Quate, C.F., Atalar, A., and Wickramasinghe, H.K., Acoustic microscope with mechanical scanning: a review, *Proc. IEEE,* 67, 1092–1113, 1979.
8. Lobkis, O.I., Kundu, T., and Zinin, P.V., A theoretical analysis of acoustic microscopy of spherical cavities, *Wave Motion,* 21, 183–201, 1995.
9. Weise, W., Zinin, P., Wilson, T., Briggs, A., and Boseck, S., Imaging of spheres with the confocal scanning optical microscope, *Opt. Lett.,* 21, 1800–1802, 1996.
10. Zinin, P., Weise, W., Lobkis, O., and Boseck, S., The theory of three-dimensional imaging of strong scatterers in scanning acoustic microscopy, *Wave Motion,* 25, 213–236, 1997.
11. Crossen, J.D., Sykes, J.M., Zhai, T., and Briggs, G.A.D., Study of the coating/substrate interface by scanning acoustic microscopy: Cathodic disbonding of epoxy-polyamide lacquer from mild steel, *Faraday Discussions,* 107, 417–424, 1997.
12. Levin, V.M., Blank, V.D., Prokhorov, V.M., Soifer, J.M., and Kobelev, N.P., Elastic properties of solid C_{60}: measurements and relationship with nanostructure, *J. Phys. Chem. Sol.,* 61, 1017–1024, 2000.
13. Drescherkrasicka, E. and Willis, J.R., Mapping stress with ultrasound, *Nature,* 384, 52–55, 1996.
14. Kolosov, O. and Yamanaka, K., Nonlinear detection of ultrasonic vibrations in an atomic-force microscope, *Jap. J. Appl. Phys. Part 2,* 32, L1095–L1098, 1993.
15. Rabe, U. and Arnold, W., Atomic-force microscopy at MHz frequencies, *Annalen Der Physik,* 3, 589–598, 1994.
16. Briggs, A., *Advances in Acoustic Microscopy*, Plenum Press, New York, 1995.
17. Briggs, A. and Arnold, W., *Advances in Acoustic Microscopy,* Plenum Press, New York, 1996.

18. Wilson, T. and Sheppard, C., *Theory and Practice of Scanning Confocal Microscopy*, Academic Press, London, 1984.
19. Kushibiki, J. and Chubachi, N., Material characterization by line-focus-beam acoustic microscope, *IEEE Trans. Son. Ultrasonics,* 32, 189–212, 1985.
20. Atalar, A. and Hoppe, M., High-performance acoustic microscope, *Rev. Sci. Instr.,* 57, 2568–2576, 1986.
21. Reinholdtsen, P. A. and Khuri-Yakub, B.T., Amplitude and phase acoustic microscope using digital heterodyning, *Rev. Sci. Instr.,* 61, 1236–1242, 1990.
22. Forgber, E., Heygster, G., and Boseck, S., Modeling the imaging properties of SAM, *Optik,* 87, 170–178, 1991.
23. Heygster, G., Block, H., Gadomski, A., and Boseck, S., Modeling of the optical transfer-function (OTF) of the scanning acoustic microscope (SAM) and its relation to the other scanning microscopes, *Optik,* 85, 89–98, 1990.
24. Weise, W., Zinin, P., Briggs, A., Wilson, T., and Boseck, S., Examination of the two-dimensional pupil function in coherent scanning microscopes using spherical particles, *J. Acoust. Soc. Am.,* 104, 181–191, 1998.
25. Hirsekorn, S., Pangraz, S., Weides, G., and Arnold, W., Measurement of elastic impedance with high-spatial-resolution using acoustic microscopy, *Appl. Phys. Lett.,* 67, 745–747, 1995.
26. Livingston, R.A., Manghnani, M.H., Wang, Y., and Zinin, P., Detection of cracks and interfacial transition zone in concrete by acoustic microscopy, in *Second US-Japan Symposium on Advances in NDT. Proceeding of the International Symposium*, Katoh, M. and Djordjevic, B.B., Eds., The Japanese Society for Non-Destructive Inspection, Tokyo, 1999, pp. 136–141.
27. Brundle, C.R., Evans, C.A., and Wilson, S., *Encyclopedia of Materials Characterization*, Butterworth-Heinemann, Boston, 1992.
28. Prasad, M., Manghnani, M.H., Wang, Y., Zinin, P., and Livingston, R.A., Acoustic microscopy of portland cement mortar aggregate/paste interfaces, *J. Mater. Sci.,* 35, 3607–3613, 2000.
29. Hauser, M.R., Weaver, R.L., and Wolfe, J.P., Internal diffraction of ultrasound in crystals: Phonon focusing at long wavelength, *Phys. Rev. Lett.,* 17, 2604–2607, 1992.
30. Weaver, R.L., Hauser, M.R., and Wolfe, J.P., Acoustic flux imaging in anisotropic media, *Zeitschrift Fur Physik B,* 90, 27–46, 1993.
31. Grill, W., Hillmann, K., Wurtz, K.U., and Wesner, J., Scanning ultrasonic microscopy with phase contrast, in *Advances in Acoustic Microscopy*, Briggs, A. and Arnold, W., Eds., Plenum Press, New York, 1996, pp. 167–218.
32. Tsukahara, Y., Nakaso, N., Ohira, K., and Yanaka, M., Interaction of acoustic waves with solid surfaces, in *Advances in Acoustic Microscopy*, Briggs, A. and Arnold, W., Eds., Plenum Press, New York, 1996, pp. 103–165.
33. Knaus, D., Zhai, T., Briggs, G.A.D., and Martin, J.M., Measuring short cracks by time-resolved acoustic microscopy, in *Advances in Acoustic Microscopy*, Briggs, A., Ed., Plenum Press, New York, 1995, pp. 49–77.
34. Daft, C.M.W. and Briggs, G.A.D., Wideband acoustic microscopy of tissue, *IEEE Trans. Ultrason. Ferroelect. Freq. Contr.,* 36, 258–263, 1989.
35. Krautkramer, J. and Krautkrämer, H., *Ultrasonic Testing of Materials*, 4th fully rev. ed. Springer-Verlag, Berlin, New York, 1990.
36. Auld, B.A., General electromechanical reciprocity relations applied to the calculation of elastic wave scattering coefficients, *Wave Motion,* 1, 3–10, 1979.
37. Atalar, A., A backscattering formula for acoustic transducers, *J. Appl. Phys.,* 51, 3093–3098, 1980.

38. Somekh, M.G., Bertoni, H.L., Briggs, G.A.D., and Burton, N.J., A two-dimensional imaging theory of surface discontinuities with the scanning acoustic microscope, *Proc. Royal Soc. London A.*, 401, 29–51, 1985.
39. Goodman, J.W., *Introduction to Fourier Optics*, 2nd ed., McGraw-Hill, New York, 1996.
40. Bracewell, R.N., *The Fourier transform and its applications.* McGraw-Hill, New York, 1987.
41. Weise, E., *Konfokale Rastermikroskopie zur Abbildung kugelförmiger Objekte*, Ph.D. thesis, University of Bremen, Germany, 1997.
42. Liang, K.K., Kino, G.S., and Khuri-Yakub, B.T., Material characterization by the inversion of V(z), *IEEE Trans. Sonics Ultrasonics,* 32, 213–224, 1985a.
43. Sasaki, Y., Endo, T., Yamagishi, T., and Sakai, M., Thickness measurement of a thin-film layer on an anisotropic substrate by phase-sensitive acoustic microscope, *IEEE Trans. Ultrasonic Ferroelectric Freqency Control,* 39, 638–642, 1992.
44. Born, M. and Wolf, E., *Principles of Optics: Electromagnetic Theory of Propagation, Interference and Diffraction of Light,* Pergamon Press, Oxford, 1980.
45. Stamnes, J.J., *Waves in Focal Regions,* Adam Hilger, Bristol, 1986.
46. Emiliani, C., *Dictionary of the Physical Sciences*, Oxford University Press, Oxford, 1987.
47. Kino, G.S., *Acoustic Waves: Devices, Imaging and Analog Signal Processing,* Prentice-Hall, Englewood Cliffs, NJ, 1987.
48. Hadimioglu, B. and Quate, C.F., Water acoustic microscopy at suboptical wavelengths, *Appl. Phys. Lett.,* 43, 1006–1007, 1983.
49. Foster, J.S. and Rugar, D., High-resolution acoustic microscopy in superfluid-helium, *Appl. Phys. Lett.,* 42, 869–871, 1983.
50. Sheppard, C.J.R. and Wilson, T., Effects of high angles of convergence on V(Z) in the scanning acoustic microscope, *Appl. Phys. Lett.,* 38, 858–859, 1981.
51. Lobkis, O.I. and Zinin, P.V., Imaging of spherical object in acoustic microscope, in *Mathematical Modelling and Application of Diffraction Phenomena, Proc. All-Union Scientific Seminar. Moscow.* Moscow, 1990, pp. 59–60.
52. Howe, M.S., On the image of a cylindrical Inclusion in the scanning acoustic microscope, *Proc. Royal Soc. London A.,* 435, 393–403, 1991.
53. Rebinsky, D.A. and Harris, J.G., The acoustic signature for a surface-breaking crack produced by a point focus microscope, *Proc. Royal Soc. London A.,* 438, 47–65, 1992.
54. Parmon, W. and Bertoni, H.L., Ray interpretation of the material signature in the acoustic microscope, *Electron.Lett.,* 15, 684–686, 1979.
55. Bertoni, H.L. and Somekh, M.G., Ray-optical analysis of spherical focusing transducers for acoustic microscopy, in *IEEE 1985 Ultrasonics Symp. Proc.*, McAvoy, B.R., Ed., IEEE Press, New York, 1985, pp. 715–719.
56. Brekhovskikh, L.M., *Waves in Layered Media*, 2nd ed., Academic Press, New York, 1980.
57. Weise, W., Zinin, P., and Boseck, S., Modeling of inclined and curved surfaces in the reflection scanning acoustic microscope, *J. Microsc.,* 176, 245–253, 1994.
58. Levin, V.M., Lobkis, O.I., and Maev, R.G., Investigation of the spatial structure of acoustic field by a spherical focusing transducer, *Sov. Phys. Acous.,* 36, 391–395, 1990.
59. Zinin, P., Maslov, K., Lobkis, O., and Kolosov, O., The effect of spherical-particle size reduction in imaging of species by the reflection acoustic microscope, in *Ultrasonics Int. 93: Conf. Proc.,* Butterworth-Heinemann, Oxford, U.K., 1993, pp. 65–68.

60. Hildebrand, J.A., Liang, K., and Bennett, S.D., Fourier-transform approach to materials characterization with the acoustic microscope, *J. Appl. Phys.*, 54, 7016–7019, 1983.
61. Sheppard, C.J.R., Confocal interference microscopy, in *Confocal Microscopy,* Wilson, T., Ed., Academic Press, London, 1990, pp. 389–411.
62. Liang, K.K., Kino, G.S., and Khuri-Yakub, B.T., Material characterization by the inversion of V(z), *IEEE Trans. Sonics Ultrasonics,* 32, 213–224, 1985b.
63. Duquesne, J.Y., Inversion of complex V(Z) at high-frequencies for acoustic microscopy, *Rev. Sci. Instr.,* 67, 2656–2657, 1996.
64. Atalar, A., Quate, C.F., and Wickramasinghe, H.K., Phase imaging in reflection with the acoustic microscope, *Appl. Phys. Lett.,* 31, 791–793, 1977.
65. Weglein, R.D. and Wilson, R.G., Characteristic material signatures by acoustic microscopy, *Electron. Lett.,* 14, 352–354, 1978.
66. Atalar, A., An angular-spectrum approach to contrast in reflection acoustic microscopy, *J. Appl. Phys.,* 49, 5130–5139, 1978.
67. Kushibiki, J., Ohkubo, A., and Chubachi, N., Anisotropy detection in sapphire by acoustic microscope using line-focus beam, *Electron. Lett.,* 17, 534–536, 1981.
68. Kundu, T., Mal, A.K., and Weglein, R.D., Calculation of the acoustic material signature of a layered solid, *J. Acoust. Soc. Amer.,* 77, 353–361, 1985.
69. Kundu, T., A complete acoustic microscopic analysis of multilayered specimens, *J. Appl. Mech.,* 59, 54–60, 1992.
70. Kundu, T. and Mal, A.K., Acoustic material signature of a layered plate, *Int. J. Eng. Sci.,* 24, 1819–1829, 1986.
71. Somekh, M.G., Briggs, G.A.D., and Ilett, C., The effect of elastic anisotropy on contrast in the scanning acoustic microscope, *Phil. Mag. A,* 49, 179–204, 1984.
72. Every, A.G. and Deschamps, M., Principal surface wave velocities in the point focus acoustic materials signature V(z) of an anisotropic solid, in *Review of Progress in Quantitative Nondestructive Evaluation*, Thompson, D.O. and Chimenti, D.E., Eds., American Institute of Physics, College Park, MD, 2003, pp. 51–58.
73. Kushibiki, J., Ishikawa, T., and Chubachi, N., Cut-off characteristic of leaky Sezawa and pseudo-Sezawa wave modes for thin-film characterization, *Appl. Phys. Lett.,* 57, 1967–1969, 1990.
74. Chan, K.H. and Bertoni, H.L., Ray representation of longitudinal lateral waves in acoustic microscopy, *IEEE Trans. Ultrasonic Ferroelectric Frequency Control,* 38, 27–34, 1991.
75. Weglein, R.D., Acoustic microscopy of curved surfaces, *Appl. Phys. Lett.,* 38, 516–518, 1981.
76. Maslov, K.I., Zinin, P.V., Lobkis, O.I., and Kundu, T., V(z) curve formation of solid spherical microparticles in scanning acoustic microscopy, *J. Microsc.,* 178 (Pt2), 125–133, 1995.
77. Reinholdtsen, P.A. and Khuri-Yakub, B.T., Image processing for a scanning acoustic microscope that measures amplitude and phase, *IEEE Trans. Ultrasonic Ferroelectric Frequency Control* 38, 141–147, 1991.
78. Baker, L., Optical transfer function: foundation and theory. selected papers, in *SPI Milestone Series,* SPIE Optical Engineering Press., Bellingham, 1992.
79. Baker, L., Optical transfer function: measurement. selected papers, in *SPI Milestone Series,* SPIE Optical Engineering Press., Bellingham, 1992.
80. Lee, U.W. and Bond, L.J., Characterising of ultrasonic imaging system using transfer function, *Ultrasonics,* 141, 48–56, 1993.

81. Atalar, A., Modulation transfer function for the acoustic microscope, *Electron. Lett.,* 15, 321–323, 1979.
82. Zinin, P., Weise, W., Zhai, T., Briggs, G.A.D., and Boseck, S., Determination of the defocused transfer function of a confocal reflection microscope by imaging of a sphere, *Optik,* 107, 45–48, 1997.
83. Sheppard, C.J.R., Hamilton, D.K., and Cox, I.J., Optical microscopy with extended depth of field, *Proc. Royal Soc. London A.,* A387, 171–186, 1983.
84. Yamanaka, K. and Enomoto, Y., Fringe pattern around surface crack observed with scanning acoustic microscope, *Electron. Lett.,* 17, 638–640, 1981.
85. Ilett, C., Somekh, M.G., and Briggs, G.A.D., Acoustic microscopy of elastic discontinuities, *Proc. Royal Soc. London A.,* 393, 171–183, 1984.
86. Yamanaka, K. and Enomoto, Y., Observation of surface cracks with scanning acoustic microscope, *J. Appl. Phys.,* 53, 846–850, 1982.
87. Manghnani, M.H., Tkachev, S., Zinin, P.V., Zhang, X., Brazhkin, V.V., Lyapin, A.G., and Trojan, I.A., Elastic properties of superhard amorphous carbon pressure- synthesized from C_{60} by surface Brillouin scattering, *Phys. Rev. B,* 6412, 121403, 2001.
88. Steibl, N, Three-dimensional imaging by a microscope, *J. Opt. Soc. Amer. A.,* A2, 121–127, 1985.
89. McNally, J.G., Preza, C., Conchello, J., and Thomas, L.J., Artifacts in computational optical-sectioning microscopy, *J. Opt. Soc. Amer. A.,* 11, 1056–1067, 1994.
90. Hamilton, D.K. and Wilson, T., Surface profile measurement using the confocal microscope, *J. Appl. Phys.,* 53, 5320–5322, 1982.
91. Landau, L.D. and Lifshits, E.M., *Quantum mechanics: non-relativistic theory,* 2d, rev. and enl. ed. Pergamon Press; [sole distributors in the U.S.A.] Addison-Wesley Pub. Co., Reading, MA, Oxford, New York,, 1965.
92. Mandel, L. and Wolf, E., *Optical Coherence and Quantum Optics,* Cambridge University Press, Cambridge, 1995.
93. Zinin, P., Weise, W., Lobkis, O., Kolosov, O., and Boseck, S., Fourier optics analysis of spherical particles image formation in reflection acoustic microscopy, *Optik,* 98, 45–60, 1994.
94. Jackson, J.D., *Classical Electrodynamics,* John Wiley, New York, 1995.
95. Kolosov, O.V., Yamanaka, K., Lobkis, O.I. and Zinin, P.V., Direct spatial evaluation of the point-spread function of axially symmetric and asymmetric acoustic imaging focusing systems using a spherical ball reflector, in *NDTE Int.,* 25(4), 219–220, 1992.
96. Kolosov, O.V., Lobkis, O.I., Maslov, K.I., and Zinin, P.V., The effect of the focal plane position on the images of spherical objects in the reflection acoustic microscope, *Acoust. Lett.,* 16, 84–88, 1992.
97. Aguilar, J.F., Lera, M., and Sheppard, C.J.R., Imaging of spheres and surface profiling by confocal microscopy, *Appl. Opt.,* 39, 4621–4628, 2000.
98. Truell, R., Elbaum, C., and Chick, B.B., *Ultrasonic Methods in Solid State Physics,* Academic Press, New York, 1969.
99. Einspruch, N.G., Witterbolt, E.J., and Truel, R., Scattering of a plane transverse wave by a spherical obsticale in an isotropic elastic solid, *J. Acoust. Soc. Amer.,* 31, 806, 1960.
100. Ying, C.F. and Truel, R., Scattering of a plane longitudinal wave by a spherical obstacle in an isotropic elastic solid, *J. Acoust. Soc. Amer.,* 27, 1086, 1956.
101. Lobkis, O.I., Maslov, K.I., Kundu, T., and Zinin, P.V., Spherical inclusion characterization by the acoustical microscope - axisymmetrical case, *J. Acoust. Soc. Amer.,* 99, 33–45, 1996.

102. Yamanaka, K., Surface acoustic wave measurement using an impulse converging beam, *J. Appl. Phys.,* 54, 4323–4329, 1983.
103. Daft, C.M.W., Briggs, G.A.D., and Obrien, W.D., Frequency-Dependence of Tissue Attenuation Measured By Acoustic Microscopy, *J. Acoust. Soc. Amer.,* 85, 2194–2201, 1989.
104. Weaver, J.M.R., Daft, C.M.W., and Briggs, G.A.D., A quantitative acoustic microscope with multiple detection modes, *IEEE Trans. Ultrasonic Ferroelectric Frequency Control,* 36, 554–560, 1989.
105. Sinton, A.M., Briggs, G.A.D., and Tsukahara, Y., Time-resolved acoustic microscopy of polymer-coatings, in *Acoustical Imaging*, Kushibiki, J., Ed., Plenum Press, New York, 1989, pp. 87–95.
106. Zhang, J., Baboux, J.C., and Guy, P., PVDF large aperture spherical transducer in the transient mode, in *Proc. IEEE 1994 Ultrasonic Symp.*, McAvoy, B.R., Levy, M., and Scheider, S.C., Eds., IEEE Press, New York, 1994, pp. 517–520.
107. Xiang, D., Hsu, N.N. and Blessing, G.V., The design, construction and application of a large-aperture lens-less line-focus PVDF transducer, *Ultrasonics,* 34, 641–647, 1996.
108. Li, W. and Achenbach, J.D., Determination of elastic constants by time-resolved line-focus acoustic microscopy, *IEEE Trans. Ultrasonic Ferroelectric Frequency Control,* 44, 681–687, 1997.
109. Papoulis, A., *The Fourier Integral and Its Applications,* McGraw-Hill, New York, 1962.
110. Zhang, J., Guy, P., Baboux, J.C., and Jayet, Y., Theoretical and experimental responses for a large-aperture broadband spherical transducer probing a liquid-solid boundary, *J. Appl. Phys.,* 86, 2825–2835, 1999.
111. Hollis, R.L. and Hammer, R., Defect detection for microelectronics by acoustic microscopy, in *Scanned Image Microscopy.*, Ash, E.A., Ed., Academic Press, 1980, pp. 155–164.
112. Khuriyakub, B.T., Reinholdtsen, P., and Jun, K.S., Subsurface Defect Detection Using Acoustic Microscopy, in *IEEEE 1984 Ultrasonics Symp. Proc., Vols. 1&2*, Piscataway, NJ, 1984, pp. 580–583.
113. Ishikawa, I., Kanda, H., and Katakura, K., An acoustic microscope for subsurface defect characterization, *IEEE Trans. Sonics Ultrasonics,* 32, 325–331, 1985.
114. Atalar, A., Penetration depth of the scanning acoustic microscope, *IEEE Trans. Sonics Ultrasonics,* 32, 164–167, 1985.
115. Miyasaka, C., Tittmann, B.R., and Ohno, M., Practical shear wave lens design for improved resolution with acoustic microscope, *Res. Nondestructive Evaluation,* 11, 97–116, 1999.
116. Levin, V.M., Maev, R.G., Maslov, K.I., Senjushkina, T.A., Grigorieva, I.G., and Baranchikova, I., Study of structure and properties of highly anisotropic materials by acoustomicroscopic methods, in *Acoustical Imaging*, Ermert, H. and Harjes, H.P. Plenum Press, New York., 1992, pp. 651–656.
117. O'Neill, B.E. and Maev, R.G., Integral approximation method for calculating ultrasonic beam propagation in anisotropic materials, *Phys. Rev. B,* 58, 5479–5485, 1998.
118. Miyasaka, C., Tittmann, B.R., and Ohno, M., Practical shear wave lens design fro improved resolution with acoustic microscope, *Res. Nondestructive Evaluation*, 11, 97–116, 1999.
119. Bechou, L., Angrisiani, L., Ousten, Y., Dallet, D., Levi, H., Daponte, P., and Danto, Y., Localization of defects in die-attach assembly by continuous wavelet transform using scanning acoustic microscopy, *Microelectron. Reliab.,* 39, 1095–1101, 1999.

120. Angrisani, L., Bechou, L., Dallet, D., Daponte, P., and Ousten, Y., Detection and location of defects in electronic devices by means of scanning ultrasonic microscopy and the wavelet transform, *Measurement*, 31, 77–91, 2002.
121. Maslov, K.I., Kundu, T., and Lobkis, O.I., Acoustic microscopy for spherical inclusion characterization, *J. Acoust. Soc. Am.,* 100, 80–85, 1996.
122. Berezina, S., Blank, V., Levin, V., and Prokhorov, V., Observation of ultrasound velocity gradient in fullerene ceramics by acoustic microscopy, *Ultrasonics,* 38, 327–330, 2000.
123. Zinin, P., Manghnani, M.H., Newtson, C., and Livingston, R. A., Acoustic microscopy of steel reinforcing bar in concrete, *J. Nondestrucive. Evaluation,* 31, 153–161, 2002.
124. Weglein, R.D., Integrated-circuit inspection via acoustic microscopy, *IEEE Trans. Sonics Ultrasonics,* 30, 40–42, 1983.
125. Attal, J., Acoustic microscopy: imaging microelectronic circuits with liquid metals, in *Scanned Image Microscopy*, Ash, E.A., Ed., Academic Press., London, 1980, pp. 97–118.
126. Pfannschmidt, G., Characterization of electronic components in acoustic microscopy, in *Advances in Acoustic Microscopy*, Briggs, A. and Arnold, W., Eds., Plenum Press, New York, 1996, pp. 1–38.
127. Crean, G.M., Flannery, C.M., and Mathuna, S.C., Acoustic microscopy analysis of microelectronic interconnection and packing technologies, in *Advanced in Acoustic Microscopy*, Briggs, A., Ed., Plenum Press, New York, 1995, pp. 1–48.
128. Ousten, Y., Mejdi, S., Fenech, A., Deletage, J.Y., Bechou, L., Perichaud, M.G., and Danto, Y., The use of impedance spectroscopy, SEM and SAM imaging for early detection of failure in SMT assemblies, *Microelectron. Reliab.,* 38, 1539–1545, 1998.
129. Moore, T.M., C-Mode acoustic microscopy applied to integrated-circuit package inspection, *Solid-State Electronics,* 35, 411–421, 1992.
130. Barton, J., Compagno, T., and Barrett, J., Scanning acoustic mycroscopy studies of microelectronic packging, in *Acoustical Imaging*, Halliwell, M. and Wells, P.N.T., Kluwer Academic, New York, 2000.
131. Benstetter, G., Ruprecht, M.W., and Hunt, D.B., A review of ULSI failure analysis techniques for DRAMs 1. Defect localization and verification, *Microelectron. Reliab.,* 42, 307–316, 2002.
132. Jipson, V.B., Acoustic microscopy of interior planes, *Appl. Phys. Lett.,* 35, 385–387, 1979.
133. Levin, V.M., Blank, V.D., Prokhorov, V.M., Soife, J.M., and Kobelev, N.P., Elastic properties of solid C_{60}: Measurements and relationship with nanostructure, *J. Phys. Chem. Sol.,* 61(7), 1017–1024, 2000.
134. Wickramasinghe, H.K., Mechanically scanned B-scan system for acoustic microscopy of solids, *Appl. Phys. Lett.,* 39, 305–307, 1981.
135. Bray, R.C., Quate, C.F., Calhoun, J., and Koch, R., Film adhesion studies with the acoustic microscope, *Thin Solid Films,* 74, 295–302, 1980.
136. Addison, R.C., Somekh, M., and Briggs, G.A.D., Techniques for the characterization of film adhesion, *IEEE 1986 Ultrason. Symp. Proc.,* New York, 1986, pp. 775–782.
137. Parthasarathi, S., Tittmann, B.R., and Ianno, R J., Quantitative acoustic microscopy for characterization of the interface strength of diamond-like carbon thin films, *Thin Solid Films,* 300, 42–50, 1997.
138. Wang, L., The contrast mechanism of bond defects with the scanning acoustic microscopy, *J. Acoust. Soc. Am.,* 104, 2750, 1998.

139. Guo, Z., Achenbach, J.D., Madan, A., Martin, K., and Graham, M.E., Modeling and acoustic microscopy measurements for evaluation of the adhesion between a film and a substrate, *Thin Solid Films*, 394, 188–200, 2001.
140. Kendig, M., Abdelgawad, M., and Addison, R., Cathodic disbonding in microelectronics observed by insitu scanning acoustic microscopy, *Corrosion*, 48, 368–372, 1992.
141. Lawrence, C.W., Briggs, G.A.D., and Scruby, C.B., Acoustic microscopy of ceramic-fiber composites. 3. Metal-matrix composites, *J. Mater. Sci.*, 28, 3653–3660, 1993.
142. Lawrence, C.W., Briggs, G.A.D., and Scruby, C.B., Acoustic microscopy of ceramic-fiber composites.2. Glass ceramic- matrix composites, *J. Mater. Sci.*, 28, 3645–3652, 1993.
143. Lawrence, C.W., Briggs, G.A.D., Scruby, C.B., and Davies, J.R.R., Acoustic microscopy of ceramic-fiber composites. 1. Glass-matrix composites, *J. Mater. Sci.*, 28, 3635–3644, 1993.
144. Zhai, T., Knauss, D., Briggs, G.A.D., and Martin, J.W., Mixed-mode crack mouth reflection in time-resolved acoustic microscopy of short fatigue cracks in single-crystal aluminum, *J. Phys. D*, 27, 719–725, 1994.
145. Yen, C.E. and Tittmann, B.R., Fiber-matrix interface study of carbon-carbon composites using ultrasonics and acoustic microscopy, *Composit. Eng.*, 5, 649, 1995.
146. Rats, D., von Stebut, J., and Augereau, F., High frequency scanning acoustic microscopy: a novel non-destructive surface analytical tool for assessment of coating-specific elastic moduli and tomographic study of subsurface defects, *Thin Solid Films*, 355–356, 347–352, 1999.
147. Connor, Z.M., Fine, M.E., Achenbach, J.D., and Seniw, M.E., Using scanning acoustic microscopy to study subsurface defects and crack propagation in materials, *JOM-e* 50, http://www.tms.org/pubs/journals/JOM/9811/Connor/Connor-9811.html, 1998.
148. Arnold, W., Fassbender, S.U., and Weides, G., Measurement of elastic properties related to the R-Curve-behavior of ceramics, (in press), 2002.
149. Drescher-Krasicka, E. and Willis, J.R., Mapping stress with ultrasound, *Nature*, 384, 52–55, 1996.
150. Landa, M. and Plesek, J., Contrast enhancement of ultrasonic imaging of internal stresses in materials, *Ultrasonics*, 40, 531–535, 2002.
151. Grill, W., Hillmann, K., Kim, T.J., Lenkeit, O., Ndop, J., and Schubert, M., Scanning acoustic microscopy with vector contrast, *Physica B*, 263, 553–558, 1999.
152. Schubert, M., Lenkeit, O., and Grill, W., Volume imaging by three dimensional scanning acoustic microscopy with phase contrast, *Instrum. Sci. Tech.*, 27, 227, 1999.
153. Ihara, I., Jen, C.-K., and Ramos França, D., Ultrasonic imaging, particle detection, and V(z) measurements in molten zinc using focused clad buffer rods, *Rev. Sci. Instrum.*, 71, 3579–3586, 2000.
154. Lefeuvre, O., Characterisation of Stiffening Layers by Acoustic Microscopy and Brillouin Spectroscopy, D. Phil. thesis, University of Oxford, 1998.
155. Manghnani, M.H., Elastic properties of cBN as a function of temperature and pressure: a comparison with diamond, in *5th NIRIM Int. Symp. Adv. Mater. (ISAM' 98)*, National Institute for Research in Inorganic Materials, Chicherster, 1998, pp. 73–78.
156. Field, J.E., *The Properties of Natural and Synthetic Diamond*, Academic Press, London, 1992.
157. Dragonette, L.R. and Uberall, H., RST analysis pf monostatic and bistatic acoustic echoes from an elastic sphere, *J. Acoust. Soc. Am.*, 73, 1–12, 1983.

12

Ultrasonic Characterization of Biological Cells

Jürgen Bereiter-Hahn and Christopher Blase

CONTENTS

0-8493-1462-3/02/$0.00+$1.50

12.1 Mechanical Characterization of Cytoplasm by Acoustic Microscopy

Cytoplasm and cellular organelles exhibit visco-elastic properties (i.e., they are adequately described neither as solid bodies nor as fluids). In addition, cytoplasm and the organelles form microdomains that differ in their mechanical properties. The integration of viscosity and elasticity has been described in terms of a Maxwell body or a Voigt body or by other combinations of viscous and elastic elements arranged in series and rows. The models are derived from the frequency related response of strain on the application of stresses (Fung, 1981, 1984). With increasing frequency of stress application, fewer forces are taken up by the viscous elements, and the reaction is dominated by the elastic properties (Sato et al., 1987). Viscous flow of cytoplasm occurs in the range of seconds or minutes; at very small strains viscosity influences may be detectable down to the kilohertz range. Acoustic microscopy, however, is performed in the upper megahertz and the gigahertz range and is far above the influence of viscous elements on the mechanical behavior of cytoplasm. The interaction of cells with ultrasound will depend almost exclusively on its elastic properties in addition to structural properties responsible for attenuation (see Section 12.6.1.3).

When a cell is exposed to gigahertz ultrasound, should it be described as a fluid or a solid? Cells are composite bodies containing about 80% of water, which chemically and mechanically determines cytoplasmic properties (Letterier, 2001). The dry mass (the solid fraction), however, largely consists of proteins that may be able to polymerize and depolymerize and to contract and relax. The proteins are responsible for the production of forces required (e.g., for migration in embryonic development, wound healing and tumor invasivity, for the movement of chromosomes toward the spindle poles in mitosis or for cytokinesis).

Compression modulus and density determine the longitudinal wave speed of sound in fluids (see Chapter 1). In the case of cytoplasm this compression modulus is a compound parameter consisting of the compression modulus

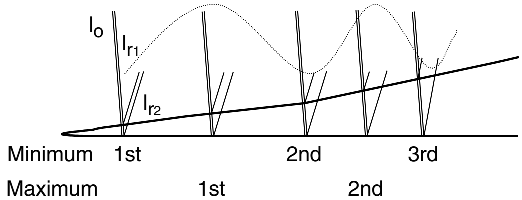

FIGURE 12.1
Schematic representation of one half of a cell as a wedge-shaped structure on a solid substratum. The incident sound waves I_0 will in part be reflected at the medium/cell interface (I_{r1}), and another fraction penetrates through the cell to the solid substratum where again a certain fraction will be reflected (I_{r2}) that can then interfere with the wave reflected from the cell/medium interface. Depending on the cell thickness the phase differences cause destructive and constructive interferences. The course of amplitude is indicated by the wave pattern above the tapering structure. Multiple reflections are highly attenuated and therefore have not been considered in this scheme.

of the saline (water plus dissolved ions) and of the compression modulus of the dry matter (proteins, nucleic acids, fat, etc.).

As a consequence of the fluid character of cytoplasm, no shear waves will be generated, and if generated, they would be highly attenuated. Neither Rayleigh waves nor other surface leaky waves interfere with the waves reflected from the cell surface. The V(z) characterization that is of high value in the determination of thin-layered solid material does not apply to cells. Cells may only influence the V(z) relations of the underlying solid by acting as a thin layer of liquid with specific properties on top of the solid (Kundu et al., 1991; Litniewski and Bereiter-Hahn, 1991).

A second feature significant in acoustic microscopic investigation of cells is shape. Because acoustic microscopy in general is limited to structures with a small degree of roughness, most of the investigations have been done on cells in culture. In this case cells reside on the surface of a solid substratum. Their shape can be approximated by an ascending and declining wedge (Figure 12.1). Longitudinal sound waves are reflected at least at two boundaries: at the culture medium/upper cell surface and at the lower cell surface/solid surface where the cells are residing. These waves will interfere with each other if the pulse length exceeds the acoustical path length through the cytoplasm, giving rise to an interference pattern that delineates cell shape (Figure 12.3, Figure 12.5, and Figure 12.8).

12.2 Alternative Methods to Determine Cell Mechanics

A broad range of methods has been developed to determine cytoplasmic elasticity. Recently atomic force microscopy (Radmacher et al., 1993, 1994, 1996; Vesenka, 1997) and the related poking methods became the most widely used methods to test cell elasticity. They are used to repeat in part the experiments performed to establish scanning acoustic microscopy (SAM). More recently magnetic twisting cytometry added considerably to cytomechanical measurements and the analysis of the physiological transduction of mechanical signals (Wang and Ingber, 1995). The main power of acoustic microscopy lies in its very small interaction with the probe and its high temporal and spatial resolution. The lateral resolution does not reach that of the scanning force microscopy, but most forces do not act on a small submicrometer area; they only distribute throughout a larger area of several microns.

Temporal resolution is a very significant parameter in the analysis of living cells because the dynamics of cells and their organelles restrict the time of data acquisition. Some cells move at speeds up to 30 μm/min. In addition, organelles inside a cell may move or the surface topography may change within a few seconds. Thus, data acquisition must be a fast process. Depending on the lateral resolution required, one or more pictures have been taken by SAM. A picture of 256 lines and 512 pixels width requires 5 sec; this is much less than for one atomic force microscopy (AFM) image.

Two types of microscopes are presently used and commercially manufactured: the scanning laser acoustic microscope (SLAM) operated at about 100 MHz and the SAM operated in reflection mode. In the SAM, frequencies up to 2 GHz (at room temperature) allow lateral resolutions in the submicrometer range, and in the direction of the acoustical axis (z-axis) resolution of 10 to 20 nm is easily achieved if interference phenomena are evaluated. At lower temperatures (< 100°K and 8 GHz) much higher resolutions can be reached. The technical expenditure, however, is enormous for operating a microscope in this temperature range. The SLAM technique in life sciences primarily has been applied to the investigation of tissue slices (e.g., O'Brien et al., 1988).

12.3 Principles of Cytomechanics Analysis by SAM

For calculating the elasticity of isolated cells and soft tissue, the measurement of impedance differences from the intensity of the reflected acoustic signal seems to be a relatively simple method. The reason why is that the contribution of surface waves and Rayleigh waves can be neglected (see above). Problems arise because reflectivity for ultrasound at the culture medium/cell surface boundary is low and sound reflection may be modulated by the slope of the reflecting surface (i.e., surface topography). This depends on the overall cell shape and the presence of microstructures on top of the cells (glycokalix, ridges, microvill, etc.) and at their surfaces adhering to a solid substratum. In general, these structures deteriorate procedures for precise measurements of surface elasticity. In part they can be overcome by preincubation of the cells in serum-free media for about 24 hours before starting the measurements.

12.4 Parameters of Cells That Have to Be Determined

The primary data acquired by SAM of cells and tissues are the intensity of p-wave reflection (corresponding to the impedance differences at the boundaries) and longitudinal wave attenuation. Depending on the type of microscope, phase information may supplement amplitude values and the time of flight can be determined by temporal resolution of the signals. From these data several unknowns determining the mechanical parameters of a cell have to be derived: cell thickness (topography), cytoplasmic elasticity, density, and probably viscosity have to be calculated from the acoustic parameters. In case cells do not adhere tightly and smoothly to their solid base, the thickness of the intermediate layer also has to be considered (Kundu et al., 1992).

How can one cope with these many unknowns? A variety of methods has been developed to solve this problem and to calculate physiologically relevant parameters from SAM images. Table 12.1 summarizes the most important approaches.

No method has gained superiority over others in handling and reliability. In general, V(z) and V(f) procedures (V(z) and V(f) curves) require focus or frequency variations and need several images to be taken before the calculations can be done. This limits temporal resolution. Methods based on the evaluation of interference fringes provide high temporal resolution combined with loss in spatial resolution; they also do not allow measurements of very thin cytoplasmic layers. Procedures taking advantage of the information in phase *and* amplitude of the acoustical signal seem to be superior for resolution in time and space. However, they are very sensitive to external disturbances (temperature, scanning plane, vibrations) that impose big difficulties for practical work.

Similar difficulties may arise using time-resolved SAM that in principle are equivalent to the combined amplitude and phase methods, but also take a long time for image acquisition (which may be overcome by technical refinements). Their resolution in z-direction in practical use is in the range of several micrometers (at 500 MHz), depending on the evaluation procedure applied.

In the next section, the application of those methods will be exemplified that have been used in the authors' laboratory.

12.5 SAM Methods to Determine Mechanical Properties of Cells

12.5.1 Surface Reflection

In the case only one boundary exists, measuring sound reflected at the interface between coupling fluid and specimen (I_r/I_0) at normal incidence,

TABLE 12.1

SAM Approaches to Determine Mechanical Properties of Cells

Method	Advantages	Shortcomings	Ref.
Surface reflection method	Sound velocity is determined straightforward	No background reflection is a must; limited applicability to thick structures only; surface topography of crucial influence	
Time-resolved SAM	All parameters can be determined directly (thickness, density, sound velocity, attenuation); high lateral resolution	Very long acquisition time; thin cytoplasmic layers cannot be measured	Briggs et al., 1993
Interference fringe contrast method	Fast; a single frame is sufficient; semiquantitative estimations of tension distributions	Low lateral resolution; density is assumed to be constant; problems with thin cytoplasmic layers; substrates with high acoustic impedance are required to minimize errors	Litniewski and Bereiter-Hahn, J., 1990
V(z) methods	Well-developed theory; high lateral resolution; thin cytoplasmic layers can be analyzed; all parameters can be calculated separately; only bounds for the values are required for mathematical iteration	Long acquisition time (several images are required); dependence on substrate properties	Grattarola et al.; Boseck et al.; 1993 Kundu et al., 1991
V(f) methods	Independent from background material; working in focus; electronic switching frequency does not involve mechanical elements as in V(z); all parameters can be calculated separately; only bounds for the values are required	Relatively long acquisition time depending on number of frequencies; lens transfer function may be very different for different frequencies	Kushibiki et al.; 1995 Kundu et al. 2000
Phase and amplitude imaging (also to be combined with V(f))	High sensitivity; thin cytoplasmic layers can be studied; high lateral resolution; all parameters can be calculated separately; only bounds for the values are required; if low lateral resolution is acceptable one image is sufficient to calculate all parameters	High sensitivity of phase imaging requires extremely well-controlled temperature and mechanical conditions, and a series of image preprocessing before starting calculations	

allows straightforward calculation of impedance (Z_C) and sound velocity (c_P) of a cell using

$$I_r / I_0 = \left(\frac{(Z_C - Z_F)}{(Z_C + Z_F)} \right)^2 \tag{12.1}$$

where (I_0) is the incident sound intensity, (I_r) is the reflected sound intensity, Z_C is the acoustic impedance of the probe (i.e., cytoplasm), and Z_F is the acoustic impedance of the coupling fluid (i.e., water or saline)

$$Z = \rho c_P \tag{12.2}$$

where ρ is the density of the propagating medium.

The confocality of SAM is in favor of this method. However, the operating aperture of acoustic lenses is much smaller than that of high-resolution light microscope objectives, making the power for producing acoustical sectioning of the probe smaller as well. While this method is well applicable to thick tissue slices or to the polished surface of a quasi-solid material as is bone (see Chapter 13), its application to cell imaging is very limited. An image showing cell surface reflectivity can be obtained only when the reflectivity of the supporting substratum is very low and the thickness of the cell is high, relative to the extension of the focal spot of the acoustical lens along its axis of propagation. In the case of an isolated rat cardiomyocyte shown in Figure 12.2, a series of images was taken with 0.5 μm increment in focal position. The brightest value for each pixel position (xi, yi) found in the whole set of about 20 images was then written into a new image, showing only the brightest reflections at each point (all max image). Because of cell thickness and low reflectivity of the supporting plastic material, no background signal reaches the acoustic lens.

For calculations of mechanical properties of cells from such all max images, the following parameters have to be considered: normal incidence, uneven surface topography, and interference with reflections from the supporting surface.

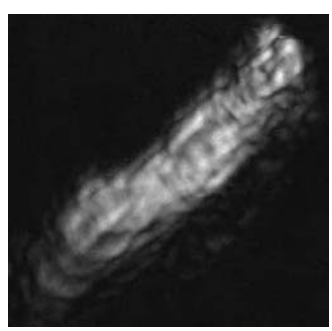

FIGURE 12.2
Maximum ultrasound image of an isolated rat cardiomyocyte. The 19 z-plane images used to calculate the image covered 9.5 μm inthe z-direction and were obtained at 1.0 GHz (30°C). Areas of high reflectivity are interspersed with areas of low reflectivity. No subcellular structures could be identified in z-direction. (From Mathis O. Riehle, Glasgow, U.K. With permission.)

12.5.1.1 Normal Incidence and Uneven Surface Topography

The simple relationship described by Equation 12.1 is valid only for normal incidence. The assumption of normal incidence of ultrasound focused on a plane surface is justified in the focal plane in the very center of the focal spot. If the focal plane of a lens is positioned several wavelengths above the surface to be imaged, only normally incident sound waves contribute to image formation. In many cases the slope of the reflecting surface is not exactly known. As a result, the extended formula (including the angular spectrum of the sound waves) cannot be applied, and only those parts of specimens that lay at approximately 90° to the incident sound beam can be studied. Examples with almost plane surfaces are tissue sections and very flat cells in culture; reflectivity does not change more than 5% if the slope of the reflecting surface of a cell is up to 15° (Boseck, 1993). Using combined amplitude and phase imaging of the reflected sound waves overcomes this problem because the changes in phase allow for the determination of distances and surface slopes. This method has not been systematically applied to cells and tissues until now.

Oblique specimens or those with surface modulations up to the focal distance of the lens can be imaged properly by acquisition of a focus series of images with an increment smaller than the focal depth of the acoustic lens to fulfill the Nyquist sampling theorem. In the case of 1 GHz, vertical resolution of the amplitude image is in the range of 3 μm; a recommended step size of 0.5 μm corresponds to extensive oversampling. From this set of images an all max image is calculated as generally applied in confocal microscopies (Figure 12.2).

12.5.1.2 Interference with Reflections from the Supporting Surface

Glass or plastic materials are used as supporting material for the microscopic observation of cells. The reflection coefficients of these materials, especially glass, are higher than those of soft biological tissues. Under defocusing conditions reflections from these surfaces may also contribute to image formation. This can be avoided by using substrates with an impedance close to that of the specimen under investigation and by sufficiently large defocusing. Materials almost matching cytoplasmic impedance are concentrated agar (> 3%) or soft polyvinylchloride (Kanngiesser and Anliker, 1991). The necessary degree of defocusing depends on the reflectivity of the substratum. On the other hand, reflections from the substratum and from the surface of the biological sample may interfere with each other; it is this interference that provides a useful signal for further analysis (see Chapter 13).

12.5.2 Time-Resolved SAM

Time-resolved acoustic microscopy has been realized several times in the past (Briggs, 1992; Briggs et al., 1993; Hänel and Kleffner, 1998; Sinton et al., 1989) and has been used for characterization of soft and hard biological tissues (Daft and Briggs, 1989; Hänel and Kleffner, 1998). The short temporal extent of the impulse excitation allows the separation of echo pulses from the top and bottom of a thin specimen or from separate interfaces in a layered specimen to be identified in the received signal. Because of this separation, the vertical structure in specimens can be resolved. High reflectivity of the supporting surface combined with low reflectivity of the specimens and attenuation by the samples normally impede this type of imaging soft biological samples. Cells grown on a polyvinyl-chloride surface that almost matches the acoustical impedance of the coupling fluid (reflectivity 18 dB lower than the reflection of the surface of a polystyrene petri dish) were viewed using ultrasound pulses in the ns range. This method permitted acoustical sectioning and thus three-dimensional imaging and x-/z-scans (brightness-scans [B-scans]) with a resolution of 1.24 μm in the axial direction (0,54 μm lateral resolution at 1.5 GHz) (Kanngiesser and Anliker, 1991). Although in time resolved SAM interference fringes appear, they are not used for further analysis.

If the echoes in time resolved SAM are adequately separated in time from the height and position of each maximum in the echo-four crucial parameters can be separated:

- The difference in time between the reference signal and the reflection from the top layer
- The difference in time between the interface of the top surface and the substrate-facing surface of a cell
- The relative amplitudes reflected from the top of the cell
- The relative amplitudes reflected from the substrate interface of the cell

From these parameters' cell thickness, acoustic velocity in the cell, impedance, attenuation, and density of the cell can be calculated. The main advantage is that analysis of time-resolved measurements does not require any *a priori* assumptions about the acoustic properties of the specimen. However, in most cases observing cells in culture the signals are so close together that they are not adequately separated to follow the procedure outlined above. In addition, the very long times of image acquisition (more than 1 min) often are prohibitory for the investigation of living cells (see Section 12.6.2).

12.5.3 The Interference Fringe Contrast Method

A biological sample on a slide or petri dish functions as a thin layer on a solid substratum. Sound reflected from the surface of such a sample may interfere with sound waves reflected from the surface of the supporting material (i.e., glass or plastic). The amplitude of the sound wave reflected from the solid can be used as a constant reference. As a result, the modulation of the amplitude of the wave resulting from interference is due to the properties of the specimen only. Contrast (the amplitude difference between constructive and destructive interferences) is related to the impedance differences at the reflecting interface of the biological sample, while mean brightness of the resulting image (calculated from the sum of maxima and minima of the amplitudes) is related to attenuation in the specimen. This relationship was described first by Hildebrand and Rugar (1984; Hildebrand et al., 1981), and then formulated mathematically and used for quantitation of longitudinal sound velocity and attenuation by Litniewski and Bereiter-Hahn (1990).

The approximate cell shape (topography) is immediately obvious from the pattern of interference fringes seen in SAM images. When applied to cells growing on a flat, solid substratum, these interference fringes delineate zones of equal acoustical path lengths between the reflecting boundaries cell/culture medium and cell/substratum (Figure 12.1). Local variations in c_P would shift the position of an interference fringe as well. Their pattern is only a first approximation to surface topography that is convolved by sound velocity.

The big advantage of this method is its speed. A single amplitude image of a specimen is sufficient to calculate local sound velocity in fringe minima and maxima to give an estimation of elasticity. However, the method has several shortcomings and requires assumptions that may not always be sufficiently reliable:

- Lateral resolution is limited by the distance between adjacent maxima and minima of interferences, and mechanical properties must be assumed to be constant over this space.
- Reliable measurements require a solid substratum with relatively high impedance (i.e., glass), and the overall contrast of these images is low.
- The method works well on the assumption of normal incidence of the sound waves (see above), and an optimal lens position is about five to seven wavelengths above the reflecting surface of the specimen.
- The procedure is limited to those areas showing interferences, and the order of interferences must be determined properly.
- The density of the cytoplasm is assumed to be constant at an estimated level. This assumption will be fulfilled in most cases.

Because of these shortcomings, this method primarily was used to follow dynamic events when changes of mechanical parameters are more important than their absolute values. Qualitatively the local dynamics of elasticity are easily visualized by Sobel-filtering of the primary images taken at z-values a few wavelengths above the specimen. Sobel-filtering reveals the steepness of gray-level changes in between constructive and destructive interferences and visualizes contrast. As a first approximation this filtering can be used to show the dynamics of elasticity distribution and is well suited for comparative observations of force distributions (Figure 12.3) in migrating cells

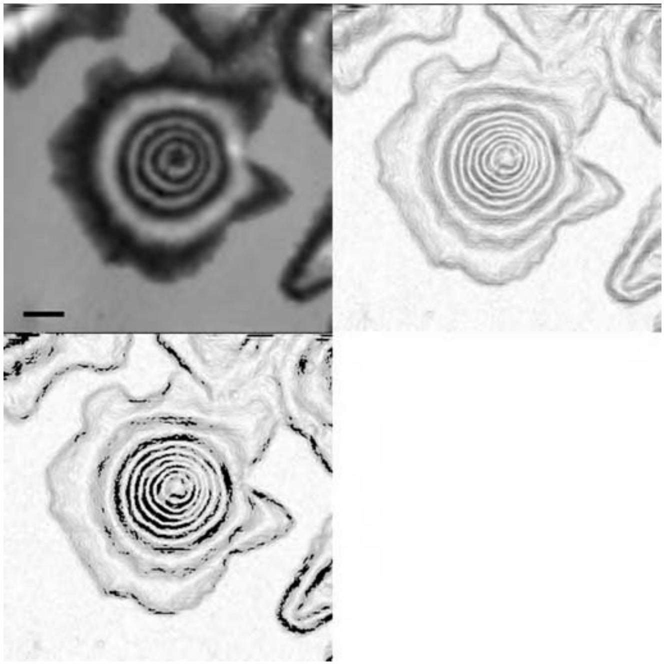

FIGURE 12.3
Example for the formation of the first derivation (Sobel Filtering) of the SAM image of a cell in culture (upper left image). In the Sobel filtered image (upper-right image), twice the number of concentric rings appears because the rings represent the gray-level changes from dark to bright and from bright to dark as well. By inversion of the Sobel filtered image, zones with high contrast appear dark, while those with low contrast (small change of image brightness from one pixel to the next) appear gray to white. Image processing allows to mark (e.g., areas with particularly high contrast) (lower image). Bar in this and following micrographs corresponds to 10 μm.

(Bereiter-Hahn and Lüers, 1998; Lüers et al., 1992b) or in cells undergoing fast volume changes.

12.5.4 V(z) Methods

Rayleigh waves result from a total conversion of a longitudinal wave into a surface wave at certain angles of incidence. They then leak back into the coupling fluid and the lens, causing intensity variations of the signal (V) with the distance (z) of this lens to the reflecting surface while moving the focus beyond this surface. A characteristic relationship results that is described as the V(z) curve. For soft tissues this procedure does not make sense because of the lack of Rayleigh waves in fluids and soft materials. However, the V(z) characteristics of a solid with a plane surface are modulated by overlying a thin layer of cytoplasm. The theory of this model has been developed independently (Bianco et al., 1992; Chubachi et al., 1991; Yu

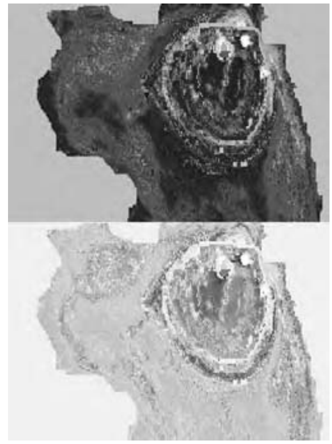

FIGURE 12.4
Endothelial cell derived from *Xenopus laevis* tadpole heart. Pattern of (a) elasticity (square of p-wave velocity) and (b) attenuation has been calculated from a series of six single pictures taken at different z-values (V(z) series). Dark areas in (a) show low sound velocity (1580 to 1620 m/sec), while bright areas show high sound velocity (>1700 m/s). Attenuation in (b) is low in the bright areas while it is high in the dark areas (ca. 3.5 times that of water). Diameter of the image: 100 μm. Size of the single pictures in the stack: 512 ×256 pixels.

and Boseck, 1992; Sathish et al., 1994; Kundu et al., 1991). For the first time this method allowed mapping of elasticity (sound velocity) and attenuation over a cell with full resolution of the SAM (Bereiter-Hahn et al., 1992; Bereiter-Hahn and Wagner, 2001) (Figure 12.4).

The main advantages of this method are:

- It is based on a well-developed theory.
- It is widely used in materials sciences.
- It offers high lateral resolution.
- It allows for the analysis of thin cytoplasmic layers (Figure 12.4).

All the parameters (local thickness, longitudinal sound velocity, attenuation, density, and thickness of a thin fluid layer in between the biological material and the solid support) can be calculated separately; only bounds for these values are required to allow the simplex algorithm to converge to the correct set of values (Kundu et al., 1991). A variety of substrata can be used to mount the specimen, and no interferences are required for the calculations.

The main disadvantages are the long acquisition time (at least one image more than the number of unknown parameters must be acquired) and the dependence on substrate properties, which must give clear V(z) curves, (i.e., support the development of Rayleigh waves).

12.5.5 V(f) Methods

The variation of frequency has been used in light interference microscopy for the determinations of the two unknowns thickness and refractive index (Beck and Bereiter-Hahn, 1981). A similar procedure can be applied in SAM (Kundu et al., 2000). Using a phase and amplitude sensitive modulation of an SAM (Hilmann et al. 1994, Grill et al., 1996; Pluta and Grill, 2002), longitudinal wave speed, attenuation, and thickness profile in a cell or tissue section are

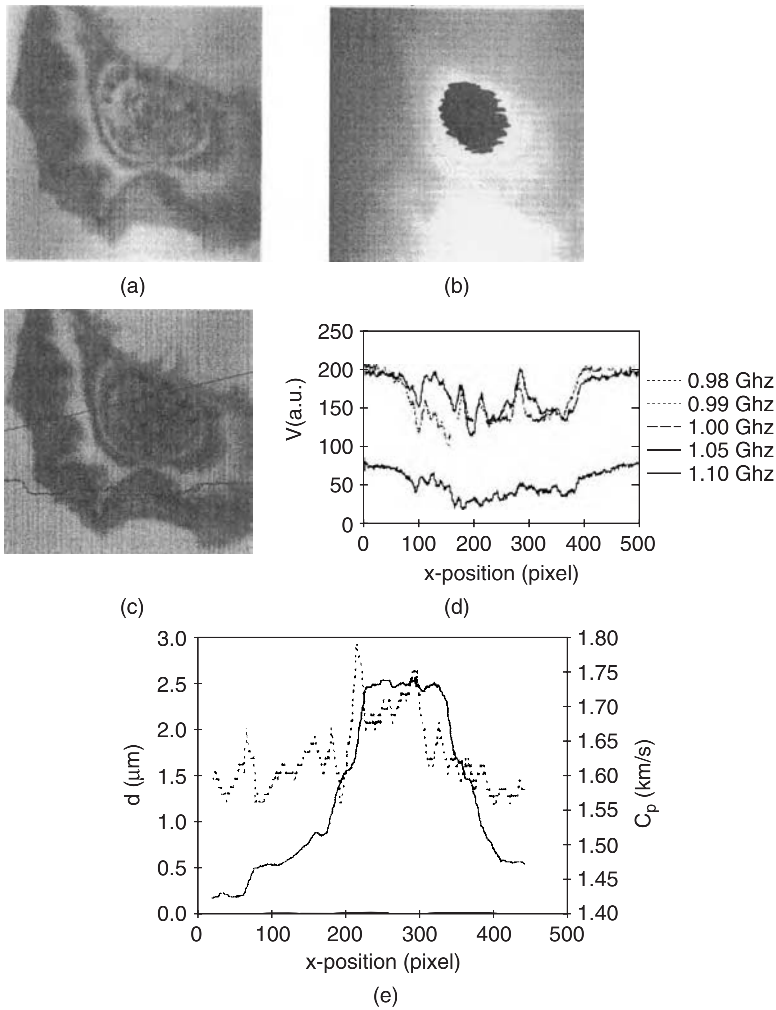

FIGURE 12.5
Endothelial cell in culture: (a) amplitude image; (b) phase image taken at 0.98 GHz; (c) course of a line through the image along which the amplitude and phase values are measured at different frequencies; (d) resulting distributions of amplitude along the measurement line; (e) sound velocities (full line) and thickness (broken line) calculated from the frequency-dependent amplitudes shown in (d).

obtained from the voltage vs. frequency or V(f) curves. Acquiring a series of pictures in the range from 980 to 1100 MHz with an increment of 20 MHz allows the experimental generation of V(f) curves for each pixel by simply changing the signal frequency, while keeping the lens-specimen distance constant (Figure 12.5). Both amplitude and phase values of the V(f) curves are used for obtaining the cell properties and the cell thickness profile. Both the cell thickness and its longitudinal wave speed can be estimated from the phase values and the order of the interference ring corresponding to a pixel.

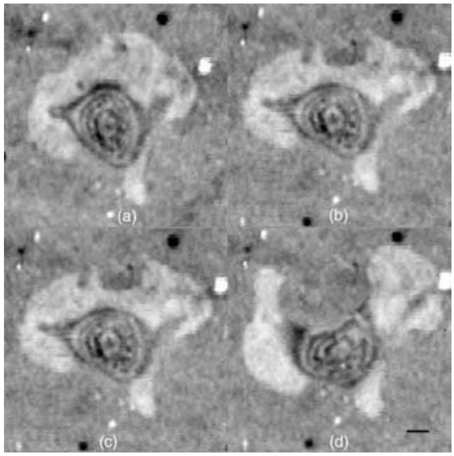

FIGURE 12.6
Shape changes of an endothelial cells growing on silicon rubber induced by a 15% uniaxial stretch. (a) control condition; (b) 5 min after onset of stretch; (c) 20 min in stretched condition; (d) 60 min in stretched condition. Cells extend lamellae in the direction of the applied stretch.

The theoretical analysis shows that the thin liquid layer between the cell and the substrate has a strong effect on the reflection coefficient and should not be ignored during the analysis. Cell properties, cell profile, and the thickness of the thin liquid layer are then calculated from the V(f) curves again using e.g., the simplex inversion algorithm.

The main advantages of this method are:

- Imaging can be done near the focal plane, achieving an optimal signal-to-noise ratio.
- No interference with Rayleigh waves occurs (focus at $z = 0$).
- The method is independent from the properties of the solid substratum on which the cells are growing.

This method allowed us to monitor by SAM the reaction of cells to mechanical stretch (Figure 12.6) (Karl and Bereiter-Hahn, 1999).

12.5.6 Phase and Amplitude Imaging

A few attempts have been made to take advantage of the information contained in a reflected acoustic wave — the phase shift relative to a reference and its amplitude (Hillmann et al., 1994; Khuri Jakub et al., 1988; Grill et al., 1996). The probe-dependent phase shift of the signal can be achieved by comparing it with a reference derived from the sending oscillator. This multiplication is technically realized with a mixer followed by a low pass filter.

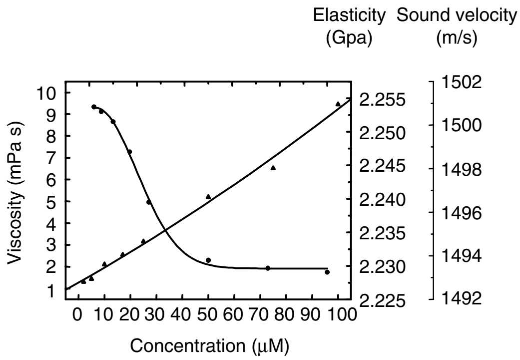

FIGURE 12.7
Concentration dependence of viscoelasticity of skeletal actin after having completed polymerization. Viscosity = •, Elasticity and sound velocity = ▲. Sound velocities of F-actin (monitored at 25°C). One symbol represents the mean of 2-5 different measurements. (From Wagner et al., *Biophys. J.*, 76, 2784, 1999. With permission.)

Then the phase shift and the amplitude resulting from interaction with the specimen can be calculated (Hillmann et al., 1994; Grill et al., 1996). The phase shift corresponds to acoustical path lengths, while the amplitude shows attenuation of sound. This is of particular interest for the investigation of specimens with a large topographical surface modulation. In such specimens (e.g., the surface of a leaf with stomatal cells) the surface topography is represented by a series of lines similar to interference fringes. In the case of phase imaging these lines result from the type of representation: A phase shift from 0° to 360° may be represented by a gray-level scale ranging from white to black, and thus every 360° phase shift induce a new start of the grayscale. This broadens the application of SAM to objects with topographical modulations in the range of up to 10 times the wavelength of the longitudinal sound wave (Figure 12.7 in Bereiter-Hahn, 1995; Pluta and Grill, 2002).

In the case of cells on a solid substratum, the amplitude image is still dominated by interferences that can be treated as normal interference images (see Section 12.5.3). However, additional information is provided by the phase image that can be used for simple calculation of cell mechanical parameters, longitudinal sound velocity, attenuation, and thickness when spatial resolution can be reduced to the distances between the minima and maxima of the interferences. In the minima of the interference fringes (dark lines) of the order m_d, the thickness (d) of the specimen is

$$d = \frac{m_d \times c_{pc}}{4f} \qquad \textbf{(12.3)}$$

when f is the frequency of the sound, c_{pc} is the longitudinal sound velocity in the specimen, and c_{ps} is the sound velocity in the surrounding fluid. In the first-order dark (the phase difference is half wavelength), this corresponds to a thickness of a quarter wavelength because in the reflection mode the sound wave travels the specimen twice.

From this c_{pc} can be calculated by

$$c_{pc} = \frac{4d \times f}{m_d} \tag{12.4}$$

The phase difference (φ) imposed to the sound wave after passing through the specimen depends on the acoustical path length (thickness times impedance) and can be written as follows:

$$\Phi = \frac{d}{m_d\left(\frac{c_{pc}}{f} - \frac{c_{ps}}{f}\right)}$$

$$\Phi = \frac{d \times f}{m_d(c_{pc} - c_{ps})} \tag{12.5}$$

Combining Equation 12.3 and Equation 12.5 results in

$$c_{pc} = \frac{c_{pf}}{\left(1 - \frac{1}{4\Phi}\right)} \tag{12.6}$$

Because values are obtained at the minima and maxima of interferences only, the intermediate zones are approached by interpolations. This limitation in lateral resolution can be overcome by a combination of V(f) with amplitude and phase acquisition. Variation of frequency shifts the interference fringes. If this shift covers a range of π, the distance between a constructive to a destructive interference, then for all points in a cell a set of minima and maxima of interference fringes is generated that can be used for calculations according to Equations 12.3 through 12.6.

12.6 Biological Significance of Acoustic Parameters of Cells

Cell biologists are used to estimating structural and chemical parameters as significant for the characterization of cells, their physiological state, and functional activities. Acoustic microscopy finally reveals the mechanical parameters elasticity and attenuation in addition to thickness and density. These features are more difficult to include into the prevalent type of cell biology. Mechanical parameters are important in all those processes that are directly related to mechanical interactions as are movements and reinforcement of a cell, tissue, or organism by tensile elements (e.g., Lüers et al., 1992b; Bereiter-Hahn et al., 1995; Bereiter-Hahn and Lüers, 1998). In addition, mechanosensing recently has been regarded a general phenomenon involved in proliferation control and differentiation (Ingber et al., 1995; Wang et al., 1995; Weaver et al., 1997) and a crucial factor in embryogenesis: Beloussov (1998; Beloussov et al., 1994, 1997) emphasized the role of morphomechanical fields acting in concert with morphogenetic fields. Local and generalized mechanical stimulation may induce a cascade of signal transduction events comparable to those induced by receptor-ligand binding. Generally accepted is the concept of integrin mediated mechanosensing (Ingber et al., 1995). The mechanism has not been fully elucidated until now.

Another example for the physiological significance of elasticity is volume control. Anisotonic media induce swelling or shrinking that can be reversed within 3 to 40 min in many cells. The cells control their volume to a certain set value. Acoustic microscopy is well suited to determine the volume of adhering cells (Hegner and Bereiter-Hahn, 1993), and it revealed that the size of cell volume is coded in the tension at the cell cortex (Bereiter-Hahn and Yastas, 1995), influencing mechanosensitive ion channels. Evidence for biochemical and structural consequences of mechanical stimulation and of the mechanical properties of cells is increasing.

A field that has been totally neglected in acousto-microscope research is plant cell biology, although the role of elasticity and swelling forces for plant cell growth are well established and several groups are working in biomechanics of plants. Because of this lack of investigations, the next section will be restricted to the situation in animal cells (in culture).

12.6.1 Interpretation of SAM Images of Cells in Culture

Before interpreting the biological significance of the parameters determined by SAM, determining which of the main components of the cytoskeleton affects sound velocity in the cytoplasm and the modulus of elasticity is important. In addition, the structural basis of sound attenuation must be identified. Both these questions can be approached experimentally.

Cellular elasticity depends highly on the strain rate; in slow deformation processes viscous creep may become prominent. In the SAM operated in the megahertz or gigahertz range, the probes are exposed to an extremely high strain rate together with an extremely small deformation (in the nm range). Impedance values reflect exclusively elastic stiffness, and the viscous properties of cytoplasm may only be reflected by the attenuation of ultrasound.

12.6.1.1 Impedance and Cell Elasticity

Intracellular sound velocity and reflectivity of a cell boundary are closely related. The reflectivity coefficient is determined by the impedance differences at the boundary. Basic assumptions on the physical state of cytoplasm, meaning that it has to be treated as a visco-elastic fluid including a quasi solid, fibrous (or porous) matrix filled with fluid, guide the interpretation that bulk modulus (K) determines the longitudinal sound velocity according to

$$c_{pc}^2 = \frac{(K + 4/3\mu)}{\rho} \tag{12.7}$$

Because of the small value of the shear modulus μ in cells, the equation can be simplified to

$$c_{pc}^2 = \frac{K}{\rho} \tag{12.8}$$

where c_c is the longitudinal sound velocity in cytoplasm, K is the bulk modulus, μ is the shear modulus, and ρ is the density.

Physiological interpretation of data derived from SAM measurements requires some further considerations. In the case of cells or tissues in an aqueous medium, the sound velocity derived for the sample includes the sound velocity of the aqueous medium and the proteinaceous content. The latter contribution is the one of physiological interest. It can be evaluated only when an assumption is made on the volume fractions of the protein (p) and the fluid space (q) of a cell:

$$p + q = 1 \tag{12.9}$$

where p and q are a measure of the relative path a sound wave travels through a specimen. The time-of-flight (t) is

$$t = \frac{d}{c_p} = \frac{p \times d}{c_{ps}} + \frac{q \times d}{c_{pr}} \tag{12.10}$$

where d is the geometrical thickness of the specimen, c_{ps} is the longitudinal sound speed in the saline, c_{pr} is the protein fraction of cytoplasm, and c_p is the resulting speed of sound through the specimen (measured speed).

From Equation 12.10 follows

$$c_{pr} = \frac{q \times d}{\left(\frac{1}{c_p} - \frac{p \times d}{c_{ps}}\right)} \tag{12.11}$$

TABLE 12.2

Relation of the Sound Velocity Determined for a Compound Material (cell: C_p) to the Sound Velocity in the Protein Fraction (C_{Pr}) and the Resulting Compression Modulus of the Protein (K_{pr})

C_p	C_{Pr}	K_{pr} (MPa)
1600	1837	3.37
1650	2224	4.95
1700	2774	7.69
1750	3617	13.08
1800	5073	25.73
1850	8193	67.12

The sound velocities (c_{pr}) and the corresponding elasticity values of the protein fraction according to Equation 12.11 have been summarized in Table 12.2. In this case, c_{ps} (longitudinal sound speed in the fluid phase in a cell) has been assumed to be 1550 m/sec at 30°C.

The values in Table 12.2 represent elasticity of the pure protein, not that of a living cell. A range of a few megapascals is reasonable, because Holwill and Satir (1987) mention 5 MPa as the Young's modulus for axonemal microtubules. The Poisson ratio (ν) relates Young´s modulus (E) to bulk modulus (K) by

$$E = 3K(1 - 2\nu) \qquad \textbf{(12.12)}$$

Mechanical properties of cells highly depend on the tension of F-actin (see below). The Poission ratio determined for this cytoskeletal element opens the possibility to relate cytoplasmic compressibility to its modulus of elasticity (Young's modulus). Schmidt et al. (1996) determined a Poission ratio of 0.33. As a result, the scalar values of bulk modulus and Young's modulus in cytoplasm will be almost equal.

In living cells locally more than 1800 m/sec have been measured (Bereiter-Hahn, 1995; Lüers et al., 1992a) corresponding to very high elasticity moduli that cannot be explained on the basis of protein properties only. The reason is because the increase of protein concentration alone may reduce sound velocity in cytogels rather than increasing it (Wagner et al., 1999; Bereiter-Hahn and Wagner, 2001). Also, the polymerization status would not be sufficient to explain these values (Wagner et al., 1999). In addition, the high sound velocities measured in living cells by far exceed those determined for a variety of tissues that in general are in the range of 1650 m/sec. A set of experiments described below reveals tension in the cytoskeletal fibrils of cells in culture, particularly the actin fibrillar system, as the reason for high elasticity.

12.6.1.1.1 Experiment 1

Treating cells with cytochalasin D, a drug that severs specifically actin fibrils suddenly (within 1 or 2 min) reduces sound velocity and thus elasticity

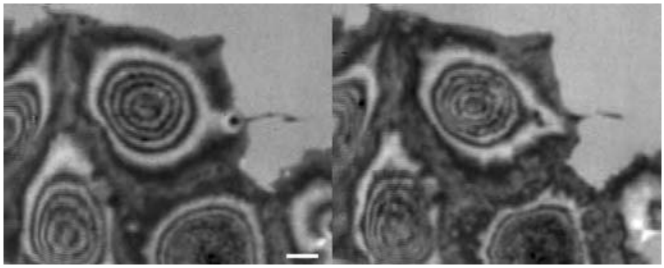

FIGURE 12.8
Human keratinocytes (HaCaT) in culture as seen with the SAM (1.0 GHz). Left panel: control condition. Right panel: 15 min after addition of 0.5 μg/ml cytochalasin D. Loss of contrast is obvious; some of the interference fringes move toward the cell periphery indicating a small volume increase.

FIGURE 12.9
Single endothelial cells being shortly exposed to cytochalasin D (2 min, 2 μg/ml). The bundles of actin fibrils have been stained with TRITC-phalloidin and therefore became visible. Because of the action of the cytochalasin D, many actin fibrils are ruptured and large gaps appear in between them. This is accompanied by a loss of stiffness of the cytoplasm indicated by the loss of contrast shown in Figure 12.8.

(Bereiter-Hahn, 1987). Qualitatively this can be seen in a loss of contrast (Figure 12.8a, b), but quantitatively the loss is largest in the cell periphery where in general high sound velocities are measured because of the existence of thick actin bundles (Figure 12.9) and less in the cell center, which has a very low sound velocity under control conditions. The structural basis of this loss of elasticity is revealed by fluorescence microscopy of F-actin stained with TRITC-phalloidin (Figure 12.9). Immediately after addition of the drug, actin fibrils start rupturing and tension from the whole fibrillar system that was previously built up by actin and myosin interaction.

12.6.1.1.2 Experiment 2

Cytoplasmic calcium ion concentration can be increased by exposing the cells to a Ca^{2+} ionphore, ionomycin (Lüers et al., 1992a). This treatment first activates myosin light chain kinase and then activates actin-myosin–based contractions, followed by the disassembly of most of the actin fibrils and of microtubules. Such a treatment immediately increases sound velocity (due to contractions), which then is followed by a marked decrease in parallel to the disassembly of the filaments.

12.6.1.1.3 Experiment 3

The third type of experiment has primarily been undertaken to distinguish the contribution of microtubules from that of the actin fibrils on sound velocity. Such a separation is not possible because of the close structural interactions of both these types of fibrils and because of cross-control in signal transduction pathways. Disassembly of microtubules by colchicin or by nocodazole also results in the activation of myosin light chain kinase, stimulating actin-myosin–based contractions (Kolodney and Elson, 1995). Consequently, sound velocity increases up to maximum values until the cytoplasm ruptures (Karl and Bereiter-Hahn, 1998).

In all three cases the protein content of the cells remains constant, with the limitation that in the very beginning of the cytochalasin D treatment the cells slightly swell. It cannot be the protein content that is responsible for the high sound velocity; it is the tension in the fibrillar system.

12.6.1.2 Membrane-Bound Organelles

As mentioned above, c_{pc} may vary along the acoustical path inside a cell as a consequence of a variety of interfaces of the cytoplasm with membranous organelles, the endoplasmic reticulum, mitochondria, and the nucleus. In addition, distribution of tension forces in the cytoskeleton varies on a subcellular level. Major vesicles either filled with fluid or lipids are easily discernable in SAM images (Figure 12.11). No hints for the demonstration of cisternae of the endoplasmic reticulum have been found until now, and mitochondria can be seen only occasionally. At 1 GHz this may be attributed to the low resolution, but at higher frequencies (e.g., 1.3 to 1.5 GHz) resolution is sufficient to resolve these organelles. Their invisibility primarily seems to result from their intimate integration into the cytoplasmic matrix; no sound reflecting interfaces will be formed.

This interpretation is supported by observing cell death while viewing with a SAM. (Hoppe and Bereiter-Hahn, 1985). Mitochondria were invisible as long as the cells were alive and immediately became visible when the cytoplasm changed its consistency on cell death. Nucleus and cytoplasmic matrix do not match mechanically. Although no special measurements of the mechanical properties of nuclei have been performed, an impedance higher than the rest of the cytoplasm can be deduced from the cytochalasin D experiments: Reducing cytoplasmic elasticity by severing actin fibrils with this drug renders the nuclei more clearly visible than they were before. In cells with a high nuclear volume fraction, the high mechanical stiffness of the nuclei may significantly influence the sonographic appearance of the tissue.

12.6.1.3 Attenuation and Cytoplasmic Structure

Attenuation (S) of sound in a fluid occurs by scattering, diffraction, and absorption. The first two parameters are based on inhomogenities of the fluid. The latter is more complex and is based on viscosity (S_{vis}) and thermal conductivity (thermal relaxation) (S_{th})

$$S_{vis} = \frac{8\pi^3 \times \eta}{3\rho \times c_p^3} \tag{12.13}$$

where η is the viscosity, ρ the density, and c_p the sound velocity (Cracknell, 1980).

In fluids, S_{th} can be neglected (Cracknell, 1980); only S_{vis} will be discussed. S_{vis} inversely goes with the third power of the ultrasound velocity. This parameter can be assumed to determine attenuation, and the distribution of relative attenuation should follow that of sound velocity. No conclusive evidence of a change in attenuation with frequency was found, but all workers agreed that ultrasound absorption was often much greater than that to be expected from viscosity according to Stokes' formula (Equation 12.13). In some liquids the observed attenuation was 100 times that calculated. Many attempts have been made to explain this anomaly for liquids. Long ago, the experimental results of Pinkerton (1949) suggest that the absorption in associated liquids is due to a different mechanism from that in nonassociated liquids. In the latter, the absorption is probably due to a slow exchange of energy between different degrees of freedom.

The same problem applies to cytoplasm. Indeed, in most cellular regions the relative course of attenuation is just inverse that of sound velocity (high sound velocity corresponds with low attenuation and vice versa; see Figure 12.4), but this is not always the case. A more detailed understanding of this parameter is required. Model experiments have been undertaken with a variety of cytogels combining structural data as revealed by electron microscopy with those gained from an oscillating rod rheometer (ORR) (Wagner et al., 1999). This instrument synchronously shows sound velocity, viscosity, and sound attenuation of a liquid sample (see the appendix). In separated cytoskeletal protein solutions (cytogels), the influence of polymerization, cross-linking of fibrils, and associations of the monomers or the filaments with other proteins can easily be assessed, and the ORR shows the altering mechanical properties. These investigations provided important insights for the interpretation of SAM images of living and chemically fixed cells. In the case of sound attenuation of actin gels, it revealed that attenuation does not follow the course of viscosity during polymerization (Figure 12.10) and in cytochalasin D-exposed F-actin (Wagner et al., 2001). The main source for increasing attenuation is the formation of higher order structures (e.g., bundling of filaments). The increase in attenuation during actin polymerization occurs at the end of polymerization when plenty of filaments have been formed and start to assemble laterally. The reason for attenuation increase can be seen in increased scattering at these higher order structures.

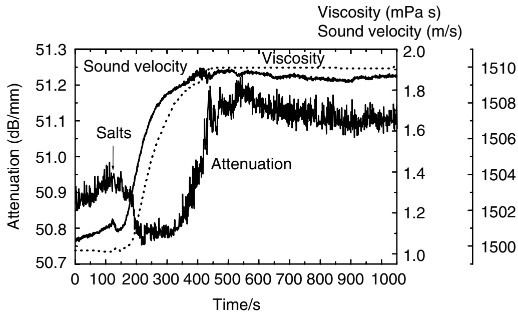

FIGURE 12.10
Time course of attenuation and sound velocity upon polymerization of 10 μM non-muscle actin, as measured synchronously with the ORR. The prominent increase of sound velocity during the lag phase of viscosity reflects assembly of G-actin to aggregates (primer formation) with solid-like properties. Simultaneously attenuation decreases notably. During most of the elongation phase attenuation remains constant, but rises strongly prior to the viscosity maximum. The time course of attenuation was highly reproducible and reflects a typical measurement. Arrows indicate the addition of polymerization buffer (2 mM $MgCl_2$, 50 mM KCl). Each point of the lines represents one measurement. Repetition rate of the measurements: 1 Hz. (From Wagner et al., *Biochem. J.*, 355, 771, 2001. With permission.)

12.6.2 Acquisition Time: A Parameter Relevant for the Investigation of Living Cells (SubSAM)

At least five images have to be taken to allow the evaluation of a V(z) or V(f) series. By definition, the sample must remain constant during the time required for image acquisition which was about 40 sec for the V(z) series (Kundu et al., 1992) and has now been reduced to 25 sec for a V(f) series (Kundu et al., 2000). Cells are dynamic as long as they are alive. As a consequence, fast-moving cells cannot be analyzed using V(z)- or V(f)-based evaluation methods. Cells that remain stationary on the scale for a few minutes might undergo shape changes or show surface movements. Therefore we analyzed the overall cytoplasmic motility of nonlocomoting cells (i.e., keeping a constant position for at least several minutes) in culture. This is performed by subtracting two subsequent images taken at a certain time interval (SubSAM) (Figure 12.11). The differences were very small in most of the cultures, but led to the detection of clearly outlined domains of cytoplasmic motility (Figure 12.11) (Vesely et al., 1994).

These activities depended on cell density in those cultures that show contact mediated control of locomotion and proliferation (Zoller et al., 1997). The motile activity measured by SubSAM correlates well with the invasive potential of rat sarcoma cells and seems to be mediated by rac-activation (Zoller et al., 1997; Karl and Vesely, personal communication). Because the motility domains become visible through the subtraction of interference images (sound waves reflected from the medium facing surface interfere with those reflected from the substratum), surface topography changes down to about 15 nm are

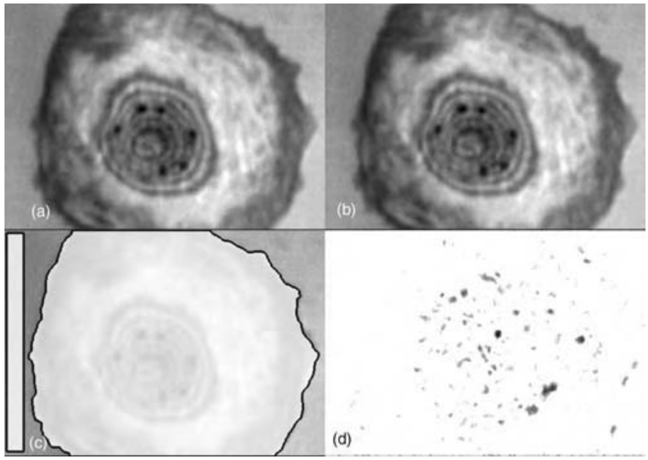

FIGURE 12.11
Principle of SubSAM. Two pictures from a single cell have been taken at 10-sec interval (a,b). The absolute difference (skalar of gray-level difference) between each corresponding pixel is shown in (d), but the log value of the differences is given to enhance visibility. For calculation of the *M* value, the differences are determined in two regions of interest: the cell area and a reference area in the background (c).

revealed. The brightness at a given point in a cell image results from interference of sound reflected from the substratum and from the cell surface. If small thickness changes take place, this is revealed by these interference phenomena. Using electronic image processing and analysis interferometry goes down to 1/200 of the wavelength, which then can be calculated from the difference images. The acoustic wavelength reflected at the cell/substratum interface passes the cytoplasm twice; about 1/400 of the wavelength of the p-wave can be detected, corresponding to a theoretical value of 3 to 4 nm (wavelength at 1 GHz: < 1500 nm). Because of background noise this full sensitivity cannot be reached taking nonaveraged, single images only. The final sensitivity is estimated to about 15 nm.

12.6.2.1 Quantitation of Motility by SubSAM

This topographical type of motility has been quantitated to be used for a more sophisticated cell motility analysis, introducing a motility factor *M* (Zoller et al., 1997). Images were taken at a time interval of 5 sec, 8 images for 1 series (Figure 12.11). Subsequent images were then subtracted from each other pixel by pixel, and the results were taken as absolute values. For better contrast, logarithmic scaling was applied twice and gray levels were inverted (Figure 12.9d). The area covered by the cell was outlined (Figure 12.9c), the area determined and the *M* value for the gray level changes (Figure 12.11) was calculated (see below). A virtual *M*-value resulting from background noise was calculated separately for each image and subtracted from the value of the corresponding cell. In images of confluent cultures, calculation of the background was not possible. In these cases, a mean background M value was calculated from other images of that series and subtracted. A principal difficulty lies in the fact that the difference values not only depend on the motility of a cell, but also on the contrast of an image. At low contrast the gray-level difference can never reach those of high contrast images. Motility is therefore represented by the median of the gray-level distribution curve of the SubSAM images and its variation. Following the principles of variance calculations in Gaussian distributions, variance (d^2) is calculated, which gives a measure for the frequency of gray level changes, as well as the dynamic range of the gray-level distribution.

$$d^2 = \sum_{i=0}^{255} (x_i - \bar{x})^2 \times \frac{f(x_i)}{A} \quad \textbf{(12.14)}$$

where x_i is the gray level in each pixel and x is the median of the gray level distribution curve, f is the frequency of the category (gray level), and A is the area of measurements in pixels. The d^2 value referring to the background ($d^2{}_{ref}$) was calculated in the same way. For motility measurements and background measurements the variation values and medians were added; both terms were then subtracted from each other according to the following:

$$M = x_{cell} \times d_{cell}^2 - x_{ref} \times d_{ref}^2 \quad \textbf{(12.15)}$$

12.7 Correlative Microscopy: Combining SAM with Optical Microscopy

A single parameter in most cases is not sufficient to characterize a cell's state and behavior. This is particularly true in cytomechanics. The mechanical properties result from the interaction of a large number of molecules tied together by very sophisticated and interacting control circuits involving receptors, ion channels, and other membrane-bound proteins, transducing information from the environment to the cytoskeleton and to the genome. The combination of SAM with light microscopic methods is indispensable (see also Chapter 14). On this basis the structures have been identified that determine the acoustic properties of cells (Lüers et al. 1992b). Investigation of the same cell with SAM and with reflection interference microscopy proved the coincidence of thickness measurements performed by these two independent methods (Bereiter-Hahn, 1997). If combined with micro-interferometry (e.g., with a Mach-Zehnder type interference microscope), precise tissue characterization will result (Bereiter-Hahn and Buhles, 1987).

Most of these comparative investigations have been conducted by retrieving cells with one microscope system after investigation with the other one.

FIGURE 12.12
Combination of an acoustic microscope (EL-SAM) with a fluorescence microscope (Leica DMB) equipped with a CCD camera. The acoustic lens can be seen in the center of the image.

The integration of SAM with the broad range of light microscopic methods is not easy with the commercially available instruments. Kanngiesser and Anliker (1991) produced a lab version of such an integrated system on the basis of a Zeiss inverted microscope.

More recently, in research from both the author's laboratory and Lemor et al. (in preparation) a SAM has been coassembled with an inverted fluorescence microscope (Figure 12.12) to allow for comparative fluorescence and SAM studies (Figure 12.13). This technique allows, for instance, for a comparison of release of calcium ions into the cytosol and the concomitant contractile events. The difficulties using a commercially available SAM lie in the small distance between the stage and the lens of the acoustic microscope, which is too small to insert a research-type inverted microscope. Therefore we use a DMB Leica laboratory microscope instead.

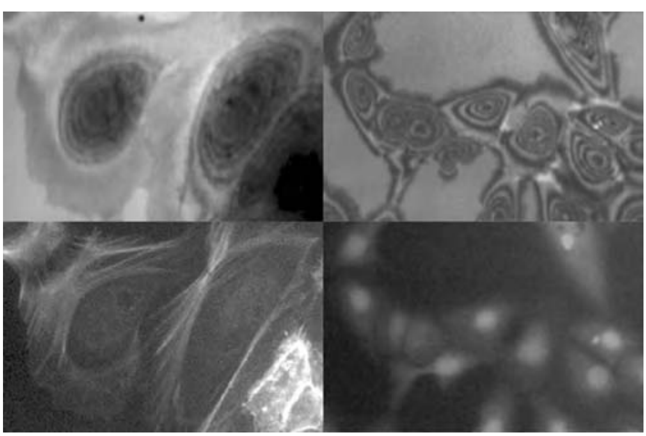

FIGURE 12.13
Examples for correlative microscopy including SAM. Image pair on the left: distribution of actin fibrils made visible with TRITC-phalloidin; pair on the right: cytosolic calcium visualized by fluorescence of cells stained with calcium green 1; upper row: SAM images; lower row: corresponding fluorescence images.

12.8 Conclusions

SAM has reached a state of development that allows routine investigations of biological samples (isolated cells, tissue sections, and tissue blocks). Specimens with large surface topographic variations may be reconstructed from focus series and phase sensitive imaging. The evaluation of V(z) and V(f), when combined with phase-sensitive imaging, provides a convenient key to subcellular distribution of elasticity, structure, and motility.

Acknowledgments

Funding by the Vereinigung der Freunde und Förderer der Johann Wolfgang Goethe-Universitat is gratefully acknowledged. Our work has continuously been supported by the Deutsche Forschungsgemeinschaft under the "Schwerpunkt: Neue mikroskopische Techniken für Biologie und Medizin."

Appendix

The Oscillating Rod Rheometer

The ORR has first been described by Kojro et al. (1996) and then was applied first to cytogels by Wagner and Bereiter-Hahn (1996) and Wagner et al. (1999). It allows for synchronous determination of sound velocity, dynamic viscosity, and sound attenuation. This was a prerequisite to collect data on cytogels that then formed the basis for the interpretation of the mechanical properties of living cells as revealed by acoustic microscopy. Because cytogels show non-Newtonian behavior, the measurements had to impose an impact as small as possible to the gels, or they would be destroyed or behave differently. Extreme care was taken to use minimal strain for the measurements.

Description of the ORR

A glass fiber rod (diameter ≈ 50 μm, length ≈ 2 mm) is immersed in the fluid probe and is stimulated to transversal oscillations (about 1 to 4 kHz, depending on the viscosity of the fluid and the length of the fiber) via a piezomechanical bimorph actuator (Figure 12.14). The resonance frequency of the rod oscillation is, among others (e.g., the density of the specimen), a function of the viscosity of the surrounding fluid. The extremely small displacements (≥ 1> 100 nm) of the rod are monitored by an acoustic microscope with phase-sensitive detection (Grill et al., 1996; Hillmann et al., 1994). High-frequency

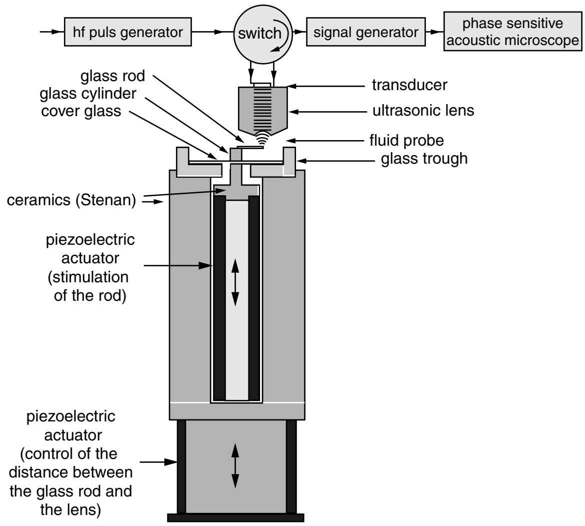

FIGURE 12.14
Principle of the ORR. For description see Section 12.6.1.3 and the appendix. (From Wagner et al., *Biophys. J.*, 76, 2784, 1999. With permission.)

pulses (1 GHz) are converted by a transducer into longitudinal acoustic waves, coupling into a sapphire, and focused onto the free tip of the glass fiber. A circulating switch directs the high-frequency pulses either to the acoustic lens or the detected signal to amplification and filtering components. A Boxcar-Integrator averages the received ultrasound pulses and filters undesirable interfering signals (e.g., lens echoes).

The oscillation frequency of the rod is held at its resonance frequency via a feedback control: the phase of the rod oscillation is permanently compared with the phase of the piezo excitation frequency and is kept to a phase shift of $\pi/2$ by frequency adjustments. This function is accomplished by using a lock-in amplifier (model SR810, Stanford Research System Inc., Stanford, CA) that also feeds the mean of the resonance frequency during 1 sec into a PC.

Changes of the propagation speed of the longitudinal acoustic waves in the sample shift the phase difference between the reflected ultrasound wave and the generating 1 GHz electric oscillation (e.g., the detected ultrasound signal is delayed when the sound velocity decreases). This phase shift is compensated by regulating the distance between the acoustic lens and the free tip of the glass fiber via a second piezoelectric actuator (Figure 12.14). The voltage controlling this piezo actuator is a measure for the change of sound velocity, which is related to the volume elasticity of the probe (Equation 12.11 and Equation 12.12).

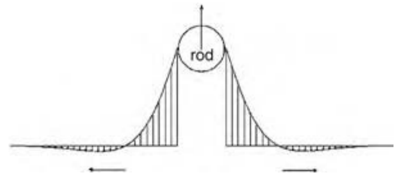

FIGURE 12.15
Diagram illustrating the mass drag effect and the shear wave generation by the oscillating rod in the ORR. (From Wagner et al., *Biophys. J.*, 76, 2784, 1999. With permission.)

*Calculation of the Viscosity**

The actual oscillation of the rod stimulated externally at the fixed end with an amplitude (A) and the frequency (ω_A) is determined by the sum of the inertia force, the friction force, and the resistance force.

The effective mass (M) of the rod and the friction constant (R) are given by

$$M = m_g + \rho(a + b\delta + c\delta^2) \quad \textbf{(12.16)}$$

$$R = \rho \times b' \times \delta \times \omega_A \quad \textbf{(12.17)}$$

where

$$\delta = \sqrt{\frac{2\eta}{\rho\omega}} \quad \textbf{(12.18)}$$

where is the penetration depth of the shear wave (Lamb, 1932; Landau and Lifshitz, 1987) in a liquid (Figure 12.14); η is the dynamic viscosity of the liquid; ρ is the density of the liquid; m_g is the mass of the rod (without adhering liquid); and a, b, b', and c are geometric constants.

It is obvious that the "oscillating mass" of the rod increases with the dimension of the induced viscous shear wave. This can be described as a mass drag effect (Figure 12.15).

The solution of the differential equation (Equation 12.1) is

$$x(t) = a(\omega) \times \cos(\omega t - \Phi(\omega)) \quad \textbf{(12.19)}$$

where $a(\omega)$ is the amplitude of the rod oscillations and $\varphi(\omega)$ is the phase shift between the excitation frequency and the frequency of the rod oscillation.

With Equation 12.1 and Equation 12.5 we obtain the phase law described by Kojro et al. (1996):

* Adapted from Kojro et al., 1996.

$$\frac{\left(\frac{\omega_0^2}{\omega_A^2}\right) - 1}{\rho} = \alpha + \left(\beta + \frac{\beta'}{\tan\varphi}\right)\delta + \gamma\delta^2 \tag{12.20}$$

where ω_0 is the resonance frequency of the rod in vacuum (approximate in air) and α, β, β', δ, and γ are constants of the apparatus.

Finally the dynamic viscosity η (in milliPascal seconds, where 1 milliPascal second is 0.01 poise = 1 cP) is given by the following:

$$\eta = \left(\frac{\left(\beta + \frac{\beta'}{\tan\varphi}\right)\sqrt{\frac{\omega_A \rho}{8}}}{\gamma} + \sqrt{\frac{\left(\beta + \frac{\beta'}{\tan\varphi}\right)^2 \omega_A \rho}{8\gamma^2} + \left(\frac{\omega_0{}^2}{\omega_A{}^2} - 1\right)\frac{\omega_A}{2\gamma} - \frac{\alpha\omega_A\rho}{2\gamma}} \right)^2 \tag{12.21}$$

The constants β, β', and are derived from the determinations of the resonance frequencies in water-glycerol mixtures (0%, 5%, 10%,…0%) of known viscosities determined with a commercial micro falling ball viscosimeter (HAAKE Mess-Technik GmbH u. Co., Karlsruhe, Germany).

Comparison of the ORR with Other Types of Rheometers

The main advantage of the ORR is the possibility for synchronous measurements of dynamic viscosity and sound velocity (equivalent to elasticity), as well as the extremely small strain and the ratio of the dimension of the sensor to the penetration depth of the viscosity shear wave. Because the amplitude of the moving glass rod is in the nanometer range and freely variable, interactions and properties of macromolecules can be determined nondestructively (Figure 12.16).

Measurements of viscoelastic properties of actin gels using minimum strain were also achieved by Zaner et al. (1981) and Sato et al. (1985) with cone-plate rheometers. However, the sample volume was some milliliters and — as for most rheometers — during the measurement, the device has to be closed. Because the ORR requires a few microliters only and it is an open system, the online addition of substances gives access to a broad range of experimental control.

The polymerization rate was considerably higher when measured using the ORR as compared with a falling ball viscosimeter. Since the ORR is not air sealed, evaporation may influence measurements. Because of the overall construction, evaporation from the specimen drop is very small. This is demonstrated by a change of less than 0.01 milliPascal seconds for the viscosity of actin buffer measured for 40 min.

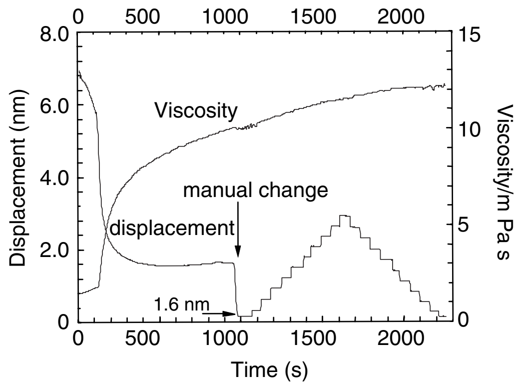

FIGURE 12.16
Time course of the polymerization of 5 μM of actin from skeletal muscle as calculated according to formula 13.20 based on the oscillation frequency of the oscillating rod. With increasing viscosity the oscillation amplitude of the rod decreases; it was then tuned via the piezo-electric actor to an amplitude of 1.6 nm and stepwise increased with an increment of 3 nm. Even at these very small amplitudes the viscosity curve remains continuous, showing that the measurement also at extremely small strains remained reliable. (From Wagner et al., *Biophys. J.*, 76, 2784, 1999. With permission.)

References

Beck, K. and Bereiter-Hahn, J., Evaluation of reflection interference contrast microscope images of living cells. *Micr. Acta.*, 84, 153, 1981.

Beloussov L., Bereiter-Hahn J., and Green P., Morphogenetic dynamics in tissues: expectations of developmental and cell biologists, in *Dynamics of Cell and Tissue Motion*, Alt, W., Deutsch, A., and Dunn, G., Eds., Birkhäuser, Zürich, 1997, p. 215.

Beloussov, L., Saveliev, S., Naumidi, I., and Novoselov, V., Mechanical stresses in embryonic tissues: patterns, morphogenetic role, and involvement in regulatory feedback, *Int. Rev. Cytol.*, 150, 1, 1994.

Beloussov, L.V., *The Dynamic Architecture of a Developing Organism*, Kluwer, Dordrecht, 1998, p. 238.

Bereiter-Hahn, J., Comparison of the scanning acoustomicroscopic appearance of culture cells with those obtained by reflection interference contrast and fluorescence microscopy, *Opt. Optoelctr. Sci. Eng.*, 809, 162, 1997.

Bereiter-Hahn, J., Probing biological cells and tissues with acoustic microscopy, *Adv. Acous. Microsc.*, 1, 79, 1995.

Bereiter-Hahn, J., Akustische mikroskopie, in *Mikroskopie in Forschung und Praxis*, Robenek, H., Ed., GIT Verlag, Darmstadt, 1995, p. 261.

Bereiter-Hahn, J., Scanning acoustic microscopy visualized cytomechanical responses to cytochalasin D., *J. Microsc.*, 146, 29, 1987.

Bereiter-Hahn, J., Berghofer, F., Kundu, T., Penzkofer, C., and Hillmann K., Evaluation of mechanical properties of cells by scanning acoustic microscopy using V(z) characteristics, in *Acousto-Optics and Acoustic microscopy*, 140, Graceweski, S.M., Kundu, T., Eds., American Society of Civil Engineers, Reston, VA, 1992, p. 71.

Bereiter-Hahn, J. and Buhles, N., Basic principles of interpretation of scanning acoustic images obtained from cell cultures and histological sections, in *Imaging and Visual Documentation in Medicine*, 2nd ed., Wamsteker, K. et al., Eds., Excerpta Medica, Amsterdam, 1987, p. 537.

Bereiter-Hahn, J., Karl, I., Lüers, H., and Vöth, M., Mechanical basis of cell shape: investigations with the scanning acoustic microscope, *Biochem. Cell Biol.*, 73, 337, 1995.

Bereiter-Hahn, J. and Lüers, H., Subcellular tension fields and mechanical resistance of the lamella front related to the direction of locomotion, *Cell Biochem. Biophys.,* 29, 243, 1998.

Bereiter-Hahn J. and Wagner, O., Characterization of cytogels using acoustomicroscopy-based oscillating rod rheometry, in *Advanced Nondestructive Evaluation for Structural and Biological Health Monitoring*, Kundu, T., Ed., Proc. SPIE 4335, 2001, p. 236.

Bereiter-Hahn, J. and Yastas, S., Mechanical basis of cell morphogenesis and volume control, *Appl. Mech. Rev.*, 48, 674, 1995.

Bianco, B., Cambiaso, A., Paradiso, R., and Tommasi, T., Experimental and theoretical surface acoustic wave analysis of thin-film lipid multilayers, *Appl. Phys. Lett*., 61, 402, 1992.

Boseck, S., Akustische Mikroskopie, *Phys. Bl.*, 49, 497, 1993.

Briggs, A., Acoustic microscopy, in *Monographs on the Physics and Chemistry of Materials 47*, Clarendon Press, Oxford, 1992, 325.

Briggs, G.A., Wang, J., and Gundle, R., Quantitative acoustic microscopy of individual living human cells, *J. Microsc.,* 172, 3, 1993.

Chubachi, N., Kanai, H., Sannomiya, T., and Wakahara T., Acoustic microscope for measuring acoustic properties by micro-defocusing method, *Acoust. Imaging,* 19, 685, 1991.

Cracknell, A.P., *Ultrasonics*, Wykeham Publishing, London, 1980, p. 200.

Daft, C.M. and Briggs, G.A., The elastic microstructure of various tissues. *J. Acoust. Soc. Am.* 85, 416, 1989.

Fung, Y.C., Structure and stress-strain relationship of soft tissues. *Amer. Zool.* 24, 13, 1984.

Fung, Y.C., *Biomechanics*, Springer, Berlin, Heidelberg, New York, 1981.

Grill, W., Hillmann, K., Würz, K., and Wesner, J., Scanning ultrasonic microscopy with phase contrast, *Adv. Acoust. Microsc.*, 2, 167, 1996.

Hänel, V. and Kleffner, B., Double focus technique for simultaneous measurement of sound velocity and thickness of thin samples using sound velocity and thickness of thin samples by time-resolved acoustic microscopy, *J. Appl. Phys.* 84, 668, 1998.

Hegner S. and Bereiter-Hahn, J., Volume determination of adhering cells in culture by means of acoustic interferometry, in *Cell and Tissue Culture Models in Dermatological Research*, Bernd A., Bereiter-Hahn J., Hevert F., and Holzmann H., Eds., Springer, Heidelberg, New York, 1993, p. 53.

Hildebrand, J.A., Rugar D., Measurement of cellular elastic properties by acoustic microscopy., *J. Microsc.*, 134, 245, 1984.

Hildebrand, J.A., Rugar, D., Johnston, R.N., and Quate, C.F., Acoustic microscopy of living cells, *Proc. Natl. Acad. Sci. USA*, 78, 1656, 1981.

Hillmann, K., Grill, W., and Bereiter-Hahn, J., Determination of ultrasonic attenuation in small samples of solid material by scanning acoustic microscopy with phase contrast. *J. Alloys Compounds,* 211/212, 625, 1994.

Holwill, M.E.J. and Satir, P., Generation of propulsive forces by cilia and flagella, in *Cytomechanics: The Mechanical Basis of Cell Form and Structure*, Bereiter-Hahn, J., Anderson O.R., and Reif, W.E., Eds., Springer, Berlin, Heidelberg, 1987, p. 120.

Hoppe, M. and Bereiter-Hahn, J., Applications of scanning acoustic microscopy: survey and new aspects, *IEEE Trans. Sonics Ultrasonics,* SU-32, 289, 1985.

Ingber, D.E., Prusty, D., Sun, Z.Q., Betensky, H., and Wang, N., Cell shape, cytoskeletal mechanics, and cell cycle control in angiogenesis, *J. Biomech.*, 28, 1471, 1995.

Kanngiesser, H. and Anliker, M., Ultrasound microscopy of biological structures with weak reflecting properties, *Acoust. Imaging*, 19, 517, 1991.

Karl, I., personal communication, 1999.

Karl, I. and Bereiter-Hahn, J., Tension modulates cell surface motility: a scanning acoustic microscopy study, *Cell Motil. Cytoskeleton*, 43, 349, 1999.

Karl, I. and Bereiter-Hahn, J., Cell contraction caused by microtubule disruption is accompanied by shape changes and an increased elasticity measured by scanning acoustic microscopy, *Cell Biochem. Biophys.*, 29, 225, 1998.

Khuri-Yakub, B.T., Reinholdtsen, T., Chou, C.-H., Paren, P., and Cinbis, C., Amplitude and phase acoustic microscopy and its application to QNDE, *Acoust. Imaging*, 17, 173, 1988.

Kojro, Z., v.d. Burg, E., Zinke, J., Hillmann, K., and Grill, W., Viscosity shear waves and mass drag effect in liquids, *Z. Phys. B.,* 101, 433, 1996.

Kolodney, M. and Elson, E., Contraction due to microtubule disruption is associated with increased phosphorylation of myosin regulatory light chain, *Proc. Natl. Acad. Sci. USA*, 92, 10252, 1995.

Kundu, T., Bereiter-Hahn, J., and Karl, I., Cell property determination from the acoustic microscope generated voltage versus frequency curves, *Biophys. J.,* 78, 2270, 2000.

Kundu, T., Bereiter-Hahn, J., and Hillmann, K., Calculating acoustical properties of cells: Influence of surface topography and liquid layer between cell and substrate, *J. Acoust. Soc. Am.*, 91, 3008, 1992.

Kundu, T., Bereiter-Hahn, J., and Hillmann, K., Measuring elastic properties of cells by evaluation of scanning acoustic microscopy V(z) values using simplex algorithm, *Biophys. J.*, 59, 1194, 1991.

Kushibiki, J., Akashi, N., Sannomiya, T., Chubachi, N. and Dunn, F., VHF/UHF range bioultrasonic spectroscopy system and method, *IEEE Trans*., 42, 1028, 1995.

Lamb, H., Hydrodynamics, 6th ed. Dover Publications, New York, 1932.

Landau, L.D. and Lifshitz, E.M., *Course of Theoretical Physics*, 2nd ed. vol. 6, Fluid Mechanics, Pergamon Press, Oxford, 1987.

Lemor, R. and Pilarczyk, G., Combination of acoustic and optical microscopy for investigation of biological cell properties, *Acoust. Imaging,* 28 (in preparation).

Leterrier, J.F., Water and the cytoskeleton, *Cell Mol. Biol. (Noisy-le-grand)*, 47, 901, 2001.

Litniewski, J. and Bereiter-Hahn, J., Acoustic velocity determination in cytoplasm by V(z) shift, *Acoust. Imaging,* 19, 535, 1991.

Litniewski, J. and Bereiter-Hahn, J., Measurements of cells in culture by scanning acoustic microscopy, *J. Microsc.*, 158, 95, 1990.

Lüers, H., Bereiter-Hahn, J., and Litniewski, J., Observation of cultured cells with the SAM: the structural basis of elasticity, *Acoust. Imaging*, 19, 511, 1992a.

Lüers, H., Hillmann, K., Litniewski, J., and Bereiter-Hahn, J., Acoustic microscopy of cultured cells: distribution of forces and cytoskeletal elements, *Cell Biophys.* 18, 279, 1992b.

O'Brien, W.D., Jr., Erdman, J.W., Jr., and Hebner, T.B., Ultrasonic propagation properties (a-100 MHz) in excessively fatty rat liver, *J. Acoust. Soc. Am.*, 83, 1166, 1988.

Pinkerton, J.M., The absorption of ultrasonic waves in liquids and its relations to molecular constitution, *Proc. Phys. Soc*. 62, 129, 1949.

Pluta, M. and Grill, W., Phase sensitive acoustic microscopy image quality estimation by volume imaging in anisotropic media: acoustic microscopy, *Acoust. Imaging,* 26, 213, 2002.

Radmacher, M., Fritz, M., Cleveland, J., Walters, D., and Hansma, P., Imaging adhesion forces and elasticity of lysozyme adsorbed on mica with the atomic force microscope, *Langmuir*, 10, 3809, 1994.

Radmacher, M., Fritz, M., Kacher, C., Cleveland, J., and Hansma, P., Measuring the viscoelastic properties of human platelets with the atomic force microscope, *Biophys. J.*, 70, 556, 1996.

Radmacher, M., Tillman, R.W., and Gaub, H.E., Imaging viscoelasticity by force modulation with the atomic force microscope, *Biophys. J.*, 64, 735, 1993.

Sathish, S., Gremaud, G., Kulik, A., and Richard, P., V(z) of continuous wave reflection scanning acoustic microscope, *J. Acoust. Soc. Am.*, 96, 2769, 1994.

Sato, M., Leimbach, G., Schwarz, W.H., and Pollard, T.D., Mechanical properties of actin, *J. Biol. Chem.*, 260, 8585, 1985.

Sato, M., Schwarz, W.H., and Pollard, T.D., Dependence of the mechanical properties of actin/alpha-actinin gels on deformation rate, *Nature,* 325, 829, 1987.

Schmidt, F.G., Ziemann, F., and Sackmann, E., Shear field mapping in actin networks by using magnetic tweezers, *Eur. Biophys. J.,* 24, 348, 1996.

Sinton, A.M., Briggs, G.A.D., and Tsukahara, Y., Time-resolved acoustic microscopy of polymer coatings, *Acoust. Imaging,* 17, 87, 1989.

Tommasi, T., Cambiaso, A., Buzzoni, G., Grattarola, M., and Bianco, B., Acoustic microscopy investigations for living cell investigations, *Acoust. Imaging*, 19, 529, 1992.

Vesely, P., personal communication, 1999.

Vesely, P., Lüers, H., Riehle, M., and Bereiter-Hahn, J., Subtraction scanning acoustic microscopy reveals motility domains in cells in vitro, *Cell Motil. Cytoskeleton*, 29, 231, 1994.

Vesenka, J., Biological applications of scanning probe microscopies, *Scanning*, 19, 135, 1997.

Wagner, O. and Bereiter-Hahn, J., The oscillating rod viscosimeter: a new method for simultaneously measurement of dynamic viscosity and velocity of sound in cytogels using nanometer strains, *Eur. J. Cell. Biol.*, 42, 469, 1996.

Wagner, O., Schüler, H., Hofmann, P., Langer, D., Dancker, P., and Bereiter-Hahn, J., Sound attenuation of polymerizing actin reflects supramolecular structures: viscoelastic properties of actin gels modified by cytochalasin D, profilin and a-actinin, *Biochem. J.*, 355, 771, 2001.

Wagner, O., Zinke, J., Dancker, P., Grill, W., and Bereiter-Hahn J., Viscoelastic properties of f-actin, microtubules, f-actin/a-actinin, and f-actin/hexokinase determined in microliter volumes with a novel nondestructive method, *Biophys. J.*, 76, 2784, 1999.

Wang, D.L., Wung, B.S., Peng, Y.C., and Wang, J.J., Mechanical strain increases endothelin-1 gene expression via protein kinase c pathway in human endothelial cells, *J. Cell Physiol.*, 163, 400, 1995.

Wang, N. and Ingber, D.E., Probing transmembrane mechanical coupling and cytomechanics using magnetic twisting cytometry, *Biochem. Cell Biol.*, 73, 327, 1995.

Weaver, V.M., Petersen, O.W., Wang, F., Larabell, C.A., Briand, P., Damsky, C., and Bissell, M.J., Reversion of the malignant phenotype of human breast cells in three-dimensional culture and *in vivo* by integrin blocking antibodies, *J. Cell. Biol.*, 137, 231, 1997.

Yu, Z. and Boseck, S., Inversion of V(z) data in the scanning acoustic microscope (SAM) to determine material properties of a layered solid, *Acoust. Imaging*, 19, 617, 1992.

Zaner, K.S., Fotland, R., and Stossel, T.P., Low-shear, small volume, viscoelastometer. *Rev. Sci. Instrum.*, 52, 85, 1981.

Zoller, J., Brändle, K., and Bereiter-Hahn, J., Cellular motility *in vitro* as revealed by scanning acoustic microscopy depends on cell-cell contacts, *Cell Tiss. Res.*, 290, 43, 1997.

13

Ultrasonic Characterization of Hard Tissues

Kay Raum

CONTENTS

13.1 *In Vivo* Characterization of Bone with Low Frequencies

Low-frequency ultrasound has been extensively used for the characterization of the macroscopic elastic properties of bone for many years.[1] With frequencies in the range from 500 kHz to 2 MHz, the wavelengths and acoustic beam dimensions are much larger than the dimensions of the trabecular structure. The wave propagation through this porous structure is influenced by scattering, interference, and diffraction. Quantitative imaging of the calcaneus was introduced more than 10 years ago and is now widely accepted as a clinical tool of assessment of skeletal status in osteoporosis.[2,3] In these systems, two low-frequency, slightly focused transducers are coaxially and confocally aligned (Figure 13.1).

For the measurement in transmission mode, one transducer emits a broadband pulse and the other one acts as a receiver. Both transducers are moved simultaneously in order to scan the ultrasound beam through the heel.

0-8493-1462-3/02/$0.00+$1.50

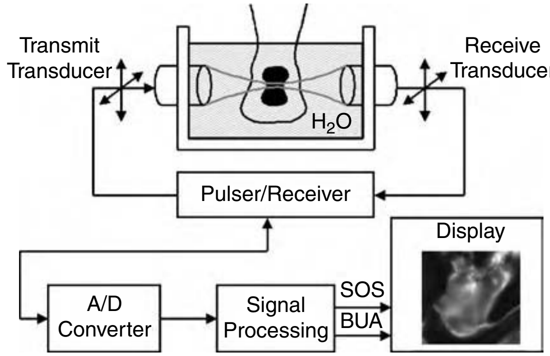

FIGURE 13.1
Principle of U.S. parametric imaging of the os calcis. Usually slightly focused transducers with center frequencies between 500 kHz and 2 MHz are applied.

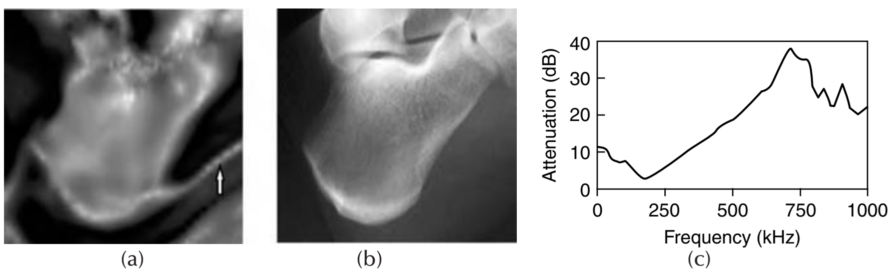

FIGURE 13.2
Comparison between the BUA (a) and radiograph (b) images of the calcaneus. The BUA values are derived from the linear slope of the frequency dependent attenuation (c). (From Laugier, P. et al., *Calcif. Tissue Int.*, 54, 83, 1994. Copyright 1996 by Springer-Verlag. With permission.)

For each scan position the received signal is digitized. The speed of sound (SOS) is calculated using a substitution method:[4,5]

$$c(x_1, x_2) = \frac{c_f \cdot d}{d - (c_f \Delta TOF)} \tag{13.1}$$

where d is the thickness of the heel and ΔTOF is the difference of the pulse travel times with and without the sample in the propagation path. The frequency dependent attenuation [$\alpha(x_1,x_2,f)$] is found from the ratio of the magnitude spectrum [$A(x_1,x_2,f)$] of the signal transmitted through the heel and a reference spectrum [$A_r(x_1,x_2,f)$] of a signal transmitted through water:

$$\alpha(x_1, x_2, f) = 20 \log_{10} \frac{A(x_1, x_2, f)}{A_r(x_1, x_2, f)} \tag{13.2}$$

In cancellous bone, the attenuation displays nearly a linear frequency dependence (Figure 13.2c). The slope of the attenuation or broadband ultrasonic attenuation (BUA) is found by a linear regression of $\alpha_P(x_1,x_2,f)$ within the usable bandwidth of the transducers.

Quantitative parametric imaging allows a precise and reproducible determination of SOS and BUA in standardized measurement sites. Numerous clinical studies have shown that these parameters correlate significantly with bone mass density and that they are dependent upon the anisotropic elasticity and structure of cancellous bone. They have the ability to discriminate between normal and osteoporotic bone and to predict the fracture risk.[6–14] Comprehensive summaries can be found elsewhere.[15–20]

Although a general consensus of the important clinical role of low-frequency ultrasound for the assessment of osteoporosis exists, there is still a lack of clear understanding of the fundamental principles of ultrasound wave propagation through cancellous bone. A physical model that could explain the individual influences of structural and constitutional properties of the bone compound on the sound propagation properties does not yet exist. In order to assess these parameters separately, higher frequencies are necessary.

13.2 Acoustic Microscopy of Hard Tissues

While contrast in acoustic microscopy of soft tissues is dominated by interference and attenuation, the situation for stiff tissues is quite different. The sound velocities can be several times higher than those of common coupling fluids. Complex transmission and reflectance characteristics at the interfaces result in mode conversions that remarkably complicate the data interpretation. The heterogeneous microstructure causes problems both for the preparation and for the investigation of those tissues.

In high-frequency microscopes, the pulse echoes are usually not available for analysis. Mostly the echoes are time gated, demodulated, and envelope detected. The amplitude varies very sensitively with the distance between the focal plane and the surface of the specimen (x_3 or z direction). For an isotropic homogeneous half space, the detected amplitude can be expressed by the pupil function $[P(\theta_{Pf})]$ of the lens, the, complex reflectance function $[R(\theta_{Pf})]$ between the two materials, and the distance of the boundary relative to the focal plane of the lens:

$$V(x_3) = \int_0^{\pi/2} P(\theta_{Pf})R(\theta_{Pf})e^{-i2x_3k_f\cos\theta_{Pf}}\sin(\theta_{Pf})\cos(\theta_{Pf})d\theta_{Pf} \qquad \textbf{(13.3)}$$

The two prominent features in the so-called V(z) curve are the confocal amplitude and oscillations at negative defocus respectively (Figure 13.3).

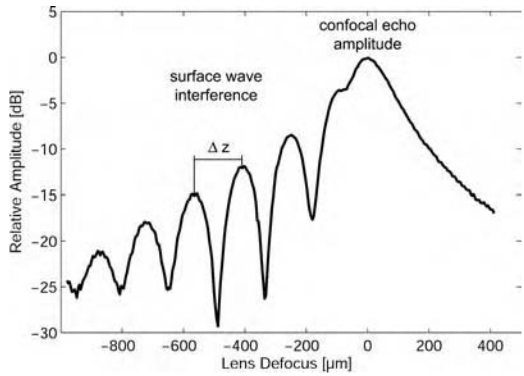

FIGURE 13.3
A typical V(z) curve of a quartz glass, obtained at 50 MHz.

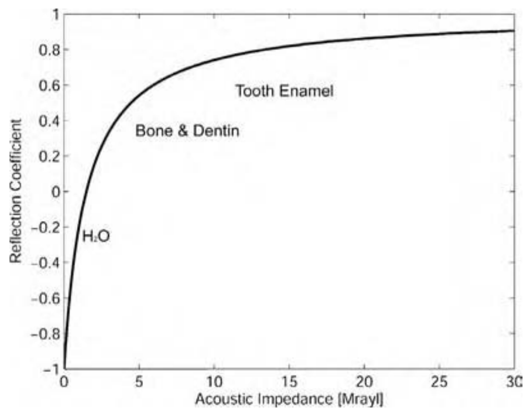

FIGURE 13.4
Reflection coefficient R as a function of the acoustic impedance Z. Water at 25°C (Z = 1.49 Mrayl) was assumed as a coupling fluid.

If the focal plane of the transducer coincides with the surface of the sample, all parts of the incident waves are in phase. Lateral stress components are extinguished and plane wave propagation can be assumed. As described in Chapter 11, the resulting echo amplitude [V(x_3 = 0)] is proportional to the reflection coefficient R, and the acoustic impedance of the sample can be determined from the confocal echo amplitude via Equation 1.142. Figure 13.4 shows the reflection coefficient as a function of the acoustic impedance for the usual measurement condition with water serving as a coupling fluid.

The sensitivity of the estimation of the acoustic impedance from the amplitude of the reflected wave is not linear. A good discrimination of varying acoustic properties is only obtained for materials with intermediate or very low acoustic impedances. As the impedance increases, the reflection coefficient converges toward one and the confocal contrast is diminished. In very stiff tissues the most dominant contrast arises from surface wave interferences when the lens is defocused.

13.2.1 Wave Interference Contrast

Rayleigh (R) waves are excited, if the semiaperture angle of the lens exceeds the Rayleigh angle θ_R:

$$\sin\theta_R = \frac{c_f}{c_R} \tag{13.4}$$

where c_R is the R-wave velocity. Moreover, P-waves can propagate parallel to the fluid-solid interface when the angle of refraction is 90°. For this case the semiaperture angle has to be larger than the longitudinal critical angle θ_L:

$$\sin\theta_L = \frac{c_f}{c_P} \tag{13.5}$$

These waves, also known as surface skimming compressional waves (SSCW), give rise to similar oscillations in the V(z) curve as obtained with R-wave interference. The periodicity of the oscillations for both cases is:

$$\Delta x_{3_i} = \frac{\lambda_f}{2(1-\cos\theta_i)} \tag{13.6}$$

where i indicates either the Rayleigh angle or the longitudinal critical angle. In principle, both waves can occur at the same time; therrefore, a spatial spectrum approach is required to determine the individual wave velocities.

The determination of the sound velocities from oscillations in the V(z) curve is relatively straightforward if these oscillations can be observed reliably. Tooth enamel contains around 96% mineral and is the stiffest material found in the body. It is relatively homogeneous and the orientation of the mineral crystals is highly oriented. The speed of sound is in the order of 6000 m/sec for normal enamel. R-waves have a velocity of around 3000 m/sec and are easily excited. The V(z) technique can be successfully exploited with either a point or a line focus system. Dentin and bone are less stiff and the Rayleigh velocities are relatively small. With a 120° aperture lens velocities as small as 1720 m/sec could be theoretically detected. The drawback of such a large aperture is that the sampled volume is increased as well. The radius of the illuminated surface area is

$$r_{\max} = -x_{3\max}\tan\theta_i \tag{13.7}$$

where z_{max} is the maximum defocus position used for the analysis. Even with a 2-GHz lens, where the maximum defocus is approximately 20 µm,

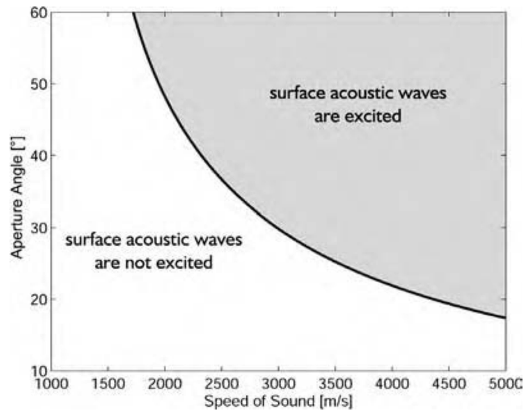

FIGURE 13.5
Critical angle for the generation of a surface acoustic wave as a function of the wave velocity. Water at 25°C ($\nu_0 = 1492$ m/sec) was assumed as a coupling fluid.

the corresponding sampled surface radius would be about 35 μm. Most of biological tissues are neither isotropic nor homogeneous within such an area. An important feature especially in bone is its heterogeneous microstructure with greatly varying properties. Consequently, the analysis becomes far more complex and in many cases Rayleigh wave interference cannot be seen at all. The situation is similar for SSCWs, although the velocities are much higher and can be observed with lower aperture lenses. Figure 13.5 summarizes for which velocities wave interference contrast can be expected.

13.2.2 Confocal Amplitude Contrast

One of the most promising features of acoustic microscopes is the striking spatial resolution that can be obtained at very high frequencies. Major advantages of confocal measurements are that the beam width is minimal, the sample volume interacting with the acoustic wave is minimized, and transmission and reflection phenomena are considerably simplified. The reflection from the surface of the sample is usually measured over a rectangular scan area (C-Scan, Figure 13.6).

The resulting grayscale image can then be converted into a two-dimensional impedance map. The resolution ($D_{lateral}$) is determined by the 3-dB beam width in the focal plane:

$$D_{lateral} = 1.028 \cdot \lambda_f \cdot \frac{ROC}{2a} \quad \textbf{(13.8)}$$

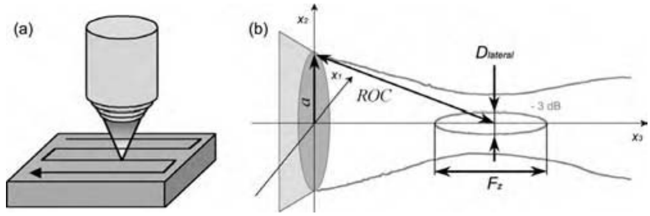

FIGURE 13.6
For a C-Scan a spherically focused transducer is scanned over the sample (a). If the waves are reflected in the focal plane, an acoustic impedance map can be derived from the echo amplitudes. Lateral resolution ($D_{lateral}$) and depth of focus (F_z) are determined by the transducer diameter (a), the radius of curvature (*ROC*) of the focusing lens, and the acousic wavelength (λ), respectively (b).

where *ROC* is the radius of curvature and a is the aperture radius, respectively. The semiangle of the lens-aperture θ_0 is:[21]

$$\sin\theta_0 = \frac{a}{ROC} \tag{13.9}$$

The depth of focus (F_z), defined as the distance between points along the beam axis where the intensity is 3 dB less compared to the focal point, is:[21]

$$F_z = 7.08 \cdot \lambda \left(\frac{ROC}{2 \cdot a} \right)^2 \tag{13.10}$$

A crucial requirement for a quantitative analysis is that the waves are reflected at normal incidence in the focal plane for each scanned point. Consequently, a well-prepared flat surface is essential. Mechanical preparation techniques will remove softer materials more easily than stiffer ones, leading to a remaining surface roughness in heterogeneous materials with varying mechanical properties. Other problems arise from imperfections in the flatness of the scan plane of the microscope and in cases where the sample surface is not perfectly parallel to the scan plane. At very high frequencies, the dimensions of these variations become comparable to the depth of focus of the acoustic lens (Figure 13.7). It is necessary to separate topographical influences in the image contrast from those caused by varying material properties.

13.2.3 Time-Resolved Techniques

Short pulse microscopy with time of flight (TOF) recording can be used to measure the sound velocity both in transmission and in reflection mode. Although systems operating with center frequencies up to 750 MHz have been

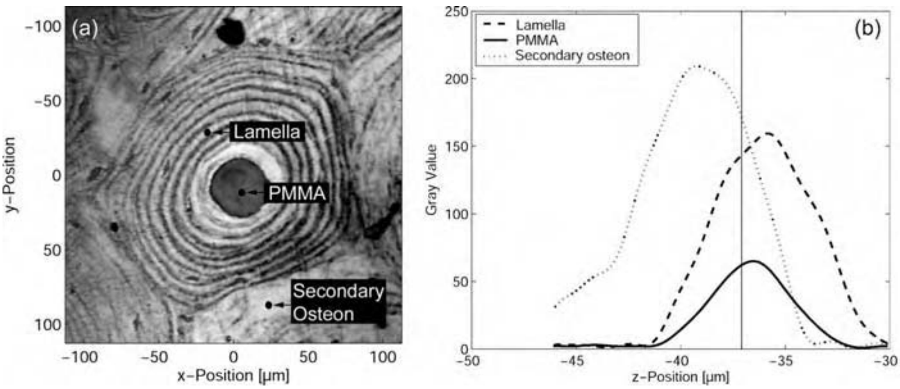

FIGURE 13.7
C-Scan of an osteon, measured at 900 MHz (a). V(z) scans at three different locations are plotted in (b). The vertical line in (b) indicates the x_1x_2-plane of the C-scan image. While the image appears to be focused, V(z) analysis reveals that none of the three marked points were measured in the focal plane.

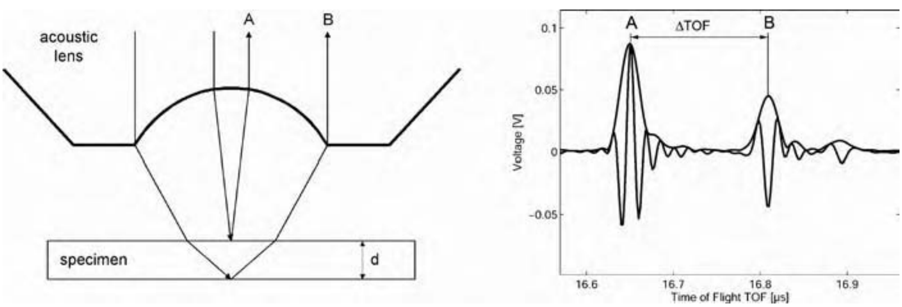

FIGURE 13.8
The time delay between waves reflected at the front (A) and back (B) side of a thin specimen can be used to calculate the P-wave velocity. Mode conversions can result in additional echoes, if focused beams are used. Because of the lower sound velocities, these waves have larger time delays compared to P-waves.

available for more than a decade now,[22] the high attenuation in hard tissues usually limits the applicable frequency bandwidth. Usually broadband pulses with center frequencies around 50 MHz are applied to measure the delay time between front and back side echoes of thin samples (Figure 13.8).

The P-wave velocity is calculated as twice the sample thickness (d) divided by the delay time (ΔTOF) between front and back side echoes:

$$c_P = \frac{2d}{\Delta TOF} \tag{13.11}$$

TABLE 13.1

P-Wave Velocities in Different Layers of Dentin

Structure	c_P (m/sec)
Dentin in bulk	3870 ± 300
Dark mantle dentin near the enamel	3530 ± 300
Dark dentin near the pulp chamber	3200 ± 290
Destroyed dentin close to a carious lesion	3570 ± 200

Source: From Maev et al. *Ultrasound Med. Biol*, 28, 131, 2002. With permission.

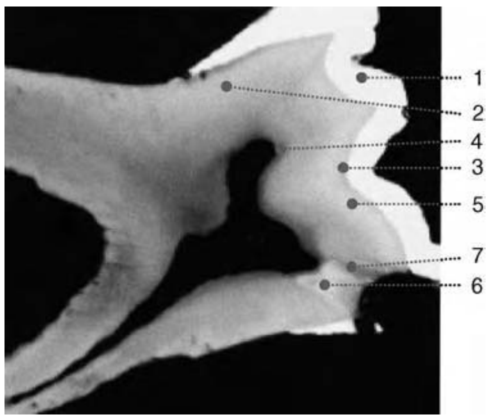

FIGURE 13.9
Differences in the reflected sound intensity caused by variation of acoustic impedance in different tooth areas. Image size: 12 × 12 mm; frequency: 50 MHz. 1 = enamel; 2 = bulk dentin; 3 = thin layer of dark mantel dentin; 4 = dark dentin around pulp chamber; 5 = light layer of dentin beneath mantle dentin; 6 = dense transparent dentin; 7 = dark destroyed dentin. (Reprinted by permission of Elsevier Science from Maev, R.G., *Ultrasound Med. Biol.*, 28, 131. Copyright 2002 by World Federation of Ultrasound in Medicine and Biology.)

13.2.4 Tooth Enamel and Dentin

An acoustic image of a section through a human tooth is shown in Figure 13.9. Differences of the reflectivity can be particularly seen between enamel and dentin and also within various regions of the dentin.

Maev et al.[23] determined P-wave velocities in thin sections of human premolar dentin with TOF measurements. The highest velocities were observed in bulk dentin. The velocities in dark mantel dentin were about 8% lower near the enamel and 15% lower near the pulp chamber. In cases with destroyed dentin close to carious cavities the decrease was about 17% (see Table 13.1). Maev et al.[23] and Mezava et al.[24] found a good correlation between P-wave velocity and acoustic impedance.

The P-wave velocity in enamel is about 1.5 to 2 times higher than in dentin, and R-waves are easily excited. V(z) analysis is the most suitable technique

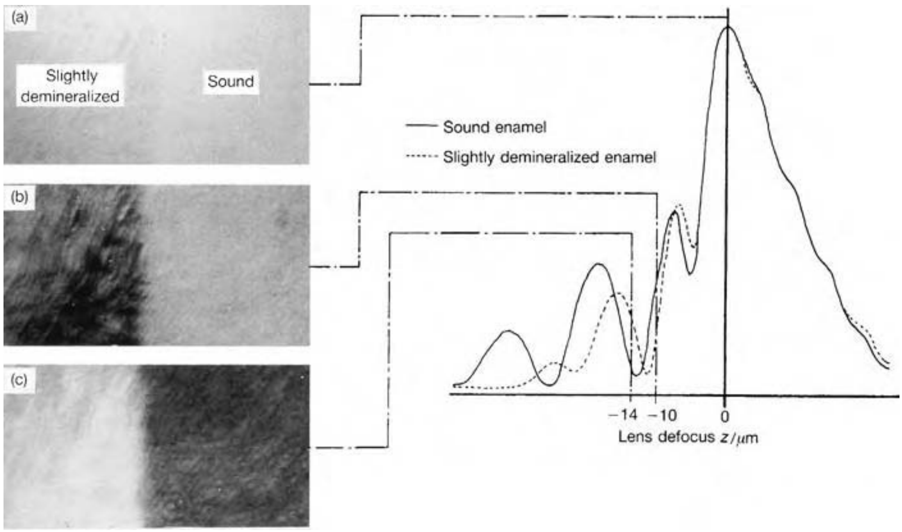

FIGURE 13.10
Acoustic images and V(z) curves for a specimen of human tooth enamel prepared with the left half slightly demineralized and the right half sound. V(z) curves: sound enamel (——); slightly demineralized (-----). Micrographs: (a) z = 0; (b) z = −10 μm; (c) z = −14 μm. 370 MHz. (Republished with the permission of the International and American Associations for Dental Research, from Peck, S.D. and Briggs G.A., The caries lesion under the scanning microscope, *Adv. Dent. Res.*, 1(1), 1987. Permission conveyed through Copyright Clearance Center, Inc.)

for a quantitative characterization. Peck et al.[25] first demonstrated the potential of using wave interference contrast in order to distinguish a caries lesion from sound enamel. The contrast arises from different peak and dip locations at negative defocus due to variations of the R-wave velocities (Figure 13.10).

Quantitative evaluation of the R-wave velocities revealed a decrease of about 15% in the core of a lesion compared with sound enamel.[26] It is interesting to notice that destruction of dentin and enamel is accompanied with a reduction of density, acoustic impedance, and sound velocity, respectively. Since the specific acoustic impedance varies proportionally with the square root of density and the P-wave velocity varies inversely with the square root of density, the reduction of the elastic stiffness is assumed to be predominant over the reduction of density.[22,23,26]

The anisotropy of tooth enamel can be measured using a line-focus beam technique with a cylindrical lens.[26,27] Figure 13.11 shows measurements made on a buccal surface of a human molar tooth. V(z) measurements were made over 180° at 10° intervals. The location of the sketches indicates angles at which the R-wave propagation would have been roughly perpendicular and parallel to the long axis of the tooth.

It can be seen in Figure 13.11 that the R-wave velocity is least perpendicular to and greatest parallel to the long axis of the tooth. The difference is about 2%. Similar results were found by Kushibiki et al.[27] in incisor teeth, where

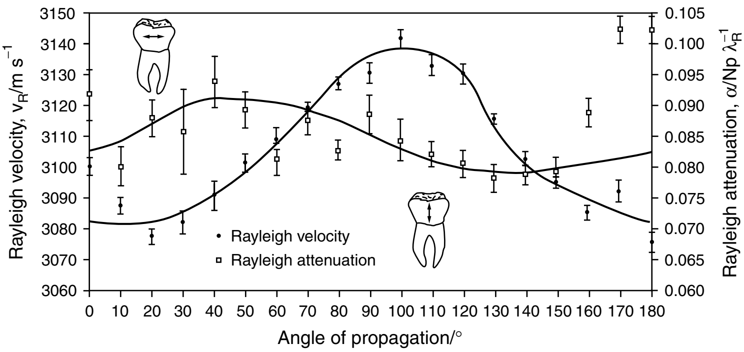

FIGURE 13.11
Buccal surface of human molar tooth. Rayleigh velocity and attenuation measured using a line-focus-beam lens at 225 MHz. The sketches indicate the approximate measurement angles at which the Rayleigh wave propagation was in the direction of the arrows (From Peck, S.D., *J. Dent. Res.*, 68, 107, 1989. Reprinted with permission from the *Journal of Dental Research*.)

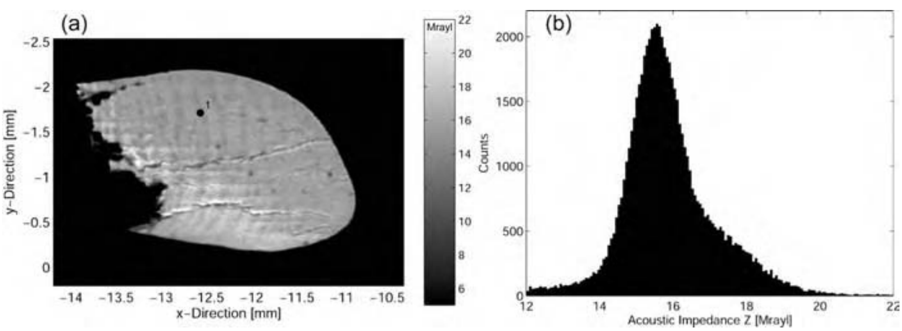

FIGURE 13.12
C-Scan image of tooth enamel, measured at 50 MHz (a). On the left-hand side there is a carious lesion. The two large cracks probably occurred during the preparation with a micromilling machine. Histogram of the image (b).

the wave velocities ranged from 3106 to 3153 m/sec. Measurements on longitudinal sections of human molar tooth revealed a greater spread of velocities, ranging from 3124 ± 10 m/sec parallel to the axis of the keyhole-shaped apatite bundles, and 2943 ± 10 m/sec perpendicular to it. Although the estimation of the attenuation is less accurate, an opposite trend as for the velocity was hypothesized.[26]

Another section of human tooth enamel is shown in Figure 13.12. Except for a slightly increased impedance in the lower part of the image little contrast is seen due to the high acoustic impedances in the range between 14 and 19 Mrayl. The variation of the reflected voltage is only about 1.3%.

The V(z) curve in Figure 13.13a was obtained from point 1 in the C-scan of Figure 13.12a. Oscillations at negative defocus are clearly visible. The voltages

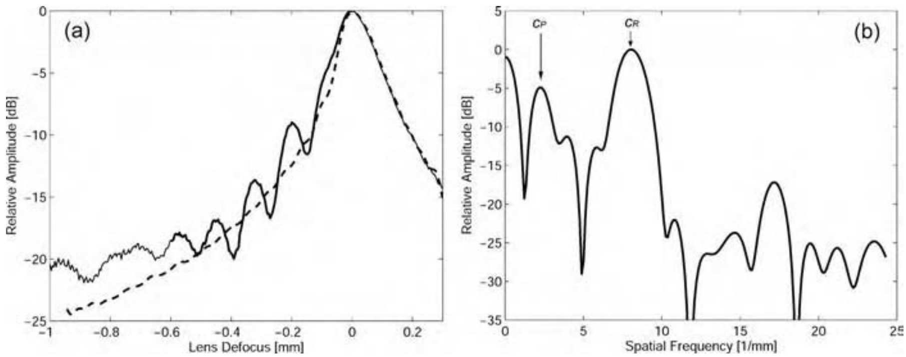

FIGURE 13.13
V(z) curve measured at point 1 indicated in 13.12a. The dashed line is the V(z) signal of teflon. The confocal amplitude corresponds to an acoustic impedance of 17.26 Mrayl. The bold section was used for an (FFT) analysis. The two peaks in the spatial frequency spectrum in (b) correspond to oscillations caused by R- and P-waves with sound velocities of 3119 and 6140 m/sec, respectively. Frequency: 50 MHz; semiaperture: 30°.

were converted into decibel and normalized to the confocal amplitude. After subtracting the normalized V(z) signal of a reference material, for which oscillations do not occur, the individual surface wave contributions of P- and R-waves can be analyzed in the Fourier transform (Figure 13.13b).

13.2.5 Bone

The investigation of bone is far more complex due to its heterogeneous macro- and microstructure. Weiner and Wagner[28] classified bone into seven levels of hierarchical organization. Size, orientation, distribution, and properties of the assembling units at each level can vary dramatically even within a single bone. At the macroscopic scale one can distinguish between cancellous and compact bone (Figure 13.14).

Many studies were conducted with the time-resolved technique described in Section 0 by Turner et al. and other colleagues.[29–31] Significant differences of the P-wave velocities were found between pre- and postmenopausal and osteoporotic iliac crest specimen of 40 Caucasian women.[32] Canine femoral bone specimens were measured at 10° increments from the long axis of the bone.[33] A significant anisotropy of the P-wave velocity with an off-axis maximum at around 30° was observed. From a comparison of the anisotropic velocity of demineralized and decollagenized samples it was concluded that the principal orientation of bone mineral was along the long axis of the femur, while bone collagen was aligned at a 30-degree angle to it. No significant differences were observed between cancellous and cortical bone.[34] Table 13.2 summarizes the observed velocities for different species, types of tissue, and orientations.

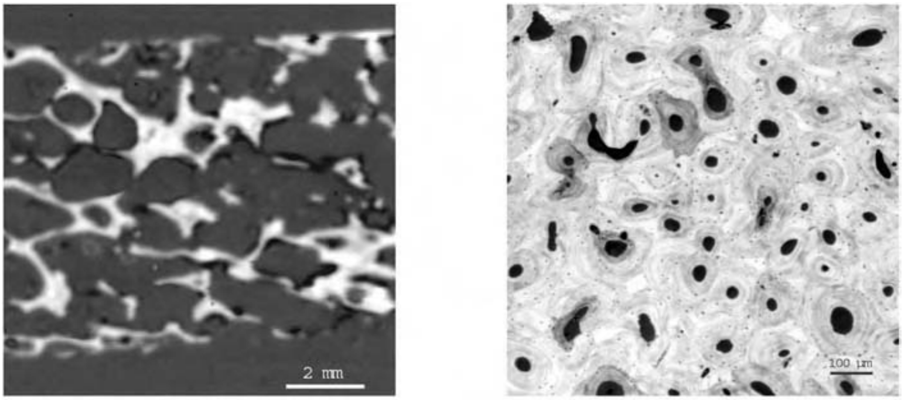

(a) (b)

FIGURE 13.14
Cancellous (a) and compact (b) bone. The measurement frequencies were 25 and 200 MHz, respectively. While cancellous bone is characterized by a mesh of thin trabeculae and large voids filled with bone marrow, compact bone consists of a dense matrix of osteons and secondary osteons. The osteons are composed of a central Haversian channel and surrounding layers of mineralized collagen lamellae. The small dark spots are osteocytes. Varying gray levels of osteons are related to their age and mineralization, respectively.

TABLE 13.2
P-Wave Velocities in Different Bone Samples

Structure	c_P (m/sec)	Ref.
Human iliac crest, premenopausal	3318 ± 319.1	32
Human iliac crest, postmenopausal	3663 ± 62.5	32
Human iliac crest, osteoporotic	3436 ± 209.3	32
Rat femur, cortical bone, transverse direction	3782 ± 20	30
Rat femur, cortical bone, longitudinal direction	4246 ± 17	30

Elastic parameters (e.g., stiffness and Young's modulus) were calculated from the P-wave velocities using relations derived in Chapter 1. Macroscopic densities and Poission ratios had to be used for the conversion. Both parameters are presumably not homogenous at the microscopic scale, resulting in inherent uncertainties in the estimation.

Wave interference contrast works well for the characterization of tooth enamel, but it is much less pronounced in bone. Fourier analysis of the example in Figure 13.15 still reveals a peak that can be assigned to a reasonable P-wave velocity of about 3980 m/sec, but the peak width is much broader than those observed in enamel. Using Equation 13.7 we can estimate the contributing surface radius for this measurement to be about 240 μm. In Figure 13.14 it can be easily seen that bone is neither homogeneous nor isotropic within such a large area.

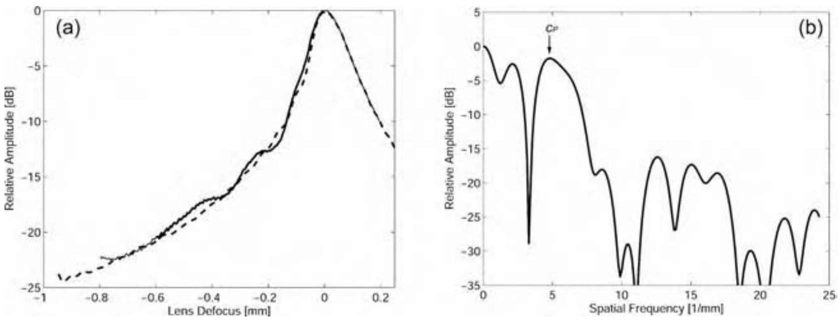

FIGURE 13.15
Example of a V(z) curve measured in human cortical bone (a). The dashed line is the V(z) signal of teflon. The confocal amplitude corresponds to an acoustic impedance of 8.8 Mrayl. The bold section was used for an FFT analysis. The peak in the spatial frequency spectrum in (b) corresponds to a P-wave velocity of 3982 m/sec. Frequency: 50 MHz; semiaperture: 30°.

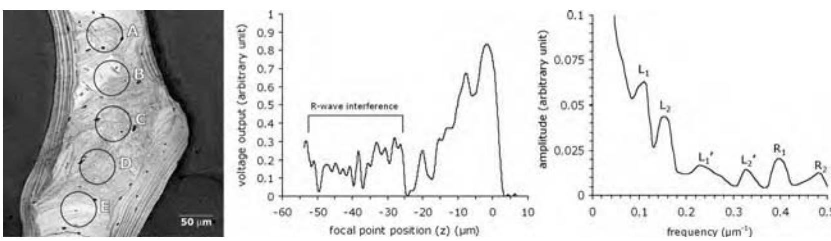

FIGURE 13.16
Acoustic image of a canine trabecular strut taken at 1 GHz (a). A V(z) curve recorded in the region indicated by circle A is plotted in (b). The size of the circle corresponds to the contributing surface area for the V(z) analysis. The peaks in the spatial spectrogram (b) were assigned to two different P-waves (L_1 and L_2) and their corresponding R-waves (R_1 and R_2). (Reprinted by permission of Elsevier Science from Jørgensen, C.S. and Kundu, T., *J. Orthopaed. Res.*, 28, 131. Copyright 2002 by Orthopaedic Research Society.)

A solution is to increase the frequency, and some promising results were recently reported by Jørgensen and Kundu.[35] They performed V(z) measurements in a single canine trabecular strut at 1 GHz and observed both P- and R-waves (Figure 13.16).

Up to four different P-wave velocities were recorded in individual measurements that were attributed to elastic anisotropy. The estimated velocities were in the range from 2330 to 4330 m/sec for the P-waves and 1930 to 2070 m/sec for the R-waves, respectively. The large contributing surface area with a radius of about 25 μm in this case is still a limiting factor. The heterogeneous structure within the measurement spots is clearly visible in Figure 13.16a. Each spot consists of structures with different elastic properties. Surface wave propagation along these structures (e.g., mineralized collagen lamellae) is presumably preferred over propagation in other directions, and, hence, carefulness is required for the interpretation of these multipeak spectrograms.

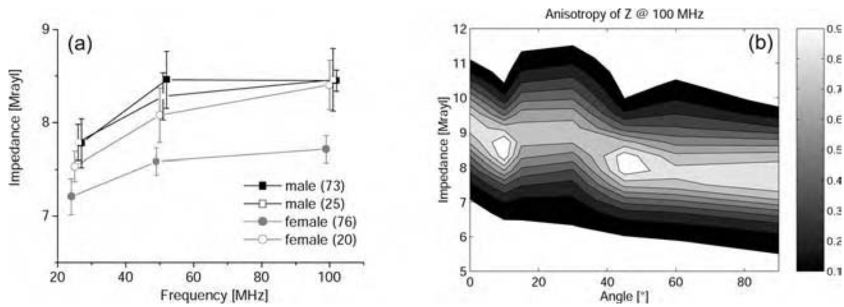

FIGURE 13.17
Frequency dependence of the acoustic impedance (a) and anisotropy of impedance distributions in human cortical bone (b). (FromRaum, K., et al., Frequency dependence of the anisotropic impedance estimation in cortical bone using time-resolved scanning acoustic microscopy, *Proc. IEEE Ultrason. Symp.*, Munich, 2002, p. 1269. With permission.)

The alternate way to assess the heterogeneous microstructure of bone is to map the confocal echo amplitude. At 100 MHz the nominal beam width in the focal plane of a transducer with a 60° aperture is about 15 µm, which is already more than three times better than the resolution with V(z) contrast at 1 GHz. Two-dimensional impedance mapping allows a more rapid evaluation of the diversity of elastic properties. Figure 13.17 shows results obtained from human femur sections. Cortical samples were prepared with different surface orientations relative to the long axis of the femur (0° perpendicular, 90° parallel to the long axis). Measurements made at 25 MHz exhibited significantly lower mean impedance values compared to those obtained at higher frequencies. This was partly attributed to an insufficient spatial resolution (142 µm) of this transducer. Decreased impedance values were observed in the femur of the 76-year-old female donor. In order to explore the complex relations between loading angle and impedance distribution, the normalized angular dependent histograms were represented as color-coded contour plots.

Width and peak values of the impedance histograms (vertical direction in Figure 13.17b) varied considerably for different observation angles. The narrowest distributions can be seen at 15 and 45°. In between the distributions are broadened and the peak reaches a local maximum. At 0 and 90° the peaks have a maximum and a minimum, respectively.

If the frequency is increased up to the gigahertz range, the resolution becomes comparable to that of light microscopy. To achieve a reliable impedance estimation it has to be assured that the surface reflection occurs at normal incidence in the focal plane of the lens. This can be done by a combination of C- and V(z) scans. Raum et al.[37] introduced the multilayer analysis (MLA) where a set of C-scan images is acquired (Figure 13.18). Starting from an x_3-position where the focus of the lens is well above the sample surface (positive defocus), images are captured with a successively decreasing lens-surface distance. The image acquisition is stopped when the focus is well below the surface everywhere in the scanned image (negative defocus). The x_3-distance between

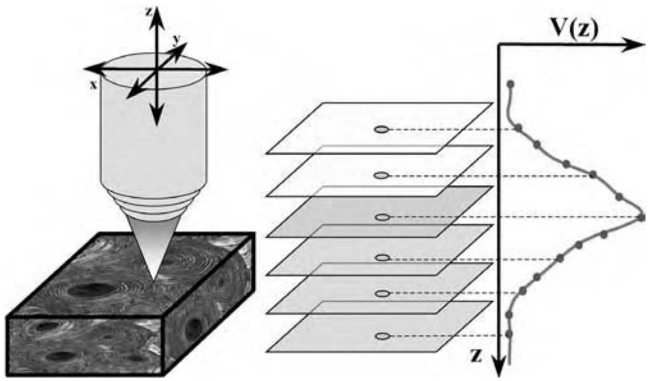

FIGURE 13.18
A high-frequency focused field, produced by an acoustic lens, is scanned in a plane parallel to the sample surface (a). For an MLA a set of C-scan images with successively decreasing distances between lens and surface is acquired (b). After interpolation in x_3 direction, the amplitude and position of the maximum in the $V(x_3)$-signal is determined for each x_1x_2-scan position (c). (From Raum et al. Multi layer analysis: Quantitative scanning acoustic microscopy for tissue characterization at a microscopic scale, *IEEE Trans.* 50, 507, 2003. With permission).

two adjacent images should be a fraction of the depth of focus of the lens. In this way it is guaranteed that each scanned surface point is measured at or close to the focus once. After resampling the data set in x_3-direction, both the focus position and the confocal amplitude are obtained for each scanned point.

These values are used to compute the two-dimensional surface topography and a topographically corrected amplitude map, respectively (Figure 13.19).

The maps were reconstructed from 17 individual C-scan images. They show a typical example of a cross section of compact bone. Large variations of the reflectivity can be particularly seen in the osteon. A three-dimensional reconstruction of the surface reflectivity in Figure 13.20 reveals that higher values in the maximum image are well correlated with a surface elevation. The average distance between two elevated lamellae is approximately 8 microns and the elevation is in the range between 1 and 2 microns. Such an increased surface roughness is not found in more homogenous regions (e.g., in the lower right secondary osteon or in the central polymethylmethacrylate [PMMA] region of the Haversian channel).

Apparently the amplitude of the reflection is reduced if the beam axis is not perpendicular to the surface. A part of the reflected waves is directed away from the transducer. The magnitude of the reflectance function usually decreases continuously until the critical angle for the total reflection of the longitudinal wave is reached. This needs to be incorporated in the impedance estimation. The local inclination angles can be assessed from the topography map. It is then possible to plot the calculated impedance of segmented regions of interest as a function of the inclination angle (Figure 13.21).

It can be seen in Figure 13.21) that oblique incidence leads to an underestimation of Z. The slopes of the curves, however, can be used to estimate

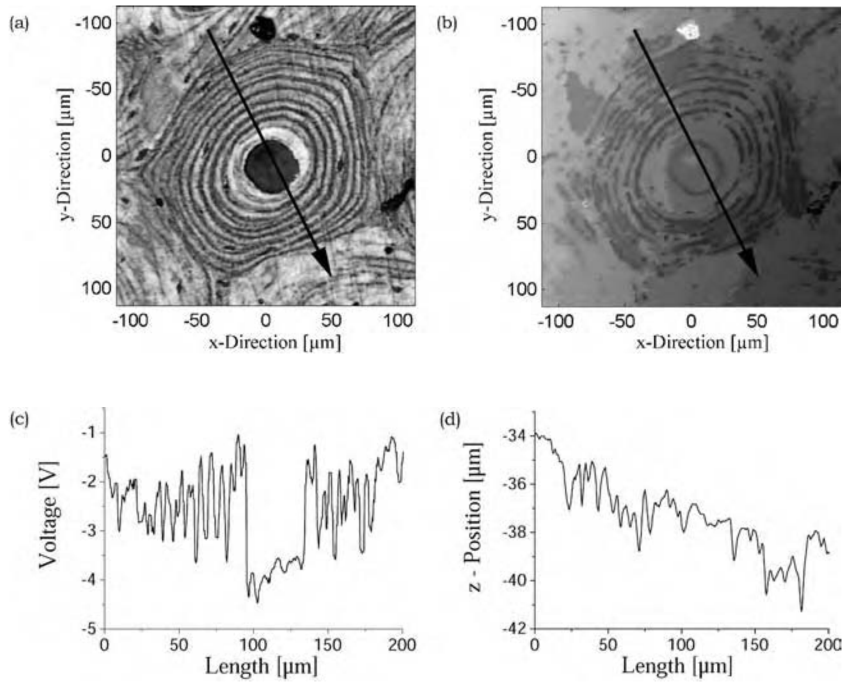

FIGURE 13.19
Maximum and topography images of an osteon (a and b). Frequency: 900 MHz. The Haversian channel (which is filled with the embedding material) in the center is surrounded by alternating lamellae of mineralized collagen fibers. Adjacent to the circular osteon fractions of less structured secondary osteons are visible. The small dark spots are cavities that used to host bone cells. The values along the plotted lines in the images are drawn below (c and d). (From Raum et al., Multi layer analysis: Quantitative scanning acoustic microscopy for tissue characterization at a microscopic scale, *IEEE Trans.* 50, 507, 2003. With permission).

the impedance values for the normal incidence condition. The error without considering the inclination angle depends on both the absolute impedance value and on the heterogeneity of the material. For the osteon shown in Figure 13.20, ignoring the local inclination angles led to an underestimation of 22.7%.

The MLA method was used to investigate anisotropy, age, and gender dependence of human cortical femur bone.[38] Statistical analysis of histograms of 900-MHz impedance maps revealed a significant anisotropy with an off-axis maximum at 15° (Figure 13.22). While the general shape of the curve is similar to that observed at lower frequencies (Figure 13.17b) and to the anisotropy of the P-wave velocity found by Turner et al.,[33] the absolute impedance values were considerably lower than those measured at lower frequencies. Inclination angles up to 10 degrees were accepted for the voltage-to-impedance conversion in this study, presumably leading to an underestimation of 10 to 15%. Structural effects and dispersion of the sound

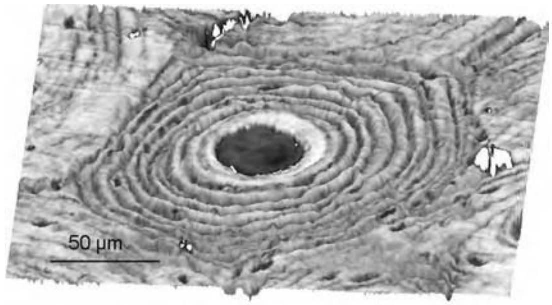

FIGURE 13.20
Three-dimensional reconstruction of the bone surface from Figure 13.19. A considerable surface roughness is visible mainly in the region of the osteon. The elevated lamellae exhibit a higher degree of reflectivity. (From Raum et al., Multi layer analysis: Quantitative scanning acoustic microscopy for tissue characterization at a microscopic scale, *IEEE Trans.* 50, 507, 2003. With permission.)

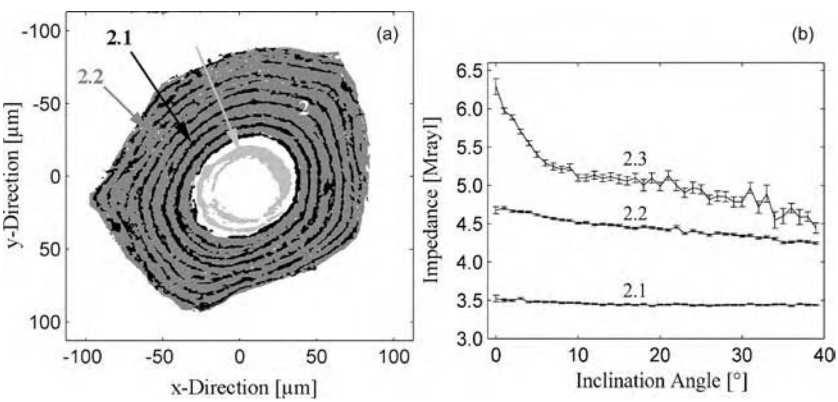

FIGURE 13.21
Segmented regions of interests (a) of the bone surface from Figure 13.19. The ROIs are: 2.1 — lamellae with low reflectivity, 2.2 — lamellae with high reflectivity, 2.3 — innermost thick lamella with very high reflectivity. Angular dependent impedance plots (mean and standard error) of the segmented substructures of the osteon (b). (From Raum et al., Multi layer analysis: Quantitative scanning acoustic microscopy for tissue characterization at a microscopic scale, *IEEE Trans.* 50, 507, 2003. With permission.)

velocity were proposed to be additional factors for the discrepancy between low- and high-frequency impedance values.

After dividing the samples into four age groups, a slight, but insignificant increase of the impedance with age was observed. The difference between the youngest and oldest groups was about 5% (Figure 13.22b). This is consistent with findings of Hasegawa et al.,[32] where the P-wave velocity in premenopausal women was about 10% lower compared with postmenopausal women.

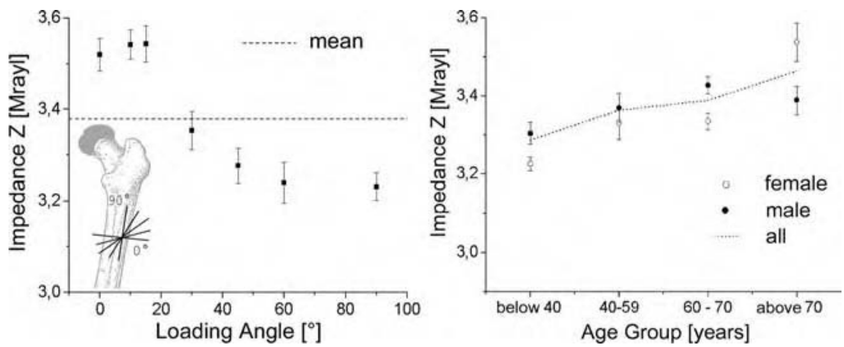

FIGURE 13.22
Anisotropy (a) and age dependence (b) of the acoustic impedance of human cortical bone. The study was conducted at 900 MHz. (From Smitmans, L. et al., *Proc. IEEE Ultrason. Symp.*, 2001, p. 1379. Copyright 2001 IEEE. With permission.)

13.3 Conclusions

Ultrasound offers many different possibilities for the evaluation of hard tissues. The acoustic wavelength can be varied over more than four orders of magnitude. Acoustic parameters (e.g., impedance, sound velocities, and attenuation) depend on the elastic interaction of the wave with the tissue. In relatively homogeneous tissues elastic parameters can easily be deduced, either from the macro- or microstructure. Carefulness is required for investigating a heterogeneous material like bone. It can be considered as a tissue compound with greatly varying mechanical properties at different levels of organization (e.g., trabeculae — bone marrow; osteon — Haversian channel; osteon lamellae with high and low mineralization, mineral — collagen), which has had considerable effects on the interaction with acoustic waves. Wavelength and beam dimensions have to be conscientiously adjusted to the tissue level under inspection.

References

1. Langton, C.M., Palmer, S.B., and Porter, R.W., The measurement of broadband ultrasonic attenuation in cancellous bone, *Eng. Med.*, 13, 89, 1984.
2. Laugier, P., Giat, P., and Berger, G., Broadband ultrasonic attenuation imaging: a new imaging technique of the os calcis, *Calcif. Tissue Int.*, 54, 83, 1994.
3. Laugier, P., Fournier, B., and Berger, G., Ultrasound parametric imaging of the calcaneus: *in vivo* results with a new device, *Calcif. Tissue Int.*, 58, 326, 1996.

4. Evans, J.A. and Tavakoli, M.B., Ultrasonic attenuation and velocity in bone, *Phys. Med. Biol.*, 35, 1387, 1990.
5. Strelitzki, R., Clarke, A.J., and Evans, J.A., The measurement of the velocity of ultrasound in fixed trabecular bone using broadband pulses and single-frequency tone bursts, *Phys. Med. Biol.*, 41, 743, 1996.
6. Alves, J.M., Xu, W., Lin, D. et al. Ultrasonic assessment of human and bovine trabecular bone: a comparison study, *IEEE Trans. Biomed. Eng.*, 43, 249, 1996.
7. Bauer, D.C., Gluer, C.C., Genant, H.K., and Stone, K., Quantitative ultrasound and vertebral fracture in postmenopausal women. Fracture Intervention Trial Research Group, *J. Bone Miner. Res.*, 10, 353, 1995.
8. Bauer, D.C., Gluer, C.C., Cauley, J.A. et al. Broadband ultrasound attenuation predicts fractures strongly and independently of densitometry in older women. A prospective study. Study of Osteoporotic Fractures Research Group, *Arch. Intern. Med.*, 157, 629, 1997.
9. Bauer, D.C., Sklarin, P.M., Stone, K.L. et al. Biochemical markers of bone turnover and prediction of hip bone loss in older women: the study of osteoporotic fractures, *J. Bone Miner. Res.*, 14, 1404, 1999.
10. Bouxsein, M.L. and Radloff, S.E., Quantitative ultrasound of the calcaneus reflects the mechanical properties of calcaneal trabecular bone, *J. Bone Miner. Res.*, 12, 839, 1997.
11. Chappard, C., Laugier, P., Fournier, B. et al. Assessment of the relationship between broadband ultrasound attenuation and bone mineral density at the calcaneus using BUA imaging and DXA, *Osteoporos. Int.*, 7, 316, 1997.
12. Hans, D., Dargent-Molina, P., Schott, A.M. et al. Ultrasonographic heel measurements to predict hip fracture in elderly women: the EPIDOS prospective study, *Lancet*, 348, 511, 1996.
13. Nicholson, P.H., Muller, R., Lowet, G. et al. Do quantitative ultrasound measurements reflect structure independently of density in human vertebral cancellous bone?, *Bone*, 23, 425, 1998.
14. Njeh, C.F., Kuo, C.W., Langton, C.M. et al. Prediction of human femoral bone strength using ultrasound velocity and BMD: an *in vitro* study, *Osteoporos. Int.*, 7, 471, 1997.
15. Blake, G.M., Gluer, C.C., and Fogelman, I., Bone densitometry: current status and future prospects, *Br. J Radiol.*, 70 Spec No. S177-S186, 1997.
16. Genant, H.K., Engelke, K., Fuerst, T. et al. Noninvasive assessment of bone mineral and structure: state of the art, *J. Bone Miner. Res.*, 11, 707, 1996.
17. Gluer, C.C., Quantitative ultrasound techniques for the assessment of osteoporosis: expert agreement on current status. The International Quantitative Ultrasound Consensus Group, *J. Bone Miner. Res.*, 12, 1280, 1997.
18. Gluer, C.C., Barkmann, R., and Heller, M., Quantitative ultrasound. State of the art 1999, *Radiologe*, 39, 213, 1999.
19. Langton, C.M. and Njeh, C.F., Acoustic and ultrasonic tissue characterization: assessment of osteoporosis, *Proc. Inst. Mech. Eng.*, 213, 261, 1999.
20. Laugier, P., Berger, G., and de Vernejoul, M.C., Bone remodeling: evaluation methods, *Rev. Prat.*, 48, 1185, 1998.
21. Kino, G.S., *Acoustic Waves: Devices, Imaging and Analog Signal Processing*, Prentice Hall, Englewood Cliffs, NJ, 1987.
22. Briggs, G.A., *Acoustic Microscopy*, Clarendon Press, Oxford, 1992.

23. Maev, R.G., Denisova, L.A., Maeva, E.Y., and Denissov, A.A., New data on histology and physico-mechanical properties of human tooth tissue obtained with acoustic microscopy, *Ultrasound Med. Biol.*, 28, 131, 2002.
24. Mezawa, S., Kawato, T., Yoshida, K. et al. Evaluation of human tooth structure with the ultrasonic imaging technique, *J. Oral Sci.*, 41, 191, 1999.
25. Peck, S.D. and Briggs, G.A., A scanning acoustic microscope study of the small caries lesion in human enamel, *Caries Res.*, 20, 356, 1986.
26. Peck, S.D., Rowe, J.M., and Briggs, G.A., Studies on sound and carious enamel with the quantitative acoustic microscope, *J. Dent. Res.*, 68, 107, 1989.
27. Kushibiki, J., Ha, K.L., Kato, H. et al. Application of acoustic microscopy to dental material characterization, *Proc. IEEE Ultrason. Symp.*, New York, 1987, p. 837.
28. Weiner, S. and Wagner, H.D., The material bone: Structure mechanical function relations, *Ann. Rev. Mat. Sci.*, 28, 271, 1998.
29. Hasegawa, K., Turner, C.H., and Burr, D.B., Contribution of collagen and mineral to the elastic anisotropy of bone, *Calcif. Tissue Int.*, 55, 381, 1994.
30. Takano, Y., Turner, C.H., and Burr, D.B., Mineral anisotropy in mineralized tissues is similar among species and mineral growth occurs independently of collagen orientation in rats: results from acoustic velocity measurements, *J. Bone Miner. Res.*, 11, 1292, 1996.
31. Takano, Y., Turner, C.H., Owan, I. et al. Elastic anisotropy and collagen orientation of osteonal bone are dependent on the mechanical strain distribution, *J. Orthop. Res.*, 17, 59, 1999.
32. Hasegawa, K., Turner, C.H., Recker, R.R. et al. Elastic properties of osteoporotic bone measured by scanning acoustic microscopy, *Bone*, 16, 85, 1995.
33. Turner, C.H., Chandran, A., and Pidaparti, R.M., The anisotropy of osteonal bone and its ultrastructural implications, *Bone*, 17, 85, 1995.
34. Turner, C.H., Rho, J.Y., Takano, Y. et al. The elastic properties of trabecular and cortical bone tissues are similar: results from two microscopic measurement techniques, *J. Biomech.*, 32, 437, 1999.
35. Jorgensen, C.S. and Kundu, T., Measurement of material elastic constants of trabecular bone: a micromechanical analytic study using a 1 GHz acoustic microscope, *J. Orthop. Res.*, 20, 151, 2002.
36. Raum, K., Reißhauer, J., and Brandt, J., Frequency dependence of the anisotropic impedance estimation in cortical bone using time-resolved scanning acoustic microscopy, Proc. IEEE Ultrason. Symp., Munich, 2002, p. 1269.
37. Raum, K., Jenderka, K.V., Klemenz, A., and Brandt, J., Multi layer analysis: Quantitative scanning acoustic microscopy for tissue characterization at a microscopic scale, *IEEE Trans. Ultrason., Ferroelect., Freq. Contr.*, 2002.
38. Smitmans, L., Raum, K., Brandt, J. et al. Variations in the microstructural acousto-mechanical properties of cortical bone revealed by a quantitative acoustic microscopy study, *Proc. IEEE Ultrason. Symp.*, San Juan, Puerto Rico, 2001, p. 1379.

14

Clinical Applications of Ultrasonic Nondestructive Evaluation

Yoshifumi Saijo

CONTENTS

14.1 History of Medical Ultrasound

Applications of ultrasound started as underwater detection systems. Sound navigation and ranging (SONAR) systems were developed after the Titanic sank in 1912 and, during World Wars I and II, for submarine navigation. Pulsed echo ultrasound was developed as metal flaw detectors for integrity of metal hulls of large ships and tanks. The history of ultrasound was related to tragedies in those days.

After World War II, the applications of ultrasound dramatically changed direction to avoid tragedies; it was now used in medical applications. Subsequent development of the instruments made it possible to use higher frequency of ultrasound with shorter pulse durations. These refinements resulted in finer resolution to detect smaller targets. The development of

0-8493-1462-3/02/$0.00+$1.50

high-input impedance amplifiers helped to improve the sensitivity and stability of signals.

Dussik, a neurologist at the University of Vienna, was generally regarded as the first physician to employ ultrasound in medical diagnosis. In 1942, he located brain tumors and the cerebral ventricles by measuring the transmission of an ultrasound beam through the skull.[1]

The finer-resolution flaw-detection systems became the precursor of pulse-echo medical ultrasonic devices. In the early 1950s, the unidirectional A-mode started to be used to examine brain lesions. Edler and Hertz in Lund, Sweden, began to employ metal flaw detectors for cardiac investigation in 1953.[2] Researchers in Japan were also actively investigating, but their findings have been sparsely documented in the English-language literature. Japan's first A-mode scanner was built in 1949 from a modified metal flaw-detector.[3] In 1952, Wagai at Juntendo University, Tokyo, together with Kikuchi at Tohoku University, Sendai, Japan, reported on the detection of intracerebral hematomas and tumors.[4] In the era of A-mode devices, Wild[7] at the Medico Technical Research Institute reported that patterns of A-mode spikes were different according to the malignancy of breast tumors, not just the thickness of tissues.[5,6] This concept later led to ultrasonic tissue characterization.

In 1952, Wild and Reid reported on a linear, manually scanned, handheld B-mode (B standing for brightness) instrument to visualize a breast tumor.[7] They named the imaging device *echography* and it marked the beginning of long history of echography.

Howry and Bliss had also started pioneering ultrasonic investigations.[8] They invented the immersion tank ultrasound system, the first two-dimensional B-mode linear compound scanner in 1951. The patient was immersed in water and the transducer was mechanically scanned around the patient.

Some important developments also took place in the 1970s. Among them were the grayscale with the scan converter and the real-time B-mode scan.

The B-scan in the early days used threshold detection. In 1973, Kossoff et al. published the new analog scan converter with grayscale capabilities.[9] They also demonstrated that the different magnitude of the echoes came from the internal texture of soft tissues. This finding was the evidence that ultrasound could be used for tissue characterization and was what Wild had proposed 20 years before. The echo was not only reflected from the interfaces, but also from the smaller structures of biological materials. In the late 1970s, several reports on the digital scan converter were published from Australia and Japan.

Real-time imaging is also an important technical innovation for medical ultrasonic practice. Besides the improvement of the image quality, real-time imaging is the most important feature of medical ultrasound compared with other imaging modalities of today. The first real-time scanner was manufactured by Siemens Medical Systems of Germany in 1965. Siemens equipped three rotating transducers housed in front of a parabolic mirror in a water-coupling system to realize a real-time scan with 15 ft/sec.

The concept of multielement linear electronic arrays was first described in 1964. In 1971, Uchida et al., at Aloka, published (in Japanese) that they had produced a prototype array system with a frame rate of 17 ft/sec.[10] Bom et al., at Erasmus University in the Netherlands ,produced the world's first commercially available and notable linear array transducer for cardiac investigation in 1972.[11,12]

The early array systems were large because they equipped probes housing an array of some 64 transducer elements arranged in a linear row that operated with sequential electronic switching. The phased-array scanning mechanism was first described by Somer at the University of Limberg in 1968.[13] After the introduction of phased-array and convex-array transducers, the ultrasonic diagnostic systems had become portable.

The M-mode (time–motion, M standing for motion) display was first described by Edler and Hertz in 1954[2] and marked the beginning of echocardiography. They equipped a modified metal-flaw detector and demonstrated the feasibility of recording cardiac valvular motion. Although the early M-mode investigations provided important information on cardiac motion, the methods were blind procedures. In the early 1970s, the two-dimensional B-mode was developed, and the M-mode was used with it to detect the location.

The Doppler principle was first described by Doppler in Austria in 1842. He observed that the color of stars and the changes in their color (i.e., the change of the frequency) were made from the difference of propagating velocities between the observer and observed object. Ultrasonic Doppler techniques were first implemented by Nimura and Satomura in Osaka, Japan, in 1955. They used the technique for the study of cardiac valvular motion and peripheral vessel pulsations. Their group also equipped the Doppler technique to detect blood flow because blood was considered as a suspension of point backscatters with varying density and compressibility. Baker developed a pulsed Doppler system in 1970.[14] The concept was based on the repetitive propagation of short ultrasound bursts, and analysis of the signal received at a preselected time delay with respect to emission. The technique helped to determine the blood flow from Doppler velocity measurements. Combining two-dimensional grayscale imaging and pulsed Doppler signal acquisition, the duplex scanner was developed in 1974.

In 1981, Brandestini, at the University of Washington, obtained two-dimensional color images using a 128-point multigated pulsed Doppler system, where velocity waveforms and flow images were encoded in color and superimposed on M-mode and two-dimensional grayscale images.[15] Around the same time, Namekawa et al., at Aloka, were developing a phase-detector system. They used a phase detector based on an autocorrelation technique in which the changing phase of the received signal gave information about changing velocity along the ultrasonic beam.[16] This approach provided real-time frequency estimation and is still used in color flow mapping today. Aloka produced its first commercially available color flow mapping in 1984.[17]

In the 1990s, there were significant improvements in imaging. One improvement was that the beamformer and signal processing stages were changed from analog circuit to digital processing because of the development of very powerful computers.

Another development was that the broadband, wide-aperture transducers improved definition of tissue textures and dynamic range. The number of channels in high-end systems is up to 256 to make wide-aperture transducers. Beam width is determined by the following equation:

$$BD = \frac{1.02Fc}{fD} \quad \textbf{(14.1)}$$

where

BD = beam width,
F = focus length,
c = sound speed,
f = frequency, and
D = aperture.

Both wider aperture and higher frequency of ultrasound enabled a sharper ultrasonic beam, leading to improvements in lateral resolution.

The recent development in image quality improvements has been tissue harmonic imaging. Generation of harmonic frequencies occurs when an ultrasound wave propagates through tissue. This harmonic frequency ultrasound reduces near-field and side robe artifacts.

14.2 Basic Principles of Clinical Echography

The technique for displaying echo motion utilizes intensity modulation. This type of modification converts the amplitude of the echo to intensity; the signal is converted from a spike (A-mode) to a dot (B-mode). This presentation is known as B-mode, the B standing for brightness. Figure 14.1 is an example of A-mode and B-mode presentations of one scan line. Having converted the signal to a dot, another dimension available for the recording develops. Because the heart is a moving object, one can record the motion by introducing time as the second dimension. The term for this type of echo presentation is M-mode.

Ultrasonic scans can be obtained in various ways. Figure 14.2 demonstrates some types of scans available in medical diagnostic settings. The linear scan is the first real-type scan and is still used for the body surface (carotid artery, thyroid, breast) organs. As the echo window for the heart is narrow because it must be through the ribs, the sector scan is usually equipped for cardiac examination. For abdominal organs, the convex scan is most popular because it has both usability and good quality of images.

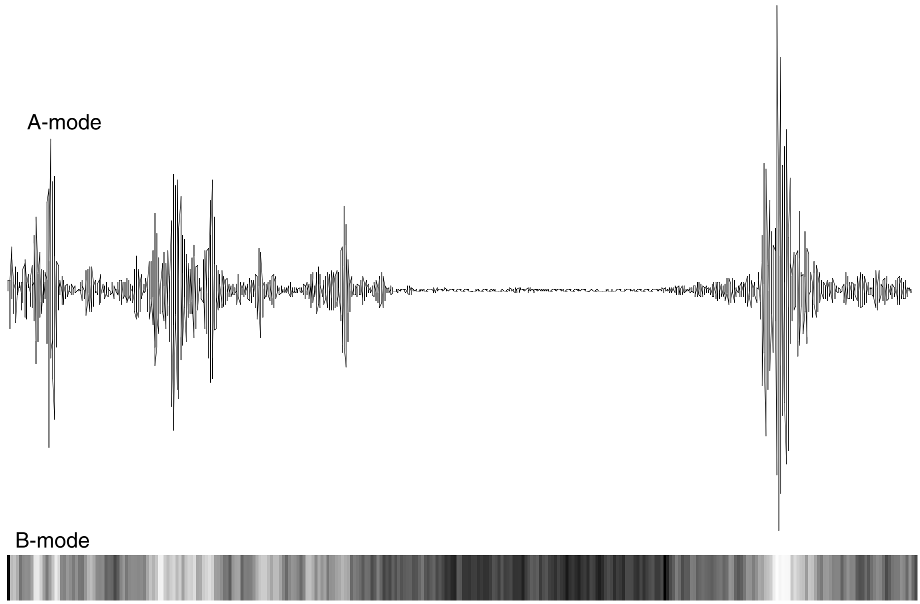

FIGURE 14.1
Schematic illustration of A-mode presentation and grayscale B-mode presentation.

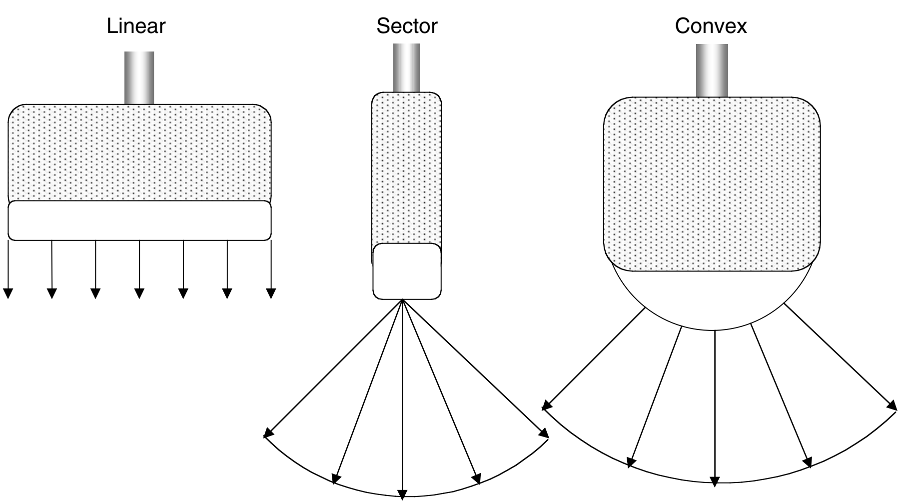

FIGURE 14.2
Types of scan frequently used in clinical settings.

Another important technology is Doppler ultrasound. The Doppler examination is based on the Doppler effect. If a source of sound is stationary, then the wavelength and frequency of the sound emanating from the source are constant. If the source of the sound is moving toward one's ear, then the wavelength is decreasing and the frequency is increasing. If the source of sound moves away from the ear, then the wavelength is increasing and the frequency is decreasing. Figure 14.3 demonstrates the Doppler effect using reflected sound from a target. The reflected frequency (f_r) is greater than the transmitted frequency (f_t) when the target is moving toward the transducer. The reflected frequency is smaller than the transmitted frequency when the target moves away from the transducer. The Doppler shift can be calculated from the following equations:

$$f_d = f_r - f_t \tag{14.2}$$

$$f_d = 2f_t \frac{v \cdot \cos\theta}{c} \tag{14.3}$$

where

f_d = Doppler shift frequency
f_r = received frequency
f_t = transmitted frequency,
θ = the angle between the direction of the moving target and the path of the ultrasonic beam
c = sound speed

The advantage of the pulsed Doppler system is that one has the ability to obtain an M-mode or two-dimensional image as with any other pulsed ultrasonic device. A pulsed Doppler system can obtain a Doppler signal from a specific area of the cardiovascular system. The major disadvantage of the pulsed Doppler system is that the velocity one can measure is limited. The pulsed system inherently has a pulse repetition frequency (PRF). The PRF determines how high a Doppler frequency the pulse system can detect. The upper limit of frequency that can be detected with a given pulsed system is known as the *Nyquist* limit or number. The inability of a pulsed Doppler system to detect high-frequency Doppler shifts is known as *aliasing*. Aliasing occurs when the Doppler shift is larger than half of the PRF. Then the Nyquist number is expressed as

$$Nyquist\ number = \frac{PRF}{2} \tag{14.4}$$

Maximum velocity is also determined by the carrier frequency and range of the region of interest.

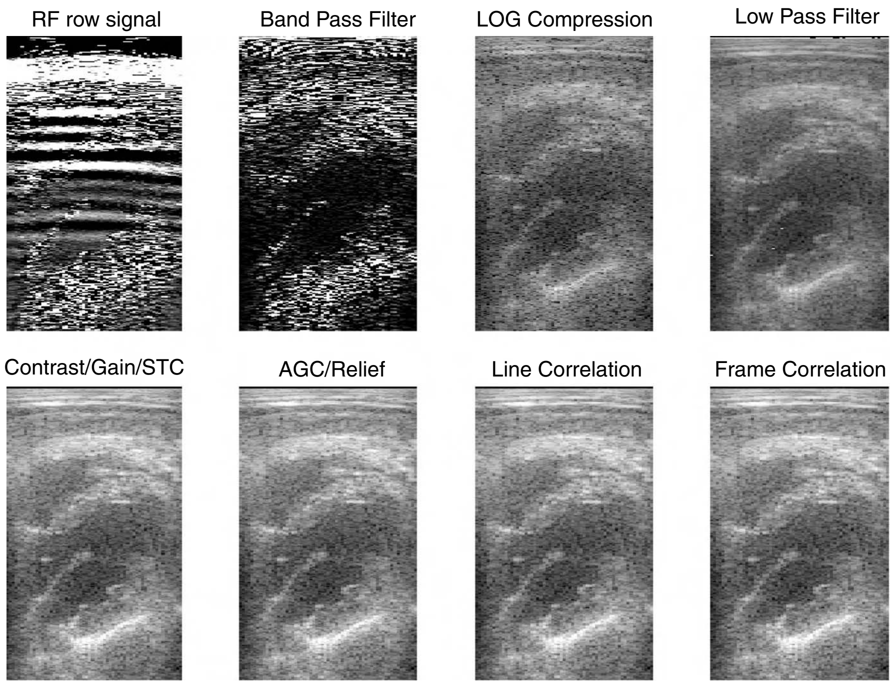

FIGURE 14.3
Schematic illustration of the Doppler effect.

$$v_m = \frac{c^2}{8 f_0 R} \tag{14.5}$$

where
v_m = maximum velocity
f_0 = carrier frequency
R = range

Doppler echocardiography provides other information that M-mode or B-mode echocardiography does. It can measure blood flow if one knows the mean velocity of flow (v) and the cross-sectional area (A) of the vessel or orifice through which the blood is flowing:

$$Cardiac\ output = A \times v \times HR \tag{14.6}$$

where
A = area,
v = mean velocity,
HR = heart rate.

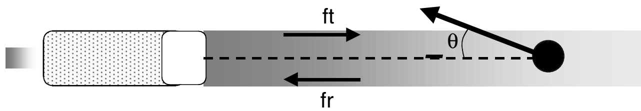

FIGURE 14.4
Pulsed Doppler method and calculation of blood flow volume.

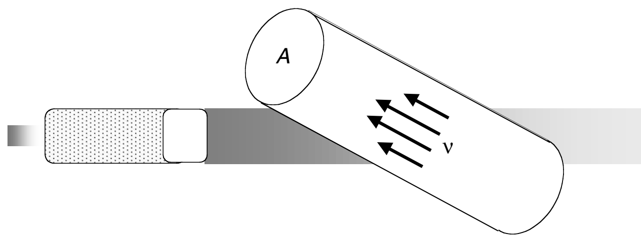

FIGURE 14.5
Continuous Doppler method and calculation of pressure drop at the stenosis.

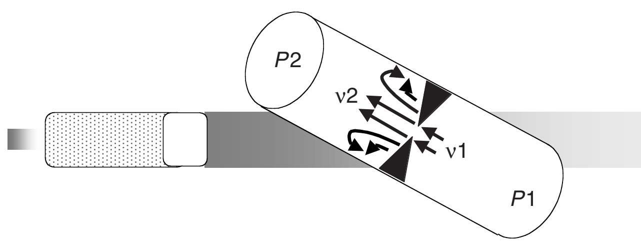

FIGURE 14.6
An example of image processing.

Figure 14.4 shows the schematic illustration of the blood flow volume derived from the flow velocity and area of rube-like structure.

Pressure drop or pressure gradient is assessed by the following:

$$P_1 - P_2 = \frac{1}{2}\rho\left(v_2^2 - v_1^2\right) + \rho\int_1^2 \frac{DV}{DT} + R(v) \tag{14.7}$$

$$P_1 - P_2 = \frac{1}{2}\rho\left(v_2^2 - v_1^2\right) \approx 4v_2^2 \tag{14.8}$$

where

P_1 = pressure proximal to obstruction
P_2 = pressure distal to obstruction

v_1 = velocity proximal to obstruction
v_2 = velocity distal to obstruction
ρ = density of blood (1.06×10^3 kg/m^3)

Figure 14.5 shows the schematic illustration of pressure drop. The velocity of the main stream is increased downward the stenosis, and many small eddies around the main stream are generated.

Today, a B-mode image is generated by the following processes. First, a band pass filter is used for the raw radio frequency (RF) signal. Then the signal is compressed logarithmically, and a low pass filter is applied to exclude the noise. The contrast, gain, and sensitivity time control (STC) effects and other smoothing techniques (i.e., line correlation, frame correlation) are added to improve the image. Figure 14.6 shows an example of image processing.

14.3 Examples of Clinical Images

Clinical images are shown in Figure 14.7 through Figure 14.12. Figure 14.7 shows an example of a B-mode image of a human liver. A high-intensity echo is represented in white, while a low echo is represented in black in standard B-mode images. In this figure, the gray dotted zone indicates the liver; the black, sonolucent zone indicates the hepatic veins. Figure 14.8 is an example of a human heart. The transducer is placed on the left margin of the sternum, and ultrasound beams are transmitted through the rib. This is a long axis view of the heart.

Figure 14.9 is an example of B-mode and M-mode images focused on the mitral valve. Time series displacement of the echo on the cursor is represented in an M-mode image. The trace of the mitral valve in the M-mode image is M-shaped. The M-mode image was the only method to display heart or valvular motion on a static picture until the B-mode movie was easily recorded on videotape.

Figure 14.10 is an example of color flow mapping. Usually, blood flow toward the transducer is represented in red, and blood flow away from the transducer is represented in blue. Turbulent flow is often represented as mosaic pattern of color flow mapping because the turbulent flow contains various vectors and scalars of flow. The left image was recorded in the systolic phase and the blood flow toward the aorta from the left ventricle is represented in blue. The regurgitation jet fromthe left ventricle to the left atrium is represented in a mosaic pattern. The right image was recorded in the diastolic phase, and aortic regurgitation is represented in red and a mosaic pattern.

Figure 14.11 is an example of color flow mapping and pulsed Doppler signal at the cursor. The cursor is located between the tips of the mitral valve. The flow pattern shows an M-shape like M-mode of the mitral valvular movement.

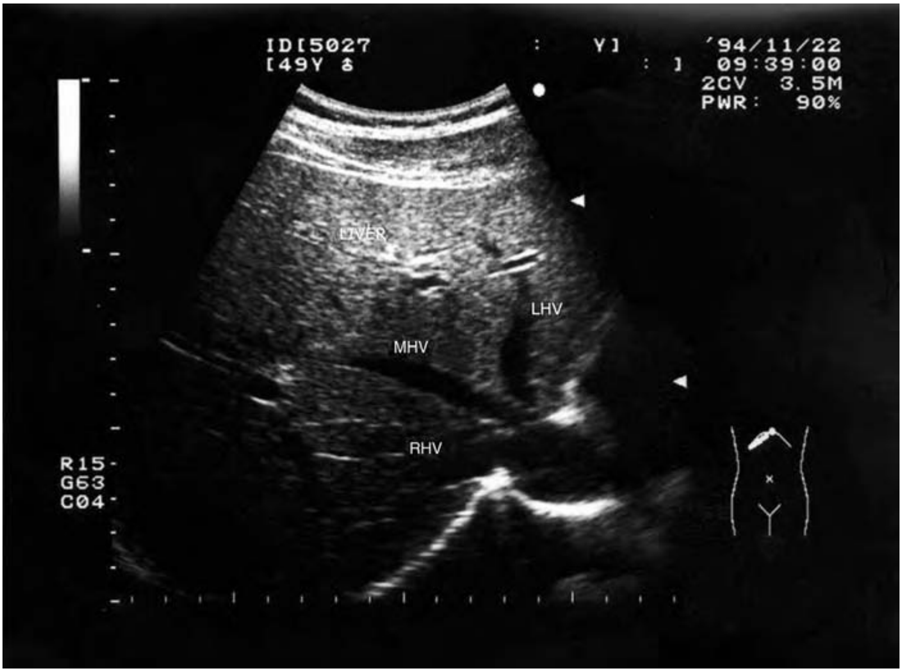

FIGURE 14.7
B-mode echogram of normal liver (LHV: left hepatic vein; MHV: main hepatic vein; RHV: right hepatic vein).

The pulsed Doppler spectrum is the velocity profile at the region of interest (ROI).

Figure 14.12 is an example of color flow mapping and a continuous wave Doppler (CWD) signal in a case of aortic valvular stenosis. CWD uses a continuous wave to detect the maximum velocity along the ultrasonic beam. CWD is mainly used to measure the higher velocity that pulsed Doppler can measure. In stenotic valvular diseases and regurgitation flow, the maximum velocity exceeds more than 300 cm/sec. By applying Bernouli's law, pressure gradient over the stenosis can be assessed by a simple equation, as shown in Chapter 14, Equation 14.8.

In this case, the maximum velocity of aortic root is 347 cm/sec and the pressure gradient between the left ventricle and the aorta is calculated as 48.0 mmHg. The severity of valvular stenosis here is assessed as moderate.

Both B-mode and M-mode demonstrate wall and valvular motion of the heart, while Doppler techniques show the blood flow velocity. With the combination of these ultrasound techniques and other physiological data, cardiac function can be assessed noninvasively, providing great information to cardiologists.

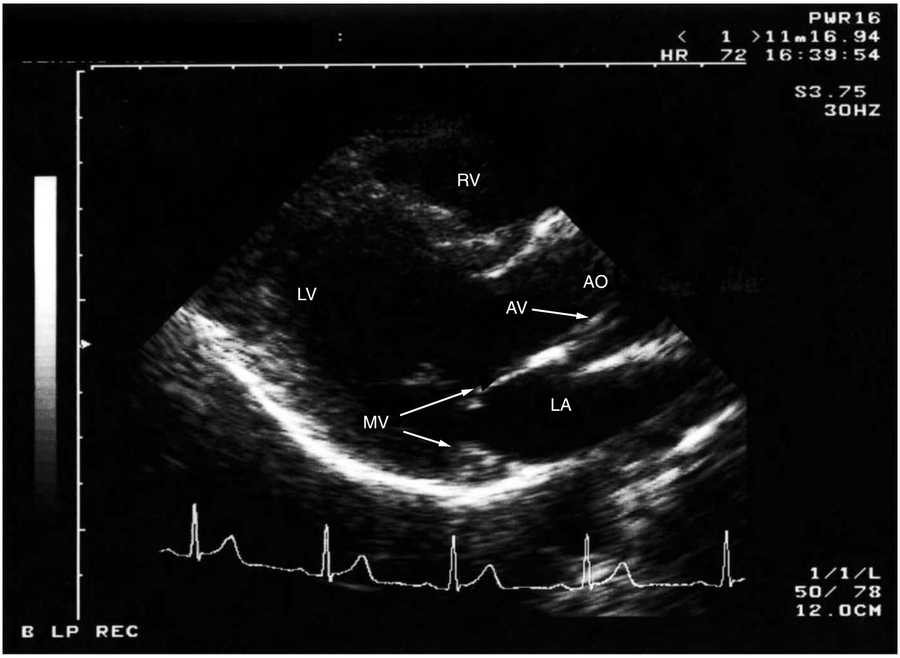

FIGURE 14.8
B-mode echocardiogram of normal heart in left parasternal long axis view (LV: left ventricle; RV: right ventricle; LA: left atrium; AO: aorta; MV: mitral valve; AV: aortic valve).

14.4 Ultrasonic Tissue Characterization at Lower Frequencies

At the dawn of echo in the 1950s, Wild described that the reflection pattern could be used for tissue characterization. The echo is not only produced at the boundary of different acoustic impedance, but it is also produced in the tissue. Thus, the echo from inside the tissue is related to the chemical components and mechanical structure of the biological tissue.

In 1964, Tanaka and colleagues, at Tohoku University,[48,49] found that the intensity of the echo from human myocardium changed during one cardiac cycle. The sensitivity changing method was used to semiquantitatively evaluate the echo intensity. They assumed that the highest echo came from the epicardium of the left ventricular posterior wall, and the lowest intensity echo came from the blood in the left ventricular cavity. The difference in intensity between the tissue and the epicardium was measured by changing the total gain. They also applied this technique to characterize abnormal granular echoes in hypertrophic cardiomyopathy. The intensity was highest in the diastolic phase and lowest in the systolic phase of the cardiac cycle.

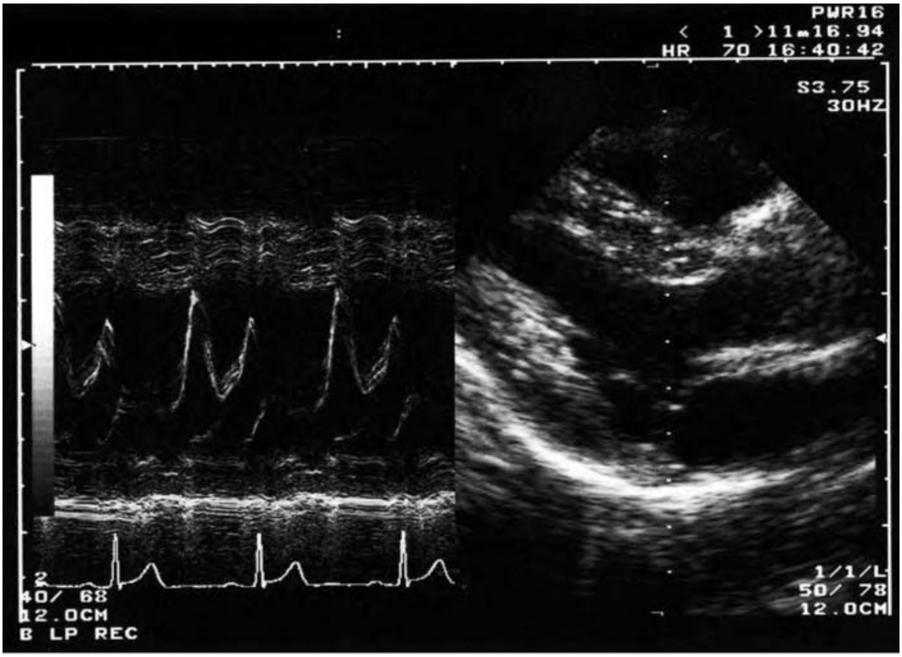

FIGURE 14.9
B-mode and M-mode echocardiograms of the mitral valve.

In the 1980s, the technique to detect the phasic change of echo intensity was refined by Mimbs et al. at the University of Washington.[18,19] As shown in the upper column in Figure 14.5, the RF signal contains both plus and minus components. If the signal is simply averaged, the result becomes zero. Then the envelope of the RF signal is drawn and the envelope is logarithmically compressed by an analog circuit in conventional ultrasound machines. The group performed FFT analysis before the raw RF signal went through these circuits. The intensity in the frequency domain was integrated, and they determined the value as the integrated backscatter to analyze the echo intensity of myocardium quantitatively. In other words, the method is to increase the sensitivity of intensity by reducing the sensitivity of axial resolution. This technique can measure the change of intensity very precisely; it can assess the viability of myocardium from other views of conventional wall motion analysis; they also found it useful in detecting stunned myocardium after myocardial infarction.

Figure 14.13 is an example of integrated backscatter imaging. This short-axis view of the left ventricle was recorded at the weaning from extracorporeal circulation during cardiac surgery. The myocardial function has already recovered, but the myocardium does not move because the left ventricle has not yet been filled with blood. The region of interest is placed on a papillary muscle

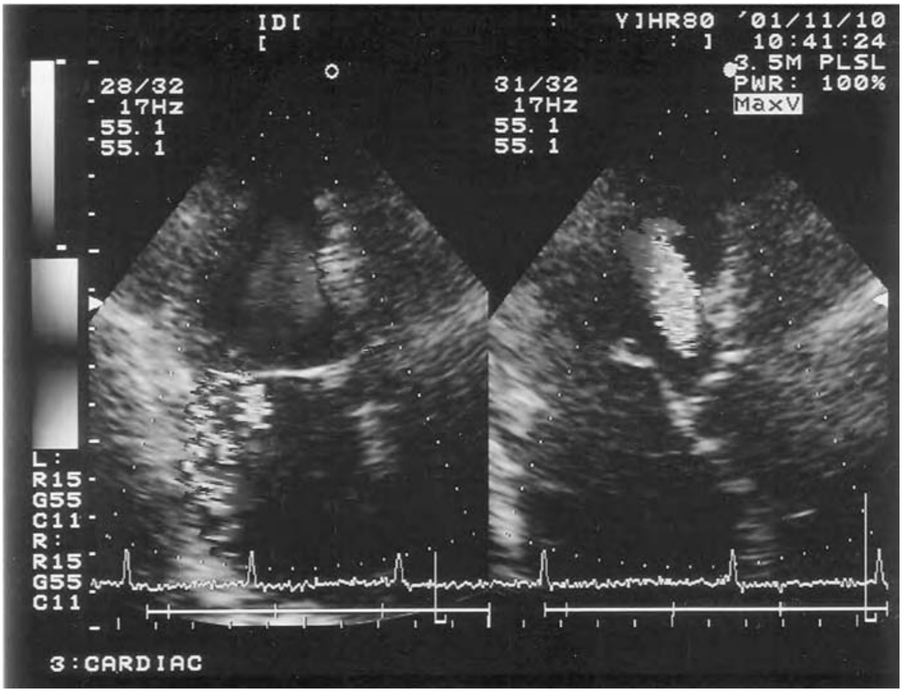

FIGURE 14.10
Two examples of color flow mapping (left: mitral regurgitation; right: aortic regurgitation).

of the left ventricle and the cyclic variation of backscatter is shown in the graph. The value increased in diastolic phase and decreased in systolic phase, showing the viability has already recovered in spite of poor wall motion.

Baba et al., at the University of Tokyo, first reported on a three-dimensional ultrasound system in 1984, and succeeded in obtaining three-dimensional fetal images by processing the raw two-dimensional images in 1989.[20] It took a long time to obtain data and generate three-dimensional images because a surface-rendering algorithm was employed for the three-dimensional reconstruction. Recently, very powerful computers and the volume-rendering technique have enabled nearly real-time three-dimensional reconstruction.

Figure 14.14 is an example of reconstructed three-dimensional ultrasound image of aortic valve of a patient with dissecting aortic aneurysm. The tear is clearly shown and the geometry of aortic valve can be assessed precisely.

In 1991, a group of researchers at Duke University produced a matrix array scanner that could image cardiac structure in three-dimensional real-time.[21,22] Similar attempts have been made in several companies, and commercially available real-time three-dimensional ultrasound machines are available today.

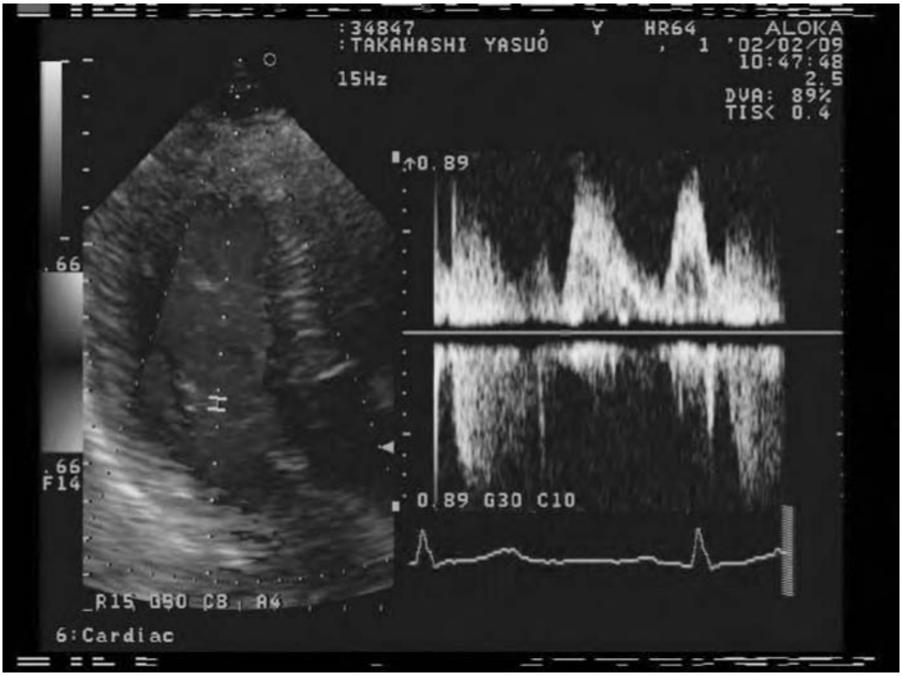

FIGURE 14.11
Color flow mapping and pulsed Doppler signal between the tips of the mitral valve.

14.5 Intravascular Ultrasound

Intravascular ultrasound (IVUS) has been clinically applied since the early 1990s. It has become an important clinical tool in investigation, especially the investigation of the coronary artery during interventional cardiology procedures. IVUS uses radial scan, and there are two types of systems available today. One is the rotating transducer with a frequency range of 30 to 40 MHz, and the other is the phased-array transducer with a frequency range of 20 MHz. IVUS is mainly used to measure the luminal area and expansion of the stent. IVUS has also provided important clinical aspects on coronary arterial remodeling.

Recently, some techniques of ultrasonic tissue characterization have been reported. Jeremias et al. measured the attenuation in the adventitia of normal and allograft aorta.[23] The attenuation was smaller in the area of allograft when rejection occurred. Schartl et al. used IVUS for evaluation of effect of lipid-lowering therapy on regression of atherosclerosis in the coronary artery.[24] Angiographically normal and ultrasonically atherosclerotic lesions were observed before and after the treatment. Six months after the first observation, the coronary artery was again examined by IVUS. The plaque

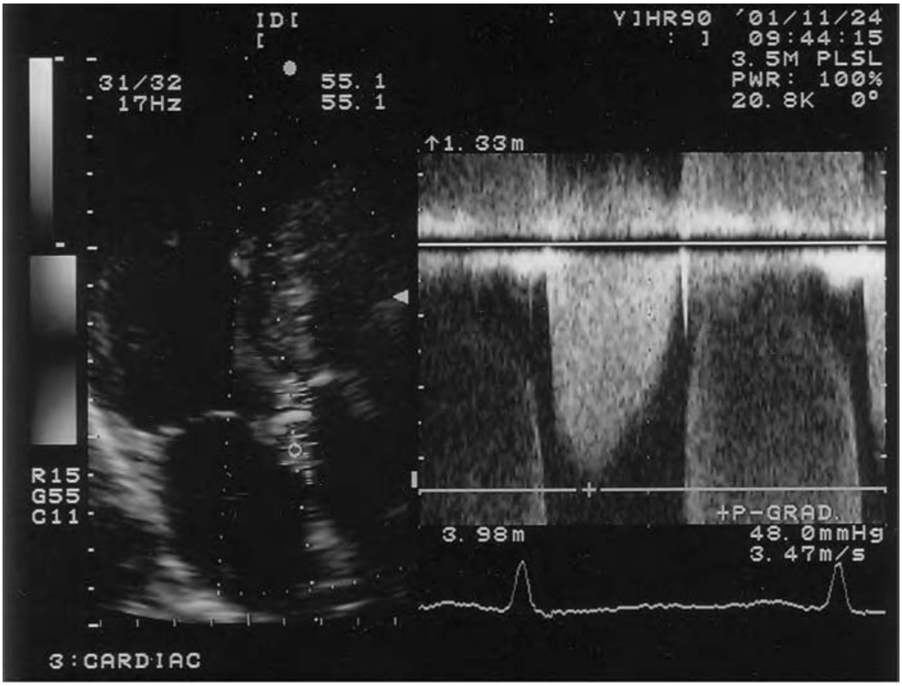

FIGURE 14.12
Color flow mapping and continuous Doppler signal at the aortic valve.

volume was not changed significantly, but the intensity of the soft plaque increased significantly. This result suggests that atherosclerotic plaque was stabilized by lipid-lowering therapy. This is an example showing that ultrasonic tissue characterization is more sensitive than the conventional use of ultrasound for measuring dimensions of the artery.

These two analyses were based on the static character of the tissue. Because the coronary artery is always receiving blood flow and blood pressure, the dynamic characteristics of the artery were also examined. A group of researchers at Erasmus University led by van der Steen developed vascular elastography technique using phased array IVUS.[25] The RF signal from the IVUS transducer was digitized and the correlation and change of two consecutive frames were analyzed. The luminal pressure was also measured. As the displacement was caused by luminal pressure, tissue elasticity can be assessed by dividing the displacement by pressure change. We have developed a similar technique using a rotating probe. Figure 14.15 is an example of the normal IVUS image and tissue elasticity image showing a clear internal border and inhomogeneous plaque composition. In this case, a directional coronary atherectomy (DCA) procedure was performed to cut the plaque specimen from the coronary artery. The optical image shows the stable region with collagen fibers and vulnerable regions with foam cell

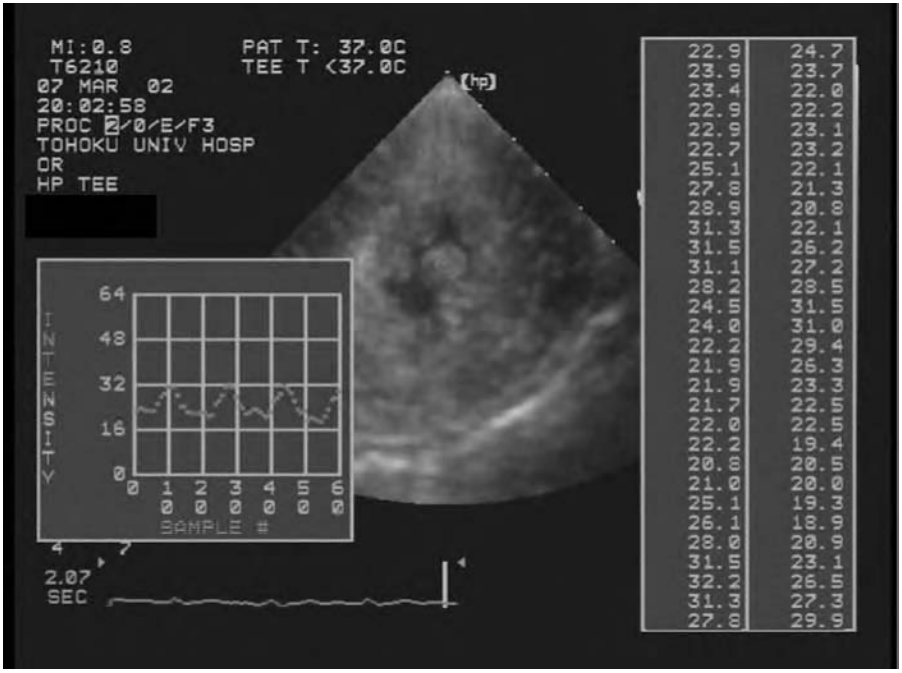

FIGURE 14.13
Integrated backscatter image of the left ventricle in the short axis view. ROI is placed at the papillary muscle of the left ventricle. The graph represents the cyclic variation of the integrated backscatter of ROI.

infiltration. These techniques suggest that IVUS provides microscopic pathology of the coronary artery.

14.6 Biomedical Application of Acoustic Microscopy

Tohoku University has been applying scanning acoustic microscopy (SAM) in medicine and biology since 1980.[26–27] Several objectives for using SAM for medicine and biology are described below.

First, SAM can be applied for intraoperative pathological examination since it does not require a special staining technique. A group of researchers at University of California at Irvine determined that an obtainable resolution of 600 MHz SAM was sufficient to render a microscopic diagnosis.[28,29] We have shown that SAM can also classify the types of cancer in the stomach[30] and kidney[31] by quantitative measurement of ultrasonic attenuation and sound speed at 200 MHz.

Second, ultrasonic data obtained with high-frequency SAM can be used for assessing reflectability or texture in clinical echographic imaging. Density

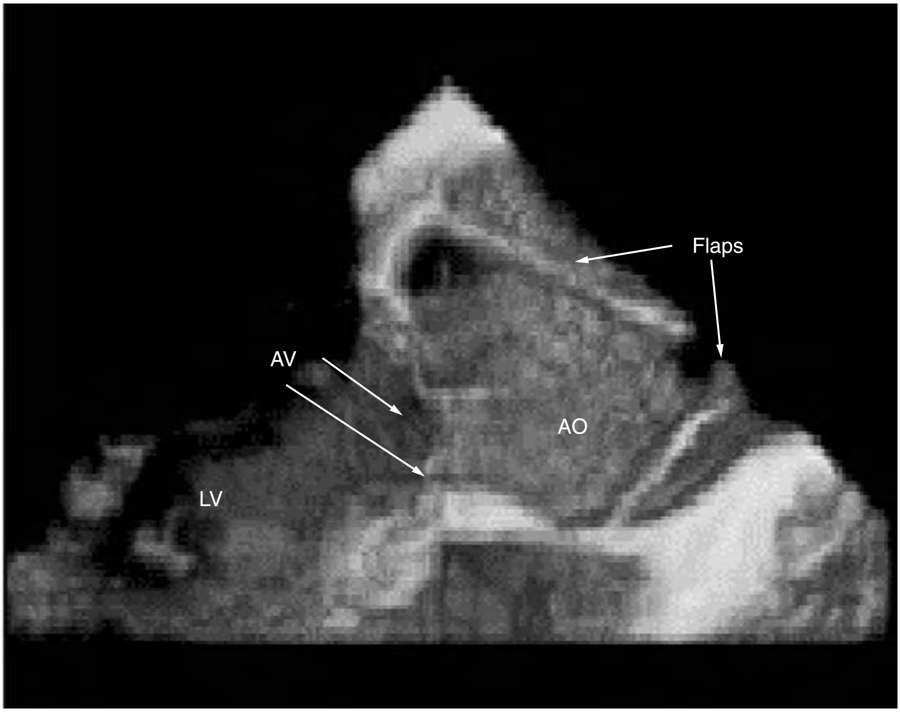

FIGURE 14.14
An example of a three-dimensional echocardiogram of a patient with dissecting aortic aneurysm (LV: left ventricle; AO: aorta; AV: aortic valve; flap: intimal flap caused by aortic dissection).

(Ò) and sound speed (c) determine the characteristic acoustic impedance $\boldsymbol{Z}$ of the material as

$$Z = \rho c \tag{14.9}$$

On the assumption that the interface between two fluid-like media is infinite and plane, the relative reflected sound power (dB) would be determined by the specific acoustic impedance of each medium.

$$dB = 10\log_{10}\frac{P_r}{P_i} = 10\log_{10}\frac{(Z_a - Z_b)^2}{(Z_a + Z_b)^2} \tag{14.10}$$

where

P_r = sound power reflected at interface
P_i = incident sound power
Z_a = acoustic impedance of medium a
Z_b = acoustic impedance of medium b

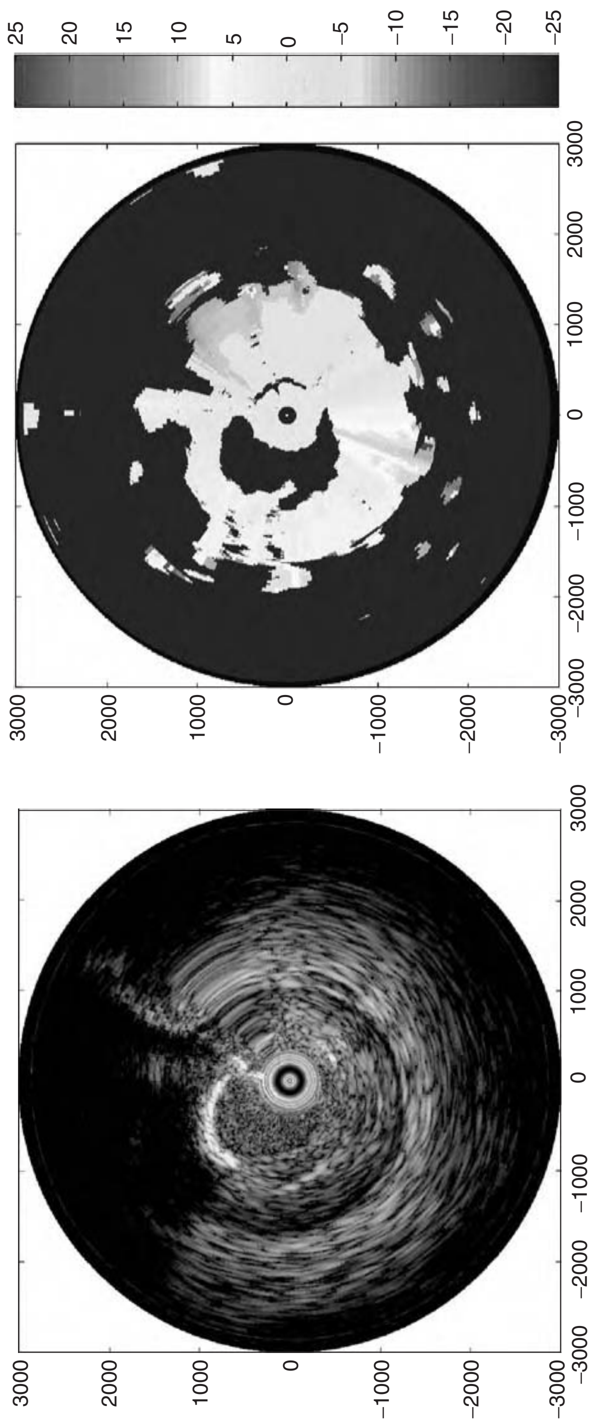

FIGURE 14.15
Conventional IVUS image (left) and an example of parametric IVUS (right).

Although the assumption is not applied for biological tissues alone, we have shown that the calculated reflection and clinical data were matched in the myocardium.[32] Chandraratna et al. also assessed the echo-bright area in the myocardium by using 600-MHz SAM.[33]

Third, the acoustics have strong correlation to physics. In the simplest form, the relation between the sound speed and the elastic bulk modulus of the liquid material is described in the following equation:

$$c = \sqrt{\frac{K}{\rho}} \tag{14.11}$$

where

c = sound speed
K = elastic bulk modulus
Ò = density

Because a biological tissue is assumed to be a liquid material, the equation used to be applied to assess the elastic properties of biological tissues. Recent studies on biomechanics revealed that the mechanical properties of tissues are not completely liquid, so biological tissues should be treated as soft solid material. However, the relationship between acoustics and a solid material can also be described by modifying the above equation.

$$c = \sqrt{\frac{E(1-\sigma)}{(1+\sigma)(1-2\sigma)}} \tag{14.12}$$

where

c = sound speed
E = Young's modulus
σ = Poission's ratio
ρ = density

As seen in Equation 14.12, the relationship between the Young's modulus of the tissue and the sound speed still represents close correlation. As shown in both the above equations, the value of sound speed has close relation to elasticity of the tissues.

The pathophysiology of atherosclerosis is closely related to the biomechanical properties because the arteries are always faced with mechanical stress caused by blood pressure or blood flow. Both the dynamic and the static mechanical properties of arteries would change in dramatically changed circumstances. As the term *arteriosclerosis* means hardening of the artery, atherosclerotic tissues have been known to increase in stiffness or hardness in the development of atherosclerosis. Assessment of the mechanical properties of atherosclerosis is important, in addition to determining the chemical components of the tissue.

Coronary plaque disruption with superimposed thrombus is the main cause of acute coronary syndrome such as unstable angina or acute myocardial infarction.[34] Pathological investigations have shown that plaque size or degree of the lumen narrowing is less important than the composition of the plaque; lipid-rich soft plaques are more vulnerable than collagen-rich hard plaques. In clinical settings, IVUS imaging has been applied to detect a vulnerable plaque, which is sometimes found in an angiographically normal coronary artery. The composition of atherosclerosis is defined as the collagen fibers, lipid and calcification in the intima, the smooth muscle and elastic fiber in the media, and the collagen fibers in the adventitia, respectively. The variety of the degree of staining for optical microscopy indicates that the collagen content or the chemical property is not homogeneous in fibrotic lesions in the intima.

In the present study, two kinds of SAM systems were employed to characterize the tissue components in normal and atherosclerotic arteries. The values of attenuation and sound speed in six types of tissue components in atherosclerosis were measured by 100- to 200-MHz SAM.[35] The collagen type was assessed by 800- to 1300-MHz SAM and polarized microscopy for qualitative and quantitative analysis of characterization of collagen fibers.

14.6.1 Acoustic Microscopy in 100 to 200 MHz

Figure 14.16 shows the block diagram of the SAM system developed at Tohoku University. The acoustic focusing element comprises a ZnO piezoelectric transducer with a sapphire lens. The ultrasonic frequency is variable over the range of 100 to 210 MHz and the beam width at the focal volume ranges from 5 (at 210 MHz) to 10 mm (at 100 MHz). The focusing element is mechanically scanned at 60 Hz in the lateral direction (x) above the specimen, which remains stationary on the specimen holder, while the holder is scanned in the other lateral direction (y) in 8 sec, providing two-dimensional scanning. The mechanical scanner is arranged so that the ultrasonic beam will be transmitted at 1-mm intervals over a 0.5-mm width. The number of sampling points is 480 in one scanning line and 480×480 points make one frame. Both amplitude and phase images can be obtained in a field of view 2×2 mm. Either the reflection or transmission mode is selectable in the system. In the present study, the reflection mode was used. Distilled water, which was maintained at 37°C, was used for the coupling medium between the transducer and the specimen.

The ROI was determined by observing the two-dimensional amplitude image. Both the amplitude and phase in the ROI were measured at every 10-MHz interval between 100 to 210 MHz to obtain the quantitative values of acoustic properties. Thus, the frequency varying change of the amplitude and phase was obtained.

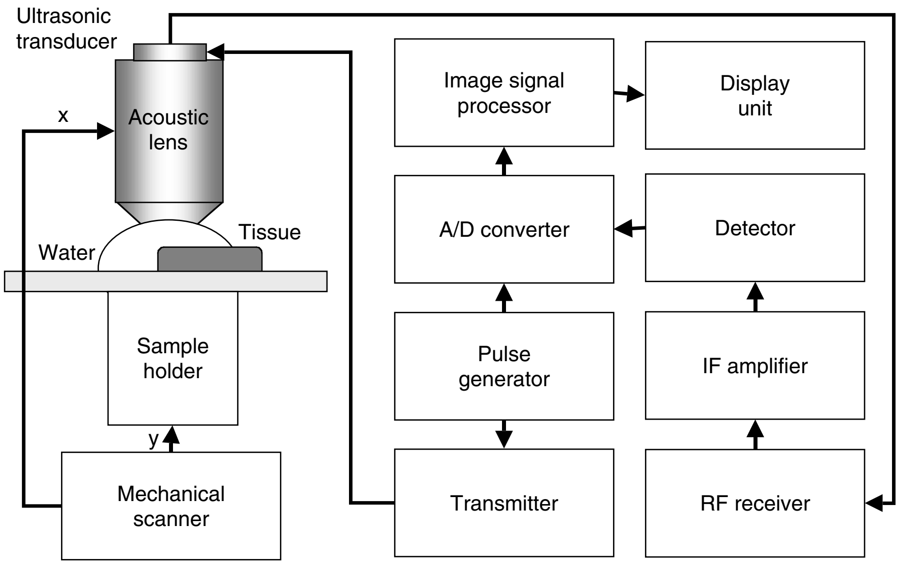

FIGURE 14.16
The block diagram of the scanning acoustic microscope system developed at Tohoku University.

The equation shows the relationship between the frequency, amplitude, and phase due to the interference between the reflection of the surface and bottom of the specimen. By fitting the obtained frequency varying curve with the calculated values, the thickness of the tissue in the ROI was obtained.

$$\begin{aligned} y_r &= y_s + y_b \\ &= e^{-\left(\alpha + j\frac{2\pi f}{c}\right)d} \\ &= e^{-j\frac{2\pi f}{c}d} \cdot e^{-A_0 f^n d} \end{aligned} \quad \textbf{(14.13)}$$

where
y_r = received signal
y_s = reflection from the surface of the specimen
y_b = reflection from the bottom of the specimen
f = frequency
c = sound speed of the specimen
d = thickness of the specimen)

Figures 14.17a and 14.7b show the graphs representing the relationship between frequency and amplitude (Figure 14.17a) or phase (Figure 14.17b) in 6 μm thickness specimen. Once the thickness of the specimen was determined, the attenuation and sound speed were calculated by the following equation:

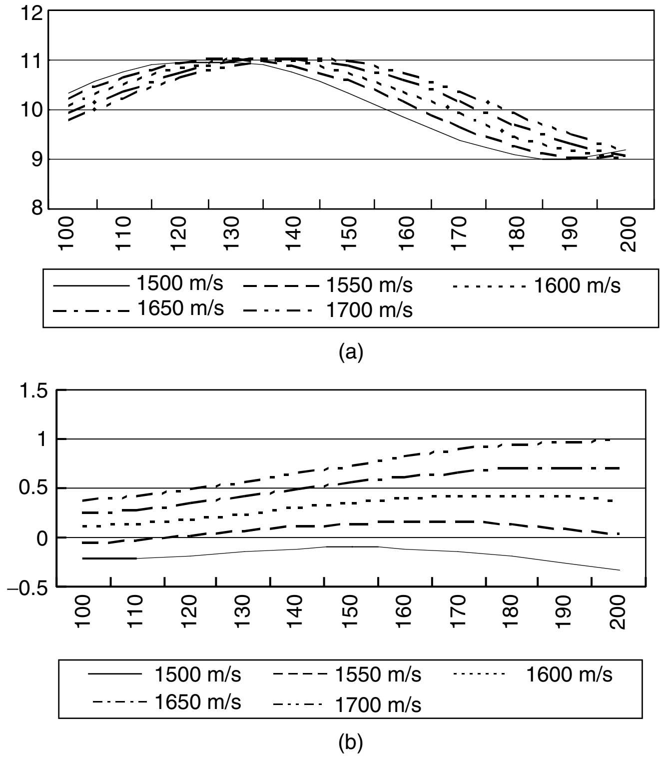

FIGURE 14.17
Graph showing (a) the frequency-dependent intensity characteristics and (b) the frequency-dependent phase characteristics at the frequency range of 100 to 200 MHz.

$$A = \frac{L}{fd} \tag{14.14}$$

where
- A = slope of attenuation
- f = frequency
- d = thickness

$$c = \frac{1}{\dfrac{1}{c_w} - \dfrac{\theta}{2\pi f d}} \tag{14.15}$$

where
- f = frequency
- d = thickness of the specimen
- c = sound speed in the specimen
- c_w = sound speed in the coupling medium,
- *Ë* = phase shift.

As a result, quantitative values of slope of attenuation and sound speed of each pixel can be obtained; this is the most important specification of our scanning acoustic microscope system. The data of slope of attenuation and sound speed were converted into color signals and were displayed on a color monitor as two-dimensional distribution patterns.

A neighboring section of the SAM specimen was stained with Elastica-Masson's trichrome stain and used for optical microscopy. The ROI for acoustic microscopy was determined by the optical microscopic observations. The tissue components in normal and atherosclerotic arteries were classified as the following tissue components: normal intima, fibrosis, calcification, lipid, normal media, and normal adventitia. ROI was so determined that a single tissue component was included in the ROI. The mean values of attenuation and sound speed of each tissue component were then averaged.

14.6.2 Acoustic Microscopy in 800 to 1300 MHz

A scanning acoustic microscope (SAM2000 [KSI, Herborn, Germany]) was equipped for semiquantitative ultrasonic measurements. In the present study, an acoustic lens with the optimal frequency range between 800 MHz and 1.3 GHz was used. The SAM frequency in the experiments was 1.1 GHz because the image quality was best at this measurement. Distilled water was used for the coupling medium between the transducer and the sample. The temperature of the transducer, coupling medium, sample, and the glass substrate was kept at 37°C by a heating plate. The RF output gain was fixed for the whole experiment. In the SAM system, a 80-dB difference of ultrasonic intensity corresponded to 256 grayscales (0 to 255). The reflection from the glass surface was set at level 255 (white). The average thickness of the specimen was determined by laser micrometer. Ultrasonic attenuation at each pixel was calculated from the number of the gray level and the thickness. All of the SAM images were stored in a personal computer for statistical analysis.

The optical and polarized images of atherosclerotic plaque were captured to make the same field taken by SAM. The images were analyzed using the following computer-assisted image analysis equipment:

1. Leitz DMRBE light microscope — Leica Wetzlar, Germany
2. JVC KY-F55 color video camera — Victor Co.Ltd., Tokyo, Japan
3. Scion CG-7 RGB color frame grabber and ScionImage — Scion Corporation, Frederick, Maryland
4. Photoshop — Adobe Systems Inc., Seattle, Washington

Although the picrosirius red staining was not a specific staining technique, the area with collagen was specifically visualized by polarized microscopy. The areas were differentiated according to the polarized color — longer wavelength (red or yellowish color) or shorter wavelength (green).

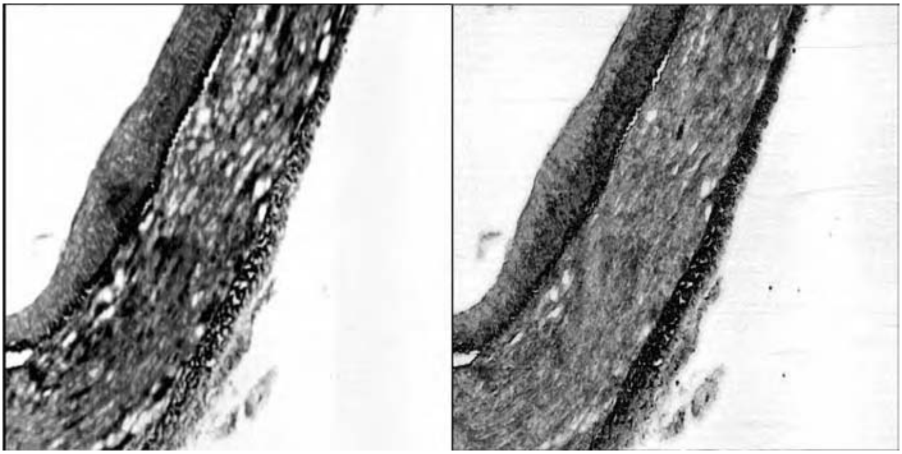

FIGURE 14.18
Attenuation (left) and sound speed (right) images of a normal coronary artery obtained with the scanning acoustic microscope at 160 MHz.

For the study in 800 to 1300 MHz, the specimen was perfusion-fixed at 100 mmHg with phosphate-buffered 4% formaldehyde (pH 7.2) and immersed in fixative overnight. The specimen was sectioned at 4 μm and embedded in paraffin. The paraffin was removed by coconut oil and graded alcohol process. The sections were unstained and used for the SAM investigations. After the SAM investigation, the sample was stained with Sirius red and covered by a cover glass. The same field observed by SAM is also observed by normal and polarized optical microscopy for comparing the tissue components.

Figure 14.18shows the attenuation and sound speed images of a normal human coronary artery visualized with 100- to 200-MHz SAM. Coronary artery comprises three layers: the intima, consisting of endothelium and collagen fiber; media, consisting of smooth muscle and elastic fiber; and adventitia, consisting of collagen fiber. In the acoustic microscopy images, the three-layered appearance is clearly represented. Figure 14.19 shows attenuation and sound speed images of an atheroscletoric human coronary artery.

Figure 14.20 shows the normal ligh, polarized light, and acoustic microscopy images of a normal coronary artery. The ultrasonic frequency is 1.1 GHz. Endothelial cells aligning in a single layer and thin fibrosis make up the intima. The smooth muscle cells and elastic fibers consisting of the media are shown by the acoustic image. Collagen fibers in the adventitia are highlighted by the polarized image. No pathological atherosclerotic lesions were found.

Figure 14.21 shows an atherosclerotic plaque. The collagen network in the intima is shown in the acoustic image. Although the lipid in the plaque was completely removed by alcohol dehydration, the remaining outer shape of the cholesterol crystal indicates that the cholesterol had existed in the spaces.

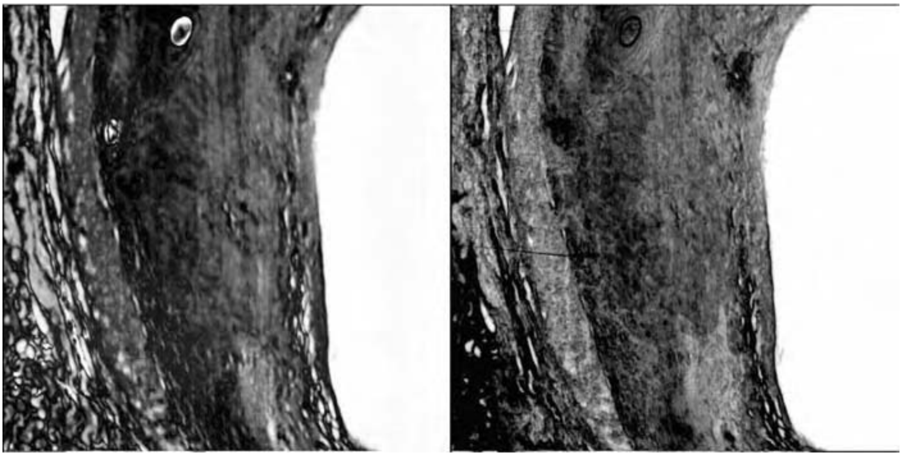

FIGURE 14.19
Attenuation (left) and sound speed (right) images of an atherosclerotic coronary artery obtained with the scanning acoustic microscope at 160 MHz.

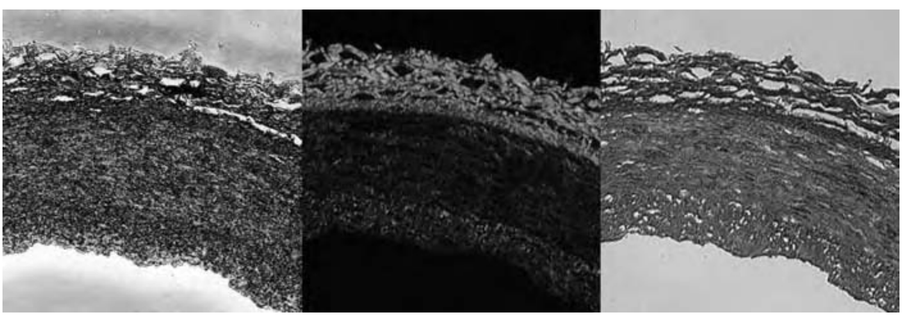

FIGURE 14.20
Normal light (left), polarized light (center), and acoustic (right) microscopt images of normal coronary artery obtained with the scanning acoustic microscope at 1.1 GHz.

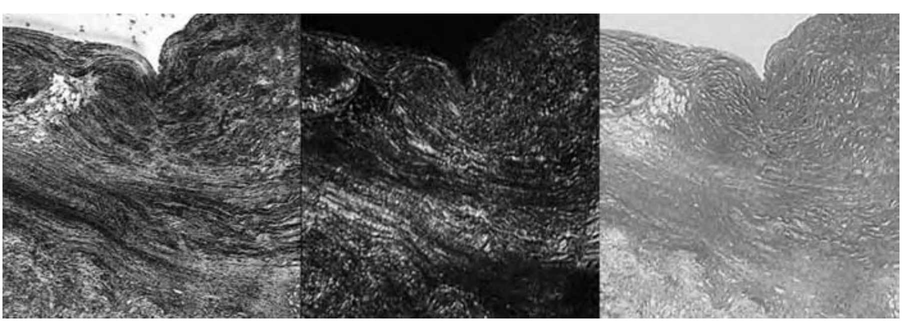

FIGURE 14.21
Normal light (left), polarized light (center), and acoustic (right) microscopt images of atheroscletoric coronary artery obtained with the scanning acoustic microscope at 1.1 GHz.

The fibrosis in the plaque would be classified into two categories: low ultrasonic attenuation and weak polarization, and high ultrasonic attenuation and strong polarization.

The complete results of the study showed that the fibrous caps in the advanced atherosclerotic plaques consisted of thick collagen fibrils. In these regions, the polarized color was orange and the polarized intensity was the highest. In acoustic images, these regions showed high attenuation. In contrast, thin collagen fibrils exhibited green polarized color, showing low polarized intensity.

As the pathophysiology of atherosclerosis is currently understood, the rupture of a fibrous cap overlying a lipid pool is considered to be the most common initial event to worsen the state. Biomechanical factors, such as hemodynamic shear stress,[36] transient compression,[37] and sudden increase in intraluminal pressure,[38] have been postulated to play an important role in plaque rupture. As a result, the assessment of both chemical composition and the mechanical properties of the plaque has become an important aspect of evaluating atherosclerosis. In previous studies, pulsed wave velocity (PWV)[39] and stiffness parameter[40] were proposed to assess the elastic properties of arteries, but these methods provide information about the elasticity of entire arterial wall. The mechanical properties of the tissue components in atherosclerosis should be measured because the pathological finding of plaque rupture is often found in the complex microstructure of atherosclerosis.

Because of ultrasound's strong correlation to mechanical properties, acoustic microscopy provides only morphological and mechanical information on the biological tissues. In the present study, fibrosis showed greater values of attenuation and sound speed than those of normal media consisting of smooth muscle. This result suggests that the increase of collagen fiber in arteries would lead to hardening of the arteries.[41] PWV of aorta is known to increase at aging, and the phenomenon is explained by the increase and maturation of collagen fiber in the arteries.

In atheromatous plaques, lipid is covered with various thickness of collagen fiber. This structure is called a *fibrous cap*. A vulnerable plaque is characterized by a thin fibrous cap and infiltration of macrophages. In the previous studies assessing stress distribution on the fibrous caps by using finite element analysis, the circumferential stress was concentrated to the thin fibrous cap.[42] In those studies, a single set of values of mechanical properties was given to either a thick or a thin fibrous cap. As shown in the present study, the sound speed distribution was not uniform in fibrous caps. We have previously applied the sound speed data in stress distribution analysis by a finite element method.[43] Our study suggested that the adaptive change of the elasticity of the thin fibrous cap prevented plaque rupture. Further evaluation is needed to prove the mechanical property change and the stress on these thin caps from both actual mechanical testing and computer simulation.

Under polarized light, the collagen fiber stained with picrosirius red is highlighted by induced birefringence.[44] The collagen content is known to be proportional to the intensity of polarization. In other words, the intensity of polarization demonstrates the quantity of the collagen. In the present study, the thick fibrous caps showed high-intensity polarization, while the thin fibrous caps showed weak polarization. The results indicate that the collagen content is rich in thick fibrous caps, and that thin caps contained low amount of collagen.

The wavelength of the birefringence light depends on the collagen type and thickness of the fibril; orange indicates thick collagen fibrils, while green indicates thin fibrils.[45] Usually, the thick collagen fibrils compose Type I collagen, and the thin fibrils compose Type III collagen. The color of polarization demonstrates the quality of the collagen. Because Type III collagen is often associated with macrophage infiltration, green polarized collagen may correlate with vulnerable plaques. The acoustic microscopy revealed that the attenuation of green polarized collagen was significantly lower than that of orange polarized collagen. Consequently, with high-frequency ultrasound, it is possible to differentiate collagen types I and III in atherosclerosis.[46,47]

When comparing 200-MHz and 1.1-GHz images of SAM, the better spatial resolution was confirmed in 1.1 GHz. This is natural because the beam width is determined by the frequency. A single elastic fiber in media or collagen fiber orientation in intima was clearly visualized in 1.1 GHz. However, the 200-MHz image was better in identifying the three-layered structure of the coronary artery. In this aspect, 200-MHz SAM may better interpret normal and abnormal images of IVUS with 20 to 40 MHz in clinical settings.

Two sets of acoustic microscope systems were equipped for visualizing the microstructure of coronary arteries. The difference of acoustic properties of each tissue component in atherosclerosis indicated the change of the mechanical properties according to the pathophysiological state in developing atherosclerosis. The ultrasonic tissue characterization of Type I and Type III collagen was possible, and this would be very important for detecting a vulnerable plaque leading to acute coronary syndrome. The results of the high-frequency ultrasound should also provide important information to understand IUVS imaging in clinical situations.

14.7 Summary

Ultrasonic nondestructive evaluation in medical applications started as an A-mode flaw detector to detect a reflection at the interface of biological materials with large acoustic impedance difference. Then the technique was developed to measure the distance of the echoes and to obtain real-time two-dimensional images. Today, development of computer technologies has enabled us to obtain three-dimensional reconstructed images or even three-dimensional real-time images. Comparing other medical imaging modalities, the features of ultrasound include portability, repeatability, real-time imaging, and, especially, real-time blood flow measurement.

Besides the visualization of the organ structure, analysis of reflected ultrasound has help to assess the internal chemical and mechanical properties of the tissue.

Around 1970, the development of satellite communication enabled researchers to use higher-frequency ultrasound, which led to IVUS or SAM. As higher-frequency ultrasound provides a higher resolution of imaging, the ultrasound of today can visualize tissue structure on a microscopic level.

References

1. Dussik, K.T., On the possibility of using ultrasound waves as a diagnostic aid, *Neurol. Psychiat.*, 174, 153–168, 1942.
2. Edler, I. and Hertz, C.H., The use of ultrasonic reflectoscope for the continuous recording of the movements of heart walls, *K. Fysiogr. Sallsk. Lund. Forh.*, 24, 40, 1954.
3. Tanaka, K., Miyajima, G., Wagai, T., Yasuura, M., Kikuchi, Y., and Uchida, R., Detection of intracranial anatomical abnormalities by ultrasound. *Tokyo Med. J.*, 69, 525, 1950.
4. Miyajima, G., Wagai, T., Fukushima, Y., Uchida, R., and Hagiwara, I., Detection of intracranial disease by pulsed ultrasound, *Tokyo Med. J.*, 72, 37, 1952.
5. Wild, J.J., The use of ultrasonic pulses for the measurement of biological tissues and the detection of tissue density changes, *Surgery*, 27, 183–188, 1950.
6. Wild, J.J. and Neal, D., Use of high frequency ultrasonic waves for detecting changes in texture in living tissue, *Lancet*, 1, 655, 1951.
7. Wild, J.J. and Reid, J.M., Application of echo-ranging techniques to the determination of structure of biological tissues, *Science*, 115, 226–230, 1952.
8. Howry, D.H. and Bliss, W.R., Ultrasonic visualization of soft tissue structures of the body, *J. Lab. Clin. Med.*, 40, 579–592, 1952.
9. Kossoff, G., Garrett, W.J., and Radovanovich, G., Gray scale echography in obstetrics and gynaecology, *Australas. Radiol.*, 18, 62–111, 1974.
10. Uchida, R., Hagiwara, Y., and Irie, T., Electro-scanning ultrasonic diagnostic equipment. *Jap Med El.*, 58, 1971, 1971.
11. Bom, N., Lancee, C.T., Honkoop J., and Hugenholtz, P.G., Ultrasonic Viewer for cross-sectional analyses of moving cardiac structures, *BioMed Eng.*, 6, 500, 1971.
12. Bom, N., Lancee, C.T., Van Zweten, G., Kloster, F.E., and Roelandt, J., Multiscan echocardiography. 1. Technical description, *Circulation*, 48, 1066–1074, 1973.
13. Somer, J.C., Instantaneus and continuous pictures obtained by a new two-dimensional scan technique with a stationary transducer, *Proc. Echo-encephalography,* Kazner, E., Schiefer W., and Zulch., K., Eds. 234–236, 1968.
14. Baker, D.W. and Watkins, D., A phase coherent pulse doppler system for cardiovascular measurement, *Proc. 20th Ann. Conf. Eng. Med. Biol.,* 27, 2, 1967.
15. Eyer, M.K., Brandestini, M.A., Phillips, D.J., and Baker D.W., Color digital echo/Doppler image presentation, *Ultrasound Med. Biol.*, 7, 21–31, 1981.
16. Kasai, C., Namekawa, K., Tsukamoto, M., and Koyano A., Realtime bloodflow imaging system utilizing auto-correlation techniques, *Ultrasound Med. Biol.,* Suppl. 2, 203–208, 1983.

17. Kasai, C., Namekawa, K., and Koyano. A., Realtime two-dimensional blood flow imaging using autocorrelation technique, *IEEE. Trans. Sonics. Ultrason.*, 32, 460, 1985.
18. Mimbs, J.W., O'Donnell, M., Miller, J.G., and Sobel, B.E., Detection of cardiomyopathic changes induced by doxorubicin based on quantitative analysis of ultrasonic backscatter, *Am. J. Cardiol.*, 47, 1056–1060, 1981.
19. Mimbs, J.W., Bauwens, D., Cohen, R.D., O'Donnell, M., Miller, J.G., and Sobel, B.E., Effects of myocardial ischemia on quantitative ultrasonic backscatter and identification of responsible determinants, *Circ. Res.*, 49, 89–96, 1981.
20. Baba, K., Satoh, K., Sakamoto, S., Okai, T., and Ishii, S., Development of an ultrasonic system for three-dimensional reconstruction of the fetus, *J. Perinat. Med.*, 17, 19–24, 1989.
21. von Ramm, O.T. and Smith, S.W., Real-time volumetric ultrasound imaging system, *J. Digit. Imaging*, 3, 261–266, 1990.
22. Smith, S.W., Pavy, H.G., and von Ramm, O.T., High-speed ultrasound volumetric imaging system-Part I: transducer design and beam steering, *IEEE Trans. Ultrason. Frequency Control*, 38, 100–108, 1991.
23. Jeremias, A., Kolz, M.L., Ikonen, T.S., Gummert, J.F., Oshima, A., Hayase, M., Honda, Y., Komiyama, N., Berry, G.J., Morris, R.E., Yock, P.G., and Fitzgerald, P.J., Feasibility of *in vivo* intravascular ultrasound tissue characterization in the detection of early vascular transplant rejection, *Circulation*, 100, 2127–2130, 1999.
24. Schartl, M., Bocksch, W., Koschyk, D.H., Voelker, W., Karsch, K.R., Kreuzer, J., Hausmann, D., Beckmann, S., and Gross, M., Use of intravascular ultrasound to compare effects of different strategies of lipid-lowering therapy on plaque volume and composition in patients with coronary artery disease, *Circulation*, 104, 387–392, 2001.
25. de Korte, C.L., van der Steen, A.F., Cespedes, E.I., and Pasterkamp, G., Intravascular ultrasound elastography in human arteries: initial experience in vitro, *Ultrasound Med. Biol.*, 24, 401–408, 1998.
26. Kushibiki, J. and Chubachi, N., Material characterization by line-focused-beam acoustic microscope, *IEEE. Trans. Sonics. Ultrason.*, SU-32, 132–135, 1985.
27. Okawai, H., Tanaka, M., Chubachi, N., and Kushibiki, J., Non-contact simultaneous measurement of thickness and acoustic properties of a biological tissue using focused wave in a scanning acoustic microscope, *Jpn. J. Appl. Phys.*, 26, 52–54, 1987.
28. Barr, R.J., White, G.M., Jones, J.P., Shaw, L.B., and Ross, P.A., Scanning acoustic microscopy of neoplastic and inflammatory cutaneous tissue specimens, *J. Invest. Dermatol.*, 96, 38–42, 1991.
29. Jones, J.P., Applications of acoustical microscopy in dermatology, in *Ultrasonic Tissue Characterization*, Dunn, F., Tanaka, M., Ohtsuki, S., and Saijo, Y., Eds., Springer-Verlag, Tokyo, 201–212, 1996.
30. Saijo, Y., Tanaka, M., Okawai, H., and Dunn, F., The ultrasonic properties of gastric cancer tissues obtained with a scanning acoustic microscope system, *Ultrasound Med. Biol.*, 17, 709–714, 1991.
31. Sasaki, H., Saijo, Y., Tanaka, M., Okawai, H., Terasawa, Y., Yambe, T., and Nitta, S., Influence of tissue preparation on the high-frequency acoustic properties of normal kidney tissue, *Ultrasound Med. Biol.*, 22, 1261-1265, 1996.
32. Saijo, Y., Tanaka, M., Okawai, H., Sasaki, H., Nitta, S., and Dunn, F., Ultrasonic tissue characterization of infarcted myocardium by scanning acoustic microscopy, *Ultrasound Med. Biol.*, 23, 77–85, 1997.

33. Chandraratna, P.A.N., Whittaker, P., Chandraratna, P.M., Gallet, J., Kloner, R.A., and Hla, A., Characterization of collagen by high-frequency ultrasound: Evidence for different acoustic properties based on collagen fiber morphologic characteristics, *Am. Heart J.*, 133, 364–368, 1997.
34. Falk, E., Why do plaques rupture? *Circulation*, 86, III30-42, 1992.
35. Saijo, Y., Sasaki, H., Okawai, H., Nitta, S., Tanaka, M., Acoustic properties of atherosclerosis of human aorta obtained with high-frequency ultrasound, *Ultrasound Med Biol.*, 24, 1061–1064, 1998.
36. Gerz, S.D. and Roberts, W.C., Hemodynamic shear force in rupture of coronary arterial atheroscleorotic plaques, *Am. J. Cardiol.*, 66, 1368–1372, 1990.
37. Binns, R.L. and Ku, D.N., Effect of stenosis on wall motion: a possible mechanism of stroke and transient ischemic attack, *Arteriosclerosis*, 9, 842–847, 1989.
38. Muller, J.E., Tofler, G.H., and Stone, P.H., Circadian variation and triggers of onset of acute cardiovascular disease, *Circulation*, 79, 733–743, 1989.
39. Kanai, H., Kawabe, K., Takano, M., Murata, R., Chubachi, N., and Koiwa, Y., New method for evaluating local pulse wave velocity by measuring vibrations on arterial wall, *Electron. Lett.*, 30, 534–536, 1994.
40. Hayashi, K., Sato, M., Handa, H., and Moritake, K., Biomechanical study of constitutive laws of vascular walls, *Exp. Mech.*, 14, 440–444, 1974.
41. Greenberg, S.R., The association of medial collagenous tissue with atheroma formation in the aging human aorta as revealed by a special technique, *Histol. Histopathol.*, 1, 323–326, 1986.
42. Lee, R.T., Grodzinsky, A.J., Frank, E.H., Kamm, R.D., and Schoen, F.J., Structure-dependent dynamic mechanical behavior of fibrous caps from human atherosclerotic plaques, *Circulation*, 83, 1764–1770, 1991.
43. Saijo, Y., Ohashi, T., Sasaki, H., Sato, M., Jorgensen, C.S., and Nitta, S., Application of scanning acoustic microscopy for assessing stress distribution in atherosclerotic plaque, *Ann. Biomed. Eng.*, 29, 1048–1053, 2001.
44. Junqueira, L.C., Montes, G.S., and Sanchez, E.M., The influence of tissue thickness on the study of collagen by the Picrosirius-polarization method, *Histochemistry*, 74, 153–156, 1982.
45. Whittaker, P., Kloner, R.A., Boughner, D.R., and Pickering, J.G., Quantitative assessment of myocardial collagen with picrosirius red staining and circularly polarized light, *Basic Res. Cardiol.*, 89, 397–410, 1994.
46. Saijo, Y., Jorgensen, C.S., and Falk, E., Ultrasonic tissue characterization of collagen in lipid-rich plaques in apoE-deficient mice, *Atherosclerosis*, 158, 289–295, 2001.
47. Saijo, Y., Jorgensen, C.S., Mondek, P., Sefranek, V., and Paaske, W., Acoustic inhomogeneity of carotid arterial plaques determined by GHz frequency range acoustic microscopy, *Ultrasound Med. Biol.*, 28, 933–937, 2002.
48. Tanaka, M., Neyazaki, T., Kosaka, S. , Sugi, H., Oka, S., Ebina, T., Terasawa, Y., Unno, K., and Nitta, K., Ultrasonic evaluation of anatomical abnormalities of heart in congenital and acquired heart diseases, *Br. Heart J.* , 33, 686–698, 1971.
49. Tanaka, M., Nitta, S., Sogo, Y., Yamamoto, A., Katahira, Y., Sato, N., Ohkawai, H., and Tezuka, F., Noninvasive estimation by cross-sectional echocardiography of myocardial damage in cardiomyopathy, *Br. Heart J.*, 53, 137–152, 1985.

Index

B

C

D

E

F

G

H

I

J

K

L

M

N

O

P

Q

R

S

U

V

W

X

Y

Z

Mechanical Engineering

ULTRASONIC NONDESTRUCTIVE EVALUATION

Engineering and Biological Material Characterization

Edited by Tribikram Kundu

While most books on ultrasonic nondestructive evaluation (NDE) focus either on its theoretical background or on advanced applications, ***Ultrasonic Nondestructive Evaluation: Engineering and Biological Material Characterization*** has integrated these aspects into one comprehensive treatment.

This book brings together the principles, equations, and applications of ultrasonic NDE, both traditional and state of the art. It begins with the relevant fundamentals of mechanics, derives the basic equations of the mechanics of elastic wave propagation, and then covers the advanced topics and applications of ultrasonic NDE that are at the forefront of today's research. These include engineering, biological, and clinical applications, such as structural health monitoring, the characterization of biological cells, and real-time blood flow measurement.

Written in plain language by some of the world's leading experts, the chapters are filled with case studies, worked examples, and exercises that help make this book an outstanding resource for course work, as well as for reference.

THIS VOLUME CONTAINS:

- A broad range of engineering and biological material characterization techniques
- Expert coverage of ultrasonic NDE fundamentals and state-of-the-art applications
- Modeling tools, including derived equations, numerical results, and MATLAB® code, that enable you to easily model ultrasonic transducers
- More than 400 illustrations, including 20 in full color

1462
ISBN 0-8493-1462-3
90000
9 780849 314629

CRC PRESS
www.crcpress.com